

HELICOPTER DYNAMICS

Inderjit Chopra
Anubhav Datta

ENAE 633 Helicopter Dynamics
Spring 2011

Contents

1	Introduction to Rotor Dynamics	9
1.1	Basic Rotor Aerodynamics	9
1.1.1	Hover	9
1.1.2	Axial Climb	23
1.1.3	Axial Descent	25
1.1.4	Forward Flight	26
1.2	Basic Structural Dynamics	32
1.2.1	Second-Order Systems	32
1.2.2	Reduction to First-Order Form	39
1.2.3	Rotor Blade Dynamics	41
1.2.4	Flap motion of a rotor blade	42
1.3	Aero-elastic Response	45
1.3.1	Flap response for non-rotating blades	46
1.3.2	Flap response for rotating blades in vacuum	46
1.3.3	Flap response in hover	47
1.3.4	Flap response in forward flight	48
1.4	Introduction to Loads	52
1.4.1	Root shear load	53
1.4.2	Root bending load	53
1.4.3	Rotating frame hub loads	53
1.4.4	Fixed frame hub loads	54
1.5	Rotor planes of reference	57
1.6	Helicopter Trim	61
1.6.1	Rotor Forces and Moments	62
1.6.2	Uncoupled trim	64
1.6.3	Coupled trim for an isolated rotor	65
1.6.4	Coupled trim for a full aircraft	66
1.6.5	Rotor Power and Lift to Drag Ratio	71
1.6.6	The Jacobian Method for Trim	76
2	Flap Dynamics	79
2.1	Rigid Blade Model	79
2.1.1	Hinged Blade with zero offset	79
2.1.2	Hinged Blade with Offset	82
2.1.3	Hingeless Blade with Equivalent Hinge Offset	85
2.2	Flexible Beam Model	86
2.2.1	Axial Deformation	86
2.2.2	Euler-Bernoulli Theory of Bending	86
2.2.3	Flap Bending Equation using Newtons's Laws	87
2.2.4	Second Order Nonlinear Coupled Axial Elongation-Flap Bending	90

2.2.5	Axial Elongation as a Quasi-coordinate	94
2.2.6	Boundary Conditions	94
2.3	Non-rotating beam vibration	95
2.3.1	Cantilevered Beam	96
2.3.2	Simple-Supported Beam	99
2.3.3	Beam Functions	99
2.4	Rotating Beam Vibration	100
2.4.1	Approximate solution Methods	101
2.4.2	Galerkin Method	101
2.4.3	Rayleigh-Ritz Method	105
2.5	Finite Element Method (FEM)	111
2.5.1	Element properties	112
2.5.2	Assembly of elements	114
2.5.3	Constraint conditions	117
2.6	Fan plot and frequency plots for rotating beams	119
2.6.1	Rotating versus non-rotating frequencies	119
2.6.2	Rotating frequencies vs. rotational speed	119
2.6.3	Rotating versus non-rotating mode shapes	127
2.7	Response Solution in time	129
2.7.1	Fourier series methods	130
2.7.2	Finite Element in Time (FET) method	133
2.7.3	Time Integration Methods	136
2.8	Bending Moments and Stresses	136
2.8.1	Deflection and Force Summation methods	136
2.8.2	Force summation vs. modal method	138
2.9	Fourier Coordinate Transformation	138
2.9.1	FCT of governing equations	140
2.10	Aeroelastic Stability	145
2.10.1	Stability roots in hover	146
2.11	Stability Analysis in Forward flight	151
2.11.1	Constant Coefficient System	151
2.11.2	Periodic coefficient systems	153
2.11.3	Floquet stability solution	153
2.11.4	Floquet response solution	154
3	Coupled Flap-Lag-Torsion Dynamics	163
3.1	Lag Dynamics	163
3.1.1	Rigid Lag Model with Hinge Offset	163
3.1.2	Elastic Lag Model	165
3.1.3	Natural Vibrations of Lag Motion	167
3.1.4	Finite Element Formulation	169
3.2	Torsion Dynamics	171
3.2.1	Rigid Torsion Model	172
3.2.2	Elastic Torsion	175
3.2.3	Natural Vibrations of Torsion Motion	177
3.2.4	Beam Functions for Torsion	177
3.3	Coupled Flap-Lag Dynamics	178
3.3.1	Rigid Model	178
3.3.2	Flexible Model	183
3.4	Coupled Pitch-Flap Dynamics	185

3.4.1	Rigid Model	185
3.4.2	Kinematic Pitch-Flap Coupling: δ_3 Effect	188
3.4.3	δ_3 Effect in Hover	189
3.4.4	Kinematic Pitch-Lag Coupling: δ_4 Effect	191
3.5	Rigid Flap-Lag-Torsion	192
3.6	Flexible Flap-Lag-Torsion-extension	196
3.6.1	Second order non-linear beam model	196
3.6.2	Equations for uniform beams	196
3.6.3	Detailed model for non-uniform beams	197
3.6.4	Blade Coordinate Systems	197
3.6.5	Blade Deformation Geometry	198
3.6.6	Nondimensionalization and Ordering scheme	202
3.6.7	Formulation Using Hamilton's Principle	203
3.6.8	Derivation of Strain Energy	204
3.6.9	Derivation of Kinetic Energy	207
3.6.10	Virtual Work	210
3.6.11	Equations of Motion	210
3.7	Structural loads	211
3.7.1	Modal Curvature Method	212
3.7.2	Force Summation Method	212
3.8	Hub Reactions	214
4	Unsteady Aerodynamics	221
4.1	Basic Fluid Mechanics Equations	221
4.1.1	Navier-Stokes equations	222
4.1.2	Euler equations	226
4.1.3	Velocity Potential Equation for Unsteady Flows	226
4.1.4	The Acceleration Potential	229
4.1.5	Vorticity Conservation Equation	230
4.1.6	Potential Equation for Steady Flow	231
4.1.7	Potential Equation for Incompressible Flow	231
4.2	The Rotor Flow Field	232
4.2.1	Wake Structure of a Lifting Wing	232
4.2.2	Coupled Airloads and Wake	233
4.2.3	Non-steady Excitation in Rotor Blades	234
4.2.4	Trailed and Shed Wake Structure of a Rotor	234
4.2.5	Unsteady Aerodynamics	235
4.2.6	Dynamic Stall	235
4.3	Unsteady Thin Airfoil Theory	237
4.3.1	Steady Airloads	239
4.3.2	Quasi-Steady Airloads	240
4.3.3	Unsteady Airloads	242
4.3.4	A Simple Interpretation	246
4.3.5	The Theodorsen Lift Deficiency Function	247
4.3.6	Application to Rotary Wings	248
4.3.7	Near Shed Wake	251
4.3.8	Time-Varying Free Stream	252
4.3.9	Returning Wake	252
4.3.10	Miller's Conclusion	254
4.4	Time Domain Methods for Unsteady Aerodynamics	254

4.4.1	Leishman-Beddoes indicial model	257
4.4.2	Frequency response of indicial model	258
4.4.3	Recursive formulation of an indicial model	263
4.4.4	Leishman-Beddoes dynamic stall formulation	265
4.5	Wing Models	269
4.5.1	Prandtl Lifting Line Theory	269
4.5.2	Weissinger-L Lifting-surface Theory	270
4.5.3	Unsteady Lifting-Line Analysis	272
4.6	Perturbation Aerodynamic Forces	274
4.7	Dynamic Inflow Models	280
4.7.1	Hover	280
4.7.2	Forward Flight	280
5	Aeroelastic Stability in Hover	287
5.1	Flag-Lag Flutter	287
5.1.1	Comment on Flap-Lag Flutter	295
5.2	Pitch-Flap Instabilities	300
5.2.1	Pitch Divergence	302
5.2.2	Flutter	304
5.3	Flap-Lag-Torsion Flutter	307
6	Ground and Air Resonance	319
6.1	Ground Resonance	319
6.1.1	Blade Lag Motion in Fixed Coordinates	319
6.1.2	Three and Four bladed Rotors	320
6.1.3	Ground Resonance Equations	322
6.2	Ground Resonance of Two-Bladed Rotors	330
6.3	Air Resonance	333
6.3.1	Body Pitch and Roll with a Rigid Spinning Rotor	335
6.3.2	Rotor Flap and Lag	335
6.3.3	Rotor Flap and Body Pitch	339
6.3.4	Rotor Flap and Body Pitch and Roll	339
6.3.5	Rotor Flap and Lag and Body Pitch in Vacuum	340
6.3.6	Rotor Flap and Lag coupled to Body Pitch and Roll in Air	344
6.4	Experimental Data on Aeromechanical Stability	347
7	Aeroelastic Stability in Forward Flight	363
7.1	Flap Motion in forward flight	363
7.2	Hover Stability Roots	365
7.3	Forward Flight Stability Roots	366
7.3.1	Stability Roots in Rotating Coordinates	367
7.3.2	Stability Roots in Fixed Coordinates	367
7.4	Flap-lag Stability in Forward Flight	369
7.4.1	Perturbation Stability Solution	371
7.4.2	Constant Coefficient Approximation	373
7.4.3	Floquet Theory	373

8	Trailing Edge Flaps and Tabs	377
8.1	Flap-Torsion-Aileron Dynamics of a Wing Section	377
8.1.1	Flap-Torsion dynamics	377
8.1.2	Flap-torsion-Aileron dynamics: Force method	378
8.1.3	Flap-torsion-Aileron dynamics: Energy method	379
8.2	Flap-Torsion-Aileron-Tab Dynamics of a Rotor Blade	380
8.2.1	Governing equations	380
8.2.2	Hinge Moments	391
8.2.3	Initial condition response	391
8.2.4	Response with prescribed tab deflections	391
8.2.5	Flap-Torsion-Aileron Dynamics for a Rotor Blade	392
8.2.6	Response using prescribed aileron deflections	393
8.2.7	Flap-Torsion-Aileron-Tab equations in non-dimensional form	393
8.3	Aerodynamic Model	395
8.3.1	Theodorsen model for aileron	395
8.3.2	Theodorsen and Garrick model for aileron and tab	396
8.3.3	2D airfoil data	402
8.4	Flexible blade equations	405
9	CFD for Rotors	415
9.1	Isentropic Flow Relations	415
9.1.1	Unsteady Bernoulli's Equation	417
9.1.2	Pressure coefficient	418
9.2	Potential equation in the non-conservation form	418
9.2.1	Blade fixed moving frame	419
9.2.2	Velocity and acceleration in the moving frame	420
9.2.3	Derivatives in the moving frame	421
9.2.4	Full Potential Equations	422
9.2.5	Boundary conditions	424
9.2.6	Small disturbance equations for subsonic and transonic flows	425
9.2.7	Literature	427
9.3	Potential equation in conservation form	427
9.3.1	Full potential equation	428
9.3.2	Generalized coordinate transformation	428
9.3.3	Literature	430
9.4	Euler and Navier-Stokes equations	430
9.4.1	Review of Curvilinear coordinates	430
9.4.2	Generalized coordinate transformation	433
9.4.3	Euler equation in generalized coordinates	434
9.4.4	Thomas and Lombard's Geometric Conservation Law	438
9.4.5	Navier-Stokes equations in generalized coordinates	439
9.4.6	Surface Boundary Conditions	441
10	Helicopter Vibration	443
10.1	Measure of Helicopter Vibration	443
10.2	Sources of Helicopter Vibration	444
10.3	Analysis of Helicopter Vibration	445
10.4	Rotor Vibratory Loads	446
10.4.1	Periodic Blade Forcing	448
10.4.2	Hub Loads in Rotating Frame	449
10.4.3	Hub Loads in Fixed Frame	450

10.5	Vibration Control	452
10.6	Passive Vibration Control	453
10.6.1	Vibration Isolators	453
10.6.2	Vibration Absorbers	454
10.6.3	Bifilar Pendulum absorber	454
10.7	Active Vibration Control	455
10.7.1	Multicyclic Vibration Control or Higher Harmonic Control (HHC)	455
10.7.2	Control Algorithms	457
10.7.3	Off-line Identification	459
10.7.4	On-line Identification	460
10.7.5	Open-Loop Off-Line Control	461
10.7.6	Closed-Loop Off-Line Control	461
10.7.7	Open-Loop On-Line Control	462
10.7.8	Closed-Loop On-Line Control	463
11	Rotor Tests in Wind Tunnel and in Flight	469
11.1	Wind Tunnel Models	469
11.1.1	Froude-Scaled Models	470
11.1.2	Mach-Scaled Models	472
11.1.3	Model Fabrication	473
11.1.4	Model Instrumentation	473
11.2	Model Testing	474
11.2.1	Testing for Isolated Rotor Stability	475
11.2.2	Spectra for Various Inputs	475
11.3	Major Model and Full Scale Rotor Tests	475

Chapter 1

Introduction to Rotor Dynamics

The objective of this chapter is to introduce the topic of rotor dynamics, as applied to rotorcraft. Helicopters are the most common form of a rotorcraft. It has a single main rotor, and a smaller tail rotor. Some rotorcraft have multiple main rotors like the tandem, co-axial, and tilt-rotor aircraft. Some have unusual configurations like a compound with a wing and propeller, a stopped or slowed rotor, or a quad tilt-rotor with two wings and 4 main rotors. The main rotor, or rotors form the heart of every rotorcraft. To begin the study of rotor dynamics one needs familiarity with the following concepts. The purpose of this chapter is to introduce these concepts.

- 1) Basic rotor aerodynamics
- 2) Basic Structural Dynamics
- 3) Aero-elastic Response
- 4) Loads
- 5) Helicopter trim

Typically, a helicopter rotor has a large diameter, and produces thrust at disk loadings (thrust per unit area) of 2-10 lbs/ft² (200-450 N/m²). It consists of two, three, four or sometimes five to seven blades. The blades are like large aspect ratio wings (chord/Radius ~ 15), made of special airfoil sections. The U.S. manufactured blades rotate counter clockwise (looking from above facing toward helicopter). The rotor RPM is generally around 300-400. The tip speeds are of the order of 700 ft/sec. The speed at which it sucks in air, called the downwash velocity, is in comparison around 30-50 ft/sec. There is a small diameter rotor at the far end of the body called the tail rotor. The purpose of the tail rotor is to counterbalance the shaft torque reaction of main rotor and provide directional stability to the vehicle. Let us briefly examine the aerodynamics of two major flight modes of the helicopter, hover and forward flight.

1.1 Basic Rotor Aerodynamics

1.1.1 Hover

Hover is a flight condition of the helicopter with zero forward speed and zero vertical speed. The flow condition on the rotor disk is axisymmetric. Momentum theory is widely used to calculate the minimum power that is necessary to generate a given thrust using a given disk area. First, the velocity with which the surrounding air needs to be sucked in through the rotor to generate the thrust, is calculated. This velocity is also called rotor downwash or inflow. The power is then simply the thrust multiplied with inflow. Larger the rotor diameter, smaller the inflow for a given thrust, and hence smaller the power requirement.

Momentum theory does not tell us whether a rotor will be able to generate a given thrust. The rotor may stall before an intended thrust level is achieved. The blade element theory can be used to calculate the maximum thrust capability. The blade element theory is discussed later.

Momentum Theory

Momentum theory assumes a uniform, incompressible, zero-swirl flow through the rotor disk. It uses the three basic laws of fluid mechanics: conservation of mass, conservation of momentum, and conservation of energy. It solves for the three unknowns: the inflow velocity, v , the velocity of the fully contracted far wake, w , and the fully contracted flow area, A_4 . The flow around a rotor in hover is shown in Fig. 1.1 The total pressures at each of the four stations are

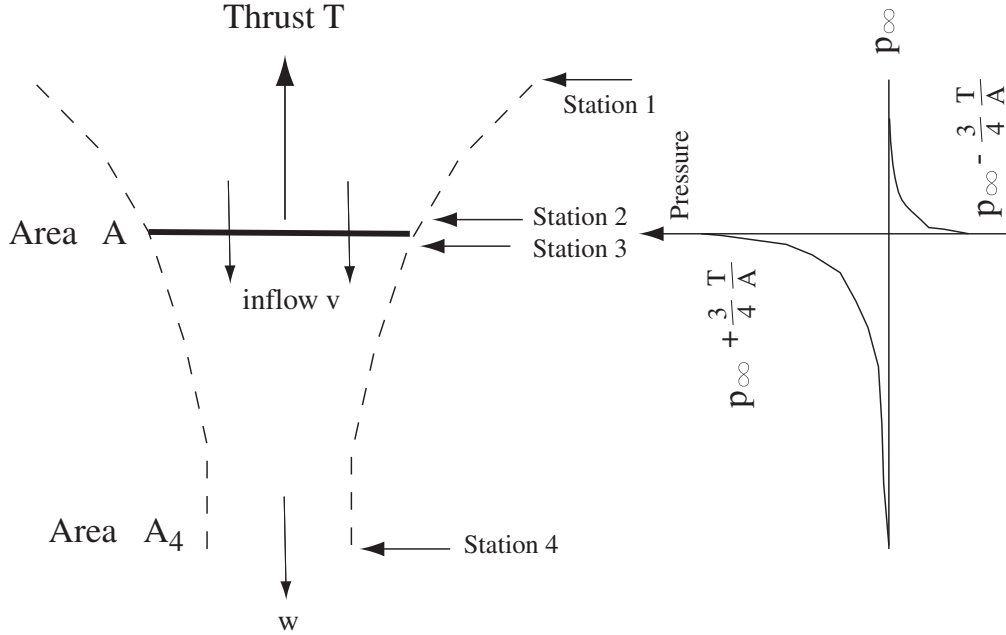


Figure 1.1: Flow around a rotor in hover

$$\begin{aligned} p_{01} &= p_\infty \text{ static pressure far upstream} \\ p_{02} &= p_2 + \frac{1}{2}\rho v^2 \\ p_{03} &= p_3 + \frac{1}{2}\rho v^2 \\ p_{04} &= p_\infty + \frac{1}{2}\rho w^2 \end{aligned}$$

As no force is applied on the fluid between sections 1 and 2, and then between sections 3 and 4, there is no change in total pressure.

$$\begin{aligned} p_{02} &= p_{01} \\ p_{03} &= p_{04} \end{aligned}$$

Force is only applied on the fluid between sections 2 and 3, leading to the pressure differential

$$p_3 - p_2 = \frac{T}{A}$$

Thus

$$\begin{aligned} p_2 &= p_{02} - \frac{1}{2}\rho v^2 \\ &= p_\infty - \frac{1}{2}\rho v^2 \\ p_3 &= p_{03} - \frac{1}{2}\rho v^2 \\ &= p_{04} - \frac{1}{2}\rho v^2 \\ &= p_\infty + \frac{1}{2}\rho w^2 - \frac{1}{2}\rho v^2 \end{aligned}$$

Therefore

$$p_3 - p_2 = \frac{1}{2}\rho w^2$$

Equating this with the pressure differential we have

$$T = \frac{1}{2}\rho A w^2$$

where A is the disk area. Upto this was conservation of energy. Conservation of momentum gives

$$\begin{aligned} T &= \text{mass flow rate} \cdot \text{change in fluid velocity} \\ &= \rho A v (w - 0) \end{aligned}$$

Equating the expressions from conservation of momentum and conservation of energy we have

$$w = 2v$$

Thus the air which is at rest far upstream is accelerated by the rotor to velocity v at the disc, and then to velocity $2v$ far downstream. It follows

$$T = 2\rho A v^2$$

The induced velocity and induced power are then

$$v = \sqrt{\frac{T}{2\rho A}}$$

$$P = \frac{T^{3/2}}{\sqrt{2\rho A}}$$

In addition, from conservation of mass, the far downstream flow area is

$$A_4 = \frac{A}{2}$$

The pressures above and below the rotor disk are given as

$$\begin{aligned} p_2 &= p_\infty - \frac{1}{2}\rho v^2 \\ &= p_\infty - \frac{1}{4}\frac{T}{A} \\ p_3 &= p_\infty + \frac{1}{2}\rho w^2 - \frac{1}{2}\rho v^2 \\ &= p_\infty + \frac{3}{2}\rho v^2 \\ &= p_\infty + \frac{3}{4}\frac{T}{A} \end{aligned}$$

The induced velocity v can be non-dimensionalized as

$$\lambda = \frac{v}{\Omega R}$$

where

$$\begin{aligned} \Omega &= \text{rotational speed (rad/sec)} \\ R &= \text{rotor radius (ft)} \end{aligned}$$

The thrust and power can be non-dimensionalized as

$$C_T = \frac{T}{\rho A (\Omega R)^2}$$

$$C_P = \frac{P}{\rho A (\Omega R)^3}$$

Using $T = 2\rho A v^2$ in the above expression produces a relation between inflow ratio λ and the thrust coefficient

$$\lambda = \sqrt{\frac{c_T}{2}}$$

Note that this relation is based on uniform flow through the entire rotor disk. To cover nonuniform flow, tip losses, and momentum loss due to swirl flow, an empirical correction factor κ_h is used

$$\lambda = \kappa_h \sqrt{\frac{c_T}{2}}$$

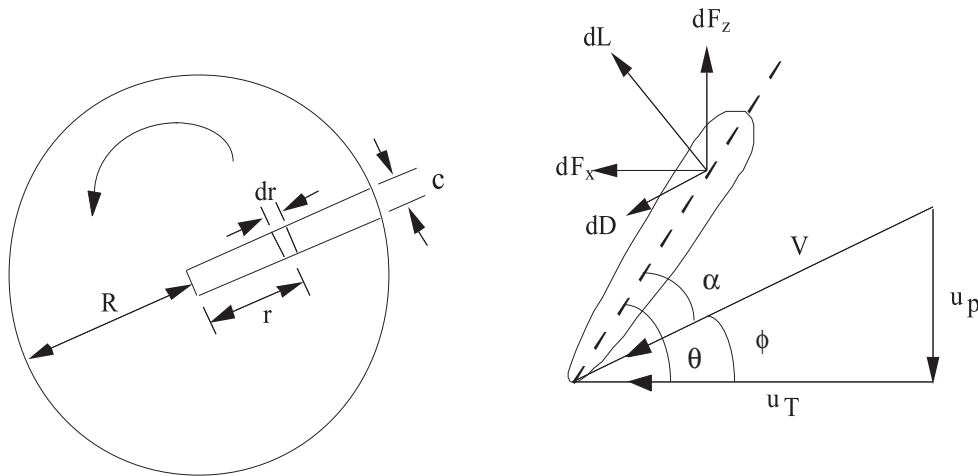
Typically, $\kappa_h = 1.15$. The power coefficient then becomes

$$C_P = \lambda C_T = \kappa_h \frac{C_T^{3/2}}{\sqrt{2}}$$

The Momentum theory assists in the preliminary evaluation of a rotor and helps in the comparison of various rotors. However, the theory does not help directly with the design of a rotor.

Blade Element Theory

To calculate the aerodynamic force distribution on the blade, the simple blade element theory is widely used. It is also called 2-dimensional (2D) Strip Theory. Each blade element is a 2D airfoil which is assumed to operate independantly of the other elements. The aerodynamic forces acting on each blade element are the lift, drag, and pitching moments. They are called air loads.



$$\begin{aligned}
U_T &= \text{tangential velocity (in the plane of rotation)} \\
U_P &= \text{normal velocity} \\
V &= \text{resultant velocity } \sqrt{U_P^2 + U_T^2} \\
&\cong U_T^2 \\
\theta &= \text{pitch angle} \\
\alpha &= \text{effective angle of attack} \\
&= \theta - \tan^{-1} \frac{U_P}{U_T} \cong \theta - \frac{U_P}{U_T} \\
dL &= \text{lift generated on an element of length } dr \text{ located at a radial station } r \\
&= \frac{1}{2} \rho V^2 c_l c dr \\
c &= \text{chord} \\
c_l &= \text{lift coefficient} \\
&= a \left(\theta - \frac{U_P}{U_T} \right) \\
a &= \text{airfoil lift curve slope (linear below stall)} \\
dD &= \text{element drag force} \\
&= \frac{1}{2} \rho V^2 c_d c dr
\end{aligned}$$

Resolved force components are

$$\begin{aligned}
dF_z &= dL \cos \phi - dD \sin \phi \\
&\cong dL \\
&= \frac{1}{2} \rho U_T^2 c a \left(\theta - \frac{U_P}{U_T} \right) dr \\
&= \frac{1}{2} \rho c a (\theta U_T^2 - U_P U_T) dr \\
dF_x &= dL \sin \phi + dD \cos \phi \\
&\cong \frac{U_P}{U_T} dL + dD \\
&= \frac{1}{2} \rho c a (\theta U_T U_P - U_P^2) dr + \frac{1}{2} \rho U_T^2 c c_d dr
\end{aligned}$$

The rotor thrust T, torque Q, and power P are

$$\begin{aligned}
T &= \text{Total forces from } N_b \text{ blades} \\
&= N_b \int_0^R dF_z \\
Q &= \text{Total torque from } N_b \text{ blades} \\
&= N_b \int_0^R r dF_x \\
P &= \Omega Q
\end{aligned}$$

Assume, for simplicity, an uniform induced inflow on the disk. Later on we will see that this assumption is strictly true only for ideally twisted blades. Before we study ideal twist, and other

twist distributions, consider a zero twist case. For a zero twist rotor, the blades have a constant pitch angle, θ across the blade span. We have

$$c_l = a \left(\theta - \frac{U_P}{U_T} \right)$$

For hover

$$\begin{aligned} U_T &= \Omega r \\ U_p &= \lambda \Omega R \end{aligned}$$

Consider the following non-dimensionalizations. First, define a solidity ratio as the ratio of total blade area to disk area. For uniform chord blades

$$\sigma = \frac{N_b c}{\pi R}$$

A local solidity ratio can be defined as

$$\sigma(r) = \frac{N_b c(r)}{\pi R}$$

Also

$$\begin{aligned} x &= \frac{r}{R} \\ u_t &= \frac{U_T}{\Omega R} = x \\ u_p &= \frac{U_P}{\Omega R} = \lambda \end{aligned}$$

Thrust coefficient

$$\begin{aligned} c_T &= \frac{T}{\rho A (\Omega R)^2} \\ &= \frac{N_b \int_0^R \frac{1}{2} \rho c a (\theta u_t^2 - u_p u_t) dr}{\rho (\pi R^2)} \\ &= \frac{\frac{1}{2} a N_b c \int_0^1 (\theta x^2 - \lambda x) dx}{\pi R} \\ &= \frac{\sigma a}{2} \int_0^1 (\theta x^2 - \lambda x) dx \\ &= \frac{\sigma a}{2} \left(\frac{\theta}{3} - \frac{\lambda}{2} \right) \end{aligned}$$

Now consider a linear twist distribution

$$\theta = \theta_{75} + \theta_{tw} \left(\frac{r}{R} - \frac{3}{4} \right)$$

Here θ_{75} is the pitch at 75% radius position and θ_{tw} is the linear twist distribution. Again assuming a uniform induced inflow λ , one obtains

$$\begin{aligned} c_T &= \frac{\sigma a}{2} \int_0^1 \left(\theta_{75} x^2 + \theta_{tw} x^3 - \frac{3}{4} \theta_{tw} x^2 - \lambda x \right) dx \\ &= \frac{\sigma a}{2} \left(\frac{\theta_{75}}{3} - \frac{\lambda}{2} \right) \end{aligned}$$

Note that the twist distribution θ_{tw} has got cancelled. Thus, it is a general relationship valid for both uniform pitch and linearly twisted blades. From momentum theory, induced inflow is

$$\lambda = \kappa_h \sqrt{\frac{c_T}{2}}$$

The thrust level is related to the pitch setting

$$c_T = \frac{\sigma a}{2} \left(\frac{\theta_{75}}{3} - \frac{1}{2} \kappa_h \sqrt{\frac{c_T}{2}} \right)$$

$$\theta_{75} = 6 \frac{c_T}{\sigma a} + \frac{3}{2} \kappa_h \sqrt{\frac{c_T}{2}}$$

Thus, blade element theory gives the blade setting required to generate an inflow of $\kappa_h \sqrt{\frac{c_T}{2}}$, which in turn is necessary to produce a particular thrust coefficient C_T . Note that the assumption here is that the airfoils do not stall at angle of attack produced by this pitch setting, and operates at the lift curve slope a .

Now consider the torque coefficient for a constant pitch setting and uniform chord.

$$\begin{aligned} \text{Torque } Q &= N_b \int_0^R r dF_x \\ &= N_b \int_0^R \frac{1}{2} \rho c a \left(U_P U_T \theta - U_P^2 + U_T^2 \frac{C_{do}}{a} \right) r dr \quad \text{assuming } c_d = c_{do} \end{aligned}$$

The Torque coefficient is

$$\begin{aligned} C_Q &= \frac{Q}{\rho(\pi R^2)(\Omega R)^2 R} \\ &= \frac{N_b \frac{1}{2} \rho a c \int_0^R [\lambda \Omega R \cdot \Omega r \theta - (\lambda \Omega R)^2 + (\Omega R)^2 \frac{c_{do}}{a}] r dr}{\rho(\pi R^2)(\Omega R)^2 R} \\ &= \frac{\sigma a}{2} \int_0^1 \left(\theta \lambda x^2 - \lambda^2 x + \frac{c_{do}}{a} x^3 \right) dx \\ &= \lambda \frac{\sigma a}{2} \int_0^1 (\theta x^2 - \lambda x) dx + \frac{\sigma a}{2} \int_0^1 \frac{c_{do}}{a} x^3 dx \\ &= \lambda C_T + \frac{\sigma a}{2} \int_0^1 \frac{c_{do}}{a} x^3 dx \\ &= \lambda C_T + \frac{\sigma c_{do}}{8} \end{aligned}$$

For example, using the C_T expression for uniform pitch we can get

$$C_Q = \frac{\sigma a}{2} \lambda \left(\frac{\theta}{3} - \frac{\lambda}{2} \right) + \frac{\sigma}{8} C_{do}$$

Note that C_Q has broken up into two parts, one related to C_T , the other related to sectional drag.

$$C_Q = C_{Qi} + C_{Qo}$$

These are called the induced torque, and profile torque.

The Power coefficient, by definition, is identical to the torque coefficient. Thus the induced power and profile power are identical to induced torque and profile torque.

$$\begin{aligned}
 C_P &= \frac{P}{\rho(\pi R^2)(\Omega R)^3} \\
 &= \frac{\Omega Q}{\Omega \rho(\pi R^2)(\Omega R)^2 R} \\
 &= C_Q \\
 &= C_{Pi} + C_{Po}
 \end{aligned}$$

The induced power is the power spent to generate thrust. It is an absolute minimum, without which the thrust cannot be sustained. It is spent to push the airflow downwards. In an ideal case the entire induced power would be spent on pushing the airflow downwards. In reality a part of the induced power is lost in swirl flow, tip losses, non-uniform inflow. This can be accounted for, as we saw before, using the factor κ_h . The profile power is spent to overcome drag. We would like this to be minimized as much as possible. An important parameter is used to estimate the hover performance of a rotor. It is called the Figure of Merit, M. The Figure of Merit, M, is defined as the ration of ideal power to the actual power.

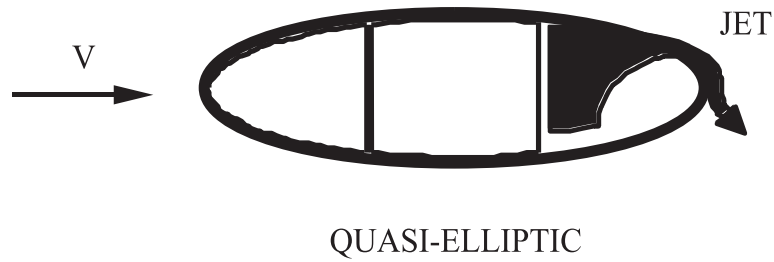
$$\begin{aligned}
 M &= \frac{(C_{pi})_{ideal}}{(C_{pi})_{real} + C_{po}} \\
 &= \frac{(\lambda C_T)_{ideal}}{(\lambda C_T)_{real} + \frac{\sigma}{8} C_{do}} \\
 &= \frac{\frac{C_T^{3/2}}{\sqrt{2}}}{\kappa_h \frac{C_T^{3/2}}{\sqrt{2}} + \frac{\sigma}{8} C_{do}}
 \end{aligned}$$

Typically, the value of M lies between 0.6 to 0.8. The higher value is more true for recent rotors. From the above expression it seems that a rotor operating at high C_T would have a high M, other factors remaining constant. Indeed, as C_T increases, M asymptotes to κ_h . In reality it is different. Airfoil stall prevents the other factors from remaining constant. Even though C_T is high, the sectional c_l should still be below stall. The sectional c_l is directly related to rotor $\frac{C_T}{\sigma}$. Thus the solidity, σ , has to be increased as well. Alternatively, the sectional c_l may be pushed up close to stall. In this case the airfoil drag increases. Using simply c_{do} as a constant drag is no longer an acceptable assumption. Thus it is impossible to keep increasing C_T indefinitely without increasing the second factor in the denominator.

Shaft horsepower

$$\text{HP} = \frac{P}{550} \quad (\text{P ft-lb})$$

Example 1.1: In a circulation-controlled airfoil, a thin jet of air is blown from a spanwise slot along a rounded trailing edge. Due to the Coanda effect, the jet remains attached by balance of centrifugal force and suction pressure. For a CCR, the thrust can be controlled by geometric pitch as well as blowing.

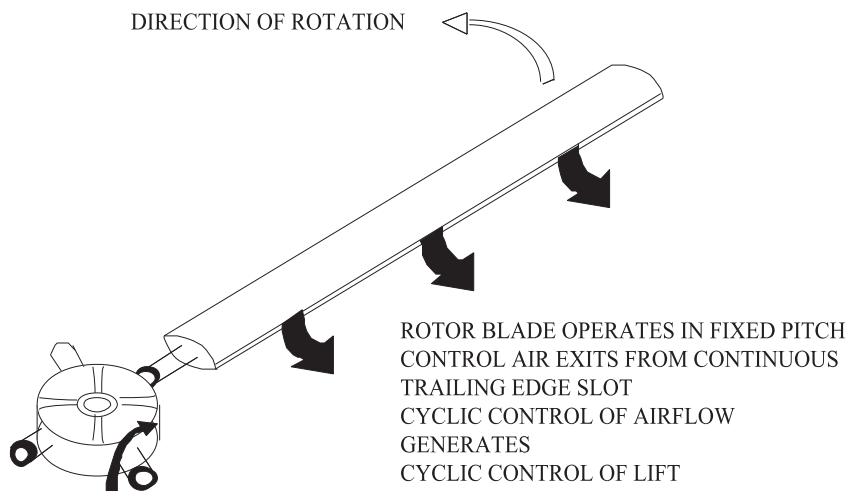


Assuming lift coefficient $c_l = c_1\alpha + c_2\mu$, establish a relationship between thrust coefficient, c_T , geometric pitch, θ_o (uniform), and blowing coefficient, c_μ (uniform), for a hovering rotor. Assume a uniform inflow condition.

For hover

$$\begin{aligned}
 U_P &= \lambda\Omega R \\
 U_T &= \Omega r \\
 T &= N_b \int_0^R dF_z \\
 &= N_b \int_0^R \frac{1}{2}\rho c \Omega^2 r^2 c_l dr \\
 c_l &= c_1\alpha + c_2\mu \\
 &= c_1 \left(\theta_0 - \frac{\lambda}{x} \right) + c_2\mu
 \end{aligned}$$

CIRCULATION CONTROL CONCEPT



$$\begin{aligned}
c_T &= \frac{T}{\rho\pi R^2(\Omega R)^2} \quad \text{and} \quad \sigma = \frac{N_b c}{\pi R} \\
&= \frac{\sigma}{2} \int_0^1 x^2 \left[c_1 \left(\theta_0 - \frac{\lambda}{x} \right) + c_2 c_\mu \right] dx \\
&= \frac{\sigma}{2} \left[c_1 \left(\frac{\theta_0}{3} - \frac{\lambda}{2} \right) + \frac{1}{3} c_2 c_\mu \right] \\
\lambda &= \kappa_h \sqrt{\frac{c_T}{2}} \\
\theta_0 &= \frac{6c_T}{\sigma c_1} + \frac{3}{2} \lambda + \frac{c_2}{c_1} c_\mu
\end{aligned}$$

Momentum Theory in Annular Form

In the earlier derivations, the induced velocity was assumed to be uniform over the rotor disk. In reality, the inflow is highly non-uniform. The non-uniformity in inflow can be calculated and accounted for by using what is called the Combined Blade Element Momentum Theory. It combines Blade Element Theory with Momentum Theory. The momentum theory is used in its annular form. The idea is simple. The momentum theory is simply applied to an annular ring of thickness, dr , located at radial position, r , extended both far upstream and far downstream. For this elemental ring, the induced velocity in the far wake is again twice the induced velocity at the disk. Thus the thrust on the annular ring

$$\begin{aligned}
dT &= \text{mass flow rate} \cdot \text{change in fluid velocity} \\
&= \rho dA v (w - 0) \\
&= \rho (2\pi r dr) v (2v - 0) \\
&= 4\rho v^2 \pi r dr \\
dC_T &= 4\lambda^2 x dx
\end{aligned}$$

Combined Blade Element Momentum Theory

Combines momentum theory and blade element theory to obtain non-uniform spanwise induced velocity, or inflow, distribution. From blade element theory we had the following expressions.

$$\begin{aligned}
dC_T &= \frac{N_b dF_z}{\rho A (\Omega R)^2} \\
&= \frac{1}{2} \sigma a \left(\theta - \frac{\lambda}{x} \right) x^2 dx \\
&= \frac{1}{2} \sigma c_l(x) x^2 dx
\end{aligned}$$

Earlier when we integrated the above expression to obtain C_T , we assumed $\sigma(x) = \sigma$, a constant for convenience. Here, we leave it in general to be a function of radial station. Thus is it the local solidity.

$$c_l(x) = a \left(\theta - \frac{\lambda}{x} \right)$$

$$\begin{aligned}
dC_P &= dC_Q \\
&= \frac{N_b r dF_x}{\rho A (\Omega R)^2 R} \\
&= \frac{1}{2} \sigma (c_l \phi + c_d) x^3 dx && \text{where } \phi = \frac{\lambda}{x} \\
&= \frac{1}{2} \sigma c_l \phi x^3 dx + \frac{1}{2} \sigma c_d x^3 dx \\
&= dC_{P_i} + dC_{P_0}
\end{aligned}$$

Let us obtain an expression for sectional bound circulation. The bound circulation is obtained using 2D Kutta condition. The Kutta condition relates the span-wise gradient of blade lift $\frac{dL}{dr}$ to the bound circulation $\Gamma(r)$ using following the simple relation

$$\frac{dL}{dr} = \rho U \Gamma(r)$$

where U is the local incident flow velocity. Keeping in mind, that the blade lift in hover is simply the rotor thrust divided by the number of blades, it follows

$$\begin{aligned}
dL(r) &= \rho U_T \Gamma(r) dr \\
dT(r) &= N_b \rho U_T \Gamma(r) dr \\
dC_T(r) &= \frac{N_b}{\Omega A} x \Gamma(x) dx && \text{Now use blade element expression on the left} \\
\frac{1}{2} c_l(x) x^2 dx &= \frac{N_b}{\Omega A} x \Gamma(x) dx && \text{From here it follows} \\
\Gamma(x) &= \frac{1}{2} \Omega \frac{\sigma A}{N_b} c_l(x) x \\
&= \frac{1}{2} \Omega c(x) R c_l(x) x && \text{dimension } m^2/s \\
\gamma(x) &= \frac{\Gamma(x)}{\Omega R} \\
&= \frac{1}{2} \frac{c(x)}{R} c_l(x) x && \text{non-dimensional}
\end{aligned}$$

Now we have all the necessary equations to study the results of Combined Blade Element Momentum Theory. The theory gives us a method to calculate non-uniform inflow across the span. Simply relate the dC_T expressions from Blade Element and Annular Momentum theories.

$$\frac{1}{2} \sigma a \left(\theta - \frac{\lambda}{x} \right) x^2 dx = 4 \lambda^2 x dx$$

Solve for λ as a function of x

$$\lambda(x) = \sqrt{A^2 + B \theta x} - A \tag{1.1}$$

where

$$\begin{aligned}
A &= \frac{\sigma a}{16} \\
B &= \frac{\sigma a}{8}
\end{aligned}$$

Another interesting expression can be obtained as follows. Instead of really solving for λ we can re-arrange the above equation to read as

$$\begin{aligned}\frac{1}{2}\sigma(x)c_l x^2 dx &= 4\lambda^2 dx \\ \frac{1}{2}\sigma(x)a\alpha x^2 dx &= 4\lambda^2 dx\end{aligned}$$

which gives

$$\lambda = \sqrt{\frac{\sigma x a \alpha}{8}} \quad (1.2)$$

Note that, the α above is the sectional angle of attack $\theta - \lambda/x$, with a λ hiding inside. Let us now study the effect of different twist distributions. Consider the following cases one by one.

Case I : $\theta = \theta_{75} = \text{const}$

$$\begin{aligned}\lambda(x) &\cong \text{linear} \cong \lambda_0 x \\ c_l(x) &\cong a(\theta_{75} - \lambda_0) = \text{constant} \\ \Gamma(x) &\cong \text{linear} \\ dC_T(x) &\cong \text{parabolic} \\ C_T &= \frac{1}{2}\sigma a \left(\frac{\theta_{75}}{3} - \frac{\lambda}{2} \right)\end{aligned}$$

Case II : $\theta(x) = \theta_0 + x\theta_{tw}$

$$\begin{aligned}\lambda(x) &= \text{non-uniform} \\ c_l(x) &= \text{non-uniform} \\ \Gamma(x) &= \text{non-uniform} \\ dC_T(x) &= \text{non-uniform} \\ C_T &= \frac{1}{2}\sigma a \left(\frac{\theta_0}{3} + \frac{\theta_{tw}}{4} - \frac{\lambda}{2} \right) \\ &= \frac{1}{2}\sigma a \left(\frac{\theta_{75}}{3} - \frac{\lambda}{2} \right)\end{aligned}$$

Case III : $\theta(x) = \frac{\theta_{tip}}{x}$

$$\begin{aligned}\lambda(x) &= \text{const} \\ &= \phi x \\ &= \phi_{tip} \\ c_l(x) &= \frac{1}{x}a(\theta_{tip} - \phi_{tip}) \\ &= \frac{1}{x}\alpha_{tip} \quad \text{hyperbolic} \\ \Gamma(x) &= \text{const} \\ dC_T(x) &= \text{linear} \\ &= \frac{1}{2}\sigma a \alpha_{tip} x dx \\ C_T &= \frac{1}{4}\sigma a \alpha_{tip} \quad \text{assume constant } \sigma\end{aligned}$$

Thus for the twist distribution given above, α_{tip} has to equal $\frac{4C_T}{\sigma a}$ to produce a given thrust C_T . The lift coefficient distribution, c_l , then equals $\frac{4C_T}{\sigma x}$. Two ideas follow: (1) the inflow distribution is $\lambda = \sqrt{\sigma x c_l / 8} = \sqrt{C_T / 2}$. This is the uniform inflow expression as obtained earlier using the momentum theory. Recall that momentum theory gives the absolute minimum power that must be supplied to the rotor to sustain a given thrust. Thus the above twist requires minimum induced power. (2) $\theta_{tip} = \frac{4C_T}{\sigma a} + \phi_{tip} = \frac{4C_T}{\sigma a} + \sqrt{C_T / 2}$. Thus the twist depends on one particular C_T value. The twist distribution, as it minimizes induced power, is called ideal twist, and such a rotor an ideal rotor. Note that it is ideal only for a given C_T . If C_T changes it no longer remains ideal. For example, if a higher (or lower) C_T is required a constant pitch must be added (or subtracted) to the hyperbolic distribution. This makes the inflow distribution non-uniform again.

A similar case is that of an optimum rotor. An optimum rotor, given as Case IV below, seeks to minimize both induced and profile power at the same time. Again, it is optimum only for a given thrust level. Minimum induced power can be achieved only if the inflow is forced to be uniform $\lambda = \sqrt{C_T / 2}$. The question is, what should be the form of twist $\theta(x)$ that would minimize profile power in addition to induced power.

Case IV : Choose $\theta(x) = \alpha_0 + \frac{\lambda}{x}$, where α_0 is an unknown. λ is known, and must be uniform with value $\sqrt{C_T / 2}$ in order to minimize induced power.

$$\begin{aligned}\alpha(x) &= \theta(x) - \frac{\lambda}{x} \\ &= \text{constant} = \alpha_0 \\ c_l(x) &= \text{constant} = a\alpha_0\end{aligned}$$

Now equate the inflow expressions and solve for solidity

$$\lambda = \sqrt{\frac{\sigma(x) x a \alpha_0}{8}} = \sqrt{\frac{C_T}{2}}$$

Thus the solidity must be chosen such that it equals

$$\sigma(x) = \frac{4C_T}{a\alpha_0} = \frac{\sigma_{tip}}{x}$$

This value of solidity will realize the minimize induced power criteria. The only unknown that remains is α_0 . However, we know that this is the angle of attack all sections will operate in. What angle of attack do we want the sections to operate in? Such, that the profile power is minimized. Using the expression for profile power obtained above, and remembering that the sectional drag c_d remains constant along the span (because the angle of attack remains constant α_0) we have

$$\begin{aligned}C_{P0} &= \frac{1}{2} \int_0^1 \sigma(x) c_d x^3 dx \\ &= \frac{4C_T}{a\alpha_0} \int_0^1 c_d x^2 dx \\ &= \frac{2}{3} C_T \frac{c_d}{c_l}\end{aligned}$$

So to minimize profile power, simply choose α_0 such that it maximizes C_l / C_d based on airfoil property data. Once this α_0 has been chosen, the geometric properties of the optimum rotor are set as

$$\begin{aligned}\sigma(x) &= \frac{1}{x} \frac{4C_T}{a\alpha_0} \\ \theta(x) &= \alpha_0 + \frac{1}{x} \sqrt{\frac{C_T}{2}}\end{aligned}$$

Solidity Ratio

To examine the performance of non-rectangular blades, we saw that the local solidity can be defined as

$$\sigma(r) = \frac{N_b c(r)}{\pi R}$$

where $c(r)$ is the local chord at station r and N_b is total number of blades. For rectangular blades, the overall solidity, σ , is the same as the local solidity, σ . For non-rectangular blades, often, there is a need to define an equivalent solidity, σ_e . That is, what would be the solidity of a rectangular blade that is equivalent to a given non-uniform blade? Then the question is, equivalent in what sense? Generates same thrust? Or requires same power? Naturally then, there are two types of equivalent solidities, thrust basis and power basis. The power basis is based on profile power. First equate the following two expressions

$$C_T = \frac{1}{2} \sigma_e \int_0^1 c_l x^2 dx = \frac{1}{2} \int_0^1 \frac{N_b c(x)}{\pi R} c_l x^2 dx$$

$$C_{P0} = \frac{1}{2} \sigma_e \int_0^1 c_d x^3 dx = \frac{1}{2} \int_0^1 \frac{N_b c(x)}{\pi R} c_d x^3 dx$$

Then assume c_l , c_d to be constant over span to obtain

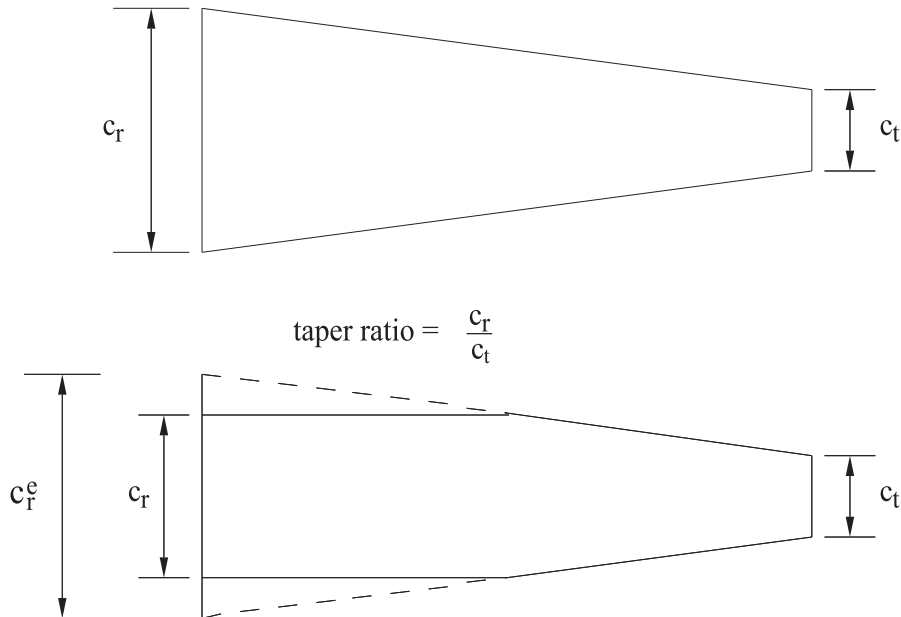
$$\sigma_e = \frac{3N_b}{\pi R} \int_0^1 c x^2 dx \quad \text{thrust basis } (x = \frac{r}{R})$$

$$\sigma_e = \frac{4N_b}{\pi R} \int_0^1 c x^3 dx \quad \text{power basis}$$

The equivalent solidity is used for performance comparison of two different rotors. They are of limited importance however, because of the following assumptions: (1) the sectional coefficients remain constant over span, and (2) the sectional coefficients would remain the same between the real and equivalent rotors. In reality, none of them hold true. The best way to compare two rotors is simply to compare their power requirements at the same thrust, or their Figure of Merits.

Taper Ratio

Linear variation of solidity is sometimes expressed as a taper ratio. For linearly tapering planform, the taper ratio is defined as root chord over tip chord.



For partial linear tapered planform

$$\text{taper ratio} = \frac{\text{extended root chord}}{\text{tip chord}} = \frac{c_r^e}{c_t}$$

For large diameter rotors, the taper appears viable for performance gains.

1.1.2 Axial Climb

Upto now only the hover condition was considered. The analysis of axial climb and descent are shown using momentum theory, and combined blade element momentum theory. The theories, as before, are methods to related rotor inflow to rotor thrust.

Axial climb: Momentum theory

The fluid flow around the rotor looks very similar to that of hover, except that now a constant downwash, V_c is superimposed on the velocities. Thus the total far upstream, disk, and far downstream velocities are now $0 + V_c$, $v_i + V_c$, and $w + V_c$ respectively. Again, as in the case of hover, the thrust T can be easily related to the far downstream induced velocity w , using a momentum balance. The next step is then to simply relate w to v_i . This is done using energy balance. It can be shown that w is again equal to $2v_i$. The slipstream contraction then, follows obviously from mass balance. The steps are shown below.

In hover, the energy balance was formulated by conserving total pressure. It can also be formulated easily by conserving kinetic energy. The kinetic energy of the fluid moving out of the control volume per unit time is $\frac{1}{2}\dot{m}(v_c + w)^2$. The kinetic energy moving in per unit time is $\frac{1}{2}\dot{m}v_c^2$. The balance is the work done on the fluid per unit time, i.e., thrust times the displacement of the fluid per unit time $T(v_c + v_i)$. Thus

$$\begin{aligned} T(v_c + v_i) &= \frac{1}{2}\dot{m}(v_c + w)^2 - \frac{1}{2}\dot{m}v_c^2 && \text{energy balance} \\ T &= \dot{m}(v_c + w) - \dot{m}v_c = \dot{m}w && \text{momentum balance} \end{aligned}$$

Using the second expression in the first equation it follows, $w = 2v_i$.

Keeping in mind $\dot{m} = \rho A(v_c + v_i)$, we have $T = \rho A(v_c + v_i)w$. This can be expressed either in terms of only v_i or w . Thus $T = 2\rho A v_i(v_c + v_i) = \rho A w(v_c + w/2)$. The first expression is usually used to directly relate v_i to T. Often, instead of T, v_i is related to the hover induced velocity, i.e., what v_i would be in case of hover. Recall, that v_i in case of hover is related to thrust by the relation $v_h^2 = \frac{T}{2\rho A}$. Thus we have

$$v_h^2 = (v_c + v_i)v_i$$

It follows

$$\frac{v_i}{v_h} = -\frac{v_c}{2v_h} \pm \sqrt{\left(\frac{v_c}{2v_h}\right)^2 + 1}$$

The positive sign provides the physically meaningful solution, as v_i should always be positive, i.e, downwards, for a positive thrust T upwards. The power required to climb, as a fraction of power required to hover, is simply

$$\frac{P}{P_h} = \frac{P_i + P_c}{P_h} = \frac{T(v_i + v_c)}{T v_h} = \frac{v_i}{v_h} + \frac{v_c}{v_h} = \frac{v_c}{2v_h} \pm \sqrt{\left(\frac{v_c}{2v_h}\right)^2 + 1}$$

where the positive sign provides the physically meaningful solution.

Consider a case when the rate of climb is such that $v_c/v_h \ll 2$.

$$\begin{aligned} \frac{v_i}{v_h} &\cong -\frac{v_c}{2v_h} + 1 \\ v_i &\cong v_h - \frac{1}{2}v_c \\ P_i &= T(v_h - \frac{1}{2}v_c) + Tv_c + P_0 \\ &= Tv_h + P_0 + T\frac{v_c}{2} \\ &= P_h + T\frac{v_c}{2} \quad \text{assuming profile power remains same as in hover} \end{aligned}$$

This means that the increased power required for steady climb is half the rate of change of potential energy. Which means that if the maximum power of an aircraft is P_{max} , and the hover power is P_h , then a steady rate of climb of twice the excess power to thrust ratio can be established, $v_c = 2(P_{max} - P_h)/T$. This approximation holds as long as the rate of climb remains much lesser compared to the hover induced velocity.

Note that the initial climb rate is $(P_{max} - P_h)/T$, but a final steady-state climb rate of twice this value can be reached. This is because the induced velocity in steady climb is reduced by twice the climb velocity from induced velocity in hover.

Axial climb: Combined Blade Element Momentum theory

We have for an annulus

$$\begin{aligned} dT &= \rho(2\pi r dr)(v_c + v_i)(2v_i - 0) \\ dC_T &= 4\lambda(\lambda - \lambda_c)x dx \end{aligned}$$

where

$$\begin{aligned} \lambda &= \frac{v_c + v_i}{\Omega R} \\ \lambda_c &= \frac{v_c}{\Omega R} \end{aligned}$$

Then equate dC_T Blade Element theory and Momentum theory

$$\frac{1}{2}\sigma a \left(\theta - \frac{\lambda}{x} \right) x^2 dx = 4\lambda(\lambda - \lambda_c)x dx$$

Solve for λ as a function of x

$$\lambda(x) = \sqrt{A^2 + B\theta x} - A \tag{1.3}$$

where

$$\begin{aligned} A &= \frac{\sigma a}{16} - \frac{\lambda_c}{2} \\ B &= \frac{\sigma a}{8} \end{aligned}$$

1.1.3 Axial Descent

Descending flight is similar to ascent, except that v_c is negative. For example, a descent of 5 m/s can be viewed as an ascent of -5 m/s. However the same expressions as ascent cannot be used.

Note that in all three conditions, hover, ascent, and descent the thrust must act upwards. Thus the force on the fluid must be downwards. The control volumes therefore have a similar geometry, constricted below the rotor and expanded above. In all three cases the rotor pushes the fluid down. However, during descent, unlike in hover and climb, the freestream velocity is from below the rotor. As a result, the fluid, in response to the rotor pushing it down, slows down or decelerates above the rotor. The far upstream, disk, and far downstream velocities are still v_c , $v_c + v_i$, and $v_c + w$, except far upstream is now below the rotor, and far downstream is above the rotor.

Axial descent: Momentum theory

Define positive direction to be downwards.

$$\begin{aligned} T(v_c + v_i) &= \frac{1}{2}\dot{m}(v_c)^2 - \frac{1}{2}\dot{m}(v_c + w)^2 && \text{energy balance} \\ T &= \dot{m}(v_c) - \dot{m}(v_c + v_i) = -\dot{m}v_i && \text{momentum balance} \end{aligned}$$

Using the second expression in the first equation it follows, $w = 2v_i$.

Following the same procedure as in axial climb we have

$$\begin{aligned} T &= -\dot{m}w = -2\rho A(v_c + v_i)v_i \\ v_h^2 &= -(v_c + v_i)v_i \end{aligned}$$

It follows

$$\frac{v_i}{v_h} = -\frac{v_c}{2v_h} \pm \sqrt{\left(\frac{v_c}{2v_h}\right)^2 - 1}$$

The negative sign provides the physically meaningful solution. The power required to climb, as a fraction of power required to hover, is simply

$$\frac{P}{P_h} = \frac{P_i + P_c}{P_h} = \frac{T(v_i + v_c)}{Tv_h} = \frac{v_i}{v_h} + \frac{v_c}{v_h} = \frac{v_c}{2v_h} \pm \sqrt{\left(\frac{v_c}{2v_h}\right)^2 - 1}$$

where the negative sign provides the physically meaningful solution.

Axial climb: Combined Blade Element Momentum theory

We have for an annulus

$$\begin{aligned} dT &= -\rho(2\pi r dr)(v_c + v_i)(2v_i - 0) \\ dC_T &= -4\lambda(\lambda - \lambda_c)xdx \end{aligned}$$

where

$$\begin{aligned} \lambda &= \frac{v_c + v_i}{\Omega R} \\ \lambda_c &= \frac{v_c}{\Omega R} \end{aligned}$$

Then equate dC_T Blade Element theory and Momentum theory

$$\frac{1}{2}\sigma a \left(\theta - \frac{\lambda}{x} \right) x^2 dx = -4\lambda(\lambda - \lambda_c) x dx$$

Solve for λ as a function of x

$$\lambda(x) = \sqrt{A^2 + B\theta x} - A \quad (1.4)$$

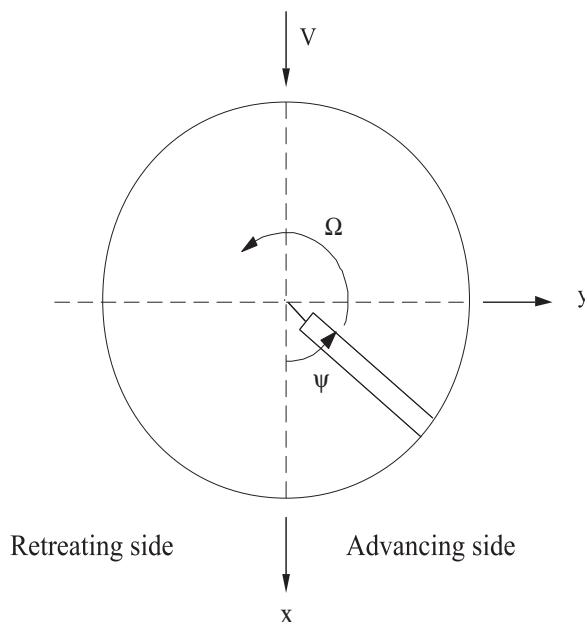
where

$$A = \frac{\sigma a}{16} + \frac{\lambda_c}{2}$$

$$B = -\frac{\sigma a}{8}$$

1.1.4 Forward Flight

In hovering flight, there is an axial symmetry of airflow, whereas, in forward flight there is no axial symmetry of airflow. There is a periodic aerodynamic environment. For an anti-clockwise rotation from the top, the blades on the starboard side advances into the oncoming airflow, and the blades on the port side retreats from it.



Clearly is a greater velocity of airflow on the advancing side of the disk as compared to the retreating side. This results in periodic variation of air loads on the blade. Left to themselves, the blades would generate more lift on the advancing side than on the retreating side and the aircraft would roll over to the left. The remedy is to put a flap hinge at the blade root, so that the blades can freely flap up about the hinge, without rolling the whole aircraft over. The idea was suggested by Charles Renard (1904), patented by Louis Breguet (1908), and applied successfully by Juan de la Cierva on the autogyro (1923). When the blades are allowed to flap, the problem is now reversed. For a lifting rotor, transitioning from hover to forward flight, the aircraft now rolls to the right. We shall see later why. The remedy is to introduce a mechanism for cyclic pitch variations along with a flap hinge. The roll moment can now be completely controlled. In addition to flapping, the other important blade motions are lag and torsion. The lag motion is extremely important for aero-elastic stability. The elastic twist is extremely important for aero-elastic loads. The blade

Momentum theory: Physical interpretation

A physical interpretation of Glauert's theory is as follows. Figure 1.2 shows the flow around the rotor disk in forward flight.

V = forward speed of the helicopter

v = normal induced velocity at the disk

w = far wake induced velocity

α = disk tilt

then, in keeping with the axial flow results, the induced velocity at the far wake is assumed to be twice the induced velocity at the disk.

$$\begin{aligned} w &= 2v \\ T &= \dot{m}2v \\ \dot{m} &= \rho AV_R \end{aligned}$$

where V_R is the resultant velocity through the disk, see figure 1.2.

$$\begin{aligned} V_R &= \sqrt{(V \cos \alpha)^2 + (V \sin \alpha + v)^2} \\ T &= 2\rho Av \sqrt{(V \cos \alpha)^2 + (V \sin \alpha + v)^2} \end{aligned}$$

Now define advance ratio μ and inflow ratio λ as follows.

$$\begin{aligned} \mu &= \frac{V \cos \alpha}{\Omega R} = \frac{\text{tangential velocity at the disk}}{\text{Tip velocity}} \\ \lambda &= \frac{V \sin \alpha + v}{\Omega R} = \frac{\text{Normal velocity at the disk}}{\text{Tip velocity}} \\ \lambda &= \mu \tan \alpha + \lambda_i \end{aligned}$$

Typically $\mu = 0.25$ to 0.4 and λ_i is of order 0.01 where $\lambda_i = \frac{v}{\Omega R}$, induced inflow ratio. Non-dimensionalising the thrust expression we have

$$\begin{aligned} C_T &= 2\lambda_i \sqrt{\lambda^2 + \mu^2} \\ \lambda_i &= \frac{C_T}{2\sqrt{\lambda^2 + \mu^2}} \\ \lambda_i &= \frac{\lambda_h^2}{\sqrt{\lambda^2 + \mu^2}} \end{aligned}$$

Thus the inflow equation becomes

$$\lambda = \mu \tan \alpha + \frac{C_T}{2\sqrt{\lambda^2 + \mu^2}}$$

The inflow equation is nonlinear and therefore an iteration procedure is used to solve it. Johnson suggested a Newton-Raphson solution scheme,

$$\lambda_{n+1} = \lambda_n - (f/f')_n$$

where

$$f(\lambda) = \lambda - \mu \tan \alpha - \frac{c_T}{2} \frac{1}{\sqrt{\mu^2 + \lambda^2}}$$

Therefore

$$\begin{aligned} \lambda_{n+1} &= \lambda_n - \frac{\lambda_n - \mu \tan \alpha - \frac{c_T}{2}(\mu^2 + \lambda_n^2)^{\frac{1}{2}}}{1 + \frac{c_T}{2}(\mu^2 + \lambda_n^2)^{-\frac{3}{2}}\lambda_n} \\ &= \left(\frac{\mu \tan \alpha + \frac{c_T}{2} \frac{(\mu^2 + 2\lambda^2)}{(\mu^2 + \lambda^2)^{3/2}}}{1 + \frac{c_T}{2} \frac{\lambda}{(\mu^2 + \lambda^2)^{3/2}}} \right)_n \end{aligned}$$

Usually 3 to 4 iterations are enough to achieve a converged solution. Figures 1.3 and 1.4 show example solutions of this equation with changing thrust levels, and shaft tilt angle.

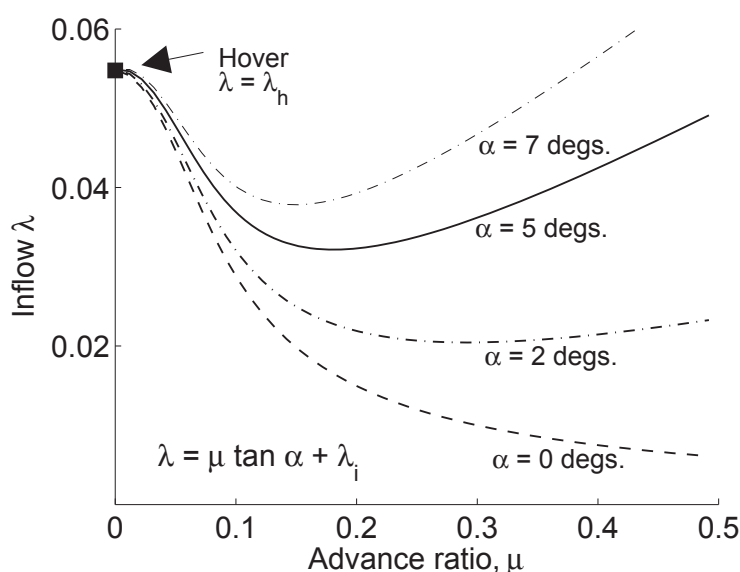


Figure 1.3: Inflow variation with forward speed for different disk tilt angles; $C_T = 0.006$

Note that, in the induced inflow expression given earlier

$$\lambda_i = \frac{\lambda_h^2}{\sqrt{\mu^2 + \lambda^2}}$$

λ_h can, in general, be modified with the empirical correction factor $\kappa_p \sqrt{C_T}/2$. κ_p is often replaced with a different correction factor in forward flight κ_f .

$$\begin{aligned} \lambda_i &= \mu \tan \alpha + \frac{\kappa_f C_T / 2}{\sqrt{\mu^2 + \lambda^2}} \\ &\cong \mu \tan \alpha + \kappa_f \frac{C_T}{2\mu} \quad \text{valid for } \mu > 1.5\lambda_h \end{aligned}$$

Thus, the effect of forward flight is to reduce induced velocity as a result of increased mass flow through the disk and thus reduce the induced power. The result is based on the assumption of uniform inflow over the entire disk. In reality, the induced power may increase at high speeds due to nonuniform inflow.

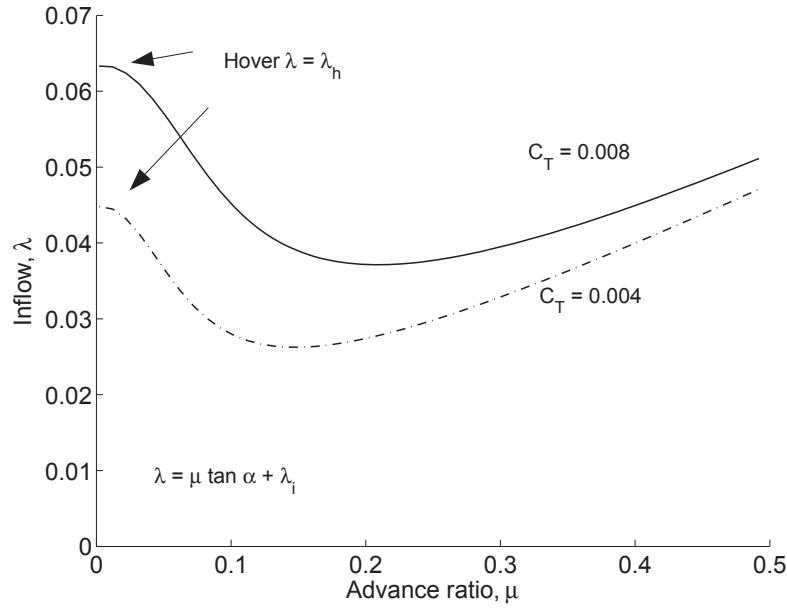


Figure 1.4: Inflow variation with forward speed for different thrust levels; $\alpha = 5^\circ$

The blade element theory for forward flight is quite similar to the one discussed for hover flight, except that the flow components, u_t, u_p , are modified. Consider a model rotor in a wind tunnel with shaft held fixed vertically. Assume that the blades are not allowed any other motion but rotation. This can be called a rigid rotor. The airflow velocity at a radial station r is $\Omega r + V \sin \psi$ where V is the incoming wind velocity and Ω is the rotational speed. Thus the non-dimensional sectional air velocities are

$$\begin{aligned} u_t &= x + \mu \sin \psi \\ u_p &= \lambda \\ u_r &= \mu \cos \psi \end{aligned}$$

The advancing blade encounters higher velocity than the retreating blade. If the pitch is held fixed, the lift on the advancing side is greater than that on the retreating side. This creates periodic bending moments at the root of the blade which rolls the rotor from the advancing side towards the retreating side, i.e. roll left for counter clockwise rotation. For example, the sectional lift, in non-dimensional form, is

$$\begin{aligned} \frac{dF_z}{\rho c a (\Omega R)^2 R} &\cong \frac{dL}{\rho c a (\Omega R)^2 R} \\ &= \frac{1}{2} (\theta u_t^2 - u_p u_t) dx \\ &= \frac{1}{2} (\theta x^2 + 2x\mu\theta \sin \psi + \theta \mu^2 \sin^2 \psi - \lambda x - \mu \lambda \sin \psi) dx \\ &= \left(\theta \frac{x^2}{2} + \theta \frac{\mu^2}{4} - \frac{\lambda x}{2} \right) + \left(\theta \mu x - \frac{\lambda x}{2} \right) \sin \psi + \left(-\theta \frac{\mu^2}{4} \right) \cos 2\psi \end{aligned}$$

In the simple example above, the lift has a constant part, a $\sin \psi$ part and a $\cos 2\psi$ part. The constant part is called the steady lift. The $\sin \psi$ part is called 1 per revolution (1/rev, or 1p) lift. It is an oscillatory lift which completes one cycle of variation over one rotor revolution, i.e., it completes one cycle of variation as the blade moves from $\psi = 0$, through $\psi = 90, 180, 270$ degrees

back to $\psi = 360 = 0$ degrees. At $\psi = 0$ it has a value of 0, at $\psi = 90$ degrees it reaches the maximum value $\theta\mu x - \frac{\lambda x}{2}$, at $\psi = 180$ degrees it is again 0, at $\psi = 270$ degrees it reaches the minimum value $-(\theta\mu x - \frac{\lambda x}{2})$, and finally back to 0 at $\psi = 360$. Similarly the $\cos 2\psi$ part is called 2/rev lift. The bending moment produced by the lift at the root of the blade is

$$\begin{aligned} \frac{dM}{\rho ca(\Omega R)^2 R^2} &= \frac{rdL}{\rho ca(\Omega R)^2 R^2} \\ &= \left(\theta \frac{x^3}{2} + \theta \frac{\mu^2}{4} x - \frac{\lambda x^2}{2} \right) + \left(\theta \mu x^2 - \frac{\lambda x^2}{2} \right) \sin \psi + \left(-\theta \frac{\mu^2}{4} x \right) \cos 2\psi \end{aligned}$$

which is simply the lift expression multiplied by x . The net bending moment at the shaft is obtained by simply integrating the above expression over the span.

$$\begin{aligned} M &= \frac{1}{\rho ac \Omega^2 R^4} \int_0^R r dF_z \\ &= \left(\frac{\theta}{8} + \theta \frac{\mu^2}{8} - \frac{\lambda}{6} \right) + \left(\theta \frac{\mu}{3} - \frac{\lambda}{6} \right) \sin \psi + \left(-\theta \frac{\mu^2}{8} \right) \cos 2\psi \end{aligned}$$

M is the aerodynamic root moment. Like lift it has a steady and two oscillatory components. Note that the root moment occurs at the blade root and has a direction perpendicular to the blade span. As the blade rotates around the azimuth, the direction of the root moment rotates along with the blade. Therefore the root moment is also termed hub rotating moment. The rotating moment can be resolved along two fixed axes, say the aircraft roll and pitch axes. The resolved moments do not change in direction and are called the hub fixed moments. The roll and pitch moments are

$$\begin{aligned} M_R &= +M \sin \psi && \text{positive to left} \\ M_P &= -M \cos \psi && \text{positive nose up} \end{aligned}$$

This leads to 2 important concepts. First, Note that the hub fixed moments are hub rotating moments multiplied with a 1/rev variation. Thus a steady rotating moment generates a 1/rev hub fixed moment. A 1/rev rotating moment generates steady and 2/rev hub fixed moments. A 2/rev rotating moment generates 1/rev and 3/rev hub fixed moments, and so on. In general, a N/rev rotating moment generates $N \pm 1/rev$ hub fixed moments. Our M_β expression had steady, 1 and 2/rev. Therefore our M_R and M_P expressions would have a highest harmonic of 3/rev. Assume M_R to have the following general form.

$$M_R(\psi) = m_0 + m_1 \sin(\psi + \phi_1) + m_2 \sin(2\psi + \phi_2) + m_3 \sin(3\psi + \phi_3)$$

where the phase lags ϕ_1 , ϕ_2 , and ϕ_3 are introduced to account for both sin and cos components of the harmonics.

Now, imagine there are three identical blades. The root moments from each will be identical, except shifted in phase by $360/3 = 120$ degrees. This is because when blade 1 is at $\psi = 0$, blade 2 is at $\psi = 120$, and blade 3 is at $\psi = 240$ degrees, where ψ is always referred with respect to blade 1. Physically it means that at $\psi = 0$ the root moment is made up of three contributions. Contribution 1 is from blade 1 at $\psi = 0$. Contribution 2 is from blade 2. The value of this contribution is exactly same as the root moment blade 1 would have when it reaches $\psi = 120$ degrees. Thus, the contribution from blade 2 is easily found by putting $\psi = 120$ degrees in the expression for blade 1 root moment. Similarly, contribution 3 is from blade 3, and it is easily found by putting $\psi = 240$ degrees in the expression for blade 1 root moment. The concept applies to hub fixed moments as well. When blade 1 contributes $M_R(\psi)$ as a hub fixed load, blade 2 contributes $M_R(\psi + 120)$, and blade 3 contributes $M_R(\psi + 240)$. All three contributions are added at the hub. The end result from simple trigonometry is only steady and 3/rev.

$$\begin{aligned} M_R(\psi)_{total} &= (M_R)_{blade1} + (M_R)_{blade2} + (M_R)_{blade3} \\ &= M_R(\psi) + M_R(\psi + 120) + M_R(\psi + 240) \\ &= 3m_0 + 3m_3(3\psi + \phi_3) \end{aligned}$$

In general, for N_b blades, the fixed frame moments (and forces in general) are always steady, and pN_b/rev components where p is an integer.

High 1/rev blade root moments, and the high steady hub fixed moment that it generates was a major cause of early rotor failures. The question is quite natural, how to minimize this oscillatory bending moment at the root and how to reduce the aircraft rolling moment. The advent of flap hinge (Renard - 1904) relieved the blade root moment, by allowing the blades to flap freely in response to oscillatory aerodynamic flap moments.

1.2 Basic Structural Dynamics

The dynamics of a single degree of freedom system is reviewed. It is then applied to a simple rotor blade flapping model.

1.2.1 Second-Order Systems

Consider a second-order ordinary differential equation describing the motion of a mass spring system.

$$m\ddot{q} + kq = f(t)$$

where q describes the motion, and \ddot{q} is the second derivative with respect to time t . $Q(t)$ is the external forcing. The motion exhibited by the mass m in absence of external forcing is called *natural motion*. Such is the case when the mass is given an initial displacement or velocity and then released. The motion is then governed by the *homogenous equation*

$$m\ddot{q} + kq = 0$$

where the forcing $f(t)$ is set to zero. We seek a solution of the following type.

$$q(t) = Ae^{st}$$

Substituting in the equation we have

$$(ms^2 + k)A = 0$$

$A = 0$ yields a trivial solution $q = 0$. For a non-trivial solution, one must have

$$ms^2 + k = 0$$

which leads to

$$s = \pm i\sqrt{k/m} = i\omega_n$$

where

$$\omega_n = \sqrt{k/m}$$

Thus the governing equation allows a solution of the above type only for these two values of s . These are called the *eigen-values* and ω_n (rad/s) the natural frequency of the system. The homogenous solution is then

$$q(t) = A_1e^{i\omega_n t} + A_2e^{-i\omega_n t} \tag{1.5}$$

The physical interpretation of the solution can be found using the Euler's theorem. Euler's theorem states

$$e^{\pm i\omega t} = \cos \omega t \pm i \sin \omega t$$

It follows from above

$$\begin{aligned} e^{i\pi/2} &= i; & e^{-i\pi/2} &= -i \\ e^{i\pi} &= -1; & e^{-i\pi} &= 1 \end{aligned} \quad (1.6)$$

The term $A_1 e^{i\omega_n t}$ can now be physically interpreted. the first term is expanded as

$$A_1 e^{i\omega_n t} = A_1 \cos \omega_n t + i A_1 \sin \omega_n t \quad (1.7)$$

The two resulting terms $A_1 \cos \omega_n t$ and $A_1 \sin \omega_n t$ are simply the projections of a rotating vector of magnitude A_1 along two mutually perpendicular axes. The rotation speed is ω_n radians/second, and the vector is initially aligned with the horizontal axis. In this sense $A_1 e^{i\omega_n t}$ represents a rotating vector. Similarly $A_2 e^{-i\omega_n t}$ represents another rotating vector. It has magnitude A_2 and rotates with the same speed ω rad/s, but, rotates in a direction opposite to $A_1 e^{i\omega_n t}$. This is easily seen from below.

$$A_2 e^{-i\omega_n t} = A_2 \cos \omega_n t - i A_2 \sin \omega_n t = A_2 \cos(-\omega_n t) + i A_2 \sin(-\omega_n t) \quad (1.8)$$

It follows that an expression of the form $A_1 e^{\pm i(\omega_n t + \phi)}$, where ϕ is a constant, represents a pair of counter-rotating vectors (corresponding to the '+' and '-' signs), which are always ahead of the vectors $A_1 e^{\pm i\omega_n t}$ by an angle ϕ in the direction of their respective rotations. ϕ is called a phase angle. The horizontal and vertical directions are simply two orthogonal directions; one of them can be chosen arbitrarily. Conventionally they are referred to as the Real and Imaginary directions.

The time derivative of $q(t)$ in eqn. 1.5 yields the following expression for velocity

$$\dot{q}(t) = A_1 i \omega_n e^{i\omega_n t} + i A_2 (-i) \omega_n e^{-i\omega_n t} \quad (1.9)$$

which, using the expressions for i and $-i$ from eqns. 1.6 produce

$$\dot{q}(t) = A_1 \omega_n e^{i(\omega_n t + \pi/2)} + i A_2 \omega_n e^{-i(\omega_n t + \pi/2)} \quad (1.10)$$

Thus the expression for velocity represents two counter-rotating vectors of magnitudes $A_1 \omega_n$ and $A_2 \omega_n$ which rotate ahead of the displacement vectors by $\pi/2$ in the direction of their respective rotations. Thus the velocities are ahead of the displacement by a phase angle of $\pi/2$ radians. Similarly the expression for acceleration represents two counter-rotating vectors which lead velocity vectors by $\pi/2$ radians in phase, and therefore the displacement vectors by π .

$$\begin{aligned} \ddot{q}(t) &= A_1 i^2 \omega_n^2 e^{i\omega_n t} + A_2 (-i)^2 \omega_n^2 e^{-i\omega_n t} \\ &= A_1 \omega_n e^{i(\omega_n t + \pi)} + i A_2 \omega_n e^{-i(\omega_n t + \pi)} \end{aligned} \quad (1.11)$$

To summarize, each of the two terms in eqn. 1.5 represents two projections of a rotating vector along two perpendicular directions. Each projection defines a harmonic oscillator. The combination of the two counter-rotating vectors leads to two harmonic oscillators of different magnitudes along the Real (or cosine) and Imaginary (or sine) axes.

$$p(t) = (A_1 + A_2) \cos \omega_n t + i(A_1 - A_2) \sin \omega_n t \quad (1.12)$$

This implies that the physical displacement of the mass m is a combination of cosine and sine harmonics of different amounts, and could be expressed in the following form

$$q(t) = A \sin \omega_n t + B \cos \omega_n t \quad (1.13)$$

It can also be expressed in a pure sine form by substituting $A = \sin \phi_1$ and $B = \cos \phi_1$

$$q(t) = C \sin(\omega_n t + \phi_1); \quad C = \sqrt{A^2 + B^2}; \quad \phi_1 = \tan^{-1}(A/B) \quad (1.14)$$

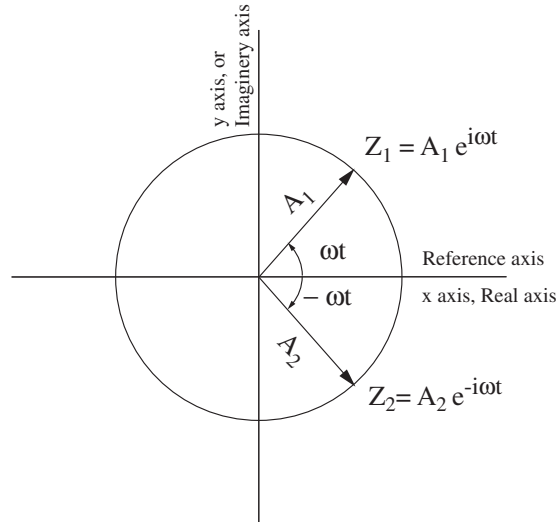


Figure 1.5: **Projections of rotating vectors along orthogonal axes produce harmonic motion**

or in a pure cosine form by substituting $A = \cos \phi_2$ and $B = \sin \phi_2$

$$q(t) = C \cos(\omega_n t - \phi_2); \quad C = \sqrt{A^2 + B^2}; \quad \phi_2 = \tan^{-1}(B/A) \quad (1.15)$$

They are identical, i.e. they yield exactly the same value at a given time t , as $\tan^{-1}(A/B) + \tan^{-1}(B/A) = \pi/2$. Two unknown constants appear in every form which are determined from the initial conditions $q(0), \dot{q}(0)$. These are the initial displacement and velocities. The final solution is called the natural response of the system. It represents perpetual motion in response to an initial perturbation.

In reality systems contain damping. Response to an initial perturbation decays depending on the amount of damping. Consider a real system with damping c in Newtons per m/s.

$$m\ddot{q} + c\dot{q} + kq = f(t) \quad (1.16)$$

For natural response, set $f(t) = 0$, and solve the resulting homogenous equation. For convenience the equation is divided by m and expressed in the following form

$$\ddot{q} + 2\xi\omega_n\dot{q} + \omega_n^2 q = 0$$

Note that k/m has been expressed in terms of the natural frequency of the system (derived earlier). c/m has been replaced with a damping ratio ξ which changes with ω_n even if the physical damper c remains same. $c/m = 2\xi\omega_n$. As before, we seek a solution of the form $q = Ae^{st}$. Substituting in the differential equation we obtain

$$s = (-\xi \pm \sqrt{\xi^2 - 1})\omega_n$$

Case 1: $\xi = 0$ undamped

Roots same as shown earlier, imaginary.

$$s = \pm i\omega_n$$

Case 2: $\xi = 1$ critically damped

Equal roots, real and negative.

$$s_1 = -\omega_n$$

$$s_2 = -\omega_n$$

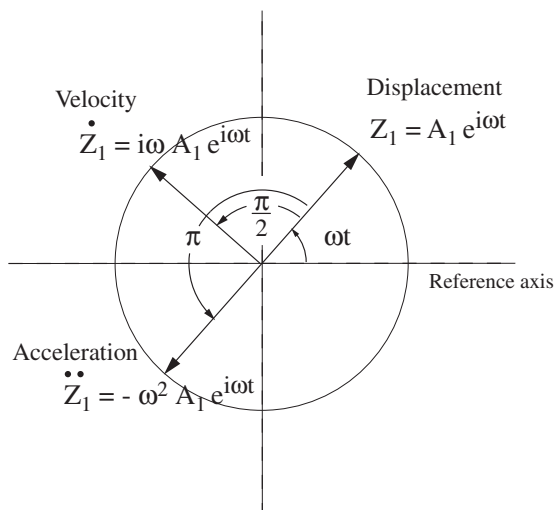


Figure 1.6: The rotating vectors representing velocity and acceleration lead the displacement by $\pi/2$ and π radians

In case of repeated roots the solution is of a slightly different from than the rest

$$\begin{aligned} q(t) &= A_1 e^{-\omega_n t} + A_2 t e^{-\omega_n t} \\ &= (A_1 + A_2 t) e^{-\omega_n t} \end{aligned}$$

Case 3: $\xi > 1$ over damped

Unequal roots, real and negative

$$s_{1,2} = (-\xi \pm \sqrt{\xi^2 - 1})\omega_n$$

$$\begin{aligned} q(t) &= A_1 e^{s_1 t} + A_2 e^{s_2 t} \\ &= e^{-\xi\omega_n t} (A_1 e^{\sqrt{\xi^2 - 1}\omega_n t} + A_2 e^{-\sqrt{\xi^2 - 1}\omega_n t}) \end{aligned}$$

Case 4: $0 < \xi < 1$

The above were all special cases, for a realistic system the damping coefficient is less than one. In this case $\sqrt{\xi^2 - 1}$ is imaginary, and better expressed as $i\sqrt{1 - \xi^2}$. Thus,

$$s_{1,2} = (-\xi \pm i\sqrt{1 - \xi^2})\omega_n$$

$$\begin{aligned} q(t) &= e^{-\xi\omega_n t} (A_1 e^{i\sqrt{1 - \xi^2}\omega_n t} + A_2 e^{-i\sqrt{1 - \xi^2}\omega_n t}) \\ &= e^{-\xi\omega_n t} A \cos(\sqrt{1 - \xi^2}\omega_n t - \phi) \end{aligned}$$

A and ϕ are two arbitrary constants that can be determined from the initial conditions. The damped frequency w_d is given by

$$w_d = \sqrt{1 - \xi^2}\omega_n$$

The decay envelope of the oscillatory response in case 4 is given by

$$E(\xi, \omega_n, t) = e^{-\xi\omega_n t}$$

In summary, the solution to

$$\ddot{q} + 2\xi\omega_n \dot{q} + \omega_n^2 q = 0$$

is given by

$$\begin{aligned} q(t) &= e^{-\xi\omega_n t} A \cos(\sqrt{1-\xi^2}\omega_n t - \phi) & 0 < \xi < 1 \\ &= A \cos(\omega_n t - \phi) & \xi = 0 \\ &= \text{no oscillations} & \xi \geq 0 \end{aligned}$$

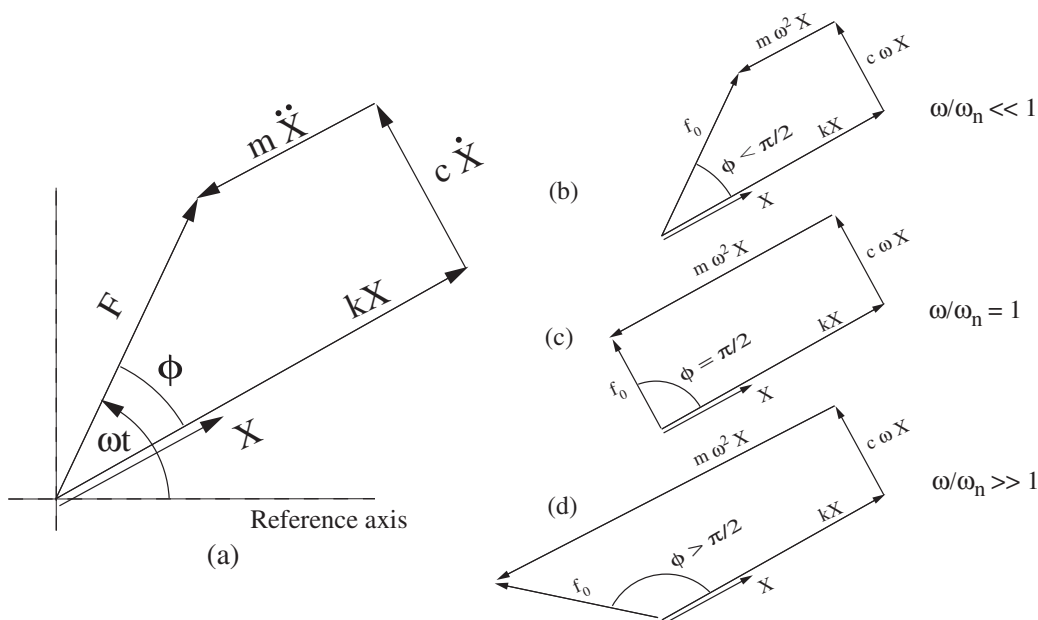


Figure 1.7: (a) **General relationship between spring force, damper force, inertia force and external force in forced vibration**; (b) when $\omega/\omega_n \ll 1$ both inertia and damper force small, ϕ small; (c) when $\omega/\omega_n = 1$ damper force equal and opposite to external force, inertial equal and opposite to spring force, $\phi = \pi$; (d) $\omega/\omega_n \gg 1$ external force almost equal to inertial force, ϕ approaches π

Now consider the forced response of the system. Here we want to solve the *inhomogenous* system as given by eqn. 1.16. Let the external forcing be $f(t) = f_0 \cos \omega t$. The equation then takes the following form.

$$m\ddot{q} + c\dot{q} + kq = f_0 \cos \omega t$$

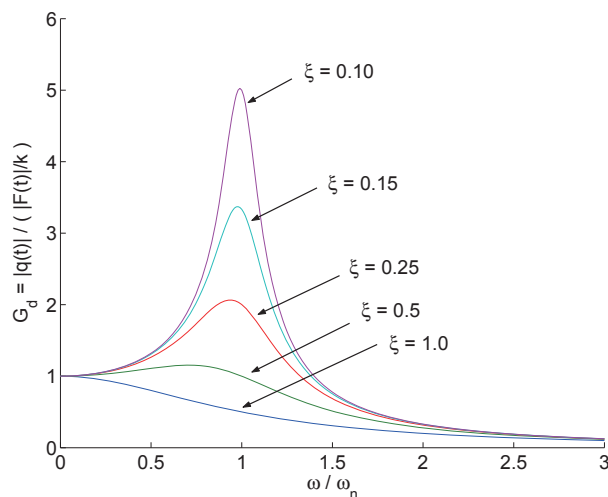
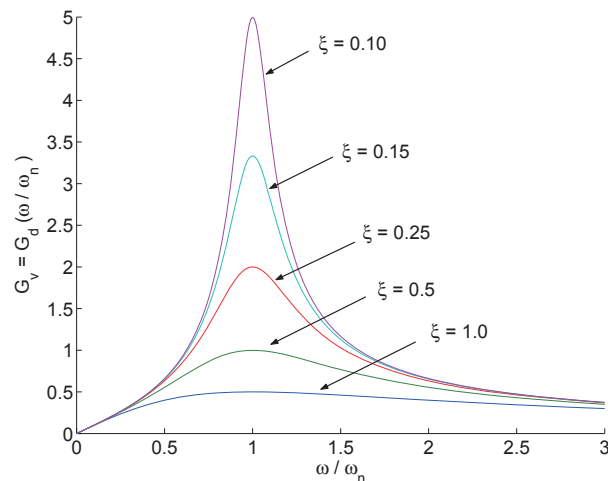
It is easy to check by substitution that the equation accepts a solution of the form

$$q(t) = c_1 \cos \omega t + c_2 \sin \omega t$$

i.e. the response is at the same frequency as that of the forcing, ω . Note that, here we have taken the forcing to be the real axis projection of a rotating vector. One can use both projections by representing the forcing as $f(t) = f_0 e^{i\omega t}$. The form of the solution should then be taken as $q(t) = ce^{i(\omega t - \phi)}$. The real (or imaginary) part of the solution would then be exactly same as the solution obtained by using the real (or imaginary) part of the forcing expressions alone.

c_1 and c_2 (or c , if one performs the calculations using the complex notation) are not arbitrary constants, as earlier in the case of natural response. Forced response of a linear system does not depend on initial conditions. The magnitude of forcing f_0 can be written as ka , where k is the spring stiffness, and a a displacement. Expressing f_0 as $f_0 = ka$ and dividing throughout by m we have

$$\ddot{q} + 2\xi\omega_n\dot{q} + \omega_n^2 q = \omega_n^2 a \cos \omega t$$

Figure 1.8: **Transfer function between forcing and displacement**Figure 1.9: **Transfer function between forcing and velocity**

Substitute $q(t)$ in the equation, and determine c_1 and c_2 by equating the cos and sin components (for complex domain calculations equate the real and imaginary parts to find c and ϕ). The final solution has the following form.

$$q(t) = \frac{f_0/k}{\sqrt{\left[1 - \left(\frac{\omega}{\omega_n}\right)^2\right]^2 + \left[2\xi\frac{\omega}{\omega_n}\right]^2}} \cos(\omega t - \phi) \quad := \quad a\mathbf{G}_d \cos(\omega t - \phi)$$

$$\phi = \tan^{-1} \frac{2\xi\frac{\omega}{\omega_n}}{1 - \left(\frac{\omega}{\omega_n}\right)^2}$$

where ϕ is the phase angle by which the displacement lags the forcing. The ratio of the magnitude of displacement to the magnitude of forcing is a transfer function

$$\frac{|q|}{|f|} = \frac{a\mathbf{G}_d}{f_0} = \frac{a\mathbf{G}_d}{ka}$$

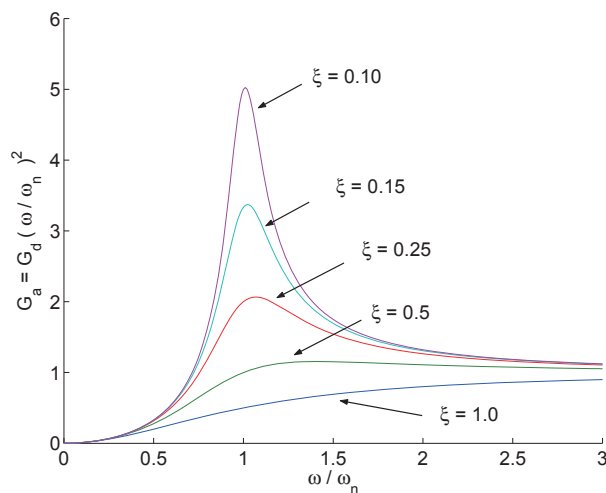


Figure 1.10: **Transfer function between forcing and acceleration**

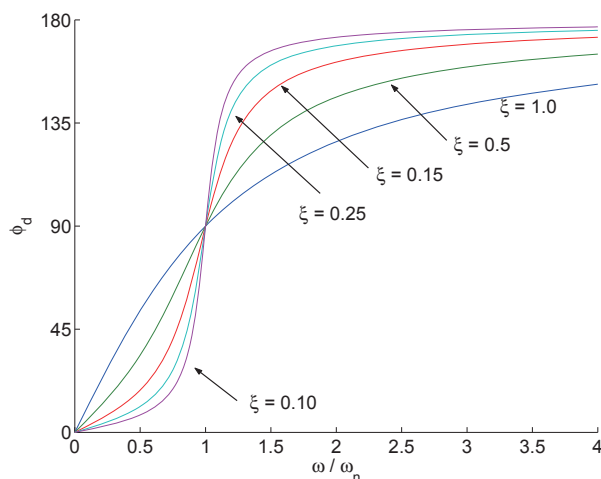


Figure 1.11: **Phase by which response (displacement) lags forcing**

Re-arrange to obtain

$$\frac{|q|}{|f|/k} = \mathbf{G}_d$$

The numerator of the left hand side is the maximum displacement including dynamics. The denominator of the left hand side is the maximum displacement ignoring dynamics. Thus the ratio gives a magnification factor due to the dynamics. This can be termed the displacement gain function, \mathbf{G}_d . \mathbf{G}_d is a function of ω/ω_n and ξ .

For $\xi = 0$ and $\omega/\omega_n = 1$ we have an infinite response. Physically, the response blows up in time domain. The equation and the solution take the following form.

$$\begin{aligned} \ddot{q} + \omega_n^2 q &= \omega_n^2 a \cos \omega_n t \\ q(t) &= \frac{a}{2} \omega_n t \cos(\omega_n t - \pi/2) \end{aligned}$$

The velocity-force, and acceleration-force transfer functions are $|\dot{q}|/|F|$ and $|\ddot{q}|/|F|$. To express

them as functions of ω/ω_n non-dimensionalize as

$$\frac{|\dot{q}|}{\frac{|f|}{k}\omega_n} = \mathbf{G}_d \frac{\omega}{\omega_n} = \mathbf{G}_v$$

$$\frac{|\ddot{q}|}{\frac{|f|}{k}\omega_n^2} = \mathbf{G}_d \left(\frac{\omega}{\omega_n} \right)^2 = \mathbf{G}_a$$

Note that the denominator of the left hand side expression for \mathbf{G}_a represents the rigid body acceleration of m in absence of dynamics. To obtain the phase by which the velocity and acceleration lags the forcing, differentiate the response

$$\dot{q}(t) = -a\mathbf{G}_d\omega \sin(\omega t - \phi) = a\mathbf{G}_d\omega \cos(\omega t - [\phi - \pi/2]) = a\mathbf{G}_d\omega \cos(\omega t - \phi_v)$$

$$\ddot{q}(t) = a\mathbf{G}_d\omega \cos(\omega t - [\phi - \pi]) = a\mathbf{G}_d\omega \cos(\omega t - \phi_a)$$

It follows, as we expect

$$\phi_v = \phi - \pi/2$$

$$\phi_a = \phi - \pi$$

The displacement, velocity, and acceleration transfer functions are shown in figures 1.8, 1.9, and 1.10. The displacement phase lag with respect to forcing is shown in figure 1.11.

The total response of the system, for a realistic case, then becomes

$$q(t) = e^{-\xi\omega_n t} A \cos(\sqrt{1 - \xi^2}\omega_n t - \phi) + \frac{a}{\sqrt{\left[1 - \left(\frac{\omega}{\omega_n}\right)^2\right]^2 + \left[2\xi\frac{\omega}{\omega_n}\right]^2}} \cos(\omega t - \phi)$$

By realistic case, it is assumed that $0 \leq \xi < 1$, and $\omega \neq \omega_n$ if $\xi = 0$.

The first part is the initial condition response. The second part is the steady state response. In case of numerical integration both are obtained as part of the solution. If the periodic response is desired, one must wait till the initial condition response dies down. For high damping, the initial condition response dies down quickly. For low damping, it takes a long time. For zero damping it remains forever. Methods like Harmonic Balance and Finite Element in Time are used to obtain the steady state solution in such cases, when the steady state solution is desired uncontaminated with the initial condition response.

1.2.2 Reduction to First-Order Form

The second-order eqn. 1.16 can be reduced to first-order form by the substitution

$$x_1 = q, \quad x_2 = \dot{q}$$

It follows

$$\dot{x}_1 = \dot{q} = x_2$$

$$\dot{x}_2 = \ddot{q} = (-c/m)x_2 + (-k/m)x_1 + (1/m)f$$

leading to

$$\begin{pmatrix} \dot{x}_1 \\ \dot{x}_2 \end{pmatrix} = \begin{bmatrix} 0 & 1 \\ -k/m & -c/m \end{bmatrix} \begin{pmatrix} x_1 \\ x_2 \end{pmatrix} + \begin{pmatrix} 0 \\ f/m \end{pmatrix}$$

In matrix notation

$$\dot{\mathbf{x}} = \mathbf{A}\mathbf{x} + \mathbf{f} \quad (1.17)$$

\mathbf{x} is the vector of *states* describing the system and \mathbf{f} is a vector of excitations. For a general second-order system with n degrees of freedom, q_1, q_2, \dots, q_n , eqn. 1.16 becomes

$$\mathbf{M}\ddot{\mathbf{q}} + \mathbf{C}\dot{\mathbf{q}} + \mathbf{K}\mathbf{q} = \mathbf{F}$$

The corresponding first-order system now has a state vector \mathbf{x} of size $2n$ containing q_1, q_2, \dots, q_n and $\dot{q}_1, \dot{q}_2, \dots, \dot{q}_n$, with

$$\mathbf{A} = \begin{bmatrix} \mathbf{0} & \mathbf{I}_n \\ -\mathbf{M}^{-1}\mathbf{K} & -\mathbf{M}^{-1}\mathbf{C} \end{bmatrix} \quad \text{of size } 2n \times 2n$$

$$\mathbf{f} = \begin{bmatrix} \mathbf{0} \\ \mathbf{M}^{-1}\mathbf{F} \end{bmatrix} \quad \text{of size } 2n \times 1$$

The forcing \mathbf{F} can be a superposition of m separate excitations u_1, u_2, \dots, u_m .

$$\mathbf{F} = \mathbf{G}\mathbf{u}$$

where \mathbf{G} is of size $n \times m$. The first-order system then takes the following form

$$\dot{\mathbf{x}} = \mathbf{A}\mathbf{x} + \mathbf{B}\mathbf{u} \quad (1.18)$$

where \mathbf{B} is now given as

$$\mathbf{B} = \begin{bmatrix} \mathbf{0} \\ \mathbf{M}^{-1}\mathbf{G} \end{bmatrix} \quad \text{of size } 2n \times m$$

In the previous section we had obtained transfer functions between q , \dot{q} and f , directly using the solution of the second-order equation. The same transfer functions can also be obtained using the first-order eqn. 1.18. For this simple case, $n = m = 1$, $\mathbf{G} = 1$, $\mathbf{u} = f$, and

$$\mathbf{B} = \begin{bmatrix} 0 \\ 1/m \end{bmatrix}$$

Under many circumstances, often encountered in control theory, the second-order system has the following form

$$\ddot{\mathbf{q}} + \mathbf{A}'\dot{\mathbf{q}} + \mathbf{B}'\mathbf{q} = \mathbf{C}'\ddot{\mathbf{u}} + \mathbf{D}'\dot{\mathbf{u}} + \mathbf{E}'\mathbf{u}$$

where the forcing is a function of the excitation and its derivatives. The corresponding first-order form is given by

$$\mathbf{A} = \begin{bmatrix} \mathbf{0} & \mathbf{I}_n \\ -\mathbf{B}' & -\mathbf{A}' \end{bmatrix} \quad \text{of size } 2n \times 2n$$

$$\mathbf{B} = \begin{bmatrix} \mathbf{B}_1 \\ \mathbf{B}_2 \end{bmatrix} \quad \text{of size } 2n \times m$$

where

$$\mathbf{B}_1 = \mathbf{D}' - \mathbf{A}'\mathbf{C}'$$

$$\mathbf{B}_2 = \mathbf{E}' - \mathbf{A}'\mathbf{B}_1 - \mathbf{B}'\mathbf{C}'$$

The states are defined as

$$\mathbf{x}_1 = \mathbf{q} - \mathbf{C}'\mathbf{u}$$

$$\mathbf{x}_2 = \dot{\mathbf{q}} - \mathbf{C}'\dot{\mathbf{u}} - \mathbf{B}_1\mathbf{u}$$

1.2.3 Rotor Blade Dynamics

The rotor blades undergo three dominant dynamic motions.

β : flap motion

normal to the plane of rotation

positive for upward motion

ζ : lag motion

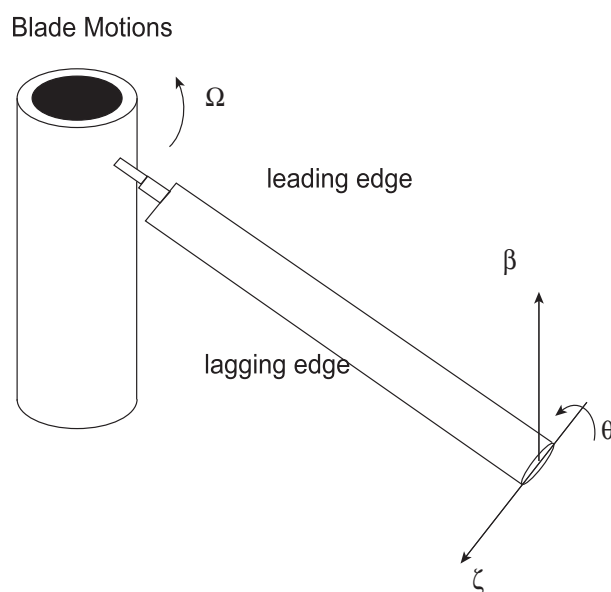
motion in the plane of rotation

positive lag opposes rotation lead-lag is in opposite direction to lag-motion

θ : pitch motion

rotation of blade about elastic axis

positive for nose up motion



The flap motion of the blades, we shall see, relieves the root moments. The letting the blades flap freely, in response to lift, the blades are allowed to take up a certain orientation in space. The direction of the rotor thrust is determined by this orientation.

The flap motion will induce Coriolis moment in the lag direction. To relieve this lag moment at the root of the blade, a lag hinge is introduced.

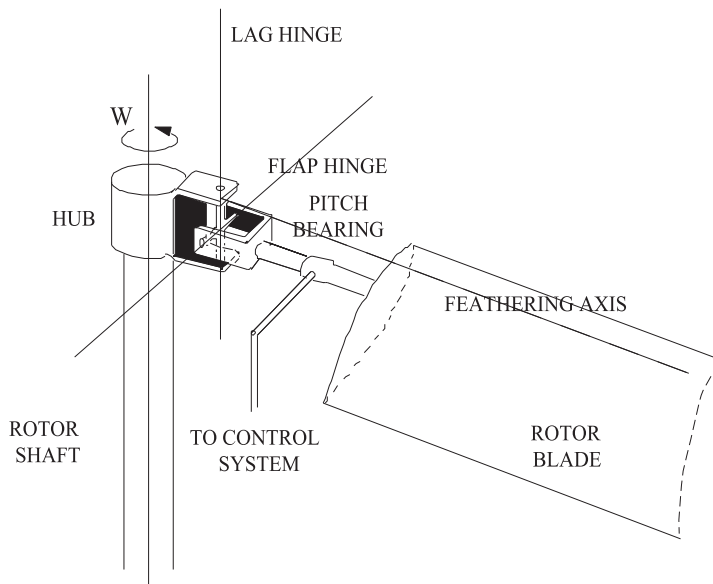
The pitch motion is a blade dynamic response to aerodynamic pitching moments. The pitch control angle, $\theta_{con}(\psi)$, on the other hand, is a pilot input provided via a hub mechanism e.g. a pitch bearing or torque tube. Note that the net pitch angle at a blade section consists of three components: (1) pitch motion $\theta(r, \psi)$, (2) pitch control angle $\theta_{con}(\psi)$, and (3) the in-built twist $\theta_{tw}(r)$. The first component, pitch motion, is also called elastic twist. The second component, pitch control angle, is a means to control the direction of thrust vector. The blades are still free to flap, but they flap in response to a lift distribution which is influenced via the pitch control angles. Thus the blade orientation in space, and the resultant thrust direction can be controlled. The pitch control angles have a steady (called collective) and 1/rev components. The sin part of the 1/rev component is called the longitudinal cyclic, and the cos part is called the lateral cyclic.

The advent of cyclic pitch (Pescare - 1924) helped to control the thrust vector. The thrust vector can be oriented to the desired direction without changing the shaft orientation. Therefore,

the inclusion of the flap hinge and the cyclic pitch converts a static problem into a dynamic one because the blade motion now becomes important. In this chapter we shall study the flap motion to understand the basic principles behind the rotor and moments generated by the rotor.

The next figure shows a typical articulated rotor blade with mechanical flap and lag hinges, and a pitch bearing.

For hingeless rotor, the mechanical flap and lag hinges are eliminated. Virtual hinges are introduced by making the the blade quite flexible structurally near the root so that it behaves as if there are hinges for flap and lag motions.



1.2.4 Flap motion of a rotor blade

Consider the general model where a blade flaps about a hinge located at a distance e from the shaft axis. See Fig. 6.2. The equation governing the blade flapping motion is obtained as follows

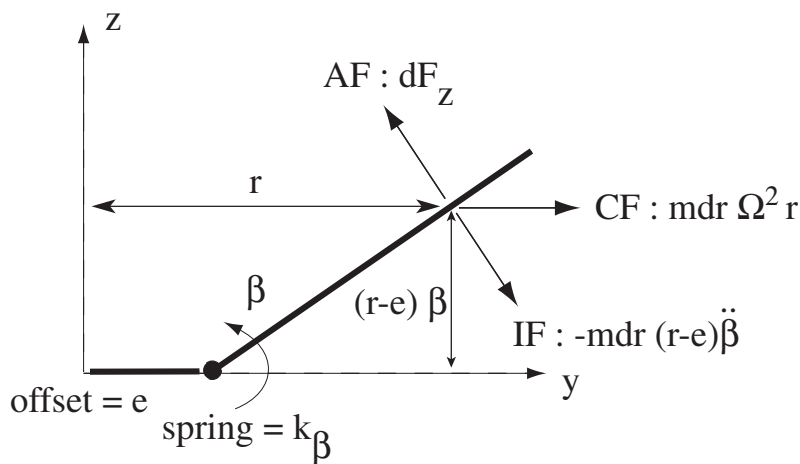


Figure 1.12: Flapping motion about a hinge

External moments about hinge = (Blade inertia about hinge). (angular acceleration $\ddot{\beta}$)

The right hand side of the above equation can be defined as the negative of inertial moment about the hinge. Then we have

$$\begin{aligned} \text{External moments about hinge} &= -\text{Inertial moment about hinge} \\ \text{External moments about hinge} &+ \text{Inertial moment about hinge} = 0 \\ \text{Net moments about hinge} &= 0 \end{aligned}$$

The blade inertia about the hinge is $\int_e^R m(r-e)^2 dr$. Thus the inertial moment is $-\int_e^R m(r-e)^2 \ddot{\beta} dr$. This is a moment generated by the spanwise integration of a force $-m(r-e)\ddot{\beta} dr$ acting on an element of length dr . This is defined here as the inertial force (IF) on the element. The external moments are the moments generated by the aerodynamic force (AF) and the centrifugal force (CF), and the restoring spring moment. The moment due to aerodynamic force is $\int_e^R (r-e)dF_z$. The moment due to centrifugal force is $\int_e^R (m dr)\Omega^2 r(r-e)\beta$. The restoring spring moment is $k_\beta \beta$. The forces are shown in Fig. 6.2. The moment balance about the hinge is then as follows.

$$\int_e^R (r-e)dF_z - \int_e^R (m dr)\Omega^2 r(r-e)\beta - k_\beta \beta = \int_e^R m(r-e)^2 \ddot{\beta} dr$$

which can be re-arranged to read

$$\int_e^R (r-e)dF_z - \int_e^R (m dr)\Omega^2 r(r-e)\beta - \int_e^R m(r-e)^2 \ddot{\beta} dr = k_\beta \beta$$

Physically, the above equation means that the aerodynamic moment is cancelled partly by the centrifugal moment, used partly to generate acceleration in flap, and the remainder is balanced by the spring at the hinge. Thus the net balance of moments at the hinge is provided by the spring, where $k_\beta \beta$ is the spring moment. This quantity is called the hinge moment or the root moment. Note that, in the case of perfectly articulated blade with a free hinge, i.e. $k_\beta = 0$, then the balance of aerodynamic and centrifugal moments is used up entirely by the blade acceleration. The root moment in this case is forced to zero. For hingeless blades or articulated blades with a spring the root moment is $k_\beta \beta$. Often a pre-cone angle β_p pre-set to reduce the hinge moment. For example β_p could be an estimate of steady flap angle. The equation then becomes

$$\int_e^R r dF_z - \int_e^R (m dr)\Omega^2 r(r-e)\beta - \int_e^R m(r-e)^2 \ddot{\beta} dr = k_\beta (\beta - \beta_p) \quad (1.19)$$

Define

$$\begin{aligned} I_\beta &= \int_e^R (r-e)^2 m dr \\ S_\beta &= \int_e^R (r-e) m dr \end{aligned}$$

The moment balance then becomes

$$k_\beta (\beta - \beta_p) = \int_e^R (r-e)dF_z - I_\beta \ddot{\beta} - \left(1 + \frac{eS_\beta}{I_\beta}\right) \Omega^2 I_\beta \beta \quad (1.20)$$

The above expression is important. It says that the root moment can be calculated either using the left hand side, or the right hand side. They are identical, and their equality generates the flap equation. The expression can be further simplified. First club the β terms together to obtain

$$I_\beta \ddot{\beta} + \left(1 + \frac{eS_\beta}{I_\beta} + \frac{k_\beta}{I_\beta \Omega^2}\right) \Omega^2 I_\beta \beta = \int_e^R (r-e)dF_z + k_\beta \beta_p$$

Then define $\left(1 + \frac{eS_\beta}{I_\beta} + \frac{k_\beta}{I_\beta\Omega^2}\right) = \nu_\beta^2$.

$$I_\beta\ddot{\beta} + \nu_\beta^2\Omega^2 I_\beta\beta = \int_e^R (r - e)dF_z + k_\beta\beta_p$$

Divide by I_b . I_b is the inertia about the shaft axis, i.e. $\int_0^R r^2 m dr$. I_β was the inertia about the hinge. For practical purposes we make the assumption $I_\beta \cong I_b$. Thus we have

$$\ddot{\beta} + \nu_\beta^2\Omega^2\beta = \frac{1}{I_b} \int_e^R (r - e)dF_z + \frac{k_\beta}{I_\beta}\beta_p \quad (1.21)$$

The above equation determines flap dynamics and shows a natural frequency of $\nu_\beta\Omega$, equal to ω_β say. The unit of this frequency ω_β is radians per second. Note that the unit of Ω is itself radians per second. Thus ν_β is a non-dimensional number with no units. If it is 1, that means ω_β , the natural frequency of flap dynamics is simply Ω . Physically, it means that the flap degree of freedom, when excited, completes one full cycle of oscillation just when the blade finishes one full circle of rotation. Recall, that this type of motion, which completes one cycle just in time for one circle of rotation, is called a 1/rev motion. Thus the ν_β is 1/rev. It is a non-dimensional frequency such that a phenomenon at that frequency just has time to finish one cycle within one blade revolution. A ν_β of say 1.15/rev means, that the flap motion when excited finishes one cycle well within one complete blade rotation and has time for a bit more. It finishes 1.15 cycles within one blade rotation.

The dynamics with time can be recast into dynamics with rotor azimuth, a more physically insightful expression for rotor problems. Divide by Ω^2 .

$$\frac{1}{\Omega^2}\ddot{\beta} + \nu_\beta^2\beta = \frac{1}{I_\beta\Omega^2} \int_e^R (r - e)dF_z + k_\beta\beta_p$$

Now

$$\begin{aligned} \psi &= \Omega t \\ \ddot{\beta} &= \frac{\partial^2\beta}{\partial t^2} = \Omega^2 \frac{\partial^2\beta}{\partial \psi^2} = \Omega^2 \beta^{**} \end{aligned}$$

The equation takes the following form.

$$\beta^{**} + \nu_\beta^2\beta = \gamma\overline{M}_\beta + \frac{\omega_{\beta_0}^2}{\Omega^2}\beta_p \quad \text{where} \quad \beta^{**} = \frac{\partial^2\beta}{\partial \psi^2} \quad (1.22)$$

Equation (1.22) describes the evolution of flap angle as the blade moves around the azimuth ψ .

$$\begin{aligned} \gamma &= \frac{\rho acR^4}{I_b} \\ \overline{M}_\beta &= \frac{1}{\rho ca(\Omega R)^2 R^2} \int_e^R (r - e)dF_z \\ \omega_{\beta_0}^2 &= \frac{k_\beta}{I_\beta} \end{aligned}$$

γ is called Lock number. \overline{M}_β is the aerodynamic flap moment in non-dimensional form. It is the same form as given earlier. ω_{β_0} is the non-rotating flap frequency. Note that it is zero in case of a perfect hinge with zero spring constant. ν_β is the rotating natural frequency of flap dynamics.

$$\begin{aligned}
\nu_\beta &= \sqrt{1 + \frac{eS_\beta}{I_\beta} + \frac{k_\beta}{I_\beta\Omega^2}} && \text{non-dimensional in /rev} \\
\omega_\beta &= \Omega \sqrt{1 + \frac{eS_\beta}{I_\beta} + \frac{k_\beta}{I_\beta\Omega^2}} && \text{dimensional in radians/sec} \\
S_\beta &= \frac{1}{2}m(R-e)^2 && \text{for uniform blade} \\
I_\beta &= \frac{1}{3}m(R-e)^3 && \text{for uniform blade} \\
\frac{eS_\beta}{I_\beta} &\cong \frac{3}{2} \frac{e}{R}
\end{aligned} \tag{1.23}$$

Now consider the case where the flap hinge contains both a spring and a damper. Equation 1.20 is then modified to read

$$k_\beta(\beta - \beta_p) + c_\beta\dot{\beta} = \int_e^R (r-e)dF_z - I_\beta\ddot{\beta} - \left(1 + \frac{eS_\beta}{I_\beta}\right)\Omega^2 I_\beta\beta \tag{1.24}$$

which simply means that the balance of moment at the hinge is provided by the spring and damper moments. Following the same procedure, equation 1.21 modifies to

$$\ddot{\beta} + \left(\frac{c_\beta}{I_\beta}\right)\dot{\beta} + \nu_\beta^2\Omega^2\beta = \frac{1}{I_b}\int_e^R (r-e)dF_z + \frac{k_\beta}{I_\beta}\beta_p \tag{1.25}$$

Equation 1.22 modifies to

$$\beta^{**} + \left(\frac{c_\beta}{I_b\Omega}\right)^*\dot{\beta} + \nu_\beta^2\beta = \gamma\overline{M}_\beta + \frac{\omega_{\beta_0}^2}{\Omega^2}\beta_p$$

or

$$\beta^{**} + (2\xi\nu_\beta)^*\dot{\beta} + \nu_\beta^2\beta = \gamma\overline{M}_\beta + \frac{\omega_{\beta_0}^2}{\Omega^2}\beta_p \tag{1.26}$$

where $c_\beta/I_b\Omega$ is conveniently expressed as $2\xi\nu_\beta$. ν_β is the flap frequency. ξ is defined as the damping ratio. This is simply one possible way of expressing the damping. Physically it means

$$\begin{aligned}
c_\beta &= 2\xi\nu_\beta I_b\Omega \\
&= 2\xi\omega_\beta I_b
\end{aligned}$$

c_β is a physical damper value. It does not depend on operating conditions. The damping ratio ξ , on the other hand, depends on the operating condition Ω , and blade property I_b . In general any frequency can be chosen to determine a corresponding ξ , as long as the physical value c_β remains unchanged. For example, in terms of the non-rotating frequency c_β can be expressed as follows.

$$c_\beta = 2\xi_{nr}\omega_{\beta_0}I_b$$

This ξ_{nr} is different from the ξ above obtained using the rotating frequency, but the physical flap damper value c_β ofcourse is the same.

1.3 Aero-elastic Response

Assume that a blade exhibits only flapping motion. Assume further a simple case when the blade has no pre-cone angle, no root-damper, i.e. $\beta_p=0$, $\xi=0$, and the flap hinge is at the center of rotation.

1.3.1 Flap response for non-rotating blades

First consider a stationary blade with no rotation. The flap equation 1.21 then becomes

$$\ddot{\beta} + \omega_{\beta 0}^2 \beta = 0$$

When perturbed the blade exhibits a motion

$$\beta(t) = A \cos(\omega_{\beta 0} t - \phi)$$

where A and ϕ are constants to be determined from the initial conditions $\beta(0)$ and $\dot{\beta}(0)$, and $\omega_{\beta 0} = \sqrt{k_{\beta}/I_{\beta}}$.

1.3.2 Flap response for rotating blades in vacuum

Now consider that the rotor is rotating in a vacuum chamber. There is a centrifugal force but no aerodynamic force. Equations 1.21 then becomes

$$\ddot{\beta} + \omega_{\beta}^2 \beta = 0$$

When perturbed the blade exhibits a motion

$$\beta(t) = A \cos(\omega_{\beta} t - \phi)$$

where A and ϕ are constants to be determined from the initial conditions $\beta(0)$ and $\dot{\beta}(0)$, and

$$\begin{aligned} \omega_{\beta} &= \Omega \sqrt{1 + \frac{3e}{2R} + \frac{\omega_{\beta 0}^2}{\Omega^2}} \\ &= \Omega \sqrt{1 + \frac{3e}{2R}} && \text{if } \omega_{\beta 0} = 0 \text{ i.e. } k_{\beta} = 0 \\ &= \Omega, && \text{if } k_{\beta} = 0, \text{ and } e = 0 \end{aligned}$$

However, for a rotating blade it is more convenient to non-dimensionalize the governing differential equation with Ω^2 which, as derived earlier, leads to the following

$$\beta^{**} + \nu_{\beta}^2 \beta = 0$$

$$\beta(\psi) = A \cos(\nu_{\beta} \psi - \phi)$$

where A and ϕ are constants to be determined from the initial conditions $\beta(0)$ and $\dot{\beta}^*(0)$, and

$$\begin{aligned} \nu_{\beta} &= \sqrt{1 + \frac{3e}{2R} + \frac{\omega_{\beta 0}^2}{\Omega^2}} \\ &= \sqrt{1 + \frac{3e}{2R}} && \text{if } \omega_{\beta 0} = 0 \text{ i.e. } k_{\beta} = 0 \\ &= 1 && \text{if } k_{\beta} = 0, \text{ and } e = 0 \end{aligned}$$

1.3.3 Flap response in hover

Consider a rotor in a hover stand. Or a helicopter in hover. From equation 1.22 we have

$$\beta^{**} + \nu_{\beta}^2 \beta = \gamma \overline{M_{\beta}}$$

where the aerodynamic flap moment is given by

$$\begin{aligned} \overline{M_{\beta}} &= \frac{1}{\rho c a (\Omega R)^2 R^2} \int_0^R (r - e) dF_z \\ &\cong \frac{1}{\rho c a (\Omega R)^2 R^2} \int_0^R r dF_z \quad \text{simplifying assumption for small } e \\ &= \frac{1}{\rho c a (\Omega R)^2 R^2} \int_0^R r \frac{1}{2} \rho c c_l U_T^2 dr \\ &= \frac{1}{\rho c a (\Omega R)^2 R^2} \int_0^R r \frac{1}{2} \rho c a \left(\theta - \frac{U_P}{U_T} \right) U_T^2 dr \\ &= \frac{1}{2} \int_0^1 x (\theta u_t^2 - u_p u_t) dx \end{aligned}$$

For hover we have

$$\begin{aligned} U_T &= \Omega r \\ U_P &= \lambda \Omega R + r \dot{\beta} \end{aligned}$$

Note that, compared to the simple blade element formulation given earlier, U_P now has an addition component $r\dot{\beta}$ from blade flapping. Thus the blade dynamics, or elastic deformation affects the aerodynamic forces. In non-dimensional form we have

$$\begin{aligned} u_t &= x \\ u_p &= \lambda + x \dot{\beta}^* \end{aligned}$$

Assume θ to be constant in hover, θ_0 . The aerodynamic hinge moment then becomes

$$\begin{aligned} \overline{M_{\beta}} &= \frac{1}{2} \int_0^1 x (\theta_0 x^2 - x^2 \dot{\beta}^* - \lambda x) dx \\ &= \frac{\theta_0}{8} - \frac{\lambda}{6} - \frac{\dot{\beta}^*}{8} \end{aligned}$$

The aero-elastic form of the flap equation then becomes

$$\beta^{**} + \frac{\gamma}{8} \dot{\beta}^* + \nu_{\beta}^2 \beta = \gamma \left(\frac{\theta_0}{8} - \frac{\lambda}{6} \right)$$

The steady state solution is a constant

$$\beta_0 = \frac{\gamma}{\nu_{\beta}^2} \left(\frac{\theta_0}{8} - \frac{\lambda}{6} \right)$$

Suppose the pilot provides a 1/rev control input in addition to a collective θ_0

$$\begin{aligned} \theta(t) &= \theta_0 + \theta_{1s} \sin \Omega t \\ \theta(\psi) &= \theta_0 + \theta_{1s} \sin \psi \end{aligned}$$

The steady state response contains not only a constant term but also a periodic term.

$$\beta(\psi) = \beta_0 + A \sin(\psi - \phi)$$

The constant term is same as before. The magnitude and phase of the periodic term can be obtained from the expression derived earlier for single degree of freedom systems. We have

$$\begin{aligned}\omega_n &= \nu_\beta \\ \omega &= 1 \\ 2\xi\omega_n &= \frac{\gamma}{8}\end{aligned}$$

Using the above expressions we have

$$\begin{aligned}A &= \frac{\theta_{1s}}{\sqrt{(\nu_\beta^2 - 1)^2 + (\frac{\gamma}{8})^2}} \\ \phi &= \tan^{-1} \frac{\frac{\gamma}{8}}{\nu_\beta^2 - 1} \\ &= \frac{\pi}{2} - \tan^{-1} \frac{\nu_\beta^2 - 1}{\frac{\gamma}{8}}\end{aligned}$$

Thus the maximum flap response occurs almost 90° after maximum forcing. For $\nu_\beta = 1$, ϕ exactly 90° . Generally ν_β is slightly greater than one. Then ϕ is close to, but slightly lower than 90° . The flap solution is

$$\beta(\psi) = \frac{\gamma}{\nu_\beta^2} \left(\frac{\theta_0}{8} - \frac{\lambda}{6} \right) + \frac{\theta_{1s}}{\sqrt{(\nu_\beta^2 - 1)^2 + (\frac{\gamma}{8})^2}} \sin \left(\psi - \frac{\pi}{2} + \tan^{-1} \frac{\nu_\beta^2 - 1}{\frac{\gamma}{8}} \right)$$

Assume $\nu_\beta = 1$. Then,

$$\begin{aligned}\beta(\psi) &= \gamma \left(\frac{\theta_0}{8} - \frac{\lambda}{6} \right) + \frac{8\theta_{1s}}{\gamma} \sin(\psi - \frac{\pi}{2}) \\ &= \gamma \left(\frac{\theta_0}{8} - \frac{\lambda}{6} \right) + \left(-\frac{8\theta_{1s}}{\gamma} \right) \cos \psi \\ &= \gamma \left(\frac{\theta_0}{8} - \frac{\lambda}{6} \right) + \beta_{1c} \cos \psi\end{aligned}$$

β_{1c} is, by definition, the cosine component of the flap response. Here $\beta_{1c} = (-8\theta_{1s})/\gamma$. Note that a sine input to the controls produce a cosine response in flap and vice-versa. This is simply because the flap motion occurs in resonance to the applied forcing, and therefore has a 90° phase lag with respect to it. This is the case for rotors with flap frequency exactly at $1/\text{rev}$. For slightly higher flap frequencies, a sine input generates both a cosine as well as a sine output. However, as long as the flap frequency is near $1/\text{rev}$ (e.g. $1.15/\text{rev}$ for hingeless rotors, and $1.05/\text{rev}$ for articulated rotors), a sine input generates a dominant cosine output, and vice-versa.

1.3.4 Flap response in forward flight

Consider a rotor in a wind tunnel, or in forward flight. In forward flight the sectional velocity components vary with azimuth. The pitch variation in forward flight is of the form

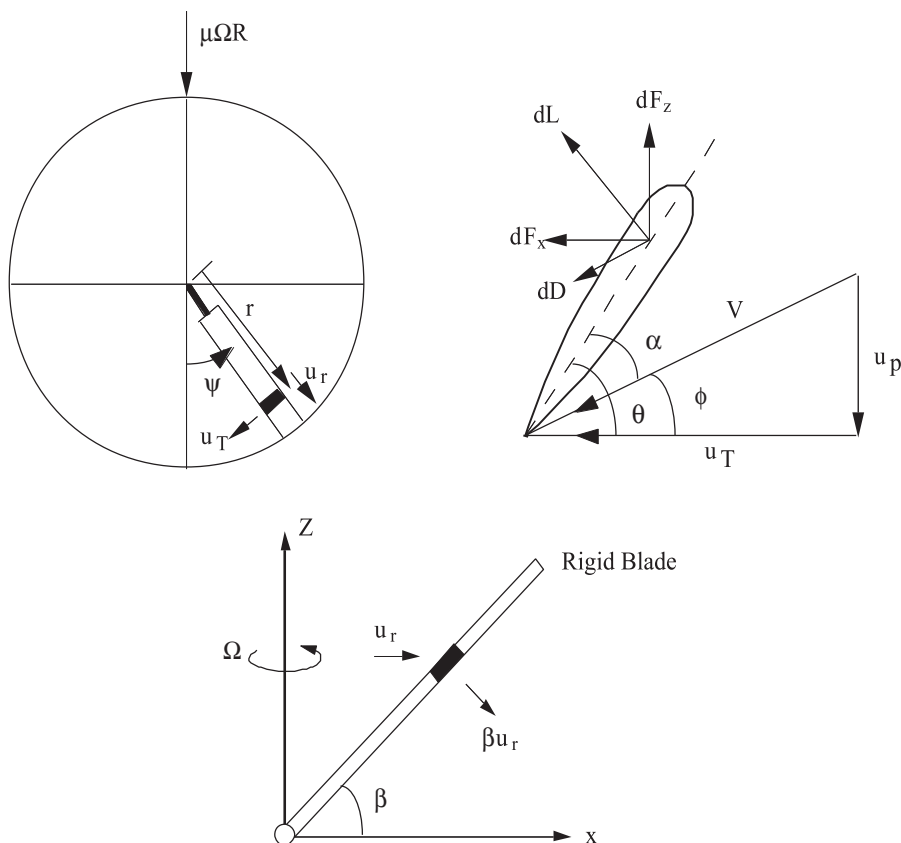
$$\theta(r, \psi) = \theta_0 + \theta_{tw} \frac{r}{R} + \theta_{1c} \cos \psi + \theta_{1s} \sin \psi \quad (1.27)$$

where θ_0 , θ_{1c} , and θ_{1s} are called trim control inputs. They are provided to influence the steady and first harmonic flap response. The total flap response in forward flight contains a large number of harmonics.

$$\beta(\psi) = \beta_0 + \beta_{1c} \cos \psi + \beta_{1s} \sin \psi + \text{higher harmonics} \quad (1.28)$$

For simplicity, let us consider only the first harmonics for the time being. Retaining only the first harmonics are often adequate for performance evaluations of a helicopter. By performance we mean rotor power, lift, drag, and aircraft trim attitudes. We shall study aircraft trim in a later section. Here, let us first see the sectional velocity components. Then the blade element forces. And then calculate the flap response.

The airflow components at a section are shown in the following figures.



$$\phi = \frac{U_P}{U_T}$$

$$\Gamma = \frac{U_R}{U_T}$$

where Γ is the incident yaw angle at the section. The sectional drag acts along this angle. U_T and U_P are the tangential and perpendicular velocity components at a section. U_R is radial, not along the blade. Along the blade, and perpendicular to the blade components of U_R would be

$$U_R \cos \beta = \mu \Omega R \cos \psi \cos \beta$$

$$U_R \sin \beta = \mu \Omega R \cos \psi \sin \beta$$

Let us define the inflow $\lambda\Omega R$ to be positive downwards acting along the Z axis. The Z axis is aligned parallel to the rotor shaft. Then the mutually perpendicular velocity components at each section are

$$U_T = \Omega r + \mu\Omega R \sin \psi$$

$$U_P = \lambda\Omega R \cos \beta + r\dot{\beta} + \mu\Omega R \cos \psi \sin \beta$$

$$U_R = \mu\Omega R \cos \psi$$

U_S is the spanwise component acting along the blade. Assume $\cos \beta \cong 1$ and $\sin \beta \cong \beta$. Non-dimensionalize the velocity components w.r.t ΩR to obtain:

$$\frac{u_t}{\Omega R} = x + \mu \sin \psi$$

$$\frac{u_p}{\Omega R} = \lambda + x \beta^* + \beta \mu \cos \psi$$

$$\frac{u_r}{\Omega R} = \mu \cos \psi$$

The blade forces are

$$\begin{aligned} dF_z &= (dL \cos \phi - dD \sin \phi) \cos \beta \\ &\cong dL \quad \text{because } dD \cong 0.1dL \\ &= \frac{1}{2} \rho c a U_T^2 \left(\theta - \frac{U_P}{U_T} \right) dr \\ &= \frac{1}{2} \rho c a dr (U_T^2 \theta - U_P U_T) \end{aligned} \tag{1.29}$$

$$\begin{aligned} dF_x &= dL \sin \phi + dD \cos \phi \cos \Gamma \\ &\cong dF_z \frac{U_P}{U_T} + dD \\ &= \frac{1}{2} \rho c a U_T^2 \left(\theta - \frac{U_P}{U_T} \right) \frac{U_T}{U_P} dr + \frac{1}{2} \rho c a U_T^2 C_d dr \\ &= \frac{1}{2} \rho c a dr \left(U_P U_T \theta - U_P^2 + \frac{C_d}{a} U_T^2 \right) \end{aligned} \tag{1.30}$$

$$\begin{aligned} dF_r &= -dL \sin \beta + dD \sin \Gamma \\ &\cong -\beta dL \\ &= -\beta \frac{1}{2} \rho c a dr (U_T^2 \theta - U_P U_T) \end{aligned} \tag{1.31}$$

The aerodynamic flap moment is then

$$\begin{aligned}
\overline{M}_\beta &= \frac{1}{\rho ac \Omega^2 R^4} \int_0^R r dF_z \\
&= \frac{1}{2} \int_0^1 x \left[\left(\frac{u_T}{\Omega R} \right)^2 \theta - \left(\frac{u_p}{\Omega R} \right) \left(\frac{u_T}{\Omega R} \right) \right] dx \\
&= \frac{1}{2} \int_0^1 x (u_t^2 \theta - u_p u_t) dx \\
&= \left(\frac{1}{8} + \frac{\mu}{3} \sin \psi + \frac{\mu^2}{4} \sin^2 \psi \right) (\theta_0 + \theta_{1c} \cos \psi + \theta_{1s} \sin \psi) \\
&\quad + \theta_{tw} \left(\frac{1}{10} + \frac{\mu^2}{6} \sin^2 \psi + \frac{\mu}{4} \sin \psi \right) - \lambda \left(\frac{1}{6} + \frac{\mu}{4} \sin \psi \right) \\
&\quad - \beta^* \left(\frac{1}{8} + \frac{\mu}{6} \sin \psi \right) - \mu \beta \cos \psi \left(\frac{1}{6} + \frac{\mu}{4} \sin \psi \right)
\end{aligned}$$

Recall the flap equation (1.22)

$$\beta^{**} + \nu_\beta^2 \beta = \gamma \overline{M}_\beta + \frac{\omega_{\beta_0}^2}{\Omega^2} \beta_p$$

where γ is the Lock number, $(\rho ac R^4 / I_b)$, ω_{β_0} is the nonrotating flap frequency, β_p is the precone angle and ν_β is the rotating flap frequency in terms of rotational speed. The term $\omega_{\beta_0}^2$ is used to model a hingeless blade, or an articulated blade with a flap spring. For an articulated blade without a flap spring, this term is zero. In addition, if there is no hinge offset (teetering blade or gimbal blade) $\nu_\beta = 1$. The simplified flap equation in this case becomes

$$\beta^{**} + \beta = \gamma \overline{M}_\beta \quad (1.32)$$

Substitute \overline{M}_β and β in the flap equation (1.21) and match the constant, $\cos \psi$, and $\sin \psi$ terms on both sides to obtain the solution as follows.

$$\begin{aligned}
\nu_\beta^2 \beta_0 &= \gamma \left[\frac{\theta_0}{8} (1 + \mu^2) + \frac{\theta_{tw}}{10} (1 + \frac{5}{6} \mu^2) + \frac{\mu}{6} \theta_{1s} - \frac{\lambda}{6} \right] + \frac{\omega_{\beta_0}^2}{\Omega^2} \beta_p \\
(\nu_\beta^2 - 1) \beta_{1c} &= \gamma \left[\frac{1}{8} (\theta_{1c} - \beta_{1s}) \left(1 + \frac{1}{2} \mu^2 \right) - \frac{\mu}{6} \beta_0 \right] \\
(\nu_\beta^2 - 1) \beta_{1s} &= \gamma \left[\frac{1}{8} (\theta_{1s} + \beta_{1c}) \left(1 - \frac{1}{2} \mu^2 \right) + \frac{\mu}{3} \theta_0 - \frac{\mu}{4} \lambda + \frac{\mu^2}{4} \theta_{1s} + \frac{\mu}{4} \theta_{tw} \right]
\end{aligned} \quad (1.33)$$

The solution to (1.32) can be obtained by simply putting $\nu_\beta = 1$ in the above expressions.

$$\begin{aligned}
\beta_0 &= \gamma \left[\frac{\theta_0}{8} (1 + \mu^2) + \frac{\theta_{tw}}{10} (1 + \frac{5}{6} \mu^2) - \frac{\mu}{6} \theta_{1s} - \frac{\lambda}{6} \right] \\
\beta_{1s} - \theta_{1c} &= \frac{-\frac{4}{3} \mu \beta_0}{1 + \frac{1}{2} \mu^2} \\
\beta_{1c} + \theta_{1s} &= \frac{-\left(\frac{8}{3}\right) \mu \left[\theta_0 - \frac{3}{4} \lambda + \frac{3}{4} \mu \theta_{1s} + \frac{3}{4} \theta_{tw} \right]}{1 - \frac{1}{2} \mu^2}
\end{aligned} \quad (1.34)$$

Recall that we studied the effect of cyclic pitch variation in hover. A sine input in cyclic produced a cosine output in flap, and vice-versa. This was when the rotor operated under resonance conditions where $\nu_\beta = 1$. The flap solution in forward flight for $\nu_\beta = 1$ is given above. Substitute $\mu = 0$ in the above expression to re-obtain the hover results.

Put $\mu = 0$ in the solution of equation (1.21).

$$\beta_{1s} - \theta_{1c} = 0$$

$$\beta_{1c} + \theta_{1s} = 0$$

This means for pitch variation

$$\theta = \theta_0 + \theta_{1c} \cos \psi + \theta_{1s} \sin \psi$$

The flap response will be

$$\beta = \beta_0 + \theta_{1c} \cos(\psi - 90^\circ) + \theta_{1s} \sin(\psi - 90^\circ)$$

Therefore, for articulated blades with zero hinge spring and zero hinge offset, the flap response lags pitch motion by 90° (resonance condition).

For a hingeless blades, or articulated blades with non-zero hinge springs, or articulated blades with non-zero hinge offsets, put $\mu = 0$ in the solution of (1.21).

$$\begin{aligned} \beta_0 &= \frac{\gamma}{v_\beta^2} \left[\frac{\theta_0}{8} - \frac{\lambda}{6} \right] + \frac{\omega_{\beta 0}^2}{\Omega^2} \beta_p \\ \beta_{1s} &= \frac{\theta_{1c} + (v_\beta^2 - 1) \frac{8}{\gamma} \theta_{1s}}{1 + \left[(v_\beta^2 - 1) \frac{8}{\gamma} \right]^2} \\ \beta_{1c} &= \frac{-\theta_{1s} + (v_\beta^2 - 1) \frac{8}{\gamma} \theta_{1c}}{1 + \left[(v_\beta^2 - 1) \frac{8}{\gamma} \right]^2} \end{aligned} \tag{1.35}$$

Thus θ_{1s} produces both β_{1s} and β_{1c} . Similarly θ_{1c} produces both β_{1s} and β_{1c} . This is an off-resonance condition where the forcing frequency is less than the natural frequency. Lateral flap deflection is now caused by longitudinal cyclic pitch θ_{1s} , in addition to lateral pitch θ_{1c} . Recall that the phase lag of flap response with respect to the pitch motion was shown earlier to be

$$\phi = 90^\circ - \tan^{-1} \frac{(v_\beta^2 - 1)}{\frac{8}{\gamma}}$$

1.4 Introduction to Loads

The distribution of aerodynamic and centrifugal forces along the span, and the structural dynamics of the blade in response to these forces create shear loads and bending loads at the blade root. For a zero hinge offset, the blade root is at the center of rotation. For a non-zero hinge offset, it is at a distance e outboard from the center of rotation. By 'loads' we mean 'reaction' forces generated by the net balance of all forces acting over the blade span. Let s_x , s_r , and s_z be the three shear loads, in-plane, radial, and vertical. Let n_f , n_t , and n_l be the bending loads, flap bending moment, torsion moment (positive for leading edge up), and chord bending moment (positive in lag direction). They occur at the blade root, rotate with the blade, and vary with the azimuth angle. Thus they are called the rotating root loads. Or simply root loads or root reactions.

1.4.1 Root shear load

The vertical, in-plane, and radial root shear are as follows

$$\begin{aligned} s_z &= \int_e^R \left[\frac{dF_z}{dr} - m(r-e)\ddot{\beta} \right] dr \\ s_x &= \int_e^R \left[\frac{dF_x}{dr} \right] dr \\ s_r &= \int_e^R \left[m\Omega^2 r - \beta \frac{dF_r}{dr} \right] dr \end{aligned}$$

1.4.2 Root bending load

Like in the case of root shears, the root bending loads are obtained by integrating the moments generated by the sectional forces about the root. The flap bending moment n_f is as follows. Recall, that the same expression was derived in equation (1.19).

$$\begin{aligned} n_f &= \int_e^R (r-e)dF_z - \int_e^R (m dr)\Omega^2 r(r-e)\beta - \int_e^R m(r-e)^2 \ddot{\beta} dr \\ &= k_\beta(\beta - \beta_p) \end{aligned} \tag{1.36}$$

Now use the non-dimensional form of the flap frequency as given in equation (1.23) to replace k_β in terms of the flap frequency ν_β .

$$\begin{aligned} n_f &= k_\beta(\beta - \beta_p) \\ &= \left(\nu_\beta^2 - 1 - \frac{3}{2} \frac{e}{R} \right) I_\beta \Omega^2 (\beta - \beta_p) \\ &= (\nu_\beta^2 - 1) I_\beta \Omega^2 (\beta - \beta_p) \quad \text{for hinge offset } e/R = 0 \\ &= (\nu_\beta^2 - 1) I_\beta \Omega^2 \beta \quad \text{for } e/R = 0, \text{ and precone } \beta_p = 0 \end{aligned} \tag{1.37}$$

Thus, the flap bending moment at the root is related to the flap frequency, and flap dynamics. Similarly, later we shall see that the lag and torsion moments depend on lag and torsion frequencies, and lag and torsion dynamics. Here, we have considered only the flap motion. The lag and torsion moments then simply become

$$n_l = \int_e^R \left[(r-e) \frac{dF_x}{dr} \right] dr \tag{1.38}$$

$$n_t = \int_e^R \left[\frac{dM_x}{dr} \right] dr \tag{1.39}$$

where dM_x is the nose-up aerodynamic pitching moment acting on the airfoils over each section of length dr . dM_x is about the elastic axis, which is generally close to quarter-chord.

1.4.3 Rotating frame hub loads

The rotating frame hub loads are obtained by simply transferring the root loads to the hub. By hub we mean the center of rotation, i.e. the rotor shaft axis. Note that in the case of zero hinge offset, $e/R = 0$, then the root loads are directly the rotating frame hub loads.

$$\begin{aligned} f_x &= s_x & m_x &= n_f \\ f_y &= s_r & m_y &= n_t \\ f_z &= s_z & m_z &= -n_l \end{aligned} \tag{1.40}$$

For a non-zero hinge offset

$$\begin{aligned}
 f_x &= s_x & m_x &= n_f + es_z \\
 f_y &= s_r & m_y &= n_t \\
 f_z &= s_z & m_z &= -n_l - es_x
 \end{aligned}
 \tag{1.41}$$

In the case of non-zero hinge offset, m_x and m_z can be obtained directly by integrating the moments generated by the blade forces about the hub, instead of about the hinge.

It is important to note that the rotating frame hub loads are associated with each blade. At any instant of time, each blade produces six rotating frame hub loads. For each blade, they act in three directions along an axis system stuck to its root. This local axis system rotates with the blade. Thus, before the contribution from all blades at the hub can be added up, the rotating frame loads from each blade must be resolved into three fixed directions which do not rotate with any of the blades. This is called a fixed frame.

1.4.4 Fixed frame hub loads

The fixed frame hub loads are often simply called the hub loads. They are obtained from the rotating frame loads by the following two steps.

1. Resolve the rotating frame loads of each blade in a fixed frame.
2. Sum the fixed frame loads from all N_b blades.

Let $m = 1, 2, \dots, N_b$ be the blade number. ψ_m be the azimuthal location of each blade m . Then we have

$$\begin{aligned}
 F_x &= \sum_{m=1}^{N_b} (f_y \cos \psi_m + f_x \sin \psi_m) \\
 F_y &= \sum_{m=1}^{N_b} (f_y \sin \psi_m - f_x \cos \psi_m) \\
 F_z &= \sum_{m=1}^{N_b} f_z \\
 M_x &= \sum_{m=1}^{N_b} (m_x \sin \psi_m + m_y \cos \psi_m) \\
 M_y &= \sum_{m=1}^{N_b} (-m_x \cos \psi_m + m_y \sin \psi_m) \\
 M_z &= \sum_{m=1}^{N_b} m_z
 \end{aligned}
 \tag{1.42}$$

In general f_x, f_y, f_z and m_x, m_y, m_z contain all harmonics $1, 2, 3, \dots, \infty/\text{rev}$.

Step 1 redistributes the magnitudes of individual harmonics, but retains all harmonics. For example in the calculation of F_x , the $f_y \sin \psi$ term would re-distribute a steady f_y component into a $1/\text{rev}$ harmonic, a $1/\text{rev}$ f_y component into $0/\text{rev}$ (steady) and $1/\text{rev}$ components. In general, a p/rev component in the rotating frame loads can, when resolved in a fixed frame, give rise to $p \pm 1/\text{rev}$ components. F_z , and M_z are exceptions. Here f_z , and m_z are not multiplied with sine or cosine components. Thus p/rev loads remain p/rev loads when resolved in a fixed frame.

Step2, i.e. the summation over all blades, filters out all non- pN_b/rev harmonics. For example in the case of a four bladed rotor, $N_b = 4$, the fixed frame hub loads contain only 0, 4, 8, 12, .../rev harmonics. The N_b/rev harmonic is called the blade passage frequency. Thus the fixed frame hub loads contain only integral multiples of the blade passage frequency. Consider for example

$$\begin{aligned} f_z(\psi) &= a_0 + a_1 \sin \psi + a_2 \sin 2\psi + a_3 \sin 3\psi + a_4 \sin 4\psi \\ F_z(\psi) &= f_z(\psi_1) + f_z(\psi_2) + f_z(\psi_3) + f_z(\psi_4) \\ &= f_z(\psi) + f_z(\psi + 90^\circ) + f_z(\psi + 180^\circ) + f_z(\psi + 270^\circ) \\ &= 4a_0 + 4a_4 \sin 4\psi \end{aligned}$$

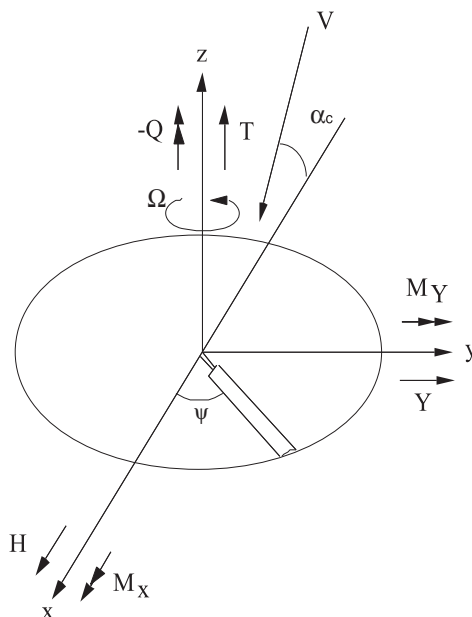
Note that the assumption here is that all blades have identical root loads, only shifted in phase. In case the blades are dissimilar this assumption does not hold. The hub loads in that case transmit all harmonics. Such is the case for damaged or dissimilar rotors. The goal is to make all the blades identical.

The pN_b/rev harmonics of the hub loads, e.g. the $4a_4 \sin 4\psi$ component, create enormous vibration in the fuselage. The steady component, e.g. the $4a_0$ component is used to trim the helicopter. The steady component is the average force generated by the rotor. In this case $4a_0$ was the rotor thrust. The steady components of F_x, F_y, F_z are often denoted as H, Y, T , the rotor drag, side force, and thrust. The steady components of M_x and M_y are denoted as M_X and M_Y , the roll-left, and pitch-up moments. The steady component of $-M_z$ is denoted by Q , the rotor torque.

The steady components can be more easily obtained by averaging the rotating frame loads over the rotor disk, and then multiplying by N_b to account for all blades. Using the same example as above, the thrust can be calculated as

$$\begin{aligned} T &= \frac{N_b}{2\pi} \int_0^{2\pi} f_z(\psi) d\psi \\ &= \frac{4}{2\pi} \int_0^{2\pi} a_0 + a_1 \sin \psi + a_2 \sin 2\psi + a_3 \sin 3\psi + a_4 \sin 4\psi \\ &= \frac{4}{2\pi} 2\pi a_0 \\ &= 4a_0 \end{aligned}$$

Thus in general we have the steady rotor forces H, Y, T , and moments M_X, M_Y, Q as follows.



Rotor Thrust T:

$$\begin{aligned}
T &= \frac{N_b}{2\pi} \int_0^{2\pi} f_z d\psi \\
&= \frac{N_b}{2\pi} \int_0^{2\pi} s_z d\psi \\
&= \frac{N_b}{2\pi} \int_0^{2\pi} \int_e^R \left[\frac{dF_z}{dr} - m(r-e)\ddot{\beta} \right] dr d\psi \\
&= \frac{N_b}{2\pi} \int_0^{2\pi} \int_e^R dF_z d\psi
\end{aligned} \tag{1.43}$$

This is because $\ddot{\beta}$ cannot have a steady component, and all harmonics integrate to zero over the azimuth.

Rotor Drag H:

$$\begin{aligned}
H &= \frac{N_b}{2\pi} \int_0^{2\pi} (f_y \cos \psi + f_x \sin \psi) d\psi \\
&= \frac{N_b}{2\pi} \int_0^{2\pi} (s_r \cos \psi + s_x \sin \psi) d\psi \\
&= \frac{N_b}{2\pi} \int_0^{2\pi} \int_e^R (dF_r \cos \psi + dF_x \sin \psi) d\psi
\end{aligned} \tag{1.44}$$

where the centrifugal component of s_r integrates to zero.

Rotor Side Force Y:

$$\begin{aligned}
Y &= \frac{N_b}{2\pi} \int_0^{2\pi} (f_y \sin \psi - f_x \cos \psi) d\psi \\
&= \frac{N_b}{2\pi} \int_0^{2\pi} (s_r \sin \psi - s_x \cos \psi) d\psi \\
&= \frac{N_b}{2\pi} \int_0^{2\pi} \int_e^R (dF_r \sin \psi - dF_x \cos \psi) d\psi
\end{aligned} \tag{1.45}$$

Rotor Torque Q:

$$\begin{aligned}
Q &= -\frac{N_b}{2\pi} \int_0^{2\pi} m_z d\psi \\
&= \frac{N_b}{2\pi} \int_0^{2\pi} (n_l + es_x) d\psi \\
&= \frac{N_b}{2\pi} \int_0^{2\pi} \int_e^R [(r-e)dF_x + edF_x] d\psi \\
&= \frac{N_b}{2\pi} \int_0^{2\pi} \int_e^R r dF_x d\psi
\end{aligned} \tag{1.46}$$

Rotor Roll Moment M_x : Assume that the torsion moment is zero, i.e. $m_y = n_t \cong 0$.

$$\begin{aligned}
M_X &= \frac{N_b}{2\pi} \int_0^{2\pi} m_x \sin \psi d\psi \\
&= \frac{N_b}{2\pi} \int_0^{2\pi} (n_f + es_z) \sin \psi d\psi \\
&= \frac{N_b}{2\pi} \int_0^{2\pi} \left(\nu_\beta^2 - 1 - \frac{3e}{2R} \right) I_\beta \Omega^2 (\beta - \beta_p) \sin \psi d\psi + \frac{N_b}{2\pi} \int_0^{2\pi} \int_e^R e dF_z \sin \psi d\psi
\end{aligned} \tag{1.47}$$

For $e = 0$ and $\beta_p = 0$ an useful expression is obtained

$$\begin{aligned}
M_X &= \frac{N_b}{2\pi} \int_0^{2\pi} (\nu_\beta^2 - 1) I_\beta \Omega^2 \beta \sin \psi d\psi \\
&= N_b (\nu_\beta^2 - 1) I_\beta \Omega^2 \frac{1}{N_b} \int_0^{2\pi} \beta \sin \psi d\psi \\
&= N_b (\nu_\beta^2 - 1) I_\beta \Omega^2 \beta_{1s}
\end{aligned} \tag{1.48}$$

In non-dimensional form we have

$$C_{MX} = \frac{M_X}{\rho A (\Omega R)^2 R} = \frac{\sigma a}{2\gamma} (\nu_\beta^2 - 1) \beta_{1s} \tag{1.49}$$

Rotor Pitch Moment M_Y : Assume that the torsion moment is zero, i.e. $m_y = n_t \cong 0$.

$$\begin{aligned}
M_Y &= \frac{N_b}{2\pi} \int_0^{2\pi} -m_x \cos \psi d\psi \\
&= \frac{N_b}{2\pi} \int_0^{2\pi} -(n_f + e s_z) \cos \psi d\psi \\
&= -\frac{N_b}{2\pi} \int_0^{2\pi} \left(\nu_\beta^2 - 1 - \frac{3}{2} \frac{e}{R} \right) I_\beta \Omega^2 (\beta - \beta_p) \cos \psi d\psi - \frac{N_b}{2\pi} \int_0^{2\pi} \int_e^R e dF_z \cos \psi d\psi
\end{aligned} \tag{1.50}$$

For $e = 0$ and $\beta_p = 0$ an useful expression is obtained

$$\begin{aligned}
M_Y &= -\frac{N_b}{2\pi} \int_0^{2\pi} (\nu_\beta^2 - 1) I_\beta \Omega^2 \beta \cos \psi d\psi \\
&= -N_b (\nu_\beta^2 - 1) I_\beta \Omega^2 \frac{1}{N_b} \int_0^{2\pi} \beta \cos \psi d\psi \\
&= -N_b (\nu_\beta^2 - 1) I_\beta \Omega^2 \beta_{1c}
\end{aligned} \tag{1.51}$$

In non-dimensional form we have

$$C_{MY} = \frac{M_Y}{\rho A (\Omega R)^2 R} = -\frac{\sigma a}{2\gamma} (\nu_\beta^2 - 1) \beta_{1c} \tag{1.52}$$

1.5 Rotor planes of reference

There are various physical planes which can be used to describe the rotor motion. Researchers and engineers use different planes for different purposes. For example, the expressions for inflow derived earlier were perpendicular to the plane of the disk tilt. This plane is also called the tip path plane (TPP). The tip of the blades lie in this plane, hence the name. For the purposes of rotor dynamic analysis, the hub plane (HP) is the most convenient plane. The hub plane is perpendicular to the rotor shaft. The rotor RPM, Ω , is along the shaft. Recall fig. 6.2. The vertical axis z was perpendicular to the hub plane. The inflow λ used in the expression for U_P was along z , i.e., it was perpendicular to the hub plane. This inflow must be calculated from the inflow expression derived using momentum theory earlier by transformation between TPP and HP. In general, it is often necessary to transform variables from one type of axes system to another.

For hover and vertical flight, the control is the thrust level which is obtained by the collective pitch setting. There is no variation of pitch or flap angle along the azimuth.

$$\theta(\psi) = \theta_0 \text{ collective}$$

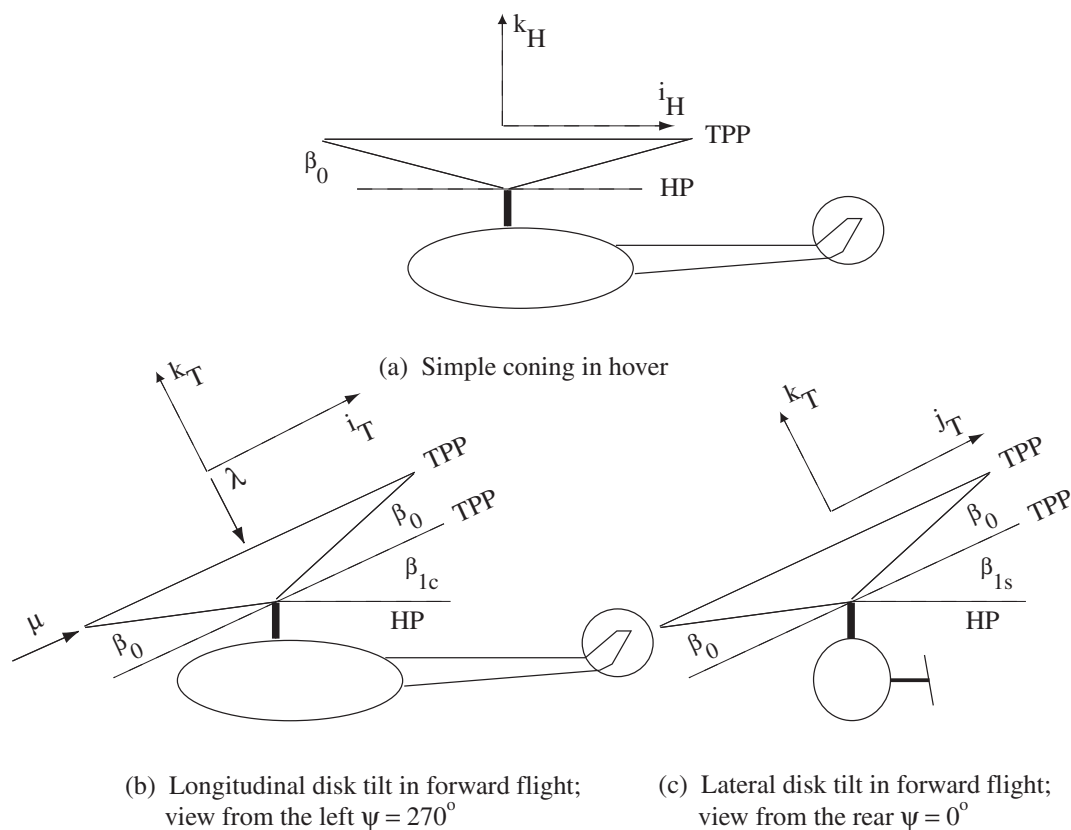


Figure 1.13: Definition of tip path plane (TPP) and hub plane (HP)

$$\beta(\psi) = \beta_0 \text{ coning}$$

TPP is parallel to HP, see Fig. 1.13(a). Both are perpendicular to the shaft axis. The thrust vector acts along the shaft and is normal to both planes. In forward flight, the TPP is tilted longitudinally and laterally. Consider the following flapping motion.

$$\beta(\psi) = \underbrace{\beta_0}_{\text{coning}} + \underbrace{\beta_{1c} \cos \psi}_{\text{longitudinal TPP tilt}} + \underbrace{\beta_{1s} \sin \psi}_{\text{lateral TPP tilt}}$$

Figures 1.13(b) and (c) show the longitudinal and lateral tilts for positive β_{1c} and β_{1s} . The tilt of the tip path plane tilts the thrust vector. The longitudinal tilt is forward. The vertical component of the thrust balances the weight and the horizontal component of the thrust provides a propulsive force. The lateral tilt is to the left or right depending on the roll moment requirement to trim the rotor. The transformation between the TPP and HP is obtained by subsequent rotations of the hub plane by β_{1c} and β_{1s} . If i_H, j_H, k_H and i_T, j_T, k_T are the unit vectors in HP and TPP, we have

$$\begin{Bmatrix} i_T \\ j_T \\ k_T \end{Bmatrix} = \begin{bmatrix} c\beta_{1c} & 0 & s\beta_{1c} \\ -s\beta_{1c}s\beta_{1s} & c\beta_{1s} & s\beta_{1s}c\beta_{1c} \\ -s\beta_{1c}c\beta_{1s} & -s\beta_{1s} & c\beta_{1s}c\beta_{1s} \end{bmatrix} \begin{Bmatrix} i_H \\ j_H \\ k_H \end{Bmatrix} \cong \begin{bmatrix} 1 & 0 & \beta_{1c} \\ 0 & 1 & \beta_{1s} \\ -\beta_{1c} & -\beta_{1s} & 1 \end{bmatrix} \begin{Bmatrix} i_H \\ j_H \\ k_H \end{Bmatrix} \quad (1.53)$$

It follows for example,

$$\begin{aligned} \lambda_H &= \lambda_{TPP} - \mu\beta_{1c} \\ H_H &= H_{TPP} - \beta_{1c}T_T \\ Y_H &= Y_{TPP} - \beta_{1s}T_T \end{aligned} \quad (1.54)$$

The flapping motion is controlled by introducing collective and cyclic pitch angles through the swashplate.

$$\theta(\psi) = \underbrace{\theta_0}_{\text{collective}} + \underbrace{\theta_{1c} \cos \psi}_{\substack{\text{lateral} \\ \text{cyclic}}} + \underbrace{\theta_{1s} \sin \psi}_{\substack{\text{longitudinal} \\ \text{cyclic}}}$$

The cyclic pitch angles lie in a plane. This is a plane from which one observes no variation of cyclic pitch. The longitudinal and lateral tilts of this plane are shown in Figs. 1.14(a) and (b). The

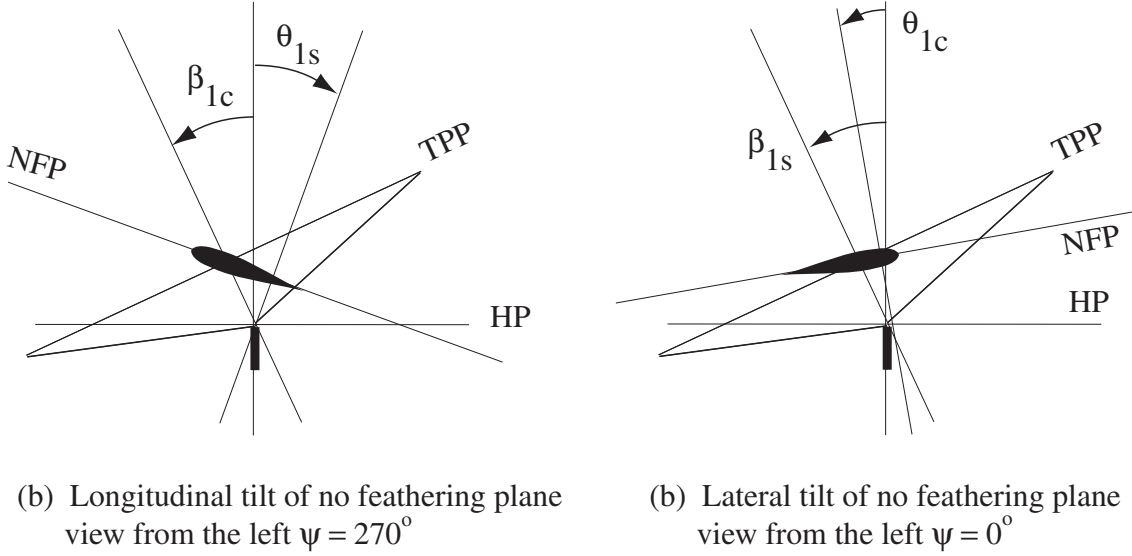


Figure 1.14: Definition of no feathering plane (NFP), tip path plane (TPP) and hub plane (HP)

transformation between the NFP and HP is obtained by subsequent rotations of the hub plane by θ_{1s} and θ_{1c} . If i_H, j_H, k_H and i_N, j_N, k_N are the unit vectors in HP and TPP, we have

$$\begin{Bmatrix} i_N \\ j_N \\ k_N \end{Bmatrix} = \begin{bmatrix} c\theta_{1s} & 0 & -s\theta_{1s} \\ s\theta_{1s}s\theta_{1c} & c\theta_{1c} & s\theta_{1c}c\theta_{1s} \\ c\theta_{1c}s\theta_{1s} & -s\theta_{1c} & c\theta_{1c}c\theta_{1s} \end{bmatrix} \begin{Bmatrix} i_H \\ j_H \\ k_H \end{Bmatrix} \cong \begin{bmatrix} 1 & 0 & \beta_{1c} \\ 0 & 1 & \theta_{1c} \\ \theta_{1s} & -\theta_{1c} & 1 \end{bmatrix} \begin{Bmatrix} i_H \\ j_H \\ k_H \end{Bmatrix} \quad (1.55)$$

It follows for example,

$$\begin{aligned} \lambda_H &= \lambda_{NFP} + \mu\theta_{1c} \\ H_H &= H_{NFP} + \theta_{1s}T_T \\ Y_H &= Y_{NFP} - \theta_{1c}T_T \end{aligned} \quad (1.56)$$

It is important to keep in mind the reference frame from which the flap and cyclic pitch angles are measured. From the hub plane, the flap and pitch angles are β_{1c} , β_{1s} and θ_{1c} , θ_{1s} . From the tip path plane, the flap angles are zero. Similarly, from the no feathering plane, the cyclic pitch angles are zero. Note that the angle between any two planes remain the same, irrespective of the plane from which they are measured. For example, the longitudinal tilt angle between NFP and TPP when measured from the hub plane is $(\beta_{1c} + \theta_{1s})$, see fig. 1.14(a). The same angle is only β_{1c} when measured from NFP. However this β_{1c} is different from the β_{1c} measured from the HP, but is equal to $(\beta_{1c} + \theta_{1s})$ as measured from the HP. Thus,

$$(\beta_{1c} + \theta_{1s})_H = (\beta_{1c})_N = (\theta_{1s})_T$$

Similarly for the lateral tilt, we have from fig. 1.14(b),

$$(\beta_{1s} - \theta_{1c})_H = (\beta_{1s})_N = -(\theta_{1c})_T$$

In addition to TPP, HP, and NFP, another plane can be defined. This is the plane of the swashplate, called the control plane (CP). See Fig. 1.15. As shown in the figure, if the pitch links are connected

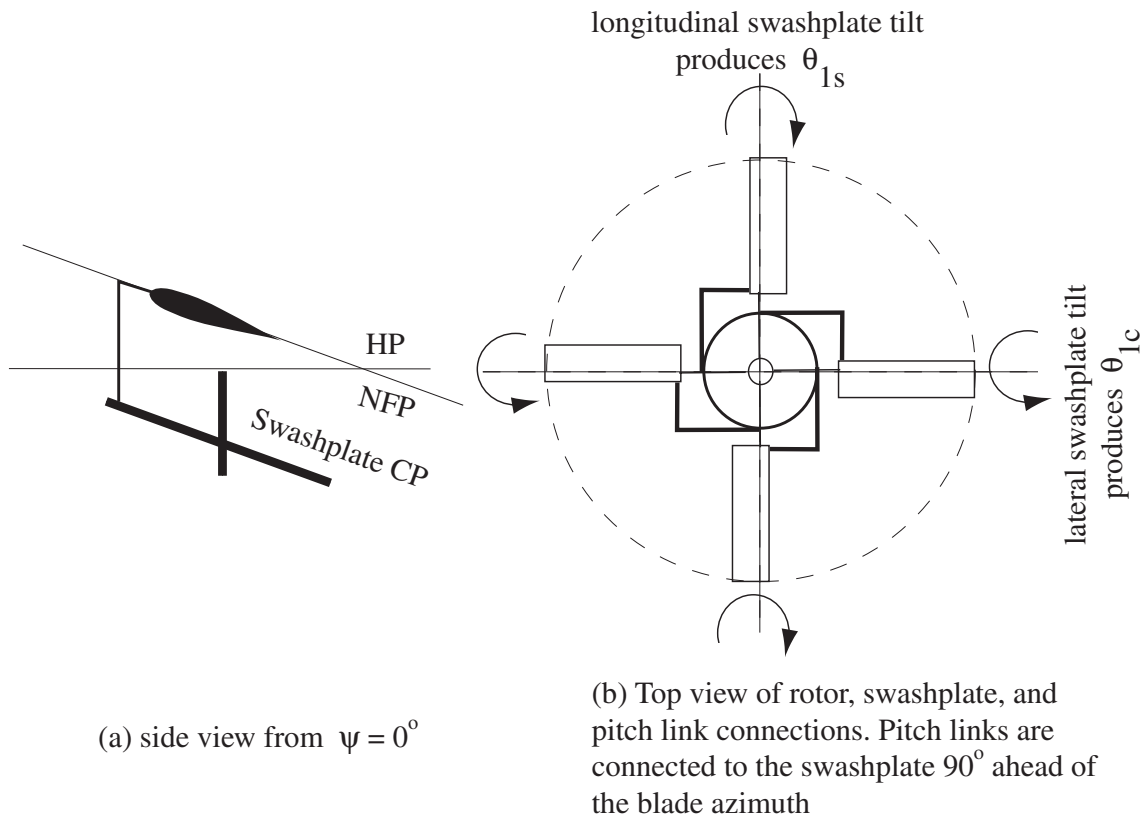


Figure 1.15: **Definition of control plane (CP)**

90° ahead of the blade azimuth, the CP is parallel to the NFP. In addition, the pitch flap coupling must be zero for this condition to hold. The different rotor reference planes, and their use are briefly summarized below.

(a) Tip Path Plane (TPP): This is a plane described by blade tips, so that there is no cyclic variation of flap angles when measured from this plane. This plane is frequently used for wake studies and acoustic studies. The expressions for inflow derived earlier using moment theory were with respect to this plane. The TPP is same as the disk tilt plane.

(b) No Feather Plane (NFP): This is a plane from which there is no cyclic variation of control pitch. This is often used for performance and stability analysis, especially for autogyros. In Gessow and Myers' book, this plane is used for performance studies.

(c) Control Plate (CP): It represents the swashplate plane. This plane is important for servo-actuators.

(d) Hub Plane (HP): This plane is normal to the rotor shaft. Both cyclic flap and cyclic pitch control angles are non-zero when measured from this plane. This plane is routinely adopted for the blade dynamic analysis.

Finally, note that the concept of TPP and NFP is applicable only with the assumption of $1/\text{rev}$ variations of flap and cyclic pitch. In reality the flapping motion contains all harmonics, the $2/\text{rev}$ and higher harmonics create ripples over the tip path plane. Similarly in the case of higher

harmonic control, when the swashplate is used to input higher harmonics of pitch angle, the NFP is no longer defined. Also note that, in Gessow and Myers book, the pitch and flap angles (including higher harmonics) are defined as

$$\theta(\psi) = A_0 - A_1 \cos \psi - B_1 \sin \psi - A_2 \cos 2\psi - B_2 \sin 2\psi \dots$$

$$\beta(\psi) = a_0 - a_1 \cos \psi - b_1 \sin \psi - a_2 \cos 2\psi - b_2 \sin 2\psi \dots$$

where

$$\theta_0 = A_0$$

$$\theta_{nc} = -A_n$$

$$\theta_{ns} = -B_n$$

$$\beta_0 = a_0$$

$$\beta_{nc} = -a_n$$

$$\beta_{ns} = -b_n$$

1.6 Helicopter Trim

Trimming an helicopter means maintaining equilibrium in space. The steady forces and moments generated by the rotor should be equal and opposite to those generated by the other parts of the helicopter, e.g. the tail rotor, the fuselage, the horizontal stabilizer etc. The steady forces and moments generated by the rotor should remain the same from one rotor revolution to another. In order to satisfy this condition it is necessary that the blades exhibit periodic motion. Therefore, helicopter trim involves two steps:

1. Achieving periodic blade response. Also called *uncoupled trim*.
2. Achieving periodic blade response such that specific targets are met. Also called *coupled trim*.

A trimmed flight can be achieved under any steady condition – axial flight, ascent and descent along a coordinated banked turn, and straight and level flight. In this section we consider a straight and level flight. Coupled trim is broadly classified into two types:

1. Isolated rotor trim.
2. Full aircraft trim.

For an isolated rotor trim, the three rotor control angles are determined based on three specified targets, e.g. the thrust, and rotor pitch and roll moments. When the targetted moments are zero, it is called moment trim. Alternatively, the thrust, and the first harmonic flapping motions, β_{1c} and β_{1s} , are specified. One popular approach is to specify zero first harmonic flapping. This procedure is widely used in wind tunnel trim. Isolated rotor trim is used in wind-tunnels to achieve specific flight conditions in a controlled environment.

Full aircraft trim is also called propulsive trim. The only assumption is that sufficient rotor power is available from the powerplants. The target rotor forces and moments are equal and opposite to those produced by the rest of the aircraft. The three rotor controls, the tail rotor collective, and the two aircraft attitude angles, longitudinal and lateral, are determined using the six vehicle equilibrium equations.

The trim procedures require the calculation of rotor forces and moments.

1.6.1 Rotor Forces and Moments

The steady rotor forces and moments in the hub plane can be derived using equations 9.83–8.88, and equations 1.29–1.31. Assume uniform inflow, linear lift curve slope $c_l = a\alpha$, and a constant drag coefficient $c_d = c_{d0}$. Recall, that in forward flight we have

$$\begin{aligned} u_t &= x + \mu \sin \psi \\ u_p &= \lambda + x \beta + \beta \mu \cos \psi \\ \beta &= \beta_0 + \beta_{1c} \cos \psi + \beta_{1s} \sin \psi \\ \theta &= \theta_0 + x \theta_{tw} + \theta_{1c} \cos \psi + \theta_{1s} \sin \psi \end{aligned}$$

where

$$\lambda = \lambda_H = \lambda_{TTP} - \mu \beta_{1c}$$

and

$$\lambda_{TTP} = \mu \tan \alpha + \frac{k_f C_T}{2\sqrt{\mu^2 + \lambda_{TTP}^2}} \quad (1.57)$$

$$\alpha = \alpha_s + \beta_{1c} + \theta_{FP}$$

where α_s is the longitudinal shaft tilt angle with respect to the horizontal plane, θ_{FP} is the flight path angle positive for climb. The rotor thrust coefficient C_T , same in all planes for small angles, is given by

$$\begin{aligned} C_T &= \frac{T}{\rho A (\Omega R)^2} \\ &= \frac{\sigma a}{2} \frac{1}{2\pi} \int_0^{2\pi} \int_0^1 (u_t^2 \theta - u_p u_t) dx d\psi \\ &= \frac{\sigma a}{2} \left[\frac{\theta_0}{3} \left(1 + \frac{3}{2} \mu^2 \right) + \frac{\theta_{tw}}{4} (1 + \mu^2) + \frac{\mu}{2} \theta_{1s} - \frac{\lambda}{2} \right] \end{aligned} \quad (1.58)$$

If the twist is expressed as $\theta_{75} + (x - 3/4)\theta_{tw} + \theta_{1c} \cos \psi + \theta_{1s} \sin \psi$, then we have

$$C_T = \frac{\sigma a}{2} \left[\frac{\theta_{75}}{3} \left(1 + \frac{3}{2} \mu^2 \right) + \frac{\theta_{tw}}{8} \mu^2 + \frac{\mu}{2} \theta_{1s} - \frac{\lambda}{2} \right]$$

The inflow can be expressed in NFP and TPP as follows.

$$C_T = \frac{\sigma a}{2} \left[\frac{\theta_0}{3} \left(1 + \frac{3}{2} \mu^2 \right) + \frac{\theta_{tw}}{4} (1 + \mu^2) - \frac{\lambda_{NFP}}{2} \right] \quad (1.59)$$

$$C_T = \frac{\sigma a}{2} \left[\frac{\theta_0}{3} \left(1 + \frac{3}{2} \mu^2 \right) + \frac{\theta_{tw}}{4} (1 + \mu^2) - \frac{\lambda_{TTP}}{2} + \frac{\mu}{2} (\beta_{1c} + \theta_{1s}) \right] \quad (1.60)$$

The rotor drag force is given by

$$\begin{aligned} C_H &= \frac{H}{\rho A (\Omega R)^2} \\ &= \frac{\sigma a}{2} \frac{1}{2\pi} \int_0^{2\pi} \int_0^1 \left[(u_p u_t \theta - u_p^2 + \frac{c_{d0}}{a} u_t^2) \sin \psi - \beta \cos \psi (u_t^2 \theta - u_p u_t) \right] dx d\psi \\ &= \frac{\sigma a}{2} \left[\theta_0 \left(-\frac{1}{3} \beta_{1c} + \frac{1}{2} \mu \lambda \right) + \theta_{tw} \left(-\frac{1}{4} \beta_{1c} + \frac{1}{4} \mu \lambda \right) \right. \\ &\quad \left. + \theta_{1c} \left(-\frac{1}{6} \beta_0 - \frac{1}{8} \mu \beta_{1s} \right) + \theta_{1s} \left(-\frac{1}{4} \mu \beta_{1c} + \frac{1}{4} \lambda \right) \right. \\ &\quad \left. + \frac{3}{4} \lambda \beta_{1c} + \frac{1}{6} \beta_0 \beta_{1s} + \frac{1}{4} \mu (\beta_0^2 + \beta_{1c}^2) + \frac{C_{d0}}{a} \left(\frac{\mu}{2} \right) \right] \end{aligned} \quad (1.61)$$

Now use

$$C_{H_{TPP}} = C_H + \beta_{1c}C_T; \quad \lambda = \lambda_{TPP} - \mu\beta_{1c}$$

to obtain

$$\begin{aligned} C_{H_{TPP}} = & \frac{\sigma a}{2} \left[\theta_0 \left(\frac{1}{2} \mu \lambda_{TPP} \right) + \theta_{tw} \left(\frac{1}{4} \mu \lambda_{TPP} \right) + \theta_{1c} \left(-\frac{1}{6} \beta_0 - \frac{1}{8} \mu \beta_{1s} \right) + \theta_{1s} \left(\frac{1}{4} \lambda_{TPP} \right) \right. \\ & \left. + \frac{1}{4} \lambda_{TPP} \beta_{1c} + \frac{1}{6} \beta_0 \beta_{1s} + \frac{1}{4} \mu \beta_0^2 \right] + \frac{\sigma C_{d_0}}{4} \mu \end{aligned} \quad (1.62)$$

The rotor side force is given by

$$\begin{aligned} C_Y = & \frac{Y}{\rho A (\Omega R)^2} \\ = & \frac{\sigma a}{2} \frac{1}{2\pi} \int_0^{2\pi} \int_0^1 \left[- \left(u_p u_t \theta - u_p^2 + \frac{c_{d_0}}{a} u_t^2 \right) \cos \psi - \beta \sin \psi (u_t^2 \theta - u_p u_t) \right] dx d\psi \\ = & \frac{\sigma a}{2} \left[-\theta_0 \left(\frac{3}{4} \mu \beta_0 + \frac{1}{3} \beta_{1s} \right) - \theta_{tw} \left(\frac{1}{4} \beta_{1s} + \frac{1}{2} \mu \beta_0 \right) - \theta_{1c} \left(\frac{1}{4} \lambda + \frac{1}{4} \mu \beta_{1c} \right) \right. \\ & \left. - \theta_{1s} \left(\frac{1}{6} \beta_0 + \frac{1}{2} \mu \beta_{1s} \right) + \frac{3}{4} \lambda \beta_{1s} + \frac{3}{2} \mu \lambda \beta_0 - \frac{1}{6} \beta_0 \beta_{1c} + \frac{1}{4} \mu \beta_{1c} \beta_{1s} \right] \end{aligned} \quad (1.63)$$

Now use

$$C_{Y_{TPP}} = C_Y + \beta_{1s}C_T; \quad \lambda = \lambda_{TPP} - \mu\beta_{1c}$$

to obtain

$$\begin{aligned} C_{Y_{TPP}} = & \frac{\sigma a}{2} \left[-\theta_0 \left(\frac{3}{4} \mu \beta_0 \right) - \theta_{tw} \left(\frac{1}{2} \mu \beta_0 \right) - \theta_{1c} \left(\frac{1}{4} \lambda_{TPP} \right) - \theta_{1s} \left(\frac{1}{6} \beta_0 \right) \right. \\ & \left. + \frac{1}{4} \lambda_{TPP} \beta_{1s} + \frac{3}{2} \mu \lambda_{TPP} \beta_0 - \frac{1}{6} \beta_0 \beta_{1c} \right] \end{aligned} \quad (1.64)$$

The rotor torque is

$$\begin{aligned} C_Q = & \frac{Q}{\rho A (\Omega R)^2 R} \\ = & \frac{\sigma a}{2} \frac{1}{2\pi} \int_0^{2\pi} \int_0^1 x \left(u_p u_t \theta - u_p^2 + \frac{c_{d_0}}{a} u_t^2 \right) dx \\ = & \frac{\sigma a}{2} \left[\lambda \left(\frac{\theta_0}{3} + \frac{\theta_{tw}}{4} + \frac{1}{4} \mu \theta_{1s} - \frac{1}{2} \mu \beta_{1c} - \frac{\lambda}{2} \right) + \mu \left(\frac{1}{6} \theta_{1c} \beta_0 - \frac{1}{3} \beta_0 \beta_{1s} \right) \right. \\ & \left. + \mu^2 \left(\frac{1}{16} \beta_{1s} \theta_{1c} + \frac{1}{16} \beta_{1c} \theta_{1s} - \frac{1}{4} \beta_0^2 - \frac{3}{16} \beta_{1c}^2 - \frac{1}{16} \beta_{1s}^2 \right) \right. \\ & \left. + \frac{1}{8} \theta_{1c} \beta_{1s} - \frac{1}{8} \theta_{1s} \beta_{1c} - \frac{1}{8} (\beta_{1c}^2 + \beta_{1s}^2) \right] + \frac{\sigma c d_0}{8} (1 + \mu^2) \end{aligned} \quad (1.65)$$

Replace λ with $\lambda_{TPP} - \mu\beta_{1c}$, in the first term of the above expression to produce

$$\begin{aligned} C_Q = & \frac{\sigma a}{2} \left[\lambda_{TPP} \left(\frac{\theta_0}{3} + \frac{\theta_{tw}}{4} - \frac{\lambda_{TPP}}{2} + \frac{1}{2} \mu \beta_{1c} + \frac{1}{4} \mu \theta_{1s} \right) \right. \\ & \left. - \mu \left(\frac{1}{3} \beta_{1c} \theta_0 + \frac{1}{4} \beta_{1c} \theta_{tw} - \frac{1}{6} \theta_{1c} \beta_0 + \frac{1}{3} \beta_0 \beta_{1s} \right) \right. \\ & \left. + \mu^2 \left(\frac{1}{16} \beta_{1s} \theta_{1c} + \frac{1}{16} \beta_{1c} \theta_{1s} - \frac{1}{4} \beta_0^2 - \frac{3}{16} \beta_{1c}^2 - \frac{1}{16} \beta_{1s}^2 \right) \right. \\ & \left. + \frac{1}{8} \theta_{1c} \beta_{1s} - \frac{1}{8} \theta_{1s} \beta_{1c} - \frac{1}{8} (\beta_{1c}^2 + \beta_{1s}^2) \right] + \frac{\sigma c d_0}{8} (1 + \mu^2) \end{aligned} \quad (1.66)$$

The expressions given above for torque are exact. It is important that all terms are retained for accurate predictions beyond advance ratio $\mu = 0.3$. The roll and pitch moment coefficients are derived from equations 1.47 and 1.50 as

$$\begin{aligned} C_{MX} &= \frac{\sigma a}{2\gamma} \left(\nu_\beta^2 - 1 - \frac{3e}{2R} \right) \beta_{1s} + \frac{e}{R} \frac{\sigma a}{2} \frac{1}{2\pi} \int_0^{2\pi} \int_0^1 (u_t^2 \theta - u_p u_t) \cos \psi dx d\psi \\ C_{MY} &= -\frac{\sigma a}{2\gamma} \left(\nu_\beta^2 - 1 - \frac{3e}{2R} \right) \beta_{1c} + \frac{e}{R} \frac{\sigma a}{2} \frac{1}{2\pi} \int_0^{2\pi} \int_0^1 (u_t^2 \theta - u_p u_t) \sin \psi dx d\psi \end{aligned}$$

Assume $e/R \cong 0$ for the following simple expressions.

$$\begin{aligned} C_{MX} &= \frac{\sigma a}{2\gamma} (\nu_\beta^2 - 1) \beta_{1s} \\ C_{MY} &= -\frac{\sigma a}{2\gamma} (\nu_\beta^2 - 1) \beta_{1c} \end{aligned} \tag{1.67}$$

1.6.2 Uncoupled trim

Uncoupled trim is a periodic blade response obtained for a given set of rotor control angles. The forward speed, shaft tilt angle, and flight path angle are prescribed. The following procedure can be used.

1. Start with $\lambda_{TPP} = \mu \tan(\alpha_s + \theta_{FP})$, $\beta_{1c} = \beta_{1s} = 0$, $\mu = V/(\Omega R)$.
2. Calculate β_0 , β_{1c} , and β_{1s} from eqns. 1.33.
3. Update $\mu = V \cos(\alpha_s + \beta_{1c} + \theta_{FP})/(\Omega R)$.
4. Calculate C_T from eqn. 1.60.
5. Update λ_{TPP} from eqn. 1.57.

Iterate steps 2 to 5 till convergence.

Example 1.2: An articulated rotor model with 4% flap hinge offset is exposed to a wind speed of 200 ft/sec in the wind tunnel. If the blade tip speed is 600 ft/sec and the blades are set at collective pitch of 5° , calculate the tip path plane orientation with shaft angle, α_s , of 0° , 10° and -10° . Assume Lock number, $\gamma = 8$, solidity ratio, $\sigma = 0.05$ and lift curve slope, $a = 6$.

Use the above procedure to obtain the following results.

	$\alpha_s = 0^\circ$	$\alpha_s = 10^\circ$	$\alpha_s = -10^\circ$
μ	0.3323	0.3303	0.3197
β_0	0.083	0.017	0.1418
β_{1c}	-4.52°	-2.32°	-6.44°
β_{1s}	-0.0303	-0.00489	-0.0536
C_T	0.00457	0.00066	0.00845
λ_{TPP}	-0.0194	0.0456	-0.0816
$(\alpha_s + \beta_{1c})$	-4.52°	7.68°	-16.44°

For a backward tilt of the shaft of 10° , the TPP is tilted back further by 16.44° . For a zero tilt of the shaft, TPP is tilted back by 4.52° . The change in TPP tilt is 11.92° . For a forward tilt of shaft of 10° , the TPP is tilted forward by 7.68° . The change in TPP tilt is 12.2° . This means that for a forward tilt of shaft, the TPP tilts forward at a faster rate. This results in an instability of rotor disk with respect to the angle of attack and is called the angle of attack of instability.

1.6.3 Coupled trim for an isolated rotor

In a coupled trim for an isolated rotor, the three control pitch angles are determined based on specific targets. The following two targets are useful.

1. Target rotor thrust and the hub roll and pitch moments.
2. Target rotor thrust and the first harmonic flapping β_{1c} and β_{1s} .

The first type produces similar airloads and structural loads on the rotor as in real flight. The second type produces similar wake geometries and acoustic characteristics.

The second type is used during wind tunnel tests. For a given longitudinal shaft tilt α_s , a popular set of targets are the thrust and zero first harmonic flapping angles. Such a condition can occur in free flight only if the aircraft center of gravity is located at the rotor hub.

The following procedure can be used for wind tunnel trim. Here, C_T , and β_{1c} , β_{1s} are the targets. θ_0 , θ_{1s} , θ_{1c} are the unknowns. Initialize the unknowns to zero.

1 : Calculate λ_{TTPP} from eqn. 1.57.

2 : Calculate θ_0 , β_0 , θ_{1s} , θ_{1c} .

From eqns. 1.33 we have

$$\beta_0 = \frac{\gamma}{v_\beta^2} \left[\frac{\theta_0}{8}(1 + \mu^2) + \frac{\theta_{tw}}{10} \left(1 + \frac{5}{6}\mu^2\right) + \frac{\mu}{6}(\theta_{1s} + \beta_{1c}) - \frac{\lambda_{TTPP}}{6} \right] + \frac{\omega_{\beta_0}^2}{\Omega^2 v_\beta^2} \beta_p \quad (1.68)$$

$$\theta_{1c} = \beta_{1s} + \frac{1}{(1 + \frac{1}{2}\mu^2)} \left[\frac{8}{\gamma}(v_\beta^2 - 1)\beta_{1c} + \frac{4}{3}\mu\beta_0 \right] \quad (1.69)$$

$$\theta_{1s} = -\beta_{1c} + \frac{1}{(1 + \frac{3}{2}\mu^2)} \left[-\frac{8}{3}\mu \left(\theta_0 + \frac{3}{4}\theta_{tw} - \frac{3}{4}\lambda_{TTPP} \right) + \frac{8}{\gamma}(v_\beta^2 - 1)\beta_{1s} \right] \quad (1.70)$$

where λ has been replaced with $\lambda_{TTPP} - \mu\beta_{1c}$.

Substituting β_{1c} + θ_{1s} from eqn. 1.70 into eqn. 1.60 we have

$$\theta_0 = \frac{\frac{6C_T}{\sigma a}(1 + \frac{3}{2}\mu^2) - \frac{3}{4}\theta_{tw}(1 - \frac{3}{2}\mu^2 + \frac{3}{2}\mu^4) + \frac{3}{2}\lambda_{TTPP}(1 - \frac{1}{2}\mu^2) + \frac{12}{\gamma}\mu(v_\beta^2 - 1)\beta_{1s}}{1 - \mu^2 + \frac{9}{4}\mu^4} \quad (1.71)$$

Iterate step 2 till convergence.

A similar procedure can be used for moment trim. Here C_T , and C_{MX} , C_{MY} are the targets. θ_0 , θ_{1s} , θ_{1c} are the unknowns. Initialize the unknowns to zero.

1 : Calculate λ_{TTPP} from eqn. 1.57.

2 : Calculate β_{1c} , β_{1s} using the pitch and roll moment expressions, e.g., eqns. 1.67.

3 : Calculate θ_0 from eqn. 1.71, and β_0 , θ_{1s} , θ_{1c} from eqns. 1.68, 1.70 and 1.69.

Iterate steps 2 and 3 till convergence.

1.6.4 Coupled trim for a full aircraft

The target is to achieve 3 force and 3 moment equilibriums. It is necessary to have 6 control variables.

The rotor control angles, which can be set by the pilot, are θ_0 , θ_{1c} , and θ_{1s} . The yaw control is via the tail rotor collective θ_t . The two aircraft attitude angles, the longitudinal tilt α_s , and lateral tilt ϕ_s can be used as the two additional control variables. Note that the pilot does not have a direct control over these variables. The helicopter must be *flown into* these vehicle orientations to achieve trim.

Mathematically, the problem is formulated as follows. For a specified aircraft gross weight and forward speed, the trim solution evaluates rotor controls, θ_0 , θ_{1c} and θ_{1s} , rotor dynamics e.g. flapping $\beta(\psi)$, the vehicle orientation, α_s and ϕ_s , tail rotor collective setting, and the rotor inflow, λ . The equations are the flap equation, inflow equation, and the 6 vehicle equilibrium equations. A popular approach is to neglect altogether the yawing moment equilibrium equation and thereby neglect the influence of the tail rotor on the solution. Thus we have 7 unknowns – 3 rotor controls,

2 fuselage attitudes, plus flapping and inflow, and 7 equations – 3 vehicle forces, 2 vehicle moments, plus flapping and inflow.

The flapping equation can be solved for any number of harmonics. Let us consider three harmonics here – β_0 , β_{1c} , and β_{1s} .

Aircraft Force and Moment Equilibrium Equations

Consider the left side view and front view of a helicopter in flight.

T = rotor thrust

H = rotor drag force

Y = rotor side force

W = weight

D = airframe drag in direction of V

Y_F = tail rotor thrust

M_X = rotor roll moment

M_y = rotor pitch moment

V = helicopter speed

M_{XF} = airframe roll moment

M_{YF} = airframe pitch moment

α_s = longitudinal shaft tilt with respect to vertical axis

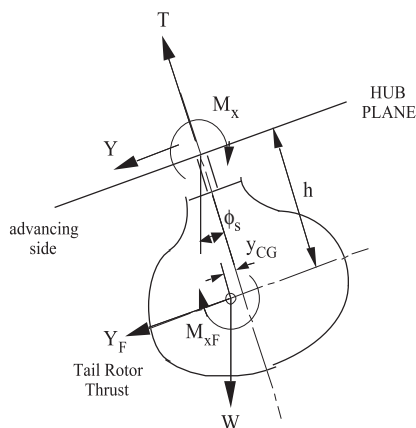
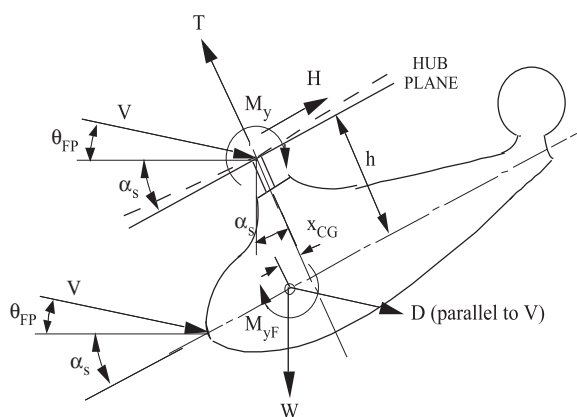
ϕ_s = lateral shaft tilt with respect to vertical axis

X_{cg} = forward shift of cg from shaft axis

Y_{cg} = side shift of cg from shaft axis (positive right) towards advancing side

θ_{FP} = flight path angle

Note that the disk tilt, i.e. the TPP tilt $\alpha = \alpha_s + \beta_{1c} + \theta_{FP}$.



Vertical force equilibrium:

$$W - T \cos \alpha_s \cos \phi_s + D \sin \theta_{FP} - H \sin \alpha_s + Y \sin \phi_s + Y_F \sin \phi_s = 0 \quad (1.72)$$

Longitudinal force equilibrium:

$$D \cos \theta_{FB} + H \cos \alpha_s - T \sin \alpha_s \cos \phi_s = 0 \quad (1.73)$$

Lateral force equilibrium:

$$Y \cos \phi_s + Y_F \cos \phi_s + T \cos \alpha_s \sin \phi_s = 0 \quad (1.74)$$

Pitch moment equilibrium about hub:

$$M_y + M_{y_F} - W(X_{cg} \cos \alpha_s - h \sin \alpha_s) - D(x_{cg} \sin \alpha_s + h \cos \alpha_s) = 0 \quad (1.75)$$

Roll moment equilibrium about hub:

$$M_x + M_{x_F} + Y_F h + W(h \sin \phi_s - Y_{cg} \cos \phi_s) = 0 \quad (1.76)$$

Torque equilibrium about shaft:

$$Q - Y_F l_T = 0 \quad (1.77)$$

In addition to the six vehicle equilibrium equations we have an equation for the inflow and an equation for blade flapping. From the flapping equation, linear equations for the flap harmonics can be extracted, as many equations as the number of assumed harmonics. For example, eqns. 1.33 are three equations for three harmonics.

The trim equations can be simplified assuming: (1) small shaft tilt angles, and (2) zero flight path angle $\theta_{FP} = 0$. Additionally, the yaw degree of freedom can be ignored, i.e. remove the torque equation and the tail rotor collective θ_t as a trim variable.

$$W = T \quad (1.78)$$

$$D + H = T \alpha_s \quad (1.79)$$

$$Y + Y_F = -T \phi_s \quad (1.80)$$

$$M_y + M_{y_F} + W(h \alpha_s - X_{cg}) - hD = 0 \quad (1.81)$$

$$M_x + M_{x_F} + W(h \phi_s - Y_{cg}) + Y_F h = 0 \quad (1.82)$$

Non-dimensionalize all forces and moments by $\rho A (\Omega R)^2$ and $\rho A (\Omega R)^2 R$ respectively. Define the fuselage drag D as

$$D = \frac{1}{2} \rho V^2 f \quad (1.83)$$

where f has units of area. It is the equivalent flat plate area of the hub, fuselage, landing gear etc. The drag coefficient then becomes

$$C_D = \frac{1}{2} \mu^2 (f/A) \quad (1.84)$$

where A is the rotor disk area. Typically f/A varies from 1 to 3%. From eqn. 1.78

$$C_T = C_W \quad (1.85)$$

From eqns. 1.79 and 1.81 extract equations for α_s and β_{1c} . From eqn. 1.79

$$\begin{aligned} \alpha_s &= \frac{D}{W} + \frac{C_H}{C_T} = \frac{1}{2}\mu^2 \frac{f}{A} \frac{1}{C_T} + \frac{C_H}{C_T} \\ &= \frac{1}{2}\mu^2 \frac{f}{A} \frac{1}{C_T} + \frac{C_{HTPP}}{C_T} - \beta_{1c} \end{aligned} \quad (1.86)$$

From eqn. 1.81

$$\begin{aligned} \alpha_s &= \frac{X_{cg}}{h} + \frac{D}{W} - \frac{M_y}{hW} - \frac{M_{yF}}{hW} \\ &= \frac{X_{cg}}{h} + \frac{1}{2}\mu^2 \frac{f}{A} \frac{1}{C_T} + \frac{(v_\beta^2 - 1)/\gamma}{\frac{h}{R} \frac{2C_T}{\sigma a}} \beta_{1c} - \frac{M_{yF}}{hW} \end{aligned} \quad (1.87)$$

Equating the above two eqns. 1.86 and 1.87 obtain

$$\beta_{1c} = \frac{-\frac{X_{cg}}{h} + \frac{M_{yF}}{hW} + C_{HTPP}/C_T}{1 + \frac{(v_\beta^2 - 1)/\gamma}{\frac{h}{R} \frac{2C_T}{\sigma a}}} \quad (1.88)$$

Now use the above eqn. 1.88 in eqn. 1.86 to obtain

$$\alpha_s = \frac{\frac{x_{cg}}{h} - \frac{M_{yF}}{hW} + \frac{(v_\beta^2 - 1)/\gamma}{\frac{h}{R} \frac{2C_T}{\sigma a}} \frac{C_{HTPP}}{C_T}}{1 + \frac{(v_\beta^2 - 1)/\gamma}{\frac{h}{R} \frac{2C_T}{\sigma a}}} + \frac{1}{2} \frac{f}{A} \frac{\mu^2}{C_T} \quad (1.89)$$

Similarly use eqns. 1.80 and 1.82 to extract equations for ϕ_s and β_{1s} . From eqn. 1.80

$$\begin{aligned} \phi_s &= -\frac{Y_F}{W} - \frac{C_y}{C_T} \\ &= -\frac{Y_F}{W} - \frac{C_{yTPP}}{C_T} + \beta_{1s} \end{aligned} \quad (1.90)$$

$Y_F/W = 0$ if the tail rotor is ignored. $Y_F/W = C_Q R / (C_T l_T)$ if the tail rotor is considered. l_T is the distance of the tail rotor thrust from the rotor hub. From eqn. 1.82

$$\begin{aligned} \phi_s &= \frac{y_{cg}}{h} - \frac{Y_F}{W} - \frac{M_x}{hW} - \frac{M_{xF}}{hW} \\ &= \frac{y_{cg}}{h} - \frac{Y_F}{W} - \frac{(v_\beta^2 - 1)/\gamma}{\frac{h}{R} \frac{2C_T}{\sigma a}} \beta_{1s} - \frac{M_{xF}}{hW} \end{aligned} \quad (1.91)$$

Equating the above two eqns. 1.90 and 1.91 obtain

$$\beta_{1s} = \frac{\frac{y_{cg}}{h} - \frac{M_{xF}}{hW} + \frac{C_{yTPP}}{C_T}}{1 + \frac{(v_\beta^2 - 1)/\gamma}{\frac{h}{R} \frac{2C_T}{\sigma a}}} \quad (1.92)$$

Now use the above eqn. 1.92 in eqn. 1.90 to obtain

$$\phi_s = \frac{\frac{y_{cg}}{h} - \frac{M_{xF}}{hW} - \frac{(v_\beta^2 - 1)/\gamma}{\frac{h}{R} \frac{2C_T}{\sigma a}} \frac{C_{yTPP}}{C_T}}{1 + \frac{(v_\beta^2 - 1)/\gamma}{\frac{h}{R} \frac{2C_T}{\sigma a}}} - \frac{C_Q}{C_T} \frac{R}{l_T} \quad (1.93)$$

Recall, that the inflow equation was (see eqn. 1.57)

$$\begin{aligned}
\lambda_{TTPP} &= \mu \tan(\alpha_s + \beta_{1c} + \theta_{FP}) + \frac{k_f C_T}{2\sqrt{\mu^2 + \lambda_{TTPP}^2}} \\
&\cong \mu(\alpha_s + \beta_{1c} + \theta_{FP}) + \frac{k_f C_T}{2\sqrt{\mu^2 + \lambda_{TTPP}^2}} \\
&= \mu \left(\frac{C_D + C_H}{C_T} \right) + \mu\beta_{1c} + \lambda_c + \frac{k_f C_T}{2\sqrt{\mu^2 + \lambda_{TTPP}^2}} \\
&= \mu \left(\frac{C_D + C_H + \beta_{1c} C_T}{C_T} \right) + \lambda_c + \frac{k_f C_T}{2\sqrt{\mu^2 + \lambda_{TTPP}^2}} \\
&= \frac{1}{2}\mu^3 \left(\frac{f}{A} \right) \frac{1}{C_T} + \mu \frac{C_{HTPP}}{C_T} + \lambda_c + \frac{k_f C_T}{2\sqrt{\mu^2 + \lambda_{TTPP}^2}}
\end{aligned} \tag{1.94}$$

The control angles θ_0 , θ_{1c} , θ_{1s} , and coning β_0 can be calculated in the same manner as was done in coupled trim for an isolated rotor. The description is repeated here. From eqns. 1.33 we have

$$\beta_0 = \frac{\gamma}{v_\beta^2} \left[\frac{\theta_0}{8}(1 + \mu^2) + \frac{\theta_{tw}}{10} \left(1 + \frac{5}{6}\mu^2 \right) + \frac{\mu}{6}(\theta_{1s} + \beta_{1c}) - \frac{\lambda_{TTPP}}{6} \right] + \frac{\omega_{\beta_0}^2}{\Omega^2 v_\beta^2} \beta_p \tag{1.95}$$

$$\theta_{1c} = \beta_{1s} + \frac{1}{(1 + \frac{1}{2}\mu^2)} \left[\frac{8}{\gamma}(v_\beta^2 - 1)\beta_{1c} + \frac{4}{3}\mu\beta_0 \right] \tag{1.96}$$

$$\theta_{1s} = -\beta_{1c} + \frac{1}{(1 + \frac{3}{2}\mu^2)} \left[-\frac{8}{3}\mu \left(\theta_0 + \frac{3}{4}\theta_{tw} - \frac{3}{4}\lambda_{TTPP} \right) + \frac{8}{\gamma}(v_\beta^2 - 1)\beta_{1s} \right] \tag{1.97}$$

where λ has been replaced with $\lambda_{TTPP} - \mu\beta_{1c}$. Substituting $\beta_{1c} + \theta_{1s}$ from the above equation into eqn. 1.60 for C_T , and solving for θ_0 we have

$$\theta_0 = \frac{\frac{6C_T}{\sigma a} \left(1 + \frac{3}{2}\mu^2 \right) - \frac{3}{4}\theta_{tw} \left(1 - \frac{3}{2}\mu^2 + \frac{3}{2}\mu^4 \right) + \frac{3}{2}\lambda_{TTPP} \left(1 - \frac{1}{2}\mu^2 \right) + \frac{12}{\gamma}\mu(v_\beta^2 - 1)\beta_{1s}}{1 - \mu^2 + \frac{9}{4}\mu^4} \tag{1.98}$$

The rotor drag and side forces are obtained from eqns. 1.62 and 1.64.

The above expressions can be used to calculate rotor trim iteratively using the following sequence.

1: Calculate C_T

$$C_T \cong C_W = \frac{W}{\rho\pi R^2(\Omega R)^2}$$

Initialize λ_{TTPP}

$$\lambda_{TTPP} = \kappa_f \frac{C_T}{2\mu} + \frac{1}{2} \left(\frac{f}{A} \right) \frac{\mu^3}{C_T}$$

Initialize C_{HTPP} and C_{YTPP} to zero

Now iterate until λ_{TTPP} converges as follows:

- 2 : Calculate β_{1c} using eqn. 1.88
- 3 : Calculate β_{1s} using eqn. 1.92
- 4 : Calculate α_s using eqn. 1.89
- 5 : Calculate ϕ_s using eqn. 1.93
- 6 : Calculate θ_0 using eqn. 1.98
- 7 : Calculate θ_{1s} using eqn. 1.97

- 8 : Calculate β_0 using eqn. 1.95
- 9 : Calculate θ_{1c} using eqn. 1.96
- 10 : Update λ_{TTPP} using the last of eqns. 1.94
- 11 : Calculate C_{HTPP} using eqn. 1.62
- 12 : Calculate C_{YTPP} using eqn. 1.64
- Back to beginning of iteration.

In case of hover, λ_{TTPP} remains fixed to the uniform inflow value. Any one of the other variables can be iterated over.

The rotor power can be calculated using eqn. 1.66. A simpler alternative expression is given in the next section. When yaw equilibrium is considered, then for a conventional configuration, the tail rotor collective is a trim variable. The yaw equilibrium equation is given by eqn. 1.77. In non-dimensional form

$$C_Q - \frac{l_T}{R} C_{YF} \frac{(\Omega_T R_T)^2}{(\Omega R)^2} \frac{A_T}{A} = 0$$

where $(\Omega_T R_T)^2/(\Omega R)^2$ is the tip speed ratio of the tail rotor to the main rotor, $C_{YF} = Y_F/\rho A_T (\Omega_T R_T)^2$ is the tail rotor thrust coefficient, and A_T/A is the ratio of tail rotor disk area to main rotor disk area. The tail rotor collective is then related to the tail rotor thrust by

$$\theta_{75T} = \frac{6C_{YF}}{\sigma_T a_T} + \frac{3}{2} \kappa_h \sqrt{\frac{C_{YF}}{2}}$$

with assumption of uniform inflow and linear tail rotor twist. σ_T and a_T are the tail rotor solidity and blade element lift curve slopes.

1.6.5 Rotor Power and Lift to Drag Ratio

Consider the non-dimensional torque C_Q , as in eqn. 1.66. Recall, that the non-dimensional power is equal to the non-dimensional torque C_Q . The expression was of the following form

$$C_Q = \frac{\sigma a}{2} \left[\lambda_{TTPP} \left(\frac{\theta_0}{3} + \frac{\theta_{tw}}{4} - \frac{\lambda_{TTPP}}{2} + \frac{\mu\beta_{1c}}{2} + \frac{\mu\theta_{1s}}{4} \right) \right] + \frac{\sigma a}{2} \frac{1}{4} \frac{C_{do}}{a} (1 + \mu^2) + \dots \text{ other terms} \quad (1.99)$$

where the ‘... other terms’ are terms that are independent of inflow λ_{TTPP} and profile drag c_{do} , and are functions of only the blade flapping angle and the control angles. From the expression of thrust in the tip path plane (eqn. 1.60) we have

$$\frac{\sigma a}{2} \left(\frac{\theta_0}{3} + \frac{\theta_{tw}}{4} - \frac{\lambda_{TTPP}}{2} + \frac{\mu\beta_{1c}}{2} + \frac{\mu\theta_{1s}}{4} \right) = C_T - \frac{\sigma a}{2} \left(\frac{\theta_0 \mu^2}{2} + \frac{\theta_{tw} \mu^2}{4} + \frac{\theta_{1s} \mu}{4} \right) \quad (1.100)$$

Using the above expression we have

$$C_Q = \lambda_{TTPP} C_T - \lambda_{TTPP} \frac{\sigma a}{2} \left(\frac{\theta_0 \mu^2}{2} + \frac{\theta_{tw} \mu^2}{4} + \frac{\theta_{1s} \mu}{4} \right) + \frac{\sigma a}{2} \frac{1}{4} \frac{C_{do}}{a} (1 + \mu^2) + \dots \text{ other terms} \quad (1.101)$$

Now from eqns. 1.94 we have

$$\lambda_{TTPP} = \mu \left(\frac{C_D + C_H}{C_T} \right) + \mu\beta_{1c} + \lambda_c + \lambda_i \quad (1.102)$$

Hence

$$\begin{aligned} \lambda_{TTPP} C_T &= \mu C_D + \mu (C_H + \beta_{1c} C_T) \lambda_c C_T + \lambda_i C_T \\ &= \mu C_D + \mu C_{HTPP} + \lambda_c C_T + \lambda_i C_T \end{aligned} \quad (1.103)$$

Substitute the above expression of $\lambda_{TTPP}C_T$ in the expression for C_Q

$$C_Q = \mu C_D + \mu C_{HTPP} + \lambda_c C_T + \lambda_i C_T - \lambda_{TTPP} \frac{\sigma a}{2} \left(\frac{\theta_0 \mu^2}{2} + \frac{\theta_{tw} \mu^2}{4} + \frac{\theta_{1s} \mu}{4} \right) + \frac{\sigma a}{2} \frac{1}{4} \frac{C_{d0}}{a} (1 + \mu^2) + \dots \text{ other terms} \quad (1.104)$$

Now, μC_{HTPP} can be calculated from eqn. 1.62 as

$$\mu C_{HTPP} = \lambda_{TTPP} \frac{\sigma a}{2} \left(\frac{\theta_0 \mu^2}{2} + \frac{\theta_{tw} \mu^2}{4} + \frac{\theta_{1s} \mu}{4} \right) + \frac{\sigma a}{2} \frac{1}{4} \frac{C_{d0}}{a} 2\mu^2 + (\dots) \quad (1.105)$$

It can be shown that the terms (\dots) cancel with those described earlier as ... other terms. Also, recall that

$$\mu C_D = \frac{1}{2} \mu^3 \left(\frac{f}{A} \right)$$

Thus the final expression of non-dimensional power (or torque) in forward flight takes the following form

$$C_P = \lambda_i C_T + \frac{\sigma C_{d0}}{8} (1 + 3\mu^2) + \frac{1}{2} \mu^3 \left(\frac{f}{A} \right) + \lambda_c C_T = \frac{\kappa_f C_T}{2\sqrt{\lambda_{TTPP}^2 + \mu^2}} + \frac{\sigma C_{d0}}{8} (1 + 3\mu^2) + \frac{1}{2} \mu^3 \left(\frac{f}{A} \right) + \lambda_c C_T \quad (1.106)$$

λ_i is the induced inflow perpendicular to the tip path plane. The above is the familiar form used in a simple momentum theory analysis of a rotor in forward flight using uniform inflow.

$$C_P = C_{Pi} + C_{Po} + C_{Pp} + C_{Pc}$$

C_{Pi} = rotor induced power required to produce thrust

C_{Po} = rotor profile power required to overcome rotor drag (turn in real fluid)

C_{Pp} = parasite power required to overcome airframe drag

C_{Pc} = rotor climb power required to increase gravitational potential.

The induced power is given by

$$C_{Pi} = \frac{\kappa_f C_T}{2\sqrt{\lambda_{TTPP}^2 + \mu^2}} \approx \kappa_f \frac{C_T^2}{2\mu} \quad \text{for } \mu > 0.15 \quad (1.107)$$

The profile power is often modified empirically to include radial flow and reversed flow effects

$$C_{Po} = \frac{\sigma C_{d0}}{8} (1 + 4.6\mu^2) \quad (1.108)$$

The parasite power is

$$C_{Pp} = \frac{1}{2} \mu^3 \left(\frac{f}{A} \right)$$

The climb power is given by

$$C_{Pc} = \lambda_c C_T \quad \left(\lambda_c = \frac{V_c}{\Omega R} \right)$$

where V_c is the climb velocity. Thus, the climb velocity can be calculated from the available power and level flight power as

$$V_c = \frac{P_a - (P_i + P_o + P_p)}{T} = \frac{\Delta P}{W}$$

Note that, while using blade element theory, the required rotor power is calculated directly from eqn. 1.66. This expression includes all components of power and is difficult to extract the individual components. The analytical extraction is given above to identify the different components and have a physical feel regarding the growth and decay of each with forward speed. The induced power decreases with forward speed. The profile power increases as square of forward speed. The parasite power increases as cube of forward speed. The reduction of induced power with forward speed is due to the uniform inflow assumption. In real flight the induced power increases, gradually above $\mu > 0.25$ due to nonuniform inflow. Either of the expressions, eqn. 1.66 or eqn. 1.106, can be used. Both produce the same result. If eqn. 1.106 is used, often the radial flow corrected expression of profile power (eqn. 1.108) is used.

The power to generate thrust (induced power) and to overcome rotor drag (profile power) together can be associated with an effective drag of a rotor C_{DE} .

$$C_{P_i} + C_{P_o} = \mu C_{DE}$$

That is,

$$\mu C_{DE} = C_P - (C_{P_p} + C_{P_c}) = C_P - (\mu C_D + \lambda_c C_T)$$

In level flight then,

$$C_{DE} = \frac{C_P}{\mu} - C_D$$

Under trim condition the net rotor propulsive force C_X must equal the airframe drag C_D , hence the above expression is also written as

$$C_{DE} = \frac{C_P}{\mu} - C_X$$

where $X = T \sin \alpha_s \cos \phi_s - H \cos \alpha_s = D$. The rotor lift-to-drag ratio is given by the ratio between lift and effective drag

$$(L/D_E) = \frac{C_L}{C_P/\mu - C_D} \approx \frac{C_T}{C_P/\mu - C_D}$$

Just as Figure of Merit is the measure of rotor efficiency in hover, L/D_E is the measure of rotor efficiency in forward flight. Note that during autorotation, $C_P = 0$, and the rotor effective drag equals the airframe drag (or propulsive force).

$$C_{DE} = -C_X \quad \text{in autorotation}$$

Example 1.3:

Numerical results are calculated for a rotor with the following characteristics. Yaw equilibrium is ignored.

Rotor

$$\begin{array}{llll} N_b = 4 & R = 25ft & c = 1.5ft & \Omega R = 700ft/s \\ v_\beta = 1.05/rev & \gamma = 8.0 & C_{l_a} = 5.73 & C_{d0} = 0.01 \end{array}$$

Vehicle

$$\begin{array}{llll}
 W = 15,000\text{lbs} & h = 6.0\text{ft} & l_T = 32\text{ft} & f = 20\text{ft}^2 \\
 x_{cg} = -2\text{ft} & y_{cg} = 0\text{ft} & \text{Engine} = 2000\text{HP} & \rho = 0.002377\text{slugs/ft}^3 \\
 M_{xF} = 0\text{ft} - \text{lbs} & M_{yF} = 0\text{ft} - \text{lbs} & \kappa_h = 1.15 & \kappa_f = 1.00
 \end{array}$$

(a) Hover at sea level

shaft HP required = 1535 HP

$$\theta_0 = 10.81^\circ \quad \theta_{1c} = 1.31^\circ \quad \theta_{1s} = -5.47^\circ$$

$$\alpha_s = -9.22^\circ \quad \alpha_s = -4.92^\circ$$

$$\beta_0 = 5.24^\circ \quad \beta_{1c} = 5.55^\circ \quad \beta_{1s} = 0.74^\circ$$

Maximum climb velocity $v_c = 34.08$ ft/sec**(b) Forward flight of 200 ft/sec at sea level**

shaft HP required = 947 HP

$$\mu = 0.2857 \quad C_T = 0.006559 \quad \lambda_{TPP} = 0.02284$$

$$C_P = 0.000325$$

$$\theta_0 = 8.25^\circ \quad \theta_{1c} = 3.31^\circ \quad \theta_{1s} = -11.24^\circ$$

$$\beta_0 = 4.84^\circ \quad \beta_{1c} = 6.38^\circ \quad \beta_{1s} = 0.91^\circ$$

$$\alpha_s = -4.10^\circ \quad \phi_s = -3.84^\circ$$

Maximum climb velocity $v_c = 38.6$ ft/sec

The variation of trim parameters with advance ratio are shown in figure 1.16

Example 1.4:

The rotor and vehicle characteristics are given below.

Rotor

4-bladed, radius = 27 ft, chord = 1.75 ft

Tip speed $\Omega R = 700$ ft/sec, Lock number $\gamma = 8$

Hingeless blades with flap frequency = 1.08 /rev

Airfoil $C_{la} = 6$, $C_{d0} = 0.01$ VehicleWeight = 16,000 lbs $h/R = 0.2R$ Assume $M_{xF} = M_{yF} = Y_F = 0$ $f/A = 0.1$ (flat plate area/Disk Area) $x_{cg} = 0.01R$ (forward of shaft axis), $y_{cg} = 0$

Engine Shaft Power = 2000 HP

Assume uniform inflow in hover and forward flight ($\kappa_h = \kappa_f = 1.15$).

Calculate for hover

(a) shaft HP needed

(b) control settings

(c) maximum climb velocity

(d) flap response

Calculate for a forward flight of 280 ft/sec

(e) shaft HP needed

(f) control settings

(g) maximum climb velocity

(h) flap response

Ignore yaw equilibrium.

Hover

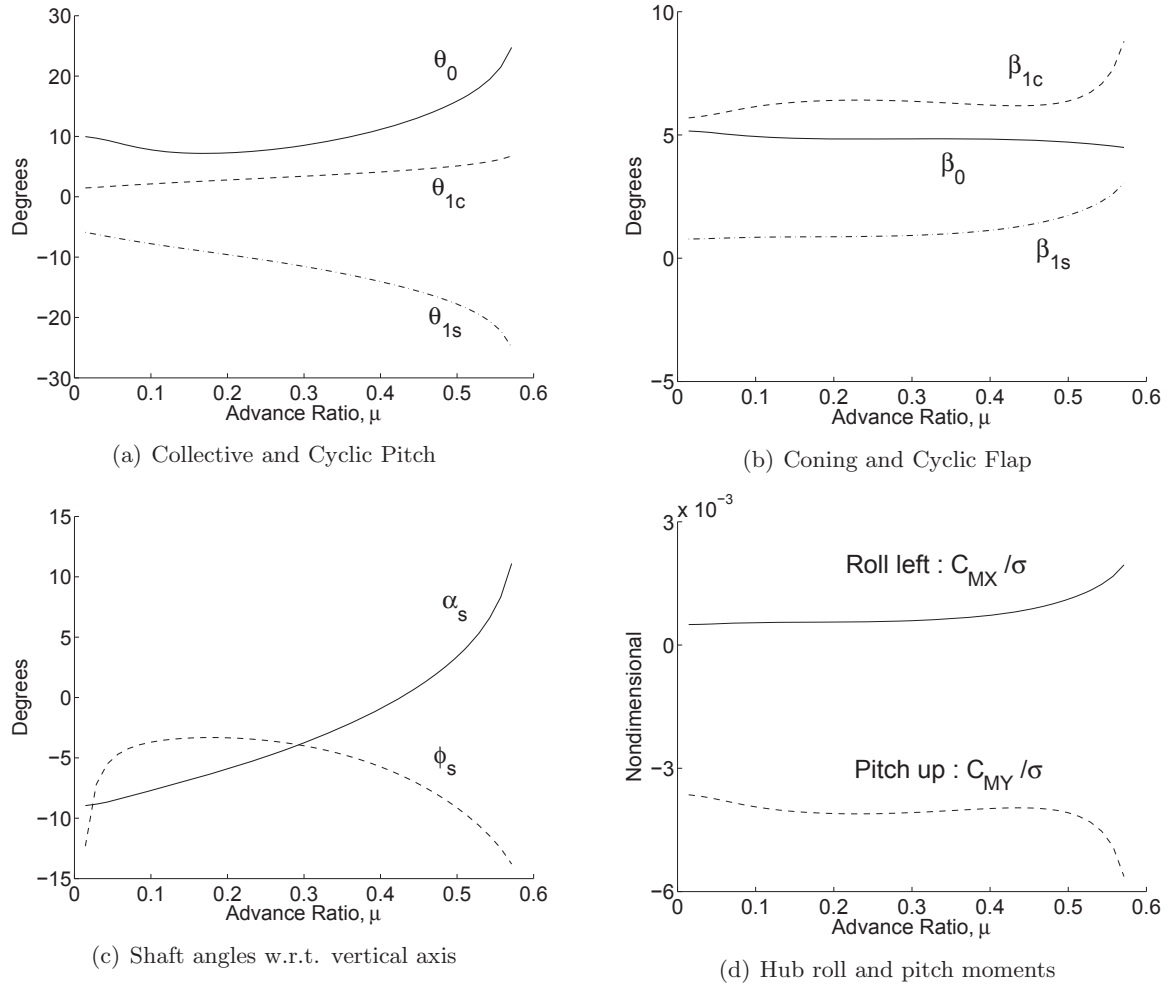


Figure 1.16: Variation of aircraft trim angles with forward flight speed (Example 1.3)

$$C_T = \frac{W}{\rho \pi R^2 (\Omega R)^2} = \frac{1600}{(0.002378) \pi (27)^2 (700)^2} = 0.006$$

$$\sigma = \frac{N_b c}{\pi R} = \frac{4(1.75)}{\pi(27)} = 0.0825$$

$$\lambda = \kappa \sqrt{\frac{C_T}{2}} = 0.063$$

$$C_P = \lambda C_T + \frac{\sigma C_{do}}{8} = 0.063(0.006) + \frac{0.0825(0.01)}{8} = 0.00048$$

(a) The shaft HP is given by

$$\begin{aligned} P &= C_p \pi R^2 \rho (\Omega R)^3 = 0.00048 \pi (27)^2 (0.002378) (700)^3 = 8.988 \times 10^5 \text{ ft-lb/sec} \\ &= \frac{8.988 \times 10^5}{550} = 1634 \text{ HP} \end{aligned}$$

(b) Using the iterative procedure with $\mu = 0$

$$\theta_0 = 9.57^\circ$$

$$\theta_{1c} = -0.109^\circ$$

$$\theta_{1s} = 0.469^\circ$$

$$\alpha_s = 0.166^\circ$$

$$\phi_s = -0.026^\circ$$

(c) Maximum climb velocity

$$V_c = \frac{2\Delta P}{W} = \frac{2(2000 - 1634)}{16000} 550 = 25.2 \text{ ft/sec}$$

(d) Flap Response

$$\beta_0 = 4.09^\circ$$

$$\beta_{1c} = -0.48^\circ$$

$$\beta_{1s} = -0.03^\circ$$

Forward Flight

(e) Using the iterative procedure, the Shaft HP is

$$\mu = 0.3947$$

$$C_T = 0.0060$$

$$\lambda = 0.05877 \quad \alpha = 9.559, \quad \phi_s = -0.1291^\circ$$

$$C_P = 0.0005369 \quad P = 1823\text{HP}$$

$$C_{HTPP} = 0.0002034 \quad C_{YTPP} = 0.0000167$$

(f) Control angles

$$\theta_0 = 10.9^\circ$$

$$\theta_{1c} = 1.823^\circ$$

$$\theta_{1s} = -9.963^\circ$$

(g) Maximum climb velocity

$$V = \frac{\Delta P}{W} = 6.08 \text{ ft/sec}$$

(h) Flap response

$$\beta_0 = 3.728^\circ$$

$$\beta_{1c} = 0.174^\circ$$

$$\beta_{1s} = -0.0301^\circ$$

1.6.6 The Jacobian Method for Trim

The method described earlier, using analytical expressions for rotor forces and moments, was a point iteration procedure, also called Picard's iterations. In this procedure, the general approach to solving a set of nonlinear equations

$$f_1(x_1, x_2, \dots, x_n) = 0$$

$$f_2(x_1, x_2, \dots, x_n) = 0$$

...

$$f_n(x_1, x_2, \dots, x_n) = 0$$

or in vector notation

$$\mathbf{f}(\mathbf{x}) = \mathbf{0}$$

is to re-express $\mathbf{f}(\mathbf{x})$ as $\mathbf{g}(\mathbf{x}) - \mathbf{x}$ so that the equation takes the following form

$$\mathbf{x} = \mathbf{g}(\mathbf{x})$$

The solution procedure is then simply to iterate

$$\mathbf{x}^{k+1} = \mathbf{g}(\mathbf{x}^k); \quad k = 0, 1, 2, \dots,$$

The procedure is useful for simple models and initial design calculations – even though convergence is not guaranteed. For non-uniform inflow, higher frequencies of blade dynamics, unsteady aerodynamics, and for the nonlinear trim equations, there will not be analytical expressions. The rotor forces and moments are then obtained numerically by integrating the blade element forces. The non-linear trim equations are then solved using the Newton-Raphson procedure.

The Newton-Raphson procedure is based on the calculation of trim Jacobian. Start from an initial estimate of the six trim variables $\mathbf{x}^0 = x_1^0, x_2^0, \dots, x_6^0$. Calculate the rotor forces and moments using these initial estimates. Initial estimates are often obtained using the simple model given in the previous section. Now substitute in the vehicle equilibrium eqns. 1.72 – 1.77. These equations have the general form $\mathbf{f}(\mathbf{x}) = \mathbf{0}$. Upon substitution, the right hand side of the equations will not be zero but have non-zero residuals, since obviously $\mathbf{f}(\mathbf{x}^0) \neq \mathbf{0}$. The objective is to determine an increment $\Delta\mathbf{x}$ such that

$$\mathbf{f}(\mathbf{x}^0 + \Delta\mathbf{x}) = \mathbf{0}$$

A Taylor expansion of the above leads to

$$\begin{aligned} f_1 + \frac{\partial f_1}{\partial x_1} \Delta x_1 + \frac{\partial f_1}{\partial x_2} \Delta x_2 + \dots + \frac{\partial f_1}{\partial x_6} \Delta x_6 + \text{higher order terms} &= 0 \\ f_2 + \frac{\partial f_2}{\partial x_1} \Delta x_1 + \frac{\partial f_2}{\partial x_2} \Delta x_2 + \dots + \frac{\partial f_2}{\partial x_6} \Delta x_6 + \text{higher order terms} &= 0 \\ \dots & \\ f_6 + \frac{\partial f_6}{\partial x_1} \Delta x_1 + \frac{\partial f_6}{\partial x_2} \Delta x_2 + \dots + \frac{\partial f_6}{\partial x_6} \Delta x_6 + \text{higher order terms} &= 0 \end{aligned} \tag{1.109}$$

where the derivatives and functions are evaluated about the solution \mathbf{x}^0 . Dropping the higher order terms we have the requirement

$$\mathbf{f}^0 + \mathbf{J}\Delta\mathbf{x} = \mathbf{0}$$

Therefore the update is given by

$$\Delta \mathbf{x} = \mathbf{J}^{-1}(\mathbf{0} - \mathbf{f}^0)$$

or in general

$$\Delta \mathbf{x} = \mathbf{J}^{-1}(\mathbf{f}^T - \mathbf{f}^0)$$

where the targets are not zero but \mathbf{f}^T . For the complete aircraft, of course, the targets are zero. \mathbf{J} is called the Jacobian matrix.

For an isolated rotor, moment trim, the updates are based on the following Jacobian.

$$\mathbf{J} \begin{Bmatrix} \Delta \theta_0 \\ \Delta \theta_{1c} \\ \Delta \theta_{1s} \end{Bmatrix} = \begin{bmatrix} \frac{\partial T}{\partial \theta_0} & \frac{\partial T}{\partial \theta_{1c}} & \frac{\partial T}{\partial \theta_{1s}} \\ \frac{\partial M_X}{\partial \theta_0} & \frac{\partial M_X}{\partial \theta_{1c}} & \frac{\partial M_X}{\partial \theta_{1s}} \\ \frac{\partial M_Y}{\partial \theta_0} & \frac{\partial M_Y}{\partial \theta_{1c}} & \frac{\partial M_Y}{\partial \theta_{1s}} \end{bmatrix} \begin{Bmatrix} \Delta \theta_0 \\ \Delta \theta_{1c} \\ \Delta \theta_{1s} \end{Bmatrix} = \begin{Bmatrix} T_0 - T \\ M_{X0} - M_X \\ M_{Y0} - M_Y \end{Bmatrix} \quad (1.110)$$

where T_0 , M_{X0} and M_{Y0} are the trim targets.

For an isolated rotor wind tunnel trim the trim variable updates are based on the following Jacobian.

$$\mathbf{J} \begin{Bmatrix} \Delta \theta_0 \\ \Delta \theta_{1c} \\ \Delta \theta_{1s} \end{Bmatrix} = \begin{bmatrix} \frac{\partial T}{\partial \theta_0} & \frac{\partial T}{\partial \theta_{1c}} & \frac{\partial T}{\partial \theta_{1s}} \\ \frac{\partial \beta_{1c0}}{\partial \theta_0} & \frac{\partial \beta_{1c0}}{\partial \theta_{1c}} & \frac{\partial \beta_{1c0}}{\partial \theta_{1s}} \\ \frac{\partial \beta_{1s0}}{\partial \theta_0} & \frac{\partial \beta_{1s0}}{\partial \theta_{1c}} & \frac{\partial \beta_{1s0}}{\partial \theta_{1s}} \end{bmatrix} \begin{Bmatrix} \Delta \theta_0 \\ \Delta \theta_{1c} \\ \Delta \theta_{1s} \end{Bmatrix} = \begin{Bmatrix} T_0 - T \\ \beta_{1c0} - \beta_{1c} \\ \beta_{1s0} - \beta_{1s} \end{Bmatrix} \quad (1.111)$$

where T_0 , β_{1c0} and β_{1s0} are the trim targets.

The Jacobians are calculated by perturbing the initial estimates of each trim variable by 5%–10%, and using the finite differences of the perturbed trim targets. If the trim targets are linear functions of the trim variables the solution is obtained in one iteration. Generally they are nonlinear functions and several iterations are necessary. After each iteration, the Jacobian must be recalculated, about the current trim variables. For rotors, except in the case of severe stall, this is often not necessary. The Jacobian is often calculated only once, before the trim iterations begin, and stored for all subsequent iterations. This procedure is called the *modified Newton* procedure.

Questions

1. What are the advantages and the disadvantages of the tractor and pusher type tail rotors?
2. Which one of the following rotors need tail rotors for hovering?
 - i) Coaxial rotor (ABC-Sikorsky)
 - ii) Circulation controlled rotor (X-wing-NSRDC)
 - iii) Tilt rotor (XV-15-Bell)
 - iv) Tandem rotor (Chinook-Boeing Vertol)
 - v) Tip jet rotor
3. Justify the following:
 - The helicopters with conventional rotors are limited to a forward speed of about 170 knots.
 - In hovering flight, the rotor disk follows the shaft (in about 3 revs).
 - A rotation of the tail boom in the opposite direction of the blades rotation can be troublesome.
 - For a rotor with hinge offset, the phase lag of the flapping motion, with respect to the pitch motion is not 90° .
 - For a fixed wing, control surfaces such as flaps and ailerons are used to control the lift, but that is not the case with rotor blades.
 - It is quite common that a small precone of 2 to 3 degrees is given to hingeless blades.
 - For a flapping rotor with no cyclic pitch (tail rotor), the hub and control planes are equivalent.
 - For a feathering rotor with non flapping (propeller with cyclic pitch), the hub plane and TPP are identical.
 - The rotor behaves as a gyro, maintaining its orientation relative to the inertial space in vacuum.
 - A teetering rotor perhaps is not practical for large helicopters.
 - An optimum rotor is a hypothetical rotor that is efficient in hover for one thrust level.
 - The induced rotor power is the largest in hover.

REFERENCES

1. Johnson, W., Helicopter Theory, Princeton University Press, (1980), Ch. 1, 2, 4 and 5.
2. Gessow, A., and Meyers, G.C., Aerodynamics of the Helicopter, Frederick Ungar Publishing Co., (1952) Ch. 3, 4, 7, 8 and 9.

Chapter 2

Flap Dynamics

Blade flapping is the motion of the blade normal to the rotation plane. In this chapter, the natural vibration characteristics and response due to external force such as an aerodynamic force is examined for a flapping blade. Initially, a simplified model is used, where the blade is assumed rigid with a hinge offset. Later on, a more refined model is used, where the blade is represented as an elastic beam. The primary objective of this chapter is to grasp various mathematical tools as applicable to rotor analyses through an application to isolated flap mode dynamics. It is very important to understand the need and usage of these tools for a simple case of flapping blade, such that these could be extended to more complex coupled blade dynamics in later chapters.

It should be kept in mind that the dynamics of flap mode is by itself an important step towards the understanding of coupled rotor dynamics. The knowledge of natural vibration characteristics of isolated flap motion is important for vibration, loads, blade stresses and aeromechanical stability. In fact, the fundamental rotating flap frequency is a key physical parameter and has a direct influence on vehicle performance, flight stability and rotor dynamics. Typically for an articulated blade, this frequency varies from 1.03 to 1.05 times the rotational speed, whereas for hingeless blades, the flap frequency varies from 1.08 to 1.15 times the rotational speed. For an articulated rotor, the maximum bending stress takes place about mid-span of the blade whereas for a hingeless rotor, it takes place near the root. We shall see later that higher the flap frequency, the larger will be the bending stresses in the blade.

2.1 Rigid Blade Model

The rotor blade is assumed to be rigid undergoing a single degree of motion, i.e., flapping motion about a hinge. A real rotor can have : (1) a mechanical hinge, or (2) a virtual hinge. Articulated rotors have mechanical hinges. Hingeless rotors, even though they are called hingeless, have virtual hinges. Virtual hinges are created by flexible structures near the blade root which are softer than the rest of the blade. Thus a hingeless rotor can also be modeled as a rigid rotor flapping about a hinge. Except that in this case, the hinge location or offset is an equivalent one determined from experiment, or a flexible blade analysis.

2.1.1 Hinged Blade with zero offset

Consider a rigid blade hinged at the rotation axis. See Fig. 2.2 (a). This simple configuration represents an articulated rotor blade. The blade undergoes a single degree of motion, i.e. flapping. Assume that there is no spring restraint and the flap hinge offset is set to zero. The forces acting on an element of length dr , and their moment arms, are listed below. The flapping angle, β is assumed to be small. The inertial force (IF) on the element is defined as the mass of the element

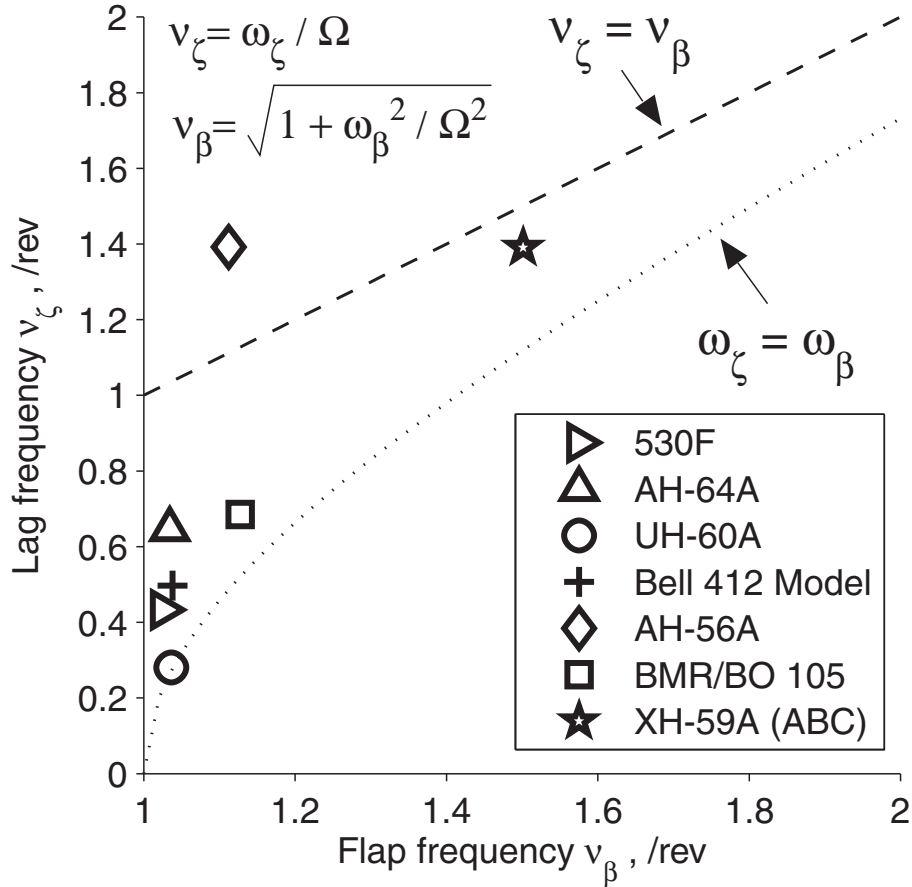


Figure 2.1: **Flap and lag frequencies of rotor blades**

multiplied with the flapping acceleration of the element, acting opposite to the direction of the flapping acceleration (See Chapter 1, Section 1.2.3).

a) inertia force (IF): $m dr r \ddot{\beta}$ arm r with respect to rotation axis

b) centrifugal force (CF): $m dr \Omega^2 r$ arm $z = r\beta$

c) aerodynamic force (AF): $F_z dr$ arm r

Taking moment about flap hinge

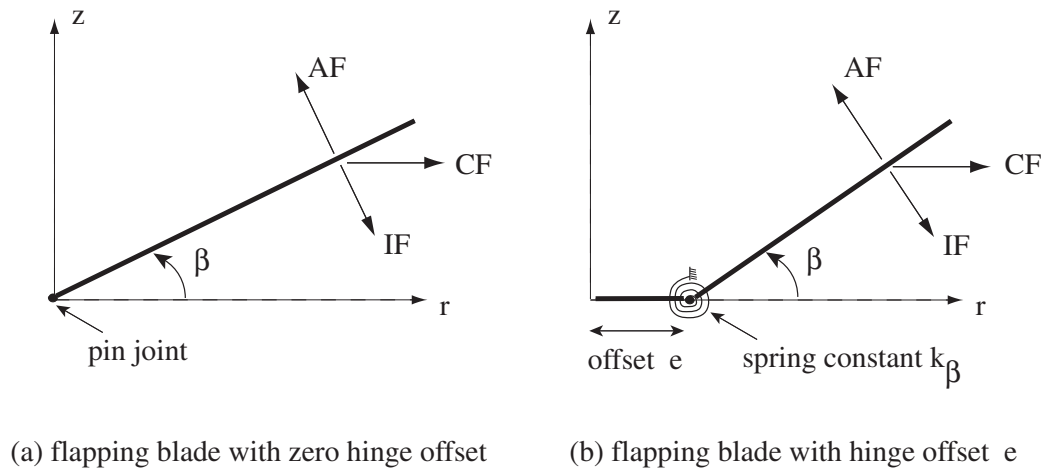
$$\int_0^R (mr \ddot{\beta} dr)r + \int_0^R (m\Omega^2 r dr)r\beta - \int_0^R (F_z dr)r = 0$$

$$\left(\int_0^R mr^2 dr \right) (\ddot{\beta} + \Omega^2 \beta) = \int_0^R r F_z dr$$

$\int_0^R mr^2 dr =$ mass moment of inertia about flap hinge $= I_b$, with units $(lb - in - sec)^2$ or $kg - m^2$

For a uniform blade $I_b = \frac{mR^3}{3}$ where m is the mass per unit length ($lb - sec^2/in^2$ or kg/m). The above expression leads to the flap equation

$$\ddot{\beta} + \Omega^2 \beta = \frac{1}{I_b} \int_0^R r F_z dr \quad (2.1)$$



(a) flapping blade with zero hinge offset (b) flapping blade with hinge offset e

Figure 2.2: Rigid blade flapping model

Now express time in terms of azimuth angle

$$\psi = \Omega t$$

where Ω is the rotational speed, rad/sec. The derivatives are

$$\dot{\beta} = \frac{\partial \beta}{\partial t} = \Omega \frac{\partial \beta}{\partial \psi} = \Omega^* \beta \quad \ddot{\beta} = \Omega^2 \beta^{**}$$

$\dot{\beta}$ was the rate of change of flapping with time (rad/sec), whereas β^* is the rate of change of flapping with azimuth of rotation (rad/rad). The flap equation then becomes

$$\frac{\partial^2 \beta}{\partial \psi^2} + \beta = \frac{1}{I_b \Omega^2} \int_0^R r F_z dr$$

or

$$\beta^{**} + \beta = \gamma \overline{M}_\beta \quad (2.2)$$

where

$$\beta^{**} = \frac{\partial^2 \beta}{\partial \psi^2} \quad \gamma = \frac{\rho a c R^4}{I_b} \quad \overline{M}_\beta = \frac{1}{\rho a c R^4 \Omega^2} \int_0^R r F_z dr$$

γ is called the Lock number, ρ is the air density, a is the aerodynamic lift curve slope, c is the chord and R is the rotor radius. The Lock number represents the ratio of aerodynamic force and inertia force. Typically, the value of γ varies from 5 to 10, the smaller number for a heavy blade whereas the larger value for a light blade.

The flapping equation can be imagined to represent a single degree of freedom spring-mass system. The natural frequency of the system, from eqn. 2.1, is Ω rad/sec.

$$\text{i. e.,} \quad \omega_\beta = \Omega \quad \text{rad/sec}$$

The natural frequency of the system, from eqn. 2.2, is 1 rad/rad.

$$\text{i. e.,} \quad \nu_\beta = 1 \quad \text{rad/sec}$$

where

$$\nu_\beta = \frac{\omega_\beta}{\Omega}$$

The unit of rad/rad is also defined as per rev (/rev or p). Thus, 1 rad/rad is 1/rev (or 1p), 2 rad/rad is 2/rev (or 2p) and so on. For this configuration, the spring stiffness is a result of centrifugal force. To visualize this spring, consider the simple example of a stone tied to a thread and rotated. Very soon the thread is taut, and the stone stretches out due to centrifugal force. The natural frequency of this system will be the rotational frequency itself. The aerodynamic force \overline{M}_β can be motion dependent and will be discussed in later sections.

2.1.2 Hinged Blade with Offset

Consider a rigid blade hinged at a distance e from the rotation axis. It is assumed that there is a flap bending spring at the hinge. See Fig. 2.2(b). This configuration represents an articulated blade with a hinge offset. It can also be a simple approximation for a hingeless blade (as shown in the next section).

$$h(q_1, q_2, q_3, \dots, t) = 0 \quad (2.3)$$

$$\ddot{h} + \alpha \dot{h} + \beta h = 0 \quad (2.4)$$

Force acting on an element dr are

- a) inertia force (IF): $m dr (r - e) \ddot{\beta}$ arm($r - e$) about hinge
- b) centrifugal force (CF): $m dr \Omega^2 r$ arm($r - e$) β
- c) aerodynamic force (AF): $F_z dr$ arm($r - e$)
- d) spring moment (SF): $k_\beta (\beta - \beta_p)$ about hinge

β_p is a precone angle. Taking moment about flap hinge,

$$\int_e^R m(r - e)^2 dr \ddot{\beta} + \int_e^R m \Omega^2 r (r - e) dr \beta - \int_e^R F_z (r - e) dr + k_\beta (\beta - \beta_p) = 0$$

or

$$k_\beta (\beta - \beta_p) = \int_e^R F_z (r - e) dr - \int_e^R m \Omega^2 r (r - e) dr \beta - \int_e^R m (r - e)^2 dr \ddot{\beta} \quad (2.5)$$

The spring moment $k_\beta (\beta - \beta_p)$ is the flapping moment, or the flap bending moment, at the hinge. It is a dynamic load, i.e., the balance of external forcing, minus centrifugal forcing, minus the part used up by blade acceleration.

$$I_\beta = \int_e^R m (r - e)^2 dr, \quad \text{mass moment of inertia about flap hinge}$$

$$\begin{aligned} \int_e^R m r (r - e) dr &= \int_e^R m (r - e)^2 dr + \int_e^R m e (r - e) dr \\ &= I_\beta \left(1 + \frac{e \int_e^R m (r - e) dr}{\int_e^R m (r - e)^2 dr} \right) \end{aligned}$$

Flap equation

$$I_\beta \left\{ \ddot{\beta} + \Omega^2 \left(1 + \frac{e \int_e^R m(r-e) dr}{I_\beta} \right) \beta + \frac{k_\beta}{I_\beta} (\beta - \beta_p) \right\} = \int_e^R F_z(r-e) dr$$

Writing in non-dimensional form by dividing with $I_b \Omega^2$.

$$I_\beta^* (\beta + \nu_\beta^2 \beta) = \frac{k_\beta}{I_b} \frac{1}{\Omega^2} \beta_p + \gamma \overline{M}_\beta \quad I_\beta^* = \frac{I_\beta}{I_b}$$

ν_β is the non-dimensional flap frequency

$$\nu_\beta^2 = 1 + \frac{e \int_e^R m(r-e) dr}{I_b} + \frac{k_\beta}{I_b \Omega^2} \quad / \text{rev}$$

For uniform blade, the second term is

$$\frac{e}{I_\beta} \int_e^R m(r-e) dr = \frac{3e}{2(R-e)} \simeq \frac{3}{2} \frac{e}{R}$$

The third term represents the non-rotating natural frequency made dimensionless using rotational frequency

$$\frac{k_\beta}{I_b} = \omega_{\beta 0}^2 \quad \text{rad/sec}$$

The term $I_\beta^* = I_\beta / I_b$ is nearly equal to unity. Thus the flap equation can be written as

$$\beta + \nu_\beta^2 \beta = \frac{\omega_0^2}{\Omega^2} \beta_p + \gamma \overline{M}_\beta$$

The β_p is the precone angle given to the blade to reduce the steady flap moment about the hinge and typically its value is about 2 to 3°. Again this represents a single degree spring-mass system, as shown in Fig. 2.3.

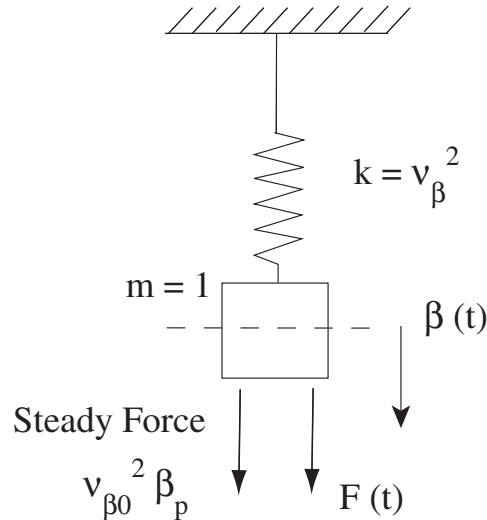


Figure 2.3: The rigid blade flapping equation represents a single degree of freedom spring-mass system

The natural frequency of the system

$$\begin{aligned} \frac{\omega_\beta}{\Omega} &= \nu_\beta && \text{/rev} \\ \omega_\beta &= \nu_\beta \Omega && \text{rad/sec} \\ &= \left(1 + \frac{3}{2} \frac{e}{R} + \frac{\omega_{\beta 0}^2}{\Omega^2}\right)^{1/2} \Omega && \text{for a uniform blade} \end{aligned}$$

where $\omega_{\beta 0}$ is the non-rotating natural frequency, rad/sec. For zero spring case

$$\omega_n = \left(1 + \frac{3}{2} \frac{e}{R}\right)^{1/2} \Omega \quad \text{rad/sec}$$

Typically e varies between 4 to 6 % of rotor radius for an articulated blade. The variation of flap frequency with hinge offset is given in Fig. 2.4

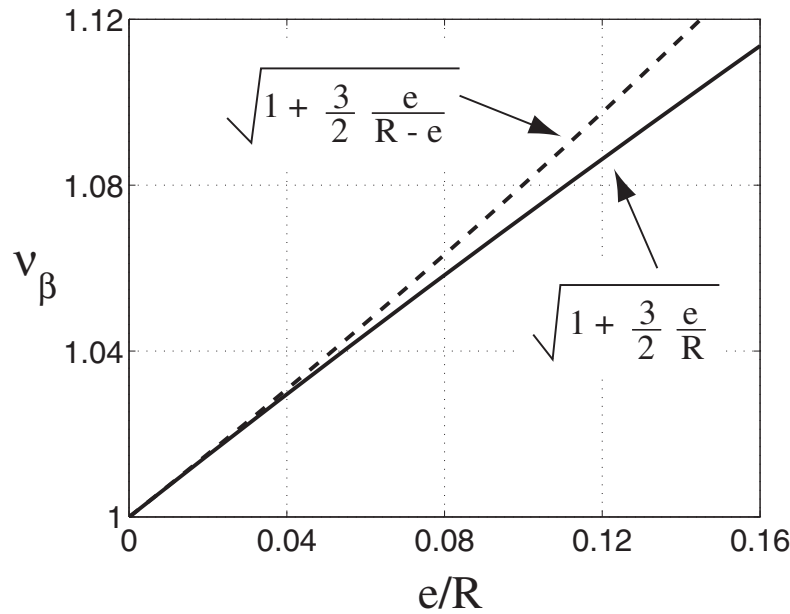


Figure 2.4: **Variation of flapping frequency with hinge offset; Spring constant $k_\beta = 0$**

Example 2.1:

Calculate the rotating flap frequency of an articulated rotor blade with hinge offset of 1 ft. from the rotation axis. Given are the rotor radius = 20 feet and the RPM = 360.

$$\frac{e}{R} = \frac{1}{20} = 0.05$$

$$1 + \frac{3}{2} \frac{e}{R} = 1.075$$

$$\begin{aligned} \text{Flap frequency} &= \left(1 + \frac{3}{2} \frac{e}{R}\right)^{1/2} = 1.037 && \text{per rev} \\ &= 1.037 \Omega && \text{rad/sec} \\ &= 1.037 \times \frac{360}{60} \times 2\pi && \\ &= 39.1 && \text{rad/sec} \end{aligned}$$

2.1.3 Hingeless Blade with Equivalent Hinge Offset

To simplify analysis, a hingeless blade can be idealized into a rigid blade with an offset hinge and a bending spring at the hinge. This representation can be useful for the calculation of flight dynamic and aeroelastic stability because the global characteristics are well represented with this simple model. It is assumed that the fundamental mode shape and the fundamental frequency is available for the hingeless blade, either using a flexible blade model (described later) or determined through an experiment. To obtain an equivalent simplified configuration, two constants are to be determined, e and k_β . Two simple methods to calculate these constants are as follows.

One method is to compare the nonrotating and rotating natural frequencies.

$$\nu_\beta = \frac{\omega_\beta}{\Omega} = \left(1 + \frac{3e}{2R} + \frac{\omega_{\beta 0}^2}{\Omega^2} \right)^{1/2}$$

where $\omega_{\beta 0}$ and ω_β are the non-rotating and rotating flap frequencies for basic hingeless blade. Then,

$$k_\beta = \omega_{\beta 0}^2 I_b$$

$$e = \frac{2}{3} R \left(\nu_\beta^2 - \frac{\omega_{\beta 0}^2}{\Omega^2} - 1 \right)$$

where I_b is the flap mass moment of inertia. A second method is to compare the rotating bending

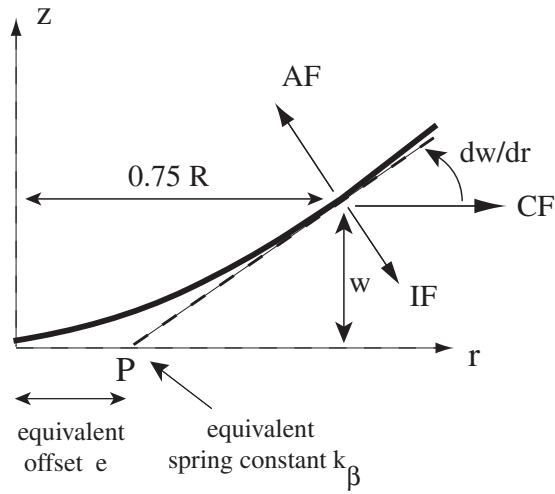


Figure 2.5: Equivalent rigid blade flapping model for a hingeless blade

slope and displacement at a reference station 75% R (see Fig. 2.5) and the rotating frequency. Extend the slope line to find point P on the undeflected blade axis. Then,

$$e = R - \frac{w}{\left(\frac{dw}{dr}\right)}$$

This spring stiffness can be calculated comparing the rotating flap frequency.

$$k_\beta = I_\beta \Omega^2 \left(\nu_\beta^2 - 1 - \frac{3e}{2R} \right)$$

2.2 Flexible Beam Model

A better representation for a rotor blade is to assume it is an elastic beam restrained at the root. The blade undergoes bending deflection distribution under loading. The assumption of treating blade as a slender beam is quite appropriate because the cross sectional dimensions are much smaller than the length. In this chapter, only flap bending (out of plane) is considered. The lead-lag bending (in-plane) and torsion will be introduced in the next chapter. The physics of a rotating beam in bending differs from that of a non-rotating beam because of nonlinear coupling with axial elongation. To understand this coupling, consider first the dynamics of axial elongation alone for a rotating beam.

2.2.1 Axial Deformation

A beam element located at a distance r from the rotation axis before deformation is at a location $r + u$ after deformation. The centrifugal force acting on the element is then $m dr \Omega^2 (r + u)$. A force balance on the element gives

$$(T + T' dr) - T + m dr \Omega^2 (r + u) - m dr \ddot{u} + f_h dr = 0$$

from which the gradient of tensile force follows

$$T' = m \ddot{u} - m \Omega^2 (r + u) - f_h \quad (2.6)$$

The tensile force is related to the axial elongation as

$$T = EAu'$$

Substituting in eqn. 2.6 we obtain the governing equation for axial elongation

$$m \ddot{u} - m \Omega^2 u - (EAu')' = f_h + m \Omega^2 r \quad (2.7)$$

Note that a force balance at a section gives the following expression for the tensile force

$$T = \int_r^R (-m \ddot{u} + m \Omega^2 u + m \Omega^2 \rho + f_h) d\rho \quad (2.8)$$

which when differentiated once using Leibnitz theorem gives back eqn. 2.6.

2.2.2 Euler-Bernoulli Theory of Bending

The Euler-Bernoulli assumption states that a plane section normal to the beam centerline remains plane and normal after deformation (see Fig. 2.6). This is a valid assumption when the shear deflection is negligible. The assumption helps to uncouple bending and shear deflections. The assumption lets one express the rotation of a section solely in terms of its translation. If the out of plane bending deflection is w then the bending slope is simply the derivative of the deflection, i.e. $w^+ = \frac{dw}{ds}$, where w^+ is the derivative with respect to the span coordinate along the deformed beam s . For small deflections, the derivative can be taken with respect to the undeformed beam coordinate r . Thus $w^+ \simeq \frac{dw}{dr} = w'$. The bending curvature κ , and the radius of curvature ρ , are then related to the deflection by the following kinematic relation

$$\kappa = \frac{1}{\rho} = \frac{w^{++}}{[1 + w^{+2}]^{\frac{3}{2}}} \simeq \frac{w''}{[1 + w'^2]^{\frac{3}{2}}} \quad (2.9)$$

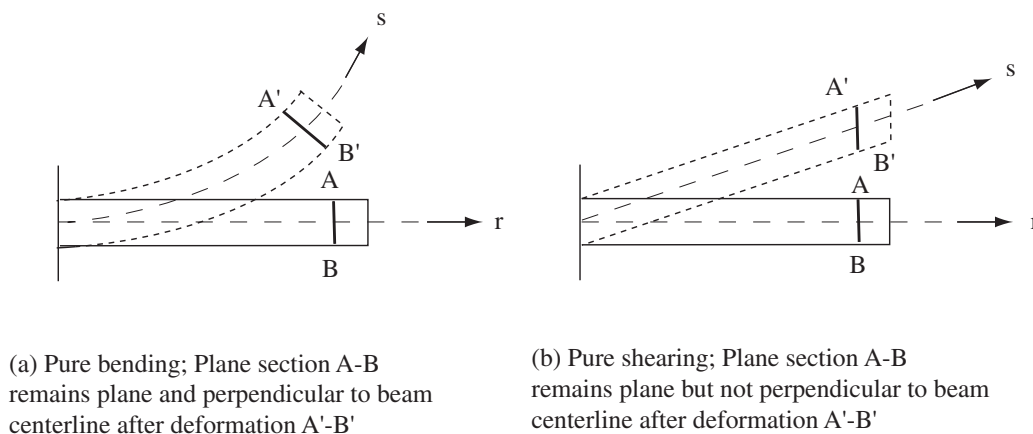


Figure 2.6: Pure bending and pure shearing of beams

The strain due to bending ϵ_{rr} at a distance z from the beam centerline is related to the curvature by $\epsilon_{rr} = z/\rho$. The strain is then related to the stress σ_{rr} by the constitutive relation

$$\sigma_{rr} = E\epsilon_{rr} = E\frac{z}{\rho} \quad (2.10)$$

The bending moment at any section is then given by the resultant

$$M(r) = \int_{\text{Area}} \sigma_{rr} z dA = \int_{\text{Area}} E\frac{z^2}{\rho} dA = \frac{EI}{\rho} = EI\frac{w''}{[1+w'^2]^{\frac{3}{2}}} \simeq EIw'' \quad (2.11)$$

The kinematic relation 2.9, the constitutive relation 2.10, and the resultant relation 2.11 together form the Euler-Bernoulli beam theory. Note that the constitutive relation 2.10 and the resultant 2.11 generates the well-known identity

$$\frac{M}{I} = \frac{E}{\rho} = \frac{\sigma_{rr}}{z} \quad (2.12)$$

2.2.3 Flap Bending Equation using Newton's Laws

Let us derive a general equation of motion of a beam under external loading. It is assumed small deflections as compared to its dimensions. Also, it is assumed that the rotation of the element is small as compared to the vertical displacement. Thus, the rotary inertia effects are neglected in the derivation. For convenience, structural damping is neglected. The geometry of the deformed beam is shown in Fig. 2.7. where $f_z(r, t)$ is the vertical load per unit span (kg/m, lb/in) and $w(r, t)$ is the vertical deflection at station r (m, in). Consider an element dr of mass $m dr$, where m is mass per unit span, with units kg/m or lb/in. The forces acting on it are the inertia force $m\ddot{w} dr$, the external vertical force f_z , the external axial force f_H , and the internal tensile, shear, and bending loads T (N, lbf), S (N, lbf), and M (N-m, lbf-in). S is positive when it acts in the positive direction z (i.e., upward) on a negative x plane (i.e., left face of element). M is positive when top fiber under compression. T is positive in tension. The bending slope $w' = dw/dr$ is assumed to be small, i.e. w'^2 will be neglected with respect to unity. Thus $\cos w' \simeq 1$ and $\sin w' \simeq w'$.

Consider the equilibrium of forces and moment on the element. Force equilibrium in the z -direction gives

$$f_z dr + S - S - \frac{dS}{dr} dr - m\ddot{w} dr - T\frac{dw}{dr} + \left(T + \frac{dT}{dr}\right) \left(\frac{dw}{dr} + \frac{d^2w}{dr^2} dr\right) = 0$$

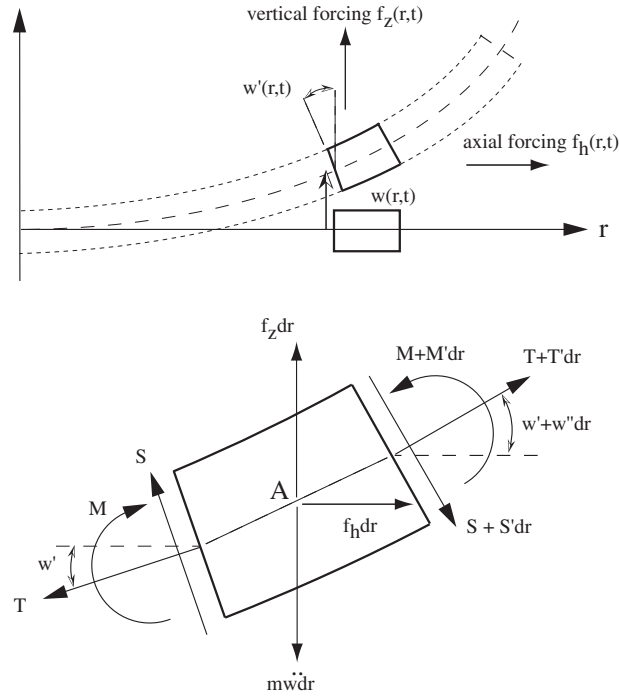


Figure 2.7: Pure bending of a rotating beam and free body diagram of a beam segment

or

$$f_z - \frac{dS}{dr} - m\ddot{w} + T \frac{d^2 w}{dr^2} + \frac{dT}{dr} \frac{dw}{dr} = 0$$

or

$$\frac{dS}{dr} = f_z - m\ddot{w} + \frac{d}{dr} \left(T \frac{dw}{dr} \right) \quad (2.13)$$

The above expression states that the spatial derivative of shear is equal to the sectional loading distribution. The expression leads to the governing partial differential equation (PDE) for deflection w . To this end, S and T must be expressed in terms of either w or other known quantities. S can be expressed in terms of w by considering the moment equilibrium about the center of the element, point A. Moment about A gives

$$M + S dr - M - \frac{dM}{dr} dr = 0$$

or

$$\frac{dM}{dr} = S \quad (2.14)$$

The above expression states that the spatial derivative of bending moment is the shear distribution. Now use the Euler-Bernoulli beam theory result to obtain the beam model. Consider a rectangular beam cross-section as shown in Fig. 2.8. Let O be the shear center of the section. The shear center, by definition, is such point where a force applied vertically creates a pure bending deformation with no accompanying twist. For a rectangular closed section this point is the area centroid. Let (ξ, η) be the principle axes at this section, i.e. $I_{\xi\eta} = 0$. The Euler-Bernoulli beam theory gives

$$M = EI \frac{d^2 w}{dr^2} \quad (2.15)$$

where I equals $I_{\eta\eta}$, the area moment of inertia about the principle axis η , with units m^2 or in^2 . For a rectangular section

$$I_{\eta\eta} = \frac{bd^3}{12} \quad \text{m}^4 \text{ or } \text{in}^4$$

E is the Young's Modulus of the beam material, with units N/m^2 or lbf/in^2 . EI is the flexural stiffness about the principle axis η , with units $\text{N}\cdot\text{m}^2$ or $\text{lbf}\cdot\text{in}^2$. Thus eqn.2.14 becomes

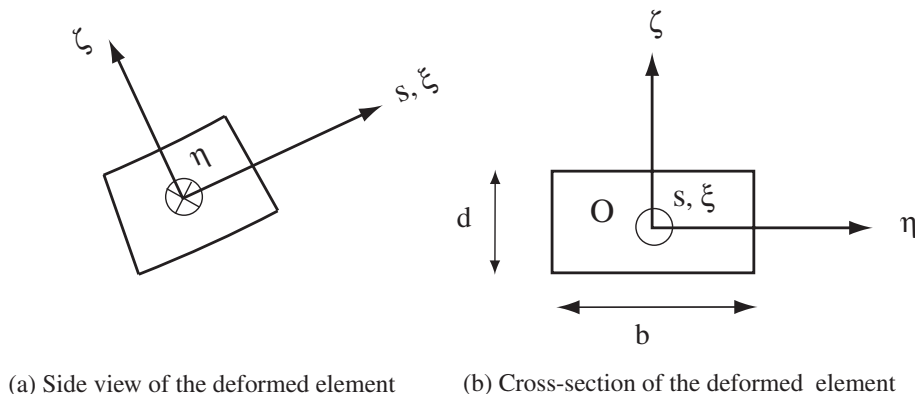


Figure 2.8: **Rectangular cross-section of a beam with centroid O**

$$S = \frac{d}{dr} \left(EI \frac{d^2 w}{dr^2} \right)$$

Substitute the above expression in eqn.2.13 to obtain

$$\frac{d^2}{dr^2} \left(EI \frac{d^2 w}{dr^2} \right) + m \frac{\partial^2 w}{\partial t^2} - \frac{d}{dr} \left(T \frac{dw}{dr} \right) = f_z(r, t) \quad (2.16)$$

T is related to axial elongation via eqn. 2.6. Thus the governing equation in bending takes the following form.

$$m\ddot{w} + (EIw'')'' - (EAu'w')' = f_z(r, t) \quad (2.17)$$

The difference between the above equation and the non-rotating beam equation is the nonlinear coupling term $EAu'w'$. The coupling term can also be expressed in a different manner. Recall that T is also expressed as eqn. 2.8 Thus the governing equation can also be written in the following form.

$$m\ddot{w} + (EIw'')'' - \left[w' \int_x^R (-m\ddot{u} + m\Omega^2 u + m\Omega^2 \rho + f_h) d\rho \right]' = f_z(r, t) \quad (2.18)$$

The above form is useful for a simple flapping blade analysis without axial dynamics. Without axial dynamics, i.e. $u = 0$, eqn. 2.17 reduces to the non-rotating beam equation. The form given in eqn. 2.18, however, can be used to retain the centrifugal term $m\Omega^2 \rho$. Physically, the centrifugal term affects u which affects w via the nonlinear coupling term $EAu'w'$, but eqn. 2.18 helps us recast the fundamentally non-linear problem into a linear form by ignoring the axial elongation but retaining the effect of centrifugal stiffness.

Let us study this centrifugal stiffness term further. Using force equilibrium in axial direction, i.e. eqn. 2.6, ignoring axial elongation, and assuming no external forcing in the axial direction, we have

$$\frac{dT}{dr} + m\Omega^2 r = 0$$

or

$$\frac{dT}{dr} = -m\Omega^2 r$$

For a uniform beam, integration of the above expression yields

$$T = -\frac{1}{2}m\Omega^2 r^2 + C$$

$$\text{At } r = R, T = 0 \quad \text{therefore} \quad C = \frac{1}{2}m\Omega^2 R^2$$

$$T = \frac{m\Omega^2}{2}(R^2 - r^2)$$

where Ω is the rotation speed, rad/sec. In general for a non-uniform blade we have

$$T = \int_r^R m\Omega^2 \rho d\rho \tag{2.19}$$

which is same as eqn. 2.8 with axial deformation u and axial forcing f_h ignored.

To summarize, under static conditions, $T = 0$ and $\ddot{w} = 0$, the shear force and bending moment at any spanwise station can be calculated directly using eqns. 2.13 and 2.14 using the external loading f_z . Under dynamic conditions, but non-rotating, the inertial term in eqn. 2.13 depends on the vertical displacement w . Therefore it is necessary to combine eqns. 2.13 and 2.14 and solve for the vertical displacement w . Rotation of the beam adds the tensile force term on the right hand side of eqn. 2.13. The tensile force term depends on the axial elongation u via eqn. 2.8. Therefore now it is necessary to combine eqns. 2.13 and 2.14 with eqn. 2.8. This combination is nonlinear in nature. But in its simplest form, ignoring axial dynamics but still retaining the centrifugal effect of rotation, it can be expressed in the following form.

$$\begin{aligned} m\ddot{w} + (EIw'')'' - (Tw')' &= f_z(r, t) \\ T &= \int_r^R m\Omega^2 \rho d\rho \end{aligned} \tag{2.20}$$

2.2.4 Second Order Nonlinear Coupled Axial Elongation-Flap Bending

In the previous section, the governing equation for a rotating flapping blade was derived as follows

$$\begin{aligned} m\ddot{w} + (EIw'')'' - (EAu'w')' &= f_z(r, t) \quad : \text{Flap} \\ m\ddot{u} - m\Omega^2 u - (EAu')' &= f_h + m\Omega^2 r \quad : \text{Axial} \end{aligned}$$

The equations were then reduced to the simplest linear form as given in eqn. 2.20. The above non-linear equations assumed small deformations. For large deformations, non-linearities upto second order can be retained. It is important to note that these equations are of little engineering value by themselves. In fact, even the non-linear equations given above for small deformations provide no significant improvement in the prediction of w compared to the simpler formulation given in eqn. 2.20; unless ofcourse the axial deformation is desired. For rotor dynamics however, axial deformations by themselves are of lesser engineering value. The non-linear couplings due to large deformations will be critical later, while analyzing the coupled flap-lag-torsion dynamics of real rotor blades. There, several sources of nonlinear structural couplings will be encountered - geometric, coriolis, and centrifugal. The purpose in this section is to provide a simple illustration of the physical source, and a second order treatment, of one such nonlinear coupling: the elongation-flap bending coupling that occurs for large deformation in the presence of centrifugal force.

Large deformations require two changes in the previous formulation.

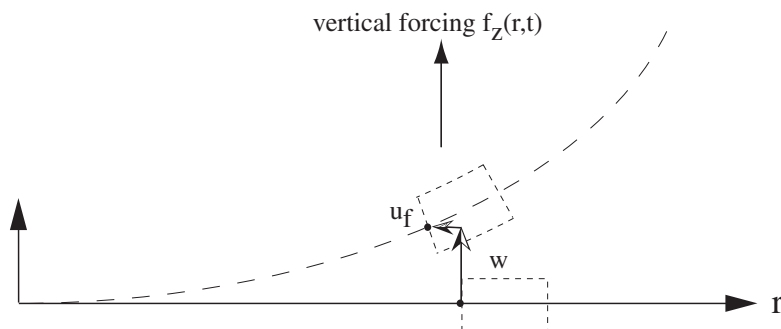
(a) Deformation $u_e(r,t)$ in axial direction due to axial flexibility(b) Deformation $u_f(r,t)$ in axial direction due to axial fore-shortening because of bending flexibility

Figure 2.9: Axial dynamics of a beam

1. The axial force balance term: $(T + T'dr) - T$, is now modified to $(T + T'dr) \cos(w' + w''dr) - T \cos w'$.
2. The tensile force T is no longer expressible as $E Au'$. It must be replaced with $E Au'_e$ where u_e is the axial elongation of the beam. Note that u is the deformation in the axial direction. For large deformations u and u_e are not the same.

Let us first understand the axial elongation u_e and the axial deformation u physically. u is not simply the component of u_e in the radial direction, or vice versa. The bending deflection w introduces a axial deformation simply by virtue of the fact that the length of the beam must remain the same after bending. This is an axial foreshortening effect, u_f . The total axial deformation u is the sum of these two effects (see Fig. 2.9).

$$u = u_e + u_f$$

The axial foreshortening u_f is caused by the bending of the beam and can therefore be expressed as a function of w . Figure 2.10 shows a beam element dr in the undeformed and deformed positions.

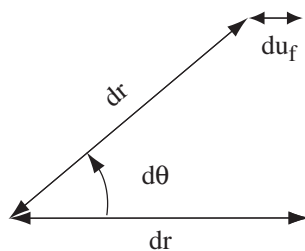


Figure 2.10: Axial foreshortening of a beam due to bending

Because the length of the element remains constant during pure bending the rotation creates an axial foreshortening du_f .

$$\begin{aligned} du_f &= \text{axial length of } dr \text{ after deformation} - \text{axial length of } dr \text{ before deformation} \\ &= dr \cos d\theta - dr \\ &= -2 \sin^2(d\theta/2) dr \\ &= -(1/2)w'^2 dr \quad \text{using } d\theta = w', \text{ and } d\theta \text{ is small} \end{aligned}$$

Thus at any station r

$$\begin{aligned} u_f(r) &= -\frac{1}{2} \int_0^r w'^2 dr \\ \dot{u}_f(r) &= -\int_0^r w' \dot{w}' dr \\ \ddot{u}_f(r) &= -\int_0^r (\dot{w}'^2 + w' \ddot{w}') dr \end{aligned} \tag{2.21}$$

The equation for axial equilibrium now contains the following expression

$$(T + T' dr) \cos(w' + w'' dr) - T \cos w'$$

Noting that upto second order, $\cos \theta = 1 - \theta^2/2$, we have

$$\begin{aligned} \cos(w' + w'' dr) &= 1 - \frac{1}{2}w'^2 - w'w'' \\ \cos w' &= 1 - \frac{1}{2}w'^2 \end{aligned}$$

It follows

$$\begin{aligned} (T + T' dr) \cos(w' + w'' dr) - T \cos w' &= T' \left(1 - \frac{1}{2}w'^2\right) - Tw'w'' \\ &= \left[T \left(1 - \frac{1}{2}w'^2\right)\right]' \end{aligned} \tag{2.22}$$

Thus the former eqn. 2.6 now takes the following form

$$\left[T \left(1 - \frac{1}{2}w'^2\right)\right]' = m\ddot{u} - m\Omega^2(r + u) - f_h \tag{2.23}$$

T remains to be replaced in terms of u . $T = EAu'_e$, thus u_e needs to be expressed in terms of u . To this end, note that

$$\begin{aligned} du &= (dr + du_e) \cos d\theta - dx \\ &= dr \left(-\frac{1}{2}w'^2\right) + du_e \left(1 - \frac{1}{2}w'^2\right) \end{aligned} \tag{2.24}$$

It follows

$$u'_e \left(1 - \frac{1}{2}w'^2\right) = u' + \frac{1}{2}w'^2$$

Thus

$$T \left(1 - \frac{1}{2}w'^2\right) = EAu'_e \left(1 - \frac{1}{2}w'^2\right) = EA \left(u' + \frac{1}{2}w'^2\right)$$

The new axial dynamics equation becomes

$$\left[EA \left(u' + \frac{1}{2} w'^2 \right) \right]' = m\ddot{u} - m\Omega^2 (r + u) - f_h \quad (2.25)$$

The flap equation requires the term $(Tw)'$. Note that we have, to second order

$$\begin{aligned} u'_e &\approx \left(u' + \frac{1}{2} w'^2 \right) \left(1 + \frac{1}{2} w'^2 \right) \\ &\approx u' + \frac{1}{2} w'^2 \end{aligned} \quad (2.26)$$

Thus

$$Tw' = EAu'_e w' \approx EA \left(\approx u' + \frac{1}{2} w'^2 \right) w'$$

which to second order remains same as before, i.e.

$$Tw' = EAu'w'$$

Thus the flap equation remains the same as before, eqn. 2.17. The final equations for this case are therefore

$$\begin{aligned} m\ddot{w} + (EIw'')'' - (EAu'w')' &= f_z(r, t) \\ \left[EA \left(u' + \frac{1}{2} w'^2 \right) \right]' &= m\ddot{u} - m\Omega^2 (r + u) - f_h \end{aligned} \quad (2.27)$$

The time varying aerodynamic forcing in the axial direction is an order of magnitude smaller than the lift. Both the axial flexibility u_e and the axial forshortening u_f are in general an order of magnitude smaller than the bending displacement w . The natural frequency in axial flexibility u_e is usually greater than 10/rev. The axial dynamics is therefore often neglected during a simple analysis, and only eqn. 2.17 is considered.

However, it is important to understand that the nonlinear term $(EAu'w')'$ in the bending equation cannot be dropped. For a rotating beam this term introduces the centrifugal stiffening. Thus care must be taken while linearizing the beam bending equation. It must be replaced with $(Tw)'$, where

$$T = \int_r^R m\Omega^2 \rho d\rho$$

The axial dynamics can then be ignored. The axial forshortening can be found from eqn. 2.21 once w is known. The steady axial deflection can be found simply from

$$T = EAu'_e$$

While this procedure was well-understood by rotorcraft designers, it created a hurdle for space-craft dynamicists during the development of flexible multibody analysis. Dropping the nonlinear term led to what was known as the ‘spin-up’ problem, an erroneous dynamic softening of the rotor beam during spin up which led to unbounded tip deflection. This was because the multibody analyses were made for general purpose structures which could not incorporate specific linearization methods depending on the topology of the problem. The problem was subsequently rectified by adding the necessary corrections termed ‘geometric stiffness due to operating loads’ [10]. Thus, to summarize, if axial dynamics is neglected in the analysis, eqn. 2.20 must be used. If axial dynamics is included, eqn. 2.27 must be used.

2.2.5 Axial Elongation as a Quasi-coordinate

The axial elongation u_e presented above is called a quasi-coordinate. A coordinate is called a quasi-coordinate when it is related to physical displacements and angles through integrals that cannot be evaluated in closed form. The integrals cannot be evaluated because they involve velocities or angular velocities (or their kinetic analogues in terms of gradients and curvature) of the physical displacements. For example, the quasi-coordinate u_e is related to the axial displacement u in the following manner

$$u = u_e - \frac{1}{2} \int_0^r w'^2 dr + O(\epsilon^4)$$

Similarly, in the presence of both flap and lag bending deflections, we have

$$u = u_e - \frac{1}{2} \int_0^r (v'^2 + w'^2) dr + O(\epsilon^4)$$

where w and v are the flap and lag deflections.

Torsion dynamics can also be formulated in terms of a quasi-coordinate (we shall see later). In this case we have

$$\hat{\phi} = \phi - \frac{1}{2} \int_0^r v'' w' dr + O(\epsilon^2)$$

where $\hat{\phi}$ is an angle defining the rotation of a section, and ϕ is the elastic torsion of the section. The torsion moment is given by $GJ\phi'$. ϕ is a quasi-coordinate. Note how in the case of large deformations the rotation of a section depends not only on the elastic torsion but also on the flap and lag bending deflections.

2.2.6 Boundary Conditions

Consider the pure bending equation 2.20. It is fourth order in r , and requires four boundary conditions, two on either edge. The order-0 and order-1 boundary conditions are called the Dirichlet conditions. They are the geometric boundary conditions imposed on the displacement and slope at the boundary. The order-2 and order-3 boundary conditions are the Neumann conditions. They are the force boundary conditions imposed on the bending moment and shear force at the boundary. Figure 2.11 shows some of the important boundary conditions at an edge. They can be combined to provide more general conditions.

Figure 2.11(a) shows a cantilevered or fixed end condition where the deformation and slope are zero. Figure 2.11(b) shows a simple supported or pin ended condition where the deformation and bending moment are zero. Figure 2.11(c) shows a shear spring restrained condition. Here the bending moment is zero. The shear force is as restrained by the linear spring. For a positive deformation (upwards), the shear force is downwards on the left edge, hence the negative sign as per convention. Note that for a spring on the other end of the beam the boundary condition would be $(EIw'')' = +k_1 w$. Figure 2.11(d) shows a bending spring restrained boundary condition. Here the shear force is zero. The bending moment is as restrained by the rotary spring. Again, for a positive deformation (counter-clockwise rotation) the bending moment is clockwise, and on the left face, hence positive as per convention. Note that for a spring on the other end of the beam the boundary condition would be $EIw'' = -k_2 w$.

The beam equation is second order in time, hence requires two initial conditions to obtain response solution. At time = 0, the velocity $\dot{w}(r)$ and displacement w are prescribed.

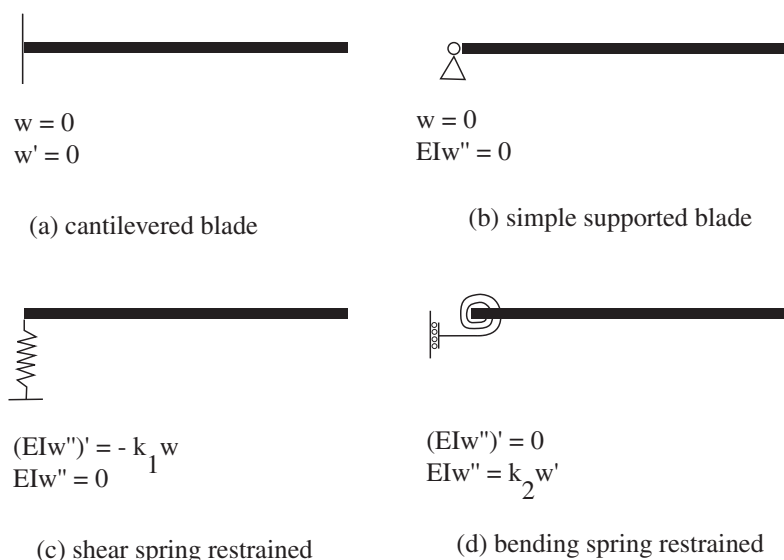


Figure 2.11: Boundary conditions of a beam

2.3 Non-rotating beam vibration

To understand beam vibration, we begin without any axial force and without rotation. See Fig. 2.12. Assuming the beam to be uniform and with no axial force, the partial differential equation ??

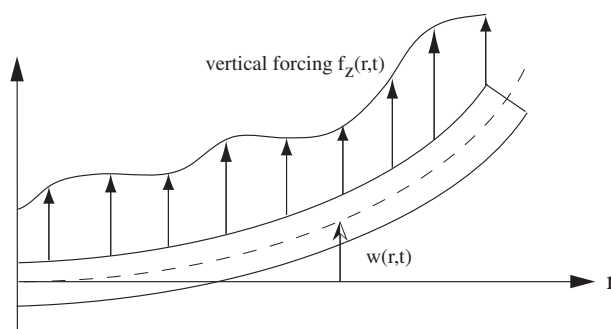


Figure 2.12: Non-rotating beam in pure bending

becomes

$$m\ddot{w} + (EIw'')'' = f_z(r, t) \tag{2.28}$$

If the beam is initially disturbed and then left to vibrate on its own, it follows what is called the natural vibration characteristics. During this time there is no forcing on the beam. Thus, to determine the natural vibration characteristics, one needs to calculate only the homogeneous solution by setting $f_z(r, t) = 0$.

$$m\ddot{w} + (EIw'')'' = 0 \tag{2.29}$$

The solution is of the following form.

$$w(r, t) = \phi(r)q(t)$$

One out of the two functions $\phi(r)$, or $q(t)$, can be assigned the dimension of $w(r, t)$, the other remains nondimensional. Here, we assume $q(t)$ to have the same dimension as $w(r, t)$, with units

of displacement (m or in) in this case. $\phi(r)$ is considered nondimensional. Assuming that there is no damping in the structure, we seek $q(t)$ of the form

$$q(t) = q_0 e^{i\omega t}$$

In presence of damping, we seek $q(t)$ of the form

$$q(t) = q_0 e^{\alpha + i\omega t} = q_0 e^{st}$$

To obtain natural vibration characteristics we assume there is no damping. We seek such solutions because a linear combination of such solutions can be used to construct any continuous function of time. Substituting the solution type in the homogenous equation yields

$$\left[\phi^{IV} - \frac{m\omega^2}{EI} \phi \right] q_0 e^{i\omega t} = 0$$

For a non-trivial $q(t)$, i.e. a non-zero q_0 , we must have

$$\phi^{IV} - \omega^2 \frac{m}{EI} \phi = 0 \quad (2.30)$$

which is a fourth order ordinary differential equation (ODE). This equation has an analytical solution. Assume

$$\phi(r) = C e^{pr}$$

where C is a nondimensional constant and p has dimension of 1/length. Solve for p to obtain

$$p^4 = \frac{m\omega^2}{EI}$$

This gives four roots $p = \pm\lambda, \pm i\lambda$ where

$$\lambda = \left(\frac{m\omega^2}{EI} \right)^{1/4} \quad \text{units: 1/m or 1/in} \quad (2.31)$$

Therefore $\phi(r)$ becomes

$$\phi(r) = C_1 \sinh \lambda r + C_2 \cosh \lambda r + C_3 \sin \lambda r + C_4 \cos \lambda r \quad (2.32)$$

The constants C_1, C_2, C_3 and C_4 are evaluated using the four boundary conditions specific to the beam. The constants have units of m or in.

2.3.1 Cantilevered Beam

For a cantilevered beam, the boundary conditions are as follows. At $r = 0$, displacement and slopes are zero at all times. Thus

$$\begin{aligned} w(0, t) = 0 &\implies \phi(0)q(t) = 0 \implies \phi(0) = 0 \\ w'(0, t) = 0 &\implies \phi'(0)q(t) = 0 \implies \phi'(0) = 0 \end{aligned} \quad (2.33)$$

At $r = R$, the bending moment and shear forces are zero at all times. Thus

$$\begin{aligned} EIw''(0, t) = 0 &\implies \phi''(0)q(t) = 0 \implies \phi''(0) = 0 \\ EIw'''(0, t) = 0 &\implies \phi'''(0)q(t) = 0 \implies \phi'''(0) = 0 \end{aligned} \quad (2.34)$$

Substituting the four conditions in eqn. 2.32

$$\begin{bmatrix} 0 & 1 & 0 & 1 \\ 1 & 0 & 1 & 0 \\ \sinh \lambda R & \cosh \lambda R & -\sin \lambda R & -\cos \lambda R \\ \cosh \lambda R & \sinh \lambda R & -\cos \lambda R & -\sin \lambda R \end{bmatrix} \begin{bmatrix} C_1 \\ C_2 \\ C_3 \\ C_4 \end{bmatrix} = 0 \quad (2.35)$$

For non-trivial solution, the determinant of square matrix must be zero. This results in

$$\cos \lambda R \cosh \lambda R = -1$$

or

$$\cos \lambda R = -1/\cosh \lambda R$$

which is a transcendental equation. The solutions are obtained by plotting the left hand side and right hand side components individually and mark the points where these two graphs cross each other. See Fig. 2.13. The solution is given by

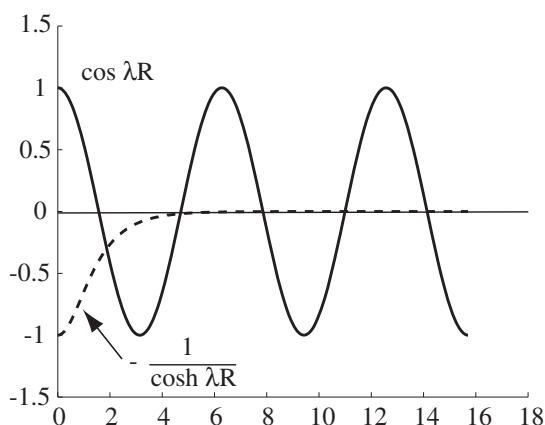


Figure 2.13: **Solution of transcendental equation for cantilevered beam natural frequencies**

$$\begin{aligned} (\lambda R)_1 &= 1.87 \\ (\lambda R)_2 &= 4.69 \\ (\lambda R)_3 &= 7.85 \\ (\lambda R)_j &\cong (2j-1)\frac{\pi}{2} \quad \text{for } j > 3 \end{aligned} \quad (2.36)$$

The natural frequencies can now be easily calculated from equation 2.31, which can be reorganized as follows

$$\omega_j = (\lambda R)_j^2 \sqrt{\frac{EI}{mR^4}} = f_j \sqrt{\frac{EI}{mR^4}} \quad (2.37)$$

f_j in equation 2.37 represent an infinite set of eigenvalues which produce an infinite number of natural frequencies of the beam. The mode shape corresponding to any particular natural frequency is obtained by solving for C_1 , C_2 , C_3 , and C_4 from equation 2.35. Note that, for an equation of this

form, one cannot solve for C_1 , C_2 , C_4 , and C_5 . Any three can be solved for in terms of the fourth, for example solve for C_1 , C_2 , and C_3 in terms of C_4 .

$$\begin{bmatrix} 0 & 1 & 0 \\ 1 & 0 & 1 \\ \sinh \lambda R & \cosh \lambda R & -\cos \lambda R \end{bmatrix} \begin{bmatrix} C_1 \\ C_2 \\ C_3 \end{bmatrix} = \begin{bmatrix} 1 \\ 0 \\ -\cos \lambda R \end{bmatrix} C_4$$

Set $C_4 = 1$. The mode shape from equation 2.32 then becomes

$$\begin{aligned} \phi_j(r) &= \cosh \lambda_j r - \cos \lambda_j r - \frac{\cosh(\lambda R)_j + \cos(\lambda R)_j}{\sinh(\lambda R)_j + \sin(\lambda R)_j} (\sinh \lambda_j r - \sin \lambda_j r) \\ \phi_j(x) &= \cosh f_j x - \cos f_j x - \frac{\cosh f_j + \cos f_j}{\sinh f_j + \sin f_j} (\sinh f_j x - \sin f_j x) \\ f_j &= (\lambda R)_j \quad x = r/R \end{aligned} \tag{2.38}$$

Corresponding to each λR , we have a different $\phi(r)$. These mode shapes are plotted in Fig. 2.14. These are the free vibration modes or natural modes. Note that the magnitude of the mode shapes are not unique. They depend on the value of C_4 chosen. Often it is chosen such that $\phi_j(R) = 1$. Each homogeneous solution is of the general form

$$w_j(r, t) = c_j \phi_j(r) e^{i(\omega_j t + d_j)}$$

where c_j and d_j are constants determined by the the initial displacement and velocity of each mode. If an initial velocity or displacement is applied on the beam, all modes get excited. The total response of the beam is the sum of all the modal responses

$$w(r, t) = \sum_{j=1}^{j=\infty} w_j(r, t)$$

However, most of the contribution comes from the first three or four modes.

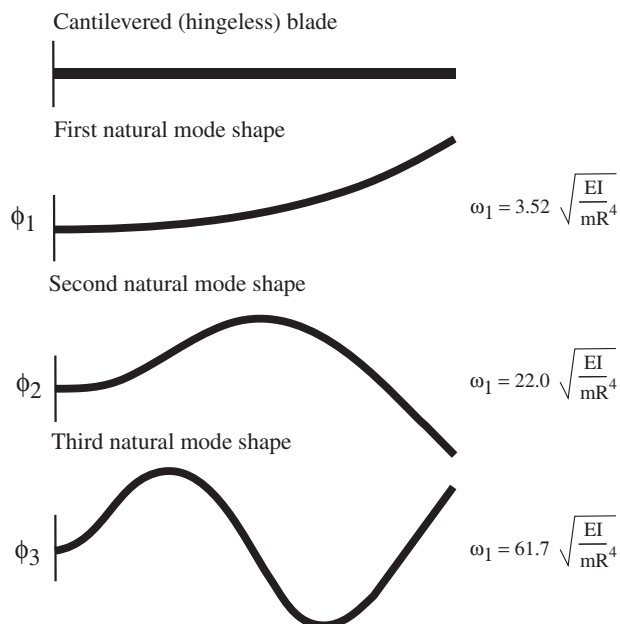


Figure 2.14: Cantilevered beam natural frequencies and mode shapes

2.3.2 Simple-Supported Beam

For a simple supported beam, the boundary conditions are as follows. Both at $r = 0$ and at $r = R$, displacement and bending moments are zero at all times. Thus

$$\begin{aligned} w(0, t) = 0 &\implies \phi(0) = 0 \\ EIw''(0, t) = 0 &\implies \phi''(0) = 0 \end{aligned} \quad (2.39)$$

$$\begin{aligned} w(R, t) = 0 &\implies \phi(R) = 0 \\ EIw''(R, t) = 0 &\implies \phi''(R) = 0 \end{aligned} \quad (2.40)$$

Substituting the four conditions in eqn. 2.32 and proceeding similarly as earlier, one obtains the eigenvalues of λR , natural frequencies, and mode shapes as follows

$$\begin{aligned} (\lambda R)_j &= j\pi \\ \omega_j &= (\lambda R)_j^2 \sqrt{\frac{EI}{mR^4}} \\ \phi_j(r) &= \sqrt{2} \sin \frac{r(\lambda R)_j}{R} \end{aligned} \quad (2.41)$$

2.3.3 Beam Functions

The nonrotating natural vibration characteristics are available for uniform beams with different boundary conditions. Felgar and Young (1952) tabulated the numerical values for the constants.

$$\begin{aligned} \phi_j(x) &= \cosh f_j x - \cos f_j x - \alpha_j (\sinh f_j x - \sin f_j x) \\ x &= r/R \end{aligned} \quad (2.42)$$

For cantilever beam

j	1	2	3	4	j > 4
f_j	1.8751	4.6941	7.8548	10.9955	$(2j-1)\frac{\pi}{2}$
α_j	.7341	1.0185	.9992	1.0000	1.0

The nonrotating natural frequency for uniform beam is obtained as

$$\omega_j = (f_j)^2 \sqrt{\frac{EI}{mR^4}} \quad (2.43)$$

An important property of these modes is that these are orthogonal

$$\begin{aligned} \int_0^R m\phi_i(r)\phi_j(r) dr &= 0 \quad i \neq j \\ &= \delta_{ij} M_i \end{aligned} \quad (2.44)$$

and

$$\begin{aligned} \int_0^R \phi_i \frac{d^2}{dr^2} \left(EI \frac{d^2 \phi_j}{dr^2} \right) dr &= 0 \quad i \neq j \\ &= \delta_{ij} \omega_i^2 M_i \end{aligned} \quad (2.45)$$

where δ_{ij} is Kronecker's delta and M_i is generalized mass

$$M_i = \int_0^R m\phi_i^2 dr$$

The beam functions can be of great value for calculating an approximate solution, by assuming the deflection in terms of a series of beam functions. Because of the orthogality properties, these functions generally result into good convergence characteristics.

2.4 Rotating Beam Vibration

A rotating beam, unlike a stationary beam, can generate aerodynamic forces which affects its response to an initial disturbance. By natural vibration characteristics of a rotating beam we mean characteristics obtained in a vacuum. This is obtained from the homogeneous solution of the PDE given in eqn. ??.

$$m\ddot{w} + \frac{\partial^2}{\partial r^2} \left(EI_{\eta\eta} \frac{\partial^2 w}{\partial r^2} \right) - \frac{\partial}{\partial r} \left(T \frac{\partial w}{\partial r} \right) = 0$$

$$T(r) = \int_r^R mr\Omega^2 dr$$
(2.46)

As in the case of a non-rotating beam we seek a solution of the form

$$w(r, t) = \phi(r)q(t) = \phi(r)q_0 e^{i\omega t}$$

where $\phi(r)$ is assumed to be nondimensional. $q(t)$ is assumed to have the same dimension as $w(r, t)$, here that of length, m or in. Substitution in the homogenous equation leads to the following ODE, for non-trivial $q(t)$,

$$\frac{\partial^2}{\partial r^2} \left(EI_{\eta\eta} \frac{\partial^2 \phi}{\partial r^2} \right) - \frac{\partial}{\partial r} \left(\int_r^R m\Omega^2 r dr \frac{\partial \phi}{\partial r} \right) - m\omega^2 \phi = 0$$
(2.47)

Unlike the non-rotating case, the above ODE cannot be solved analytically even for a beam with uniform properties. Approximate solution methods must be employed. Before we discuss approximate methods, it is instructive to re-write the governing eqn. ?? in a nondimensional form. To this end substitute

$$x = \frac{r}{R}, \quad \bar{w} = \frac{w}{R}, \quad \psi = \Omega t$$

The PDE then becomes

$$m\Omega^2 R \bar{w}^{**} + \frac{\partial^2}{\partial x^2} \left(\frac{EI_{\eta\eta}}{R^3} \frac{\partial^2 \bar{w}}{\partial x^2} \right) - \frac{\partial}{\partial x} \left(\frac{T}{R} \frac{\partial \bar{w}}{\partial x} \right) = f_z(x, R, t)$$
(2.48)

where $\bar{w}^{**} = \partial^2 \bar{w} / \partial \psi^2$. Divide by $m_0 \Omega^2 R$ throughout, where m_0 is a reference mass per unit span, to obtain

$$\frac{m}{m_0} \bar{w}^{**} + \left(\frac{EI_{\eta\eta}}{m_0 \Omega^2 R^4} \bar{w}'' \right)'' - \left(\frac{T}{m_0 \Omega^2 R^2} \bar{w}' \right)' = \frac{f_z(x, R, t)}{m_0 \Omega^2 R}$$

$$\frac{T}{m_0 \Omega^2 R^2} = \int_x^1 \frac{m}{m_0} x dx$$
(2.49)

where $(\)' = \partial / \partial x$. To specify the reference mass per unit span, it is convenient to use an imaginary uniform beam which has the same flap inertia about the root as the real beam

$$I_b = \frac{m_0 R^3}{3} \quad \text{or} \quad m_0 = \frac{3I_b}{R}$$

Note than for an uniform beam $m/m_0 = 1$. The homogenous equation corresponding to eqn. 2.46 is then

$$\frac{m}{m_0} \bar{w}^{**} + \left(\frac{EI_{\eta\eta}}{m_0 \Omega^2 R^4} \bar{w}'' \right)'' - \left(\bar{w}' \int_x^1 \frac{m}{m_0} x dx \right)' = 0$$
(2.50)

where $EI/m_0\Omega^2R^4$ is the nondimensional flexural stiffness. Proceeding similarly as before, assume a solution of the form

$$\bar{w}_a(x, \psi) = \phi_j(x)\bar{q}_j(\psi) = \phi_j(x)\bar{q}_{0j}e^{j\nu\psi} \quad (2.51)$$

where $\phi_j(x)$ are the same nondimensional shape functions as before, expressed now as a function of $x = r/R$, $\bar{q}(t)$ is now nondimensional $\bar{q}(t) = q(t)/R$, and ν is the nondimensional frequency in per rev $\nu = \omega/\Omega$. The nondimensional modal equation, corresponding to eqn. 2.47, then takes the following form

$$\frac{d^2}{dx^2} \left(\frac{EI_{\eta\eta}}{m_0\Omega^2R^4} \frac{d^2\phi}{dx^2} \right) - \frac{d}{dx} \left(\int_x^1 \frac{m}{m_0} x dx \frac{d\phi}{dx} \right) - \frac{m}{m_0} \nu^2 \phi = 0 \quad (2.52)$$

The nondimensional mass and stiffness distributions determine the nondimensional frequency ν (in /rev). For the non-rotating case, $\Omega = 0$ the entire equation is multiplied by $m_0\Omega^2R^4$ to prevent division by zero. The equation then takes the following form

$$\frac{d^2}{dx^2} \left(EI_{\eta\eta} \frac{d^2\phi}{dx^2} \right) - m_0\Omega^2R^4 \frac{d}{dx} \left(\int_x^1 \frac{m}{m_0} x dx \frac{d\phi}{dx} \right) - mR^4\omega^2\phi = 0 \quad (2.53)$$

which is the appropriate form for solving a non-rotating case. Note that $\Omega = 0$ gives back eqn. 2.30 with the substitution of $x = r/R$.

2.4.1 Approximate solution Methods

Two types of approximate methods are described: (1) a weighted residual method, and (2) a variational method. An example of each is discussed. An example of the first type is the Galerkin method. An example of the second type is the Rayleigh-Ritz method. The weighted residual methods are used to solve the governing PDEs. The governing PDEs, as we saw before are derived based on the principles of Newtonian mechanics (force and moment equilibrium). The weighted residual methods reduces the governing PDEs to a set of ODEs. The variational methods bypass the governing PDEs and formulates the ODEs directly. They are based on the principles of Analytical mechanics, a branch distinct and independant from Newtonian mechanics. The only variational principle in analytical mechanics is the principle of least action. Methods which formulate the governing ODEs using this principle are called variational methods. Variational methods are also called energy methods.

All modern structural dynamic analyses use a discretization technique called the Finite Element Method (FEM). It is a method of discretizing a system, while using any type of an approximate method of solution, that renders the formulation more suitable for numerical analysis. Thus one can have a FEM of Galerkin type, FEM of Rayleigh-Ritz type, etc. FEM is discussed as a separate section later on. In this section, two approximate methods are described, one of each type.

2.4.2 Galerkin Method

This method is based on the equilibrium equation. The deflection is expressed as the sum of a series of assumed functions each of which satisfies all the boundary conditions. If we substitute this approximate deflection into the equilibrium equation it will result in an error, or a residual. There are many ways to reduce this residual. In the weighted residual method, it is reduced by projecting it orthogonally onto a subspace spanned by a chosen set of weighing functions. When the chosen set of weighing functions are same as the assumed functions the method is called the Galerkin method. The process is similar to the error orthogonalization of polynomials. Consider the equilibrium equation for the rotating beam blade, eqn. ??

$$m\ddot{w} + (EI_{\eta\eta}w'')'' - (Tw')' = f_z(r, t) \quad (2.54)$$

Assume an approximate deflection $w_a(r, t)$ of the form

$$w_a(r, t) = \sum_{j=1}^n \phi_j(r) q_j(t) \quad (2.55)$$

where $\phi_i(r)$, assumed deflection shape, must satisfy both geometric and force boundary conditions. If it would have been an exact solution, then its substitution in the governing partial differential equation would be identically satisfied. Being an approximate solution, it will result into error

$$\epsilon(r, t) = \sum_{j=1}^n \{m\phi_j \ddot{q}_j + (EI\phi_j'')'' q_j - (T\phi_j')' q_j - f_z\}$$

To determine q_i that will reduce this error, the error is projected orthogonally onto a subspace spanned by a set of weighing functions. In the Galerkin method the assumed deflection shapes are chosen as the weighing functions.

$$\text{i.e. } \int_0^R \phi_i \epsilon(r, t) dr = 0 \quad i = 1, 2, \dots, n$$

or

$$\sum_{j=1}^n \left\{ \left(\int_0^R \phi_i m \phi_j dr \right) \ddot{q}_j + \left(\int_0^R \phi_i (EI\phi_j'')'' dr - \int_0^R \phi_i (T\phi_j')' dr \right) q_j - \left(\int_0^R \phi_i f_z dr \right) \right\} = 0$$

or,

$$\sum_{j=1}^n \{m_{ij} \ddot{q}_j + k_{ij} q_j\} = Q_j \quad i = 1, 2, \dots, N$$

where

$$m_{ij} = \int_0^R m \phi_i \phi_j dr$$

$$k_{ij} = \int_0^R \phi_i (EI\phi_j'')'' dr - \int_0^R \phi_i (T\phi_j')' dr$$

$$Q_i = \int_0^R \phi_i f_z(r, t) dr$$

In matrix notation

$$M \ddot{\underline{q}} + K \underline{q} = \underline{Q} \quad (2.56)$$

where M and K are mass and stiffness matrices of size $(n \times n)$. \underline{Q} is the forcing vector of size n , and \underline{q} are the degrees of freedom. The degrees of freedom \underline{q} have units of radians. M has units of kg. K has units of N/m. \underline{Q} has units of N. For natural response, set $\underline{Q} = \underline{0}$ and seek solution of the form $\underline{q} = \underline{q}_0 e^{j\omega t}$. This leads to

$$\begin{aligned} K \underline{q}_0 &= \omega^2 M \underline{q}_0 \\ (K - \omega^2 M) \underline{q}_0 &= \underline{0} \end{aligned} \quad (2.57)$$

The above is an algebraic eigenvalue problem. It means that there are only n values of ω^2 for which a non-trivial solution of \underline{q}_0 exists, for all other values of ω^2 , $\underline{q}_0 = \underline{0}$. For non-trivial solution,

$$|K - \omega^2 M| = 0$$

which leads to the solutions ω_i where $i = 1, 2, \dots, n$. Corresponding to each ω_i there exists a solution \underline{q}_{0i} which satisfies the equation

$$K \underline{q}_{0i} = \omega_i^2 M \underline{q}_{0i}$$

ω_i and its corresponding \underline{q}_{0i} are called the eigenvalues and eigenvectors of the system.

As an example, consider a case where the assumed deflection functions are the non-rotating beam functions as given in eqn. 2.42.

$$w_a(r, t) = \sum_{j=1}^n \phi_j(r) q_j(t) \quad (2.58)$$

where ϕ_j is the mode shape for a non-rotating beam corresponding to its j^{th} natural frequency of vibration. Using the orthogonality property of these functions (eqns. 2.44 and 2.45), we have

$$\begin{aligned} m_{ij} &= \delta_{ij} M_i \\ k_{ij} &= \delta_{ij} \omega_{0i}^2 M_i - \int_0^R \phi_j (T \phi_i')' dr \end{aligned} \quad (2.59)$$

where

$$M_i = \int_0^R m \phi_i^2 dr \quad T = \int_r^R m \Omega^2 r dr = (1/2) m \Omega^2 (R^2 - r^2) \quad \text{for an uniform beam}$$

$\omega_{0i} = i^{\text{th}}$ non-rotating natural frequency

Recall, that the governing PDE eqn. 2.54 can also be expressed in the following non-dimensional form (from eqn. 2.49)

$$\begin{aligned} \frac{m}{m_0} \frac{**}{\bar{w}} + \left(\frac{EI \eta \eta}{m_0 \Omega^2 R^4} \bar{w}'' \right)'' - \left(\frac{T}{m_0 \Omega^2 R^2} \bar{w}' \right)' &= \frac{f_z(x, R, t)}{m_0 \Omega^2 R} \\ \frac{T}{m_0 \Omega^2 R^2} &= \int_x^1 \frac{m}{m_0} x dx \end{aligned} \quad (2.60)$$

An assumed solution of the form

$$\bar{w}_a(x, \psi) = \sum_{i=1}^n \phi_j(x) \bar{q}_j(\psi) = \sum_{i=1}^n \phi_j(x) \bar{q}_{0j} e^{j\nu\psi}$$

where $\bar{w} = w/R$ and $\bar{q}(t) = q(t)/R$ leads to the eigenvalue problem

$$\begin{aligned} \bar{K} \bar{q}_0 &= \nu^2 \bar{M} \bar{q}_0 \\ (\bar{K} - \nu^2 \bar{M}) \bar{q}_0 &= 0 \end{aligned} \quad (2.61)$$

which is the nondimensional form of the eigenvalue eqn. 2.57, where \bar{K} and \bar{M} are the nondimensional stiffness and mass matrices given by

$$\begin{aligned}\bar{m}_{ij} &= \int_0^1 \frac{m}{m_0} \phi_i \phi_j dx \\ \bar{k}_{ij} &= \int_0^1 \phi_j \frac{d^2}{dx^2} \left(\frac{EI}{m_0 \Omega^2 R^4} \frac{d^2 \phi_i}{dx^2} \right) dx - \int_0^1 \phi_j \frac{d}{dx} \left(\frac{T}{m_0 \Omega^2 R^2} \frac{d \phi_i}{dx} \right) dx\end{aligned}$$

The procedure is simple, but it is difficult to choose functions which satisfies all the boundary conditions. The Galerkin method overestimates the natural frequencies, the error progressively increasing for higher mode frequencies. For accurate prediction of higher mode frequencies a large number of modes must be assumed.

Example: 2.2

For a hingeless uniform rotating blade, calculate approximately the fundamental flap bending frequency using the Galerkin method. Assume a one term deflection series

$$w(r, t) = \left[3 \left(\frac{r}{R} \right)^2 - 2 \left(\frac{r}{R} \right)^3 + \frac{1}{2} \left(\frac{r}{R} \right)^4 \right] q_1(t)$$

First note that

$$\phi_1(r) = 3 \left(\frac{r}{R} \right)^2 - 2 \left(\frac{r}{R} \right)^3 + \frac{1}{2} \left(\frac{r}{R} \right)^4 = 3x^2 - 2x^3 + \frac{1}{2}x^4$$

Cantilever boundary conditions

$$\begin{aligned}r = 0 \quad w = \phi_1 = 0 \quad \frac{dw}{dr} = \frac{1}{R} \frac{d\phi_1}{dx} = 0 \\ r = R \quad M = 0 \text{ or } \frac{1}{R^2} \frac{d^2 \phi_1}{dx^2} = 0 \quad S = 0 \text{ or } \frac{1}{R^3} \frac{d^3 \phi_1}{dx^3} = 0\end{aligned}$$

All boundary conditions are satisfied. Therefore, the assumed displacement function can be used to calculate Galerkin solution.

$$m_{11} = \int_0^R m \phi_1^2 dr = mR \int_0^1 \left(3x^2 - 2x^3 + \frac{1}{2}x^4 \right)^2 dx = \frac{26}{45} mR$$

$$T = \frac{m}{2} \Omega^2 (R^2 - r^2) = \frac{m}{2} \Omega^2 R^2 (1 - x^2)$$

$$\begin{aligned}k_{11} &= \int_0^R EI \phi_1 \frac{d^4 \phi_1}{dr^4} dr - \int_0^R T \phi_1 \frac{d^2 \phi_1}{dr^2} dr \\ &= \frac{EI}{R^3} \int_0^R 12 \left(3x^2 - 2x^3 + \frac{1}{2}x^4 \right) dx \\ &\quad - \frac{1}{2} m \Omega^2 R \int_0^R (1 - x^2) (x - 6x^2 + 2x^3) \left(3x^2 - 2x^3 + \frac{1}{2}x^4 \right) dx \\ &= \frac{36}{5} \frac{EI}{R^3} + \frac{61}{90} m \Omega^2 R\end{aligned}$$

$$\omega_1^2 = \frac{k_{11}}{m_{11}} = 12.46 \frac{EI}{mR^4} + 1.173 \Omega^2$$

$$\nu_1^2 = 12.46 \frac{EI}{m \Omega^2 R^4} + 1.173$$

$$\text{For } \Omega = 0 \quad \omega_1 = 3.53 \sqrt{\frac{EI}{mR^4}} \quad \text{Exact soln: } 3.52 \sqrt{\frac{EI}{mR^4}}$$

In this case, the assumed one term approximation was adequate for the fundamental mode.

2.4.3 Rayleigh-Ritz Method

Assume the deflection as a series of functions that need to satisfy only geometric boundary conditions. Using this deflection, calculate the kinetic energy, potential energy and virtual work. Substitute in the Euler-Lagrange equation of motion. This generates the governing ODEs directly.

The Euler-Lagrange equation of motion is a statement of the principle of Least Action in a differential form. The principle of Least Action, or more correctly the principle of stationary action, requires that the degrees of freedom $[q_1 q_2 q_3 \dots q_n]^T$ must evolve with time in such a manner so as to render a certain integral I stationary with respect to arbitrary variations in the manner of their evolution. The evolution of the degrees of freedom with time can be thought of as a path of motion of the system from a certain time t_1 to time t_2 . The integral I is called the action integral. For mechanical systems, an appropriate action integral I is the integration of the kinetic energy U of the system, and work done W on the system, over the time t_1 to t_2 , calculated along the path of motion. The action integral in this form was provided by Hamilton. Therefore, this formulation of the principle of Least Action for mechanical systems is known as Hamilton's Principle. Thus, Hamilton's Principle states that out of all possible paths of motion of a mechanical system between t_1 and t_2 , the true motion is such that the integral $I = \int_{t_1}^{t_2} (U + W) dt$ attains an extremum, given that the end points of all possible paths at t_1 and t_2 are the same. Hamilton's Principle is a statement of the principle of Least Action, in an integral form. The differential form, as noted earlier, is the Euler-Lagrange equation. The connection between Hamilton's Principle and the Euler-Lagrange equation is given in the next section. Here, the Euler-Lagrange equation is used to provide an approximate solution of a rotating beam. Assume

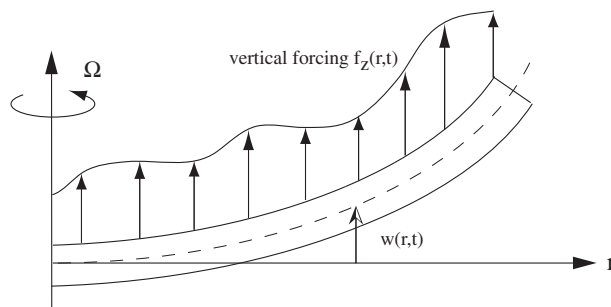


Figure 2.15: Rotating cantilevered beam

$$w_a(r, t) = \sum_{j=1}^n \phi_j(r) q_j(t) \quad (2.62)$$

where $\phi_j(r)$ need to satisfy only the geometric boundary conditions. For example for a cantilevered beam, it is enough that $\phi_j(0) = 0$ and $\phi_j'(0) = 0$. Now calculate the kinetic energy, potential energy and virtual work associated with the deflection of the beam. The kinetic energy U is given by

$$U = \frac{1}{2} \int_0^R m \dot{w}^2 dr = \frac{1}{2} \int_0^R m \left(\sum_{i=1}^n \phi_i(r) \dot{q}_i \right) \left(\sum_{j=1}^n \phi_j(r) \dot{q}_j \right) dr = \frac{1}{2} \sum_{i=1}^n \sum_{j=1}^n m_{ij} \dot{q}_i \dot{q}_j \quad (2.63)$$

where

$$m_{ij} = \int_0^R m \phi_i \phi_j dr \quad (2.64)$$

The potential energy or strain energy V is given by

$$\begin{aligned}
V &= \text{strain energy due to flexure} + \text{strain energy due to centrifugal force} \\
&= \frac{1}{2} \int_0^R EI \left(\frac{d^2 w_a}{dr^2} \right)^2 dr + \frac{1}{2} \int_0^R T \left(\frac{dw_a}{dr} \right)^2 dr \\
&= \frac{1}{2} \int_0^R EI \left(\sum_{i=1}^n \phi_i'' q_i \right) \left(\sum_{j=1}^n \phi_j'' q_j \right) dr + \frac{1}{2} \int_0^R T \left(\sum_{i=1}^n \phi_i' q_i \right) \left(\sum_{j=1}^n \phi_j' q_j \right) dr \\
&= \frac{1}{2} \sum_{i=1}^n \sum_{j=1}^n k_{ij} q_i q_j
\end{aligned} \tag{2.65}$$

where

$$k_{ij} = \int_0^R EI \phi_i'' \phi_j'' dr + \int_0^R T \phi_i' \phi_j' dr \tag{2.66}$$

and

$$T = \int_r^R m \Omega^2 r dr$$

Virtual work done by $f_z(r, t)$ through virtual displacements δw is given by

$$\begin{aligned}
\delta W &= \int_0^R f_z(r, t) \delta w dr \\
&= \int_0^R f_z \sum_{i=1}^n \phi_i \delta q_i dr \\
&= \sum_{i=1}^n Q_i \delta q_i
\end{aligned} \tag{2.67}$$

where

$$Q_i = \int_0^R f_z \phi_i dr \tag{2.68}$$

Substitute in the Euler-Lagrange equation

$$\frac{\partial}{\partial t} \left(\frac{\partial T}{\partial \dot{q}_i} \right) - \frac{\partial T}{\partial q_i} + \frac{\partial V}{\partial q_i} = Q_i \quad i = 1, 2, \dots, n \tag{2.69}$$

to obtain

$$\sum_{j=1}^n (m_{ij} \ddot{q}_j + k_{ij} q_j) = Q_i \quad i = 1, 2, \dots, n$$

These are n coupled equations and can be put together in matrix form

$$M \ddot{\underline{q}} + K \underline{q} = \underline{Q}$$

where M and K are mass and stiffness matrices of size $(n \times n)$. \underline{Q} is the forcing vector of size n , and \underline{q} are the degrees of freedom. The degrees of freedom \underline{q} have units of displacement w in m or

in. M has units of kg^2 . K has units of N/m . Q has units of N . For natural response, set $\underline{Q} = \underline{0}$ and seek solution of the form $\underline{q} = \underline{q}_0 e^{j\omega t}$. This leads to the same algebraic eigenvalue problem as discussed earlier in the case of Galerkin method,

$$\begin{aligned} K\underline{q}_0 &= \omega^2 M\underline{q}_0 \\ (K - \omega^2 M)\underline{q}_0 &= 0 \end{aligned} \quad (2.70)$$

It leads to the solutions ω_i where $i = 1, 2, \dots, n$. Corresponding to each ω_i there exists a solution \underline{q}_{0i} which satisfies the equation

$$K\underline{q}_{0i} = \omega_i^2 M\underline{q}_{0i}$$

ω_i and its corresponding \underline{q}_{0i} are called the eigenvalues and eigenvectors of the system. For example, consider the simplest case of a one term solution. This is also called a Rayleigh solution.

$$w_a(r, t) = \phi_1(r) q_1(t)$$

This results in

$$\begin{aligned} M &= m_{11} = \int_0^R m \phi_1^2 dr \\ K &= k_{11} = \int_0^R EI(\phi_1'')^2 dr + \int_0^R T(\phi_1')^2 dr \end{aligned}$$

Eqn. 2.88 then leads to

$$\omega^2 = \frac{k_{11}}{m_{11}} = \frac{\int_0^R EI(\phi_1'')^2 dr + \int_0^R T(\phi_1')^2 dr}{\int_0^R m \phi_1^2 dr}$$

The energy expressions can be nondimensionalized using $m_0 \Omega^2 R^3$, with units of N-m . The kinetic energy, potential energy, and virtual work corresponding to eqns. 9.93, 2.65 and 2.67 become

$$\begin{aligned} \frac{U}{m_0 \Omega^2 R^3} &= \frac{1}{2} \sum_{i=1}^n \sum_{j=1}^n \bar{m}_{ij} \bar{q}_i^* \bar{q}_j^* \\ \frac{V}{m_0 \Omega^2 R^3} &= \frac{1}{2} \sum_{i=1}^n \sum_{j=1}^n \bar{k}_{ij} \bar{q}_i \bar{q}_j \\ \frac{\delta W}{m_0 \Omega^2 R^3} &= \sum_{i=1}^n \bar{Q}_i \delta \bar{q}_i \end{aligned} \quad (2.71)$$

where $\bar{q} = q/R$. The nondimensional mass corresponding to eqn. 2.64 is then

$$\begin{aligned} \bar{m}_{ij} &= \frac{\int_0^R m \phi_i \phi_j dr}{m_0 R} \\ &= \frac{\int_0^1 m \phi_i(x) \phi_j(x) d(xR)}{m_0 R} \\ &= \int_0^1 \frac{m}{m_0} \phi_i(x) \phi_j(x) dx \end{aligned} \quad (2.72)$$

where $x = r/R$. Similarly, the the nondimensional stiffness corresponding to eqn. 2.66 is

$$\begin{aligned}\bar{k}_{ij} &= \frac{\int_0^R EI \phi_i'' \phi_j'' dr + \int_0^R T \phi_i' \phi_j' dr}{m_0 \Omega^2 R^3} \\ &= \frac{\int_0^1 EI \frac{d^2 \phi_i}{d(xR)^2} \frac{d^2 \phi_j}{d(xR)^2} d(xR) + \int_0^1 T \frac{d\phi_i}{d(xR)} \frac{d\phi_j}{d(xR)} d(xR)}{m_0 \Omega^2 R} \\ &= \int_0^1 \frac{EI}{m_0 \Omega^2 R^4} \frac{d^2 \phi_i}{dx^2} \frac{d^2 \phi_j}{dx^2} dx + \int_0^1 \frac{T}{m_0 \Omega^2 R^2} \frac{d\phi_i}{dx} \frac{d\phi_j}{dx} dx\end{aligned}\quad (2.73)$$

where

$$\frac{T}{m_0 \Omega^2 R^2} = \int_0^1 \frac{m}{m_0} x dx$$

The nondimensional force vector corresponding to eqn. 2.68 is

$$\bar{Q}_i = \int_0^1 \frac{f_z}{m_0 \Omega^2 R} \phi_i dx \quad (2.74)$$

The energy and work expressions as given in eqns. 2.71, when substituted in the Euler-Lagrange equation generates

$$\bar{M} \ddot{\bar{q}} + \bar{K} \bar{q} = \bar{Q}$$

with the corresponding eigenvalue problem

$$\begin{aligned}\bar{K} \bar{q}_0 &= \nu^2 \bar{M} \bar{q}_0 \\ (\bar{K} - \nu^2 \bar{M}) \bar{q}_0 &= 0\end{aligned}\quad (2.75)$$

where $\nu = \omega/\Omega$.

Example: 2.3

Calculate Rayleigh's solution for a uniform rotating blade. Assume displacement as

$$w(r, t) = \left(\frac{r}{R}\right)^2 q_i(t)$$

First note that

$$\phi_1(r) = \left(\frac{r}{R}\right)^2 = x^2$$

The geometric boundary conditions are satisfied

$$r = 0 \quad w = \frac{dw}{dr} = 0$$

thus the assumed form is a permissible deflection.

$$m_{11} = \int_0^R m \phi_1^2 dr = \int_0^R m \frac{r^4}{R^4} dr = \frac{mR}{5}$$

$$T = \frac{m}{2} (R^2 - r^2) \Omega^2$$

$$\begin{aligned}
k_{11} &= \int_0^R EI(\phi_1'')^2 dr + \int_0^R T(\phi_1')^2 dr \\
&= EI \int_0^R \frac{4}{R^4} dr + \int_0^R \frac{1}{2} m(R^2 - r^2) \Omega^2 \frac{4r^2}{R^4} dr \\
&= \frac{4EI}{R^3} + \frac{4}{15} m \Omega^2 R
\end{aligned}$$

$$\omega_1^2 = \frac{k_{11}}{m_{11}} = \frac{\frac{4EI}{R^3} + \frac{4}{15} m \Omega^2 R}{\frac{mR}{5}} = 20 \frac{EI}{mR^4} + \frac{4}{3} \Omega^2$$

$$\text{For } \Omega = 0 \quad \omega_1 = 4.47 \sqrt{\frac{EI}{mR^4}} \quad \text{Exact soln: } 3.52 \sqrt{\frac{EI}{mR^4}}$$

In this case, the assumed one term approximation was not adequate. Only a very rough estimate of the solution is obtained.

Example: 2.4

A radially tapered solid blade is idealized into two uniform segments of equal lengths, with EI of 0.8 and 0.5 of root value EI_0 and mass distribution m of .9 and .7 of root value m_0 . Calculate the fundamental flap bending frequency approximately using the Rayleigh-Ritz method. Assume a one term deflection series

$$w(r, t) = \left(\frac{r}{R}\right)^2 q_1(t)$$

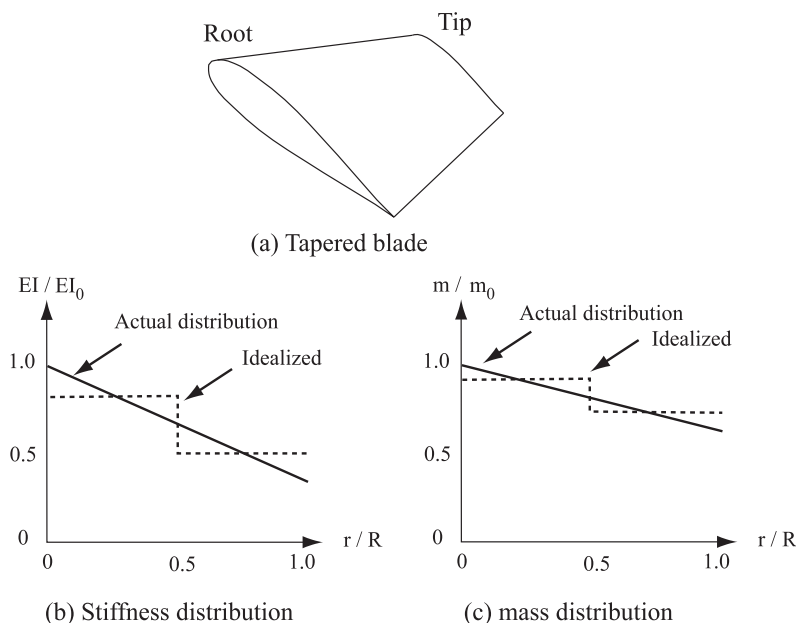


Figure 2.16: Non-uniform tapered blade natural frequencies and mode shapes

$$\phi_1 = x^2$$

The geometric boundary conditions are satisfied.

$$r = 0 \quad w = \frac{dw}{dr} = 0$$

The mass is given by

$$\begin{aligned}
 m_{11} &= \int_0^R m\phi_1^2 dr \\
 &= \int_0^{R/2} m\phi_1^2 dr + \int_{R/2}^R m\phi_1^2 dr \\
 &= 0.9m_0R \int_0^{1/2} x^4 dx + 0.7m_0R \int_{1/2}^1 x^4 dx \\
 &= 0.14m_0R
 \end{aligned}$$

The stiffness is given by

$$\begin{aligned}
 k_{11} &= (k_{11})_{\text{bending}} + (k_{11})_{\text{centrifugal}} \\
 (k_{11})_{\text{bending}} &= \int_0^{R/2} EI_1(\phi_1'')^2 dr + \int_{R/2}^R EI_2(\phi_1'')^2 dr \\
 &= 0.8\frac{EI_0}{R^3} \int_0^{1/2} 4 dx + 0.5\frac{EI_0}{R^3} \int_{1/2}^1 4 dx \\
 &= 2.6\frac{EI_0}{R^3}
 \end{aligned}$$

The centrifugal stiffness depends on the tensile force T

$$T = \int_r^R m\Omega^2 r dr$$

For $\frac{R}{2} < r < R$

$$T = \Omega^2 R^2 \int_x^1 0.7m_0 x dx = 0.35m_0\Omega^2 R^2(1 - x^2) = 0.35m_0\Omega^2(R^2 - r^2)$$

For $r < R/2$

$$\begin{aligned}
 T &= \Omega^2 R^2 \int_x^{1/2} 0.9m_0 x dx + \Omega^2 R^2 \int_{1/2}^1 0.7m_0 x dx \\
 &= m_0\Omega^2 R^2(0.375 - 0.45x^2) = m_0\Omega^2(0.375R^2 - 0.45r^2)
 \end{aligned}$$

Therefore

$$\begin{aligned}
 (k_{11})_{\text{centrifugal}} &= \int_0^R T(\phi_1')^2 dr \\
 &= \int_0^{R/2} (m_0\Omega^2)(0.375R^2 - 0.45r^2)\frac{4r^2}{R^4} dr + \int_{R/2}^R 0.35m_0\Omega^2(R^2 - r^2)\frac{4r^2}{R^4} dr \\
 &= m_0\Omega^2 R \int_0^{1/2} (0.375 - 0.45x^2)4x^2 dx + 0.35m_0\Omega^2 R \int_{1/2}^1 (1 - x^2)4x^2 dx \\
 &= 0.188m_0\Omega^2 R
 \end{aligned}$$

$$k_{11} = 2.6\frac{EI_0}{R^3} + 0.188m_0\Omega^2 R$$

$$\omega_1^2 = \frac{k_{11}}{m_{11}} = 18.41\frac{EI_0}{m_0R^4} + 1.33\Omega^2$$

$$\nu^2 = 18.41\frac{EI_0}{m_0\Omega^2 R^4} + 1.33$$

2.5 Finite Element Method (FEM)

The Finite Element Method (FEM) forms the basis of all modern structural analysis because of its easy adaptability to different configurations and boundary conditions. The present section introduces a simple displacement based one dimensional FEM. FEM is a discretization technique. Any of the approximate methods, e.g. Galerkin or Rayleigh-Ritz, can be applied in combination with FEM. Thus, one can have a Galerkin type FEM, a Rayleigh-Ritz type FEM, etc. In general, one can have a FEM based on weighted residual methods or a FEM based on energy methods. In this section we will use a Rayleigh-Ritz type FEM to solve the Euler-Bernoulli rotating beam problem.

The first step is to discretize the rotating beam into a number of finite elements as shown in Fig. 2.17. Each element is free of constraints. This is followed by three major steps: (a) Development of elemental properties, (b) Assembly of elemental properties, and (3) Application of constraints and determination of solution. These steps are discussed below.

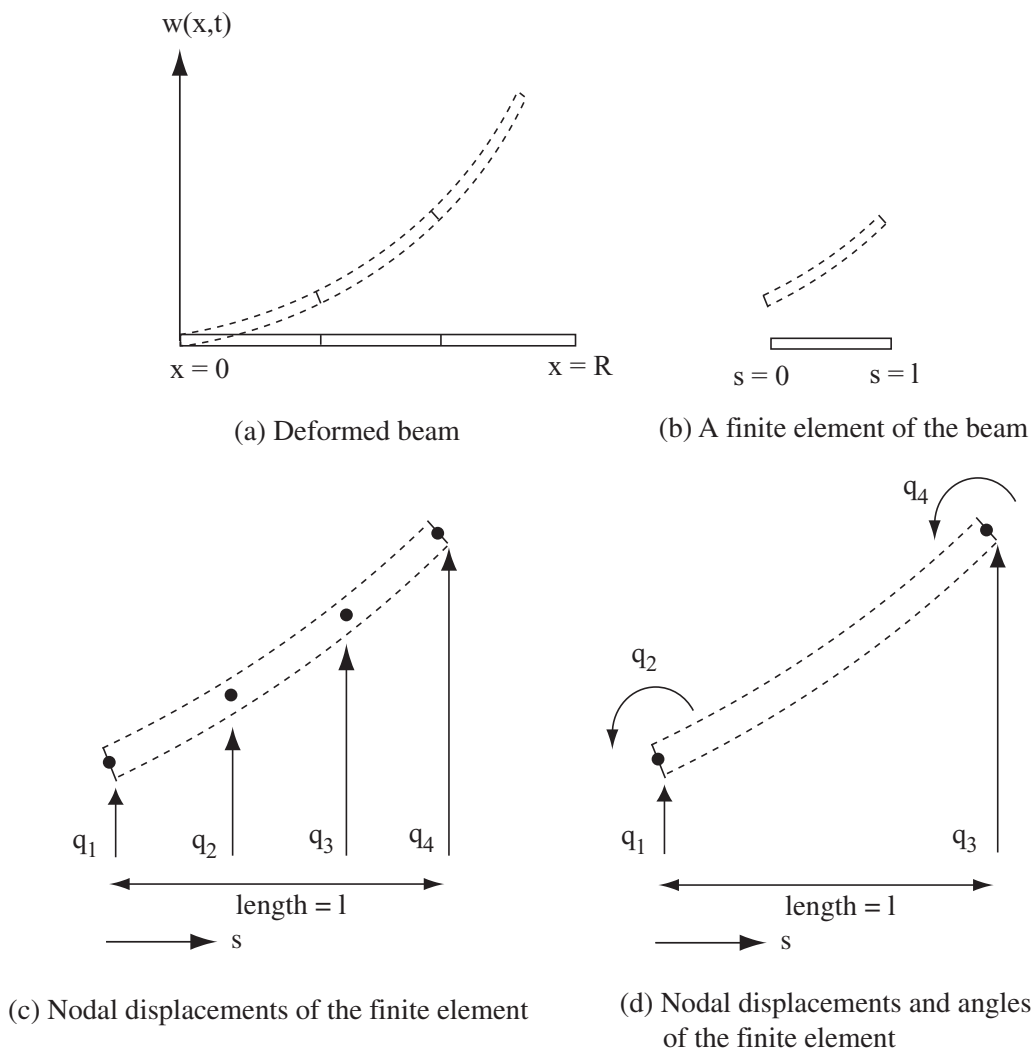


Figure 2.17: Finite element discretization of a beam

2.5.1 Element properties

Figure 2.17(a) shows a rotating beam in its undeformed and deformed positions. Figure 2.17(b) shows a finite element of the beam. The beam extends from $x = 0$ to $x = R$. Each element extends from, say, $s = 0$ to $s = l$ where s is a local variable within each element. The goal is to represent the deformation within each element w as a function of s and in the following form.

$$w(s) = \sum_{i=1}^{i=n} H_i(s)q_i(t) \quad (2.76)$$

Here $q_i(t)$, $i = 1, 2, 3, \dots, n$ are displacements at n 'chosen' points within the element. These points are also called nodes. $H_i(s)$, $i = 1, 2, 3, \dots, n$ are interpolation functions, also called shape functions, automatically extracted based on this choice. The order of each $H(s)$ depend on the chosen value of n . The type of each $H(s)$ depend on the chosen nature of $q_i(t)$. The above form is generated in the following manner.

First, assume a polynomial distribution for displacement w in the element

$$w(s, t) = \alpha_1 + \alpha_2 s + \alpha_3 s^2 + \alpha_4 s^3 \quad (2.77)$$

A third order polynomial is chosen because anything less will provide zero shear forces. The order must be at least three, i.e. the highest derivative for loads. The order can be greater than three, however, this implies that added number of unknowns need to be determined. For the third order polynomial, as chosen above, we have the unknowns α_{0-3} to be determined. It is here that the choice of $q_i(t)$ plays a role.

To determine the four constants α_{0-3} , four $q_i(t)$ need to be chosen, i.e. $i = 1, 2, 3, n = 4$. Consider first a choice of the type shown in Fig. 2.17(c). $q_i(t)$ are the displacements (same dimension as w , in m or in) at four equidistant nodes within the element. Thus

$$\begin{aligned} w(0, t) &= q_1 = \alpha_0 \\ w(l/3, t) &= q_2 = \alpha_0 + \alpha_1(l/3) + \alpha_2(l/3)^2 + \alpha_3(l/3)^3 \\ w(2l/3, t) &= q_3 = \alpha_0 + \alpha_1(2l/3) + \alpha_2(2l/3)^2 + \alpha_3(2l/3)^3 \\ w(l, t) &= q_4 = \alpha_0 + \alpha_1(l) + \alpha_2(l)^2 + \alpha_3(l)^3 \end{aligned}$$

Solving for α_{0-3} in terms of q_{1-4} , and substitution into eqn. 2.77 leads to a form given by eqn. 2.76. The shape functions $H(s)$ are Lagrange polynomials.

A more suitable choice of nodal displacements $q_i(t)$ for beam problems is shown in Fig. 2.17(d). Here q_1 and q_2 are the displacement and angles at node 1 (in m or in, and in rads), q_2 and q_3 are the displacement and angles at node 2 (in m or in, and in rads). This is a more suitable choice because it ensures continuity of both displacement and slope between adjacent finite elements. Based on this choice we have

$$\begin{aligned} w(0, t) &= q_1 = \alpha_0 \\ w'(0, t) &= \frac{dw}{ds}(\text{at } s=0) = q_2 = \alpha_2 \\ w(l, t) &= q_3 = \alpha_0 + \alpha_1(l) + \alpha_2(l)^2 + \alpha_3(l)^3 \\ w'(l, t) &= \frac{dw}{ds}(\text{at } s=l) = q_4 = \alpha_2 + 2\alpha_3(l) + 3\alpha_4(l)^2 \end{aligned}$$

Solving for α_{0-3} in terms of q_{1-4} , and substitution into eqn. 2.77 leads to a form given by eqn. 2.76. The shape functions $H(s)$ are in this case Hermite polynomials.

$$H_1 = 2 \left(\frac{s}{l} \right)^3 - 3 \left(\frac{s}{l} \right)^2 + 1$$

$$H_2 = \left[\left(\frac{s}{l} \right)^3 - 2 \left(\frac{s}{l} \right)^2 + \frac{s}{l} \right] l$$

$$H_3 = -2 \left(\frac{s}{l} \right)^3 + 3 \left(\frac{s}{l} \right)^2$$

$$H_4 = \left[\left(\frac{s}{l} \right)^3 - \left(\frac{s}{l} \right)^2 \right] l$$

Now calculate the elemental energies using the Rayleigh-Ritz method. Note that this step is same as that done earlier in the section on Rayleigh-Ritz method, except that here the integration is only over each element $s = 0$ to $s = l$, not the entire beam. The kinetic energy of the element U_e is given by

$$U_e = \frac{1}{2} \int_0^l m \dot{w}^2 ds = \frac{1}{2} \int_0^l \left(\sum_{i=1}^4 H_i \dot{q}_i \right) \left(\sum_{j=1}^4 H_j \dot{q}_j \right) ds = \frac{1}{2} \sum_{i=1}^4 \sum_{j=1}^4 m_{ij} \dot{q}_i \dot{q}_j$$

where

$$m_{ij} = \int_0^l m H_i H_j ds \quad (2.78)$$

The potential energy of the element is given by the strain energy V_e

$$\begin{aligned} V_e &= \frac{1}{2} \int_0^l EI \left(\frac{d^2 w}{ds^2} \right)^2 ds + \frac{1}{2} \int_0^l T \left(\frac{dw}{ds} \right)^2 ds \\ &= \frac{1}{2} \int_0^l EI \left(\sum_{i=1}^4 \frac{d^2 H_i}{ds^2} q_i \right) \left(\sum_{j=1}^4 \frac{d^2 H_j}{ds^2} q_j \right) ds + \frac{1}{2} \int_0^l T \left(\sum_{i=1}^4 \frac{dH_i}{ds} q_i \right) \left(\sum_{j=1}^4 \frac{dH_j}{ds} q_j \right) ds \\ &= \frac{1}{2} \sum_{i=1}^4 \sum_{j=1}^4 k_{ij} q_i q_j \end{aligned}$$

where

$$k_{ij} = \int_0^l EI \frac{d^2 H_i}{ds^2} \frac{d^2 H_j}{ds^2} ds + \int_0^l T \frac{dH_i}{ds} \frac{dH_j}{ds} ds \quad (2.79)$$

The virtual work done by the external forces are given by

$$\delta W_e = \int_0^l f_z \delta w(s, t) ds = \int_0^l f_z \sum_{i=1}^4 H_i \delta q_i ds = \sum_{i=1}^4 Q_i \delta q_i$$

where

$$Q_i = \int_0^l f_z H_i ds \quad (2.80)$$

The above energy expressions can be put together in matrix form

$$T_e = \frac{1}{2} \dot{\underline{q}}^T M_e \dot{\underline{q}} \quad V_e = \frac{1}{2} \underline{q}^T K_e \underline{q} \quad \delta W_e = \underline{Q}_e^T \delta \underline{q}$$

where $\underline{q} = [q_1 \ q_2 \ q_3 \ q_4]^T$. Consider a beam element with uniform properties within it, i.e., EI and m constant within the element. The tensile force T depends on the distance of a point $s = s$ from the rotation axis. For this purpose consider that the left hand edge of a general element i is at a

distance x_i from the rotation axis. The length of the element is l . The mass matrix and the EI dependant part of the stiffness matrix calculation are straight forward. The centrifugal stiffness part can be easily treated by noting

$$T(s) = \int_{x_i+s}^R m\Omega^2 \rho d\rho = \int_{x_i}^R m\Omega^2 \rho d\rho - \int_{x_i}^{x_i+s} m\Omega^2 \rho d\rho$$

The first term is a successive integration over all elements from i to N and leads to $\sum_{j=i}^N m_j \Omega^2 (x_{j+1}^2 - x_j^2)/2$. The second term, with a change in integration variable, leads to

$$\int_{x_i}^{x_i+s} m\Omega^2 \rho d\rho = \int_0^s m\Omega^2 (x_i + \eta) d\eta = m_i \Omega^2 (x_i s + s^2/2)$$

Thus

$$\int_0^l T(s) \frac{dH_i}{ds} \frac{dH_j}{ds} ds = \sum_{j=i}^N \frac{m_j \Omega^2}{2} (x_{j+1}^2 - x_j^2) \int_0^l \frac{dH_i}{ds} \frac{dH_j}{ds} ds - m_i \Omega^2 \int_0^l \left(x_i s + \frac{1}{2} s^2 \right) \frac{dH_i}{ds} \frac{dH_j}{ds} ds$$

Finally we have the following elemental matrices for the element i

$$M_e = m \begin{bmatrix} \frac{13}{35}l & \frac{11}{210}l^2 & \frac{9}{70}l & -\frac{13}{420}l^2 \\ \frac{11}{210}l^2 & \frac{1}{105}l^3 & \frac{13}{420}l^2 & -\frac{1}{140}l^3 \\ \frac{9}{70}l & \frac{13}{420}l^2 & \frac{13}{35}l & -\frac{11}{210}l^2 \\ -\frac{13}{420}l^2 & -\frac{1}{140}l^3 & -\frac{11}{210}l^2 & \frac{1}{105}l^3 \end{bmatrix} \quad (2.81)$$

$$K_e = EI \begin{bmatrix} \frac{12}{l^3} & \frac{6}{l^2} & -\frac{12}{l^3} & \frac{6}{l^2} \\ \frac{6}{l^2} & \frac{4}{l} & -\frac{6}{l^2} & \frac{2}{l} \\ -\frac{12}{l^3} & -\frac{6}{l^2} & \frac{12}{l^3} & -\frac{6}{l^2} \\ \frac{6}{l^2} & \frac{2}{l} & -\frac{6}{l^2} & \frac{4}{l} \end{bmatrix} + \frac{\Omega^2 A_i}{2} \begin{bmatrix} \frac{6}{5l} & \frac{1}{10} & -\frac{6}{5l} & \frac{1}{10} \\ \frac{1}{10} & \frac{2l}{15} & -\frac{1}{10} & -\frac{l}{30} \\ -\frac{6}{5l} & -\frac{1}{10} & \frac{6}{5l} & -\frac{1}{10} \\ \frac{1}{10} & -\frac{l}{30} & -\frac{1}{10} & \frac{2l}{15} \end{bmatrix} \quad (2.82)$$

$$-m_i \Omega^2 \begin{bmatrix} \frac{3}{5}x_i + \frac{6l}{35} & \frac{lx_i}{10} + \frac{l^2}{28} & -\frac{3}{5}x_i - \frac{6l}{35} & -\frac{l^2}{70} \\ \frac{lx_i}{10} + \frac{l^2}{28} & \frac{lx_i}{30} + \frac{l^3}{105} & -\frac{lx_i}{10} - \frac{l^2}{28} & -\frac{l^2 x_i}{60} + \frac{l^3}{70} \\ -\frac{3}{5}x_i - \frac{6l}{35} & -\frac{lx_i}{10} - \frac{l^2}{28} & \frac{3}{5}x_i + \frac{6l}{35} & \frac{l^2}{70} \\ -\frac{l^2}{70} & -\frac{l^2 x_i}{60} + \frac{l^3}{70} & +\frac{l^2}{70} & \frac{l^2 x_i}{10} + \frac{3l^3}{70} \end{bmatrix}$$

and

$$A_i = \sum_{j=i}^N m_j (x_{j+1}^2 - x_j^2)$$

2.5.2 Assembly of elements

We have the energies and virtual work for each element. The next step is to assemble them to obtain the global or total energies and virtual work T , V , and δW . For illustration of the assembly procedure, consider a case where the beam is discretized into three finite elements, with a total of eight degrees of freedom. The total potential energy is the sum of the elemental energies.

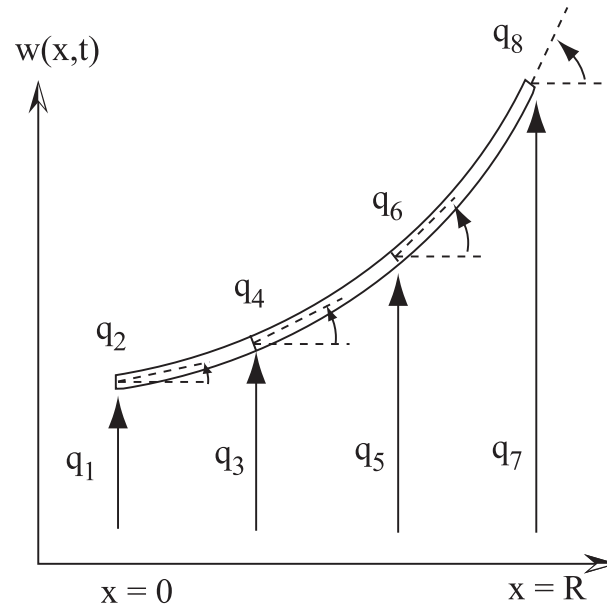


Figure 2.18: Finite element discretization of a beam into three elements using Hermite polynomial interpolation within each element

$$V = (V_e)_1 + (V_e)_2 + (V_e)_3$$

The elemental energies involve only four degrees of freedom. Thus they can be written as follows

$$(V)_1 = \frac{1}{2} \begin{Bmatrix} q_1 \\ q_2 \\ q_3 \\ q_4 \\ q_5 \\ q_6 \\ q_7 \\ q_8 \end{Bmatrix}^T \begin{bmatrix} \times & \times & \times & \times & & & & \\ \times & \times & \times & \times & & & & \\ \times & \times & \times & \times & & & & \\ \times & \times & \times & \times & & & & \\ & & & & & & & \\ & & & & & & & \\ & & & & & & & \\ & & & & & & & \end{bmatrix} \begin{Bmatrix} q_1 \\ q_2 \\ q_3 \\ q_4 \\ q_5 \\ q_6 \\ q_7 \\ q_8 \end{Bmatrix} = \frac{1}{2} \underline{q}^T (K_e)_1 \underline{q}$$

The matrix $(K_e)_1$ contains nonzero values only at marked places. The column numbers have been marked over the matrix. Similarly

$$(V)_2 = \frac{1}{2} \begin{Bmatrix} q_1 \\ q_2 \\ q_3 \\ q_4 \\ q_5 \\ q_6 \\ q_7 \\ q_8 \end{Bmatrix}^T \begin{bmatrix} & & & & & & & \\ & & & & & & & \\ & & + & + & + & + & & \\ & & + & + & + & + & & \\ & & + & + & + & + & & \\ & & + & + & + & + & & \\ & & & & & & & \\ & & & & & & & \end{bmatrix} \begin{Bmatrix} q_1 \\ q_2 \\ q_3 \\ q_4 \\ q_5 \\ q_6 \\ q_7 \\ q_8 \end{Bmatrix} = \frac{1}{2} \underline{q}^T (K_e)_2 \underline{q}$$

Substitute the total energies and the total load vector into the Euler-Lagrange equation to determine the ODE's governing the degrees of freedom $q_1, q_2, q_3, \dots, q_N$. Note that the virtual work expression includes only the external loading on each element, not the work done by the constraint forces acting on each face. The work done by the constraint forces however cancel when the elements are assembled. This is the reason why the elemental properties must be assembled before substitution into the Euler-Lagrange equation.

$$\frac{\partial}{\partial t} \left(\frac{\partial U}{\partial \dot{q}_i} \right) - \frac{\partial U}{\partial q_i} + \frac{\partial V}{\partial q_i} = Q_i \quad i = 1, 2, \dots, N. \quad (2.83)$$

For the case of three elements we have the following ODE's.

$$\begin{bmatrix} m_{11} & m_{12} & \dots & m_{18} \\ m_{21} & m_{22} & \dots & m_{28} \\ \vdots & \vdots & \vdots & \vdots \\ m_{81} & m_{82} & \dots & m_{88} \end{bmatrix} \begin{bmatrix} \ddot{q}_1 \\ \ddot{q}_2 \\ \vdots \\ \ddot{q}_8 \end{bmatrix} + \begin{bmatrix} k_{11} & k_{12} & \dots & k_{18} \\ k_{21} & k_{22} & \dots & k_{28} \\ \vdots & \vdots & \vdots & \vdots \\ k_{81} & k_{82} & \dots & k_{88} \end{bmatrix} \begin{bmatrix} q_1 \\ q_2 \\ \vdots \\ q_8 \end{bmatrix} = \begin{bmatrix} Q_1 \\ Q_2 \\ \vdots \\ Q_8 \end{bmatrix} \quad (2.84)$$

Note that at this point the stiffness matrix above K is singular. This is because the elements were free-free in nature and no constraints have yet been implemented on either end of the beam. Thus the entire beam is still free-free and as such, the above ODE's include the rigid body modes of the beam. The next step is to apply the constraints posed by the geometric boundary conditions.

2.5.3 Constraint conditions

Constraints conditions can be easily incorporated by modifying eqn. 2.84, by simple removal of certain degrees of freedom. For example, for a cantilevered boundary condition at the root end we have

$$\begin{aligned} w(0, t) = 0 &\implies q_1(t) = 0 \\ w'(0, t) = 0 &\implies q_2(t) = 0 \end{aligned} \quad (2.85)$$

which can be incorporated by removing the first two rows and columns of eqn. 2.84. Thus in this case the governing ODE's become

$$\begin{bmatrix} m_{33} & m_{34} & \dots & m_{38} \\ m_{43} & m_{44} & \dots & m_{48} \\ \vdots & \vdots & \vdots & \vdots \\ m_{83} & m_{84} & \dots & m_{88} \end{bmatrix} \begin{bmatrix} \ddot{q}_3 \\ \ddot{q}_4 \\ \vdots \\ \ddot{q}_8 \end{bmatrix} + \begin{bmatrix} k_{33} & k_{34} & \dots & k_{38} \\ k_{43} & k_{44} & \dots & k_{48} \\ \vdots & \vdots & \vdots & \vdots \\ k_{83} & k_{84} & \dots & k_{88} \end{bmatrix} \begin{bmatrix} q_3 \\ q_4 \\ \vdots \\ q_8 \end{bmatrix} = \begin{bmatrix} Q_3 \\ Q_4 \\ \vdots \\ Q_8 \end{bmatrix}$$

The new K matrix is no longer singular. For a simply-supported beam we have

$$\begin{aligned} w(0, t) = 0 &\implies q_1(t) = 0 \\ w(R, t) = 0 &\implies q_7(t) = 0 \end{aligned} \quad (2.86)$$

which can be incorporated by removing the first and seventh rows and columns of eqn. 2.84. Similarly a statically indeterminate problem where one end is cantilevered and the other end simply-supported

$$\begin{aligned} w(0, t) = 0 &\implies q_1(t) = 0 \\ w'(0, t) = 0 &\implies q_2(t) = 0 \\ w(R, t) = 0 &\implies q_7(t) = 0 \end{aligned} \quad (2.87)$$

can be easily realized by removing the first, second and seventh rows and columns. The mass and stiffness matrices are in general banded, a fact that can be used to reduce computations and memory

storage requirements during the solution of the ODE's. After the application of constraints, the n coupled equations can be put together in matrix form.

$$M\ddot{\underline{q}} + K\underline{q} = \underline{Q}$$

where M and K are mass and stiffness matrices of size $(n \times n)$. \underline{Q} is the forcing vector of size n , and \underline{q} are the degrees of freedom. The degrees of freedom \underline{q} are generalized displacements (displacement or angles, with units of m or in, and radians). M has units of kg. K has units of N/m. \underline{Q} has units of N. For natural response, set $\underline{Q} = \underline{0}$ and seek solution of the form $\underline{q} = \underline{q}_0 e^{j\omega t}$. This leads to the same algebraic eigenvalue problem as discussed earlier in the case of Galerkin and Rayleigh-Ritz methods,

$$\begin{aligned} K\underline{q}_0 &= \omega^2 M\underline{q}_0 \\ (K - \omega^2 M)\underline{q}_0 &= 0 \end{aligned} \tag{2.88}$$

It leads to the solutions ω_i where $i = 1, 2, \dots, n$. Corresponding to each ω_i there exists a solution \underline{q}_{0i} which satisfies the equation

$$K\underline{q}_{0i} = \omega_i^2 M\underline{q}_{0i}$$

ω_i and its corresponding \underline{q}_{0i} are called the eigenvalues and eigenvectors of the system. The mode shapes of the beam can be extracted from the eigenvectors. Consider the example of the beam discretized into three elements as before. Consider a simply-supported case at the root end. Let the i -th eigenvector be $\underline{q}_{0i} = [q_{02} \ q_{03} \ q_{04} \ q_{05} \ q_{06} \ q_{07} \ q_{08}]^T$. The mode shape ϕ_i corresponding to this eigenvectors can then be constructed using the shape functions as follows.

$$\phi_j(r) = \begin{cases} w_1(r) = & H_2(s)q_{02} + H_3(s)q_{03} + H_4(s)q_{04} & r_1 < r < r_2 & s = r - r_1 \\ w_2(r) = & H_1(s)q_{03} + H_2(s)q_{04} + H_3(s)q_{05} + H_4(s)q_{06} & r_2 < r < r_3 & s = r - r_2 \\ w_3(r) = & H_1(s)q_{05} + H_2(s)q_{06} + H_3(s)q_{07} + H_4(s)q_{08} & r_3 < r < R & s = r - r_3 \end{cases}$$

Note that the shape functions obtained here correspond to the rotating beam. Thus an important property is that they are orthogonal with respect to mass and rotational stiffness.

$$\int_0^R m\phi_i(r)\phi_j(r) dr = \delta_{ij}M_i \tag{2.89}$$

and

$$\int_0^R \left[EI \frac{d^2\phi_i(r)}{dr^2} \frac{d^2\phi_j(r)}{dr^2} + T \frac{d\phi_i(r)}{dr} \frac{d\phi_j(r)}{dr} \right] dr = \delta_{ij}\omega_i^2 M_i \tag{2.90}$$

where δ_{ij} is Kronecker's delta and M_i is generalized mass

$$M_i = \int_0^R m(r)\phi_i^2 dr$$

2.6 Fan plot and frequency plots for rotating beams

The natural modes of a structure represent the unique ways it can vibrate in vacuum and without damping. The lowest frequency is called the fundamental frequency and the corresponding mode is called the fundamental mode. The natural frequencies of a rotating blade depend on its mass and stiffness properties, boundary conditions, and rotational speed. The rotational speed supplies centrifugal stiffness. At low rotational speeds, the beam stiffness is more important than the centrifugal stiffness. At higher rotational speeds, the centrifugal stiffness is more important than the beam stiffness. At still higher rotational speeds, the beam behaves like a string, the fundamental natural frequency asymptotes to the rotational frequency. The rotating frequencies are always greater than non-rotating frequencies. However, there is only a slight change in mode shapes from non-rotating to the rotating ones. In the following sub-sections the natural frequencies of a uniform, rotating beam are studied. The frequency and mode shape calculations are performed using a Rayleigh-Ritz type finite element analysis with ten equal length elements.

2.6.1 Rotating versus non-rotating frequencies

For a given rotational speed, the blade rotating frequencies are determined by the mass and stiffness of the blade, and the boundary conditions. Consider a cantilevered non-rotating beam with uniform properties EI and m . This is a simple model for a hingeless blade.

First, solve eqn.2.29 to get the non-rotating frequencies ω_{NR_1} , ω_{NR_2} , ω_{NR_3} etc. The first frequency, or the lowest, $\omega_{NR_1} = \omega_{NR}$ say, is called the fundamental frequency. Note that these frequencies are of the form $f_j \sqrt{EI/mR^4}$ as given in eqns.2.37 and 2.41. Now consider a rotational speed Ω . Corresponding to this Ω solve eqn.2.46 to obtain the rotating frequencies ω_{R_1} , ω_{R_2} , ω_{R_3} etc. Again, $\omega_{R_1} = \omega_R$ is the fundamental frequency, this time that of the rotating beam. Varying the stiffness EI , a set of ω_{NR} and ω_R can be obtained. Thus one can obtain a plot of ω_R versus ω_{NR} . This plot corresponds to the specific set of beam properties and a given Ω .

If the frequencies are non-dimensionalized with respect to rotational speed Ω , i.e. ω_R/Ω versus ω_{NR}/Ω , then the plot becomes representative of all uniform cantilevered beams at any given rotational speed. This is due to the following. We have

$$\frac{\omega_{NR}}{\Omega} = f_j \sqrt{\frac{EI}{m\Omega^2 R^4}} \quad \text{where } m = m_0 \text{ for uniform beams}$$

Recall that, eqn.2.50 showed that the only parameter on which the non-dimensional rotational frequency, ω_R/Ω , of a uniform beam depend is $EI/m\Omega^2 R^4$. This is the same parameter on the right hand side of the above expression. Varying ω_{NR}/Ω from zero onwards includes all variations of this parameter. Thus all beams, regardless of their properties EI , m , dimension R , and rotational speed Ω would correspond to a point on the plot of ω_R/Ω versus ω_{NR}/Ω . Such a plot, for the first mode, is shown in figure 2.19. Note that, different beams with different EI , m , R , and Ω can correspond to the same point on the plot as long as they have the same $EI/m_0\Omega^2 R^4$. Therefore ω_{R_j}/Ω versus ω_{NR_j}/Ω plots are representative of all uniform beams of a specific boundary condition type. Figure 2.20 shows the variation of two higher modes in addition to the fundamental mode.

2.6.2 Rotating frequencies vs. rotational speed

For a given mass and stiffness, the rotating frequencies vary with the rotational speed (RPM). At zero RPM the frequency corresponds to a non-rotating beam. As RPM increases, the centrifugal force gradually stiffens the blade. Figure 2.21(a) shows the variation of rotating frequencies in Hz with RPM. The value at zero RPM is $3.52\sqrt{EI/mR^4}$ from eqns.2.36 and 2.37, where the following values have been assumed: $EI = 4.225 e5 \text{ Nm}^2$, $m = 13 \text{ kg/m}$, and $R = 8.2 \text{ m}$.

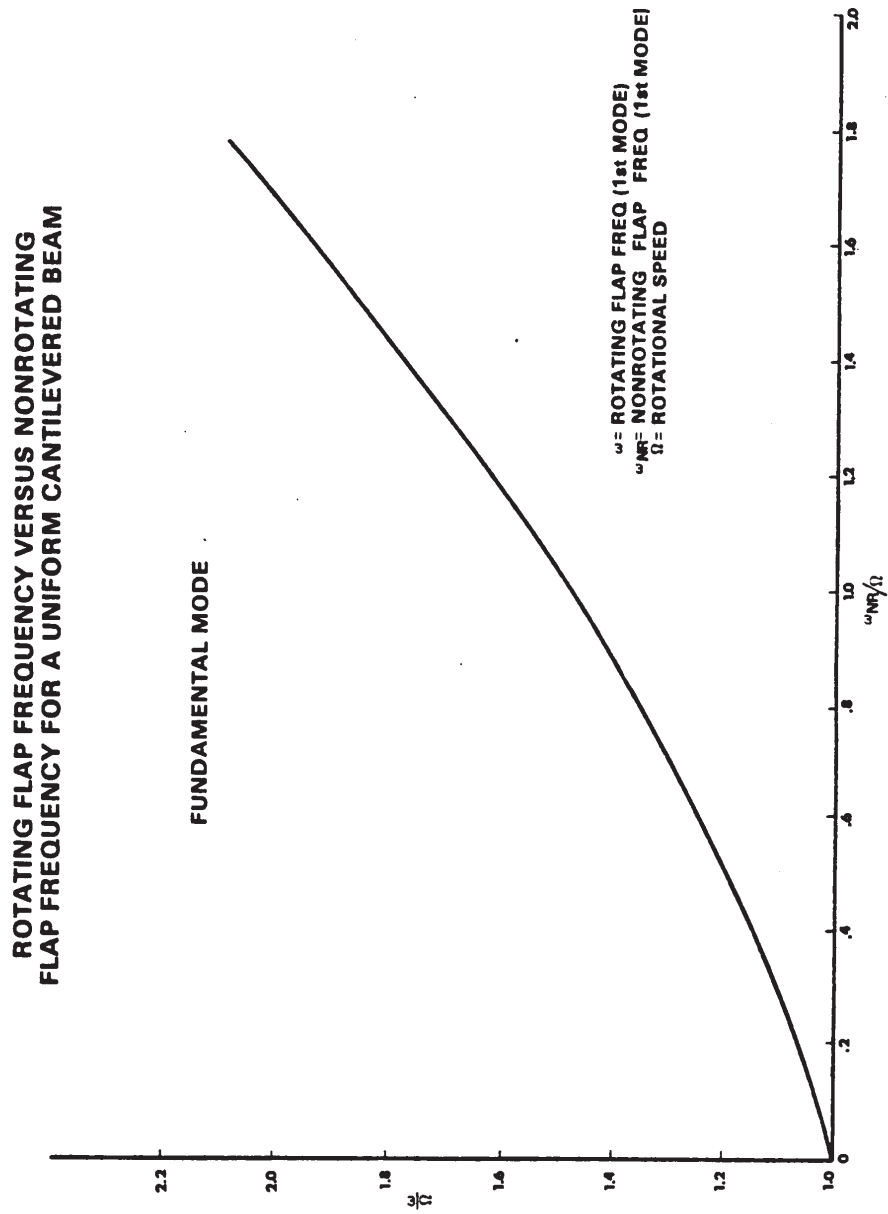


Figure 2.19: Rotating natural frequencies as function of non-rotating natural frequencies for a uniform cantilevered beam: Fundamental mode

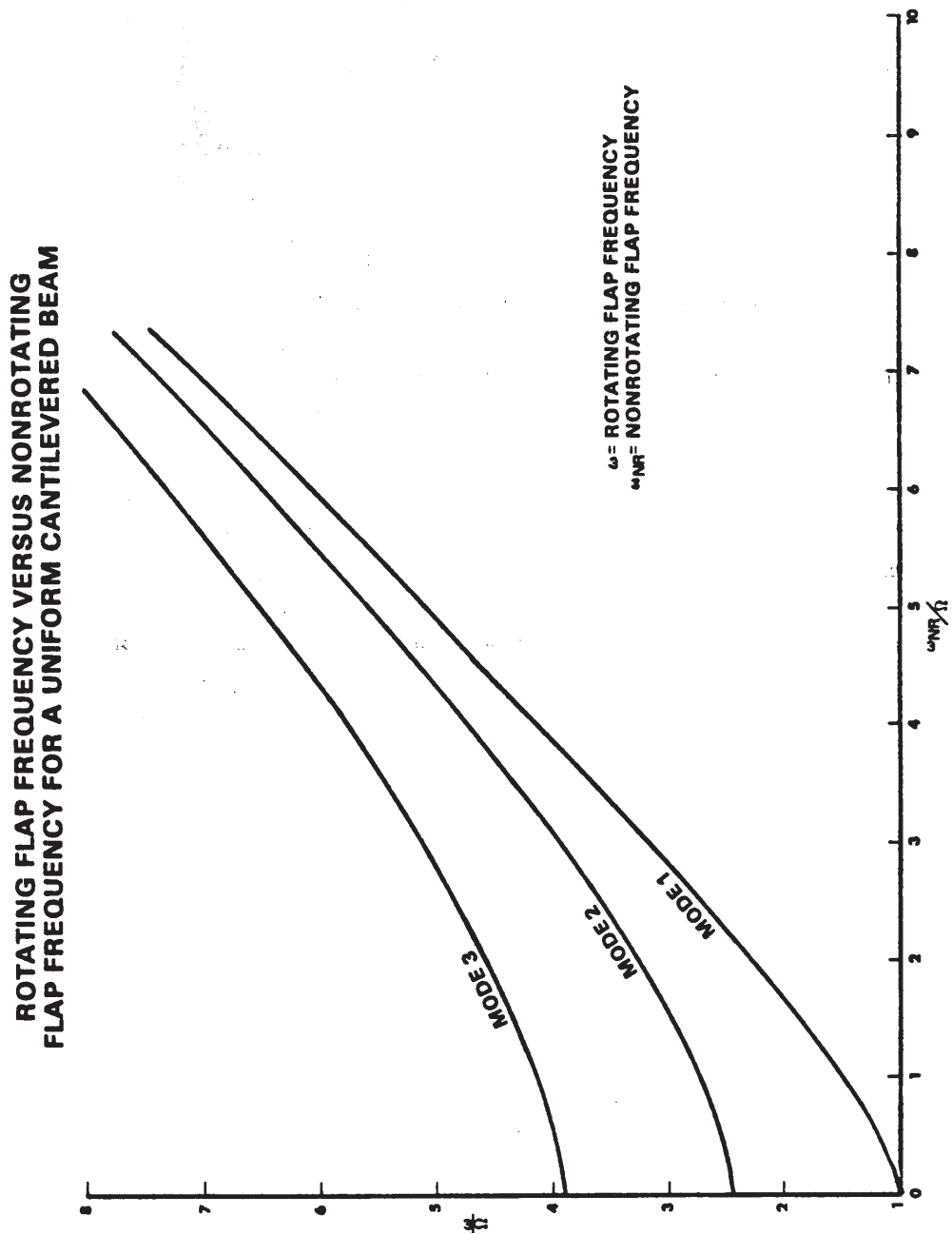


Figure 2.20: Rotating natural frequencies as function of non-rotating natural frequencies for a uniform cantilevered beam: First three modes

Let the operating RPM be 260. Then the x-axis is often conveniently represented in terms of the operating RPM, see Fig. 2.21(b)). The frequencies, instead of being in Hz can be non-dimensionalized at each rotor RPM. These frequencies, in per rev, are plotted in Figs. 2.21(c) and 2.21(d). These plots show the relative dominance of the centrifugal stiffness. A very high per rev value, as is the case for very lower RPM, signifies the dominance of bending stiffness. A lower per rev value, as is the case of higher RPM, signifies the dominance of centrifugal stiffness.

For design purposes it is often convenient to represent the frequencies in the following two formats. The first is called a fan plot. The second is called the non-dimensional frequency plot. The fan plot is same as the frequency plot of figure 2.21(b), except that it shows the 1/rev, 2/rev, 3/rev, etc lines in addition to the rotor frequencies. The rotor frequency can be read off in Hz. In addition, at any RPM an approximate per rev value can be estimated. For example, at the operating RPM the second mode lies between 3 and 4/rev, the third mode lies between 7 and 8/rev. It is desirable to design the blade structurally in such a way that the modal frequencies lie in between /rev lines. The aerodynamic forcing in steady flight occurs at 1/rev, 2/rev, 3/rev etc. Structural frequencies near these forcing harmonics expose the rotor to resonance. The non-dimensional frequency plot is same as the frequency plot of figure 2.21(b), except that the frequencies are non-dimensionalized with respect to the *operating RPM*. Note that this is different from figure 2.21(d) in that the frequencies are not divided by the rotor RPM, but the rotor RPM at the operating condition. Thus these are not /rev values. They equal the /rev values only at the operating RPM.

Frequency plots for a simple-supported beam (articulated rotor model) is shown in figures 2.23 and 2.24. The simple-supported beam has exactly the same properties as the cantilevered beam (hingeless rotor model). The only difference is in the boundary condition. The frequency trends are very similar for the higher modes. The key difference is in the fundamental mode. Figure 2.23(c) shows that the fundamental frequency is determined by the centrifugal stiffness regardless of the RPM. Thus it is always at 1/rev. Resonance is not a problem because of the high aerodynamic damping present in the flap mode (around 50%). On the contrary it is desirable to place the first frequency as close to 1/rev as possible to relieve the root bending moments. Under this condition the balance of the centrifugal and aerodynamic forces on the blade is used up completely by the blade flapping motion with zero moment transmitted to the root.

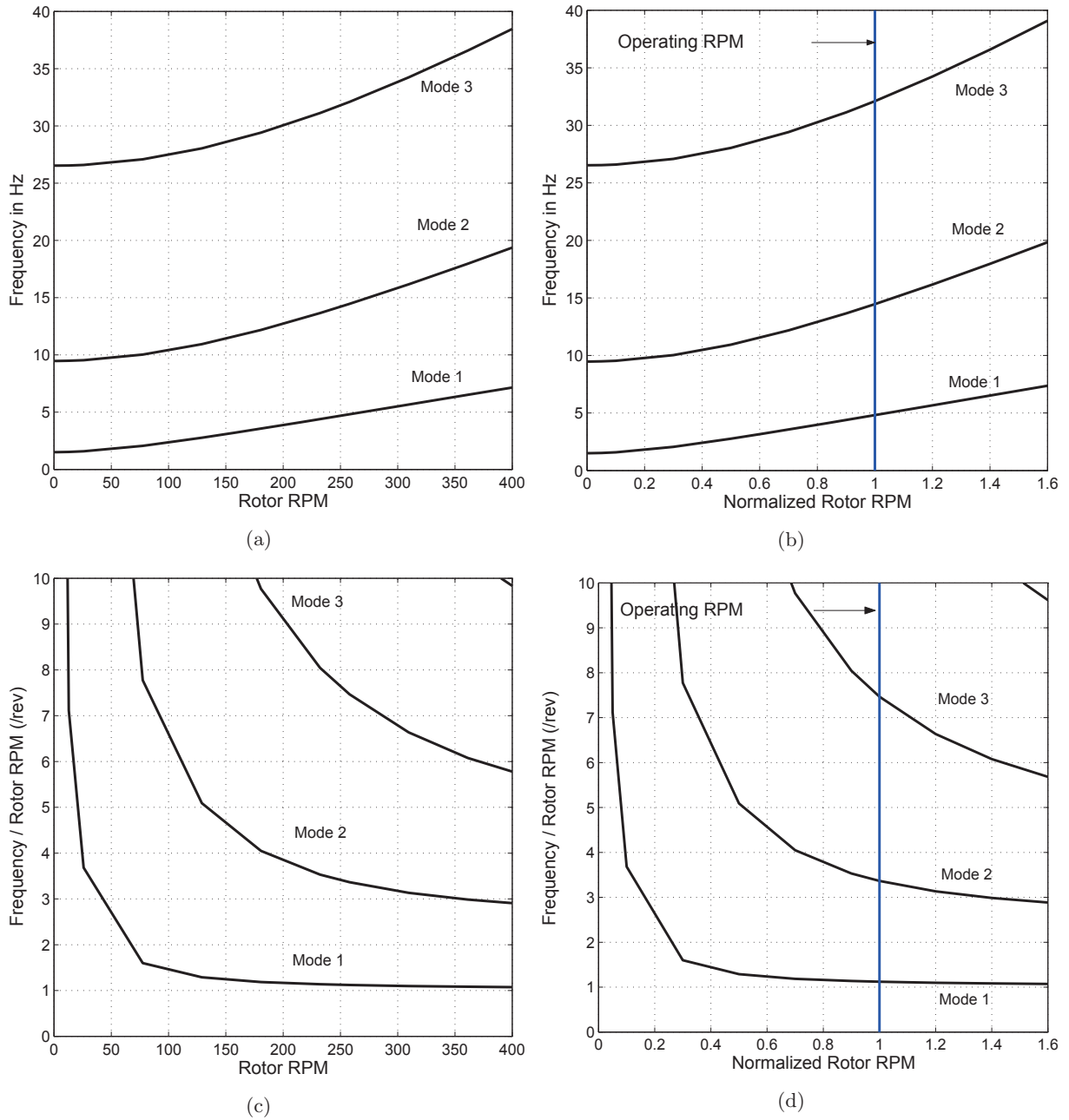
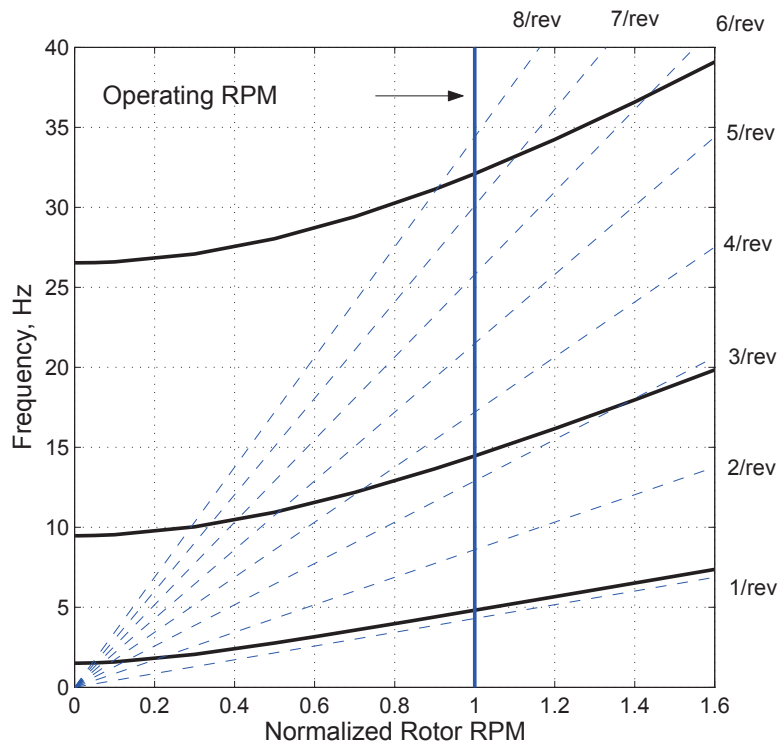
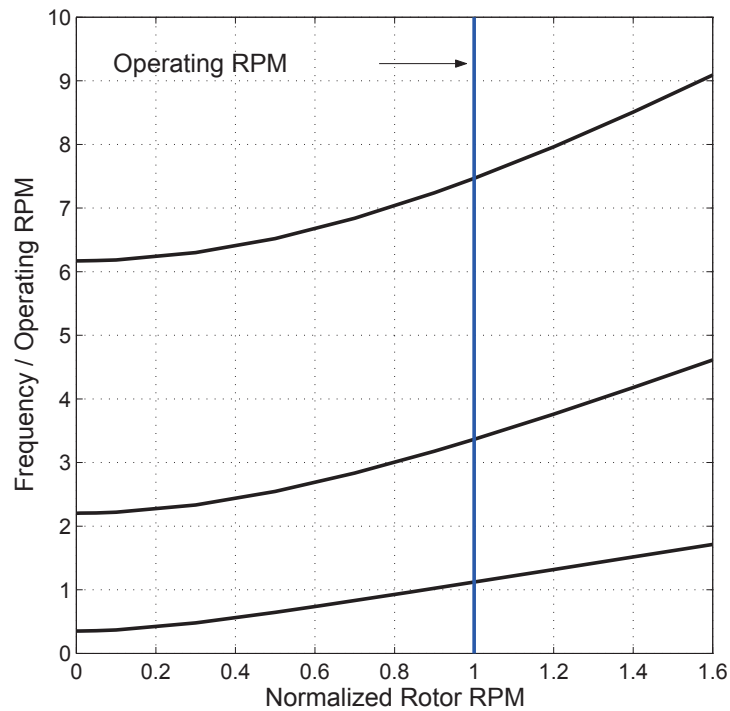


Figure 2.21: Natural frequencies of a uniform cantilevered beam varying with RPM



(a) Fan plot in Hz



(b) Frequency plot non-dimensionalized with respect to operating RPM

Figure 2.22: Fan plot and Non-dimensional frequency plot for a hingeless rotor blade

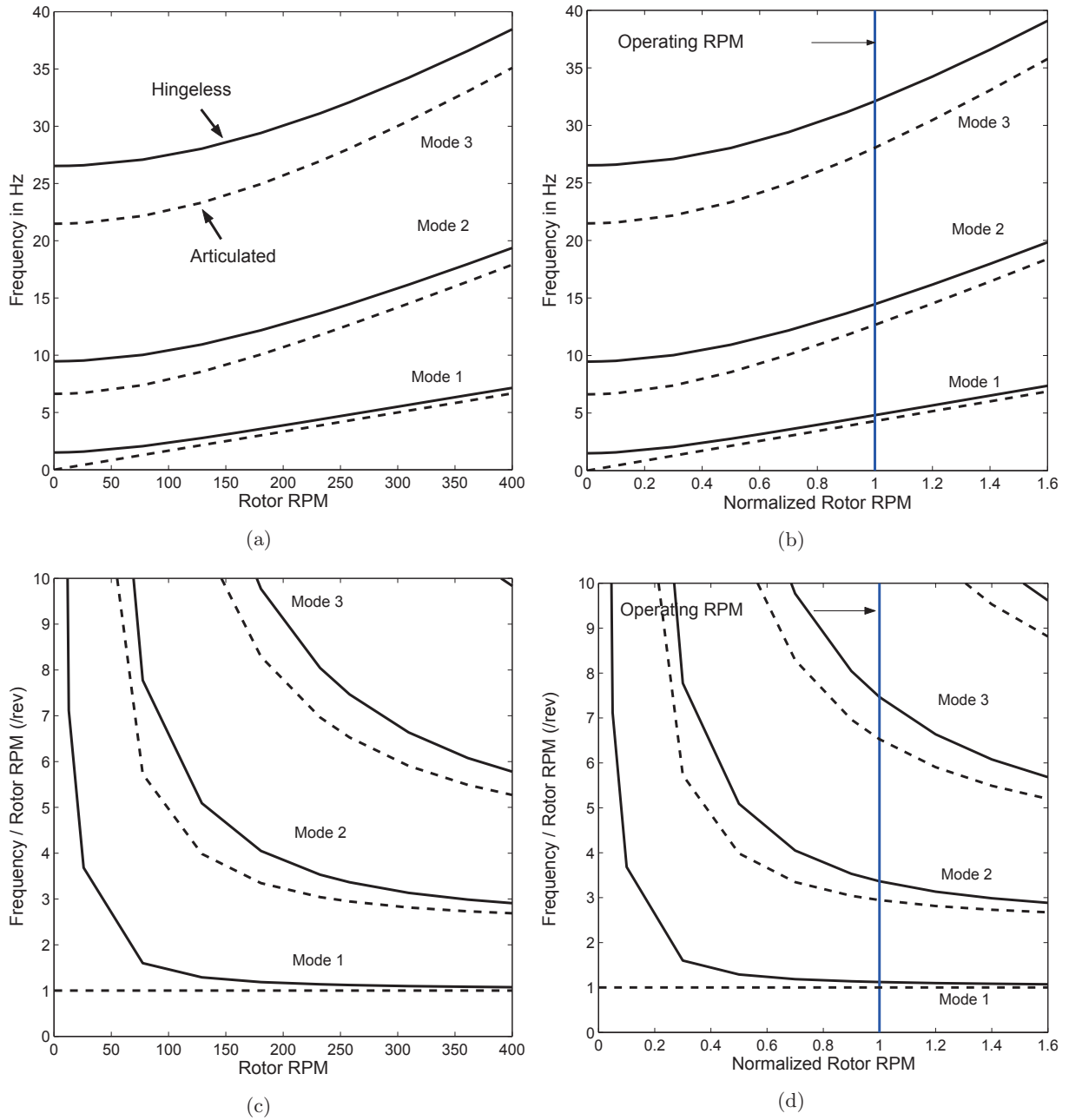
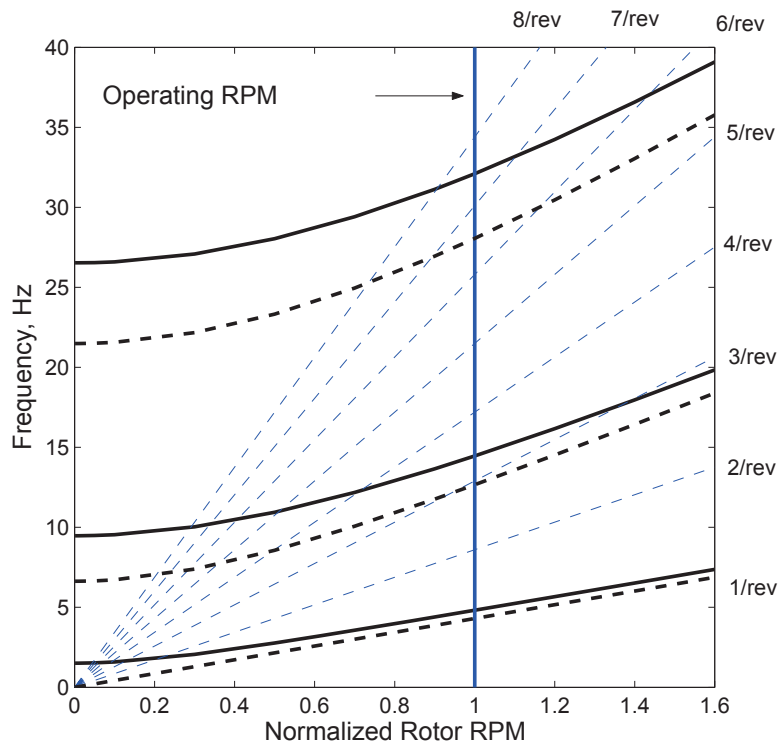
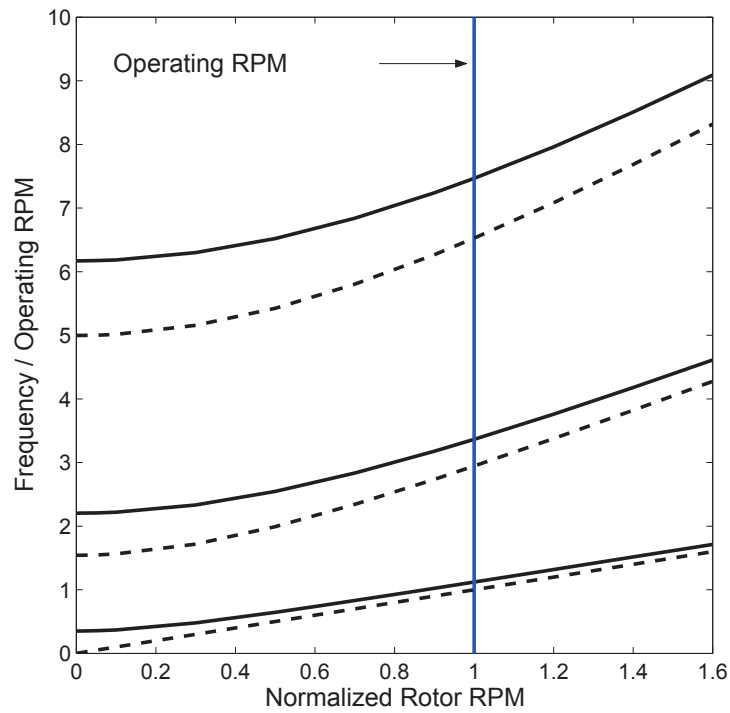


Figure 2.23: Natural frequencies of an articulated rotor blade compared with a hingeless rotor blade



(a) Fan plot in Hz



(b) Frequency plot non-dimensionalized with respect to operating RPM

Figure 2.24: Fan plot and Non-dimensional frequency plot for a hingeless rotor blade

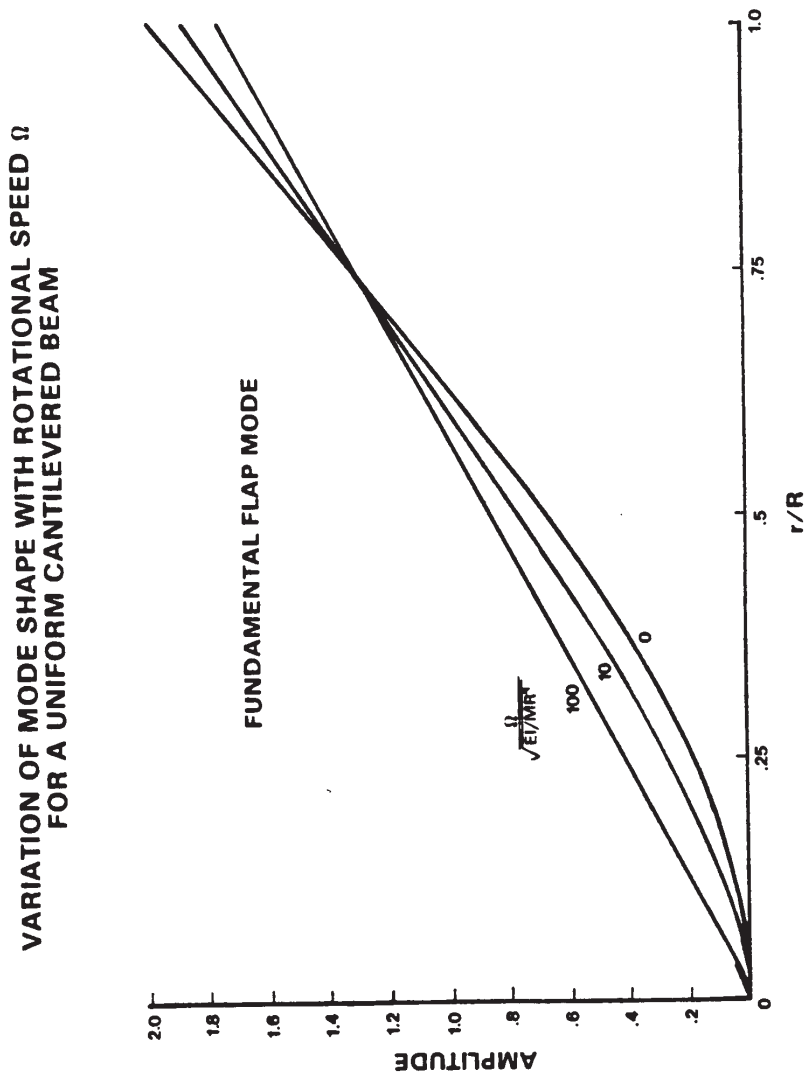


Figure 2.25: Rotating mode shapes for a uniform cantilevered beam: Fundamental mode

2.6.3 Rotating versus non-rotating mode shapes

It is clear that the parameter which makes the non-dimensional frequencies and mode shapes differ from one uniform beam to another is $EI/m\Omega^2R^4$. The parameter can be re-arranged to read $\Omega/\sqrt{EI/mR^4}$. The frequencies and mode shapes of two beams operating at different values of Ω can still be same if EI , m , and R are such that the above parameter remains same. The effect of rotational speed on the mode shape can be seen only if this parameter is varied. Figure 3 and 4 shows such plots for the first and the second modes for cantilevered beams. Note that each line on a plot can represent the mode shape of different cantilevered beams with different rotational speeds, but all having the same $\Omega/\sqrt{EI/mR^4}$.

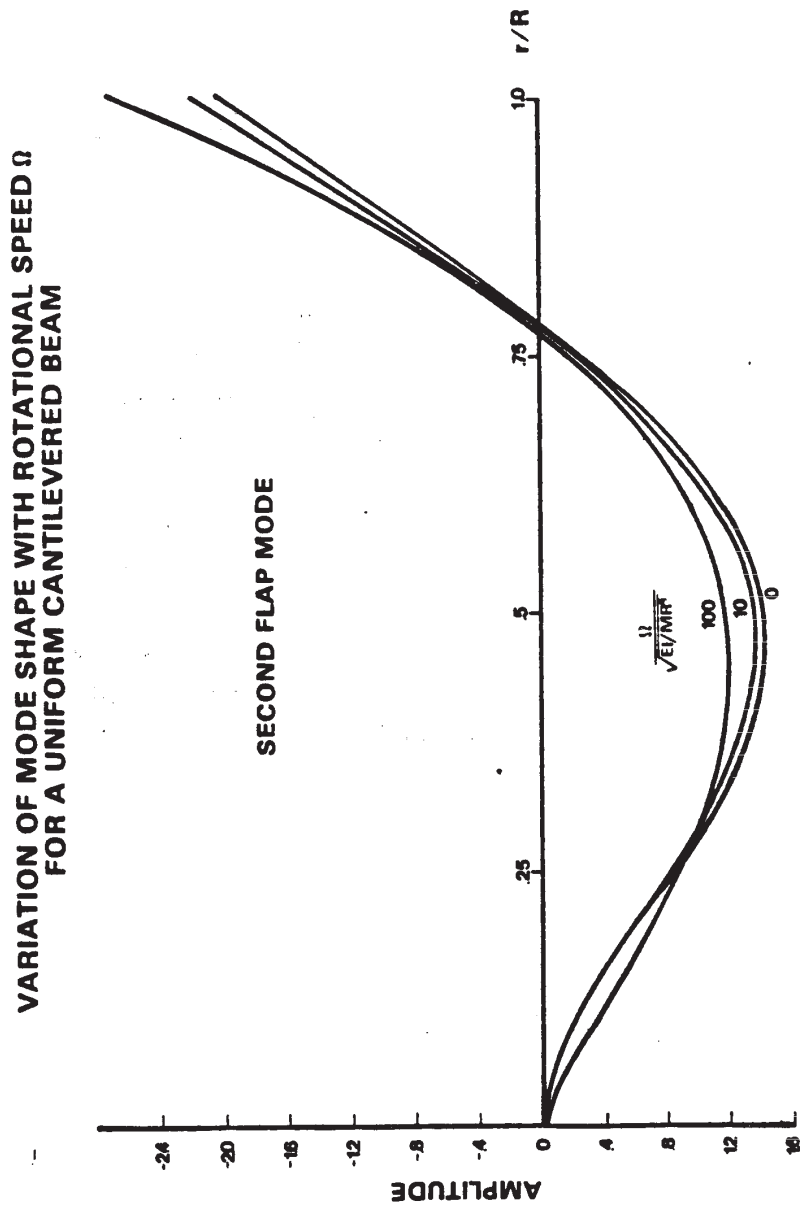


Figure 2.26: Rotating mode shapes for a uniform cantilevered beam: First three modes

2.7 Response Solution in time

After the natural vibration characteristics of the blade has been determined, the next step is to calculate dynamic response to a given forcing. Let us examine the equations of motion. For the rigid blade model, the flap equation was given by

$$\beta^{**} + \nu_\beta^2 \beta = \frac{\omega_0^2}{\Omega^2} \beta_p + \gamma \overline{M}_\beta \quad (2.91)$$

The aerodynamic moment term \overline{M}_β may contain motion dependent terms like β and β^* . It may also contain periodic terms, particularly for forward flight condition. One of the simplest and most commonly used method is Fourier series. The method will be discussed later. For the flexible blade model, the flap bending equation was given by

$$\frac{d^2}{dr^2} \left(EI_{\eta\eta} \frac{d^2 w}{dr^2} \right) + m\ddot{w} - \frac{d}{dr} \left(T \frac{dw}{dr} \right) = f_z(r, t) \quad (2.92)$$

where $f_z(r, t)$ was the aerodynamic force. Again, it may contain motion dependent terms as well as periodic terms. Recall, that the first step of the solution was to obtain the natural frequencies and mode shapes by solving the homogenous form of the equation, i.e. with $f_z(r, t) = 0$. The next step is to reduce the governing PDE to a set of ODE's using the mode shapes. The ODE's are then called normal mode equations. To this end, assume that the loading is a series of N natural modes

$$w(r, t) = \sum_{j=1}^N \phi_j(r) \xi_j(t) \quad (2.93)$$

where $\phi_j(r)$ is j^{th} natural mode. $\xi_j(t)$ is the j^{th} modal response. Substitute in the governing eqn.2.92, project the error onto a subspace spanned by the mode shapes themselves and set to zero.

$$\int_0^R \phi_i(r) \epsilon(r, t) dr = 0 \quad i = 1, 2, \dots, N \quad (2.94)$$

Use the orthogonality relations 2.89 and 2.90 to obtain

$$M_i \ddot{\xi}_i + \omega_i^2 M_i \xi_i = S_i \quad i = 1, 2, \dots, N \quad (2.95)$$

where

$$\begin{aligned} M_i &= \int_0^R m \phi_i^2(r) dr \\ S_i &= \int_0^R \phi_i f_z(r, t) dr \end{aligned} \quad (2.96)$$

These are N modally reduced equations.

The external forcing on the beam is f_z . For a pure structural dynamics problem, f_z is purely a function of r and t . In this case S_i is only a function of time. For an aeroelastic problem, as is the case for rotor blades, f_z is motion dependant, i.e. it depends on the response itself. In this case S_i contain deflection dependant terms. First, consider the case where S_i is only a function of time. The modally reduced equations simply represent a series of one degree of freedom spring-mass systems. Generally, $N = 2$ to 3 are adequate to describe the response of a system. The higher modes contribute comparatively little to the response. The normal mode coordinates $\xi_1(t)$, $\xi_2(t)$, ..., etc may be solved in time using various methods. The most commonly used methods for rotor

problems are Fourier series and time integration technique and these will be discussed later. For non-rotor problems, Duhamel's integral is often used to calculate.

Now consider the case of motion dependant forcing. In this case $f_z(r, t)$ depends on displacement w as well as time t . In general, we have

$$f_z(r, t) = \bar{f}_z(r, t) + aw + b\dot{w} + cw' + d\dot{w}' + \dots \text{etc} \quad (2.97)$$

In this case the modally reduced equations take the following form.

$$M_i \ddot{\xi}_i + M_i \omega_i^2 \xi_i = S_i \quad i = 1, 2, \dots, N$$

where

$$S_i = \sum_{j=1}^N \bar{S}_i(t) + (A_{ij} + C_{ij})\xi_i + (B_{ij} + D_{ij})\dot{\xi}_j + \dots \text{etc} \quad (2.98)$$

and

$$\begin{aligned} \bar{S}_i &= \int_0^R \phi_i \bar{f}_z(r, t) dr & A_{ij} &= \int_0^R \phi_i a \phi_j dr & B_{ij} &= \int_0^R \phi_i b \phi_j dr \\ C_{ij} &= \int_0^R \phi_i c \phi_j' dr & D_{ij} &= \int_0^R \phi_i d \phi_j' dr \end{aligned}$$

The mode shapes ϕ are not orthogonal with respect to a, b, c, d . Thus the matrices A, B, C, D are not diagonal. Therefore the resultant ODE's are now coupled. $A + C$ represent aerodynamic stiffness. $B + D$ represent aerodynamic damping. Unlike the structural properties, the aerodynamic stiffness and damping matrices are no longer symmetric. Further, unlike the mechanical system without aerodynamics, the aerodynamic forcing adds a damping to the system. Thus the system is no longer a energy conserving system. The aerodynamic damping need not be necessarily positive. A negative damping can lead to instability, typically called aeroelastic instability. It is more involved to solve these equations. Three widely used variety of methods are: (1) Fourier series based methods, (2) Finite Element in Time method, and (3) Time integration methods. The first two methods provide the steady state forced response solution and are well suited for rotorcraft applications. The third, is a general time marching procedure with provide both the natural response as well as the forced response.

2.7.1 Fourier series methods

In the Fourier series method the response is assumed to be periodic and consisting of a sum of harmonics. For example, for the rigid blade model, the response $\beta(\psi)$ is assumed to be a linear combination of sine and cosine terms as

$$\begin{aligned} \beta(\psi) &= \beta_0 + \beta_{1c} \cos \psi + \beta_{1s} \sin \psi + \beta_{2c} \cos 2\psi + \beta_{2s} \sin 2\psi + \dots \infty \\ &= \beta_0 + \sum_{n=1}^{\infty} (\beta_{nc} \cos n\psi + \beta_{ns} \sin n\psi) \end{aligned}$$

where the fundamental period is 2π . The fourier constants $\beta_0, \beta_{1c}, \beta_{1s}, \dots$ are constant with time. They are given by

$$\begin{aligned} \beta_0 &= \frac{1}{2\pi} \int_0^{2\pi} \beta(\psi) d\psi \\ \beta_{nc} &= \frac{1}{\pi} \int_0^{2\pi} \beta(\psi) \cos n\psi d\psi \\ \beta_{ns} &= \frac{1}{\pi} \int_0^{2\pi} \beta(\psi) \sin n\psi d\psi \end{aligned} \quad (2.99)$$

The number of harmonics necessary for satisfactory solution depends on the intended results of the analysis. For preliminary performance and flight dynamic calculations the first harmonic is often adequate. For vibratory loads at least the first five harmonics must be retained. The flapping harmonics can be computed from measured data. If the sample of data points taken over one revolution is N_s , where N_s is the total number of azimuthal intervals such that $\beta(N_s + 1) = \beta(1)$, then

$$\begin{aligned}\beta_0 &= \frac{1}{N_s} \sum_{i=1}^{N_s} \beta_i \\ \beta_{nc} &= \frac{2}{N_s} \sum_{i=1}^{N_s} \beta_i \cos n\psi_i \\ \beta_{ns} &= \frac{2}{N_s} \sum_{i=1}^{N_s} \beta_i \sin n\psi_i\end{aligned}\tag{2.100}$$

where $\psi_i = 2\pi(i - 1)/N_s$. Using the fourier series method, the governing ODE's can be solved using two approaches: (1) the Substitutional or Harmonic Balance method and (2) the Operational method.

The harmonic balance method is well suited for analytical solution. In this method the fourier series is truncated to a finite number of terms

$$\beta(\psi) = \beta_0 + \sum_{n=1}^N (\beta_{nc} \cos n\psi + \beta_{ns} \sin n\psi)$$

and substituted in the ODE. The coefficients of the equation are also written as fourier series by reducing the products of sines and cosines to sums of sines and cosines. The coefficients of the sine and cosine components are then collected

$$(\dots) + (\dots) \sin \psi + (\dots) \cos \psi + (\dots) \sin 2\psi + (\dots) \cos 2\psi + \dots = 0$$

These coefficients are then separately set to zero leading to $2N + 1$ algebraic equations for the same number of unknown fourier coefficients.

In the operational method, the following operators are used directly on the ODEs.

$$\begin{aligned}\frac{1}{2\pi} \int_0^{2\pi} (de) d\psi &= 0 \\ \frac{1}{\pi} \int_0^{2\pi} (de) \cos n\psi d\psi &= 0 \quad n = 1, 2, \dots, N \\ \frac{1}{\pi} \int_0^{2\pi} (de) \sin n\psi d\psi &= 0 \quad n = 1, 2, \dots, N\end{aligned}\tag{2.101}$$

The coefficients of the equation are again written as fourier series but the degrees of freedom are not. The operators act on the product of the degrees of freedom and the sin or cosine harmonics reducing them to appropriate fourier coefficients. Both the harmonic balance and the operational method yield the same algebraic equations. In the later, the equations can be derived one at a time. The following standard formulas are helpful in reducing the products of sines and cosines to sums of sines and cosines.

$$\begin{aligned}\sin \psi \cos \psi &= \frac{1}{2} \sin 2\psi & \sin^2 \psi &= \frac{1}{2}(1 - \cos 2\psi) & \cos^2 \psi &= \frac{1}{2}(1 + \cos 2\psi) \\ \sin^3 \psi &= \frac{3}{4} \sin \psi - \frac{1}{4} \sin 3\psi & \cos^3 \psi &= \frac{3}{4} \cos \psi + \frac{1}{4} \cos 3\psi\end{aligned}$$

$$\sin \psi \cos^2 \psi = \frac{1}{4}(\sin \psi + \sin 3\psi) \quad \sin^2 \psi \cos \psi = \frac{1}{4}(\cos \psi - \cos 3\psi)$$

Example 2.5:

A rotor blade is idealized into a rigid blade with spring at the hinge ($\nu_\beta = 1.10/\text{rev}$) and is in hovering flight condition. The blade is excited by an oscillatory aerodynamic lift produced by oscillating the outermost 25% of the blade segment so that $\Delta\theta = 1^\circ \cos \psi$. Calculate the vibratory response assuming the following fourier series

$$\beta(\psi) = \beta_0 + \beta_{1c} \cos \psi + \beta_{1s} \sin \psi$$

Use $\gamma = 8.0$ and assume uniform remains constant.

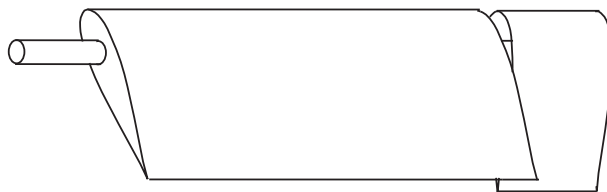


Figure 2.27: **Excitation of outboard blade segment to generate oscillatory lift**

We have the flap equation as follows

$$\beta^{**} + \nu_\beta^2 \beta = \gamma \overline{M}_\beta$$

where

$$\overline{M}_\beta = \frac{1}{2} \int_0^1 x \left\{ \left(\frac{U_T}{\Omega R} \right)^2 \theta - \frac{U_P}{\Omega R} \frac{U_T}{\Omega R} \right\} dx$$

$$\frac{U_T}{\Omega R} = x \quad \frac{U_P}{\Omega R} = \lambda + x \beta^*$$

$$\overline{M}_\beta = \frac{1}{2} \int_0^{3/4} (x^3 \theta - \lambda x^2 - \beta^* x^3) dx + \frac{1}{2} \int_{3/4}^1 \{x^3(\theta + \Delta\theta) - \lambda x^2 - \beta^* x^3\} dx = \frac{\theta}{8} - \frac{\lambda}{6} - \frac{\beta^*}{8} + 0.0854 \Delta\theta$$

The flapping equation is then

$$\beta^{**} + \nu_\beta^2 \beta = \frac{\gamma \theta}{8} - \frac{\gamma \lambda}{6} + \gamma \cdot 0.0854 \frac{1 \times \pi}{180} \cos \psi$$

Substituting

$$\beta = \beta_0 + \beta_{1c} \cos \psi + \beta_{1s} \sin \psi$$

in the flapping equation, collect $\cos \psi$ and $\sin \psi$ terms and set to zero.

$$\text{constant term: } \beta_0 = \frac{\gamma}{2} \left(\frac{\theta_0}{8} - \frac{\gamma}{6} \right)$$

$$\text{cosine term: } (\nu_\beta^2 - 1) \beta_{1c} + \frac{\gamma}{8} \beta_{1s} = \gamma \cdot 0.0854 \frac{1 \times \pi}{180}$$

$$\text{sine term: } (\nu_\beta^2 - 1) \beta_{1s} - \frac{\gamma}{8} \beta_{1c} = 0$$

It follows

$$\begin{bmatrix} 0.21 & 1.00 \\ -1.00 & 0.21 \end{bmatrix} \begin{bmatrix} \beta_{1c} \\ \beta_{1s} \end{bmatrix} = \begin{bmatrix} 0.0119 \\ 0.0000 \end{bmatrix}$$

$$\beta_{1c} = 0.137^\circ, \quad \beta_{1s} = 0.65^\circ$$

2.7.2 Finite Element in Time (FET) method

Finite element in time is a method to calculate the periodic response of a rotor blade. The method can be formulated in two ways: (1) Direct Energy approach, and (2) Indirect Governing Equations approach. We will discuss the Indirect Governing Equations approach. The discretization procedure is the same in both.

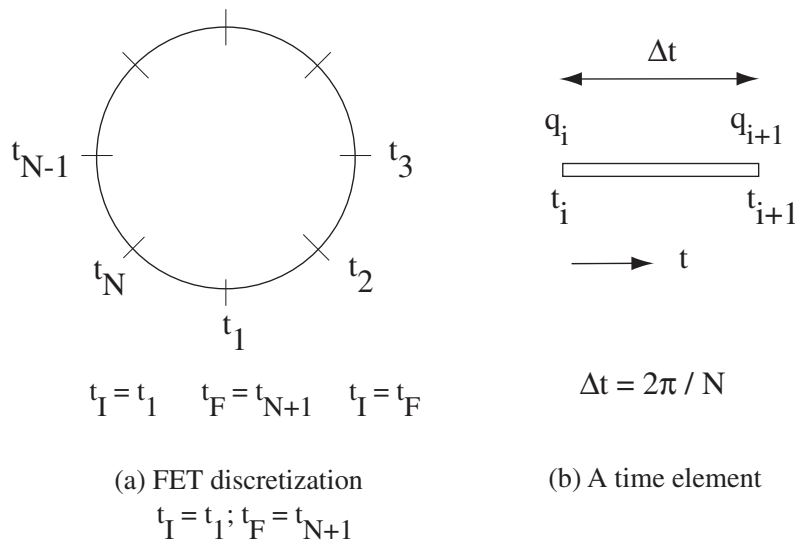


Figure 2.28: **Finite Element in Time (FET) discretization of one period of oscillatory motion**

Consider a single period of oscillatory motion as shown in Fig. 2.28(a). Let the period be T be discretized into N time elements of length $T/2\pi$. For rotors $T = 2\pi$. The initial and final times are the same.

$$t_I = t_1 \quad t_F = t_{N+1} \quad \text{where} \quad t_{N+1} = t_I$$

Similarly the response, say q , at the initial and final times are also the same. For purposes of illustration consider a single degree of freedom system. Now consider a single time element as shown in Fig. 2.28(b). Within the element the degree of freedom q is assumed to vary as a function of time. For example, for a linear variation we have

$$q(t) = \alpha_1 + \alpha_2 t$$

where the constants α are determined in terms of values of q at certain chosen points, called nodes, within the time element. The procedure is same as that described in FEM in space earlier. For purposes of illustration consider the first order element. To determine the two constants α , two nodal degrees of freedom are needed. Let these be the values at the two end points. Then for element-1, for example, we have

$$\eta_1 = q(t_1) = \alpha_1 + \alpha_2 t_1$$

$$\eta_2 = q(t_2) = \alpha_1 + \alpha_2 t_2$$

Solve for $\alpha_{1,2}$

$$\alpha_2 = \frac{\eta_2 - \eta_1}{t_2 - t_1} \quad \alpha_1 = \frac{\eta_1 t_2 - \eta_2 t_1}{t_2 - t_1}$$

It follows

$$\begin{aligned} q(t) &= H_1(t)\eta_1 + H_2(t)\eta_2 \\ H_1(t) &= \left(1 - \frac{t-t_1}{\Delta t}\right) \\ H_2(t) &= \left(\frac{t-t_1}{\Delta t}\right) \end{aligned}$$

where H_1 and H_2 are the time shape functions. The nodal values of q , denoted by η , have no time dependence. The derivatives are

$$\begin{aligned} \dot{q}(t) &= \dot{H}_1(t)\eta_1 + \dot{H}_2(t)\eta_2 \\ \dot{H}_1(t) &= -\frac{1}{\Delta t} \\ \dot{H}_2(t) &= \frac{1}{\Delta t} \end{aligned}$$

The solution procedure begins by putting the governing ODEs in a variational form.

$$\int_{t_I}^{t_F} \delta \underline{q}^T \left(m \ddot{\underline{q}} + c \dot{\underline{q}} + k \underline{q} - \underline{f} \right) dt = 0 \quad (2.102)$$

For a constant m the acceleration term reduces to

$$\int_{t_I}^{t_F} \delta \underline{q}^T m \ddot{\underline{q}} dt = \delta \underline{q}^T m \dot{\underline{q}} \Big|_{t_I}^{t_F} - \int_{t_I}^{t_F} \delta \dot{\underline{q}}^T m \dot{\underline{q}} dt = - \int_{t_I}^{t_F} \delta \dot{\underline{q}}^T m \dot{\underline{q}} dt \quad (2.103)$$

where the first term is cancelled due to periodicity of the response. Using the above, eqn.2.102 becomes

$$I = \int_{t_I}^{t_F} \left(-\delta \dot{\underline{q}}^T m \dot{\underline{q}} + \delta \underline{q}^T c \dot{\underline{q}} + \delta \underline{q}^T k \underline{q} - \delta \underline{q}^T \underline{f} \right) dt = 0 \quad (2.104)$$

where

$$I = \int_{t_1}^{t_2} () dt + \int_{t_1}^{t_2} () dt + \int_{t_1}^{t_2} () dt \dots + \int_{t_{N-1}}^{t_N} () dt = I_1 + I_2 + I_3 + \dots + I_N \quad (2.105)$$

Each integral is of the following form. Consider for example, I_1 .

$$\begin{aligned} I_1 &= - \int_{t_1}^{t_2} \begin{Bmatrix} \delta \eta_1 \\ \delta \eta_2 \end{Bmatrix}^T \begin{Bmatrix} \dot{H}_1 \\ \dot{H}_2 \end{Bmatrix} m [\dot{H}_1 \dot{H}_2] \begin{Bmatrix} \eta_1 \\ \eta_2 \end{Bmatrix} dt \\ &+ \int_{t_1}^{t_2} \begin{Bmatrix} \delta \eta_1 \\ \delta \eta_2 \end{Bmatrix}^T \begin{Bmatrix} H_1 \\ H_2 \end{Bmatrix} c [\dot{H}_1 \dot{H}_2] \begin{Bmatrix} \eta_1 \\ \eta_2 \end{Bmatrix} dt \\ &+ \int_{t_1}^{t_2} \begin{Bmatrix} \delta \eta_1 \\ \delta \eta_2 \end{Bmatrix}^T \begin{Bmatrix} H_1 \\ H_2 \end{Bmatrix} c [H_1 H_2] \begin{Bmatrix} \eta_1 \\ \eta_2 \end{Bmatrix} dt \\ &- \int_{t_1}^{t_2} \begin{Bmatrix} \delta \eta_1 \\ \delta \eta_2 \end{Bmatrix}^T \begin{Bmatrix} H_1 \\ H_2 \end{Bmatrix} \underline{f} dt \\ &= \begin{Bmatrix} \delta \eta_1 \\ \delta \eta_2 \end{Bmatrix}^T \begin{bmatrix} A_{11} & A_{12} \\ A_{21} & A_{22} \end{bmatrix} \begin{Bmatrix} \eta_1 \\ \eta_2 \end{Bmatrix} - \begin{Bmatrix} \delta \eta_1 \\ \delta \eta_2 \end{Bmatrix}^T \begin{Bmatrix} Q_1 \\ Q_2 \end{Bmatrix} \end{aligned} \quad (2.106)$$

where

$$A_{11} = -\frac{m}{\Delta t} - \int_{t_1}^{t_2} \frac{c}{\Delta t} \left(1 - \frac{t-t_1}{\Delta t}\right) dt + \int_{t_1}^{t_2} k \left(1 - \frac{t-t_1}{\Delta t}\right)^2 dt$$

$$\begin{aligned}
A_{12} &= \frac{m}{\Delta t} + \int_{t_1}^{t_2} \frac{c}{\Delta t} \left(1 - \frac{t-t_1}{\Delta t}\right) dt + \int_{t_1}^{t_2} k \frac{t-t_1}{\Delta t} \left(1 - \frac{t-t_1}{\Delta t}\right) dt \\
A_{21} &= \frac{m}{\Delta t} - \int_{t_1}^{t_2} \frac{c}{\Delta t} (t-t_1) dt + \int_{t_1}^{t_2} k \frac{t-t_1}{\Delta t} \left(1 - \frac{t-t_1}{\Delta t}\right) dt \\
A_{22} &= -\frac{m}{\Delta t} + \int_{t_1}^{t_2} \frac{c}{\Delta t} (t-t_1) dt + \int_{t_1}^{t_2} k \left(\frac{t-t_1}{\Delta t}\right)^2 dt \\
Q_1 &= \int_{t_1}^{t_2} f \left(1 - \frac{t-t_1}{\Delta t}\right) dt \\
Q_2 &= \int_{t_1}^{t_2} f \frac{t-t_1}{\Delta t} dt
\end{aligned}$$

Similar expressions can be found for I_2, I_3, \dots etc. The following step is to add the individual integrals as in eqn.2.105. This is an assembly procedure. For illustration consider a case where the time period is discretized into 4 time elements, see Fig.2.29. For the four elements we have the

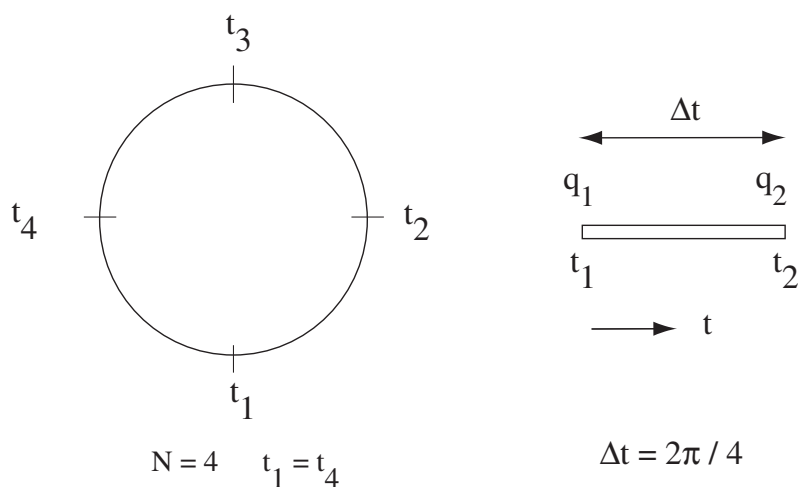


Figure 2.29: **Finite Element in Time (FET) discretization of one period of oscillatory motion**

following

$$\begin{aligned}
I_1 &= \begin{Bmatrix} \delta\eta_1 \\ \delta\eta_2 \end{Bmatrix}^T \begin{bmatrix} A_{11} & A_{12} \\ A_{21} & A_{22} \end{bmatrix}_1 \begin{Bmatrix} \eta_1 \\ \eta_2 \end{Bmatrix} - \begin{Bmatrix} \delta\eta_1 \\ \delta\eta_2 \end{Bmatrix}^T \begin{Bmatrix} Q_1 \\ Q_2 \end{Bmatrix}_1 \\
I_2 &= \begin{Bmatrix} \delta\eta_2 \\ \delta\eta_3 \end{Bmatrix}^T \begin{bmatrix} A_{11} & A_{12} \\ A_{21} & A_{22} \end{bmatrix}_2 \begin{Bmatrix} \eta_2 \\ \eta_3 \end{Bmatrix} - \begin{Bmatrix} \delta\eta_2 \\ \delta\eta_3 \end{Bmatrix}^T \begin{Bmatrix} Q_1 \\ Q_2 \end{Bmatrix}_2 \\
I_3 &= \begin{Bmatrix} \delta\eta_3 \\ \delta\eta_4 \end{Bmatrix}^T \begin{bmatrix} A_{11} & A_{12} \\ A_{21} & A_{22} \end{bmatrix}_3 \begin{Bmatrix} \eta_3 \\ \eta_4 \end{Bmatrix} - \begin{Bmatrix} \delta\eta_3 \\ \delta\eta_4 \end{Bmatrix}^T \begin{Bmatrix} Q_1 \\ Q_2 \end{Bmatrix}_3 \\
I_4 &= \begin{Bmatrix} \delta\eta_4 \\ \delta\eta_1 \end{Bmatrix}^T \begin{bmatrix} A_{11} & A_{12} \\ A_{21} & A_{22} \end{bmatrix}_4 \begin{Bmatrix} \eta_4 \\ \eta_1 \end{Bmatrix} - \begin{Bmatrix} \delta\eta_4 \\ \delta\eta_1 \end{Bmatrix}^T \begin{Bmatrix} Q_1 \\ Q_2 \end{Bmatrix}_4
\end{aligned} \tag{2.107}$$

Add the individual integrals and set $I = 0$ to obtain

$$\begin{Bmatrix} \delta\eta_1 \\ \delta\eta_2 \\ \delta\eta_3 \\ \delta\eta_4 \end{Bmatrix}^T A \begin{Bmatrix} \eta_1 \\ \eta_2 \\ \eta_3 \\ \eta_4 \end{Bmatrix} = \begin{Bmatrix} \delta\eta_1 \\ \delta\eta_2 \\ \delta\eta_3 \\ \delta\eta_4 \end{Bmatrix}^T Q \tag{2.108}$$

Because $\delta\eta$ is arbitrary we have

$$A\eta = Q \quad (2.109)$$

where A and Q are as follows

$$A = \begin{bmatrix} \boxed{\times} & \times & \square & \\ \times & \bullet & \bullet & \\ & \bullet & \bullet & 0 \\ \square & & 0 & \boxed{0} \end{bmatrix} \quad \begin{array}{l} \times \rightarrow \text{from element 1} \\ \bullet \rightarrow \text{from element 2} \\ 0 \rightarrow \text{from element 3} \\ \square \rightarrow \text{from element 4} \end{array}$$

$$= \begin{bmatrix} (A_{11})_1 + (A_{22})_4 & (A_{12})_1 & 0 & (A_{21})_4 \\ (A_{21})_1 & (A_{22})_1 + (A_{11})_2 & (A_{12})_2 & 0 \\ 0 & (A_{21})_2 & (A_{22})_3 + (A_{11})_3 & (A_{12})_3 \\ (A_{12})_4 & 0 & (A_{21})_3 & (A_{12})_3 + (A_{11})_4 \end{bmatrix} \quad (2.110)$$

$$Q = \left\{ \begin{array}{l} \boxed{\times} \\ \bullet \\ \bullet \\ \boxed{0} \end{array} \right\} \quad \begin{array}{l} \times \rightarrow \text{from element 1} \\ \bullet \rightarrow \text{from element 2} \\ 0 \rightarrow \text{from element 3} \\ \square \rightarrow \text{from element 4} \end{array} = \left\{ \begin{array}{l} (Q_1)_1 \quad \quad \quad + (Q_2)_4 \\ (Q_2)_1 + (Q_1)_2 \\ (Q_2)_2 + (Q_1)_3 \\ (Q_2)_3 + (Q_1)_4 \end{array} \right\}$$

2.7.3 Time Integration Methods

A commonly used method for response solution of linear and non-linear equations is the time integration technique. There are many solution procedures used for time integration of equations. Some of these are the Runge-Kutta method, the Adams predictor corrector method, the Gear variable order method, the Newmark method, and the Energy-Momentum method.

2.8 Bending Moments and Stresses

Once the blade deformations in response to external loading are known, the bending moments and shear loads at any section can be determined. The stresses at a point in a section can then be calculated based on the bending moment and shear load at the section. The bending moment and shear loads at any section are determined using two methods: (1) Curvature method and (2) Force Summation method. The curvature method is also called the deflection method, as the curvature can be expressed as a function of deflection. If the deflection is calculated based on a modally reduced set of ODEs, the method is also called the modal method. For the purposes of illustration, assume that the deflection of the beam is of the following form

$$w(r, t) = \sum_{j=1}^n \phi_j(r) q_j(t) \quad (2.111)$$

where q_i due to the external loading have been solved for, and ϕ_j are known shape functions, either assumed as in the case of Galerkin or Rayleigh-Ritz, or determined using FEM.

2.8.1 Deflection and Force Summation methods

In the deflection method the resultant relation given in eqn.2.11 is used. The bending moment at a station r is given by

$$M(r) = EI_{\eta\eta}\kappa = \frac{EI_{\eta\eta}}{\rho} \cong EI_{\eta\eta} \frac{d^2w}{dr^2} = EI_{\eta\eta} \sum_{j=1}^n \phi_j'' q_j$$

The bending stress, from eqn.2.12 is then simply

$$\sigma_{rr}(z) = \frac{M(r)}{I_{\eta\eta}} z = z E \sum_{j=1}^n \phi_j'' q_j$$

where z is the distance from the beam centerline. The bending stress is proportional to the second derivative of displacement. Usually a large number of terms is needed to accurately calculate the bending stress. The method is simple but yields poor results for small n . The shear load at a station is given by

$$S(r) = \frac{\delta M}{\delta r} = \left(EI_{\eta\eta} \sum_{j=1}^n \phi_j'' \right)' q_j = EI_{\eta\eta} \sum_{j=1}^n \phi_j''' q_j \quad \text{for uniform beam}$$

The shear deformation was neglected in the analysis, thus the shear stress cannot be accurately calculated. For a rough estimate divide the shear load with the sectional area.

$$\tau_{rz} = S(r)/A$$

Again, a large number of terms is needed to calculate the shear load. The shear load is proportional to the third derivative of displacement. In general, error increases with the order of derivative. The error in shear load is greater than that in bending moment. By error, one refers to the difference in solution between using n terms and as many terms required for a converged solution.

The alternative to the deflection method, which relies on the derivative of the response solution, is to use the Force Summation method. See Fig.2.30. The bending moment at a station r is obtained

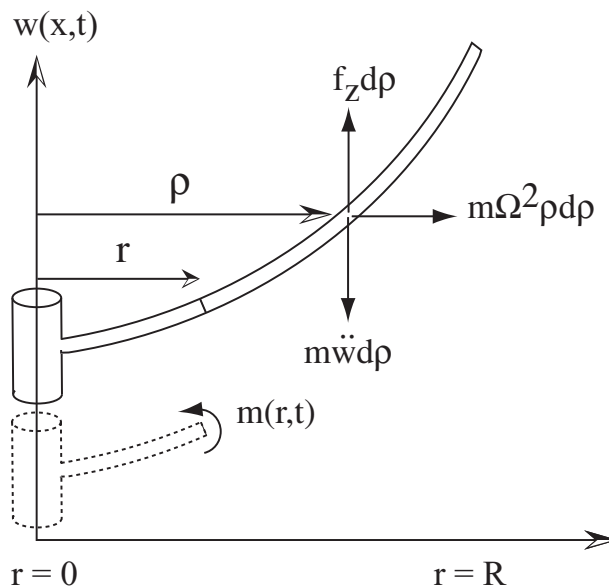


Figure 2.30: Flap bending moment at a blade section using force summation method

by integrating all of the elemental forces outboard of r .

$$M(r) = \int_{\rho=r}^{\rho=R} [(F_z - m\ddot{w})(\rho - r)] d\rho - \int_{\rho=r}^{\rho=R} m\Omega^2 \rho [w(\rho) - w(r)] d\rho \quad (2.112)$$

Because integrations are involved with respect to spatial coordinate r , this method generally produces less error for smaller n . However, the method is more involved compared to the deflection

method. The statement of equality between bending moments calculated using the deflection method and using force summation method reproduces the beam bending equation. To verify, substitute $M(r) = EI_{\eta\eta}w''$ on the left hand side of the above equation and differentiate twice with respect to r . Note that r occurs in the limits of integration on the right hand side, hence use the Leibnitz theorem. The Leibnitz theorem gives

$$\begin{aligned} \text{If } \phi(r) &= \int_{u_1(r)}^{u_2(r)} F(r, \rho) d\rho \\ \text{then, } \frac{\partial \phi}{\partial r} &= \int_{u_1(r)}^{u_2(r)} \frac{\partial F}{\partial r} d\rho - \frac{\partial u_1}{\partial r} F(r, u_1) - \frac{\partial u_2}{\partial r} F(r, u_2) \end{aligned} \quad (2.113)$$

Using the Leibnitz theorem twice it follows

$$\frac{\partial^2}{\partial r^2} \left(EI_{\eta\eta} \frac{\partial^2 w}{\partial r^2} \right) = -m\ddot{w} + \frac{\partial}{\partial r} \left(\int_r^R mr\Omega^2 dr \frac{\partial w}{\partial r} \right) \quad (2.114)$$

which is the flexible flap equation. Note that the equivalent expression for the rigid blade was given by eqn.2.5. There, the left hand side was the flap moment at the hinge via deflection method. The right hand side was the flap moment at the hinge via force summation method. Their equality generated the rigid flap equation.

2.8.2 Force summation vs. modal method

In the curvature method (also called modal method if the deflection is obtained using normal modes), the loads at a given section are determined by the elastic motion induced curvature and structural properties at that section. If there is a radial step change in structural properties, e.g. bending stiffness, or a concentrated loading, e.g. damper force, then there should be a corresponding step change in curvature, to keep the physical loads continuous. With a small number modes or shape functions this discontinuity cannot be captured. Moreover, the curvature method gives zero load on an element without elastic degrees of freedom. A force summation method rectifies the above deficiencies. It is a force balance method which obtains the section loads from the difference between the applied forces and the inertial forces acting on the blade on one side of the section. The forces used for this purpose must be exactly same as those used for solving the structural dynamic equations, otherwise inconsistent loads are obtained. For example, the bending moments at a pure hinge would not be identically zero. With lesser number of modes, the force summation method better captures the effects of concentrated loading and radial discontinuities of structural properties. However, with increase in number of modes the curvature method and the force summation method must approach the same solution.

2.9 Fourier Coordinate Transformation

Fourier Coordinate Transformation is also called Multi-blade Coordinate Transformation. Let $\beta^{(m)}(\psi)$ be the flapping motion of the m -th blade of a rotor with N_b blades, where $m = 1, 2, 3, \dots, N_b$.

Then the forward Fourier Coordinate Transformation is defined as

$$\begin{aligned}
B_0 &= \frac{1}{N_b} \sum_{m=1}^{N_b} \beta^{(m)} \\
B_{nc} &= \frac{2}{N_b} \sum_{m=1}^{N_b} \beta^{(m)} \cos n\psi_m \\
B_{ns} &= \frac{2}{N_b} \sum_{m=1}^{N_b} \beta^{(m)} \sin n\psi_m \\
B_d &= \frac{1}{N_b} \sum_{m=1}^{N_b} \beta^{(m)} (-1)^{(m)}
\end{aligned} \tag{2.115}$$

where ψ_m is the azimuthal angle for the m^{th} blade

$$\psi_m = \psi_1 + \frac{2\pi}{N_b}(m-1) = \psi + \frac{2\pi}{N_b}(m-1)$$

and ψ_1 is defined as ψ . n and d are defined as follows.

$$n = 1, 2, 3, \dots, \frac{N_b - 2}{2} \quad \text{for } N_b \text{ even; } \frac{N_b - 1}{2} \quad \text{for } N_b \text{ odd}$$

$$d = \frac{N_b}{2} \quad \text{for } N_b \text{ even; does not exist for } N_b \text{ odd}$$

For a 5-bladed rotor, the rotating coordinates are the flapping motion of the five blades, $\beta^1, \beta^2, \beta^3, \beta^4, \beta^5$. The fixed coordinates are also five in number, they are $B_0, B_{1c}, B_{1s}, B_{2c}, B_{2s}$. Note that N_b being odd, B_d does not exist. Similarly, for a 4-bladed rotor the rotating and fixed coordinates are $\beta^1, \beta^2, \beta^3, \beta^4$, and B_0, B_{1c}, B_{1s}, B_2 respectively. For a 3-bladed rotor they are $\beta^1, \beta^2, \beta^3$, and B_0, B_{1c}, B_{1s} respectively. For a 2-bladed rotor they are β^1, β^2 , and B_0, B_1 respectively. In the last case there are no cosine or sine coordinates. Note that the transformation does not require that the flapping motion $\beta^{(m)}(\psi)$ be periodic.

For a physical feel, consider a rotor with 4 blades. For purposes of illustration assume that the blades undergo a periodic flapping motion. At any instant of time one of the blades, designated as say blade-1, occurs in the azimuth ψ_1 . Define $\psi_1 = \psi$. Blade-2 at that instant occupies $\psi_2 = \psi + \pi/2$. Blade-3 occupies $\psi_3 = \psi + \pi$. Blade-4 occupies $\psi_4 = \psi + 3\pi/2$. Let $\beta^1(\psi)$, $\beta^2(\psi)$, $\beta^3(\psi)$, and $\beta^4(\psi)$, describe the flapping motion of the blades. If blade-1 exhibits the following flapping motion

$$\beta^1(\psi) = \beta_0 + \beta_{1c} \cos \psi + \beta_{1s} \sin \psi + \beta_{2c} \cos 2\psi + \beta_{2s} \sin 2\psi + \dots \infty$$

then blades 2, 3 and 4 exhibit

$$\beta^2(\psi) = \beta^1(\psi_2) = \beta_0 - \beta_{1c} \sin \psi + \beta_{1s} \cos \psi - \beta_{2c} \cos 2\psi - \beta_{2s} \sin 2\psi + \dots \infty$$

$$\beta^3(\psi) = \beta^1(\psi_3) = \beta_0 - \beta_{1c} \cos \psi - \beta_{1s} \sin \psi + \beta_{2c} \cos 2\psi + \beta_{2s} \sin 2\psi + \dots \infty$$

$$\beta^4(\psi) = \beta^1(\psi_4) = \beta_0 + \beta_{1c} \sin \psi - \beta_{1s} \cos \psi - \beta_{2c} \cos 2\psi - \beta_{2s} \sin 2\psi + \dots \infty$$

The fixed coordinates are then given by

$$B_0(\psi) = \frac{1}{4} [\beta^1(\psi) + \beta^2(\psi) + \beta^3(\psi) + \beta^4(\psi)]$$

$$B_{1c}(\psi) = \frac{2}{4} [\beta^1(\psi) \cos \psi_1 + \beta^2(\psi) \cos \psi_2 + \beta^3(\psi) \cos \psi_3 + \beta^4(\psi) \cos \psi_4]$$

$$B_{1s}(\psi) = \frac{2}{4} [\beta^1(\psi) \sin \psi_1 + \beta^2(\psi) \sin \psi_2 + \beta^3(\psi) \sin \psi_3 + \beta^4(\psi) \sin \psi_4]$$

$$B_2(\psi) = \frac{1}{4} [\beta^1(\psi)(-1)^1 + \beta^2(\psi)(-1)^2 + \beta^3(\psi)(-1)^3 + \beta^4(\psi)(-1)^4]$$

The reverse Fourier Coordinate Transformation is given by

$$\begin{aligned}\beta^{(m)}(\psi) &= B_0(\psi) + \sum_{n=1}^{(N_b-2)/2} [B_{nc}(\psi) \cos n\psi_m + B_{ns}(\psi) \sin n\psi_m] + B_d(-1)^m \quad \text{for } N_b \text{ even} \\ \beta^{(m)}(\psi) &= B_0(\psi) + \sum_{n=1}^{(N_b-1)/2} [B_{nc}(\psi) \cos n\psi_m + B_{ns}(\psi) \sin n\psi_m] \quad \text{for } N_b \text{ odd}\end{aligned}\tag{2.116}$$

The fourier coordinates $B_0, B_{1c}, B_{1s}, \dots$ etc are functions of ψ , and are different from fourier series coefficients which are constants. The forward and reverse transformations, eqns.2.115 and 2.116, are exact not approximate. As a result governing equations in fourier coordinates retain the same information as those in rotating coordinates. A complete description of rotor motion can be obtained by solving for the rotating coordinates $\beta^m(\psi), m = 1, 2, 3, \dots, N_b$. Alternatively it can be obtained by solving for the fixed coordinates, equal in number, $B_0(\psi), B_{nc}(\psi), B_{ns}(\psi), B_d(\psi)$. The governing equations in rotating coordinates can be transformed into fixed coordinates in the following manner.

2.9.1 FCT of governing equations

To carry out FCT of governing equations the following expressions are required. We have by definition

$$B_{nc} = \frac{2}{N_b} \sum \beta^{(m)} \cos n\psi_m \tag{2.117}$$

Differentiate once to obtain

$$B_{nc}^* = \frac{2}{N_b} \sum \beta^{*(m)} \cos n\psi_m - \frac{2}{N_b} n \sum \beta^{(m)} \sin n\psi_m = \frac{2}{N_b} \sum \beta^{*(m)} \cos n\psi_m - nB_{ns}$$

where the definition of B_{ns} has been used in the second term on the right hand side. Hence we have

$$\frac{2}{N_b} \sum \beta^{*(m)} \cos n\psi_m = B_{nc}^* + nB_{ns} \tag{2.118}$$

Similarly starting from the definition of B_{ns} , differentiating once, and using the definition of B_{nc} we have

$$\frac{2}{N_b} \sum \beta^{*(m)} \sin n\psi_m = B_{ns}^* - nB_{nc} \tag{2.119}$$

Now differentiate eqn.2.118 to obtain

$$\frac{2}{N_b} \sum \beta^{**(m)} \cos n\psi_m - \frac{2}{N_b} n \sum \beta^{*(m)} \sin n\psi_m = B_{nc}^{**} + n B_{ns}^*$$

Use eqn.2.119 on the second term on the left hand side to obtain

$$\frac{2}{N_b} \sum \beta^{**(m)} \cos n\psi_m = B_{nc}^{**} + 2n B_{ns}^* - n^2 B_{nc} \tag{2.120}$$

Similarly differentiating eqn.2.119 and using eqn.2.118 we have

$$\frac{2}{N_b} \sum \beta^{**(m)} \sin n\psi_m = B_{ns}^{**} - 2n B_{nc}^* - n^2 B_{ns} \tag{2.121}$$

The derivatives of B_0 and B_d are straightforward as they do not involve sin or cosine harmonics. The final derivative expressions, necessary for FCT, are listed below. The B_0 expressions are

$$\begin{aligned}\frac{1}{N_b} \sum_m^{N_b} \beta^{(m)} &= B_0 \\ \frac{1}{N_b} \sum_m^{N_b} \beta^{*(m)} &= B_0^* \\ \frac{1}{N_b} \sum_m^{N_b} \beta^{**(m)} &= B_0^{**}\end{aligned}\tag{2.122}$$

The B_d expressions are

$$\begin{aligned}\frac{1}{N_b} \sum_m^{N_b} \beta^{(m)} (-1)^m &= B_d \\ \frac{1}{N_b} \sum_m^{N_b} \beta^{*(m)} (-1)^m &= B_d^* \\ \frac{1}{N_b} \sum_m^{N_b} \beta^{**(m)} (-1)^m &= B_d^{**}\end{aligned}\tag{2.123}$$

The B_{nc} expressions are

$$\begin{aligned}\frac{2}{N_b} \sum_m^{N_b} \beta^{(m)} \cos n\psi_m &= B_{nc} \\ \frac{2}{N_b} \sum_m^{N_b} \beta^{*(m)} \cos n\psi_m &= B_{nc}^* + nB_{ns} \\ \frac{2}{N_b} \sum_m^{N_b} \beta^{**(m)} \cos n\psi_m &= B_{nc}^{**} + 2n B_{ns}^* - n^2 B_{nc}\end{aligned}\tag{2.124}$$

The B_{ns} expressions are

$$\begin{aligned}\frac{2}{N_b} \sum_m^{N_b} \beta^{(m)} \sin n\psi_m &= B_{ns} \\ \frac{2}{N_b} \sum_m^{N_b} \beta^{*(m)} \sin n\psi_m &= B_{ns}^* - nB_{nc} \\ \frac{2}{N_b} \sum_m^{N_b} \beta^{**(m)} \sin n\psi_m &= B_{ns}^{**} - 2n B_{nc}^* - n^2 B_{ns}\end{aligned}\tag{2.125}$$

The conversion of the governing equations to fixed coordinates is now carried out as follows

$$\begin{aligned}
B_0 \text{ equation} &: \frac{1}{N_b} \sum_{m=1}^{N_b} (\text{Equation of motion}) \\
B_{nc} \text{ equation} &: \frac{2}{N_b} \sum_{m=1}^{N_b} (\text{Equation of motion}) \cos n\psi_m \\
B_{ns} \text{ equation} &: \frac{2}{N_b} \sum_{m=1}^{N_b} (\text{Equation of motion}) \sin n\psi_m \\
B_d \text{ equation} &: \frac{1}{N_b} \sum_{m=1}^{N_b} (\text{Equation of motion}) (-1)^m
\end{aligned} \tag{2.126}$$

During this operation, certain expressions can arise which are not straightforward application of the above formulae and need to be substituted correctly. These are described below. For purposes of illustration consider $N_b = 4$. The fourier coordinates in this case are B_0 , B_{1c} , B_{1s} and B_2 . First consider summations over trigonometric functions.

$$\begin{aligned}
\frac{1}{4} \sum_{m=1}^4 \sin \psi_m &= \sin \psi_1 + \sin \psi_2 + \sin \psi_3 + \sin \psi_4 = 0 \\
\frac{1}{4} \sum_{m=1}^4 \sin 2\psi_m &= 0 \\
\frac{1}{4} \sum_{m=1}^4 \sin 3\psi_m &= 0 \\
\frac{1}{4} \sum_{m=1}^4 \sin 4\psi_m &= \sin 4\psi_1 = \sin 4\psi
\end{aligned} \tag{2.127}$$

In general

$$\frac{1}{N_b} \sum_{m=1}^{N_b} \cos n\psi_m = \cos n\psi \quad \text{and} \quad \frac{1}{N_b} \sum_{m=1}^{N_b} \sin n\psi_m = \sin n\psi$$

only when $n = pN_b$ where p is an integer, and zero otherwise. It follows that a harmonic which is an integral multiple of blade number can be taken outside the summation side. For example,

$$\frac{2}{4} \sum_{m=1}^4 \beta^{(m)} \cos 4\psi_m \cos \psi_m = \cos 4\psi \frac{2}{4} \sum_{m=1}^4 \beta^{(m)} \cos \psi_m = B_{1c} \cos 4\psi$$

Thus note the following treatment

$$\frac{2}{4} \sum_{m=1}^4 \beta^{(m)} \cos 3\psi_m = \frac{2}{4} \sum_{m=1}^4 \beta^{(m)} \cos(4\psi_m - \psi_m) = B_{1c} \cos 4\psi + B_{1s} \sin 4\psi$$

Just as harmonics which are integral multiples of blade number can be taken outside the summation, a special treatment is needed for harmonics which are integral multiples of half the blade number. For example

$$\begin{aligned}
\frac{2}{4} \sum_{m=1}^4 \beta^{(m)} \cos 2\psi_m &= \frac{2}{4} \left[\beta^{(1)} \sin 2\psi_1 + \beta^{(1)} \sin 2\psi_2 + \beta^{(1)} \sin 2\psi_3 + \beta^{(1)} \sin 2\psi_4 \right] \\
&= \frac{2}{4} \left[\beta^{(1)} \sin 2\psi - \beta^{(1)} \sin 2\psi + \beta^{(1)} \sin 2\psi - \beta^{(1)} \sin 2\psi \right] = -2B_2 \sin 2\psi
\end{aligned}$$

Another set of special cases arise during transformation of the B_d equation. They involve $(-1)^m$ multiplied with with sine and cosine terms. First consider the sum of harmonics

$$\begin{aligned}
\frac{1}{4} \sum_{m=1}^4 (-1)^m \sin \psi_m &= -\sin \psi_1 + \sin \psi_2 - \sin \psi_3 + \sin \psi_4 = 0 \\
\frac{1}{4} \sum_{m=1}^4 (-1)^m \sin 2\psi_m &= -\sin 2\psi \\
\frac{1}{4} \sum_{m=1}^4 (-1)^m \sin 3\psi_m &= 0 \\
\frac{1}{4} \sum_{m=1}^4 (-1)^m \sin 4\psi_m &= 0
\end{aligned} \tag{2.128}$$

In general

$$\frac{1}{N_b} \sum_{m=1}^{N_b} (-1)^m \cos n\psi_m = -\cos n\psi \quad \text{and} \quad \frac{1}{N} \sum_{m=1}^N (-1)^m \sin n\psi_m = -\sin n\psi$$

only when $n = pN_b + N_b/2$, where p is an integer and N_b is even, zero otherwise. It follows that a harmonic of frequency $n = pN_b + N_b/2$ can be taken outside the summation sign in the presence of the factor $(-1)^m$. Thus note the following treatment

$$\begin{aligned}
&\frac{1}{4} \sum_{m=1}^4 \beta^{(m)} (-1)^m \sin \psi_m \\
&= \frac{1}{4} \sum_{m=1}^4 \beta^{(m)} (-1)^m \sin(2\psi_m - \psi_m) \\
&= \frac{1}{4} \sum_{m=1}^4 \beta^{(m)} (-1)^m \sin 2\psi_m \cos \psi_m - \frac{1}{4} \sum_{m=1}^4 \beta^{(m)} (-1)^m \cos 2\psi_m \sin \psi_m \\
&= +\frac{1}{4} \left[-\beta^{(1)} \sin 2\psi \cos \psi_1 - \beta^{(2)} \sin 2\psi \cos \psi_2 - \beta^{(3)} \sin 2\psi \cos \psi_3 - \beta^{(4)} \sin 2\psi \cos \psi_4 \right] \\
&\quad -\frac{1}{4} \left[-\beta^{(1)} \cos 2\psi \sin \psi_1 - \beta^{(2)} \cos 2\psi \sin \psi_2 - \beta^{(3)} \cos 2\psi \sin \psi_3 - \beta^{(4)} \cos 2\psi \sin \psi_4 \right] \\
&= -\frac{1}{2} B_{1c} \sin 2\psi + \frac{1}{2} B_{1s} \cos 2\psi
\end{aligned}$$

Consider the rigid blade flapping equation in forward flight. The blade twist and the cyclic control angles are assumed to be zero.

$$\begin{aligned}
\beta^{**} + \left(\frac{\gamma}{8} + \mu \frac{\gamma}{6} \sin \psi \right) \beta^* + \left(\nu_\beta^2 + \mu \frac{\gamma}{6} \cos \psi + \mu^2 \frac{\gamma}{8} \sin 2\psi \right) \beta = \\
\gamma \theta_0 \left(\frac{1}{8} + \frac{\mu}{3} \sin \psi + \frac{\mu^2}{4} \sin^2 \psi \right) - \gamma \lambda \left(\frac{1}{6} + \frac{\mu}{4} \sin \psi \right)
\end{aligned} \tag{2.129}$$

Consider the transformation of the above equation for $N_b = 4$. The fixed coordinates are B_0 , B_{1c} , B_{1s} , and B_2 . Use the operators given by eqns.2.126, and the definitions given by eqns.2.122–2.125 Apply the first operator to obtain the B_0 equation.

$$\begin{aligned}
\beta^{**} + \frac{\gamma}{8} \beta^* + \mu \frac{\gamma}{6} \frac{1}{2} \left(B_{1s}^* - B_{1c}^* \right) + \nu_\beta^2 B_0 + \mu \frac{\gamma}{6} \frac{1}{2} B_{1c} + \mu^2 \frac{\gamma}{8} \frac{1}{4} \sum \beta \sin 2\psi \\
= \gamma \theta_0 \left(\frac{1}{8} + \frac{1}{4} \sum \sin^2 \psi \right) - \gamma \lambda \frac{1}{6}
\end{aligned}$$

The underlined terms are to be replaced by

$$\frac{1}{4} \sum \beta \sin 2\psi = -B_2 \sin 2\psi$$

$$\frac{1}{4} \sum \sin^2 \psi = \frac{1}{4} \sum \frac{1}{2} (1 - \cos 2\psi) = \frac{1}{2}$$

Apply the second operator to obtain the B_{1c} equation.

$$\begin{aligned} & B_{1c}^{**} + 2 B_{1s}^* - B_{1c} + \frac{\gamma}{8} (B_{1c}^* + B_{1s}) + \mu \frac{\gamma}{6} \frac{2}{4} \sum \beta \sin \psi \cos \psi + \nu_{\beta}^2 B_{1c} + \mu \frac{\gamma}{6} \frac{2}{4} \sum \beta \cos^2 \psi \\ & + \mu^2 \frac{\gamma}{8} \frac{2}{4} \sum \beta \sin 2\psi \cos \psi = \gamma \theta_0 \left(\frac{\mu}{3} \frac{2}{4} \sum \sin \psi \cos \psi + \frac{\mu^2}{4} \frac{2}{4} \sum \sin^2 \psi \cos \psi \right) - \gamma \lambda \frac{\mu}{4} \frac{2}{4} \sum \sin \psi \cos \psi \end{aligned}$$

The underlined terms are to be replaced by

$$\begin{aligned} \frac{2}{4} \sum \beta \sin \psi \cos \psi &= \frac{2}{4} \sum \beta \frac{1}{2} \sin 2\psi = -B_2 \sin 2\psi \\ \frac{2}{4} \sum \beta \cos^2 \psi &= \frac{2}{4} \sum \beta \frac{1}{2} (1 + \cos 2\psi) = B_0 - 2B_2 \cos 2\psi \\ \frac{2}{4} \sum \beta \sin 2\psi \cos \psi &= \frac{2}{4} \sum \beta \frac{1}{2} (\sin 3\psi + \sin \psi) \\ &= \frac{2}{4} \sum \beta \frac{1}{2} (\sin 4\psi \cos \psi - \cos 4\psi \sin \psi + \sin \psi) \\ &= \frac{1}{2} B_{1c} \sin 4\psi - \frac{1}{2} B_{1s} \cos 4\psi + \frac{1}{2} B_{1s} \\ \frac{2}{4} \sum \sin^2 \psi \cos \psi &= \frac{2}{4} \sum \frac{1}{2} (\cos \psi - \cos 2\psi \cos \psi) = 0 \\ \frac{2}{4} \sum \sin \psi \cos \psi &= 0 \end{aligned}$$

Apply the third operator to obtain the B_{1s} equation.

$$\begin{aligned} & B_{1s}^{**} - 2 B_{1c}^* - B_{1s} + \frac{\gamma}{8} (B_{1s}^* + B_{1c}) + \mu \frac{\gamma}{6} \frac{2}{4} \sum \beta \sin^2 \psi + \nu_{\beta}^2 B_{1c} + \mu \frac{\gamma}{6} \frac{2}{4} \sum \beta \cos \psi \sin \psi \\ & + \mu^2 \frac{\gamma}{8} \frac{2}{4} \sum \beta \sin 2\psi \sin \psi = \gamma \theta_0 \left(\frac{\mu}{3} \frac{2}{4} \sum \sin^2 \psi + \frac{\mu^2}{4} \frac{2}{4} \sum \sin^3 \psi \right) - \gamma \lambda \frac{\mu}{4} \frac{2}{4} \sum \sin^2 \psi \end{aligned}$$

The underlined terms are to be replaced by

$$\begin{aligned} \frac{2}{4} \sum \beta \sin^2 \psi &= \frac{2}{4} \sum \beta \frac{1}{2} (1 - \cos 2\psi) = B_0 + \frac{1}{2} B_2 \cos 2\psi \\ \frac{2}{4} \sum \beta \cos \psi \sin \psi &= \frac{2}{4} \sum \beta \frac{1}{2} \sin 2\psi = -2B_2 \sin 2\psi \\ \frac{2}{4} \sum \beta \sin 2\psi \sin \psi &= \frac{2}{4} \sum \beta \frac{1}{2} (\cos \psi - \cos 3\psi) \\ &= \frac{1}{2} B_{1c} - \frac{2}{4} \sum \beta \frac{1}{2} (\cos 4\psi \cos \psi + \sin 4\psi \sin \psi) \\ &= \frac{1}{2} B_{1c} - \frac{1}{2} B_{1c} \cos 4\psi - \frac{1}{2} B_{1s} \sin 4\psi \\ \frac{2}{4} \sum \sin^2 \psi &= \frac{2}{4} \sum \frac{1}{2} (1 - \cos 2\psi) = \frac{1}{4} \\ \frac{2}{4} \sum \sin^3 \psi &= \frac{2}{4} \sum \left(\frac{3}{4} \sin \psi - \frac{1}{4} \sin 3\psi \right) = 0 \end{aligned}$$

Apply the fourth operator to obtain the B_2 equation.

$$\begin{aligned} B_2^{**} + \frac{\gamma}{8} B_2^* + \mu \frac{\gamma}{6} \frac{1}{4} \sum \beta^* (-1)^m \sin \psi + \nu_\beta^2 B_2 + \mu \frac{\gamma}{6} \frac{1}{4} \sum \beta (-1)^m \cos \psi + \mu^2 \frac{\gamma}{8} \frac{1}{4} \sum \beta (-1)^m \sin 2\psi \\ = \gamma \theta_0 \frac{\mu^2}{4} \frac{1}{4} \sum (-1)^m \sin^2 \psi \end{aligned}$$

The underlined terms are to be replaced by

$$\begin{aligned} \frac{1}{4} \sum \beta^* (-1)^m \sin \psi &= \frac{1}{4} \sum \beta^* (-1)^m \sin(2\psi - \psi) \\ &= \frac{1}{4} \sum \beta^* (-1)^m (\sin 2\psi \cos \psi - \cos 2\psi \sin \psi) \\ &= \frac{1}{4} \left[-\beta^{(1)*} \sin 2\psi \cos \psi_1 - \beta^{(2)*} \sin 2\psi \cos \psi_2 - \beta^{(3)*} \sin 2\psi \cos \psi_3 - \beta^{(4)*} \sin 2\psi \cos \psi_4 \right] \\ &\quad - \frac{1}{4} \left[-\beta^{(1)*} \cos 2\psi \sin \psi_1 - \beta^{(2)*} \cos 2\psi \sin \psi_2 - \beta^{(3)*} \cos 2\psi \sin \psi_3 - \beta^{(4)*} \cos 2\psi \sin \psi_4 \right] \\ &= -\frac{1}{2} \sin 2\psi \frac{2}{4} \sum \beta^* \cos \psi + \frac{1}{2} \cos 2\psi \frac{2}{4} \sum \beta^* \sin \psi \\ &= -\frac{1}{2} \sin 2\psi (B_{1c}^* + B_{1s}^*) + \frac{1}{2} \cos 2\psi (B_{1s}^* - B_{1c}^*) \\ \frac{1}{4} \sum \beta (-1)^m \cos \psi &= -\frac{1}{2} B_{1c} \cos 2\psi - \frac{1}{2} B_{1s} \sin 2\psi \\ \frac{1}{4} \sum \beta (-1)^m \sin 2\psi &= -B_0 \sin 2\psi \\ \frac{1}{4} \sum (-1)^m \sin^2 \psi &= \frac{1}{4} \sum (-1)^m \frac{1}{2} (1 - \cos 2\psi) = \frac{1}{2} \cos 2\psi \end{aligned}$$

Consider the flap equation in the rotating coordinates, eqn.2.129. The terms associated with forward speed, μ , and μ^2 terms, are all periodic in nature associated with sine and cosine harmonics. Now consider the equations in the fixed coordinates. Note that all the μ terms now occur as constants, not in association with sine and cosine harmonics. The μ^2 terms are still periodic in nature and occur as sine or cosine harmonics. The fact that the constant coefficients in the fixed coordinate equations retain the effect of forward speed can be utilized during the calculation of aeroelastic stability.

2.10 Aeroelastic Stability

Consider the rigid flap equation in forward flight. Assume that the twist $\theta_{tw} = 0$ for simplicity. Let $\beta_s(\psi)$ be the steady state flap solution. Then we have

$$\begin{aligned} \beta_s^{**} + \left(\frac{\gamma}{8} + \mu \frac{\gamma}{6} \sin \psi \right) \beta_s^* + \left(\nu_\beta^2 + \mu \frac{\gamma}{6} \cos \psi + \mu^2 \frac{\gamma}{8} \sin 2\psi \right) \beta_s = \\ \gamma \theta \left(\frac{1}{8} + \frac{\mu}{3} \sin \psi + \frac{\mu^2}{4} \sin^2 \psi \right) - \gamma \lambda \left(\frac{1}{6} + \frac{\mu}{4} \sin \psi \right) \end{aligned} \quad (2.130)$$

where $\theta = \theta(\psi) = \theta_0 + \theta_{1c} \cos \psi + \theta_{1s} \sin \psi$ in forward flight. Suppose a perturbation $\delta\beta$ is applied to the steady state flap motion at $\psi = \psi_0$. We seek the nature of its evolution with time $\delta\beta(\psi)$. At any instant $\beta(\psi) = \beta_s(\psi) + \delta\beta(\psi)$ must satisfy the governing eqn.2.129. Substituting $\beta(\psi)$ in the governing equation and noting that the steady state solution $\beta_s(\psi)$ must satisfy eqn.2.130, we have the governing equation for the perturbation

$$\delta\beta^{**} + \left(\frac{\gamma}{8} + \mu \frac{\gamma}{6} \sin \psi \right) \delta\beta^* + \left(\nu_\beta^2 + \mu \frac{\gamma}{6} \cos \psi + \mu^2 \frac{\gamma}{8} \sin 2\psi \right) \delta\beta = 0 \quad (2.131)$$

The ‘ δ ’s are dropped.

$$\beta^{**} + \left(\frac{\gamma}{8} + \mu\frac{\gamma}{6}\sin\psi\right)\beta^* + \left(\nu_\beta^2 + \mu\frac{\gamma}{6}\cos\psi + \mu^2\frac{\gamma}{8}\sin 2\psi\right)\beta = 0 \quad (2.132)$$

Note that for a linear system, the perturbation equation is identical to the main equation with zero forcing.

2.10.1 Stability roots in hover

In hover, the perturbation equation becomes

$$\beta^{**} + \frac{\gamma}{8}\beta^* + \nu_\beta^2\beta = 0 \quad (2.133)$$

Seek a perturbation solution of the form

$$\beta = \beta_0 e^{s\psi}$$

The nature of s determines whether the perturbation grows or dies down with time. Substitute in the governing equation. For non-trivial β_0 , i.e., $\beta_0 \neq 0$, s must satisfy the following equation

$$s^2 + \frac{\gamma}{8}s + \nu_\beta^2 = 0$$

which leads to the following eigenvalues

$$s_R = -\frac{\gamma}{16} \pm i\sqrt{\nu_\beta^2 - \left(\frac{\gamma}{16}\right)^2} \quad (2.134)$$

where s_R denotes the stability roots of the rotating coordinates. These are complex conjugate pairs. There are four pairs of such roots, one for each blade. Note that in the absence of aerodynamics, and structural damping if any, the stability roots are simply the natural frequencies of the system. For example, here they would be simply $\pm\nu_\beta$. The evolution of the perturbation with time is then

$$\beta = \beta_0 e^{s_R\psi} = \beta_0 e^{-\frac{\gamma}{16}\psi} e^{\pm i\sqrt{\nu_\beta^2 - \left(\frac{\gamma}{16}\right)^2}\psi}$$

The real part of the eigenvalue represents damping of the perturbation. The imaginary part represents the frequency of oscillation of the perturbation. The stability roots in eqn.2.134 can be written in standard notation as

$$s_R = -\text{decay rate} \pm i \text{damped frequency} = -\zeta\nu_n \pm i\nu_n\sqrt{1 - \zeta^2}$$

where $\nu_n\sqrt{1 - \zeta^2} = \nu_d$ is the damped frequency in /rev and ζ is the damping ratio as a percentage of critical. These are the frequency of oscillation of the perturbation and its decay rate. They are expressed in terms of ν_n , the natural frequency of the system. The natural frequency is the frequency of oscillation of the perturbation in the case of zero damping and no aerodynamics. In general, these parameters can be extracted from stability roots by making use of the above standard notation as follows

$$\begin{aligned} \nu_d &= \text{Im}(s) \\ \zeta &= -\frac{\text{Re}(s)}{|s|} \\ \nu_n &= |s| \end{aligned} \quad (2.135)$$

A positive ζ means stable system, negative ζ means unstable system, and $\zeta = 0$ means neutral stability. In the last case, the perturbation once introduced neither grows nor decays with time.

To get a feel of these numbers, consider a typical Lock number $\gamma = 8$ and an articulated rotor with flap frequency $\nu_\beta = 1$.

$$\text{critical damping ratio } \zeta = \frac{\gamma}{16\nu_\beta} = 0.5 \implies 50\% \text{ damping}$$

$$\text{damped frequency } \nu_d = \sqrt{\nu_\beta^2 - \left(\frac{\gamma}{16}\right)^2} = 0.87/\text{rev}$$

Therefore, the flap mode is highly damped and the frequency of oscillation as a perturbation dies down is less than 1/rev. The damped frequency in Hz and the time period are given by

$$f_d = \frac{\nu_d \Omega}{2\pi} \quad \text{in cycles/sec or Hertz}$$

$$T_d = \frac{1}{f_d} \quad \text{in sec/cycle}$$

Consider now the stability roots in the fixed coordinates. The flap perturbation eqn.2.133 in fixed coordinates produce the following equations for a N_b bladed rotor. The B_0 and B_d perturbation equations (where B_d exists only in the case of even N_b) are

$$B_0^{**} + \frac{\gamma}{8} B_0 + \nu_\beta^2 B_0 = 0$$

$$B_d^{**} + \frac{\gamma}{8} B_d^* + \nu_\beta^2 B_d = 0$$

These equations are identical to the rotating frame equation. Therefore, for B_0 and B_d the fixed coordinate eigenvalues are the same as the rotating coordinate eigenvalue.

$$s_F = s_R$$

The B_{nc} and B_{ns} perturbation equations (B_{nc} and B_{ns} exist only in the case of $N_b > 2$) are

$$\begin{Bmatrix} B_{nc}^{**} \\ B_{ns} \end{Bmatrix} + \begin{bmatrix} \frac{\gamma}{8} & 2n \\ -2n & \frac{\gamma}{8} \end{bmatrix} \begin{Bmatrix} B_{nc}^* \\ B_{ns} \end{Bmatrix} + \begin{bmatrix} \nu_\beta^2 - n^2 & \frac{\gamma}{8}n \\ -\frac{\gamma}{8}n & \nu_\beta^2 - n^2 \end{bmatrix} \begin{Bmatrix} B_{nc} \\ B_{ns} \end{Bmatrix} = \begin{Bmatrix} 0 \\ 0 \end{Bmatrix}$$

For a particular n , seek solution of the type

$$\begin{Bmatrix} B_{nc}(\psi) \\ B_{ns}(\psi) \end{Bmatrix} = \begin{Bmatrix} B_{nc0} \\ B_{ns0} \end{Bmatrix} e^{s\psi}$$

where s is an eigenvalue in the fixed coordinate which determines the azimuthal evolution of perturbations in B_{nc} and B_{ns} . Substitute the solution type into the governing equation.

$$\begin{bmatrix} s^2 + \frac{\gamma}{8}s + \nu_\beta^2 - n^2 & 2ns + \frac{\gamma}{8}n \\ -(2ns + \frac{\gamma}{8}n) & s^2 + \frac{\gamma}{8}s + \nu_\beta^2 - n^2 \end{bmatrix} \begin{bmatrix} B_{nc0} \\ B_{ns0} \end{bmatrix} = 0 \quad (2.136)$$

For nontrivial $[B_{nc0} \ B_{ns0}]^T$ set the determinant of the left hand side matrix to zero. It follows

$$(s^2 + \frac{\gamma}{8}s + \nu_\beta^2 - n^2)^2 = -\left(2ns + \frac{\gamma}{8}n\right)^2 \quad (2.137)$$

This leads to two complex conjugate pairs of eigenvalues, i.e. four eigenvalues in total

$$\begin{aligned} s_F &= -\frac{\gamma}{16} \mp i\sqrt{\nu_\beta^2 - \left(\frac{\gamma}{16}\right)^2} \pm in \\ &= s_R \pm in \end{aligned} \quad (2.138)$$

Thus the eigenvalues for B_{nc} and B_{ns} are shifted by $\pm n/\text{rev}$ from the rotating eigenvalue. The exponential decay rate is the same in both the fixed frame and the rotating frame. The corresponding eigenvectors, using eqn.2.137 are given by

$$\frac{B_{nc0}}{B_{ns0}} = -\frac{2ns_F + \frac{\gamma}{8}n}{s_F^2 + \frac{\gamma}{8}s_F + \nu_\beta^2 - n^2} = \pm i = e^{\pm i\frac{\pi}{2}} \quad (2.139)$$

The eigenvalues and their corresponding eigenvectors are tabulated below. Out of the two complex conjugate pairs, one has higher frequency compared to the other. These are noted as high frequency and low frequency eigenvalues.

$$\begin{aligned} s_F = -\frac{\gamma}{16} + i(\sqrt{\dots} + 1) & \quad \text{High Frequency,} & \text{obtained using: } s_F = s_R + i & \implies \frac{B_{nc0}}{B_{ns0}} = +i \\ s_F = -\frac{\gamma}{16} - i(\sqrt{\dots} + 1) & \quad \text{High Frequency,} & \text{obtained using: } s_F = s_R - i & \implies \frac{B_{nc0}}{B_{ns0}} = -i \\ s_F = -\frac{\gamma}{16} + i(\sqrt{\dots} - 1) & \quad \text{Low Frequency,} & \text{obtained using: } s_F = s_R - i & \implies \frac{B_{nc0}}{B_{ns0}} = -i \\ s_F = -\frac{\gamma}{16} - i(\sqrt{\dots} - 1) & \quad \text{Low Frequency,} & \text{obtained using: } s_F = s_R + i & \implies \frac{B_{nc0}}{B_{ns0}} = +i \end{aligned}$$

where the entry within the square root, $\nu_\beta^2 - (\gamma/16)^2$ has been replaced with \dots for brevity. The first line means s_F as given is a high frequency. It has been obtained by using $s_R + i$, which implies that the corresponding eigenvector $B_{nc0}/B_{ns0} = +i$. Each frequency with its associated eigenvector is referred to as a mode. Note that $s_R + i$ is not necessarily the high frequency mode. Similarly $s_R - i$ is not necessarily the low frequency mode. Consider each mode one by one. The first high frequency mode is given by

$$\begin{aligned} B_{nc}(\psi) &= B_{nc0} e^{s_F \psi} \\ &= B_{ns0} (+i)e^{s_F \psi} \\ &= B_{ns0} e^{i\frac{\pi}{2}} e^{s_F \psi} \\ &= B_{ns0} e^{-\frac{\gamma}{16}\psi} e^{i(\sqrt{\dots}+1)\psi} e^{i\frac{\pi}{2}} \\ &\approx B_{ns0} e^{-\frac{\gamma}{16}\psi} \cos \left[(\sqrt{\dots} + 1) \psi + \frac{\pi}{2} \right] \end{aligned} \quad (2.140)$$

Thus $B_{nc}(\psi)$ has the same magnitude as $B_{ns}(\psi)$, same decay rate $-\gamma/16$, same frequency $\sqrt{\dots} + 1$, except that it is ahead of $B_{ns}(\psi)$ by $\pi/2$. Consider the second high frequency mode

$$\begin{aligned} B_{nc}(\psi) &= B_{nc0} e^{s_F \psi} \\ &= B_{ns0} (-i)e^{s_F \psi} \\ &= B_{ns0} e^{-i\frac{\pi}{2}} e^{s_F \psi} \\ &= B_{ns0} e^{-\frac{\gamma}{16}\psi} e^{i(\sqrt{\dots}+1)\psi} e^{-i\frac{\pi}{2}} \\ &\approx B_{ns0} e^{-\frac{\gamma}{16}\psi} \cos \left[(\sqrt{\dots} + 1) \psi + \frac{\pi}{2} \right] \end{aligned} \quad (2.141)$$

Again, $B_{nc}(\psi)$ has the same magnitude as $B_{ns}(\psi)$, same decay rate $-\gamma/16$, same frequency $\sqrt{\dots} + 1$, except that it is ahead of $B_{ns}(\psi)$ by $\pi/2$. In both the high frequency modes $B_{nc}(\psi)$ leads $B_{ns}(\psi)$ by $\pi/2$. This is defined as a ‘Progressive Mode’. Figure 2.31 shows the fixed coordinate perturbation variations for $B_{nc}(\psi)$ and $B_{ns}(\psi)$ for a Progressive Mode.

Now consider the low frequency modes. From the first mode, we have

$$\begin{aligned}
 B_{nc}(\psi) &= B_{nc0} e^{s_F \psi} \\
 &= B_{ns0} (-i) e^{s_F \psi} \\
 &= B_{ns0} e^{-i\frac{\pi}{2}} e^{s_F \psi} \\
 &= B_{ns0} e^{-\frac{\gamma}{16}\psi} e^{i(\sqrt{\dots}-1)\psi} e^{-i\frac{\pi}{2}} \\
 &\approx B_{ns0} e^{-\frac{\gamma}{16}\psi} \cos \left[(\sqrt{\dots} - 1) \psi - \frac{\pi}{2} \right]
 \end{aligned} \tag{2.142}$$

Similarly, from the second mode, we have

$$\begin{aligned}
 B_{nc}(\psi) &= B_{nc0} e^{s_F \psi} \\
 &= B_{ns0} (+i) e^{s_F \psi} \\
 &= B_{ns0} e^{i\frac{\pi}{2}} e^{s_F \psi} \\
 &= B_{ns0} e^{-\frac{\gamma}{16}\psi} e^{i(\sqrt{\dots}-1)\psi} e^{i\frac{\pi}{2}} \\
 &\approx B_{ns0} e^{-\frac{\gamma}{16}\psi} \cos \left[(\sqrt{\dots} - 1) \psi - \frac{\pi}{2} \right]
 \end{aligned} \tag{2.143}$$

Here $B_{nc}(\psi)$ can again lead $B_{ns}(\psi)$ by $\pi/2$, but only if

$$\sqrt{\nu_\beta^2 - \left(\frac{\gamma}{16}\right)^2} - 1 < 0 \quad \text{i.e., if} \quad \sqrt{\nu_\beta^2 - \left(\frac{\gamma}{16}\right)^2} < 1$$

In this case the low frequency mode is again a ‘Progressive Mode’. Otherwise, if

$$\sqrt{\nu_\beta^2 - \left(\frac{\gamma}{16}\right)^2} - 1 > 0 \quad \text{i.e., if} \quad \sqrt{\nu_\beta^2 - \left(\frac{\gamma}{16}\right)^2} > 1$$

$B_{nc}(\psi)$ lags $B_{ns}(\psi)$ by $\pi/2$. This is defined as a ‘Regressive Mode’.

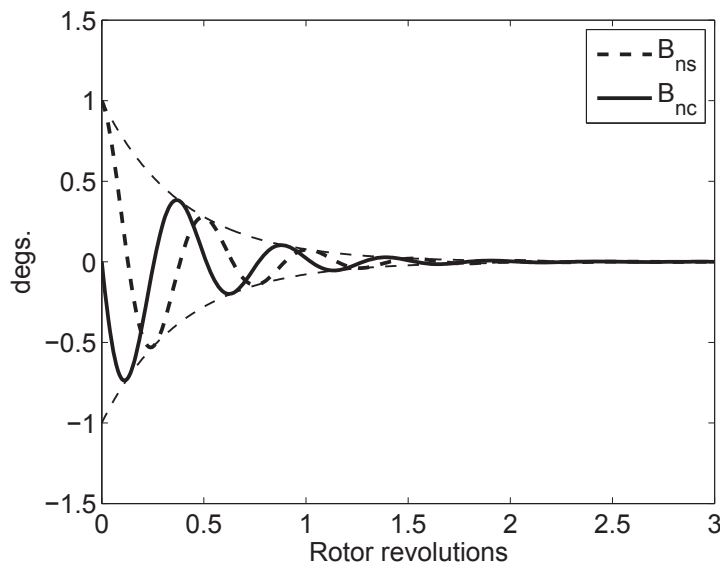


Figure 2.31: **Progressive mode of flapping: Fixed coordinate B_{nc} leads B_{ns} by $\pi/2$**

Example: 2.9

A four bladed rotor has a fundamental flap frequency of 1.12 /rev and a Lock number of 8. Calculate the hover eigenvalues in the rotating and the fixed coordinates. Discuss the nature of the modes in the fixed coordinates.

In the rotating coordinates, we have

$$\nu_\beta = 1.12 \quad \gamma = 8$$

$$s_R = -\frac{\gamma}{16} \pm i\sqrt{\nu_\beta^2 - \left(\frac{\gamma}{16}\right)^2} = -0.5 \pm i 1.002$$

Four blades have four identical pairs of rotating stability roots. In the fixed coordinates, we have $n = 1$, four complex conjugate pairs of roots. For collective B_0 and differential B_2 , the eigenvalues are the same as the rotating roots

$$s_F = s_R = -0.5 \pm i 1.002$$

For B_{1c} and B_{1s}

$$s_F = s_R \pm i$$

Thus the high frequency mode is

$$s_F = -0.5 \pm i 2.002$$

The low frequency mode is

$$s_F = -0.5 \pm i 0.002$$

The high frequency modes are always progressive. The low frequency mode can be either progressive or regressive. Here

$$\sqrt{\nu_\beta^2 - \left(\frac{\gamma}{16}\right)^2} = 1.002 \quad \text{i.e.} \quad > 1.0$$

Therefore the low frequency mode is regressive.

Example: 2.10

For the flutter testing of a helicopter blade, the rotor was excited by wobbling the swash plate and the response was measured from the pick-ups mounted on all the four blades. The response of the lowest mode in the fixed system was analyzed using the Moving Block method. The frequency of oscillations and the damping coefficient were obtained as 1.25 Hz and 0.5 respectively. Calculate the corresponding blade frequency and damping coefficient (in rotating system) for a rotor rpm of 350.

We have in the fixed coordinates

$$\omega_d = 1.25 \text{ Hz} = 7.854 \text{ rad/sec}$$

$$\zeta = .5$$

$$\Omega = 350 \text{ RPM} = 36.65 \text{ rad/sec}$$

$$\nu_d = \frac{\omega_d}{\Omega} = \frac{7.854}{36.65} = 0.2143/\text{rev}$$

$$\text{Natural} \quad \omega_n = \frac{\omega_d}{\sqrt{1 - \zeta^2}}$$

$$\frac{\omega_n}{\Omega} = .2475$$

$$\zeta \frac{\omega_n}{\Omega} = .1238$$

$$\text{Eigenvalue } S = \zeta \frac{\omega_n}{\Omega} + i \frac{\omega_d}{\Omega} = .1238 \pm i .2143$$

$$\text{Rotating frame: } S_R = S + i$$

$$= .1238 + i 1.2143$$

$$\frac{\zeta}{\sqrt{1 - \zeta^2}} = \frac{.1238}{1.2143} = .1019$$

$$\zeta = .1010$$

$$\text{Frequency} = 1.2143/\text{rev} = 7.08Hz$$

2.11 Stability Analysis in Forward flight

In dynamic analysis of rotating systems, one frequently encounters with the equations of motion with periodic coefficients. For example, the equation of motion expressing the dynamic response of a flapping blade in forward flight contains many periodic terms. For some dynamic problems, one also gets equations with constant coefficients. Here, the example is the flapping motion of a blade in hovering flight. The analysis techniques for constant coefficient systems are simple and familiar whereas analysis for periodic systems is more involved and the analysis techniques are less familiar.

2.11.1 Constant Coefficient System

Let us consider N linear differential equations with constant coefficients,

$$\begin{array}{ccccccc} \widetilde{M}\ddot{\tilde{q}} & + & \widetilde{C}\dot{\tilde{q}} & + & \widetilde{K}\tilde{q} & = & \widetilde{F}(t) \\ \text{inertia} & & \downarrow & & \text{stiffness} & & \downarrow \\ & & \text{damping} & & & & \text{force} \end{array} \quad (2.144)$$

where \widetilde{M} , \widetilde{C} and \widetilde{K} are square matrices of order N x N while displacement vector \tilde{q} and force vector \widetilde{F} are of order N x 1.

These equations can be rewritten as

$$\begin{bmatrix} \widetilde{I} & \widetilde{0} \\ \widetilde{0} & \widetilde{M} \end{bmatrix} \begin{bmatrix} \dot{\tilde{q}} \\ \tilde{q} \end{bmatrix} - \begin{bmatrix} \widetilde{0} & \widetilde{I} \\ -\widetilde{K} & -\widetilde{C} \end{bmatrix} \begin{bmatrix} \tilde{q} \\ \dot{\tilde{q}} \end{bmatrix} = \begin{bmatrix} \widetilde{0} \\ \widetilde{F} \end{bmatrix}$$

where \widetilde{I} = identity matrix (unity on diagonal)

order N x N

$\widetilde{0}$ = null matrix (zeros)

order N x N

Let us define

$$\tilde{y} = \begin{bmatrix} \tilde{q} \\ \dot{\tilde{q}} \end{bmatrix}_{2N \times 1}$$

The above equations can be rearranged as

$$\dot{\tilde{y}} = \widetilde{A}\tilde{y} + \widetilde{G} \quad (2.145)$$

This results into $2N$ first order equations.

$$\tilde{A} = \begin{bmatrix} \tilde{0} & \tilde{I} \\ -\tilde{M}^{-1}\tilde{K} & -\tilde{M}^{-1}\tilde{C} \end{bmatrix}_{2N \times 2N}$$

$$\tilde{G} = \begin{bmatrix} \tilde{0} \\ -\tilde{M}^{-1}\tilde{F} \end{bmatrix}_{2N \times 1}$$

The above arrangements are valid provided \tilde{M} is not singular.

Stability

To examine stability of the system, set $\tilde{F} = 0$ i.e., $\tilde{G} = 0$. This results into a set of homogeneous equations and then seek the solution as

$$\tilde{y}(t) = \tilde{y}e^{\lambda t}$$

The equation (78) becomes

$$\tilde{A}\tilde{y} = \lambda\tilde{y} \quad (2.146)$$

This results into a standard algebraic eigenvalue problem and can be solved using any standard eigenvalue routine. This gives $2N$ eigenvalues, complex in nature.

$$\lambda_k = \begin{array}{c} \alpha_k \\ \text{real} \end{array} + \begin{array}{c} i\omega_k \\ \text{imaginary} \end{array}$$

The real part of the eigenvalue represents the damping of the mode whereas the imaginary part represents the frequency of the mode. If any one of the eigenvalues has a positive real part, the system is unstable.

Forced response

Under steady conditions, the external forces $F(t)$ in a rotating system are generally periodic, in multiples of the rotation frequency Ω . Let us say the forcing function is m^{th} harmonic, frequency $\omega_m = m\Omega$.

$$\tilde{q}(t) = \text{Re}(\tilde{q}e^{i\omega_m t}) \quad (2.147)$$

$$= \tilde{F}_R \cos \omega_m t - \tilde{F}_I \sin \omega_m t$$

where \tilde{F}_R and \tilde{F}_I are real and imaginary parts of \tilde{F} . Assuming the steady response to be m^{th} harmonic

$$\tilde{q}(t) = \text{Re}(\tilde{q}e^{i\omega_m t})$$

$$= \tilde{q}_R \cos \omega_m t - \tilde{q}_I \sin \omega_m t$$

Placing this in basic equation (78) and using the harmonic balance method (discussed earlier). Comparing $\sin \omega_m t$ and $\cos \omega_m t$ terms, one gets,

$$\begin{bmatrix} \tilde{G} & \tilde{H} \\ -\tilde{H} & \tilde{G} \end{bmatrix} \begin{Bmatrix} \tilde{q}_R \\ \tilde{q}_I \end{Bmatrix} = \begin{Bmatrix} \tilde{F}_R \\ \tilde{F}_I \end{Bmatrix} \quad (2.148)$$

$$2N \times 2N \quad 2N \times 1 \quad 2N \times 1$$

where

$$\tilde{G} = \tilde{K} - \omega_m^2 \tilde{M}$$

$$\tilde{H} = \omega_m \tilde{C}$$

For the known external forces, these equations can be solved to calculate \tilde{q}_R and \tilde{q}_I . The total response can be calculated by summing up the response components from all harmonics.

$$\tilde{q}(t) = \sum_{m=0}^N q_R^{(m)} \cos \omega_m t - \sum_{m=0}^N q_I^{(m)} \sin \omega_m t \quad (2.149)$$

This method is more physical than the direct numerical integration because individual harmonic components are calculated and assessed. One can also use the finite difference method to calculate response but it generally results into more involved analysis for rotor problems.

2.11.2 Periodic coefficient systems

The governing equations are

$$\tilde{M}(t)\ddot{\tilde{q}} + \tilde{C}(t)\dot{\tilde{q}} + \tilde{K}\tilde{q} = \tilde{F}(t) \quad (2.150)$$

where matrices \tilde{M} , \tilde{C} and \tilde{K} contain periodic terms. These equations can be rearranged as first order equations,

$$\dot{\tilde{y}} - \tilde{A}(t)\tilde{y} = \tilde{G}(t) \quad (2.151)$$

where $\tilde{A}(t)$ and $\tilde{G}(t)$ are periodic over an interval T .

2.11.3 Floquet stability solution

To investigate stability, set $\tilde{G}(t)$. Seek solution of the form

$$\begin{array}{ccc} \tilde{y}(t) & = & \tilde{B}(t) \{c_k e^{p_k t}\} \\ 2N \times 1 & & 2N \times 2N \quad 2N \times 1 \end{array} \quad (2.152)$$

The square matrix $\tilde{B}(t)$ is periodic over period T .

$$\tilde{B}(T) = \tilde{B}(0)$$

$$\tilde{y}(0) = \tilde{B}(0)\{c_k\}$$

$$\tilde{y}(T) = \tilde{B}(T)\{c_k e^{p_k T}\}$$

$$= \tilde{B}(0)\{c_k e^{p_k T}\}$$

Also, one can express $y(T)$ as,

$$\tilde{y}(T) = [\tilde{y}^{(1)} \quad \tilde{y}^{(2)} \quad \dots] \begin{Bmatrix} y_1(0) \\ y_1(0) \\ \vdots \end{Bmatrix}$$

where $\tilde{y}^{(1)}$ is the solution at $t = T$ of the basic equation with $\tilde{G}(t) = 0$ for the initial condition $y_1(0) = 1$ and all remaining $y_i(0) = 0$, etc.

$$[Q] = [\tilde{y}^{(1)} \quad \tilde{y}^{(2)} \quad \dots] \quad (2.153)$$

This is a square matrix of order $2N$ and is called as "transition matrix". Thus

$$\begin{aligned}\{y(T)\} &= [Q]\{y(0)\} \\ &= [Q][B(0)]\{c_k\} \\ &= [Q](\{B(0)\}_1 c_1 + \{B(0)\}_2 c_2 + \dots)\end{aligned}\quad (2.154)$$

Another form is

$$\begin{aligned}\{y(T)\} &= [B(0)]\{c_k e^{p_k T}\} \\ &= \{B(0)\}_1 c_1 e^{p_1 T} + \{B(0)\}_2 c_2 e^{p_2 T} + \dots\end{aligned}\quad (2.155)$$

Comparing Eqs. (86) and (87) one gets

$$[Q]\{B(0)\} = \lambda_k \{B(0)\}_k \quad (2.156)$$

where

$$\lambda_k = e^{p_k T}$$

This is a standard eigenvalue problem, where λ_k are the eigenvalues of the transition matrix $[Q]$.

$$p_k = \frac{1}{T} \ln(\lambda_k) = \alpha_k + i \omega_k$$

The real and imaginary parts of stability exponent p_k are

$$\alpha_k = \frac{1}{T} \ln|\lambda_k| \quad (2.157)$$

$$\begin{aligned}\omega_k &= \frac{1}{2T} \ln[(\lambda_k)_R^2 + (\lambda_k)_I^2] \\ \omega_k &= \frac{1}{T} \tan^{-1}[(\lambda_k)_I/(\lambda_k)_R]\end{aligned}\quad (2.158)$$

The α_k measures the growth or decay of the response. The α_k positive (>0) or λ_k greater than one indicates instability of the mode. The ω_k represents frequency of vibration. However, the \tan^{-1} is multivalued, one will get multivalues for ω_k . Taking physical consideration one can choose the right value of ω_k .

2.11.4 Floquet response solution

The governing equation is

$$\tilde{y}' = \tilde{A}\tilde{y} + \tilde{G} \quad (2.159)$$

The solution of this equation can be obtained by direct numerical integration using some standard time integration techniques. With arbitrary initial conditions one needs many cycles of integration before a converged solution is obtained. Through a proper choice of initial conditions, one can however eliminate all transients from the response and the steady dynamic response can be calculated by integrating through only one period T . The objective of the Floquet method is to calculate the proper initial conditions.

Let us assume a general solution

$$\tilde{y}(t) = \tilde{y}_H(t) + \tilde{y}_p(t) \quad (2.160)$$

where \tilde{y}_H is the homogeneous solution and \tilde{y}_p is the particular solution. Let us say $\tilde{y}_E(t)$ is the complete solution of the governing equation for a given set of initial conditions. One can add any

number of additional homogeneous solutions $\Delta\tilde{y}_H(t)$ for different initial conditions to this solution, $\tilde{y}_E(t)$. This would be a new solution.

$$\tilde{y}(t) = \tilde{y}_E(t) + \Delta\tilde{y}_H(t) \quad (2.161)$$

One can obtain all the homogeneous solutions of the governing equation by setting $G \equiv 0$, a total of $2N$ solutions, subject to the initial conditions $y_1 = 1$ and all remaining $y_i = 0$, then $y_2 = 1$ and all remaining $y_i = 0$, etc. The similar set of solutions are calculated for the transition matrix.

$$\Delta\tilde{y}_H(t) = [\tilde{y}^{(1)}(t) \quad \tilde{y}^{(2)}(t) \quad \dots] \begin{bmatrix} c_1 \\ c_2 \\ \vdots \end{bmatrix} \quad (2.162)$$

$$= [Q(t)]\tilde{c}$$

The matrix $[Q(t)]$ is the transition matrix at any instant of time.

$$\tilde{y}(t) = \tilde{y}_E(t) + [Q(t)]\tilde{c} \quad (2.163)$$

For a periodic solution over period $T = 2\pi/\Omega$, one gets

$$y(t) = y(O)$$

$$\tilde{y}_E(t) + [Q(T)]\tilde{c} = \tilde{y}_E(0) + [Q(0)]\tilde{c}$$

$$\begin{array}{ccc} \downarrow & & \downarrow \\ \tilde{Q} & & \tilde{I} \end{array}$$

Transition matrix unity matrix

$$\tilde{c} = [\tilde{I} - \tilde{Q}]^{-1}\{y_E(T) - y_E(0)\}$$

$$\tilde{y}(0) = \tilde{y}_E(0) + [\tilde{I} - \tilde{Q}]^{-1}\{y_E(T) - y_E(0)\} \quad (2.164)$$

This gives the initial conditions. Once these initial conditions are known we can calculate the forced response numerically, and we do not need to repeat beyond one cycle. For simplicity we can select $\tilde{y}_E(0) = 0$. This gives

$$\tilde{y}(0) = [\tilde{I} - \tilde{Q}]^{-1}\tilde{y}_E(T) \quad (2.165)$$

Here $\tilde{y}_E(T)$ is the complete solution of the governing equation for zero initial conditions.

The above form of initial conditions is given by Dugundji (1983). An alternate form for the initial conditions is given by Friedmann group (1979)

$$\tilde{y}(0) = [\tilde{I} - \tilde{Q}]^{-1}\tilde{Q} \int_0^T [Q(t)]^{-1}\tilde{G}(t) dt \quad (2.166)$$

This does not use $\tilde{y}_E(T)$.

This procedure may be extended to deal with nonlinear equations

$$\tilde{y} - \tilde{A}(t)\tilde{y} = \tilde{G}(t, \tilde{y}, \dot{\tilde{y}}) \quad (2.167)$$

The forcing term on the right hand side contains nonlinear terms. See Dugundji (1983) for details.

Example: 2.11

The dynamic behavior of a system is represented by the following equations

$$\dot{x} = x \sin \psi$$

$$\dot{y} = x e^{\cos \psi} + F \sin \psi$$

Using the Floquet transition matrix, find out whether the system is stable or not.

$$\begin{aligned} \dot{x} &= x \sin \psi \\ \text{Sol. } x &= c_1 e^{-\cos \psi} \\ \dot{x} &= c_1 e^{-\cos \psi} = x \sin \psi \end{aligned}$$

For stability purpose, set $F = 0$

$$\begin{aligned} \dot{y} &= x e^{\cos \psi} = c_1 \\ y &= c_1 \psi + c_2 \end{aligned}$$

Let us now generate Floquet transition matrix. First set of initial conditions.

$$\text{@ } \psi = 0 \quad x = 1.0 \quad \text{and} \quad y = 0$$

This gives

$$c_1 = \frac{1}{e} \quad c_2 = 0$$

For $\psi = 2\pi$

$$\begin{aligned} x &= \frac{1}{e} e^{\cos 2\pi} = 1 = Q_{11} \\ y &= \frac{2\pi}{e} = Q_{21} \end{aligned}$$

For the second set of initial conditions

$$\text{@ } \psi = 0 \quad x = 0 \quad \text{and} \quad y = 1.0$$

This gives

$$c_1 = 0 \quad c_2 = 1.0$$

For $\psi = 2\pi$

$$\begin{aligned} x &= 0 = Q_{12} \\ y &= 1.0 = Q_{22} \end{aligned}$$

Floquet transition matrix

$$[Q] = \begin{bmatrix} 1 & 0 \\ 2\pi & 1 \end{bmatrix}$$

Eigenvalues

$$\begin{vmatrix} \lambda - 1 & 0 \\ 2\pi & \lambda - 1 \end{vmatrix} = 0$$

$$(\lambda - 1)^2 = 0$$

$$\lambda_1 = 1 \quad \text{and} \quad \lambda_2 = 1$$

This is a condition of neutral stability.

Example: 2.12

The flapping equation for a blade in forward flight is given in the rotating frame as

$$\begin{aligned} \beta^{**} + \left(\frac{\gamma}{8} + \mu \frac{\gamma}{8} \sin \psi\right) \beta^* + (\nu_\beta^2 + \mu \frac{\gamma}{8} \cos \psi + \mu^2 \frac{\gamma}{8} \sin 2\psi) \beta \\ = \left[\frac{\gamma}{8}(1 + \mu^2) + \frac{\gamma}{3}\mu \sin \psi - \frac{\gamma}{8}\mu^2 \cos 2\psi\right] \theta - \left(\frac{\gamma}{6} + \frac{\gamma}{4}\mu \sin \psi\right) \lambda \end{aligned}$$

For a known advance ratio μ and a prescribed pitch $\theta(\psi)$ you would like to find the steady response of the blade for a full period of 2π . Without solving, show the steps to carry out the analysis using the Floquet method.

Periodic equation

Time period = 2π

Step 1

Reduce the equation to the first order form.

$$\begin{aligned} \begin{bmatrix} \beta^* \\ \beta^{**} \\ \beta \end{bmatrix} &= \begin{bmatrix} 0 & 1.0 \\ -(\nu_\beta^2 + \mu \frac{\gamma}{8} \cos \psi + \mu^2 \frac{\gamma}{8} \sin 2\psi) & -(\frac{\gamma}{8} + \mu \frac{\gamma}{8} \sin \psi) \end{bmatrix} \begin{bmatrix} \beta \\ \beta^* \\ \beta \end{bmatrix} \\ &+ \begin{bmatrix} 0 \\ [\frac{\gamma}{8}(1 + \mu^2) + \frac{\gamma}{3}\mu \sin \psi - \frac{\gamma}{8}\mu^2 \cos 2\psi] \theta(\psi) - (\frac{\gamma}{6} + \frac{\gamma}{4}\mu \sin \psi) \lambda \end{bmatrix} \\ \tilde{y}^* &= \tilde{A}\tilde{y} + \tilde{G} \end{aligned}$$

Step 2

Calculate for the complete system with zero initial conditions (using numerical integration)

$$\text{@ } \psi = 0, \quad \begin{Bmatrix} \beta \\ \beta^* \\ \beta \end{Bmatrix} = 0$$

Step 3

Calculate the Floquet transition matrix $[Q(2\pi)]$

For this set $\tilde{G} = \tilde{0}$.

Response at $\psi = 2\pi$ with two sets of initial conditions

First set @ $\psi = 0$ $\beta = 1.0$ $\beta^* = 0$ gives Q11, Q21

Second set @ $\psi = 0$ $\beta = 0$ $\beta^* = 1.0$ gives Q12, Q22

Step 4

Calculate the initial conditions.

$$\tilde{y}(0) = (\tilde{I} - \tilde{Q}(2\pi))^{-1} y_E(2\pi)$$

Step 5

Using these initial conditions, calculate the response at different time steps ψ using the numerical integration for the complete system.

Questions

Justify the following

- The flap mode is highly damped.
- In an articulated rotor blade, the rotating flap frequency was found to be less than one per revolution.
- Most of the flying rotors have fundamental flap frequencies (rotating) of less than 1.2 per revolution.
- Propeller blades have fundamental flap frequencies much higher than those of helicopter blades.
- Most of the rotors operate at one fixed rotational speed.
- Free decay vibration frequency is not natural frequency.
- At higher rotational speeds, the fundamental flap frequency becomes rotational speed itself.
- To calculate accurately the first few modes (2 to 3), one needs only a few terms in the assumed deflection series (4 to 6), but to calculate the bending stresses at the root of the blade, one needs a large number of terms in the series.
- Frequencies calculated using Galerkin method and Rayleigh-Ritz method are always higher than exact values.
- If an assumed deflection series satisfies all the boundary conditions, will there be any difference in the results obtained using the Galerkin method and Rayleigh-Ritz method.
- The solution converges monotonically to the exact solution with the increasing number of terms in the approximate series (R-R method). For one particular series, the solution fluctuated with an increasing number of terms. Any possible source of trouble.
- The lumped parameter formulation (Myklestad) is a crude form of finite element analysis.
- To increase the polynomial distribution for displacement within a beam element one can include the continuity of the second derivative of displacement between elements, but it is never done that way.
- The beauty of finite element analysis is its adaptability to different configurations which is not possible with other approximate methods.
- A great care is taken to calculate the natural vibration characteristics (rotating) of the blade.
- For calculating the bending stresses, the force summation is preferred over the modal method.
- For dynamic response, the normal mode approach results in key simplification of the multi-degree system.
- The Fourier series is quite different from the Fourier coordinate transformation.
- One has to be careful using the Fourier series solution to transient response problems.
- During the wind tunnel testing of a rotor, a 1/rev signal was observed from an accelerometer mounted on the top of the hub and the test was immediately stopped.

- For multicyclic vibration control, the swash plate is excited at 4/rev to eliminate 3, 4 and 5/rev bending stresses at the blade root.
- The progressive mode is quite different from the regressive mode.
- The rotor acts as a filter for many harmonics.
- The longitudinal and lateral TPP tilt equations are coupled in hovering flight.
- High dynamic stresses on blades does not necessarily mean high vibration in body.
- Finite different method is quite commonly used for structural response problems whereas Fourier series and Floquet methods are more commonly used for blade response problems.
- For solving stability and response problems using Floquet theory, one needs to find the initial conditions as a first step. However, for stability calculations using the Floquet method, there is no need to find the initial conditions.
- The nature of the eigenvalue explains the system behavior.
- For the dynamics of a blade, the mass distribution of the outermost part and the stiffness distribution of the innermost part play an important role.

Bibliography

- [1] Johnson, W., Helicopter Theory, Princeton University Press, Princeton, N.J. 1980, Ch. 8 and 9.
- [2] Dungundji, J. and Wendell, J.H., "Some Analysis Methods for Rotating Systems with Periodic Coefficients," AIAA Journal, Vol. 21, No. 6, June 1983, pp. 890-897.
- [3] Meirovitch, L., Analytical Methods in Vibration, The MacMillan Company, New York, 1967. Chapter 5.
- [4] Young, D. and Felgar, R.P., "Tables of Characteristic Functions Representing Normal modes of vibration of a Beam," Engr. Res. Series No. 44, Bureau of Engr. Research, The University of Texas, Austin, TX, 1949.
- [5] Meirovitch, L., Computational Methods in Structural Dynamics, Sijthoff and Noordhoff, 1980, Ch. 9.
- [6] Sivaneri, N.T. and Chopra, I., "Dynamic Stability of a Rotor Blade Using Finite Element Theory," AIAA Journal, Vol. 25, No. 5, May 1982, pp. 716-723.
- [7] Friedmann, P.P., Hammond, C.E. and Woo, T.H., "Efficient Treatment of Periodic Systems with Application to Stability Problems," International Journal of Numerical Methods in Engineering, Vol. 11, No. 7, 1977, pp. 1117-1136.
- [8] Kottapalli, S.B. R., Friedmann, P.P. and Rosen, A., "Aeroelastic Stability and Response of Horizontal Axis Wind Turbine Blades," AIAA Journal, Vol. 17, No. 12, Dec. 1979, pp. 1381-1389.
- [9] Sivaneri, N.T. and Chopra, I., "Finite Element Analysis for Bearingless Rotor Blade Aeroelasticity," Journal of the American Helicopter Society, Vol. 29, No. 2, April 1984, pp. 716-723.
- [10] Banerjee, A. K., "Contributions of Multibody Dynamics to Space Flight: A Brief Review," *Journal of Guidance, Control, and Dynamics*, Vol. 26, (3), May-June 2003, pp. 385-394.

Chapter 3

Coupled Flap-Lag-Torsion Dynamics

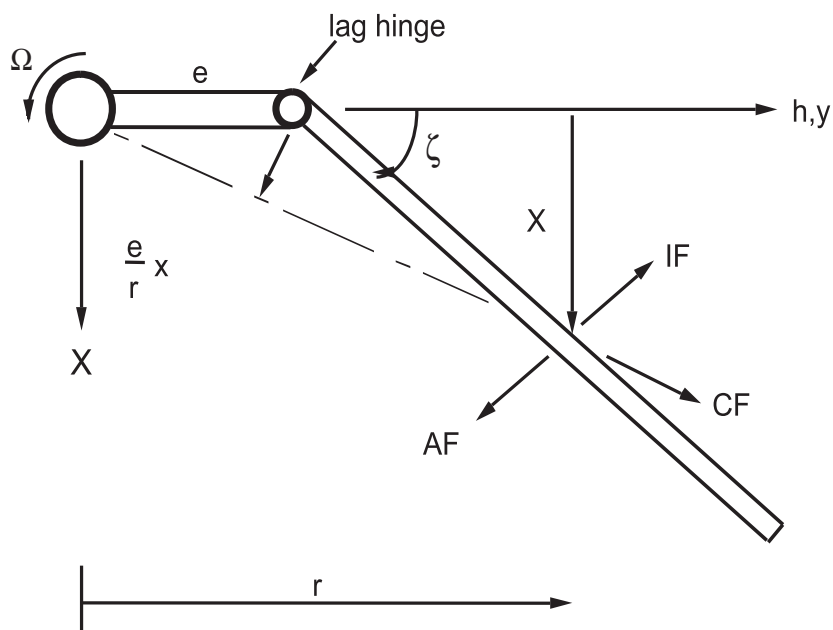
The objective of this chapter is to understand the equations of motion for a blade undergoing flap and lag bending and torsional deflection. In the last chapter, uncoupled flap dynamics was discussed. In this chapter, first the equations of motion for the uncoupled lag and torsion modes are discussed followed by coupled motions. The principle concern here is the structural and inertial terms, then the important coupling terms due to coupled motion due to flap, lag and torsion are identified. The Newtonian approach is used to derive the equations of motion. Also, one can derive these equations using the energy approach, but it is not a physical approach and therefore does not help to understand different forces. The resultant blade forces in the rotating frame and the hub forces in the fixed frame are also derived.

3.1 Lag Dynamics

The dynamics of lag motion is studied below.

3.1.1 Rigid Lag Model with Hinge Offset

The blade is assumed rigid and undergoes a single degree of motion in the plane of rotation. It has a hinge offset at a distance e from the rotation axis. The simple configuration represents an articulated blade with lag hinge. This type of modeling can be an approximate representation for a hingeless blade with a possible leaf spring at the hinge. The lag motion opposes rotation. Let us examine various forces acting on the blade for small angle assumption. For a blade element of length dr



- (a) IF: inertia force $m\ddot{x} dr = m(r - e)\ddot{\zeta} dr$ arm $(r - e)$ about lag hinge
 (b) CF: centrifugal force $m\Omega^2 r dr$ arm $\frac{e}{r}(r - e)\zeta$
 (c) AF: aerodynamic force F_ζ arm $r - e$
 (d) SF: spring moment about hinge $k_\zeta \zeta$
- where m is mass per unit length (lb sec²/in²) and F_ζ is external force per unit length (lb/in).
 Taking moment of all forces about lag hinge

$$\int_e^R m(r - e)^2 dr \ddot{\zeta} + \int_e^R m\Omega^2 r(r - e) \frac{e}{r} dr \zeta - \int_e^R F_\zeta(r - e) dr + k_\zeta \zeta = 0$$

$$\int_e^R m(r - e)^2 dr = \text{mass moment of inertia about lag hinge, } I_\zeta$$

$$I_\zeta(\ddot{\zeta} + \nu_\zeta^2 \zeta) = \frac{1}{\Omega^2} \int_e^R F_\zeta(r - e) dr \quad (3.1)$$

where ν_ζ is nondimensional lag frequency in terms of rotational speed.

$$\nu_\zeta^2 = \frac{k_\zeta}{I_\zeta \Omega^2} + \frac{e \int_e^R m(r - e) dr}{I_\zeta} \quad (3.2)$$

The second term is due to centrifugal spring and is zero if there is no hinge offset. The first term is due to spring bending at the hinge and this represents the nonrotating natural frequency of the blade made nondimensional with respect to rotational speed

$$\nu_\zeta^2 = \frac{\omega_{\zeta 0}^2}{\Omega^2} + e \frac{S_\zeta}{I_\zeta}$$

where S_ζ is the first moment of mass about lag hinge and I_ζ is the second moment of mass about lag hinge. For a uniform blade

$$S_\zeta = \frac{m}{2}(R - e)^2$$

$$I_{\zeta} = \frac{m}{3}(R - e)^3$$

The lag frequency becomes

$$\nu_{\zeta}^2 = \frac{\omega_{\zeta 0}^2}{\Omega^2} + \frac{3}{2} \frac{e}{R - e} \text{ per rev.}$$

For an articulated blade (zero offset)

$$\nu_{\zeta} = 0$$

This is not a realistic case and there will be no transfer of torque.

For an articulated blade with hinge offset, the lag equation becomes

$$\zeta^{**} + \nu_{\zeta}^2 \zeta = \gamma \overline{M}_{\zeta} \quad (3.3)$$

The lag mode is inherently very low damped and is quite susceptible to various aeroelastic instabilities. In particular, the soft lag rotor can get into mechanical instability called ground resonance. This is the reason that most of the existing rotors have mechanical lag dampers to stabilize the lag motion.

Let us look at uncoupled flap and lag frequencies for hinged blades,

$$\text{Flap: } \nu_{\beta}^2 = 1 + \frac{3}{2} \frac{e_{\beta}}{R} + \frac{\omega_{\beta 0}^2}{\Omega^2}$$

$$\text{Lag: } \nu_{\zeta}^2 = \frac{3}{2} \frac{e_{\zeta}}{R} + \frac{\omega_{\zeta 0}^2}{\Omega^2}$$

where e_{β} and e_{ζ} are respectively the flap and lag hinges from the rotation axis. Generally these are very close, and for making analysis simple these are assumed coincidental.

$$e_{\beta} = e_{\zeta} = e$$

For matched stiffness blades, the nonrotating flap and lag frequencies are equal

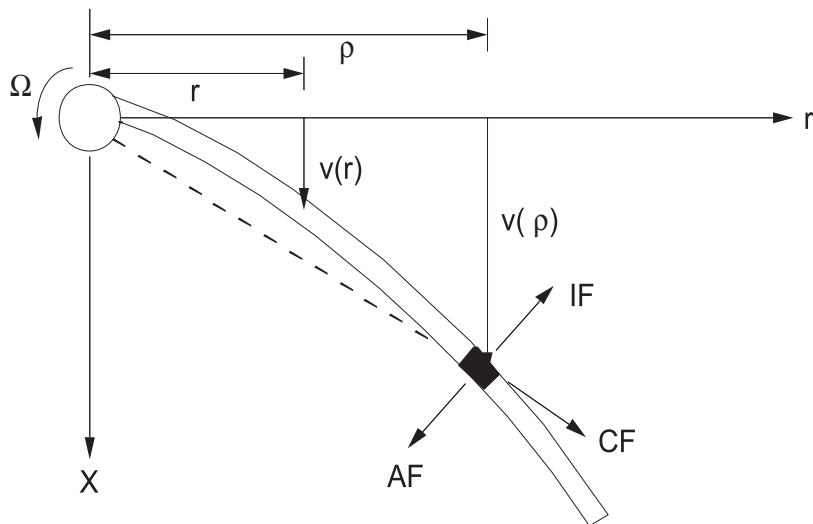
$$\omega_{\beta 0} = \omega_{\zeta 0}$$

This results into an important relationship between flap and lag rotating frequencies.

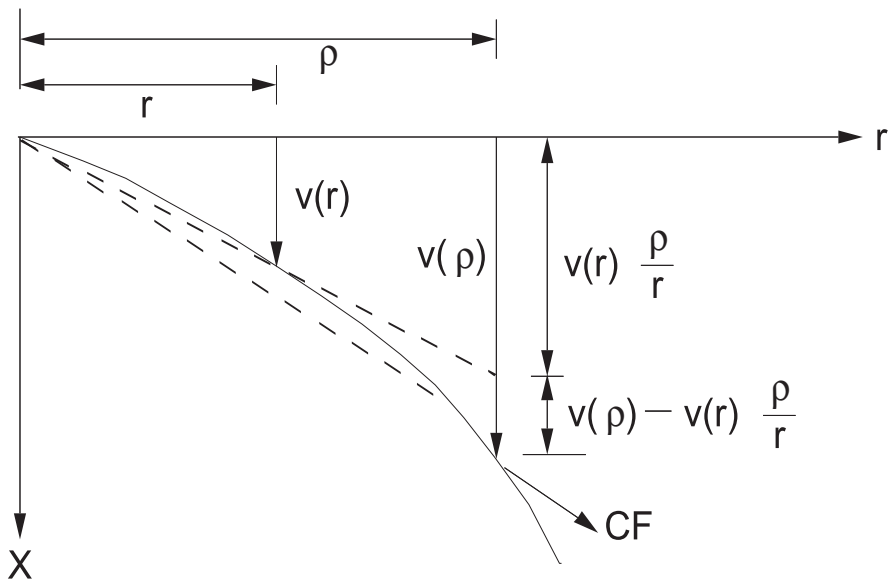
$$\nu_{\beta}^2 = 1 + \nu_{\zeta}^2 \quad (3.4)$$

3.1.2 Elastic Lag Model

A better representation for a blade is to assume it as an elastic beam undergoing in-plane bending. At the moment, it is assumed to be pure lag motion and the coupling terms due to other modes of motion will be considered later on. This type of modeling is also applicable to articulated blades if one needs to know more than the fundamental vibration mode. Let us examine the forces acting on an element of length dr a distance ρ



$v(\rho)$ = lag bending deflection at r
 $v(r)$ = lag bending deflection at r
 z axis is normal to the rotation plane



- (a) IF: inertia force $m\ddot{v}(\rho) d\rho$ arm $(\rho - r)$ about r
 (b) CF: centrifugal force $m\Omega^2 \rho d\rho$ arm $\frac{r}{\rho}v(\rho) - v(r)$
 (c) AF: aerodynamic force $F_x dr$ arm $(\rho - r)$

The lag moment at r is

$$\begin{aligned}
 M_z(r) &= \int_r^R (F_x - m\ddot{v})(\rho - r) d\rho \\
 &= - \int_r^R m\Omega^2 \rho \left\{ \frac{r}{\rho}v(\rho) - v(r) \right\} d\rho
 \end{aligned} \tag{3.5}$$

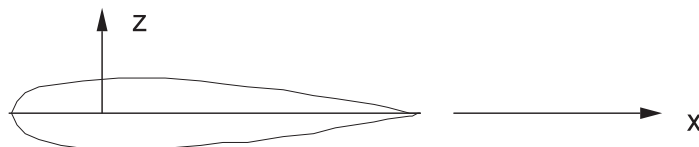
Let us recall the Leibnitz theorem

$$\begin{aligned}\phi &= \int_{u_1(r)}^{u_2(r)} f(\rho, r) d\rho \\ \frac{\partial \phi}{\partial r} &= \int_{u_1(r)}^{u_2(r)} \frac{\partial f}{\partial r}(\rho, r) d\rho + \frac{\partial u_2(r)}{\partial r} f(u_2(r), r) \\ &\quad - \frac{\partial u_1(r)}{\partial r} f(u_1(r), r)\end{aligned}\quad (3.6)$$

The beam bending equation is

$$M_z = EI_z \frac{d^2 v}{dr^2} \quad (3.7)$$

Let us consider an airfoil section



M_z = moment of forces about z axis at station r, in-lb

E = Young's modulus of elasticity, lb/in². Typically for aluminum
 10.5×10^6 lb/in²

I_z = area moment of inertia about z-axis

$$= \int_{\text{section}} x^2 dA, \text{ in}^4$$

x and z are section principle axes.

Taking the second derivative of the moment (Eq. (3.7)) and using Leibnitz's theorem one gets

$$\frac{d^2}{dr^2} (EI_z \frac{d^2 v}{dr^2}) - \frac{d}{dr} \left[\int_r^R m\Omega^2 \rho d\rho \frac{dv}{dr} \right] + m\ddot{v} - m\Omega^2 v = F_x(r, t) \quad (3.8)$$

This equation can be also derived like the flap bending equation. The first term is the flexural term, the second term is due to centrifugal force, the third term is the inertia term and the fourth term is the vertical component of centrifugal force. The boundary conditions here are quite similar to those of flap bending described in Chapter 2.

3.1.3 Natural Vibrations of Lag Motion

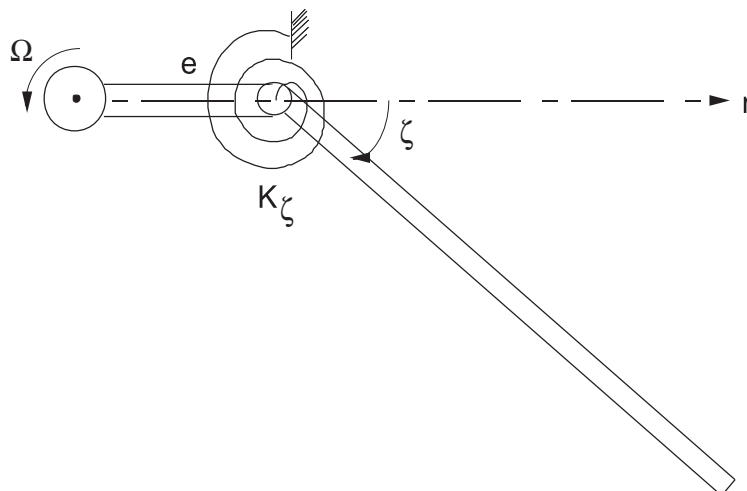
The natural vibration characteristics of a rotating blade in pure lag bending mode are obtained from the homogeneous solution of lag bending equation (3.8)

$$\frac{d^2}{dr^2} (EI_z \frac{d^2 v}{dr^2}) - \frac{d}{dr} \left[\left(\int_r^R m\Omega^2 \rho d\rho \right) \frac{dv}{dr} \right] + m\ddot{v} - m\Omega^2 v = 0 \quad (3.9)$$

The boundary conditions for a hingeless blade are

$$\begin{aligned}\text{@ } r = 0 \quad v &= 0 \quad \frac{dv}{dr} = 0 \\ \text{@ } r = R \quad M_z &= EI_z \frac{d^2 v}{dr^2} = 0 \quad (\text{moment}) \\ S_x &= \frac{d}{dr} (EI_z \frac{d^2 v}{dr^2}) = 0 \quad (\text{shear})\end{aligned}$$

The boundary conditions for a hinged blade with a lag hinge at distance e from rotation axis and a leaf spring k_ζ at the hinge



$$\begin{aligned} @r = e \quad V &= 0 \\ M_z &= EI_z \frac{d^2 v}{dr^2} = k_\zeta v \quad (\text{Bending}) \end{aligned}$$

$$\begin{aligned} @r = R \quad M_z &= EI_z \frac{d^2 v}{dr^2} = 0 \quad (\text{Bending}) \\ S_x &= \frac{d}{dr} (EI_z \frac{d^2 v}{dr^2}) = 0 \quad (\text{Shear}) \end{aligned}$$

Let us consider a hingeless blade. The closed form (exact) solution is available only for a uniform nonrotating blade. For a rotating blade, one has to apply some approximate method to calculate the natural frequencies and mode shapes. Three approximate methods to solve this problem have been discussed in Chapter 2.

Note that the nonrotating natural vibration characteristics for a uniform beam with different boundary conditions were given in Chapter 2 as beam functions. Recall that the tabulated numerical values by Felgar and Young (1950) were given as follows.

For a cantilever beam, the j^{th} mode shape is expressed as

$$\phi_j(r) = \cosh \lambda_j r - \cos \lambda_j r - \alpha_j (\sinh \lambda_j r - \sin \lambda_j r) \quad (3.10)$$

Mode j	1	2	3	4	j
λ_j	1.8751	4.6941	7.8548	10.995	$(2j-1)\pi/2$
α_j	.7341	1.0185	.9992	1.0	1.0

The nonrotating natural frequency for a uniform beam for j^{th} mode is

$$\omega_{j0} = (\lambda_j)^2 \sqrt{\frac{EI_z}{mR^4}} \quad (3.11)$$

where EI_z = flexural stiffness about chord, lb-in²
 m = mass per unit length, lb-sec²/in²
 R = blade length, in

Again, these beam modes are orthogonal as discussed in Chapter 2.

3.1.4 Finite Element Formulation

Quite similar to flap bending vibrations, it is quite convenient to calculate lag bending vibration characteristics of a rotating blade using finite element formulation. The procedure is similar to one discussed in art. 2.7. The shape functions for a beam element are the same. The element energy expressions are slightly modified for lag bending of a rotating beam.

$$\text{Kinetic energy} \quad T = \frac{1}{2} \int_0^l m \dot{v}^2 dx$$

$$\text{Strain energy} \quad v = \frac{1}{2} \int_0^l EI_z \left(\frac{d^2 v}{dx^2} \right)^2 + \frac{1}{2} \int_0^l T(x) \left(\frac{dv}{dx} \right)^2 - \frac{1}{2} \int_0^l m \Omega^2 v^2 dx$$

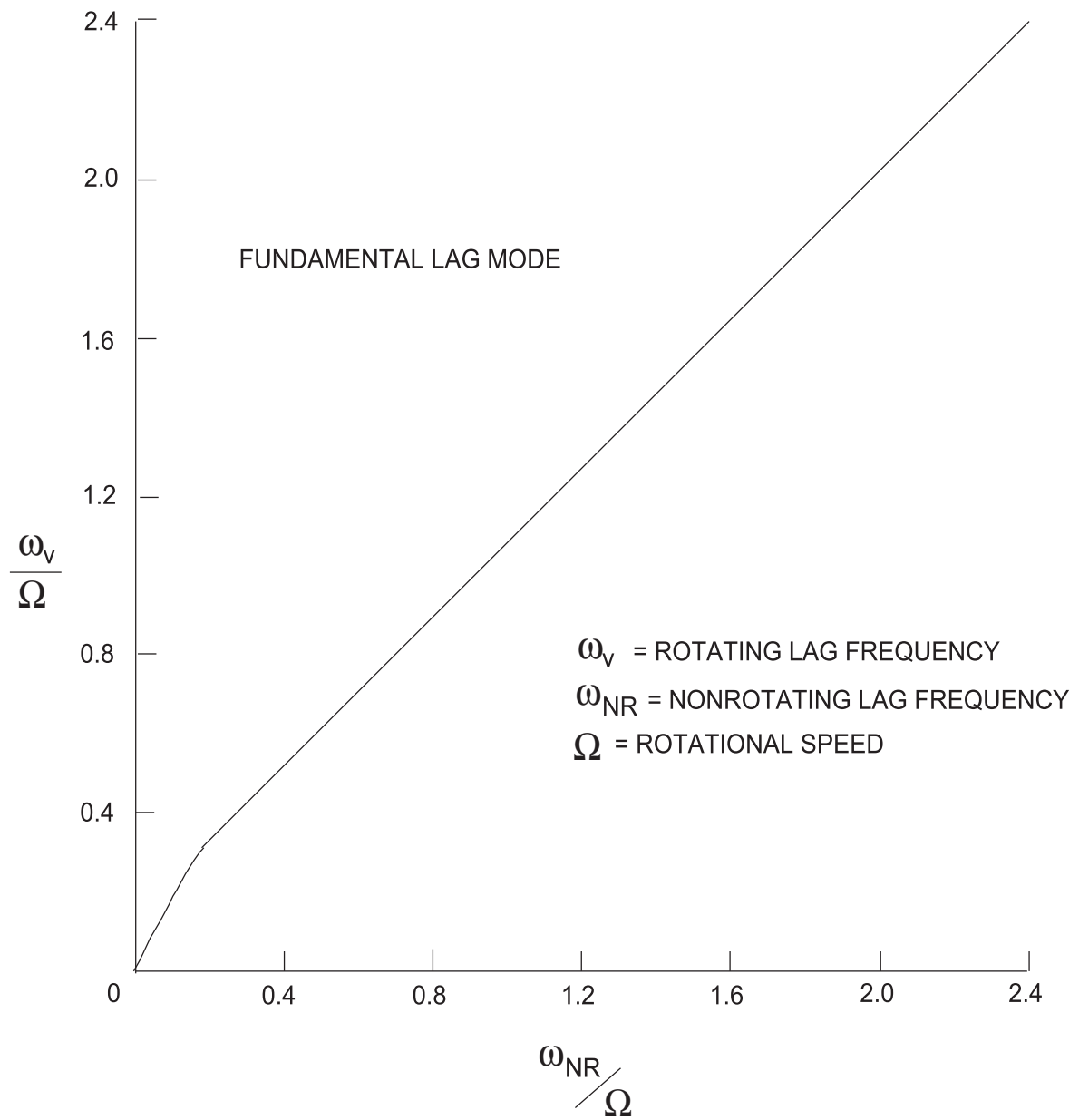
The kinetic energy expression is the same as that of flap bending, whereas for the strain energy expression, the last term is an additional term. The inertial and stiffness matrices are

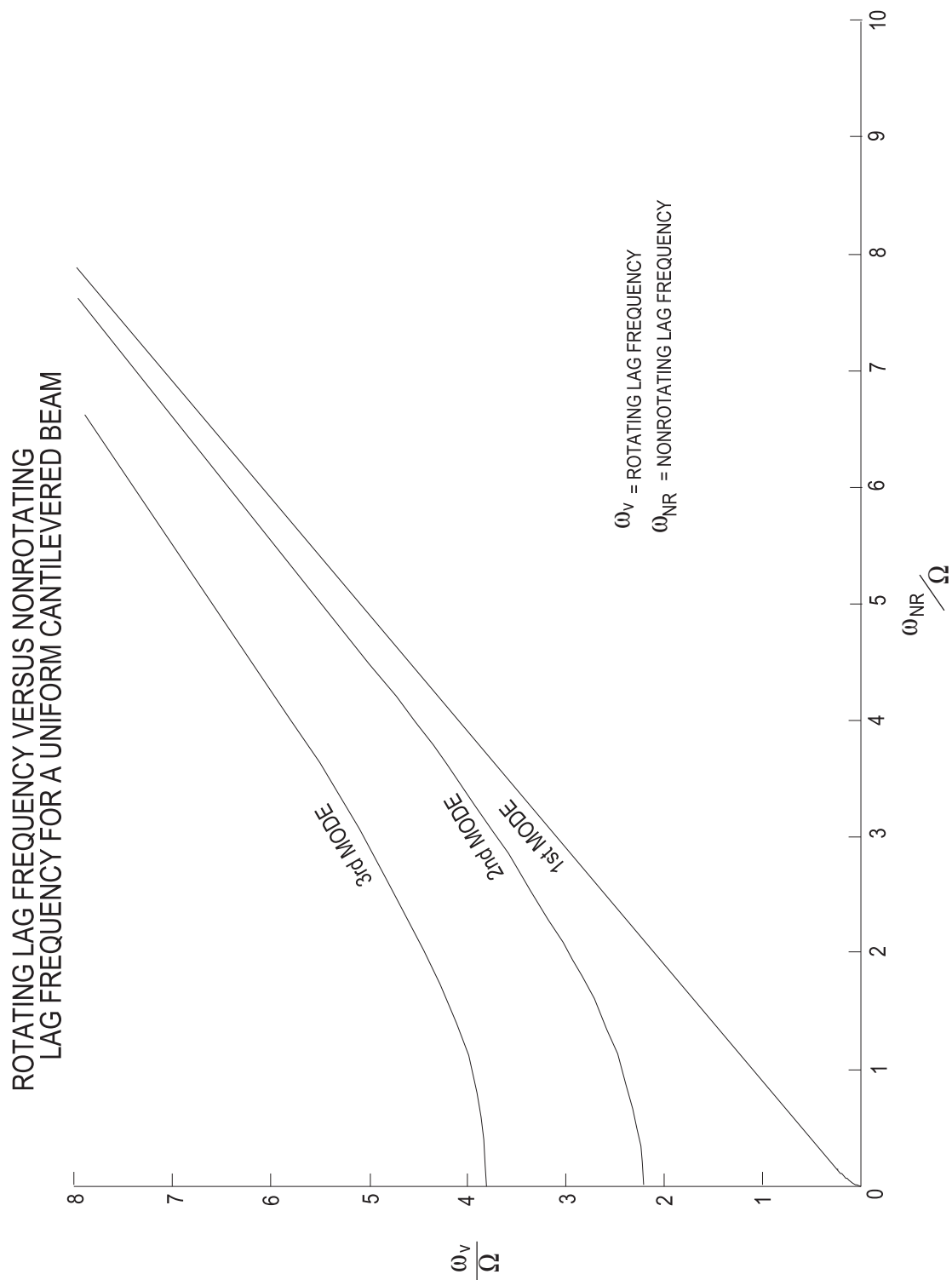
$$[\tilde{m}_{ij}]_{\text{lag}} = [\tilde{m}_{ij}]_{\text{flap}}$$

$$[\tilde{k}_{ij}]_{\text{lag}} = [\tilde{k}_{ij}]_{\text{flap}} - m_i \Omega^2 \begin{bmatrix} \frac{13}{35}l & \frac{11}{210}l^2 & \frac{9}{70}l & -\frac{13}{420}l^2 \\ \frac{11}{210}l^2 & \frac{1}{105}l^3 & \frac{13}{420}l^2 & -\frac{140}{1}l^3 \\ \frac{9}{70}l & \frac{13}{420}l^2 & \frac{13}{35}l & -\frac{11}{210}l^2 \\ -\frac{13}{420}l^2 & -\frac{1}{140}l^3 & -\frac{11}{210}l^2 & \frac{1}{105}l^3 \end{bmatrix}$$

In the subsequent figures, the lag vibration results are presented for uniform rotating beams. These results are calculated using finite element analysis. Four to ten finite elements are used; more elements are required for $\omega_{NR}/\Omega < .1$.

ROTATING LAG FREQUENCY VERSUS NONROTATING LAG
FREQUENCY FOR A UNIFORM CANTILEVERED BEAM



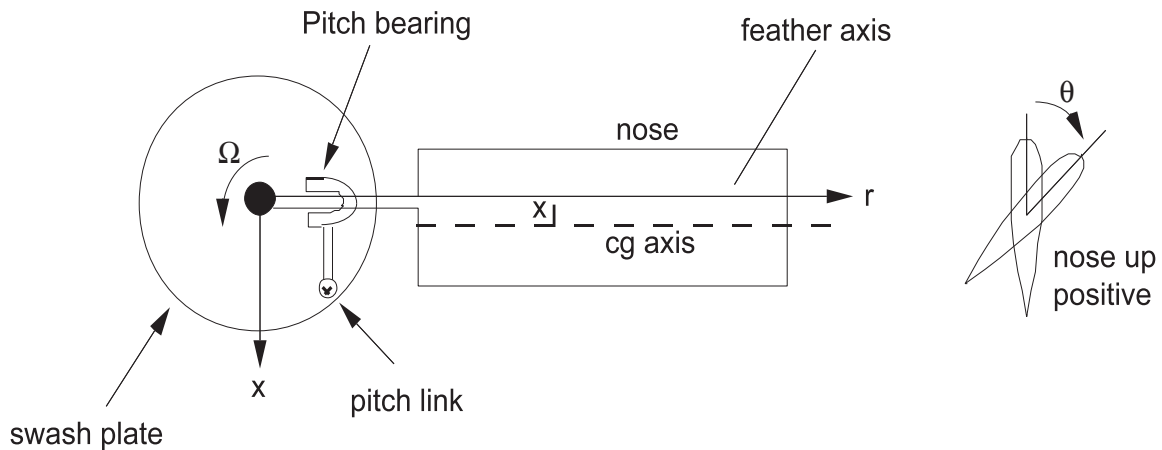


3.2 Torsion Dynamics

As in the case of flap, and lag, the torsion dynamics is studied both using a simple rigid model and a detailed flexible model.

3.2.1 Rigid Torsion Model

This is also called rigid pitch. The blade is assumed rigid and it undergoes a single degree pitch motion about the feathering axis. There is a torsional spring at the root of the blade. This type of modeling is quite satisfactory with helicopter blades because the control system (pitch link) stiffness is less than the blade elastic torsional stiffness. The nose up motion is positive feathering motion. Let us examine the various forces acting on an element dr undergoing torsional motion about the feathering axis,



$\theta =$ pitch angle

$\theta_{\text{CON}} =$ control system command pitch

$\theta - \theta_{\text{CON}} =$ pitch change due to control flexibility

$x_I =$ chordwise cg offset behind feathering axis

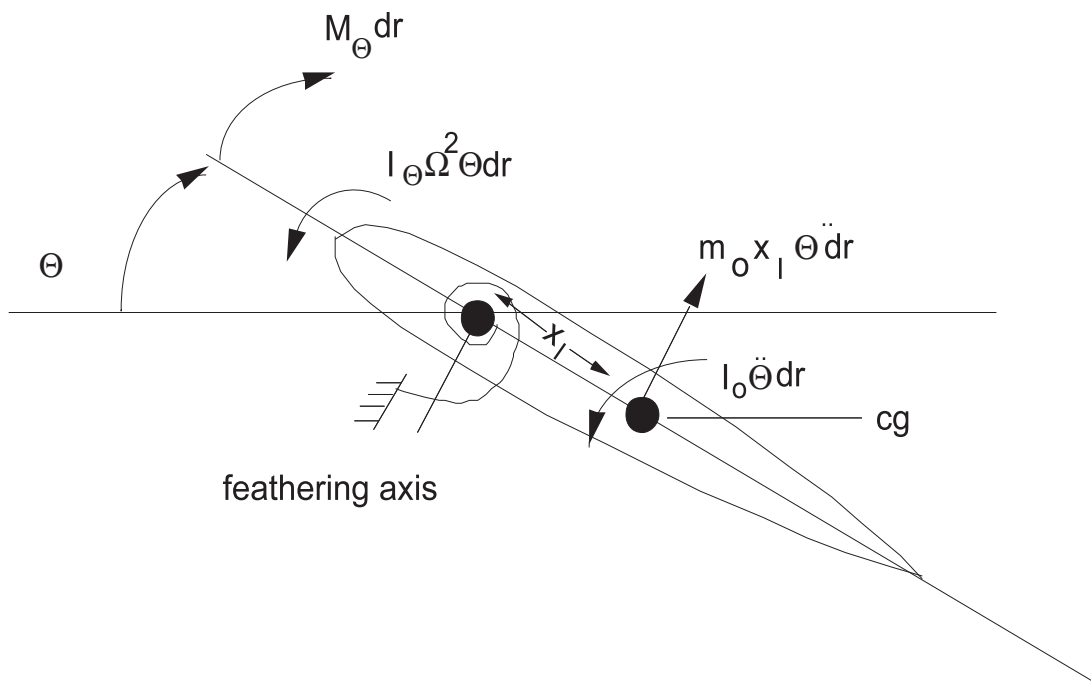
$I_o =$ mass moment of inertia about cg axis per unit length, lb-sec²

$I_\theta =$ mass moment of inertia about feathering axis per unit length

$$= I_o + mx_I^2, \quad \text{lb} - \text{sec}^2$$

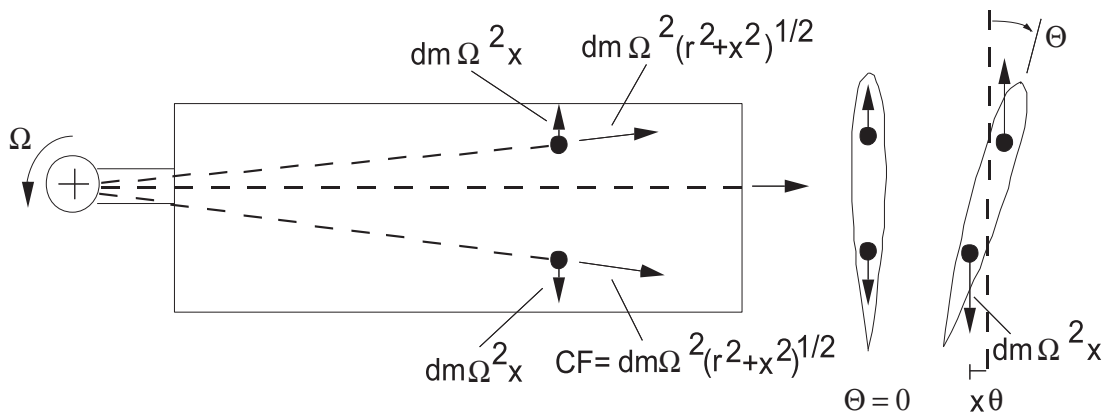
$m =$ mass per unit length lb-sec²/in²

$k_\theta =$ control system stiffness in-lb/rad



- a) inertia force $m x_I \ddot{\theta} dr$ arm x_I about feathering axis
- b) inertia torque $I_o \ddot{\theta} dr$ about cg axis
- c) propeller moment $I_\theta \Omega^2 \theta dr$ about feathering axis
- d) aerodynamic moment $M_\theta dr$ about feathering axis
- e) spring moment $k_\theta(\theta - \theta_{con})$

Let us examine carefully the propeller moment caused by the centrifugal action. Let us consider



two mass elements 'dm' on either side of the feathering axis. The elements are being pulled away by the centrifugal force, $dm \Omega^2 (r^2 + x^2)^{1/2}$. The chordwise resolved component

$$dm \Omega^2 (r^2 + x^2)^{1/2} \frac{x}{(r^2 + x^2)^{1/2}} = dm \Omega^2 x$$

Now let us say that the blade undergoes nose up pitch motion. The chordwise resolved component now produces a nose down couple about the feathering axis

$$\int_{\text{section}} (dm \Omega^2 x)(x\theta) = I_\theta \Omega^2 \theta$$

This is also called “Tennis racket effect”. A tilt of the racket face can be used to produce a pitching motion in the ball. Summing up the torque moments about the feathering axis

$$\int_0^R m x_I^2 \ddot{\theta} dr + \int_0^R I_0 \ddot{\theta} dr + \int_0^R I_\theta \Omega^2 \theta dr - \int_0^R M_\theta dr$$

$$+ k_\theta (\theta - \theta_{\text{con}}) = 0$$

$$\int_0^R I_\theta dr = I_f = \text{total mass moment of inertia about feather axis, lb-sec}^2\text{-in}$$

This results in

$$I_f (\ddot{\theta} + \Omega^2 \theta) + I_f \omega_{\theta 0}^2 (\theta - \theta_{\text{con}}) = \int_0^R M_\theta dr$$

where $\omega_{\theta 0}$ is the nonrotating natural torsional frequency. Let us nondimensionalize by dividing through $I_b \Omega^2$

$$I_f^* (\ddot{\theta} + \nu_\theta^2 \theta) = \gamma \overline{M}_\theta + I_f^* \frac{\omega_{\theta 0}^2}{\Omega^2} \theta_{\text{con}} \quad (3.12)$$

where

$$\overline{M}_\theta = \frac{1}{\rho a c \Omega^2 R^4} \int_0^R M_\theta dr$$

and

$$I_f^* = I_f / I_b$$

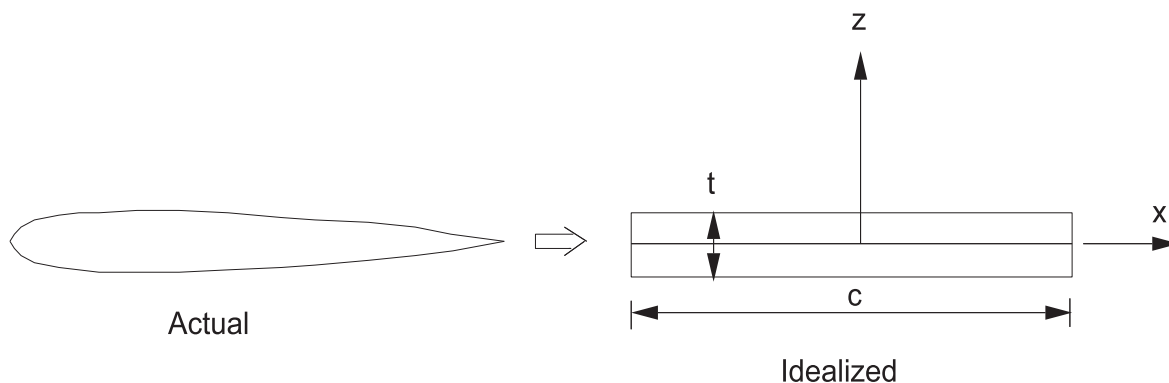
The ν_θ is the rotating natural frequency for torsion mode,

$$\nu_\theta^2 = 1 + \frac{\omega_{\theta 0}^2}{\Omega^2} \quad (3.13)$$

For zero spring, the torsional frequency is equal to the rotational speed and this is caused by propeller moment.

For helicopter blades, typically, the ν_θ varies from 5 to 10. The blades are much stiffer in the torsion mode than the flap and lag modes.

Let us examine an order of magnitude for I_f^* . Let us consider a solid airfoil, idealized into a rectangular strip.



$$I_0 = \rho_m(I_x + I_z) = \rho_m\left(\frac{ct^3}{12} + \frac{tc^3}{12}\right)$$

$$\simeq \rho_m \frac{tc^3}{12} \quad (\rho_m = \text{mass density})$$

$$I_f = \rho_m \frac{tc^3}{12} R$$

$$I_b = \frac{mR^3}{3}$$

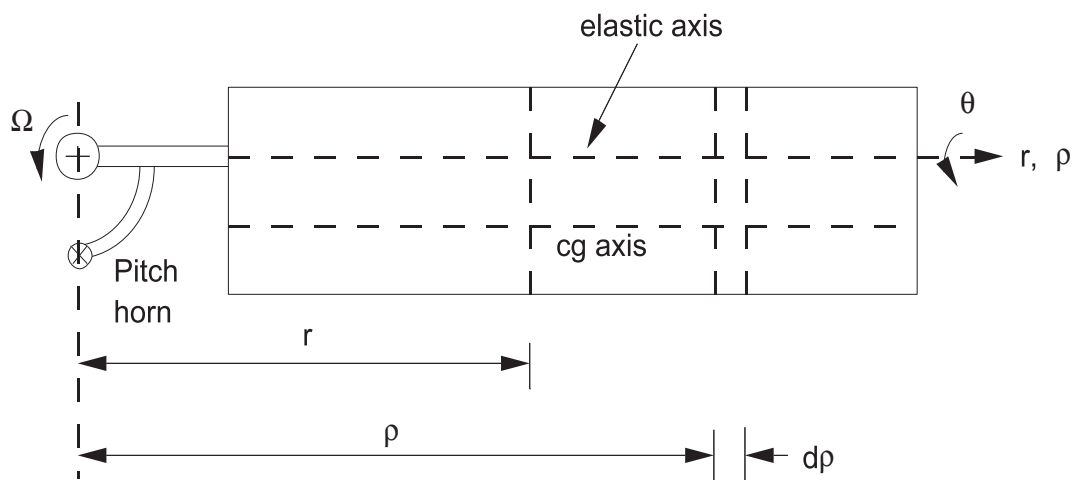
$$\frac{I_f}{I_b} = \rho_m 3 \frac{tc^3 R}{12mR^3} \quad m = \rho_m ct$$

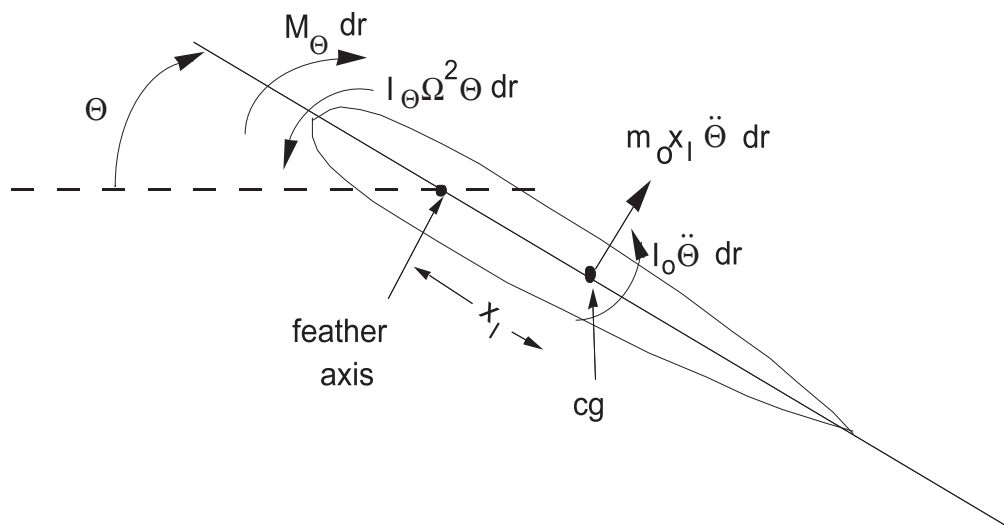
$$= \frac{\rho_m tc^3 R}{\rho_m tcR^3} = \frac{1}{4} \left(\frac{c}{R}\right)^2$$

For $c/R = 20$, $I_f^* = .00063$, a very small number.

3.2.2 Elastic Torsion

A better representation for the blade is to consider it as torsionally flexible and it undergoes elastic twist distribution. Again here the analysis is made for the pure torsion mode and coupling terms due to other modes are neglected. The blade twists about the elastic axis and for simplicity of analysis, the elastic axis is assumed to be a straight line coinciding with the feathering axis. Let us say θ is pitch change at a station, which consists of elastic twist ϕ plus rigid pitch due to control flexibility. Let us examine various forces acting at an element at station ρ





- inertia force $m_0 x_I \ddot{\theta} d\rho$ arm x_I about elastic axis
- inertia torque $I_0 \ddot{\theta} d\rho$ about cg axis
- propeller moment $I_\theta \Omega^2 \theta d\rho$ about elastic axis
- aerodynamic moment $M_\theta d\rho$ about elastic axis

Torsional moment at station r

$$\begin{aligned} M(r) &= \int_r^R [M_\theta - m_0 x_I^2 \ddot{\theta} - I_0 \ddot{\theta} - I_\theta \Omega^2 \theta] d\rho \\ &= \int_r^R [M_\theta - I_\theta (\ddot{\theta} + \Omega^2 \theta)] d\rho \end{aligned}$$

Using the engineering torsion theory for slender bars

$$M(r) = GJ \frac{d\theta}{dr}$$

where θ is the elastic twist distribution. Taking the first derivative of torque, one gets

$$-\frac{d}{dr} \left(GJ \frac{d\theta}{dr} \right) + I_\theta (\ddot{\theta} + \Omega^2 \theta) = M_\theta \quad (3.14)$$

The effect of control flexibility can be introduced through the boundary condition. Let us say at a distance r_a from the rotation axis, pitch link is located. Also assume that for $r = 0$ to r_a , the blade is rigid torsionally. Boundary conditions are:

$$\begin{aligned} @r = r_a \quad GJ\theta' &= -k_\theta (\theta - \theta_{con}) \quad (\text{Spring}) \\ @r = R \quad GJ\theta' &= 0 \quad (\text{Free}) \end{aligned} \quad (3.15)$$

For cantilevered blades, the boundary conditions are

$$\begin{aligned} @r = 0 \quad \theta &= 0 \quad (\text{fixed}) \\ @r = R \quad GJ\theta' &= 0 \quad (\text{free}) \end{aligned} \quad (3.16)$$

Another form of expression for the governing equations to be put in non-dimensional by dividing through Eq. (14) with $I_b \Omega^2$.

$$I_\theta^* (\theta'' + \theta) - \frac{d}{d\xi} \left(\frac{GJ}{I_b \Omega^2} \frac{d\theta}{d\xi} \right) = M_\theta / I_b \Omega^2 \quad (3.17)$$

where $I_\theta^* = I_\theta / I_b$ and $\xi = r / R$.

3.2.3 Natural Vibrations of Torsion Motion

The natural vibration characteristics of a rotating blade in pure torsion mode are obtained from the homogeneous solution of governing equation (14)

$$I_\theta(\ddot{\theta} + \Omega^2\theta) - \frac{d}{dr}(GJ\frac{d\theta}{dr}) = 0 \quad (3.18)$$

The corresponding governing equation for the nonrotating blade is

$$I_\theta\ddot{\theta} - \frac{d}{dr}(GJ\frac{d\theta}{dr}) = 0 \quad (3.19)$$

From the identity of these two equations one obtains

$$\omega_\theta^2 = \omega_{\theta_0}^2 + \Omega^2 \quad (3.20)$$

where ω_θ and ω_{θ_0} are respectively rotating and nonrotating natural frequencies. The mode shapes are the same for the rotating and nonrotating shafts.

3.2.4 Beam Functions for Torsion

The non-rotating natural torsional vibration characteristics are available for uniform bars with different boundary conditions.

For a cantilever bar, the j^{th} mode shape is expressed as

$$\phi_j(r) = \sqrt{2} \sin \lambda_j r \quad (3.21)$$

where

$$\lambda_j = \pi(j - \frac{1}{2})$$

The non-rotating natural torsional frequency for a uniform bar for the j^{th} mode is

$$\omega_{j0} = (\lambda_j) \sqrt{\frac{GJ}{I_\theta R^2}} \quad \text{rad/sec} \quad (3.22)$$

or

$$= (\lambda_j) \sqrt{\frac{GJ}{mk_m^2 R^2}}$$

where

GJ = torsional stiffness, lb-in²

I_θ = mass moment of inertia per unit length about the elastic axis, lb-sec² (= mk_m²)

R = blade radius, in

m = mass per unit length, lb-sec²/in²

k_m = radius of gyration, in

These mode shapes are orthogonal

$$\int_0^R I_\theta \phi_i \phi_j dr = 0 \quad \text{for } i \neq j \quad (3.23)$$

The rotating torsional frequency for a particular mode can be obtained from the nonrotating frequency as

$$\omega_j^2 = \omega_{j0}^2 + \Omega^2$$

and the mode shapes are identical.

rotating ϕ_j = nonrotating ϕ_j

Rotating torsion frequency versus nonrotating torsion frequency for uniform cantilevered bar

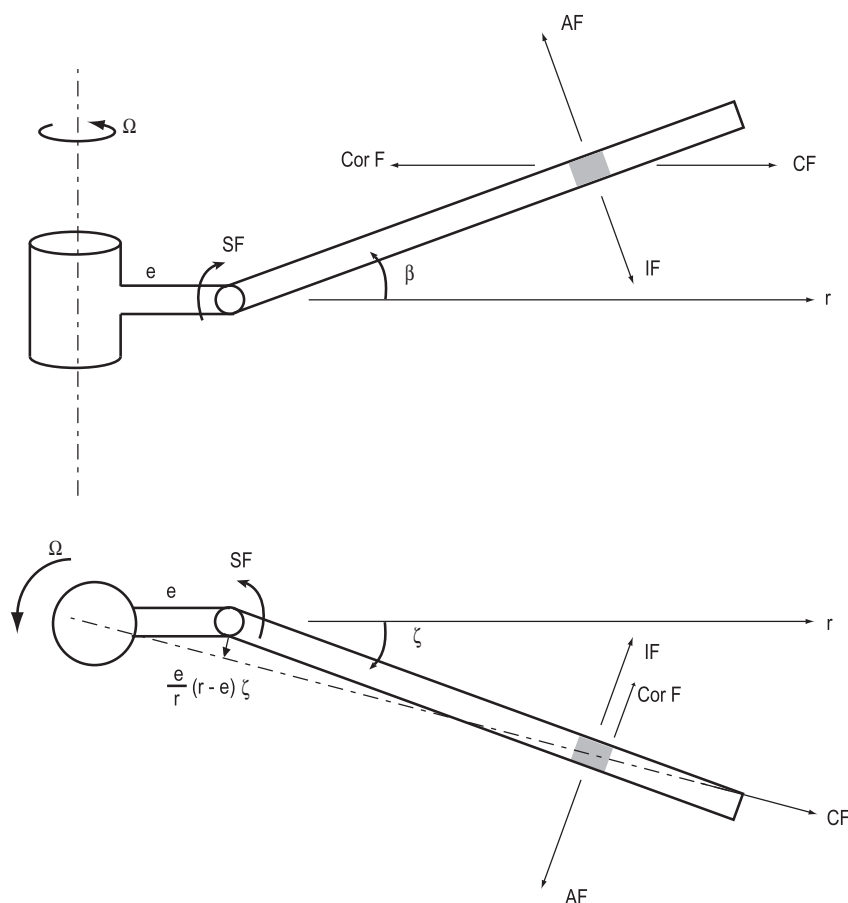
3.3 Coupled Flap-Lag Dynamics

First a rigid model is studied to understand the effect of non-linear flap-lag coupling. Then a detailed flap-lag bending model is considered.

3.3.1 Rigid Model

The blade is assumed rigid and it undergoes two degrees of motion, flap and lag rotations. For simplicity of analysis, it is assumed that the flap and lag hinges are identical. However, a small difference in hinge location can be taken care of by a suitable modification of the rotating flap and lag frequencies. This type of modeling is a good representation for dynamics of an articulated blade with large torsional frequency. It can also be a good approximation for the dynamics of hingeless blades.

Here, the flap and lag motions are coupled due to Coriolis and aerodynamic forces. The flap displacement β is positive up normal to the rotation plane and the lag displacement ζ is positive in the direction opposite to the rotation. Let us examine various forces acting on the element in flap and lag modes for small angles assumption.



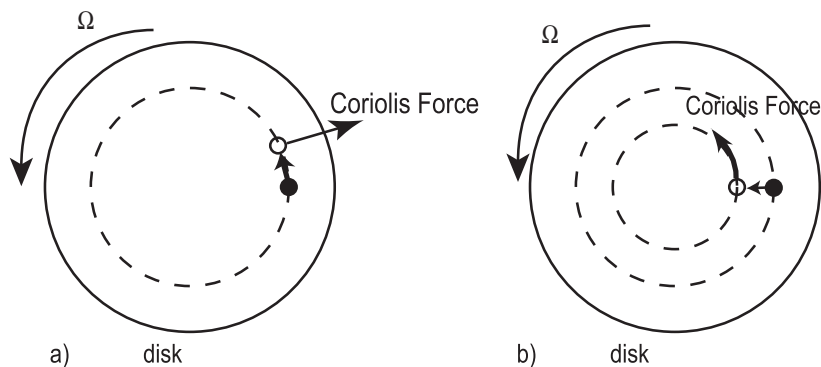
Flap mode forces

- (a) IF: inertia force $m(r-e)\ddot{\beta} dr$ arm $(r-e)$ about flap hinge
- (b) CF: centrifugal force $m\Omega^2 r dr$ arm $(r-e)\beta$
- (d) Cor F: Coriolis force $2m(r-e)\Omega\dot{\zeta} dr$ arm $(r-e)\beta$
- (c) AF: aerodynamic force $F_\beta dr$ arm $(r-e)$
- (e) SF: spring moment due to hinge spring, $k_\beta(\beta - \beta_p)$ where β_p is initial setting.

Lag mode forces

- (a) IF: $m(r - e)\ddot{\zeta}$ arm $(r - e)$ about lag hinge
- (b) CF: $m\Omega^2 r dr$ arm $(r - e)\frac{e}{r}\zeta$
- (c) Cor F: $2m(r - e)\beta\Omega\dot{\beta} dr$ arm $(r - e)$
- (c) AF: $F_\zeta dr$ arm $(r - e)$
- (d) SF: spring moment $k_\zeta\zeta$

Let us understand first the Coriolis forces. Imagine a person is standing on a circular disk rotating with a speed Ω .



There are two cases. In the first case he attempts to walk on the circumference (radius fixed) in the direction of rotation. He acquires more angular momentum than needed to sustain in equilibrium, so he is pushed towards region needing larger momentum. Thus the person feels a Coriolis force radially outward.

$$\text{Coriolis force} = 2\Omega mv$$

where v is the velocity of the person along the circumferential direction. In the second case, the person moves radially, let us say toward the center. He goes to a region where less angular momentum is required to sustain in equilibrium condition. He gets a push along the direction of rotation. Therefore the person feels a Coriolis force in the circumferential direction. Again, the force expression for this second case is the same as given except that the velocity v is interpreted as the radial velocity.

Taking the moment of forces about the flap hinge

$$\int_e^R \{m(r - e)^2 \ddot{\beta} + m\Omega^2(r - e)r\beta - 2m\Omega(r - e)^2\beta\dot{\zeta} - F_\beta(r - e)\} dr$$

$$+ k_\beta(\beta - \beta_p) = 0$$

or

$$I_\beta(\ddot{\beta} + \nu_\beta^2 \Omega^2 \beta - 2\Omega\dot{\zeta}) = \omega_{\beta 0}^2 I_\beta \beta_p + \int_e^R (r - e) F_\beta dr \quad (3.24)$$

where

$$\nu_\beta^2 = \frac{e \int_e^R m(r - e) dr}{I_\beta} + \frac{\omega_{\beta 0}^2}{\Omega^2} + 1 \quad (3.25)$$

The ν_β is nondimensional rotating flap frequency (uncoupled) and I_β is flap inertia.

$$\omega_{\beta 0} = \sqrt{\frac{k_\beta}{I_\beta}} \text{ rad/sec} \quad \text{nonrotating flap frequency}$$

Taking moments about lag hinge

$$\int_e^R \{m(r-e)^2 \ddot{\zeta} + m\Omega^2(r-e)e\zeta + 2m(r-e)^2\Omega\dot{\beta}\beta - F_\zeta(r-e)\} dr$$

$$+k_\zeta\zeta = 0$$

or

$$I_\zeta(\ddot{\zeta} + \nu_\zeta^2\Omega^2\zeta + 2\Omega\dot{\beta}\beta) = \int_e^R F_\zeta(r-e) dr \quad (3.26)$$

where

$$\nu_\zeta^2 = \frac{e \int_e^R m(r-e) dr}{I_\zeta} + \frac{w_{\zeta_0}^2}{\Omega^2} \quad (3.27)$$

The ν_ζ is nondimensional rotating lag frequency (uncoupled) and I_ζ is lag inertia.

$$w_{\zeta_0} = \sqrt{\frac{k_\zeta}{I_\zeta}} \text{ rad/sec} \quad \text{nonrotating lag frequency}$$

Dividing the flap and lag equations by $I_b\Omega^2$ and assuming $I_\beta = I_\zeta \simeq I_b$, the nondimensional equations are

$$\begin{aligned} \text{Flap:} \quad & \beta + \nu_\beta^2\beta - 2\beta \zeta = \gamma\overline{M}_\beta + \frac{\omega_{\beta_0}^2}{\Omega^2}\beta_p \\ \text{Lag:} \quad & \zeta + \nu_\zeta^2\zeta + 2\beta \beta = \gamma\overline{M}_\zeta \end{aligned} \quad (3.28)$$

where

$$\overline{M}_\beta = \frac{1}{\rho ac R^4 \Omega^2} \int_e^R F_\beta(r-e) dr$$

and

$$\overline{M}_\zeta = \frac{1}{\rho ac R^4 \Omega^2} \int_e^R F_\zeta(r-e) dr$$

The flap-lag equations are coupled inertially through the Coriolis force terms.

Some authors prefer to use lead-lag motion instead of lag motion. The lead-lag displacement has a sign convention opposite to lag displacement. For this convention, there will be a change of sign for Coriolis force terms.

$$\begin{aligned} \text{Flap:} \quad & \beta + \nu_\beta^2\beta + 2\beta \zeta = \gamma\overline{M}_\beta + \frac{\omega_{\beta_0}^2}{\Omega^2}\beta_p \\ \text{Lead-Lag:} \quad & \zeta + \nu_\zeta^2\zeta - 2\beta \beta = \gamma\overline{M}_\zeta \end{aligned} \quad (3.29)$$

The flap and lag equations are nonlinear. the equations are linearized by assuming that the dynamic motion is the small perturbation about the steady solution.

$$\beta = \underbrace{\beta_0}_{\text{steady}} + \underbrace{\beta}_{\text{perturbation}}$$

This helps in linearizing the perturbation equations. The β_0 is the steady coning angle.

Perturbation equations

Flap:

$$\beta^{**} + \nu_{\beta}^2 \beta - 2\beta_0 \zeta^* = \gamma \overline{M}_{\beta}$$

Lead-Lag:

$$\zeta^{**} + \nu_{\zeta}^2 \zeta + 2\beta_0 \beta^* = \gamma \overline{M}_{\zeta}$$

(3.30)

Since lag moment is much smaller than flap moment, therefore, Coriolis force in lag equation though nonlinear is quite important.

Example: 3.1

The blade and the hub flexibility is represented by two orthogonal spring systems, attached to the hub and the blade inboard and outboard of the pitch bearing respectively. The blade spring system, which rotates during collective pitch changes produces a significant cross coupling of flapping moments with lead-lag deflections and vice versa. The hub spring system does not rotate with the blade pitch and is oriented parallel and perpendicular to the shaft. Obtain the flap-lag equations for the following cases.

- (a) Hub flexible and blade rigid
- (b) Blade flexible and hub rigid
- (c) Both blade and hub flexible
- (a) Hub Flexible and Blade rigid

$$\beta^{**} + \nu_{\beta}^2 \beta - 2\beta_0 \zeta^* = \gamma \overline{M}_{\beta}$$

$$\zeta^{**} + \nu_{\zeta}^2 \zeta - 2\beta_0 \beta^* = \gamma \overline{M}_{\zeta}$$

$$\nu_{\beta}^2 = 1 + \frac{k_{\beta H}}{I_{\beta} \Omega^2}$$

$$\nu_{\zeta}^2 = \frac{k_{\zeta H}}{I_{\zeta} \Omega^2}$$

- (b) Blade flexible and hub rigid

$$\beta_1 = \beta \cos \theta - \zeta \sin \theta$$

$$\zeta_1 = \beta \sin \theta + \zeta \cos \theta$$

$$M_{\beta_1} = k_{\beta B} (\beta \cos \theta - \zeta \sin \theta)$$

$$M_{\zeta_1} = k_{\zeta B} (\beta \sin \theta + \zeta \cos \theta)$$

$$M_{\beta} = M_{\beta_1} \cos \theta + M_{\zeta_1} \sin \theta$$

$$= k_{\beta B} (\beta \cos^2 \theta - \zeta \sin \theta \cos \theta) + k_{\zeta B} (\beta \sin^2 \theta + \zeta \sin \theta \cos \theta)$$

$$M_{\zeta} = -M_{\beta_1} \sin \theta + M_{\zeta_1} \cos \theta$$

$$= -k_{\beta B} (\beta \sin \theta \cos \theta - \zeta \sin^2 \theta) + k_{\zeta B} (\beta \sin \theta \cos \theta + \zeta \cos^2 \theta)$$

$$M_{\beta} = \beta (k_{\beta B} \cos^2 \theta + k_{\zeta B} \sin^2 \theta) - \zeta (k_{\beta B} - k_{\zeta B}) \sin \theta \cos \theta$$

$$M_{\zeta} = -\beta (k_{\beta B} - k_{\zeta B}) \sin \theta \cos \theta + \zeta (k_{\beta B} \sin^2 \theta + k_{\zeta B} \cos^2 \theta)$$

$$\begin{Bmatrix} M_\beta \\ M_\zeta \end{Bmatrix} = \begin{bmatrix} k_{11} & k_{12} \\ k_{21} & k_{22} \end{bmatrix} \begin{Bmatrix} \beta \\ \zeta \end{Bmatrix}$$

$$k_{11} = k_{\beta_B} \cos^2 \theta + k_{\zeta_\beta} \sin^2 \theta$$

$$k_{12} = k_{21} = -(k_{\beta_B} - k_{\zeta_\beta}) \sin \theta \cos \theta$$

$$k_{22} = k_{\beta_B} \sin^2 \theta + k_{\zeta_\beta} \cos^2 \theta$$

(c) Hub flexible blade flexible

$$\begin{Bmatrix} \beta \\ \zeta \end{Bmatrix}_{\text{Total}} = \begin{Bmatrix} \beta \\ \zeta \end{Bmatrix}_{\text{Blade}} + \begin{Bmatrix} \beta \\ \zeta \end{Bmatrix}_{\text{Hub}}$$

$$\begin{Bmatrix} M_\beta \\ M_\zeta \end{Bmatrix} = [K_I] \begin{Bmatrix} \beta \\ \zeta \end{Bmatrix}_{\text{Blade}}$$

$$\begin{Bmatrix} M_\beta \\ M_\zeta \end{Bmatrix} = [K_{II}] \begin{Bmatrix} \beta \\ \zeta \end{Bmatrix}_{\text{Hub}}$$

$$[K_{\text{eff}}]^{-1} = [K_I]^{-1} + [K_{II}]^{-1}$$

Assuming a fraction of total stiffness is contributed by blade spring and the rest by hub springs.

$$R = k_\beta/k_{\beta_B} = k_\zeta/k_{\zeta_B}$$

$$\frac{k_\beta}{k_{\beta_H}} = 1 - R = \frac{k_\zeta}{k_{\zeta_H}}$$

$$[K_I] = \begin{bmatrix} \frac{1}{R}(k_\beta \cos^2 \theta + k_\zeta \sin^2 \theta) & -\frac{1}{R}(k_\beta - k_\zeta) \sin \theta \cos \theta \\ -\frac{1}{R}(k_\beta - k_\zeta) \sin \theta \cos \theta & \frac{1}{R}(k_\beta \sin^2 \theta + k_\zeta \cos^2 \theta) \end{bmatrix}$$

$$[K_{II}] = \begin{bmatrix} \frac{k_\beta}{1-R} & 0 \\ 0 & \frac{k_\zeta}{1-R} \end{bmatrix}$$

$$[K_{\text{eff}}] = \frac{1}{\Delta} \begin{bmatrix} k_\beta + R(k_\zeta - k_\beta) \sin^2 \theta & \frac{1}{2}R(k_\zeta - k_\beta) \sin 2\theta \\ \frac{1}{2}R(k_\zeta - k_\beta) \sin 2\theta & k_\zeta - R(k_\zeta - k_\beta) \sin^2 \theta \end{bmatrix}$$

$$\Delta = 1 + R(1 - R) \frac{(k_\beta - k_\zeta)^2}{k_\beta k_\zeta} \sin^2 \theta$$

3.3.2 Flexible Model

In this section the coupled flap and lag bending dynamics is studied. The blade is assumed as an elastic beam undergoing in-plane and out of plane bending motions. It is also assumed that the forces are applied along the principal axes and there is no structural coupling of bending motions.

Flap bending

- (a) IF: $m\ddot{w}(\rho) d\rho$ arm $(\rho - r)$ about r
- (b) CF: $m\Omega^2 \rho d\rho$ arm $w(\rho) - w(r)$
- (c) Cor F: $2m\Omega\dot{v}(\rho) d\rho$ arm $w(\rho) - w(r)$
- (d) AF: $F_z d\rho$ arm $(\rho - r)$

Taking moment at station r

$$M_x(r) = \int_r^R \{(F_z - m\ddot{w}(\rho))(\rho - r) - (m\Omega^2 \rho - 2m\Omega\dot{v})(w(\rho) - w(r))\} d\rho \quad (3.31)$$

Lag bending

- (a) IF: $m\ddot{v}(\rho) d\rho$ arm $(\rho - r)$ about r
- (b) CF: $m\Omega^2 \rho d\rho$ arm $r/\rho v(\rho) - v(r)$
- (c) Cor F₁: $2m\Omega\dot{v}$ arm $v(\rho) - v(r)$
- (d) Cor F₂: $2m\Omega \int_0^\rho (v'\dot{v}' + w'\dot{w}') d\rho$ arm $(\rho - r)$
- (e) AF: $F_x d\rho$ arm $(\rho - r)$

The force Cor F₂ is the Coriolis force caused by the radial shortening of the blade. The v and w are inplane and out of plane displacements producing a radial shortening of the blade length

$$-\frac{1}{2} \int_0^\rho (v'^2 + w'^2) d\rho$$

This causes radial inward velocity of the element

$$-\int_0^\rho (v'\dot{v}' + w'\dot{w}') d\rho$$

resulting in the coriolis force in the in-plane direction. Taking the lag bending moment at station r

$$M_z(r) = \int_r^R \left\{ (F_x - m\ddot{v}(\rho))(\rho - r) - m\Omega^2 \rho \left(v(\rho) \frac{r}{\rho} - v(r) \right) + 2\Omega\dot{v}m(v(\rho) - v(r)) - 2m\Omega \left(\int_0^\rho (v'\dot{v}' + w'\dot{w}') d\rho \right) (\rho - r) \right\} d\rho \quad (3.32)$$

Differentiate both $M_x(r)$ and $M_z(r)$ twice wrt r from Eqs. (31) and (32).

$$\frac{d^2 M_x}{dr^2} = \frac{d^2}{dr^2} \left(EI_x \frac{d^2 w}{dr^2} \right)$$

and

$$\frac{d^2 M_z}{dr^2} = \frac{d^2}{dr^2} \left(EI_z \frac{d^2 v}{dr^2} \right)$$

Using the Leibnitz theorem of integrations, the above equations become:

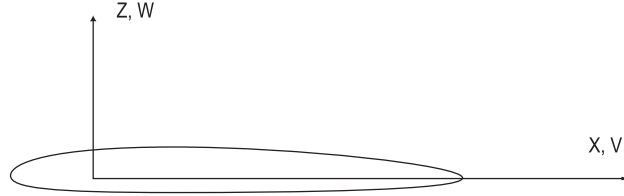
Flap bending Eq.:

$$\begin{aligned} \frac{d^2}{dr^2} \left(EI_x \frac{d^2 w}{dr^2} \right) + m\ddot{w} + \frac{d}{dr} \left(\frac{dw}{dr} \int_r^R 2m\Omega\dot{v} d\rho \right) \\ - \frac{d}{dr} \left(\frac{dw}{dr} \int_r^R m\Omega^2 \rho d\rho \right) = F_z \end{aligned} \quad (3.33)$$

Lag bending Eq.:

$$\begin{aligned} & \frac{d^2}{dr^2}(EI_z \frac{d^2 v}{dr^2}) + m\ddot{v} - m\Omega^2 v - \frac{d}{dr}(\frac{dv}{dr} \int_r^R m\Omega^2 \rho d\rho) \\ & + \frac{d}{dr}(2\Omega \frac{dv}{dr} \int_r^R \dot{v} m d\rho) + 2m\Omega \int_0^r (\frac{dv}{dr} \frac{d\dot{v}}{dr} + \frac{dw}{dr} \frac{d\dot{w}}{dr}) d\rho = F_x \end{aligned} \quad (3.34)$$

Let us consider an airfoil system



I_x = area moment of inertia about x-axis

$$= \int_{\text{section}} z^2 dA, \text{ in}^4$$

I_z = area moment of inertia about z axis

$$= \int_{\text{section}} x^2 dA, \text{ in}^4$$

E = Young's modulus of elasticity, lb/in²

v = bending deflection along x-axis, in

w = bending deflection along z-axis, in

m = mass per unit length, lb-sec²/in²

x,z = section principal axes

The flap and lag bending equations can be nondimensionalized by dividing through with $m_0\Omega^2 R$

Flap bending:

$$\begin{aligned} & \frac{d^2}{d\xi^2}(\frac{EI_x}{m_0\Omega^2 R^4} \frac{d^2 w}{d\xi^2}) + \frac{m}{m_0} \ddot{w} + \frac{d}{d\xi}(\frac{dw}{d\xi} \int_\xi^1 \frac{m}{m_0} 2 \dot{v} d\xi) - \frac{d}{d\xi}(\frac{dw}{d\xi} \int_\xi^1 \frac{m}{m_0} \xi d\xi) \\ & = \frac{F_z}{m_0\Omega^2 R} \end{aligned} \quad (3.35)$$

Lag bending:

$$\begin{aligned} & \frac{d^2}{d\xi^2}(\frac{EI_z}{m\Omega^2 R^4} \frac{d^2 v}{d\xi^2}) + (\ddot{v} - v) \frac{m}{m_0} - \frac{d}{d\xi}(\frac{dv}{d\xi} \int_\xi^1 \frac{m}{m_0} d\xi) + \frac{d}{d\xi}(2 \frac{dv}{d\xi} \int_\xi^1 \frac{m}{m_0} \dot{v} d\xi) \\ & + 2 \frac{m}{m_0} \int_0^\xi (\frac{dv}{d\xi} \frac{d\dot{v}}{d\xi} + \frac{dw}{d\xi} \frac{d\dot{w}}{d\xi}) d\xi = \frac{F_x}{m_0\Omega^2 R} \end{aligned} \quad (3.36)$$

where

$$v = v/R$$

$$w = w/R$$

$$\xi = r/R$$

Boundary conditions

For hingeless blades

$$\text{@ } r = 0 \quad v = w = 0$$

$$\frac{dv}{dr} = \frac{dw}{dr} = 0 \quad (\text{fixed})$$

$$\text{@ } r = R \quad EI_z \frac{d^2 v}{dr^2} = EI_x \frac{d^2 w}{dr^2} = 0$$

$$\frac{d}{dr}(EI_z \frac{d^2 v}{dr^2}) = \frac{d}{dr}(EI_x \frac{d^2 w}{dr^2}) = 0 \quad (\text{free})$$

Using these boundary conditions, the governing coupled equations for flap bending and lag bending can be solved.

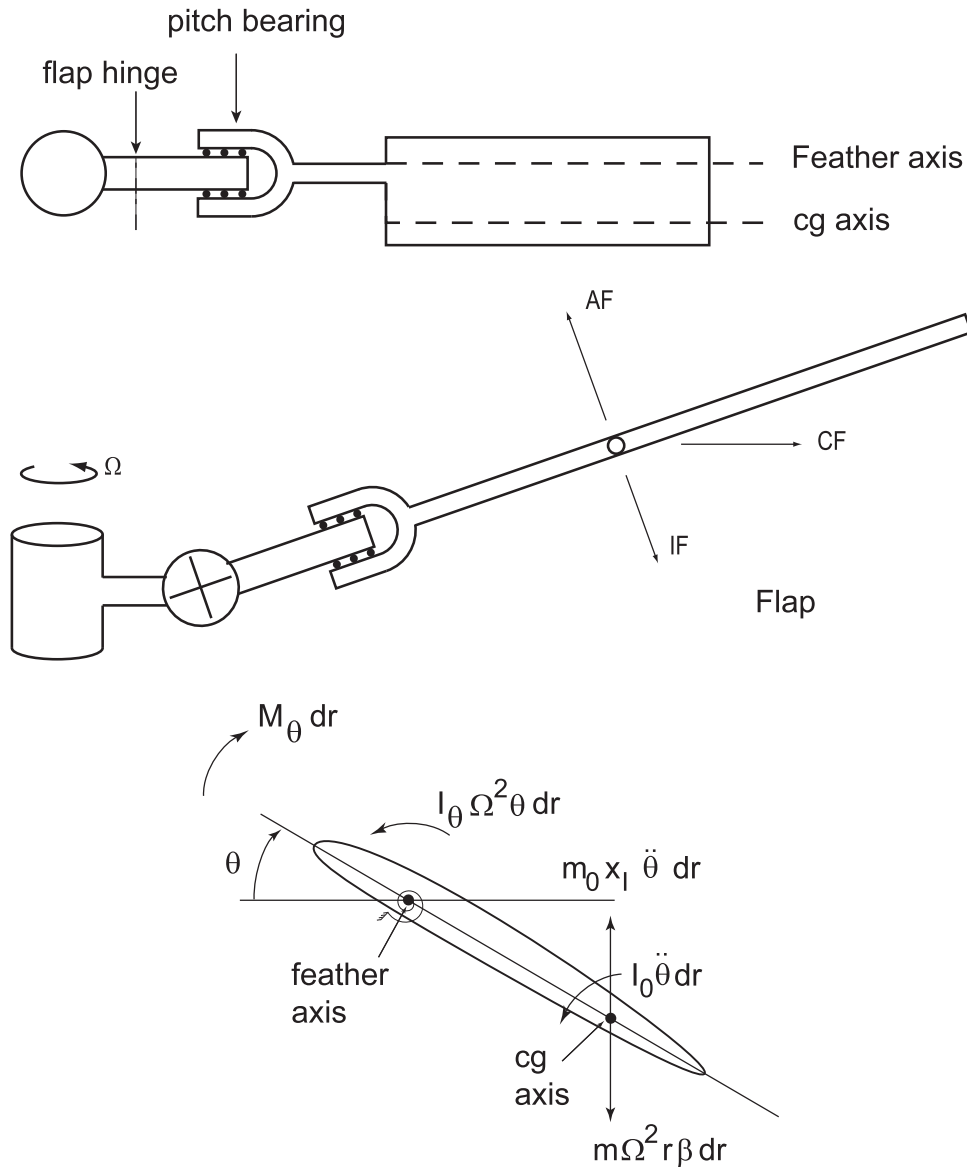
If there is a pitch change there is another coupling term called structural coupling which needs to be included. This effect will be included later on for coupled flap bending, lag bending and torsion equations.

3.4 Coupled Pitch-Flap Dynamics

The rigid and flexible blade models are discussed below

3.4.1 Rigid Model

The blade is assumed rigid and it undergoes two degrees of motion, flap and feather rotations. This model represents an articulated blade with flexible control system. It is also assumed that the pitch bearing is outboard for the flap hinge. Also it is assumed that the flap motion does not introduce pitch change, which means pitch-flap coupling ' δ_3 ' is neglected.



Flap mode forces

- (a) IF: $m(r-e)\ddot{\beta}$ dr arm $(r-e)$ about flap hinge
 $-mx_I\ddot{\theta}$ dr arm $(r-e)$
 (b) CF: $m\Omega^2 r$ dr arm $((r-e)\beta - x_I\theta)$
 (c) AF: F_β dr arm $(r-e)$
 (d) SM: $k_\beta(\beta - \beta_p)$

Pitch mode forces

- (a) IF: $mx_I\ddot{\theta}$ dr arm x_I about feathering axis
 $I_0\ddot{\theta}$ dr torque
 $-m(r-e)\ddot{\beta}$ dr arm x_I
 (b) CF: $I_\theta\Omega^2\theta$ dr torque
 $-m\Omega^2 r\beta$ dr arm x_I
 (c) AF: M_θ dr torque
 (d) SM: $k_\theta(\theta - \theta_{\text{con}})$ torque

Taking moment of forces about flap hinge

$$\int_e^R \{m(r-e)^2\ddot{\beta} - mx_I(r-e)\ddot{\theta} + m\Omega^2 r(r-e)\beta - m\Omega^2 x_I\theta - F_\beta(r-e)\} dr + k_\beta(\beta - \beta_p) = 0$$

Moments about pitch bearing

$$\int_{e_\theta}^R \{I_0\ddot{\theta} + mx_I^2\ddot{\theta} - m(r-e)x_I\ddot{\beta} + I_\theta\Omega^2\theta - M_\theta + m\Omega^2 r\beta x_I\} dr + k_\theta(\theta - \theta_{\text{con}}) = 0$$

Writing these equations in nondimensional form

$$\beta^{**} + \nu_\beta^2 \beta - I_x^*(\theta^{**} + \theta) = \gamma \overline{M}_\beta + \frac{\omega_{\beta 0}^2}{\Omega^2} \beta_p \quad (3.37)$$

$$I_f^*(\beta^{**} + \nu_\beta^2 \theta) - I_x^*(\beta^{**} + \beta) = \gamma \overline{M}_\theta + I_f^* \frac{\omega_{\theta 0}^2}{\Omega^2} \theta_{\text{con}} \quad (3.38)$$

where ν_β and ν_θ are respectively rotating flap and feather natural frequencies and

$$I_x^* = \frac{I_x}{I_b} = \int_{e_\theta}^R x_I r m dr / I_b$$

$$\overline{M}_\beta = \frac{1}{\rho a c \Omega^2 R^4} \int_e^R F_\beta(r-e) dr$$

$$\overline{M}_\theta = \frac{1}{\rho a c \Omega^2 R^4} \int_{e_\theta}^R M_\theta dr$$

and e_θ is the pitch bearing offset from the rotation axis. The pitch-flap equations are coupled through inertial and centrifugal force terms. If cg and feather axis are coincident, I_x^* becomes zero and these coupling terms are eliminated.

For uniform blades

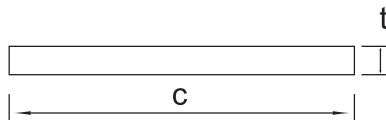
$$I_x^* = x_I \frac{mR^2}{2} / \frac{mR^3}{3} = \frac{3x_I}{2R}$$

Typically $x_I = .1c$ and $\frac{c}{R} = 20$

$$I_x^* = \frac{3}{400} = .0075 (\sim \epsilon^2)$$

$$I_f^* = \frac{I_f}{I_b}$$

Let us consider a rectangular strip



$$I_f = \rho \frac{c^3 t}{12} R$$

$$= \frac{mc^2}{12} R$$

$$I_f^* = \frac{1}{4} \left(\frac{c}{R}\right)^2 = \frac{1}{1600} \sim (\epsilon^2 \text{ to } \epsilon^3)$$

Let us examine now flap and pitch equations. In the flap equations, the I_x^* is of the order of ϵ^2 where as other terms are of order unity. The coupling has a negligible influence in the flap equation. In the pitch equation, the I_x^* is of the order of ϵ^2 and the I_f^* is of the same order. Therefore the coupling term plays an important role in the feather equation. One can write it as

$$\beta^{**} + \nu_\beta^2 \beta = \gamma \overline{M}_\beta + \frac{\omega_{\beta 0}^2}{\Omega^2} \beta_p \quad (3.39)$$

$$I_f^* (\theta^{**} + \nu_\theta^2 \theta) - (\beta^{**} + \beta) = \gamma \overline{M}_\theta + I_f^* \frac{\omega_{\theta 0}^2}{\Omega^2} \theta_{\text{con}}$$

Example: 3.2

Write the equation of motion and the boundary conditions for flap bending and elastic twist of a rotating blade with a flap hinge and pitch bearing located at a distance e from the rotation axis.

Flap Bending equation

$$(EIw'')'' - \left[\left(\int_r^R m\Omega^2 \rho d\rho \right) w' \right]' + m\ddot{w} - mx_I \ddot{\theta}$$

$$+ [(r\theta)' \int_r^R m\Omega^2 x_I d\rho]' = f_z(r, t)$$

Boundary conditions

$$\text{@ } r = e \quad w = 0, \quad EIw'' = k_\beta w' \quad (k_\beta = \text{bending spring at hinge})$$

$$\text{@ } r = R \quad EIw'' = 0, \quad (EIw''')'' = 0$$

Torsion Equation

$$-(GJ\theta')' + I_\theta \ddot{\theta} + I_\theta \Omega^2 \theta - mx_I \ddot{w}$$

$$+ r[w' \int_r^R m\Omega^2 x_I d\rho]' = M_\theta(r, t)$$

Boundary conditions

$$\text{@ } r = e \quad GJ\theta' = -k_\theta (\theta - \theta_{\text{con}})$$

($k_\theta = \text{control spring stiffness}$)

$$\text{@ } r = R \quad GJ\theta' = 0$$

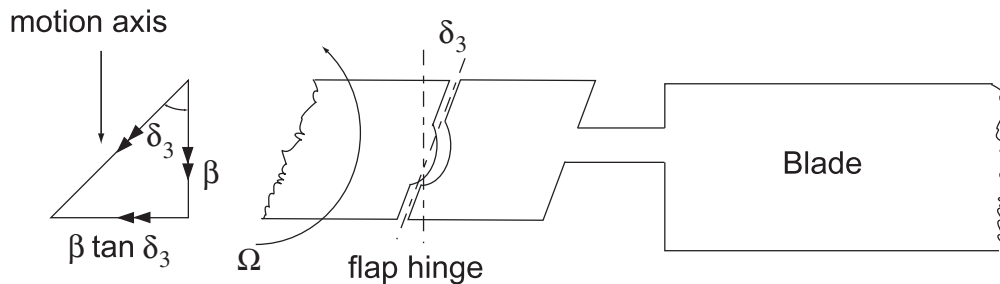
3.4.2 Kinematic Pitch-Flap Coupling: δ_3 Effect

Pitch-flap coupling is a kinematic feedback of the flapping displacement to the blade pitch motion.

$$\Delta\theta = -k_{p\beta}\beta \tag{3.40}$$

where $k_{p\beta}$ is the pitch-flap coupling and is positive when the flap up motion results in a nose down pitch motion. This will act as an aerodynamic spring for the flap mode because the lower pitch means less lift. The pitch-flap coupling plays an important role in flight stability and handling qualities of the vehicle as well as aeroelastic stability of the blade. There are many ways to achieve pitch-flap coupling.

(a) Skewed Flapping Hinge



If flap hinge is not normal to blade axis the flap motion will be accompanied with the pitch change of the blade. Let us say there is flap motion β then there will be reduction in pitch by

$$\Delta\theta = -\tan \delta_3\beta$$

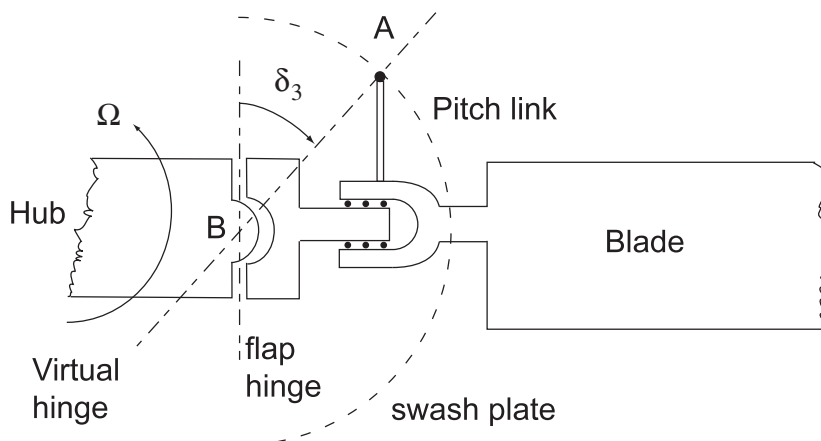
therefore

$$k_{p\beta} = \tan \delta_3$$

where δ_3 is skewing of the flap hinge in radians. The negative pitch-flap coupling can be achieved by skewing the flap hinge in the opposite direction.

(b) Location of pitch link

The second way to introduce pitch-flap coupling is through the pitch control system.



The pitch setting of the blade is obtained by vertical motion of the pitch link which is connected at one end to the moving part of the swashplate and at the end to the blade through the pitch horn. If the position of pitch link (A) is not in line with the flap hinge, it will form a virtual hinge. Now

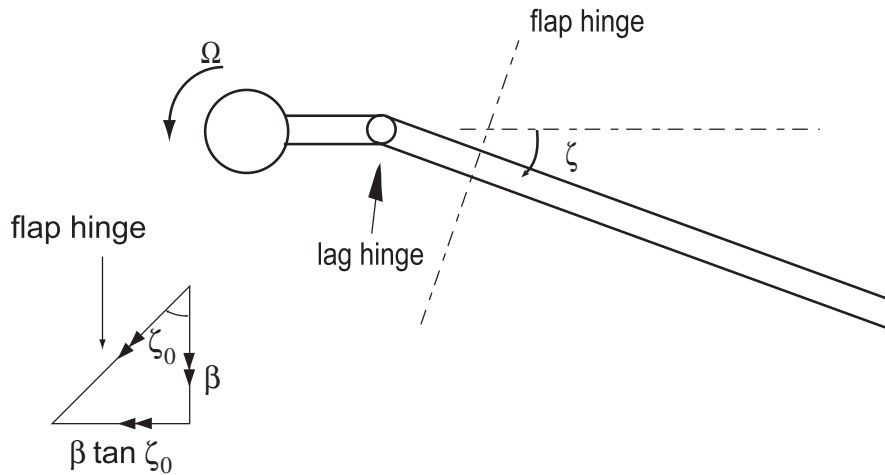
if the blade flaps, it will result into a change in the pitch producing pitch-flap coupling. This is possible only if the pitch bearing is outboard of the flap hinge.

$$k_{p\beta} = \tan \delta_3 \tag{3.41}$$

The negative pitch-flap coupling can be obtained by locating the pitch link on the other side of the blade.

(c) Position of Lag Hinge

If flap hinge is outboard of lag hinge, this will result in the δ_3 effect due to steady lag deflection.



The flap motion results in a change of pitch, since the effective flap hinge gets skewed.

$$\delta_3 = \zeta_0$$

This type of pitch-flap coupling is possible even for hingeless blades.

(d) Using Feedback System

Any amount of pitch-flap coupling can be introduced using a feedback system.

$$\Delta\theta = -k_{p\beta} \beta$$

\swarrow feedback on pitch link \downarrow gain \searrow signal from the pick up on the blade

3.4.3 δ_3 Effect in Hover

Let us examine the rigid flap equation in hovering flight. For a constant pitch blade with uniform inflow and without pitch-flap coupling, the equation of motion is

$$\beta^{**} + \frac{\gamma}{8} \beta^* + \nu_{\beta}^2 \beta = \frac{\gamma}{8} \theta - \frac{\gamma \lambda}{6}$$

With pitch-flap coupling, the blade pitch gets modified

$$\theta = \theta + \Delta\theta$$

where

$$\Delta\theta = -k_{p\beta} \beta$$

So, the new flapping equation becomes

$$\beta^{**} + \frac{\gamma}{8} \beta^* + (\nu_\beta^2 + \frac{\gamma}{8} k_{p\beta})\beta = \frac{\gamma}{8}\theta - \frac{\gamma\lambda}{6}$$

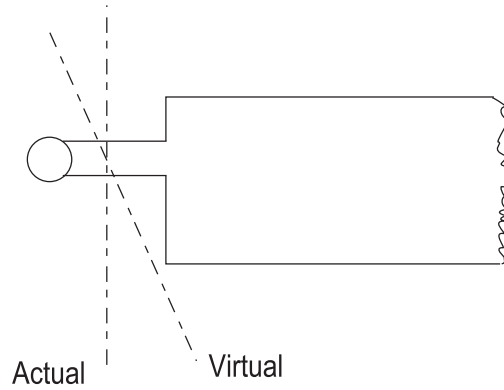
The new rotating flap frequency, ν_{β_e}

$$\nu_{\beta_e}^2 = \nu_\beta^2 + \frac{\gamma}{8} k_{p\beta} \quad (3.42)$$

The pitch-flap coupling has a direct effect on rotating flap frequency. Through a negative pitch-flap coupling, it is possible to reduce the rotating flap frequency below one.

Example: 3.3

Through the skewing of the flap hinge axis, the rotating flap frequency of a blade is reduced by 25%. Calculate the skew angle for a rotor with a Lock number of 8, and the hinge offset is given as 6% of the blade length.



Flap frequency with pitch-flap coupling

$$\nu_{\beta_e}^2 = \nu_\beta^2 + \frac{\gamma}{8} k_{p\beta}$$

$$\nu_\beta^2 = 1 + \frac{3}{2} \times .06 = 1.09$$

$$\nu_{\beta_e} = .75\nu_\beta$$

$$\begin{aligned} k_{p\beta} &= -1.09\left(1 - \frac{9}{16}\right) = -.4769 \\ &= \tan \delta_3 \end{aligned}$$

$$\delta_3 = 25.5^\circ$$

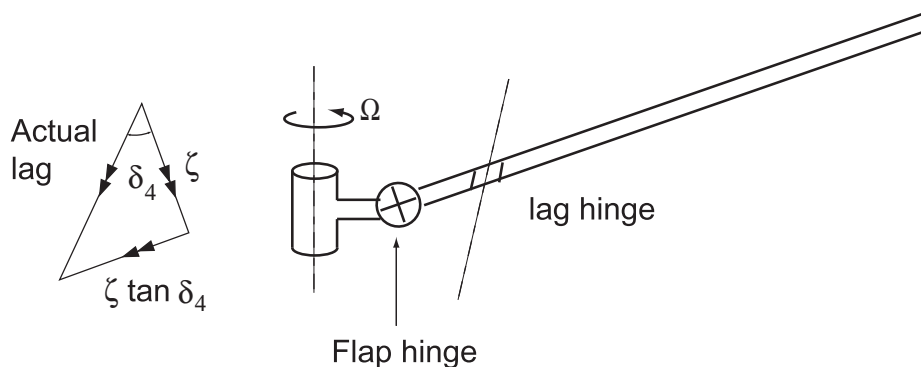
3.4.4 Kinematic Pitch-Lag Coupling: δ_4 Effect

Pitch-lag coupling is a kinematic feedback of lag displacement to the blade pitch motion

$$\delta\theta = -k_{p\zeta}\zeta \quad (3.43)$$

where $k_{p\zeta}$ is the pitch-lag coupling and is positive when lag back produces a nose down pitch motion. The pitch-lag coupling has considerable influence on aeroelastic stability of the blades. Again there are many ways to achieve pitch-lag coupling.

(a) Skewed Lag Hinge



If lag hinge is not normal to the blade axis, the lag motion will be accompanied with the pitch change of the blade. If ζ is the lag displacement then, the reduction of blade pitch will be

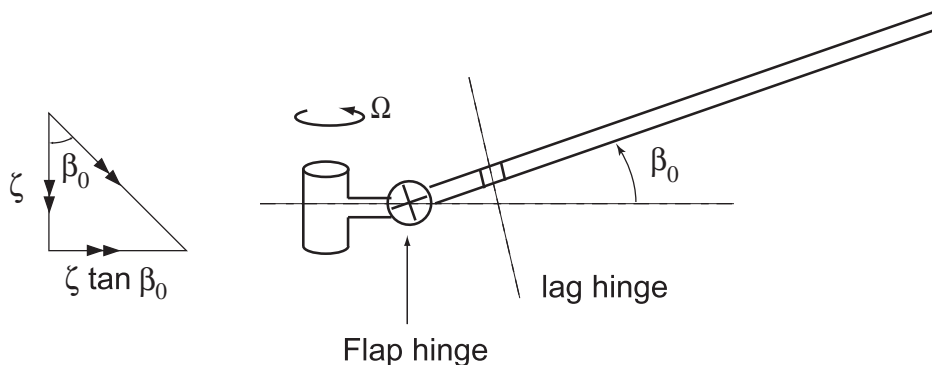
$$\Delta\theta = -\tan \alpha_4 \zeta$$

Therefore

$$k_{p\zeta} = \tan \alpha_4 \tag{3.44}$$

where δ_4 is skewing of lag hinge in radians. The negative pitch-lag coupling can be achieved by skewing the lag hinge in the opposite direction.

(b) Position of Flap Hinge



If lag hinge is outboard of flap hinge this will result into α_4 effect due to steady flap deflection.

$$\alpha_4 = -\beta_0$$

(c) Pitch Control Linkage

Through a creative design of pitch control linkages at the root end of blades, desired pitch-lag coupling can be introduced.

(d) Using Feedback System

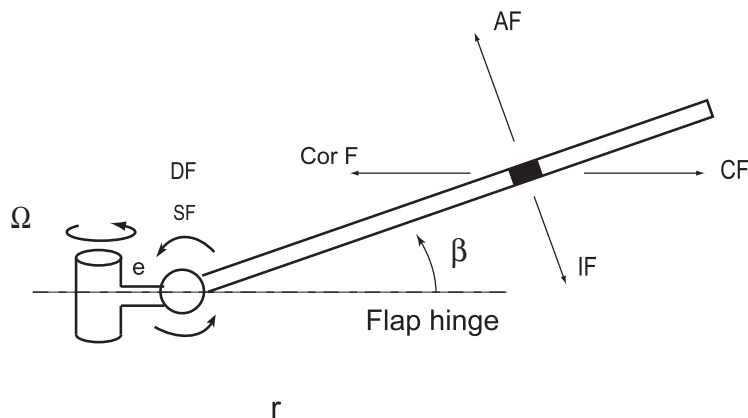
Any amount of pitch-lag coupling can be introduced using a feedback system

$$\begin{array}{ccccc} \Delta\theta & = & -k_{p\zeta} & \zeta & \\ \swarrow & & \downarrow & \swarrow & \\ \text{feedback on} & & \text{gain} & & \text{signal from the} \\ \text{pitch link} & & & & \text{pickup on the blade} \end{array}$$

3.5 Rigid Flap-Lag-Torsion

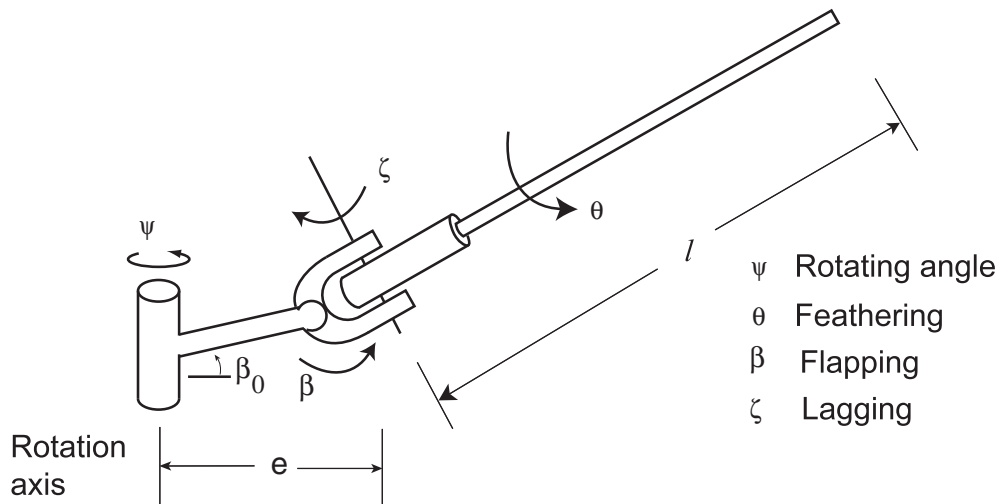
The blade is assumed rigid and it undergoes three degrees of motion, flap, lag and feather rotations about three hinges. The hinge sequence assumed here is, from the rotation axis the flap hinge is followed by lag hinge and then at the outboard is pitch bearing. with the changed hinge sequence, there will be modification in some of the nonlinear terms. This model not only represents articulated blades but also can be a good approximation of hingeless blades for dynamic analysis. For simplicity of analysis, it is assumed that all the hinges are located at the same place. The important nonlinear terms up to second order are retained. Let us examine the element forces in each mode of vibration.

Flap Mode



- (a) IF: inertia force $m(r - e)\ddot{\beta} dr$ arm $(r - e)$
 $-m x_I \dot{\theta}^2 dr$ arm $(r - e)$
- (b) CF: centrifugal force $m\Omega^2 r dr$ arm $(r - e)\beta$
 $-m\Omega^2 r dr$ arm $x_I \theta$

BLADE CONFIGURATION



- (c) CorF: coriolis force $2m\Omega\dot{\zeta}$ arm $(r - e)\beta$
- (d) AF: aerodynamic force $F_\beta dr$ arm $(r - e)$
- (e) SF: spring force $k_\beta(\beta - \beta_p)$ moment
- (f) DF: damping force $c_\beta\dot{\beta}$ moment

where

x_I = chordwise offset of cg behind feathering axis

β_p = precone angle

k_β = flap bending spring at hinge

c_β = damping constant

$$= 2\zeta\omega_{\beta 0}I_\beta$$

ζ_β = viscous damping ratio in flap mode

$\omega_{\beta 0}$ = non-rotating flap frequency, rad/sec

I_β = mass moment of inertia about flap hinge

Taking moment of forces about flap hinge

$$\int_e^R \{m(r-e)^2\ddot{\beta} - mx_I(r-e)\ddot{\theta} + m\Omega^2 r(r-e)\beta - m\Omega^2 rx_I\theta - 2m\Omega(r-e)\beta\dot{\zeta} - F_\beta(r-e)\} dr + k_\beta(\beta - \beta_p) + 2\zeta_\beta\omega_{\beta 0}I_\beta\dot{\beta} = 0$$

Assuming $I_\beta \simeq I_b$ where I_b is the total flap inertia. Dividing the above equation by $I_b\Omega^2$ gives the flap equation in nondimensional form.

$$\beta^{**} + \nu_\beta^2\beta + 2\omega_{\beta 0}\zeta_\beta\dot{\beta} - 2\beta\zeta^* - I_x^*(\theta^{**} + \theta) = \gamma\overline{M}_\beta + \frac{\omega_{\beta 0}^2}{\Omega^2}\beta_p \quad (3.45)$$

where ν_β is the rotating flap frequency,

$$\nu_\beta^2 = 1 + \frac{e \int_e^R m(r-e) dr}{I_\beta} + \frac{\omega_{\beta 0}^2}{\Omega^2} \quad \text{per rev.}$$

and

$$I_x^* = \frac{I_x}{I_b} = \frac{\int_e^R mx_I r dr}{I_b}$$

For uniform blades

$$\nu_\beta^2 = 1 + \frac{3}{2} \frac{e}{R-e} + \frac{\omega_{\beta 0}^2}{I_b}$$

and

$$I_x^* = \frac{3}{2} x_I/R$$

The γ is the Lock number,

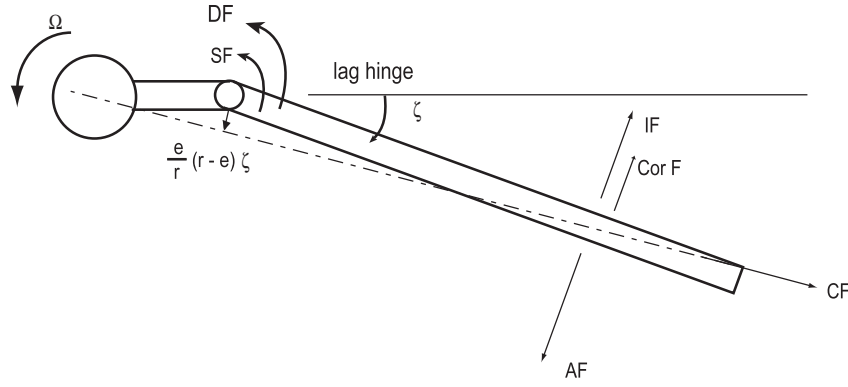
$$\frac{\rho ac R^4}{I_b}$$

and

$$\overline{M}_\beta = \frac{1}{\rho ac R^4 \Omega^2} \int_e^R F_\beta(r-e) dr$$

Also note that $\beta^* = \frac{\partial \beta}{\partial \psi}$ and $\psi = \Omega t$.

II. Lag Mode



- (a) IF: $m(r-e)\ddot{\zeta} dr$ arm $(r-e)$ about lag hinge
 (b) CF: $m\Omega^2 r dr$ arm $\frac{e}{r}(r-e)\zeta$
 (c) CorF: $2m\Omega(r-e)\dot{\beta}\beta dr$ arm $(r-e)$ $-mx_I\dot{\theta}\beta dr$ arm $(r-e)$
 (d) AF: $F_\zeta dr$ arm $(r-e)$
 (e) SF: $k_\zeta\zeta$ moment
 (f) DF: $2I_\zeta\omega_{\zeta 0}\zeta_L\dot{\zeta}$ moment

where

ζ_L = viscous damping ratio in lag mode

$\omega_{\zeta 0}$ = non-rotating lag frequency

Taking moment of forces about lag hinge

$$\int_e^R \{m(r-e)^2\ddot{\zeta} + m\Omega^2 e(r-e)\zeta + 2m\Omega(r-e)^2\dot{\beta}\beta - mx_I(r-e)\dot{\theta}\beta - F_\zeta\} dr + k_\zeta\zeta + 2I_\zeta\omega_{\zeta 0}\zeta_L\dot{\zeta} = 0$$

Assuming $I_\zeta \simeq I_b$ and dividing through $I_b\Omega^2$ gives the lag equation in nondimensional form

$$\zeta^{**} + \nu_\zeta^2\zeta + 2\frac{\omega_{\zeta 0}}{\Omega}\zeta_L\dot{\zeta} + 2\beta\beta^* - I_x^*(2\beta\dot{\theta}^*) = \gamma\overline{M}_\zeta \quad (3.46)$$

where ν_ζ is the rotating frequency

$$\nu_\zeta^2 = \frac{e \int_e^R m(r-e) dr}{I_b} + \frac{\omega_{\zeta 0}^2}{\Omega^2}$$

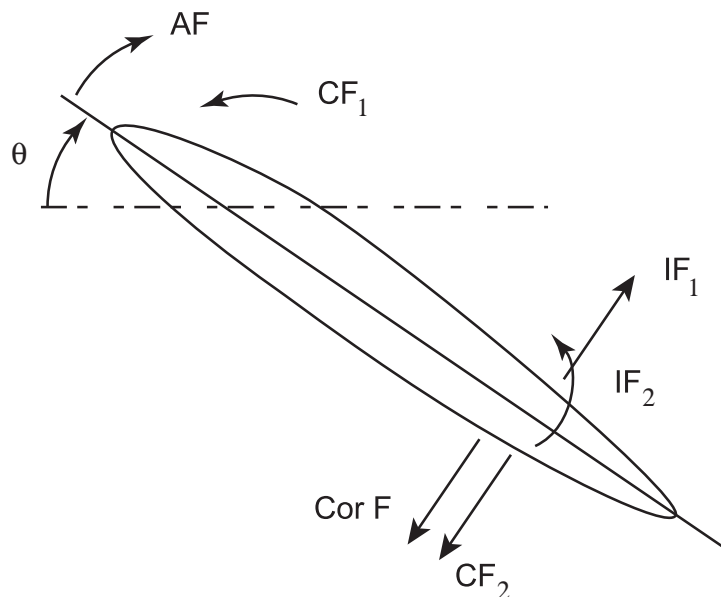
For uniform blades

$$\nu_\zeta^2 = \frac{3}{2} \frac{e}{R-e} + \frac{\omega_{\zeta 0}^2}{\Omega^2}$$

and also $I_x^* = \frac{3}{2}x_I/R$. The aerodynamic moment is

$$\overline{M}_\zeta = \frac{1}{\rho ac\Omega^2 R^4} \int_e^R F_\zeta(r-e) dr$$

III. Torsion Mode



- (a) $IF_1: mx_I \ddot{\theta} dr$ arm x_I about feathering axis
 $-m(r-e)\ddot{\beta} dr$ arm x_I
 $IF_2: I_0 \ddot{\theta} dr$ moment
- (b) $CF_1: I_\theta \Omega^2 \theta dr$ moment
 $CF_2: mr \Omega^2 \beta dr$ arm x_I
- (c) $Cor F: 2m\Omega r \dot{\zeta} \beta$ arm x_I
- (d) $AF: M_\theta dr$ moment
- (e) $SF: k_\theta(\theta - \theta_{con})$ moment
- (f) $DF: 2I_f \omega_{\theta 0} \zeta_\theta \dot{\theta}$ moment

where

$$\overline{M}_\theta = \frac{1}{\rho ac \Omega^2 R^4} \int_e^R M_\theta dr$$

and the ν_θ is the rotating torsion frequency.

$$\nu_\theta^2 = 1 + \frac{\omega_{\theta 0}^2}{\Omega^2}$$

The flap, lag and torsion equations can be rewritten as

$$\begin{aligned} & \begin{bmatrix} 1 & 0 & -I_x^* \\ 0 & 1 & 0 \\ -I_x^* & 0 & I_f^* \end{bmatrix} \begin{bmatrix} \beta \\ \zeta \\ \theta \end{bmatrix} + \begin{bmatrix} 2\frac{\omega_{\beta 0}}{\Omega} \zeta_\beta & -2\beta & 0 \\ 2\beta & 2\frac{\omega_{\zeta 0}}{\Omega} \zeta_L & -2\beta I_x^* \\ 0 & 2\beta I_x^* & 2\frac{\omega_{\theta 0}}{\Omega} \zeta_\theta I_f^* \end{bmatrix} \begin{bmatrix} \beta \\ \zeta \\ \theta \end{bmatrix} \\ & \text{inertia} \qquad \qquad \qquad \text{damping} \\ & + \begin{bmatrix} \nu_\beta^2 & 0 & -I_x^* \\ 0 & \nu_\zeta^2 & 0 \\ -I_x^* & 0 & -I_f^* \nu_\theta^2 \end{bmatrix} \begin{bmatrix} \beta \\ \zeta \\ \theta \end{bmatrix} = \gamma \begin{bmatrix} \overline{M}_\beta \\ \overline{M}_\zeta \\ \overline{M}_\theta \end{bmatrix} + \begin{bmatrix} \frac{\omega_{\beta 0}^2}{\Omega^2} \beta_p \\ 0 \\ I_f^* \frac{\omega_{\theta 0}^2}{\Omega^2} \theta_{con} \end{bmatrix} \end{aligned} \quad (3.47)$$

These equations are coupled inertially. The inertia and stiffness matrices are symmetric. The damping matrix consists of two parts. The viscous damping terms are diagonal terms whereas

coriolis force terms are antisymmetric. Also, the coriolis force terms are nonlinear in nature, but these are important coupling terms.

The complete nonlinear equations for this hinge sequence are also available (Chopra (83)). With changed hinge sequence one will get a new set of equations with different coupling terms. For example, Chopra and Dugundji (1979) derived nonlinear equations for a blade with pitch bearing inboard, followed by flap hinge and the lag hinge outboard.

3.6 Flexible Flap-Lag-Torsion-extension

An appropriate model for rotor blade is to assume it as an elastic beam undergoing flap bending, lead-lag bending and elastic torsion. These motions are coupled through inertial and aerodynamic forces. The derivation of the equations of motion for the coupled flap-lag-torsion blade is lengthy and involved. Many authors have derived these equations with different approximations in mind. Among notable works are Houbolt and Brooks (1958), Hodges and Dowell (1974), and Johnson (1977).

3.6.1 Second order non-linear beam model

The blade is idealized into a twisted beam. Due to pitch and twist distribution, there is a structural coupling between the out of plane bending and inplane bending. The derivation details are not given here. The equations of motion are given here for uniform blades.

u	axial deflection, in
v	lead-lag deflection, in
w	flap deflection, in
ϕ	elastic twist, rad
θ	blade pitch, rad

3.6.2 Equations for uniform beams

Assumptions

1. Uniform blade
2. Slender beam
3. Moderate slopes (terms 2nd order retained)
4. No droop, sweep or torque offset
5. Tension axis lies on elastic axis

$$x_I = \text{chordwise offset of cg from ea} \quad (+ \text{ ve aft})$$

$$EI_y = \text{flapwise stiffness, lb - in}^2$$

$$EI_z = \text{chordwise stiffness, lb-in}^2$$

$$GJ = \text{torsional stiffness, lb-in}^2$$

$$k_A = \text{polar radius of gyration, in}$$

$$m = \text{mass per unit length, lb-sec}^2/\text{in}^2$$

$$mk_{m_1}^2 = \text{flapwise principal mass moment of inertia}$$

$$mk_{m_2}^2 = \text{chordwise principal mass moment of inertia}$$

$$mk_m^2 = \text{torsional mass moment of inertia}$$

Flap Equation:

$$\begin{aligned} & [EI_y + (EI_z - EI_y) \sin^2 \theta] w^{IV} + \frac{1}{2} (EI_z - EI_y) \sin 2\theta v^{IV} \\ & + (EI_z - EI_y) [\cos 2\theta (\phi v'')'' + \sin 2\theta (\phi w'')''] - \frac{1}{2} m \Omega^2 [w' (R^2 - r^2)]' \\ & + m \ddot{w} + 2m \Omega \beta_p \dot{v} - 2m \Omega (w' \int_r^R \dot{v} dx) - m x_I \ddot{\phi} \\ & + \{m x_I [\Omega^2 r \phi \cos \theta + 2\Omega \dot{v} \sin \theta]\}' = L_w - m \Omega^2 r \beta_p \end{aligned}$$

Lag Equation:

$$\begin{aligned}
& [EI_z - (EI_z - EI_y) \sin^2 \theta] v^{IV} + \frac{1}{2} (EI_z - EI_y) \sin 2\theta w^{IV} \\
& + (EI_z - EI_y) [-\sin 2\theta (\phi v'')'' + \cos 2\theta (\phi w'')''] - \frac{1}{2} m \Omega^2 [v'(R^2 - r^2)]' \\
& + m\ddot{v} - m\Omega^2 v - 2m\Omega\beta_p \dot{w} - 2m\Omega \int_0^r (v'\dot{v}' + w'\dot{w}') dr \\
& - 2m\Omega (v' \int_r^R \dot{v} dx)' + mx_I \ddot{\phi} \sin \theta + 2m\Omega x_I (\dot{v} \cos \theta + \dot{w} \sin \theta) \\
& - m\Omega^2 x_I \sin \theta \phi = L_v
\end{aligned}$$

Torsion Equation:

$$\begin{aligned}
& -GJ\phi'' + \frac{1}{2} (EI_z - EI_y) [(w''^2 - v''^2) \sin 2\theta + v'' w'' \cos 2\theta] \\
& - \frac{1}{2} m \Omega^2 k_A^2 [\phi'(R^2 - r^2)]' + mk_m^2 \ddot{\phi} + m\Omega^2 (k_{m_2}^2 - k_{m_1}^2) \phi \cos 2\theta \\
& - mx_I [\Omega^2 r (w' \cos \theta - v' \sin \theta) - (\ddot{v} - \Omega^2 v) \sin \theta + \ddot{w} \cos \theta] \\
& = M_\phi - \frac{1}{2} m \Omega^2 (k_{m_2}^2 - k_{m_1}^2) \sin 2\theta
\end{aligned}$$

3.6.3 Detailed model for non-uniform beams

The rotor blades are modeled as long, slender, homogeneous, isotropic beams undergoing axial, flap, lag and torsion deformations. The deformations can be moderate as the model includes geometric non-linearities up-to second order. Radial non-uniformities of mass, stiffness, twist, etc., chordwise offsets of mass centroid (center of gravity) and area centroid (tension axis) from the elastic axis, precone, and warp of the cross section are included. The model follows the Hodges and Dowell formulation (1974) while treating elastic torsion and elastic axial deformation as quasi-coordinates based on Ormiston (1980). The model assumes a straight blade. Modeling refinements required to incorporate structural sweep and droop were first treated by Celi and Friedmann (1992), and Kim and Chopra (1995). The governing equations and their derivations can remain same, the swept and drooped elements can be formulated using additional coordinate transformations and a modified finite element assembly procedure. The following derivation is taken from Datta (2004). Details of the validation can be found in Datta and Chopra (2006).

The equations of motion are developed using Hamilton's Principle, a statement of the Principle of Least Action. The governing partial differential equations can be solved using finite element method in time and space. The finite element method provides flexibility in the implementation of boundary conditions for modern helicopter rotors. For example, specialized details like blade root pitch flexibility (pitch link stiffness), pitch damping, elastomeric bearing stiffness and damping can be incorporated within a finite element model.

3.6.4 Blade Coordinate Systems

There are 4 coordinate systems of interest, the hub-fixed system, (X_H, Y_H, Z_H) with unit vectors $\hat{I}_H, \hat{J}_H, \hat{K}_H$, the hub-rotating system, (X, Y, Z) with unit vectors $\hat{I}, \hat{J}, \hat{K}$, the undeformed blade coordinate system, (x, y, z) with unit vectors $\hat{i}, \hat{j}, \hat{k}$ and the deformed blade coordinate system, (ξ, η, ζ) with the unit vectors $\hat{i}_\xi, \hat{j}_\eta, \hat{k}_\zeta$. These frames of references are denoted as H, R, U and D respectively. The hub-rotating coordinate system is rotating at a constant angular velocity $\Omega \hat{K}$ with respect to the hub-fixed coordinate system. The transformation between the hub-fixed system

and the hub-rotating system is defined as

$$\begin{Bmatrix} \hat{I} \\ \hat{J} \\ \hat{K} \end{Bmatrix} = \begin{bmatrix} \cos \psi & \sin \psi & 0 \\ -\sin \psi & \cos \psi & 0 \\ 0 & 0 & 1 \end{bmatrix} \begin{Bmatrix} \hat{I}_H \\ \hat{J}_H \\ \hat{K}_H \end{Bmatrix} = \mathbf{T}_{RH} \begin{Bmatrix} \hat{I}_H \\ \hat{J}_H \\ \hat{K}_H \end{Bmatrix} \quad (3.48)$$

where the azimuth angle, ψ , equals Ωt . The undeformed blade coordinate system is at a precone angle of β_p with respect to the hub-fixed system. The transformation between the undeformed blade coordinate system and the hub-fixed system is defined as

$$\begin{Bmatrix} \hat{i} \\ \hat{j} \\ \hat{k} \end{Bmatrix} = \begin{bmatrix} \cos \beta_p & 0 & \sin \beta_p \\ 0 & 1 & 0 \\ -\sin \beta_p & 0 & \cos \beta_p \end{bmatrix} \begin{Bmatrix} \hat{I} \\ \hat{J} \\ \hat{K} \end{Bmatrix} = \mathbf{T}_{UR} \begin{Bmatrix} \hat{I} \\ \hat{J} \\ \hat{K} \end{Bmatrix} \quad (3.49)$$

The transformation between the undeformed blade coordinate system and the deformed blade coordinate system remains to be determined.

3.6.5 Blade Deformation Geometry

Consider a generic point P on the undeformed blade elastic axis. The orientation of a frame consisting of the axes normal to and along principle axes for the cross section at P defines the undeformed coordinate system (x, y, z) . When the blade deforms, P reaches P' . The orientation of a frame consisting of the axes normal to and along principle axes for the cross section at P' defines the deformed coordinate system (ξ, η, ζ) . Figure 3.1 shows the undeformed and deformed coordinate systems. Adequate description of the deformed blade requires in general a total of six variables : three translational variables from P to P' , u, v, w along x, y, z , and three rotational variables from (x, y, z) system to (ξ, η, ζ) system, and any out of plane deformations of the cross section, e.g., warp. These out of plane deformations are neglected, which results in plane sections remaining plane after deformation i.e., the Euler-Bernoulli beam assumption. The Euler-Bernoulli assumption leads to a further simplification - two of the three angles can be expressed as derivatives of the deflection variables. Thus four deformation variables - three deflections u, v, w and one rotational angle, completely determine the deformed geometry. The definition of this rotation angle - the angle of elastic twist is described below.

The coordinate transformation matrix between the undeformed system and the deformed system is defined by the direction cosines of (ξ, η, ζ) with respect to (x, y, z) , where x is tangent to the elastic axis of the undeformed blade and ξ is tangent to the elastic axis of the deformed blade. The transformation matrix can be written as

$$\begin{Bmatrix} \hat{i}_\xi \\ \hat{j}_\eta \\ \hat{k}_\zeta \end{Bmatrix} = \mathbf{T}_{DU} \begin{Bmatrix} \hat{i} \\ \hat{j} \\ \hat{k} \end{Bmatrix} \quad (3.50)$$

where \mathbf{T}_{DU} can be described as a function of three successive angular rotations in space required to align (x, y, z) along (ξ, η, ζ) . The two intermediate orientations can be described as (x_1, y_1, z_1) and (x_2, y_2, z_2) with unit vectors $(\hat{i}_1, \hat{j}_1, \hat{k}_1)$ and $(\hat{i}_2, \hat{j}_2, \hat{k}_2)$. Classical Euler angles use rotation ψ about z , θ about x_1 and ϕ about z_2 to orient (x, y, z) along (ξ, η, ζ) . Singularities result when the second angle is zero because the first and third transformations are then about the same axis. Small angle rotations are important for a rotor problem, zero rotations being a special case. Therefore, instead of Euler angles, modified Euler angles are used where the axes do not approach one another for rotations in the neighborhood of zero. The unit vectors $\hat{i}, \hat{j}, \hat{k}$, initially coincident with (x, y, z) , can be made to align with $\hat{i}_\xi, \hat{j}_\eta, \hat{k}_\zeta$ by rotation through three orientation angles in space ξ, β, θ . Depending on the choice of their sequence, six combinations are possible. The

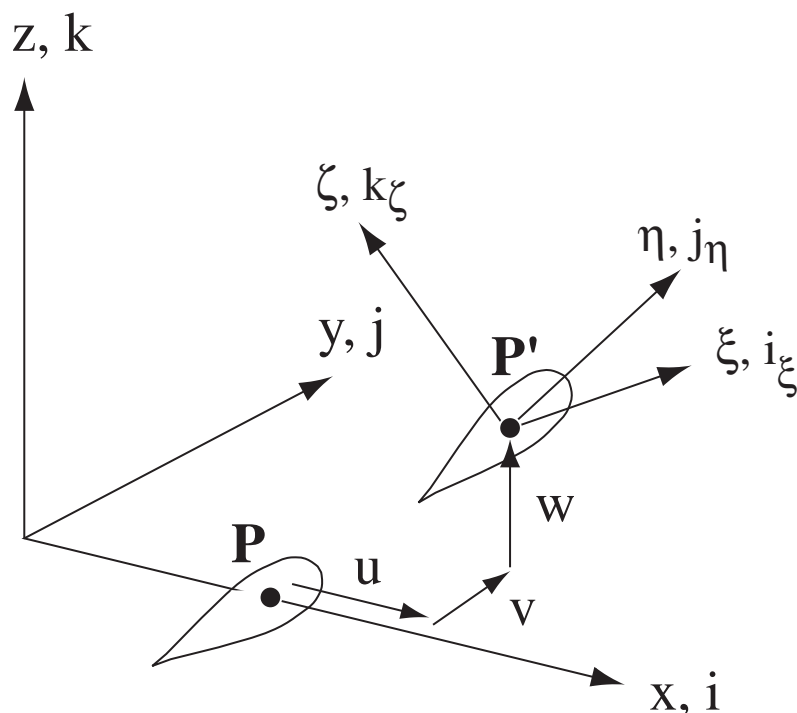


Figure 3.1: **Beam cross-section before and after deformation showing undeformed and deformed coordinate systems**

resulting transformation matrix takes a different form depending on the selected combination. The numerical values of the matrix elements, i.e. the direction cosines of the unit vectors $\hat{i}_\xi, \hat{j}_\eta, \hat{k}_\zeta$ with respect to $\hat{i}, \hat{j}, \hat{k}$, are of course independent of the choice of combination. The direction cosines are intrinsic properties, i.e., they are uniquely determined by the loading and boundary conditions. Here, we consider a rotation sequence ξ_1, β_1, θ_1 about $\hat{k}, -\hat{j}_1, \hat{i}_2$ respectively, in that order. That is, the first rotation ξ_1 is about z resulting in the new set (x_1, y_1, z_1) , β_1 about $-y_1$ resulting in (x_2, y_2, z_2) and θ_1 about x_2 resulting in (ξ, η, ζ) . This produces

$$\mathbf{T}_{\mathbf{DU}} = \begin{bmatrix} c_{\beta_1} c_{\xi_1} & c_{\beta_1} s_{\xi_1} & s_{\beta_1} \\ -c_{\xi_1} s_{\beta_1} s_{\theta_1} - c_{\theta_1} s_{\xi_1} & c_{\xi_1} c_{\theta_1} - s_{\xi_1} s_{\beta_1} s_{\theta_1} & c_{\beta_1} s_{\theta_1} \\ -c_{\xi_1} s_{\beta_1} c_{\theta_1} + s_{\theta_1} s_{\xi_1} & -c_{\xi_1} s_{\theta_1} - s_{\xi_1} s_{\beta_1} c_{\theta_1} & c_{\beta_1} c_{\theta_1} \end{bmatrix} \quad (3.51)$$

where $c_{(\cdot)} = \cos(\cdot)$, $s_{(\cdot)} = \sin(\cdot)$ and $\mathbf{T}_{\mathbf{DU}}^{-1} = \mathbf{T}_{\mathbf{DU}}^{\mathbf{T}}$. The goal is to express this transformation as a function of blade deflections and one rotation angle.

The position vector of any point on the deformed-blade elastic axis can be written as

$$\bar{\mathbf{r}} = (x + u)\hat{i} + v\hat{j} + w\hat{k} \quad (3.52)$$

and the unit vector tangent to the elastic axis of the deformed blade is

$$\frac{\partial \bar{\mathbf{r}}}{\partial r} = (x + u)^+ \hat{i} + v^+ \hat{j} + w^+ \hat{k} \quad (3.53)$$

where r is the curvilinear distance coordinate along the deformed-beam elastic axis and $(\cdot)^+ = \partial/\partial r(\cdot)$. Assuming pure bending and the cross sections remain normal to the elastic axis during deformation

$$\frac{\partial \bar{\mathbf{r}}}{\partial r} = \hat{i}_\xi = T_{11}\hat{i} + T_{12}\hat{j} + T_{13}\hat{k} \quad (3.54)$$

where T_{ij} is the element on the i th row and j th column of \mathbf{T}_{DU} . Thus

$$\left. \begin{aligned} T_{11} &= (x+u)^+ \\ T_{12} &= v^+ \\ T_{13} &= w^+ \end{aligned} \right\} \quad (3.55)$$

In the case of a pure elastic axial elongation, u_e , in addition to pure bending, it is subtracted from total axial elongation to calculate the unit vector tangent to the elastic axis of the deformed blade.

$$\hat{i}_\xi = (x+u-u_e)^+ \hat{i} + v^+ \hat{j} + w^+ \hat{k} \quad (3.56)$$

and then

$$\left. \begin{aligned} T_{11} &= (x+u-u_e)^+ \\ T_{12} &= v^+ \\ T_{13} &= w^+ \end{aligned} \right\} \quad (3.57)$$

Because \mathbf{T}_{DU} is orthonormal

$$T_{11}^2 + T_{12}^2 + T_{13}^2 = 1 \quad (3.58)$$

and therefore

$$(x+u-u_e)^+ = \sqrt{1-v^{+2}-w^{+2}} \quad (3.59)$$

Using equations (3.51) and (3.57) it can be deduced

$$\left. \begin{aligned} s_{\beta_1} &= w^+ \\ c_{\beta_1} &= \sqrt{1-w^{+2}} \\ s_{\xi_1} &= \frac{v^+}{\sqrt{1-w^{+2}}} \\ c_{\xi_1} &= \frac{\sqrt{1-v^{+2}-w^{+2}}}{\sqrt{1-w^{+2}}} \end{aligned} \right\} \quad (3.60)$$

c_{θ_1} and s_{θ_1} remain to be expressed in terms of the blade deflections and some appropriate measure of elastic torsion. The angular velocity of the frame (x, y, z) as it moves to (ξ, η, ζ) is

$$\begin{aligned} \omega &= \dot{\xi}_1 \hat{k} - \dot{\beta}_1 \hat{j}_1 + \dot{\theta}_1 \hat{i}_2 \\ &= \omega_\xi \hat{i}_\xi + \omega_\eta \hat{i}_\eta + \omega_\zeta \hat{i}_\zeta \end{aligned} \quad (3.61)$$

where \hat{j}_1 and \hat{i}_2 are unit vectors of the intermediate frames (x_1, y_1, z_1) and (x_2, y_2, z_2) , and $(\dot{}) = \partial/\partial t()$. The components of the angular velocity are

$$\left. \begin{aligned} \omega_\xi &= \dot{\theta}_1 + \dot{\xi}_1 s_{\beta_1} \\ \omega_\eta &= -\dot{\beta}_1 c_{\theta_1} + \dot{\xi}_1 c_{\beta_1} s_{\theta_1} \\ \omega_\zeta &= \dot{\xi}_1 c_{\beta_1} c_{\theta_1} + \dot{\beta}_1 s_{\theta_1} \end{aligned} \right\} \quad (3.62)$$

The bending curvatures and torsion (or angle of twist per unit length) can be deduced with the use of Kirchhoff's kinetic analog by replacing $(\dot{})$ with $()^+$. Thus,

$$\left. \begin{aligned} \kappa_\xi &= \theta_1^+ + \xi_1^+ s_{\beta_1} \\ \kappa_\eta &= -\beta_1^+ c_{\theta_1} + \xi_1^+ c_{\beta_1} s_{\theta_1} \\ \kappa_\zeta &= \xi_1^+ c_{\beta_1} c_{\theta_1} + \beta_1^+ s_{\theta_1} \end{aligned} \right\} \quad (3.63)$$

where κ_ξ , κ_η and κ_ζ are the components of bending curvatures in the deformed blade ξ, η, ζ directions. κ_ξ is the torsion. The angle of elastic twist, ϕ is defined such that

$$(\theta_t + \phi)^+ = \kappa_\xi \quad (3.64)$$

where $\theta_t^+ = \theta'_t x^+$. θ_t is the rigid pretwist of the blade. From (3.63a) and (3.64) we have

$$\theta_1^+ = (\theta_t + \phi)^+ - \xi^+ w^+ \quad (3.65)$$

ξ can be expressed as a function of blade deflections. Using (3.51), (3.57b) and (3.60b) we have

$$s_\xi = \frac{v^+}{\sqrt{(1-w^+)}} \quad (3.66)$$

Differentiating equation (3.66) and substituting equation (3.60d) we have

$$\xi_1^+ = \frac{v^{++}}{\sqrt{1-v^{+2}-w^{+2}}} + \frac{v^+ w^+ w^{++}}{(1-w^{+2})\sqrt{1-v^{+2}-w^{+2}}} \quad (3.67)$$

From (3.67) and (3.65) we have

$$\theta_1^+ = (\theta_t + \phi)^+ - \frac{w^+}{\sqrt{1-v^{+2}-w^{+2}}} \left(v^{++} + \frac{v^+ w^+ w^{++}}{1-w^{+2}} \right) \quad (3.68)$$

or

$$\theta_1 = \theta_t + \phi - \int_0^r \frac{w^+}{\sqrt{1-v^{+2}-w^{+2}}} \left(v^{++} + \frac{v^+ w^+ w^{++}}{1-w^{+2}} \right) dr \quad (3.69)$$

and

$$\theta_1 = \theta_t + \hat{\phi} \quad (3.70)$$

where θ_t is the blade rigid twist arising from pre-twist and control angles. ϕ is the blade elastic twist which is used in Hodges(1974) as the rotation variable. $\hat{\phi}$ is the blade elastic twist including the kinematic integral component and is used in the present work as the rotation variable. The T_{DU} matrix can now be expressed as a function of the unknown blade deflections and one rotation angle θ_1 related to the unknown blade twist $\hat{\phi}$ via equation (3.70).

$$\mathbf{T}_{DU} = \begin{bmatrix} \frac{\sqrt{(1-v^{+2}-w^{+2})}}{-v^+ c_{\theta_1} - w^+ s_{\theta_1} \sqrt{(1-v^{+2}-w^{+2})}} & \frac{v^+}{c_{\theta_1} \sqrt{(1-v^{+2}-w^{+2})} - v^+ w^+ s_{\theta_1}} & \frac{w^+}{s_{\theta_1} \sqrt{(1-w^{+2})}} \\ \frac{v^+ s_{\theta_1} - w^+ c_{\theta_1} \sqrt{(1-v^{+2}-w^{+2})}}{\sqrt{(1-w^{+2})}} & \frac{-s_{\theta_1} \sqrt{(1-v^{+2}-w^{+2})} - v^+ w^+ c_{\theta_1}}{\sqrt{(1-w^{+2})}} & c_{\theta_1} \sqrt{(1-w^{+2})} \end{bmatrix} \quad (3.71)$$

The above expressions and coordinate transformation T_{DU} are exact. Now they are reduced to second order. To second order $()^+ = ()'$. To second order

$$\begin{aligned} \frac{\sqrt{1-v^{+2}-w^{+2}}}{\sqrt{1-w^{+2}}} &= \frac{1 - \frac{1}{2}(v'^2 + w'^2)}{1 - \frac{1}{2}w'^2} \\ &= \frac{1 - \frac{1}{2}w'^2}{1 - \frac{1}{2}w'^2} - \frac{\frac{1}{2}v'^2}{1 - \frac{1}{2}w'^2} \\ &= 1 - \frac{1}{2}v'^2 \end{aligned} \quad (3.72)$$

Finally we have

$$\mathbf{T}_{DU} = \begin{bmatrix} 1 - \frac{v'^2}{2} - \frac{w'^2}{2} & v' & w' \\ -v' c_{\theta_1} - w' s_{\theta_1} & (1 - \frac{v'^2}{2})c_{\theta_1} - v' w' s_{\theta_1} & (1 - \frac{w'^2}{2})s_{\theta_1} \\ v' s_{\theta_1} - w' c_{\theta_1} & -(1 - \frac{v'^2}{2})s_{\theta_1} - v' w' c_{\theta_1} & (1 - \frac{w'^2}{2})c_{\theta_1} \end{bmatrix} \quad (3.73)$$

where θ is expressed as

$$\begin{aligned}\theta_1 &= \theta_0 + \theta_{1C} \cos(\psi) + \theta_{1S} \sin(\psi) + \theta_{tw} + \hat{\phi} \\ &= \theta + \hat{\phi}\end{aligned}\tag{3.74}$$

$\theta_0, \theta_{1C}, \theta_{1S}$ are the collective, lateral and longitudinal cyclic angles respectively, ψ is the blade azimuth location, θ_{tw} is the rigid twist angle and $\hat{\phi}$ is the elastic rotation angle. From equation (3.69), the elastic rotation is related to the blade elastic twist as follows

$$\hat{\phi} = \phi - \int_0^r w' v'' dr\tag{3.75}$$

where r denotes a blade radial station. Now the blade equations can be formulated using Hamilton's Principle. The equations are formulated in a non-dimensional form.

3.6.6 Nondimensionalization and Ordering scheme

The entire analysis has been done in a nondimensional form. This avoids scaling problems while computing results and increases the generality of the analysis. Table 3.1 shows the reference parameters used to nondimensionalize the relevant physical quantities.

Physical Quantity	Reference Parameter
Length	R
Time	$1/\Omega$
Mass/Length	m_0
Velocity	ΩR
Acceleration	$\Omega^2 R$
Force	$m_0 \Omega^2 R^2$
Moment	$m_0 \Omega^2 R^3$
Energy or Work	$m_0 \Omega^2 R^3$

Table 3.1: Nondimensionalization of Physical Quantities

In deriving a nonlinear system of equations, it is necessary to neglect higher-order terms to avoid over-complicating the equations of motion. A systematic and consistent set of guidelines has been adopted for determining which terms to retain and which to ignore. The ordering scheme is same as that in Hodges (1974). It is based on a parameter ε which is of the order of nondimensional flap deflection w or lag deflection v (nondimensionalized with respect to radius, R , as described in table 3.1). u is of the same order as the square of w or v . The elastic twist ϕ is a small angle in the sense that $\sin \phi \approx \phi$ and $\cos \phi \approx 1$. The axial coordinate x is of order R and the lateral coordinates are of order chord, c , and thickness, t . Chord, c , thickness, t and rigid blade twist θ_t are all of same order as v and w . The warp function λ_T is of the same order of magnitude as u so that the warp displacement, which is λ_T multiplied with twist is one order of magnitude less than u . Thus,

$$\left. \begin{aligned} \frac{u}{R} &= O(\varepsilon^2) & \frac{\lambda}{R} &= O(\varepsilon^2) \\ \frac{v}{R} &= O(\varepsilon) & \frac{w}{R} &= O(\varepsilon) \\ \frac{\eta}{R} &= O(\varepsilon) & \frac{\zeta}{R} &= O(\varepsilon) \\ \phi &= O(\varepsilon) & \frac{\delta\lambda/\delta\eta}{R} &= O(\varepsilon) \\ \frac{x}{R} &= O(\varepsilon) & \frac{\delta\lambda/\delta\zeta}{R} &= O(\varepsilon) \end{aligned} \right\}\tag{3.76}$$

The order of magnitude of the other nondimensional physical quantities are as follows.

$$\left. \begin{aligned} \frac{EA}{m_0\Omega^2 R^2} &= O(\varepsilon^{-2}) \\ \frac{x}{R}, \frac{h}{R}, \frac{xcg}{R}, \frac{ycg}{R}, \frac{m}{m_0}, \frac{\delta}{\delta\psi}, \frac{\delta}{\delta x} &= O(1) \\ \mu, \cos\psi, \sin\psi, \theta, \theta_t, \frac{c_1}{a}, \frac{d_2}{a} &= O(1) \\ \frac{EI_y}{m_0\Omega^2 R^4}, \frac{EI_z}{m_0\Omega^2 R^4}, \frac{GJ}{m_0\Omega^2 R^4} &= O(1) \\ \beta_p, \frac{k_A}{R}, \frac{k_{m1}}{R}, \frac{k_{m2}}{R} &= O(\varepsilon) \\ \alpha_s, \phi_s &= 0(\varepsilon) \\ \lambda, \frac{\eta_c}{R}, \frac{c_0}{a}, \frac{d_1}{a}, \frac{f_0}{a} &= O(\varepsilon) \\ \frac{EB_2}{m_0\Omega^2 R^5}, \frac{EC_2}{m_0\Omega^2 R^5} &= O(\varepsilon) \\ \frac{e_d}{R}, \frac{e_g}{R}, \frac{e_a}{R} &= O(\varepsilon^{\frac{3}{2}}) \\ \dot{\alpha}_s, \dot{\phi}_s &= 0(\varepsilon^{\frac{3}{2}}) \\ \frac{EB_1}{m_0\Omega^2 R^6}, \frac{EC_1}{m_0\Omega^2 R^6} &= O(\varepsilon^2) \\ \frac{d_0}{a}, \frac{f_1}{a} &= O(\varepsilon^2) \end{aligned} \right\} \quad (3.77)$$

R is the rotor radius, Ω is the rotational speed, E is the Young's Modulus, G is the shear modulus, I_y and I_z are cross-section moment of inertia from the y and z axis in the undeformed blade frame, J is the torsional rigidity constant, a is the lift curve slope and m_0 is mass per unit length of the blade. Rest of the symbols are defined in the beginning and later on as they appear. m_0 is defined as the mass per unit length of an uniform beam which has the same flap moment of inertia as the actual beam. Therefore

$$m_0 = \frac{3I_\beta}{R^3} \approx \frac{3 \int_0^R mr^2 dr}{R^3} \quad (3.78)$$

Azimuth angle is considered as nondimensional time, therefore

$$\left. \begin{aligned} (\dot{}) &= \frac{\delta()}{\delta t} = \frac{\delta()}{\delta\psi} \frac{\delta\psi}{\delta t} = \Omega \frac{\delta()}{\delta\psi} \\ (\ddot{}) &= \frac{\delta^2()}{\delta t^2} = \frac{\delta^2()}{\delta^2\psi} \frac{\delta^2\psi}{\delta t^2} = \Omega^2 \frac{\delta^2()}{\delta^2\psi} \end{aligned} \right\} \quad (3.79)$$

The ordering scheme is systematically and consistently adopted within the total energy context as is explained during the calculation of the energy terms. However, while following the scheme, terms are lost, which destroy the symmetric nature of the mass and stiffness matrix of the system, or, the antisymmetric gyroscopic nature of the modal equations, then those terms must be retained in violation to the ordering scheme.

3.6.7 Formulation Using Hamilton's Principle

Hamilton's variational principle is used to derive the blade equations of motion. For a conservative system, Hamilton's principle states that the true motion of a system, between prescribed initial conditions at time t_1 and final conditions at time t_2 , is that particular motion for which the time integral of the difference between the potential and kinetic energies is a minimum. For an aeroelastic system, e.g., the rotor, there are nonconservative forces which are not derived from a potential function. The generalized Hamilton's Principle, applicable to nonconservative systems, is expressed as

$$\delta\Pi_b = \int_{t_1}^{t_2} (\delta U - \delta T - \delta W) dt = 0 \quad (3.80)$$

where δU is the virtual variation of strain energy and δT is the virtual variation of kinetic energy. The δW is the virtual work done by the external forces. These virtual variations have contributions from the rotor blades and the fuselage.

The variations can be written as

$$\delta U = \delta U_R + \delta U_F = \left(\sum_{b=1}^{N_b} \delta U_b \right) + \delta U_F \quad (3.81)$$

$$\delta T = \delta T_R + \delta T_F = \left(\sum_{b=1}^{N_b} \delta T_b \right) + \delta T_F \quad (3.82)$$

$$\delta W = \delta W_R + \delta W_F = \left(\sum_{b=1}^{N_b} \delta W_b \right) + \delta W_F \quad (3.83)$$

where the subscript R denotes the contribution from the rotor, which is the sum of individual contributions from the N_b blades, and F denotes the contribution from the fuselage. In the present study, only the rotor contribution is considered. Strain energy variation from the flexible pitch links are included in the blade energy terms. The expression for the virtual work δW has been dealt with in the chapter on Aerodynamic Modeling.

3.6.8 Derivation of Strain Energy

Because each blade is assumed to be a long slender isotropic beam, the uniaxial stress assumption ($\sigma_{yy} = \sigma_{yz} = \sigma_{zz} = 0$) can be used. The relation between stresses and classical engineering strains are

$$\sigma_{xx} = E\epsilon_{xx} \quad (3.84)$$

$$\sigma_{x\eta} = G\epsilon_{x\eta} \quad (3.85)$$

$$\sigma_{x\zeta} = G\epsilon_{x\zeta} \quad (3.86)$$

where ϵ_{xx} is axial strain, and $\epsilon_{x\eta}$ and $\epsilon_{x\zeta}$ are engineering shear strains. The expression for strain energy of the b th blade is

$$U_b = \frac{1}{2} \int_0^R \int \int_A (\sigma_{xx}\epsilon_{xx} + \sigma_{x\eta}\epsilon_{x\eta} + \sigma_{x\zeta}\epsilon_{x\zeta}) d\eta d\zeta dx \quad (3.87)$$

Using the stress-strain relations the variation of strain energy becomes

$$\delta U_b = \int_0^R \int \int_A (E\epsilon_{xx}\delta\epsilon_{xx} + G\epsilon_{x\eta}\delta\epsilon_{x\eta} + G\epsilon_{x\zeta}\delta\epsilon_{x\zeta}) d\eta d\zeta dx \quad (3.88)$$

The general non-linear strain displacement equations to second order are

$$\begin{aligned} \epsilon_{xx} = & u' + \frac{v'^2}{2} + \frac{w'^2}{2} - \lambda_T \phi'' + (\eta^2 + \zeta^2)(\theta' \phi' + \frac{\phi'^2}{2}) \\ & - v'' [\eta \cos(\theta + \phi) - \zeta \sin(\theta + \phi)] \\ & - w'' [\eta \sin(\theta + \phi) + \zeta \cos(\theta + \phi)] \end{aligned} \quad (3.89)$$

$$\epsilon_{x\eta} = - \left(\zeta + \frac{\partial \lambda_T}{\partial \eta} \right) \phi' = -\hat{\zeta} \phi' \quad (3.90)$$

$$\epsilon_{x\zeta} = - \left(\eta - \frac{\partial \lambda_T}{\partial \zeta} \right) \phi' = \hat{\eta} \phi' \quad (3.91)$$

where λ_T is the cross-sectional warping function. From equation (3.75) we have the relations between the deformation variable ϕ and quasi-coordinate $\hat{\phi}$.

$$\left. \begin{aligned} \phi' &= \hat{\phi}' + w'v'' \\ \delta\phi' &= \delta\hat{\phi}' + w'\delta v'' + v''\delta w' \end{aligned} \right\} \quad (3.92)$$

From equation (3.59) we have the relations between the deformation variable u and the quasi-coordinate u_e .

$$\left. \begin{aligned} u' &= u'_e - \frac{1}{2}(v'^2 + w'^2) \\ u &= u_e - \frac{1}{2}\int_0^x (v'^2 + w'^2) \\ \delta u' &= \delta u'_e - v'\delta v' - w'\delta w' \\ \delta u &= \delta u_e - \int_0^x (v'\delta v' + w'\delta w')dx \end{aligned} \right\} \quad (3.93)$$

Using equations (3.92) and (3.93) we obtain the strains as follows.

$$\begin{aligned} \epsilon_{xx} &= u'_e - \lambda_T(\hat{\phi}'' + w'v''' + v''w'') + (\eta^2 + \zeta^2)(\theta'\hat{\phi}' + \theta'w'v'' + \frac{\hat{\phi}'^2}{2} + \frac{w'^2v''^2}{2} + \hat{\phi}'w'v'') \\ &\quad - v'' [\eta \cos(\theta + \hat{\phi}) - \zeta \sin(\theta + \hat{\phi})] - w'' [\eta \sin(\theta + \hat{\phi}) + \zeta \cos(\theta + \hat{\phi})] \end{aligned} \quad (3.94)$$

$$\epsilon_{x\eta} = -\hat{\zeta}(\hat{\phi}' + w'v'') \quad (3.95)$$

$$\epsilon_{x\zeta} = \hat{\eta}(\hat{\phi}' + w'v'') \quad (3.96)$$

The variation of the strains are

$$\begin{aligned} \delta\epsilon_{xx} &= \delta u'_e + \lambda_T(\delta\hat{\phi}'' + w'\delta v''' + v''\delta w'' + v'''\delta w' + w''\delta v'') \\ &\quad + (\eta^2 + \zeta^2)[\theta'\delta\hat{\phi}' + \theta'w'\delta v'' + \theta'v''\delta w' + (\hat{\phi}' + w'v'')(\delta\hat{\phi}' + w'\delta v'' + v''\delta w')] \\ &\quad - [\eta \cos(\theta + \hat{\phi}) - \zeta \sin(\theta + \hat{\phi})]\delta v'' + [\eta \sin(\theta + \hat{\phi}) + \zeta \cos(\theta + \hat{\phi})]v''\delta\hat{\phi} \\ &\quad - [\eta \sin(\theta + \hat{\phi}) + \zeta \cos(\theta + \hat{\phi})]\delta w'' - [\eta \cos(\theta + \hat{\phi}) - \zeta \sin(\theta + \hat{\phi})]w''\delta\hat{\phi} \end{aligned} \quad (3.97)$$

$$\delta\epsilon_{x\eta} = -\hat{\zeta}(\delta\phi' + w'\delta v'' + v''\delta w') \quad (3.98)$$

$$\delta\epsilon_{x\zeta} = \hat{\eta}(\delta\phi' + w'\delta v'' + v''\delta w') \quad (3.99)$$

Substituting equations (3.97), (3.98) and (3.99) in equation (3.88) gives the variation of strain energy as function of the deformation variables. It can be expressed in nondimensional form as follows.

$$\begin{aligned} \delta U &= \frac{\delta U_b}{m_0\Omega^2 R^3} = \int_0^1 (U_{u'_e}\delta u'_e + U_{v'}\delta v' + U_{w'}\delta w' + U_{v''}\delta v'' + U_{w''}\delta w'' \\ &\quad + U_{\hat{\phi}}\delta\hat{\phi} + U_{\hat{\phi}'}\delta\hat{\phi}' + U_{\hat{\phi}''}\delta\hat{\phi}'')dx \end{aligned} \quad (3.100)$$

In deriving the expressions the following section properties are used.

$$\left. \begin{aligned} \int \int_A d\eta d\zeta &= A \\ \int \int_A \eta d\eta d\zeta &= Ae_A \\ \int \int_A \zeta d\eta d\zeta &= 0 \\ \int \int_A \lambda_T d\eta d\zeta &= 0 \\ \int \int_A (\eta^2 + \zeta^2) d\eta d\zeta &= AK_A^2 \\ \int \int_A (\eta^2 + \zeta^2)^2 d\eta d\zeta &= B_1 \\ \int \int_A \eta(\eta^2 + \zeta^2)^2 d\eta d\zeta &= B_2 \\ \int \int_A \eta^2 d\eta d\zeta &= I_Z \\ \int \int_A \zeta^2 d\eta d\zeta &= I_Y \\ \int \int_A \lambda_T^2 d\eta d\zeta &= EC_1 \\ \int \int_A \zeta \lambda_T d\eta d\zeta &= EC_2 \end{aligned} \right\} \quad (3.101)$$

The coefficients, up to second order of non-linearities are given below.

$$U_{u'_e} = EA \left[u'_e + K_A^2 (\theta' \hat{\phi}' + \theta' w' v'' + \frac{\hat{\phi}'^2}{2}) \right] - EAe_A \left[v'' (\cos \theta - \hat{\phi} \sin \theta) + w'' (\sin \theta + \hat{\phi} \cos \theta) \right] \quad (3.102)$$

$$U_{v'} = 0 \quad (3.103)$$

$$U_{w'} = (GJ + EB_1 \theta'^2) \hat{\phi}' v'' + EAK_A^2 \theta' v'' u'_e \quad (3.104)$$

$$U_{v''} = v'' [EI_Z \cos^2(\theta + \hat{\phi}) + EI_Y \sin^2(\theta + \hat{\phi})] + w'' (EI_Z - EI_Y) \cos(\theta + \hat{\phi}) \sin(\theta + \hat{\phi}) - EB_2 \theta' \hat{\phi}' \cos \theta - EAe_A u'_e (\cos \theta - \hat{\phi} \sin \theta) + EAK_A^2 u'_e w' \theta' + (GJ + EB_1 \theta'^2) \hat{\phi}' w' - EC_2 \hat{\phi}'' \sin \theta \quad (3.105)$$

$$U_{w''} = w'' [EI_Z \sin^2(\theta + \hat{\phi}) + EI_Y \cos^2(\theta + \hat{\phi})] + v'' [EI_Z - EI_Y] \cos(\theta + \hat{\phi}) \sin(\theta + \hat{\phi}) - EAe_A u'_e (\sin \theta + \hat{\phi} \cos \theta) - EB_2 \hat{\phi}' \theta' \sin \theta + EC_2 \hat{\phi}'' \cos \theta \quad (3.106)$$

$$U_{\hat{\phi}} = w''^2 (EI_Z - EI_Y) \cos(\theta + \hat{\phi}) \sin(\theta + \hat{\phi}) - v''^2 (EI_Z - EI_Y) \cos(\theta + \hat{\phi}) \sin(\theta + \hat{\phi}) + v'' w'' (EI_Z - EI_Y) \cos 2(\theta + \hat{\phi}) \quad (3.107)$$

$$U_{\hat{\phi}'} = GJ(\hat{\phi}' + w' v'') + EAK_A^2 (\theta' + \phi') u'_e + EB_1 \theta'^2 \hat{\phi}' - EB_2 \theta' (v'' \cos \theta + w'' \sin \theta) \quad (3.108)$$

$$U_{\hat{\phi}''} = EC_1 \hat{\phi}'' + EC_2 (w'' \cos \theta - v'' \sin \theta) \quad (3.109)$$

Note that in the above expressions, the $\cos(\theta + \hat{\phi})$ and $\sin(\theta + \hat{\phi})$ terms associated with bending curvature, i.e., with EI_Z and EI_Y , have been retained. These terms are expanded to second order as

$$\left. \begin{aligned} \sin(\theta + \hat{\phi}) &= \left(1 - \frac{\hat{\phi}^2}{2}\right) \sin \theta + \hat{\phi} \cos \theta \\ \cos(\theta + \hat{\phi}) &= \left(1 - \frac{\hat{\phi}^2}{2}\right) \cos \theta - \hat{\phi} \sin \theta \end{aligned} \right\} \quad (3.110)$$

This expansion introduces third order terms in $U_{v''}$, $U_{w''}$ and $U_{\hat{\phi}}$ which are retained in violation of the ordering scheme. This is to maintain consistency between the force-summation and modal methods of blade loads calculation. Thus we have the following

$$U_{v''} = v'' (EI_Z \cos^2 \theta + EI_Y \sin^2 \theta) + w'' (EI_Z - EI_Y) \cos \theta \sin \theta - v'' \hat{\phi} \sin 2\theta (EI_Z - EI_Y) + w'' \hat{\phi} \cos 2\theta (EI_Z - EI_Y) - v'' \hat{\phi}^2 \cos 2\theta (EI_Z - EI_Y) - w'' \hat{\phi}^2 \sin 2\theta (EI_Z - EI_Y) - EB_2 \theta' \hat{\phi}' \cos \theta - EAe_A u'_e (\cos \theta - \hat{\phi} \sin \theta) + EAK_A^2 u'_e w' \theta' + (GJ + EB_1 \theta'^2) \hat{\phi}' w' - EC_2 \hat{\phi}'' \sin \theta \quad (3.111)$$

$$U_{w''} = w'' (EI_Z \sin^2 \theta + EI_Y \cos^2 \theta) + v'' (EI_Z - EI_Y) \cos \theta \sin \theta + w'' \hat{\phi} \sin 2\theta (EI_Z - EI_Y) + v'' \hat{\phi} \cos 2\theta (EI_Z - EI_Y) + w'' \hat{\phi}^2 \cos 2\theta (EI_Z - EI_Y) - v'' \hat{\phi}^2 \sin 2\theta (EI_Z - EI_Y) - EAe_A u'_e (\sin \theta + \hat{\phi} \cos \theta) - EB_2 \hat{\phi}' \theta' \sin \theta + EC_2 \hat{\phi}'' \cos \theta \quad (3.112)$$

$$U_{\hat{\phi}} = (w''^2 - v''^2) \cos \theta \sin \theta (EI_Z - EI_Y) + v'' w'' \cos 2\theta \hat{\phi} (w''^2 - v''^2) \cos 2\theta (EI_Z - EI_Y) - 2\hat{\phi} v'' w'' \sin 2\theta \quad (3.113)$$

3.6.9 Derivation of Kinetic Energy

The kinetic energy of the bth blade, δT_b depends on the blade velocity relative to the hub and the velocity of the hub itself. The velocity of the hub originates from fuselage dynamics and is neglected in the present analysis.

Let the position of an arbitrary point after the beam has deformed is given by (x_1, y_1, z_1) where

$$\begin{aligned} \bar{\mathbf{r}} = [x_1 \quad y_1 \quad z_1] \begin{Bmatrix} \hat{i} \\ \hat{j} \\ \hat{k} \end{Bmatrix} &= [x+u \quad v \quad w] \begin{Bmatrix} \hat{i} \\ \hat{j} \\ \hat{k} \end{Bmatrix} + [-\lambda\phi' \quad \eta \quad \zeta] \begin{Bmatrix} \hat{i}_\xi \\ \hat{j}_\eta \\ \hat{k}_\zeta \end{Bmatrix} \\ &= \{ [x+u \quad v \quad w] + [-\lambda\phi' \quad \eta \quad \zeta] \mathbf{T}_{\mathbf{DU}} \} \begin{Bmatrix} \hat{i} \\ \hat{j} \\ \hat{k} \end{Bmatrix} \end{aligned} \quad (3.114)$$

Using equation (3.73) we obtain

$$\left. \begin{aligned} x_1 &= x + u - \lambda\phi' - v'(y_1 - v) - w'(z_1 - w) \\ y_1 &= v + (y_1 - v) \\ z_1 &= w + (z_1 - w) \end{aligned} \right\} \quad (3.115)$$

where

$$\left. \begin{aligned} y_1 - v &= \eta \cos(\theta + \hat{\phi}) - \zeta \sin(\theta + \hat{\phi}) \\ z_1 - w &= \eta \sin(\theta + \hat{\phi}) + \zeta \cos(\theta + \hat{\phi}) \end{aligned} \right\} \quad (3.116)$$

Now,

$$\bar{V}_b = \frac{\partial \bar{\mathbf{r}}}{\partial t} + \bar{\Omega} \times \bar{\mathbf{r}} \quad (3.117)$$

where using equation (3.49) we have

$$\bar{\Omega} = \Omega \hat{K} = \Omega \sin \beta_p \hat{i} + \Omega \cos \beta_p \hat{k} \quad (3.118)$$

and

$$\frac{\partial \bar{\mathbf{r}}}{\partial t} = \dot{x}_1 \hat{i} + \dot{y}_1 \hat{j} + \dot{z}_1 \hat{k} \quad (3.119)$$

Using equations (3.119) and (3.49) in equation (3.117) we have

$$\bar{V}_b = V_{bx} \hat{i} + V_{by} \hat{j} + V_{bz} \hat{k} \quad (3.120)$$

where all velocities are non-dimensionalized with respect to ΩR and $(\dot{}) = \partial()/\partial\psi$.

$$V_{bx} = \dot{x}_1 - y_1 \cos \beta_p \quad (3.121)$$

$$V_{by} = \dot{y}_1 + x_1 \cos \beta_p - z_1 \sin \beta_p \quad (3.122)$$

$$V_{bz} = \dot{z}_1 + y_1 \sin \beta_p \quad (3.123)$$

Taking variations of the velocities we have

$$\begin{aligned} \bar{V} \cdot d\bar{V} &= \dot{x}_1 \delta \dot{x}_1 - y_1 \cos \beta_p \delta \dot{x}_1 - \dot{x}_1 \cos \beta_p \delta y_1 + y_1 \cos^2 \beta_p \delta y_1 \\ &\quad + \dot{y}_1 \delta \dot{y}_1 + x_1 \cos \beta_p \delta \dot{y}_1 - z_1 \sin \beta_p \delta \dot{y}_1 + \dot{y}_1 \cos \beta_p \delta x_1 \\ &\quad + x_1 \cos^2 \beta_p \delta x_1 - z_1 \sin \beta_p \cos \beta_p \delta x_1 - \dot{y}_1 \sin \beta_p \delta z_1 - x_1 \cos \beta_p \sin \beta_p \delta z_1 \\ &\quad + \dot{z}_1 \sin^2 \beta_p \delta z_1 + \dot{z}_1 \delta \dot{z}_1 + y_1 \sin \beta_p \delta \dot{z}_1 + \dot{z}_1 \sin \beta_p \delta y_1 + y_1 \sin^2 \beta_p \delta y_1 \end{aligned} \quad (3.124)$$

According to variational method, this equation must be integrated in time between two arbitrary points in time, t_1 and t_2 . The initial and final values (e.g., $\dot{x}_1 \delta x_1|_{t_1}^2$) are taken as zero. Anticipating integration by parts the various terms can be combined in equation (3.124) to obtain

$$\begin{aligned} \bar{V}.d\bar{V} = & -\ddot{x}_1 \delta x_1 + 2\dot{y}_1 \cos \beta_p \delta x_1 + y_1 \cos^2 \beta_p \delta y_1 - \dot{y}_1 \delta y_1 \\ & - 2\dot{x}_1 \cos \beta_p \delta y_1 + 2\dot{z}_1 \sin \beta_p \delta y_1 + x_1 \cos^2 \beta_p \delta x_1 \\ & - z_1 \sin \beta_p \cos \beta_p \delta x_1 - 2\dot{y}_1 \sin \beta_p \delta z_1 - x_1 \cos \beta_p \sin \beta_p \delta z_1 + z_1 \sin^2 \beta_p \delta z_1 \\ & - \dot{z}_1 \delta z_1 + y_1 \sin^2 \beta_p \delta y_1 \end{aligned} \quad (3.125)$$

For the b th, the resultant kinetic energy expression in non-dimensional form is given by

$$\frac{\delta T_b}{m_0 \Omega^2 R^3} = \int_0^1 \iint_A \rho \bar{V}.d\bar{V} \, d\eta \, d\zeta \, dx \quad (3.126)$$

where ρ is the structural mass density. Substituting the velocity expressions as given before we have

$$\frac{\delta T_b}{m_0 \Omega^2 R^3} = \int_0^1 \left[\iint_A \rho (T_{x_1} \delta x_1 + T_{y_1} \delta y_1 + T_{z_1} \delta z_1) \, d\eta \, d\zeta \right] dx \quad (3.127)$$

where

$$T_{x_1} = -\ddot{x}_1 + 2\dot{y}_1 \cos \beta_p + x_1 \cos^2 \beta_p - z_1 \sin \beta_p \cos \beta_p \quad (3.128)$$

$$T_{y_1} = y_1 \cos^2 \beta_p - \dot{y}_1 - 2\dot{x}_1 \cos \beta_p + y_1 \sin^2 \beta_p + 2\dot{z}_1 \sin \beta_p \quad (3.129)$$

$$T_{z_1} = -2\dot{y}_1 \sin \beta_p - \dot{z}_1 + z_1 \sin^2 \beta_p - x_1 \cos \beta_p \sin \beta_p \quad (3.130)$$

Now, using equations (8.32) and (3.116) we have

$$\left. \begin{aligned} y_1 &= \dot{v} - (z_1 - w)\dot{\theta}_1 \\ z_1 &= \dot{w} + (y_1 - v)\dot{\theta}_1 \\ x_1 &= \dot{u} - \lambda_T \dot{\phi}' - (\dot{v}' + w'\dot{\theta}_1)(y_1 - v) - (\dot{w}' - v'\dot{\theta}_1)(z_1 - w) \end{aligned} \right\} \quad (3.131)$$

and

$$\left. \begin{aligned} \ddot{y}_1 &= \ddot{v} - (z_1 - w)\ddot{\theta}_1 - (y_1 - v)\dot{\theta}_1^2 \\ \ddot{z}_1 &= \ddot{w} + (y_1 - v)\ddot{\theta}_1 - (z_1 - w)\dot{\theta}_1^2 \\ \ddot{x}_1 &= \ddot{u} - \lambda_T \ddot{\phi}' - (y_1 - v)(\ddot{v}' + w'\ddot{\theta}_1 - v'\dot{\theta}_1^2 + 2\dot{w}'\dot{\theta}_1) \\ &\quad - (z_1 - w)(\ddot{w}' - v'\ddot{\theta}_1 - w'\dot{\theta}_1^2 - 2\dot{v}'\dot{\theta}_1) \end{aligned} \right\} \quad (3.132)$$

The variations are as follows

$$\left. \begin{aligned} \delta y_1 &= \delta v - \delta \hat{\phi}(z_1 - w) \\ \delta z_1 &= \delta w + \delta \hat{\phi}(y_1 - v) \\ \delta x_1 &= \delta u - \lambda_T \delta \hat{\phi}' - (y_1 - v)(\delta v' + w'\delta \hat{\phi}) \\ &\quad - (z_1 - w)(\delta w' - v'\delta \hat{\phi}) \end{aligned} \right\} \quad (3.133)$$

Using equations (3.133), (3.132), (3.131), (8.32) in (3.126) we obtain

$$\delta T = \frac{\delta T_b}{m_0 \Omega^2 R^3} = \int_0^1 m (T_{u_e} \delta u_e + T_v \delta v + T_w \delta w + T_{w'} \delta w' + T_{v'} \delta v' + T_\phi \delta \phi + T_F) dx \quad (3.134)$$

In deriving the expressions the following section properties are used.

$$\left. \begin{aligned} \int \int_A \rho d\eta d\zeta &= m \\ \int \int_A \rho \eta d\eta d\zeta &= m e_g \\ \int \int_A \rho \zeta^2 d\eta d\zeta &= m k_{m_1}^2 \\ \int \int_A \rho \eta^2 d\eta d\zeta &= m k_{m_2}^2 \\ k_{m_1}^2 + k_{m_2}^2 &= k_m^2 \\ \int \int_A \rho \zeta d\eta d\zeta &= 0 \\ \int \int_A \rho \eta \zeta d\eta d\zeta &= 0 \\ \int \int_A \rho \lambda_T d\eta d\zeta &= 0 \end{aligned} \right\} \quad (3.135)$$

assuming cross-section symmetry about the η axis and an antisymmetric warp function λ_T . The terms involving $(y_1 - v)$ and $(z_1 - w)$ are given by

$$\left. \begin{aligned} \int \int_A \rho (y_1 - v) d\eta d\zeta &= m e_g \cos(\theta + \hat{\phi}) \\ \int \int_A \rho (z_1 - w) d\eta d\zeta &= m e_g \sin(\theta + \hat{\phi}) \\ \int \int_A \rho (z_1 - w)(y_1 - v) d\eta d\zeta &= m (k_{m_2}^2 - k_{m_1}^2) \sin(\theta + \hat{\phi}) \cos(\theta + \hat{\phi}) \\ \int \int_A \rho [(y_1 - v)^2 - (z_1 - w)^2] d\eta d\zeta &= m k_m^2 \end{aligned} \right\} \quad (3.136)$$

The coefficients in equation (3.134) are written up to second order, $O(\epsilon^2)$, as follows

$$T_{U_e} = -\ddot{u} + u + x + 2\dot{v} \quad (3.137)$$

where

$$\left. \begin{aligned} u &= u_e - \frac{1}{2} \int_0^x (v'^2 + w'^2) dx \\ \ddot{u} &= \ddot{u}_e - \int_0^x (\dot{v}'^2 + v'\ddot{v}' + \dot{w}'^2 + w'\ddot{w}') dx \end{aligned} \right\} \quad (3.138)$$

$$\begin{aligned} T_v &= -\ddot{v} + e_g \ddot{\theta} \sin \theta + e_g \cos \theta + v - \hat{\phi} \sin \theta + 2\dot{w} \beta_p + 2e_g \dot{v}' \cos \theta \\ &\quad + 2e_g \dot{w}' \sin \theta + \ddot{\hat{\phi}} e_g \sin \theta - 2\dot{u}_e + 2 \int_0^x (v'\dot{v}' + w'\dot{w}') dx \end{aligned} \quad (3.139)$$

$$T_{v'} = -e_g (x \cos \theta - \hat{\phi} x \sin \theta + 2\dot{v} \cos \theta) \quad (3.140)$$

$$\begin{aligned} T_w &= -\ddot{w} - e_g \ddot{\theta} \cos \theta - e_g \ddot{\hat{\phi}} \cos \theta \\ &\quad - 2\dot{v} \beta_p - x \beta_p \end{aligned} \quad (3.141)$$

$$T_{w'} = -e_g (x \sin \theta + \hat{x} \cos \theta + 2\dot{v} \sin \theta) \quad (3.142)$$

$$\begin{aligned} T_{\hat{\phi}} &= -k_m^2 \ddot{\hat{\phi}} - \hat{\phi} (k_{m_2}^2 - k_{m_1}^2) \cos 2\theta - (k_{m_2}^2 - k_{m_1}^2) \cos \theta \sin \theta - x \beta_p e_g \cos \theta \\ &\quad - v e_g \sin \theta + x v' e_g \sin \theta - x w' e_g \cos \theta + \ddot{v} e_g \sin \theta - \ddot{w} e_g \cos \theta - k_m^2 \ddot{\theta} \end{aligned} \quad (3.143)$$

The non-variation term T_F is given by

$$\begin{aligned} T_F &= -(-\ddot{u} + u + x + 2\dot{v}) \int_0^x (v' \delta v' + w' \delta w') \\ &= -T_{U_e} \int_0^x (v' \delta v' + w' \delta w') \end{aligned} \quad (3.144)$$

Note that the ordering scheme is violated in equation (3.144). It is important to keep the entire T_{U_e} in the non-variation form for articulated rotors where the bending moments at the hinge must go to zero. For hingeless rotors with large bending moments at the blade root the error is negligible.

3.6.10 Virtual Work

For each degree of freedom, there is a corresponding external force (or moment) which contribute to virtual work on the system. The general expression is given by

$$\frac{\delta W_b}{m_0 \Omega^2 R^3} = \int_0^1 (L_u^A \delta u + L_v^A \delta v + L_w^A \delta w + M_{\hat{\phi}}^A \delta \hat{\phi}) dx \quad (3.145)$$

where L_u^A , L_v^A , L_w^A , $M_{\hat{\phi}}^A$ are the distributed air loads in the x , y and z directions and $M_{\hat{\phi}}^A$ is the aerodynamic pitching moment about the undeformed elastic axis. Calculated air loads are motion dependent. Measured air loads are not motion dependent.

In addition to distributed air loads, there can be concentrated forces and moments acting on locations over the blade span, e.g. a prescribed damper force. They can be included as follows.

$$\begin{aligned} \frac{\delta W_b}{m_0 \Omega^2 R^3} &= \int_0^1 (L_u^A \delta u + L_v^A \delta v + L_w^A \delta w + M_{\hat{\phi}}^A \delta \hat{\phi}) dx \\ &+ \int_0^1 (F_x \delta u + F_y \delta v + F_z \delta w + M_x \delta \hat{\phi} - M_y \delta w' + M_z \delta v') \delta(x - x_f) dx \end{aligned} \quad (3.146)$$

where F_x , F_y , F_z , M_x , M_y , M_z are the concentrated forces and moments acting at $x = x_f$ along the blade span. The calculated forces and moments are described in Chapter 3.

3.6.11 Equations of Motion

Integrating the strain energy, kinetic energy and virtual work expressions (3.100), (3.134) and (3.145) by parts we obtain

$$\left. \begin{aligned} \delta U &= \int_0^1 (Y_{u_e} \delta u_e + Y_v \delta v + Y_w \delta w + Y_{\hat{\phi}} \delta \hat{\phi}) dx + b(U) \\ \delta T &= \int_0^1 (Z_{u_e} \delta u_e + Z_v \delta v + Z_w \delta w + Z_{\hat{\phi}} \delta \hat{\phi}) dx + b(T) \\ \delta W &= \int_0^1 (W_{u_e} \delta u_e + W_v \delta v + W_w \delta w + W_{\hat{\phi}} \delta \hat{\phi}) dx + b(W) \end{aligned} \right\} \quad (3.147)$$

where $b(U)$, $b(T)$ and $b(W)$ are the force and displacement boundary conditions. Using equation (3.80) and collecting terms associated with δu , δv , δw and $\delta \hat{\phi}$ we obtain the blade equations as follows.

u_e equation :

$$\begin{aligned} &\left[EAu_e' + EAK_A^2 \left(\theta' \hat{\phi}' + \theta' w' v'' + \frac{\hat{\phi}'^2}{2} \right) \right. \\ &\quad \left. - EAe_A v'' (\cos \theta - \hat{\phi} \sin \theta) + EA w'' (\sin \theta + \hat{\phi} \cos \theta) \right]' \\ &+ m(\ddot{u}_e - u_e - x - 2\dot{v}) = L_u \end{aligned} \quad (3.148)$$

v equation :

$$\begin{aligned}
& \left[v''(EI_Z \cos^2 \theta + EI_Y \sin^2 \theta) + w''(EI_Z - EI_Y) \cos \theta \sin \theta \right. \\
& - v'' \hat{\phi} \sin 2\theta (EI_Z - EI_Y) + w'' \hat{\phi} \cos 2\theta (EI_Z - EI_Y) \\
& - v'' \hat{\phi}^2 \cos 2\theta (EI_Z - EI_Y) - w'' \hat{\phi}^2 \sin 2\theta (EI_Z - EI_Y) \\
& - EB_2 \theta' \hat{\phi}' \cos \theta - EAe_A u_e' (\cos \theta - \hat{\phi} \sin \theta) + EAK_A^2 u_e' w' \theta' \\
& \left. + (GJ + EB_1 \theta'^2) \hat{\phi}' w' - EC_2 \hat{\phi}'' \sin \theta \right]'' \\
& - m \left[-\ddot{v} + e_g \ddot{\theta} \sin \theta + e_g \cos \theta + v - \hat{\phi} \sin \theta + 2\dot{w} \beta_p + 2e_g v' \cos \theta \right. \\
& \left. + 2e_g w' \sin \theta + \ddot{\hat{\phi}} e_g \sin \theta - 2\dot{u}_e + 2 \int_0^x (v' \dot{v}' + w' \dot{w}') dx \right] \\
& - me_g \left(x \cos \theta - \hat{\phi} x \sin \theta + 2\dot{v} \cos \theta \right)' + \left\{ mv' \int_x^1 (-\ddot{u}_e + u_e + x + 2\dot{v}) \right\}' = L_v
\end{aligned} \tag{3.149}$$

w equation :

$$\begin{aligned}
& \left[w''(EI_Z \sin^2 \theta + EI_Y \cos^2 \theta) + v''(EI_Z - EI_Y) \cos \theta \sin \theta \right. \\
& + w'' \hat{\phi} \sin 2\theta (EI_Z - EI_Y) + v'' \hat{\phi} \cos 2\theta (EI_Z - EI_Y) \\
& + w'' \hat{\phi}^2 \cos 2\theta (EI_Z - EI_Y) - v'' \hat{\phi}^2 \sin 2\theta (EI_Z - EI_Y) \\
& - EAe_A u_e' (\sin \theta + \hat{\phi} \cos \theta) - EB_2 \hat{\phi}' \theta' \sin \theta + EC_2 \hat{\phi}'' \cos \theta \left. \right]'' \\
& - m \left(-\ddot{w} - e_g \ddot{\theta} \cos \theta - e_g \ddot{\hat{\phi}} \cos \theta - 2\dot{v} \beta_p - x \beta_p \right) \\
& - me_g (x \sin \theta + \hat{x} \cos \theta + 2\dot{v} \sin \theta)' + \left\{ mw' \int_x^1 (-\ddot{u}_e + u_e + x + 2\dot{v}) \right\}' = L_w
\end{aligned} \tag{3.150}$$

$\hat{\phi}$ equation :

$$\begin{aligned}
& (w''^2 - v''^2) \cos \theta \sin \theta (EI_Z - EI_Y) + v'' w'' \cos 2\theta \\
& \hat{\phi} (w''^2 - v''^2) \cos 2\theta (EI_Z - EI_Y) - 2\hat{\phi} v'' w'' \sin 2\theta \\
& + \left[GJ(\hat{\phi}' + w' v'') + EAK_A^2 (\theta' + \phi') u_e' \right. \\
& \left. + EB_1 \theta'^2 \hat{\phi}' - EB_2 \theta' (v'' \cos \theta + w'' \sin \theta) \right]' \\
& - \left[-k_m^2 \ddot{\hat{\phi}} - \hat{\phi} (k_{m_2}^2 - k_{m_1}^2) \cos 2\theta - (k_{m_2}^2 - k_{m_1}^2) \cos \theta \sin \theta - x \beta_p e_g \cos \theta \right. \\
& \left. - v e_g \sin \theta + x v' e_g \sin \theta - x w' e_g \cos \theta + \ddot{v} e_g \sin \theta - \ddot{w} e_g \cos \theta - k_m^2 \ddot{\theta} \right] = L_{\hat{\phi}}
\end{aligned} \tag{3.151}$$

3.7 Structural loads

The blade sectional loads, i.e. the flap, lag and torsion bending moments, are calculated using two methods - (1) Modal Curvature and (2) Force Summation Method. For converged blade response, i.e. when the response does not change with increase in the number of blade normal modes, both methods should produce identical loads. In the immediate vicinity of a concentrated loading, e.g.,

lag damper force, the force summation method captures the blade loads with lesser number of modes.

To obtain the same loads using force summation and modal curvature methods, the response equations must be consistent with loads calculations. Consistency is specially important for articulated rotors where the bending loads must reduce to zero at the hinge.

3.7.1 Modal Curvature Method

The flap and lag bending moments, M_η and M_ζ are obtained as follows.

$$\begin{aligned} M_\eta &= \int \int_A \zeta \sigma d\eta d\zeta = \int \int_A E\zeta \epsilon_{xx} d\eta d\zeta \\ &= EI_\eta [v'' \sin(\theta + \hat{\phi}) - w'' \cos(\theta + \hat{\phi})] - EC_1 \hat{\phi}'' \end{aligned} \quad (3.152)$$

$$\begin{aligned} M_\zeta &= - \int \int_A \eta \sigma d\eta d\zeta = - \int \int_A E\eta \epsilon_{xx} d\eta d\zeta \\ &= EI_\zeta [v'' \cos(\theta + \hat{\phi}) + w'' \sin(\theta + \hat{\phi})] - EAe_A u'_e - EB_2 \theta' \hat{\phi}' \end{aligned} \quad (3.153)$$

The expression for torsion bending moment is given by

$$\begin{aligned} M_\xi &= \int \int_A \left[\eta \sigma_{x\zeta} - \zeta \sigma_{x\eta} + \lambda_T \left(\frac{\partial \sigma_{x\eta}}{\partial \eta} + \frac{\partial \sigma_{x\zeta}}{\partial \zeta} \right) \right] d\eta d\zeta \\ &+ \frac{\partial}{\partial x} \int \int_A \lambda_T \sigma_{xx} d\eta d\zeta \\ &+ (\theta + \hat{\phi})' \int \int_A (\eta^2 + \zeta^2) \sigma_{xx} d\eta d\zeta \\ &= E A k_A^2 (\theta + \hat{\phi})' u'_e + E B_1 \theta'^2 \hat{\phi}' - E B_2 \theta' (v'' \cos \theta + w'' \sin \theta) \\ &+ GJ (\hat{\phi}' + w' v'') \\ &- [EC_1 \hat{\phi}'' + EC_2 (w'' \cos \theta - v'' \sin \theta)]' \end{aligned} \quad (3.154)$$

3.7.2 Force Summation Method

The loads occurring at a blade section are the reaction forces (and moments) to those occurring outboard. It is equal (and opposite) to the integrated air loads and inertial loads from blade tip to the desired section. The inertial forces and moments at each blade section are given by the following.

$$\left. \begin{aligned} F^I &= - \int \int_A \rho \bar{a} d\eta d\zeta \\ M^I &= - \int \int_A \bar{s} \times \rho d\eta d\zeta \end{aligned} \right\} \quad (3.155)$$

The acceleration of the section, \bar{a} is given by

$$\bar{a} = \ddot{\bar{r}} + \Omega \times (\Omega \times \bar{r}) + 2(\Omega \times \dot{\bar{r}}) \quad (3.156)$$

The moment arm of a point on the blade section measured from the deformed shear center, \bar{s} is obtained from equation(8.32) as

$$\bar{s} = -[v'(y_1 - v) + w'(z_1 - w)]\hat{i} + (y_1 - v)\hat{j} + (z_1 - w)\hat{k} \quad (3.157)$$

Using equations (8.32), (3.118), (3.131), and (3.132) we obtain

$$\bar{a} = a_x \hat{i} + a_y \hat{j} + a_z \hat{k} \quad (3.158)$$

where

$$\begin{aligned} a_x = & \ddot{u} - \lambda_T \ddot{\theta}_1' - (y_1 - v)(\ddot{v}' + w' \ddot{\theta}_1' + 2\dot{w}' \dot{\theta}_1' - v' \dot{\theta}_1'^2) \\ & - (z_1 - w)(\ddot{w}' - 2\dot{v}' \dot{\theta}_1' - v' \ddot{\theta}_1' - w' \dot{\theta}_1'^2) - 2[\dot{v} - \dot{\theta}_1'(z_1 - w)] \\ & + \beta_p[w + (z_1 - w)] - [x + u - v'(y_1 - v) - w'(z_1 - w)] \end{aligned} \quad (3.159)$$

$$\begin{aligned} a_y = & \ddot{v} - \ddot{\theta}_1'(z_1 - w) - \dot{\theta}_1'^2(y_1 - v) - 2\beta_p[\dot{w} + \dot{\theta}_1'(y_1 - v)] \\ & 2[\dot{u} - \lambda_T \dot{\theta}_1' - (y_1 - v)(\dot{v}' + w' \dot{\theta}_1') - (z_1 - w)(\dot{w}' - v' \dot{\theta}_1')] - \\ & \beta_p[v + (y_1 - v)] - [v + (y_1 - v)] \end{aligned} \quad (3.160)$$

$$\begin{aligned} a_z = & \ddot{w} + (y_1 - v) \ddot{\theta}_1' - (z_1 - w) \dot{\theta}_1'^2 + 2\beta_p[\dot{v} - \dot{\theta}_1'(z_1 - w)] \\ & + \beta_p[x + u - v'(y_1 - v) - w'(z_1 - w)] \end{aligned} \quad (3.161)$$

Let L_u^I , L_v^I , L_w^I and M_u^I , M_v^I , M_w^I be the inertial forces and moments in the undeformed frame x, y, z directions. Then, to second order, we have the following.

$$L_u^I = - \int \int_A \rho a_x d\eta d\zeta = T_{U_e} \quad (3.162)$$

$$L_v^I = - \int \int_A \rho a_y d\eta d\zeta = T_v \quad (3.163)$$

$$L_w^I = - \int \int_A \rho a_z d\eta d\zeta = T_w \quad (3.164)$$

$$\begin{aligned} M_v^I &= - \int \int_A [v'(y_1 - v) + w'(z_1 - w)a_z + (z_1 - w)a_x] d\eta d\zeta \\ &\approx - \int \int_A (z_1 - w)a_x d\eta d\zeta \\ &= -T_w' \end{aligned} \quad (3.165)$$

$$\begin{aligned} M_w^I &= \int \int_A [v'(y_1 - v) + w'(z_1 - w)a_y + (z_1 - w)a_x] d\eta d\zeta \\ &\approx \int \int_A (y_1 - v)a_x d\eta d\zeta \\ &= T_v' \end{aligned} \quad (3.166)$$

$$\begin{aligned} M_u^I &= \int \int_A [(z_1 - w)a_y - (y_1 - v)a_z] d\eta d\zeta \\ &= T_{\hat{\phi}} - v' M_v^I - w' M_w^I \\ &= T_{\hat{\phi}} + v' T_w' - w' T_v' \end{aligned} \quad (3.167)$$

where T_{U_e} , T_v , T_w , T_v' , T_w' , $T_{\hat{\phi}}$ are identical to those given in equations (3.137) to (3.143). Thus the kinetic energy terms derived before are identical to the inertial terms obtained here. This shows the equivalence of Hamilton's Principle and Newton's Laws.

Let the external loads (air loads and other concentrated loadings if any e.g., a prescribed lag damper force) be denoted by the superscript A . Then the total loads distribution at a section is given by the sum of inertial and external loads

$$\left. \begin{aligned} L_u &= L_u^A + L_u^I \\ L_v &= L_v^A + L_v^I \\ L_w &= L_w^A + L_w^I \\ M_u &= M_{\hat{\phi}}^A + M_u^I \\ M_v &= v' M_{\hat{\phi}}^A + M_v^I \\ M_w &= w' M_{\hat{\phi}}^A + M_w^I \end{aligned} \right\} \quad (3.168)$$

$M_{\hat{\phi}}^A$ is the external pitching moment (e.g. aerodynamic pitching moment) acting in the blade deformed frame. Its components in the x, y, z directions, $M_{\hat{\phi}}^A, v' M_{\hat{\phi}}^A, w' M_{\hat{\phi}}^A$ are obtained using T_{DU} from equation (3.73).

The resultant shear forces and bending moments at any blade section x_0 is given by the following.

$$\left\{ \begin{array}{c} f_x \\ f_y \\ f_z \end{array} \right\} = \int_{x_0}^1 \left\{ \begin{array}{c} L_u \\ L_v \\ L_w \end{array} \right\} dx \quad (3.169)$$

$$\left\{ \begin{array}{c} m_x \\ m_y \\ m_z \end{array} \right\} = \int_{x_0}^1 \left\{ \begin{array}{c} -L_v(w - w_0) + L_w(v - v_0) + M_u \\ L_u(w - w_0) - L_w(x + u - x_0 - u_0) + M_v \\ -L_u(v - v_0) + L_v(x + u - x_0 - u_0) + M_w \end{array} \right\} dx \quad (3.170)$$

To compute the contribution of the blade loads to the hub loads in the rotating frame, the spanwise integration is carried out from the hub center to the blade tip, and $u_0, v_0, w_0, x_0 = 0$. The hub loads in the fixed frame is calculated using transformation (3.48).

$$\left. \begin{aligned} F_X(\psi) &= \sum_{m=1}^{N_b} (f_x^m \cos \psi_m - f_y^m \sin \psi_m - f_z^m \cos \psi_m \beta_p) \\ F_Y(\psi) &= \sum_{m=1}^{N_b} (f_x^m \sin \psi_m + f_y^m \cos \psi_m - f_z^m \sin \psi_m \beta_p) \\ F_Z(\psi) &= \sum_{m=1}^{N_b} (f_z^m + f_x^m \beta_p) \\ M_X(\psi) &= \sum_{m=1}^{N_b} (m_x^m \cos \psi_m - m_y^m \sin \psi_m - m_z^m \cos \psi_m \beta_p) \\ M_Y(\psi) &= \sum_{m=1}^{N_b} (m_x^m \sin \psi_m + m_y^m \cos \psi_m - m_z^m \sin \psi_m \beta_p) \\ M_Z(\psi) &= \sum_{m=1}^{N_b} (m_z^m + m_x^m \beta_p) \end{aligned} \right\} \quad (3.171)$$

where $f_x, f_y, f_z, m_x, m_y, m_z$ are the rotating frame hub loads, i.e., blade loads integrated up to the hub. The steady values of the fixed frame hub loads (3.171) are used for trimming the helicopter. The higher harmonics cause helicopter vibration. For a tracked rotor, with identical structural and aerodynamic behavior, the higher harmonics contain only those frequencies which are integral multiples of rotor frequency. These harmonics are generated by harmonics of rotating frame blade loads which are one higher and one lower than the rotor frequency.

For example, for an N_b bladed rotor, the higher harmonics in the fixed frame hub loads are pN_b/rev , where p is an integer. These harmonics are generated by $pN_b \pm 1/\text{rev}$ in-plane shear forces (f_x, f_y), pN_b/rev vertical shear force (f_z), $pN_b \pm 1/\text{rev}$ flap and torsion bending moments (m_x, m_y) and pN_b/rev chord bending moment (m_z). To predict helicopter vibration these rotating frame blade loads must be predicted correctly.

3.8 Hub Reactions

The forces and moments acting on the root of the blade are transmitted to the body. If we sum up all the like forces and like moments from various blades in the fixed frame, these form the

hub reactions. The hub reactions are important for the calculation of the helicopter trim, body vibrations and helicopter stability and control characteristics.

Rotating Frame (Blade)

The root forces and moments for a blade,

S_z = vertical shear force

S_x = drag shear force

S_r = radial shear force

N_F = flapwise bending moment

N_L = lag bending moment

Fixed Frame (Rotor)

The resultant rotor forces and moments are,

T = thrust

H = drag force

Y = Side force

M_x = roll moment

M_y = pitching moment

Q = rotor torque, positive opposing rotor rotation

The total non-rotating forces and moments on the rotor hub are obtained by resolving the rotating forces and moment of various blades in the fixed frame and summing these for N blades:

$$T = \sum_{m=1}^N S_z$$

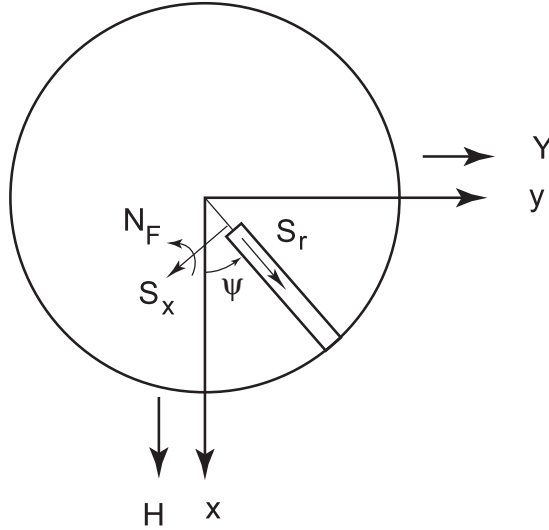
$$H = \sum_{m=1}^N (S_r \cos \psi_m + S_x \sin \psi_m)$$

$$Y = \sum_{m=1}^N (S_r \sin \psi_m - S_x \cos \psi_m)$$

$$M_x = \sum_{m=1}^N N_F \sin \psi_m$$

$$M_y = - \sum_{m=1}^N N_F \cos \psi_m$$

$$Q = \sum_{m=1}^N N_L$$



The above relations can be put in nondimensional form

$$\gamma \frac{c_T}{\sigma a} = \left(\frac{R}{I_b \Omega^2} \right) \frac{1}{N} \sum_{m=1}^N S_z$$

$$\gamma \frac{2c_{m_x}}{\sigma a} = \frac{1}{I_b \Omega^2} \frac{2}{N} \sum_{m=1}^N N_F \sin \psi_m$$

$$\gamma \frac{2c_{m_y}}{\sigma a} = -\frac{1}{I_b \Omega^2} \frac{2}{N} \sum_{m=1}^N N_F \cos \psi_m$$

$$\gamma \frac{c_Q}{\sigma a} = \frac{1}{I_b \Omega^2} \frac{1}{N} \sum_{m=1}^N N_L$$

$$\gamma \frac{c_H}{\sigma a} = \frac{R}{I_b \Omega^2} \frac{1}{N} \sum_{m=1}^N (S_r \cos \psi_m + S_x \sin \psi_m)$$

$$\gamma \frac{c_y}{\sigma a} = \frac{R}{I_b \Omega^2} \frac{1}{N} \sum_{m=1}^N (S_r \sin \psi_m - S_x \cos \psi_m)$$

Example: 3.4

The flap-lag equations of motion for a blade with springs at hinges located at a distance ee from the rotation axis are

$$\beta^{**} + \frac{\gamma}{8} \beta^* + [2\beta_0 - \frac{\gamma}{8}(2\theta - \lambda) \zeta^* + \nu_\beta^2 \beta] = 0$$

$$\zeta^{**} + [-2\beta_0 + \frac{\gamma}{8}(\theta - 2\lambda) \beta^* + \nu_\beta^2 \zeta^*] = 0$$

- (a) Calculate the various forces and moments at the blade hinge.
 (b) Reduce the blade forces to the fixed system.

IF $x \beta^{**}$ arm x	IF $x \zeta^{**}$ arm x
CF x arm $x\beta_0$	CF x arm $x\epsilon\zeta$
CorR $2 \zeta^*$ arm x	CorF $2\beta_0 \beta^*$ arm x
AR F_β arm x	AF F_ζ arm x

$$dL = \frac{1}{2} \rho a c \Omega^2 R^2 \left\{ \left(\frac{u_T}{R} \right)^2 - \frac{u_p}{R} \frac{u_T}{r} \right\}$$

$$\frac{u_T}{\Omega R} = x \quad \frac{u_p}{\Omega R} = x \quad \frac{\partial u_T}{\Omega R} = x \zeta^*$$

Vertical Shear

$$S_z = \frac{I_b \Omega^2}{R} \left\{ \frac{\gamma}{6} (2\theta - \lambda) \zeta^* - \frac{\gamma}{6} \beta^* - \frac{3}{2} \beta^{**} \right\}$$

Lead-Lag Shear

$$S_x = \frac{I_b \Omega^2}{R} \left\{ -\frac{\gamma}{6} (\theta - 2\lambda) \beta^* + \frac{3}{2} \zeta^* - \frac{3}{2} \zeta^{**} \right\}$$

Radial Force

$$S_x = \frac{I_b \Omega^2}{R} \{ 2 - 3 \zeta^* \}$$

Flap Moment

$$N_F = I_b \Omega^2 \left\{ \beta (\nu_\beta^2 - 1 - \frac{3}{2} e) \right\}$$

Lead-Lag Moment

$$N_L = I_b \Omega^2 \left\{ \zeta (\nu_\zeta^2 - \frac{3}{2} e) \right\}$$

Fixed System

Thrust:

$$c_T = \frac{\sigma a}{6} \left\{ (2\theta - \lambda) \zeta_0^* - \beta_0^* \right\} - \frac{3 \sigma a}{2 \gamma} \beta_0^{**}$$

Roll Moment M_x

$$\gamma 2 \frac{c_{mx}}{\sigma a} = (\nu_\beta^2 - 1 - \frac{3}{2} e) \beta_{1s}$$

Pitch Moment M_y

$$\gamma 2 \frac{c_{mx}}{\sigma a} = -(\nu_\beta^2 - 1 - \frac{3}{2} e) \beta_{1c}$$

Rotor Torque Q

$$\frac{\gamma c_Q}{\sigma a} = (\nu_\zeta^2 - \frac{3}{2}e)\zeta_0$$

Drag Force $H = \sum(S_R \cos \psi_m + S_x \sin \psi_m)$

$$\begin{aligned} \gamma 2 \frac{c_H}{\sigma a} &= \frac{\gamma}{6}(\theta - 2\lambda)(\beta_{1s}^* - \beta_{1c}) - \frac{3}{2}(\zeta_{1s}^{**} - 2\zeta_{1c}^* - \zeta_{1s}) \\ &\quad + \frac{3}{2}\zeta_{1s} - 3(\zeta_{1c}^* + \zeta_{1s}) \end{aligned}$$

$$= \frac{\gamma}{6}(\theta - 2\lambda)(\beta_{1s}^* - \beta_{1c}) - \frac{3}{2}(\zeta_{1s}^{**})$$

Side Force $Y = \sum(S_R \sin \psi_m - S_x \cos \psi_m)$

$$\begin{aligned} \gamma 2 \frac{c_Y}{\sigma a} &= \frac{\gamma}{6}(\theta - 2\lambda)(\beta_{1c}^* + \beta_{1s}) + \frac{3}{2}(\zeta_{1c}^{**} + 2\zeta_{1s}^* - \zeta_{1c}) \\ &\quad + \frac{3}{2}\zeta_{1c} - 3(\zeta_{1s}^* - \zeta_{1c}) \end{aligned}$$

$$= \frac{\gamma}{6}(\theta - 2\lambda)(\beta_{1c}^* + \beta_{1s}) + \frac{3}{2}(\zeta_{1c}^{**})$$

Questions

Justify the following:

- Let us look at the “tennis racket effect” on the tennis ball. To give clockwise spin to the ball how should the racket be tilted.
- Generally pitch bearing is located outboard of flap hinge.
- Inplane rotating frequency is generally kept away from the rotational speed, but that is not the case with the flapping mode.
- If the pitch axis lies on the cg axis, there is no structural coupling between flap and pitch motions, but in actuality, these motions are coupled.
- The coriolis forces depend on velocity like damping forces, but their nature is quite different from damping forces.
- In a bearingless main rotor (BMR), the pitch bearing is replaced by an elastic flexure consisting of flexbeams and a torque tube to facilitate pitch changes. From outset, the BMR configuration appears quite similar to the hingeless blade, but in actual, the analysis is quite different for a BMR blade.
- A large δ_3 (like 45°) is not uncommon for tail rotors.
- A zero lag offset is not physical.
- Pitch and lag equations are coupled through coriolis terms.
- External damping in the lag mode is beneficial, but it is quite difficult to add such damping for a hingeless blade.
- Generally it is possible to achieve a matched stiffness condition with soft lag rotors.
- A small offset of cg from feather axis may have a negligible influence on flap mode, but that may not be the case with torsion mode.
- The corolis forces produce a 2/rev lag motion proportional to the square of the 1/rev flap amplitude.
- There will be inherently some pitch-flap and pitch-lag coupling for an elastic blade.
- A vertical gust would induce only vertical oscillations in an articulated rotor with no hinge offset, but that may not be the case with hingeless rotors.

References

1. Johnson, W., Helicopter Theory, Princeton University Press, 1980, Ch. 9.
2. Chopra, I. and Johnson, W., "Flap-Lag-Torsion Aeroelastic Stability of Circulation Controlled Rotors," *Journal of the American Helicopter Society*, Vol. 23, No. 2, April 1979, pp. 37-46.
3. Chopra, I., "Dynamic Analysis of Constant-Lift and Free-Tip Rotors," *Journal of the American Helicopter Society*, Vol. 28, No. 1, Jan. 1983, pp. 24-33.
4. Houbolt, J.C. and Brooks, G. W., "Differential Equations of Motion for Combined Flapwise Bending, Chordwise Bending, and Torsion of Twisted, Nonuniform Rotor Blades," NASA Report 1346, 1958.
5. Hodges, D. H. and Dowell, E. H., "Nonlinear Equations of Motion for Elastic Bending and Torsion of Twisted Nonuniform Blades," NASA TND-7818, Dec. 1974.
6. Johnson, W., "Aeroelastic Analysis for Rotorcraft in Flight or in a Wind Tunnel," NASA TND-8515, July 1977.
Ormiston, R. A., Hodges, D. H., and Peters, D. A., "On the Nonlinear Deformation Geometry of Euler-Bernoulli Beams," NASA Technical Paper 1566, 1980.
7. Chopra, I. and Dugundji, J., "Nonlinear Dynamic Response of a Wind Tunnel Blade," *Journal of Sound and Vibration*, Vol. 63, No. 2, 1979, pp. 265-286.
8. Hong, C. H. and Chopra, I., "Aeroelastic Stability Analysis of a Composite Blade," *Journal of the American Helicopter Society*, Vol. 30, No. 2,
9. Celi, R., Friedmann, P. P., "Structural Optimization with Aeroelastic Constraints of Rotor Blades with Straight and Swept Tips," *AIAA Journal*, Vol. 28, No. 5, 1992.
10. Kim, K. C., Chopra, I., "Aeroelastic Analysis of Helicopter Blades with Advanced Tip Shapes," *Journal of the American Helicopter Society*, Vol. 37, No. 1, Jan 1992. April 1985, pp. 57-67.
11. Sivaneri, N.T. and Chopra, I., "Dynamic Stability of a Rotor Blade Using Finite Element Analysis," *AIAA Journal*, Vol. 20, No. 5, May 1982, pp. 716 - 723.
12. Datta, A., "Fundamental Understanding, Prediction, and Validation of Rotor Vibratory Loads in Steady Level Flight," *PhD Thesis*, University of Maryland, September 2004.
13. Datta, A., and Chopra, I., "Validation of Structural and Aerodynamic Modeling using UH-60A Flight Test Data," *Journal of the American Helicopter Society*, 50th Anniversary Special Edition, Vol. 50, No. 1, January 2006.

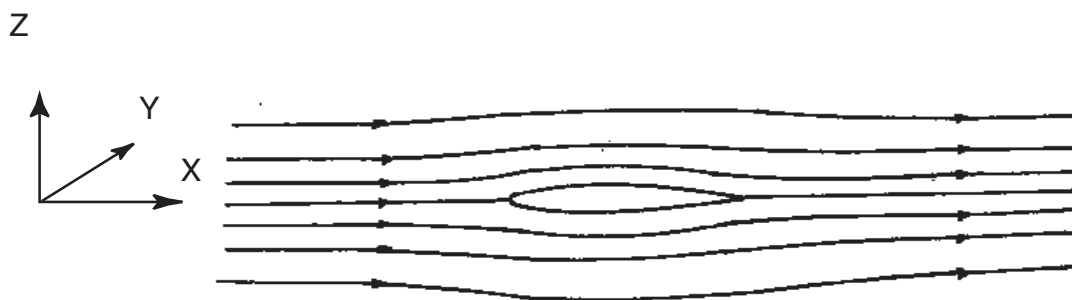
Chapter 4

Unsteady Aerodynamics

The subject of unsteady aerodynamics deals with time dependent aerodynamic forces. The objective of this chapter is to discuss briefly some basic principles of unsteady aerodynamics that concern a rotary wing system. As far as possible, lengthy mathematical derivations are avoided. There are many unique features of the unsteady aerodynamics of the rotary wing as compared to the fixed wing that merit attention. Some of these are: time varying free stream, returning wake, inflow dynamics, radial flow, dynamic stall, reversed flow and complex blade motions. It is important to first understand some of the basic phenomena related to fixed wing unsteady aerodynamics and then expand and reformulate these, wherever possible, to the rotary wing aerodynamics.

4.1 Basic Fluid Mechanics Equations

Assume a wind tunnel case where body is stationary and fluid is flowing over it. The objective is to obtain the state of the fluid at any station x, y, z at a time t . The state consists of six variables and these are pressure (p), fluid density (ρ), temperature (T), and three flow velocity components u, v, w along $x, y,$ and z axes respectively.



There are two forces of interaction between the fluid and the body - (1) pressure force normal to the body surface, and (2) shear force, tangential to the body surface. In addition, a temperature gradient may exist between the fluid and the body. Typically, one would like to determine the pressure distribution and shear force distribution over the body. The shear force depends on the viscosity of the fluid, and velocity gradients near the wall. Without viscosity, the fluid slips past the body without exerting any tangential shear force. The governing partial differential equations are based on conservation of mass, momentum, and energy. Additionally, an algebraic equation of state is used to relate pressure and density to temperature. With the inclusion of viscosity, the equations become involved and it is extremely difficult to solve these equations, even for simple cases.

The governing equations are discussed in the following sections. The derivations of the governing equations can be found in textbooks like Refs. [1, 2].

4.1.1 Navier-Stokes equations

The continuity equation describes the conservation of mass.

1. Conservation of mass

The velocity component in the x direction is u . The velocity components in the y and z direction are v and w .

$$\begin{aligned} \frac{\partial \rho}{\partial t} + \frac{\partial(\rho u)}{\partial x} + \frac{\partial(\rho v)}{\partial y} + \frac{\partial(\rho w)}{\partial z} &= 0 \\ \frac{\partial \rho}{\partial t} + \nabla \cdot (\rho \mathbf{V}) &= \mathbf{0} \end{aligned} \quad (4.1)$$

When all spatial terms are expressed in the form of divergence, as above, the equations are said to be in a *conservation form*.

2. Conservation of momentum

Three equations, each for x, y, and z directions. First consider the equation for x direction. In *conservation form* it is given as follows.

$$\frac{\partial(\rho u)}{\partial t} + \frac{\partial(\rho u^2)}{\partial x} + \frac{\partial(\rho uv)}{\partial y} + \frac{\partial(\rho uw)}{\partial z} = \rho f_x + \frac{\partial \sigma_{xx}}{\partial x} + \frac{\partial \sigma_{xy}}{\partial y} + \frac{\partial \sigma_{xz}}{\partial z} \quad (4.2)$$

where the fluid stresses are given as

$$\sigma_{xx} = -p + \tau_{xx} \quad (4.3)$$

$$\sigma_{xy} = \tau_{xy} \quad (4.4)$$

$$\sigma_{xz} = \tau_{xz} \quad (4.5)$$

The viscous stresses can be related to velocity gradients for Newtonian fluids. Air is a Newtonian fluid. Blood is a non-Newtonian fluid.

$$\tau_{xx} = \mu \frac{\partial u}{\partial x} - \frac{2}{3} \mu \left(\frac{\partial u}{\partial x} + \frac{\partial v}{\partial y} + \frac{\partial w}{\partial z} \right) \quad (4.6)$$

$$\tau_{xy} = \mu \left(\frac{\partial u}{\partial y} + \frac{\partial v}{\partial x} \right) \quad (4.7)$$

$$\tau_{xz} = \mu \left(\frac{\partial u}{\partial z} + \frac{\partial w}{\partial x} \right) \quad (4.8)$$

The momentum equations in y and z directions are similarly given as follows.

$$\frac{\partial(\rho v)}{\partial t} + \frac{\partial(\rho uv)}{\partial x} + \frac{\partial(\rho v^2)}{\partial y} + \frac{\partial(\rho vw)}{\partial z} = \rho f_y + \frac{\partial \sigma_{yx}}{\partial x} + \frac{\partial \sigma_{yy}}{\partial y} + \frac{\partial \sigma_{yz}}{\partial z} \quad (4.9)$$

$$\frac{\partial(\rho w)}{\partial t} + \frac{\partial(\rho wu)}{\partial x} + \frac{\partial(\rho wv)}{\partial y} + \frac{\partial(\rho w^2)}{\partial z} = \rho f_z + \frac{\partial \sigma_{zx}}{\partial x} + \frac{\partial \sigma_{zy}}{\partial y} + \frac{\partial \sigma_{zz}}{\partial z} \quad (4.10)$$

The stress tensor σ is given by

$$\sigma = \left(-p + \frac{2}{3} \mu \nabla \cdot \mathbf{V} \right) \mathbf{I} + 2\mu \mathbf{D} \quad (4.11)$$

\mathbf{I} is an unit tensor. \mathbf{D} is the deformation tensor defined as

$$\mathbf{D} = \frac{1}{2} [\nabla\mathbf{V} + (\nabla\mathbf{V})^T] \quad (4.12)$$

where $\nabla\mathbf{V}$ is the gradient tensor.

$$\nabla\mathbf{V} = \begin{bmatrix} \frac{\partial u}{\partial x} & \frac{\partial u}{\partial y} & \frac{\partial u}{\partial z} \\ \frac{\partial v}{\partial x} & \frac{\partial v}{\partial y} & \frac{\partial v}{\partial z} \\ \frac{\partial w}{\partial x} & \frac{\partial w}{\partial y} & \frac{\partial w}{\partial z} \end{bmatrix} \quad (4.13)$$

Alternatively, in Einstein notation we have

$$\sigma_{ij} = -p\delta_{ij} - \frac{2}{3}\mu\nabla \cdot \mathbf{V}\delta_{ij} + 2\mu D_{ij} \quad (4.14)$$

Consider equations 4.2, 4.9, and 4.10. The spatial derivatives on the left hand side (LHS) are called the convection fluxes. The spatial derivatives on the right hand side (RHS) are called the diffusive fluxes. ρf , the body forces are called the source terms. The equations can be transformed to *non-conservative* forms as follows. Consider the left hand side of any one equation, say equation 4.2. They can be simplified using the continuity equation as follows.

$$\begin{aligned} LHS &= \frac{\partial \rho u}{\partial t} + \frac{\partial(\rho u^2)}{\partial x} + \frac{\partial(\rho uv)}{\partial y} + \frac{\partial(\rho uw)}{\partial z} \\ &= \rho \frac{\partial u}{\partial t} + \rho u \frac{\partial u}{\partial x} + \rho v \frac{\partial u}{\partial y} + \rho w \frac{\partial u}{\partial z} + u \left[\frac{\partial \rho}{\partial t} + \frac{\partial(\rho u)}{\partial x} + \frac{\partial(\rho v)}{\partial y} + \frac{\partial(\rho w)}{\partial z} \right] \\ &= \rho \left(\frac{\partial}{\partial t} + u \frac{\partial}{\partial x} + v \frac{\partial}{\partial y} + w \frac{\partial}{\partial z} \right) u + u(0) \quad \text{using continuity equation} \\ &= \rho \left(\frac{\partial}{\partial t} + \mathbf{V} \cdot \nabla \right) u \\ &= \rho \frac{Du}{Dt} \end{aligned} \quad (4.15)$$

where Du/Dt is called the substantial derivative operator. Thus equation 4.2 can be written in non-conservation form as follows.

$$\begin{aligned} \rho \frac{Du}{Dt} &= \frac{\partial \sigma_{xx}}{\partial x} + \frac{\partial \sigma_{xy}}{\partial y} + \frac{\partial \sigma_{xz}}{\partial z} + \rho f_x \\ &= \frac{\partial p}{\partial x} + \frac{\partial \tau_{xx}}{\partial x} + \frac{\partial \tau_{xy}}{\partial y} + \frac{\partial \tau_{xz}}{\partial z} + \rho f_x \end{aligned} \quad (4.16)$$

The three equations along three directions can be written together as

$$\rho \frac{D\mathbf{V}}{Dt} = -\nabla p + \nabla \cdot \boldsymbol{\tau} + \rho \mathbf{f} \quad (4.17)$$

3. Conservation of energy

The conservation of energy equation is based on the first law of thermodynamics. The total energy per unit mass of a fluid, E is given by

$$E = e + \frac{1}{2}\mathbf{v}^2$$

where e is the internal energy, and $1/2v^2$ is the kinetic energy per unit mass. The enthalpy is given by

$$h = e + pv$$

where p is the pressure, and v is specific volume. In general

$$\begin{aligned} e &= e(T, v) \\ h &= h(T, p) \end{aligned}$$

When the intermolecular forces are negligible, and the fluid is not chemically reacting, we obtain a thermally perfect gas

$$\begin{aligned} e &= e(T) \\ h &= h(T) \\ de &= c_v dT \\ dh &= c_p dT \end{aligned}$$

If the specific heats, c_v and c_p are not functions of temperature, we obtain a calorically perfect gas where

$$\begin{aligned} e &= c_v T \\ h &= c_p T \end{aligned}$$

It has been assumed that $h(T = 0) = 0$ and $e(T = 0) = 0$. The energy conservation equation is given as follows

$$\frac{\partial(\rho E)}{\partial t} + \frac{\partial F_x}{\partial x} + \frac{\partial F_y}{\partial y} + \frac{\partial F_z}{\partial z} + \frac{\partial G_x}{\partial x} + \frac{\partial G_y}{\partial y} + \frac{\partial G_z}{\partial z} = B \quad (4.18)$$

where the convective fluxes are

$$\begin{aligned} F_x &= \rho u E + p u \\ F_y &= \rho v E + p v \\ F_z &= \rho w E + p w \end{aligned} \quad (4.19)$$

The diffusive fluxes are

$$\begin{aligned} G_x &= -\tau_{xx}u - \tau_{xy}v - \tau_{xz}w + q_x \\ G_y &= -\tau_{yx}u - \tau_{yy}v - \tau_{yz}w + q_y \\ G_z &= -\tau_{zx}u - \tau_{zy}v - \tau_{zz}w + q_z \end{aligned} \quad (4.20)$$

q are the heat fluxes into the control volume. They can be related to the temperature gradients. For example, from Fourier's law of heat conduction one can write

$$q_x = -k_x A \frac{\partial T}{\partial x}$$

Similarity for the other directions. A is the area perpendicular to heat flux.

$$B = \rho \dot{q} + \rho u f_x + \rho v f_y + \rho w f_z$$

where $\rho \dot{q}$ is the heat supply per unit mass. Equation 4.18 is in the conservation form. It can be reduced to the non-conservation form to read

$$\begin{aligned} \rho \frac{DE}{Dt} &= -\nabla \cdot (pV) - \nabla \cdot G + B \\ \rho \frac{De}{Dt} + \rho V \cdot \frac{DV}{Dt} &= -\nabla \cdot (pV) - \nabla \cdot G + B \end{aligned} \quad (4.21)$$

The *conservation* form and the *non-conservation* forms are also called the *strong*, and *weak* conservation forms.

4. Equation of state

The equation of state for a perfect gas (where intermolecular forces are neglected) is given by

$$p = \rho RT \quad (4.22)$$

where R is the Rankine gas constant, 287 Joules/kg.Kelvin.

$$R = \frac{\Re}{M} \quad (4.23)$$

where \Re is the universal gas constant, same for all gases, 8314 Joules/(kg.mole.Kelvin). M is the molecular weight of the gas.

These are six basic equations and there are six unknowns to be evaluated. From outset it appears straight forward. But, in reality, it is not possible to get a closed form solution even for very simple problems. Naturally, we have to depend on an approximate analysis. The equations are non-linear and coupled. There are no analytical solutions.

Numerical solutions can be obtained using either finite difference, or finite element discretization. Both these discretization techniques can be cast into a finite volume method. The finite volume method when applied to the equations in conservation form ensures global conservation of mass, momentum and energy. A finite volume method is implemented in the following manner.

$$\begin{aligned} \int_{\Omega} \left(\frac{\partial u}{\partial t} + \frac{\partial F}{\partial x} + \frac{\partial G}{\partial x} - B \right) d\Omega &= 0 \\ \int_{\Omega} \left(\frac{\partial u}{\partial t} - B \right) d\Omega + \int_{\Gamma} (F + G) n_i d\Gamma &= 0 \end{aligned} \quad (4.24)$$

where \int_{Ω} is a volume integral, \int_{Γ} is a surface integral. The following two theorems are very useful.

Divergence Theorem

The volume integral of a divergence of a quantity is equal to the surface integral of the component of the quantity normal to the surface.

$$\int_{\Omega} \nabla \cdot E dV = \int_{\Gamma} E dA \quad (4.25)$$

Stokes Theorem

The area integral of the curl of a vector is equal to the line integral of the vector around the boundary of the area.

$$\int_{\Gamma} \nabla \times E dA = \int_L E dl \quad (4.26)$$

The Navier-Stokes equations can be non-dimensionalized. However, for practical applications with complicated geometries, varying fluid properties, and unsteady boundary conditions the number of non-dimensional parameters become very large. Hence for many practical applications are dimensional equations are used. From experiments it has been observed that the Navier-Stokes equations describe the flow of a Newtonian fluid satisfactorily, even though, for a given boundary condition the uniqueness of a solution is difficult to prove.

The Navier-Stokes equations can be simplified for special cases. These simplified cases are also of great value to an analyst. They are incompressible flows (constant density), isothermal flows (constant viscosity), inviscid flows (zero viscosity), potential flow (zero viscosity and irrotational), creeping or Stokes flow (convective fluxes are negligible except for pressure, i.e. flow occurs under viscous, pressure and body forces only), Boussinesq flow (density is constant in the unsteady and convective fluxes, but varying in the gravitational body forces), boundary layer flow (thin shear layer), and steady flows, where the time derivatives are set to zero. The simplified equations relevant for rotorcraft flows are discussed below.

4.1.2 Euler equations

The fluid is assumed to have no viscosity. The Euler equations are obtained by simply setting the diffusive fluxes to zero in the conservation form of the equations. The continuity equation remains same as equation 4.1.

The momentum equation, in its non-conservation form, equation 4.17, reduces to

$$\rho \frac{DV}{Dt} = -\nabla p + \rho \mathbf{f} \quad (4.27)$$

The energy equation, equation 4.18, can be re-arranged in several ways. One way is to proceed from equation 4.18 as follows. First set the diffusive fluxes to zero, $G = 0$.

$$\begin{aligned} \rho \frac{De}{Dt} &= -\rho V \cdot \frac{DV}{Dt} - \nabla \cdot (pV) + B \\ &= +V \cdot \nabla p - \nabla \cdot (pV) + B && \text{using the momentum equation} \\ &= -p \nabla \cdot V + B && \text{using } \nabla \cdot (pV) = p \nabla \cdot V + V \cdot \nabla p \end{aligned} \quad (4.28)$$

The continuity equation gives the following

$$\begin{aligned} \frac{\partial \rho}{\partial t} + (V \cdot \nabla) \rho + \rho \nabla \cdot V &= 0 \\ \nabla \cdot V &= -\frac{1}{\rho} \frac{D\rho}{Dt} \end{aligned} \quad (4.29)$$

Thus the energy equation becomes

$$\begin{aligned} \rho \frac{De}{Dt} &= \frac{p}{\rho} \frac{D\rho}{Dt} + B \\ \rho c_v \frac{De}{Dt} &= \frac{p}{\rho} \frac{D\rho}{Dt} \end{aligned} \quad (4.30)$$

Assuming the body forces and heat fluxes to be zero.

The Euler equations cannot be solved analytically. The next level of approximation is to assume irrotational flow. The assumption of irrotational flow leads to the existence of velocity and acceleration potential functions. Thus, these flows are called potential flows.

4.1.3 Velocity Potential Equation for Unsteady Flows

The assumption of irrotationality reduces the momentum equations to the unsteady Bernoulli equation, also called Kelvin's equation. This is the Bernoulli equation in its most non-restrictive form, applicable for unsteady, compressible flows. The governing equation is obtained from the continuity equation. The equations are derived in ref. [3], and given below.

Flow irrotationality means that the curl of the flow velocity is zero. The curl of the flow velocity is vorticity, ξ .

$$\xi = \nabla \times V = 0 \quad (4.31)$$

This is a necessary and sufficient condition for the existence of a velocity potential such that

$$V = \nabla \phi \quad (4.32)$$

For an irrotational flow, the force field must be irrotational. A conservative force field is an irrotational force field. Consider the Euler equation 4.27. The body force per unit mass \mathbf{f} can then be represented as $\nabla \Omega$. The equation is written as

$$\frac{DV}{Dt} = -\frac{\nabla p}{\rho} + \nabla \Omega \quad (4.33)$$

Now

$$\begin{aligned}
 \frac{DV}{Dt} &= \frac{\partial V}{\partial t} + (V \cdot \nabla)V \\
 &= \frac{\partial V}{\partial t} + \nabla \frac{V^2}{2} - V \times (\nabla \times V) \\
 &= \frac{\partial V}{\partial t} + \nabla \frac{V^2}{2} - 0 \\
 &= \frac{\partial \nabla \phi}{\partial t} + \nabla \frac{V^2}{2} \\
 &= \nabla \left(\phi_t + \frac{V^2}{2} \right)
 \end{aligned} \tag{4.34}$$

where $\phi_t = \partial \phi / \partial t$. The momentum conservation equation now becomes

$$\begin{aligned}
 \nabla \left(\phi_t + \frac{V^2}{2} \right) &= -\frac{\nabla p}{\rho} + \nabla \Omega \\
 &= -\nabla \int \frac{dp}{\rho} + \nabla \Omega
 \end{aligned} \tag{4.35}$$

It follows

$$\nabla \left(\phi_t + \frac{V^2}{2} + \int \frac{dp}{\rho} - \Omega \right) = 0 \tag{4.36}$$

The term within the bracket can only be a constant, at most a function of time.

$$\phi_t + \frac{V^2}{2} + \int \frac{dp}{\rho} - \Omega = F(t) \tag{4.37}$$

The above equation is the most non-restrictive form of Bernoulli's equation. The right hand side can be related to conditions at a remote point where ϕ will be a constant. Thus,

$$F(t) = \frac{U_\infty^2}{2} + \int_{p_\infty}^{p_\infty} \frac{dp}{\rho} - \Omega_\infty \tag{4.38}$$

Thus equation 4.37 can be written as

$$\phi_t + \frac{1}{2} (V^2 - U_\infty^2) + \int_{p_\infty}^p \frac{dp}{\rho} + (\Omega_\infty - \Omega) = 0 \tag{4.39}$$

For isentropic flow

$$\int_{p_\infty}^p \frac{dp}{\rho} = \frac{1}{\gamma - 1} (a^2 - a_\infty^2) \tag{4.40}$$

The local pressure coefficient and the local speed of sound (or absolute temperature T) can be obtained from the above equation.

$$\begin{aligned}
 C_p &= \frac{p - p_\infty}{\frac{1}{2} \rho_\infty U_\infty^2} \\
 &= \frac{2}{\gamma M^2} \left\{ \left[1 - \frac{\gamma - 1}{a_\infty^2} \left(\phi_t + \frac{V^2 - U_\infty^2}{2} + \Omega_\infty - \Omega \right) \right]^{\frac{\gamma}{\gamma - 1}} - 1 \right\}
 \end{aligned} \tag{4.41}$$

From equations 4.40 and 9.18 we have

$$a^2 - a_\infty^2 = -(\gamma - 1) \left[\phi_t + \frac{1}{2} (V^2 - U_\infty^2) + (\Omega_\infty - \Omega) \right] \quad (4.42)$$

We saw above how the Euler equations for momentum conservation reduce to the unsteady Bernoulli's equation (or Kelvin's equation) under the assumption of flow irrotationality. The continuity equation for mass conservation reduces to the governing governing PDE for the velocity potential ϕ .

$$\begin{aligned} \frac{D\rho}{Dt} + \rho \nabla \cdot V &= 0 \\ \frac{D\rho}{Dt} + \rho \nabla^2 V &= 0 \\ \int_{p_\infty}^p \frac{dp}{\rho} &= -\phi_t - \frac{1}{2} (V^2 - U_\infty^2) \end{aligned} \quad (4.43)$$

Now using Leibnitz theorem we have

$$\frac{d}{dp} \int_{p_\infty}^p \frac{dp}{\rho} = \frac{1}{\rho} \quad (4.44)$$

Then

$$\begin{aligned} \frac{D}{Dt} \int_{p_\infty}^p \frac{dp}{\rho} &= \left[\frac{d}{dp} \int_{p_\infty}^p \frac{dp}{\rho} \right] \frac{Dp}{Dt} \\ &= \frac{1}{\rho} \frac{dp}{d\rho} \frac{D\rho}{Dt} \\ &= \frac{a^2}{\rho} \frac{D\rho}{Dt} \end{aligned} \quad (4.45)$$

Using the above result with the third of equation 4.43 we have

$$\begin{aligned} \frac{1}{\rho} \frac{D\rho}{Dt} &= -\frac{1}{a^2} \frac{D}{Dt} \left(\phi_t + \frac{1}{2} V^2 \right) \\ \frac{1}{\rho} \frac{D\rho}{Dt} &= -\frac{1}{a^2} \left(\frac{\partial}{\partial t} + V \cdot \nabla \right) \left(\phi_t + \frac{V^2}{2} \right) \end{aligned} \quad (4.46)$$

Replace the left hand side of the above expression from the second of equation 4.43. Expand the right hand side to obtain

$$\nabla^2 \phi - \frac{1}{a^2} \left[\phi_{tt} + V \cdot \nabla \phi_t + V \cdot \frac{\partial V}{\partial t} + V \cdot \nabla \left(\frac{V^2}{2} \right) \right] \quad (4.47)$$

Thus the governing equation can be written in any of the following forms

$$\begin{aligned} \nabla^2 \phi - \frac{1}{a^2} \left[\phi_{tt} + \frac{\partial}{\partial t} V^2 + V \cdot \nabla \frac{V^2}{2} \right] &= 0 \\ \nabla^2 \phi - \frac{1}{a^2} \left(\frac{\partial}{\partial t} + V \cdot \nabla \right) \left(\phi_t + \frac{V^2}{2} \right) &= 0 \\ \nabla^2 \phi - \frac{1}{a^2} \frac{D}{Dt} \left(\phi_t + \frac{V^2}{2} \right) &= 0 \end{aligned} \quad (4.48)$$

These equations describe an inviscid potential flow, but non-stationary and not limited to small disturbances. It has the same form as the equation of wave motion. The disturbance represented by the velocity potential partakes of the local fluid velocity and is propagated as a wave which spreads at a rate equal to the local speed of sound.

At this stage it is important to note the following. Consider the following two assumptions, one by one.

1. The fluid is incompressible, ρ is constant everywhere.
2. The fluid flow is steady, $\partial/\partial t$ terms are zero.

Under each of these two conditions, the governing equation reduces to the same Laplace equation

$$\nabla^2 \phi = 0 \quad (4.49)$$

Under the first assumption, the speed of sound goes to infinity. Under the second assumption, the unsteady terms go to zero. Thus for incompressible flow, the governing equation is indistinguishable between steady and unsteady flows. The boundary conditions, however, are to be treated differently. The classical unsteady solutions (obtained during the 1930s by several researchers) are obtained from such differences. This is treated in the section on thin airfoil theory. Thin airfoil theory deals with incompressible potential flow in 2-dimensions.

The above potential flow equations (4.48) is in its invariant form. It can be converted easily to any coordinate system, fixed or moving in space. For example, in cartesian coordinates it reduces to the following form [4]

$$\begin{aligned} \left(1 - \frac{u^2}{a^2}\right) \phi_{xx} + \left(1 - \frac{v^2}{a^2}\right) \phi_{yy} + \left(1 - \frac{w^2}{a^2}\right) \phi_{zz} - 2\frac{uv}{a^2} \phi_{xy} - 2\frac{vw}{a^2} \phi_{yz} \\ - 2\frac{wu}{a^2} \phi_{zx} - 2\frac{u}{a^2} \phi_{xt} - 2\frac{v}{a^2} \phi_{yt} - 2\frac{w}{a^2} \phi_{zt} - \frac{1}{a^2} \phi_{tt} = 0 \end{aligned} \quad (4.50)$$

where $u = \phi_x$, $v = \phi_y$, $w = \phi_z$, and a is the velocity of propagation of disturbances, i.e. the local speed of sound.

4.1.4 The Acceleration Potential

Like velocity potential ϕ , an acceleration potential Ψ can be defined for potential flows. For an irrotational flow to remain irrotational, the force field must be irrotational. The Euler equation from equation 4.27 is then given by

$$\frac{D\mathbf{V}}{Dt} = -\frac{\nabla p}{\rho} + \frac{\mathbf{f}}{\rho} \quad (4.51)$$

where Ω is the potential of the force field per unit mass. It follows

$$\begin{aligned} \frac{DV}{Dt} &= -\frac{\nabla p}{\rho} + \nabla \Omega \\ &= \nabla \left[\Omega - \int \frac{dp}{\rho} \right] \end{aligned} \quad (4.52)$$

Thus

$$\nabla \times \frac{DV}{Dt} = 0 \quad (4.53)$$

which implies DV/Dt can be expressed as a gradient of a potential $\nabla \Psi$. This is called the acceleration potential.

$$\Psi = \Omega - \int \frac{dp}{\rho} \quad (4.54)$$

or at most

$$\Psi = \Omega - \int \frac{dp}{\rho} + G(t) \quad (4.55)$$

where $G(t)$ can be function of time, generally discarded. When disturbances are small, the acceleration potential is useful.

$$\int_{p_\infty}^p \frac{dp}{\rho} \approx \frac{p - p_\infty}{\rho_\infty}$$

$$\Psi = -\frac{p - p_\infty}{\rho_\infty}$$
(4.56)

Thus the acceleration potential Ψ denotes a pressure difference. Doublets of Ψ are useful tools to represent lifting surfaces.

4.1.5 Vorticity Conservation Equation

The Euler equations for momentum conservation can be recast into a vorticity conservation form. This form is often used by researchers for problems where preservation of flow vorticity is of great importance over large flow domains. Consider the substantive derivative of velocity (left hand side of the Euler equation).

$$\begin{aligned} \frac{DV}{Dt} &= \frac{\partial V}{\partial t} + (V \cdot \nabla)V \\ &= \frac{\partial V}{\partial t} + \nabla \frac{V^2}{2} - V \times (\nabla \times V) \\ &= \frac{\partial V}{\partial t} + \nabla \frac{V^2}{2} - V \times \xi \end{aligned}$$
(4.57)

Now take curl of the equation above

$$\begin{aligned} \nabla \times \frac{DV}{Dt} &= \nabla \times \frac{\partial V}{\partial t} + \nabla \times \nabla \frac{V^2}{2} - \nabla \times (V \times \xi) \\ &= \frac{\partial \xi}{\partial t} + 0 - \nabla \times (V \times \xi) \end{aligned}$$
(4.58)

Note the following identity

$$\nabla \times (A \times B) = (B \cdot \nabla)A - (A \cdot \nabla)B - B(\nabla \cdot A) + A(\nabla \cdot B)$$
(4.59)

It follows

$$\nabla \times (V \times \xi) = (\xi \cdot \nabla)V - (V \cdot \nabla)\xi - \xi(\nabla \cdot V) + V(\nabla \cdot \xi)$$
(4.60)

Note that $\nabla \cdot \xi = 0$. This is similar to the Maxwell equation for magnetic induction B , $\nabla \cdot B = 0$. Hence we have

$$\begin{aligned} \nabla \times \frac{DV}{Dt} &= \frac{\partial \xi}{\partial t} + (V \cdot \nabla)\xi - (\xi \cdot \nabla)V + \xi(\nabla \cdot V) \\ &= \frac{D\xi}{Dt} - (\xi \cdot \nabla)V + \xi(\nabla \cdot V) \end{aligned}$$
(4.61)

The final equation is then

$$\frac{D\xi}{Dt} = (\xi \cdot \nabla)V + \xi(\nabla \cdot V) + \nabla \times \mathbf{f}$$
(4.62)

where \mathbf{f} is the body force per unit mass.

4.1.6 Potential Equation for Steady Flow

The potential equation for steady flow can be obtained by setting the time derivatives in equation 4.48 or equation 4.50 to zero. The later gives the following

$$\begin{aligned} \left(1 - \frac{\phi_x^2}{a^2}\right) \phi_{xx} + \left(1 - \frac{\phi_y^2}{a^2}\right) \phi_{yy} + \left(1 - \frac{\phi_z^2}{a^2}\right) \phi_{zz} \\ - 2\frac{\phi_x\phi_y}{a^2} \phi_{xy} - 2\frac{\phi_y\phi_z}{a^2} \phi_{yz} - 2\frac{\phi_z\phi_x}{a^2} \phi_{zx} = 0 \end{aligned} \quad (4.63)$$

where all velocities have been expressed in terms of the potential. Note that this equation, combines both the continuity and momentum conservation laws. The energy conservation law leads to the following. Conserving enthalpy per unit mass and assuming a calorically perfect fluid we have

$$\begin{aligned} C_p T + \frac{V^2}{2} &= C_p T_0 \\ C_p &= \frac{\gamma R}{\gamma - 1} \\ a &= \sqrt{\gamma R T} \end{aligned}$$

where T_0 is the stagnation temperature corresponding to zero velocity. Using the above we obtain

$$a^2 - a_0^2 = -\frac{\gamma - 1}{2} (\phi_x^2 + \phi_y^2 + \phi_z^2) \quad (4.64)$$

Note that the above equation 4.64 is same as equation 4.42 for a steady case. Only that in the present case the local properties have been related to stagnation properties, whereas in the previous case they were related to un-disturbed conditions at infinity. Equations 4.63 and 4.64, as before, represent one equation for continuity, momentum and energy conservation. The non-linear PDE is applicable to subsonic, transonic, supersonic as well as hypersonic flows. The only assumptions are that of irrotational and isentropic flow.

4.1.7 Potential Equation for Incompressible Flow

In the case of incompressible flow, the continuity equation 4.1 reduces to the following form

$$\nabla \cdot \mathbf{V} = 0 \quad (4.65)$$

The condition of flow irrotationality, $\xi = \nabla \times V = 0$, gaurantees the existance of a velocity potential $V = \nabla\phi$. The continuity equation then produces the Laplace Equation.

$$\nabla^2 \phi = 0 \quad (4.66)$$

In cartesian coordinates

$$\phi_{xx} + \phi_{yy} + \phi_{zz} = 0 \quad (4.67)$$

Both are readily deducible from equations 4.48 and 4.50. As noted earlier, for an incompressible flow the time dependancies vanish, and hence the governing equation is indistinguishable between steady and unsteady flows. The momentum conservation equation reduces to the Bernoulli's equation for steady flows. From equation 9.18 we have

$$p + \frac{1}{2} \rho V^2 = \text{Constant} \quad (4.68)$$

The equations 4.83, 4.67 can be solved with values of the potential or its normal derivatives (or combinations thereof) prescribed at the boundaries. A large volume of knowledge exists on the solution of such classical boundary value problems, see for example Lamb ([5], 1945), Milne-Thompson ([6], 1960), Thwaites ([7], 1960). The equation cannot be solved directly for arbitrary geometries. Analytical solutions exist for simple flows which can be combined to obtain solutions for practical applications. Such solutions are the uniform flow, source, sink, and a vortex flow. The strength of these solutions are treated as unknowns and determined from boundary conditions. One such application is the basis for the thin airfoil.

4.2 The Rotor Flow Field

The rotor blades operate in a high Reynolds number, typically 1–6 million, highly vortical flowfield. The aerodynamics of a rotor blade differ from that of a fixed wing due to the following phenomenon.

1. Rotor inflow, generated by high RPM of the blades (around 250 for conventional main rotors), necessary for vertical flight.
2. Cyclic variation of blade pitch angle, necessary for control.
3. Time varying, asymmetric flow in forward flight with large variations of angle of attack in the advancing and retreating sides.
4. Enormous compressibility effects including shocks on the advancing side and stalled flow on the retreating side.
5. The complex, unsteady wake structure of each blade interacting with following blades.

4.2.1 Wake Structure of a Lifting Wing

Consider an un-twisted wing with symmetric airfoils in steady flight. If the angle of incidence of with respect to the oncoming flow is zero then the flow over the wing is symmetric in the vertical direction. It need not be so in the horizontal direction. If the airfoil sections are thick, and if there is sufficient skin friction the flow will separate towards the trailing edge of the wing. This asymmetry creates skin friction drag and pressure drag forces on the wing. In turn, the disturbance imparted by the wing on the surrounding air can be turbulent and unsteady. The flows on the top and bottom surfaces however, being symmetric, generates no vertical force. This symmetry is broken in the case of a wing at an angle of incidence to the oncoming flow, or in the case of a wing with cambered airfoils. The asymmetry between the flow on the top and flow on the bottom generates a vertical lifting force. The magnitude of this lifting force, or lift, is generally an order of magnitude greater than the drag force. It is the key determinant of wing performance and the performance of the aircraft as a whole. The asymmetry between the flow on the top and bottom surfaces also generates an additional horizontal drag force called the induced drag. This horizontal force is produced only in the case of a finite wing. While the net pressure determines lift, the distribution of pressure determines the pitching moment about any point on a wing section. The lift, pitching moment, and drag are called airloads. The pitching moment divided by the lift force gives a distance. This is the distance from the point about which the pitching moment was calculated and the point at which the lift force acts. The later is called the center of pressure. The definition of center of pressure becomes less meaningful when the lift force approaches zero. This happens at small angles of incidences. The center of pressure then approaches infinity, oscillating wildly between positive and negative values depending on the relative signs of the lift and pitching moments. The goal is to calculate the airloads as accurately as possible.

The disturbance imparted by a lifting wing to its surrounding air is highly vortical in nature. Lanchester was the first to show that the effect of the wing on the surrounding air, and the effect of the surrounding air on the wing in terms of the lifting force can be closely simulated by a system of vortices. Lanchester's system of vortices greatly aids in understanding the basic character of the disturbance, or wake, behind finite, lifting wings. The system comprises of what is called a bound vortex system, a trailing vortex system and a starting vortex system. The trailing and starting vortex systems can be related to physical flow characteristics in the wake and are often visible to the naked eye if the conditions are right. The bound vortex system is hypothetical and forms the crux of the model. The bound vortex system replaces the wing. The finite wing theory is concerned with the determination of an equivalent bound vortex system which re-creates the real airloads, and the real disturbances imparted to the fluid, from as close to the wing as possible.

The strength of the bound vortices are related to the strengths of the trailing and starting vortices via the four fundamental theorems of vortex motion, Helmholtz's Theorems. These theorems require that a fluid initially free from vortices remain so permanently - vortices can neither be created nor destroyed. The lift force is related to the strength of the bound vortices via Kutta Joukowski condition. These inter-relations only emphasize the coupled nature of airloads and wake where one determines the other and vice versa.

4.2.2 Coupled Airloads and Wake

For a 2D airfoil, there is no trailing vortex system. If the airfoil is held steady to the oncoming flow, the starting vortex is at infinity. The bound vortex system, which models the airfoil, moves through the flow, and tries to simulate the airloads on the airfoil, and the disturbances imparted by the airfoil on the surrounding air. The strength of the bound vortex system is obtained by zero impenetrability condition, and by ensuring smooth flow over the trailing edge. The later is also called the Kutta condition. The forms the subject of thin airfoil theory. That is, given an airfoil at an angle of incidence the goal is to determine the bound vortex strength which generates the correct lift.

For a 3D wing, the objective is the same, but there is an added complication. That is the trailing vortex system. Depending on the strength of the trailing vortex system a downwash is induced on the airfoil, which modifies the oncoming flow, and this induced effect must be taken into account while calculating the bound vortex system. However, the strength of the trailing vortex system is itself determined by the bound vortex system. Thus, the wake (trailing vortex system) and the airloads (determined by the bound vortex system) are coupled together and must be treated as a whole.

Prandtl's lifting line model conceptually separates the two. It says the following: (1) use thin airfoil theory for each wing section just as if it were 2D, with the only modification, that instead of using the actual angle of incidence use a modified or reduced angle of incidence, and (2) calculate the angle of reduction that is required in step 1. To carry out step 2, the bound vortex distribution used in step 1 is collapsed to a single bound vortex. The wing model then becomes a line of bound vortices extending over the span. The trailing vortex system is then calculated using this line distribution of bound vortices across the span, hence the name lifting-line. The lifting-line forms the wing, which is used to modify the local airfoil incidences. The assumption is that the global induced flow effects of the wake can be simulated disregarding the details of the local airfoil surface flow. It works well for large aspect ratio wings without a sharp spanwise lift variation. As long as the spanwise lift distribution do not show sharp gradients the predictions are satisfactory. This method is called breaking up the wing problem into inner and outer problems. The inner problem deals with the airfoil section. The outer problem deals with the 3D reduction in angle of incidence needed in the inner problem. For wings with low aspect ratio, sweep, delta wings, etc., this approach is no longer effective. Note also, that the spanwise lift change is necessarily sharp at the tip because it drops to zero. Thus a lifting-line model is unsatisfactory near the tip. In general,

a lifting model gives good lift variations for aspect ratios above 4, and for straight wings.

In the next level of modeling the wing is not idealized as a bound vortex line, but treated as a distribution of vortices. The vortex system is then treated in an unified manner. For conventional helicopter rotors, blades have a high aspect ratio (8 to 10) and are nominally straight. However the lift variation is not uniform over span due to the rotational motion of the wing. Still, the lifting line model can be successfully used for the calculation of lift. It is often modified to account for measured airfoil properties. The airfoil properties provide 2D lift, drag, and pitching moment data for realistic airfoils. In this case step 1 of the lifting line procedure can be avoided. However, step 2 must be done in a systematic manner such that the bound vortex strengths, trailing vortex strengths and the airfoil properties are all consistent. This means: (1) the predicted lift satisfies Kutta Joukowski theory as well as the airfoil properties, and (2) the reduced angle of incidences are consistent with the trailing vortex system which is consistent with the airfoil lift. A lifting line model is a simplified potential flow solution. The advantage is that the effects of compressibility and viscosity can be easily incorporated externally using prescribed airfoil tables. To understand lifting line models that are classically adopted for rotary wing calculations we begin with the concept of breaking up the problem of calculation of lift into inner and outer problems.

The inner problem is the airfoil response problem. The outer problem is the wake problem. Note that, as mentioned earlier, this break-up is only for the ease of analytical treatment. In reality the 3D wing or rotor problem is a coupled problem of airloads and wake.

4.2.3 Non-steady Excitation in Rotor Blades

In the case of a rotor blade the angle of incidence varies with time. This is due to the time varying control inputs and blade deformations. As a result the trailing vortex system is time varying. In addition, there is a shed vortex system. It can be thought of as a system of starting vortices generated due to a time varying angle of incidence on the blade. In the case of rotor blades

Physically, the problem has two parts - excitation and response. The excitation is due to blade motions and control angles. The response involves the calculation of airloads on the blade and the motion imparted to the surrounding air by the blade, i.e. the wake comprised of the trailed and shed vortex system. The airloads and the wake system, as mentioned earlier, forms a coupled problem. Given the blade excitation, modern CFD methods seek to solve the response problem directly.

For many applications a lifting line approach is adopted to a rotor. In this approach the problem is again broken into an inner and an outer part. The advantage, as mentioned earlier, in this approach of breaking up the problem into inner and outer parts is the ease of including compressible and viscous effects using corrections to a potential flow solution. The conceptual departure from physics here is the treatment of wake as an agent of excitation, not part of the response. This is discussed in the next subsection.

4.2.4 Trailed and Shed Wake Structure of a Rotor

Consider the wake system one by one. First the trailed wake. As in the case of a fixed wing, a lifting line model can be used to calculate a modified angle of incidence. The key difference here is that the modification must account for the trailed wake from all blades. Next consider the shed wake. The shed wake can be incorporated in two ways. One way is to treat it in the same way as the trailed wake. That is, determine the effect of the shed wake from all blades to modify the angle of incidence. In this case the shed wake is treated as an agent of excitation. A disadvantage here is that, the shed wake being modeled as a vortex system, is necessarily incompressible and inviscid. The second way is to ignore the shed wake while calculating the airfoil excitation. Incorporate the shed wake by modifying the airfoil response. This second approach forms the subject matter of the theory of unsteady aerodynamics. This approach has the advantage that compressibility, and

dynamic stall effects can be incorporated using semi-empirical models. The effect of shed wake is called the circulatory effect. The unsteady airfoil response also contains a non-circulatory or apparant mass effect. This effect must be accounted for in either approach. The effect of trailed and shed wake from all the blades generate the rotor inflow.

If the rotor blades experience a constant angle of incidence, for example in the case of hover with only a collective angle, then there is no shed wake. The trailed wake, all the blades create a steady inflow through the rotor disk, varying over the blade span.

One approximate way to calculate the steady rotor inflow is to use momentum theory. This inflow can then be used to modify the blade angle of incidence. This is the blade element momentum theory. Note that it is not a lifting line model, as the inflow has not been calculated using a blade aerodynamic model, but by simple implementation of energy conservation laws.

4.2.5 Unsteady Aerodynamics

Classical 2D unsteady aerodynamic theory is concerned with calculating the effect of shed wake on airfoil airload response. For example, the effective angle of incidence of the airfoil sections on the rotor blade can be determined based on blade motions, control angles, and trailed wake from all blades. The angle of incidence is also called the effective blade element angle of attack. Based on the angle of attack and its rate of change the airload response can be modified to incorporate the effect of shed wake. The geometry of the shed wake will be different depending on the type of excitation. The effective angle of attack excitation can consist of several parts. For example, the blade pitching motions supply both an angle of attack as well as a rate of change of angle of attack, the flapping motion supplies a plunging motion, the inflow supplies a gust type velocity pattern, the unsteady response to all these stimuli are different and complex. An comprehensive treatment of these effects can be found in Leishman [8]. In general, most rotor simulations combine these effects to define an instantaneous angle of attack for each airfoil section calculated at the 3/4 chord location. The airloads are then calculated using the 'look-up' tables obtained from wind tunnel tests. These are termed quasi-steady airloads. The quasi-steady airloads can then be corrected using unsteady aerodynamic theory. The quasi-steady airloads vary with time. The unsteady correction reduces the peak magnitude and alters the phase. The correction can be made either in the frequency domain or in the time domain. They are equivalent. For example, the classical Theodorsen's theory provides the correction in the frequency domain. On the other hand Wagner's formulation is in the time domain. It is exactly equivalent to Theodorsen's theory in the frequency domain, except that it also includes the non-circulatory forces. These classical 2D theories are based on potential flow solutions to oscillating thin airfoils. Thus they ignore compressibility, viscous effects, affect of airfoil shape and most significantly flow separation. Over the last three decades, significant improvements have been made in unsteady aerodynamic modeling. Oscillating airfoil wind tunnel data have been used to develop semi-empirical models that attempt to capture the real fluid effects, including specific airfoil properties, compressibility, and flow separation. Flow separation on rotor blades produce the phenomenon of dynamic stall. Whereas the attached flow unsteady effects are produced by continuous vortex shedding from the trailing edge, dynamic stall is characterised by abrupt vortex shedding from the leading edge. For example, semi-empirical indicial models were developed for high sub-sonic (up to Mach number 0.8) 2D unsteady aerodynamics by Leishman and Beddoes [11, 10]. The models were further extended to include nonlinear effects of flow separation [9], dynamic stall [12] and effects of blade sweep on dynamic stall [13].

4.2.6 Dynamic Stall

Dynamic stall is an unsteady flow separation phenomenon that occurs on a heavily loaded rotor or a moderately loaded rotor at high speed. The rotor blades can encounter dynamic stall on the retreating blade because of high angle of attack, and on the advancing blade because of shock

induced leading-edge separation. Dynamic stall generates high oscillatory and vibratory torsion loads on the blades and the swash-plate servos. Predicting dynamic stall is necessary for initial sizing and stall flutter calculations. It is also key to achieving higher forward speed capabilities for heavily loaded rotor systems.

Numerous experiments have revealed the general sequence of events. For an airfoil pitching up, a progressive trailing edge separation due to flow reversal in the boundary layer, is accompanied by the formation of a leading edge vortex. The onset of a critical leading edge pressure triggers a leading-edge separation where the vortex detaches and starts moving downstream. This phenomenon of vortex detachment generates a strong pitching moment stall. However, as long as the vortex traverses over the airfoil, the lift does not stall and continues to increase. The lift stalls when the vortex leaves the trailing edge. At this time, the pitching moment reaches its maximum negative value. A period of progressive flow re-attachment follows as the airfoil pitches down. During this time one or more weaker vortices can be shed from the upper surface, creating additional fluctuations in lift and pitching moment. This sequence of events lead to large hysteresis loops in airloads when plotted versus the angle of incidence. Typical hysteresis loops in airfoil lift coefficient and pitching moment coefficients are shown in Fig.4.1. The figure shows the airloads on a 2D SC-1095 airfoil section undergoing pitch oscillations at a nondimensional frequency $k = \omega c/2U$, where ω is the frequency of oscillation in radians/sec, c is the airfoil chord, and U is the incident velocity. The incident velocity corresponds to a Mach number of 0.3. When the angle of attack variation is such that the airfoil goes slightly out of the static stall regime with each oscillation, it is called a light stall. When a large part of the angle of oscillation occurs outside the static stall regime, it is called a deep stall.

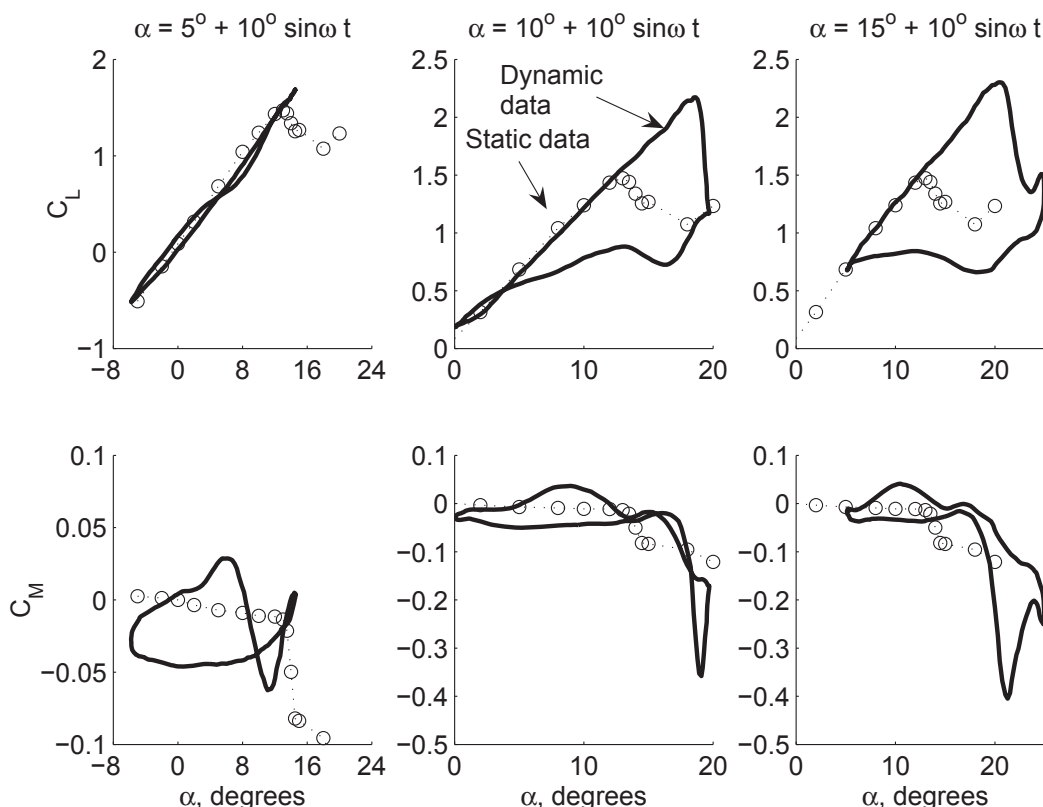


Figure 4.1: SC-1095 light and deep dynamic stall cycles; static and dynamic data from McCroskey et al NASA TM-84245, 1982, at Mach 0.3, reduced frequency $k = 0.1$

Fundamental understanding of dynamic stall began with the seminal work of Liiva [16] on helicopter rotors and Carta [17] on axial-flow turbomachines. Subsequently, many experimental investigations have provided greater insights into the phenomena.

Current comprehensive analyses calculates dynamic stall using semi-empirical models. like the UTRC Method 1970, the Beddoes Time-Delay Method 1976, Gangwani's Method 1982 (all reviewed in [8]), the Boeing-Vertol gamma function method 1973 [18], Johnson's Method 1969 [19], the Leishman-Beddoes Method 1986 [12], ONERA EDLIN (Equations Differentielles Lineaires) model 1990 [20] and the ONERA BH (Bifurcation de Hopf) model 1998 [21].

Dynamic stall is characterized by a delay in angle of attack before stall (or separation) and high transient loads induced by a leading edge vortex after stall. All dynamic stall models, model the delay in angle of attack and the aerodynamic coefficient increments after stall. In the Leishman-Beddoes model uses first-order differential equations for the delayed angle of attack and leading-edge vortex lift. All models are 2-D and semi-empirical in nature. The ONERA EDLIN model and BH model both use second-order differential equations to calculate delayed angle of attack and lift, drag and moment increments. The Johnson model uses an angle of attack delay proportional to the rate of change of angle of attack. The Boeing model uses an angle of attack delay proportional to the square-root of the rate of change of angle of attack. In general the agreement between different models are good considering the simplicity of the models, but correlation with test data show significant errors, as expected with empirical models. Johnson [22] compared 2D airloads, PUMA blade sectional airloads, and power predictions under stall conditions using the different models. The predictions were similar but correlation with test data showed errors, as expected of all semi-empirical models.

4.3 Unsteady Thin Airfoil Theory

Thin airfoil theory is widely used to calculate the lift force on an airfoil. The theory tries to solve the Laplace equation in two dimensions while implementing boundary conditions that produce useful aerodynamic solutions. The assumption of inviscid potential flow implies that the governing equation remains the same for both steady and unsteady flows. The treatment of unsteady flows is via boundary conditions.

Normally, the problem is divided into two parts, lift and drag. Typically, the lift problem is normally solved using the inviscid flow assumption. On the other hand, the viscosity plays an important role near the surface and it influences the drag force. The drag solution is separately obtained for the real fluid either using some empirical relations or the experimental data. For most of the problems, viscosity has little influence on the pressure solution. An airfoil is assumed sufficiently thin so that for a small angle of attack the disturbances in the flow are small perturbations.

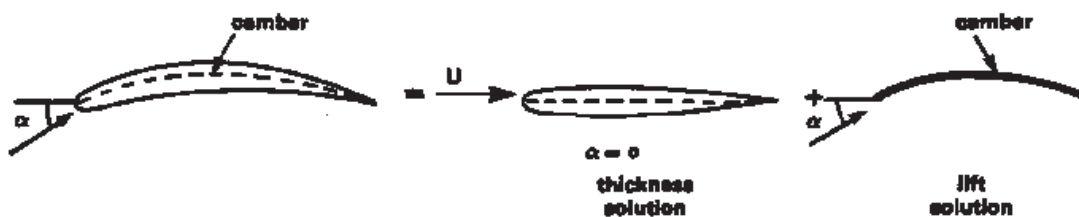


The assumptions are:

1. Flow disturbances are small perturbations.
2. Flow on the surface is tangential.

3. Flow leaves trailing edge smoothly (Kutta condition).

Break the problem into two parts.



Part I: Thickness solution

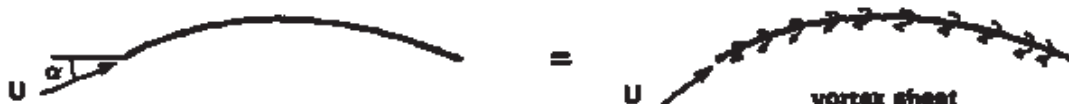
The airfoil camber as well as the angle of attack are set to zero. A symmetric airfoil at zero angle of attack gives symmetric pressure resulting in zero net lift. The airfoil is replaced by a source distribution on the chord line.



We would like to find the strength of the source distribution, and this is done using the tangential flow condition on the surface. Once the strength is known then the pressure distribution can be calculated.

Part II: Lift solution

The airfoil thickness is set to zero, so the camber line is set at an angle of attack. The lift solution is obtained by replacing the camber line with the vortex sheet. The solution is anti-symmetric in character.

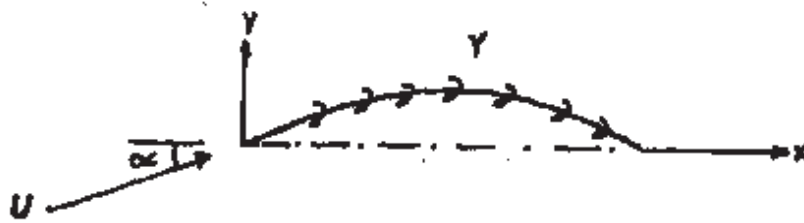


Using the boundary condition on the surface and the Kutta condition at the trailing edge, the strength of the vorticity distribution is evaluated. Then the pressure distribution can be calculated. Glauert used a Fourier series to solve the problem. Note that, without the Kutta condition the airfoil generates zero forces and moments. The assumption of inviscid irrotational flow guarantees that the flow slips past the body without producing any net forces. The Kutta condition ensures that at least a lift is produced. This lift happens to be close to measured values, implying that the Kutta condition has a physical basis.

It was Helmholtz who first proposed an idea to obtain a lift solution for a thin airfoil, essentially a flat plate. It is impossible he reasoned that a real flow with viscosity would negotiate a sharp turn (zero radius of curvature) at the leading and trailing edges. One way to indirectly incorporate viscous behavior within a potential flow solution was to impose flow smoothness at the leading and trailing edges. The lift solution he obtained was far off, but the idea was correct. Kutta and Joukowski, independantly, imposed the condition only at the trailing edge. Their solution was quite accurate. We now know that the effects of viscosity is pronounced at the trailing edge, not the leading edge. The boundary layer is thick near the trailing edge.

4.3.1 Steady Airloads

Let us examine the lifting problem through the thin airfoil theory. The flow is assumed to be inviscid, irrotational (i.e. potential) and in addition incompressible.



The airfoil camber is given by $z = z(x)$, $z(x) \ll c$, where c is the airfoil chord. The camber line is replaced by the vorticity distribution $\gamma(x)$. For steady flow, the shed vorticity is neglected. The induced velocity $w(x)$ perpendicular to the camber line at any x is approximated to be the same as that perpendicular to the x axis. This is the thin airfoil assumption.

$$w_b(x) = \int_0^c \frac{\gamma_b(\xi)d\xi}{2\pi(\xi - x)}$$

For flow tangency, or impenetrability along the camber line, the induced velocity from the free stream should be equal and opposite to the vortex induced velocity. Thus

$$\int_0^c \frac{\gamma(\xi)d\xi}{2\pi(\xi - x)} + \left(\alpha - \frac{dz}{dx} \right) U = 0$$

or

$$\int_0^c \frac{\gamma(\xi)d\xi}{2\pi(x - \xi)} = \left(\alpha - \frac{dz}{dx} \right) U$$

The Kutta condition is given by

$$\gamma(c) = 0$$

Solve for $\gamma(x)$. Then the lift and moment about the leading edge can be calculated using

$$L = \int_0^c \rho U \gamma dx$$

$$M_{le} = \int_0^c \rho U \gamma x dx$$

The moment can be transferred to any chord-wise location based on requirements.

Glauert calculated the solution using the Fourier series. The results are summarized here. The non-dimensional lift and pitching moment coefficient at quarter chord are given by

$$Cl = 2\pi(A_0 + A_1/2)$$

$$Cm_{\frac{1}{4}c} = -\frac{\pi}{4}(A_1 - A_2)$$

where

$$A_0 = \alpha - \frac{1}{\pi} \int_0^\pi \frac{dz}{dx} d\theta$$

$$A_n = \frac{2}{\pi} \int_0^\pi \frac{dz}{dx} \cos n\theta d\theta$$

$$\theta = \cos^{-1} \left(1 - \frac{2x}{c} \right)$$

4.3.2 Quasi-Steady Airloads

The steady airloads results can be adapted to unsteady airfoil motions. It provides quasi-steady airloads solutions that are quite useful for simple aero-elastic stability analysis. The world quasi-steady is used because the effects of shed wake is still being neglected.

Note that the slope of the camberline dz/dx satisfies the following equation to maintain impenetrability conditions.

$$\left(\alpha - \frac{dz}{dx}\right)U = w_a(x)$$

where $w_a(x)$ is the component of free stream perpendicular to the camberline. Thus

$$\frac{dz}{dx} = \alpha - \frac{w_a(x)}{U}$$

In the case of a flat plate we have

$$\frac{dz}{dx} = 0$$

Consider a flat plate with a plunge velocity \dot{h} downwards (so that the relative air velocity is \dot{h} positive upwards).

$$w_a(x) = U\alpha + \dot{h}$$

$$\frac{w_a(x)}{U} = \alpha + \frac{\dot{h}}{U}$$

$$\frac{dz}{dx} = -\frac{\dot{h}}{U}$$

Now consider a flat plate pitching with a angular rate $\dot{\alpha}$. The point with zero translational velocity (center of rotation, elastic axis) is at a distance $a_h b$ from the mid-chord, where $b = c/2$.

$$w_a(x) = U\alpha + (x - b - a_h b)\dot{\alpha}$$

$$\frac{w_a(x)}{U} = \alpha + (x - b - a_h b)\frac{\dot{\alpha}}{U}$$

$$\frac{dz}{dx} = -(x - b - a_h b)\frac{\dot{\alpha}}{U}$$

For an airfoil both pitching and plunging we have

$$\frac{dz}{dx} = -\frac{\dot{h}}{U} - (x - b - a_h b)\frac{\dot{\alpha}}{U}$$

Using the above expression in the steady airload results and noting that $x = b(1 - \cos \theta)$, we have

$$\begin{aligned} A_0 &= \alpha + \frac{1}{\pi} \int_0^\pi \left[\frac{\dot{h}}{U} + (x - b - a_h b)\frac{\dot{\alpha}}{U} \right] d\theta \\ &= \alpha + \frac{\dot{h}}{U} - \frac{a_h b}{U}\dot{\alpha} \end{aligned} \tag{4.69}$$

For pitching about $1/4c$, i.e. if the elastic axis is at $1/4c$ then

$$a_h b = -b/2$$

$$a_h = -1/2$$

$$A_0 = \alpha + \frac{\dot{h}}{U} + \frac{b\dot{\alpha}}{2U}$$

or

$$A_0 = \alpha + \frac{\dot{h}}{U} + \frac{c\dot{\alpha}}{4U}$$

Similarly

$$\begin{aligned} A_1 &= -\frac{2}{\pi} \int_0^\pi \left[\frac{\dot{h}}{U} + (x - b - a_h b) \frac{\dot{\alpha}}{U} \right] \cos \theta d\theta \\ &= -\frac{2}{\pi} \frac{\dot{\alpha}}{U} \int_0^\pi x \cos \theta d\theta \\ &= \frac{\dot{\alpha}}{U} b \end{aligned} \quad (4.70)$$

Thus

$$\begin{aligned} Cl &= 2\pi \left[\alpha + \frac{\dot{h}}{U} + \frac{\dot{\alpha}}{U} \left(\frac{b}{2} - a_h b \right) \right] \\ L_{qs} &= \frac{1}{2} \rho U^2 (2b) \\ &= 2\pi b \rho U \left[U\alpha + \dot{h} + \dot{\alpha} \left(\frac{b}{2} - a_h b \right) \right] \end{aligned} \quad (4.71)$$

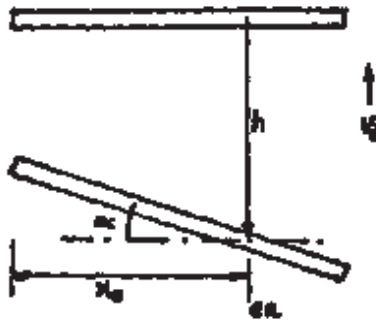
where L_{qs} is the quasi-steady lift per unit span. Note that

$$\begin{aligned} \frac{b}{2} - a_h b &= \left(b + \frac{b}{2} \right) - (b + a_h b) \\ &= \frac{3}{4}c - x_{ea} \end{aligned} \quad (4.72)$$

Thus

$$\begin{aligned} Cl &= 2\pi \left[\alpha + \frac{\dot{h}}{U} + \frac{\dot{\alpha}}{U} \left(\frac{3}{4}c - x_{ea} \right) \right] \\ &= 2\pi \left[\alpha + \frac{\text{downward velocity at } 3/4 \text{ chord}}{U} \right] \\ &= 2\pi \alpha_g \end{aligned} \quad (4.73)$$

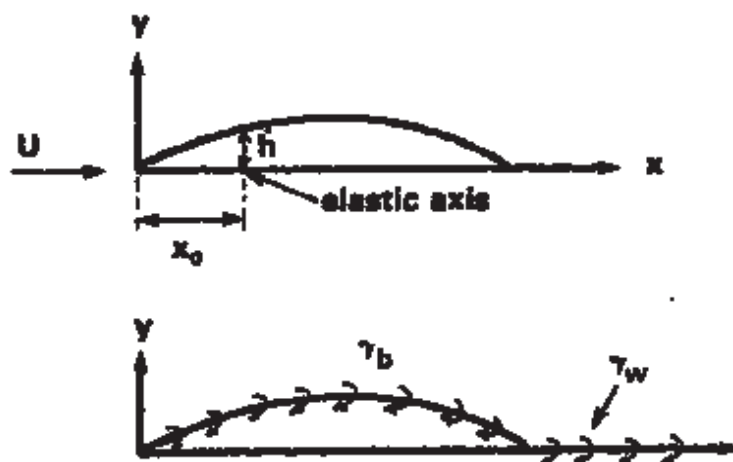
where α_g is defined as a geometric angle of attack, arising out of the unsteady blade motions. α_g is the angle of attack at $3/4c$.



Thus, the quasi-steady assumption boils down to the following. At any instant of time, freeze the motion of the body. Calculate the effective angle of attack at $3/4c$. Then use the static aerodynamic characteristics to evaluate the forces on the body.

4.3.3 Unsteady Airloads

For unsteady flow, the shed vorticity plays an important role. The Laplace solutions are retained with the addition of shed vorticity. Consider a similar pitching and plunging airfoil motion as before.



The bound vorticity strength is γ_b as before. In addition we have a shed (or wake) vorticity strength of γ_w .

$$w_a(x) = U\alpha + \dot{h} + \dot{\alpha}(x - a_h b)$$

where, as in the case of steady and quasi-steady airloads, the geometric camber has been neglected. The airfoil is assumed to behave as a flat plate.

$$w_b(x) = \int_{-b}^b \frac{\gamma_b(\xi)d\xi}{2\pi(\xi - x)}$$

$$\lambda_s(x) = \int_b^\infty \frac{\gamma_w(\xi)d\xi}{2\pi(\xi - x)}$$

For flow tangency or impenetrability as before we have

$$w_b + \lambda_s + w_a = 0$$

The unknown is γ_b . Note that γ_w is not an unknown. It can be related to γ_b , as follows. The total bound circulation is $\Gamma = \int_{-b}^{+b} \gamma_b dx$. The shed vorticity is the time rate of change in total bound circulation Γ . Suppose in time Δt the airfoil has traversed a distance Δs . Then

$$\gamma_w \Delta s = -\Delta \Gamma$$

It follows

$$\gamma_w \frac{\Delta s}{\Delta t} = -\frac{\Delta \Gamma}{\Delta t}$$

In differential form

$$\gamma_w = -\frac{1}{U} \frac{d\Gamma}{dt}$$

where the derivative is take at time $t - (x - b)/U$ when the vorticity was shed from the airfoil. The Kutta condition is same as before $\gamma_b(c) = 0$. In addition the condition $\gamma_w(t) = \gamma_w(x - Ut)$ is satisfied to enforce the shed vorticity to convect with free stream. This ensures that there is no pressure differential across the shed wake. The solution of the impenetrability condition, along with the above boundary conditions produce a γ_b of the following form. For details of the derivaion see Johnson [23].

$$\int_{-b}^b \gamma_b dx = 2\pi b \left[\left(w_0 + \frac{1}{2} w_1 \right) - \left(\lambda_0 + \frac{1}{2} \lambda_1 \right) \right]$$

where

$$w_0 = U\alpha + \dot{h} - a_h b \dot{\alpha}$$

$$w_1 = b \dot{\alpha}$$

$$\lambda_n = \frac{2}{\pi} \int_0^\pi \lambda_s(x) \cos n\theta d\theta = -\frac{1}{\pi} \int_b^\infty \gamma_w \frac{(\xi - \sqrt{\xi^2 - 1})^n}{b^n \sqrt{\xi^2 - b^2}} d\xi$$

γ_b can be broken into two parts

$$\gamma_b = \gamma_{bc} + \gamma_{bnc}$$

such that the circulatory part γ_{bc} provides the net circulation Γ but does not affect the boundary conditions, whereas the non-circulatory part γ_{bnc} does not affect the circulation but satisfies the boundary condition. Thus

$$\int_{-b}^b \gamma_{bc} dx = \Gamma$$

$$\int_{-b}^b \frac{\gamma_{bc}}{2\pi(x - \xi)} dx = 0$$

and

$$\int_{-b}^b \gamma_{bnc} dx = 0$$

$$\int_{-b}^b \frac{\gamma_{bnc}}{2\pi(x - \xi)} dx = w_a - \lambda_s$$

The solution γ_b is then related to the differential pressure on the top and bottom surfaces of the airfoil and then to lift and pitching moments. The differential pressure is obtained from the linearized form of the unsteady Bernoulli's equation. This is valid for small perturbations of the flow.

$$p = -\rho \left(U \frac{\partial \phi}{\partial x} + \frac{\partial \phi}{\partial t} \right)$$

$$-\Delta p = \rho \left(U \frac{\partial \Delta \phi}{\partial x} + \frac{\partial \Delta \phi}{\partial t} \right)$$

$$\begin{aligned}\frac{\partial \Delta \phi}{\partial x} &= \Delta u = \gamma_b \\ \frac{\partial \Delta \phi}{\partial t} &= \frac{\partial}{\partial t} \int_{-\infty}^x \Delta u dx\end{aligned}$$

Finally

$$-\Delta p = \rho \left(U \gamma_b + \frac{\partial}{\partial t} \int_{-\infty}^x \gamma_{bnc} dx \right)$$

where the effect of the time derivative of γ_{bc} has already been accounted for via $\lambda_s(x)$. The lift and pitching moments about the elastic axis then become

$$\begin{aligned}L &= \int_{-b}^b (-\Delta p) dx \\ M_{a_h b} &= \int_{-b}^b (-\Delta p)(-x + a_h b) dx\end{aligned}$$

Substitute the expression for Δp to obtain

$$\begin{aligned}L &= \rho \left(U \Gamma - \frac{\partial}{\partial t} \Gamma_{nc}^{(1)} \right) \\ M_{a_h b} &= -\rho \left(U \Gamma^{(1)} - \frac{1}{2} \frac{\partial}{\partial t} \Gamma_{nc}^{(2)} \right)\end{aligned}$$

where

$$\begin{aligned}\Gamma^{(n)} &= \int_{-b}^b x^n \gamma_b dx \\ \Gamma_{nc}^{(n)} &= \int_{-b}^b x^n \gamma_{bnc} dx \\ \Gamma &= \Gamma^{(0)}\end{aligned}$$

From the solution of γ_b , and using equation 4.71 we can obtain

$$\begin{aligned}\Gamma &= 2\pi b \left[U \alpha + \dot{h} + \dot{\alpha} \left(\frac{b}{2} - a_h b \right) \right] + \int_b^\infty \left(\sqrt{\frac{\xi+b}{\xi-b}} - 1 \right) \gamma_w d\xi \\ &= \frac{L_{qs}}{\rho U} + \int_b^\infty \left(\sqrt{\frac{\xi+b}{\xi-b}} - 1 \right) \gamma_w d\xi\end{aligned}\tag{4.74}$$

and

$$\frac{\partial}{\partial t} \Gamma_{nc}^{(1)} = -\pi b^2 (U \dot{\alpha} + \ddot{h} - a_h b \ddot{\alpha}) - U \int_b^\infty \left(1 - \frac{\xi}{\sqrt{\xi^2 - b^2}} \right) \gamma_w d\xi$$

Substituting in the lift expression we have per unit span

$$\begin{aligned}L &= 2\pi b \rho U \left[U \alpha + \dot{h} + \dot{\alpha} \left(\frac{b}{2} - a_h b \right) \right] + \rho \pi b^2 (U \dot{\alpha} + \ddot{h} - a_h b \ddot{\alpha}) \\ &\quad + \rho U \int_b^\infty \frac{b}{\sqrt{\xi^2 - b^2}} \gamma_w d\xi \\ &= L_{qs} + L_{nc} + L_w \\ &= L_c + L_{nc}\end{aligned}\tag{4.75}$$

L_{qs} is the same expression as obtained earlier in equation 4.71. L_{nc} and L_w are the new terms. The shed wake contribution L_w can be re-arranged as follows. Note that, from conservation of vorticity we have

$$\Gamma = - \int_b^\infty \gamma_w d\xi$$

Using the above in the second line of equation 4.74 we obtain

$$L_{qs} = -\rho U \int_b^\infty \sqrt{\frac{\xi+b}{\xi-b}} \gamma_w d\xi$$

It follows

$$L_c = L_{qs} + L_w = -\rho U \int_b^\infty \frac{\xi}{\sqrt{\xi^2 - b^2}} \gamma_w d\xi$$

Finally the total lift can be expressed as

$$\begin{aligned} L &= L_c + L_{nc} \\ &= (L_{qs} + L_w) + L_{nc} \\ &= \frac{L_{qs} + L_w}{L_{qs}} L_{qs} + L_{nc} \\ &= \frac{\int_b^\infty \frac{\xi}{\sqrt{\xi^2 - b^2}} \gamma_w d\xi}{\int_b^\infty \sqrt{\frac{\xi+b}{\xi-b}} \gamma_w d\xi} L_{qs} + L_{nc} \\ &= C L_{qs} + L_{nc} \end{aligned} \tag{4.76}$$

where C is a lift deficiency function. The form of C depend on the specific time history of excitation. For example, for $\alpha = \bar{\alpha} e^{i\omega t}$ and $h = \bar{h} e^{i\omega t}$, the shed wake is of the form $\gamma_w = \bar{\gamma}_w e^{i\omega(t-\xi/U)}$ and C has the following form

$$C(k) = \frac{H_1^{(2)}(k)}{H_1^{(2)}(k) + iH_0^{(2)}(k)} \tag{4.77}$$

where $H_n^{(2)}$ are Hankel functions, expressed in terms of Bessel functions

$$H_n^{(2)} = J_n - iY_n$$

and k is defined as the reduced frequency.

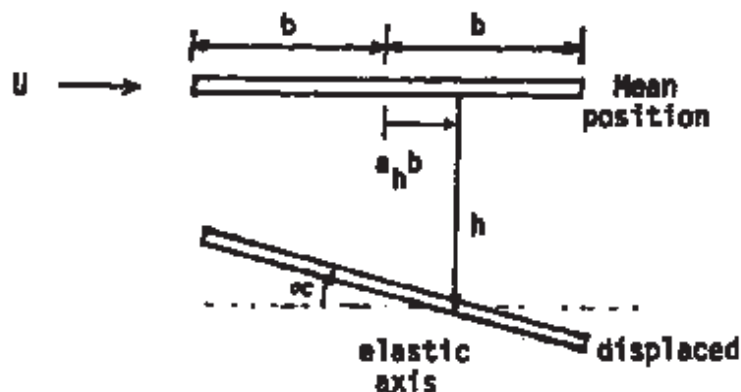
$$k = \frac{\omega b}{U}$$

$C(k)$ for this type of excitation is called the Theodorsen Lift Deficiency Function as discussed later. The circulatory lift L_c acts at quarter chord for thin airfoil theory. The moment $M_{a_h b}$ about the elastic axis is given by

$$\begin{aligned} M_{a_h b} &= L_c \cdot \left(\frac{b}{2} + a_h b \right) - \frac{1}{2} \rho \pi b^3 \left[2U \dot{\alpha} + \ddot{h} + b \left(\frac{1}{4} - a_h \right) \ddot{\alpha} \right] \\ &= L_{qs} C(k) \cdot \left(\frac{b}{2} + a_h b \right) - \frac{1}{2} \rho \pi b^3 \left[2U \dot{\alpha} + \ddot{h} + b \left(\frac{1}{4} - a_h \right) \ddot{\alpha} \right] \end{aligned} \tag{4.78}$$

4.3.4 A Simple Interpretation

The unsteady results above are often interpreted as follows. The unsteady forces generated over the wing can be classified into two categories; circulatory and non-circulatory forces. The circulatory forces are caused by circulation, which means the origin of the forces is vorticity. The non-circulatory forces are called virtual or apparent forces. Let us examine the various component of forces. The airfoil chord is $2b$.



\dot{h} = vertical motion, positive down

$\dot{\alpha}$ = pitch motion about elastic axis, positive nose up

1. Lift ' L_1 ' caused by circulation. The downwash is computed at $3/4$ -chord. It lies at the aerodynamic center.

$$L_1 = \frac{1}{2} \rho C_{l_\alpha} U^2 2b \left[\alpha + \frac{\dot{h}}{U} + \frac{\dot{\alpha}}{U} \left(\frac{b}{2} - a_h b \right) \right]$$

In the case of thin airfoil theory, the lift curve slope, $C_{l_\alpha} = 2\pi$. The aerodynamic center lies at $1/4c$.

2. Lift ' L_2 ' is noncirculatory with the center of pressure at mid-chord.

$$L_2 = (\text{apparent mass}) \times (\text{vertical acceleration at mid-chord}) = \pi \rho b^2 (\ddot{h} - a_h b \ddot{\alpha})$$

For an apparent mass, a cylinder of air with diameter equal to chord and length of unity assumed to oscillate with the wing

3. Lift L_3 is noncirculatory with the center of pressure at $3/4$ -chord. The nature of the force is of centrifugal force type.

$$\begin{aligned} L_3 &= (\text{apparent mass}) \times (U \dot{\alpha}) \\ &= \pi \rho b^2 U \dot{\alpha} \end{aligned}$$

4. Noncirculatory nose down moment ' M_a '

$$M_a = (\text{apparent moment of inertia}) \times (\text{angular acceleration})$$

For an apparent mass moment of inertia, a one-quarter inertia of a cylinder with diameter equal to chord and length unity is used.

$$M_a = -\frac{\pi \rho b^4}{8} \ddot{\alpha}$$

Total lift $L = L_1 + L_2 + L_3$

Total moment about elastic axis

$$= \left(\frac{b}{2} + a_h b\right) L_1 + a_h b L_2 - \left(\frac{b}{2} - a_h b\right) L_3 - \frac{\pi \rho b^4}{8} \ddot{\alpha}$$

Circulatory lift $L_Q = L_1$

Noncirculatory lift $L_{NC} = L_2 + L_3$

The effect of shed vorticity is only on circulatory lift.

4.3.5 The Theodorsen Lift Deficiency Function

The Theodorsen Lift Deficiency function is obtained for a pure harmonic excitation of a pitching and plunging airfoil. Let us consider that the wing is undergoing pure harmonic motion at frequency ω

$$h(t) = \bar{h} e^{i\omega t}$$

$$\alpha(t) = \bar{\alpha} e^{i\omega t}$$

It follows then that the wake vorticity γ_w is also periodic in time with frequency ω . The circulation lift build up depend on the reduced frequency.

$$L = C(k)L_Q + L_{NC}$$

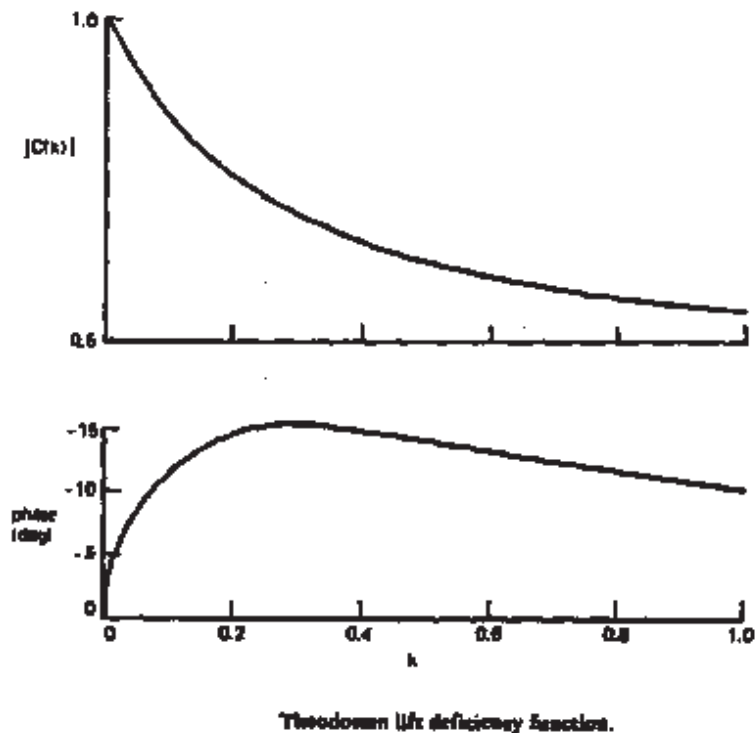
where $C(k)$ is called Theodorsen lift deficiency function and it depends on reduced frequency

$$k = \frac{\omega b}{U}$$

where ω is the frequency of oscillation, rad/sec, b is the semi-chord, m, and U = free stream velocity, m/sec. The magnitude of C varies from 1 at low frequency to .5 at high frequency. The lift deficiency C takes care of the effect of shed vorticity on the lift due to unsteady motion and this always reduces the quasi-steady lift value. On the following figure, the lift deficiency function in terms of magnitude and phase is plotted for various k . The magnitude gives deficiency of lift and phase shows the lag in the lift build up. Thus the $C(k)$ is a type of feed-back parameter of wake vorticity.

Lift and moment expressions are

$$\begin{aligned} L &= 2\pi b \rho U \left[U \alpha + \dot{h} + \dot{\alpha} \left(\frac{b}{2} - a_h b \right) \right] + \rho \pi b^2 (U \dot{\alpha} + \ddot{h} - a_h b \ddot{\alpha}) \\ M &= 2\pi b \rho U \left[U \alpha + \dot{h} + \dot{\alpha} \left(\frac{b}{2} - a_h b \right) \right] \cdot \left(\frac{b}{2} + a_h \right) C(k) \\ &\quad + \pi \rho b^2 \left[(\ddot{h} - a_h b \ddot{\alpha}) a_h b - U \dot{\alpha} \left(\frac{b}{2} - a_h b \right) - \frac{b^2}{8} \ddot{\alpha} \right] \end{aligned} \quad (4.79)$$



Let us examine a typical reduced frequency for a rotor blade

$$k = \frac{\omega b}{U} = \frac{\omega c/2}{\Omega r}$$

say $\omega = n\Omega$

$$k = \frac{nc}{2r}$$

Consider a representative section at 3/4-radius

$$k = \frac{nc}{2 \times \frac{3}{4}R} = \frac{2n}{3} \left(\frac{c}{R}\right)$$

Assume

$$\frac{c}{R} = \frac{1}{20}$$

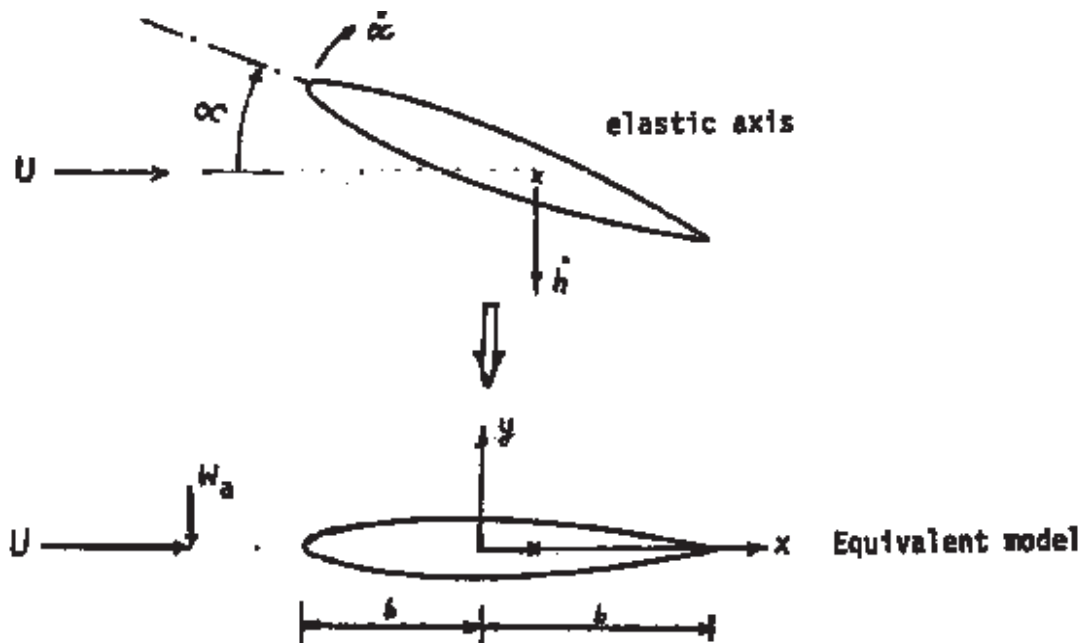
For 1/rev motion, $n = 1$, $k = 0.033$

$$|C(k)| \sim .97$$

The unsteady circulatory lift is about 97% of quasi-steady lift. This means that the unsteady effect due to shedding of vorticity are negligible. This shows that the quasi-steady assumption is quite adequate for 1/rev motion. For high frequency motion, say $n = 4$ (4/rev), there is about a 15% reduction in lift. Therefore unsteady effect has to be included for higher harmonic motion.

4.3.6 Application to Rotary Wings

The objective is to apply unsteady forces results derived earlier for fixed wing to rotary wing problems. For the fixed wing the blade undergoes two degrees of motion, pitching and heaving motions. The rotor blade motion as well as flow environment are complex, and for simplicity the effect of blade motion is taken care of in the velocity components. Let us examine the normal velocity due to airfoil motion.



where the first component is air velocity normal to the airfoil section at the pitch axis. The normal velocity component W_a is a function of $\dot{h} + U\alpha$ and $\dot{\alpha}$, it follows that the linear solution for aerodynamic lift and moment must also depend on these two quantities. Therefore, rewriting the lift and moment expressions.

$$L = 2\pi\rho UbC(k) \left[(\dot{h} + U\alpha) + \left(\frac{b}{2} - a_h b\right) \dot{\alpha} \right] + \pi\rho b^2 \left[(\ddot{h} + U\dot{\alpha}) - a_h b \ddot{\alpha} \right]$$

$$M = 2\pi\rho UbC(k) \left[(\dot{h} + U\alpha) + \left(\frac{b}{2} - a_h b\right) \dot{\alpha} \right] \cdot \left(\frac{b}{2} + a_h b\right) + \pi\rho b^2 \left[a_h b (\ddot{h} + U\dot{\alpha}) - \frac{1}{2} Ub \dot{\alpha} - b^2 \left(\frac{1}{8} + a_h^2\right) \ddot{\alpha} \right]$$

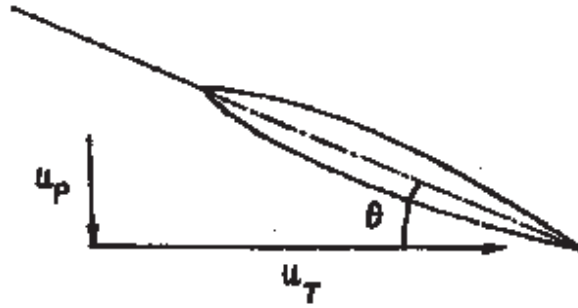
Writing the forces in this manner, one does not need to identify the section pitch and heave motions, but on the other hand one needs the mean and linear components of the normal velocity distribution over the airfoil chord. It is useful to identify, in the above expressions, the normal and inplane velocity components U_P and U_T .

$$\dot{h} + \left(\frac{b}{2} - a_h b\right) \dot{\alpha} = -U_P$$

$$U = U_T$$

$$\alpha = \theta$$

For rotor problems, h and θ are obtained based on the blade structural dynamic model. The inflow and forward velocity components are added appropriately.

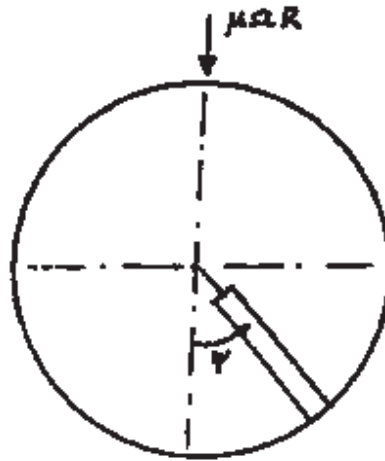


For example, consider an articulated rotor blade with rigid flap and rigid pitch motions.

$$\dot{h} = -r\dot{\beta}$$

$$\dot{\alpha} = \dot{\theta}$$

$$b = c/2$$



In hover

$$U_T = \Omega r$$

$$U_P = \lambda \Omega R + r\dot{\beta} - \left(\frac{c}{4} - a_h \frac{c}{2} \right) \dot{\theta}$$

In forward flight

$$U_T = \Omega r + \Omega R \mu \sin \psi$$

$$U_P = \lambda \Omega R + \beta \Omega R \mu \cos \psi + r\dot{\beta} - \left(\frac{c}{4} - a_h \frac{c}{2} \right) \dot{\theta}$$

where

λ is wake induced inflow

β is flap motion

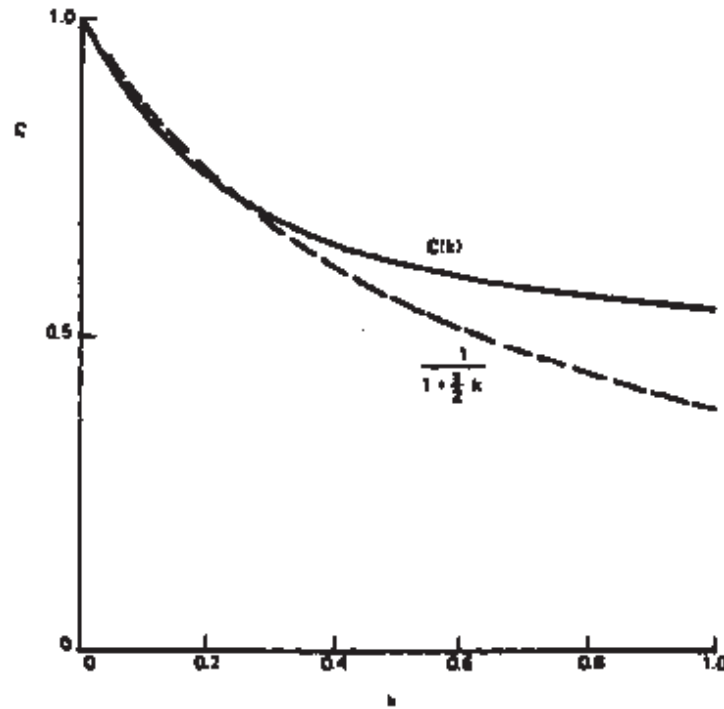
μ is advance ratio

$$\lambda = \lambda_{Tpp} - \mu\beta_{1c}$$

4.3.7 Near Shed Wake

Shed wake plays an important role in the determination of unsteady aerodynamic forces. The rotary shed wake is in a helical sheet behind the blade. Most of the influence on airfoil loading comes from near shed wake, extending 15° to 45° in azimuth behind the blade trailing edge. Thus considering only the near shed wake and neglecting the far wake reduces the computation to a great extent.

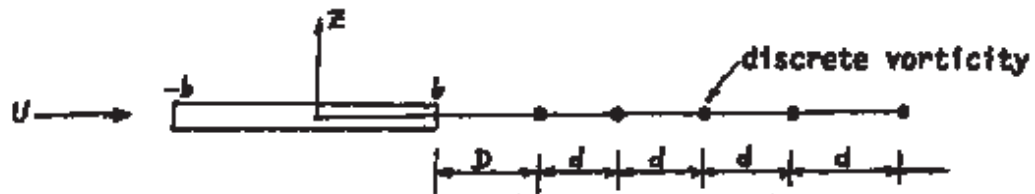
Miller (1964) considered a lifting line theory approximation for the near shed wake, implying a low reduced frequency. He derived a simple expression for the lift deficiency function.



$$C(k) = \frac{1}{1 + \frac{\pi}{2}k}$$

Piziali Model (1966):

Piziali made a discrete vortex approximation for the near wake.

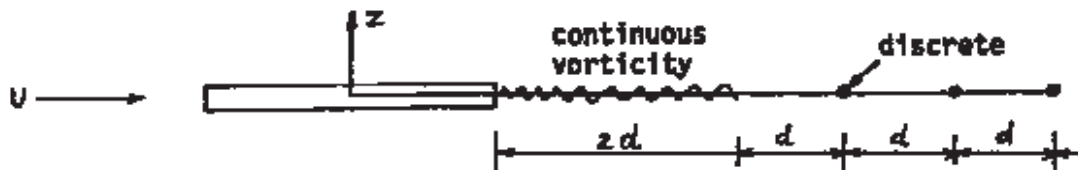


The wake is represented by a series of finite strength point vortices.

Spacing $d = \frac{2\pi U}{N\omega}$ for N vortices per cycle. (Typically 5-8)

Daughaday and Piziali (1966):

They made another model for shed wake where combined continuous and discrete shed wake vorticity is used.



4.3.8 Time-Varying Free Stream

The rotating blade in forward flight has a time varying free stream velocity at a station

$$u_T = \Omega r + \Omega R \mu \sin \psi$$

This is periodic with a period of 2π rad. Since the time varying component is of the same order of magnitude as the mean component, one has to include the effect of time variation on the unsteady forces, both the direct effect as well as the shed wake effect. This results in

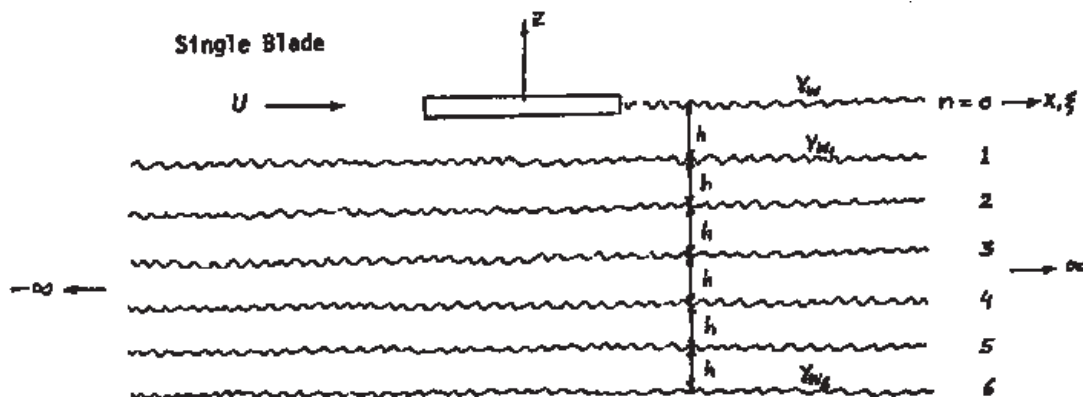
- (a) additional noncirculating forces caused by $\frac{d}{dt}(U\alpha)$
- (b) additional circulatory forces
- (c) additional influence of stretching and compressing of the vorticity in the shed wake.

A simple approximation sometimes can be very useful by choosing element $C(k)$ based on mean k .

4.3.9 Returning Wake

For a hovering rotor, the wake generally moves slowly away from the rotor disk. Therefore, for the determination of unsteady loads, one needs to consider the influence of helical vortex sheets below the disk, one from each blade. For high inflow or forward speed, the rotor wake is convected away and so the influence of the returning shed wake is not important.

Loewy (1957) developed a two-dimensional model for unsteady aerodynamics of hovering rotor.



Consider a single blade rotor, so all the vorticity is originated from the same blade. The returning wake is modeled as a series of planar two-dimensional vortex sheets with a vertical separation h . For hover, the velocity $U = \Omega r$, is constant with time and the vortex sheets are parallel to free stream U . The spacing h depends on the mean flow through the rotor disk.

The wake induced velocity λ is

$$\lambda = \frac{1}{2\pi} \int_b^\infty \frac{\gamma_w d\xi}{x - \xi} + \sum_{n=1}^\infty \frac{1}{2\pi} \int_{-\infty}^\infty \frac{\gamma_{wn}(x - \xi)}{(x - \xi)^2 + h^2 n^2} d\xi$$

As before the strength of the shed vorticity is of the form

$$\gamma_w = \bar{\gamma}_w e^{i\omega(t-x/U)}$$

The strength of the n -th sheet is of the form

$$\gamma_{wn} = \bar{\gamma}_w e^{i\omega(t-x/U-2\pi n/\Omega)}$$

The total lift can again be written in the following form

$$L = C' L_Q + L_{NC}$$

where C' is the Loewy function and it is a function of reduced frequency k , frequency of oscillation ω/Ω and wake spacing h . The wake spacing h is such that the wake goes down by a distance $N_b h$ over a single rotor revolution. Thus

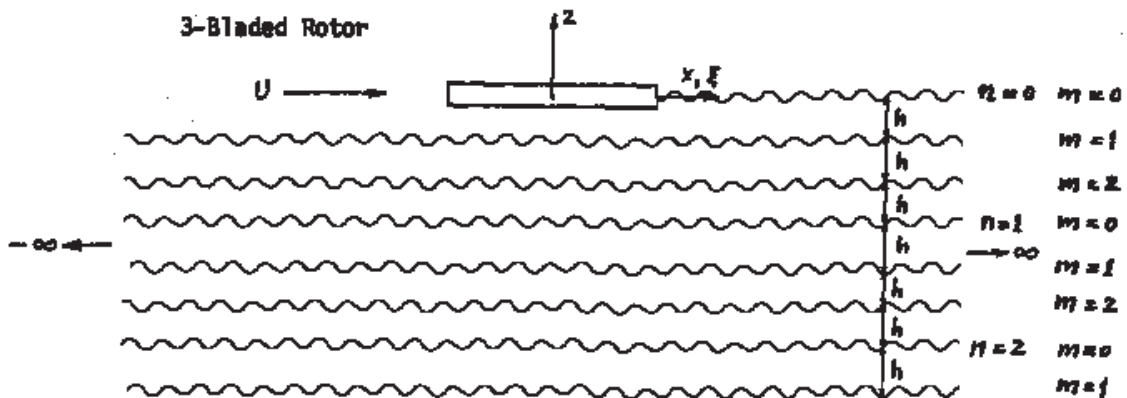
$$N_b h = v_0 \frac{2\pi}{\Omega}$$

where v_0 is the steady inflow. It follows

$$h = \frac{2\lambda_0 c}{\sigma}$$

$$\frac{h}{c} = \frac{h}{2b} = \frac{2\lambda_0}{\sigma}$$

The Loewy function is quite similar to Theodorsen function, $C(k)$. For a N blade rotor, the returning wake model gets complicated, since the wake of other blades also has to be considered.



$m = 0, 1, 2$ blade index

For $\omega/\Omega = \text{integer}$ and for low k (approximately < 0.4),

$$C' \simeq \frac{1}{1 + \frac{\pi\sigma}{4\lambda_0}}$$

where λ is the steady inflow ratio and σ is the solidity ratio. Typically,

$$\lambda_0 = .05 \text{ to } .07$$

$$\frac{h}{b} \simeq 3 \text{ or } 4$$

$$C' \simeq .5$$

This is quite important for control loads and stability. This may reduce flap damping significantly.

4.3.10 Miller's Conclusion

When system frequencies approach integers of rotational speed Ω , unsteady flow theory must be used because of a large reduction in $\frac{dc_l}{d\alpha}$ due to spiral wake. The near wake including the first quadrant or so of vorticity behind the blade is important. For this the lift acts at 1/4-chord due to angle of attack at 3/4-chord. When frequency ω are not close to integers of Ω , the far wake contribution to $C(k)$ are negligible.

For $\frac{\omega}{\Omega} = \text{integer}$,

$$\begin{aligned} C' &\simeq \frac{1}{1 + \frac{\pi\sigma}{4\lambda_0}} \\ &= F + iG \quad (G = 0) \end{aligned}$$

Where

$$\lambda_0 = \text{steady inflow.}$$

This means that there is a lift deficiency but no lag is produced.

4.4 Time Domain Methods for Unsteady Aerodynamics

Consider a unit step function at $t = h$

$$\begin{aligned} u(t - h) &= 1 \quad t \geq h \\ &= 0 \quad t < h \end{aligned}$$

Any function f at a discrete time nh can be expressed as

$$\begin{aligned} f(nh) &= f(0)u(t - 0) + \sum_{i=1}^{i=n} [f(ih) - f(\overline{i-1}h)] u(t - ih) \\ &= f(0)u(t - 0) + \sum_{i=1}^{i=n} \Delta f(ih) u(t - ih) \\ &= f(0)u(t - 0) + \sum_{i=1}^{i=n} \frac{\Delta f(ih)}{h} u(t - ih)h \end{aligned}$$

In the limit as $h \rightarrow 0$, we have at a continuous time t

$$f(t) = f(0)u(t - 0) + \int_{\sigma=0}^{\sigma=t} \frac{\partial f}{\partial \sigma} u(t - \sigma) d\sigma$$

Thus any continuous and smooth function $f(t)$ can be expressed as a superimposition of a series of step functions. Note that for $t > 0$, $u(t - 0) = 1$. Similarly an angle of attack variation can be expressed in the same manner, as a series of step functions

$$\alpha(t) = \alpha(0) + \int_0^t \frac{\partial \alpha}{\partial \sigma} u(t - \sigma) d\sigma \quad (4.80)$$

In order to calculate the airloads (normal force, pitching moment, and chord force) generated by the airfoil in response to this angle of attack variation, it is therefore sufficient to calculate only the response to a step input in angle of attack of unit magnitude. The response to any angle of attack variation can then be constructed by superposition of these responses. The response to a step input in angle of attack is called an indicial response. For example if $\theta(t - h)$ is the indicial

lift coefficient generated in response to $u(t-h)$, an unit step input in angle of attack at $t=h$, then the lift coefficient at any time t is simply

$$C_l(t) = \alpha(0)\theta(0) + \int_0^t \frac{\partial \alpha}{\partial \sigma} \theta(t-\sigma) d\sigma \quad (4.81)$$

Note that $\theta(t-h)$, the lift increment generated in response to an unit step change in angle of attack $\alpha(t-h)$ applied at time $t=h$, finally reaches a steady state value after some time. This value is the airfoil lift curve slope $C_{l\alpha}$. In the case of a flat plate, based on calculations of thin airfoil theory with no stall, we have $C_{l\alpha} = 2\pi$. Including the Glauert correction for compressibility $C_{l\alpha} = 2\pi/\beta$, where $\beta = \sqrt{1-M^2}$. For real airfoils, $C_{l\alpha}$ depends on the initial angle of attack setting at which the step change is applied. That is, the steady state increment in C_l in response to an unit step increment in angle of attack depends on whether the unit step increment is imposed while the airfoil is at 5° or 12° . At 12° , when the airfoil is already near stall, an unit step increment in angle of attack may not produce any noticeable increment in C_l at all. Thus, below stall, $C_{l\alpha}$ is same as the airfoil lift curve slope. Above stall, $C_{l\alpha}$ depends on the local angle of attack.

Instead of the lift coefficient C_l , let us consider the normal force coefficient C_n from now onwards. The direction of the normal force coefficient is defined solely by the airfoil orientation. Similarly instead of drag consider the chord force C_c . The choice is only a matter of convention, either can be used to formulate the problem without any loss in generality. For pitching moments, we consider those about the airfoil quarter-chord. In addition, we distinguish between the circulatory and non-circulatory components by the superscript C and I , where I stands for 'impulsive'. The impulsive airloads in compressible flow are similar to their the noncirculatory counterparts in incompressible flow. Let the circulatory part of the normal force indicial response to angle of attack be of the form

$$C_{n\alpha}^C(t) = C_{n\alpha} \phi_{n\alpha}^C(t)$$

where the indicial response function $\phi_{n\alpha}^C(t) \rightarrow 1$ as $t \rightarrow \infty$, so that $C_{n\alpha}^C(t) \rightarrow C_{n\alpha}$ at the steady state. Also, at $t=0$, the indicial function must vanish, $\phi_{n\alpha}^C(0) = 0$. Consider an acceptable form as the following

$$\phi_{n\alpha}^C(t) = 1 - A_1 e^{-t/T_1} - A_2 e^{-t/T_2} \quad \text{where} \quad A_1 + A_2 = 1 \quad (4.82)$$

The normal force response of the airfoil to sinusoidal inputs can be deduced from its indicial response. The response to sinusoidal inputs is the response to inputs of the general form e^{pt} , where $p = j\omega$ for sinusoidal inputs.

The response to inputs of the form e^{pt} is, by definition, the Transfer function between input and output of the system expressed in terms of the Laplace variable p , assuming that the response is related to the input via an ODE in time. A continuous function of time $f(t)$ can be expressed as a summation of basis functions each of form e^{pt} , where p is a complex variable with frequency varying from $+\infty$ to $-\infty$, and each multiplied with a magnitude $F(p)$ independent of time t but in general a function of p . Thus

$$f(t) = \frac{1}{2\pi j} \int_{\gamma-j\infty}^{\gamma+j\infty} F(p) e^{pt} dt \quad (4.83)$$

The component $F(p)$ is defined as the Laplace Transform of the function $f(t)$ and can be determined by

$$F(p) = \lim_{T \rightarrow \infty} \int_0^T f(t) e^{-pt} dt$$

Let $f(t)$ be the input to a system governed by an ODE. Let $y(t)$ be the output. The function $y(t)$ can again be expressed as a summation of basis functions as before.

$$y(t) = \frac{1}{2\pi j} \int_{\gamma-j\infty}^{\gamma+j\infty} Y(p)e^{pt} dt \quad (4.84)$$

where $Y(p)$ is the Laplace Transform of $y(t)$. Now, note that for a system (an input output relationship) governed by a linear ODE with constant coefficients, the output corresponding to an input e^{pt} must necessarily be of the form $H(p)e^{pt}$. $H(p)$ is defined as the transfer function in terms of the Laplace variable. A special case is when $p = 1$. The output corresponding to an input e^t is always e^t itself, i.e., $H(p) = 1$. Thus the output $y(t)$, corresponding to $f(t)$, which is given by eqn.4.83 is necessarily of the form

$$y(t) = \frac{1}{2\pi j} \int_{\gamma-j\infty}^{\gamma+j\infty} F(p) H(p)e^{pt} dt \quad (4.85)$$

Comparing expressions 4.84 and 4.85 we have

$$Y(p) = F(p)H(p) \quad (4.86)$$

or

$$H(p) = \frac{Y(p)}{F(p)} \quad (4.87)$$

Thus the transfer function of a system $H(p)$, which is the response of the system to an input of the form e^{pt} can be determined by the ratio of the Laplace Transforms of any output-input combination.

Assuming that the airload response to an indicial input of angle of attack is governed by a linear constant coefficient system, the response to an input angle of attack e^{pt} is simply $H(p)$ where $H(p)$ is the ratio of the Laplace Transforms of any set of output-input combination. The Laplace Transforms of the unit step input and assumed indicial output are

$$L[u(t-0)] = \frac{1}{p}$$

$$L[C_{n\alpha}^C] = C_{n\alpha} \left(\frac{1}{p} - \frac{A_1 T_1}{1 + T_1 p} - \frac{A_2 T_2}{1 + T_2 p} \right)$$

Thus

$$\begin{aligned} H_{n\alpha}^C(p) &= \frac{L[C_{n\alpha}^C]}{L[u(t-0)]} = C_{n\alpha} \left(1 - \frac{A_1 T_1 p + A_1 - A_1}{1 + T_1 p} - \frac{A_2 T_2 p + A_2 - A_2}{1 + T_2 p} \right) \\ &= C_{n\alpha} \left(1 - A_1 - A_2 + \frac{A_1}{1 + T_1 p} + \frac{A_2}{1 + T_2 p} \right) \\ &= C_{n\alpha} \left(\frac{A_1}{1 + T_1 p} + \frac{A_2}{1 + T_2 p} \right) \quad \text{using } A_1 + A_2 = 1 \end{aligned}$$

For frequency response, i.e. response to inputs of sine and cosine harmonics, substitute $p = j\omega$. The transfer function then takes the following form

$$\begin{aligned} H_{n\alpha}^C(j\omega) &= C_{n\alpha} \left(\frac{A_1}{1 + jT_1\omega} + \frac{A_2}{1 + jT_2\omega} \right) \\ &= C_{n\alpha} \left[\frac{A_1(1 - jT_1\omega)}{1 + \omega^2 T_1^2} + \frac{A_2(1 - jT_2\omega)}{1 + \omega^2 T_2^2} \right] \\ &= C_{n\alpha} \left(\frac{A_1}{1 + \omega^2 T_1^2} + \frac{A_2}{1 + \omega^2 T_2^2} \right) - jC_{n\alpha} \left(\frac{A_1 T_1 \omega}{1 + \omega^2 T_1^2} + \frac{A_2 T_2 \omega}{1 + \omega^2 T_2^2} \right) \end{aligned}$$

Consider the indicial function given in eqn.4.88. For rotor problems, the time t is often replaced with a nondimensional parameter s , where s is the distance traversed by the airfoil measured in semi-chords in time t after the step change in angle of attack.

$$s = \frac{Ut}{c/2} \quad \text{or} \quad t = \frac{c}{2U}s$$

The time constants T_1 and T_2 are replaced with constants b_1 and b_2 where

$$T_1 = \frac{c}{2U} \frac{1}{b_1\beta^2}$$

$$T_2 = \frac{c}{2U} \frac{1}{b_2\beta^2} \quad \text{where} \quad \beta^2 = 1 - M^2$$

The indicial function in terms of s and b_1 then take the following form

$$\phi_{n\alpha}^C(t) = 1 - A_1 e^{-sb_1\beta^2} - A_2 e^{-sb_2\beta^2} \quad \text{where} \quad A_1 + A_2 = 1 \quad (4.88)$$

Note that

$$\omega T_1 = \frac{\omega c}{2U} \frac{1}{b_1\beta^2} = \frac{k}{b_1\beta^2}$$

$$\omega T_2 = \frac{\omega c}{2U} \frac{1}{b_2\beta^2} = \frac{k}{b_2\beta^2} \quad \text{where} \quad k \text{ is the reduced frequency}$$

The transfer function then takes the following form

$$H_{n\alpha}^C = C_{n\alpha} \left(\frac{A_1 b_1^2 \beta^4}{b_1^2 \beta^4 + k^2} + \frac{A_2 b_2^2 \beta^4}{b_2^2 \beta^4 + k^2} \right) - j C_{n\alpha} \left(\frac{A_1 b_1 k \beta^2}{b_1^2 \beta^4 + k^2} + \frac{A_2 b_2 k \beta^2}{b_2^2 \beta^4 + k^2} \right) \quad (4.89)$$

4.4.1 Leishman-Beddoes indicial model

The Leishman-Beddoes model consists of the indicial functions given by Beddoes [9, 10] and subsequently refined by Leishman and Beddoes [11, 12, 13]. They included the effects of compressibility, and later viscous flow separation. The indicial normal force due to angle of attack, the indicial pitching moment (about quarter-chord) due to angle of attack, the indicial normal force due to 'rate' of angle of attack, and the indicial pitching moment due to 'rate' of angle of attack are given by the following expressions. The first part is the impulsive part, analogous to the non-circulatory components in incompressible flow, the second part is the circulatory part due to the effects of the shed vorticity.

$$C_{n\alpha} = \frac{4}{M} \phi_{\alpha n}^I + \frac{2\pi}{\beta} \phi_{\alpha n}^C \quad (4.90)$$

$$C_{m\alpha} = -\frac{1}{M} \phi_{\alpha m}^I - \frac{2\pi}{\beta} \phi_{\alpha n}^C (x_{ac} - 0.25) \quad (4.91)$$

$$C_{nq} = \frac{1}{M} \phi_{qn}^I + \frac{\pi}{\beta} \phi_{qn}^C \quad (4.92)$$

$$C_{mq} = -\frac{7}{12M} \phi_{qm}^I - \frac{\pi}{8\beta} \phi_{qm}^C \quad (4.93)$$

Each indicial response is assumed to consist of two parts: an exponentially decaying part for the initial non-circulatory loading, and an asymptotically growing part which reaches a steady state value. The initial non-circulatory loading is taken from piston theory [14, 15]. The circulatory component of the indicial normal force due to angle of attack is

$$\phi_{\alpha n}^C = 1 - A_1 e^{-b_1\beta^2 s} - A_2 e^{-b_2\beta^2 s}$$

The impulsive component of the indicial normal force due to angle of attack is

$$\phi_{\alpha n}^I = e^{-\frac{s}{T'_\alpha}} \quad \text{where} \quad T'_\alpha = \frac{4M}{2(1-M) + 2\pi\beta M^2(A_1b_1 + A_2b_2)}$$

The circulatory component of the indicial normal force due to 'rate' of angle of attack is the same as that due to angle of attack

$$\phi_{qn}^C = 1 - A_1e^{-b_1\beta^2s} - A_2e^{-b_2\beta^2s}$$

The impulsive component of the indicial normal force due to 'rate' of angle of attack has the same form but with a different time constant

$$\phi_{qn}^I = e^{-\frac{s}{T'_q}} \quad \text{where} \quad T'_q = \frac{2M}{(1-M) + 2\pi\beta M^2(A_1b_1 + A_2b_2)}$$

The circulatory component of the indicial pitching moment due to angle of attack is assumed to be due to the aerodynamic center offset from quarter chord. The impulsive component of the indicial pitching moment due to angle of attack is

$$\phi_{\alpha m}^I = A_3e^{-\frac{s}{b_3T'_{\alpha m}}} + A_4e^{-\frac{s}{b_4T'_{\alpha m}}} \quad \text{where} \quad T'_{\alpha m} = 2M \left[\frac{A_3b_4 + A_4b_3}{b_3b_4(1-M)} \right]$$

The circulatory component of the indicial pitching moment due to 'rate' of angle of attack is

$$\phi_{qm}^C = 1 - e^{-b_5\beta^2s}$$

The impulsive component of the indicial pitching moment due to 'rate' of angle of attack is

$$\phi_{qm}^I = e^{-\frac{s}{T'_{qm}}} \quad \text{where} \quad T'_{qm} = \frac{14M}{15(1-M) + 3\pi\beta M^2b_5}$$

The original model parameters proposed by Beddoes are

$$\begin{aligned} A_1 &= 0.3 & A_2 &= 0.7 & A_3 &= 1.5 & A_4 &= -0.5 \\ b_1 &= 0.14 & b_2 &= 0.53 & b_3 &= 0.25 & b_4 &= 0.1 & b_5 &= 0.5 \end{aligned}$$

4.4.2 Frequency response of indicial model

It was shown earlier that it is possible to deduce the frequency response (i.e. response to sinusoidal inputs) from indicial response. The frequency response of the circulatory normal force was deduced in eqn.4.89. Consider the impulsive indicial normal force in response to angle of attack.

$$C_{n\alpha}^I(s) = \frac{4}{M}e^{-\frac{s}{T'_\alpha}}$$

To convert to a function in time use $s = 2Ut/c$. The nondimensional constant T'_α can be expressed as

$$T'_\alpha = \frac{2U}{c}T_\alpha$$

where T_α has the dimension of time. Then we have

$$C_{n\alpha}^I(t) = \frac{4}{M}e^{-t/T_\alpha}$$

The Laplace Transform is

$$L[C_{n\alpha}^I] = \frac{4}{M} \frac{T_\alpha}{1 + T_\alpha p}$$

Thus

$$H_{n\alpha}^I(p) = \frac{L[C_{n\alpha}^I]}{L[u(t-0)]} = \frac{4}{M} \frac{T_\alpha p}{1 + T_\alpha p}$$

Substitute $p = j\omega$ to obtain

$$H_{n\alpha}^I(j\omega) = \frac{4}{M} \left(\frac{\omega^2 T_\alpha^2}{1 + \omega^2 T_\alpha^2} \right) + j \frac{4}{M} \left(\frac{\omega T_\alpha}{1 + \omega^2 T_\alpha^2} \right)$$

The time constant T_α can be expressed as

$$T_\alpha = \frac{c}{a} K_\alpha$$

where a is the speed of sound, and K_α is a nondimensional constant. Then

$$\omega T_\alpha = \omega \frac{c}{a} K_\alpha = \frac{2Uk}{c} \frac{c}{a} K_\alpha = 2MkK_\alpha$$

The transfer function then takes the following form

$$H_{n\alpha}^I = \frac{4}{M} \left(\frac{4K_\alpha^2 M^2 k^2}{1 + 4K_\alpha^2 M^2 k^2} \right) + j \frac{4}{M} \left(\frac{2K_\alpha M k}{1 + 4K_\alpha^2 M^2 k^2} \right) \quad (4.94)$$

The transfer function has been expressed as a function of incident Mach number M and reduced frequency k . Consider the impulsive indicial pitching moment in response to angle of attack.

$$C_{m\alpha}^I(s) = \frac{1}{M} \left(A_3 e^{-\frac{s}{b_3 T'_{\alpha m}}} + A_4 e^{-\frac{s}{b_4 T'_{\alpha m}}} \right)$$

To convert to a function in time use $s = 2Ut/c$. The nondimensional constant $T'_{\alpha m}$ can be expressed as

$$T'_{\alpha m} = \frac{2U}{c} T_{\alpha m}$$

where $T_{\alpha m}$ has the dimension of time. Then we have

$$C_{m\alpha}^I(t) = \frac{1}{M} \left(A_3 e^{-\frac{t}{b_3 T'_{\alpha m}}} + A_4 e^{-\frac{t}{b_4 T'_{\alpha m}}} \right)$$

The Laplace Transform is

$$L[C_{m\alpha}^I] = \frac{1}{M} \left(\frac{A_3 b_3 T_{\alpha m}}{1 + b_3 T_{\alpha m} p} + \frac{A_4 b_4 T_{\alpha m}}{1 + b_4 T_{\alpha m} p} \right)$$

Thus

$$H_{m\alpha}^I(p) = \frac{L[C_{m\alpha}^I]}{L[u(t-0)]} = \frac{1}{M} \left(\frac{A_3 b_3 T_{\alpha m} p}{1 + b_3 T_{\alpha m} p} + \frac{A_4 b_4 T_{\alpha m} p}{1 + b_4 T_{\alpha m} p} \right)$$

Substitute $p = j\omega$ to obtain

$$H_{m\alpha}^I(j\omega) = \frac{1}{M} \left(\frac{A_3 b_3^2 \omega^2 T_{\alpha m}^2}{1 + b_3^2 \omega^2 T_{\alpha m}^2} + \frac{A_4 b_4^2 \omega^2 T_{\alpha m}^2}{1 + b_4^2 \omega^2 T_{\alpha m}^2} \right) - j \frac{1}{M} \left(\frac{A_3 b_3 \omega T_{\alpha m}}{1 + b_3^2 \omega^2 T_{\alpha m}^2} + \frac{A_4 b_4 \omega T_{\alpha m}}{1 + b_4^2 \omega^2 T_{\alpha m}^2} \right)$$

The time constant T_α can be expressed as

$$T_{\alpha m} = \frac{c}{a} K_{\alpha m}$$

where a is the speed of sound, and K_α is a nondimensional constant. Then

$$\omega T_{\alpha m} = \omega \frac{c}{a} K_{\alpha m} = \frac{2Uk}{c} \frac{c}{a} K_{\alpha m} = 2MkK_{\alpha m}$$

The transfer function then takes the following form

$$H_{m\alpha}^I = \frac{1}{M} \left(\frac{4A_3 b_3^2 M^2 k^2 K_{\alpha m}^2}{1 + 4b_3^2 M^2 k^2 K_{\alpha m}^2} + \frac{4A_4 b_4^2 M^2 k^2 K_{\alpha m}^2}{1 + 4b_4^2 M^2 k^2 K_{\alpha m}^2} \right) - j \frac{1}{M} \left(\frac{2A_3 b_3 M k K_{\alpha m}}{1 + 4b_3^2 M^2 k^2 K_{\alpha m}^2} + \frac{2A_4 b_4 M k K_{\alpha m}^2}{1 + 4b_4^2 M^2 k^2 K_{\alpha m}^2} \right) \quad (4.95)$$

The transfer function has been expressed as a function of incident Mach number M and reduced frequency k .

Consider the impulsive indicial normal force in response to ‘rate’ of angle of attack. Note that, here, the input is still a unit step of angle of attack, and not an unit step of ‘rate’ of angle of attack.

$$C_{nq}^I(s) = \frac{1}{M} e^{-\frac{s}{T_q'}}$$

To convert to a function in time use $s = 2Ut/c$. The nondimensional constant T_q' can be expressed as

$$T_q' = \frac{2U}{c} T_q$$

where T_q has the dimension of time. Then we have

$$C_{nq}^I(t) = \frac{1}{M} e^{-t/T_q}$$

The Laplace Transform is

$$L[C_{nq}^I] = \frac{1}{M} \frac{T_q}{1 + T_q p}$$

Note that the above expressions describes the response to a sinusoidal input in pitch rate, i.e. a pitch rate of the form e^{pt} . This is not the transform we seek. We seek the response to a sinusoidal input in angle of attack, i.e. an angle of attack variation of the form e^{pt} . The response will depend on the pitch rate this angle of attack variation generates. To this end we consider a step change in input angle of attack. Then, relate in the Laplace domain, the output response with the input pitch rate it generates. If the angle of attack variation is given by $\alpha(t)$, then the rate of angle of attack is the time derivative $\dot{\alpha}(t)$, with units of rad/sec. In nondimensional form

$$q(t) = \dot{\alpha} \frac{c}{U}$$

The Laplace transform of the pitch rate is related to the Laplace transform of the angle of attack variation as follows

$$L[q] = L[\dot{\alpha}] \frac{c}{U} = pL[\alpha] \frac{c}{U}$$

Now, the transfer function between normal force due to pitch input and pitch input is given by

$$\frac{L[C_{nq}^I]}{L[q]} = \frac{1}{M} \frac{T_q p}{1 + T_q p} \quad (4.96)$$

Replace the Laplace transform of the pitch rate

$$\frac{L[C_{nq}^I]}{pL[\alpha] \frac{c}{U}} = \frac{1}{M} \frac{T_q p}{1 + T_q p}$$

The transfer function between normal force due to pitch input and the angle of attack is then obtained by simply re-arranging the above expression

$$H_{nq}^I(p) = \frac{L[C_{nq}^I]}{L[\alpha]} = \frac{1}{M} \frac{T_q p}{1 + T_q p} p \frac{c}{U} = \frac{1}{M} \frac{2T_q p}{1 + T_q p} p \frac{c}{2U} \quad (4.97)$$

Substituting $p = j\omega$ in eqn.4.102 gives C_{nq}^I when q is sinusoidal. Substituting $p = j\omega$ in eqn.4.97 gives C_{nq}^I when α is sinusoidal. This is the transfer function we seek. Substitute $p = j\omega$ in eqn.4.97 to obtain

$$\begin{aligned} H_{nq}^I(j\omega) &= \frac{1}{M} \left(\frac{j\omega T_q}{1 + j\omega T_q} j\omega \frac{c}{2U} \right) = \frac{1}{M} \left(\frac{j\omega T_q}{1 + j\omega T_q} jk \right) \\ &= -\frac{1}{M} \left(\frac{2\omega T_q k}{1 + \omega^2 T_q^2} \right) + j \frac{1}{M} \left(\frac{2\omega^2 T_q^2 k}{1 + \omega^2 T_q^2} \right) \end{aligned}$$

The time constant T_q can be expressed as

$$T_\alpha = \frac{c}{a} K_q$$

where a is the speed of sound, and K_q is a nondimensional constant. Then

$$\omega T_\alpha = \omega \frac{c}{a} K_q = \frac{2Uk}{c} \frac{c}{a} K_q = 2MkK_q$$

The transfer function then takes the following form

$$H_{nq}^I = -\frac{1}{M} \left(\frac{4K_q M k^2}{1 + 4K_q^2 M^2 k^2} \right) + j \frac{1}{M} \left(\frac{8K_q^2 M^2 k^3}{1 + 4K_q^2 M^2 k^2} \right) \quad (4.98)$$

Similarly, consider the circulatory indicial pitching moment in response to ‘rate’ of angle of attack, i.e. pitch rate.

$$C_{mq}^C(s) = -\frac{\pi}{8\beta} \left(1 - e^{-b_5 \beta^2 s} \right)$$

To convert to a function in time use $s = 2Ut/c$, and introduce the nondimensional constant T_5

$$T_5 = \frac{c}{2U} \frac{1}{b_5 \beta^2}$$

Then we have

$$C_{mq}^C(t) = -\frac{\pi}{8\beta} \left(1 - e^{-t/T_5} \right)$$

Now, the transfer function with respect to the pitch input is given by

$$\frac{L[C_{mq}^C]}{L[q]} = -\frac{\pi}{8\beta} \left(\frac{1}{1 + T_5 p} \right) \quad (4.99)$$

Following the arguments given earlier, the transfer function with respect to the angle of attack is then

$$H_{mq}^C(p) = \frac{L [C_{mq}^C]}{L [\alpha]} = -\frac{2\pi}{8\beta} \left(\frac{p}{1 + T_5 p} \right) \frac{c}{2U} \quad (4.100)$$

Substitute $p = j\omega$ to obtain

$$\begin{aligned} H_{mq}^C(j\omega) &= -\frac{\pi}{8\beta} \left(\frac{jk}{1 + j\omega T_5} \right) \\ &= -\frac{\pi}{8\beta} \left(\frac{k\omega T_5}{1 + \omega^2 T_5^2} \right) - j\frac{\pi}{8\beta} \left(\frac{k}{1 + \omega^2 T_5^2} \right) \end{aligned}$$

Use

$$\omega T_5 = \frac{k}{b_5 \beta^2}$$

to obtain

$$H_{mq}^C = -\frac{\pi}{8\beta} \left(\frac{b_5 k^2 \beta^2}{k^2 + b_5^2 \beta^4} \right) - j\frac{\pi}{8\beta} \left(\frac{k b_5^2 \beta^4}{k^2 + b_5^2 \beta^4} \right) \quad (4.101)$$

Lastly, consider the impulsive indicial pitching moment in response to pitch rate.

$$C_{mq}^I(s) = -\frac{7}{12M} e^{-\frac{s}{T'_{mq}}}$$

To convert to a function in time use $s = 2Ut/c$. The nondimensional constant T'_{mq} can be expressed as

$$T'_{mq} = \frac{2U}{c} T_{mq}$$

where T_q has the dimension of time. Then we have

$$C_{mq}^I(t) = -\frac{7}{12M} e^{-t/T_{mq}}$$

Now, the transfer function with respect to the pitch input is given by

$$\frac{L [C_{mq}^I]}{L [q]} = -\frac{7}{12M} \left(\frac{T_{qm} p}{1 + T_{qm} p} \right) \quad (4.102)$$

Following the arguments given earlier, the transfer function with respect to the angle of attack is then

$$H_{mq}^I(p) = \frac{L [C_{mq}^C]}{L [\alpha]} = -\frac{7}{12M} \left(\frac{2T_{qm} p}{1 + T_{qm} p} \right) \frac{c}{2U} \quad (4.103)$$

Substitute $p = j\omega$, and express the time constant T_{mq} as

$$T_{mq} = \frac{c}{a} K_{mq}$$

where a is the speed of sound, and K_{mq} is a nondimensional constant. Then

$$\omega T_{mq} = \omega \frac{c}{a} K_{mq} = \frac{2Uk}{c} \frac{c}{a} K_{mq} = 2MkK_{mq}$$

The transfer function then takes the following form

$$H_{mq}^I = \frac{7}{12M} \left(\frac{4K_{mq} M k^2}{1 + 4K_{mq}^2 M^2 k^2} \right) - j\frac{7}{12M} \left(\frac{8K_{mq}^2 M^2 k^3}{1 + 4K_{mq}^2 M^2 k^2} \right) \quad (4.104)$$

4.4.3 Recursive formulation of an indicial model

The normal force at any time t is the sum of normal forces due to angle of attack and pitch rate, each having a circulatory and an impulsive component.

$$\begin{aligned} C_N &= C_N^\alpha + C_N^q \\ &= C_N^{\alpha C} + C_N^{\alpha I} + C_N^{qC} + C_N^{qI} \end{aligned}$$

where the components are given in terms of the indicial response functions (see eqns.4.80 and 4.81) as follows

$$\begin{aligned} C_N^{\alpha C}(s, M) &= \frac{2\pi}{\beta} \phi_{\alpha n}^C(0) \alpha(0) + \int_0^s \frac{\partial \alpha}{\partial \sigma} \frac{2\pi}{\beta} \phi_{\alpha n}^C(s - \sigma) d\sigma \\ &= \frac{2\pi}{\beta} \left[\alpha(0) + \int_0^s \frac{\partial \alpha}{\partial \sigma} \phi_{\alpha n}^C(s - \sigma) d\sigma \right] \\ &= \frac{2\pi}{\beta} \left[\alpha(0) + \int_0^s \frac{\partial \alpha}{\partial \sigma} \left\{ 1 - A_1 e^{-b_1 \beta^2 (s - \sigma)} - A_2 e^{-b_2 \beta^2 (s - \sigma)} \right\} d\sigma \right] \\ &= \frac{2\pi}{\beta} \left[\alpha(0) + \int_0^s d\alpha - \int_0^s A_1 \frac{\partial \alpha}{\partial \sigma} e^{-b_1 \beta^2 (s - \sigma)} d\sigma - \int_0^s A_2 \frac{\partial \alpha}{\partial \sigma} e^{-b_2 \beta^2 (s - \sigma)} d\sigma \right] \\ &= \frac{2\pi}{\beta} [\alpha(s) - X(s) - Y(s)] \end{aligned} \tag{4.105}$$

where

$$\begin{aligned} X(s) &= \int_0^s A_1 \frac{\partial \alpha}{\partial \sigma} e^{-b_1 \beta^2 (s - \sigma)} d\sigma \\ Y(s) &= \int_0^s A_2 \frac{\partial \alpha}{\partial \sigma} e^{-b_2 \beta^2 (s - \sigma)} d\sigma \end{aligned} \tag{4.106}$$

The above formulation can be cast into a recursive form for discrete advances in time Δt , or reduced time Δs , where $\Delta s = 2U \Delta t / c$. For example, at $s + \Delta s$ we have

$$C_N^{\alpha C}(s + \Delta s, M) = \frac{2\pi}{\beta} [\alpha(s + \Delta s) - X(s + \Delta s) - Y(s + \Delta s)]$$

Using eqn4.106 it can be shown

$$X(s + \Delta s) = X(s) e^{-b_1 \beta^2 \Delta s} + A_1 \Delta \alpha(s + \Delta s) e^{-b_1 \beta^2 \frac{\Delta s}{2}}$$

or in terms of current s

$$X(s) = X(s - \Delta s) e^{-b_1 \beta^2 \Delta s} + A_1 \Delta \alpha e^{-b_1 \beta^2 \frac{\Delta s}{2}}$$

where $\Delta \alpha$ is at s and

$$X(0) = 0$$

Thus the recursive formulation for the circulatory normal force due to angle of attack variation can be expressed as

$$\begin{aligned} C_N^{\alpha C}(s, M) &= \frac{2\pi}{\beta} [\alpha(s) - X_1(s) - Y_1(s)] \\ X_1(s) &= X_1(s - \Delta s) e^{-b_1 \beta^2 \Delta s} + A_1 \Delta \alpha e^{-b_1 \beta^2 \frac{\Delta s}{2}} \\ Y_1(s) &= Y_1(s - \Delta s) e^{-b_2 \beta^2 \Delta s} + A_2 \Delta \alpha e^{-b_2 \beta^2 \frac{\Delta s}{2}} \\ X_1(0) &= Y_1(0) = 0 \end{aligned} \tag{4.107}$$

Using the same approach it can be shown that the recursive formulation for the impulsive normal force due to angle of attack variation is

$$\begin{aligned} C_N^{\alpha I}(s, M) &= \frac{4T'_\alpha}{M} \left[\frac{\Delta\alpha(s)}{\Delta s} - D_1(s) \right] \\ D_1(s) &= D_1(s - \Delta s)e^{-\frac{\Delta s}{T'_\alpha}} + \left\{ \frac{\Delta\alpha(s)}{\Delta s} - \frac{\Delta\alpha(s - \Delta s)}{\Delta s} \right\} e^{-\frac{\Delta s}{2T'_\alpha}} \\ C_N^{\alpha I}(0, M) &= 0 \quad , \quad D_1(0) = 0 \end{aligned} \quad (4.108)$$

The recursive formulation for the circulatory normal force due to pitch rate is

$$\begin{aligned} C_N^{qC}(s, M) &= \frac{\pi}{\beta} [q(s) - X_3(s) - Y_3(s)] \\ X_3(s) &= X_3(s - \Delta s)e^{-b_1\beta^2\Delta s} + A_1\Delta qe^{-b_1\beta^2\frac{\Delta s}{2}} \\ Y_3(s) &= Y_3(s - \Delta s)e^{-b_2\beta^2\Delta s} + A_2\Delta qe^{-b_2\beta^2\frac{\Delta s}{2}} \\ X_3(0) &= Y_3(0) = 0 \end{aligned} \quad (4.109)$$

The recursive formulation for the impulsive normal force due to pitch rate is

$$\begin{aligned} C_N^{qI}(s, M) &= \frac{T'_q}{M} \left[\frac{\Delta q(s)}{\Delta s} - D_3(s) \right] \\ D_3(s) &= D_3(s - \Delta s)e^{-\frac{\Delta s}{T'_q}} + \left\{ \frac{\Delta q(s)}{\Delta s} - \frac{\Delta q(s - \Delta s)}{\Delta s} \right\} e^{-\frac{\Delta s}{2T'_q}} \\ C_N^{qI}(0, M) &= 0 \quad , \quad D_3(0) = 0 \end{aligned} \quad (4.110)$$

The circulatory pitching moment due to angle of attack is simple due to the aerodynamic center offset from quarter-chord and is given by

$$C_M^{\alpha C}(s, M) = \left(\frac{1}{4} - x_{ac} \right) C_N^{\alpha C}(s, M) \quad (4.111)$$

The recursive formulation for the circulatory pitching moment due to pitch rate is

$$\begin{aligned} C_M^{qC}(s, M) &= -\frac{\pi}{8\beta} [q(s) - X_2(s)] \\ X_2(s) &= X_2(s - \Delta s)e^{-b_5\Delta s} + A_5\Delta qe^{-b_5\beta^2\frac{\Delta s}{2}} \\ X(0) &= 0 \end{aligned} \quad (4.112)$$

The recursive formulation for the impulsive pitching moment due to angle of attack is given by

$$\begin{aligned} C_M^{\alpha I}(s, M) &= -\frac{A_3b_3T'_{m\alpha}}{M} \left[\frac{\Delta\alpha(s)}{\Delta s} - D_4(s) \right] - \frac{A_4b_4T'_{m\alpha}}{M} \left[\frac{\Delta\alpha(s)}{\Delta s} - D_5(s) \right] \\ D_4(s) &= D_4(s - \Delta s)e^{-\frac{\Delta s}{b_3T'_{m\alpha}}} + \left\{ \frac{\Delta\alpha(s)}{\Delta s} - \frac{\Delta\alpha(s - \Delta s)}{\Delta s} \right\} e^{-\frac{\Delta s}{2b_3T'_{m\alpha}}} \\ D_5(s) &= D_5(s - \Delta s)e^{-\frac{\Delta s}{b_4T'_{m\alpha}}} + \left\{ \frac{\Delta\alpha(s)}{\Delta s} - \frac{\Delta\alpha(s - \Delta s)}{\Delta s} \right\} e^{-\frac{\Delta s}{2b_4T'_{m\alpha}}} \\ C_N^{\alpha I}(0, M) &= 0 \quad , \quad D_4(0) = 0 \quad , \quad D_5(0) = 0 \end{aligned} \quad (4.113)$$

The recursive formulation for the impulsive pitching moment due to pitch rate is

$$\begin{aligned} C_M^{qI}(s, M) &= -\frac{7T'_{mq}}{12M} \left[\frac{\Delta q(s)}{\Delta s} - D_6(s) \right] \\ D_6(s) &= D_6(s - \Delta s)e^{-\frac{\Delta s}{T'_{mq}}} + \left\{ \frac{\Delta q(s)}{\Delta s} - \frac{\Delta q(s - \Delta s)}{\Delta s} \right\} e^{-\frac{\Delta s}{2T'_{mq}}} \\ C_N^{qI}(0, M) &= 0 \quad , \quad D_6(0) = 0 \end{aligned} \quad (4.114)$$

4.4.4 Leishman-Beddoes dynamic stall formulation

The first step is to reconstruct the static airfoil property data, normal force (or lift) and pitching moments using a theoretical model for flow separation over 2D bodies. A theory which models the separated flow regions on 2D bodies is due to Kirchhoff [7, 24]. An airfoil at an angle of attack α , normal force coefficient C_N , and force curve slope 2π for incompressible flow, has a the trailing edge separation point f given by

$$C_N = 2\pi \left(\frac{1 + \sqrt{f}}{2} \right)^2 \alpha$$

For real airfoils this can be adapted to

$$C_N = C_0 + C_{n\alpha} \left(\frac{1 + \sqrt{f}}{2} \right)^2 \alpha$$

Given the static airfoil properties, f can be calculated at every α . A smooth curve is then fitted through these data points

$$f = \begin{cases} f_1 + f_2 \exp\left(\frac{\alpha - \alpha_1}{S_1}\right) & \text{if } \alpha \leq \alpha_1 \\ f_3 + f_4 \exp\left(\frac{\alpha_1 - \alpha}{S_2}\right) & \text{if } \alpha \geq \alpha_1 \end{cases}$$

α_1 is the static angle of attack at which the airfoil stalls. At $\alpha = \alpha_1$, the separation point $f = f_1 + f_2$. For incompressible flow this point often corresponds to $f = 0.7$. In the Leishman-Beddoes model, f is therefore described as

$$f = \begin{cases} 1 - 0.3 \exp\left(\frac{\alpha - \alpha_1}{S_1}\right) & \text{if } \alpha \leq \alpha_1 \\ 0.04 + 0.66 \exp\left(\frac{\alpha_1 - \alpha}{S_2}\right) & \text{if } \alpha \geq \alpha_1 \end{cases}$$

S_1 , S_2 , α_1 , and in general the constants f_1 , f_2 , f_3 , f_4 can be determined from static airfoil tables at a given Mach number. The pitching moment about quarter-chord can be constructed as a function of the separation point as

$$C_M = C_{M0} + C_N [K_0 + K_1(1 - f) + K_2 \sin(\pi f^m)] \quad (4.115)$$

where C_{M0} is the zero lift moment. The constant $K_0 = (0.25 - x_{ac})$ is the aerodynamic center offset from the quarter-chord. K_1 models the effect on the center of pressure due to the growth of the separated flow region. K_2 and m help describe the shape of the moment break at stall. The four constants are to be adjusted to provide the best static moment reconstruction for a particular airfoil.

Consider the circulatory normal force due to angle of attack variation as in eqn.4.107. Writting terms of a current time n we have

$$\begin{aligned} C_{N_n} &= C_{n\alpha} [\alpha_n - X_n - Y_n] \\ X_n &= X_{n-1} \exp(-b_1 \beta^2 \Delta s) + A_1 \Delta \alpha_n \exp\left(-b_1 \beta^2 \frac{\Delta s}{2}\right) \\ Y_n &= Y_{n-1} \exp(-b_2 \beta^2 \Delta s) + A_2 \Delta \alpha_n \exp\left(-b_2 \beta^2 \frac{\Delta s}{2}\right) \end{aligned} \quad (4.116)$$

where $C_N = C_N^{\alpha C}$, the superscript ' αC ' is dropped for brevity. $\Delta s = s_n - s_{n-1}$ is the distance, in semi-chords, traversed by the airfoil in $\Delta t = t_n - t_{n-1}$. $\Delta \alpha_n = \alpha_n - \alpha_{n-1}$ is the step change in

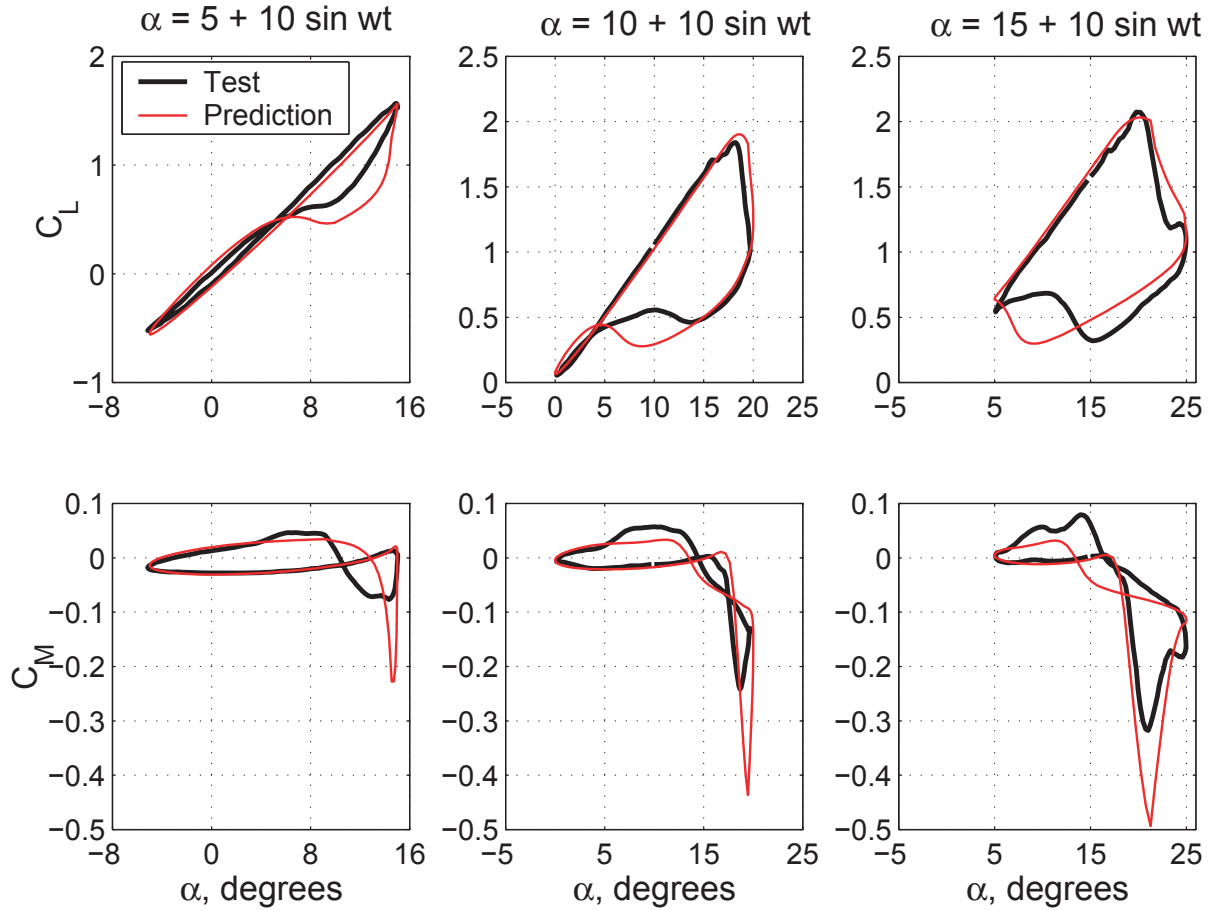


Figure 4.2: NACA 0012 light and deep dynamic stall cycles: Test data vs. prediction using Leishman-Beddoes model (data from McCroskey et al NASA TM-84245, 1982) Mach No. 0.3, reduced freq. $k = 0.1$

angle of attack at step n . Note that the flat plate lift curve slope has been replaced with a general lift curve slope $C_{n\alpha}$.

During unsteady conditions, stall is delayed due to a lag in leading edge pressure response with respect to the normal force. To implement this lag a first order reduction is applied to the circulatory normal force producing a new value

$$C'_{N_n} = C_{N_n} - D_{p_n}$$

where

$$D_{p_n} = D_{p_{n-1}} \exp\left(-\frac{\Delta s}{T_p}\right) + (C_{N_n} - C_{N_{n-1}}) \exp\left(-\frac{\Delta s}{2T_p}\right)$$

T_p is an empirical constant, a function of Mach number, and determined from unsteady experimental data. The corrected angle of attack is then

$$\alpha_f = \frac{C'_{N_n} - C_0}{C_{n\alpha}}$$

where C_0 is the normal force coefficient at zero angle of attack. The corrected angle of attack is then used to determine the effective separation point on the airfoil, f' , from the static f versus α

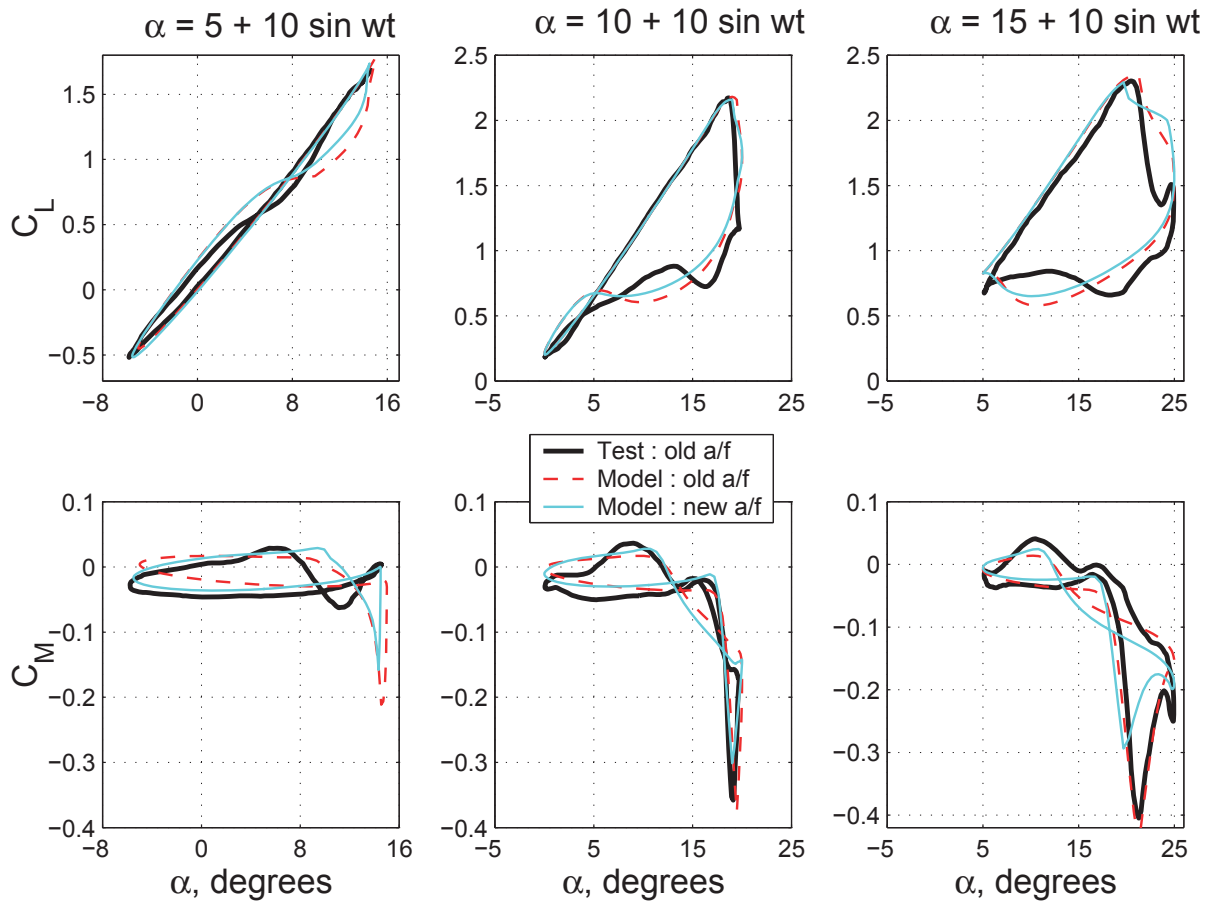


Figure 4.3: SC-1095 light and deep dynamic stall cycles: Test data vs. prediction using Leishman-Beddoes model (data from McCroskey et al NASA TM-84245, 1982) Mach No. 0.3, reduced freq. $k = 0.1$; Old airfoil data is static data from McCroskey report, New airfoil data is a refined version from U.S.Army

relationship given above. The additional effect of unsteady boundary layer response is incorporated using a first order lag

$$f_n'' = f_n' - D_{f_n}$$

where

$$D_{f_n} = D_{f_{n-1}} \exp\left(-\frac{\Delta s}{T_f}\right) + (f_n' - f_{n-1}') \exp\left(-\frac{\Delta s}{2T_f}\right)$$

T_f is an empirical constant, a function of Mach number. Can be determined from unsteady data or an unsteady boundary layer analysis, in absence of data. Once the separation parameter has been determined, the normal force can then be determined as

$$C_{N_n} = C_{n\alpha} \left(\frac{1 + \sqrt{f_n''}}{2}\right)^2 \alpha_f = C_{N_n}^C$$

where $C_{n\alpha}$ is the lift curve slope, a function of Mach number. The pitching moment is given by

$$C_{M_n} = C_{M_0} + C_{N_n}^C [K_0 + K_1(1 - f_n'') + K_2 \sin(\pi f_n''^m)] \quad (4.117)$$

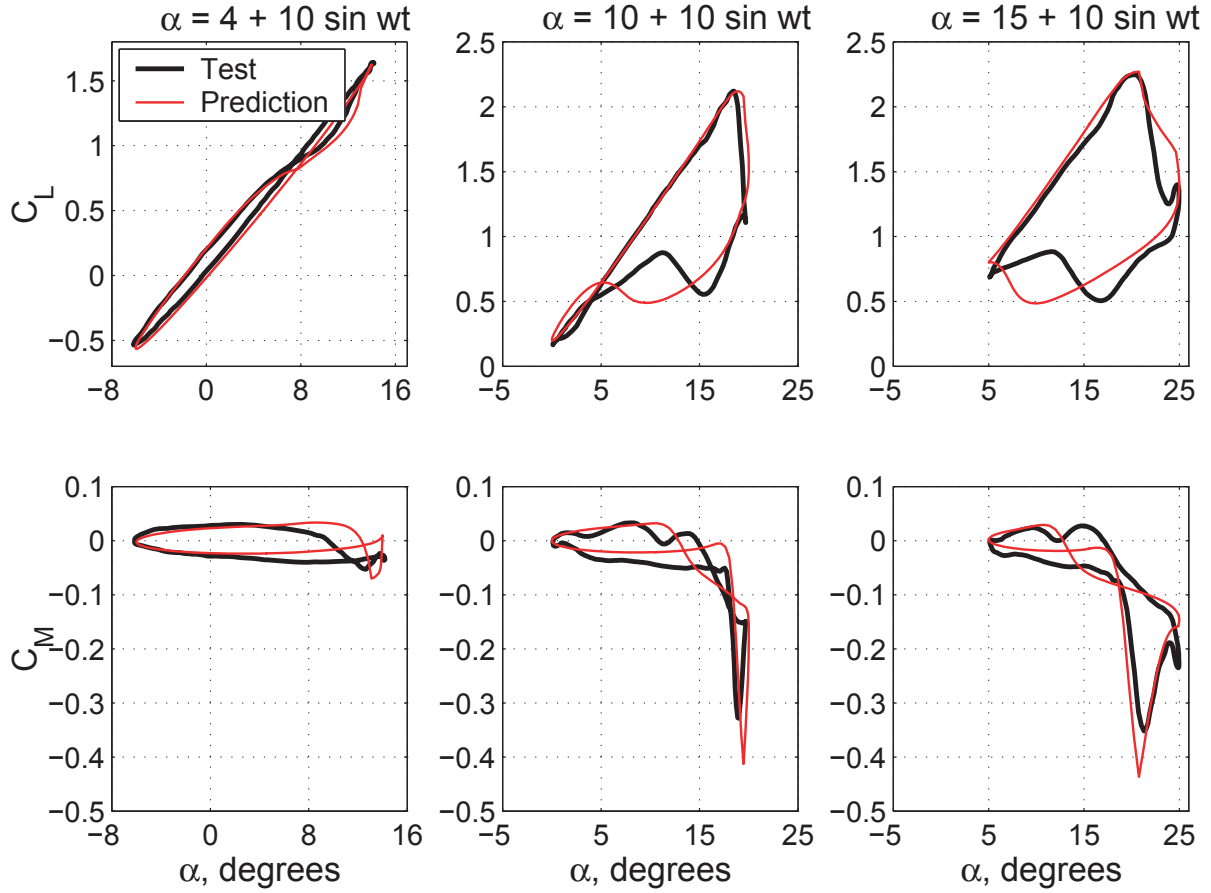


Figure 4.4: **Hughes HH-02 light and deep dynamic stall cycles: Test data vs. prediction using Leishman-Beddoes model (data from McCroskey et al NASA TM-84245, 1982) Mach No. 0.3, reduced freq. $k = 0.1$**

Note that, here C_M corresponds to $C_N^{\alpha C}$, the circulatory pitching moment due to angle of attack variation. The contributions of the pitch rate terms and the impulsive terms will be added later on. As the airfoil gradually pitches up, the separation point f progressively advances towards the leading edge. At the same time, a leading edge vortex is formed, gradually growing in strength. The gradual growth in its strength can be viewed as caused by an accumulation of circulation, such that, the lift induced by this gradually growing vortex accounts for the difference between the normal force given by the Kirchhoff approximation above, C_{N_n} , and a hypothetical normal force that would result if there was no separation, i.e. corresponding to $f_n'' = 1$. Thus the incremental vortex lift at a time step n is given by

$$C_{V_n} = C_{N_n} - C_{n\alpha}\alpha_f = C_{n\alpha} \left(\frac{1 + \sqrt{f_n''}}{2} \right)^2 \alpha_f - C_{n\alpha}\alpha_f \quad (4.118)$$

The total vortex lift, C_N^v , results from the cumulative addition of the above increments along with a simultaneous mechanism for decay.

$$C_{N_n}^v = C_{N_{n-1}}^v \exp\left(-\frac{\Delta s}{T_v}\right) + (C_n^v - C_{n-1}^v) \exp\left(-\frac{\Delta s}{2T_v}\right) \quad (4.119)$$

where T_v is another empirical constant. When a leading edge separation is triggered, the vortex lift is added to the normal force as long as the vortex traverses the chord and has not been washed

aft of the trailing edge. The condition of leading edge separation, and the duration of the vortex passage over the chord are set by empirical means. The condition for leading edge separation is when C_{N_n} exceeds the value corresponding to static stall. This value is a function of Mach number and denoted by C_{N_1} in the model. At this point the accumulated vortex is assumed to start to convect over the airfoil chord. The rate of convection has been experimentally determined to be less than half of the free stream velocity. During the vortex convection, the vortex lift evolves according to eqns.4.118 and 4.119, i.e. the total vortex lift $C_{N_n}^v$ is allowed to decay exponentially with time while being constantly updated by a new increment. The duration of vortex passage, in terms of nondimensional time τ_v (distance travelled by the airfoil in semi-chords), is from $\tau_v = 0$ to $\tau_v = \tau_{vl}$. At $\tau_v = \tau_{vl}$, the vortex leaves the trailing edge. The center of pressure movement behind quarter-chord due to the vortex movement is determined empirically to be

$$C_P^v = 0.20 \left[1 - \cos \left(\frac{\pi \tau_v}{T_{vl}} \right) \right] \quad (4.120)$$

The pitching moment contribution of the moving center of pressure is then simply

$$C_{M_n}^v = -C_P^v C_{N_n}^v \quad (4.121)$$

The final normal force and pitching moment expressions at a given time step n is then

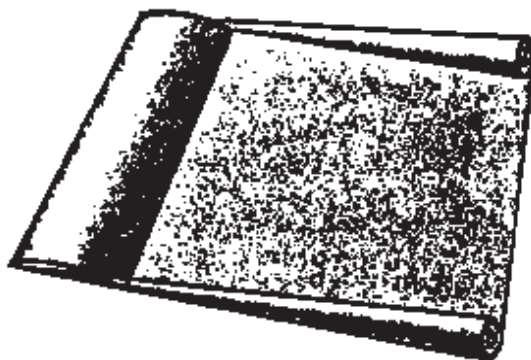
$$\begin{aligned} C_N &= C_0 + \underline{C_N^{\alpha C}} + C_N^v + C_N^{\alpha I} + C_N^{qC} + C_N^{qI} \\ C_M &= C_{M0} + \underline{C_M^{\alpha C}} + C_M^v + C_M^{\alpha I} + C_M^{qC} + C_M^{qI} \end{aligned}$$

The separated flow model is embedded in the underlined terms. The dynamic stall effects are in C_N^v and C_M^v . Dynamic stall cycles for an oscillating 2D airfoil are shown in Figs.4.2, 4.3 and 4.4.

4.5 Wing Models

4.5.1 Prandtl Lifting Line Theory

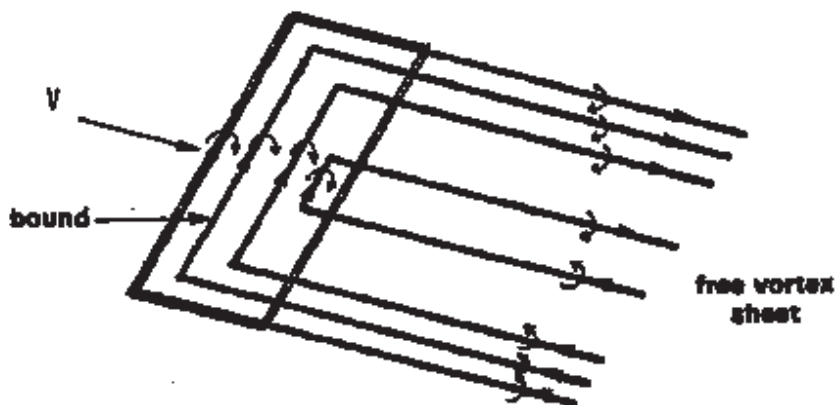
Associated with the lift on the wing, there is a circulation around the wing. At the tip, the lift is zero and therefore the circulation must vanish at the tip. This means circulation varies along the span. Whenever there is a variation of circulation spanwise, there has to be shedding of vorticity. If there is a continuous variation of circulation along the wing span, a continuous sheet of trailing vortices must proceed from the wing.



If we assume that the circulation is uniform along the span and drops to zero at the tips of the wing, then one can consider a simple model of two concentrated vorticity filaments originated at

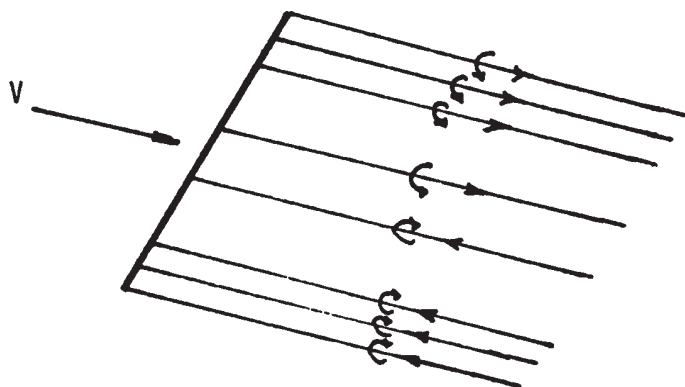
the wing tips. this concept of two tip vortices was originated by Lanchester. This model gives a good global picture but is not appropriate for analyzing flow near the wing.

A better model is to consider a continuous trailing vortex sheet distribution, as proposed by Prandtl.



The vortex sheet on the top and bottom surface is called the bound vortex sheet. Across the bound vortex sheet, a pressure difference may exist. The trailing edge sheet is called the free vortex sheet and no pressure difference exists across the sheet. The shed vortices are pulled downstream by the wind. If there is no new shedding, the old one will not have any influence on the airfoil.

For large aspect ratio wings, the bound part of the vortex sheet may be approximated by a single bound vortex line of varying strength. This is called the Prandtl lifting line theory.



For steady flow, influence on the shedding vorticity sheet on lift is negligible. For a body in motion, the lift is changing with time and so there is a continuous shedding of vorticity. The vorticity which is close to the surface plays an important role for the calculation of unsteady pressure on the surface.

4.5.2 Weissinger-L Lifting-surface Theory

The W-L model [25] is essentially a lifting-surface model with only one chord-wise element. The W-L model represents blade lift using a series of spanwise horseshoe vortex elements. The bound

circulation is located at the 1/4-chord point. The flow tangency condition is imposed at the 3/4-chord point. Compared to a lifting line model, the W-L model predicts improved loading for fixed wings with arbitrary planforms.

Let the blade be divided into N aerodynamic segments. For the i -th segment the flow tangency can be written as

$$\begin{aligned} V_{b_i} &= V_{\infty_i} \alpha_{e_i} \\ &= V_{\infty_i} (\alpha_i - \phi_{NW_i}) \\ &= V_{\infty_i} \alpha_i - V_{NW_i} \end{aligned} \quad (4.122)$$

where V_{b_i} is the bound vortex induced velocity at the i -th control point and V_{∞_i} is the incident free stream velocity at the control point. α_{e_i} is the *effective angle of attack* at the section. The *effective angle of attack* is obtained by subtracting the near wake *induced angle of attack* from the *input angle of attack*. The later includes the effect of blade deformation and far wake inflow. V_{NW_i} is the velocity induced by the nearwake at the i -th control point.

The velocities V_{b_i} and V_{NW_i} are related to the strength of the bound vortices, Γ_i through influence coefficient matrices. These matrices depend both on the blade deformations and on the blade geometry e.g., rigid twist, control angles, planform, sweep etc.

$$V_{b_i} = \sum_{j=1}^N I_{b_{i,j}} \Gamma_j \quad (4.123)$$

$$V_{NW_i} = \sum_{j=1}^N I_{NW_{i,j}} \Gamma_j \quad (4.124)$$

The linear algebraic governing equations for bound circulation (N equations, N unknowns) are thus obtained as

$$\sum_{j=1}^N \{I_{b_{i,j}} + I_{NW_{i,j}}\} \Gamma_j = V_{\infty_i} \alpha_i \quad (4.125)$$

Once the bound circulation strengths, Γ_j are known they are used to calculate α_{e_i} using equations (4.124) and (4.122). Assuming thin airfoil theory, i.e., with a lift curve slope of 2π , the local lift coefficient simply becomes

$$\begin{aligned} C_l &= 2\pi \alpha_{e_i} \\ &= \frac{2\pi}{V_{\infty_i}} \sum_{j=1}^N I_{b_{i,j}} \end{aligned} \quad (4.126)$$

using equations (4.122) and (8.34). This is the effective angle of attack approach and is consistent with K-J theorem for 3D wings which gives

$$C_l = \frac{2\pi}{V_{\infty_i}} \sum_{j=1}^N I_{b_{i,j}} \quad (4.127)$$

In the present analysis, the effective angle of attack approach is used.

The radial distribution of *input angle of attack* is influenced by the far wake (rotor inflow) which in turn is governed by the bound circulation strengths. Therefore, iterations are performed between far wake and near wake until bound circulation strengths are converged. The iterations are started with a uniform inflow far wake (based on helicopter gross weight) which is subsequently replaced with non-uniform inflow.

Within the W-L near wake model, the airfoil property tables are included using the following method. The *input angle of attack* is scaled to an equivalent *flat plate angle of attack* using the lift coefficients obtained from the airfoil tables. This scaled angle of attack is used by the W-L model to calculate bound circulation strengths at 1/4-chord locations. The bound circulation strengths are then used to calculate the circulation strengths of near wake trailers. The near wake trailers are used to estimate the *induced angle of attack* at 3/4-chord locations. This induced angle of attack is subtracted from the *input angle of attack* and the resulting *effective angle of attack* is used to obtain lift (also pitching moment and drag) from the airfoil tables.

4.5.3 Unsteady Lifting-Line Analysis

An unsteady lifting-line model can be constructed using a consistent combination of the following parts: (1) A near wake model, e.g. a W-L type lifting surface model, (2) A far wake model, with free or prescribed wake geometries (3) 2D airfoil properties and (4) An unsteady aerodynamic model for attached and separated flow flow.

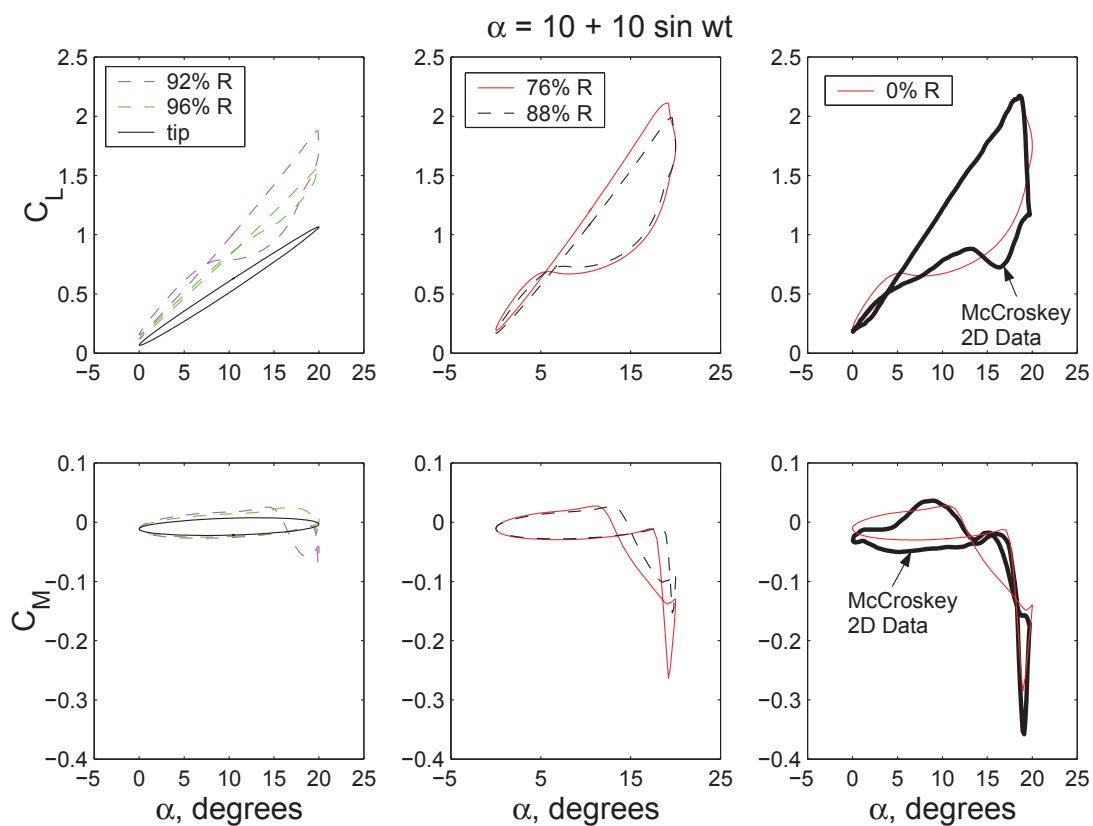


Figure 4.5: Dynamic stall prediction on a hypothetical 3D wing of Aspect ratio 15.30 with SC-1095 airfoils; Weissinger-L and Leishman Beddoes model; Inboard predictions (almost 2D) are compared with 2D airfoil data from McCroskey et al NASA TM-84245, 1982, Mach No. 0.3, reduced freq. $k = 0.1$

For a prescribed set of deformations, the airloads were calculated using the following three steps. In the first step, the blade deformations and an initial inflow distribution, for example, a uniform inflow based on the measured thrust, were used to calculate the sectional angle of attack. The sectional angle of attack was used as input to the $W - L$ near wake model, which then calculates the spanwise bound circulation distribution. The bound circulation distribution is calculated iteratively, so that it is consistent with the airfoil properties, the Kutta condition, and the

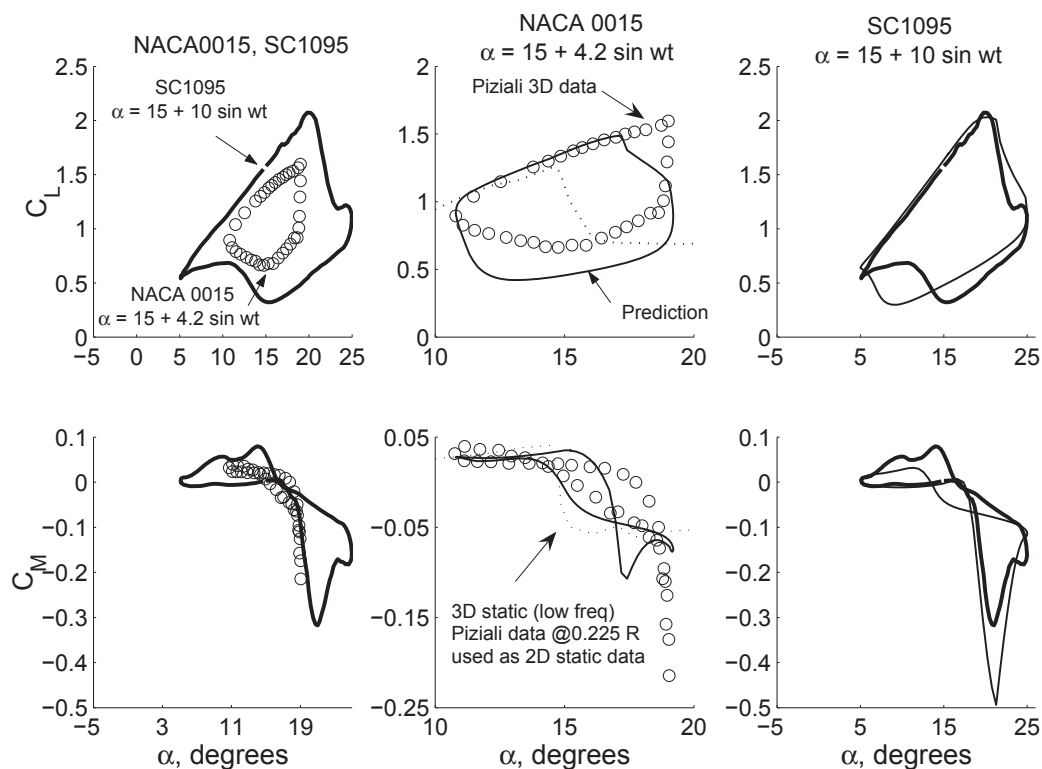


Figure 4.6: Dynamic stall prediction on a 3D wing with NACA 0015 airfoils, Mach No. 0.3, reduced freq. $k = 0.1$ Piziali test data compared with McCroskey SC1095 test, (prediction for Piziali test case uses 2D static data sent to UMD on Aug. 1991)

near-wake trailer sheet. This procedure is described later. In the second step, the bound circulation strengths were used to calculate the rotor far wake (free or prescribed). The far-wake generates a refined non-uniform inflow distribution. Using the non-uniform inflow, the sectional angles of attack are recalculated. In the third step, the new angles of attack are used as input to the near wake model to recalculate the bound circulation strengths. Steps one to three are repeated until the airloads converge. Iterations are required because the bound circulation strengths calculated by the near wake model changes the far wake inflow which changes the input angle of attack distribution of the near wake model.

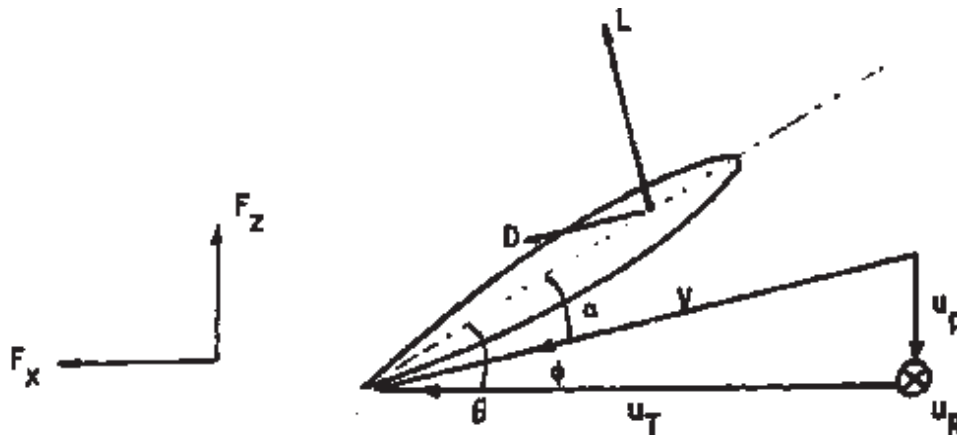
Within the $W - L$ model, the bound circulation strengths are obtained iteratively. First, the input angle of attack and incident Mach number are used to obtain the spanwise lift distribution from the airfoil tables. The bound circulation is obtained using the Kutta condition. Next, a near wake trailer sheet is layed out over thirty degree azimuth following the blade; 25 blade segments are used. The bound circulation line is at local $1/4$ -chord and swept back at the tip. The trailer sheet follows the local incident velocity. It is allowed to trail in the reverse direction in the regions of reverse flow. The velocity induced by the trailer sheet at the local $3/4$ -chord is then used to reduce the input angle of attack to an effective angle of attack. The effective angle of attack is then used to update the bound circulations using airfoil properties and the Kutta condition. The steps are repeated until the bound circulation converges. A relaxation scheme is necessary for converging the bound circulation strengths (10% used). The converged bound circulation strengths are consistent with the near wake trailers and the airfoil properties.

The $W-L$ model can be combined with the 2D static airfoil property data and a 2D unsteady dynamic stall model. The stall model is applied at each section on the effective angle of attack

distributions. Sample test data and predictions are shown in Figs.4.5 and 4.6.

4.6 Perturbation Aerodynamic Forces

The quasisteady blade element theory can be used to obtain the perturbation aerodynamic forces.



u_T = tangential flow velocity, ft/sec

u_p = normal flow velocity, ft/sec

u_R = radial flow velocity acting radially outward, ft/sec

θ = pitch, rad

α = angle of attack, $\theta - \phi$, rad

ϕ = induced angle, rad

ρ = air density, slug/ft³, lb-sec²/ft⁴

c = chord, ft

v = resultant velocity, $\sqrt{u_p^2 + u_T^2}$, ft/sec

The blade lift and drag forces per unit length

$$L = 1/2 \rho v^2 c c_l$$

$$D = 1/2 \rho v^2 c c_d$$

The moment about aerodynamic center

$$M_{ac} = 1/2 \rho v^2 c^2 c_{m_{ac}}$$

Resolving forces in hub plane

$$F_z = L \cos \phi - D \sin \phi$$

$$F_r = L \sin \phi + D \cos \phi$$

Moment about elastic axis

$$M_{ea} = 1/2 \rho v^2 c^2 c_m - L x_a$$

where x_a is the chordwise offset of aerodynamic center from elastic axis (+ ve aft). The radial force can be important for forward flight and it consists of two components; drag force due to radial velocity, and resolved component of vertical force in the radial direction.

$$F_r = D \frac{u_R}{v} - F_z \frac{dW}{dr}$$

Note

$$\sin \phi = \frac{u_p}{v}$$

$$\cos \phi = \frac{u_T}{v}$$

Thus

$$F_z = \frac{1}{2} \rho c (c_l u_T v - c_d u_p v)$$

$$F_x = \frac{1}{2} \rho c (c_l u_p v + c_d u_T v)$$

$$F_r = \frac{1}{2} \rho c (c_d v u_R) - F_z \frac{dw}{dr}$$

$$M_a = \frac{1}{2} \rho c^2 (c_{m_{ac}} - \frac{x_a}{c} c_l) v^2$$

These are the forces per unit span. These forces contain blade motion and thus these are the motion dependent aerodynamic forces.

To make analysis simple, the flow components are broken into two parts, steady and perturbation components.

$$u_T = (u_T)_{\text{trim}} + \delta u_T$$

$$u_p = (u_p)_{\text{trim}} + \delta u_p$$

$$u_R = (u_R)_{\text{trim}} + \delta u_R$$

$$\theta = \theta_{\text{trim}} + \delta \theta$$

The trim or steady components are due to the operating condition of the rotor and the perturbed components are caused by the perturbed motion. Similarly, the forces are also expressed into two parts, trim and perturbation components.

$$F_z = (F_z)_{\text{trim}} + \delta F_z$$

$$F_x = (F_x)_{\text{trim}} + \delta F_x$$

$$F_r = (F_r)_{\text{trim}} + \delta F_r$$

$$M_{ea} = (M_{ea})_{\text{trim}} + \delta M_{ea}$$

for convenience, the trim word is omitted from flow components.

Trim Forces

$$(F_z)_{\text{trim}} = \frac{1}{2} \rho c (c_l u_T v - c_d u_p v)$$

$$(F_x)_{\text{trim}} = \frac{1}{2} \rho c (c_l u_p v + c_d u_T v)$$

$$(F_r)_{\text{trim}} = \frac{1}{2} \rho c c_d u_R v - F_z \frac{dw}{dr}$$

$$(M_a)_{\text{trim}} = \frac{1}{2} \rho c^2 (c_m - \frac{x_a}{c} c_l) v^2$$

In the above expressions, the aerodynamic coefficients are obtained for trim flight.

Perturbations

Let us first examine the perturbation of resultant velocity v and pitch θ .

$$\delta v = \delta(u_p^2 + u_T^2)^{1/2}$$

$$= \frac{u_p \delta u_p + u_T \delta u_T}{v}$$

$$\delta \alpha = \delta(\theta - \tan^{-1} \frac{u_p}{u_T}) \simeq \delta(\theta - \frac{u_p}{u_T})$$

$$= \delta \theta + \frac{u_p \delta u_T - u_T \delta u_p}{u_T}$$

The aerodynamic coefficients are the functions of the angle of attack and Mach number.

$$c_l = c_l(\alpha, M)$$

$$c_d = c_d(\alpha, M)$$

$$c_m = c_m(\alpha, M)$$

The perturbation in aerodynamic coefficients are

$$\delta c_l = \frac{\partial c_l}{\partial \alpha} \delta \alpha + \frac{\partial c_l}{\partial M} \delta M$$

$$= c_{l_\alpha} \delta \alpha + c_{l_M} \delta M$$

$$\delta c_d = c_{d_\alpha} \delta \alpha + c_{d_M} \delta M$$

$$\delta c_m = c_{m_\alpha} \delta \alpha + c_{m_M} \delta M$$

The Mach number at any radial station is

$$M = \frac{M_{tip} v}{v_{tip}}$$

$$= M_{tip} \frac{v}{\Omega R}$$

and the perturbation in the Mach number is

$$\delta M = \frac{M_{tip}}{\Omega R} \delta v$$

Let us now look at the perturbation in forces

$$F_z = \frac{1}{2} \rho c \{ c_l u_T v - c_d u_p v \}$$

$$\delta F_z = \frac{1}{2} \rho c \{ \delta c_l u_T v + c_l \delta u_T v + c_l u_T \delta v$$

$$- \delta c_d u_p v - c_d \delta u_p v - c_d u_p \delta v \}$$

$$\begin{aligned}
&= \frac{1}{2}\rho c\{(c_{l_\alpha}\delta\alpha + c_{l_M}\delta M)u_T v + c_l\delta u_T v + c_l u_T\delta v \\
&\quad - (c_{d_\alpha}\delta\alpha + c_{d_M}\delta M)u_p v - c_d\delta u_p v - c_d u_p\delta v\} \\
\frac{\delta F_z}{\frac{1}{2}\rho c} &= \\
&\quad \delta u_T\left\{\frac{u_p}{v}(u_T c_{l_\alpha} - u_p c_{d_\alpha}) + \frac{u_T^2}{2}(c_l + M c_{l_M}) + c_l v \right. \\
&\quad \left. - (c_d + M c_{d_M})\frac{u_p u_T}{v} + \delta u_p\left\{-\frac{u_T}{v}(u_T c_{l_\alpha} - u_p c_{d_\alpha}) + \frac{u_p u_T}{v}(c_l + M c_{l_M}) \right. \right. \\
&\quad \left. \left. - c_D v \frac{u_p^2}{v}(c_d + M c_{d_M})\right\} + \delta\theta\{c_{l_\alpha} v u_T - c_{d_\alpha} v u_p\}\right\}
\end{aligned}$$

Similarly

$$\begin{aligned}
\frac{\delta F_x}{\frac{1}{2}\rho c} &= \delta u_T\left[\frac{u_p}{v}(u_p c_{l_\alpha} + u_T c_{d_\alpha}) + \frac{u_T^2}{v}(c_d + M c_{d_M}) \right. \\
&\quad \left. + c_d v + (c_l + M c_{l_M})\frac{u_p u_T}{v}\right\} \\
&\quad + \delta u_p\left\{-\frac{u_T}{v}(u_p c_{l_\alpha} + u_T c_{d_\alpha}) + \frac{u_p u_T}{v}(c_d + M c_{d_M}) \right. \\
&\quad \left. + c_l v + \frac{u_p^2}{v}(c_l + M c_{l_M})\right\} \\
&\quad \delta\theta\{c_{l_\alpha} v u_p + c_{d_\alpha} v u_T\}
\end{aligned}$$

$$\begin{aligned}
\frac{\delta F_r}{\frac{1}{2}\rho c} &= \delta u_T\left\{c_{d_\alpha}\frac{u_p u_R}{v} + \frac{u_T u_R}{v}(c_d + M c_{d_M}) \right. \\
&\quad \left. + \delta u_p\left\{-c_{d_\alpha}\frac{u_p u_R}{v} + \frac{u_p u_R}{v}(c_d + M c_{d_M})\right\} \right. \\
&\quad \left. + \delta u_R\{c_d v\} \right. \\
&\quad \left. \delta\theta\{c_{d_\alpha} v u_R\}\right\}
\end{aligned}$$

$$\begin{aligned}
\frac{\delta M_{ea}}{\frac{1}{2}\rho c^2} &= \delta u_T\left\{2u_T(c_m - c_l\frac{x_a}{c}) + v^2\frac{u_p}{u_T^2}(c_{m_\alpha} - c_{l_\alpha}\frac{x_a}{c}) \right. \\
&\quad \left. + \mu_T(c_{m_M} - c_{l_M}\frac{x_a}{c})\right\} \\
&\quad + \delta u_p\left\{2u_p(c_m - c_l\frac{x_a}{c}) - \frac{v^2}{u_T}(c_{m_\alpha} - c_{l_\alpha}\frac{x_a}{c}) \right. \\
&\quad \left. + M u_p(c_{m_M} - c_{l_M}\frac{x_a}{c})\right\} \\
&\quad + \delta\theta\{v^2(c_{m_\alpha} - c_{l_\alpha}\frac{x_a}{c})\}
\end{aligned}$$

To these perturbation forces, the noncirculating forces also are added. The most important component is the virtual moment.

$$\delta M_{ea} = (\delta M_{ea})_c + M_{nc}$$

$$\begin{aligned}
M_{NC} &= \text{noncirculatory moment} \\
&= \frac{1}{4}\pi\rho\Omega^2 c^3 \left[r\left(\frac{1}{4} + \frac{x_a}{c}\right)\ddot{\beta} - r\left(\frac{1}{2} + \frac{x_a}{c}\right)\dot{\theta} - c\left(\frac{3}{32} + \frac{1}{2}\frac{x_a}{c}\right)\ddot{\theta} \right]
\end{aligned}$$

Small Angle Simplification

Assume small angles

$$F_z \simeq L$$

$$F_x \simeq L \frac{u_p}{u_T} + D$$

$$\alpha \simeq \theta - \frac{u_p}{u_T}$$

Assume simplified airfoil characteristics

$$c_l = a\alpha \text{ (symmetric airfoil)}$$

$$= a\left(\theta - \frac{u_p}{u_T}\right)$$

$$c_d = c_{d0}$$

$$c_m = c_{m0} \text{ (for symmetric it is zero)}$$

$$v = u_T$$

Trim Forces

$$F_z = \frac{1}{2}\rho c a (u_T^2 \theta - u_p u_T)$$

$$F_x = \frac{1}{2}\rho c a (u_p u_T \theta - u_p^2 + \frac{c_d}{a} u_T^2)$$

$$M_a = \frac{1}{2}\rho c^2 a \left\{ \frac{c_m}{a} (u_p^2 + u_T^2) - \frac{x_a}{c} (u_T^2 \theta - u_p u_T) \right\}$$

Perturbation Forces

$$\delta F_z = \frac{1}{2}\rho c a \{ \delta u_T (2u_T \theta - u_p) + \delta u_p (-u_T) + \delta \theta (u_T^2) \}$$

$$\delta F_x = \frac{1}{2}\rho c a \{ \delta u_T (u_p \theta + \frac{c_d}{a} 2u_T) + \delta u_p (u_T \theta - 2u_p) + \delta \theta (u_p u_T) \}$$

$$\delta M_a = \frac{1}{2}\rho c^2 a \{ \delta u_T (2\frac{c_m}{a} u_T + \frac{x_a}{c} u_p - 2\frac{x_a}{c} u_T \theta)$$

$$+ \delta u_p (2\frac{c_{m_a}}{a} u_p + \frac{x_a}{c} u_T) + \delta \theta (-\frac{x_a}{c} u_T^2) \}$$

Example 4.1:

In a circulation-controlled rotor, the aerodynamic lift is a function of geometric angle as well as blowing

$$c_l = c_l(\alpha, c_\mu)$$

where

$$c_\mu = \frac{\dot{m} V_j}{\frac{1}{2}\rho V^2 c} \quad (\dot{m} V_j = \text{jet momentum})$$

calculate the perturbation in lift in terms of flow components of u_p and u_T and pitch angle θ (steady and perturbations).

$$\text{Lift } L = 1/2\rho V^2 c c_l(\alpha, c_\mu)$$

$$\text{Perturbation } \delta L = \rho c c_l V \delta V + 1/2\rho c V^2 \delta c_l$$

$$V = \sqrt{u_p^2 + u_T^2}$$

$$\delta V = \frac{u_p \delta u_p + u_T \delta u_T}{V}$$

$$\delta c_l = c_{l_\alpha} \delta \alpha + c_{l_\mu} \delta c_\mu$$

$$\delta c_\mu = -2c_\mu \frac{\delta V}{V}$$

$$\alpha = \theta - \tan^{-1} \frac{u_p}{u_T}$$

$$\delta \alpha = \delta \theta - \frac{u_T \delta u_p - u_p \delta u_T}{u_T^2}$$

$$\frac{\delta L}{1/2\rho c} = \delta u_T \left\{ 2u_T c_l + \frac{V^2}{u_T^2} u_p c_{l_\alpha} - 2u_T c_\mu c_{l_\mu} \right\}$$

$$+ \delta u_p \left\{ 2u_p c_l - \frac{V^2}{u_T^2} u_T c_{l_\alpha} - 2u_p c_\mu c_{l_\mu} \right\}$$

$$+ \delta \theta \{ V^2 c_{l_\alpha} \}$$

Example 4.2:

For an articulated rotor in hovering flight, obtain the blade flapping equation under varying pitch conditions. For unsteady aerodynamic forces, use the lift deficiency function of a typical section at 75% radius position. Assume a 6% hinge offset, and the elastic axis at mid-chord position.

$$\beta^{**} + \nu_\beta^2 \beta - \frac{3}{2} \frac{x_I}{R} (\theta^{**} + \theta) = \gamma \bar{M}_\beta$$

$$\bar{M}_\beta = \frac{1}{2} \int_0^1 x \left[\frac{\delta u_T}{\Omega R} \left(2 \frac{u_T}{\Omega R} \theta - \frac{u_p}{\Omega R} \right) + \frac{\delta u_p}{\Omega R} \left(-\frac{u_T}{\Omega R} \right) + \delta \theta \left(\frac{u_T}{\Omega R} \right)^2 \right] C(k) dx$$

$$+ \int_0^1 x L_{NC} dx$$

$$\frac{u_T}{\Omega R} = x, \quad \frac{u_p}{\Omega R} = \lambda, \quad \frac{\delta u_T}{\Omega R} = 0, \quad \frac{\delta u_p}{\Omega R} = x \dot{\beta} - \frac{1}{4} \frac{c}{R} \theta^*$$

$$\delta \theta = \theta$$

$$\bar{k} = \frac{\omega b}{U} = \frac{1}{.75} \frac{\omega c}{\Omega R}$$

$$L_{NC} = \frac{\pi \rho b^2}{\rho a c \Omega^2 R^4} [(u_T \theta - u_p) - b a_h (\theta + \Omega \beta)]$$

$$\bar{M}_\beta = C(\bar{k}) \left[-\frac{1}{8} \beta^* + \frac{1}{24} \frac{c}{R} \theta^* + \frac{1}{8} \theta \right] + \frac{c}{R} \left(\frac{\theta^*}{24} - \frac{\beta^*}{24} \right) - \frac{1}{64} \left(\frac{c}{R} \right)^2 \theta^{**}$$

4.7 Dynamic Inflow Models

Typical stability analyses normally employ steady wake induced inflow calculated from simple momentum theory. However, under unsteady flow conditions, the rotor wake will not be steady, and this will naturally result in unsteady induced inflow, called as dynamic inflow. The dynamic inflow may be a significant factor in the calculation of unsteady aerodynamic loads, and hence can have an important influence on the rotor dynamics. In fact, the dynamic inflow components should be related to the unsteady rotor loads (thrust, roll moment and pitch moment). These relationships are complex and are still subject of research. For analyses, it is important to put these relationships in simplified form. One possible way to derive these relationships is by using unsteady actuator disk theory. Let us examine the steady as well as dynamic inflow components for hover and forward flight.

4.7.1 Hover

A simple steady inflow model for hover is to assume uniform inflow over the rotor disk. Using simple momentum theory the inflow is related to the rotor thrust.

$$\lambda = \text{sign}(C_T)k_p\sqrt{\left|\frac{C_T}{2}\right|}$$

where C_T is the thrust coefficient, λ is induced inflow ($v_i/\Omega R$) and k_p is an empirical factor to cover tip losses (~ 1.15).

A simple dynamic inflow model for hover is

$$\tau\dot{\lambda} + \lambda = \text{sign}(C_T)k_p\sqrt{\left|\frac{C_T}{2}\right|}$$

or

$$\tau\Delta\dot{\lambda} + \Delta\lambda = k_p^2\frac{\Delta C_T}{4\lambda_0}$$

where τ is time lag in seconds and can be approximately taken as $.85/4\lambda_0\Omega$. The λ_0 is the mean induced inflow and Ω is rotational speed (rad/sec). Note that the C_T here consists of total thrust, i.e., the sum of steady and perturbation thrust components.

4.7.2 Forward Flight

A simple steady inflow model for forward flight is to assume it uniform over the rotor disk.

$$\lambda_i = \frac{1}{2}\frac{C_T}{\sqrt{\mu^2 + \lambda^2}}$$

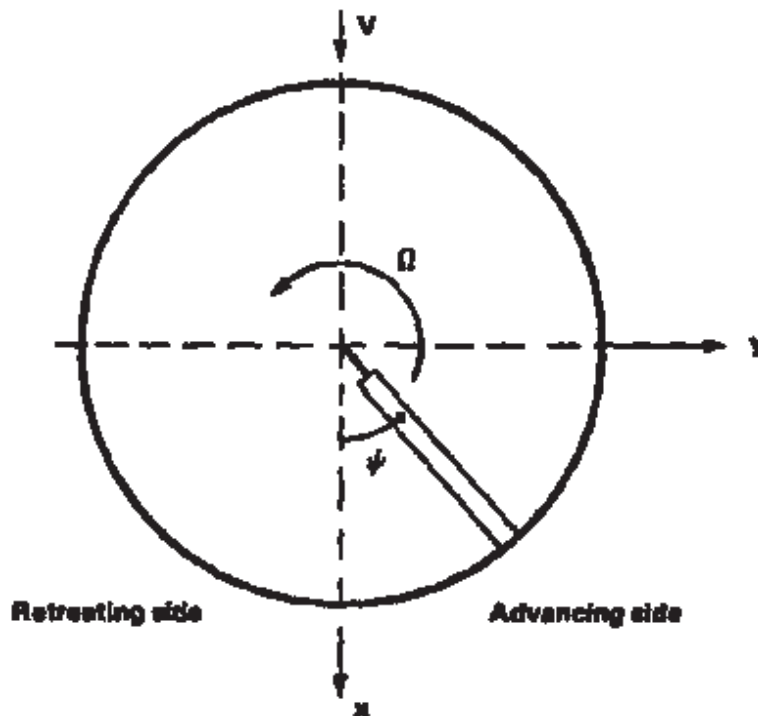
where λ_i is induced inflow ratio and μ is advance ratio and λ is inflow ratio

$$\lambda = \mu \tan \alpha + \lambda_i$$

and α is disk tilt to the free stream. An improvement over the simple uniform model is to assume a linear variation for steady induced inflow

$$\lambda_i = \lambda_m\left(1 + \kappa_x\frac{r}{R}\cos\psi + \kappa_y\frac{r}{R}\sin\psi\right)$$

where λ_m is the mean value of induced flow, and κ_x represents the longitudinal variation of inflow and κ_y represents the lateral variation of inflow.



Typically, the value of κ_x is positive and the value of κ_y is negative. This means that the induced inflow is larger at the rear of the disk and on the retreating side. At higher velocities,

$$\lambda_i \simeq \lambda_m \left(1 + \frac{r}{R} \cos \psi\right)$$

The classical vortex theory gives an estimate of parameters κ_x and κ_y . There are a number of estimates available for these parameters. A popular one is given by Drees (1949)

$$\kappa_x = \frac{4}{3} \left[(1 - 1.8\mu^2) \sqrt{1 + (\lambda/\mu)^2} - \lambda/\mu \right]$$

$$\kappa_y = -2\mu$$

Dynamic inflow in forward flight is lot more involved than the hover case. A simple dynamic inflow model is to assume a perturbation to the induced inflow of the following form

$$\Delta\lambda_i = \lambda_u + \lambda_{1c} \frac{r}{R} \cos \psi + \lambda_{1s} \frac{r}{R} \sin \psi$$

where λ_u represents the uniform perturbation component and λ_{1c} and λ_{1s} represent the linear varying components in longitudinal and lateral directions over the rotor disk. These dynamic inflow components are related to the perturbation forces on the rotor disk, namely rotor thrust C_T , pitching moment C_{M_y} and rolling moment C_{M_x} . The perturbation forces are obtained from total forces after subtracting the steady forces. A simple form of relationships between dynamic inflow components and perturbation forces is obtained using actuator disk theory.

$$\begin{bmatrix} \tau_T & \dot{\lambda}_u \\ \tau_M & \dot{\lambda}_c \\ \tau_M & \dot{\lambda}_s \end{bmatrix} + \begin{bmatrix} \lambda_u \\ \lambda_{1c} \\ \lambda_{1s} \end{bmatrix} = \begin{bmatrix} \frac{1}{2(\lambda_0 + \sqrt{\mu^2 + \lambda_0^2})} & 0 & 0 \\ 0 & \frac{2}{\sqrt{\mu^2 + \lambda_0^2}} & 0 \\ 0 & 0 & \frac{2}{\sqrt{\mu^2 + \lambda_0^2}} \end{bmatrix} \begin{bmatrix} \Delta C_T \\ -\Delta C_{M_y} \\ \Delta C_{M_x} \end{bmatrix}$$

where τ_T and τ_M are time lags in seconds and these are approximately taken as

$$\tau_T = \frac{.42}{\mu\Omega}$$

$$\tau_M = \frac{.22}{\mu\Omega}$$

The λ_0 is the rotor steady inflow ($\lambda_m + \mu \tan \alpha$) and the Ω is the rotational speed (rad/sec).

An alternate form of dynamic inflow is given by Pitt and Peters (1980).

$$[M] \begin{bmatrix} \dot{\lambda}_u \\ \dot{\lambda}_c \\ \dot{\lambda}_s \end{bmatrix} + [L]^{-1} \begin{bmatrix} \lambda_u \\ \lambda_c \\ \lambda_s \end{bmatrix} = \begin{bmatrix} c_T \\ -C_{M_y} \\ C_{M_x} \end{bmatrix}$$

The matrices M and L are of size 3 x 3. There are many forms of these matrices; typically for simple momentum theory, these matrices are diagonal, for other theories they can be fully populated. One of the popular form of these matrices is

$$[L] = \frac{1}{c_v} \begin{bmatrix} \frac{1}{2} & 0 & \frac{15\pi}{64} \sqrt{\frac{1-\sin \alpha}{1+\sin \alpha}} \\ 0 & \frac{-4}{1+\sin \alpha} & 0 \\ \frac{15\pi}{64} \sqrt{\frac{1-\sin \alpha}{1+\sin \alpha}} & 0 & -\frac{-4}{1+\sin \alpha} \end{bmatrix}$$

$$[M] = \begin{bmatrix} \frac{128}{75\pi} & 0 & 0 \\ 0 & \frac{-16}{45\pi} & 0 \\ 0 & 0 & \frac{-16}{45\pi} \end{bmatrix}$$

where c_v is a mass-flow parameter

$$c_v = \frac{\mu^2 + \lambda(\lambda + \lambda_i)}{\sqrt{\mu^2 + \lambda^2}}$$

and α is the rotor disk tilt wrt free stream.

For dynamic analysis of the blade, the dynamic inflow components are treated as additional degrees of freedom. The dynamic inflow models are well suited for aero-elastic stability calculations. For loads prediction a free wake based unsteady lifting line model or detailed CFD analysis is preferred. These are discussed in the next section.

Questions

Justify the following:

- The unsteady forces are more involved for a rotary wing than a fixed wing.
- Show the similarities and differences between the basic fluid mechanics equations and the basic structural mechanics equations.
- Virtual aerodynamic forces play an important role in the pitch dynamics of the blade.
- In a wind tunnel testing, the unsteady aerodynamic forces on a two-dimensional wing model were measured for a pure pitch motion as well as for a pure vertical vibratory motion. The discrepancy in the two sets of results was observed for identical angle of attack perturbation.
- The neglecting of the effect of shed wake and other unsteady aerodynamic forces on the analysis of rotor performance is quite justified, but for higher frequency vibrations one cannot ignore these forces.
- During the forward flight mode, there is a continuous stretching and compressing of the vorticity in the shed wake.
- One has to be very careful to include the effect of shed vorticity for higher harmonic vibrations.
- Is there any difference between the induced velocities calculated using the momentum theory and the lifting line theory?
- For blade aeroelastic analysis (flap-lag), quasi-steady aerodynamics is widely used.
- The shed wake plays a more important role in hovering flight than the forward flight.
- There are differences between the thin airfoil theory, lifting line theory, lifting surface theory and the rotor shed wake modeling.
- The larger the reversed flow region on the retreating side of the rotor, the more the vibration.
- In a circulation-controlled rotor blade, the steady lift is primarily caused by blowing circulation, causing the aerodynamic center to be close to the half-chord position. To reduce the aerodynamic moment, the elastic axis is positioned at half-chord, but this may result in an unstable torsional motion (single degree flutter).
- The Theodoresen function $C(k)$ is referred to as a feedback parameter of blade motion.
- There is no Kutta condition for circulation control airfoils.
- Dynamic inflow modeling is an approximate representation for unsteady rotor forces.

Bibliography

- [1] John, D. Anderson, *Modern Compressible Flow*, 1990, McGraw-Hill.
- [2] Karamcheti, K., *Principles of Ideal-Fluid Aerodynamics*, Robert E. Krieger Publishing Co., 1980, Chapter 17 and 19.
- [3] Ashley, H. and Landahl, M., *Aerodynamics of Wings and Bodies*, Addison-Wesley Publishing Company, Inc., 1965.
- [4] Donovan, A. F., and Lawrance, H. R., *Aerodynamic Components of Aircraft At High Speeds*, Princeton University Press, 1957. Volume VII. High Speed Aerodynamics and Jet Propulsion. Part F, Non-Steady Wing Characteristics by I. E. Garrick, pp. 658–778.
- [5] Lamb, Sir Horace, *Hydrodynamics*, Sixth Edition, Dover Publications, New York, 1945.
- [6] Milne-Thompson, L. M., *Theoretical Hydrodynamics*, Fourth Edition, Macmillan, New York, 1960.
- [7] Thwaites, B., editor, *Incompressible Aerodynamics*, Oxford University Press, Oxford, 1960.
- [8] Leishman, J. G., *Principles of Helicopter Aerodynamics*, Cambridge University Press, New York, 2000
- [9] Beddoes, T. S., “Representation of Airfoil Behaviours,” *Vertica* Vol. 7, No. 2, pp. 183-197, 1983.
- [10] T.S.Beddoes, “Practical Computation of Unsteady Lift,” *Proceedings of the 7th European Rotorcraft Forum*, Sept. 1982, see also *Vertica*, Vol. 8, No. 1, 1984, pp. 55-71.
- [11] Leishman, J.G., “Validation of Approximate Indicial Aerodynamic Functions for Two-Dimensional Subsonic Flow,” *Journal of Aircraft*, Vol. 25, No. 1, October 1, 1988.
- [12] Leishman, J. G. and Beddoes, T. S., “A Semi-Empirical Model for Dynamic Stall,” *Journal of the American Helicopter Society*, July 1989, pp. 3-17.
- [13] Leishman, J. G., “Modeling Sweep Effects on Dynamic Stall,” *Journal of the American Helicopter Society*, July 1989, pp. 18-29.
- [14] Bisplinghoff, R. L., Ashley, H., and Halfman, R. L., *Aeroelasticity*, Addison-Wesley Publishing Co., Reading, Mass., 1955.
- [15] Lomax, H., Heaslet, M. A., Fuller, F. B., and Sludder, L., “Two and Three Dimensional Unsteady Lift Problems in High Speed Flight,” *NACA Report 1077*, 1952.
- [16] Liiva, J., “Unsteady Aerodynamic and Stall Effects on Helicopter Rotor Blade Airfoil Sections,” *Journal of Aircraft*, Vol. 6, (1), January-February 1969, pp. 46–51.

- [17] Carta, F. O., "Unsteady Normal Force on an Airfoil in a Periodically Stalled Inlet Flow," *Journal of Aircraft*, Vol. 4, (5), September-October 1967, pp. 416-421.
- [18] Gormont, R. E., "A Mathematical Model of Unsteady Aerodynamics and Radial Flow for Application to Helicopter Rotors," USA AVLABS TR 72-67, May 1970.
- [19] Johnson, W., "The Response and Airloading of Helicopter Rotor Blades Due to Dynamic Stall," ASRL TR 130-1, May 1970
- [20] Petot, D., "Differential Equation Modeling of Dynamic Stall," *La Recherche Aeronautique*, Number 1989-5 (Corrections dated October 1990).
- [21] Truong, V. K., "A 2-D Dynamic Stall Model Based on a Hopf Bifurcation," Nineteenth European Rotorcraft Forum, Marseilles, France, September, 1998.
- [22] Johnson, W., "Rotorcraft Aerodynamics Models for a Comprehensive Analysis," 54th Annual Forum of the American Helicopter Society, Washington DC, May 20-22, 1998.
- [23] Johnson, W., *Helicopter Theory*, Princeton University Press, 1980, Chapter 10 and 11.
- [24] Woods, L. C., *The Theory of Subsonic Plane Flow*, Cambridge University Press, 1961.
- [25] J. Weissinger, "The Lift Distribution of Swept-Back Wings," National Advisory Committee for Aeronautics, Technical Memorandum No. 1120, 1942.
- [26] Johnson, W., "Application of Unsteady Airfoil Theory to Rotary Wings," *Journal of Aircraft*, Vol. 17, No. 4, April 1980, pp. 285-286.
- [27] Pitt, D.M., and Peters, D. A., "Theoretical Prediction of Dynamic-inflow Derivatives," *Vertica*, Vol. 5, 1981, pp. 21-34.
- [28] Johnson, W., "A Comprehensive Analytical Model of Rotorcraft Aerodynamics and Dynamics, Part I: Analysis Development," NASA TM 81182, June 1980.

Chapter 5

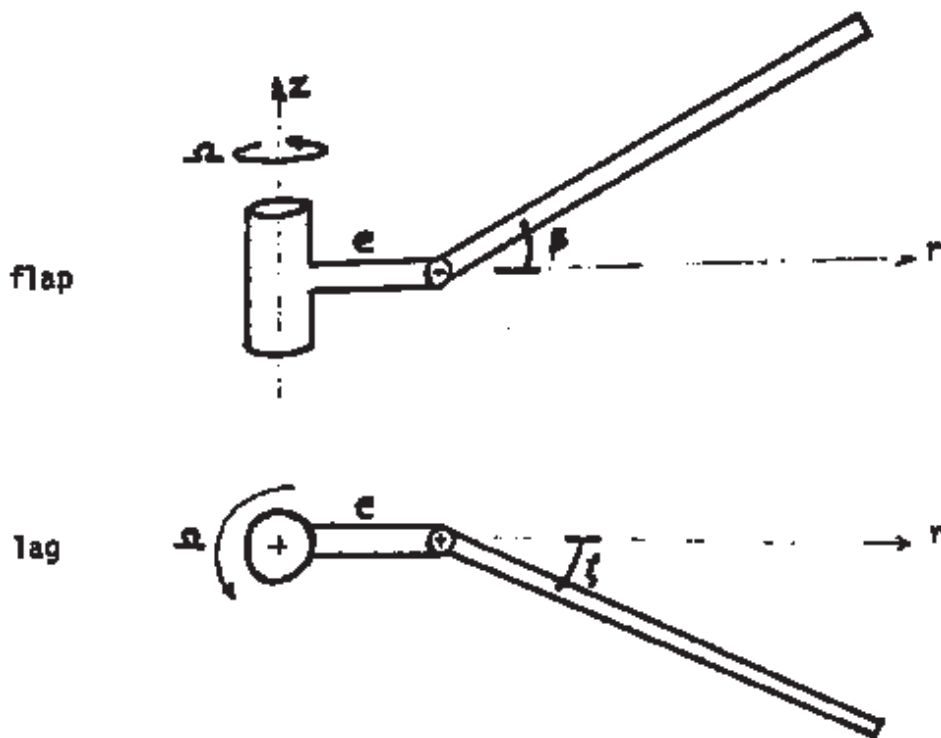
Aeroelastic Stability in Hover

Flutter is a dynamic aeroelastic instability caused by the interaction of aerodynamic, elastic and inertial forces. Flutter is self-sustained oscillations which are totally different from resonance or forced response oscillations. For flutter instability, the external forcing is not needed. The objective of this chapter is to understand the basic principles of blade flutter in hovering flight. The equations of motion are simple as compared to the forward flight case, where many periodic terms are present. The time and response solutions for forward flight are very involved as compared to those of hovering flight. For hover, it is relatively easy to determine the equilibrium position of the blade and then to determine a linearized stability analysis. There are many types of flutter. Two of the most important types of blade flutter are flap-lag and pitch-flap. The designer has to be very careful with these instabilities and has to establish the safety margin for critical flight conditions. These aeroelastic instabilities will be investigated in detail for simple blade configurations, with two-degree-of-freedom models. One can interpret these results for complex configurations and then refine these analyses.

5.1 Flap-Lag Flutter

This aeroelastic instability is unique with rotor blades, and does not take place in fixed wings. The flap and lag modes participate in causing this instability, of course, with the inclusion of unsteady aerodynamic forces. The flap mode alone is highly damped because of aerodynamic damping. The lag mode alone is a low damped mode, but does not become unstable. The flap and lag modes together are coupled, and the couplings are due to the Coriolis forces and aerodynamic forces. There is no likelihood of blade flutter if the aerodynamic forces are neglected. Again, there is no likelihood of flutter if Coriolis forces are neglected. Hence, for blade flutter, both the aerodynamic forces and the Coriolis forces play an important role.

To understand the phenomena, a simple blade configuration is studied in hovering flight. The blade is assumed rigid and it undergoes two degrees of motion, flap and lag motions about hinges. The flap and lag hinges are coincided and are offset by a distance e from the rotation axis. Also, there are bending springs at the hinges to obtain desired flap and lag frequencies.



The equations of motion in nondimensional form are,

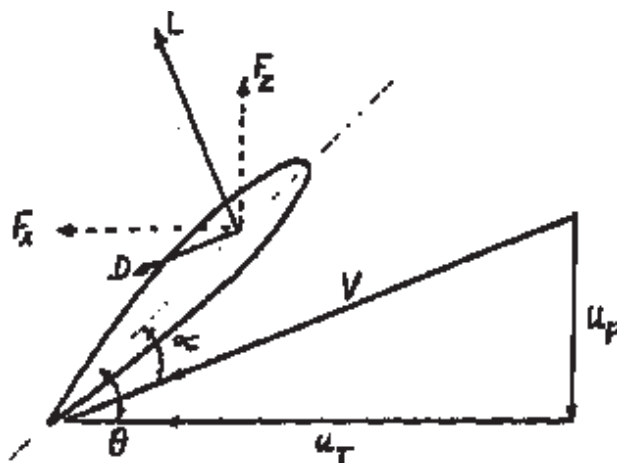
$$\text{Flap: } \beta'' + \nu_\beta^2 \beta - 2\beta_0 \zeta' = \gamma \overline{M}_\beta$$

$$\text{Lag: } \zeta'' + \nu_\zeta^2 \zeta + 2 \frac{\omega_{\zeta 0}}{\Omega} \zeta_L \zeta' + 2\beta_0 \beta' = \gamma \overline{M}_\zeta \tag{5.1}$$

These are perturbation equations. The ν_β and ν_ζ are rotating flap and lag frequencies, the ζ_L is the viscous damping coefficient due to lag damper, and β_0 is the steady flap deflection due to centrifugal and aerodynamic forces.

$$\nu_\beta^2 \beta_0 = \gamma \overline{M}_{\beta 0} + \frac{\omega_{\beta 0}^2}{\Omega^2} \beta_p$$

where β_p is a precone angle. The \overline{M}_β and \overline{M}_ζ are perturbation aerodynamic moments about flap and lag hinges and γ is the Lock number. The $\omega_{\beta 0}$ and $\omega_{\zeta 0}$ are non-rotating flap and lag frequencies. Sometimes the viscous damping ratio of mechanical lag damper is defined with respect to the rotating lag frequency. Then the third term in Eq(5.1) becomes $2\zeta_L \nu_\zeta \zeta'$. Let us derive aerodynamic forces.



Quasisteady theory is used to obtain the aerodynamic forces. The u_p and u_T are flow velocity components. Forces per unit span are

$$F_z \simeq L = \frac{1}{2} \rho a c (u_T^2 \theta - u_p u_T)$$

$$F_x \simeq L \frac{u_p}{u_T} + D = \frac{1}{2} \rho a c \left(\frac{c_d}{a} u_T^2 + u_p u_T \theta - u_p^2 \right)$$

Perturbations

$$F_z = \frac{1}{2} \rho a c \{ \delta u_T (2u_T \theta - u_p) + \delta u_p (-u_T) + \delta \theta (u_T^2) \}$$

$$F_x = \frac{1}{2} \rho a c \{ \delta u_T (2 \frac{c_d}{a} u_T + u_p \theta) + \delta u_p (u_T \theta - 2u_p) + \delta \theta (u_p u_T) \}$$

Let us examine flow components

Steady:

$$\begin{aligned} u_T &= \Omega r & \frac{u_T}{\Omega R} &= x \\ u_p &= \Omega \lambda R & \frac{u_p}{\Omega R} &= \lambda \end{aligned}$$

Perturbation:

$$\begin{aligned} \delta u_T &= -r \dot{\zeta} & \frac{\delta u_T}{\Omega R} &= -x \zeta^* \\ \delta u_p &= r \dot{\beta} & \frac{\delta u_p}{\Omega R} &= x \beta^* \\ \delta \theta &= -k_{p\beta} \beta - k_{p\zeta} \zeta \end{aligned}$$

where $x = r/R$, and λ is the wake induced inflow parameter at the rotor disk. The $k_{p\beta}$ and $k_{p\zeta}$ are pitch-flap and pitch-lag coupling terms.

$$\overline{M}_\beta = \frac{1}{\rho a c \Omega^2 R^4} \int_e^R F_z (r - e) dr$$

For making analysis simple, the effect of e is neglected in the derivation of aerodynamic forces. This is, however, not a bad assumption.

$$\overline{M}_\beta = \frac{1}{\rho a c \Omega^2 R^4} \int_0^R F_z r dr$$

$$\begin{aligned}\overline{M}_\zeta &= \frac{1}{\rho ac \Omega^2 R^4} \int_0^R F_x r dr \\ (\overline{M}_\beta)_{steady} &= \frac{1}{2} \int_0^1 \left\{ \left(\frac{u_T}{\Omega R} \right)^2 \theta - \left(\frac{u_p}{\Omega R} \right) \left(\frac{u_T}{\Omega R} \right) \right\} x dx \\ &= \frac{\theta}{8} - \frac{\lambda}{6}\end{aligned}$$

It is assumed that the pitch θ as well as inflow ratio γ are uniform along the length of the blade. The $(\overline{M}_\zeta)_{steady}$ is not important since it is negligible, because the drag force is much smaller than the lift force.

$$\begin{aligned}(\overline{M}_\beta)_{perturbation} &= \frac{1}{\rho ac \Omega^2 R^4} \int_0^R \delta F_z r dr \\ &= \frac{1}{2} \int_0^1 \left\{ \frac{\delta u_T}{\Omega R} \left(2 \frac{u_T}{\Omega R} \theta - \frac{u_p}{\Omega R} \right) - \frac{\delta u_p}{\Omega R} \frac{u_T}{\Omega R} + \delta \theta \left(\frac{u_T}{\Omega R} \right)^2 \right\} x dx \\ &= -\zeta^* \left(\frac{\theta}{4} - \frac{\lambda}{6} \right) - \frac{\beta^*}{8} - \frac{1}{8} (k_{p\beta} \beta + k_{p\zeta} \zeta) \\ (\overline{M}_\zeta)_{perturbation} &= \frac{1}{\rho ac \Omega^2 R^4} \int_0^R \delta F_x r dr \\ &= \frac{1}{2} \int_0^1 \left\{ \frac{\delta u_T}{\Omega R} \left(2 \frac{c_d}{a} \frac{u_T}{\Omega R} + \frac{u_p}{\Omega R} \theta \right) + \frac{\delta u_p}{\Omega R} \left(\frac{u_T}{\Omega R} \theta - 2 \frac{u_p}{\Omega R} \right) \right. \\ &\quad \left. + \delta \theta \left(\frac{u_T}{\Omega R} \right)^2 \right\} x dx \\ &= -\zeta^* \left(\frac{1}{4} \frac{c_d}{a} + \frac{\lambda \theta}{6} \right) + \beta^* \left(\frac{\theta}{8} - \frac{\lambda}{3} \right) - (k_{p\beta} \beta + k_{p\zeta} \zeta) \frac{\lambda}{6}\end{aligned}$$

Steady solution

$$\beta_0 = \frac{\gamma}{\nu_{\beta e}^2} \left(\frac{\theta}{8} - \frac{\lambda}{6} \right) + \frac{\omega_{\beta 0}^2}{\Omega^2} \beta_p \frac{1}{\nu_{\beta e}^2} \quad (5.2)$$

$$\zeta_0 \simeq 0$$

where

$$\nu_{\beta e}^2 = \nu_\beta^2 + \frac{\gamma}{8} k_{p\beta}$$

Perturbation Equations

Flap

$$\beta^{**} + \frac{\gamma}{8} \beta^* + (\nu_\beta^2 + \frac{\gamma}{8} k_{p\beta}) \beta + \left[-2\beta_0 + \gamma \left(\frac{\theta}{4} - \frac{\lambda}{6} \right) \right] \zeta^* + k_{p\zeta} \frac{\gamma}{8} \zeta = 0$$

Lag

$$\begin{aligned}\zeta^{**} + \left[2 \frac{\omega_{\zeta 0}}{\Omega} \zeta_L + \gamma \left(\frac{c_d}{4a} + \frac{\lambda \theta}{6} \right) \right] \zeta^* + (\nu_\zeta^2 + \frac{\gamma}{6} k_{p\zeta} \lambda) \zeta + \left[2\beta_0 - \gamma \left(\frac{\theta}{8} - \frac{\lambda}{3} \right) \right] \beta^* \\ + \frac{\gamma}{6} k_{p\beta} \lambda \beta = 0\end{aligned}$$

Rewriting these equations

$$\begin{aligned} & \begin{bmatrix} \beta^{**} \\ \zeta^{**} \end{bmatrix} + \begin{bmatrix} \frac{\gamma}{8} & -2\beta_0 + \gamma\left(\frac{\theta}{4} - \frac{\lambda}{6}\right) \\ 2\beta_0 - \gamma\left(\frac{\theta}{8} - \frac{\lambda}{3}\right) & 2\frac{\omega\zeta_0}{\Omega}\zeta_L + \gamma\left(\frac{c_d}{4a} + \frac{\lambda\theta}{6}\right) \end{bmatrix} \begin{bmatrix} \beta^* \\ \zeta^* \end{bmatrix} \\ & + \begin{bmatrix} \nu_\beta^2 + \frac{\gamma}{8}k_{p_\beta} & \frac{\gamma}{8}k_{p_\zeta} \\ \frac{\gamma}{6}k_{p_\beta}\lambda & \nu_\zeta^2 + \frac{\gamma}{6}k_{p_\zeta}\lambda \end{bmatrix} \begin{bmatrix} \beta \\ \zeta \end{bmatrix} = 0 \end{aligned} \quad (5.3)$$

For the solution of the above equations (5.3), one needs trim solution i.e., λ and θ . It is assumed that the wake induced inflow λ for hover is uniform along the length of the blade. For constant pitch θ , there may be some variation in λ , but is not considered here. Using the simple momentum theory,

$$\lambda = k_h \sqrt{\frac{c_T}{2}} \quad (5.4)$$

where c_T is the thrust coefficient and k_h is an empirical factor to cover tip losses and nonuniform distribution, typically 1.15. Comparing thrust obtained using momentum theory and blade element theory, one gets

$$\theta = \frac{6c_T}{\sigma a} + \frac{3}{2}\lambda \quad (5.5)$$

Two simple ways to calculate the solution on Eqs. (5.3) are determinant expansion and the eigenvalue solution.

I. Determinant Expansion

Assume flap and lag displacements as

$$\beta(\psi) = \beta e^{s\psi}$$

$$\zeta(\psi) = \zeta e^{s\psi}$$

Eqs. (5.3) becomes

$$\begin{bmatrix} s^2 + \frac{\gamma}{8}s + \nu_\beta^2 + \frac{\gamma}{8}k_{p_\beta} & (-2\beta_0 + \frac{\gamma\theta}{4} - \frac{\gamma\lambda}{6})s + \frac{\gamma}{8}k_{p_\zeta} \\ (2\beta_0 - \frac{\gamma\theta}{8} + \frac{\gamma\lambda}{3})s + \frac{\gamma}{6}k_{p_\beta} & s^2 + (\frac{2\omega\zeta_0}{\Omega}\zeta_L + \frac{\gamma}{4}\frac{c_d}{a} + \frac{\gamma\lambda}{6}\theta)s + \nu_\zeta^2 + \frac{\gamma}{6}k_{p_\zeta}\lambda \end{bmatrix} \begin{bmatrix} \beta \\ \zeta \end{bmatrix} = 0$$

For a nontrivial solution, the determinant of the matrix is zero. This results into

$$As^4 + Bs^3 + Cs^2 + Ds + E = 0 \quad (5.6)$$

where

$$A = 1$$

$$B = \frac{\gamma}{8} + 2\frac{\omega\zeta_0}{\Omega}\zeta_L + \frac{\gamma}{4}\frac{c_d}{a} + \frac{\gamma\lambda}{6}\theta$$

$$C = \frac{\gamma}{8}(2\frac{\omega\zeta_0}{\Omega}\zeta_L + \frac{\gamma}{4}\frac{c_d}{a} + \frac{\gamma\lambda}{6}\theta) + \nu_\beta^2 + \frac{\gamma}{8}k_{p_\beta} + \nu_\zeta^2 + \frac{\gamma}{6}k_{p_\zeta}\lambda - (-2\beta_0 + \frac{\gamma\theta}{4} - \frac{\gamma\lambda}{6})(2\beta_0 - \frac{\gamma\theta}{8} + \frac{\gamma\lambda}{3}) \quad (5.7)$$

$$\begin{aligned}
D &= (\nu_\beta^2 + \frac{\gamma}{8}k_{p\beta})\left(\frac{2\omega\zeta_0}{\Omega}\zeta_L + \frac{\gamma}{4}\frac{c_d}{a} + \frac{\gamma\lambda}{6}\theta\right) + \frac{\gamma}{8}(\nu_\zeta^2 + \frac{\gamma}{6}k_{p\zeta}\lambda) \\
&\quad - \frac{\gamma}{8}k_{p\zeta}\left(2\beta_0 - \frac{\gamma\theta}{8} + \frac{\gamma\lambda}{3}\right) - \frac{\gamma}{6}k_{p\beta}\lambda\left(-2\beta + \frac{\gamma\theta}{4} - \frac{\gamma\lambda}{4}\right) \\
E &= (\nu_\beta^2 + \frac{\gamma}{8}k_{p\beta})(\nu_\zeta^2 + \frac{\gamma}{6}k_{p\zeta}\lambda) - \left(\frac{\gamma}{8}k_{p\zeta}\right)\left(\frac{\gamma}{6}k_{p\beta}\lambda\right)
\end{aligned}$$

At the critical flutter condition, the system damping becomes zero.

$$s = i\omega$$

Substituting in Eq. (5.6),

$$A\omega^4 - iB\omega^3 - C\omega^2 + iD\omega + E = 0$$

Setting separately the real and imaginary parts to be zero, gives,

$$A\omega^4 - C\omega^2 + E = 0$$

$$-B\omega^3 + D\omega = 0$$

The second equation gives

$$\omega^2 = \frac{D}{B}$$

Substituting in the first equation

$$A\left(\frac{D}{B}\right)^2 - C\left(\frac{D}{B}\right) + E = 0$$

or

$$AD^2 - CDB + EB^2 = 0$$

This is the condition for instability. It is called as Routh's stability criteria.

Solution Procedure

Given the rotor characteristics in terms of coefficients

$$\gamma, \sigma, a, c_d, k_{p\beta}, k_{p\zeta}, \zeta_L, \nu_\beta, \nu_\zeta, \beta_p, \omega_{\beta_0}/\Omega, \omega_{\zeta_0}/\Omega$$

Step 1. Calculate the trim solution. For a given $\frac{cT}{\sigma}$ calculate λ and θ using Eqs.(5.4) and (5.5).

Step 2. Calculate the steady flap deflection β_0 using Eq. (5.2).

Step 3. Calculate the constants A, B, C, D, E for Eqs. (5.7).

Step 4. Calculate $R = AD^2 - BCD + B^2E$.

If the remainder R is zero it gives critical condition. For a non-zero value of R, select a new $\frac{cT}{\sigma}$ and repeat Steps 1-4. Vary $\frac{cT}{\sigma}$ till R changes sign. Take finer steps of $\frac{cT}{\sigma}$ to get the critical value at which R is nearly zero.

Note that Eq.(7) can also be solved using any standard subroutine for polynomial equation. The solution will give complex roots, the real part represents damping and the imaginary part presents the damping of the mode.

II. Eigen Analysis

The perturbation equations of motion (5.3) can be interpreted in a standard spring-mass-damper form.

$$[M] \begin{Bmatrix} ** \\ \beta \\ ** \\ \zeta \end{Bmatrix} + [C] \begin{Bmatrix} * \\ \beta \\ * \\ \zeta \end{Bmatrix} + [K] \begin{Bmatrix} \beta \\ \zeta \end{Bmatrix} = 0 \quad (5.8)$$

The matrices C and K are not symmetric. These can be transformed into a first order system (2.14) and solved as an eigenvalue problem. This will give two complex conjugate pairs, i.e., four eigenvalues. A typical eigenvalue λ will be

$$\lambda = \lambda_{\text{real}} + i\lambda_{\text{imaginary}}$$

(Note this eigenvalue λ is totally different from inflow λ .) The real part of the eigenvalue represents damping of the mode and the imaginary part represents the frequency of the mode.

If any one of the eigenvalue has a positive real part, the blade is unstable. The $\lambda_R = 0$ gives the stability boundary. Also note that if the frequency becomes zero in the unstable region, it represents static divergence condition.

This figure shows the flap-lag flutter stability boundaries as a function of thrust level obtained for a rotor blade in hovering flight. The following rotor parameters have been used for calculations

$$\begin{array}{llll} \gamma = 8.0 & \sigma = .05 & k_{p\beta} = k_{p\zeta} = 0 & \\ \beta_p = 0 & a = 2\pi & c_d = .01 & \zeta_L = 0 \end{array}$$

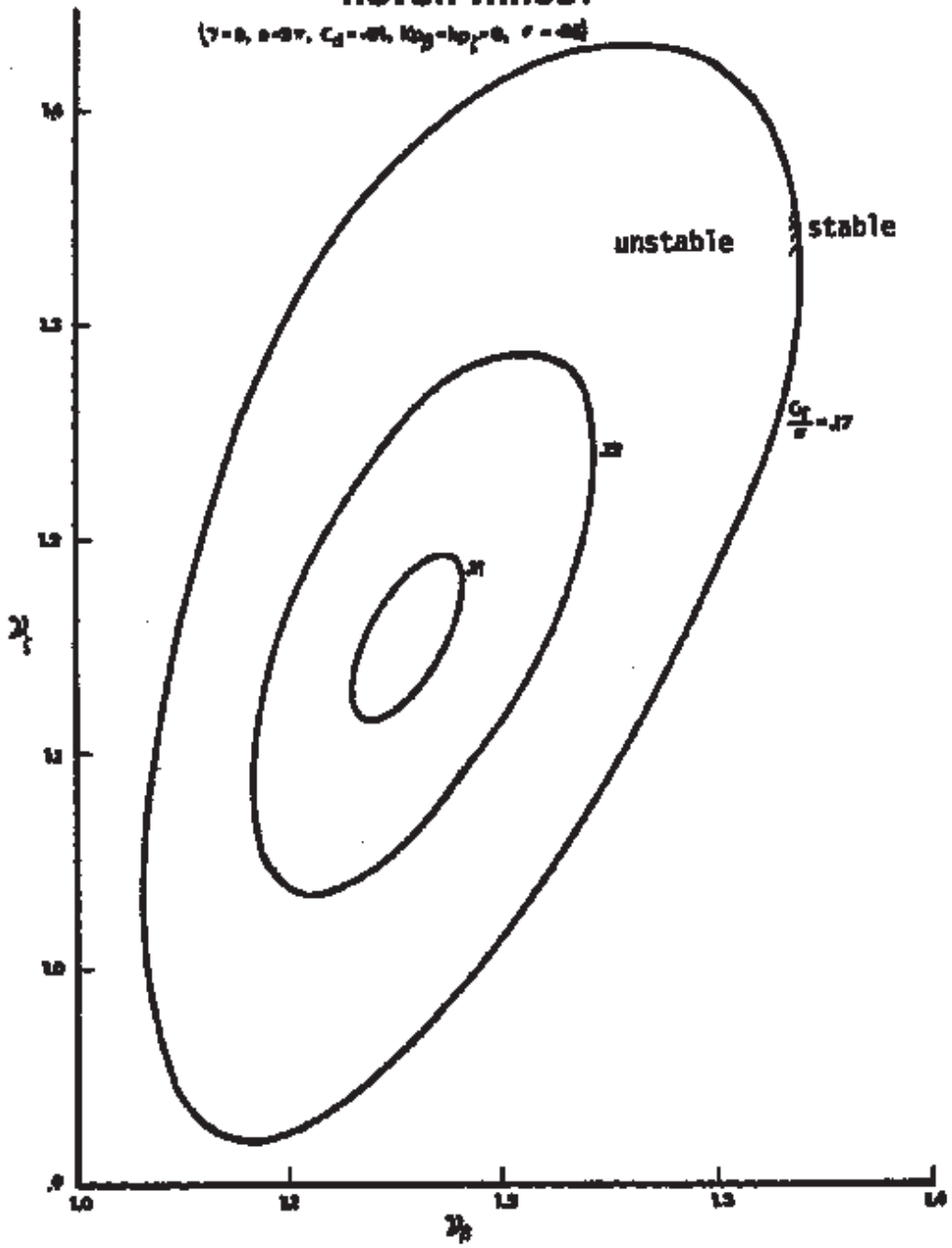
The flutter boundary is calculated using the determinant expansion. For a particular thrust level represented by $\frac{c_T}{\sigma}$, the blade is unstable inside the elliptic graph. The less damped lag mode becomes unstable and the damping ratio of the lag mode is plotted on the next figure for a fixed flap frequency, and for varying lag frequencies. These results are obtained using eigen-analysis. It is interesting to note that the lag mode instability is soft in nature and can be easily stabilized with the inclusion of a small amount of structural damping in the lag mode. Flap-lag flutter is an instability of lag mode which occurs at lag frequency. Because of low reduced frequencies, the unsteady effects play less important role here. The application of quasisteady aerodynamics theory appears adequate to predict flap-lag flutter. For hingeless rotors with no pitch-flap or pitch-lag coupling or flap-lag structural coupling, the critical condition for flap-lag stability occurs with zero precone and

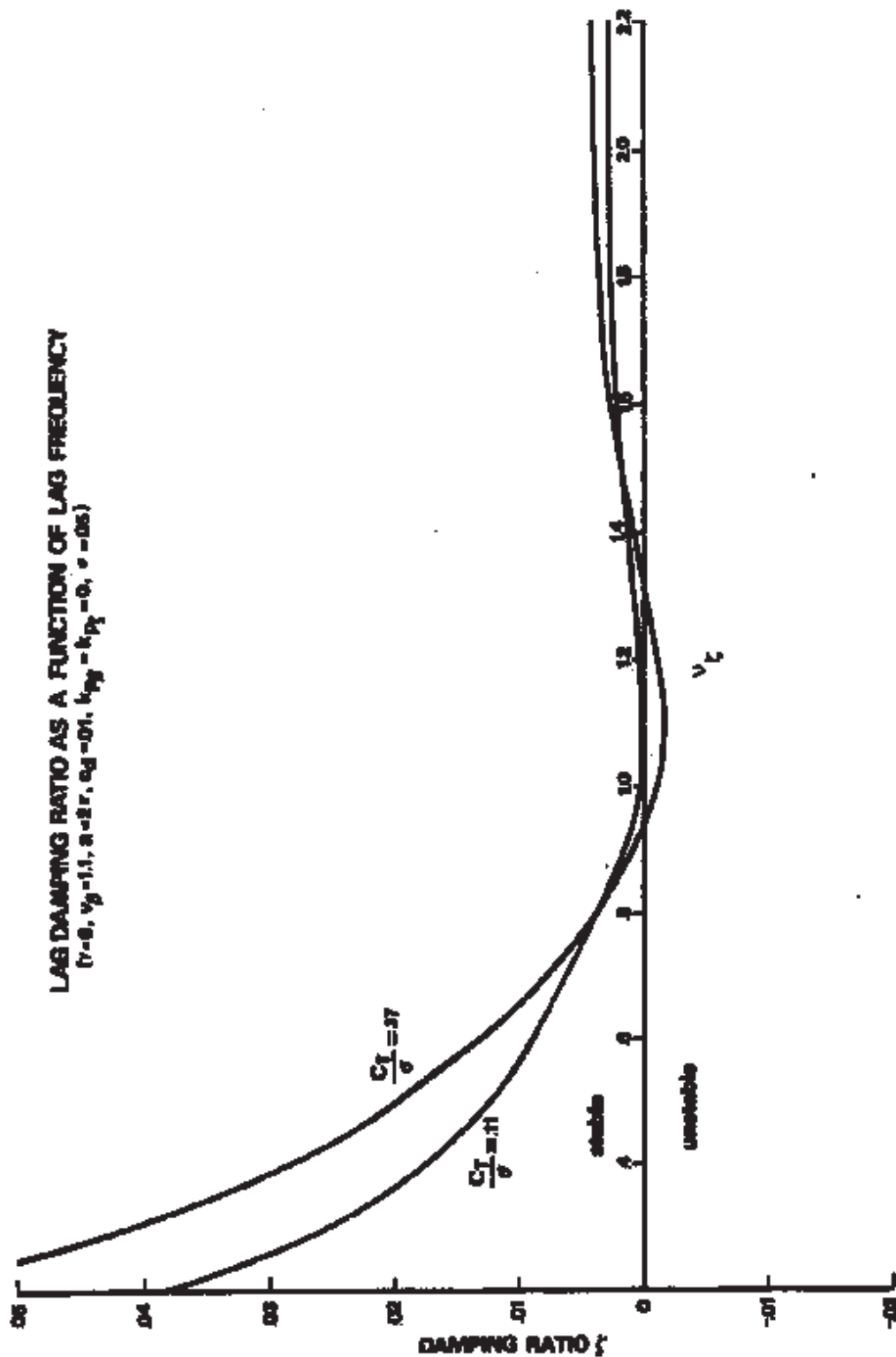
$$\text{flap frequency} = \text{lag frequency} = 1.15/\text{rev}$$

The rotor is stable for a flap frequency of less than 1/rev or greater than 1.4/rev.

FLAP-LAG STABILITY BOUNDARY AS A FUNCTION OF ROTOR THRUST

$(\gamma = 0, \delta = 0.7, C_d = 0.01, K_{\theta} = 10^7, \sigma = 0.01)$





5.1.1 Comment on Flap-Lag Flutter

Some general remarks are made on flap-lag flutter.

1. Articulated Rotor

Assume the blade with $k_{p\beta} = k_{p\zeta} = 0$ and with no hinge offset, $e = 0$. Gives $\nu_\beta = 1$. The steady solution is given in Eq. (5.2),

$$\beta_0 = \frac{\gamma\theta}{8} - \frac{\gamma\lambda}{6}$$

Let us examine the perturbation equations in Eq. (5.3),

$$\begin{aligned} \text{coupling term in flap equation} &= (-2\beta_0 + \frac{\gamma\theta}{4} - \frac{\gamma\lambda}{6}) \zeta^* \\ &= \frac{\gamma\lambda}{6} \zeta^* \end{aligned}$$

This term is small and can be neglected. This nearly uncouples the flap equation from the lag equation. It has been seen that the articulated blade with zero hinge offset, the blade is stable from the aeroelastic stability. However, the coupling term in the lag equation plays an important role for the determination of vibration and loads.

2. Ideal Precone

An ideal precone is the initial blade coning setting so that at the operating condition, the moments due to centrifugal force and aerodynamic force balance out, result in

$$\beta_0 \approx \beta_p$$

From steady solution, Eq.(5.2)

$$\beta_0 = \frac{1}{\nu_\beta^2} \left[\frac{\omega_{\beta 0}^2}{\Omega^2} \beta_p + \frac{\gamma\theta}{8} - \frac{\gamma\lambda}{6} \right] \quad (\text{assume } k_{p\beta} = k_{p\zeta} = 0)$$

$$\nu_\beta^2 = 1 + \frac{3}{2} \frac{e}{R} + \frac{\omega_{\beta 0}^2}{\Omega^2}$$

This gives

$$\beta_p = \frac{\gamma}{1 + \frac{3}{2}e} \left(\frac{\theta}{8} - \frac{\lambda}{6} \right)$$

and this does not depend on nonrotating flap frequency. Again the flap mode gets nearly uncoupled from lag mode resulting in a stable blade from flap-lag flutter instability. Otherwise, precone can be destabilizing.

3. Thrust Level

Flap-lag flutter is a high thrust phenomena. To achieve a high thrust level in hover, a high collective pitch is required. Also the inflow λ is higher for a higher thrust level. The result of this all is that the coupling terms particular in the lag equation becomes larger with higher thrust. At zero thrust, the coupling is minimum and the blade is free from aeroelastic instability.

4. Elastic Coupling

If the section principal axes do not lie along the flap and lag axes, then the flap and lag equations get coupled structurally due to elastic coupling. The elastic coupling allows the transfer of kinetic energy from weakly damped lag mode to well damped flap mode. The soft lag rotors get stabilized with small coupling. The stiff lag rotors on the other hand get destabilized with the small coupling term but generally become stabilized with the large coupling term.

5. Matched Stiffness Rotors

For matched stiffness rotors, the flap bending stiffness EI_x is equal to the lag stiffness EI_z . This is generally achieved through a circular cross-section at the root of the blade. This means that the nonrotating flap and lag frequencies are equal. Not shown so far, but it results in uncoupling, the bending and torsion equations structurally. This means that there is a less influence of torsion on flap-lag stability. Thus the matched stiffness condition stabilizes the blades.

6. Structural Damping

The flap mode is highly damped because of aerodynamic damping. The structural damping in the flap mode is unimportant. On the other hand, the lag mode is weakly damped and the flag-lag mode is instability of the lag mode. This instability is soft in nature and can be stabilized by damping in the lag mode. The other possibility is to add a mechanical lag damper at the root hinge to stabilize the blade.

7. Hinge Sequence

The earlier analysis is made for lag hinge followed by flap hinge outboard, other possibility is flap hinge followed by lag hinge outboard. The changed hinge sequence will introduce some extra nonlinear terms, in particular, in the aerodynamic forces. The flap-lag aeroelastic stability is very sensitive to small terms so the results can be somewhat different due to a change in hinge sequence (Kaza & Kvaternik.)

8. Pitch-Flap Coupling $k_{p\beta}$

Pitch-flap coupling, due to torsion dynamics or kinematic coupling is introduced in the two-degree-of-freedom problem by assuming a feather motion of the form

$$\Delta\theta = -k_{p\beta}\beta$$

The pitch-flap coupling $k_{p\beta}$ is positive for flap up/pitch down motion. The positive value of pitch-flap coupling raises the flap frequency. However, its influence on flap-lag stability is small.

9. Pitch-Lag Coupling $k_{p\zeta}$

Pitch-lag coupling due to torsion dynamics or kinematic coupling is introduced in two-degree model by assuming a feather motion of the form

$$\Delta\theta = -k_{p\zeta}\zeta$$

The pitch-lag $k_{p\zeta}$ is positive for lag back-pitch down motion. Generally, a negative coupling is stabilizing analysis.

10. Quasistatic Torsion Model

For low to moderate torsional frequencies one has to include torsion degree of motion for stability analysis. For high torsional frequencies (typically $\nu_\theta > 5$) the feathering inertia and damping terms are generally small and these do not influence the flap-lag instability. Either one can drop the torsion effect all together or one can include approximately the stiffness terms through a quasistatic torsion model assumption. Let us look at the flap-lag torsion equations.

$$[M] \begin{Bmatrix} \ddot{\beta} \\ \ddot{\zeta} \\ \ddot{\theta} \end{Bmatrix} + [C] \begin{Bmatrix} \dot{\beta} \\ \dot{\zeta} \\ \dot{\theta} \end{Bmatrix} + [k] \begin{Bmatrix} \beta \\ \zeta \\ \theta \end{Bmatrix} = 0 \quad (5.9)$$

keeping only static stiffness terms in the torsion equation, one gets

$$k_{31}\beta + k_{32}\zeta + k_{33}\theta = 0$$

$$\theta = -\frac{k_{31}}{k_{33}}\beta - \frac{k_{32}}{k_{33}}\zeta \quad (5.10)$$

Replace θ from the flap and lag equations using above expression. Again this results into a two-degree system. The effective pitch-flap and pitch-lag coupling terms due to torsion mode have been retained. These coupling terms are primarily caused by aerodynamic forces.

11. Stall

The flap-lag instability generally takes place at a high pitch setting, which also means high angle of attack. There is the likelihood of getting into stalled flow for part of the rotor blade. At stall, there is a loss of flap damping because of the reduced lift-curve slope.

12. Compressibility

Near the tip of the blade, there is a high speed region, and sometimes there can be transonic flow conditions. The compressibility effects are important near the tip, because of larger dynamic pressure there. Also due to transonic conditions, there is a shift in aerodynamic center from 1/4-chord to 1/2-chord, resulting in a large torsional moment. Also there is a large increase in the drag force. The compressibility effects can be quite destabilizing.

Ex. In a circulating controlled rotor blade, the aerodynamic characteristics are functions of geometric angle as well as blowing,

$$c_l = c_{l\alpha} + c_{l\mu}$$

$$c_d = c_{d0} + d_1 c_{l\mu}$$

Using quasisteady aerodynamics, derive the equations of motion for blade flap-lag aeroelastic stability in hover.

Flap-Lag equations

$$\beta^{**} - \nu_\beta^2 \beta - 2\beta_0 \zeta^* = \gamma \overline{M}_\beta + \frac{\omega_{\beta_0}^2}{\Omega^2} \beta_p$$

$$\zeta^{**} - \nu_\zeta^2 \zeta - 2\beta_0 \beta^* + 2\zeta_L \frac{\omega_{\beta_0}}{\Omega} \zeta = \gamma \overline{M}_\zeta$$

$$F_Z = \frac{1}{2} \rho c (c_l u_T V - c_d u_p V)$$

$$\delta F_Z = \frac{1}{2} \rho c (\delta c_l u_T V + c_l \delta u_T V + c_l u_T \delta V - \delta c_d u_p V - c_d \delta u_p V - c_d u_p \delta V)$$

$$\delta c_l = c_{l\alpha} \delta \alpha + c_{l\mu} \delta c_\mu$$

$$\delta c_d = c_{d\mu} \delta c_\mu$$

$$\delta c_\mu = -2c_\mu \frac{\delta V}{V}$$

$$\delta V = \frac{1}{V} (u_T \delta u_T + u_p \delta u_p)$$

$$\alpha = \theta - \frac{u_p}{u_T}$$

$$\begin{aligned}
\delta\alpha &= \delta\theta - \frac{1}{V^2}(u_T\delta u_p - u_p\delta u_T) \\
\frac{\delta F_z}{\frac{1}{2}\rho c} &= \delta u_T \left\{ \frac{u_p u_T}{V}(c_1 + d_1 c_\mu - c_{d_0}) + \left(\frac{u_T^2}{V} + V\right)\left(\theta - \frac{u_p}{u_T}\right)c_1 \right. \\
&\quad \left. - \left(\frac{u_T^2}{V} - V\right)c_2 c_\mu \right\} \\
&+ \delta u_p \left\{ -\frac{u_T^2}{V}c_1 + \frac{u_p u_T}{V}c_1\left(\theta - \frac{u_p}{u_T}\right) - \frac{u_p u_T}{V}c_2 c_\mu \right. \\
&\quad \left. + \frac{u_p^2}{V}(d_1 c_\mu - c_{d_0}) - V(c_{d_0} + d_1 c_\mu) \right\} \\
&+ \delta\theta(c_1 u_T V) \\
F_x &= \frac{1}{2}\rho c(c_l u_p V + c_d u_T V) \\
\frac{\delta F_x}{\frac{1}{2}\rho c} &= \delta u_T \left\{ c_1 \frac{u_p^2}{V} + \frac{u_p u_T}{V}c_1\left(\theta - \frac{u_p}{u_T}\right) - \frac{u_p u_T}{V}c_2 c_\mu \right. \\
&\quad \left. + \frac{u_T^2}{V}(c_{d_0} - d_1 c_\mu) + V(c_{d_0} + d_1 c_\mu) \right\} \\
&+ \delta u_p \left\{ -\frac{u_p u_T}{V}(c_1 + d_1 c_\mu - c_{d_0}) + \left(\frac{u_p^2}{V} + V\right)c_1\left(\theta - \frac{u_p}{u_T}\right) \right. \\
&\quad \left. - \frac{u_p^2}{V}c_2 c_\mu \right\} \\
&\delta\theta(c_1 u_p V)
\end{aligned}$$

For Hover

$$\begin{aligned}
\frac{u_T}{\Omega R} &= x, & \frac{u_p}{\Omega R} &= \lambda \\
\frac{\delta u_T}{\Omega R} &= -x^* \zeta, & \frac{\delta u_p}{\Omega R} &= x^* \beta^* & \delta\theta &= -k_{p\beta}\beta - k_{p\zeta}\zeta \\
V &\approx u_T
\end{aligned}$$

$$\overline{M}_\beta = \frac{1}{\rho a c R^4 \Omega^2} \int_0^R r \delta F_Z dr$$

$$\overline{M}_\zeta = \frac{1}{\rho a c R^4 \Omega^2} \int_0^R r \delta F_x dr$$

Perturbation Equations are

Flap:

$$\begin{aligned}
&\beta^{**} + \gamma \left(\frac{1}{8} - \frac{1}{6} \lambda \theta - \frac{1}{8} \frac{c_{d_0}}{c_1} + \frac{1}{6} \frac{c_2}{c_1} c_\mu \right) \beta^* + (\nu_\beta^2 + \frac{\gamma}{8} k_{p\beta}) \beta \\
&+ \left\{ -2\beta_0 + \gamma \left(\frac{\theta}{4} - \frac{\lambda}{6} - \frac{1}{8} \frac{c_2}{c_1} c_\mu + \frac{1}{6} \frac{d_1}{c_1} c_\mu - \frac{1}{6} \frac{c_{d_0}}{c_1} \right) \right\} \zeta^* + \frac{1}{8} k_{p\zeta} \zeta = 0
\end{aligned}$$

Lag:

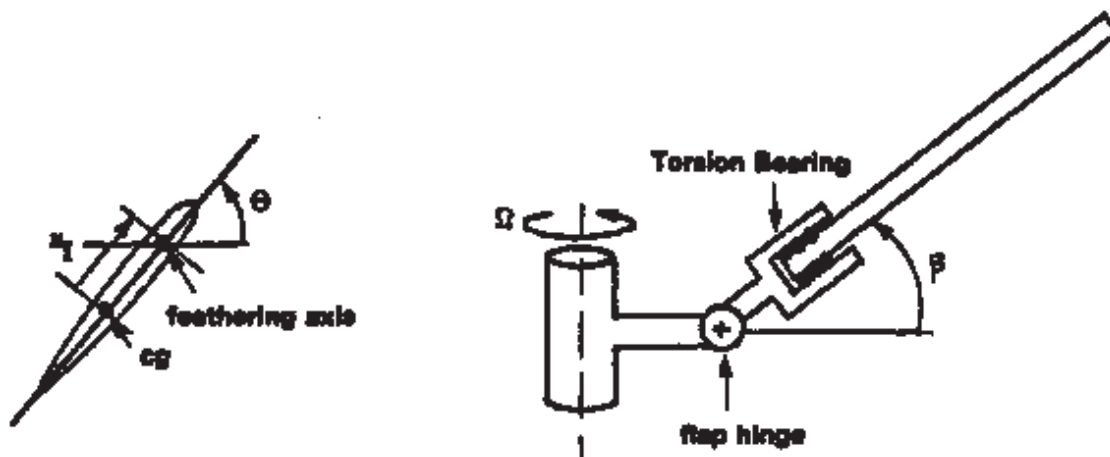
$$\begin{aligned}
&\zeta^{**} + \left\{ \frac{2\omega_{\zeta 0}}{\Omega} \zeta_L + \gamma \left(\frac{c_{d_0}}{4c_1} + \frac{\lambda \theta}{6} - \frac{1}{6} \frac{c_2}{c_1} c_\mu \lambda \right) \right\} \zeta^* + (\nu_\zeta^2 + \frac{\gamma}{6} k_{p\zeta} \lambda) \zeta \\
&+ \left\{ 2\beta_0 - \gamma \left(\frac{\theta}{8} - \frac{1}{6} \frac{d_1}{c_1} c_\mu + \frac{1}{6} \frac{c_{d_0}}{c_1} \right) \right\} \beta^* + \frac{\gamma}{6} k_{p\beta} \lambda \beta = 0
\end{aligned}$$

5.2 Pitch-Flap Instabilities

The flap and torsion modes participate causing this instability. This flutter instability is also called as classical or conventional flutter because a similar type flutter is also called as classical or conventional flutter because a similar type flutter instability takes place in fixed wings. However, there are certain differences for rotor blade flutter from fixed wing flutter.

- i) There is an important coupling due to centrifugal force if there is a cg offset from the elastic axis.
- ii) There is a tennis racket effect in the torsion equation.
- iii) Aerodynamic forces are more involved, in particular, returning wake can be important here.
- iv) Periodic forces are present if forward flight is also considered.

The result of all this is that one may not be able to apply the fixed wing results here. Let us investigate this problem for a simple blade configuration with two degrees of motion, rigid flap about flap hinge and rigid pitch about pitch bearing. The torsion bearing is assumed to be located outboard of the flap hinge (which is typical). The study is carried out for hovering flight.



The equations of motion for uniform blades in nondimensional form are

$$\text{Flap: } \beta + \nu_{\beta}^2 \beta - \frac{3}{2} \frac{X_I}{R} (\theta^{**} + \theta) = \gamma \overline{M}_{\beta} + \frac{\omega_{\beta 0}^2}{\Omega^2} \beta_p \quad (5.11)$$

$$\begin{aligned} \text{Pitch: } I_f^* (\theta^{**} + \nu_{\theta}^2 \theta + 2 \frac{\omega_{\theta 0}}{\Omega} \zeta_{\theta} \dot{\theta}) - \frac{3}{2} \frac{x_I}{R} (\beta^{**} + \beta) + K_{p\beta} \left(\frac{W_{\theta 0}}{\Omega} \right)^2 I_f^* \beta \\ = \gamma \overline{M}_{\theta} + I_f^* \frac{\omega_{\theta 0}^2}{\Omega^2} \theta_{con} \end{aligned}$$

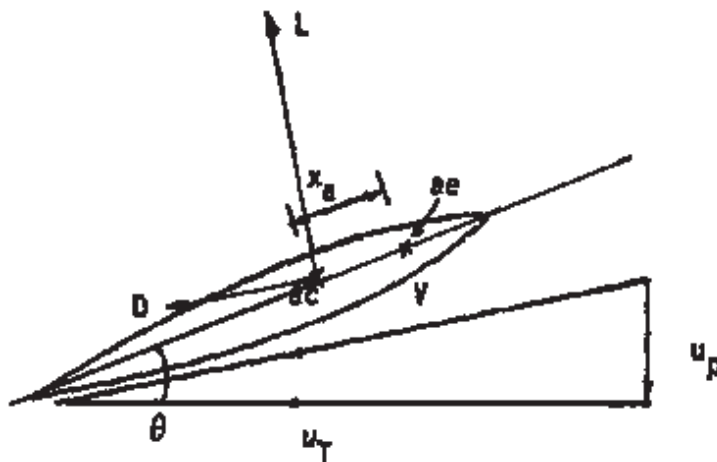
where $I_f^* = I_f/I_b$, the I_f is the feather moment of inertia and I_b is the flap moment of inertia. The $\omega_{\beta 0}$ and $\omega_{\theta 0}$ are the nonrotating flap and torsion frequencies. The ζ_{θ} is the viscous damping coefficient in the pitch mode with respect to nonrotating frequency and $K_{p\beta}$ is the pitch-flap coupling. The ν_{β} and ν_{θ} are respectively, the rotating natural frequencies of flap and torsion modes.

$$\nu_{\beta}^2 = 1 + \frac{3}{2} \frac{e}{R} + \frac{\omega_{\beta 0}^2}{\Omega^2}$$

$$\nu_\theta^2 = 1 + \frac{\omega_{\theta 0}^2}{\Omega^2}$$

where e is the offset for flap hinge. The θ_{con} is the control system command pitch.

Let us examine the aerodynamic forces



$$\overline{M}_\beta \approx \frac{1}{\rho a c \Omega^2 R^4} \int_0^R r L dr \quad (5.12)$$

$$\overline{M}_\theta \approx \frac{1}{\rho a c \Omega^2 R^4} \left[\int_0^R (-x_a) L dr + M_{Nc} \right]$$

where x_a is the chordwise offset of aerodynamic center from elastic axis, positive towards the trailing edge. The airfoils used for the rotor blades are generally symmetric and therefore the aerodynamic moment coefficient c_{mac} is zero. The M_{Nc} is the noncirculatory aerodynamic moment which is important for the pitch dynamics. The lift force per unit length is

$$(5.13)$$

where $\overline{C}(k)$ is a lift deficiency function and it depends on the reduced frequency $k = \frac{\omega b}{U}$. For simplifying the analysis, a representative value of $C(k)$ is taken at the 3/4-radius position and assumed constant for the blade. The perturbation aerodynamic force is

$$\begin{aligned} (\overline{M}_\beta)_{perturbation} &= \frac{1}{\rho a c \Omega^2 R^4} \int_0^R \delta L r dr \\ \frac{1}{2} \int_0^1 \overline{C}(k) &\left\{ \frac{\delta u_T}{\Omega R} \left(2 \frac{u_T}{\Omega R} \theta - \frac{u_p}{\Omega R} \right) - \frac{\delta u_p}{\Omega R} \frac{u_T}{\Omega R} + \delta \theta \left(\frac{u_T}{\Omega R} \right)^2 \right\} x dx \\ (\overline{M}_\theta)_{perturbation} &= -\frac{1}{2} \int_0^2 \frac{x_a}{R} \overline{C}(k) \left\{ \frac{\delta u_T}{\Omega R} \left(2 \frac{u_T}{\Omega R} \theta - \frac{u_p}{\Omega R} \right) - \frac{\delta u_p}{\Omega R} \frac{u_T}{\Omega R} \right. \\ &\left. + \delta \theta \left(\frac{u_T}{\Omega R} \right)^2 \right\} dx + \overline{M}_{nc} \end{aligned}$$

and

$$\overline{M}_{nc} = \frac{1}{\rho a c \Omega^2 R^4} \left\{ \frac{1}{4} \pi \rho \Omega^2 c^3 \left[r \left(\frac{1}{4} + \frac{x_a}{c} \right) \ddot{\beta} - r \left(\frac{1}{2} + \frac{x_a}{c} \right) \dot{\theta} \right] \right\}$$

$$-c\left(\frac{3}{32} + \frac{1}{2}\frac{x_a}{c}\right)\ddot{\theta}] \left. \vphantom{-c\left(\frac{3}{32} + \frac{1}{2}\frac{x_a}{c}\right)\ddot{\theta}} \right\}$$

The steady and perturbation flow components are

$$\begin{aligned} \frac{u_T}{\Omega R} &= x, & \frac{u_p}{\Omega R} &= \lambda \\ \frac{\delta u_T}{\Omega R} &= 0, & \frac{\delta u_p}{\Omega R} &= x \beta^* - \frac{c}{R} \left(\frac{1}{2} + \frac{x_a}{c} \right) \theta^* \\ \delta \theta &= \theta \text{ (elastic)} \end{aligned}$$

Perturbation moments become

$$\begin{aligned} \overline{M}_\beta &= \frac{1}{2} \overline{C} \left\{ -\frac{1}{4} \beta^* + \frac{1}{3} \frac{c}{R} \left(\frac{1}{2} + \frac{x_a}{c} \right) \theta^* + \frac{1}{4} \theta \right\} \\ \overline{M}_\theta &= -\frac{1}{2} \overline{C} \frac{x_a}{R} \left\{ -\frac{1}{3} \beta^* + \frac{1}{2} \frac{c}{R} \left(\frac{1}{2} + \frac{x_a}{c} \right) \theta^* + \frac{1}{3} \theta \right\} - \frac{1}{16} \left(\frac{c}{R} \right)^2 \left(\frac{1}{2} + \frac{x_a}{c} \right) \theta^* \end{aligned} \quad (5.14)$$

The equations of motion (5.11) become

$$\begin{aligned} \left[\begin{array}{cc} 1 & -\frac{3}{2} \frac{x_I}{R} \\ -\frac{3}{2} \frac{x_I}{R} & I_f^* \end{array} \right] \left[\begin{array}{c} \beta^* \\ \theta^* \end{array} \right] + \left[\begin{array}{cc} \frac{\gamma}{8} \overline{C}(k) & -\frac{\gamma}{12} \frac{c}{R} (1 + 2 \frac{x_a}{c}) \overline{C}(k) - \frac{1}{24} \frac{C}{R} \\ -\frac{\gamma}{6} \frac{c}{R} \frac{x_a}{c} \overline{C}(k) & \frac{\gamma}{8} \left(\frac{c}{R} \right)^2 \frac{x_a}{c} (1 + 2 \frac{x_a}{c}) \overline{C}(k) \\ & + \frac{1}{16} \left(\frac{c}{R} \right)^2 \left(\frac{1}{2} + \frac{x_a}{c} \right) + 2 I_f^* \frac{\omega_{\theta 0}}{\Omega} \zeta_\theta \end{array} \right] \left[\begin{array}{c} \beta^* \\ \theta^* \end{array} \right] \\ + \left[\begin{array}{cc} \nu_\beta^2 & -\frac{\gamma}{8} \overline{C}(k) - \frac{3}{2} \frac{x_I}{R} \\ -\frac{3}{2} \frac{x_I}{R} k_{p\beta} & I_f^* \nu_\theta^2 + \frac{\gamma}{6} \frac{c}{R} \frac{x_a}{c} \overline{C}(k) \end{array} \right] \left[\begin{array}{c} \beta \\ \theta \end{array} \right] = 0 \end{aligned} \quad (5.15)$$

These are second order equations expressed in standard spring-mass-damper form. These can be solved many different ways. Two possible ways are:

- (a) Expansion of the determinant
- (b) Eigen Analysis

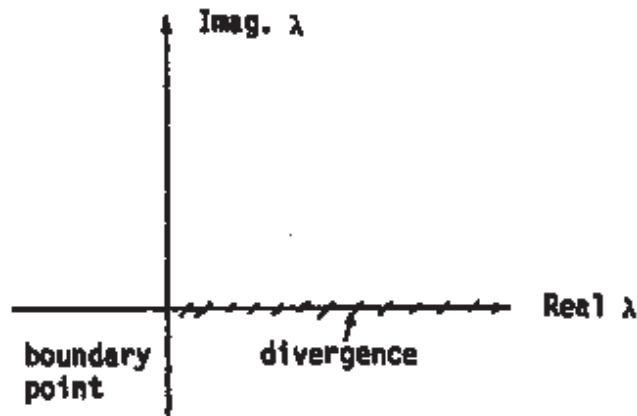
Two types of instabilities are possible

- (a) Static instability (Divergence)
- (b) Dynamic instability (Flutter)

Let us examine each one separately.

5.2.1 Pitch Divergence

At a particular operating condition, if a disturbance is given to the blade, the elastic pitch becomes larger and larger till the blade fails. This is a static instability and the dynamics of the blade does not play any role. It is only the pitch mode which becomes unstable. One can solve the governing pitch-flap equations (5.15) as an eigenvalue problem. This will result into two complex conjugates pairs.



eigen $\lambda = \lambda_{Real} + i\lambda_{Imag}$.

For divergence condition

$$\lambda_{Real} \geq 0$$

and

$$\lambda_{Imag.} = 0$$

Divergence is a zero frequency condition. For divergence, the acceleration and velocity terms are not important. Also, $\overline{C}(k) = 1$.

$$\begin{bmatrix} \nu_\beta^2 & -\frac{\gamma}{8} - \frac{3x_I}{2R} \\ -\frac{3x_I}{2R} & I_f^* \nu_\theta^2 + \frac{\gamma x_a}{6R} \end{bmatrix} \begin{bmatrix} \beta \\ \theta \end{bmatrix} = 0$$

Setting the determinant to be zero, gives the critical condition

$$R = \nu_\beta^2 (I_f^* - \nu_\theta^2 + \frac{\gamma x_a}{6R}) - \frac{3x_I}{2R} (\frac{\gamma}{8} + \frac{3x_I}{2R})$$

= 0 gives the critical condition.

If $R > 0$, the system is stable or

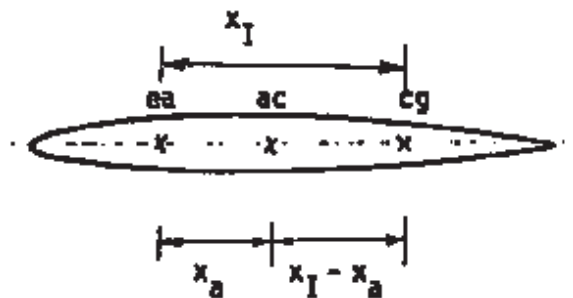
$$\frac{3}{16} \gamma \frac{x_I}{R} - \frac{\gamma}{6} \nu_\beta^2 \frac{x_a}{R} < \nu_\beta^2 I_f^* \nu_\theta^2$$

$$\frac{x_I}{R} - \frac{8}{9} \nu_\beta^2 \frac{x_a}{R} < \frac{16}{3\gamma} \nu_\beta^2 I_f^* \nu_\theta^2$$

$$\frac{8}{9} \nu_\beta^2 \approx 1$$

Thus for the stable blade from pitch divergence

$$\frac{x_I - x_a}{R} < \frac{16}{3\gamma} \nu_\beta^2 I_f^* \nu_\theta^2$$



The pitch divergence depends on the chordwise offset of the cg after aerodynamic center. The elastic axis location is unimportant for the divergence boundary.

Let us consider a typical rotor with the following properties

$$\gamma = 8 \quad \nu_\beta = 1.1 \quad I_f^* = .001 \quad \frac{R}{c} = 10$$

For the unstable blade

$$\frac{x_a - x_I}{c} \geq \frac{R}{c} \times \frac{16}{3} \times \frac{1}{8} \times 1.21 \times \nu_\theta^2 \times 0.001 \approx .01\nu_\theta^2$$

The right hand side is a positive number. The aerodynamic center is quite close to 1/4-chord. Thus if cg falls on 1/4-chord or ahead of 1/4-chord, there is no possibility of pitch divergence.

There are two important parameters for pitch divergence

- (a) cg offset from 1/4-chord
- (b) torsional frequency $\frac{\omega_\theta}{\Omega}$

It should be kept in mind that for fixed wing, the divergence depends on aerodynamic center offset from the elastic axis. For the rotor blade, the elastic axis position is unimportant and divergence can happen even if the aerodynamic center and elastic axis are coincident. This is because in rotors, as blade twists, the lift increases and this increases steady flap deflection β , resulting in larger twisting action due to the centrifugal force component ($\beta \times CF$).

5.2.2 Flutter

The self-excited oscillations are caused by the coupling of pitch and flap modes. The flutter boundary is defined by the zero damping condition. This flutter does not depend on the thrust level and in fact, it can take place at zero thrust. The rotor trim is not required for the calculation of flutter speed.

There are two simple ways to solve the dynamic pitch and flap equations (5.15), either the determinant expansion or as an eigenvalue problem. Let us discuss the first method.

Determinant Expansion:

Assume the perturbation motion as

$$\beta(\psi) = \beta e^{s\psi}$$

$$\theta(\psi) = \theta e^{s\psi}$$

Substituting in the governing Eq. (5.15),

$$\begin{bmatrix} s^2 + \frac{\gamma}{8}\overline{C}(k)s + \nu_\beta^2 & -\frac{3}{2}\frac{x_I}{R}s^2 - \frac{\gamma}{12}\frac{c}{R}(1 + 2\frac{x_a}{c})\overline{C}(k)s \\ & -\frac{\gamma}{8}\overline{C}(k) - \frac{3}{2}\frac{x_I}{R} \\ -\frac{3}{2}\frac{x_I}{R}s^2 - \frac{\gamma}{6}\frac{x_a}{R}\overline{C}(k)s & I_f^*s^2 + \frac{\gamma}{8}(\frac{c}{R})^2\frac{x_a}{c}(1 + 2\frac{x_a}{R})\overline{C}(k)s \\ & + I_f^*\nu_\theta^2 + \frac{\gamma}{6}\frac{x_a}{R}\overline{C}(k) + 2I_f^*\frac{\omega_{\theta\Omega}}{\Omega}\zeta_\theta \end{bmatrix} \begin{bmatrix} \beta \\ \theta \end{bmatrix} = 0$$

Expansion of the determinant will result in

$$As^4 + Bs^3 + Cs^2 + Ds + E = 0$$

Routh's stability criteria is

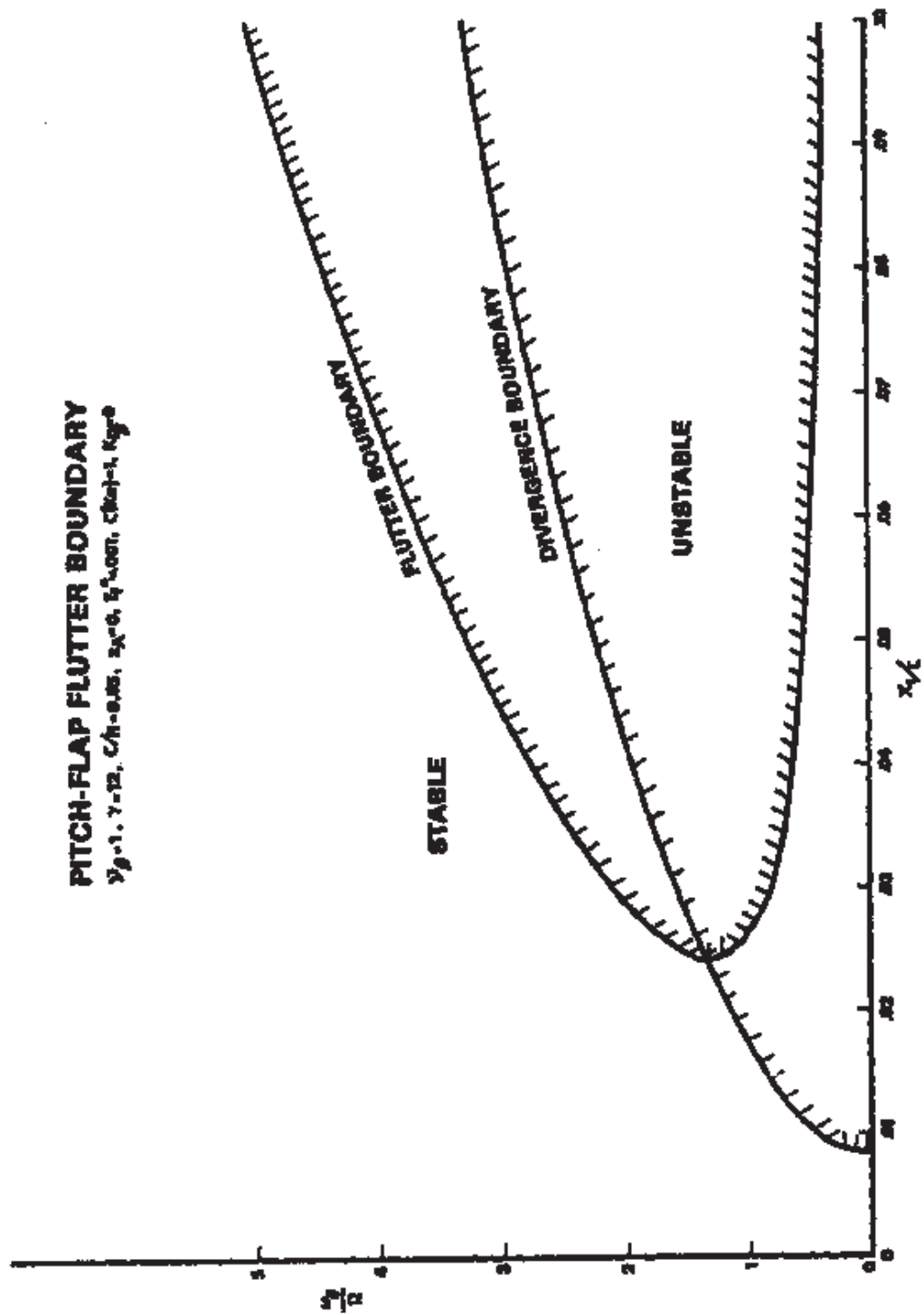
$$R = AD^2 - BCD + B^2E > 0 \text{ for stable system.}$$

Neglecting the shed wake effect. The above stability criteria can be put in an approximate form as

$$\frac{x_I - x_a}{R} < (\frac{c}{R})^2(\frac{1}{3\sqrt{2}} + \frac{\gamma}{48}) \text{ for stable blade}$$

Again it is the offset of cg behind the aerodynamic center that is important. If cg lies on the 1/4-chord or ahead of it, there is no likelihood of flutter.

Eigen Analysis



Ex. The characteristics of an articulated rotor with 6% hinge offset are given as

$$\gamma = 8.0 \quad I_f^* = .001 \quad \frac{c}{R} = 20$$

The blade cg and elastic axis lies respectively at 35% and 20% of chord. If the nonrotating torsional

frequency is 3 times the rotational speed.

- (a) Find out whether the blade is stable from pitch divergence or not.
- (b) If the elastic axis is brought to 25% chord position, you would like to find whether the blade can get into pitch-flap flutter. For simplicity assume $C(k)=1$ $C(k) = 1$
- (a) For pitch divergence,

$$\frac{x_I - x_A}{R} < \frac{16}{3\gamma} \nu_\beta^2 I_* \nu_\theta^2 \text{ for stable blade}$$

$$\nu_\beta^2 = 1 + \frac{3}{2} \times .06 = 1.09$$

$$\text{RHS} = \frac{16}{3 \times 8} \times 1.09 \times .001 \times 10 = .0073$$

$$\text{LHS} = .10 \times \frac{1}{20} = .005$$

Blade is stable

- (b) Flutter Eqs.

$$\begin{bmatrix} 1 & -.0075 \\ -.0075 & .001 \end{bmatrix} \begin{bmatrix} \beta \\ \theta \end{bmatrix} + \begin{bmatrix} 1 & -.033 \\ 0 & .000625 \end{bmatrix} \begin{bmatrix} \beta \\ \theta \end{bmatrix} + \begin{bmatrix} 1.09 & -1.0 \\ -.0075 & .01 \end{bmatrix} \begin{bmatrix} \beta \\ \theta \end{bmatrix} = 0$$

Determinant becomes

$$\begin{vmatrix} s^2s + 1.09 & -.0075s^2 - 1.0 \\ -.0075s^2 - .0075 & -.001s^2 + .000625s + .01 \end{vmatrix} = 0$$

$$= As^4 + Bs^3 + Cs^2 + Ds + E$$

$$A = .00094 \quad B = .00075 \quad C = .0035$$

$$D = .00975E = .0034$$

$$R = AD^2 - BCD + B^2E = .66 \times 10^{-8}$$

Blade stable (marginal)

5.3 Flap-Lag-Torsion Flutter

The earlier two-degrees of freedom representation of flap-lag and pitch-flap blades is quite analogous to the fixed wing “typical section” analysis that treats a two-dimensional wing undergoing rigid body pitch and heave motions. An improvement over the two-degree model will be to introduce the third degree of motion. Thus, the blade undergoes rigid body flap, lag and feather rotations about hinges at the blade root, with hinge springs to obtain arbitrary natural frequencies. With this three-degree flap-lag-torsion model, both flap-lag and pitch-flap instabilities are covered. The equations of motion for this system are covered in 3.10 and the generic aerodynamic forces are defined in 4.6. This will result into three second order equations in terms of β , ζ , and θ (like Eqs. (5.3)) and these equations can be solved as an eigenvalue problem. Again the nature of the eigenvalues tells whether the system is stable or not. For a three-degree model, the hinge sequence is quite important, and the results can be quite different for different hinge sequences. The suitability of a particular hinge sequence depends on the physical configuration of the blade. For most blade configurations, a hinge sequence of inboard flap, followed by lag and then the torsion outboard, appears quite adequate. For analysis details, see Chopra (83). These simple two-degree and three-degree models help to

understand the physics of phenomena through a systematic identification of coupling terms. Also, these simple models have often been proven very useful for rotor system design and development.

A better representation for a rotor blade is to treat it as an elastic beam undergoing flap bending, lead-lag bending and torsion deflections. Several authors have investigated the aeroelastic stability of an elastic blade (see, general review papers 4-7). The equations of motion are given in 3.11 for a uniform blade and the generic aerodynamic forces are defined in 4.6. The common approach for calculating the trim deflections, as well as the aeroelastic stability, is the model method (Galerkin or Rayleigh-Ritz) using either coupled natural modes (rotating) or uncoupled beam modes (nonrotating). In general, the trim deflections are assumed to be large and are obtained by solving nonlinear steady-state equation; and the flutter equations of motion are linearized about the trim state. With the modal approach, it becomes increasingly difficult to handle geometric complexities. For example, it is difficult to effectively model the multibeam flexure of a bearingless blade. The finite element method is perhaps an ideal choice for complex blade configurations. The blade is divided into a number of beam elements and the application of energy principles or the method of weighted residuals yields approximate expressions for forces (inertial, elastic, etc.) over each elements. The global equations for motion are obtained by assembling the elements. Nonuniform properties can be easily accommodated. The finite element method is very flexible and the formulation can be adapted to different rotor blade configurations with a few modifications. Multibeams of a bearingless blade can be modeled individually (Refs. 10-11).

Most analyses apply quasisteady strip theory to obtain aerodynamic forces. Forces of noncirculatory origin from unsteady thin airfoil theory are also included. Normally, linearized two-dimensional airfoil lift, drag, and pitch moment coefficients are used. Typically,

$$c_l = a\alpha$$

$$c_d = c_{d_0}$$

$$c_m = 0$$

The correlation of theoretical and experimental results from scaled models has shown that nonlinear airfoil section characteristics may significantly influence low-frequency flap-lag-torsion stability. For example,

$$c_l = c_0 + c_1\alpha + c_2\alpha|\alpha|$$

$$c_d = d_0 + d_1\alpha^2|\alpha|$$

$$c_m = f_0 + f_1\alpha$$

appears quite adequate representation below stall condition. Some analyses have used data tables to obtain airfoil characteristics. Linearization of airfoil lift, drag and pitch moment coefficients about a trim angle of attack provides a simple way of treating these effects in a linear stability analysis.

$$c_l(\alpha) = c_l(\alpha_0) + \frac{\delta c_l}{\delta \alpha}(\alpha_0)\Delta\alpha$$

$$c_d(\alpha) = c_d(\alpha_0) + \frac{\delta c_d}{\delta \alpha}(\alpha_0)\Delta\alpha$$

$$c_m(\alpha) = c_m(\alpha_0) + \frac{\delta c_m}{\delta \alpha}(\alpha_0)\Delta\alpha$$

and

$$\alpha = \alpha_0 + \Delta\alpha$$

where α_0 is the trim angle of attack and $\delta\alpha$ is the perturbation in the angle of attack.

The induced inflow is calculated using simple momentum theory. The assumption of uniform inflow is widely used, though it is strictly true for ideally twisted blades. It is, however, observed that a small variation in inflow distribution has negligible influence on blade stability.

Quasisteady assumption appears satisfactory for low frequency modes. For high frequency pitch-flap flutter, one needs to include unsteady aerodynamic effects. The influence of unsteady aerodynamics can be introduced through a suitable modification of the circulatory lift with a suitable lift deficiency function. The airfoil characteristics become

$$c_l = c_l(\alpha_0) + \frac{\delta c_l}{\delta\alpha}(\alpha_0)\Delta\alpha$$

$$c_d = c_d(\alpha_0) + \frac{\delta c_d}{\delta\alpha}(\alpha_0)\Delta\alpha$$

$$c_m = c_m(\alpha_0) + \frac{\delta c_m}{\delta\alpha}(\alpha_0)C(k)\Delta\alpha$$

where $C(k)$ is lift deficiency function and k is the reduced frequency, $\frac{\omega c}{2U}$. The ω is the frequency of oscillation, c is the chord, and U is the free-stream velocity. For hover, U becomes equal to Ωr , where Ω is rotational speed (rad/sec) and r is the radial position. The value of reduced frequency k varies along the length of the blade; the smaller value at the tip and the larger value near the root end of the blade. For hover, it is appropriate to use the Loewy function $C(k)$ and for forward flight Theodorsen function $C(k)$ is perhaps a better choice. There are two problems with this approach. First, the reduced frequency k varies radially and the second, $C(k)$ is a complex number. The first problem can be covered approximately through finite element formulation. The blade is divided into a number of elements and for each element an average value of reduced frequency corresponding to the mid-point is used. With the inclusion of complex numbers for lift deficiency functions, the equations become complex and there is no easy way to solve these equations. Thus,

$$C(k) = F(k) + iG(k)$$

One possible way is to arbitrarily neglect the complex component from the lift deficiency function ($G(k) = 0$) and retain the real component. There is a little justification with this assumption; more so, with higher frequencies.

Another simple way to include unsteady aerodynamic effects is to use dynamic inflow modeling. As discussed in art. 4.6, the dynamic inflow components are related to perturbation rotor loads (thrust, roll moment and pitch moment). For hovering flight, the dynamic inflow model is quite simple and is given as

$$\dot{\tilde{\lambda}} + \tilde{\lambda} = \text{sign}(c_T) k_p^2 \frac{\Delta c_T}{4\lambda_0}$$

where $\tilde{\lambda}$ is a perturbation to the induced inflow from its steady value λ_0 .

The blade motion is assumed to be small perturbation about steady deflected shape. The steady blade equilibrium position has an important influence on blade stability. The steady-state equations are obtained for hovering flight after dropping the time dependent terms. These nonlinear equations are solved iteratively using the Newton-Raphson procedure. The next step is to obtain the natural vibration characteristics of the rotating blade about its equilibrium position. This is done removing all aerodynamic terms and also neglecting damping matrix. This gives real eigenvalues. The last step is to calculate the flutter stability. Typically, this is done through the normal mode equations using few (about 6) natural vibration modes. This results in a complex eigenvalue problem. The condition of negative damping for a mode results in dynamic instability.

The correlation of experimental data with analytical results obtained using different codes for blade and rotor stability has been presented in ITR Methodology Workshop (1983). One particular example of hingeless blade in hovering flight is worked out here using finite element analysis. The blade is divided into seven elements. Each element consists of two end nodes and three internal nodes, with a total of fifteen degrees of freedom. Each of the end nodes has six degrees of freedom, namely, axial deflection u , lead-lag deflection v , v' , flap deflection w , w' , and elastic twist ϕ . The input data is given below.

Configuration Hingeless Rotor Isolated Stability
(Task IIA) Soft Flexure case

Rotor RPM	=	1000
Lock Number	γ =	5.3
Solidity ratio	σ =	.057
chord/radius	$\frac{c}{R}$ =	.09
reference life curve slope	a_r =	6.0

zero precone, zero pretwist, zero offsets of aerodynamic center, cg and tension center from elastic axis

$$c_l = 6\alpha - 10\alpha^2 \quad (\text{sign } \alpha)$$

$$c_d = .01 + 11.1(\alpha)^3 (\text{sign } \alpha)$$

$$c_m = 0$$

7 Finite Elements (No. 1 from tip)

lengths in terms of radius .1, .1, .1, .1, .25, .255, .095.

structural properties same for elements 1-6

$$\text{Flapwise } EI_y/m_0\Omega^2R^4 = .005239$$

$$\text{Chordwise } EI_z/m_0\Omega^2R^4 = .1067$$

$$\text{Torsion } GJ/m_0\Omega^2R^4 = .00157$$

$$\text{Torsion Inertia } k_m^2/R^2 = .000647 = k_a^2/R^2$$

$$m/m_0=1$$

For root element 7

$$EI_y/m_0\Omega^2R^4 = .1477 \quad EI_z/m_0\Omega^2R^4 = .1866$$

$$GJ/m_0\Omega^2R^4 = .00116 \quad k_m^2/R^2 = k_a^2/R^2 = .0131$$

$$m/m_0 = 12.1$$

Given nonrotating frequencies

$$\text{flap frequency} = .311/\text{rev}$$

$$\text{lag frequency} = 1.32/\text{rev}$$

$$\text{torsion freq.} = 2.30/\text{rev}$$

$$\text{lag structural damping } 2\zeta_L \frac{\omega\zeta_0}{\Omega} = .0196$$

For unsteady aerodynamics

Reduced frequencies k corresponding to lag mode for elements 1-7 are .066, .074, .084, .097, .133, .283 and 1.326 and Theodoresen's lift deficiency function $C(k)$ are .8825, .8699, .8363, .7922, .6746 and .5262.

Calculated rotating frequencies ($\theta = 0$)

$$\text{flap frequency} = 1.17/\text{rev}$$

$$\text{lag frequency} = 1.33/\text{rev}$$

$$\text{torsion freq.} = 2.97/\text{rev}$$

The following reports discuss aeroelastic stability in hover for different types of rotors.

(a) Hingeless rotors - Hodges and Ormiston (1976).

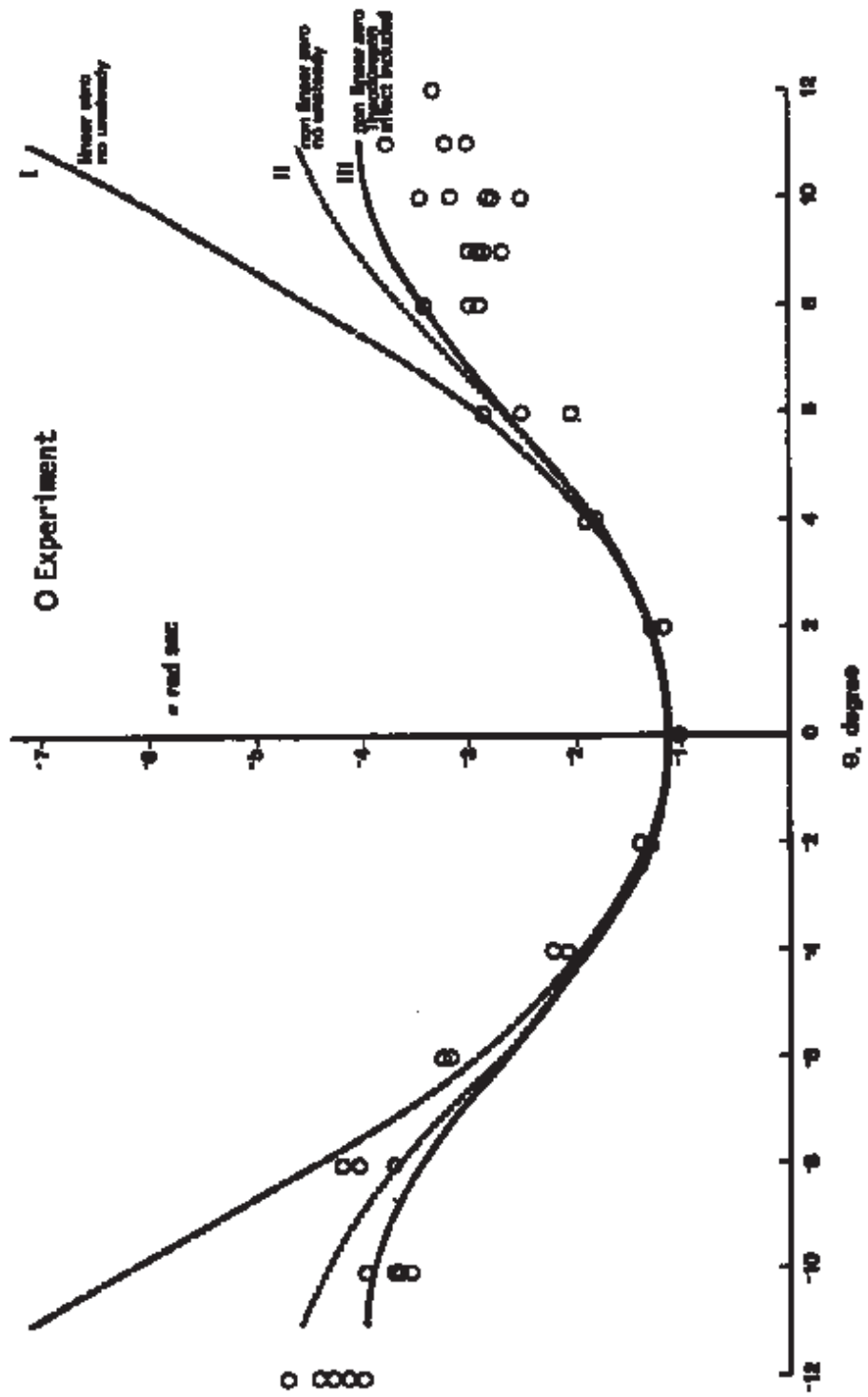
(b) Circulation control rotors Chopra and Johnson (1979) Chopra (1984).

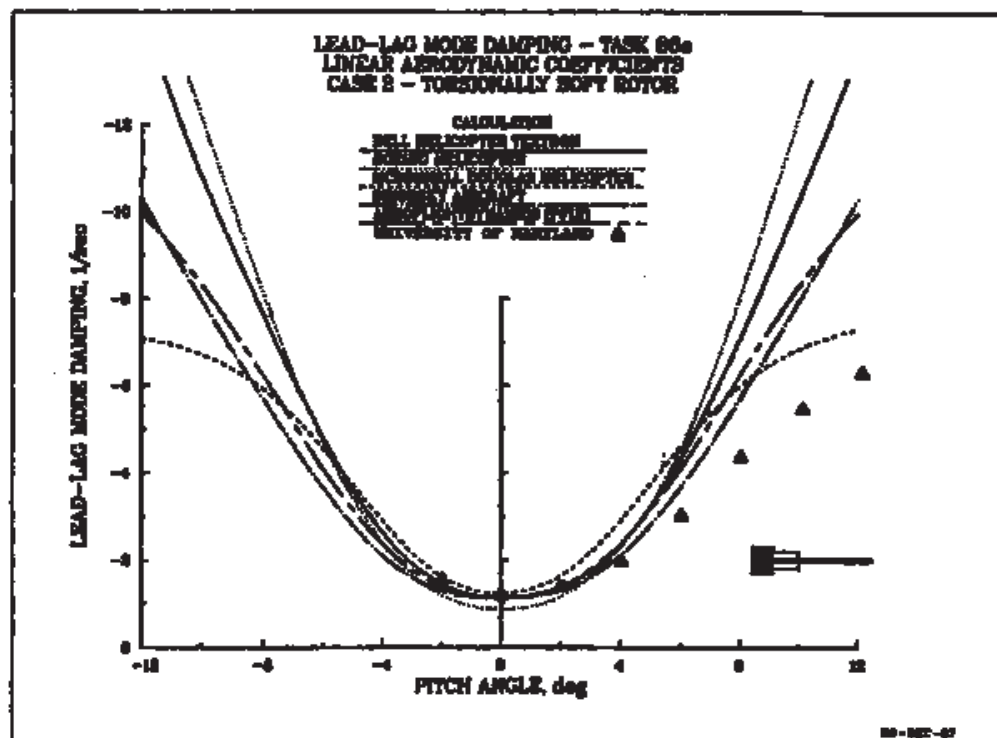
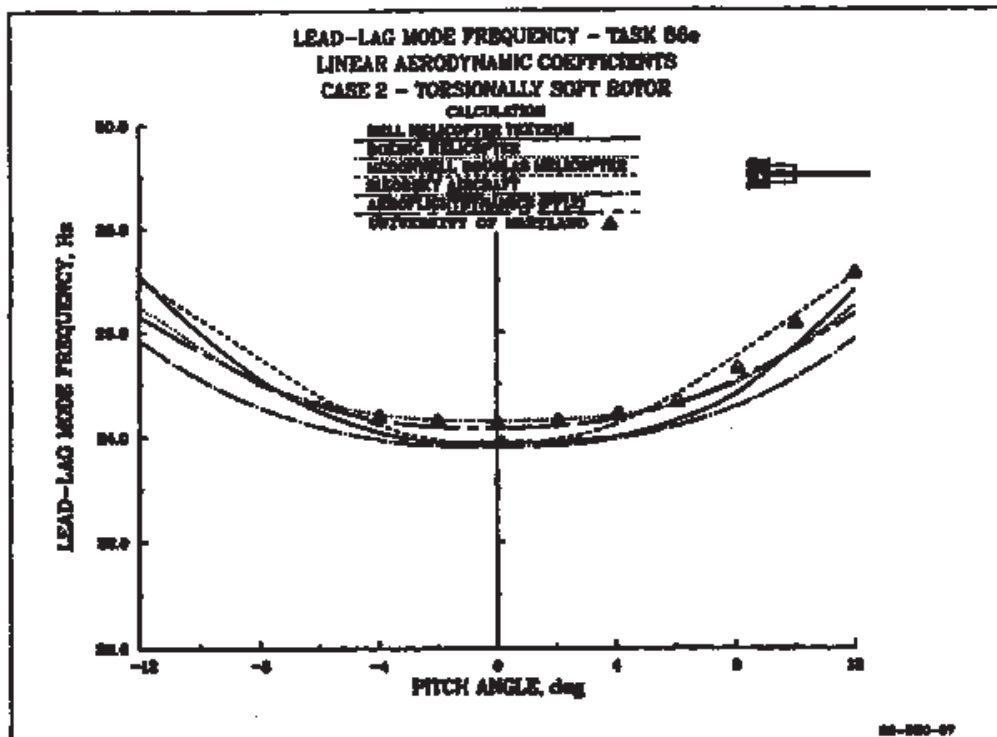
(c) Composite Blades - Hong and Chopra (1985).

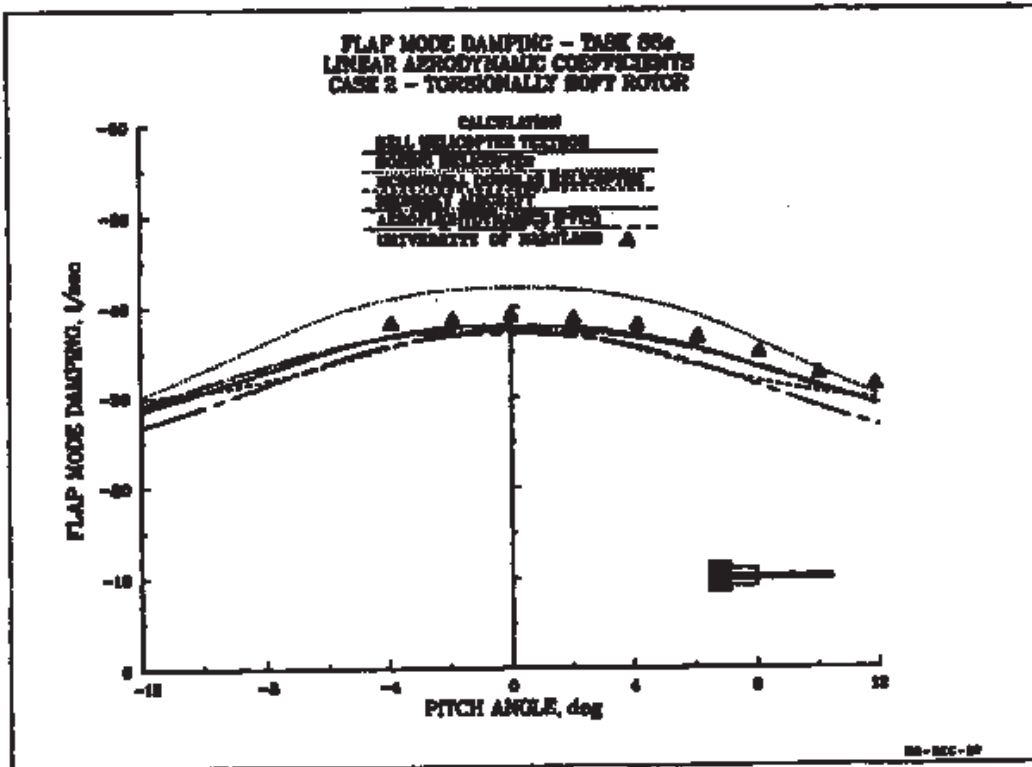
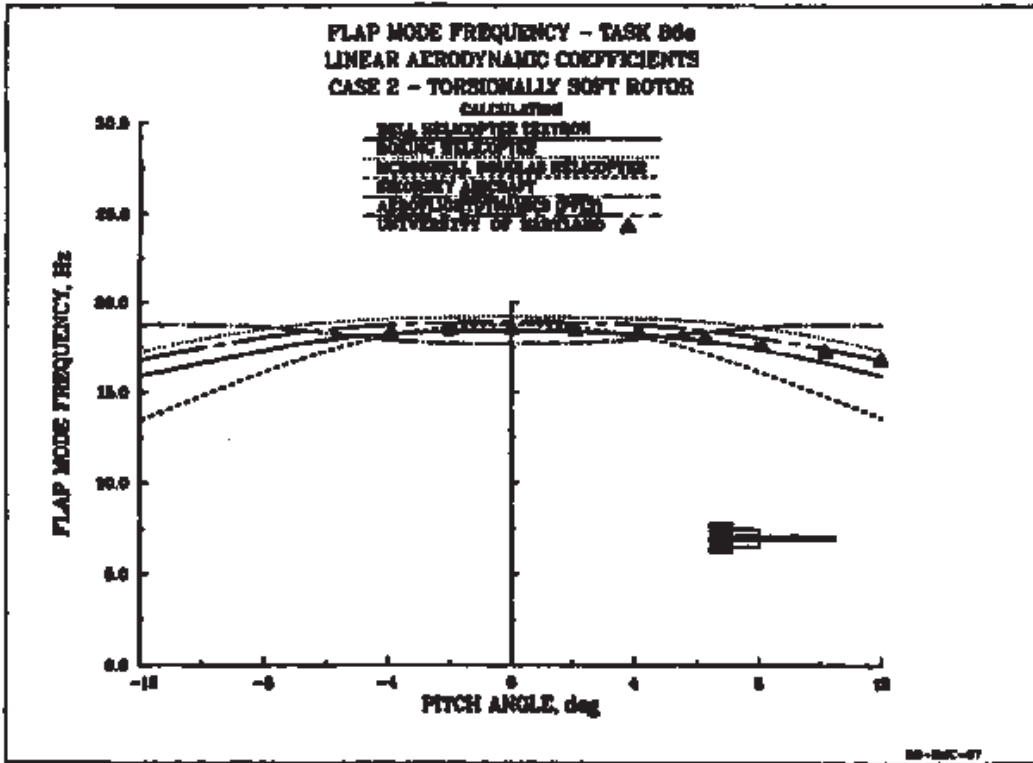
(d) Bearingless Rotors - Sivaneri and Chopra (1984), Chopra (1984), Hong and Chopra (1985), Hodges (1979).

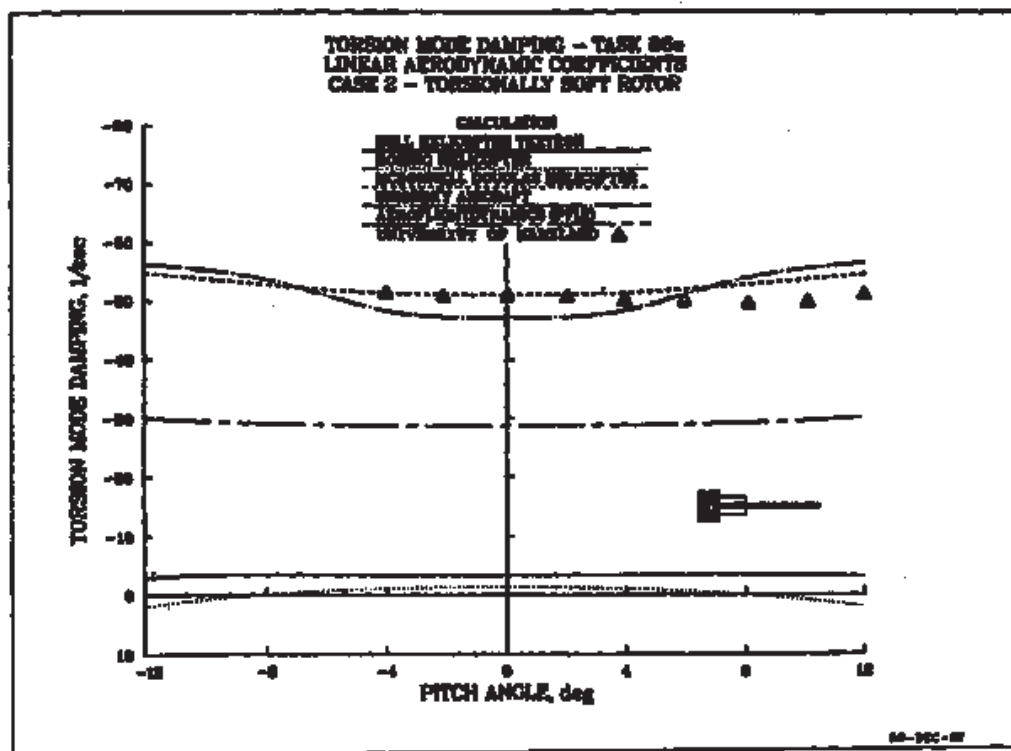
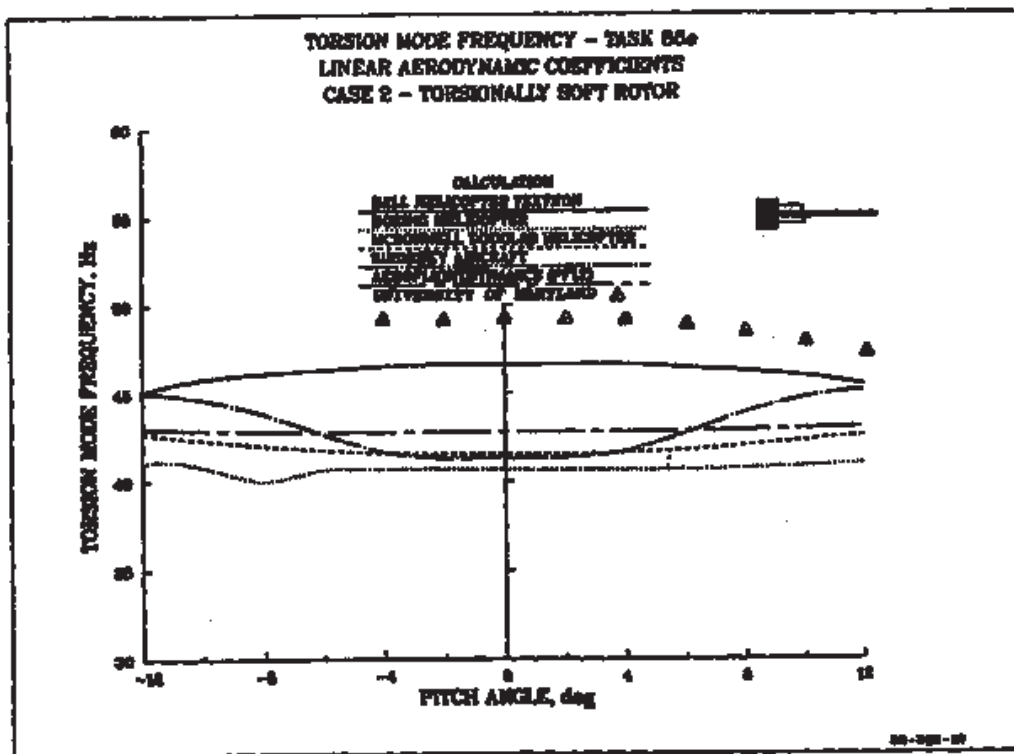
(e) Tilting Proprotor (JVX, XV-15) - Johnson (1975).

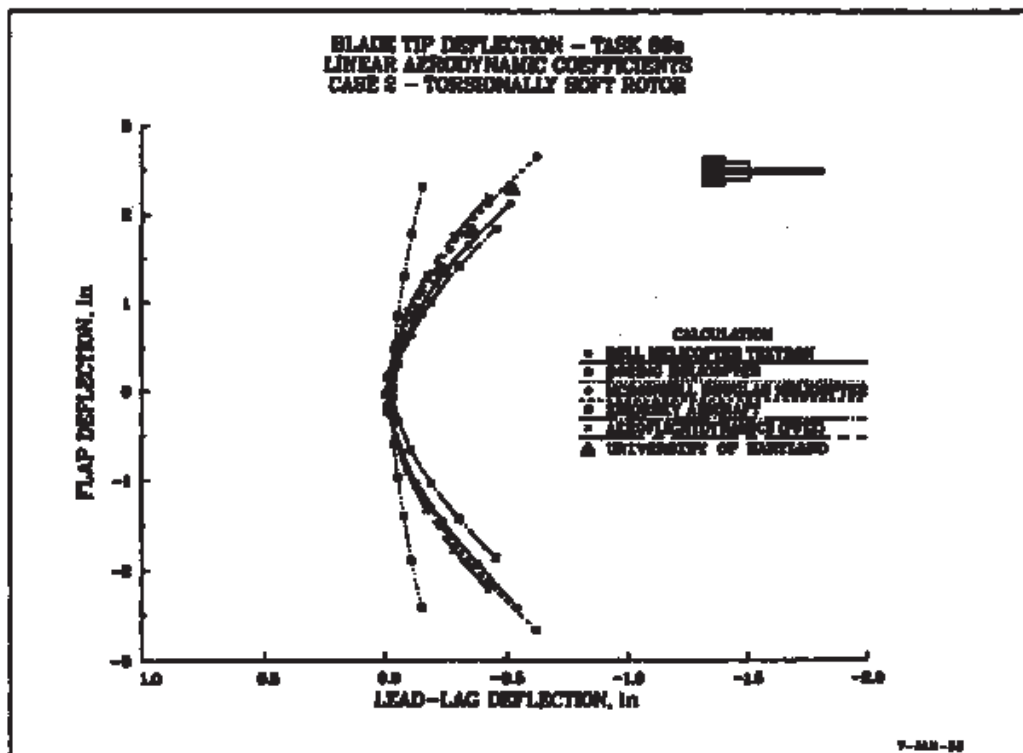
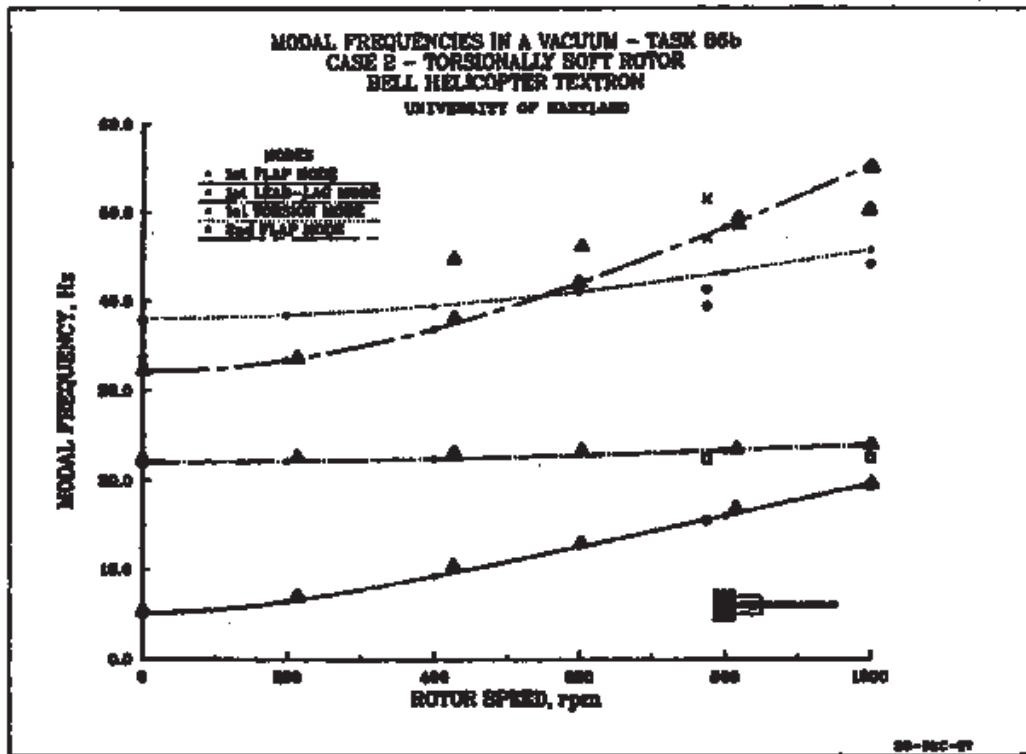
LAG DAMPING OF A HINGELESS ROTOR BLADE IN HOVER











Questions

Justify the following:

- Flutter is different from forced vibrations.

- Flap-lag flutter is a unique aeroelastic instability with rotor blades, and it has nothing to do with fixed wing.
- Flap-lag flutter is a weak instability and can be easily stabilized.
- Soft lag rotors get stabilized with a small elastic coupling.
- Pitch divergence of the blades does not depend on the elastic axis position.
- Through a simple analysis, the blade was found to be unstable from pitch-flap instability and the flutter frequency was calculated to be 18 Hz. During the hover test, the rotor model was found to be quite stable at the operating speed of 360 RPM. However, when the speed was slightly reduced, an instability appeared and the rotor started shaking violently.
- After the blade was built, the analysis showed the possibility of pitch-flap flutter. You would like to do some quick fix to the problem.
- How would you identify the wake excited flutter? Suggest ways to get rid of it.
- A great effort is made to keep the cg and the elastic axis at the quarter-chord position.
- Through a quasielastic torsion modelling, the important pitch-flap and pitch-lag terms are retained.
- The pitch divergence of the blades does not depend on the thrust level at which the rotor is being operated.

References

1. Johnson, W., *Helicopter Theory*, Princeton University Press, 1980, Chapter 12.
2. Ormiston, R.A. and Hodges, D.H., "Linear Flap-lag dynamics of hingeless helicopter rotor blades in Hover," *Journal of the American Helicopter Society*, Vol. 17, No. 2, April 1972.
3. Ham, N.D., "Helicopter Blade Flutter," AGARD Report 607, 1973.
4. Johnson, W., "Recent Developments in the Dynamics of Advanced Rotor Systems." NASA Technical Memorandum 86669, March 1985.
5. Friedmann, P., "Recent Developments in Rotary Wing Aeroelasticity," *Journal of Aircraft*, Vol. 14, No. 11, Nov. 1977, pp. 1027-1041.
6. Friedman, P., "Formulation and Solution of Rotary-wing Aeroelasticity Stability and Response Problems," *Vertica*, Vol. 7, No. 2, 1983.
7. Ormiston, R.A., "Investigation of Hingeless Rotor Stability", *Vertica*, Vol, 7, No. 2, pp. 143-181.
8. Chopra, I., "Dynamic Analysis of Constant-Lift and Free-Tip Rotors," *Journal of the American Helicopter Society*, Vol. 28, No., Jan. 1983, pp. 24-33.
9. Kaza, K.R.V., and Kvaternik, R.G., "Examination of the Flap-Lag Stability of Rigid Articulated Rotor Blades," *Journal of Aircraft*, Vol. 16, No. 12, Dec. 1979, pp. 876-884.
10. Sivaneri, N.T. and Chopra, I., "Dynamic Stability of a Rotor Blade Using Finite Element Analysis," *AIAA Journal*, Vol. 20, No. 5, May 1982, pp. 716-723.

11. Sivaneri, N.T. and Chopra, I., "Finite Element Analysis for Bearingless Rotor Blade Aeroelastic," *Journal of American Helicopter Society*, Vol. 29, No. 2, April 1984, pp. 42-51.
12. ITR Methodology Assessment Workshop" held at Ames Research Center, June 1983.
13. Chopra, I., and Johnson, W., "Flap-lag-torsion Aeroelastic Stability of Circulation Controlled Rotors," *Journal of the American Helicopter Society*, Vol. 23, No. 2, April 1979, pp.37-46.
14. Chopra, I., "Dynamic Stability of an Elastic Circulation Control Rotor Blade in Hover," *Vertica*, Dec. 1984.
15. Chopra, I., "Dynamic Stability of a Bearingless Circulation Control Rotor Blade in Hover," Presented at the Second Decennial Specialists' Meeting on Rotorcraft Dynamics at Ames Research Center, Moffett Field, Calif., Nov. 1984.
16. Hong, C.H. and Chopra, I., "Aeroelastic Stability Analysis of a Composite Blade," *Journal of American Helicopter Society*, Vol. 30, No. 2, April 1985, pp. 57-67.
17. Hong, C.H. and Chopra, I., "Aeroelastic Stability of a Composite Bearingless Rotor Blade," Presented at the International Conference on Rotorcraft Basic Research, Research Triangle Park, North Carolina, Feb. 1985.
18. Johnson, W., "Analytical Modeling Requirements for Tilting Proprotor Aircraft Dynamics," NASA TN D-8013, July 1975.
19. Hodges, D.H. and Ormiston, R.A., "Stability of Elastic Bending and Torsion of Uniform Cantilever Rotor Blades in Hover with Variable Structural Coupling," NASA TN D-8192, April 1976.
20. Hodges, D.H., "An Aeromechanical Stability Analysis for Bearingless Rotor Helicopter," *Journal of the American Helicopter Society*, Vol. 24, No. 1, Jan. 1979.

Chapter 6

Ground and Air Resonance

6.1 Ground Resonance

Ground resonance is a dynamic instability caused by the coupling of the blade lag motion and the hub inplane motion. The word resonance is used because at the instability condition one of the lag frequencies in the fixed frame becomes equal to the support frequency. It is called ground resonance because this instability takes place when the helicopter is on the ground. That is the reason that the landing gear and the supporting structure characteristics are important for this instability. It is also called mechanical instability because the aerodynamic forces do not play an important role in causing this instability. The ground resonance is a problem of soft lag rotors.

Ground resonance is a violent instability and would result in a catastrophe. A major design consideration is to avoid this instability. The selection of the operating rotor speed is made with the consideration that there is no possibility of resonance at or near this speed. The inclusion of damping in lag mode is very beneficial for this instability. This is the reason that most of the flying rotors have mechanical lag dampers near the root of the blade. This type of instability is also possible when the helicopter is in flight, then it is called air resonance. This instability is more common with hingeless blades.

6.1.1 Blade Lag Motion in Fixed Coordinates

Let us examine the Fourier coordinate transformation of blade lag motion.

$\zeta^{(m)}$ = lag motion of the m^{th} blade in rotating frame

$\zeta_o, \zeta_{nc}, \zeta_{ns}, \zeta_{N/2}$ = lag motions in fixed frame

The FCT is a linear transformation of N degrees of motion in the rotating frame to N degrees of motion in the fixed frame.

For N bladed rotor

$$\zeta_o = \frac{1}{N} \sum_{m=1}^N \zeta^{(m)}$$

$$\zeta_{nc} = \frac{2}{N} \sum_{m=1}^N \zeta^{(m)} \cos n\psi_m$$

$$\zeta_{ns} = \frac{2}{N} \sum_{m=1}^N \zeta^{(m)} \sin n\psi_m$$

$$\zeta_{N/2} = \frac{1}{N} \sum_{m=1}^N \zeta^{(m)} (-1)^m$$

and

$$\zeta^{(m)} = \zeta_o + \sum_{n=1} (\zeta_{nc} \cos n\psi_m + \zeta_{ns} \sin n\psi_m) + \zeta_{N/2} (-1)^m$$

The summation

$$\sum_n \Rightarrow \begin{matrix} n = 1 \text{ to } \frac{N-1}{2} & \text{for } N \text{ odd} \\ n = 1 \text{ to } \frac{N-2}{2} & \text{for } N \text{ even} \end{matrix}$$

and

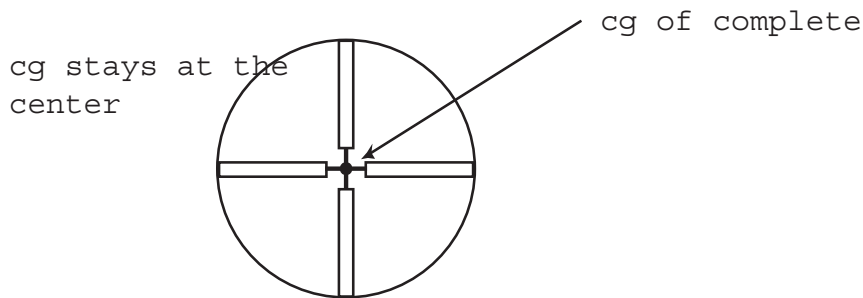
$$\begin{aligned} \psi_m &= \psi + (m - 1)\Delta\psi \quad m=1,2,\dots,N \\ \Delta\psi &= \frac{2\pi}{N} \\ \psi &= \Omega t \end{aligned} \quad \text{where } \Omega \text{ is rotational speed.}$$

Let us examine the fixed frame terms. First consider a four bladed rotor. The analysis is similar for three bladed rotors. Then consider a two bladed rotor. The analysis for two bladed rotors is distinctly different from three or higher blades.

6.1.2 Three and Four bladed Rotors

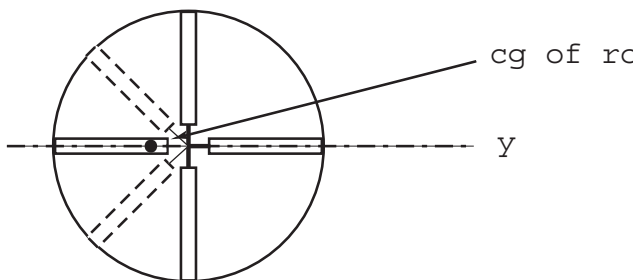
For 4-bladed rotors, N=4, there are four rigid lags in the rotating frame, one for each blade. This results in four degrees of motion in the fixed frame, i. e. , ζ_o , ζ_{lc} , ζ_{ls} , and ζ_2 .

$$\zeta^{(m)} = \zeta_o$$



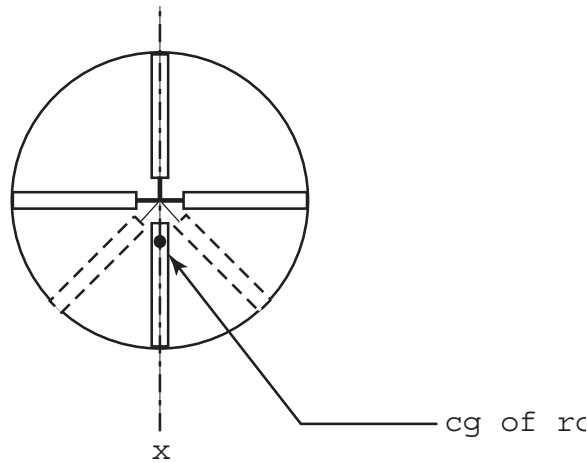
ζ_o is a collective lag motion

$$\zeta^{(m)} = \zeta_{lc} \cos \psi_m$$



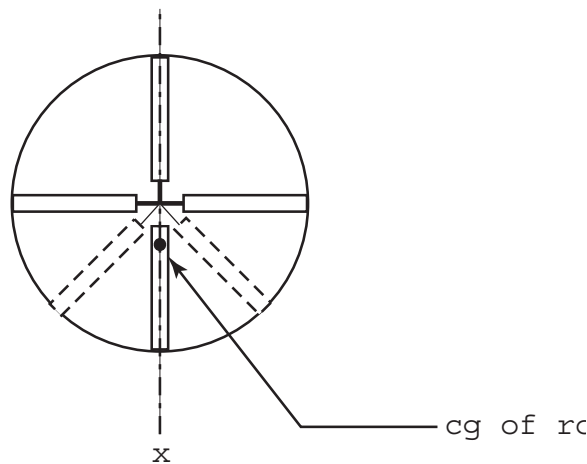
ζ_{lc} represents a lateral shift of rotor cg, in negative y directional.

$$\zeta^{(m)} = \zeta_{ls} \sin \psi_m$$



ζ_{ls} represents a longitudinal shift of rotor cg, in positive x direction.

$$\zeta^{(m)} = \zeta_2 (-1)^m$$



ζ_2 Scissoring motion, cg stays at the center.

The transformed lag motion in the fixed system can be coupled with the hub motion. The uncoupled lag equation for a blade with rigid lag is

$$I_{\zeta}(\zeta^{**} + \nu_{\zeta}^2 \zeta + C_{\zeta}^* \zeta) = \gamma \bar{M}_{\zeta}$$

The right side is the aerodynamic force which is small and its effect can be taken care of through the damping term C_{ζ}^* .

$$I_{\zeta}(\zeta^{**} + \nu_{\zeta}^2 \zeta + C_{\zeta}^* \zeta) = 0$$

Using 'FCT' for a 4-bladed rotor

$$I_{\zeta}(\zeta_o^{**} + \nu_{\zeta}^2 \zeta_o + C_{\zeta}^* \zeta_o^*) = 0$$

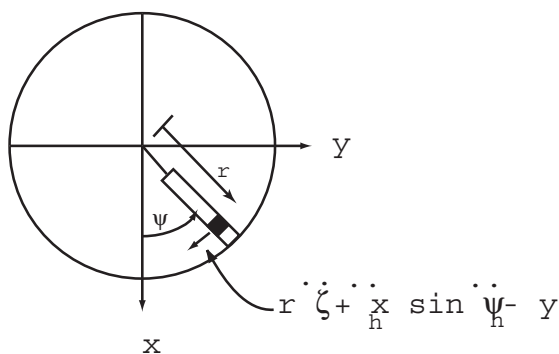
$$I_{\zeta}(\zeta_2^{**} + \nu_{\zeta}^2 \zeta_2 + C_{\zeta}^* \zeta_2^*) = 0$$

$$I_{\zeta}\{\zeta_{lc}^{**} + 2\zeta_{ls}^* - \zeta_{lc} + \nu_{\zeta}^2 \zeta_{lc} + C_{\zeta}^*(\zeta_{lc}^* + \zeta_{ls}^*)\} = 0$$

$$I_{\zeta}\{\zeta_{ls}^{**} - 2\zeta_{lc}^* - \zeta_{ls} + \nu_{\zeta}^2 \zeta_{ls} + C_{\zeta}^*(\zeta_{ls}^* - \zeta_{lc}^*)\} = 0$$

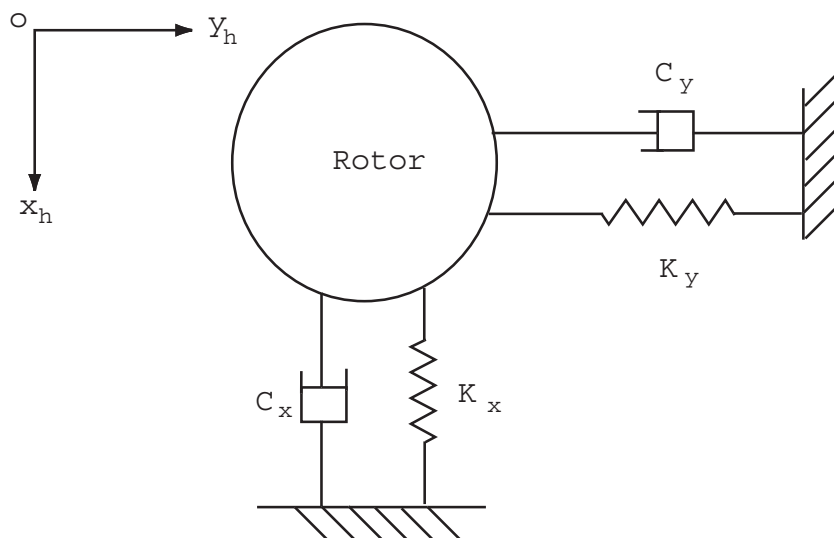
The last two equations are longitudinal and lateral inertial equations of the rotor. Now there is a hub motion of x_h and y_h superimposed on lag motion, then the blade lag equation becomes:

$$I_{\zeta}(\zeta^{**} + \nu_{\zeta}^2 \zeta + C_{\zeta}^* \zeta^*) + S_{\zeta}(\frac{\ddot{x}_h}{\Omega^2} \sin \psi - \frac{\ddot{y}_h}{\Omega^2} \cos \psi) = \gamma \overline{M}_{\zeta} I_b$$



6.1.3 Ground Resonance Equations

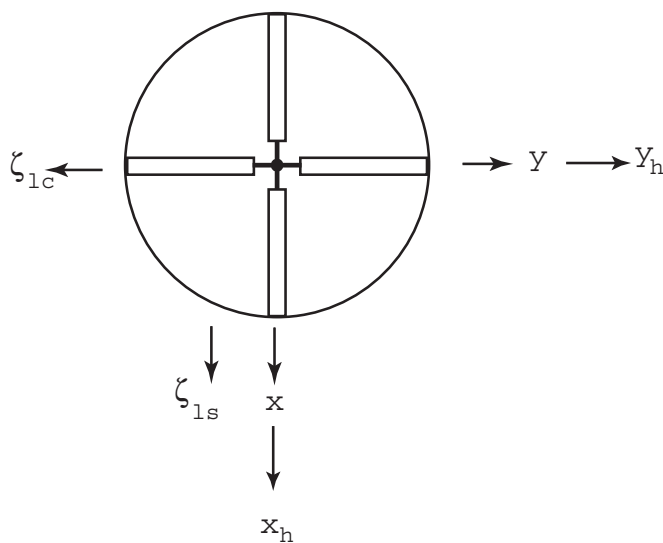
As we have seen earlier for a 4-bladed rotor that there is no shift of rotor cg with collective lag ζ_o and differential lag ζ_2 . The important lag motions are ζ_{lc} and ζ_{ls} which cause lateral and longitudinal shift of rotor cg. These motions can couple with inplane longitudinal and lateral hub motions, x_h and y_h . Therefore, a four degree of freedom model is quite useful to explain the phenomenon of ground resonance.



The equations of motion are conveniently expressed in the fixed reference frame. Neglecting the aerodynamic forces, the equations of motion for inplane rotor motion in the fixed frame are

$$I_{\zeta} \Omega^2 \{ (\zeta_{lc}^{**} + 2 \zeta_{ls}^* - \zeta_{lc}) + \nu_{\zeta}^2 \zeta_{lc} + C_{\zeta}^* (\zeta_{lc} + \zeta_{ls}) \} - S_{\zeta} \Omega^2 y_h = 0$$

$$I_{\zeta} \Omega^2 \{ (\zeta_{ls}^{**} - 2 \zeta_{lc}^* - \zeta_{ls}) + \nu_{\zeta}^2 \zeta_{ls} + C_{\zeta}^* (\zeta_{ls} - \zeta_{lc}) \} + S_{\zeta} \Omega^2 x_h = 0$$



The ν_{ζ} is the rotating lag frequency and the C_{ζ}^* is the damping coefficient in the rotating frame due to aerodynamic, structural and mechanical damping. In actuality, the nature of mechanical damping from lag and support dampers is quite nonlinear. For mathematical convenience, these dampings are represented as equivalent viscous dampings and are calculated equating the energies dissipated in one cycle of motion.

$$I_{\zeta} = \int_e^R r^2 dm \quad \text{mass moment of inertia about lag hinge}$$

$$S_{\zeta} = \int_e^R r dm \quad \text{first moment of mass about lag hinge}$$

Let us assume that M_x and M_y the effective masses of body hanging on the springs in the x and y directions respectively. The rotor forces excite the body, and the equations of motion for the body are

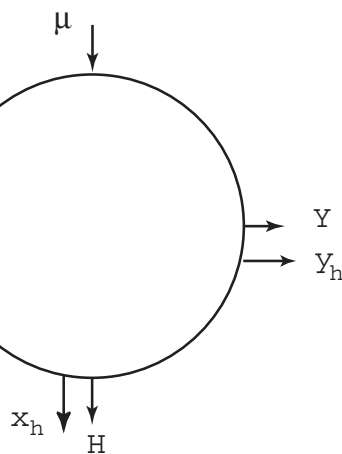
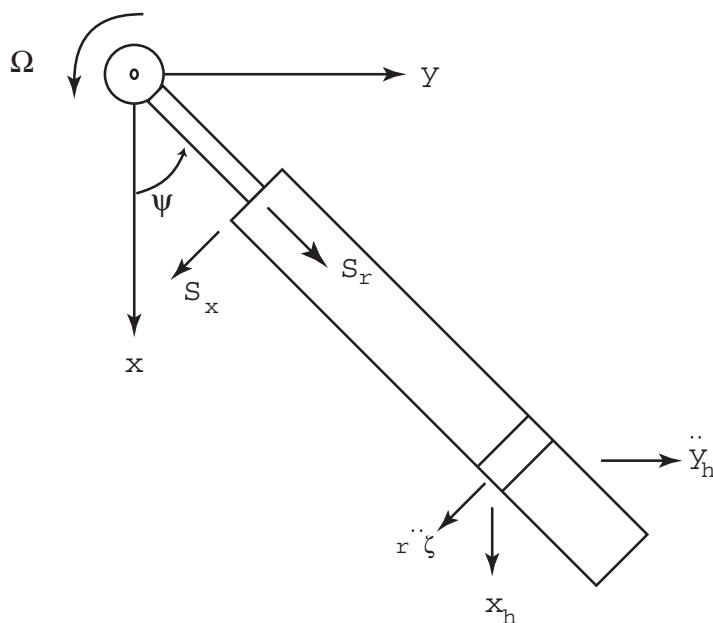
$$M_x \ddot{x}_h + k_x x_h + C_x \dot{x}_h = H$$

$$M_y \ddot{y}_h + k_y y_h + C_y \dot{y}_h = Y$$

The blade inplane forces are

$$S_r = -2\Omega \dot{\zeta} \int_e^R m r dr - (\ddot{x}_h \cos \psi + \ddot{y}_h \sin \psi) \int_e^R m dr = -2S_\zeta \Omega \dot{\zeta} - M(\ddot{x}_h \cos \psi + \ddot{y}_h \sin \psi)$$

$$\begin{aligned} S_x &= -\ddot{\zeta} \int_e^R m r dr + \Omega^2 \zeta \int_e^R m r dr - (\ddot{x}_h \sin \psi - \ddot{y}_h \cos \psi) \int_e^R m dr \\ &= -S_\zeta \ddot{\zeta} + S_\zeta \Omega^2 \zeta - M(\ddot{x}_h \sin \psi - \ddot{y}_h \cos \psi) \end{aligned}$$



where H and Y are the hub forces due to the rotor and these are expressed as

$$\begin{aligned}
 H &= \text{Total resultant drag force} = \sum_{m=1}^N (S_x \sin \psi_m + S_r \cos \psi_m) \\
 H &= \sum_{m=1}^N \sin \psi_m [-S_\zeta \ddot{\zeta}^{(m)} + M\Omega^2 \zeta^{(m)} - M(\ddot{x} \sin \psi_m - \ddot{y}_h \cos \psi_m) \\
 &\quad + \sum_{m=1}^N \cos \psi_m [-2S_\zeta \Omega \dot{\zeta}^{(m)} - M(\ddot{x}_h + \dot{y}_h \sin \psi_m)] \\
 &= -S_\zeta \Omega^2 \frac{N}{2} (\zeta_{ls}^{**} - 2\zeta_{lc}^* - \zeta_{ls}) + M\Omega^2 \frac{N}{2} \zeta_{ls} - M\ddot{x}_h \frac{N}{2} \\
 &\quad - 2S_\zeta \Omega^2 \frac{N}{2} (\zeta_{lc}^* + \zeta_{ls}) - M\ddot{x}_h \frac{N}{2} \\
 &= -S_\zeta \Omega^2 \frac{N}{2} \zeta_{ls}^{**} - NM_b \ddot{x}_h \\
 &= -\frac{N}{2} S_\zeta \ddot{\zeta}_{ls} - NM_b \ddot{x}_h
 \end{aligned}$$

Y = Total Edge Force

$$\begin{aligned}
 Y &= \sum_{m=1}^N (-S_x \cos \psi_m + S_r \sin \psi_m) \\
 &= \sum_{m=1}^N -\cos \psi_m [S_\zeta \ddot{\zeta}^{(m)} + M\Omega^2 \zeta^{(m)} - M(\ddot{x}_h \sin \psi_m - \ddot{y}_h \cos \psi_m)] \\
 &\quad + \sum_{m=1}^N \sin \psi_m [-2S_\zeta \Omega \dot{\zeta}^{(m)} - M(\ddot{x}_h \cos \psi_m - \dot{y}_h \sin \psi_m)] \\
 &= S_\zeta \Omega^2 \frac{N}{2} (\zeta_{lc}^{**} + 2\zeta_{ls}^* - \zeta_{lc}) - M\Omega^2 \frac{N}{2} \zeta_{lc} - M\dot{y}_h \frac{N}{2} \\
 &\quad - 2S_\zeta \Omega^2 \frac{N}{2} (\zeta_{ls}^* - \zeta_{lc}) - M\dot{y}_h \frac{N}{2} \\
 &= S_\zeta \Omega^2 \frac{N}{2} \zeta_{lc}^{**} - M_b N \dot{y}_h
 \end{aligned}$$

where N is the number of blades and M_b is the total blade mass. The C_x and C_y are the damping coefficients of the supporting structure.

The body equations can be rewritten as

$$\ddot{x}_h (M_x + NM_b) + C_x \dot{x}_h + k_x x_h + \frac{N}{2} S_\zeta \ddot{\zeta}_{ls} = 0$$

$$\ddot{y}_h (M_y + NM_b) + C_y \dot{y}_h + k_y y_h - \frac{N}{2} S_\zeta \ddot{\zeta}_{lc} = 0$$

Imagine that there are no coupling terms, then one can calculate natural frequencies of support as

$$\omega_x^2 = \frac{k_x}{M_x + NM_b}$$

$$\omega_y^2 = \frac{k_y}{M_y + NM_b}$$

Also, defining

$$C_x^* = \frac{C_x}{\Omega(M_x + NM_b)}$$

$$C_y^* = \frac{C_y}{\Omega(M_y + NM_b)}$$

The equations of motion expressed in nondimensional form

$$\begin{bmatrix} 1.0 & 0 & 0 & -S_\zeta^* \\ 0 & 1.0 & S_\zeta^* & 0 \\ 0 & \frac{1}{2} \frac{S_\zeta^*}{M_x^*} & 1 & 0 \\ \frac{1}{2} \frac{S_\zeta^*}{M_y^*} & 0 & 0 & 1 \end{bmatrix} \begin{bmatrix} \zeta_{lc} \\ \zeta_{ls} \\ x_h \\ y_h \end{bmatrix} + \begin{bmatrix} C_\zeta^* & 2 & 0 & 0 \\ -2 & C_\zeta^* & 0 & 0 \\ 0 & 0 & C_x^* & 0 \\ 0 & 0 & 0 & C_y^* \end{bmatrix} \begin{bmatrix} \zeta_{lc} \\ \zeta_{ls} \\ x_h \\ y_h \end{bmatrix} + \begin{bmatrix} \nu_\zeta^2 - 1 & C_\zeta^* & 0 & 0 \\ -C_\zeta^* & \nu_\zeta^2 - 1 & 0 & 0 \\ 0 & 0 & \frac{\omega_x^2}{\Omega^2} & 0 \\ 0 & 0 & 0 & \frac{\omega_y^2}{\Omega^2} \end{bmatrix} \begin{bmatrix} \zeta_{lc} \\ \zeta_{ls} \\ x_h \\ y_h \end{bmatrix} = 0$$

where

$$\begin{aligned} S_\zeta^* &= \frac{RS_\zeta}{I_\zeta} \cong \frac{RS_\zeta}{I_b} \\ &= \frac{3}{2} \text{ for uniform blades} \\ &\quad I_b \text{ is blade inertia} = M_b \frac{R^2}{3} \text{ for uniform blade} \\ M_x^* &= \frac{(M_x + NM_b)R^2}{NI_b} \\ &= 3 \left(\frac{M_x}{NM_b} + 1 \right) \text{ for uniform blades} \\ M_y^* &= \frac{(M_y + NM_b)R^2}{NI_b} \\ &= 3 \left(\frac{M_y}{NM_b} + 1 \right) \text{ for uniform blades} \\ NM_b &= \text{Total rotor mass} \end{aligned}$$

For uniform blades

$$\frac{S_\zeta^*}{M_x^*} = \frac{1}{2 \left(\frac{M_x}{NM_b} + 1 \right)} \cong \frac{1}{2} \frac{\text{Rotor mass}}{\text{Support mass}} \quad (\text{Support mass} = M_y + NM_b)$$

$$\frac{S_\zeta^*}{M_y^*} = \frac{1}{2 \left(\frac{M_y}{NM_b} + 1 \right)} \cong \frac{1}{2} \frac{\text{Rotor mass}}{\text{Support mass}}$$

The support mass is much larger than the rotor mass. In the above equations, the hub displacement x_h and y_h are also nondimensional with respect to rotor radius R .

$$\begin{aligned} \bar{x}_h &= \frac{x_h}{R} \\ \bar{y}_h &= \frac{y_h}{R} \end{aligned}$$

The governing equations are four second order differential equations. These can be solved either through determinate expansion or through the eigen analysis. Let us examine the first approach of determinate expansion. The stability determinant is

$$\begin{vmatrix} (s^2 + C_\zeta^* s + \nu_\zeta^2 - 1) & (2s + C_\zeta^*) & 0 & -s_\zeta^* s^2 \\ -(2s + C_\zeta^*) & (s^2 + C_\zeta^* s + \nu_\zeta^2 - 1) & s_\zeta^* s^2 & 0 \\ 0 & (\frac{1}{2} \frac{s_\zeta^*}{M_\zeta^*}) s^2 & (s^2 + C_x^* s + \frac{\omega_x^2}{\Omega^2}) & 0 \\ -(\frac{1}{2} \frac{s_\zeta^*}{M_\zeta^*}) s^2 & 0 & 0 & (s^2 + C_\zeta^* s + \nu_\zeta^2 - 1) \end{vmatrix} = 0$$

This is an eighth order polynomial. The solution gives eight eigenvalues, which means four complex conjugate pairs. From the physics, the divergence instability is not possible. The ground resonance is a dynamic instability where one of the modes becomes unstable, i.e., zero damping condition.

For divergence stability

$$[(\nu_\zeta^2 - 1)^2 + C_\zeta^{*2}] (\frac{\omega_x}{\Omega})^2 (\frac{\omega_y}{\Omega})^2 > 0$$

This is always satisfied. Let us first consider the uncoupled dynamics, obtained by setting S_ζ^* equal to zero. The blade lag motion is damped and its eigenvalue in the rotating frame is

$$s_R = -\frac{C_\zeta^*}{2} \pm i \sqrt{\nu_\zeta^2 - \left(\frac{C_\zeta^*}{2}\right)^2}$$

and in the fixed frame, the eigenvalue is

$$s = s_R \pm i \quad (n = 1)$$

This consists of two types of modes

(a) High frequency mode $s = s_R + i$
Frequency = $I_m s_R + 1$ per rev.

Frequency of oscillation is always greater than the rotational speed, and corresponds to a progressive whirling motion of the rotor cg.

(b) Low frequency mode $s = s_R - i$
Frequency = $I_m s_R - 1$ per rev.

There are two possibilities. For stiff lag rotors ($I_m s_R > 1$), it results into a regressive whirling motion of the rotor cg at a frequency of $(I_m s_R - 1)$ per rev. For soft lag rotors ($I_m s_R < 1$), it results into a progressive whirling mode of the rotor cg at a frequency of $(1 - I_m s_R)$ per rev. The last possibility is a typical example of an articulated rotor.

Let us examine the uncoupled inplane support eigenvalues in x and y directions.

$$s = -\frac{C_x^*}{2} \pm i \sqrt{\left(\frac{\omega_x}{\Omega}\right)^2 - \left(\frac{C_x^*}{2}\right)^2}$$

$$s = -\frac{C_y^*}{2} \pm i \sqrt{\left(\frac{\omega_y}{\Omega}\right)^2 - \left(\frac{C_y^*}{2}\right)^2}$$

These are two complex conjugate pairs in the fixed reference frame. In total, these are four conjugate pairs. Looking at the real parts, one finds that the uncoupled rotor and support motion is stable. Therefore, the ground resonance instability is a possibility due to inertial coupling s_ζ^* .

For a configuration with zero damping and zero inertial coupling, there are four frequencies, high frequency lag $\nu_\zeta + 1$, low frequency lag $1 - \nu_\zeta$, longitudinal support frequency ω_x and lateral support frequency ω_y . With the inclusion of coupling terms, the different modes coalesce resulting in instability. This is a dynamic instability and is of catastrophic type.

In the first figure the Coleman diagram is plotted for an articulated rotor with soft inplane frequency. The Coleman diagram consists of a plot of dimensional frequencies as a function of rotational speed. The frequencies corresponding to different modes in the fixed frame are obtained either from the eigen-solutions or from the roots of the eighth order polynomial. The following data is used for calculations.

$$\begin{aligned} S_\zeta^* &= 1.5 & C_\zeta^* &= C_x^* = C_y^* = 0 \\ M_x^* &= 68.175 & M_y^* &= 29.708 \\ \nu_\zeta &= .285/\text{rev} & \omega_x &= 12.148 \text{ rad/sec}, \omega_y = 18.402 \text{ rad/sec} \end{aligned}$$

There are two instability bands, caused by coalescence of rotor and body modes. For a stable condition, there are four distinct eigenvalues. For an unstable condition, two frequencies merge resulting in three distinct eigenvalues. Also the real part of the eigenvalue which represents damping of the mode becomes positive. In the next figure, the damping ratio of the unstable mode is presented. The value of damping ratio of 0.1 is quite large and represents violent instability. This also shows that a large lag damping is required to stabilize this instability.

In the next figure, the Coleman diagram is plotted for an articulated rotor with stiff inplane frequency. The following data are used for calculations.

$$\begin{aligned} S_\zeta^* &= 3.19 & C_\zeta^* &= C_x^* = C_y^* = 0 \\ M_x^* &= 178.77 & M_y^* &= 77.902 \\ \nu_\zeta &= 1.3/\text{rev} & \omega_x &= 12.148 \text{ rad/sec}, \omega_y = 18.402 \text{ rad/sec} \end{aligned}$$

There is no instability condition for stiff inplane rotors.
For a case of no-damping

$$C_\zeta^* = C_x^* = C_y^* = 0$$

The stability determinant becomes

$$\begin{vmatrix} s^2 + \nu_\zeta^2 - 1 & 2s & 0 & -s_\zeta^* s^2 \\ -2s & s^2 + \nu_\zeta^2 - 1 & s_\zeta^* s^2 & 0 \\ 0 & \frac{1}{2} \left(\frac{s_\zeta^*}{M_x^*} \right) s^2 & s^2 + \frac{\omega_x^2}{\Omega^2} & 0 \\ -\frac{1}{2} \left(\frac{s_\zeta^*}{M_y^*} \right) s^2 & 0 & 0 & s^2 + \frac{\omega_y^2}{\Omega^2} \end{vmatrix} = 0$$

This gives

$$\begin{aligned} & [(s^2 + \nu_\zeta^2 - 1)^2 + 4s^2] (s^2 + \frac{\omega_x^2}{\Omega^2}) (s^2 + \frac{\omega_y^2}{\Omega^2}) - (s^2 + \nu_\zeta^2 - 1) \frac{s_\zeta^{*2}}{M_x^* M_y^*} \\ & \times s^4 [M_y^* (s^2 + \omega_y^2) + M_x^* (s^2 + \omega_x^2)] + \frac{s_\zeta^{*4}}{M_x^* M_y^*} s^8 = 0 \end{aligned}$$

The critical condition of zero system damping can be calculated by substituting $s = i\omega$ in the above equation. The numerical solution of the polynomial represents the boundary line between stable and unstable conditions.

Deutsch Stability Criteria

Using an approximate stability criteria, a simple expression for damping required to stabilize ground resonance is obtained.

Longitudinal mode:

Assumed $\frac{\omega}{\Omega} \cong \frac{\omega_x}{\Omega} = 1 - \nu_\zeta$ and $\omega_x \neq \omega_y$ For stability

$$C_\zeta^* C_x^* > \frac{(1 - \nu_\zeta)}{4\nu_\zeta} \left(\frac{\omega_x}{\Omega}\right)^2 \frac{s_\zeta^{*2}}{M_x^*}$$

Lateral mode:

Assumed $\frac{\omega}{\Omega} \cong \frac{\omega_y}{\Omega} = 1 - \nu_\zeta$ and $\omega_x \neq \omega_y$ For stability

$$C_\zeta^* C_y^* > \frac{(1 - \nu_\zeta)}{4\nu_\zeta} \left(\frac{\omega_y}{\Omega}\right)^2 \frac{s_\zeta^{*2}}{M_y^*}$$

For a stiff-lag rotor, ($\nu_\zeta > 1$), the right hand side is negative and the system is always stable. For a soft-lag rotor, ($\nu_\zeta < 1$), the product of lag damping and support damping must be greater than the critical values given above for longitudinal and lateral modes. A larger lag damping is required for

- (a) small lag frequency (typical of articulated rotors)
- (b) large support frequency (ω_x or ω_y)
- (c) large inertial coupling s_ζ^{*2}/M_x^* or s_ζ^{*2}/M_y^* ($\cong \frac{3}{4} \frac{\text{rotor mass}}{\text{support mass}}$)

For an isotropic support condition ($\omega_x = \omega_y$). For stability

$$C_\zeta^* C_y^* > \frac{(1 - \nu_\zeta)}{2\nu_\zeta} \left(\frac{\omega_y}{\Omega}\right)^2 \frac{s_\zeta^{*2}}{M_y^*}$$

One requires twice the damping needed for an anisotropic case ($\omega_x \neq \omega_y$). This is because the longitudinal and lateral support frequencies become equal resulting in the whirling motion of the hub which couples well with the whirling motion of the low-frequency lag mode.

Ex. The shake test was performed on the helicopter on its landing gear and the natural frequencies were obtained as 1.2 and 1.8 Hz respectively in longitudinal and lateral directions. The damping ratios were calculated as 2% of critical value for both the modes. The helicopter rotor was four-bladed, articulated with 6% hinge offset. The blades are uniform and form about 10% of the total weight. You would like to check whether the rotor is stable from ground resonance at an operating speed of 360 RPM. Write the stability equation in the form of determinant.

$$\omega = 6\text{Hz}$$

$$\omega_x = \frac{1.2}{6} = .2/\text{rev}$$

$$\omega_y = \frac{1.8}{6} = .3/\text{rev}$$

$$\zeta_x = \zeta_x = .02$$

$$C_x^* = 2\zeta_x\omega_x = .008$$

$$C_y^* = 2\zeta_y\omega_y = .012$$

$$\nu_\zeta^2 = .09 \qquad \nu_\zeta = .3$$

$$I_\zeta^* = 1$$

$$s_\zeta = \frac{mR^2}{2} \qquad I_b = \frac{mR^3}{3} \qquad s_\zeta^* = \frac{3}{2}$$

$$M_x^* = \frac{R^2(M_x + NM_b)}{NI_b} = \frac{M_x + NM_b}{NM_b\frac{1}{3}} = 30 = M_y^*$$

Stability determinant

$$\begin{vmatrix} s^2 + .09 - 1 & 2s & 0 & -\frac{3}{2}s^2 \\ -2s & s^2 + .09 - 1 & \frac{3}{2}s^2 & 0 \\ 0 & \frac{3}{2}s^2 & 60(s^2 + .008s + .04) & 0 \\ -\frac{3}{2}s^2 & 0 & 0 & 60(s^2 + .012s + .09) \end{vmatrix} = 0$$

Expansion of the determinant will give 8th order polynomial. Solution will be 4 complex conjugate pairs. Nature of the roots tells us whether the system is stable or not.

6.2 Ground Resonance of Two-Bladed Rotors

Let us consider the ground resonance stability of a two-bladed rotor. Again, assume the rotor is fully tracked and the blade undergoes lag degree of motion.

Rotating frame:

$$\zeta^{(1)} = \text{lag motion of blade 1}$$

$$\zeta^{(2)} = \text{lag motion of blade 2}$$

Fixed frame:

$$\begin{aligned} \zeta_o &= \text{collective lag motion} \\ &= \frac{1}{2} (\zeta^{(2)} + \zeta^{(1)}) \end{aligned}$$

$$\begin{aligned} \zeta_1 &= \text{differential collective lag motion} \\ &= \frac{1}{2} (\zeta^{(2)} - \zeta^{(1)}) \end{aligned}$$

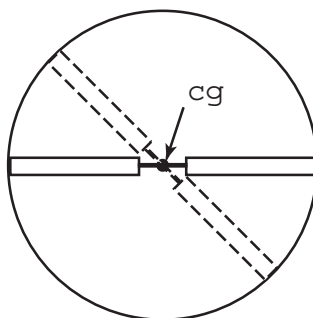
Also,

$$\zeta^{(1)} = \zeta_o - \zeta_1$$

$$\zeta^{(2)} = \zeta_o + \zeta_1$$

Let us examine the influence of lag motion on rotor cg.

ζ_o motion cg stays at center



ζ_1 motion Assuming

$$\zeta^{(1)} = \zeta_o - \zeta_{lc} \cos \psi - \zeta_{ls} \sin \psi$$

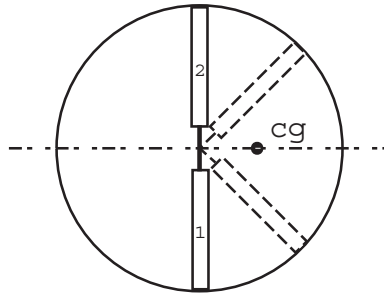
$$\zeta^{(2)} = \zeta_o + \zeta_{lc} \cos \psi + \zeta_{ls} \sin \psi$$

This gives

$$\zeta_1 = \zeta_{lc} \cos \psi + \zeta_{ls} \sin \psi$$

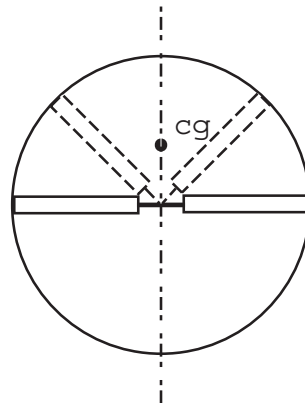
Two cases.

(a) $\zeta_1 = \zeta_{lc} \cos \psi$



A lateral shift of rotor cg in positive x-direction.

(b) $\zeta_1 = \zeta_{ls} \sin \psi$



A longitudinal shift of cg in negative x-direction.

Therefore, the differential collective lag motion ζ_1 coupled with support motion to cause ground resonance instability for the 2-bladed rotor.

The uncoupled lag equations for blades in the rotating frame are

$$\zeta^{*(1)} + C_{\zeta}^* \zeta^{*(1)} + \nu_{\zeta}^2 \zeta^{(1)} = 0$$

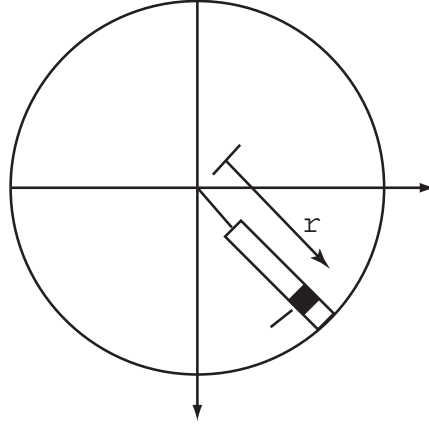
$$\zeta^{*(2)} + C_{\zeta}^* \zeta^{*(2)} + \nu_{\zeta}^2 \zeta^{(2)} = 0$$

Transformed rotor equations in fixed frame are

$$\zeta_o^{**} + C_{\zeta}^* \zeta_o^* + \nu_{\zeta}^2 \zeta_o = 0$$

$$\zeta_1^{**} + C_{\zeta}^* \zeta_1^* + \nu_{\zeta}^2 \zeta_1 = 0$$

Now, if there is a hub motion of x_h and y_h superimposed on lag motion, the lag equations become



$$I_{\zeta}(\ddot{\zeta}^{**} + C_{\zeta}^* \dot{\zeta}^{*(2)} + \nu_{\zeta}^2 \zeta^{(2)}) + S_{\zeta}(\ddot{x}_h \sin \psi - \ddot{y}_h \cos \psi) = 0$$

$$I_{\zeta}(\ddot{\zeta}^{**} + C_{\zeta}^* \dot{\zeta}^{*(1)} + \nu_{\zeta}^2 \zeta^{(1)}) - S_{\zeta}(\ddot{x}_h \sin \psi - \ddot{y}_h \cos \psi) = 0$$

and the rotor equations become

$$\ddot{\zeta}_o + C_{\zeta}^* \dot{\zeta}_o + \nu_{\zeta}^2 \zeta_o = 0$$

$$I_{\zeta}(\ddot{\zeta}_1 + C_{\zeta}^* \dot{\zeta}_1 + \nu_{\zeta}^2 \zeta_1) + S_{\zeta}(\ddot{x}_h \sin \psi - \ddot{y}_h \cos \psi) = 0$$

The first collective lag equation is unaffected by hub motion. The differential collective equation however gets modified with the hub motion. Again, assuming vehicle is supported by two sets of springs and dampers represented by k_x , C_x , k_y , C_y . The body equations of motion are

$$M_x \ddot{x}_h + C \dot{x}_h + k_x x_h = H$$

$$M_y \ddot{y}_h + C \dot{y}_h + k_y y_h = Y$$

The inplane hub forces H and Y are obtained from blade shear forces

$$S_r = -2\Omega \dot{\zeta} S_{\zeta} - M_b(\ddot{x}_h \cos \psi + \ddot{y}_h \sin \psi)$$

$$S_x = S_{\zeta}(\Omega^2 \zeta - \ddot{\zeta}) - M_b(\ddot{x}_h \sin \psi - \ddot{y}_h \cos \psi)$$

and

$$\begin{aligned} H &= \sum_{m=1}^2 (S_x^{(m)} \sin \psi_m + S_r^{(m)} \cos \psi_m) \\ &= -2M_b \ddot{x}_h + 2S_{\zeta}[(\Omega^2 \zeta_1 - \ddot{\zeta}_1) \sin \psi - 2\Omega \dot{\zeta}_1 \cos \psi] \\ Y &= \sum_{m=1}^2 (-S_x^{(m)} \cos \psi_m + S_r^{(m)} \sin \psi_m) \\ &= -2M_b \ddot{y}_h + 2S_{\zeta}[(\ddot{\zeta}_1 - \Omega^2 \zeta_1) \cos \psi - 2\Omega \dot{\zeta}_1 \sin \psi] \end{aligned}$$

Again using the previous definitions, the coupled rotor-body equations for a two-bladed rotor can be written as

$$\begin{bmatrix} 1.0 & S_\zeta^* \sin \psi & -S_\zeta^* \cos \psi \\ \frac{S_\zeta^*}{M_\zeta^*} \sin \psi & 1.0 & 0 \\ -\frac{S_\zeta^*}{M_\zeta^*} \cos \psi & 0 & 1.0 \end{bmatrix} \begin{bmatrix} \zeta_1^{**} \\ x_h^{**} \\ y_h^{**} \end{bmatrix} + \begin{bmatrix} C_\zeta^* & 0 & 0 \\ 2\frac{S_\zeta^*}{M_x^*} \cos \psi & C_x^* & 0 \\ 2\frac{S_\zeta^*}{M_y^*} \sin \psi & 0 & C_y^* \end{bmatrix} \begin{bmatrix} \zeta_1^* \\ x_h^* \\ y_h^* \end{bmatrix} \\ + \begin{bmatrix} \nu_\zeta^2 & 0 & 0 \\ -\frac{S_\zeta^*}{M_x^*} \sin \psi & \frac{\omega_x^2}{\Omega^2} & 0 \\ \frac{S_\zeta^*}{M_y^*} \cos \psi & 0 & \frac{\omega_y^2}{\Omega^2} \end{bmatrix} \begin{bmatrix} \zeta_1 \\ x_h \\ y_h \end{bmatrix} = 0$$

These are three second order differential equations and can be solved either through determinant expansion or through the eigen-analysis.

6.3 Air Resonance

An air resonance is similar to ground resonance but occurs on an airborne vehicle. It is caused by coupling of low frequency blade flap and lag modes and rigid body airframe modes. Aerodynamic forces are needed to determine this instability. Air resonance is primarily a problem for soft-inplane hingeless and bearingless rotors.

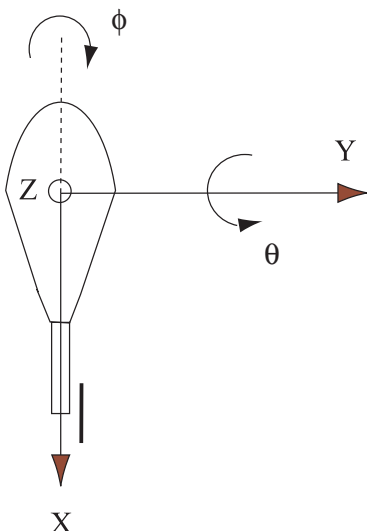
In general, hingeless and bearingless aeromechanical stability is more difficult to predict compared to articulated rotors. The frequencies of rotor flap coupled with body angular motions coalesce with the rotor lag frequency. Due to the presence of the flap motion, aerodynamic forces become important. For hingeless and bearingless rotors, flap, lag, and torsion can be highly coupled, and the torsion motion can affect ground and air resonance. The damping and frequency characteristics of coupled hingeless rotor-body modes often make the associated instabilities a mild phenomena.

Compared to ground resonance, where the body modes are relatively clear, in air resonance they are more complex. In ground resonance the body modes are determined by the rotor-body mass reacting against the fixed ground. In air resonance there is ofcourse no fixed ground against which the rotor-body mass can react. Here, the body modes are the fundamental free-free modes of the rotor-body reacting against each other through the interposed blade flap spring (mechanical or virtual) stiffness. Hence the body modes are determined by the flap spring stiffness, rotor inertia, body inertia, and rotor aerodynamics. The modes and frequencies are not well defined and show great variety from one rotor to another. The coalescences are also more obscure.

The basic mechanism of air resonance involves flap, lag, body pitch and body roll motions. For a simple analysis, blades are assumed rigid and undergo flap and lag motions about hinges. The body is also assumed rigid and undergoes pitch and roll motion about the body center of gravity. Body translation degrees of freedom are not included since they do not significantly influence air resonance stability. Let us study the behavior of the isolated modes in a step-wise manner.

The body pitch and roll degrees of freedom are shown in Fig. 6.1. If I_Y is the fuselage (or body) mass moment of inertia about the pitch axis, M_F is the fuselage mass, then the square of the body mass radius of gyration about the pitch axis, nondimensionalized with the square of the rotor radius, is given by

$$K_y^2 = \frac{M_F}{I_Y R^2}$$

Figure 6.1: **Body pitch and roll degrees of freedom**

Similarly the square of the body mass radius of gyration about the roll axis, nondimensionalized with the square of the rotor radius, is given by

$$K_x^2 = \frac{M_F}{I_x R^2}$$

Typical values are

$$K_y^2 = \frac{\text{square of body mass radius of gyration}}{R^2} \approx 0.1 \text{ to } 0.4$$

$$K_x^2 \approx 0.025$$

The body pitch and roll frequencies, nondimensionalized with respect to the operating rotational speed Ω_0 typically varies between

$$\text{body pitch frequency} = \bar{\omega}_\theta = 0 \text{ to } 0.8/\text{rev}$$

$$\text{body roll frequency} = \bar{\omega}_\phi = 0 \text{ to } 0.4/\text{rev}$$

The mass ratio and distance of rotor hub above the rotor-body c.g. are typically

$$\frac{\text{rotor mass}}{\text{total mass}} = 0.1$$

$$\frac{h}{R} = 0.2$$

The characteristic plots shown in the subsequent sections correspond to the following values, where applicable.

$$\nu_\zeta = 0.7/\text{rev}$$

$$\nu_\beta = 1.1/\text{rev}$$

$$\gamma = 5 - -15$$

$$\sigma = 0.05$$

$$c_{l\alpha} = 5.73$$

$$c_{d0} = 0.01$$

The lag and flap frequencies above are typical values for soft inplane hingeless rotors.

6.3.1 Body Pitch and Roll with a Rigid Spinning Rotor

Consider a two degree of freedom system, as shown in Fig. 6.1, with body pitch and roll modes. Consider a spinning rotor attached at the top. When the rotor is rigid, i.e. has no flapping, the frequencies in vacuum represent those of a 2 degree of freedom gyroscope. The four eigenvalues of the system are

$$\eta = 0, 0, \pm j \frac{\Omega J}{\sqrt{I_\theta I_\phi}}$$

The zeroes represent the unconstrained rigid body pitch and roll motions. The imaginary pairs are the well known nutation frequency of a gyroscope. I_θ and I_ϕ are the rotor-body pitch and roll inertia about the rotor-body center of mass.

$$I_\theta = I_y + \frac{1}{2} N_b I_b + 3 N_b I_b h^2$$

$$I_\phi = I_x + \frac{1}{2} N_b I_b + 3 N_b I_b h^2$$

$$J = \text{rotor polar mass moment of inertia} = N_b I_b$$

If the body vanishes, we have

$$I_\theta = I_\phi = \frac{1}{2} N_b I_b$$

and

$$\eta = 0, 0, \pm j 2\Omega$$

A well known result, where the gyroscopic nutation frequency is twice the rotational speed. The above results were in vacuum. In air, the spinning rigid rotor acts as a damper and the four eigenvalues of the system become

$$\eta = 0, 0, \sigma \pm j\omega$$

where

$$\begin{aligned} \sigma &= - \left(\frac{I_\theta + I_\phi}{I_\theta I_\phi} \right) \frac{J\gamma}{32} \Omega \\ \omega &= \frac{\Omega J}{\sqrt{I_\theta I_\phi}} \sqrt{1 + \left(\frac{\gamma}{16} \right)^2 \left[\frac{1}{2} - \frac{1}{4} \left(\frac{I_\theta}{I_\phi} + \frac{I_\phi}{I_\theta} \right) \right]} \end{aligned} \quad (6.1)$$

I_θ is greater than I_ϕ , hence the term associated with $(\gamma/16)^2$ in the expression for frequency is negative. For very high values of γ , the frequency can become imaginary and produce two real eigenvalues.

6.3.2 Rotor Flap and Lag

Consider the flapping motion in the rotating frame. Assuming an offset e/R and non-rotating frequency of $\omega_{\beta 0}$ rad/s, and rotational speed Ω , the rotating flap frequency ν_β is given by

$$\nu_\beta^2 = 1 + \frac{3}{2} \frac{e}{R} + \frac{\omega_{\beta 0}^2}{\Omega^2}$$

Another useful way of writing the frequency expression is to first denote the flap frequency at the operating RPM as p . That is

$$p^2 = 1 + \frac{3e}{2R} + \frac{\omega_{\beta 0}^2}{\Omega_0^2}$$

Then

$$\omega_{\beta 0}^2 = \left(p^2 - 1 - \frac{3e}{2R} \right) \Omega_0^2$$

The rotating flap frequency expression can now be written as

$$\nu_{\beta}^2 = 1 + \left(p^2 - 1 - \frac{3e}{2R} \right) \frac{\Omega_0^2}{\Omega^2}$$

where the flap frequency at the operating RPM, p , occurs explicitly. We shall drop the term $3e/2R$ at this point, as it adds no new physics, inclusion of this term by interested readers will be straight-forward. Thus we have

$$\nu_{\beta}^2 = 1 + (p^2 - 1) \frac{\Omega_0^2}{\Omega^2}$$

Recall that the flap perturbation equation in hover was

$$\beta^{**} + \frac{\gamma}{8} \beta^* + \nu_{\beta}^2 \beta = 0$$

with characteristic stability roots

$$-\frac{\gamma}{16} \pm i \sqrt{\nu_{\beta}^2 - \left(\frac{\gamma}{16} \right)^2} \text{ in } /\text{rev}$$

In dimensional form was

$$\ddot{\beta} + \frac{\gamma}{8} \Omega \dot{\beta} + \nu_{\beta}^2 \Omega^2 \beta = 0$$

with characteristic stability roots

$$\sigma \pm i\omega = -\frac{\gamma}{16} \Omega \pm i \Omega \sqrt{\nu_{\beta}^2 - \left(\frac{\gamma}{16} \right)^2} \text{ in rad/s}$$

Using the expression for flap frequency given above we can write

$$\begin{aligned} \sigma &= -\frac{\gamma}{16} \Omega \\ \omega &= \Omega \left[1 + (p^2 - 1) \frac{\Omega_0^2}{\Omega^2} - \left(\frac{\gamma}{16} \right)^2 \right]^{1/2} \end{aligned} \tag{6.2}$$

Nondimensionalized with respect to the operating RPM, Ω_0 , we have

$$\begin{aligned} \bar{\sigma} &= \frac{\sigma}{\Omega_0} = -\frac{\gamma}{16} \bar{\Omega} \\ \bar{\omega} &= \frac{\omega}{\Omega_0} = \bar{\Omega} \left[1 + (p^2 - 1) / \bar{\Omega}^2 - \left(\frac{\gamma}{16} \right)^2 \right]^{1/2} \end{aligned} \tag{6.3}$$

The frequencies in the fixed frame are simply shifted by integer multiples of the rotational speed. Consider for the sake of discussion we have a three or a four bladed rotor. Then the frequencies of the fixed frame cyclic flapping modes, β_{1c} and β_{1s} , are given by

$$\omega_F = |\omega \pm \Omega| \text{ in rad/s or, in nondimensional form } \bar{\omega}_F = |\bar{\omega} \pm \bar{\Omega}|$$

The high frequencies, obtained using the positive sign, is always positive. The low frequencies, obtained using the negative sign, decreases with increase in Ω , and in air (i.e. for a non-zero Lock number) eventually hits zero. With further increase in Ω it continues to become more and more negative, however, because the physical frequency of oscillation is the absolute value of this number, the absolute value is plotted, showing an increase with increase in Ω . Figure 6.2(a) plots the fixed frame frequencies in rad/s. Figure 6.2(b) is an identical plot, only this time in nondimensional form. Figure 6.2(a) uses the expression in eqn. 6.2. Note that for $\Omega = 0$

$$\omega_F = \Omega \pm \left[\Omega^2 + (p^2 - 1) \Omega_0^2 - \Omega^2 \left(\frac{\gamma}{16} \right)^2 \right]^{1/2} = [(p^2 - 1) \Omega_0^2]^{1/2} = \omega_{\beta 0}$$

Figure 6.2(b) uses the expression in eqn. 6.3. Note that for $\bar{\Omega} = 0$

$$\bar{\omega}_F = \bar{\Omega} \pm \left[\bar{\Omega}^2 + p^2 - 1 - \bar{\Omega}^2 \left(\frac{\gamma}{16} \right)^2 \right]^{1/2} = [(p^2 - 1)]^{1/2} = \frac{\omega_{\beta 0}}{\Omega_0}$$

The magnitudes of β_{1c} and β_{1s} define the angular motion of the rotor disc plane with respect to the body. Note that, $\beta_{1c} - \theta$ and $\beta_{1s} - \phi$ define the angular motion of the rotor disc plane with respect to a fixed-space reference frame, for the simple case when the motions are in phase. For example, if $\beta_{1c} = \theta$ implies that the spinning rotor remains fixed in space due to gyroscopic inertia as the body pitches beneath it.

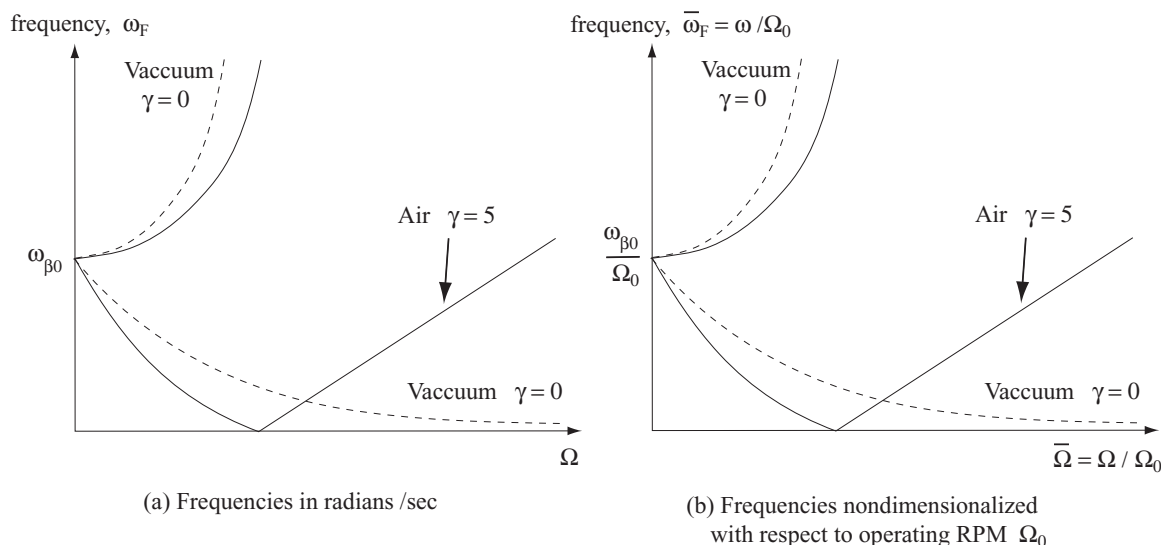


Figure 6.2: Rotor Flap Frequencies in the Fixed Frame

Consider the lagging motion in the rotating frame. The rotating lag frequency ν_ζ is given by

$$\nu_\zeta^2 = \frac{3e}{2R} + \frac{\omega_{\zeta 0}^2}{\Omega^2}$$

If the lag frequency at the operating RPM is q , then

$$q^2 = \frac{3e}{2R} + \frac{\omega_{\zeta 0}^2}{\Omega_0^2}$$

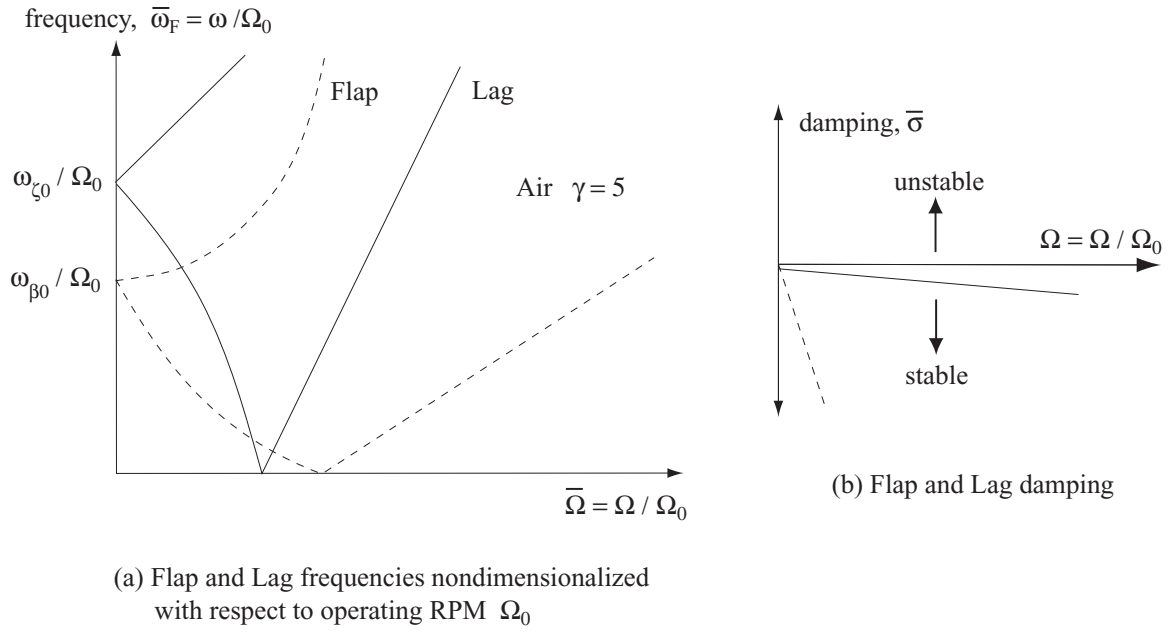


Figure 6.3: Rotor Flap and Lag Frequencies, and damping in the Fixed Frame

It follows

$$\left(q^2 - \frac{3e}{2R}\right)\Omega_0^2 = \omega_{\zeta_0}^2$$

$$\nu_{\zeta}^2 = \frac{3e}{2R} + \left(q^2 - \frac{3e}{2R}\right)\frac{\Omega_0^2}{\Omega^2}$$

where the lag frequency at the operating RPM, q , occurs explicitly. Dropping the term $3e/2R$, we have

$$\nu_{\zeta}^2 = q^2 \frac{\Omega_0^2}{\Omega^2}$$

The frequencies in the fixed frame, of the 1st cyclic lag modes ζ_{1c} and ζ_{1s} , are then simply shifted by the rotational speed. In /rev they are

$$\begin{aligned} 1 + \nu_{\zeta} &= 1 + \left[\frac{3e}{2R} + \frac{\omega_{\zeta_0}^2}{\Omega^2}\right]^{1/2} && \text{high frequency} \\ |1 - \nu_{\zeta}| &= \left|1 - \left[\frac{3e}{2R} + \frac{\omega_{\zeta_0}^2}{\Omega^2}\right]^{1/2}\right| && \text{low frequency} \end{aligned} \quad (6.4)$$

In rad/s they are

$$\begin{aligned} \Omega + \omega_{\zeta} &= \Omega + \left[\frac{3e}{2R}\Omega^2 + \omega_{\zeta_0}^2\right]^{1/2} && \text{high frequency} \\ |\Omega - \omega_{\zeta}| &= \left|\Omega + \left[\frac{3e}{2R}\Omega^2 + \omega_{\zeta_0}^2\right]^{1/2}\right| && \text{low frequency} \end{aligned} \quad (6.5)$$

which shows the variation with RPM Ω . A convenient form is to nondimensionalize with the operating RPM Ω_0 . Divide the above expressions by Ω_0 to obtain

$$\begin{aligned}\bar{\Omega} + \bar{\omega}_\zeta &= \bar{\Omega} + \bar{\Omega} \left[\frac{3}{2} \frac{e}{R} + \frac{\omega_{\zeta 0}^2 / \Omega_0^2}{\bar{\Omega}^2} \right]^{1/2} && \text{high frequency} \\ |\bar{\Omega} - \bar{\omega}_\zeta| &= \left| \bar{\Omega} - \bar{\Omega} \left[\frac{3}{2} \frac{e}{R} + \frac{\omega_{\zeta 0}^2 / \Omega_0^2}{\bar{\Omega}^2} \right]^{1/2} \right| && \text{low frequency}\end{aligned}\tag{6.6}$$

For $\Omega = 0$ (or $\bar{\Omega} = 0$), the high and low frequencies are the same and equal $\omega_{\zeta 0}$ (or $\omega_{\zeta 0} / \Omega_0$). To have the operating lag frequency q explicitly, use

$$\omega_{\zeta 0}^2 = \left(q^2 - \frac{3}{2} \frac{e}{R} \right) \Omega_0^2$$

to obtain the fixed frame frequencies as

$$\begin{aligned}\bar{\Omega} + \bar{\omega}_\zeta &= \bar{\Omega} + \bar{\Omega} \left[\frac{3}{2} \frac{e}{R} + \left(q^2 - \frac{3}{2} \frac{e}{R} \right) / \bar{\Omega}^2 \right]^{1/2} && \text{high frequency} \\ |\bar{\Omega} - \bar{\omega}_\zeta| &= \left| \bar{\Omega} - \bar{\Omega} \left[\frac{3}{2} \frac{e}{R} + \left(q^2 - \frac{3}{2} \frac{e}{R} \right) / \bar{\Omega}^2 \right]^{1/2} \right| && \text{low frequency}\end{aligned}\tag{6.7}$$

Dropping e/R we have

$$\begin{aligned}\bar{\Omega} + \bar{\omega}_\zeta &= \bar{\Omega} + q && \text{high frequency} \\ |\bar{\Omega} - \bar{\omega}_\zeta| &= |\bar{\Omega} - q| && \text{low frequency}\end{aligned}\tag{6.8}$$

For $\bar{\Omega} = 0$, the frequencies are $q = \omega_{\zeta 0} / \Omega_0$. The lag frequencies do not change in hover, because unlike flap there is no significant source of aerodynamic damping in lag. Characteristic trends for the fixed frame lag frequencies are shown in Fig. 6.3(a). Figure 6.3(b) shows the typical trends in flap and lag damping.

6.3.3 Rotor Flap and Body Pitch

Three DOF system: β_{1c} , β_{1s} , and θ .

Six roots:

2 zero frequency real roots.

1 pair of complex conjugate high frequency flap.

1 pair complex conjugate low frequency flap-pitch coupled modes.

Figure 6.4 shows the two pairs of complex conjugate roots in vacuum. The dashed lines are the isolated flap frequencies. The plots correspond to $K_y^2 = 0.1$, $p = 1.1/\text{rev}$. Figure 6.5 shows the same frequencies in air $\gamma = 5$. Again, the dashed lines are the isolated flap frequencies. The pair of low frequency pitch-flap modes degenerate into 2 unequal real roots with increase in rotational speed before becoming oscillatory again.

6.3.4 Rotor Flap and Body Pitch and Roll

Four DOF system: β_{1c} , β_{1s} , θ , and ϕ .

Eight roots:

2 zero frequency real roots.

1 pair of complex conjugate high frequency flap.

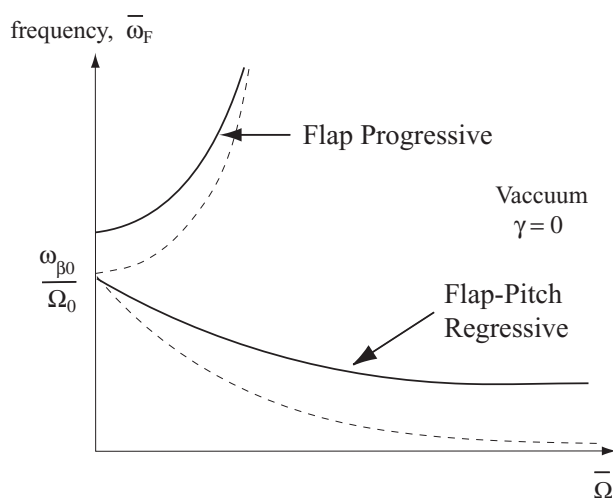


Figure 6.4: Coupled Flap and Body Pitch Frequencies in Vacuum

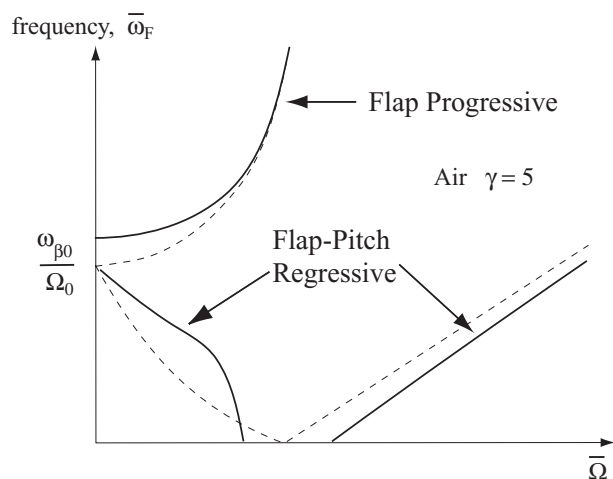


Figure 6.5: Coupled Flap and Body Pitch Frequencies in Air

2 pairs of complex conjugate coupled low frequency flap-pitch-gyroscopic modes. Figure 6.6 shows the frequencies of the three oscillatory complex conjugate modes for the values $K_x^2 = 0.025$, $K_y^2 = 0.1$, and $p = 1.1/\text{rev}$. The uncoupled roll and pitch frequencies (non-rotating) are simply due to the fuselage inertia reacting against the blade flap springs. The expressions given in the figure correspond to a four bladed rotor. Figure 6.7 shows the same frequencies including aerodynamic forces in hover for Lock number $\gamma = 5$.

6.3.5 Rotor Flap and Lag and Body Pitch in Vacuum

To avoid confusion with blade pitch angle during the derivation of aerodynamic forces, the body pitch angle will be denoted henceforth as α_y .

Blade Equations

Rotating frame:

$$\beta^{**} - 2\beta_0 \zeta^* + \nu_\beta^2 \beta - \alpha_y^{**} \cos \psi + 2 \alpha_y^* \sin \psi = 0$$

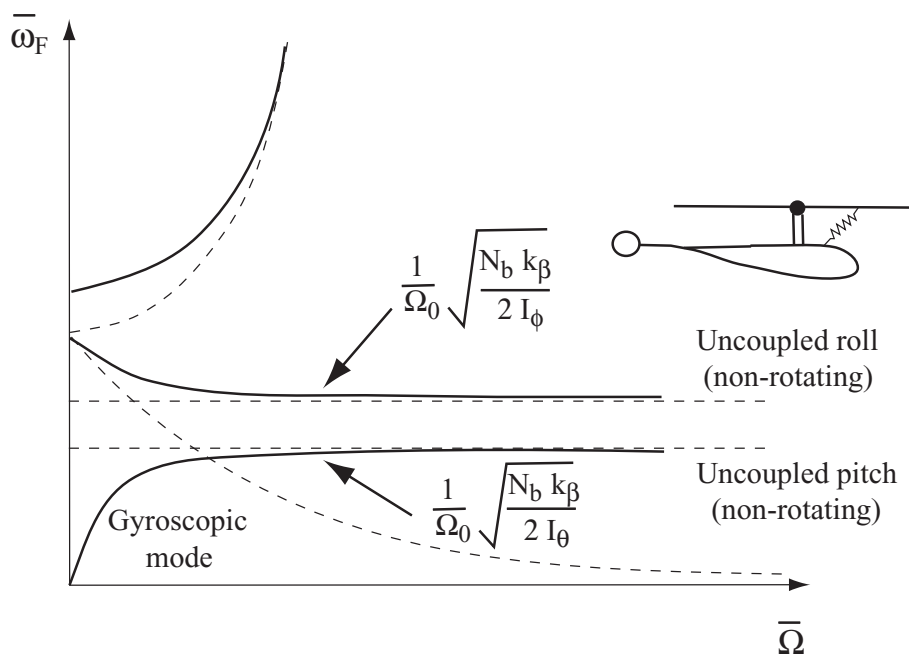


Figure 6.6: Coupled Flap Body Pitch Roll Frequencies in Vacuum

$$\zeta^{**} + 2\beta_0^* \beta + g_L \zeta^* + \nu_\beta^2 \zeta + S_\zeta \frac{h}{R} \alpha_y^{**} \sin \psi = 0$$

where h is hub center above body cg.

Fixed Frame:

$$\beta_{1c} : \beta_{1c}^{**} + 2\beta_{1s}^* - \beta_{1c} - 2\beta_0(\zeta_{1c}^* + \zeta_{1s}) + \nu_\beta^2 \beta_{1c} - \alpha_y^{**} = 0$$

$$\beta_{1s} : \beta_{1s}^{**} - 2\beta_{1c}^* - \beta_{1s} - 2\beta_0(\zeta_{1s}^* + \zeta_{1c}) + \nu_\beta^2 \beta_{1s} + 2\alpha_y^{**} = 0$$

$$\zeta_{1c} : \zeta_{1c}^{**} + 2\zeta_{1s}^* - \zeta_{1c} + 2\beta_0(\beta_{1c}^* + \beta_{1s}) + g_L(\zeta_{1c}^* + \zeta_{1s}) + \nu_\zeta^2 \zeta_{1c} = 0$$

$$\zeta_{1s} : \zeta_{1s}^{**} - 2\zeta_{1c}^* - \zeta_{1c} + 2\beta_0(\zeta_{1s}^* - \zeta_{1c}) + g_L(\zeta_{1s}^* + \zeta_{1c}) + \nu_\zeta^2 \zeta_{1s} + S_\zeta \frac{h}{R} \alpha_y^{**} = 0$$

Body Equation

$$I_y \ddot{\alpha}_y + c_y \dot{\alpha}_y + K_y \alpha_y = M_y + hH$$

I_y is pitch inertia and c_y is the pitch damping coefficient. M_y is the rotor pitch moment and H is the rotor drag force.

$$M_y = - \sum_{m=1}^N M_\beta \cos \psi_m$$

M_b = flap moment at root

$$= - \int_0^R r(m dr) r(\ddot{\beta} - \alpha \dot{\beta} \cos \psi_m - 2\beta_0 \Omega \dot{\zeta} + 2\Omega \dot{\alpha}_y \sin \psi_m + \Omega^2 \beta)$$

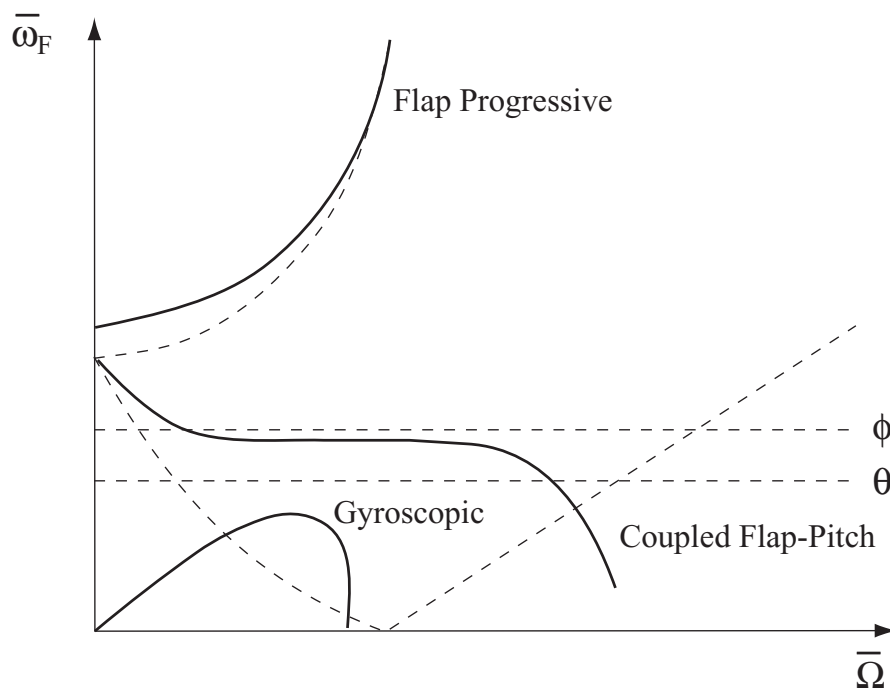


Figure 6.7: Coupled Flap Body Pitch Roll Frequencies in Air

$$= -I_b \Omega^2 (\beta^* - \alpha_y^{**} \cos \psi_m - 2\beta_0 \dot{\zeta}^* + 2\dot{\alpha}^* \sin \psi_m + \beta)$$

Radial shear:

$$\begin{aligned} S_R &= -2\Omega \dot{\zeta}^* \int_0^R m r dr - h \ddot{\alpha}_y \cos \psi_m \int_0^R m dr \\ &= -2S_\zeta \Omega \dot{\zeta}^* - h M_b \ddot{\alpha}_y \cos \psi_m \end{aligned}$$

where M_b is blade mass.

Inplane shear:

$$\begin{aligned} S_x &= -(\ddot{\zeta} - \Omega^2 \zeta) \int_0^R m r dr - h \ddot{\alpha}_y \sin \psi_m \int_0^R m dr \\ &= -(\ddot{\zeta} - \Omega^2 \zeta) S_\zeta - h M_b \ddot{\alpha}_y \sin \psi_m \end{aligned}$$

Hub drag force:

$$\begin{aligned} H &= \sum^N (S_r \cos \psi_m + S_x \sin \psi_m) \\ &= \sum^M (-2S_\zeta \Omega \dot{\zeta}^* \cos \psi_m - h M_b \ddot{\alpha}_y - \ddot{\zeta} S_\zeta \sin \psi_m + \Omega^2 \zeta^* S_\zeta \sin \psi_m) \\ &= -h M_b \ddot{\alpha}_y - S_\zeta \frac{N}{2} \zeta_{1s}^{**} \Omega^2 \end{aligned}$$

$$M_y = I_b \Omega^2 \sum_{m=1}^N (\beta^{**(m)} - \alpha^{**} \cos \psi_m - 2\beta_0 \dot{\zeta}^{*(m)} + 2\dot{\alpha}_y^* \sin \psi_m + \beta) \cos \psi_m + h H$$

$$= I_b \Omega^2 \frac{N}{2} [\beta_{1c}^{**} + 2\beta_{1s}^* - \alpha_y^{**} - 2\beta_0(\zeta_{1c}^* + \zeta_{1s})]$$

Body equation becomes (setting $c_y = K_y = 0$)

$$\alpha_y^{**} (I_y + \frac{NI_b}{2} + Nh^2 M_b) - (\beta_{1c}^{**} + 2\beta_{1s}^* - 2\beta_0 \zeta_{1c}^* - 2\beta_0 \zeta_{1s})(I_b \frac{N}{2}) + S_\zeta h \frac{N}{2} \zeta_{1s}^{**} = hH$$

$$\text{Setting } I_y = (I_y + \frac{NI_b}{2} + Nh^2 M_b) / \frac{NI_b}{2}$$

Body equation becomes

$$I_y \alpha_y^{**} - \beta_{1c}^{**} - 2\beta_{1s}^* + 2\beta_0 \zeta_{1c}^* + 2\beta_0 \zeta_{1s} + S_\zeta \frac{h}{R} \zeta_{1s}^{**} = 0$$

Rotor/Body Equations:

$$\begin{bmatrix} 1 & 0 & 0 & 0 & -1 \\ 0 & 1 & 0 & 0 & 0 \\ 0 & 0 & 1 & 0 & 0 \\ 0 & 0 & 0 & 1 & S_\zeta \frac{h}{R} \\ -1 & 0 & 0 & S_\zeta \frac{h}{R} & I_y \end{bmatrix} \begin{Bmatrix} \beta_{1c}^{**} \\ \beta_{1s}^{**} \\ \zeta_{1c}^* \\ \zeta_{1s}^* \\ \alpha_y^{**} \end{Bmatrix} + \begin{bmatrix} 0 & 2 & -2\beta_0 & 0 & 0 \\ -2 & 0 & 0 - 2\beta_0 & 2 & 0 \\ 2\beta_0 & 0 & g_L & 2 & 2\beta_0 \\ 0 & 2\beta_0 & -2 & g_L & 0 \\ 0 & -2 & 2\beta_0 & 0 & 0 \end{bmatrix} \begin{Bmatrix} \beta_{1c}^* \\ \beta_{1s}^* \\ \zeta_{1c}^* \\ \zeta_{1s}^* \\ \alpha_y^* \end{Bmatrix} + \begin{bmatrix} \nu_\beta^2 - 1 & 0 & 0 & -2\beta_0 & 0 \\ 0 & \nu_\beta^2 - 1 & 2\beta_0 & 0 & 0 \\ 0 & 2\beta_0 & \nu_\zeta^2 - 1 & g_L & 0 \\ -2\beta_0 & 0 & -g_L & \nu_\zeta^2 - 1 & 0 \\ 0 & 0 & 0 & 0 & 0 \end{bmatrix} \begin{Bmatrix} \beta_{1c} \\ \beta_{1s} \\ \zeta_{1c} \\ \zeta_{1s} \\ \alpha_y \end{Bmatrix} = 0$$

6.3.6 Rotor Flap and Lag coupled to Body Pitch and Roll in Air

Six DOF system: β_{1c} , β_{1s} , ζ_{1c} , ζ_{1s} , θ , and ϕ .

The body pitch and roll angles θ , and ϕ are henceforth denoted by α_y and α_x to avoid confusion with blade pitch angle.

Twelve roots:

2 zero frequency real roots.

5 complex conjugate pairs: 2 pairs corresponding to β_{1c} , β_{1s} ; 2 pairs for ζ_{1c} , ζ_{1s} ; and 1 pair for α_y and α_x (the other two roots of the fuselage modes are real).

Figure 6.8 shows the frequencies of the five oscillatory roots. The regressive lag mode has the danger of coalescing with two modes: the regressive flap coupled body pitch-roll and the regressive

flap coupled gyroscopic nutation mode. When it does, it produces air resonance. The damping in regressive lag mode is shown in the bottom diagram. The character of the two regressive flap coupled body modes changes with collective angle, hence the thrust level. For example, figure 6.9 shows the same frequencies at an collective pitch angle of 10° . The damping of the regressive lag mode becomes further negative, increasing air resonance instability.

$$\begin{aligned}
 & \begin{bmatrix} 1 & 0 & 0 & 0 & 0 & -1 \\ 0 & 1 & 0 & 0 & 1 & 0 \\ 0 & 0 & 1 & 0 & S_\zeta^* \frac{h}{r} & 0 \\ 0 & 0 & 0 & 1 & 0 & S_\zeta^* \frac{h}{r} \\ 0 & -1 & S_\zeta^* \frac{h}{r} & 0 & I_x & 0 \\ -1 & 0 & 0 & S_\zeta^* \frac{h}{r} & 0 & I_y \end{bmatrix} \begin{Bmatrix} \beta_{1c}^* \\ \beta_{1s}^* \\ \zeta_{1c}^* \\ \zeta_{1s}^* \\ \alpha_x^* \\ \alpha_y^* \end{Bmatrix} \\
 & + \begin{bmatrix} 0 & 2 & -2\beta_0 & 0 & 2 & 0 \\ -2 & 0 & 0 & -2\beta_0 & 0 & 2 \\ 2\beta_0 & 0 & g_L & 2 & 0 & 2\beta_0 \\ 2\beta_0 & 0 & g_L & 2 & 0 & 2\beta_0 \\ 0 & 2\beta_0 & -2 & g_L & -2\beta_0 & 0 \\ 2 & 0 & 0 & -2\beta_0 & 0 & 2 \\ 0 & -2 & 2\beta_0 & 0 & -2 & 0 \end{bmatrix} \begin{Bmatrix} \beta_{1c}^* \\ \beta_{1s}^* \\ \zeta_{1c}^* \\ \zeta_{1s}^* \\ \alpha_x^* \\ \alpha_y^* \end{Bmatrix} \\
 & + \begin{bmatrix} \nu_\beta^2 - 1 & 0 & 0 - 2\beta_0 & 0 & 0 & 0 \\ 0 & \nu_\beta^2 - 1 & 2\beta_0 & 0 & 0 & 0 \\ 0 & 2\beta_0 & \nu_\zeta^2 - 1 & g_L & 0 & 0 \\ -2\beta_0 & 0 & g_L & \nu_\zeta^2 - 1 & 0 & 0 \\ 0 & 0 & 0 & 0 & 0 & 0 \\ 0 & 0 & 0 & 0 & 0 & 0 \end{bmatrix} \begin{Bmatrix} \beta_{1c} \\ \beta_{1s} \\ \zeta_{1c} \\ \zeta_{1s} \\ \alpha_x \\ \alpha_y \end{Bmatrix} = \gamma \begin{Bmatrix} \overline{M}_{\beta_{1c}} \\ \overline{M}_{\beta_{1s}} \\ \overline{M}_{\zeta_{1c}} \\ \overline{M}_{\zeta_{1s}} \\ \overline{c}_{mx} \\ \overline{c}_{my} \end{Bmatrix}
 \end{aligned}$$

Aerodynamic forces are broken into stiffness and damping contributions.

$$\gamma \begin{Bmatrix} \overline{M}_{\beta_{1c}} \\ \overline{M}_{\beta_{1s}} \\ \overline{M}_{\zeta_{1c}} \\ \overline{M}_{\zeta_{1s}} \\ \overline{c}_{mx} \\ \overline{c}_{my} \end{Bmatrix} = K_A \begin{Bmatrix} \beta_{1c} \\ \beta_{1s} \\ \zeta_{1c} \\ \zeta_{1s} \\ \alpha_x \\ \alpha_y \end{Bmatrix} + C_A \begin{Bmatrix} \beta_{1c}^* \\ \beta_{1s}^* \\ \zeta_{1c}^* \\ \zeta_{1s}^* \\ \alpha_x^* \\ \alpha_y^* \end{Bmatrix}$$

where the components of K_A and C_A are as follows.

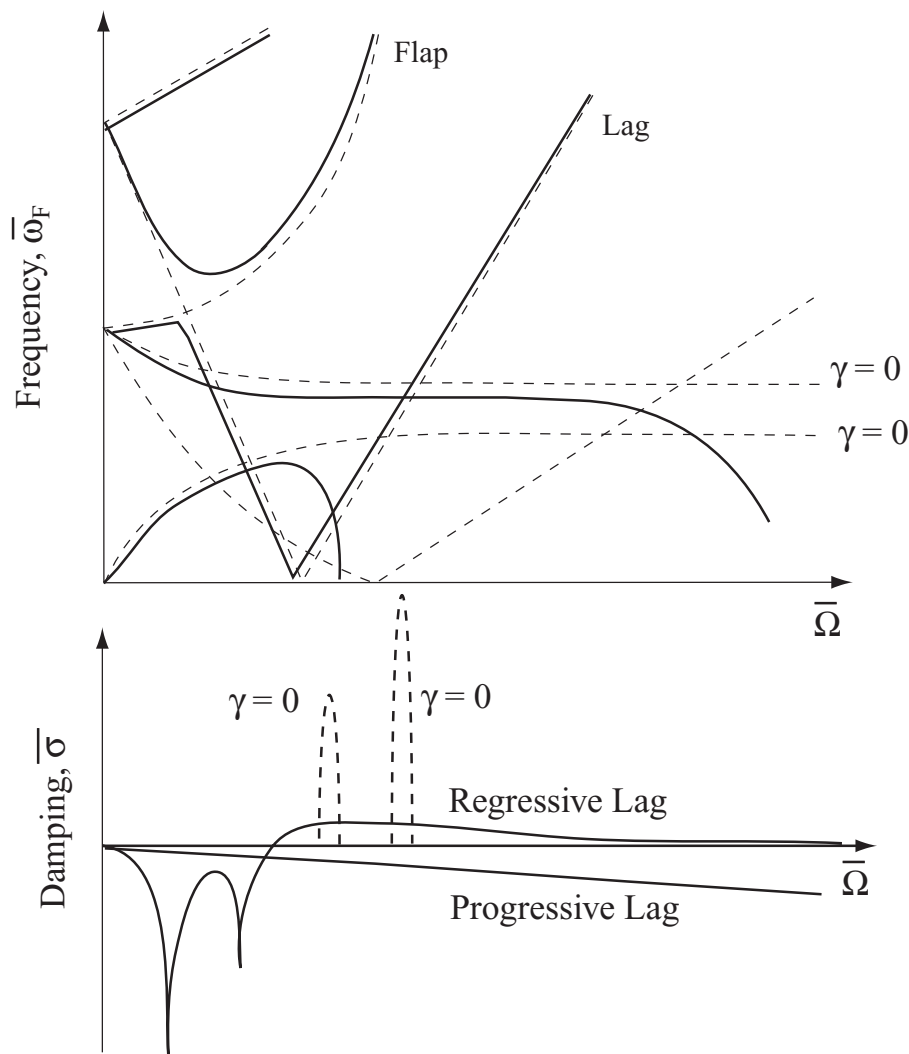


Figure 6.8: Coupled Flap, Lag, Pitch, Roll Air-Resonance Modes; Collective angle = 0°

6.4 Experimental Data on Aeromechanical Stability

A comprehensive experimental test program to measure the aeromechanical stability of a hingeless rotor was undertaken by Bousman [3]. The model was a 1.62-m diameter, three-bladed rotor mounted on a static mast. The mast was bolted to a transmission and two electric drive motors, together constituting the model. The model was supported on a gimbaled frame which allowed pitch and roll motions. The blades were rigid with flexibility concentrated at the root end flexures. The flexures created virtual lag and flap hinges. From the center of the hub, the lag hinge flexure was located inboard, followed by the flap hinge flexure outboard. When assembled, the flap and lag hinge were coincident. The lag stiffness was greater than the flap stiffness, as in conventional rotors. The flexure representing the lag hinge could be substituted with a skewed flexure to produce negative pitch lag coupling of $K_{p\zeta} = -0.4$. The flexure representing the flap hinge could be substituted with another with eight times the stiffness to produce the same non-rotating flap and lead-lag frequencies were equal with the blade set at zero pitch angle. The blade pitch angle could be changed manually, either outboard or inboard of the flexures. Five configurations were tested. They are given in table 6.1.

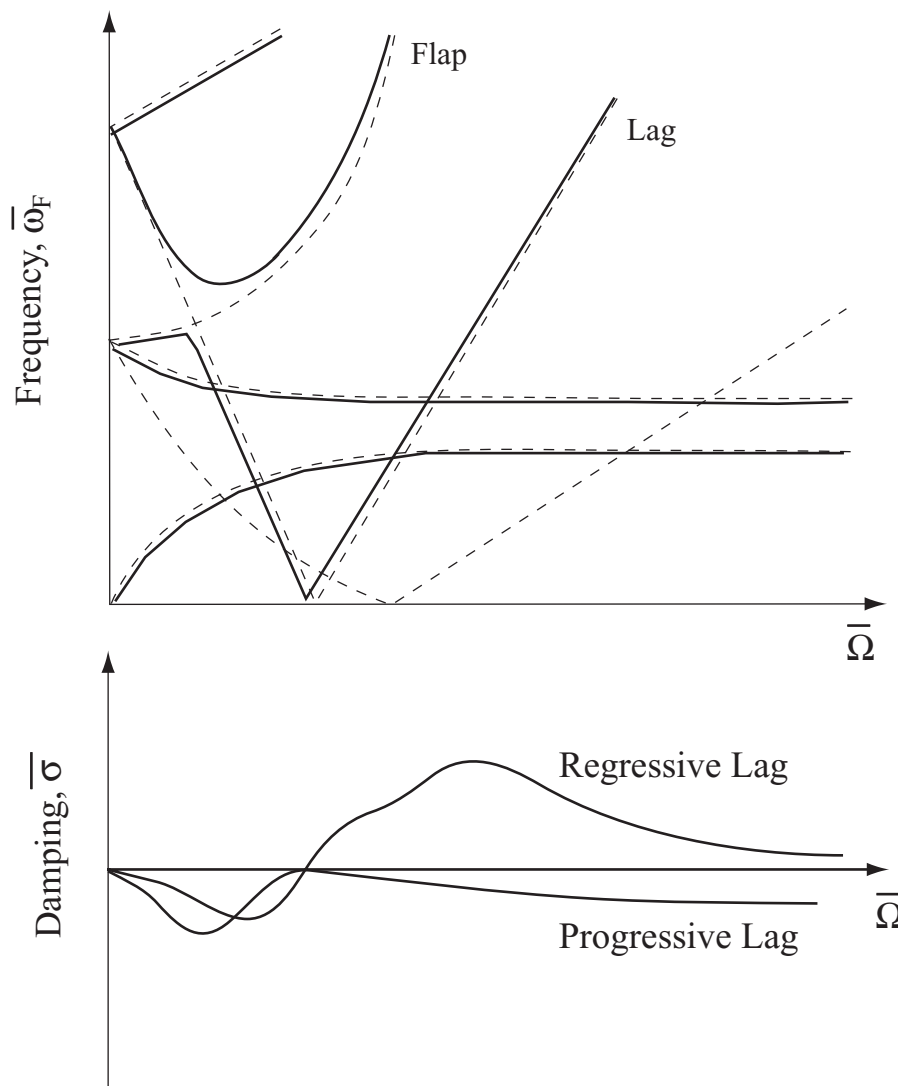


Figure 6.9: **Coupled Flap, Lag, Pitch, Roll Air-Resonance Modes; Collective angle = 10°**

The nominal rotor speed was 720 rpm. The rotor dimensionless lead-lag frequency at this rpm was 0.70/rev. The low frequency lead-lag regressing mode in the fixed coordinates was therefore at 0.30/rev. The body frequencies were controlled by cantilevered springs mounted across the gimbal flexural pivots. The springs were selected to provide body pitch and roll frequencies of 0.12/rev and 0.28/rev (2 Hz and 4 Hz at 720 rpm). The pitch mode is lower than the lead-lag regressive mode, while the roll mode is quite close and represents a critical design condition. The placement of frequencies was representative of air resonance conditions for a number of full-scale soft inplane rotor helicopters [4, 5, 6, 7]. The structural properties are given in table 6.2.

The blade properties are mean of three blades. The blade frequency and percentage critical damping are given in table 6.3. The structural properties of the body are given in table 6.4.

The gimbal frame acted as a part of the body during pitch motions, hence the difference in mass and c.g. location in pitch and roll. The vertical c.g. location is above the gimbal plane. The rotor disk was 24.10 cm above the gimbal plane. The body pitch and roll mode damping in terms of percentage critical were

$$\xi_\alpha = 3.200\% \quad \xi_\phi = 0.929\%$$

Table 6.1: Experimental Rotor Configurations

Configuration	Flap flexure	Lead-lag flexure	Blade pitch angle set
1	nominal, $\omega_{\beta 0} < \omega_{\zeta 0}$	straight, $K_{p\zeta} = 0$	outboard of flexures
2	nominal, $\omega_{\beta 0} < \omega_{\zeta 0}$	skewed, $K_{p\zeta} = -0.4$	outboard of flexures
3	nominal, $\omega_{\beta 0} < \omega_{\zeta 0}$	skewed, $K_{p\zeta} = -0.4$	outboard of flexures
4	thick, $\omega_{\beta 0} = \omega_{\zeta 0}$	straight, $K_{p\zeta} = 0$	outboard of flexures
5	thick, $\omega_{\beta 0} = \omega_{\zeta 0}$	skewed, $K_{p\zeta} = -0.4$	outboard of flexures

Table 6.2: Rotor Structural Properties

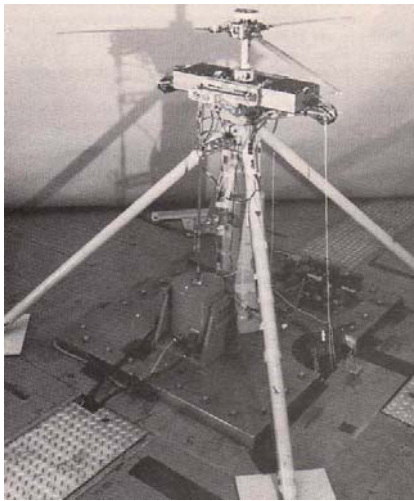
Property	Value
Radius, cm	81.10
Chord, cm	4.19
Hinge offset, cm	8.51
Lock number	7.37 (based on $a = 5.73$)
Airfoil	NACA 23012 ($C_0 = 0.15$)
Profile drag (c_{d0})	0.0079
Blade mass (to flap flexure), g	209.00
Blade mass centroid (ref. flexure centerline), cm	18.60
Blade flap inertia (ref. flexure centerline), g-m ²	17.30
Blade polar inertia (ref. hub centerline), g-m ²	85.50

Table 6.3: Blade Frequency and Damping

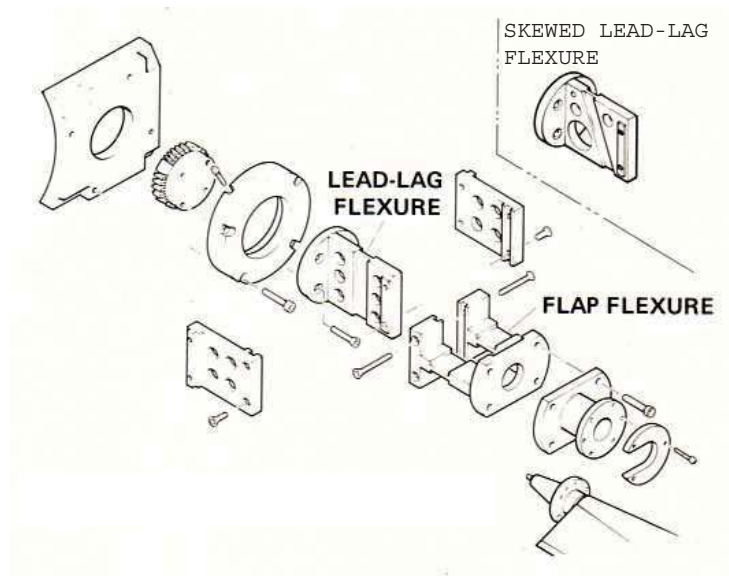
Configuration	$\omega_{\beta 0}$, Hz	$\omega_{\zeta 0}$, Hz	$\xi\%$
1	3.13	6.70	0.52
2	3.13	7.16	0.65
3	3.13	7.16	0.65
4	6.63	6.73	0.53
5	6.64	7.04	0.65

Table 6.4: Body Properties

Property	Pitch	Roll
Body mass, kg	22.60	19.06
Vertical c.g., cm	1.32	1.56
Body inertia, g-m ²	633.00	183.00



(a) Overall set up of the model



(b) Expanded view of blade root flexures

Figure 6.10: A 1.62-m diameter, three-bladed model rotor mounted on a static mast

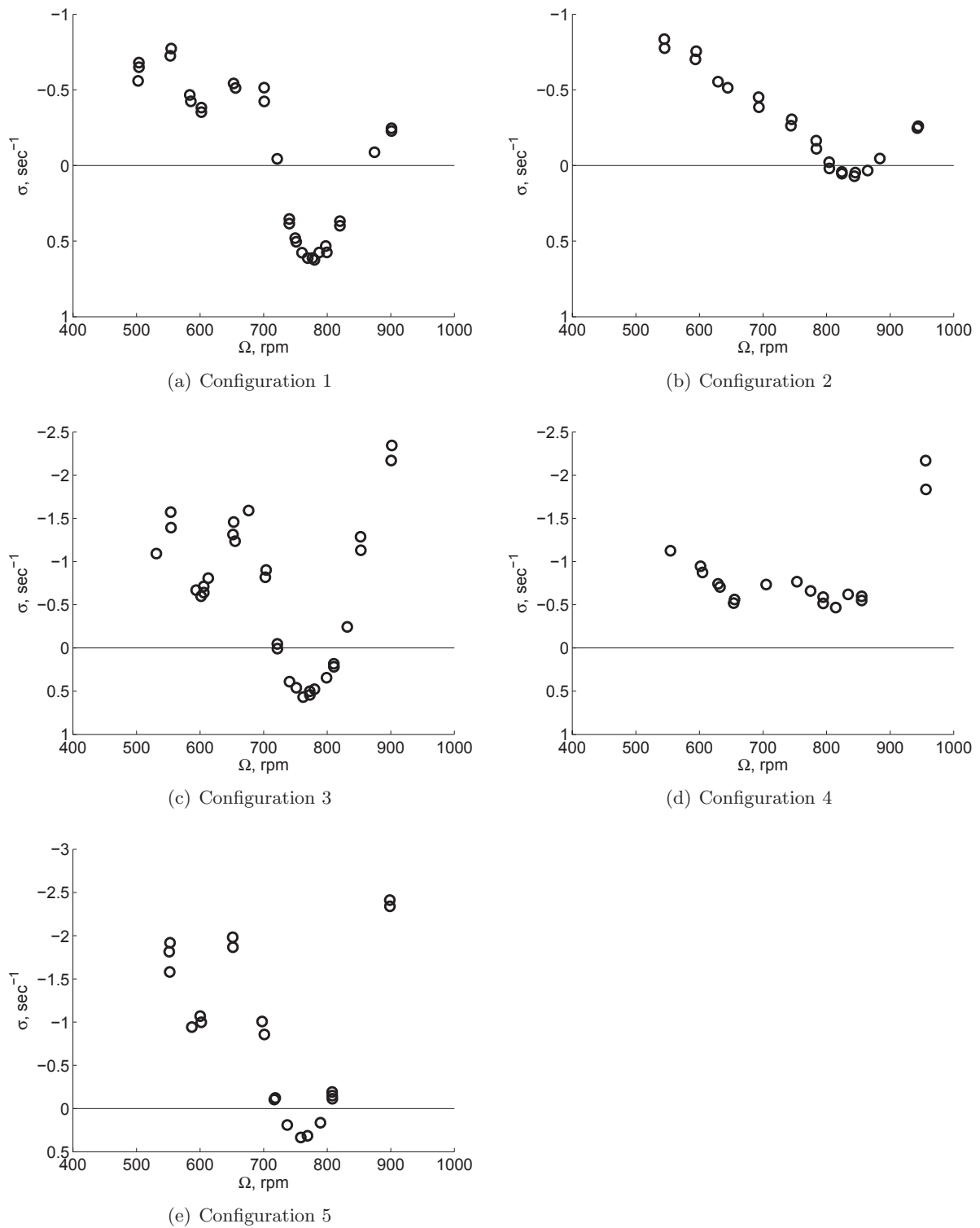


Figure 6.11: Lead-lag regressing mode damping as a function of rotor speed at blade pitch angle $\theta_0 = 9^\circ$

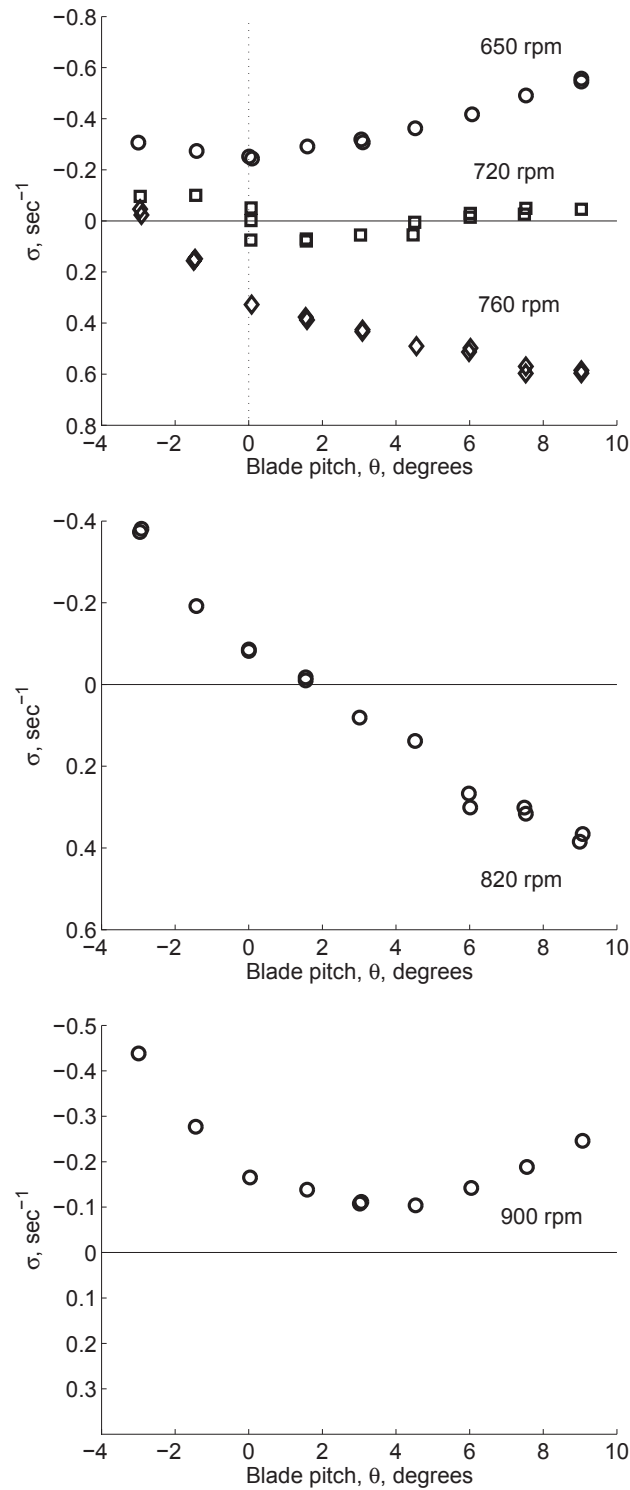


Figure 6.12: Lead-lag regressing mode damping as a function of blade pitch angle for configuration 1; $\omega_{\beta 0} < \omega_{\zeta 0}$, $K_{p\zeta} = 0$

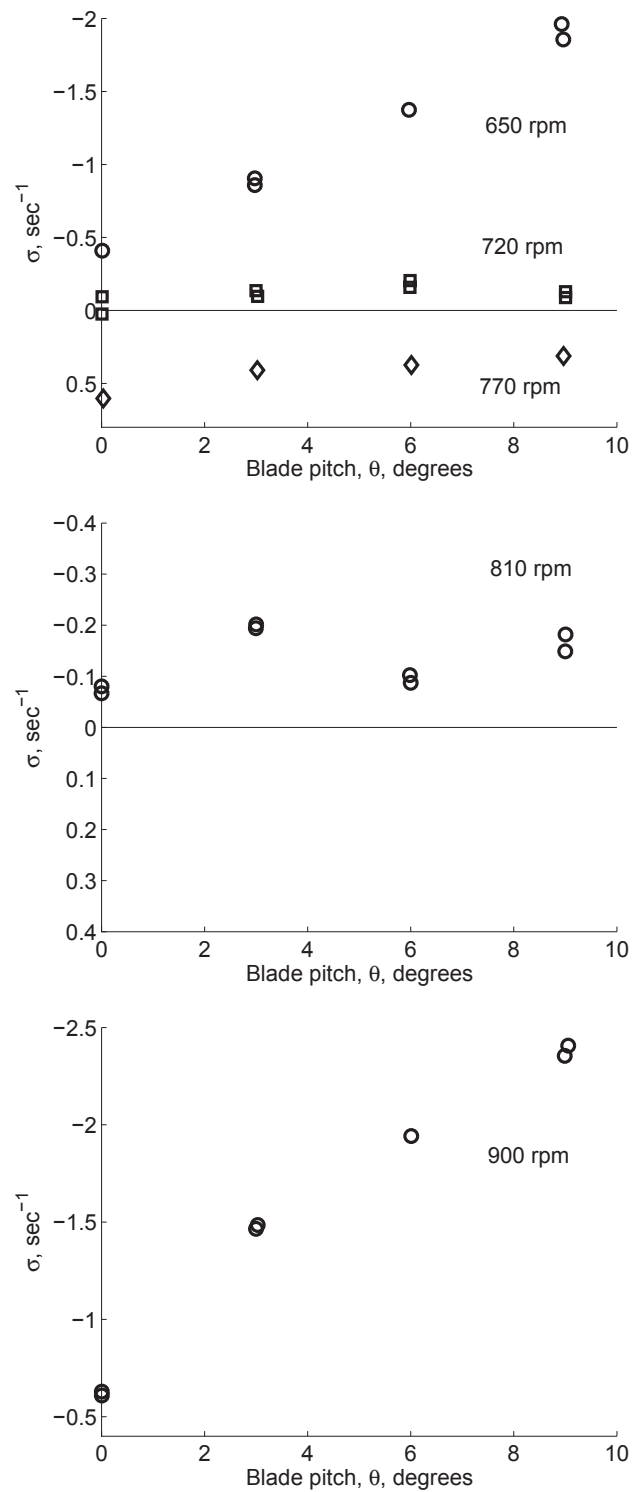


Figure 6.13: Lead-lag regressing mode damping as a function of blade pitch angle for configuration 3; $\omega_{\beta 0} < \omega_{\zeta 0}$, $K_{p\zeta} = -0.4$

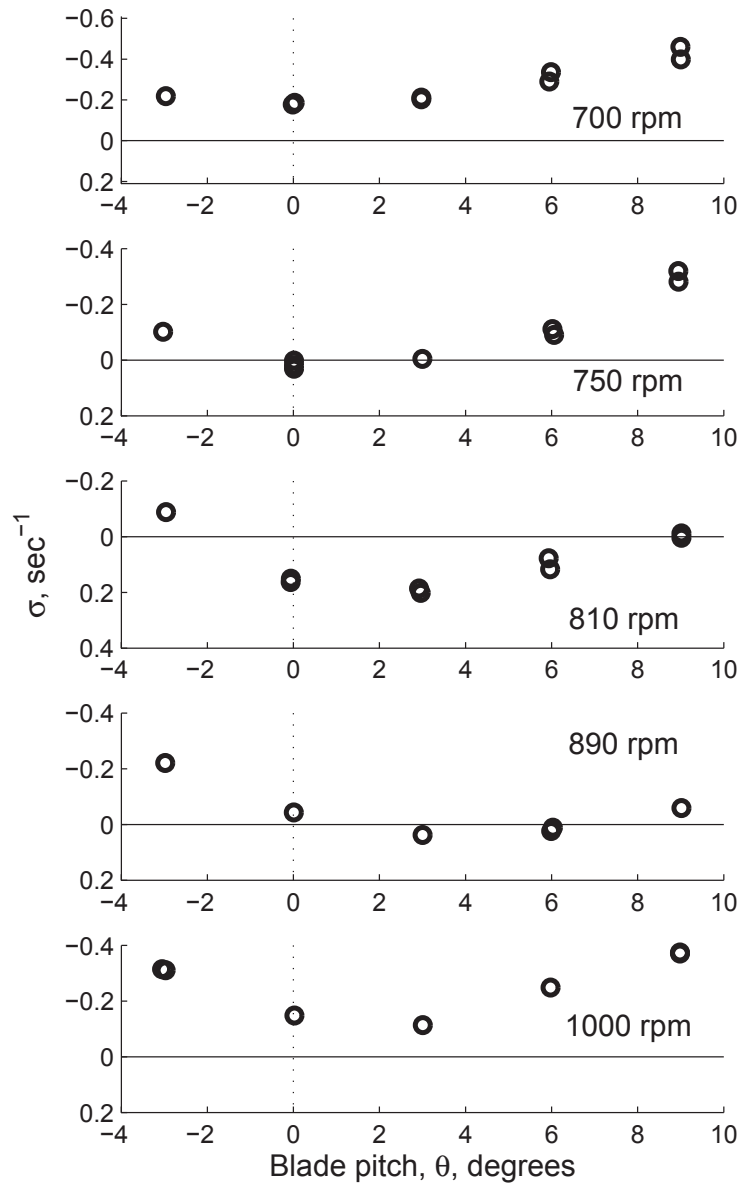


Figure 6.14: Lead-lag regressing mode damping as a function of blade pitch angle for configuration 4; $\omega_{\beta 0} = \omega_{\zeta 0}$, $K_{p\zeta} = 0$

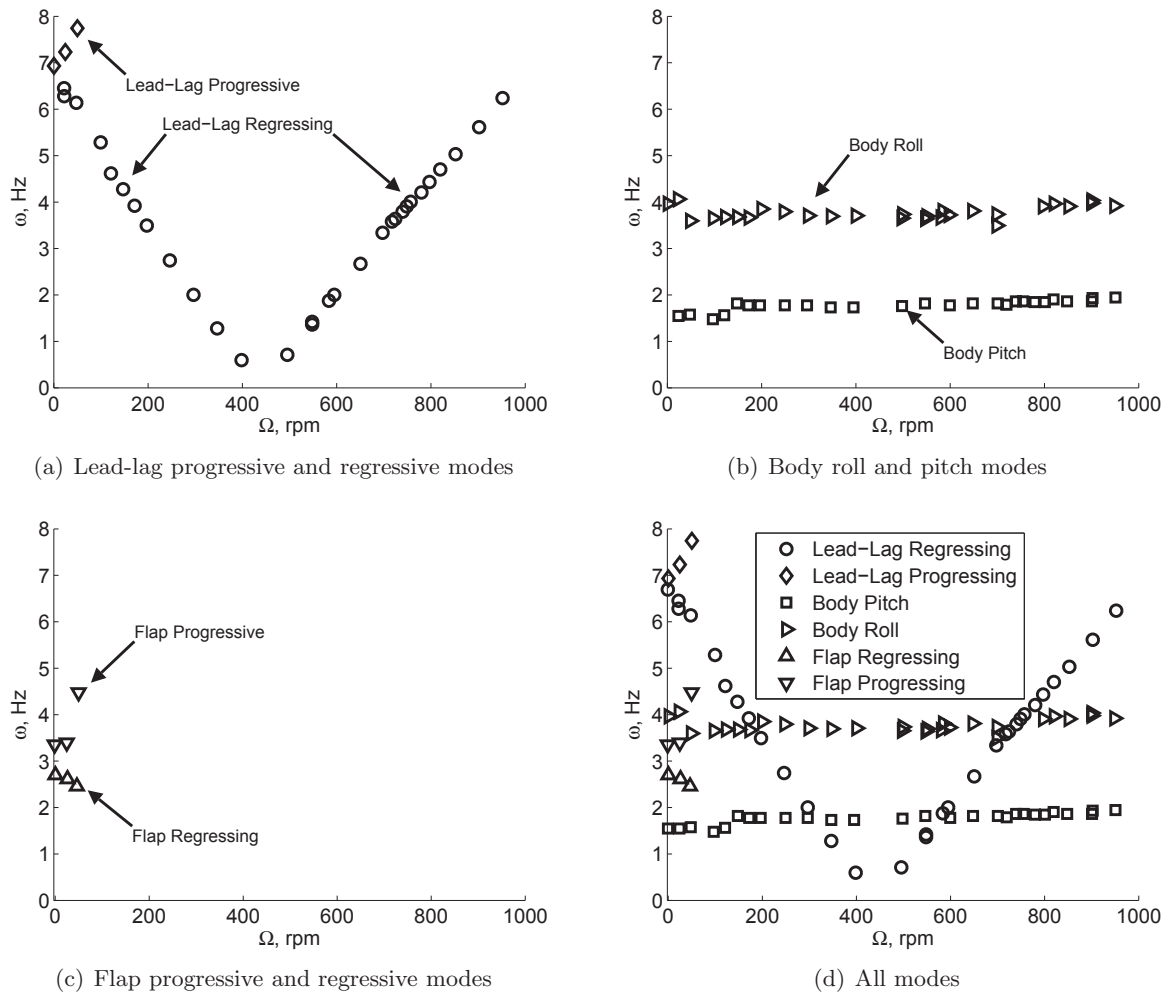
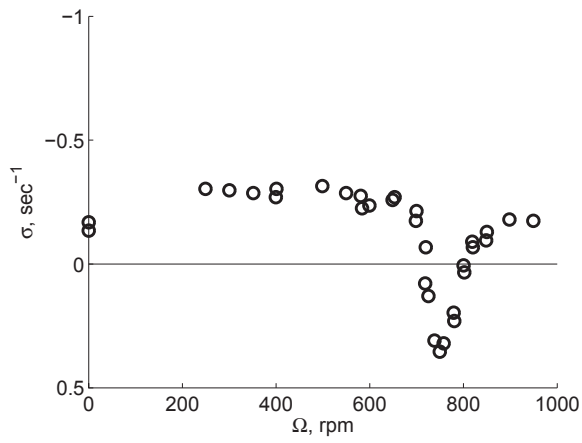
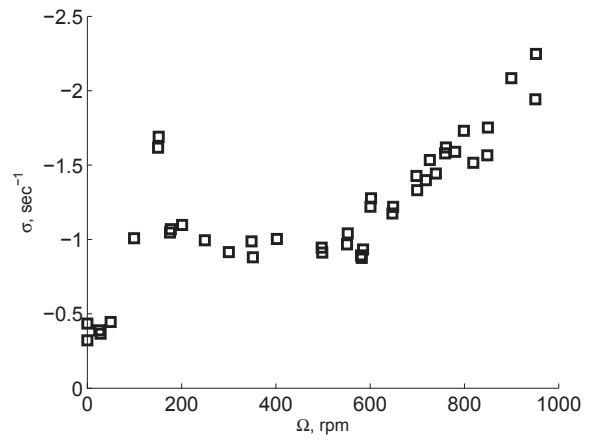


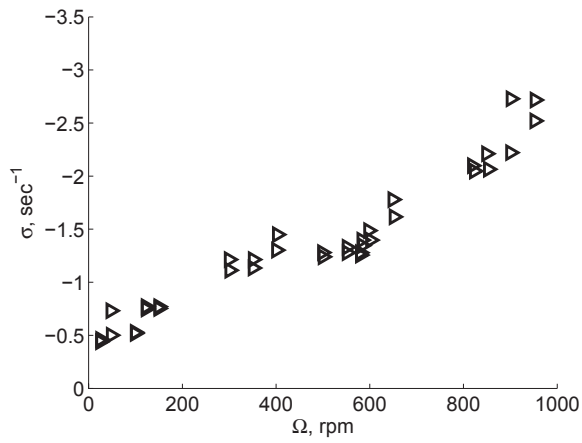
Figure 6.15: Modal frequencies as a function of rotor speed for configuration 1; $\omega_{\beta 0} < \omega_{\zeta 0}$, $K_{p\zeta} = 0$, blade pitch angle $\theta_{b_0} = 0$



(a) Lead-lag regressive mode damping

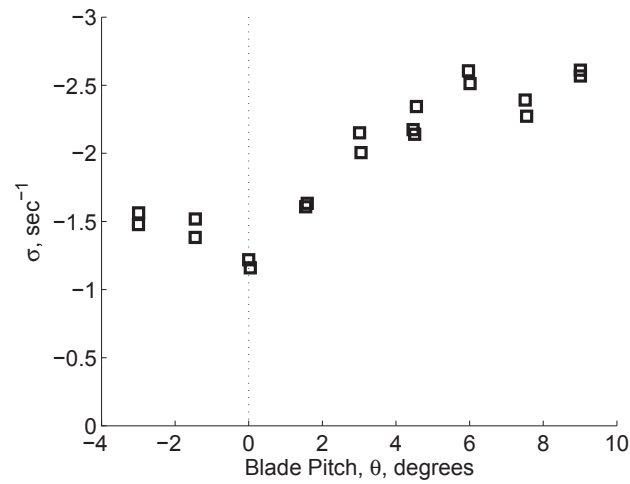


(b) Body pitch mode damping

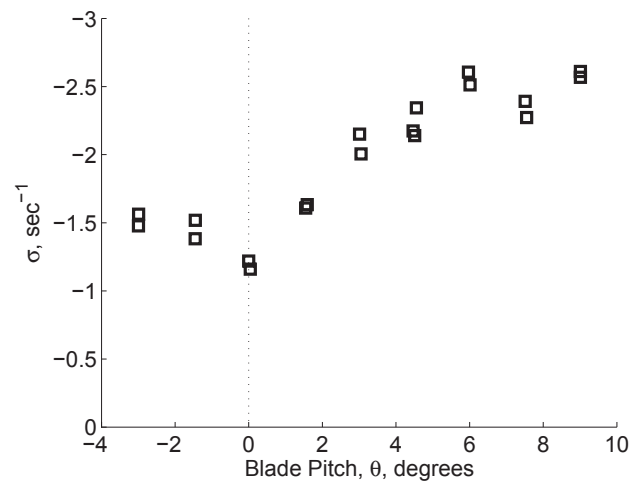


(c) Body roll mode damping

Figure 6.16: Modal damping as a function of rotor speed for configuration 1; $\omega_{\beta 0} < \omega_{\zeta 0}$, $K_{p\zeta} = 0$.

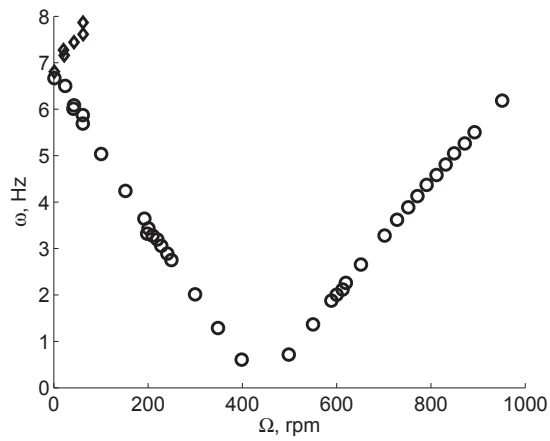


(a) Body pitch mode damping

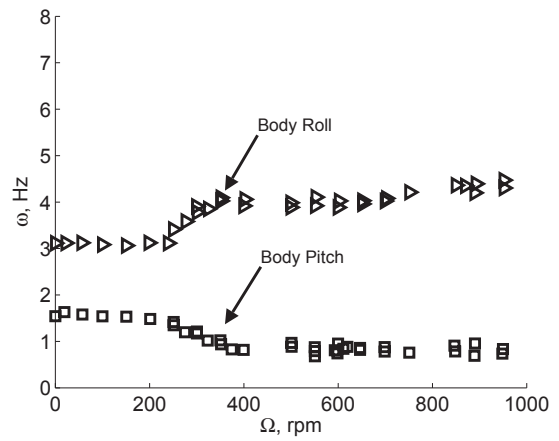


(b) Body roll mode damping

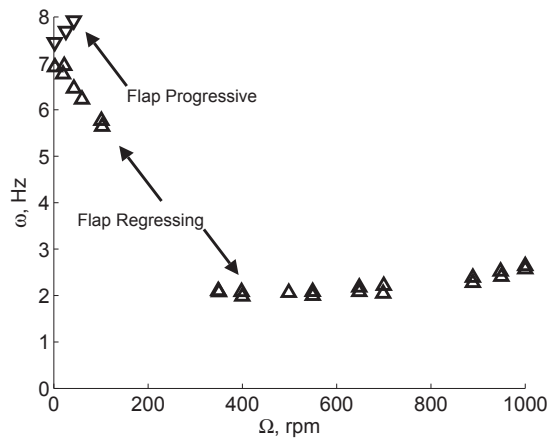
Figure 6.17: **Body pitch and roll mode damping as a function of blade pitch angle for configuration 1; $\omega_{\beta 0} < \omega_{\zeta 0}$, $K_{p\zeta} = 0$, $\Omega = 650$ rpm.**



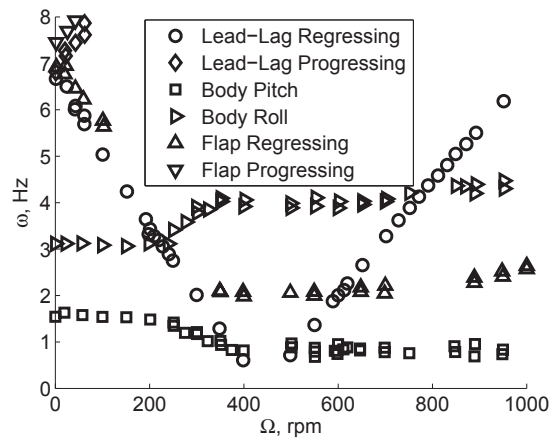
(a) Lead-lag progressive and regressive modes



(b) Body roll and pitch modes

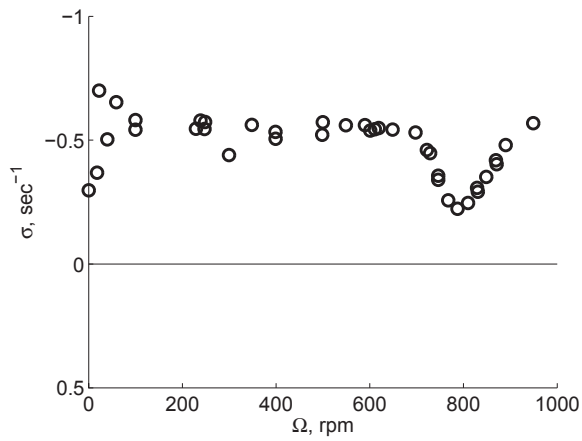


(c) Flap progressive and regressive modes

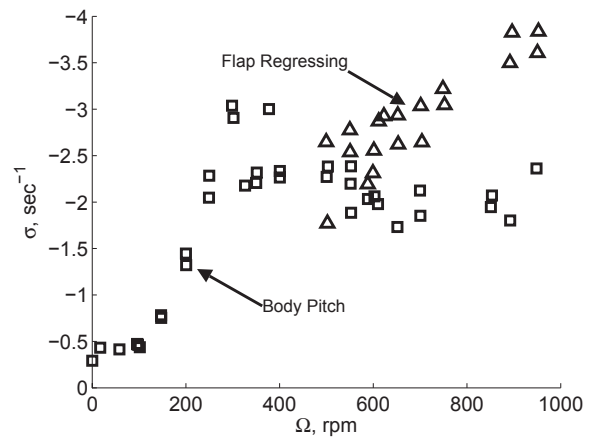


(d) All modes

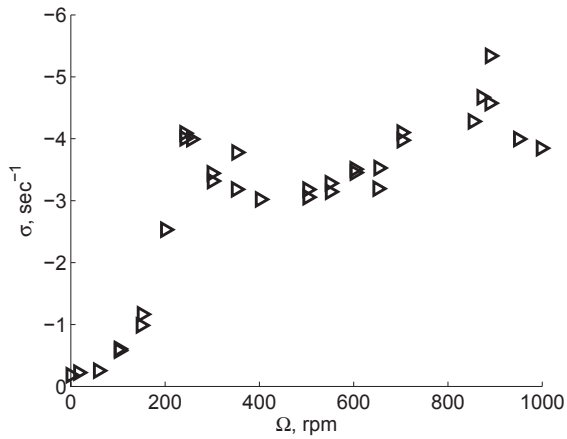
Figure 6.18: Modal frequencies as a function of rotor speed for configuration 4; $\omega_{\beta 0} = \omega_{\zeta 0}$, $K_{p\zeta} = 0$, blade pitch angle $\theta_b = 0$.



(a) Lead-lag regressive mode damping



(b) Body pitch and flap regressive mode damping



(c) Body roll mode damping

Figure 6.19: Modal damping as a function of rotor speed for configuration 1; $\omega_{\beta 0} < \omega_{\zeta 0}$, $K_{p\zeta} = 0$.

Bibliography

- [1] Coleman, R. P. and Feingold, A. M., "Theory of Self-Excited Mechanical Oscillations of Helicopter Rotors with Hinged Blades," NACA Report 1351, 1958.
- [2] Hammond, C. E., "An applicatoin of Floquet theory to the prediction of mechanical instability," *Journal of the American Helicopter Society*, Vol. 19, No.4, Oct. 1974. pp, 14-23.
- [3] Bousman, W. G., "An Experimental Investigation of the Effects of Aeroelastic Couplings on Aeromechanical Stability of a Hingeless Rotor Helicopter," *Journal of the American Helicopter Society*, Vol. 26, (1), January 1981, pp. 46-54.
- [4] Donham, R. E., Cardinale, S. V., and Sachs, I. B., "Ground and Air Resonance Characteristics of a Soft In-plane Rigid-Rotor System," *Journal of the American Helicopter Society*, Vol. 14, (4), October 1969, pp. 33-41.
- [5] Lytwyn, R. T., Miao, W., and Woitsch, W., "Airborne and Ground Resonance of Hingeless Rotors," *Journal of the American Helicopter Society*, Vol. 16, (2), April 1971, pp. 2-9.
- [6] Miao, W., Edwards, W. T., and Brandt, D. E., "Investigation of Aeroelastic Stability Phenomena of the Helicopter by In-flight Shake Test," *NASA Symposium on Flutter Testing Techniques*, NASA SP-415, 1976, pp. 473-495.
- [7] Staley, J. A., Gabel, R., and MacDonald, H. I., "Full Scale Ground and Air Resonance Testing of the Army-Boeing Vertol Bearingless Main Rotor," Preprint No. 79-23. American Helicopter Society 35th Annual Forum Proceedings, May 1979.

Chapter 7

Aeroelastic Stability in Forward Flight

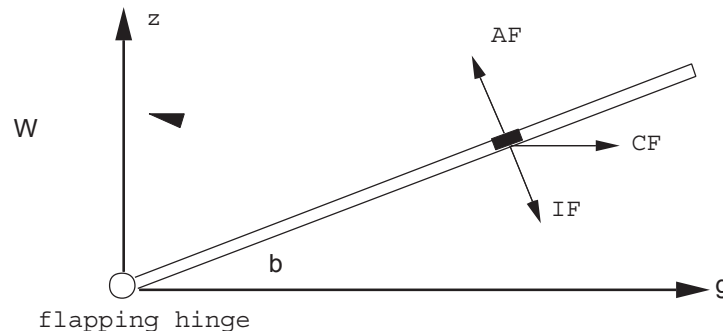
The forward flight condition introduces an extra dimension of complexity to the rotorcraft aeroelastic stability and response problems. The airflow on the disk is asymmetric, and also a part of the region is in either stalled flow or in reversed flow condition. The complexity is caused by the blade aerodynamic forces which are very much involved.

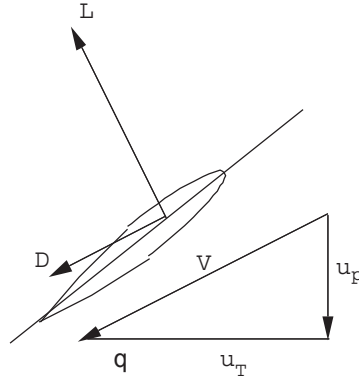
The equations of blade motion in forward flight contain many periodic terms and therefore one has to develop special mathematical tools to solve these equations. One possible way of solving these equations is to write the blade equations in the fixed reference frame using Fourier coordinate transformation, and then solve these equations approximately either neglecting altogether periodic terms or using the harmonic balance method on the periodic terms. The other involved method is to use Floquet theory in the fixed reference frame. The second approach is to keep the blade equations in the rotating reference frame and solve these using the Floquet or time integration technique or harmonic balance method. With the dynamic inflow modeling, it is more appropriate to use the first approach and solve the equations in the fixed reference frame.

To understand the fundamentals of forward flight, we shall start with a simple blade model undergoing rigid flap motion. Later on a two-degree-of-motion, flap and lag, will be investigated for aeroelastic stability in forward flight.

7.1 Flap Motion in forward flight

The blade is assumed rigid and it undergoes a single degree of motion, rigid flap, about the flap hinge. The blade is exposed to forward flight environment.





The equation of motion of a blade is

$$\beta^{**} + \nu_{\beta}^2 \beta = \gamma \overline{M}_{\beta}$$

where ν_{β} is the rotating flap frequency and γ is the Lock number. The \overline{M}_{β} represents the aerodynamic moment about the flap hinge

$$\overline{M}_{\beta} = \frac{1}{\rho a c \Omega^2 R^4} \int_0^L r F_z dr$$

$$F_z \approx L$$

$$= \frac{1}{2} \rho V^2 c a \left(\theta - \frac{u_p}{u_T} \right)$$

$$= \frac{1}{2} \rho c a (u_T^2 \theta - u_p u_T)$$

The flow components are

$$\frac{u_T}{\Omega R} = \mu \sin \psi + x$$

$$\frac{u_p}{\Omega R} = x \dot{\beta} + \lambda + \beta \mu \cos \psi$$

where $x = \frac{r}{R}$ and λ is the induced inflow. The μ is the advance ratio,

$$\mu = \frac{v \cos \alpha}{\Omega R} \approx \frac{V}{\Omega R} \quad (\alpha \text{ is tilt of TPP})$$

$$\overline{M}_{\beta} = \frac{1}{2} \int_0^1 x \left[\left(\frac{u_T}{\Omega R} \right)^2 \theta - \frac{u_p}{\Omega R} \frac{u_T}{\Omega R} \right] dx$$

Assuming θ is uniform along the blade length. It is also assumed that the induced inflow λ is uniform on the disk.

$$\begin{aligned} \overline{M}_{\beta} &= \left(\frac{1}{8} + \frac{\mu}{3} \sin \psi + \frac{\mu^2}{4} \sin^2 \psi \right) \theta - \left(\frac{1}{8} + \frac{\mu}{6} \sin \psi \right) \beta^* \\ &\quad - \left(\frac{1}{6} + \frac{\mu}{4} \sin \psi \right) \lambda - \mu \cos \psi \left(\frac{1}{6} + \frac{\mu}{4} \sin \psi \right) \beta \end{aligned}$$

The flap equation becomes

$$\beta^{**} + \left(\frac{1}{8} + \frac{\mu}{6} \sin \psi \right) \beta^* + \left[\nu_{\beta}^2 + \gamma \mu \cos \psi \left(\frac{1}{6} + \frac{\mu}{4} \sin \psi \right) \right] \beta$$

$$\begin{aligned}
&= \gamma \left(\frac{1}{8} + \frac{\mu}{3} \sin \psi + \frac{\mu^2}{4} \sin^2 \psi \right) \theta \\
&\quad - \gamma \left(\frac{1}{6} + \frac{\mu}{4} \sin \psi \right) \lambda
\end{aligned} \tag{7.1}$$

This is a linear differential equation containing periodic coefficients. If the effect of pitch-flap coupling $k_{p\beta}$ is also to be introduced, then replace θ by $\theta - k_{p\beta}$ in the above equation.

$$\begin{aligned}
&\beta^{**} + \gamma \left(\frac{1}{8} + \frac{\mu}{6} \sin \psi \right) \beta^* + \left[\nu_\beta^2 + \gamma \mu \cos \psi \left(\frac{1}{6} + \frac{\mu}{4} \sin \psi \right) \right. \\
&\quad \left. + \gamma \left(\frac{1}{8} + \frac{\mu}{3} \sin \psi + \frac{\mu^2}{4} \sin^2 \psi \right) k_{p\beta} \right] \beta \\
&= \gamma \left(\frac{1}{8} + \frac{\mu}{3} \sin \psi + \frac{\mu^2}{4} \sin^2 \psi \right) \theta - \gamma \left(\frac{1}{6} + \frac{\mu}{4} \sin \psi \right) \lambda
\end{aligned} \tag{7.2}$$

7.2 Hover Stability Roots

Let us first examine hover flight case ($\mu = 0$). The blade equation becomes

$$\beta^{**} + \frac{\gamma}{8} \beta^* + \left(\nu_\beta^2 + \frac{\gamma}{8} k_{p\beta} \right) \beta = \frac{\gamma \theta}{8} - \frac{\gamma \lambda}{6}$$

The stability of the system can be examined from the eigenvalues of this equation.

$$s = -\frac{\gamma}{16} \pm i \sqrt{\nu_\beta^2 + k_{p\beta} \frac{\gamma}{8} - \left(\frac{\gamma}{16} \right)^2}$$

This is a complex pair i.e., two eigenvalues. The real part of the eigenvalue represents the damping of the flap mode and the imaginary part represents the frequency of the flap mode.

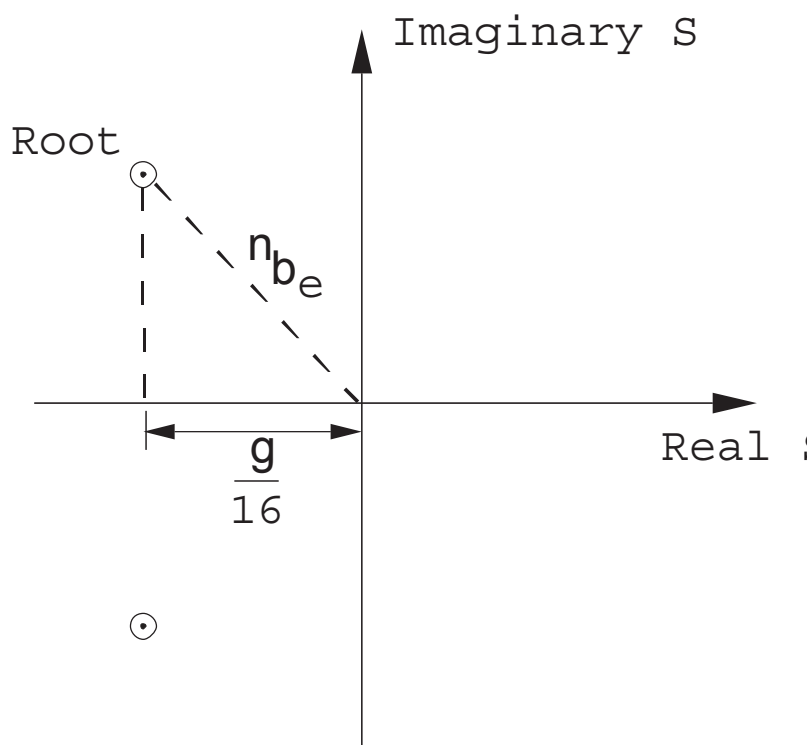
$$\text{Frequency of damped oscillations } \omega_d = \sqrt{\nu_\beta^2 + k_{p\beta} \frac{\gamma}{8} - \left(\frac{\gamma}{16} \right)^2}$$

$$\text{Natural frequency } \nu_{\beta e} = \sqrt{\nu_\beta^2 + k_{p\beta} \frac{\gamma}{8}}$$

$$\text{Damping ratio } \zeta = -\frac{\text{Real } s}{|s|}$$

$$= \frac{\gamma}{16\nu_{\beta e}}$$

Thus, the damping of the flap mode depends on the Lock number and is always a positive number. This shows that there is no likelihood of instability of the flap mode. In fact, for a typical Lock number of 8, the damping ratio is about 50%, a very high number. This damping is due to aerodynamic force caused by the flapping motion. For a 4-bladed rotor, there will be four identical pairs. Let us plot roots for a blade in a complex plane



The roots will always lie in the left half of the plane on a semi-circular arc.

7.3 Forward Flight Stability Roots

The equation of motion for a blade in forward flight (Eq. 7.2) contains periodic coefficients. This equation is expressed in the rotating reference frame. One way is to solve numerically this equation using the Floquet theory. For hover case ($\mu = 0$), the roots are complex conjugate pairs and the magnitude of the root depends on ν_β , Y and $k_{p\beta}$. For forward flight the roots, in addition, also depend on the advance ratio, μ . For low μ , the forward flight roots behavior is influenced by hover roots. Let us consider these blade cases with $k_{p\beta} = 0$.

I. $\nu_\beta = 1$ and $\gamma = 12$ (Articulated)

$$s_{\text{hover}} = -\frac{12}{16} \pm i\sqrt{1 - \left(\frac{12}{16}\right)^2}$$

$$= -\frac{3}{4} \pm i\sqrt{\frac{7}{16}}$$

Frequency of oscillation close to 1/2 per rev.

II. $\nu_\beta = 1.15$ and $\gamma = 6$ (Hingeless)

$$s_{\text{hover}} = -\frac{3}{8} \pm i\sqrt{(1.15)^2 - \frac{9}{64}}$$

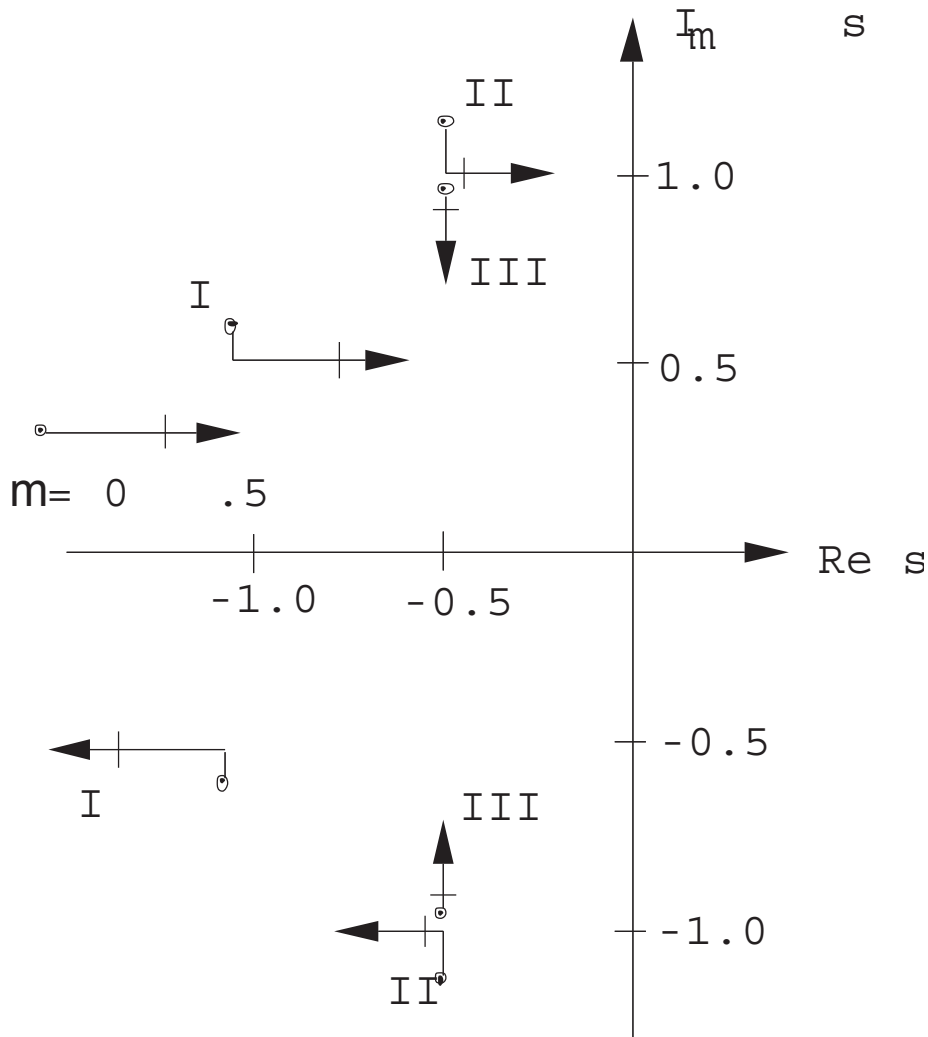
Frequency of oscillation close to 1 per rev.

III. $\nu_\beta = 1.0$ and $\gamma = 6$ (Articulated)

$$s_{\text{hover}} = -\frac{3}{8} \pm i\sqrt{1 - \frac{9}{64}}$$

Frequency of oscillation not close to 1/2 per rev. or 1 per rev.

Let us examine the behavior of roots for change of μ from 0 to 0.5.



For values of γ and ν_β such that the hover frequency ($I_m s$) is not close to a multiple of $1/2/\text{rev}$. (Case III), the roots for low μ only exhibit a second order (μ^2) change in frequency and the damping remains unchanged.

For values of γ and ν_β such that the hover frequency ($I_m s$) is close to a multiple of $1/2/\text{rev}$. (Case I), the roots for low μ exhibit a first order (μ) change. There can occur a degradation of stability, perhaps even an instability, an important characteristic of the periodic system.

For values of γ and ν_β such that the hover frequency ($I_m s$) is close to $1/\text{rev}$. (Case II), the roots exhibit similar behavior like Case I. For both cases one finds that the frequency $I_m s$ decreases while damping Real s remains constant until an integer multiple of $1/2/\text{rev}$. is reached. A further increase of μ results in a change of damping, a decrease for the upper root and an increase for the lower root, and the frequency stays constant. For larger μ , one needs to include the effect of reversed flow as well as higher modes.

7.3.1 Stability Roots in Rotating Coordinates

7.3.2 Stability Roots in Fixed Coordinates

Let us examine the flapping dynamics in the fixed reference frame. The equation of motion for the blade flapping in the rotating frame (Eq. 7.2) is converted to the fixed reference frame using the Fourier coordinate transformation.

Let us consider a 3-bladed rotor, $n = 1$

$$\beta^{(m)} = \beta_0 + \beta_{1c} \cos \psi_m + \beta_{1s} \sin \psi_m$$

Using

$$\frac{1}{N} \sum_{m=1}^N (de) = 0$$

$$\frac{2}{N} \sum_{m=1}^N (de) \cos \psi_m = 0$$

$$\frac{2}{N} \sum_{m=1}^N (de) \sin \psi_m = 0$$

results in

$$\begin{bmatrix} \beta_0^{**} \\ \beta_{1c}^{**} \\ \beta_{1s}^{**} \end{bmatrix} = \begin{bmatrix} \frac{\gamma}{8} & 0 & \frac{\mu\gamma}{12} \\ 0 & \frac{\gamma}{8} + \frac{\mu\gamma}{12} \sin 3\psi & 2 - \frac{\mu\gamma}{12} \cos 3\psi \\ \frac{\mu\gamma}{6} & -2 - \frac{\mu\gamma}{12} \cos 3\psi & \frac{\gamma}{8} - \frac{\mu\gamma}{12} \sin 3\psi \end{bmatrix} \begin{bmatrix} \beta_0^* \\ \beta_{1c}^* \\ \beta_{1s}^* \end{bmatrix} + \begin{bmatrix} \nu_\beta^2 & \frac{\mu^2\gamma}{16} \sin 3\psi & -\frac{\mu^2\gamma}{16} \cos 3\psi \\ \frac{\mu\gamma}{6} + \frac{\mu^2\gamma}{8} \sin 3\psi & \nu_\beta^2 - 1 + \frac{\mu\gamma}{6} \cos 3\psi & \frac{\gamma}{8} + \frac{\mu\gamma}{6} \sin 3\psi + \frac{\mu^2\gamma}{16} \\ -\frac{\mu^2\gamma}{8} \cos 3\psi & -\frac{\gamma}{8} + \frac{\mu^2\gamma}{16} + \frac{\mu\gamma}{6} \sin 3\psi & \nu_\beta^2 - 1 - \frac{\mu\gamma}{6} \cos 3\psi \end{bmatrix} \begin{bmatrix} \beta_0 \\ \beta_{1c} \\ \beta_{1s} \end{bmatrix} \quad (7.3)$$

Similarly for a 4-bladed rotor

$$\beta^{(m)} = \beta_0 + \beta_{1c} \cos \psi_m + \beta_{1s} \sin \psi_m + \beta_2 (-1)^{(m)}$$

results in

$$\begin{bmatrix} \beta_0^{**} \\ \beta_{1c}^{**} \\ \beta_{1s}^{**} \\ \beta_2^{**} \end{bmatrix} = \begin{bmatrix} \frac{\gamma}{8} & 0 & \frac{\mu\gamma}{12} & 0 \\ 0 & \frac{\gamma}{8} & 2 & \frac{\mu\gamma}{6} \sin 2\psi \\ -\frac{\mu\gamma}{16} & -2 & \frac{\gamma}{8} & -\frac{\mu\gamma}{6} \cos 2\psi \\ 0 & \frac{\mu\gamma}{12} \sin 2\psi & -\frac{\mu\gamma}{12} \cos 2\psi & \frac{\gamma}{8} \end{bmatrix} \begin{bmatrix} \beta_0^* \\ \beta_{1c}^* \\ \beta_{1s}^* \\ \beta_2^* \end{bmatrix} + \begin{bmatrix} \nu_\beta^2 & 0 & 0 & \frac{\mu^2\gamma}{8} \sin 2\psi \\ \frac{\mu\gamma}{6} & \nu_\beta^2 - 1 + \frac{\mu^2\gamma}{16} \sin 4\psi & \frac{\gamma}{8} + \frac{\gamma}{16} \mu^2 - \frac{\gamma}{16} \mu^2 \cos 4\psi & \frac{\mu\gamma}{6} \cos 2\psi \\ 0 & -\frac{\gamma}{8} + \frac{\gamma}{16} \mu^2 - \frac{\gamma}{16} \mu^2 \cos 4\psi & \nu_\beta^2 - 1 - \mu^2 \frac{\gamma}{16} \sin 4\psi & \frac{\mu\gamma}{8} \sin 2\psi \\ \frac{\mu^2\gamma}{8} \sin 2\psi & \frac{\mu\gamma}{6} \cos 2\psi & \frac{\mu\gamma}{6} \sin 2\psi & \nu^2 \beta \end{bmatrix} \begin{bmatrix} \beta_0 \\ \beta_{1c} \\ \beta_{1s} \\ \beta_2 \end{bmatrix} \quad (7.4)$$

It is important to note that the 3-bladed rotor equations in the fixed system contain periodic terms of 3ψ only. For a 4-bladed rotor, the equations contain periodic terms of 4ψ as well as 2ψ . Therefore, in the fixed system, the vibratory forces take place at N/rev for an odd bladed rotor and N/rev and $\frac{N}{2}/\text{rev}$ for an even bladed rotor where N is the total number of blades.

Let us examine an example of an articulated 3-bladed rotor with $\nu_\beta = 1$ and $\gamma = 12$. In the rotating frame there are three identical roots

$$s_R = -\frac{3}{4} \pm \sqrt{\frac{7}{16}}$$

and in the fixed systems, again there are three roots;

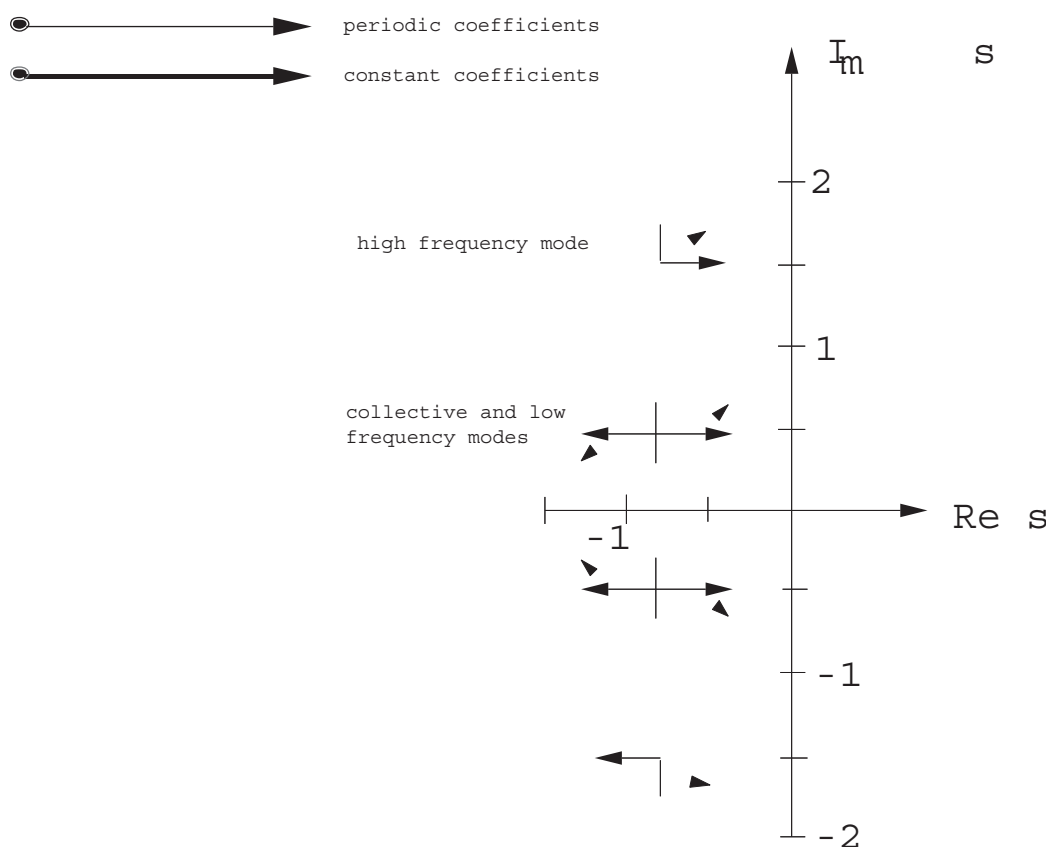
coning $s = s_R$

high frequency $s = s_R + i$

low frequency $s = s_R - i$

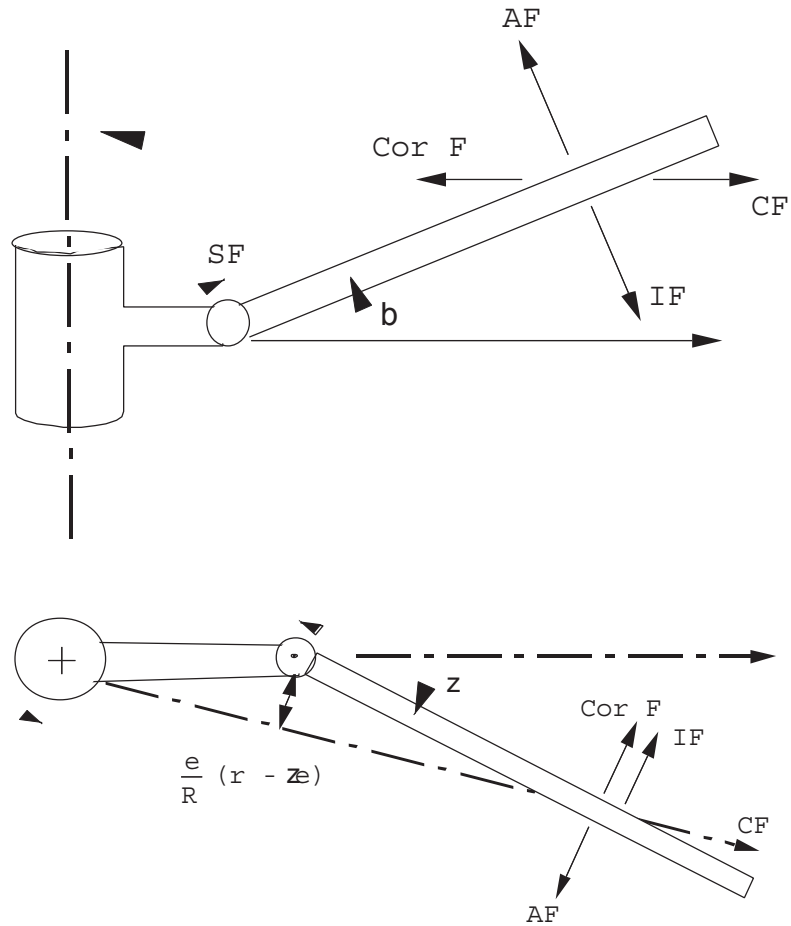
For forward flight condition, the roots of the equations can be obtained for different μ . One simple approach is to neglect all periodic terms in the fixed system equations and solve these as constant coefficient equations. The results are quite satisfactory for low advance ratios ($\mu < 0.5$), especially for the low frequency mode. One should keep in mind that this type of approximation won't work in the rotating frame. The second method is to solve the fixed frame equations numerically using the Floquet theory. Another way is to use the harmonic balance method in the fixed frame. In the figure, results are obtained using the Floquet theory and constant coefficient approximation.

The stability behavior will be identical whether the rotating reference frame or the fixed reference frame are used.



7.4 Flap-lag Stability in Forward Flight

The blade is assumed rigid and it undergoes two degrees of motion, flap and lag motions about hinges. There are bending springs at the hinges to obtain desired flap and lag frequencies.



The equations of motion become

Flap Eq.:

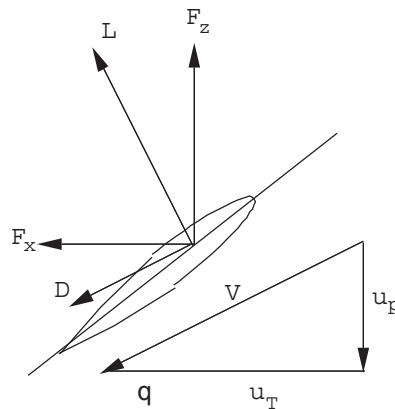
$$\beta^{**} + \nu_{\beta}^2 \beta - 2\beta \zeta^* = \gamma \overline{M}_{\beta} + \frac{\omega_{\beta_0}^2}{\Omega^2} \beta_p$$

Lag Eq.:

$$\zeta^{**} + \nu_{\zeta}^2 \zeta + 2\frac{\omega_{\zeta_0}}{\Omega} \zeta_L \zeta^* + \beta \beta^* = \gamma \overline{M}_{\zeta}$$

(7.5)

where ν_{β} and ν_{ζ} are rotating flap and lag frequencies and ζ_L is the structural damping coefficient in the lag mode. The ω_{β_0} and ω_{ζ_0} are the nonrotating flap and lag frequencies.



Quasisteady aerodynamics is used to obtain the aerodynamic forces on the blade. The reversed flow effects are neglected.

$$F_z \approx L = \frac{1}{2} \rho a c (u_T^2 \theta - u_p u_T)$$

$$F_x \approx L \frac{u_p}{u_T} + D = \frac{1}{2} \rho a c \left(\frac{c_d}{a} u_T^2 + u_p u_T \theta - u_p^2 \right)$$

Perturbation forces are

$$\delta F_z = \frac{1}{2} \rho a c [\delta u_T (2u_T \theta - u_p) - \delta u_p (u_T) + \delta \theta u_T^2]$$

$$\delta F_x = \frac{1}{2} \rho a c \left[\delta u_T \left(2u_T \frac{c_d}{a} + u_p \theta \right) + \delta u_p (u_T \theta - 2u_p) + \delta \theta (u_p u_T) \right]$$

For making analysis simple, the effect of radial force is neglected.

The flow components are

Steady:

$$\begin{aligned} \frac{u_T}{\Omega R} &= x + \mu \sin \psi \\ \frac{u_p}{\Omega R} &= \lambda + x \dot{\beta} + \beta \mu \cos \psi \end{aligned} \quad (7.6)$$

Perturbation:

$$\begin{aligned} \frac{\delta u_T}{\Omega R} &= -x \dot{\zeta} - \mu \zeta \cos \psi \\ \frac{\delta u_p}{\Omega R} &= x \dot{\beta} + \mu \beta \cos \psi \end{aligned} \quad (7.7)$$

The solution of the governing equation (7.6) consists of two major steps.

- (a) Calculation of trim.
- (b) Calculation of perturbation stability.

7.4.1 Perturbation Stability Solution

It is assumed that the flutter motion is a small perturbation about the steady trim solution.

$$(\beta)_{\text{Total}} = (\beta)_{\text{trim}} + (\beta)_{\text{perturbation}}$$

$$(\zeta)_{\text{Total}} = (\zeta)_{\text{perturbation}}$$

This is because $(\zeta)_{\text{trim}}$ trim is neglected. The trim values of β are calculated as

$$(\beta)_{\text{trim}} = -\beta_{1c} \sin \psi + \beta_{1s} \sin \psi = \beta_T$$

$$(\beta)_{\text{trim}}^* = \beta_0 + \beta_{1c} \cos \psi + \beta_{1s} \cos \psi = \beta_T^*$$

Let us remove the perturbation word from β and ζ . Substituting this in the governing equation (7.5), and also including the perturbation aerodynamic moment expressions, and keeping linear terms in perturbation motion components one gets,

$$\begin{bmatrix} ** \\ \beta \\ ** \\ \zeta \end{bmatrix} + [C(\psi)] \begin{bmatrix} * \\ \beta \\ * \\ \zeta \end{bmatrix} + [K(\psi)] \begin{bmatrix} \beta \\ \zeta \end{bmatrix} = 0 \quad (7.8)$$

These are matrices of order two, and the various terms are

$$c_{11}(\psi) = \frac{\gamma}{8} \left(1 + \frac{4}{3} \mu \sin \psi \right)$$

$$\begin{aligned}
c_{12}(\psi) &= \frac{\gamma}{8} \left(\frac{4}{3}\lambda + \frac{4}{3}\mu\beta_T \cos \psi + \beta_T^* \right) \\
&\quad - \frac{\gamma}{4}\theta \left(1 + \frac{4}{3}\mu \sin \psi \right) + 2\beta_T \\
c_{21}(\psi) &= -\frac{\gamma}{4} \left(\frac{4}{3}\lambda + \frac{4}{3}\mu\beta_T \cos \psi - \beta_T^* \right) \\
&\quad + \frac{\gamma}{8}\theta \left(1 + \frac{4}{3}\mu \sin \psi \right) - 2\beta_T \\
c_{22}(\psi) &= \frac{\gamma}{8}\theta \left(\frac{4}{3}\lambda + \frac{4}{3}\mu \cos \psi \beta_T + \beta_T^* \right) \\
&\quad + \frac{c_{d0}}{a} \frac{\gamma}{4} \left(1 + \frac{4}{3}\mu \sin \psi \right) - 2\beta_T \beta_T^* \\
k_{11}(\psi) &= \nu_\beta^2 + \frac{\gamma}{8} \left(\frac{4}{3}\mu \cos \psi + 2\mu^2 \sin \psi \cos \psi \right) \\
&\quad - \frac{\gamma}{8}k_{p\beta} \left(1 + \frac{8}{3}\mu \sin \psi + 2\mu^2 \sin^2 \psi \right) \\
k_{12}(\psi) &= \frac{\gamma}{8}\mu \cos \psi \left(2\lambda + \frac{4}{3}\beta_T^* \right) - \frac{\gamma}{4}\theta \left(\frac{4}{3}\mu \cos \psi + 2\mu^2 \sin \psi \cos \psi \right) \\
&\quad - \frac{\gamma}{4}\beta_T \left(\mu^2 \cos 2\psi - \frac{2}{3}\mu \sin \psi \right) \\
&\quad - \frac{\gamma}{8}k_{p\beta} \left(1 + \frac{8}{3}\mu \sin \psi + 2\mu^2 \sin^2 \psi \right) \\
k_{21}(\psi) &= -\frac{\gamma}{4}\mu \cos \psi \left(2\lambda + \frac{4}{3}\beta_T^* \right) + \frac{\gamma}{8}\theta \left(\frac{4}{3}\mu \cos \psi + \mu^2 \sin 2\psi \right) \\
&\quad - \frac{\gamma}{2}\beta_T \mu^2 \cos^2 \psi + \frac{\gamma}{8}k_{p\beta} \left[\frac{4}{3}\lambda \left(1 + \frac{3}{2}\mu \sin \psi \right) \right. \\
&\quad \left. + \beta_T^* \left(1 + \frac{8}{3}\mu \sin \psi \right) + \beta_T \left(\frac{4}{3}\mu \cos \psi + \mu^2 \sin 2\psi \right) \right] \\
k_{22}(\psi) &= \nu_\zeta^2 + \frac{\gamma}{8} \left[2\frac{c_{d0}}{a} \left(\frac{4}{3}\mu \cos \psi + \psi^2 \sin 2\psi \right) \right. \\
&\quad \left. + \mu \cos \psi \theta \left(2\lambda + \frac{4}{3}\beta_T^* \right) - \beta_T \theta \left(\frac{4}{3}\mu \sin \psi - 2\mu^2 \cos \psi \right) \right. \\
&\quad \left. + 2\mu\beta_T \sin \psi \left(2\lambda + \frac{4}{3}\beta_T^* + 2\mu\beta_T \cos \psi \right) \right] \\
&\quad + \frac{\gamma}{8}k_{p\beta} \left[\frac{4}{3}\lambda \left(1 + \frac{3}{2}\mu \sin \psi \right) + \beta_T \left(\frac{4}{3}\mu \cos \psi + \mu^2 \sin 2\psi \right) \right. \\
&\quad \left. + \beta_T^* \left(1 + \frac{4}{3}\mu \sin \psi \right) \right]
\end{aligned}$$

In the above expressions

$$\theta = \theta_0 + \theta_{1c} \cos \psi + \theta_{1s} \sin \psi$$

The stability of the system is calculated from the solution of the perturbation equations (7.8). There are many methods to solve these equations. Two possible approaches are discussed here

- (a) Constant coefficient approximation.
- (b) Floquet Theory.

7.4.2 Constant Coefficient Approximation

The coefficients of the matrices (\tilde{c}, \tilde{k}) contain periodic terms, and these are approximated as constant terms by taking average values over a period of 2π . For example,

$$(c_{ij})_{\text{new}} = \frac{1}{2\pi} \int_0^{2\pi} c_{ij}(\psi) d\psi$$

$$(k_{ij})_{\text{new}} = \frac{1}{2\pi} \int_0^{2\pi} k_{ij}(\psi) d\psi$$

and this results in

$$c_{11} = \frac{\gamma}{8}$$

$$c_{12} = 2\beta_0 + \frac{\gamma}{8} \left(\frac{4}{3}\lambda + \frac{2}{3}\mu\beta_{1c} \right) - \frac{\gamma}{4} \left(\theta_0 + \frac{2}{3}\mu\theta_{1s} \right)$$

$$c_{21} = -2\beta_0 - \frac{\gamma}{4} \left(\frac{4}{3}\lambda + \frac{2}{3}\mu\beta_{1c} \right) + \frac{\gamma}{8} \left(\theta_0 + \frac{2}{3}\mu\theta_{1s} \right)$$

$$c_{22} = \frac{\gamma}{8} \left[2\frac{c_{d_0}}{a} + \frac{1}{2}\theta_{1c}\beta_{1s} - \frac{1}{2}\theta_{1s}\beta_{1c} + \frac{2}{3}\mu\theta_{1c} + \frac{2}{3}\mu\theta_{1c}\beta_0 \right. \\ \left. + \theta_0 \left(\frac{4}{3}\lambda + \frac{2}{3}\mu\beta_{1c} \right) \right]$$

$$k_{11} = \nu_\beta^2 - \frac{\gamma}{8}k_{p_\beta}(1 + \mu^2)$$

$$k_{12} = -\frac{\gamma}{8}k_{p_\zeta}(1 + \mu^2) - \frac{\gamma}{6}\mu\theta_{1c}$$

$$k_{21} = \frac{\gamma}{6}\lambda k_{p_\zeta} + \frac{\gamma}{8}\mu \left(\frac{2}{3}\theta_{1c} - \frac{4}{3}\beta_{1c} - 2\mu\beta_0 \right)$$

$$k_{22} = \frac{\gamma}{8} \left[\mu\lambda\theta_{1c} - \frac{2}{3}\mu\beta_0\theta_{1s} - \frac{4}{3}\mu\beta_0\beta_{1c} + 2\mu\lambda\beta_{1s} \right] \frac{\gamma}{6}k_{p_\zeta}\lambda$$

The perturbation equations (7.8) become constant coefficient equations and these can be solved as a standard eigenvalue problem.

7.4.3 Floquet Theory

The perturbation equations (7.8) contain periodic terms and the stability of these equations can be calculated using Floquet theory. As a first step, the Floquet transition matrix is to be calculated. For this purpose, the equations (7.8) are transformed to first order form.

$$\{\dot{q}^*\} = [A(\psi)]\{q\} \tag{7.9}$$

where

$$\{q\} = \begin{bmatrix} \beta \\ \zeta \\ * \\ \beta \\ * \\ \zeta \end{bmatrix}$$

$$[A] = \begin{bmatrix} \tilde{O} & \tilde{I} \\ -\tilde{k} & -\tilde{c} \end{bmatrix}$$

To obtain the Floquet transition matrix $[Q]$, the equations (7.9) are solved numerically using some standard time integration technique (say Runge-Kutta) with unity initial conditions. The solution at $\psi = 2\pi$ gives the elements of transition matrix. For example,

$$\begin{bmatrix} \beta \\ \zeta \\ * \\ \beta \\ * \\ \zeta \end{bmatrix} = \begin{bmatrix} 1 \\ 0 \\ 0 \\ 0 \end{bmatrix}_{Ic} \Rightarrow \begin{bmatrix} Q_{11} \\ Q_{21} \\ Q_{31} \\ Q_{41} \end{bmatrix} \quad (\text{solution at } \psi = 2\pi)$$

After the transition matrix is evaluated, the next step is to obtain its eigenvalue.

$$\lambda\{q\} = [Q]\{q\}$$

If the absolute value of any of the eigenvalue (λ) is greater than one, the system is unstable.

The numerical results are obtained for a typical rotor configuration with the following characteristics

$$\begin{aligned} \nu_\beta &= 1.15 & \gamma &= 1.15 & \frac{c_T}{\sigma} &= .2 & \sigma &= .05 \\ \nu_\zeta &= 1.4 & k_{p\beta} &= k_{p\zeta} = 0 & \beta_p &= 0 & f/A &= 0.01 \\ c_{d0} &= .01 & a &= 2\pi & \frac{h}{R} &= .2 \\ x_{cg} &= y_{cg} = 0 & c_{m_{xF}} &= c_{m_{yF}} = 0 \end{aligned}$$

Earlier, the trim is calculated for this configuration. These results are plotted for various values of advance ratio μ .

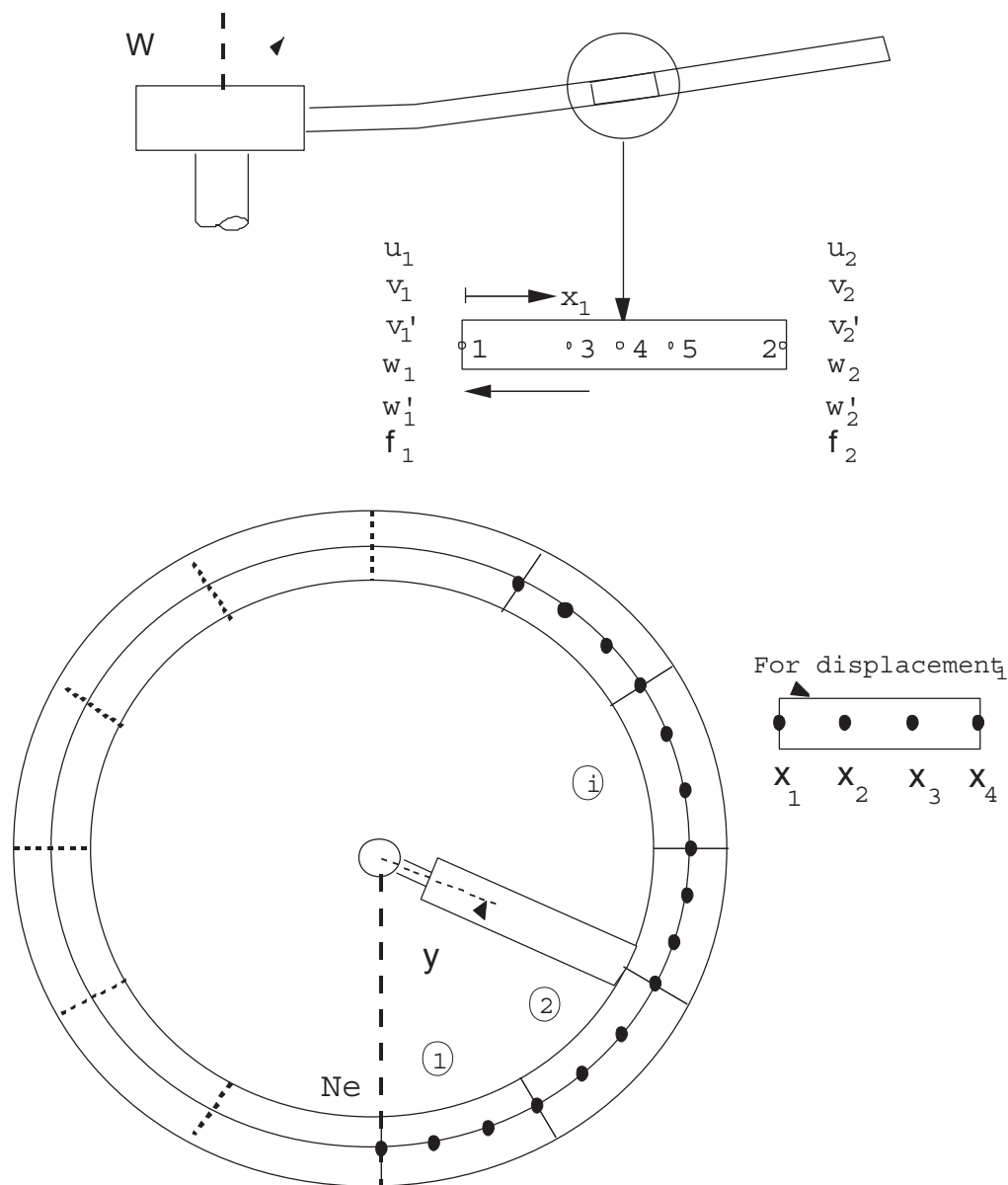
Conclusions:

1. The constant coefficient approximation in the rotating system gives satisfactory results for low advance ratio ($\mu < 0.1$).
2. The flap-lag stability in forward flight is very sensitive to the trim solution. For example, the propulsive trim results are quite different from moment trim results.
3. For large advance ratio ($\mu > 0.1$), the inflow is affected appreciably by the helicopter drag term (f/A).
4. The implicit periodic coefficients (due to β_{1c} , β_{1s} , θ_{1c} , θ_{1s}) and the explicit periodic coefficients ($\mu \sin \psi$, $\mu \cos \psi$) are important for flap-lag stability analysis.
5. The torsion degree of motion has a considerable influence on blade stability if torsional frequency is small.

References

1. Johnson, W., Helicopter Theory, Princeton University Press, 1980, Chapter 12.
2. Biggers, J. C., "Some Approximations to the Flapping Stability of Helicopter Rotors," Journal of the American Helicopter Society, Vol. 19, No. 4, Oct. 1974.
3. Friedman, P. P. and Kattapalli, S. B. R., "Coupled Flap-Lag-Torsional Dynamics of Hingeless Rotor Blades in Forward Flight," Journal of the American Helicopter Society, Vol. 24, No. 4, Oct. 1982, pp. 28-36.

4. Peters, D. A., "Flap-Lag Stability of Helicopter Rotor Blades in Forward Flight," Journal of the American Helicopter Society, Vol. 20, No. 4, Oct. 1975, pp. 2-13.
5. Panda, B. and Chopra, I., "Flap-Lag-Torsion Stability in Forward Flight," Presented at the Second Decennial Specialists' Meeting on Rotorcraft Dynamics at Ames Research Center, Moffett Field, Calif., Nov. 1984.
6. Panda, B. and Chopra, I., "Dynamic Stability of Hingeless and Bearingless Rotors in Forward Flight," Presented at the International Conference on Rotorcraft Basic Research, Research Triangle Park, North Carolina, Feb. 1985.



COUPLED TRIM ANALYSIS

- Uncoupled Vehicle Trim (Propulsive)
 - Control Settings and Vehicle Attitude
 - Initial Guess for Iteration Process

- Blade Steady Response
 - Determination of Time Dependent Blade Deflections Using Finite Element Method in Time
 - Normal Mode Equations
- Coupled Trim Solution
 - Update Control Settings and Vehicle Attitude
 - Satisfy Nonlinear Vehicle Equilibrium Equations
 - Vehicle Trim and Blade Response Calculated Iteratively as One Coupled Solution Using Modified Newton Method

Chapter 8

Trailing Edge Flaps and Tabs

This chapter deals with the dynamics of trailing edge flaps. Smart material based actuators can be used to activate on-blade trailing edge flaps. The aeroelastic response of the flaps can be used to effectively change the airload distribution on the rotor blades. In general, active surfaces like trailing edge flaps can be used for – 1. vibration control, 2. loads control, and 3. swash-plateless primary control. Trailing edge flaps have also been studied for purposes of rotor noise control.

Flaps on rotor blades operate under high centrifugal loads. Present smart actuators have been demonstrated to produce $\pm 10^\circ$ of flap deflections in vacuum, and $\pm 4^\circ$ with wind on. To obtain such values of flap deflection, the actuator deformations are amplified using mechanical, electrical, or aerodynamic means. Mechanical and electrical amplifications are widely used. Aerodynamic amplification, e.g. in form of servo tabs, is still in the exploratory phase for rotary wing applications [1].

To avoid confusion with blade flap, the trailing edge flap will be termed aileron.

8.1 Flap-Torsion-Aileron Dynamics of a Wing Section

First a classical 2 degree-of-freedom flap torsion model is shown. Then a 3 degree-of-freedom model including aileron dynamics is studied.

8.1.1 Flap-Torsion dynamics

First consider a case without aileron. In order to maintain classical notations (used in bending-torsion flutter studies) let h be the heave motion positive downwards, and θ be the nose up twist. The heave motion h is the translational motion of the shear center, i.e. elastic axis. The twist θ is ofcourse same about all points. The heave equation is obtained by balancing the net force. The moment equation is obtained by balancing the net moments about the shear center. Balancing moments about the shear center prevents the calculation of the reaction forces occuring at that point.

The moment equilibrium gives

$$\begin{aligned} I_{cg}\ddot{\theta} + mx_I^2\ddot{\theta} + mx_I\ddot{h} + k_\theta\theta &= M_{ea} \\ I_\theta\ddot{\theta} + S_\theta\ddot{h} + k_\theta\theta &= M_{ea} \end{aligned} \tag{8.1}$$

The force equilibrium gives

$$\begin{aligned} m\ddot{h} + mx_I\ddot{\theta} + k_h h &= -L \\ S_\theta\ddot{\theta} + m\ddot{h} + k_h h &= -L \end{aligned} \tag{8.2}$$

8.1.2 Flap-torsion-aileron dynamics: Force method

A coupled flap-torsion-aileron model for a wing is developed using force method (Newton). The derivation of the governing equations are simpler using the energy method. The energy method is shown in the next subsection. The force balance method is used here to illustrate the force transfer mechanism from the aileron to the wing.

Consider the free body diagram of the aileron alone. The downward acceleration of the aileron c.g. and its angular acceleration are given by

$$\ddot{h} + \{b(a+c) + y_I\} \ddot{\theta} + y_I \ddot{\delta}$$

and

$$\ddot{\theta} + \ddot{\delta}$$

Balancing moments about the aileron hinge gives

$$\begin{aligned} I_{c_{g\delta}}(\ddot{\theta} + \ddot{\delta}) + m\delta \left[\ddot{h} + \{b(a+c) + y_I\} \ddot{\theta} + y_I \ddot{\delta} \right] y_I + k_\delta \delta &= M_2 \\ I_\delta \ddot{\delta} + I_\theta \ddot{\theta} + S_\delta \ddot{h} + S_\delta b(a+c) \ddot{\theta} + k_\delta \delta &= M_2 \\ I_\delta \ddot{\delta} + [I_\delta + S_\delta b(a+c)] \ddot{\theta} + S_\delta \ddot{h} + k_\delta \delta &= M_2 \end{aligned} \quad (8.3)$$

The effect of flap is felt on the wing via the reaction force R at the flap hinge. R is obtained by balancing forces on the aileron

$$\begin{aligned} L_2 + R + m\delta \left[\ddot{h} + \{b(a+c) + y_I\} \ddot{\theta} + y_I \ddot{\delta} \right] &= 0 \\ R = -L_2 - m\delta \left[\ddot{h} + \{b(a+c) + y_I\} \ddot{\theta} + y_I \ddot{\delta} \right] \end{aligned} \quad (8.4)$$

Now consider the free body diagram of the wing alone. Using force balance the wing heave equation becomes

$$\begin{aligned} m\ddot{h} + mx_I \ddot{\theta} + k_h h - R &= -L_1 \\ M\ddot{h} + S\ddot{\theta} + S_\delta \ddot{\delta} + k_h h &= -L \end{aligned} \quad (8.5)$$

where

$$\begin{aligned} M &= m + m_\delta \\ L &= L_1 + L_2 \\ S &= S_\theta + m_\delta [b(a+c) + y_I] \end{aligned}$$

Thus the parameters involved in the heave equation contain properties pertaining to the entire section including the aileron. Now use the moment balance equation

$$I_\theta \ddot{\theta} + S_\theta \ddot{h} + k_\theta \theta - k_\delta \delta - Rb(a+c) = M_1$$

Replace $k_\delta \delta$ from equation 8.3 and R from equation 8.4 to obtain

$$I\ddot{\theta} + S\ddot{h} + [I_\delta + S_\delta b(a+c)] \ddot{\delta} = M_{ea} \quad (8.6)$$

where

$$\begin{aligned} I &= I_\theta + b^2(a+c)^2 m_\delta + 2S_\delta b(a+c) + I_\delta \\ &= I_\theta + \int_{ail} [b(a+c) + s]^2 dm_\delta \\ S &= S_\theta + S_\delta + b(a+c)m_\delta \\ M_{ea} &= M_1 + M_2 - L_2 b(a+c) \end{aligned}$$

Note that

$$\begin{aligned}
S_\theta &= \text{wing moment about wing e.a.} \\
S_\delta &= \text{aileron moment about aileron e.a.} \\
S_\delta + m_\delta b(a+c) &= \text{aileron moment about wing e.a.} \\
S &= \text{section moment about wing e.a.} \\
I_\theta &= \text{inertia of wing about wing e.a.} \\
I_\delta &= \text{inertia of aileron about aileron e.a.} \\
I_\delta + b^2(a+c)^2 m_\delta + 2S_\delta b(a+c) &= \text{inertia of aileron about wing e.a.} \\
I &= \text{inertia of section about wing e.a.}
\end{aligned} \tag{8.7}$$

All the above quantities are defined per unit span. The units for m , S , and I are kg/m , $kg-m/m$, and $kg-m^2/m$. Alternatively they can be treated as kg , $kg-m$, and $kg-m^2$ while keeping in mind they pertain to unit span of the wing.

8.1.3 Flap-torsion-Aileron dynamics: Energy method

The same equations as above are now rederived using the energy method (Euler–Lagrange). This derivation is given in Lanczos [2]. Let T be the kinetic energy of the system, U be the potential energy of the system and δW the virtual work. Then the Euler–Lagrange equations of motion are given by

$$\frac{d}{dt} \left(\frac{\partial T}{\partial \dot{q}} \right) - \frac{\partial T}{\partial q} + \frac{\partial U}{\partial q} = Q \tag{8.8}$$

where q are the degrees of freedom, here h , θ , and δ . Q is such that

$$\delta W = \int Q \delta q$$

$$\begin{aligned}
T &= T_w + T_a \\
T_w &= \int_w dT_w \\
&= \frac{1}{2} \int_w [\dot{h} + r\dot{\theta}]^2 dm \\
&= \frac{1}{2} m \dot{h}^2 + \frac{1}{2} I_\theta \dot{\theta}^2 + \dot{h} \dot{\theta} S_\theta \\
T_a &= \int_a dT_a \\
&= \frac{1}{2} \int_a [\dot{h} + \{b(a+c) + s\} \dot{\theta} + s\dot{\delta}]^2 dm_\delta \\
&= \frac{1}{2} m_\delta \dot{h}^2 + \frac{1}{2} [I_\delta + b^2(a+c)^2 m_\delta + 2b(a+c)S_\delta] \dot{\theta}^2 \\
&\quad I_\delta \dot{\delta}^2 + 2\dot{h} \dot{\theta} [b(a+c)m_\delta + S_\delta] + 2\dot{\delta} \dot{\theta} [b(a+c)S_\delta + I_\delta] + 2\dot{h} \dot{\delta} S_\delta
\end{aligned}$$

Therefore

$$T = \frac{1}{2} M \dot{h}^2 + \frac{1}{2} I \dot{\theta}^2 + \dot{h} \dot{\theta} S + \frac{1}{2} I_\delta \dot{\delta}^2 + \dot{h} \dot{\delta} S_\delta + \frac{1}{2} [b(a+c)S_\delta + I_\delta] \dot{\delta} \dot{\theta}$$

The potential energy is

$$U = \frac{1}{2} k_h h^2 + \frac{1}{2} k_\theta \theta^2 + \frac{1}{2} k_\delta \delta^2$$

The virtual work is

$$\begin{aligned}\delta W &= -L_1\delta h - L_2b(a+c)\delta\theta - L_2\delta h + M_1\delta\theta + M_2(\delta\theta + \delta\delta) \\ &= -(L_1 + L_2)\delta h + \{M_1 + M_2 - L_2b(a+c)\}\delta\theta + M_2\delta\delta \\ &= L\delta h + M_{ea}\delta\theta + M_2\delta\delta\end{aligned}$$

Now apply the Lagrange equations for h , θ , and δ separately to obtain the same equations as before

$$M\ddot{h} + S\ddot{\theta} + S_\delta\ddot{\delta} + k_h h = -L \quad (8.9)$$

$$I\ddot{\theta} + S\ddot{h} + [I_\delta + S_\delta b(a+c)]\ddot{\delta} = M_{ea} \quad (8.10)$$

$$I_\delta\ddot{\delta} + [I_\delta + S_\delta b(a+c)]\ddot{\theta} + S_\delta\ddot{h} + k_\delta\delta = M_2 \quad (8.11)$$

8.2 Flap-Torsion-Aileron-Tab Dynamics of a Rotor Blade

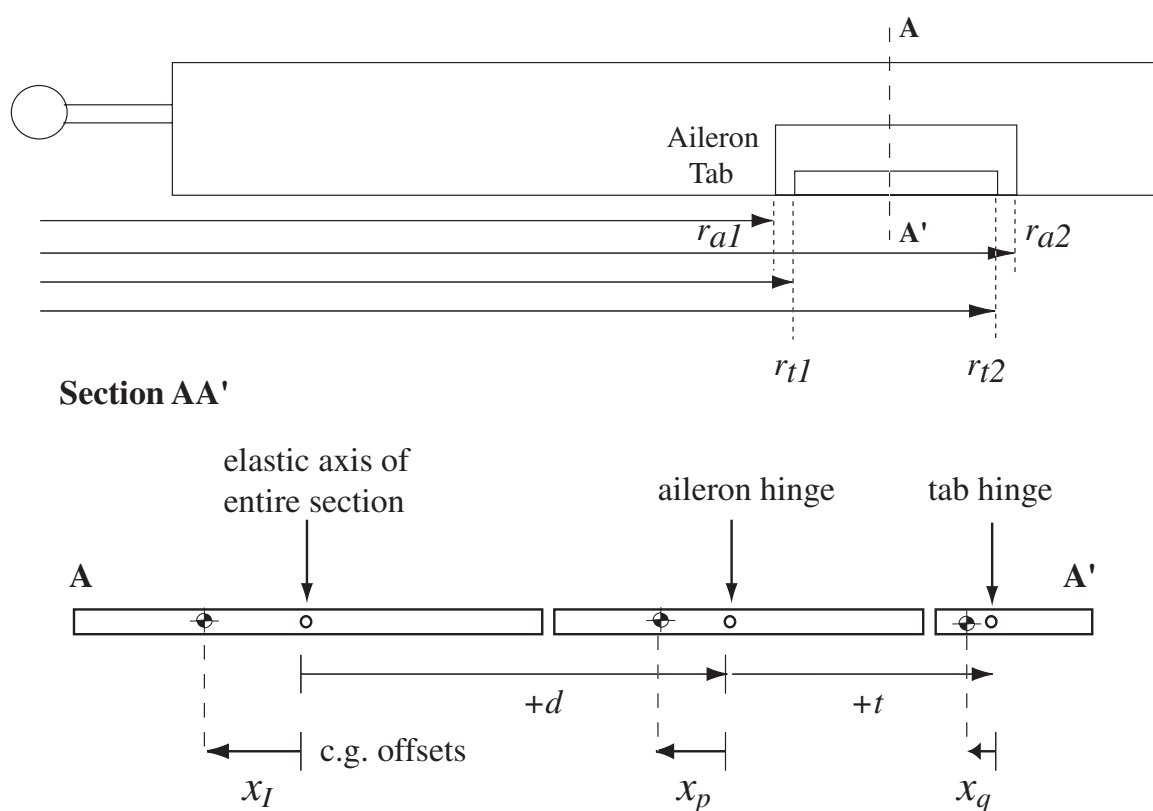


Figure 8.1: Airfoil with aileron and tab; geometry, pitch axes offsets and center of gravity offsets

8.2.1 Governing equations

Hamilton's variational principle is the general principle from which the Euler-Lagrange differential equation, and the Newton's Laws of motion can be deduced. For a conservative system, Hamilton's principle states that the true motion of a system, between prescribed initial conditions at time t_1 and final conditions at time t_2 , is that particular motion for which the time integral of the difference between the potential and kinetic energies is a minimum. For an aeroelastic system, there are non-conservative forces which are not derivable from a potential function. The generalized Hamilton's

principle, applicable to nonconservative systems, is expressed as

$$\begin{aligned}\delta\pi &= \delta \int_{t_1}^{t_2} (U - T - W)dt = 0 \quad \text{or} \\ \delta\pi &= \int_{t_1}^{t_2} (\delta U - \delta T - \delta W)dt = 0\end{aligned}\tag{8.12}$$

In order to prevent confusion between the aileron deflection δ and the variational δ , let the aileron and tab deflections be p , and q radians. The flap and torsion deflections are β and θ as before. Let the aileron span be from r_{a1} to r_{a2} . Let the tab span be from r_{t1} to r_{t2} .

A general blade section extends from the leading edge LE_b to the trailing edge TE_b . On the composite section spanning across the aileron it extends from the LE_b to a shorter trailing edge upto the aileron TE_{ba} . Similarly the aileron extends from LE_a to TE_a , except over the tab span, where it extends from LE_a to TE_{at} . TE_{at} denotes trailing edge of the aileron over the tab span. The tab extends from LE_t to the TE_t . Note that in general, TE_t or TE_a need not be the same as TE_b .

Let us define the following structural properties. η is a general local coordinate along the blade section, aileron, or tab.

Blade properties:

$$\begin{aligned}\rho &= \text{area density } kg/m^2 \\ \int_{LE_b}^{TE_b} \rho d\eta &= m_b \quad \text{mass per unit span } kg/m \\ \int_{LE_b}^{TE_b} \eta \rho d\eta &= x_I m_b = s_\theta \quad \text{first moment of mass per unit span } kg - m/m \\ \int_{LE_b}^{TE_b} \eta^2 \rho d\eta &= i_\theta \quad \text{second moment of mass per unit span } kg - m^2/m\end{aligned}\tag{8.13}$$

For each we have the following radial moments

$$\begin{aligned}\int_e^R m_b dr &= M_b \quad \text{zero-th radial moment} = \text{blade mass } kg \\ \int_e^R (r - e) m_b dr &= S_\beta \quad \text{first radial moment} = \text{first flap moment } kg - m \\ \int_e^R (r - e)^2 m_b dr &= I_\beta \quad \text{second radial moment} = \text{flap moment of inertia } kg - m^2\end{aligned}\tag{8.14}$$

Then

$$\begin{aligned}\int_e^R s_\theta dr &= \int_e^R x_I m_b dr = S_\theta \quad \text{zero-th radial moment } kg - m \\ \int_e^R (r - e) s_\theta dr &= \int_e^R (r - e) x_I m_b dr = \bar{S}_\theta \quad \text{first radial moment } kg - m^2 \\ \int_e^R (r - e)^2 s_\theta dr &= \int_e^R (r - e)^2 x_I m_b dr = \bar{\bar{S}}_\theta \quad \text{second radial moment } kg - m^2\end{aligned}\tag{8.15}$$

And finally

$$\begin{aligned}
 \int_e^R i_\theta dr &= I_\theta \quad \text{zero-th radial moment} \quad kg - m \\
 \int_e^R (r - e)i_\theta dr &= \bar{I}_\theta \quad \text{first radial moment} \quad kg - m^2 \\
 \int_e^R (r - e)^2 i_\theta dr &= \bar{\bar{I}}_\theta \quad \text{second radial moment} \quad kg - m^2
 \end{aligned} \tag{8.16}$$

Aileron properties:

$$\begin{aligned}
 \int_{LE_a}^{TE_a} \rho d\eta &= m_a \quad \text{mass per unit span} \quad kg/m \\
 \int_{LE_a}^{TE_a} \eta \rho d\eta &= x_p m_a = s_a \quad \text{first moment of mass per unit span} \quad kg - m/m \\
 \int_{LE_a}^{TE_a} \eta^2 \rho d\eta &= i_a \quad \text{second moment of mass per unit span} \quad kg - m^2/m
 \end{aligned} \tag{8.17}$$

For each we have the following radial moments

$$\begin{aligned}
 \int_{r_{a1}}^{r_{a2}} m_a dr &= M_a \quad \text{zero-th radial moment} = \text{aileron mass} \quad kg \\
 \int_{r_{a1}}^{r_{a2}} (r - e)m_a dr &= S_{\beta a} \quad \text{first radial moment} \quad kg - m \\
 \int_{r_{a1}}^{r_{a2}} (r - e)^2 m_a dr &= I_{\beta a} \quad \text{second radial moment} \quad kg - m^2
 \end{aligned} \tag{8.18}$$

Then

$$\begin{aligned}
 \int_{r_{a1}}^{r_{a2}} s_a dr &= \int_{r_{a1}}^{r_{a2}} x_p m_a dr = S_a \quad \text{zero-th radial moment} \quad kg - m \\
 \int_{r_{a1}}^{r_{a2}} (r - e)s_a dr &= \int_{r_{a1}}^{r_{a2}} (r - e)x_p m_a dr = \bar{S}_a \quad \text{first radial moment} \quad kg - m^2 \\
 \int_{r_{a1}}^{r_{a2}} (r - e)^2 s_a dr &= \int_{r_{a1}}^{r_{a2}} (r - e)^2 x_p m_a dr = \bar{\bar{S}}_a \quad \text{second radial moment} \quad kg - m^2
 \end{aligned} \tag{8.19}$$

And finally

$$\begin{aligned}
 \int_{r_{a1}}^{r_{a2}} i_a dr &= I_a \quad \text{zero-th radial moment} \quad kg - m \\
 \int_{r_{a1}}^{r_{a2}} (r - e)i_a dr &= \bar{I}_a \quad \text{first radial moment} \quad kg - m^2 \\
 \int_{r_{a1}}^{r_{a2}} (r - e)^2 i_a dr &= \bar{\bar{I}}_a \quad \text{second radial moment} \quad kg - m^2
 \end{aligned} \tag{8.20}$$

Tab properties:

$$\begin{aligned}
\int_{LE_t}^{TE_t} \rho d\eta &= m_t \quad \text{mass per unit span} \quad kg/m \\
\int_{LE_t}^{TE_t} \eta \rho d\eta &= x_q m_t = s_t \quad \text{first moment of mass per unit span} \quad kg - m/m \\
\int_{LE_t}^{TE_t} \eta^2 \rho d\eta &= i_t \quad \text{second moment of mass per unit span} \quad kg - m^2/m
\end{aligned} \tag{8.21}$$

For each we have the following radial moments

$$\begin{aligned}
\int_{r_{t1}}^{r_{t2}} m_t dr &= M_t \quad \text{zero-th radial moment} = \text{tab mass} \quad kg \\
\int_{r_{t1}}^{r_{t2}} (r - e) m_t dr &= S_{\beta t} \quad \text{first radial moment} \quad kg - m \\
\int_{r_{t1}}^{r_{t2}} (r - e)^2 m_t dr &= I_{\beta t} \quad \text{second radial moment} \quad kg - m^2
\end{aligned} \tag{8.22}$$

Then

$$\begin{aligned}
\int_{r_{t1}}^{r_{t2}} s_t dr &= \int_{r_{t1}}^{r_{t2}} x_q m_t dr = S_t \quad \text{zero-th radial moment} \quad kg - m \\
\int_{r_{t1}}^{r_{t2}} (r - e) s_t dr &= \int_{r_{t1}}^{r_{t1}} r x_q m_t dr = \bar{S}_t \quad \text{first radial moment} \quad kg - m^2 \\
\int_{r_{t1}}^{r_{t2}} (r - e)^2 s_a dr &= \int_{r_{t1}}^{r_{t2}} r^2 x_q m_t dr = \bar{\bar{S}}_t \quad \text{second radial moment} \quad kg - m^2
\end{aligned} \tag{8.23}$$

And finally

$$\begin{aligned}
\int_{r_{t1}}^{r_{t2}} i_t dr &= I_t \quad \text{zero-th radial moment} \quad kg - m \\
\int_{r_{t1}}^{r_{t2}} (r - e) i_t dr &= \bar{I}_t \quad \text{first radial moment} \quad kg - m^2 \\
\int_{r_{t1}}^{r_{t2}} (r - e)^2 i_t dr &= \bar{\bar{I}}_t \quad \text{second radial moment} \quad kg - m^2
\end{aligned} \tag{8.24}$$

The total potential energy and its variation is given by

$$\begin{aligned}
U &= \frac{1}{2} (k_\beta \beta^2 + k_\theta \theta^2 + k_p p^2 + k_q q^2) \\
\delta U &= k_\beta \delta \beta + k_\theta \delta \theta + k_p \delta p + k_q \delta q
\end{aligned} \tag{8.25}$$

The virtual work is given by

$$\delta W = M_\beta \delta \beta + M_\theta \delta \theta + M_p \delta p + M_q \delta q \tag{8.26}$$

where M_β is the aerodynamic flap hinge moment, M_θ is the aerodynamic twist moment about the blade rotation axis, M_p is the aerodynamic twist moment about the aileron rotation axis (aileron hinge), and M_q is the aerodynamic twist moment about the tab rotation axis (tab hinge).

The total kinetic energy and its variation is contributed by the blade, aileron, and the flap. Let the velocity of a point on the blade be v_b , that of a point on the aileron be v_a , and that of a point on the tab be v_t . The total kinetic energy and its variation can be expressed as

$$\begin{aligned}
T &= \frac{1}{2} \int_b \rho_b v_b^2 + \frac{1}{2} \int_a \rho_a v_a^2 + \frac{1}{2} \int_t \rho_t v_t^2 \\
\delta T &= \int_b \rho_b \bar{\mathbf{v}}_b \cdot \delta \bar{\mathbf{v}}_b + \int_a \rho_a \bar{\mathbf{v}}_a \cdot \delta \bar{\mathbf{v}}_a + \int_t \rho_t \bar{\mathbf{v}}_t \cdot \delta \bar{\mathbf{v}}_t
\end{aligned} \tag{8.27}$$

To obtain these velocities and variations, consider the following coordinate transformations:

$$\begin{Bmatrix} \hat{i}_2 \\ \hat{j}_2 \\ \hat{k}_2 \end{Bmatrix} = \begin{bmatrix} c\beta & 0 & s\beta \\ 0 & 1 & 0 \\ -s\beta & 0 & c\beta \end{bmatrix} \begin{Bmatrix} \hat{i}_1 \\ \hat{j}_1 \\ \hat{k}_1 \end{Bmatrix} \quad \text{undeformed to flap} \quad (8.28)$$

$$\begin{Bmatrix} \hat{i}_3 \\ \hat{j}_3 \\ \hat{k}_3 \end{Bmatrix} = \begin{bmatrix} 1 & 0 & 0 \\ 0 & c\theta & s\theta \\ 0 & -s\theta & c\theta \end{bmatrix} \begin{Bmatrix} \hat{i}_2 \\ \hat{j}_2 \\ \hat{k}_2 \end{Bmatrix} \quad \text{flap to torsion} \quad (8.29)$$

$$\begin{Bmatrix} \hat{i}_4 \\ \hat{j}_4 \\ \hat{k}_4 \end{Bmatrix} = \begin{bmatrix} 1 & 0 & 0 \\ 0 & c(\theta+p) & s(\theta+p) \\ 0 & -s(\theta+p) & c(\theta+p) \end{bmatrix} \begin{Bmatrix} \hat{i}_2 \\ \hat{j}_2 \\ \hat{k}_2 \end{Bmatrix} \quad \text{flap to aileron} \quad (8.30)$$

$$\begin{Bmatrix} \hat{i}_5 \\ \hat{j}_5 \\ \hat{k}_5 \end{Bmatrix} = \begin{bmatrix} 1 & 0 & 0 \\ 0 & c(\theta+p+q) & s(\theta+p+q) \\ 0 & -s(\theta+p+q) & c(\theta+p+q) \end{bmatrix} \begin{Bmatrix} \hat{i}_2 \\ \hat{j}_2 \\ \hat{k}_2 \end{Bmatrix} \quad \text{flap to tab} \quad (8.31)$$

The position of a generic point on the deformed blade can be expressed as

$$\mathbf{r} = x_1 \hat{i}_1 + y_1 \hat{j}_1 + z_1 \hat{k}_1 \quad (8.32)$$

The angular velocity vector is given by

$$\boldsymbol{\Omega} = \Omega \hat{k}_1 \quad (8.33)$$

Thus the velocity of a generic point on the deformed blade, can be expressed as

$$\begin{aligned} \mathbf{v} &= \frac{\partial \mathbf{r}}{\partial t} + \bar{\boldsymbol{\Omega}} \times \mathbf{r} \\ &= \dot{\mathbf{r}} + \boldsymbol{\Omega} \times \mathbf{r} \\ &= (\dot{x}_1 - \Omega x_1) \hat{i}_1 + (\dot{y}_1 + \Omega y_1) \hat{j}_1 + \dot{z}_1 \hat{k}_1 \end{aligned} \quad (8.34)$$

The variation is given by

$$\bar{\mathbf{v}} = (\delta \dot{x}_1 - \Omega \delta x_1) \hat{i}_1 + (\delta \dot{y}_1 + \Omega \delta y_1) \hat{j}_1 + \delta \dot{z}_1 \hat{k}_1 \quad (8.35)$$

From where it follows

$$\bar{\mathbf{v}} \cdot \delta \bar{\mathbf{v}} = (\dot{x}_1 - \Omega x_1)(\delta \dot{x}_1 - \Omega \delta x_1) + (\dot{y}_1 + \Omega y_1)(\delta \dot{y}_1 + \Omega \delta y_1) + \dot{z}_1 \delta \dot{z}_1 \quad (8.36)$$

Anticipating integration over time as in equation 8.12 we note that

$$\begin{aligned} \int_{t_1}^{t_2} \dot{x} \delta x &= \dot{x} \delta x \Big|_{t_1}^{t_2} - \int_{t_1}^{t_2} \ddot{x} \delta x \\ &= 0 + \int_{t_1}^{t_2} \ddot{x} \delta x \end{aligned}$$

Using the above, $\dot{x}_1 \delta x_1$ can be replaced with $-\ddot{x}_1 \delta x_1$, $x_1 \delta \dot{x}_1$ can be replaced with $-\dot{x}_1 \delta x_1$, etc. Thus, because

$$\begin{aligned} \int_{t_1}^{t_2} \bar{\mathbf{v}} \cdot \delta \bar{\mathbf{v}} &= \int_{t_1}^{t_2} (\dot{x}_1 - \Omega x_1)(\delta \dot{x}_1 - \Omega \delta x_1) + (\dot{y}_1 + \Omega y_1)(\delta \dot{y}_1 + \Omega \delta y_1) + \dot{z}_1 \delta \dot{z}_1 \\ &= \int_{t_1}^{t_2} (-\ddot{x}_1 + \Omega^2 x_1) \delta x_1 + (-\dot{y}_1 + \Omega^2 y_1) \delta y_1 - \dot{z}_1 \delta z_1 \end{aligned}$$

the variational expression 8.36 can be re-written as

$$\bar{\mathbf{v}} \cdot \delta \bar{\mathbf{v}} = (-\ddot{x}_1 + \Omega^2 x_1) \delta x_1 + (-\ddot{y}_1 + \Omega^2 y_1) \delta y_1 - \ddot{z}_1 \delta z_1 \quad (8.37)$$

Now we have all the tools to derive the governing equations. First, consider a generic point on the blade

$$\mathbf{r} = e \hat{i}_1 + (r - e) \hat{i}_2 + \eta \hat{j}_3$$

where η is the local chordwise coordinate. Using the transformations 8.31 and 8.28 above we have

$$\mathbf{r} = x_1 \hat{i}_1 + y_1 \hat{j}_1 + z_1 \hat{k}_1$$

where

$$\begin{aligned} x_1 &= e + (r - e) c \beta - \eta s \theta s \beta \\ y_1 &= \eta c \theta \\ z_1 &= (r - e) s \beta + \eta s \theta c \beta \end{aligned}$$

Then

$$\begin{aligned} \dot{x}_1 &= -(r - e) s \beta \dot{\beta} - \eta s \theta c \beta \dot{\beta} - \eta c \theta s \beta \dot{\theta} \\ \dot{y}_1 &= -\eta s \theta \dot{\theta} \\ \dot{z}_1 &= (r - e) c \beta \dot{\beta} - \eta s \theta s \beta \dot{\beta} + \eta c \theta c \beta \dot{\theta} \end{aligned} \quad (8.38)$$

$$\begin{aligned} \delta x_1 &= -(r - e) s \beta \delta \beta - \eta s \theta c \beta \delta \beta - \eta c \theta s \beta \delta \theta \\ \delta y_1 &= -\eta s \theta \delta \theta \\ \delta z_1 &= (r - e) c \beta \delta \beta - \eta s \theta s \beta \delta \beta + \eta c \theta c \beta \delta \theta \end{aligned}$$

Use small angle assumption and neglect non-linear terms to obtain

$$\begin{aligned} x_1 &= r \\ y_1 &= \eta \\ z_1 &= (r - e) \beta + \eta \theta \end{aligned} \quad (8.39)$$

$$\begin{aligned} \delta x_1 &= -(r - e) \beta \delta \beta - \eta \theta \delta \beta - \eta \beta \delta \theta \\ \delta y_1 &= -\eta \theta \delta \theta \\ \delta z_1 &= (r - e) \delta \beta - \eta \delta \theta \end{aligned} \quad (8.40)$$

$$\begin{aligned} \dot{x}_1 &= 0 \\ \dot{y}_1 &= 0 \\ \dot{z}_1 &= (r - e) \dot{\beta} + \eta \dot{\theta} \end{aligned} \quad (8.41)$$

Differentiating equations 8.38, making small angle assumption, and neglecting non-linear terms yield

$$\begin{aligned} \ddot{x}_1 &= 0 \\ \ddot{y}_1 &= 0 \\ \ddot{z}_1 &= (r - e) \ddot{\beta} + \eta \ddot{\theta} \end{aligned} \quad (8.42)$$

The variation in kinetic energy then becomes

$$\delta T_b = \int_{span} \int_{chord} [\mathbf{v} \cdot \delta \mathbf{v}]_b \rho d\eta dr \quad (8.43)$$

where the limit of integration for the blade, without the aileron, is

$$\int_{span} \int_{chord} = \int_e^{r_{a1}} \int_{TE_b}^{LE_b} + \int_{r_{a1}}^{r_{a2}} \int_{TE_b}^{LE_b} + \int_{r_{a2}}^R \int_{TE_b}^{LE_b} \quad (8.44)$$

$\mathbf{v} \cdot \delta \mathbf{v}$ is given by equation 8.37. Using equations 8.39 to 8.42 we have

$$\begin{aligned} (\mathbf{v} \cdot \delta \mathbf{v})_b &= \Omega^2 r [-(r-e)\beta \delta \beta - \eta \theta \delta \beta - \eta \beta \delta \theta] \\ &\quad + \Omega^2 \eta (-\eta \theta \delta \theta) \\ &\quad - \left[(r-e)\ddot{\beta} + \eta \ddot{\theta} \right] [(r-e)\delta \beta + \eta \delta \theta] \end{aligned} \quad (8.45)$$

Group the variational terms

$$\begin{aligned} (\mathbf{v} \cdot \delta \mathbf{v})_b &= \left[-\Omega^2 r (r-e)\beta - \Omega^2 r \eta \theta - (r-e)^2 \ddot{\beta} - \eta (r-e) \ddot{\theta} \right] \delta \beta \\ &\quad + \left[-\Omega^2 \eta r \beta - \Omega^2 \eta^2 \theta - \eta (r-e) \ddot{\beta} - \eta^2 \ddot{\theta} \right] \delta \theta \end{aligned} \quad (8.46)$$

Replace r with $(r-e) + e$ to have

$$\begin{aligned} (\mathbf{v} \cdot \delta \mathbf{v})_b &= \left[-\Omega^2 (r-e)^2 \beta - \Omega^2 e (r-e) \beta - \Omega^2 (r-e) \eta \theta - \Omega^2 e \eta \theta - (r-e)^2 \ddot{\beta} - \eta (r-e) \ddot{\theta} \right] \delta \beta \\ &\quad + \left[-\Omega^2 \eta (r-e) \beta - \Omega^2 \eta e \beta - \Omega^2 \eta^2 \theta - \eta (r-e) \ddot{\beta} - \eta^2 \ddot{\theta} \right] \delta \theta \end{aligned} \quad (8.47)$$

Equation 8.47 would help express the variation of kinetic energy of a point on the blade in terms of variations of flap and torsion degrees of freedom. Let us now proceed to obtain a similar expression for a point on the aileron in terms of variations of flap, torsion, and aileron degrees of freedom. The procedure is same as above, and the notations used will be same.

For a generic point on the aileron we have

$$\mathbf{r} = e \hat{i}_1 + (r-e) \hat{i}_2 - d \hat{j}_3 + \eta \hat{j}_4$$

where d is the distance of the aileron hinge lying behind the elastic axis or the center of rotation of the blade section. d is positive behind the blade. η is the local chordwise coordinate of the aileron along direction \hat{j}_4 . Thus η is zero at the aileron hinge, and positive forward to it. Using the coordinate transformations given above, small angle assumption on the degrees of freedom, and neglecting the non-linear terms we have

$$\begin{aligned} x_1 &= r \\ y_1 &= -d + \eta \\ z_1 &= (r-e)\beta + (\eta-d)\theta + \eta p \end{aligned} \quad (8.48)$$

$$\begin{aligned} \delta x_1 &= -(r-e)\beta \delta \beta - \eta \theta \delta \beta - \eta \beta \delta \theta \\ \delta y_1 &= -\eta \theta \delta \theta \\ \delta z_1 &= (r-e)\delta \beta - \eta \delta \theta \end{aligned} \quad (8.49)$$

$$\begin{aligned} \dot{x}_1 &= 0 \\ \dot{y}_1 &= 0 \\ \dot{z}_1 &= (r-e)\dot{\beta} - d\dot{\theta} + \eta\dot{\theta} + \eta\dot{p} \end{aligned} \quad (8.50)$$

$$\begin{aligned} \ddot{x}_1 &= 0 \\ \ddot{y}_1 &= 0 \\ \ddot{z}_1 &= (r-e)\ddot{\beta} - d\ddot{\theta} + \eta\ddot{\theta} + \eta\ddot{p} \end{aligned} \quad (8.51)$$

The variation in kinetic energy is

$$\delta T_a = \int_{span} \int_{chord} [\mathbf{v} \cdot \delta \mathbf{v}]_a \rho d\eta dr \quad (8.52)$$

where the limit of integration is given by

$$\int_{r_{a1}}^{r_{t1}} \int_{TE_a}^{LE_a} + \int_{r_{t1}}^{r_{t2}} \int_{TE_{at}}^{LE_a} + \int_{r_{t2}}^{r_{a2}} \int_{TE_a}^{LE_a} \quad (8.53)$$

and

$$\begin{aligned} (\mathbf{v} \cdot \delta \mathbf{v})_a = & \left[-\Omega^2 r(r-e)\beta + \Omega^2 r d\theta - \Omega^2 r\theta\eta - \Omega^2 r\eta p - (r-e)^2 \ddot{\beta} \right. \\ & \left. + d(r-e)\ddot{\theta} - \eta(r-e)\ddot{\theta} - \eta(r-e)\ddot{p} \right] \delta\beta \\ & \left[\Omega^2 r d\beta - \Omega^2 r\eta\beta + \Omega^2(\eta-d)d\theta - \Omega^2(\eta-d)\eta\theta - \Omega^2(\eta-d)\eta p \right. \\ & \left. - (\eta-d)(r-e)\ddot{\beta} + (\eta-d)d\ddot{\theta} - (\eta-d)\eta\ddot{\theta} - (\eta-d)\eta\ddot{p} \right] \delta\theta \\ & \left[-\Omega^2 r\eta\beta - \Omega^2(\eta-d)\eta p - \Omega^2(\eta-d)\eta\theta \right. \\ & \left. - \eta(r-e)\ddot{\beta} + \eta d\ddot{\theta} - \eta^2\ddot{\theta} - \eta^2\ddot{p} \right] \delta p \end{aligned} \quad (8.54)$$

Equation 8.54 would help express the variation of kinetic energy of a point on the aileron in terms of variations of flap, torsion, and aileron degrees of freedom. Let us now proceed to obtain a similar expression for a point on the tab in terms of variations of flap, torsion, aileron, and tab degrees of freedom. The procedure is same as above, and the notations used will be same.

For a generic point on the tab we have

$$\mathbf{r} = e\hat{i}_1 + (r-e)\hat{i}_2 - d\hat{j}_3 - t\hat{j}_4 + \eta\hat{j}_4$$

where t is the distance of the tab hinge lying behind the aileron hinge. t is positive behind the aileron. η is the local chordwise coordinate of the tab along direction \hat{j}_5 . Thus η is zero at the tab hinge, and positive forward to it. Using the coordinate transformations given above, small angle assumption on the degrees of freedom, and neglecting the non-linear terms we have

$$\begin{aligned} x_1 &= r \\ y_1 &= -t - d + \eta \\ z_1 &= (r-e)\beta + (\eta-d-t)\theta + (\eta-t)p + \eta q \end{aligned} \quad (8.55)$$

$$\begin{aligned} \delta x_1 &= [-(r-e)\beta + (d+t-\eta)\theta + (t-\eta)p - \eta q] \delta\beta \\ & \quad [(d+t-\eta)\beta] \delta\theta + [(t-\eta)\beta] \delta p \\ \delta y_1 &= [(d+t-\eta)\theta + (t-\eta)p - \eta q] \delta\theta \\ & \quad [(t-\eta)\theta + (t-\eta)p - \eta q] \delta p + [-\eta(\theta+p)] \delta q \\ \delta z_1 &= (r-e)\delta\beta - (d+t-\eta)\delta\theta - (t-\eta)\delta p + \eta\delta q \end{aligned} \quad (8.56)$$

$$\begin{aligned} \dot{x}_1 &= 0 \\ \dot{y}_1 &= 0 \\ \dot{z}_1 &= (r-e)\dot{\beta} + (\eta-d-t)\dot{\theta} + (\eta-t)\dot{p} + \eta\dot{q} \end{aligned} \quad (8.57)$$

$$\begin{aligned} \ddot{x}_1 &= 0 \\ \ddot{y}_1 &= 0 \\ \ddot{z}_1 &= (r-e)\ddot{\beta} - d\ddot{\theta} + \eta\ddot{\theta} + \eta\ddot{p} \end{aligned} \quad (8.58)$$

The variation in kinetic energy is

$$\delta T_a = \int_{span} \int_{chord} [\mathbf{v} \cdot \delta \mathbf{v}]_t \rho d\eta dr \quad (8.59)$$

where the limit of integration is given by

$$\int_{span} \int_{chord} = \int_{r_{t1}}^{r_{t2}} \int_{TE_t}^{LE_t} \quad (8.60)$$

and

$$\begin{aligned} (\mathbf{v} \cdot \delta \mathbf{v})_t = & \left[-\Omega^2 r(r-e)\beta - \Omega^2 r(\eta-d-t)\theta - \Omega^2 r(\eta-t)p - \Omega^2 r\eta q \right. \\ & \left. - (r-e)^2 \ddot{\beta} - (r-e)(\eta-d-t)\ddot{\theta} - (r-e)(\eta-t)\ddot{p} - \eta(r-e)\ddot{q} \right] \delta\beta \\ & \left[-\Omega^2 r(\eta-d-t)\beta - \Omega^2(\eta-d-t)^2\theta - \Omega^2(\eta-d-t)(\eta-t)p - \Omega^2\eta(\eta-d-t) \right. \\ & \left. - (r-e)(\eta-d-t)\ddot{\beta} - (\eta-d-t)^2\ddot{\theta} - (\eta-d-t)(\eta-t)\ddot{p} - \eta(\eta-d-t)\ddot{q} \right] \delta\theta \\ & \left[-\Omega^2 r(\eta-t)\beta - \Omega^2(\eta-t-d)(\eta-t)\theta \right. \\ & \left. - \Omega^2(\eta-t-d)(\eta-t)p - \Omega^2\eta(\eta-d-t)q \right. \\ & \left. - (r-e)(\eta-t)\ddot{\beta} - (\eta-t)(\eta-d-t)\ddot{\theta} - (\eta-t)^2\ddot{p} - \eta(\eta-t)\ddot{q} \right] \delta p \\ & \left[-\Omega^2 r\eta\beta - \Omega^2\eta(\eta-d-t)(\theta+p+q) \right. \\ & \left. - (r-e)\eta\ddot{\beta} - (\eta-d-t)\eta\ddot{\theta} - \eta(\eta-t)\ddot{p} - \eta^2\ddot{q} \right] \delta q \end{aligned} \quad (8.61)$$

Using equations 8.25, 8.26, and the integrated forms of equations 8.47, 8.54, and 8.61, equation 8.12 can be brought to the following form

$$\pi = \int_{t_1}^{t_2} [(\dots)\delta\beta + (\dots)\delta\theta + (\dots)\delta p + (\dots)\delta q] = 0$$

Putting the terms (...) = 0 generates the four governing equations for flap, torsion, aileron deflection, and tab deflection.

Tab equation:

The tab equation is found by collecting the terms associated with δq and setting them to zero. The kinetic energy terms are obtained from 8.59, 8.60, and eq: 8.61 as follows

$$-\Omega^2 \bar{S}_t \beta - \Omega^2 S_{te} \beta - \Omega^2 I_t (\theta + p + q) + \Omega^2 (d+t) S_t (\theta + p + q) - \bar{S}_t \ddot{\beta} - I_t \ddot{\theta} + (d+t) S_t \ddot{\theta} - I_t \ddot{p} + t S_t \ddot{p} - I_t \ddot{q}$$

Together with $-k_t$ and $-M_q$ from the potential energy and virtual work terms from equations 8.25 and 8.26 we have the equation for tab dynamics as follows

$$\begin{aligned} & \bar{S}_t \ddot{\beta} + \Omega^2 \bar{S}_t \left(1 + \frac{e S_t}{\bar{S}_t} \right) \beta \\ & + [I_t - (d+t) S_t] \ddot{\theta} + \Omega^2 I_t \left[1 - \frac{(d+t) S_t}{I_t} \right] \theta \\ & + (I_t - t S_t) \ddot{p} + \Omega^2 I_t \left[1 - \frac{(d+t) S_t}{I_t} \right] p \\ & + I_t \ddot{q} + \Omega^2 I_t \left[1 - \frac{(d+t) S_t}{I_t} + \frac{k_t}{I_t \Omega^2} \right] q = M_q \end{aligned} \quad (8.62)$$

Aileron equation:

Care must be taken while gathering the terms (...) corresponding to δp . The terms occurring in the potential energy variation, and virtual work are trivial. Consider the kinetic energy terms. Terms associated with δp occur only in equations 8.54 and 8.61. Let us write down the variation in kinetic energy

$$\begin{aligned}
& \int_{r_{a1}}^{r_{t1}} \int_{TE_a}^{LE_a} [-\Omega^2 r \eta \beta - \Omega^2 (\eta - d) \eta p - \Omega^2 (\eta - d) \eta \theta \\
& \quad - \eta (r - e) \ddot{\beta} + \eta d \ddot{\theta} - \eta^2 \ddot{\theta} - \eta^2 \ddot{p}] \\
& \int_{r_{t1}}^{r_{t2}} \int_{TE_{at}}^{LE_a} [-\Omega^2 r \eta \beta - \Omega^2 (\eta - d) \eta p - \Omega^2 (\eta - d) \eta \theta \\
& \quad - \eta (r - e) \ddot{\beta} + \eta d \ddot{\theta} - \eta^2 \ddot{\theta} - \eta^2 \ddot{p}] \\
& \int_{r_{t2}}^{r_{a2}} \int_{TE_a}^{LE_a} [-\Omega^2 r \eta \beta - \Omega^2 (\eta - d) \eta p - \Omega^2 (\eta - d) \eta \theta \\
& \quad - \eta (r - e) \ddot{\beta} + \eta d \ddot{\theta} - \eta^2 \ddot{\theta} - \eta^2 \ddot{p}] \\
& + \\
& \int_{r_{t1}}^{r_{t2}} \int_{TE_t}^{LE_t} [-\Omega^2 r (\eta - t) \beta - \Omega^2 (\eta - t - d) (\eta - t) \theta \\
& \quad - \Omega^2 (\eta - t - d) (\eta - t) p - \Omega^2 \eta (\eta - d - t) q \\
& \quad - (r - e) (\eta - t) \ddot{\beta} - (\eta - t) (\eta - d - t) \ddot{\theta} - (\eta - t)^2 \ddot{p} - \eta (\eta - t) \ddot{q}]
\end{aligned}$$

The first three integrals are contributions from aileron motion $[\mathbf{v} \cdot \delta \mathbf{v}]_a$. The fourth is a contribution from tab motion $[\mathbf{v} \cdot \delta \mathbf{v}]_t$. In the first three integrals, η , the local coordinate of integration, is the distance from aileron hinge (positive forward), say η_a . In the fourth, η , the local coordinate of integration, is the distance from the tab hinge (positive forward), say η_t . Thus, $\eta_t - t = \eta_a$. Note the second integral. It extends chord-wise over that part of the aileron which excludes the tab. Note the last integral, it extends chord-wise only over the tab. The underlined integrands of this integral are identical to those occurring in the second integral. Thus these terms can be considered together with the second integral, with the lower limit of integration for the second integral now changed from TE_{at} to TE_t . Thus the sectional properties here would now refer to the sectional properties as a whole, not excluding the tab properties. Thus, the kinetic energy terms can be re-organized as follows

$$\begin{aligned}
& \int_{r_{a1}}^{r_{t1}} \int_{TE_a}^{LE_a} [-\Omega^2 r \eta \beta - \Omega^2 (\eta - d) \eta p - \Omega^2 (\eta - d) \eta \theta \\
& \quad - \eta (r - e) \ddot{\beta} + \eta d \ddot{\theta} - \eta^2 \ddot{\theta} - \eta^2 \ddot{p}] \\
& \int_{r_{t1}}^{r_{t2}} \int_{TE_a}^{LE_a} [-\Omega^2 r \eta \beta - \Omega^2 (\eta - d) \eta p - \Omega^2 (\eta - d) \eta \theta \\
& \quad - \eta (r - e) \ddot{\beta} + \eta d \ddot{\theta} - \eta^2 \ddot{\theta} - \eta^2 \ddot{p}] \\
& \int_{r_{t2}}^{r_{a2}} \int_{TE_a}^{LE_a} [-\Omega^2 r \eta \beta - \Omega^2 (\eta - d) \eta p - \Omega^2 (\eta - d) \eta \theta \\
& \quad - \eta (r - e) \ddot{\beta} + \eta d \ddot{\theta} - \eta^2 \ddot{\theta} - \eta^2 \ddot{p}] \\
& + \\
& \int_{r_{t1}}^{r_{t2}} \int_{TE_t}^{LE_t} [-\Omega^2 \eta (\eta - d - t) q - \eta (\eta - t) \ddot{q}]
\end{aligned}$$

where the first three integrals have now the same limits of integration for the second integral. Thus the expression becomes

$$\begin{aligned} & \int_{r_{a1}}^{r_{a2}} \int_{TE_a}^{LE_a} [-\Omega^2 r \eta \beta - \Omega^2 (\eta - d) \eta p - \Omega^2 (\eta - d) \eta \theta \\ & - \eta (r - e) \ddot{\beta} + \eta d \ddot{\theta} - \eta^2 \ddot{\theta} - \eta^2 \ddot{p}] \\ & + \int_{r_{t1}}^{r_{t2}} \int_{TE_t}^{LE_t} [-\Omega^2 \eta (\eta - d - t) q - \eta (\eta - t) \ddot{q}] \end{aligned}$$

where, note that the limits of the first integral extends across the entire span of the aileron from r_{a1} to r_{a2} . The above expression equals

$$\begin{aligned} & -\Omega^2 \bar{S}_a \beta - \Omega^2 e S_a \beta + \Omega^2 d S_a p - \Omega^2 I_a p + \Omega^2 d S_a \theta - \Omega^2 I_a \theta - \\ & \bar{S}_a \ddot{\beta} + S_a d \ddot{\theta} - I_a \ddot{\theta} - I_a \ddot{p} \\ & - I_t \ddot{q} + t S_t \ddot{q} - \Omega^2 I_t q + \Omega^2 S_t (d + t) q \end{aligned}$$

Adding the potential energy and virtual work contributions, the equation for aileron dynamics becomes

$$\begin{aligned} & \bar{S}_a \ddot{\beta} + \Omega^2 \bar{S}_a \left(1 + \frac{e S_a}{\bar{S}_a} \right) \beta \\ & + [I_a - d S_a] \ddot{\theta} + \Omega^2 I_a \left[1 - \frac{d S_a}{I_a} \right] \theta \\ & + I_a \ddot{p} + \Omega^2 I_a \left[1 - \frac{d S_a}{I_a} + \frac{k_a}{I_a \Omega^2} \right] p \\ & + (I_t - t S_t) \ddot{q} + \Omega^2 I_t \left[1 - \frac{(d + t) S_t}{I_t} \right] q = M_p \end{aligned} \tag{8.63}$$

Proceeding similarly, we obtain the torsion and flapping equations as follows

Torsion equation:

$$\begin{aligned} & \bar{S}_\theta \ddot{\beta} + \Omega^2 \bar{S}_\theta \left(1 + \frac{e S_\theta}{\bar{S}_\theta} \right) \beta \\ & + I_\theta \ddot{\theta} + \Omega^2 I_\theta \left[1 + \frac{k_\theta}{I_\theta \Omega^2} \right] \theta \\ & + [I_a - d S_a] \ddot{p} + \Omega^2 I_a \left[1 - \frac{d S_a}{I_a} \right] p \\ & + (I_t - (d + t) S_t) \ddot{q} + \Omega^2 I_t \left[1 - \frac{(d + t) S_t}{I_t} \right] q = M_\theta \end{aligned} \tag{8.64}$$

Flap equation:

$$\begin{aligned}
& I_\beta \ddot{\beta} + \Omega^2 I_\beta \left[1 + \frac{eS_\beta}{I_\beta} + \frac{k_\beta}{I_\beta \Omega^2} \right] \beta \\
& + \bar{S}_\theta \ddot{\theta} + \Omega^2 \bar{S}_\theta \left(1 + \frac{eS_\theta}{\bar{S}_\theta} \right) \theta \\
& + \bar{S}_a \ddot{p} + \Omega^2 \bar{S}_a \left(1 + \frac{eS_a}{\bar{S}_a} \right) p \\
& + \bar{S}_t \ddot{q} + \Omega^2 \bar{S}_t \left(1 + \frac{eS_t}{\bar{S}_t} \right) q = M_\beta
\end{aligned} \tag{8.65}$$

8.2.2 Hinge Moments

The tab hinge moment is simply $k_t q$. From the tab equation 8.62 we have the following.

$$\begin{aligned}
k_t q &= M_q - \bar{S}_t \ddot{\beta} - \Omega^2 \bar{S}_t \left(1 + \frac{eS_t}{\bar{S}_t} \right) \beta \\
& - [I_t - (d+t)S_t] \ddot{\theta} - \Omega^2 I_t \left[1 - \frac{(d+t)S_t}{I_t} \right] \theta \\
& - (I_t - tS_t) \ddot{p} - \Omega^2 I_t \left[1 - \frac{(d+t)S_t}{I_t} \right] p \\
& - I_t \ddot{q} - \Omega^2 I_t \left[1 - \frac{(d+t)S_t}{I_t} \right] q
\end{aligned} \tag{8.66}$$

The right hand side of the above expression is useful when the tab deflection is prescribed. Similarly the aileron hinge moment is obtained from equation 8.63

$$\begin{aligned}
k_a p &= M_p - \bar{S}_a \ddot{\beta} - \Omega^2 \bar{S}_a \left(1 + \frac{eS_a}{\bar{S}_a} \right) \beta \\
& - [I_a - dS_a] \ddot{\theta} - \Omega^2 I_a \left[1 - \frac{dS_a}{I_a} \right] \theta \\
& - I_a \ddot{p} - \Omega^2 I_a \left[1 - \frac{dS_a}{I_a} \right] p \\
& - (I_t - tS_t) \ddot{q} - \Omega^2 I_t \left[1 - \frac{(d+t)S_t}{I_t} \right] q = M_p
\end{aligned} \tag{8.67}$$

The torsion and flap hinge moments at the blade root can also be easily obtained from equations 8.75 and 8.65 and is left to the reader.

8.2.3 Initial condition response

For initial condition response set M_β , M_θ , M_a , and M_t to zero and solve for β , θ , p , q with initial conditions $\beta(0)$, $\theta(0)$, $p(0)$, $q(0)$ and $\dot{\beta}(0)$, $\dot{\theta}(0)$, $\dot{p}(0)$, $\dot{q}(0)$.

8.2.4 Response with prescribed tab deflections

When $q(t)$ is prescribed, the tab equation is removed, and the flap, torsion and aileron equations take the following forms.

Flap equation:

$$\begin{aligned}
& I_\beta \ddot{\beta} + \Omega^2 I_\beta \left[1 + \frac{eS_\beta}{I_\beta} + \frac{k_\beta}{I_\beta \Omega^2} \right] \beta \\
& + \bar{S}_\theta \ddot{\theta} + \Omega^2 \bar{S}_\theta \left(1 + \frac{eS_\theta}{\bar{S}_\theta} \right) \theta \\
& + \bar{S}_a \ddot{p} + \Omega^2 \bar{S}_a \left(1 + \frac{eS_a}{\bar{S}_a} \right) p \\
& = M_\beta - \bar{S}_t \ddot{q} - \Omega^2 \bar{S}_t \left(1 + \frac{eS_t}{\bar{S}_t} \right) q
\end{aligned} \tag{8.68}$$

Torsion equation:

$$\begin{aligned}
& \bar{S}_\theta \ddot{\beta} + \Omega^2 \bar{S}_\theta \left(1 + \frac{eS_\theta}{\bar{S}_\theta} \right) \beta \\
& + I_\theta \ddot{\theta} + \Omega^2 I_\theta \left[1 + \frac{k_\theta}{I_\theta \Omega^2} \right] \theta \\
& + [I_a - dS_a] \ddot{p} + \Omega^2 I_a \left[1 - \frac{dS_a}{I_a} \right] p \\
& = M_\theta - (I_t - (d+t)S_t) \ddot{q} - \Omega^2 I_t \left[1 - \frac{(d+t)S_t}{I_t} \right] q
\end{aligned} \tag{8.69}$$

Aileron equation:

$$\begin{aligned}
& \bar{S}_a \ddot{\beta} + \Omega^2 \bar{S}_a \left(1 + \frac{eS_a}{\bar{S}_a} \right) \beta \\
& + [I_a - dS_a] \ddot{\theta} + \Omega^2 I_a \left[1 - \frac{dS_a}{I_a} \right] \theta \\
& + I_a \ddot{p} + \Omega^2 I_a \left[1 - \frac{dS_a}{I_a} + \frac{k_a}{I_a \Omega^2} \right] p \\
& = M_a - (I_t - tS_t) \ddot{q} - \Omega^2 I_t \left[1 - \frac{(d+t)S_t}{I_t} \right] q
\end{aligned} \tag{8.70}$$

8.2.5 Flap-Torsion-Aileron Dynamics for a Rotor Blade

The coupled flap-torsion-aileron dynamics follows from the flap-torsion-aileron-tab dynamics derived in the previous section, by simply removing the the tab degree of freedom $q(t)$. Thus we have

Flap equation:

$$\begin{aligned}
& I_\beta \ddot{\beta} + \Omega^2 I_\beta \left[1 + \frac{eS_\beta}{I_\beta} + \frac{k_\beta}{I_\beta \Omega^2} \right] \beta \\
& + \bar{S}_\theta \ddot{\theta} + \Omega^2 \bar{S}_\theta \left(1 + \frac{eS_\theta}{\bar{S}_\theta} \right) \theta \\
& + \bar{S}_a \ddot{p} + \Omega^2 \bar{S}_a \left(1 + \frac{eS_a}{\bar{S}_a} \right) p = M_\beta
\end{aligned} \tag{8.71}$$

Torsion equation:

$$\begin{aligned}
& \bar{S}_\theta \ddot{\beta} + \Omega^2 \bar{S}_\theta \left(1 + \frac{eS_\theta}{\bar{S}_\theta} \right) \beta \\
& + I_\theta \ddot{\theta} + \Omega^2 I_\theta \left[1 + \frac{k_\theta}{I_\theta \Omega^2} \right] \theta \\
& + [I_a - dS_a] \ddot{p} + \Omega^2 I_a \left[1 - \frac{dS_a}{I_a} \right] p = M_\theta
\end{aligned} \tag{8.72}$$

Aileron equation:

$$\begin{aligned}
& \bar{S}_a \ddot{\beta} + \Omega^2 \bar{S}_a \left(1 + \frac{eS_a}{\bar{S}_a} \right) \beta \\
& + [I_a - dS_a] \ddot{\theta} + \Omega^2 I_a \left[1 - \frac{dS_a}{I_a} \right] \theta \\
& + I_a \ddot{p} + \Omega^2 I_a \left[1 - \frac{dS_a}{I_a} + \frac{k_a}{I_a \Omega^2} \right] p = M_a
\end{aligned} \tag{8.73}$$

8.2.6 Response using prescribed aileron deflections

If the aileron deflections $p(t)$ are prescribed then the equations become

Flap equation:

$$\begin{aligned}
& I_\beta \ddot{\beta} + \Omega^2 I_\beta \left[1 + \frac{eS_\beta}{I_\beta} + \frac{k_\beta}{I_\beta \Omega^2} \right] \beta \\
& + \bar{S}_\theta \ddot{\theta} + \Omega^2 \bar{S}_\theta \left(1 + \frac{eS_\theta}{\bar{S}_\theta} \right) \theta \\
& = M_\beta - \bar{S}_a \ddot{p} - \Omega^2 \bar{S}_a \left(1 + \frac{eS_a}{\bar{S}_a} \right) p
\end{aligned} \tag{8.74}$$

Torsion equation:

$$\begin{aligned}
& \bar{S}_\theta \ddot{\beta} + \Omega^2 \bar{S}_\theta \left(1 + \frac{eS_\theta}{\bar{S}_\theta} \right) \beta \\
& + I_\theta \ddot{\theta} + \Omega^2 I_\theta \left[1 + \frac{k_\theta}{I_\theta \Omega^2} \right] \theta \\
& = M_\theta - [I_a - dS_a] \ddot{p} - \Omega^2 I_a \left[1 - \frac{dS_a}{I_a} \right] p
\end{aligned} \tag{8.75}$$

8.2.7 Flap-Torsion-Aileron-Tab equations in non-dimensional form

The coupled blade-torsion-trailing flap-tab equations are non-dimensionalized by dividing them by $I_b \Omega^2$. Thus we obtain the following

Flap equation:

$$\begin{aligned}
& \beta^{**} + \left[1 + \frac{eS_\beta}{I_\beta} + \frac{k_\beta}{I_\beta \Omega^2} \right] \beta \\
& + \frac{\bar{S}_\theta}{I_b} \theta^{**} + \frac{\bar{S}_\theta}{I_b} \left(1 + \frac{eS_\theta}{\bar{S}_\theta} \right) \theta \\
& + \frac{\bar{S}_a}{I_b} p^{**} + \frac{\bar{S}_a}{I_b} \left(1 + \frac{eS_a}{\bar{S}_a} \right) p \\
& + \frac{\bar{S}_t}{I_b} q^{**} + \frac{\bar{S}_t}{I_b} \left(1 + \frac{eS_t}{\bar{S}_t} \right) q = \gamma \bar{M}_\beta
\end{aligned} \tag{8.76}$$

where γ is the lock number, and

$$\begin{aligned}
\bar{M}_\beta &= \frac{1}{2} \int_0^1 y \bar{C}_l u_t^2 dy \\
y &= \frac{r}{R} \\
\bar{C}_l &= \frac{C_l}{a} \quad \text{where } a \text{ is a reference lift curve slope used to calculate } \gamma \\
u_t &= \frac{U_T}{\Omega R}
\end{aligned}$$

Torsion equation:

$$\begin{aligned}
& \frac{\bar{S}_\theta}{I_b} \beta^{**} + \frac{\bar{S}_\theta}{I_b} \left(1 + \frac{eS_\theta}{\bar{S}_\theta} \right) \beta \\
& + \frac{I_\theta}{I_b} \theta^{**} + \frac{I_\theta}{I_b} \left[1 + \frac{k_\theta}{I_\theta \Omega^2} \right] \theta \\
& + \left(\frac{I_a - dS_a}{I_b} \right) p^{**} + \frac{I_a}{I_b} \left[1 - \frac{dS_a}{I_a} \right] p \\
& + \left[\frac{I_t - (d+t)S_t}{I_b} \right] q^{**} + \frac{I_t}{I_b} \left[1 - \frac{(d+t)S_t}{I_t} \right] q = \gamma \bar{M}_\theta
\end{aligned} \tag{8.77}$$

$$\begin{aligned}
\bar{M}_\theta &= \frac{1}{2} \int_0^1 \bar{C}_{mea} \bar{c} u_t^2 dy \\
\bar{c} &= \frac{c}{R}
\end{aligned}$$

Aileron equation:

$$\begin{aligned}
& \frac{\bar{S}_a}{I_b} \beta^{**} + \frac{\bar{S}_a}{I_b} \left(1 + \frac{eS_a}{\bar{S}_a} \right) \beta \\
& + \left(\frac{I_a - dS_a}{I_b} \right) \theta^{**} + \frac{I_a}{I_b} \left[1 - \frac{dS_a}{I_a} \right] \theta \\
& + \frac{I_a}{I_b} p^{**} + \frac{I_a}{I_b} \left[1 - \frac{dS_a}{I_a} + \frac{k_a}{I_a \Omega^2} \right] p \\
& + \left(\frac{I_t - tS_t}{I_b} \right) q^{**} + \frac{I_t}{I_b} \left[1 - \frac{(d+t)S_t}{I_t} \right] q = \gamma \bar{M}_p
\end{aligned} \tag{8.78}$$

$$\bar{M}_p = \frac{1}{2} \int_0^1 \bar{C}_{mp} \bar{c} u_t^2 dy$$

Tab equation:

$$\begin{aligned} & \frac{\bar{S}_t}{I_b} \beta^{**} + \frac{\bar{S}_t}{I_b} \left(1 + \frac{eS_t}{\bar{S}_t}\right) \beta \\ & + \left[\frac{I_t - (d+t)S_t}{I_b} \right] \theta^{**} + \frac{I_t}{I_b} \left[1 - \frac{(d+t)S_t}{I_t}\right] \theta \\ & + \left(\frac{I_t - tS_t}{I_b} \right) p^{**} + \frac{I_t}{I_b} \left[1 - \frac{(d+t)S_t}{I_t}\right] p \\ & + \frac{I_t}{I_b} q^{**} + \frac{I_t}{I_b} \left[1 - \frac{(d+t)S_t}{I_t} + \frac{k_t}{I_t \Omega^2}\right] q = \gamma \bar{M}_q \end{aligned} \quad (8.79)$$

$$\bar{M}_q = \frac{1}{2} \int_0^1 \bar{C}_{mq} \bar{c} u_t^2 dy$$

8.3 Aerodynamic Model

The foundation of flap-torsion-aileron-tab aerodynamics was laid by Theodorsen and Garrick in 1942 [3]. It was developed to study flutter of fixed wing aircraft tails with control surfaces, including servo tabs.

8.3.1 Theodorsen model for aileron

Consider a section with flap. The section extends from $x = -b$ to $x = +b$, where b is half-chord. The pitch axis of the main part of the blade (elastic axis of the entire section) is located at $x = x_a$. The main blade ends at $x = x_c$. The pitch axis of the aileron is at the same point, i.e. there is no aerodynamic overhang.

The effective angle of attack of a 2-dimensional wing section (without aileron or tab) undergoing pitch and plunge motion is calculated at the 3/4 chord location. This is done so that the expression obtained for the sectional lift coefficient, C_l is consistent with thin airfoil theory.

$$\alpha_e = \alpha + \frac{\dot{h}}{U} + \left(\frac{1}{2} - x_a\right) b \frac{\dot{\alpha}}{U} \quad (8.80)$$

For a section with an aileron, the effective angle of attack can be extended to include the effect of aileron deflection

$$\alpha_{ep} = \alpha_e + \frac{1}{\pi} T_{10}^c p + \frac{1}{2\pi} T_{11}^c \frac{b\dot{p}}{U} \quad (8.81)$$

where T 's are geometric constants given later. Define

$$Q = U \alpha_{ep} \quad (8.82)$$

Then the lift, pitching moment, and aileron hinge moment are given as follows. The circulatory components are

$$\begin{aligned} L &= 2\pi\rho U b Q C(k) \\ M_a &= 2\pi\rho U b^2 \left[\left(x_a + \frac{1}{2}\right) C(k) - \frac{1}{2} \right] Q \\ M_p &= -\rho U b^2 [T_{12}^c C(k) - T_4] Q \end{aligned} \quad (8.83)$$

$C(k)$ is the unsteady Theodorsen constant accounting for the shed wake. The circulatory components have terms both associated with the shed wake and those not associated with the shed wake. The noncirculatory components are

$$\begin{aligned}
L &= \rho b^2 \left(\pi U \dot{\alpha} + \pi \dot{h} - \pi b a \ddot{a} - U T_4^c \dot{p} - b T_1^c \ddot{p} \right) \\
M_a &= -\rho b^2 \left[\underline{-\pi U^2 \alpha} + \pi \left(\frac{1}{8} + x_a^2 \right) b^2 \ddot{\alpha} + U^2 T_4^c p + \{ T_1^c - T_8^c - (x_c - x_a) T_4^c \} b U \dot{p} \right. \\
&\quad \left. - \{ T_7^c + (c - a) T_1^c \} b^2 \ddot{p} - \pi a b \ddot{h} - \underline{\pi U \dot{h}} \right] \\
M_p &= -\rho b^2 \left[\underline{U^2 T_4^c \alpha} + \underline{T_4^c U \dot{h}} - (2T_9^c + T_1^c) b U \dot{\alpha} + 2T_{13}^c b^2 \ddot{\alpha} + \frac{1}{\pi} T_5^c U^2 p - \frac{1}{\pi} b^2 T_3^c \ddot{p} - T_1^c b \ddot{h} \right]
\end{aligned} \tag{8.84}$$

The underlined terms in the noncirculatory components cancel with the non-shed wake related terms in the circulatory components. Grouped into shed wake related and non shed wake related terms the final expressions after addition become

$$\begin{aligned}
L &= 2\pi \rho U b Q C(k) + \rho b^2 \left(\pi U \dot{\alpha} + \pi \dot{h} - \pi b a \ddot{a} - U T_4^c \dot{p} - b T_1^c \ddot{p} \right) \\
M_a &= 2\pi \rho U b^2 \left(x_a + \frac{1}{2} \right) Q C(k) - \rho b^2 \left[\underline{\pi U b \left(\frac{1}{2} - x_a \right) \dot{\alpha}} + \pi \left(\frac{1}{8} + x_a^2 \right) b^2 \ddot{\alpha} \right. \\
&\quad \left. + U^2 (T_{10}^c + T_4^c) p + \left\{ T_1^c - T_8^c - (x_c - x_a) T_4^c + \frac{b}{2} T_{11}^c \right\} b U \dot{p} \right. \\
&\quad \left. - \{ T_7^c + (c - a) T_1^c \} b^2 \ddot{p} - \pi a b \ddot{h} \right] \\
M_p &= -\rho U b^2 T_{12}^c Q C(k) - \rho b^2 \left[- \left\{ 2T_9^c + T_1^c + T_4^c \left(\frac{1}{2} - x_a \right) \right\} b U \dot{\alpha} + 2T_{13}^c b^2 \ddot{\alpha} \right. \\
&\quad \left. + \frac{1}{\pi} (T_5^c - \underline{T_4^c T_{10}^c}) U^2 p - \underline{-\frac{1}{2\pi} b T_4^c T_{11}^c U \dot{p}} - \frac{1}{\pi} b^2 T_3^c \ddot{p} - T_1^c b \ddot{h} \right]
\end{aligned} \tag{8.85}$$

where the underlined terms are circulatory terms not related to shed wake effects. The nondimensional lift and moment coefficients are then simply

$$\begin{aligned}
C_l &= \frac{L}{\frac{1}{2} \rho U^2 (2b)} \\
C_{ma} &= \frac{M_a}{\frac{1}{2} \rho U^2 (2b)^2} \\
C_{mp} &= \frac{M_p}{\frac{1}{2} \rho U^2 (2b)^2}
\end{aligned} \tag{8.86}$$

8.3.2 Theodorsen and Garrick model for aileron and tab

Here a general airfoil section with an aileron and a tab with aerodynamic overhangs for both are considered, see Fig. 8.2. As shown in the figure, the entire section extends from $x = -b$ to $x = +b$, where b is half-chord. The pitch axis of the main part of the blade (elastic axis of the entire section) is located at $x = x_a$. The main blade ends at $x = x_c$. The pitch axis of the aileron is at $x = x_e$. The distance between x_c and x_e is the aerodynamic overhang of the aileron, l , where $l = x_e - x_c$. The aileron ends at $x = x_d$. The pitch axis of the tab is at $x = x_f$. The distance between x_f and x_d is the aerodynamic overhang of the tab, m , where $m = x_f - x_d$. The analysis assumes no leak of fluid in the gaps between the wing and the aileron, and between the aileron and the tab. These gaps are considered sealed.

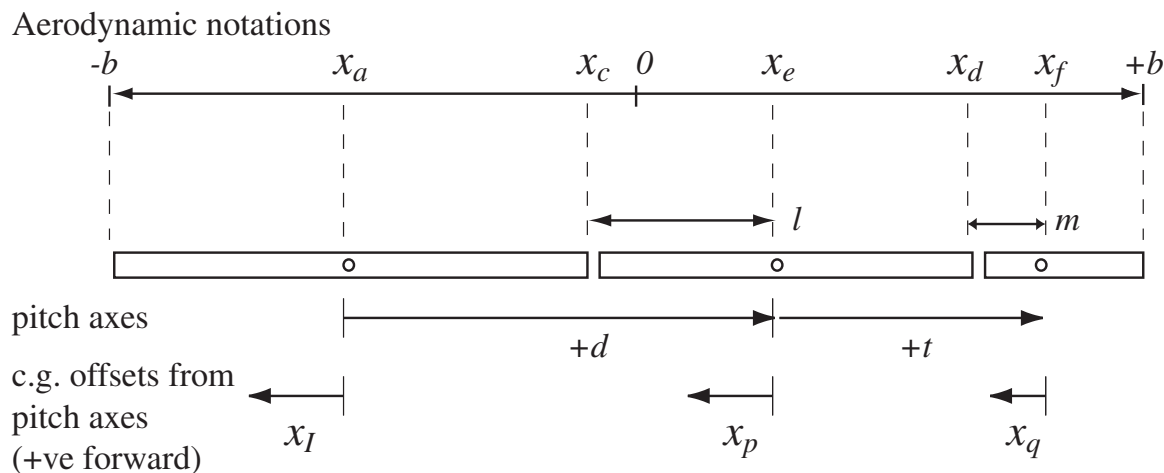


Figure 8.2: Airfoil with aileron and tab; aerodynamic notations

For a section with flap and tab the effective angle of attack can be extended to include the effect of aileron and tab deflections, p , and q .

$$\alpha_{epq} = \alpha_e + \frac{1}{\pi}(T_{10}^c - lT_{21}^c)p + \frac{1}{2\pi}(T_{11}^c - 2lT_{10}^c)\frac{b\dot{p}}{U} + \frac{1}{\pi}(T_{10}^d - mT_{21}^d)q + \frac{1}{2\pi}(T_{11}^d - 2lT_{10}^d)\frac{b\dot{q}}{U} \quad (8.87)$$

where T 's are geometric constants given later. Define Q is the same way as before

$$Q = U\alpha_{epq} \quad (8.88)$$

The final expressions for sectional lift, pitching moment and the aileron and tab hinges can be organized into shed wake and non shed wake terms are as follows

$$\begin{aligned} L &= 2\pi\rho UbQC(k) - \rho bU^2(T_{l1} + lT_{l2} + mT_{l3}) + L_I \\ M_a &= 2\pi\rho Ub^2\left(x_a + \frac{1}{2}\right)C(k)Q - \rho b^2U^2(T_{a1} + lT_{a2} + mT_{a3}) + M_{aI} \\ M_p &= -\rho Ub^2(T_{12}^c - 2lT_{20}^c)C(k)Q - \rho b^2U^2(T_{p1} + lT_{p2} + l^2T_{p3} + mT_{p4} + lmT_{p5}) + M_{pI} \\ M_q &= -\rho Ub^2(T_{12}^d - 2mT_{20}^d)C(k)Q - \rho b^2U^2(T_{q1} + mT_{q2} + m^2T_{q3} + lT_{q4} + lmT_{q5}) + M_{qI} \end{aligned} \quad (8.89)$$

$C(k)$ is the unsteady Theodorsen constant accounting for the the shed wake. L_I , M_{aI} , M_{pI} , and M_{qI} are the inertial (or acceleration) terms. In coefficient form we have

$$\begin{aligned} C_l &= \frac{L}{\frac{1}{2}\rho U^2(2b)} \\ C_{ma} &= \frac{M_a}{\frac{1}{2}\rho U^2(2b)^2} \\ C_{mp} &= \frac{M_p}{\frac{1}{2}\rho U^2(2b)^2} \\ C_{mq} &= \frac{M_q}{\frac{1}{2}\rho U^2(2b)^2} \end{aligned} \quad (8.90)$$

Using equations 8.89 and 8.90 we obtain the non-dimensional coefficients as

$$\begin{aligned}
C_l &= 2\pi \frac{Q}{U} C(k) - \frac{1}{2} T_l + C_{li} \\
C_{ma} &= 2\pi \frac{1}{2} \left(x_a + \frac{1}{2} \right) \frac{Q}{U} C(k) - \frac{1}{2} T_{ma} + C_{mai} \\
C_{mp} &= -\frac{1}{2} \frac{Q}{U} (T_{12}^c - 2lT_{20}^c) C(k) - \frac{1}{2} T_{mp} + C_{mpi} \\
C_{mq} &= -\frac{1}{2} \frac{Q}{U} (T_{12}^d - 2mT_{20}^d) C(k) - \frac{1}{2} T_{mq} + C_{mqi}
\end{aligned} \tag{8.91}$$

where Q/U is the effective angle of attack α_{epq} of the section calculated at the 3/4 chord location. T_l , T_{ma} , T_{mp} , and T_{mq} are defined as follows.

$$\begin{aligned}
T_l &= T_{l1} + lT_{l2} + mT_{l3} \\
T_{ma} &= T_{a1} + lT_{a2} + mT_{a3} \\
T_{mp} &= T_{p1} + lT_{p2} + l^2T_{p3} + mT_{p4} + lmT_{p5} \\
T_{mq} &= T_{q1} + mT_{q2} + m^2T_{q3} + lT_{q4} + lmT_{q5}
\end{aligned} \tag{8.92}$$

where

$$\begin{aligned}
T_{l1} &= \pi \frac{b\dot{\alpha}}{U} - T_4^c \frac{b\dot{p}}{U} - T_4^d \frac{b\dot{q}}{U} \\
T_{l2} &= -2 \frac{b\dot{p}}{U} \sqrt{1-x_c^2} \\
T_{l3} &= -2 \frac{b\dot{q}}{U} \sqrt{1-x_d^2}
\end{aligned} \tag{8.93}$$

and

$$\begin{aligned}
T_{a1} &= \pi \left(\frac{1}{2} - a \right) \frac{b\dot{\alpha}}{U} + T_{15}^c p + T_{16}^c \frac{b\dot{p}}{U} + T_{15}^d q + T_{16}^d \frac{b\dot{q}}{U} \\
T_{a2} &= T_{22}^c p + T_{23}^c \frac{b\dot{p}}{U} \\
T_{a3} &= T_{22}^d q + T_{23}^d \frac{b\dot{q}}{U}
\end{aligned} \tag{8.94}$$

and

$$\begin{aligned}
T_{p1} &= T_{17}^c \frac{b\dot{\alpha}}{U} + \frac{1}{\pi} T_{18}^c p + \frac{1}{\pi} T_{19}^c \frac{b\dot{p}}{U} + \frac{1}{\pi} Y_{9q} + \frac{1}{\pi} Y_{10} \frac{b\dot{q}}{U} \\
T_{p2} &= T_{25}^c \frac{b\dot{\alpha}}{U} + \frac{1}{\pi} T_{26}^c p + \frac{1}{\pi} T_{27}^c \frac{b\dot{p}}{U} + \frac{1}{\pi} Y_{11q} + \frac{1}{\pi} Y_{12} \frac{b\dot{q}}{U} \\
T_{p3} &= \frac{1}{\pi} T_{28} p + \frac{1}{\pi} T_{29} \frac{b\dot{p}}{U} \\
T_{p4} &= \frac{1}{\pi} Y_{13q} + \frac{1}{\pi} Y_{14} \frac{b\dot{q}}{U} \\
T_{p5} &= \frac{1}{\pi} Y_{15q} + \frac{1}{\pi} Y_{16} \frac{b\dot{q}}{U}
\end{aligned} \tag{8.95}$$

and

$$\begin{aligned}
T_{q1} &= T_{17}^d \frac{b\dot{\alpha}}{U} + \frac{1}{\pi} Y_{17} p + \frac{1}{\pi} Y_{13} \frac{b\dot{p}}{U} + \frac{1}{\pi} T_{18}^d q + \frac{1}{\pi} T_{19}^d \frac{b\dot{q}}{U} \\
T_{q2} &= T_{25}^d \frac{b\dot{\alpha}}{U} + \frac{1}{\pi} Y_{19} p + \frac{1}{\pi} Y_{20} \frac{b\dot{p}}{U} + \frac{1}{\pi} T_{26}^d q + \frac{1}{\pi} T_{27}^d \frac{b\dot{q}}{U} \\
T_{q3} &= \frac{1}{\pi} T_{28}^d p + \frac{1}{\pi} T_{29} \frac{b\dot{p}}{U} \\
T_{q4} &= \frac{1}{\pi} Y_{21} q + \frac{1}{\pi} Y_{22} \frac{b\dot{q}}{U} \\
T_{q5} &= \frac{1}{\pi} Y_{23} q + \frac{1}{\pi} Y_{24} \frac{b\dot{q}}{U}
\end{aligned} \tag{8.96}$$

The inertial terms L_I , M_{aI} , M_{pI} , and M_{qI} as given in equation 8.89 are as follows.

$$\begin{aligned}
L_I &= -\rho b \left(\pi b \ddot{h} - \pi b a \ddot{\alpha} - T_1^c b \ddot{p} - T_1^d b \ddot{q} \right) \\
&\quad - \rho b l \left(b^2 T_4^c \ddot{p} \right) - \rho b m \left(b^2 T_4^d \ddot{q} \right) \\
M_{aI} &= -\rho b^2 \left[\pi a h \ddot{h} + \pi b^2 \left(\frac{1}{8} + a^2 \right) \ddot{\alpha} + 2T_{13}^c b^2 \ddot{p} + 2T_{13}^d b^2 \ddot{q} \right] \\
&\quad - \rho b^2 l \left(T_{24}^c b^2 \ddot{p} \right) - \rho b^2 m \left(T_{24}^d b^2 \ddot{q} \right) \\
M_{pI} &= -\rho b^2 \left(-T_1^c b \ddot{h} + 2T_{13}^c b^2 \ddot{\alpha} - \frac{1}{\pi} T_3^c b^2 \ddot{p} - \frac{1}{\pi} Y_6 b^2 \ddot{q} \right) \\
&\quad - \rho b^2 l \left(T_4^c b \ddot{h} + T_{24}^c b^2 \ddot{\alpha} + \frac{2}{\pi} T_2^c b^2 \ddot{p} + \frac{1}{\pi} Y_3 b^2 \ddot{q} \right) \\
&\quad - \rho b^2 l^2 \left(-\frac{1}{\pi} T_5^c b^2 \ddot{p} \right) - \rho b^2 m \left(\frac{1}{\pi} Y_4 b^2 \ddot{q} \right) - \rho b^2 l m \left(-\frac{1}{\pi} Y_1 b^2 \ddot{q} \right) \\
M_{qI} &= -\rho b^2 \left(-T_1^d b \ddot{h} + 2T_{13}^d b^2 \ddot{\alpha} - \frac{1}{\pi} Y_6 b^2 \ddot{p} - \frac{1}{\pi} T_3^d b^2 \ddot{q} \right) \\
&\quad - \rho b^2 m \left(T_4^d b \ddot{h} + T_{24}^d b^2 \ddot{\alpha} + \frac{1}{\pi} Y_4 b^2 \ddot{p} + \frac{2}{\pi} T_2^d b^2 \ddot{q} \right) \\
&\quad - \rho b^2 m^2 \left(-\frac{1}{\pi} T_5^d b^2 \ddot{p} \right) - \rho b^2 l \left(\frac{1}{\pi} Y_3 b^2 \ddot{p} \right) - \rho b^2 l m \left(-\frac{1}{\pi} Y_1 b^2 \ddot{p} \right)
\end{aligned} \tag{8.97}$$

The nondimensional forms used in equations 8.91 are obtained by simply dividing the above expressions by $\rho U^2 b$ and $2\rho U^2 b^2$, for lift and moments respectively, as given in equations 8.90.

The constants are provided below.

$$\begin{aligned}
T_1^c &= -\frac{1}{3}(2+x_c^2)\sqrt{1-x_c^2} + x_c \cos^{-1} x_c \\
T_2^c &= x_c(1-x_c^2) - (1+x_c^2)\sqrt{1-x_c^2} \cos^{-1} x_c + x_c(\cos^{-1} x_c)^2 \\
T_3^c &= -\frac{1}{8}(1-x_c^2)(5x_c^2+4) + \frac{1}{4}x_c(7+2x_c^2)\sqrt{1-x_c^2} \cos^{-1} x_c - \left(\frac{1}{8}+x_c^2\right)(\cos^{-1} x_c)^2 \\
T_4^c &= x_c\sqrt{1-x_c^2} - \cos^{-1} x_c \\
T_5^c &= -(1-x_c^2) + 2x_c\sqrt{1-x_c^2} \cos^{-1} x_c - (\cos^{-1} x_c)^2 \\
T_8^c &= -\frac{1}{3}(1-x_c^2)^{3/2} - x_c T_4 \\
T_9^c &= \frac{1}{2} \left[\frac{1}{3}(1-x_c^2)^{3/2} + x_a T_4 \right] \\
T_{10}^c &= \sqrt{1-x_c^2} + \cos^{-1} x_c \\
T_{11}^c &= (2-x_c)\sqrt{1-x_c^2} + (1-2x_c) \cos^{-1} x_c \\
T_{12}^c &= (2+x_c)\sqrt{1-x_c^2} - (1+2x_c) \cos^{-1} x_c \\
T_{15}^c &= T_4^c + T_{10}^c \\
T_{16}^c &= T_1^c - T_8^c - (x_c - x_a)T_4^c + \frac{1}{2}T_{11}^c \\
T_{17}^c &= -2T_9^c - T_1^c + \left(x_a - \frac{1}{2}\right)T_4^c \\
T_{18}^c &= T_5^c - T_4^c T_{10}^c \\
T_{19}^c &= -\frac{1}{2}T_4^c T_{11}^c
\end{aligned} \tag{8.98}$$

$$\begin{aligned}
T_{20}^c &= -\sqrt{1-x_c^2} + \cos^{-1} x_c \\
T_{21}^c &= \sqrt{\frac{1+x_c}{1-x_c}} \\
T_{22}^c &= 2\sqrt{1-x_c^2} - \sqrt{\frac{1+x_c}{1-x_c}} \\
T_{23}^c &= (-1-2x_c+2x_a)\sqrt{1-x_c^2} \\
T_{25}^c &= T_4^c - (1-x_c)\sqrt{1-x_c^2} \\
T_{26}^c &= 2\sqrt{1-x_c^2}T_{20}^c + T_4^c\sqrt{\frac{1+x_c}{1-x_c}} \\
T_{27}^c &= T_4^c T_{10}^c - \sqrt{1-x_c^2}T_{11}^c \\
N_{c,c'} &= \left| \frac{1-x'_c x_c - \sqrt{1-x_c'^2}\sqrt{1-x_c^2}}{x_c - x'_c} \right| \\
T_{28}^c &= 2(1+x_c + \log_{10} N_{c,c'}) \\
T_{29}^c &= 2\sqrt{1-x_c^2}T_{10}^c
\end{aligned} \tag{8.99}$$

x'_c denotes the beginning coordinate of the aileron. x_c denotes the ending coordinate of the main blade. Thus $x'_c - x_c$ denotes the gap between the main blade and the aileron. Note that the expressions for T^d are obtained by simply replacing x_c with x_d in the above expressions. Similarly, $N_{c,d}$ is obtained by replacing x'_c with x_d in the expression for $N_{c,c'}$. $N_{d,d'}$ is obtained by replacing

x_c with x_d , and x'_c with x'_d . x'_d is the beginning coordinate of the tab. x_d is the ending coordinate of the aileron. Thus, as in the case of aileron, $x'_d - x_d$ denotes the gap between the aileron and the tab. Define the following constants.

$$\begin{aligned} q_c &= \sqrt{1 - x_c^2} \\ q_d &= \sqrt{1 - x_d^2} \\ q_{cd} &= q_c q_d \\ a_c &= \cos^{-1} x_c \\ a_d &= \cos^{-1} x_d \end{aligned}$$

The Y terms are functions of both x_c and x_d . The T terms are understood to be associated with x_c when no explicit variable is indicated. For example, T_4 in Y_9 means T_4^c .

$$\begin{aligned} Y_1 &= -q_{cd} - a_c a_d + x_d q_d a_c + x_c q_c a_d - (x_d - x_c)^2 \log_{10} N_{c,d} \\ Y_2 &= 2q_d a_c - 2(x_d - x_c) \log_{10} N_{c,d} \\ Y_3 &= \frac{1}{3}(x_c + 2x_d)q_c q_d + x_d a_c a_d - \frac{1}{3}q_d a_c (2 + x_d^2) - \frac{1}{3}q_c a_d (1 + 3x_c x_d - x_c^2) + \\ &\quad \frac{1}{3}(x_d - x_c)^3 \log_{10} N_{c,d} \\ Y_4 &= \frac{1}{3}(x_d + 2x_c)q_d q_c + x_c a_c a_d - \frac{1}{3}q_c a_d (2 + x_c^2) - \\ &\quad \frac{1}{3}q_d a_c (1 + 3x_d x_c - x_d^2) + \frac{1}{3}(x_c - x_d)^3 \log_{10} N_{c,d} \\ Y_5 &= -q_{cd} + (2x_c - x_d)q_d a_c + (x_d - x_c)^2 \log_{10} N_{c,d} \\ Y_6 &= -q_{cd} \left(1 + \frac{x_c^2}{6} + \frac{x_d^2}{6} + \frac{11}{12}x_c x_d \right) - a_c a_d \left(\frac{1}{8} + x_d x_c \right) \\ &\quad + \frac{1}{3}a_c q_d \left[\left(\frac{5}{2} - x_d^2 \right) \frac{x_d}{4} + x_c (2 + x_d^2) \right] \\ &\quad + \frac{1}{3}a_d q_c \left[\left(\frac{5}{2} - x_c^2 \right) \frac{x_c}{4} + x_d (2 + x_c^2) \right] + \frac{1}{12}(x_d - x_c)^4 \log_{10} N_{c,d} \end{aligned} \tag{8.100}$$

$$\begin{aligned}
Y_7 &= 2q_c a_c - 2(x_c - x_d) \log_{10} N_{c,d} \\
Y_8 &= -q_{cd} + (2x_d - x_c)q_c a_d + (x_c - x_d)^2 \log_{10} N_{c,d} \\
Y_9 &= Y_1 - T_4 T_{10} \\
Y_{10} &= Y_3 - Y_4 - \frac{1}{2} T_4 T_{11} \\
Y_{11} &= Y_7 - 2q_c T_{10} \\
Y_{12} &= Y_1 - Y_8 - q_c T_{11} \\
Y_{13} &= Y_2 + T_4 T_{21} \\
Y_{14} &= Y_5 - Y_9 \\
Y_{15} &= 2q_c T_{21} + 2 \log_{10} N_{c,d} \\
Y_{16} &= Y_2 - Y_7 + 2q_c T_{10} \\
Y_{17} &= Y_1 - T_4 T_{10} \\
Y_{18} &= Y_4 - Y_3 - \frac{1}{2} T_4 T_{11} \\
Y_{19} &= Y_2 - 2q_d T_{10} \\
Y_{20} &= Y_1 - Y_5 - q_d T_{11} \\
Y_{21} &= Y_7 + T_4 T_{21} \\
Y_{22} &= -Y_1 + Y_8 + T_{10} T_4 \\
Y_{23} &= 2q_d T_{21} + 2 \log_{10} N_{c,d} \\
Y_{24} &= Y_7 - Y_2 + 2q_d T_{10}
\end{aligned} \tag{8.101}$$

8.3.3 2D airfoil data

The expressions given earlier are valid for flat plate airfoils with sealed gaps and for inviscid and incompressible flows. In real applications air control surfaces are slotted. They generate hinge gaps and protrude into the flow when deflected. The flow is characterized by compressibility effects and stall at high angles of attack or deflections. Airfoil properties obtained from steady wind tunnel tests can be used to refine the steady part of the aerodynamic modeling. Calculated properties from 2D CFD analyses can be incorporated in the same manner. Let us understand which parts of the theory can be replaced with refined values. To this end we shall re-organize the coefficients given in equation 8.91 using equations 8.87 and 8.88. First consider the lift coefficient C_l . Keeping only the steady terms we can write

$$\begin{aligned}
C_l &= 2\pi \left[\alpha + \frac{1}{\pi} (T_{10}^c - lT_{21}^c) p + \frac{1}{\pi} (T_{10}^d - mT_{21}^d) q \right] \\
&= 2\pi\alpha + 2(T_{10}^c - lT_{21}^c) p + 2(T_{10}^d - mT_{21}^d) q
\end{aligned} \tag{8.102}$$

The above can be written in general as

$$C_l = C_0 + C_1 \alpha + C_{lp} p + C_{lq} q \tag{8.103}$$

where $C_0 = C_l(\alpha = 0, p = 0, q = 0)$ and C_1 is the lift curve slope. In the case of thin airfoil theory we had $C_0 = 0$, $C_1 = 2\pi$, $C_{lp} = 2(T_{10}^c - lT_{21}^c)$ and $C_{lq} = (T_{10}^d - mT_{21}^d)$. But these coefficients can in general be replaced with real airfoil properties. $C_{lp} p$ is an increment in lift brought about by the aileron deflection. It can be written as $(\Delta C_l)_p$. $C_{lq} q$ is an increment in lift brought about by the tab deflection. It can be written as $(\Delta C_l)_q$. $C_0 + C_1 \alpha$ is the baseline airfoil C_l . It can be written as $(C_l)_{af}$. Thus C_l can be written as

$$C_l = (C_l)_{af} + (\Delta C_l)_p + (\Delta C_l)_q \tag{8.104}$$

To use equation 8.103 the airfoil tables should be used to extract the coefficients C_0 , C_1 , C_{lp} , and C_{lq} . The coefficients must be extracted locally however depending on α , p and q specially in the stall regions. Alternatively, equation 8.104 can be used and incremental contributions can be read off directly from the tables.

Now consider the moments. Let the moment about any point a be C_{ma} . It can be related to the moment about any other point ac by

$$C_{ma} = C_{mac} + C_l \frac{1}{2} (x_a - x_{ac}) \quad (8.105)$$

where x_a and x_{ac} are the coordinates of the two points. The above equation simply relates the moment about any two general points. If x_{ac} is chosen as the aerodynamic center C_{mac} will be the moment about the aerodynamic center with the property that it is independant of angle of attack. Thin airfoil theory gives $x_{ac} = 1/4c$ and $C_{mac} = 0$, which gives back the expression in equation 8.91. In general for cambered airfoils x_{ac} is not at quarter chord and C_{mac} is not zero so that the above general expression should be used. x_{ac} and C_{mac} can be extracted from the airfoil property data where the moments are often measured about any convenient location. For example assume that the moments are available about the quarter chord. In equation 8.105 choose a to be at $1/4c$, which in our convention gives $x_a = -1/2$ to obtain

$$C_{m25} = C_{mac} - C_l \frac{1}{2} \left(\frac{1}{2} + x_{ac} \right) \quad (8.106)$$

Use C_{mac} from the above equation 8.106 and substitute in equation 8.105 to obtain

$$C_{ma} = C_{m25} + C_l \frac{1}{2} \left(x_a + \frac{1}{2} \right) \quad (8.107)$$

Note that the above equation 8.107 could have been directly obtained from equation 8.105 by choosing ac as the quarter chord. The above is a general expression valid for all airfoils. Expand C_l and C_{m25} as follows

$$C_l = C_0 + C_1 \alpha + C_{lp} p + C_{lq} q$$

$$C_{m25} = C_{m250} + \frac{\partial C_{m25}}{\partial \alpha} \alpha + \frac{\partial C_{m25}}{\partial p} p + \frac{\partial C_{m25}}{\partial q} q$$

where from equation 8.106 we have

$$\frac{\partial C_{m25}}{\partial \alpha} = \frac{\partial C_{mac}}{\partial \alpha} - C_l \frac{1}{2} \left(\frac{1}{2} + x_{ac} \right) = 0 - C_l \frac{1}{2} \left(\frac{1}{2} + x_{ac} \right) \quad (8.108)$$

Thus equation 8.107 becomes

$$C_{ma} = C_{m250} + C_0 \frac{1}{2} (x_a - x_{ac}) + C_1 \frac{1}{2} (x_a - x_{ac}) \alpha$$

$$+ \left[\frac{\partial C_{m25}}{\partial p} + C_{lp} \frac{1}{2} \left(x_a + \frac{1}{2} \right) \right] p + \left[\frac{\partial C_{m25}}{\partial q} + C_{lq} \frac{1}{2} \left(x_a + \frac{1}{2} \right) \right] q \quad (8.109)$$

which using equation 8.107 can be seen to be of a general form

$$C_{ma} = C_{ma0} + \frac{\partial C_{ma}}{\partial \alpha} \alpha + \frac{\partial C_{ma}}{\partial p} p + \frac{\partial C_{ma}}{\partial q} q \quad (8.110)$$

The coefficients in the above equation 8.110 can be determined from airfoil property tables via the expressions given in equation 8.109. The C_{m25} , C_0 and C_1 can be obtained from the baseline

airfoil tables with undeflected aileron and tab. The factors C_{lp} , C_{lq} , $\partial C_{m25}/\partial p$ and $\partial C_{m25}/\partial q$ can be obtained from aileron and tab tables. Let us explore the values provided by thin airfoil theory. This helps us understand which parts of the thin airfoil theory are being refined by the use of airfoil tables. The thin airfoil theory expression was

$$C_{ma} = 2\pi \left[\alpha + \frac{1}{\pi}(T_{10}^c - lT_{21}^c)p + \frac{1}{\pi}(T_{10}^d - mT_{21}^d)q \right] \frac{1}{2} \left(x_a + \frac{1}{2} \right) - \frac{1}{2} \left(T_{15}^c + lT_{22}^c + mT_{22}^d \right) p - \frac{1}{2} T_{15}^d q \quad (8.111)$$

Comparing equations 8.109 and 8.111 we have

$$\begin{aligned} C_{m250} &= 0 \\ C_0 &= 0 \\ C_1 &= 2\pi \\ C_{lp} &= 2(T_{10}^c - lT_{21}^c) \\ C_{lq} &= 2(T_{10}^d - mT_{21}^d) \\ \frac{\partial C_{m25}}{\partial p} &= -\frac{1}{2} \left(T_{15}^c + lT_{22}^c + mT_{22}^d \right) \\ \frac{\partial C_{m25}}{\partial q} &= -\frac{1}{2} T_{15}^d \end{aligned}$$

An alternative expression to equation 8.110 can be obtained by recognizing

$$C_{m250} + C_0 \frac{1}{2}(x_a - x_{ac}) + C_1 \frac{1}{2}(x_a - x_{ac})\alpha = (C_{m25})_{af} + (C_l)_{af} \frac{1}{2} \left(x_a + \frac{1}{2} \right)$$

$$\frac{\partial C_{m25}}{\partial p} p = (\Delta C_{m25})_p \quad \text{change in moment due to aileron}$$

$$\frac{\partial C_{m25}}{\partial q} q = (\Delta C_{m25})_q \quad \text{change in moment due to tab}$$

$$C_{lp} p = (\Delta C_l)_p \quad \text{change in lift due to aileron}$$

$$C_{lq} q = (\Delta C_l)_q \quad \text{change in lift due to tab}$$

Thus the expression 8.109 can be written as

$$\begin{aligned} C_{ma} &= (C_{m25})_{af} + (C_l)_{af} \frac{1}{2} \left(x_a + \frac{1}{2} \right) \\ &+ \left[(\Delta C_{m25})_p + \frac{1}{2} \left(x_a + \frac{1}{2} \right) (\Delta C_l)_p \right] + \left[(\Delta C_{m25})_q + \frac{1}{2} \left(x_a + \frac{1}{2} \right) (\Delta C_l)_q \right] \end{aligned} \quad (8.112)$$

where the quantities can be read off directly from the airfoil tables. For lift we had equations 8.103 and 8.104. For moment about the pitch axis we have equations 8.110 and 8.112.

The hinge moments for the aileron and tab can also be obtained in a similar manner. Thus for the airfoil hinge moment we have

$$\begin{aligned} C_{mp} &= C_{mp0} + \frac{\partial C_{mp}}{\partial \alpha} \alpha + \frac{\partial C_{mp}}{\partial p} p + \frac{\partial C_{mp}}{\partial q} q \\ &= (C_{mp})_{af} + \frac{\partial C_{mp}}{\partial p} p + \frac{\partial C_{mp}}{\partial q} q \\ &= (C_{mp})_{af} + (\Delta C_{mp})_p + (\Delta C_{mp})_q \end{aligned} \quad (8.113)$$

Similarly for the tab hinge moment

$$\begin{aligned}
C_{mq} &= C_{mq0} + \frac{\partial C_{mq}}{\partial \alpha} \alpha + \frac{\partial C_{mq}}{\partial p} p + \frac{\partial C_{mq}}{\partial q} q \\
&= (C_{mq})_{af} + \frac{\partial C_{mq}}{\partial p} p + \frac{\partial C_{mq}}{\partial q} q \\
&= (C_{mq})_{af} + (\Delta C_{mq})_p + (\Delta C_{mq})_q
\end{aligned} \tag{8.114}$$

As an example, figure 8.3 shows the baseline airfoil properties for a NACA 0009 airfoil. Figures 8.3(a) and 8.3(b) show the airfoil $(C_l)_{af}$ and $(C_{m25})_{af}$ variation with angle of attack. Figures 8.3(d) and (f) show the aileron and tab hinge moments of the airfoil with undeflected aileron and tab angles. These are $(C_{mp})_{af}$ and $(C_{mq})_{af}$. Figures 8.3(c) and (e) are the local lifts on the aileron and tab obtained by integrating the pressure distributions only around the aileron and the tab. The test data presented here is from Ref. [4]. The properties have been nondimensionalized in a slightly different manner compared to the analysis given earlier and are denoted with bars. The lift and pitching moment coefficients are the same. The local lift and hinge moments are nondimensionalized with respect to the local chord of the control surface.

$$\begin{aligned}
(\bar{C}_l)_p &= \frac{N_p}{\frac{1}{2}\rho U^2 c_p} \\
(\bar{C}_l)_q &= \frac{N_q}{\frac{1}{2}\rho U^2 c_q} \\
\bar{C}_{mp} &= \frac{M_p}{\frac{1}{2}\rho U^2 c_p^2} = C_{mp} \left(\frac{c}{c_p} \right)^2 \\
\bar{C}_{mq} &= \frac{M_q}{\frac{1}{2}\rho U^2 c_q^2} = C_{mq} \left(\frac{c}{c_q} \right)^2
\end{aligned}$$

Consider now an angle of attack $\alpha = 1/2^\circ$. The flap and tab are now deflected. Figure 8.4 shows the increments in lift, quarter chord pitching moment, local control surface lifts, and hinge moments brought about by the deflection. The increments are plotted versus aileron deflection over a range of tab angles. The values at zero tab angle can be assumed to correspond to an aileron only case with the aileron size of 30% chord. Figure 8.5 replots the same data with the properties now varying with tab angle over a range of aileron angle. The values at zero aileron angle can be assumed to correspond to an aileron only case with the aileron size of 9% chord.

The general expressions for lift, pitching moment and hinge moments given earlier in equations 8.103, 8.110, 8.113 and 8.114 can be extended for the unsteady case to increase sensitivity terms for the angular rates and accelerations. This form is useful for aeroelastic stability analyses as it identifies the aerodynamic damping and stiffness associated with the flap and tab deflections. Thus we have

$$C_l = C_0 + C_{l\dot{h}} \dot{h} + C_{l\ddot{h}} \ddot{h} + C_{l\alpha} \alpha + C_{lp} p + C_{lq} q + C_{l\dot{\alpha}} \dot{\alpha} + C_{l\dot{p}} \dot{p} + C_{l\dot{q}} \dot{q} + C_{l\ddot{\alpha}} \ddot{\alpha} + C_{l\ddot{p}} \ddot{p} + C_{l\ddot{q}} \ddot{q} \tag{8.115}$$

8.4 Flexible blade equations

The rotor blade is assumed flexible. The aileron and the tab are still single degrees of freedom. The flexibility of the control surface along the span is neglected. The axial extension u_e equation remains unchanged.

Elastic extension equation u_e :

$$\begin{aligned} & \left[EAu'_e + EAK_A^2 \left(\theta' \hat{\phi}' + \theta' w' v'' + \frac{\hat{\phi}'^2}{2} \right) \right. \\ & \left. - EAe_A v'' (\cos \theta - \hat{\phi} \sin \theta) + EA w'' (\sin \theta + \hat{\phi} \cos \theta) \right]' \\ & + m(\ddot{u}_e - u_e - x - 2\dot{v}) = L_u \end{aligned} \quad (8.116)$$

Chord bending equation v :

$$\begin{aligned} & [v''(EI_Z \cos^2 \theta + EI_Y \sin^2 \theta) + w''(EI_Z - EI_Y) \cos \theta \sin \theta \\ & - v'' \hat{\phi} \sin 2\theta (EI_Z - EI_Y) + w'' \hat{\phi} \cos 2\theta (EI_Z - EI_Y) \\ & - v'' \hat{\phi}^2 \cos 2\theta (EI_Z - EI_Y) - w'' \hat{\phi}^2 \sin 2\theta (EI_Z - EI_Y) \\ & - EB_2 \theta' \hat{\phi}' \cos \theta - EAe_A u'_e (\cos \theta - \hat{\phi} \sin \theta) + EAK_A^2 u'_e w' \theta' \\ & + (GJ + EB_1 \theta'^2) \hat{\phi}' w' - EC_2 \hat{\phi}'' \sin \theta]'' \\ & - m \left[-\ddot{v} + e_g \ddot{\theta} \sin \theta + e_g \cos \theta + v - \hat{\phi} \sin \theta + 2\dot{v} \beta_p + 2e_g \dot{v}' \cos \theta \right. \\ & \left. + 2e_g \dot{w}' \sin \theta + \ddot{\phi} e_g \sin \theta - 2\dot{u}_e + 2 \int_0^x (v' \dot{v}' + w' \dot{w}') dx \right] \\ & - me_g \left(x \cos \theta - \hat{\phi} x \sin \theta + 2\dot{v} \cos \theta \right)' + \left\{ mv' \int_x^1 (-\ddot{u}_e + u_e + x + 2\dot{v}) \right\}' \\ & - m_p e_p \left(\ddot{p} \sin \theta + p \ddot{\theta} \cos \theta + 2\dot{\theta} \dot{p} \cos \theta - p \dot{\theta}^2 \sin \theta - p \sin \theta \right) - m_p e_p p (x \sin \theta)' \\ & - m_q e_q \left(\ddot{q} \sin \theta + 2\dot{q} \dot{\theta} \cos \theta - q \sin \theta + q \ddot{\theta} \cos \theta - q \dot{\theta}^2 \sin \theta \right) = L_v \end{aligned} \quad (8.117)$$

Flap bending equation w :

$$\begin{aligned} & [w''(EI_Z \sin^2 \theta + EI_Y \cos^2 \theta) + v''(EI_Z - EI_Y) \cos \theta \sin \theta \\ & + w'' \hat{\phi} \sin 2\theta (EI_Z - EI_Y) + v'' \hat{\phi} \cos 2\theta (EI_Z - EI_Y) \\ & + w'' \hat{\phi}^2 \cos 2\theta (EI_Z - EI_Y) - v'' \hat{\phi}^2 \sin 2\theta (EI_Z - EI_Y) \\ & - EAe_A u'_e (\sin \theta + \hat{\phi} \cos \theta) - EB_2 \hat{\phi}' \theta' \sin \theta + EC_2 \hat{\phi}'' \cos \theta]'' \\ & - m \left(-\ddot{w} - e_g \ddot{\theta} \cos \theta - e_g \ddot{\phi} \cos \theta - 2\dot{v} \beta_p - x \beta_p \right) \\ & - me_g \left(x \sin \theta + \hat{\phi} x \cos \theta + 2\dot{v} \sin \theta \right)' + \left\{ mw' \int_x^1 (-\ddot{u}_e + u_e + x + 2\dot{v}) \right\}' \\ & - m_p e_p \left(-\ddot{p} \cos \theta + p \ddot{\theta} \sin \theta + 2\dot{\theta} \dot{p} \sin \theta + p \dot{\theta}^2 \cos \theta \right) - m_p e_p p (x \cos \theta)' \\ & - m_q e_q \left(-\ddot{q} \cos \theta - 2\dot{q} \dot{\theta} \sin \theta + q \ddot{\theta} \sin \theta + q \dot{\theta}^2 \cos \theta \right) = L_w \end{aligned} \quad (8.118)$$

Torsion equation $\hat{\phi}$:

$$\begin{aligned}
& (w''^2 - v''^2) \cos \theta \sin \theta (EI_Z - EI_Y) + v'' w'' \cos 2\theta \\
& \hat{\phi} (w''^2 - v''^2) \cos 2\theta (EI_Z - EI_Y) - 2\hat{\phi} v'' w'' \sin 2\theta \\
& + \left[GJ(\hat{\phi}' + w' v'') + EAK_A^2(\theta' + \phi') u'_e \right. \\
& \left. + EB_1 \theta'^2 \hat{\phi}' - EB_2 \theta' (v'' \cos \theta + w'' \sin \theta) \right]' \\
& - \left[-k_m^2 \hat{\phi} - \hat{\phi} (k_{m_2}^2 - k_{m_1}^2) \cos 2\theta - (k_{m_2}^2 - k_{m_1}^2) \cos \theta \sin \theta - x \beta_p e_g \cos \theta \right. \\
& \left. - v e_g \sin \theta + x v' e_g \sin \theta - x w' e_g \cos \theta + \ddot{v} e_g \sin \theta - \ddot{w} e_g \cos \theta - k_m^2 \ddot{\theta} \right] \\
& + m_p k_p^2 \ddot{p} - m_p e_p (d\ddot{p} + dp \cos 2\theta) \\
& + m_q k_q^2 \ddot{q} - m_q e_q [(t+d)\ddot{q} + (t+d)q \cos 2\theta] = L_{\hat{\phi}}
\end{aligned} \tag{8.119}$$

Aileron equation p :

$$\begin{aligned}
& m_p k_p^2 \left[-\ddot{\phi} - \ddot{p} - \ddot{\theta} - 2\dot{w}' \sin^2 \theta - (1 + 2\dot{v}') \sin \theta \cos \theta - (p + \hat{\phi}) \cos 2\theta \right] \\
& + m_p e_p \left[-\ddot{w} \cos \theta + \ddot{v} \sin \theta + d(\ddot{\phi} + \ddot{\theta}) + 2d\dot{w}' \sin^2 \theta + 2d\dot{v}' \sin \theta \cos \theta - v \sin \theta \right. \\
& \left. + x v' \sin \theta - x w' \cos \theta + d\hat{\phi} \cos 2\theta + dp \cos^2 \theta + d \cos \theta \sin \theta + dp\dot{\theta}^2 \right] \\
& + m_q k_q^2 \left[-\ddot{\phi} - \ddot{p} - \ddot{q} - \ddot{\theta} - 2\dot{w}' \sin^2 \theta - (1 + 2\dot{v}') \sin \theta \cos \theta \right. \\
& \left. - (p + q + \hat{\phi}) \cos 2\theta \right] \\
& m_q e_q \left[(t+d) (\ddot{\phi} + \ddot{\theta}) + (1 + 2\dot{v}') (t+d) \sin \theta \cos \theta + \right. \\
& \left. + (t+d)(p+q) \cos^2 \theta - tq\dot{\theta}^2 \cos^2 \theta + (t+d)\hat{\phi} \cos^2 \theta \right. \\
& \left. + (2\dot{w}' - 1)(t+d) \sin^2 \theta + (\ddot{v} - v + x v') \sin \theta + t(\ddot{p} + \ddot{q}) + (t+d)q\dot{\theta}^2 \right. \\
& \left. + (-\ddot{w} - x w' - x \beta_p) \cos \theta \right] \\
& + k_p p = M_p
\end{aligned} \tag{8.120}$$

Tab equation q :

$$\begin{aligned}
& m_q k_q^2 \left[-\ddot{\phi} - \ddot{p} - \ddot{q} - \ddot{\theta} - 2\dot{w}' \sin^2 \theta - (1 + 2\dot{v}') \sin \theta \cos \theta - (p + q + \hat{\phi}) \cos 2\theta \right] \\
& + m_q e_q \left[(t+d) (\ddot{\phi} + \ddot{\theta}) + t\ddot{p} - (t+d)\dot{\theta}^2 \sin \theta \cos \theta + (1 + 2\dot{v}') (t+d) \sin \theta \cos \theta \right. \\
& \left. + (t+d)(p+q+\hat{\phi}) \cos^2 \theta - tp \sin^2 \theta + 2(t+d)\dot{w}' \sin^2 \theta - (t+d)\hat{\phi} \sin^2 \theta + \right. \\
& \left. + (\ddot{v} - v + x v') \sin \theta + (-\ddot{w} - x w' + x \beta_p) \cos \theta \right] \\
& + k_q q = M_q
\end{aligned} \tag{8.121}$$

The sectional properties are defined as follows. The blade properties include the aileron and tab. They are assumed to remain nominally constant in presence of aileron and tab deflections. The aileron properties include the tab. They are assumed to remain nominally constant in presence of tab deflections. The blade properties are as follows.

$$\begin{aligned}
\int \int_A d\eta d\zeta &= A \\
\int \int_A \eta d\eta d\zeta &= Ae_A \\
\int \int_A \zeta d\eta d\zeta &= 0 \\
\int \int_A \lambda_T d\eta d\zeta &= 0 \\
\int \int_A (\eta^2 + \zeta^2) d\eta d\zeta &= AK_A^2 \\
\int \int_A (\eta^2 + \zeta^2)^2 d\eta d\zeta &= B_1 \\
\int \int_A \eta(\eta^2 + \zeta^2)^2 d\eta d\zeta &= B_2 \\
\int \int_A \eta^2 d\eta d\zeta &= I_Z \\
\int \int_A \zeta^2 d\eta d\zeta &= I_Y \\
\int \int_A \lambda_T^2 d\eta d\zeta &= EC_1 \\
\int \int_A \zeta \lambda_T d\eta d\zeta &= EC_2 \\
\int \int_A \rho d\eta d\zeta &= m \\
\int \int_A \rho \eta d\eta d\zeta &= me_g \\
\int \int_A \rho \zeta^2 d\eta d\zeta &= mk_{m_1}^2 \\
\int \int_A \rho \eta^2 d\eta d\zeta &= mk_{m_2}^2 \\
\int \int_A \rho(\eta^2 + \zeta^2) d\eta d\zeta &= mk_m^2 \\
\int \int_A \rho \zeta d\eta d\zeta &= 0 \\
\int \int_A \rho \eta \zeta d\eta d\zeta &= 0 \\
\int \int_A \rho \lambda_T d\eta d\zeta &= 0
\end{aligned} \tag{8.122}$$

were A is the sectional area, e_A is the tension axis offset positive in front of the elastic axis, E is the Young's modulus of the blade material, m is mass per unit span, e_g is the center of gravity offset positive in front of the elastic axis, and k_m , k_{m_1} and k_{m_2} are the radii of gyration.

The aileron and tab properties are as follows. They are the same, aileron properties are denoted with the subscript p , the tab properties with q .

$$\begin{aligned}
\int \int_{A_q} \rho d\eta d\zeta &= m_q & \int \int_{A_p} \rho d\eta d\zeta &= m_p \\
\int \int_{A_q} \rho \eta d\eta d\zeta &= me_q & \int \int_{A_p} \rho \eta d\eta d\zeta &= me_p \\
\int \int_{A_q} \rho(\eta^2 + \zeta^2) d\eta d\zeta &= m_p k_q^2 & \int \int_{A_p} \rho(\eta^2 + \zeta^2) d\eta d\zeta &= m_p k_p^2
\end{aligned} \tag{8.123}$$

m_p and m_q are the aileron and tab mass per unit span, k_p and k_q are the radii of gyration and e_p and e_q are the local c.g. offsets with respect to aileron and tab hinge axes. The c.g. offsets are positive forward.

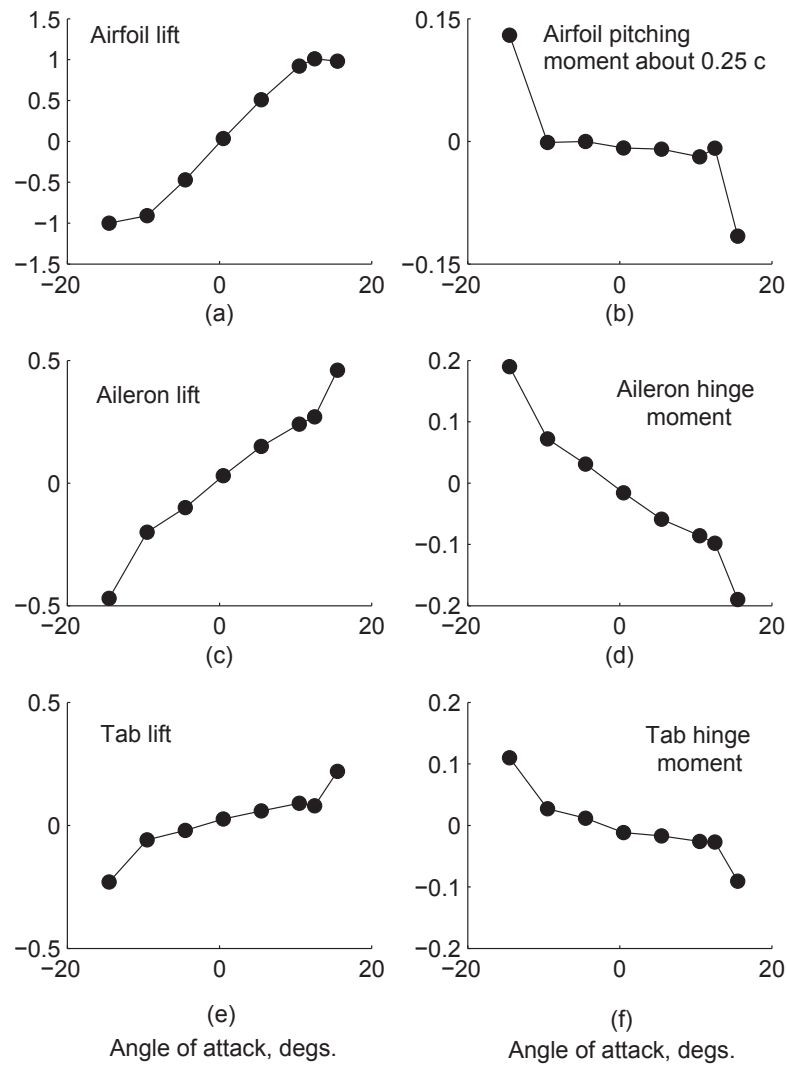


Figure 8.3: NACA 0009 airfoil property variations with section angle of attack α ; undeflected aileron and tab of size $c_p = 21\%c$, $c_q = 9\%c$, zero overhang; (a) airfoil C_l (b) airfoil $C_{m_{25}}$ (c) aileron lift $(\bar{C}_l)_p$ (d) aileron hinge moment \bar{C}_{mp} (e) tab lift $(\bar{C}_l)_q$ (f) tab hinge moment \bar{C}_{mq}

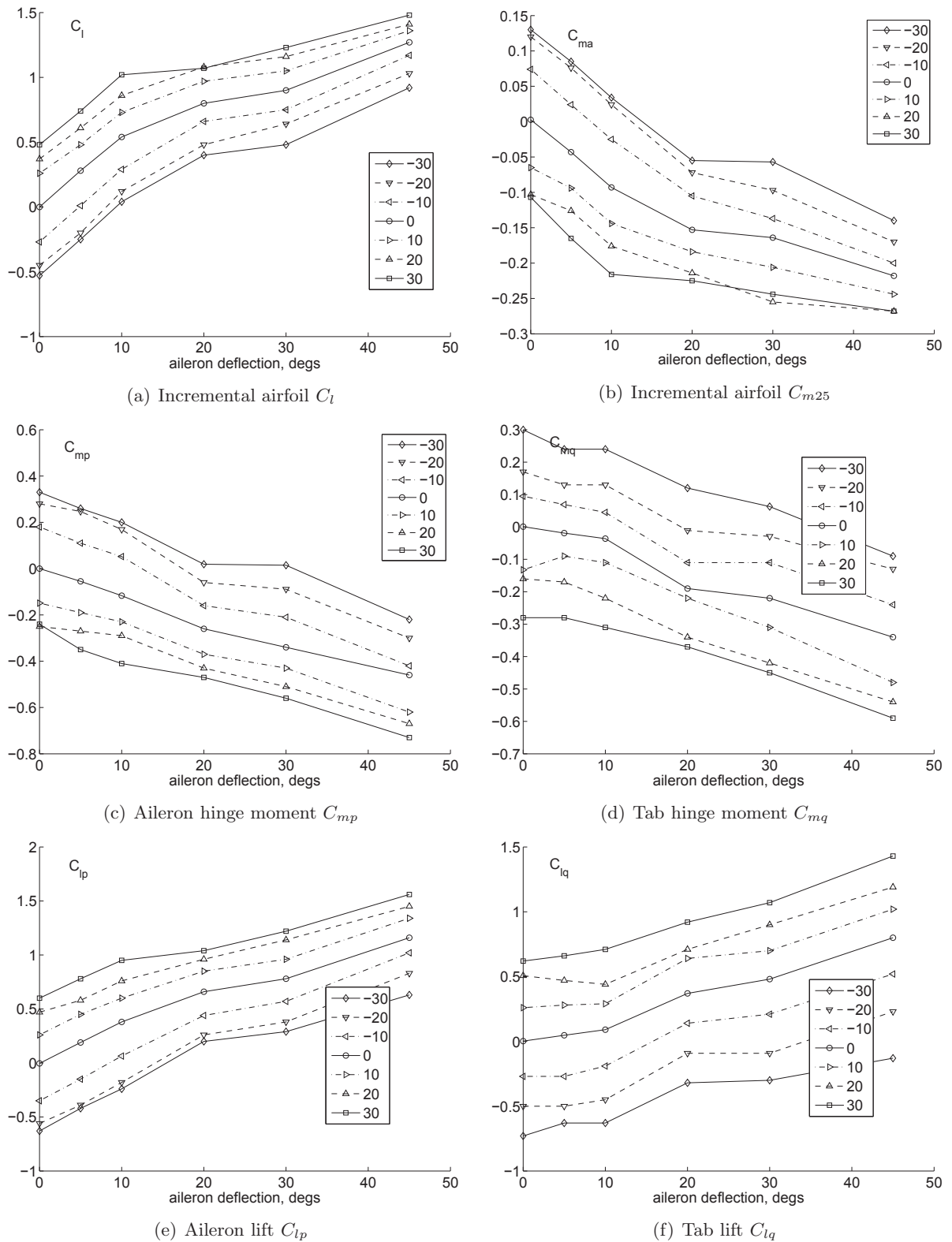


Figure 8.4: Measured properties of a NACA 0009 airfoil varying with aileron deflections at fixed tab settings; aileron and tab are 21% and 9% of total chord with zero overhang; airfoil angle of attack $1/2^\circ$

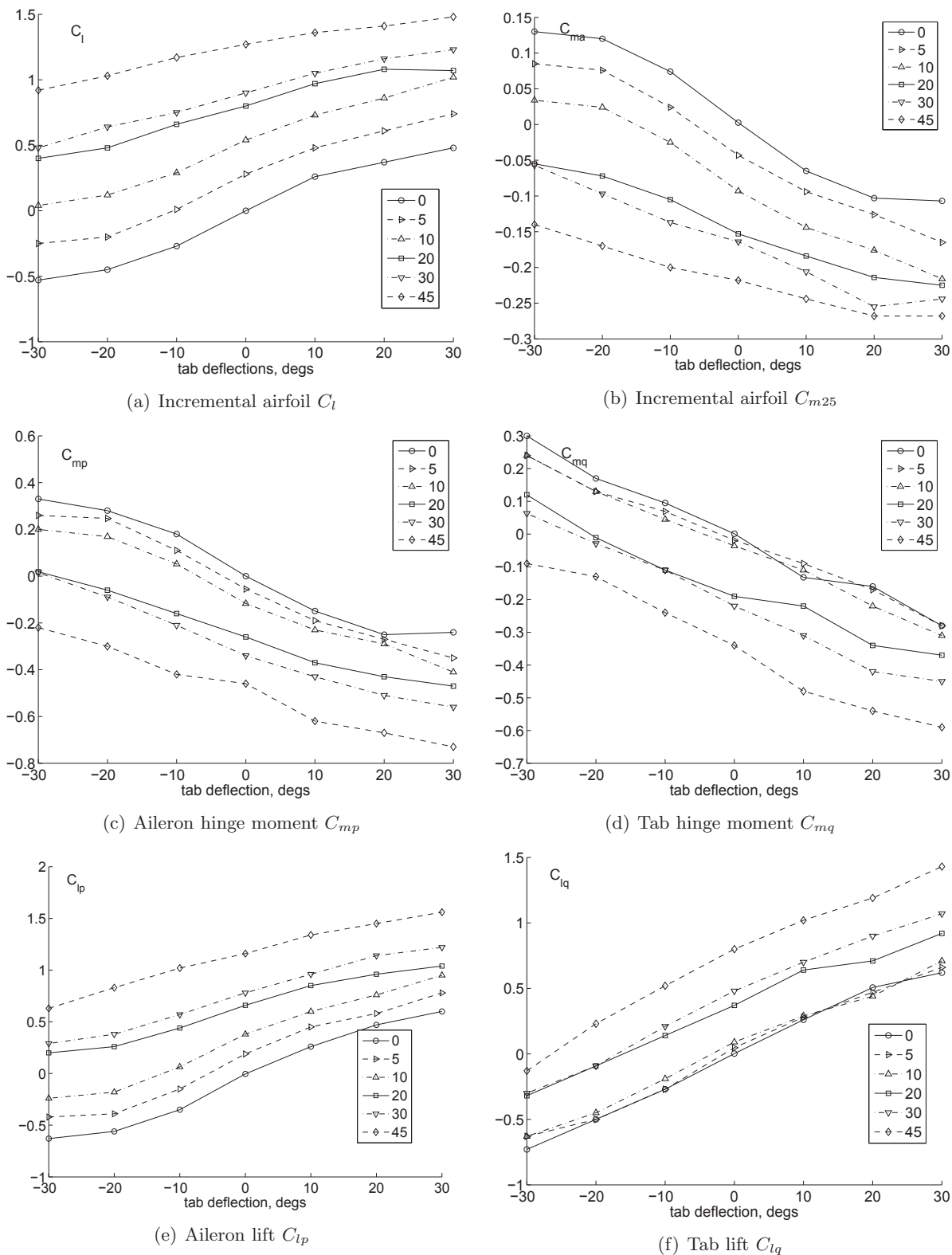


Figure 8.5: Measured properties of a NACA 0009 airfoil varying with tab deflections at fixed aileron settings; aileron and tab are 21% and 9% of total chord with zero overhang; airfoil angle of attack $1/2^\circ$

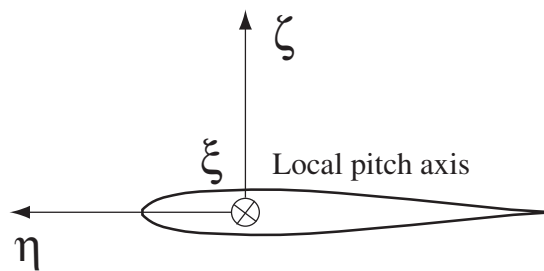


Figure 8.6: Local coordinates of a general element; blade, aileron, or the tab

Bibliography

- [1] Falls, J., Datta, A., and Chopra, I., "Integrated Servo-tabs and Trailing Edge Flaps for Helicopter Primary Control," 62nd Annual Forum of the American Helicopter Society, Phoenix, AZ, May 28-31, 2006.
- [2] Lanczos, C., *The Variational Principles of Mechanics*, Dover Publications, Inc., New York, NY, 1970.
- [3] Theodorsen, T., and Garrick, I. E., "Nonstationary Flow About a Wing-Aileron-Tab Combination Including Aerodynamic Balance," NACA Report No. 736, 1942.
- [4] Ames, M. B. and Sears, R. I., "Pressure-Distribution Investigation of an N.A.C.A. 0009 Airfoil With a 30-Percent-Chord Plain Flap and Three Tabs," NACA Technical Notes No. 759, Washington, May 1940.

Chapter 9

CFD for Rotors

This chapter describes Computational Fluid Dynamics (CFD) methods as applied to rotary wing flows.

9.1 Isentropic Flow Relations

The second law of thermodynamics states that the net rise in internal energy of a system is contributed partly by the heat added and partly by the work done on the system

$$\delta q + \delta w = de \quad (9.1)$$

The assumption is that there is no friction or dissipation losses. The work done on the system is given by $\delta w = -pdv$. p is the pressure and v is the specific volume. Thus

$$\delta q = de + pdv \quad (9.2)$$

The enthalpy h is defined as follows

$$\begin{aligned} h &= e + pv \\ &= e + RT \end{aligned}$$

where $pv = RT$ for a perfect gas. Therefore we have

$$\begin{aligned} dh &= de + pdv + vdp \\ de &= dh - pdv - vdp \end{aligned}$$

Using the above in equation 9.2 we have another expression for δq .

$$\delta q = dh - vdp \quad (9.3)$$

When heat δq is added to a system its temperature T rises. The amount of heat needed for unit rise in temperature is defined as specific heat. During the process of heat addition the volume of the system can be kept constant. Alternatively the volume may be allowed to change so as to keep its pressure constant. The specific heat value differs in the two cases. Thus there are two definitions of specific heat.

$$C_v = \left(\frac{\delta q}{dT} \right)_{\text{constant } v} \quad C_p = \left(\frac{\delta q}{dT} \right)_{\text{constant } p} \quad (9.4)$$

Using the above expressions and equations 9.2 and 9.3 it follows

$$\delta q = C_v dT \quad (9.5)$$

$$de + 0 = C_v dT \quad (9.6)$$

$$e = C_v T \quad (9.7)$$

Similarly

$$\delta q = C_p dT \quad (9.8)$$

$$dh + 0 = C_p dT \quad (9.9)$$

$$h = C_p T \quad (9.10)$$

where the assumption is that $e = 0$ and $h = 0$ at $T = 0$. Even though the above expressions have been obtained considering constant pressure and constant volume processes, the relations hold in general for any process for a perfect gas. A perfect gas is where there are no intermolecular forces. Thermodynamics is related to compressible aerodynamics through the assumption of isentropic flow. Consider the following definitions

Adiabatic process : $\delta q = 0$

Reversible process : no friction or dissipation

Isentropic process : adiabatic + reversible

For an isentropic process, set equation 9.2 to zero and use equation 9.5

$$\begin{aligned} \delta q = de + pdv &= 0 \\ -pdv &= de \\ -pdv &= C_v dT \end{aligned} \quad (9.11)$$

Similarly set equation 9.3 to zero and use equation 9.8 we have

$$\begin{aligned} \delta q = dh - vdp &= 0 \\ vdp &= dh \\ vdp &= C_p dT \end{aligned} \quad (9.12)$$

Dividing one by the other we have

$$\begin{aligned} \frac{-pdv}{vdp} &= \frac{C_v}{C_p} \\ \frac{dp}{p} &= -\gamma \frac{dv}{v} \end{aligned}$$

where $\gamma = C_p/C_v$ is the ratio of specific heats. Integration between states 1 and 2 gives

$$\frac{p_2}{p_1} = \left(\frac{v_2}{v_1} \right)^{-\gamma}$$

As $\rho = 1/v$ it follows

$$\frac{p_2}{p_1} = \left(\frac{v_2}{v_1} \right)^{-\gamma} = \left(\frac{\rho_2}{\rho_1} \right)^{\gamma}$$

Using the gas law $\rho = p/RT$

$$\frac{p_2}{p_1} = \left(\frac{T_2}{T_1} \right)^{\frac{\gamma}{\gamma-1}}$$

Thus, finally we have

$$\frac{p_2}{p_1} = \left(\frac{\rho_2}{\rho_1}\right)^\gamma = \left(\frac{T_2}{T_1}\right)^{\frac{\gamma}{\gamma-1}} \quad (9.13)$$

Further, we have

$$\begin{aligned} \frac{p}{\rho^\gamma} &= \text{constant } C \\ p &= C\rho^\gamma \\ \frac{dp}{d\rho} &= C\gamma\rho^{\gamma-1} = \left(\frac{p}{\rho^\gamma}\right)\gamma\rho^{\gamma-1} = \frac{\gamma p}{\rho} \end{aligned}$$

Relating the speed of sound to $dp/d\rho$ we have

$$\begin{aligned} a^2 &= \frac{dp}{d\rho} \\ a^2 &= \frac{\gamma p}{\rho} = \gamma RT \\ a &= \sqrt{\frac{\gamma p}{\rho}} = \sqrt{\gamma RT} \end{aligned} \quad (9.14)$$

9.1.1 Unsteady Bernoulli's Equation

Recall that the unsteady Bernoulli's equation (or the Kelvin's equation) is given by

$$\phi_t + \frac{1}{2}(V^2 - U_\infty^2) + \int_{p_\infty}^p \frac{dp}{\rho} = 0$$

where ϕ is the velocity potential. Using

$$\begin{aligned} p &= C\rho^\gamma \\ dp &= C\gamma\rho^{\gamma-1}d\rho \\ \frac{dp}{\rho} &= C\gamma\rho^{\gamma-2}d\rho \end{aligned}$$

we obtain

$$\begin{aligned} \int_{p_\infty}^p \frac{dp}{\rho} &= C\gamma \int_{p_\infty}^p \rho^{\gamma-2}d\rho \\ &= \frac{C\gamma}{\gamma-1} (\rho^{\gamma-1} - \rho_\infty^{\gamma-1}) \\ &= \frac{1}{\gamma-1} \left[\frac{\gamma(C\rho^\gamma)}{\rho} - \frac{\gamma(C\rho_\infty^\gamma)}{\rho_\infty} \right] \\ &= \frac{1}{\gamma-1} (a^2 - a_\infty^2) \end{aligned} \quad (9.15)$$

Thus the unsteady Bernoulli's equation takes the following form

$$\begin{aligned} a^2 &= a_\infty^2 - (\gamma-1) \left(\phi_t + \frac{1}{2}V^2 - \frac{1}{2}U_\infty^2 \right) \\ \frac{a^2}{a_\infty^2} &= 1 - \frac{\gamma-1}{a_\infty^2} \left(\phi_t + \frac{1}{2}V^2 - \frac{1}{2}U_\infty^2 \right) \end{aligned} \quad (9.16)$$

From the isentropic relation given in equation 9.13 we have

$$\frac{p}{p_\infty} = \left(\frac{\rho}{\rho_\infty}\right)^\gamma = \left(\frac{\gamma RT}{\gamma RT_\infty}\right)^{\frac{\gamma}{\gamma-1}} = \left(\frac{a^2}{a_\infty^2}\right)^{\frac{\gamma}{\gamma-1}} \quad (9.17)$$

The following two forms follow

$$\frac{p}{p_\infty} = \left[1 - \frac{\gamma-1}{a_\infty^2} \left(\phi_t + \frac{1}{2}V^2 - \frac{1}{2}U_\infty^2\right)\right]^{\frac{\gamma}{\gamma-1}} \quad (9.18)$$

$$\frac{\rho}{\rho_\infty} = \left[1 - \frac{\gamma-1}{a_\infty^2} \left(\phi_t + \frac{1}{2}V^2 - \frac{1}{2}U_\infty^2\right)\right]^{\frac{1}{\gamma-1}} \quad (9.19)$$

For potential flow at rest at infinity $U_\infty = 0$.

9.1.2 Pressure coefficient

From equation 9.18 we have

$$\frac{p-p_\infty}{p_\infty} = \left[1 - \frac{\gamma-1}{a_\infty^2} \left(\phi_t + \frac{1}{2}V^2 - \frac{1}{2}U_\infty^2\right)\right]^{\frac{\gamma}{\gamma-1}} - 1 \quad (9.20)$$

Now

$$\frac{p-p_\infty}{p_\infty} = \frac{p-p_\infty}{\rho_\infty} \frac{\rho_\infty}{p_\infty} = \frac{p-p_\infty}{\rho_\infty} \frac{a_\infty^2}{\gamma}$$

Using equation 9.20 we obtain

$$\frac{p-p_\infty}{\rho_\infty} = \frac{1}{\gamma} \left\{ \left[1 - \frac{\gamma-1}{a_\infty^2} \left(\phi_t + \frac{1}{2}V^2 - \frac{1}{2}U_\infty^2\right)\right]^{\frac{\gamma}{\gamma-1}} - 1 \right\}$$

Thus the pressure coefficient is given by

$$C_p = \frac{p-p_\infty}{\frac{1}{2}\rho_\infty U_\infty^2} = \frac{2}{\gamma M_\infty^2} \left\{ \left[1 - \frac{\gamma-1}{a_\infty^2} \left(\phi_t + \frac{1}{2}V^2 - \frac{1}{2}U_\infty^2\right)\right]^{\frac{\gamma}{\gamma-1}} - 1 \right\} \quad (9.21)$$

9.2 Potential equation in the non-conservation form

Recall that under potential flow assumptions, the non-conservative form of the Euler equations reduce to

$$a^2 \nabla^2 \phi = \phi_{tt} + \frac{\partial}{\partial t} V^2 + V \cdot \nabla \frac{V^2}{2}$$

where $V = \nabla \phi$. Expressed only in terms of the velocity potential, the above equation becomes

$$a^2 \nabla^2 \phi = \phi_{tt} + \frac{\partial}{\partial t} (\nabla \phi)^2 + \nabla \phi \cdot \nabla \left[\frac{1}{2} (\nabla \phi)^2 \right] \quad (9.22)$$

where a^2 is obtained from the Bernoulli's equation. From equation 9.16 we have

$$a^2 = a_\infty^2 - (\gamma-1) \left[\phi_t + \frac{1}{2} (\nabla \phi)^2 \right] \quad (9.23)$$

where U_∞ has been set to zero. Thus the velocity potential ϕ is defined with respect to a fluid at rest at infinity. The above two equations completely define the problem. It can be expanded in any coordinate system as long as the boundary conditions are correctly imposed. For rotor problems the surface boundary condition is easily incorporated using a blade fixed rotating coordinate system. This transformation is described next.

9.2.1 Blade fixed moving frame

Using a blade fixed coordinate influences the equations and boundary conditions. The definition of ϕ remains the same as before, i.e. a velocity potential with respect to fluid at rest. This statement means that the derivative of ϕ along the choosen coordinate directions still yields velocities along those coordinate directions, but still with respect to the fluid at rest. Let (x, y, z) , with unit vectors (i, j, k) be the fixed coordinates. (x', y', z') , with unit vectors (i', j', k') , translates and rotates with respect to the fixed coordinates. Let the translational velocity be V in the (x, y) plane at an angle α with the x axis. The velocities along the x and y axes are then $V \cos \alpha$ and $V \sin \alpha$. Define $V \cos \alpha / \Omega R = \mu$. Then $V \sin \alpha / \Omega R$ becomes equal to $\mu \tan \alpha$. The translational velocity is then $-\mu \Omega R i + 0j + \mu \Omega R \tan \alpha k$. The rotational velocity is $\Omega k = \Omega k'$. The coordinate directions (i', j', k') can be expressed along (i, j, k) at any instant using the following relation

$$\begin{Bmatrix} i \\ j \\ k \end{Bmatrix} = \begin{bmatrix} \sin \psi & \cos \psi & 0 \\ -\cos \psi & \sin \psi & 0 \\ 0 & 0 & 1 \end{bmatrix} \begin{Bmatrix} i' \\ j' \\ k' \end{Bmatrix} = R \begin{Bmatrix} i' \\ j' \\ k' \end{Bmatrix} \quad (9.24)$$

where $\psi = \Omega t$ and $R = R(t)$ is the rotation matrix. Consider a point P on the rotating blade. Let the coordinates of P be given by

$$\begin{Bmatrix} x' \\ y' \\ z' \end{Bmatrix}^T \begin{Bmatrix} i' \\ j' \\ k' \end{Bmatrix}$$

in the rotating frame and

$$\begin{Bmatrix} x \\ y \\ z \end{Bmatrix}^T \begin{Bmatrix} i \\ j \\ k \end{Bmatrix}$$

in the fixed frame. Then we have

$$\begin{aligned} \begin{Bmatrix} x \\ y \\ z \end{Bmatrix}^T \begin{Bmatrix} i \\ j \\ k \end{Bmatrix} &= \begin{Bmatrix} -\mu \Omega R \\ 0 \\ \mu \Omega R \tan \alpha \end{Bmatrix}^T \begin{Bmatrix} i \\ j \\ k \end{Bmatrix} t + \begin{Bmatrix} x' \\ y' \\ z' \end{Bmatrix}^T \begin{Bmatrix} i' \\ j' \\ k' \end{Bmatrix} \\ &= t \begin{Bmatrix} -\mu \Omega R \\ 0 \\ \mu \Omega R \tan \alpha \end{Bmatrix}^T \begin{Bmatrix} i \\ j \\ k \end{Bmatrix} + \begin{Bmatrix} x' \\ y' \\ z' \end{Bmatrix}^T R^T \begin{Bmatrix} i \\ j \\ k \end{Bmatrix} \end{aligned}$$

Transpose both sides to re-write

$$\begin{Bmatrix} i \\ j \\ k \end{Bmatrix}^T \begin{Bmatrix} x \\ y \\ z \end{Bmatrix} = t \begin{Bmatrix} i \\ j \\ k \end{Bmatrix}^T \begin{Bmatrix} -\mu \Omega R \\ 0 \\ \mu \Omega R \tan \alpha \end{Bmatrix} + \begin{Bmatrix} i \\ j \\ k \end{Bmatrix}^T R \begin{Bmatrix} x' \\ y' \\ z' \end{Bmatrix}$$

which can be written as

$$\mathbf{r} = \mu \mathbf{t} + \mathbf{R}(\mathbf{t}) \mathbf{r}'$$

where \mathbf{r} is the position vector in the fixed frame and \mathbf{r}' is the position vector in the rotating frame. The rotating frame coordinates are (x, y, z, t) . The fixed frame coordinates are (x', y', z', t') .

9.2.2 Velocity and acceleration in the moving frame

We saw how the position vector in the rotating frame is related to the position vector in the fixed frame. Let us determine the velocity and acceleration in the rotating frame.

Let O be the origin in the fixed frame. Let O' be the origin of the moving frame. O' translates with respect to O . Consider a point P . $O'P$ is the vector \mathbf{r}' . The rate of change of this vector is the rate at which P changes its position with respect to O' . This is denoted by $\partial\mathbf{r}'/\partial\mathbf{t}$. When measured by an observer in the moving frame this rate can be denoted by $(\partial\mathbf{r}'/\partial\mathbf{t})_{x'y'z'}$. When measured by an observer in the fixed frame this rate can be denoted by $(\partial\mathbf{r}'/\partial\mathbf{t})_{xyz}$. We know

$$\begin{aligned} \left(\frac{\partial\mathbf{r}'}{\partial\mathbf{t}}\right)_{xyz} &= \left(\frac{\partial\mathbf{r}'}{\partial\mathbf{t}}\right)_{x'y'z'} + \Omega \times \mathbf{r}' \\ &= (V_P)_{x'y'z'} + \Omega \times \mathbf{r}' \end{aligned}$$

The velocity of P in the fixed frame is $(V_P)_{xyz}$. Let the translational velocity of O' with respect to O is \dot{R} . Then,

$$\begin{aligned} (V_P)_{xyz} &= \dot{R} + \left(\frac{\partial\mathbf{r}'}{\partial\mathbf{t}}\right)_{xyz} \\ &= \dot{R} + (V_P)_{x'y'z'} + \Omega \times \mathbf{r}' \end{aligned}$$

Note that $\dot{R} = (V'_O)_{xyz}$. Therefore $(V_P)_{xyz} - (V'_O)_{xyz}$ is the rate at which P changes its position with respect to O' as measured by an observer in the fixed frame. This is $(\partial\mathbf{r}'/\partial\mathbf{t})_{xyz}$, hence we get back the first equation. Similarly consider the accelerations.

$$\begin{aligned} (a_P)_{xyz} &= \ddot{R} + \frac{d}{dt} \left[\left(\frac{\partial\mathbf{r}'}{\partial\mathbf{t}}\right)_{xyz} \right]_{xyz} \\ &= \ddot{R} + \frac{d}{dt} \left[\left(\frac{\partial\mathbf{r}'}{\partial\mathbf{t}}\right)_{x'y'z'} + \Omega \times \mathbf{r}' \right]_{xyz} \\ &= \ddot{R} + \frac{d}{dt} \left[\left(\frac{\partial\mathbf{r}'}{\partial\mathbf{t}}\right)_{x'y'z'} \right]_{x'y'z'} + \Omega \times \left(\frac{\partial\mathbf{r}'}{\partial\mathbf{t}}\right)_{x'y'z'} + \frac{d}{dt} (\Omega \times \mathbf{r}')_{x'y'z'} + \Omega \times \Omega \times \mathbf{r}' \\ &= \ddot{R} + (a_P)_{x'y'z'} + 2\Omega \times (V_P)_{x'y'z'} + \dot{\Omega} \times (V_P)_{x'y'z'} + \Omega \times \Omega \times \mathbf{r}' \end{aligned}$$

Thus to summarize we have

$$(V_P)_{xyz} = \dot{R} + (V_P)_{x'y'z'} + \Omega \times \mathbf{r}' \quad (9.25)$$

$$(a_P)_{xyz} = \ddot{R} + (a_P)_{x'y'z'} + 2\Omega \times (V_P)_{x'y'z'} + \dot{\Omega} \times (V_P)_{x'y'z'} + \Omega \times \Omega \times \mathbf{r}' \quad (9.26)$$

For the rotor in steady flight we have

$$\begin{aligned} \dot{R} &= \mu \\ \ddot{R} &= 0 \\ \dot{\Omega} &= 0 \\ (V_P)_{x'y'z'} &= V \\ (a_P)_{x'y'z'} &= V_t \end{aligned} \quad (9.27)$$

Using the above in equations 9.25 and 9.26 it follows

$$\begin{aligned} V &= -\Omega \times \mathbf{r}' - \mu \\ V_t &= -2\Omega \times V - \Omega \times \Omega \times \mathbf{r}' \end{aligned} \quad (9.28)$$

We have for the rotor

$$\begin{aligned}\Omega &= \Omega k' \\ \mathbf{r}' &= \mathbf{x}'\mathbf{i}' + \mathbf{y}'\mathbf{j}' + \mathbf{z}'\mathbf{k}' \\ \mu &= (-\mu\Omega\mathbf{R})\mathbf{i} + \mathbf{0}\mathbf{j} + (\mu\Omega\mathbf{R} \tan \alpha)\mathbf{k}\end{aligned}$$

Put the above expressions in equations 9.28 and use the transformation given in equation 9.24 to obtain the following.

$$\begin{aligned}V &= \begin{pmatrix} \Omega y' + \mu\Omega R \sin \psi \\ -\Omega x' + \mu\Omega R \cos \psi \\ -\mu\Omega R \tan \alpha \end{pmatrix}^T \begin{pmatrix} i' \\ j' \\ k' \end{pmatrix} = \begin{pmatrix} V_1 \\ V_2 \\ V_3 \end{pmatrix}^T \begin{pmatrix} i' \\ j' \\ k' \end{pmatrix} \\ V_t &= \begin{pmatrix} \Omega^2 x' + 2\Omega V_2 \\ \Omega^2 y' - 2\Omega V_1 \\ 0 \end{pmatrix}^T \begin{pmatrix} i' \\ j' \\ k' \end{pmatrix}\end{aligned}\tag{9.29}$$

Henceforth all analysis will be done in the moving frame using the expressions given in equations (9.29). The dashes (') can be dropped for convenience.

9.2.3 Derivatives in the moving frame

We now need the derivatives - one spatial derivative (the gradient), and two time derivatives (velocity and acceleration).

The gradient is frame invariant.

$$\nabla = \nabla'$$

This can be shown as follows.

$$\begin{aligned}\nabla' &= \frac{\partial}{\partial x'}i' + \frac{\partial}{\partial y'}j' + \frac{\partial}{\partial z'}k' \\ &= \begin{pmatrix} i' \\ j' \\ k' \end{pmatrix}^T \begin{pmatrix} \frac{\partial}{\partial x} \frac{\partial x}{\partial x'} + \frac{\partial}{\partial y} \frac{\partial y}{\partial x'} + \frac{\partial}{\partial z} \frac{\partial z}{\partial x'} \\ \frac{\partial}{\partial x} \frac{\partial x}{\partial y'} + \frac{\partial}{\partial y} \frac{\partial y}{\partial y'} + \frac{\partial}{\partial z} \frac{\partial z}{\partial y'} \\ \frac{\partial}{\partial x} \frac{\partial x}{\partial z'} + \frac{\partial}{\partial y} \frac{\partial y}{\partial z'} + \frac{\partial}{\partial z} \frac{\partial z}{\partial z'} \end{pmatrix} \\ &= \begin{pmatrix} i \\ j \\ k \end{pmatrix}^T R \begin{pmatrix} \frac{\partial}{\partial x} \frac{\partial x}{\partial x'} + \frac{\partial}{\partial y} \frac{\partial y}{\partial x'} + \frac{\partial}{\partial z} \frac{\partial z}{\partial x'} \\ \frac{\partial}{\partial x} \frac{\partial x}{\partial y'} + \frac{\partial}{\partial y} \frac{\partial y}{\partial y'} + \frac{\partial}{\partial z} \frac{\partial z}{\partial y'} \\ \frac{\partial}{\partial x} \frac{\partial x}{\partial z'} + \frac{\partial}{\partial y} \frac{\partial y}{\partial z'} + \frac{\partial}{\partial z} \frac{\partial z}{\partial z'} \end{pmatrix} \\ &= \begin{pmatrix} i \\ j \\ k \end{pmatrix}^T \begin{bmatrix} \sin \psi & \cos \psi & 0 \\ -\cos \psi & \sin \psi & 0 \\ 0 & 0 & 1 \end{bmatrix} \begin{pmatrix} \sin \psi \frac{\partial}{\partial x} - \cos \psi \frac{\partial}{\partial y} \\ \sin \psi \frac{\partial}{\partial y} + \cos \psi \frac{\partial}{\partial x} \\ \frac{\partial}{\partial z} \end{pmatrix} \\ &= \frac{\partial}{\partial x}i + \frac{\partial}{\partial y}j + \frac{\partial}{\partial z}k \\ &= \nabla\end{aligned}$$

Now consider the time derivative.

$$\begin{aligned}\frac{\partial}{\partial t} &= \frac{\partial}{\partial t'} \frac{\partial t'}{\partial t} + \frac{\partial}{\partial x'} \frac{\partial x'}{\partial t} + \frac{\partial}{\partial y'} \frac{\partial y'}{\partial t} + \frac{\partial}{\partial z'} \frac{\partial z'}{\partial t} \\ &= \frac{\partial}{\partial t'} + V_1 \frac{\partial}{\partial x'} + v_2 \frac{\partial}{\partial y'} + V_3 \frac{\partial}{\partial z'} \\ &= \frac{\partial}{\partial t'} + \mathbf{V} \cdot \nabla'\end{aligned}$$

where V is the velocity in the moving frame. Thus

$$\phi_t = \phi_{t'} + V \cdot \nabla' \phi \quad (9.30)$$

The second derivative with respect to time can be taken in a similar manner

$$\begin{aligned} \phi_{tt} &= \frac{\partial \phi_t}{\partial t} \\ &= \frac{\partial}{\partial t'} (\phi_t) + V \cdot \nabla' \phi_t \\ &= \frac{\partial}{\partial t'} (\phi_{t'} + V \cdot \nabla' \phi) + V \cdot \nabla' (\phi_{t'} + V \cdot \nabla' \phi) \\ &= \phi_{t't'} + V \cdot \nabla' \phi_{t'} + \nabla' \phi \cdot V_{t'} + V \cdot \nabla' \phi_{t'} + V \cdot \nabla' (V \cdot \nabla' \phi) \end{aligned}$$

Thus the second derivative of ϕ with respect to time is given by

$$\phi_{tt} = \phi_{t't'} + 2V \cdot \nabla' \phi_{t'} + \nabla' \phi \cdot V_{t'} + (V \cdot \nabla') (V \cdot \nabla' \phi) \quad (9.31)$$

9.2.4 Full Potential Equations

Use equations 9.30 and 9.31 to reduce equations 9.22 and 9.23 to the moving frame. Note that

$$\begin{aligned} \frac{\partial}{\partial t} (\nabla \phi)^2 &= \frac{\partial}{\partial t'} (\nabla \phi)^2 + V \cdot \nabla' (\nabla \phi)^2 \\ &= 2\nabla' \phi \cdot \nabla \phi_{t'} + V \cdot \nabla' (\nabla \phi)^2 \end{aligned}$$

After substitution, the dashes ($'$) can be removed. The potential and the Bernoulli equations then take the following form

$$\begin{aligned} a^2 \nabla^2 \phi &= \phi_{tt} + 2V \cdot \nabla \phi_t + \nabla \phi \cdot V_t + (V \cdot \nabla) (V \cdot \nabla \phi) + \\ &\quad 2\nabla \phi \cdot \nabla \phi_t + V \cdot \nabla (\nabla \phi)^2 + \nabla \phi \cdot \left[\frac{1}{2} (\nabla \phi)^2 \right] \\ a^2 &= a_\infty^2 - (\gamma - 1) \left[\phi_t + V \cdot \nabla \phi + \frac{1}{2} (\nabla \phi)^2 \right] \end{aligned} \quad (9.32)$$

Velocity V and acceleration V_t are given by equations 9.29. Solve for ϕ and obtain the fluid velocities ϕ_x , ϕ_y and ϕ_z directly in the moving frame.

For physical insight, the above equations can be expanded using the following.

$$\begin{aligned} V \cdot \nabla \phi &= V_1 \phi_x + V_2 \phi_y + V_3 \phi_z \\ \frac{1}{2} (\nabla \phi)^2 &= \frac{1}{2} (\phi_x^2 + \phi_y^2 + \phi_z^2) \end{aligned}$$

The Bernoulli equation then becomes

$$a^2 = a_\infty^2 - (\gamma - 1) \left[\phi_t + V_1 \phi_x + V_2 \phi_y + V_3 \phi_z + \frac{1}{2} (\phi_x^2 + \phi_y^2 + \phi_z^2) \right] \quad (9.33)$$

To expand the potential equation use the following

$$\begin{aligned}
2V \cdot \nabla \phi_t &= 2V_1 \phi_{xt} + 2V_2 \phi_{yt} + 2V_3 \phi_{zt} \\
\nabla (V \cdot \nabla \phi) &= \frac{\partial}{\partial x} (V_1 \phi_x + V_2 \phi_y + V_3 \phi_z) i + \frac{\partial}{\partial y} (V_1 \phi_x + V_2 \phi_y + V_3 \phi_z) j \\
&\quad + \frac{\partial}{\partial z} (V_1 \phi_x + V_2 \phi_y + V_3 \phi_z) k \\
&= (V_1 \phi_{xx} + V_2 \phi_{yx} - \Omega \phi_y + V_3 \phi_{zx}) i \\
&\quad + (V_1 \phi_{xy} + \Omega \phi_x + V_2 \phi_{yy} + V_3 \phi_{zy}) j \\
&\quad + (V_1 \phi_{xz} + V_2 \phi_{yz} + V_3 \phi_{zz}) k \\
(V \cdot \nabla) (V \cdot \nabla \phi) &= V_1^2 \phi_{xx} + V_2^2 \phi_{yy} + V_3^2 \phi_{zz} \\
&\quad + 2V_1 V_2 \phi_{yx} + 2V_2 V_3 \phi_{yz} + 2V_3 V_1 \phi_{xz} - V_1 \Omega \phi_y + V_2 \Omega \phi_x \\
\nabla \phi \cdot V_t &= (\Omega^2 x + 2\Omega V_2) \phi_x + (\Omega^2 y - 2\Omega V_1) \phi_y \\
2\nabla \phi \cdot \nabla \phi_t &= 2\phi_x \phi_{xt} + 2\phi_y \phi_{yt} + 2\phi_z \phi_{zt} \\
(\nabla \phi)^2 &= \phi_x^2 + \phi_y^2 + \phi_z^2 \\
V \cdot (\nabla \phi)^2 &= (2\phi_x \phi_{xx} + 2\phi_y \phi_{yx} + 2\phi_z \phi_{zx}) V_1 \\
&\quad (2\phi_x \phi_{xy} + 2\phi_y \phi_{yy} + 2\phi_z \phi_{zy}) V_2 \\
&\quad (2\phi_x \phi_{xz} + 2\phi_y \phi_{yz} + 2\phi_z \phi_{zz}) V_3 \\
\nabla \phi \cdot \nabla \left[\frac{1}{2} (\nabla \phi)^2 \right] &= (\phi_x \phi_{xx} + \phi_y \phi_{yx} + \phi_z \phi_{zx}) \phi_x \\
&\quad (\phi_x \phi_{xy} + \phi_y \phi_{yy} + \phi_z \phi_{zy}) \phi_y \\
&\quad (\phi_x \phi_{xz} + \phi_y \phi_{yz} + \phi_z \phi_{zz}) \phi_z
\end{aligned}$$

Now define the total velocities as

$$\begin{aligned}
q_1 &= \phi_x + V_1 \\
q_2 &= \phi_y + V_2 \\
q_3 &= \phi_z + V_3
\end{aligned}$$

Then the potential equation takes the following form

$$\begin{aligned}
a^2 (\phi_{xx} + \phi_{yy} + \phi_{zz}) &= \phi_{tt} + 2q_1 \phi_{xt} + 2q_2 \phi_{yt} + 2q_3 \phi_{zt} \\
&\quad q_1^2 \phi_{xx} + q_2^2 \phi_{yy} + q_3^2 \phi_{zz} + 2q_1 q_2 \phi_{xy} + 2q_2 q_3 \phi_{yz} + 2q_3 q_1 \phi_{zx} \\
&\quad \phi_x (\Omega^2 x + 2\Omega V_2) + \phi_y (\Omega^2 y - 2\Omega V_1)
\end{aligned} \tag{9.34}$$

In Einstein notation equations 9.33 and 9.34 are also expressible as

$$\begin{aligned}
a^2 \nabla^2 \phi &= \phi_{tt} + 2q_i \phi_{tx_i} + \dot{V}_i \phi_{x_i} + q_i q_j \phi_{x_i x_j} \\
a^2 &= a_\infty^2 - (\gamma - 1) \left[\phi_t + V_j \phi_{x_j} + \frac{1}{2} \phi_{x_j} \phi_{x_j} \right]
\end{aligned} \tag{9.35}$$

where the pressure is related to velocity of sound as

$$\frac{p}{p_\infty} = \left(\frac{a^2}{a_\infty^2} \right)^{\frac{\gamma}{\gamma-1}}$$

9.2.5 Boundary conditions

The near field boundary conditions are that the flow is tangential to the blade. Let the blade surface be given by

$$F(x, y, z, t) = 0 \quad (9.36)$$

then the flow tangency condition is that the substantial derivative $DF/Dt = 0$.

$$\frac{\partial F}{\partial t} + q \cdot \nabla F = 0 \quad (9.37)$$

where q is the total velocity as given in the previous section. The blade surface description can be recast as

$$F(x, y, z, t) = z - g(x, y, t) \quad (9.38)$$

Then from 9.37

$$\begin{aligned} -g_t + q \cdot (-g_x i - g_y j + k) &= 0 \\ -g_t + (-q_x g_x - q_y g_y + q_z) &= 0 \end{aligned} \quad (9.39)$$

which reduces to

$$q_z = g_t + q_x g_x + q_y g_y \quad (9.40)$$

on the surface $z = g(x, y, t)$. Expanding the q 's and ignoring the second order terms, the linearized boundary conditions are given by

$$\begin{aligned} \phi_z + V_3 &= g_t + (V_1 + \phi_x) g_x + (V_2 + \phi_y) g_y \\ \phi_z &= g_t + V_1 g_x + V_2 g_y - V_3 \end{aligned} \quad (9.41)$$

The wake boundary condition is implemented in the following manner. The wake is a vortex surface which allows a tangential velocity jump but not a normal velocity jump. Similarly it allows a tangential pressure jump but not a normal pressure jump. The normal velocity jump is Δv_n where Δ signifies the difference between the upper and lower surfaces v_u and v_l . Thus

$$v_u - v_l = \Delta v_n = 0$$

$$\Delta p = 0$$

Consider a two dimensional airfoil wake. It follows from Kelvin's equation

$$\left(\phi_t + \frac{1}{2} v^2 \right)_u = \left(\phi_t + \frac{1}{2} v^2 \right)_l$$

or

$$\Delta \phi_t + \frac{1}{2} (v_u - v_l)(v_u + v_l) = 0$$

or

$$\Delta \phi_t + \frac{\Delta \phi}{\Delta x} v_w = 0$$

where $(v_u + v_l)/2$ has been defined as the wake velocity. The above expression can be written in general for a 3-dimensional flow

$$\Delta \phi_t + v_w \cdot \nabla (\Delta \phi) = 0$$

$$\frac{D\Delta\phi}{Dt} = 0$$

This states that the potential difference $\Delta\phi$ is constant for a point on the wake surface that is convected with the wake velocity. The wake velocity is taken as the mean of the upper and lower velocities at each point on the vortex sheet. The wake is treated as a planar surface without accounting for its curvature. The tip vortices from previous blades can be incorporated into the computational domain as additional potential jump.

The far field boundary conditions are

$$\phi_t = 0$$

$$\nabla\phi = 0$$

They can be imposed as a Neumann condition. The time derivatives of the velocity potential along the characteristics of the flow equation vanish for each spanwise plane.

$$\phi_t + v_a \cdot \nabla\phi = 0$$

9.2.6 Small disturbance equations for subsonic and transonic flows

The small disturbance assumption helps to understand the essential character of the flow. In earlier days they were attractive due to their reduced computational requirements. The unsteady compressible potential flow equations for the rotor are given by 9.35. The Laplace operator on the left hand side of the first equation is

$$\nabla^2\phi = \phi_{x_i}\phi_{x_j}\delta_{ij} \quad (9.42)$$

Equation 9.35 has no assumptions for the disturbance. The following scaling parameters are used to make small disturbance assumptions under subsonic and transonic flow conditions. The assumptions are made so that the essential features of the equation under each condition are maintained.

$$\phi = \Omega R c \delta$$

$$g(x, y) = c \tau$$

Subsonic

For subsonic flow we make the following assumption

$$a^2 \approx a_\infty^2 \quad (9.43)$$

This is because

$$V_i \ll a_\infty \quad (9.44)$$

Recall that the total velocity at a point in the flow field q_i is the sum of V_i and ϕ_x , where i are the coordinate directions, V_i is the local free stream corresponding to the translation and rotation of the rotor in these directions, and ϕ_i is the potential of the additional velocity induced by the rotor blades. The later is assumed to be small compared to the free stream under subsonic flow conditions. The second order terms in ϕ_i are neglected.

$$\begin{aligned} q_i q_j &= V_i V_j + \phi_{x_i} V_j + \phi_{x_j} V_i + \phi_{x_i} \phi_{x_j} \\ &\approx V_i V_j + \phi_{x_i} V_j + \phi_{x_j} V_i \end{aligned} \quad (9.45)$$

Use assumptions 9.43 and 9.45, and the notation 9.42 to reduce the potential equation 9.35 to the following form. The potential equation reduces to

$$(a_\infty^2 \delta_{ij} - V_i V_j) \phi_{x_i} \phi_{x_j} = \phi_{tt} + 2V_i \phi_{tx_i} + \dot{V}_i \phi_{x_i} \quad (9.46)$$

Expanding in cartesian coordinates

$$\begin{aligned} a_\infty^2 (\phi_{xx} + \phi_{yy} + \phi_{zz}) - V_1^2 \phi_{xx} - 2V_1 V_2 \phi_{xy} - 2V_1 V_3 \phi_{xz} - V_2^2 \phi_{yy} - V_3^2 \phi_{zz} - 2V_2 V_3 \phi_{xz} \\ = \phi_{tt} + 2V_1 \phi_{xt} + 2V_2 \phi_{yt} + 2V_3 \phi_{zt} + (\Omega^2 x + 2\Omega V_2) \phi_x + (\Omega^2 y - 2\Omega V_1) \phi_y \end{aligned} \quad (9.47)$$

The equation can be further simplified by making the following assumptions. For a small tip path plane tilt,

$$V_3 \approx 0 \quad (9.48)$$

. For subsonic flow we have

$$(\Omega^2 x + 2\Omega V_2) \phi_x + (\Omega^2 y - 2\Omega V_1) \phi_y \ll a_\infty^2 \phi_{xx} \quad (9.49)$$

With these assumptions equation 9.47 becomes

$$\begin{aligned} (a_\infty^2 - V_1^2) \phi_{xx} - 2V_1 V_2 \phi_{xy} + (a_\infty^2 - V_2^2) \phi_{yy} + a_\infty^2 \phi_{zz} \\ = \phi_{tt} + 2V_1 \phi_{xt} + 2V_2 \phi_{yt} \end{aligned} \quad (9.50)$$

For quasi-steady assumption, e.g. for small 1/rev flapping, the right hand side of equation 9.50 is set to zero.

$$(a_\infty^2 - V_1^2) \phi_{xx} - 2V_1 V_2 \phi_{xy} + (a_\infty^2 - V_2^2) \phi_{yy} + a_\infty^2 \phi_{zz} = 0 \quad (9.51)$$

Note that even though the time derivatives of the perturbation potential have been set to zero, the effect of rotation is still included via the $\sin \psi$ and $\cos \psi$ terms within V_1 and V_2 . Similarly the boundary conditions also retain a time dependance by being a function of blade azimuth. Hence the assumption is called quasi-steady.

Transonic flow

Here the assumption $a^2 \approx a_\infty^2$ as given by equation 9.43 is no longer valid. In the transonic range V_1 is of the same order as a_∞^2 . However the square of the potential is still negligible with respect to the square of the speed of sound.

$$\phi^2 \ll a^2 \quad (9.52)$$

With this assumption, the Bernoulli's equation in 9.35 becomes

$$a^2 = a_\infty^2 - (\gamma - 1) [\phi_t + V_j \phi_{x_j}]$$

Keep the assumption given by equation 9.48.

$$V_3 \approx 0$$

With the above two assumptions the potential equation 9.35 becomes

$$\begin{aligned} (\phi_{xx} + \phi_{yy} + \phi_{zz}) [a_\infty^2 - (\gamma - 1) (\phi_t + V_1 \phi_x + V_2 \phi_y)] = \\ \phi_{tt} + 2V_1 \phi_{xt} + 2V_2 \phi_{yt} + \phi_{xx} (V_1^2 + 2\phi_x V_1) + \phi_{yy} (V_2^2 + 2\phi_y V_2) \\ 2\phi_{xy} (V_1 \phi_y + V_2 \phi_x + V_1 V_2) + 2\phi_{yz} V_2 \phi_z + 2\phi_{zx} V_1 \phi_z \\ \phi_x (\Omega^2 x + 2\Omega V_2) + \phi_y (\Omega^2 y - 2\Omega V_1) \end{aligned} \quad (9.53)$$

For 3D flows ϕ_{xx} and ϕ_{yy} are of the same order of magnitude. The chordwise flow gradient is of the same order as the spanwise flow gradient. The following terms can be neglected.

$$\begin{aligned}\phi_{xz}\phi_z &\approx 0 \\ \phi_{yz}\phi_z &\approx 0\end{aligned}\tag{9.54}$$

Then equation 9.53 takes the following form.

$$\begin{aligned}\phi_{xx} [a_\infty^2 - V_1^2 - (\gamma + 1)V_1\phi_x - (\gamma - 1)V_2\phi_y] \\ \phi_{yy} [a_\infty^2 - V_2^2 - (\gamma - 1)V_1\phi_x - (\gamma + 1)V_2\phi_y] \\ \phi_{zz} [a_\infty^2 - (\gamma - 1)V_1\phi_x - (\gamma - 1)V_2\phi_y] \\ - 2\phi_{xy} (V_1V_2 + V_1\phi_y + V_2\phi_x) \\ = 2V_1\phi_{xt} + 2V_2\phi_{yt} + \phi_x (\Omega^2x + 2\Omega V_2) + \phi_y (\Omega^2y - 2\Omega V_1)\end{aligned}\tag{9.55}$$

Equation 9.55 is the non-conservative transonic small perturbation equation.

9.2.7 Literature

Non-conservative small disturbance

1. Caradonna, F. X. and Isom, M. P., "Subsonic and Transonic Potential Flow Over Helicopter Rotor Blades," AIAA Journal, Vol. 10, Dec. 1972, pp. 1606-1612. Steady-state formulation.
2. Caradonna, F. X. and Isom, M. P., "Numerical Calculation of Unsteady Transonic Potential Flow Over Helicopter Rotor Blades," AIAA Journal, Vol. 14, April 1976, pp. 482-488. Unsteady formulation. Forward flight. Spanwise freestream velocity component due to changing blade position was assumed to be small and was incompletely modeled.
3. Grant, J. "Calculation of the Supercritical Flow Over the Tip Region of Non-Lifting Rotor Blade at Arbitrary Azimuth," Royal Aircraft Establishment Tech. Rept. 77180, Dec. 1977. Included all free stream terms. However, quasi-steady formation.

Non-conservative full potential

1. Jameson, A. and Caughey, D. A., "Numerical Calculation of Transonic Flow Past a Swept Wing," Courant Institute of Mathematical Sciences, New York University, New York, C00-3077-140, June 1977. Fixed wing code FLO22. Non-conservative with respect to mass flux.
2. Arieli, R. and Tauber, M. E., "Computation of Transonic Flow About Helicopter Rotor Blades," AIAA Journal, Vol. 24, No. 5, May 1986, pp. 722-727. Quasi-steady. Exact boundary conditions, not small disturbance.
3. Chang, I-Chung and Tung, C., "Computation of Subsonic and Transonic Flow about Lifting Rotor Blades," AIAA Paper 79-1667, Aug. 1979.

9.3 Potential equation in conservation form

The potential equation in conservation form is the continuity equation in conservation form.

9.3.1 Full potential equation

The full potential equation is obtained by replacing the velocities in the continuity equation with derivatives of the potential function.

$$\frac{\partial \rho}{\partial t} + \frac{\partial}{\partial x} (\rho \Phi_x) + \frac{\partial}{\partial y} (\rho \Phi_y) + \frac{\partial}{\partial z} (\rho \Phi_z) = 0 \quad (9.56)$$

where Φ is the potential of the total velocity. The density is obtained from the unsteady Bernoulli's equation 9.19. The velocity potential is defined with respect to fluid at rest, hence U_∞ is set to zero. $V^2 = (\nabla \phi)^2 = \phi_x^2 + \phi_y^2 + \phi_z^2$.

$$\frac{\rho}{\rho_\infty} = \left[1 - \frac{\gamma - 1}{a_\infty^2} \left(\Phi_t + \frac{1}{2} \Phi_x^2 + \frac{1}{2} \Phi_y^2 + \frac{1}{2} \Phi_z^2 \right) \right]^{\frac{1}{\gamma - 1}} \quad (9.57)$$

The equations can be non-dimensionalized as follows :

$$\Phi = \bar{\Phi} a_\infty c$$

where c is a characteristic length, e.g. blade mean chord. Similarly Φ_y and Φ_z .

$$x = \bar{x} c \quad y = \bar{y} c \quad z = \bar{z} c$$

$$t = \bar{t} (c/a_\infty)$$

Then

$$\frac{\partial \Phi}{\partial x} = \frac{\partial \bar{\Phi} a_\infty c}{\partial \bar{x} c} = a_\infty \frac{\partial \bar{\Phi}}{\partial \bar{x}}$$

$$\frac{\partial \Phi}{\partial t} = \frac{\partial \bar{\Phi} a_\infty c}{\partial \bar{t} (c/a_\infty)} = a_\infty^2 \frac{\partial \bar{\Phi}}{\partial \bar{t}}$$

$$\rho = \bar{\rho} \rho_\infty$$

Thus the equations reduce to the following non-dimensional form

$$\begin{aligned} \frac{\partial \rho}{\partial \bar{t}} + \frac{\partial}{\partial \bar{x}} (\rho \Phi_x) + \frac{\partial}{\partial \bar{y}} (\rho \Phi_y) + \frac{\partial}{\partial \bar{z}} (\rho \Phi_z) &= 0 \\ \rho &= \left[1 - \frac{\gamma - 1}{2} (2\Phi_t + \Phi_x^2 + \Phi_y^2 + \Phi_z^2) \right]^{\frac{1}{\gamma - 1}} \end{aligned} \quad (9.58)$$

where the bars ($\bar{\quad}$) have been dropped for convenience.

9.3.2 Generalized coordinate transformation

A generalized transformation can be used to map an arbitrary body surface like a rotor blade to a rectangular coordinate surface in a transformed plane. Boundary conditions on the body can be accurately treated. The grids can be clustered as desired. Transformation to rectangular coordinates is needed only for a finite difference discretization of the governing equations. The finite difference discretization is usually used in conjunction with structured grids. The transformation is given by

$$\begin{aligned} \xi &= \xi(x, y, z, t) \\ \eta &= \eta(x, y, z, t) \\ \zeta &= \zeta(x, y, z, t) \\ \tau &= t \end{aligned} \quad (9.59)$$

The Bernoulli's equation transforms as follows.

$$\begin{aligned}\Phi_t &= \Phi_\tau + \Phi_\xi \xi_t + \Phi_\eta \eta_t + \Phi_\zeta \zeta_t \\ \Phi_x &= \Phi_\xi \xi_x + \Phi_\eta \eta_x + \Phi_\zeta \zeta_x \\ \Phi_y &= \Phi_\xi \xi_y + \Phi_\eta \eta_y + \Phi_\zeta \zeta_y \\ \Phi_z &= \Phi_\xi \xi_z + \Phi_\eta \eta_z + \Phi_\zeta \zeta_z\end{aligned}$$

It follows

$$\Phi_x^2 + \Phi_y^2 + \Phi_z^2 = A_1 \Phi_\xi^2 + A_2 \Phi_\eta^2 + A_3 \Phi_\zeta^2 + 2A_4 \Phi_\xi \phi_\eta + 2A_5 \Phi_\eta \Phi_\zeta + 2A_6 \Phi_\zeta \phi_\xi$$

where

$$\begin{aligned}A_1 &= \xi_x^2 + \xi_y^2 + \xi_z^2 \\ A_2 &= \eta_x^2 + \eta_y^2 + \eta_z^2 \\ A_3 &= \zeta_x^2 + \zeta_y^2 + \zeta_z^2 \\ A_4 &= \xi_x \eta_x + \xi_y \eta_y + \xi_z \eta_z \\ A_5 &= \eta_x \zeta_x + \eta_y \zeta_y + \eta_z \zeta_z \\ A_6 &= \zeta_x \xi_x + \zeta_y \xi_y + \zeta_z \xi_z\end{aligned}$$

Therefore

$$\begin{aligned}2\Phi_t + \Phi_x^2 + \Phi_y^2 + \Phi_z^2 &= 2\Phi_\tau + 2\Phi_\xi \xi_t + 2\Phi_\eta \eta_t + 2\Phi_\zeta \zeta_t + A_1 \Phi_\xi^2 + A_2 \Phi_\eta^2 + A_3 \Phi_\zeta^2 \\ &\quad + 2A_4 \Phi_\xi \phi_\eta + 2A_5 \Phi_\eta \Phi_\zeta + 2A_6 \Phi_\zeta \phi_\xi \\ &= 2\Phi_\tau + \Phi_\xi (2\xi_t + A_1 \Phi_\xi + 2A_4 \Phi_\eta + 2A_6 \Phi_\zeta) \\ &\quad + \Phi_\eta (2\eta_t + A_2 \Phi_\eta + 2A_5 \Phi_\zeta) \\ &\quad + \Phi_\zeta (2\zeta_t + A_3 \Phi_\zeta) \\ &= 2\Phi_\tau + \Phi_\xi (2\xi_t + A_1 \Phi_\xi + A_4 \Phi_\eta + A_6 \Phi_\zeta) \\ &\quad + \Phi_\eta (2\eta_t + A_4 \Phi_\xi + A_2 \Phi_\eta + A_5 \Phi_\zeta) \\ &\quad + \Phi_\zeta (2\zeta_t + A_6 \Phi_\xi + A_5 \Phi_\eta + A_3 \Phi_\zeta) \\ &= \Phi_\xi (\xi_t + U) + \Phi_\eta (\eta_t + V) + \Phi_\zeta (\zeta_t + W)\end{aligned}$$

where

$$\begin{aligned}U &= \xi_t + A_1 \Phi_\xi + A_4 \Phi_\eta + A_6 \Phi_\zeta \\ V &= \eta_t + A_4 \Phi_\xi + A_2 \Phi_\eta + A_5 \Phi_\zeta \\ W &= \zeta_t + A_6 \Phi_\xi + A_5 \Phi_\eta + A_3 \Phi_\zeta\end{aligned}$$

The Bernoulli's equation then becomes

$$\rho = \left\{ 1 - \frac{\gamma - 1}{2} [2\Phi_\tau + (\xi_t + U) \Phi_\xi + (\eta_t + V) \Phi_\eta + (\zeta_t + W) \Phi_\zeta] \right\}^{\frac{1}{\gamma - 1}} \quad (9.60)$$

U , V , and W defined as above are called the contravariant velocities along the ξ , η , and ζ coordinate directions. Now consider the transformation of the potential equation 9.56. The transformed potential equation is given as follows.

$$\frac{\partial}{\partial \tau} \left(\frac{\rho}{J} \right) + \frac{\partial}{\partial \xi} \left(\frac{\rho U}{J} \right) + \frac{\partial}{\partial \eta} \left(\frac{\rho V}{J} \right) + \frac{\partial}{\partial \zeta} \left(\frac{\rho W}{J} \right) = 0 \quad (9.61)$$

where J is the jacobian of the transformation.

$$J = \begin{bmatrix} \xi_x & \eta_x & \zeta_x \\ \xi_y & \eta_y & \zeta_y \\ \xi_z & \eta_z & \zeta_z \end{bmatrix}$$

The details of the derivation will be described later.

9.3.3 Literature

Conservative small disturbance

1. Caradonna, F. X. and Phillippe, J. J., "The Flow Over a Helicopter Blade Tip in the Transonic Regime," *Vertica*, Vol. 2, April 1978, pp. 43-60.
2. Phillippe, J. J. and Chattot, J. J., "Experimental and Theoretical Studies on Helicopter Blade Tips at ONERA," Sixth European Rotorcraft Forum, Bristol, England, Paper 46, Sept. 1980, pp. 16-19.

Conservative Full Potential

1. Bridgeman, J. O., Steger, J. L., and Caradonna, F. X., "A Conservative Finite-Difference Algorithm for the Unsteady Transonic Potential Equation in Generalized Coordinates," AIAA Paper 82-1388, Aug. 1982. Fixed wing.
2. Sankar, L. N. and Prichard, D., "Solution of Transonic Flow Past Rotor Blades Using the Conservative Full Potential Equation," AIAA Paper 85-5012, Oct. 1985.
3. Strawn, R. C., and Caradonna, F. X., "Conservative Full-Potential Model for Unsteady Transonic Rotor Flows," AIAA Journal, Vol. 25, No.2, Feb. 1987.

9.4 Euler and Navier-Stokes equations

The governing equations are again transformed into a body-fitted coordinate system. This transformation is necessary only for structured grids. It was given by equation 9.59 where the coordinates x, y, z, t were transformed to $\xi, \eta, \zeta,$ and τ . The meaning of body-fitted coordinates is that the body surface is completely described by constant ξ, η and ζ lines. Thus the body surface can be simply and accurately treated. In addition, as previously mentioned the transformation can be used to cluster grids in regions of the flow with high gradients. It is important to understand certain features of this transformation.

9.4.1 Review of Curvilinear coordinates

Consider a vector \vec{r} in a three dimensional space. It can be represented in different ways. One way is the cartesian representation that we are familiar with. Here, three rectilinear coordinate directions are chosen which are mutually orthogonal. The vector is projected along the coordinate directions. The projected lengths are then multiplied with tangent vectors along the directions to complete the representation of the vector. The tangent vectors are called base vectors. For example, if the coordinate directions are $(x_1x_2x_3)$ then the tangent vector, or base vector, along x_1 would be

$$\lim_{\Delta x_1 \rightarrow 0} \frac{\vec{r}(x_1 + \Delta x_1) - \vec{r}(x_1)}{\Delta x_1} = \frac{\Delta x_1 \vec{i}}{\Delta x_1} = \vec{i}$$

where \vec{i} is an unit vector along x_1 . Similarly the tangent vectors along x_2 and x_3 may be denoted by \vec{j} and \vec{k} . A differential increment of the position vector, $d\vec{r}$, can be represented by adding the differential increments along the coordinate directions multiplied by tangent vectors along those

directions.

$$\begin{aligned}\vec{dr} &= \begin{Bmatrix} dx_1 \\ dx_2 \\ dx_3 \end{Bmatrix}^T \begin{Bmatrix} i \\ j \\ k \end{Bmatrix} \\ &= \begin{Bmatrix} 1 \\ 0 \\ 0 \end{Bmatrix}^T \begin{Bmatrix} i \\ j \\ k \end{Bmatrix} dx_1 + \begin{Bmatrix} 0 \\ 1 \\ 0 \end{Bmatrix}^T \begin{Bmatrix} i \\ j \\ k \end{Bmatrix} dx_2 + \begin{Bmatrix} 0 \\ 0 \\ 1 \end{Bmatrix}^T \begin{Bmatrix} i \\ j \\ k \end{Bmatrix} dx_3\end{aligned}$$

or in vector notation

$$\vec{dr} = \begin{Bmatrix} dx_1 \\ dx_2 \\ dx_3 \end{Bmatrix} = dx_1 \begin{Bmatrix} 1 \\ 0 \\ 0 \end{Bmatrix} + dx_2 \begin{Bmatrix} 0 \\ 1 \\ 0 \end{Bmatrix} + dx_3 \begin{Bmatrix} 0 \\ 0 \\ 1 \end{Bmatrix} \quad (9.62)$$

Instead of $(x_1x_2x_3)$ the vector \underline{r} can also be represented using a set of generalized curvilinear coordinate directions $(\xi_1\xi_2\xi_3)$. The base vectors can be chosen as before, i.e., along the tangent directions. For example, the base vector along ξ_1 , would be the tangent vector given by

$$\lim_{\Delta\xi_1 \rightarrow 0} \frac{\vec{r}(\xi_1 + \Delta\xi_1) - \vec{r}(\xi_1)}{\Delta\xi_1} = \frac{\Delta\xi_1 \underline{a}_1}{\Delta\xi_1} = \underline{a}_1$$

where \underline{a}_1 is now an unit vector tangent to ξ_1 . Similarly in the other directions the base vectors would be \underline{a}_2 and \underline{a}_3 . Thus in a curvilinear coordinate system the differential increment expression 9.62 takes the following form

$$\underline{dr} = \underline{a}_1 d\xi_1 + \underline{a}_2 d\xi_2 + \underline{a}_3 d\xi_3 \quad (9.63)$$

A tangential system of base vectors, as described above, are called covariant base vectors. A perpendicular system of base vectors is called contravariant base vectors. In the later case the base vectors are chosen perpendicular to the coordinate directions.

The differential increment expression 9.63 leads to the definition of the fundamental metric tensor.

Fundamental metric tensor

The magnitude of the differential increment is given by

$$\begin{aligned}(\text{arc length } ds)^2 &= \underline{dr} \cdot \underline{dr} \\ &= \sum_i \sum_j \underline{a}_i \cdot \underline{a}_j d\xi_i d\xi_j \\ &= \sum_i \sum_j g_{ij} d\xi_i d\xi_j\end{aligned} \quad (9.64)$$

where $g_{ij} = \underline{a}_i \cdot \underline{a}_j$ are the nine covariant metric tensor components.

Incremental arc length

An incremental arc length along ξ_1 direction is given by

$$ds_1 = |\underline{a}_1| d\xi_1 = \sqrt{g_{11}} d\xi_1 \quad (9.65)$$

To generalize

$$ds_i = |\underline{a}_i| d\xi_i = \sqrt{g_{ii}} d\xi_i \quad i = 1, 2, 3 \quad (9.66)$$

Incremental area

An incremental area on a coordinate surface of constant ξ_i is given by

$$\begin{aligned} dS_i &= |\underline{a}_j \times \underline{a}_k| d\xi_j d\xi_k \\ |\underline{a}_j \times \underline{a}_k|^2 &= (\underline{a}_j \cdot \underline{a}_j)(\underline{a}_k \cdot \underline{a}_k) - (\underline{a}_k \cdot \underline{a}_j)^2 = g_{jj}g_{kk} - g_{jk}^2 \end{aligned}$$

Therefore

$$dS_i = \sqrt{g_{jj}g_{kk} - g_{jk}^2} d\xi_j d\xi_k \quad (i,j,k) = (1,2,3) \text{ in a cyclic manner} \quad (9.67)$$

Incremental volume

An incremental volume enclosed by the three coordinate directions is given by

$$dV = \underline{a}_1 \cdot (\underline{a}_2 \times \underline{a}_3) d\xi_1 d\xi_2 d\xi_3 \quad (9.68)$$

Use the following

$$(A \times B)(C \times D) = (A \cdot C)(B \cdot D) - (A \cdot D)(B \cdot C)$$

or

$$(A \cdot D)(B \cdot C) = (A \cdot C)(B \cdot D) - (A \times B)(C \times D)$$

Now

$$\begin{aligned} \left[\underline{a}_1 \cdot (\underline{a}_2 \times \underline{a}_3) \right]^2 &= \left[\underline{a}_1 \cdot (\underline{a}_2 \times \underline{a}_3) \right] \left[(\underline{a}_2 \times \underline{a}_3) \cdot \underline{a}_1 \right] \\ &= (\underline{a}_1 \cdot \underline{a}_1) \left[(\underline{a}_2 \times \underline{a}_3) \cdot (\underline{a}_2 \times \underline{a}_3) \right] - |\underline{a}_1 \times (\underline{a}_2 \times \underline{a}_3)|^2 \\ &= (\underline{a}_1 \cdot \underline{a}_1) \left[(\underline{a}_2 \cdot \underline{a}_2)(\underline{a}_3 \cdot \underline{a}_3) - (\underline{a}_2 \cdot \underline{a}_3)^2 \right] - |\underline{a}_1 \times (\underline{a}_2 \times \underline{a}_3)|^2 \end{aligned}$$

Now use

$$A \times (B \times C) = (A \cdot C)B - (A \cdot B)C$$

to obtain

$$\begin{aligned} \left[\underline{a}_1 \cdot (\underline{a}_2 \times \underline{a}_3) \right]^2 &= g_{11}(g_{22}g_{33} - g_{23}^2) - (g_{13}a_2 - g_{12}a_3)^2 \\ &= \Delta(g_{ij}) \\ &= g \end{aligned}$$

where $\Delta(g_{ij}) = g$ is the determinant of the nine element covariant symmetric metric tensor. Thus equation (9.68) can be written as

$$dV = \sqrt{g} d\xi_1 d\xi_2 d\xi_3 \quad (9.69)$$

9.4.2 Generalized coordinate transformation

Consider again the transformation 9.59. This is the forward transformation, if x, y, z, t are known, ξ, η, ζ , and τ can be determined. The jacobian of the transformation J is given as follows.

$$\begin{pmatrix} d\xi \\ d\eta \\ d\zeta \end{pmatrix} = \begin{bmatrix} \xi_x & \eta_x & \zeta_x \\ \xi_y & \eta_y & \zeta_y \\ \xi_z & \eta_z & \zeta_z \end{bmatrix} \begin{pmatrix} dx \\ dy \\ dz \end{pmatrix} + \begin{pmatrix} \xi_t \\ \eta_t \\ \zeta_t \end{pmatrix} dt = J \begin{pmatrix} dx \\ dy \\ dz \end{pmatrix} + \begin{pmatrix} \xi_t \\ \eta_t \\ \zeta_t \end{pmatrix} dt \quad (9.70)$$

The jacobian also relates the partial derivatives.

$$\begin{pmatrix} \frac{\partial}{\partial x} \\ \frac{\partial}{\partial y} \\ \frac{\partial}{\partial z} \end{pmatrix} = \begin{bmatrix} \xi_x & \eta_x & \zeta_x \\ \xi_y & \eta_y & \zeta_y \\ \xi_z & \eta_z & \zeta_z \end{bmatrix} \begin{pmatrix} \frac{\partial}{\partial \xi} \\ \frac{\partial}{\partial \eta} \\ \frac{\partial}{\partial \zeta} \end{pmatrix} = J \begin{pmatrix} \frac{\partial}{\partial \xi} \\ \frac{\partial}{\partial \eta} \\ \frac{\partial}{\partial \zeta} \end{pmatrix} \quad (9.71)$$

We have

$$\begin{aligned} \begin{pmatrix} \frac{\partial}{\partial x} \\ \frac{\partial}{\partial y} \\ \frac{\partial}{\partial z} \end{pmatrix} &= \begin{bmatrix} \xi_x & \eta_x & \zeta_x \\ \xi_y & \eta_y & \zeta_y \\ \xi_z & \eta_z & \zeta_z \end{bmatrix} \begin{pmatrix} \frac{\partial}{\partial \xi} \\ \frac{\partial}{\partial \eta} \\ \frac{\partial}{\partial \zeta} \end{pmatrix} \\ &= \begin{bmatrix} \xi_x & \eta_x & \zeta_x \\ \xi_y & \eta_y & \zeta_y \\ \xi_z & \eta_z & \zeta_z \end{bmatrix} \begin{bmatrix} x_\xi & y_\xi & z_\xi \\ x_\eta & y_\eta & z_\eta \\ x_\zeta & y_\zeta & z_\zeta \end{bmatrix} \begin{pmatrix} \frac{\partial}{\partial \xi} \\ \frac{\partial}{\partial \eta} \\ \frac{\partial}{\partial \zeta} \end{pmatrix} \end{aligned} \quad (9.72)$$

It follows

$$\begin{bmatrix} \xi_x & \eta_x & \zeta_x \\ \xi_y & \eta_y & \zeta_y \\ \xi_z & \eta_z & \zeta_z \end{bmatrix} \begin{bmatrix} x_\xi & y_\xi & z_\xi \\ x_\eta & y_\eta & z_\eta \\ x_\zeta & y_\zeta & z_\zeta \end{bmatrix} = I \quad (9.73)$$

From the above equation 9.73 we have

$$\begin{bmatrix} x_\xi & y_\xi & z_\xi \\ x_\eta & y_\eta & z_\eta \\ x_\zeta & y_\zeta & z_\zeta \end{bmatrix} = \begin{bmatrix} \xi_x & \eta_x & \zeta_x \\ \xi_y & \eta_y & \zeta_y \\ \xi_z & \eta_z & \zeta_z \end{bmatrix}^{-1} = J^{-1} \quad (9.74)$$

Thus

$$J^{-1} = x_\xi(y_\eta z_\zeta - z_\eta y_\zeta) + y_\xi(x_\zeta z_\eta - z_\zeta x_\eta) + z_\xi(x_\eta y_\zeta - x_\zeta y_\eta) \quad (9.75)$$

Before we go any further, let us study the transformation. At any instant of time, which is the same in both coordinates as $\tau = t$, we have (x, y, z) as the cartesian coordinates, and (ξ, η, ζ) as the curvilinear coordinates. A differential increment of a position vector \underline{dr} in the cartesian coordinates is given by $[dx dy dz]^T$, where dx, dy , and dz are increments along the cartesian axes. These can be expressed in terms of increments along the curvilinear axes using the chain rule.

$$\begin{aligned} dx &= x_\xi d\xi + x_\eta d\eta + x_\zeta d\zeta \\ dy &= y_\xi d\xi + y_\eta d\eta + y_\zeta d\zeta \\ dz &= z_\xi d\xi + z_\eta d\eta + z_\zeta d\zeta \end{aligned}$$

The above is in the same form as equation 9.63. ξ_1 is now ξ , ξ_2 is now η and ξ_3 is now ζ . The differential increment \underline{dr} is

$$\underline{dr} = \begin{pmatrix} dx \\ dy \\ dz \end{pmatrix} = d\xi \begin{pmatrix} x_\xi \\ x_\eta \\ x_\zeta \end{pmatrix} + d\eta \begin{pmatrix} y_\xi \\ y_\eta \\ y_\zeta \end{pmatrix} + d\zeta \begin{pmatrix} z_\xi \\ z_\eta \\ z_\zeta \end{pmatrix} \quad (9.76)$$

and the covariant base vectors in the curvilinear coordinates are

$$\underline{a}_1 = \begin{Bmatrix} x_\xi \\ x_\eta \\ x_\zeta \end{Bmatrix} \quad \underline{a}_2 = \begin{Bmatrix} y_\xi \\ y_\eta \\ y_\zeta \end{Bmatrix} \quad \underline{a}_3 = \begin{Bmatrix} z_\xi \\ z_\eta \\ z_\zeta \end{Bmatrix} \quad (9.77)$$

Thus x_ξ, y_ξ , etc are called the covariants of the transformation. They are tangents to the curvilinear coordinate directions. Note that they are obtained by taking partial derivatives from the inverse transformation. The inverse transformation is as follows.

$$\begin{aligned} x &= x(\xi, \eta, \zeta, \tau) \\ y &= y(\xi, \eta, \zeta, \tau) \\ z &= z(\xi, \eta, \zeta, \tau) \\ t &= \tau \end{aligned} \quad (9.78)$$

From equation 9.73 we have

$$\begin{bmatrix} \xi_x & \eta_x & \zeta_x \\ \xi_y & \eta_y & \zeta_y \\ \xi_z & \eta_z & \zeta_z \end{bmatrix} = \begin{bmatrix} x_\xi & y_\xi & z_\xi \\ x_\eta & y_\eta & z_\eta \\ x_\zeta & y_\zeta & z_\zeta \end{bmatrix}^{-1} = \frac{\text{cofactor of entry } x_{ji}}{J^{-1}} \quad (9.79)$$

The metrics of the transformation ξ_x, ξ_y , etc are thus related to the covariants x_ξ, x_η by the following expression.

$$\begin{aligned} \xi_x &= J(y_\eta z_\zeta - y_\zeta z_\eta) \\ \eta_x &= J(y_\zeta z_\xi - y_\xi z_\zeta) \\ \zeta_x &= J(y_\xi z_\eta - y_\eta z_\xi) \\ \\ \xi_y &= J(x_\zeta z_\eta - x_\eta z_\zeta) \\ \eta_y &= J(x_\xi z_\zeta - x_\zeta z_\xi) \\ \zeta_y &= J(x_\eta z_\xi - x_\xi z_\eta) \\ \\ \xi_z &= J(x_\eta y_\zeta - x_\zeta y_\eta) \\ \eta_z &= J(x_\zeta y_\xi - x_\xi y_\zeta) \\ \zeta_z &= J(x_\xi y_\eta - x_\eta y_\xi) \end{aligned} \quad (9.80)$$

9.4.3 Euler equation in generalized coordinates

The Euler equation in cartesian form is given as

$$\frac{\partial q}{\partial t} + \frac{\partial F}{\partial x} + \frac{\partial G}{\partial y} + \frac{\partial H}{\partial z} = 0 \quad (9.81)$$

where

$$q = \begin{Bmatrix} \rho \\ \rho u \\ \rho v \\ \rho w \\ \rho E \end{Bmatrix} \quad F = \begin{Bmatrix} \rho u \\ \rho u^2 + p \\ \rho uv \\ \rho uw \\ \rho u(E + p) \end{Bmatrix} \quad G = \begin{Bmatrix} \rho v \\ \rho vu \\ \rho v^2 + p \\ \rho vw \\ \rho v(E + p) \end{Bmatrix} \quad H = \begin{Bmatrix} \rho w \\ \rho wu \\ \rho wv \\ \rho w^2 + p \\ \rho w(E + p) \end{Bmatrix} \quad (9.82)$$

Note that the convective fluxes F, G, H were earlier denoted as F_x, F_y, F_z in chapter 4. The pressure p and temperature T can be determined from the total energy per unit mass E as follows. The internal energy by unit mass is $e = E - 0.5(u^2 + v^2 + w^2) = C_v T$. Thus

$$T = \frac{1}{C_v} \left[E - \frac{1}{2}(u^2 + v^2 + w^2) \right] \quad (9.83)$$

Now $p = \rho RT$. Therefore

$$\begin{aligned} p &= \frac{\rho R}{C_v} \left[E - \frac{1}{2}(u^2 + v^2 + w^2) \right] \\ &= \frac{\rho RT}{C_v T} \left[E - \frac{1}{2}(u^2 + v^2 + w^2) \right] \\ &= \frac{\rho(h - e)}{C_v T} \left[E - \frac{1}{2}(u^2 + v^2 + w^2) \right] \\ &= \frac{\rho(C_p - C_v)T}{C_v T} \left[E - \frac{1}{2}(u^2 + v^2 + w^2) \right] \\ &= (\gamma - 1)\rho \left[E - \frac{1}{2}(u^2 + v^2 + w^2) \right] \end{aligned} \quad (9.84)$$

The generalized coordinate transformation preserves the conservation form of the equations. First pre-multiply equation (9.81) by J^{-1} . Now, consider the terms one by one. First the time derivative.

$$\begin{aligned} J^{-1} \frac{\partial q}{\partial t} &= J^{-1} \left(\frac{\partial q}{\partial \tau} + \xi_t \frac{\partial q}{\partial \xi} + \eta_t \frac{\partial q}{\partial \eta} + \zeta_t \frac{\partial q}{\partial \zeta} \right) \\ &= \frac{\partial}{\partial \tau} (J^{-1}q) + \frac{\partial}{\partial \xi} (J^{-1}\xi_t q) + \frac{\partial}{\partial \eta} (J^{-1}\eta_t q) + \frac{\partial}{\partial \zeta} (J^{-1}\zeta_t q) \\ &\quad - q \left[\frac{\partial}{\partial \tau} (J^{-1}) + \frac{\partial}{\partial \xi} (J^{-1}\xi_t) + \frac{\partial}{\partial \eta} (J^{-1}\eta_t) + \frac{\partial}{\partial \zeta} (J^{-1}\zeta_t) \right] \end{aligned} \quad (9.85)$$

Now consider the spatial derivatives

$$\begin{aligned} &J^{-1} \left(\frac{\partial F}{\partial x} + \frac{\partial G}{\partial y} + \frac{\partial H}{\partial z} \right) \\ &= J^{-1} \left[\xi_x \frac{\partial F}{\partial \xi} + \eta_x \frac{\partial F}{\partial \eta} + \zeta_x \frac{\partial F}{\partial \zeta} + \xi_y \frac{\partial G}{\partial \xi} + \eta_y \frac{\partial G}{\partial \eta} + \zeta_y \frac{\partial G}{\partial \zeta} + \xi_z \frac{\partial H}{\partial \xi} + \eta_z \frac{\partial H}{\partial \eta} + \zeta_z \frac{\partial H}{\partial \zeta} \right] \\ &= J^{-1} \left[\xi_x \frac{\partial F}{\partial \xi} + \eta_x \frac{\partial F}{\partial \eta} + \zeta_x \frac{\partial F}{\partial \zeta} + \xi_y \frac{\partial G}{\partial \xi} + \eta_y \frac{\partial G}{\partial \eta} + \zeta_y \frac{\partial G}{\partial \zeta} + \xi_z \frac{\partial H}{\partial \xi} + \eta_z \frac{\partial H}{\partial \eta} + \zeta_z \frac{\partial H}{\partial \zeta} \right] \\ &= (y_\eta z_\zeta - y_\zeta z_\eta) F_\xi + (x_\zeta z_\eta - x_\eta z_\zeta) G_\xi + (x_\eta y_\zeta - x_\zeta y_\eta) H_\xi + \\ &\quad (y_\zeta z_\xi - z_\zeta y_\xi) F_\eta + (x_\xi z_\zeta - x_\zeta z_\xi) G_\eta + (x_\zeta y_\xi - x_\xi y_\zeta) H_\eta + \\ &\quad (y_\xi z_\eta - y_\eta z_\xi) F_\zeta + (x_\eta z_\xi - x_\xi z_\eta) G_\zeta + (x_\xi y_\eta - x_\eta y_\xi) H_\zeta \end{aligned} \quad (9.86)$$

Use equations 9.80 to rewrite the above expression as

$$\begin{aligned}
& [(y_\eta z_\zeta - y_\zeta z_\eta)F]_\xi - \underline{F(y_\eta z_\zeta - y_\zeta z_\eta)_\xi} \\
& [(x_\zeta z_\eta - x_\eta z_\zeta)G]_\xi - \underline{G(x_\zeta z_\eta - x_\eta z_\zeta)_\xi} \\
& [(x_\eta y_\zeta - x_\zeta y_\eta)H]_\xi - \underline{H(x_\eta y_\zeta - x_\zeta y_\eta)_\xi} \\
& [(y_\zeta z_\xi - z_\zeta y_\xi)F]_\eta - \underline{F(y_\zeta z_\xi - z_\zeta y_\xi)_\eta} \\
& [(x_\xi z_\zeta - x_\zeta z_\xi)G]_\eta - \underline{G(x_\xi z_\zeta - x_\zeta z_\xi)_\eta} \\
& [(x_\zeta y_\xi - x_\xi y_\zeta)H]_\eta - \underline{H(x_\zeta y_\xi - x_\xi y_\zeta)_\eta} \\
& [(y_\xi z_\eta - y_\eta z_\xi)F]_\zeta - \underline{F(y_\xi z_\eta - y_\eta z_\xi)_\zeta} \\
& [(x_\eta z_\xi - x_\xi z_\eta)G]_\zeta - \underline{G(x_\eta z_\xi - x_\xi z_\eta)_\zeta} \\
& [(x_\xi y_\eta - x_\eta y_\xi)H]_\zeta - \underline{H(x_\xi y_\eta - x_\eta y_\xi)_\zeta}
\end{aligned} \tag{9.87}$$

The underlined expressions, when expanded, assuming necessary smoothness of the transformation cancel out to zero. Thus the transformed equation becomes

$$\begin{aligned}
\frac{\partial}{\partial \tau} \left(\frac{q}{J} \right) &+ \frac{\partial}{\partial \xi} \left(\frac{\xi_t q + \xi_x F + \xi_y G + \xi_z H}{J} \right) \\
&+ \frac{\partial}{\partial \eta} \left(\frac{\eta_t q + \eta_x F + \eta_y G + \eta_z H}{J} \right) \\
&+ \frac{\partial}{\partial \zeta} \left(\frac{\zeta_t q + \zeta_x F + \zeta_y G + \zeta_z H}{J} \right) \\
&- q \left[\frac{\partial}{\partial \tau} \left(\frac{1}{J} \right) + \frac{\partial}{\partial \xi} \left(\frac{\xi_t}{J} \right) + \frac{\partial}{\partial \eta} \left(\frac{\eta_t}{J} \right) + \frac{\partial}{\partial \zeta} \left(\frac{\zeta_t}{J} \right) \right]
\end{aligned}$$

The above equation is in the following strong conservation form

$$\hat{q}_\tau + \hat{F}_\xi + \hat{G}_\eta + \hat{H}_\zeta = 0 \tag{9.88}$$

provided the expression multiplied with q vanishes.

$$\frac{\partial}{\partial \tau} \left(\frac{1}{J} \right) + \frac{\partial}{\partial \xi} \left(\frac{\xi_t}{J} \right) + \frac{\partial}{\partial \eta} \left(\frac{\eta_t}{J} \right) + \frac{\partial}{\partial \zeta} \left(\frac{\zeta_t}{J} \right) = 0 \tag{9.89}$$

The above equation 9.89 is called the geometric conservation law. The expression was suggested by Thomas and Lombard in 1970 and states that the rate at which the volume of a discretized mesh element changes with time must be same as the rate at which its six faces sweep the domain. It is important to satisfy this relationship in order to avoid spurious production of mass, momentum, and energy within the computational mesh elements.

Thus the flow equations 9.88 is solved along with the geometric conservation law 9.89. It is also necessary to prescribe a physically consistent set of boundary conditions on all the solid and fluid boundaries in the computational domain. We shall discuss boundary conditions later. Consider equation 9.88. This equation has exactly the same form as the original equation 9.81 in the cartesian

domain. Now consider the expression \hat{F} in equation (9.88).

$$\hat{F}_\xi = J^{-1} [\xi_t q + \xi_x F + \xi_y G + \xi_z H] \quad (9.90)$$

$$= J^{-1} \begin{bmatrix} \xi_t \rho + \xi_x \rho u + \xi_y \rho v + \xi_z \rho w \\ \xi_t \rho u + \xi_x \rho u u + \xi_x p + \xi_y \rho v u + \xi_z \rho w u \\ \xi_t \rho v + \xi_x \rho u v + \xi_y \rho v v + \xi_y p + \xi_z \rho w v \\ \xi_t \rho w + \xi_x \rho u w + \xi_y \rho v w + \xi_z \rho w w + \xi_z p \\ \xi_t (E + p) - \xi_t p + \xi_x \rho u (E + p) + \xi_y \rho v (E + p) + \xi_z \rho w (E + p) \end{bmatrix} \quad (9.91)$$

$$= J^{-1} \begin{bmatrix} \rho U \\ \rho u U + \xi_x p \\ \rho v U + \xi_y p \\ \rho w U + \xi_z p \\ (E + p)U - \xi_t p \end{bmatrix} \quad (9.92)$$

where

$$U = \xi_t + \xi_x u + \xi_y v + \xi_z w \quad (9.93)$$

Similarly \hat{F} and \hat{G} can be expressed as

$$\hat{F} = J^{-1} \begin{bmatrix} \rho V \\ \rho u V + \eta_x p \\ \rho v V + \eta_y p \\ \rho w V + \eta_z p \\ (E + p)V - \eta_t p \end{bmatrix} \quad \hat{G} = J^{-1} \begin{bmatrix} \rho W \\ \rho u W + \zeta_x p \\ \rho v W + \zeta_y p \\ \rho w W + \zeta_z p \\ (E + p)W - \zeta_t p \end{bmatrix} \quad (9.94)$$

where

$$V = \eta_t + \eta_x u + \eta_y v + \eta_z w \quad (9.95)$$

$$W = \zeta_t + \zeta_x u + \zeta_y v + \zeta_z w \quad (9.96)$$

U, V, W are the contravariant velocities along ξ, η, ζ directions. ξ_t, η_t, ζ_t incorporate the effect of grid motion. ξ, η, ζ do not depend on τ . Therefore we have

$$\begin{aligned} \xi_\tau = 0 &= \xi_t + \xi_x x_\tau + \xi_y y_\tau + \xi_z z_\tau \\ \eta_\tau = 0 &= \eta_t + \eta_x x_\tau + \eta_y y_\tau + \eta_z z_\tau \\ \zeta_\tau = 0 &= \zeta_t + \zeta_x x_\tau + \zeta_y y_\tau + \zeta_z z_\tau \end{aligned} \quad (9.97)$$

Thus

$$\begin{aligned} \xi_t &= -x_\tau \xi_x - y_\tau \xi_y + z_\tau \xi_z \\ \eta_t &= -x_\tau \eta_x - y_\tau \eta_y + z_\tau \eta_z \\ \zeta_t &= -x_\tau \zeta_x - y_\tau \zeta_y + z_\tau \zeta_z \end{aligned} \quad (9.98)$$

The above expressions are used to account for the unsteady motion of the grid. Using the above expressions, U, V, W can also be written in the following form.

$$\begin{aligned} U &= (u - x_\tau) \xi_x + (v - y_\tau) \xi_y + (w - z_\tau) \xi_z \\ V &= (u - x_\tau) \eta_x + (v - y_\tau) \eta_y + (w - z_\tau) \eta_z \\ W &= (u - x_\tau) \zeta_x + (v - y_\tau) \zeta_y + (w - z_\tau) \zeta_z \end{aligned} \quad (9.99)$$

9.4.4 Thomas and Lombard's Geometric Conservation Law

Consider a cell volume Δv_i where i is the cell number. It has j surfaces denoted by S_{ij} . The time variation of cell volume is related to the areas, orientations, and velocities of cell faces.

$$\frac{d}{dt} \int_{\Delta v_i} dv = \sum_j \int_{S_{ij}} W_s \cdot ds$$

W_S is the local velocity of boundary surface S . For an entire flow domain R

$$\frac{d}{dt} \int_{\Delta v} dv = \int_s W_s \cdot ds \quad (9.100)$$

Note that the above equation is very similar to the mass conservation law in integral form. In fact it can be deduced straight away from the mass conservation law by replacing ρ with 1, and setting the fluid velocity to zero. Recall that the integral statement of the law of mass conservation for a spatial region R of volume v bounded by a closed surface s and fluid velocity V is given by

$$\frac{d}{dt} \int_{\Delta v_i} \rho dv + \int_s \rho(V - W_s) \cdot ds$$

Using the above mentioned substitution, it reduces to equation (9.100). The integral form of the geometric conservation law (9.100) can be recast into a differential form. Consider the computation domain. Consider now the transformation ξ, η, ζ . The incremental volume in the cartesian coordinates is $dx dy dz$. Use equation (9.68) and the definitions (9.77) and (9.75) to obtain

$$dv = dx dy dz = J^{-1} d\xi d\eta d\zeta \quad (9.101)$$

Therefore equation (9.100) is transformed into

$$\frac{d}{d\tau} \int_{\Delta v} J^{-1} d\xi d\eta d\zeta = \int_s W_s \cdot J^{-1} d\xi d\eta d\zeta \quad (9.102)$$

The transformation ξ, η, ζ generates a boundary conforming curvilinear coordinates. Boundary conforming means that the boundary s of the body is composed only of segments of the form $\xi = \text{constant}$, $\eta = \text{constant}$, and $\zeta = \text{constant}$. In the cartesian coordinates, the velocities at any point on the boundary is given by $W_s = (x_\tau, y_\tau, z_\tau)$. In general the transformation defines a velocity field $W = (x_\tau, y_\tau, z_\tau)$ throughout a region R that coincides with W_s in the boundary. Thus the divergence theorem can be applied to reduce the surface integral to a volume integral.

$$\frac{d}{d\tau} \int_{\Delta v} J^{-1} d\xi d\eta d\zeta = \int_v (\nabla \cdot W) J^{-1} d\xi d\eta d\zeta \quad (9.103)$$

Consider the expressions on the right hand side first. We have

$$\begin{aligned} \nabla \cdot W &= (W_1)_x + (W_2)_y + (W_3)_z \\ &= \xi_x(W_1)_\xi + \eta_x(W_1)_\eta + \zeta_x(W_1)_\zeta + \\ &\quad \xi_y(W_2)_\xi + \eta_y(W_2)_\eta + \zeta_y(W_2)_\zeta + \\ &\quad \xi_z(W_3)_\xi + \eta_z(W_3)_\eta + \zeta_z(W_3)_\zeta \\ &= \nabla \xi \cdot W_\xi + \nabla \eta \cdot W_\eta + \nabla \zeta \cdot W_\zeta \end{aligned}$$

Therefore

$$\begin{aligned} J^{-1}(\nabla \cdot W) &= (J^{-1} \nabla \xi \cdot W)_\xi + (J^{-1} \nabla \eta \cdot W)_\eta + (J^{-1} \nabla \zeta \cdot W)_\zeta \\ &\quad - [(J^{-1} \nabla \xi)_\xi + (J^{-1} \nabla \eta)_\eta + (J^{-1} \nabla \zeta)_\zeta] \cdot W \end{aligned}$$

Now we have

$$\begin{aligned}\xi_\tau = 0 &= \xi_t + \xi_x x_\tau + \xi_y y_\tau + \xi_z z_\tau \\ &= \xi_t + \nabla \xi \cdot W\end{aligned}$$

Hence

$$\begin{aligned}\xi_t &= -\nabla \xi \cdot W \\ \eta_t &= -\nabla \eta \cdot W \\ \zeta_t &= -\nabla \zeta \cdot W\end{aligned}$$

and

$$\begin{aligned}J^{-1}(\nabla \cdot W) &= -(J^{-1}\xi_t)_\xi - (J^{-1}\eta_t)_\eta - (J^{-1}\zeta_t)_\zeta \\ &\quad - W \cdot [(J^{-1}\nabla \xi)_\xi + (J^{-1}\nabla \eta)_\eta + (J^{-1}\nabla \zeta)_\zeta] \\ &= \underline{(J^{-1}\xi_t)_\xi} - (J^{-1}\eta_t)_\eta - (J^{-1}\zeta_t)_\zeta \\ &\quad - x_\tau \underline{[(J^{-1}\xi_x)_\xi + (J^{-1}\eta_x)_\eta + (J^{-1}\zeta_x)_\zeta]} \\ &\quad - y_\tau \underline{[(J^{-1}\xi_y)_\xi + (J^{-1}\eta_y)_\eta + (J^{-1}\zeta_y)_\zeta]} \\ &\quad - z_\tau \underline{[(J^{-1}\xi_z)_\xi + (J^{-1}\eta_z)_\eta + (J^{-1}\zeta_z)_\zeta]}\end{aligned}$$

Each of the underlined expressions cancel to zero. For example,

$$\begin{aligned}(J^{-1}\xi_y)_\xi + (J^{-1}\eta_y)_\eta + (J^{-1}\zeta_y)_\zeta &= [J^{-1}J(y_\eta z_\zeta - y_\zeta z_\eta)]_\xi + \\ &\quad [J^{-1}J(y_\zeta z_\xi - y_\xi z_\zeta)]_\eta + \\ &\quad [J^{-1}J(y_\xi z_\eta - y_\eta z_\xi)]_\eta \\ &= 0\end{aligned}$$

Now consider the left hand side of equation (9.103). Because ξ, η, ζ are boundary-confirming, the surface s and volume v are fixed in time τ . Hence the operator $\partial/\partial\tau$ can be moved inside the integral. Thus, equation (9.103) finally reduces to

$$\int_v [(J^{-1})_\tau + (J^{-1}\xi_t)_\xi + (J^{-1}\eta_t)_\eta + (J^{-1}\zeta_t)_\zeta] d\xi d\eta d\zeta = 0 \quad (9.104)$$

As v is fixed in time τ the above reduces to equation (9.89) which is the differential statement of the geometric conservation law. Again, it can be verified that we can obtain the same expression from the mass conservation equation, which is the first component of the vector equation (9.88) by putting $\rho = 1$ and $u, v, w = 0$.

9.4.5 Navier-Stokes equations in generalized coordinates

The Navier-Stokes equations in cartesian form is given by

$$\frac{\partial q}{\partial t} + \frac{\partial(F - F_v)}{\partial x} + \frac{\partial(G - G_v)}{\partial y} + \frac{\partial(H - H_v)}{\partial z} = 0 \quad (9.105)$$

where F, G, H are same as in the Euler equations. F_v, G_v, H_v are the additional diffusive fluxes. Recall from chapter 4 that they are given by

$$F_v = \begin{Bmatrix} 0 \\ \tau_{xx} \\ \tau_{yx} \\ \tau_{zx} \\ \beta_x \end{Bmatrix} \quad G_v = \begin{Bmatrix} 0 \\ \tau_{xy} \\ \tau_{yy} \\ \tau_{zy} \\ \beta_y \end{Bmatrix} \quad H_v = \begin{Bmatrix} 0 \\ \tau_{xz} \\ \tau_{yz} \\ \tau_{zz} \\ \beta_z \end{Bmatrix} \quad \begin{aligned} \beta_x &= u\tau_{xx} + v\tau_{xy} + w\tau_{xz} + q_x \\ \beta_y &= u\tau_{yx} + v\tau_{yy} + w\tau_{yz} + q_y \\ \beta_z &= u\tau_{zx} + v\tau_{zy} + w\tau_{zz} + q_z \end{aligned} \quad (9.106)$$

where τ 's are the shear stresses and q 's the heat fluxes. The pressure and temperature are again related to the internal energy per unit mass E and the flow velocities u, v, w via equations (9.84) and (9.83).

The transformed equation in body-conforming curvilinear coordinates is similar to equation (9.88) with the additional terms F_v, G_v, H_v .

$$\hat{q}_\tau + (\hat{F} - \hat{F}_v)_\xi + (\hat{G} - \hat{G}_v)_\eta + (\hat{H} - \hat{H}_v)_\zeta = 0 \quad (9.107)$$

where

$$\hat{F}_v = J^{-1} \begin{pmatrix} 0 \\ \xi_x \tau_{xx} + \xi_y \tau_{xy} + \xi_z \tau_{xz} \\ \xi_x \tau_{yx} + \xi_y \tau_{yy} + \xi_z \tau_{yz} \\ \xi_x \tau_{zx} + \xi_y \tau_{zy} + \xi_z \tau_{zz} \\ \xi_x \beta_x + \xi_y \beta_y + \xi_z \beta_z \end{pmatrix} \quad (9.108)$$

$$\hat{G}_v = J^{-1} \begin{pmatrix} 0 \\ \eta_x \tau_{xx} + \eta_y \tau_{xy} + \eta_z \tau_{xz} \\ \eta_x \tau_{yx} + \eta_y \tau_{yy} + \eta_z \tau_{yz} \\ \eta_x \tau_{zx} + \eta_y \tau_{zy} + \eta_z \tau_{zz} \\ \eta_x \beta_x + \eta_y \beta_y + \eta_z \beta_z \end{pmatrix} \quad (9.109)$$

$$\hat{H}_v = J^{-1} \begin{pmatrix} 0 \\ \zeta_x \tau_{xx} + \zeta_y \tau_{xy} + \zeta_z \tau_{xz} \\ \zeta_x \tau_{yx} + \zeta_y \tau_{yy} + \zeta_z \tau_{yz} \\ \zeta_x \tau_{zx} + \zeta_y \tau_{zy} + \zeta_z \tau_{zz} \\ \zeta_x \beta_x + \zeta_y \beta_y + \zeta_z \beta_z \end{pmatrix} \quad (9.110)$$

The geometric conservation law remains same as equation (9.89).

Thin layer approximation

Capturing the viscous gradients near the body is difficult for high Reynolds number flows. Often the gradients perpendicular to the body are targeted for accurate calculation, the gradients along the body are neglected. In the case of body-conforming grids the body surface is mapped onto a $\zeta = \text{constant}$ line. In this case all viscous derivatives along the ξ and η directions are neglected.

$$\hat{q}_\tau + \hat{F}_\xi + \hat{G}_\eta + \hat{H}_\zeta = \hat{H}_{v\zeta} \quad (9.111)$$

The velocity derivatives are

$$u_x = \zeta_x u_\zeta$$

$$u_y = \zeta_y u_\zeta$$

$$u_z = \zeta_z u_\zeta$$

$$v_x = \zeta_x v_\zeta$$

$$v_y = \zeta_y v_\zeta$$

$$v_z = \zeta_z v_\zeta$$

$$(9.112)$$

$$w_x = \zeta_x w_\zeta$$

$$w_y = \zeta_y w_\zeta$$

$$w_z = \zeta_z w_\zeta$$

9.4.6 Surface Boundary Conditions

From equations (9.93) and (9.95) we have

$$\begin{Bmatrix} U - \xi_t \\ V - \eta_t \\ W - \zeta_t \end{Bmatrix} = \begin{bmatrix} \xi_x & \xi_y & \xi_z \\ \eta_x & \eta_y & \eta_z \\ \zeta_x & \zeta_y & \zeta_z \end{bmatrix} \begin{Bmatrix} u \\ v \\ w \end{Bmatrix} \quad (9.113)$$

Inverting, we have

$$\begin{aligned} \begin{Bmatrix} u \\ v \\ w \end{Bmatrix} &= \begin{bmatrix} \xi_x & \xi_y & \xi_z \\ \eta_x & \eta_y & \eta_z \\ \zeta_x & \zeta_y & \zeta_z \end{bmatrix}^{-1} \begin{Bmatrix} U - \xi_t \\ V - \eta_t \\ W - \zeta_t \end{Bmatrix} \\ &= J^{-1} \begin{bmatrix} (\eta_y \zeta_z - \eta_z \zeta_y) & -(\xi_y \zeta_z - \zeta_y \xi_z) & (\xi_y \eta_z - \eta_y \xi_z) \\ -(\eta_x \zeta_z - \eta_z \zeta_x) & (\xi_x \zeta_z - \zeta_z \xi_x) & -(\xi_x \eta_z - \zeta_z \eta_x) \\ (\eta_x \zeta_y - \eta_y \zeta_x) & -(\xi_x \zeta_y - \zeta_y \xi_x) & (\xi_x \eta_y - \zeta_y \eta_x) \end{bmatrix} \begin{Bmatrix} U - \xi_t \\ V - \eta_t \\ W - \zeta_t \end{Bmatrix} \end{aligned} \quad (9.114)$$

For inviscid flow, as in the case of Euler equations, the boundary condition is

$$W = 0$$

The corresponding u, v, w are obtained from equation (9.114). For viscous flow, as in the case of Navier-Stokes equations, the boundary conditions are

$$U = V = W = 0$$

Chapter 10

Helicopter Vibration

Vibration in helicopters is only one of the many major problems. Helicopter vibration is the unsteady acceleration of any given location inside the fuselage, e.g. at the pilot seat, co-pilot seat or at a given crew or passenger station measured along three mutually orthogonal axes (as a fraction of acceleration due to gravity, g). Vibration not only effects the ride quality but also influences the fatigue life of the various components. The prime source of helicopter vibration is the main rotor. In this chapter we shall concentrate mainly on the vibration caused by the main rotor.

10.1 Measure of Helicopter Vibration

The basic measure of helicopter vibration, as given in the Aeronautical Design Standard (released in 1986 as ADS-27 by the U.S. Army Aviation Systems Command, AVSCOM), is the Intrusion Index (II) [1]. This is computed by normalizing triaxial accelerometer data for the four largest spectral peaks up to 60 Hz. The four largest spectral peaks generally correspond to multiples of the rotor RPM (Revolutions Per Minute) e.g. 1/rev (once per revolution, same as the rotor RPM), 2/rev, 3/rev etc, indicating that they arise from main rotor loads. For conventional helicopter rotors, the RPM corresponds to around 4 to 4.5 Hz. The ADS-27 measure does not include the 1/rev vibration. This is to emphasize the special importance of this harmonic. The 1/rev vibration arises in the fuselage if the blades are out of track - i.e, when all the blades do not follow the same trajectory in space. For tracked and identical rotor blades, the frequencies, in /rev, transmitted to the fuselage via the rotor hub are integral multiples of blade number. For example for a 4-bladed helicopter like the UH-60A, 4/rev, 8/rev, 12/rev and so on are transmitted to the fuselage. The frequency corresponding to the blade number, 4/rev in this case, is called the blade passage frequency. Non-integral multiples are transmitted only in the case of non-identical (damaged or dissimilar) or out of track blades.

The four largest harmonics are measured along each axis and their norm is used to obtain the intrusion index. This produces a single scalar quantity as a measure of vibration which combines 12 harmonics (four each in three axes). The three axes are weighted differently, the vertical vibrations are weighted most heavily, the lateral vibrations have a 0.75 weight relative to the vertical and the longitudinal vibrations have a 0.50 weight relative to the vertical. This is done to allow designers the freedom to trade off between directions and frequency within the confines of a single scalar measure of vibration.

The ADS-27 relaxed the fuselage vibration levels compared to original standards set by the Utility Tactical Transport Aircraft System (UTTAS) and Advanced Attack Helicopter (AAH) developmental programs [2]. None of the helicopter designs even came close to those original specifications. The revised ADS-27 standards are still too stringent. For example, for the UH-60A Black Hawk helicopter with an articulated 4 bladed main rotor system, the vibration levels can be 100% higher in forward flight compared to the ADS-27 requirements [3], see Fig. 10.1.

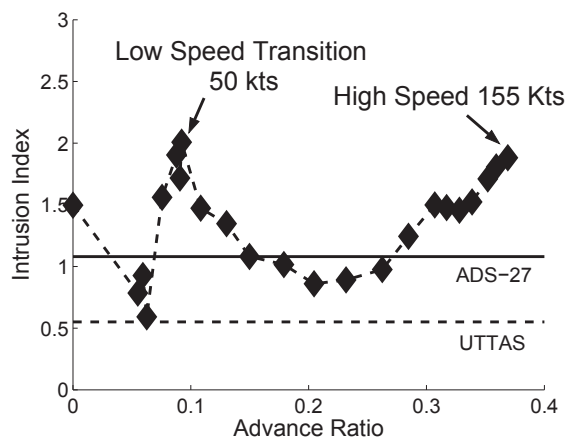


Figure 10.1: Measured Vibration at Pilot Seat of the UH-60A in Steady Level Flight, take off weight 16,500 lbs; Bousman 1999

The intrusion index at the pilot floor for the UH-60A at transition speed of around 40 kts is about 2.1 (ADS-27 level is about 1.1). 4/rev and 8/rev harmonics account for 91% of this number. At high speed of about 155 kts, 4 and 8/rev contribute to around 67% of the index. 2/rev and 6/rev contribute to 19% and 5% of the index. This shows that frequencies corresponding to non-integer multiples of blade number can contribute significantly to fuselage vibration at certain flight conditions.

Currently, vibration reduction devices, active and passive, are used to meet these requirements. Their cost and weight penalty has been excessive in part because of inadequate vibration prediction capability. Accurate prediction capability at an early design stage may enable the design of low vibration helicopter systems.

10.2 Sources of Helicopter Vibration

The prime source of helicopter vibration is the main rotor. The frequency of vibration caused by the main rotor is at integer multiples of the rotor RPM - 1 per revolution (1/rev) is the rotor RPM, then 2/rev, 3/rev and so on. In addition to the main rotor, other sources of vibration are - the engine/fan system, the main rotor transmission/drive-shaft/gear system, the tail rotor and its transmission system and loose components that are a regular or external part of the aircraft. Examples are out of balance rotor blades, loose tail fins, loose engine shaft mounts, unsecured canopy, landing gear system or external weapons or cargo systems.

As shown in Fig. 10.1, the vibration level is generally low in hover and it increases with higher forward speeds. One encounters large vibration amplitudes at a low forward speed, i.e. at the transition flight speed, and then at very high speeds. Therefore, there are two regimes: low speed flight (transition) and high speed flight, where the vibration levels are critical. The rotor flow field in the first regime is characterized by wake induced loadings in the first and fourth quadrants. The rotor flow field in the second regime is characterized by tip compressibility effects between the first and second quadrants. The mechanisms behind vibratory loads at low speed is the intertwining of tip vortices which lie close to the rotor disk [4]. As the speed increases, the disk tilts forward and the vortex wake is swept away from the disk plane and the wake-induced vibrations become smaller. At still higher speeds, the vibration level starts to increase again. The mechanism of vibratory loads at high speed is the large elastic twist deformation of the rotor blades due to unsteady transonic pitching moments occurring near the blade tips (80% R to tip). The wake has a secondary role at the relatively inboard stations (60%–80% R) [5, 6].

If there is a slight dissimilarity between the blades, there is a likelihood of 1/rev hub forces and moments which can cause a large 1/rev vibration in the airframe. This is the reason that a major effort is made in the rotorcraft industry to manufacture an identical set of blades. Then, whatever small differences of structural and aerodynamic properties for different blades exist, they are covered during the tracking and balancing operations. The dissimilarity of the inertial unbalance is corrected by suitably placing a small balancing weight at the tip of the blade. The aerodynamic dissimilarity is corrected by adjusting the trim tab as well as the pitch link.

The fuselage vibration at any station depends not only on the external loadings but also on the fuselage dynamic characteristics. The fuselage dynamic characteristics are in general coupled with the dynamics of other component structures. For example, the main rotor loads are transmitted to the fuselage via the rotor hub. The fuselage dynamic response feeds back into the blade motions via the hub and pylon assembly.

In addition to dynamic coupling, a significant amount of aerodynamic interference or coupling exists between the main rotor, airframe and tail rotor structures. The flow around the fuselage affect the aerodynamics of the main rotor and the tail rotor. The downwash from the main rotor changes the aerodynamics of the fuselage, tail rotor and horizontal tail and stabilizers. Under certain low speed conditions, the vortex wake from the main rotor impinges directly on the tail boom that gives rise to fuselage vibration at the blade passage frequency.

10.3 Analysis of Helicopter Vibration

For accurate prediction of helicopter vibration at any fuselage station, the following physical mechanisms must be modeled.

1. Structural dynamics of the main rotor with non-linear inertial couplings, moderately large deformations, boundary conditions with multiple load paths, pitch link and damper properties at the root, advanced geometry blades with sweep, droop and pre-twist and rotor-airframe coupling terms.
2. Aerodynamics of the main rotor which accounts for time varying unsteady effects, attached flow, stalled flow, dynamic stall, free or prescribed rotor wake, a lifting-line or lifting-surface model for calculating the blade airloads compatible with airfoil property data.
3. Aerodynamic and structural dynamic model of the airframe or fuselage which includes a tail rotor model, properties of the vertical and horizontal tail and fuselage center of gravity location. A detailed structural model of the flexible fuselage would include rotor-body coupling terms and modeling of rotor hub, pylon, tail boom and other difficult components.
4. Rotor-fuselage aerodynamic interaction effects. The downwash from the rotor and the upwash from the fuselage affect the fuselage and rotor airflows respectively as well as coupling their aerodynamic characteristics.
5. A vehicle trim model using a isolated rotor wind tunnel trim, or a free flight propulsive trim under steady level or steady maneuvering conditions.
6. Computation Fluid Dynamic models can be used to replace - from parts of the aerodynamic modeling of the main rotor, to the full rotor system to the entire rotor-fuselage-tail rotor flow field, depending on the level of details sought, scope of analysis and resources available.
7. Active on-blade components like trailing edge flaps, actuators and blade to blade structural and aerodynamic dissimilarities and damage.

The above models can be combined together to synthesize a comprehensive analysis to predict helicopter performance, airloads, blade loads and fuselage vibration. Detailed modeling of all the above mechanisms are prohibitive in terms of computational and modeling costs and cannot be routinely used for design purposes. Nor is it necessary for preliminary design. Depending on the level of accuracy and type of results sought from the analysis, simplifying assumptions can be made which focuses on the key mechanisms. For example, for calculation of basic rotor performance, blade airloads are more important than rotor-fuselage aerodynamic interactions. For calculation of blade airloads at low thrust conditions, dynamic stall models need not be used. For calculation of bending moments, flexible blade modes are more important than fuselage dynamics. At low speed transition flight, a free wake model is more important than transonic effects. At a high speed, transonic effects are more important than free wake. Thus, if the underlying key mechanisms of a particular flight condition are understood and modeled, reasonably accurate solutions can be obtained from a simplified analysis. In general, for accurate prediction of fuselage vibration at all flight conditions, all the above mechanisms need to be modeled.

10.4 Rotor Vibratory Loads

For accurate prediction of fuselage vibration, the dynamics and aerodynamics of all components - main rotor, airframe, tail rotor etc and their mutual interactions must be modeled accurately. However, the most significant contribution to fuselage vibration is the loads of the main rotor system. Because only the harmonics of the blade passage frequency are dominantly transferred to the fuselage, main rotor loads which generate those harmonics are termed vibratory loads. In addition to the vibratory loads, oscillatory blade loads arising out of blade dynamics are also critical. They are important for the design of blades, control linkages, hub attachments as well as rotor performance.

As discussed above, the dominant contributor to fuselage vibration is the main rotor - the oscillatory loads that are transmitted to the airframe via the rotor hub and pylon assembly. The oscillatory and vibratory blade loads originate due to : (1) unsteady aerodynamic environment and (2) dynamic response of the flexible rotor blades. The dynamic response of the blades are determined by non-linear inertial couplings between flap, lag, elastic torsion and axial degrees of motion, moderately large deformations, large pitch angles required for rotor trim, damper properties, material non-linearities and rotor-fuselage dynamic interactions.

The problem of rotor loads and vibration has been the focus of dynamics research since the beginning of the industry. The aerodynamics of a rotor blade differ from that of a fixed wing due to the following phenomenon.

- Rotor inflow, generated by high RPM of the blades (around 250 for conventional main rotors), necessary for vertical flight.
- Cyclic variation of blade pitch angle, necessary for control.
- Time varying, asymmetric flow in forward flight with large variations of angle of attack in the advancing and retreating sides.
- Enormous compressibility effects including shocks on the advancing side and stalled flow on the retreating side.
- The complex, unsteady wake structure of each blade interacting with following blades.

Because of rotation, the outboard span stations of the blades generate more lift and trail strong tip vortices. The tip vortices are the dominant features of the wake and in general contribute to non-uniform inflow variation around the rotor disk. Unlike airplane wings, these vortices remain in the vicinity of the rotor disk and interact with the following blades.

A fixed wing aircraft uses wings for lift, control surfaces for vehicle control and thrusters for propulsion. On the other hand, in a rotary wing aircraft, the main rotor performs all three functions at the same time. The rotor disk angle is controlled by time varying 1/rev pitch inputs to the blades (using swash-plate). The rotor thrust is controlled by steady pitch input to the blades (collective angle). This generates steady and 1/rev air loads at each blade section which collectively determine the magnitude and orientation of the rotor thrust.

In forward flight, the asymmetric velocity variation around the rotor disk together with cyclic pitch angles and complex inflow distribution generate higher harmonic air loads, 3/rev and higher. For example, a velocity variation of zero and 1/rev creates a zero, 1 and 2/rev variation in the square of velocity, which when multiplied with 1/rev cyclic angles generates zero, 1, 2 and 3/rev airloads. The steady components are used to trim the vehicle, the 1/rev components are required for control, the higher harmonics give rise to rotor vibration. At certain flight conditions, significant higher harmonic air loads are generated creating severe rotor vibration - e.g., tip vortex induced airloads in transition flight, dynamic stall air loads in high thrust flight, unsteady transonic air loads at high speed flights and a combination of all in maneuvering flight.

The long slender rotor blades are highly flexible. As a result significant elastic bending deformations occur in flap, lag and twist in response to airloads. Because they are equi-spaced from one another in azimuth angle, and identical, their aerodynamic loading and structural dynamic response is expected to differ only in phase. And because they are all joined at the hub, the individual blade loads at the hub add up to cancel the non-integral harmonics of blade passage frequency. For example, as mentioned before, in the case of a 4 bladed rotor system like the UH-60A Black Hawk, only steady, 4/rev, 8/rev, 12/rev, i.e., in general pN_b/rev , where p is an integer, are transmitted from the rotor system to the hub. Dissimilarities or damage of the blades make them non-identical and generate non pN_b/rev loads.

For identical blades, only integral harmonics are transmitted. Because of simple trigonometry, the integral blade number harmonics in the fixed hub system are generated by the adjoining harmonics in the rotating blades. Thus, (3/4/5)/rev blade loads in the rotating frame generate 4/rev hub loads in the fixed frame, (7/8/9)/rev blade loads generate 8/rev hub loads and in general $(p+1)N_b$, pN_b , $(p-1)N_b/\text{rev}$ blade loads in the rotating frame generate pN_b/rev hub loads in the fixed frame. All harmonics of blade loads are important for blade design, but only blade passage harmonics (and multiples) and their adjoining harmonics have the potential for hub and fuselage vibration. The large deflection response of the rotor blades feeds back to the air loads which generate time varying aerodynamic stiffness and damping matrices. The damping of the rotor system comes primarily from aerodynamics. The structural response of the rotor blades are therefore aeroelastic in nature and governed by the periodic stiffness, damping and forcing functions. In addition, the moderate to large flap, lag and elastic torsion deformations of the blades form a nonlinear coupled system with complex boundary conditions and multiple load paths at the root.

Accurate prediction of rotor loads is key to advanced rotorcraft design. Attractive and radical low noise, high performance (range and endurance) rotor designs may be evaluated quickly and at low cost using reliable analyses methods. For a reliable analysis, it is necessary to understand and model the physics of structural dynamics and aerodynamics accurately. Such a capability does not exist today (discussed later). Designers rely on costly and time consuming wind tunnel and flight tests. Rotor aeromechanics is at the heart of the helicopter system and any modification in existing design cannot be undertaken unless its impact on blade loads, control loads and vibration are clearly ascertained. Prediction of control loads is important for designing more agile and maneuverable rotor systems. While the peak magnitudes are important for sizing and design of the control system components, the phase of the response is important for implementing control algorithms.

Apart from degraded ride quality, high vibration directly increases maintenance and operating costs because of frequent replacement schedules of critical fatigued components. The maintenance, and direct operating cost of a helicopter is the greatest hindrance toward its becoming a serious

candidate for civilian short haul flight. A helicopter with its unique vertical take off and landing capability offers the most promising solution for reducing airport and air traffic congestion. Vibration is one of the major hindrances to fulfilling this potential.

Smart structure actuated on-blade active control mechanisms show enormous potential for reducing and controlling rotor vibration [7, 8, 9, 10]. The actuator requirements and control limits can be reliably designed and tested, without expensive wind tunnel or flight tests, provided the mechanisms of helicopter vibration are well understood and predicted. Passive vibration reduction techniques, using composite tailoring [11] and structural optimization, can be devised and tested with confidence without expensive wind tunnel tests. A detailed discussion on smart structures technology can be found in Chopra [12].

10.4.1 Periodic Blade Forcing

In forward flight, the blade is exposed to periodic aerodynamic forcing consisting of many harmonics. Consider a simple example of a lift force occurring at a radial station r from the rotation axis.

$$L = \frac{1}{2}\rho V^2 c_a \alpha \quad \text{where } c_l = a\alpha$$

We have for small angles of attack

$$V^2 \approx U_T^2$$

$$\alpha \approx \theta - \frac{U_P}{U_T}$$

The lift force is then

$$L \approx \frac{1}{2}\rho a c (U_T^2 \theta - U_P U_T)$$

In forward flight we have

$$\theta = \theta_C(\psi) + \phi(\psi) = \theta_0 + \theta_{1C} \cos \psi + \theta_{1S} \sin \psi + \phi(\psi)$$

$$U_T = \Omega r + \mu \Omega R \sin \psi$$

$$U_P = \lambda \Omega R + r \dot{\beta} + \mu \beta \Omega R \cos \psi$$

$$\lambda = \lambda_0 + \lambda_{1C} \cos \psi + \lambda_{1S} \sin \psi + \lambda_{2C} \cos 2\psi + \lambda_{2S} \sin 2\psi \dots$$

The general steady state flap and twist responses are given by

$$\beta(\psi) = \beta_0 + \beta_{1C} \cos \psi + \beta_{1S} \sin \psi + \beta_{2C} \cos 2\psi + \beta_{2S} \sin 2\psi + \dots$$

$$\phi(\psi) = \phi_0 + \phi_{1C} \cos \psi + \phi_{1S} \sin \psi + \phi_{2C} \cos 2\psi + \phi_{2S} \sin 2\psi + \dots$$

The lift becomes

$$L = \frac{1}{2}\rho a c [(\Omega r + \mu \Omega R \sin \psi)^2 (\theta_0 + \theta_{1C} \cos \psi + \theta_{1S} \sin \psi + \phi_0 + \phi_{1C} \cos \psi + \phi_{1S} \sin \psi + \dots) - (\lambda_0 \Omega R + \lambda_{1C} \Omega R \cos \psi + \lambda_{1S} \Omega R \sin \psi + \lambda_{2C} \Omega R \cos 2\psi + \lambda_{2S} \Omega R \sin 2\psi + \dots - r \beta_{1C} \sin \psi + r \beta_{1S} \cos \psi - 2r \beta_{2C} \sin 2\psi + \dots) (\Omega r + \mu \Omega R \sin \psi)]$$

Thus

$$L = L(r, \sin \psi, \cos \psi, \sin 2\psi, \cos 2\psi, \sin 3\psi, \cos 3\psi, \sin 4\psi, \cos 4\psi, \dots)$$

Thus, the blade section lift is a function of radial position and consists of many harmonics. In a similar way, the other aerodynamic forces and moments acting on the blade are also periodic and consist of many harmonics. Typically, the magnitude of harmonics higher than 5/rev become smaller and are less important for the prediction of vibration.

10.4.2 Hub Loads in Rotating Frame

The aeroelastic response of the blades are determined using the aerodynamic forcing. The sectional blade loads can then be obtained using either the response (curvature method) or a combination of response and forcing (force summation). The sectional blade loads at the root are called the root loads or reaction forces at the blade root. The root loads can then be transferred to the hub. These are the hub loads in the rotating frame. The hub loads in the rotating frame can be denoted by f_x, f_y, f_z , (shear loads) and m_x, m_y, m_z (moments). For a physical feel, consider the case of a hingeless rotor, or an articulated rotor with zero hinge offset. Then the hub loads in the rotating frame are simply the blade root shears and bending moments

$$f_x(\psi) = s_x = \text{Drag shear load}$$

$$f_y(\psi) = s_r = \text{Radial shear load}$$

$$f_z(\psi) = s_z = \text{Vertical shear load}$$

$$m_x(\psi) = n_f = \text{Flap bending moment}$$

$$m_y(\psi) = n_t = \text{Torsion moment}$$

$$m_z(\psi) = -n_l = - \text{Lag bending moment}$$

Consider the general form of the blade root loads. Let ψ_m denote the azimuthal position of the m -th blade, where $m = 1, 2, \dots, N$. Then, the vertical shear load at the root of the m -th blade can be written as

$$\begin{aligned} s_z^{(m)} &= s_{z_0} + s_{z_{1C}} \cos \psi_m + s_{z_{1S}} \sin \psi_m + s_{z_{2C}} \cos 2\psi_m + s_{z_{2S}} \sin 2\psi_m + \\ &\quad s_{z_{3C}} \cos 3\psi_m + s_{z_{3S}} \sin 3\psi_m + \dots \quad m = 1, 2, \dots, N \\ &= s_{z_0} + \sum_{n=1}^{\infty} (s_{z_{nC}} \cos n\psi_m + s_{z_{nS}} \sin n\psi_m) \end{aligned} \quad (10.1)$$

Similarly the radial shear and drag shear loads can be written as

$$s_r^{(m)} = s_{r_0} + \sum_{n=1}^{\infty} (s_{r_{nC}} \cos n\psi_m + s_{r_{nS}} \sin n\psi_m) \quad m = 1, 2, \dots, N \quad (10.2)$$

$$s_x^{(m)} = s_{x_0} + \sum_{n=1}^{\infty} (s_{x_{nC}} \cos n\psi_m + s_{x_{nS}} \sin n\psi_m) \quad m = 1, 2, \dots, N \quad (10.3)$$

The flap, lag, and torsion moments can be written as

$$n_f^{(m)} = n_{f_0} + \sum_{n=1}^{\infty} (n_{f_{nC}} \cos n\psi_m + n_{f_{nS}} \sin n\psi_m) \quad m = 1, 2, \dots, N \quad (10.4)$$

$$n_l^{(m)} = n_{l_0} + \sum_{n=1}^{\infty} (n_{l_{nC}} \cos n\psi_m + n_{l_{nS}} \sin n\psi_m) \quad m = 1, 2, \dots, N \quad (10.5)$$

$$n_t^{(m)} = n_{t_0} + \sum_{n=1}^{\infty} (n_{t_{nC}} \cos n\psi_m + n_{t_{nS}} \sin n\psi_m) \quad m = 1, 2, \dots, N \quad (10.6)$$

10.4.3 Hub Loads in Fixed Frame

The hub loads in fixed frame are obtained by summation of the loads from all the blades. For a tracked rotor, this procedure cancels out many harmonics of the hub loads in the rotating frame. The hub loads in the fixed frame are

$$\begin{aligned}
 T = \text{Thrust} &= \sum_{m=1}^N s_z^{(m)} \\
 H = \text{Drag force} &= \sum_{m=1}^N (s_r^{(m)} \cos \psi_m + s_x^{(m)} \sin \psi_m) \\
 Y = \text{Side force} &= \sum_{m=1}^N (s_r^{(m)} \sin \psi_m - s_x^{(m)} \cos \psi_m) \\
 M_x = \text{Rolling moment} &= \sum_{m=1}^N n_f^{(m)} \sin \psi_m \\
 M_y = \text{Pitching moment} &= - \sum_{m=1}^N n_f^{(m)} \cos \psi_m \\
 Q = \text{Torque} &= \sum_{m=1}^N n_t^{(m)}
 \end{aligned} \tag{10.7}$$

For a tracked rotor, the thrust becomes

$$\begin{aligned}
 T &= N s_{z_0} + \sum_{m=1}^N \left[\sum_{n=1}^{\infty} (s_{z_{nC}} \cos n\psi_m + s_{z_{nS}} \sin n\psi_m) \right] \\
 &= N s_{z_0} + \sum_{n=1}^{\infty} \left[\sum_{m=1}^N (s_{z_{nC}} \cos n\psi_m + s_{z_{nS}} \sin n\psi_m) \right]
 \end{aligned} \tag{10.8}$$

Using

$$\begin{aligned}
 \frac{1}{N} \sum_{m=1}^N \cos n\psi_m &= f_n \cos n\psi \\
 \frac{1}{N} \sum_{m=1}^N \sin n\psi_m &= f_n \sin n\psi
 \end{aligned} \tag{10.9}$$

where

$$\begin{aligned}
 f_n &= 1 & \text{if } n &= pN \quad p \text{ integer} \\
 f_n &= 0 & \text{otherwise}
 \end{aligned} \tag{10.10}$$

and psi is the azimuthal location of the first blade, the thrust becomes

$$T = N s_{z_0} + N \sum_{p=1}^{\infty} (s_{z_{pNC}} \cos pN\psi_m + s_{z_{pNS}} \sin pN\psi_m) \tag{10.11}$$

The first component is the steady thrust. The other components are all pN/rev harmonics. The rest of the harmonics get cancelled at the hub. Note that the pN -th harmonic of the thrust is

caused by the pN -th harmonic of the blade root shear. Consider the rotor drag force. Again, assume a tracked rotor.

$$\begin{aligned}
 H &= \sum_{m=1}^N \left[s_{r_0} + \sum_{n=1}^{\infty} (s_{r_{nC}} \cos n\psi_m + s_{r_{nS}} \sin n\psi_m) \right] \cos \psi_m \\
 &\quad \sum_{m=1}^N \left[s_{x_0} + \sum_{n=1}^{\infty} (s_{x_{nC}} \cos n\psi_m + s_{x_{nS}} \sin n\psi_m) \right] \sin \psi_m \\
 &= \sum_{m=1}^N [s_{r_0} \cos \psi_m + s_{x_0} \sin \psi_m] + \frac{1}{2} \sum_{m=1}^N \sum_{n=1}^{\infty} \{s_{r_{nC}} [\cos(n+1)\psi_m + \cos(n-1)\psi_m] \\
 &\quad + s_{r_{nS}} [\sin(n+1)\psi_m + \sin(n-1)\psi_m] + s_{x_{nC}} [\sin(n+1)\psi_m - \sin(n-1)\psi_m] \\
 &\quad + s_{x_{nS}} [\cos(n-1)\psi_m - \cos(n+1)\psi_m]\}
 \end{aligned} \tag{10.12}$$

Note that

$$\begin{aligned}
 \sum_{m=1}^N \cos \psi_m &= \sum_{m=1}^N \sin \psi_m = 0 \\
 \frac{1}{N} \sum_{m=1}^N \cos(n+1)\psi_m &= \cos(n+1)\psi, \quad \text{for } n = pN - 1, \quad p \text{ integer} \\
 \frac{1}{N} \sum_{m=1}^N \cos(n-1)\psi_m &= \cos(n-1)\psi, \quad \text{for } n = pN + 1, \quad p \text{ integer}
 \end{aligned}$$

Therefore the following terms can be written as

$$\begin{aligned}
 \sum_{m=1}^N \sum_{n=1}^{\infty} s_{r_{nC}} \cos(n+1)\psi_m &= \sum_{n=1}^{\infty} \sum_{m=1}^N s_{r_{nC}} \cos(n+1)\psi_m = \sum_{n=1}^{\infty} N s_{r_{(pN-1)C}} \cos pN\psi \\
 \sum_{m=1}^N \sum_{n=1}^{\infty} s_{r_{nC}} \cos(n-1)\psi_m &= \sum_{n=1}^{\infty} \sum_{m=1}^N s_{r_{nC}} \cos(n-1)\psi_m = \sum_{n=1}^{\infty} N s_{r_{(pN+1)C}} \cos pN\psi
 \end{aligned}$$

The final expression for rotor drag then becomes

$$\begin{aligned}
 H &= \frac{N}{2} \sum_{p=1}^{\infty} \left[(s_{r_{(pN-1)C}} - s_{x_{(pN-1)S}}) \cos pN\psi + (s_{r_{(pN-1)S}} + s_{x_{(pN-1)C}}) \sin pN\psi \right] \\
 &\quad \frac{N}{2} \sum_{p=1}^{\infty} \left[(s_{r_{(pN+1)C}} + s_{x_{(pN+1)S}}) \cos pN\psi + (s_{r_{(pN+1)S}} - s_{x_{(pN+1)C}}) \sin pN\psi \right]
 \end{aligned} \tag{10.13}$$

Similarly the side force is

$$\begin{aligned}
 Y &= \frac{N}{2} \sum_{p=1}^{\infty} \left[- (s_{r_{(pN-1)S}} + s_{x_{(pN-1)C}}) \cos pN\psi + (s_{r_{(pN-1)C}} - s_{x_{(pN-1)S}}) \sin pN\psi \right] \\
 &\quad + \frac{N}{2} \sum_{p=1}^{\infty} \left[(s_{r_{(pN+1)S}} - s_{x_{(pN+1)C}}) \cos pN\psi - (s_{r_{(pN+1)C}} + s_{x_{(pN+1)S}}) \sin pN\psi \right]
 \end{aligned} \tag{10.14}$$

Again, the inplane hub loads H and Y consists of harmonics which are multiples of N/rev . Note that unlike the thrust T , the pN/rev harmonics here are caused by the $pN + 1$ and $pN - 1/\text{rev}$

harmonics of blade inplane shears in the rotating frame. The hub roll moment is

$$\begin{aligned}
 M_x &= \sum_{m=1}^N \left[n_{f_0} + \sum_{n=1}^{\infty} (n_{f_{nC}} \cos n\psi_m + n_{f_{nS}} \sin n\psi_m) \right] \sin \psi_m \\
 &= \sum_{m=1}^N n_{f_0} \sin \psi_m + \frac{1}{2} \sum_{m=1}^N \sum_{n=1}^{\infty} \{ n_{f_{nC}} [\sin(n+1)\psi_m - \sin(n-1)\psi_m] \\
 &\quad + n_{f_{nS}} [\cos(n-1)\psi_m - \cos(n+1)\psi_m] \} \\
 &= \frac{N}{2} \sum_{p=1}^{\infty} \left[-n_{f_{(pN-1)C}} \sin pN\psi - n_{f_{(pN-1)S}} \cos pN\psi \right] \\
 &\quad + \frac{N}{2} \sum_{p=1}^{\infty} \left[-n_{f_{(pN+1)C}} \sin pN\psi + n_{f_{(pN+1)S}} \cos pN\psi \right]
 \end{aligned} \tag{10.15}$$

Similarly the hub pitch moment is

$$\begin{aligned}
 M_y &= -\frac{N}{2} \sum_{p=1}^{\infty} \left[n_{f_{(pN-1)C}} \cos pN\psi + n_{f_{(pN-1)S}} \sin pN\psi \right] \\
 &\quad - \frac{N}{2} \sum_{p=1}^{\infty} \left[n_{f_{(pN+1)C}} \cos pN\psi + n_{f_{(pN+1)S}} \sin pN\psi \right]
 \end{aligned} \tag{10.16}$$

Thus the pN/rev harmonics of the rotor roll and pitch moments are caused by the $pN+1$ and $pN-1/\text{rev}$ harmonics of the flap bending moments. The hub loads in the fixed frame for 2, 3, and 4 bladed rotors are summarized in the following tables.

Table 10.1: Vertical Loads Transmitted by Blades to Hub

Vertical Shear at Blade Root s_z Harmonics	Hub Load T in Fixed Frame		
	2-Bladed Rotor	3-Bladed Rotor	4-Bladed Rotor
s_{z_0}	$2s_{z_0}$	$3s_{z_0}$	$4s_{z_0}$
$s_{z_{1c}} \cos \psi_m$	0	0	0
$s_{z_{1s}} \sin \psi_m$	0	0	0
$s_{z_{2c}} \cos 2\psi_m$	$2s_{z_{2c}} \cos 2\psi$	0	0
$s_{z_{2s}} \sin 2\psi_m$	$2s_{z_{2s}} \sin 2\psi$	0	0
$s_{z_{3c}} \cos 3\psi_m$	0	$2s_{z_{3c}} \cos 3\psi$	0
$s_{z_{3s}} \sin 3\psi_m$	0	$2s_{z_{3s}} \sin 3\psi$	0
$s_{z_{4c}} \cos 4\psi_m$	$2s_{z_{4c}} \cos 4\psi$	0	$4s_{z_{4c}} \cos 4\psi$
$s_{z_{4s}} \sin 4\psi_m$	$2s_{z_{4s}} \sin 4\psi$	0	$4s_{z_{4s}} \sin 4\psi$
$s_{z_{5c}} \cos 5\psi_m$	0	0	0
$s_{z_{5s}} \sin 5\psi_m$	0	0	0
$s_{z_{6c}} \cos 6\psi_m$	$2s_{z_{6c}} \cos 6\psi$	$3s_{z_{6c}} \cos 6\psi$	0
$s_{z_{6s}} \sin 6\psi_m$	$2s_{z_{6s}} \sin 6\psi$	$3s_{z_{6s}} \sin 6\psi$	0

10.5 Vibration Control

For purposes of a simple illustration the helicopter can be thought of as a system of springs, dampers and masses connected to each other, which are being forced by external vibratory forces. There

are many natural frequencies and so one expects a complex response. If we can assume that all the blades are identical, structurally and aerodynamically (a tracked rotor case), then the vibration in the fixed system is simplified. The periodic blade loads in the rotating system are transmitted to the body in the fixed frame at a dominant frequency of $N\Omega$ rad/s, where N is the number of blades and Ω is the rotational speed. Sometimes, the higher multiple harmonics of this frequency, $2N\Omega$ and $3N\Omega$, are also important. The rotor acts as a big filter and transmits only pN /rev harmonics to the body, where p is an integer, and all other harmonics cancel themselves at the rotor hub.

The pN hub vertical force and yaw moment (torque) in the fixed frame are caused by vertical shear and lag moments in the rotating system at the same frequency (pN /rev). This is because the excitation forces are symmetric and there is no change of frequency due to the transformation from one frame to another reference frame. However, the pN /rev inplane hub forces and pitch and roll moments in the fixed frame are caused by the blade oscillatory lag shear and flapwise moments at two frequencies of $pN \pm 1$ /rev in the rotating frame. This makes vibration reduction easier since only selected harmonics are to be suppressed.

There are two methods to reduce vibration.

1. Design Process
2. Suppression Devices

In the Design Process, the structural and aerodynamic characteristics of the blade are tailored to achieve reduction in vibration. This requires an optimization procedure during during. The key parameters like disk loading, tip speed, solidity and blade chord are not designed based on vibration requirements, but they influence vibration. The selection of other parameters like blade twist and tip shape can be made to reduce vibration. An important requirement is to avoid resonances with excitation harmonics. But suitable use of composite materials and application of structural optimization techniques on the blade and blade, vibration can be reduced by a significant amount.

The Suppression Devices can be of many types. Broadly, they are classified into two categories:

1. Passive control devices
2. Active control devices

In passive control devices the vibration source is either isolated or diffused. When the vibration source is isolated the device is called an isolator. When the vibration source is diffused the device is called an absorber. Passive devices are tuned to a particular flight condition. In general, they incur a large weight penalty. About 70% reduction of vibration is possible with a passive device at the tuned frequency.

In active control devices the vibration source is suppressed. Compared to passive devices, active devices can be tuned in flight, and can easily target multiple frequencies. The weight penalty is less than passive devices. More than 90% reduction in vibration is possible with a passive device.

10.6 Passive Vibration Control

10.6.1 Vibration Isolators

Vibration isolators are often used to reduce helicopter vibration. Isolating materials are pads of rubber, cork or felt, or metalli springs. These are placed between the vibrating system and its supporting structure. All of these materials possess damping as well as elastic properties and can be effective in reducing the maximum transmitted force from the vibrating system to the support. It is not uncommon to use a soft mounting of the rotor and transmission to the airframe. However one has to be careful with the soft mounting, in particular with articulated rotors, in order not to seriously impair the ground resonance instability.

10.6.2 Vibration Absorbers

Dynamic absorbers are used to reduce vibration in helicopters. In its simplest form, a dynamic absorber is a single-degree-of-freedom spring-mass system that is added to a structure whose vibration needs to be reduced. For example, consider a mass M attached to a foundation by a spring k vibrating in response to a force $F \sin \omega t$ applied on the mass. See Fig. 10.2. By itself, the support reaction at the foundation would be $R = F \sin \omega t$.

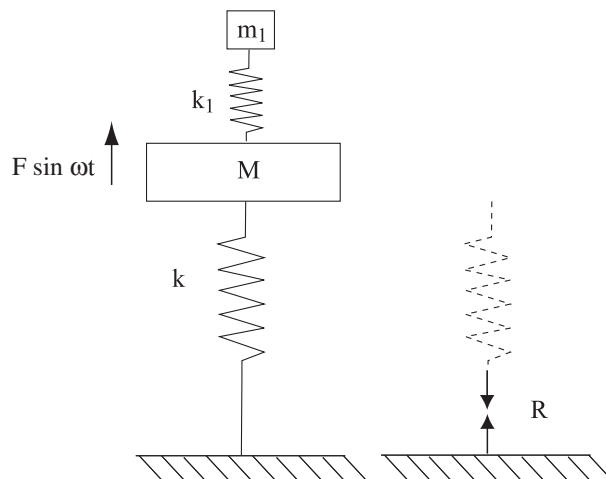


Figure 10.2: A simple two degree of freedom spring-mass vibration absorber

The support reaction can be reduced to zero, $R = 0$, by the following method. Attach an auxiliary single-degree-of-freedom spring-mass system of mass m_1 and stiffness k_1 to the existing structure such that

$$\sqrt{\frac{k_1}{m_1}} = \omega$$

The amplitude of vibration of M now becomes zero. The absorber is effective when the excitation frequency is fixed. Sometimes a damper is introduced. This is called the damped dynamic absorber. In the case of a helicopter, a dynamic absorber can be installed on the body tuned to the troublesome frequency, say N/rev . If the design is perfect and the frequency is fixed, the auxiliary mass vibrates to add to the support structure an oscillating force that is equal and opposite to the force that is causing the vibration.

The best design is not to use any extra weight for vibration absorbers. Sikorsky has used batteries and Bell has developed the Node-Matic system that uses transmissions as the moving weight.

10.6.3 Bifilar Pendulum absorber

An example of the dynamic absorber is a simple or bifilar pendulum mounted on each rotor blade near the hub. Typically it is a spherical ball of small mass compared to the blade mass and is mounted on a cantilevered beam. It is tuned to a particular frequency and acts as a dynamic absorber.

Sikorsky has successfully applied a bifilar pendulum to its 4-bladed helicopters (S-76, S-92, UH-60 series), tuned to two frequencies, $3/\text{rev}$ and $5/\text{rev}$ in the inplane direction. See Fig. 10.3. The S-92 has four heavy pendulum masses that oscillate at small amplitudes. F is the force produced by opposing bifilar masses at one instant in time. This force rotates in the direction of rotor rotation at $N - 1/\text{rev}$.

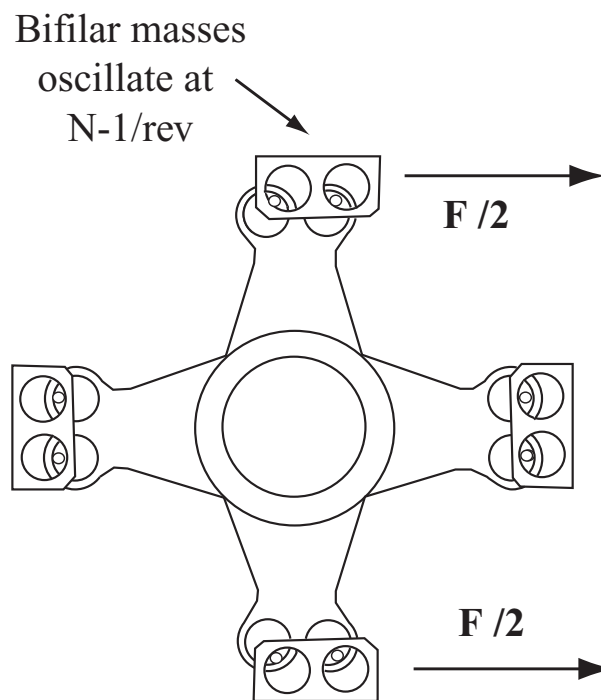


Figure 10.3: Bifilar pendulum of the S-92 helicopter

10.7 Active Vibration Control

In active vibration control the vibration is suppressed by eliminating the prime source of excitation – the unsteady aerodynamic forces on the blades. The primary components of an active vibration suppression system are:

1. Acceleration transducers that sense the vibratory response of the fuselage.
2. A actuator system to implement the control algorithm.
3. A flightworthy micro-computer, which incorporates the algorithm for suppressing vibration.
4. A signal conditioning system, i.e. an electronic control unit, which interfaces between the sensors, the computer, and the actuators.

10.7.1 Multicyclic Vibration Control or Higher Harmonic Control (HHC)

In Higher Harmonic Control (HHC) the entire blade is excited at higher harmonics of rotational speed ($2/\text{rev}$ and higher) in addition to the $1/\text{rev}$ control inputs. The unsteady airloads are changed to cancel the existing troublesome harmonics. The net effect is that the existing airloads at higher frequencies are reduced with little effect on the basic rotor performance.

Many options of implementation of higher harmonic control of different types of rotors have been considered. The most common one is full blade feathering at the root. In addition to vibration reduction, the application of HHC can be used for blade stress reduction, for improved performance by delaying the onset of retreating blade stall, and for gust load alleviation.

Both, small scale and full scale models have been tested in the wind tunnel for HHC of vibration. McDonnell Douglas Helicopters (formerly Hughes, now Boeing, Mesa) has successfully applied HHC on the OH-6 helicopter and demonstrated the concept through flight testing of the aircraft. For the modified OH-6A, higher harmonic blade pitch control was achieved by superimposing $4/\text{rev}$

swashplate motion on top of the basic collective and cyclic control inputs. Consider a swashplate lateral tilt of ϕ_X . The pitch link is attached to the swashplate at a radial distance of r_p . It is ahead of the blade azimuth by an angle α_p . If the blade is at an azimuth ψ the vertical displacement of the pitch link is

$$d = \phi_X r_p \sin(\psi + \alpha_p)$$

If the pitch horn length is a_p , then assuming a straight pitch link, the blade root angle is given by

$$\sin \theta = \left(\frac{\phi_X r_p}{a_p} \right) \sin(\psi + \alpha_p)$$

Similarly for a swashplate longitudinal tilt of ϕ_Y , the blade root angle is given by

$$\sin \theta = - \left(\frac{\phi_Y r_p}{a_p} \right) \cos(\psi + \alpha_p)$$

When both ϕ_X and ϕ_Y are prescribed, we have assuming a small θ ,

$$\theta(\psi) = \left(\frac{\phi_X r_p}{a_p} \right) \sin(\psi + \alpha_p) - \left(\frac{\phi_Y r_p}{a_p} \right) \cos(\psi + \alpha_p)$$

In addition to longitudinal and lateral tilts, a vertical displacement Z can be prescribed. Thus in general the swashplate displacement and tilts are related to the blade root pitch angle by

$$\theta(\psi) = Z + \left(\frac{\phi_X r_p}{a_p} \right) \sin(\psi + \alpha_p) - \left(\frac{\phi_Y r_p}{a_p} \right) \cos(\psi + \alpha_p)$$

A special case is when the pitch link is attached 90° ahead of the blade, i.e. $\alpha_p = \pi/2$. Then

$$\theta(\psi) = Z + \left(\frac{\phi_X r_p}{a_p} \right) \cos \psi + \left(\frac{\phi_Y r_p}{a_p} \right) \sin \psi$$

First, constant values of swashplate tilt introduces 1/rev cyclic inputs at the blade root. Second, N /rev harmonics of swashplate tilt introduces $N \pm 1$ /rev harmonics of cyclic inputs. Third, a vertical displacement get transferred to the blades directly as a collective input. Thus, perturbing the swashplate at 4/rev both collectively (in Z) and in pitch (ϕ_Y) and roll (ϕ_X) results in 3, 4, and 5/rev blade feathering in the rotating system. The main rotor rotational speed for the OH-6A is 8 Hz. Thus a 4/rev input is 32 Hz. The pitch, roll, and collective motion of the stationary swashplate at this frequency was provided by three electro-hydraulic high frequency servo-actuators. The three actuators were installed in the stationary system where they replaced the conventional rod-end links between the control mixer and the stationary swashplate.

Generally, the helicopter model is expressed in the frequency domain through a transfer function relating the input harmonics to the output response harmonics. Different control concepts have been tried to implement the higher harmonic controls. A complete discussion on these controllers can be found in Chopra and McCloud [13].

HHC model testing in wind tunnel have been performed by McCloud (71,78), Sissingh (75), Shaw (75,80,85), Hammond (78), Lehmann (85). HHC flight testing have been reported in Bell (62), U.S.Army-McDonnell Douglas (82), Sikorsky (86), Aerospatiale (86). Numerical simulations mostly have been limited to unstalled conditions.

10.7.2 Control Algorithms

Different control algorithms have been implemented for HHC of helicopter vibration. In order to implement the algorithms a helicopter model is required. The model relates the HHC inputs to the vibration. One simple linear quasi-static frequency-domain representation of the helicopter is given below. Here, Z is the response vector, Θ is the multi-cyclic input vector, T is the transfer function which relate the two, and Z_0 is the uncontrolled response vector. Also added is the measurement noise v which is random in nature.

$$Z = Z_0 + T\Theta + v \tag{10.17}$$

A pictorial representation is given in Fig. 10.4. The vibrations Z , Z_0 and the control inputs Θ can be in the rotating or fixed frame. T and Z_0 depend on flight conditions. For example, Z can be a vector of 12 components (dimension 12×1) consisting of the sine and cosine harmonics of the six 4/rev vibratory hub loads in the fixed frame. The input vector Θ can be a vector of 6 components (dimension 6×1) consisting of the sine and cosine components of the 3, 4, and 5/rev multi-cyclic root pitch inputs in the rotating frame. The transfer matrix T then has a dimension of (12×6) . The measurement noise v is assumed to be Gaussian white noise with zero mean that has a variance or noise level defined by

$$E(v_n v_i) = r_n \delta_{ni}$$

The r_n represents measurement noise and is based on sensor accuracy. A meaningful value can be assigned to r_n . The above representation of the helicopter can be cast into two types of models: (i)

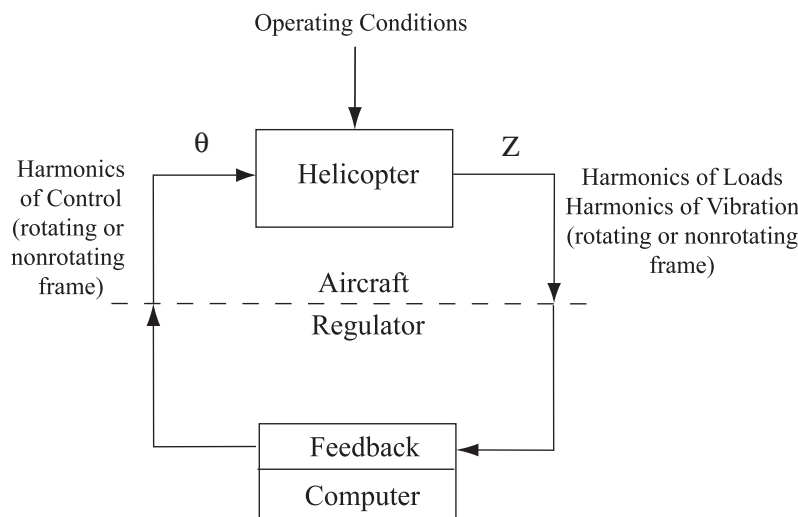


Figure 10.4: Multicyclic Control of Helicopter Vibration

a global model and (ii) a local model. The global model is linear over the entire range or duration of control. At any time step n we have

$$Z_n = Z_0 + T\Theta_n + v \tag{10.18}$$

The local model is linear only about a current control value

$$Z_n = Z_{n-1} + T_{n-1} (\Theta_n - \Theta_{n-1}) + v \tag{10.19}$$

Thus the local model is applicable even for nonlinear conditions. The T -matrix is linearized about the current control value and the range of $\Delta\Theta_n = \Theta_n - \Theta_{n-1}$ is assumed small. The current time t_n is given by

$$t_n = n\Delta t$$

where Δt is assumed to be long enough so that the transients have died down. This is typically about one or two rotor revolutions. Before the HHC control algorithms can be implemented, the model characteristics, Z_0 and T must be estimated. This estimation can be performed using flight test data, wind tunnel data, or from a mathematical model e.g. a comprehensive analysis. The procedure is called model identification.

The different control algorithms implemented for HHC were classified by Johnson [14]. From the simplest to the most refined they are as follows.

1. **Open-loop, off-line:** Model behavior (i.e., Z_0 and T) is identified off-line. The inputs (i.e., Θ) are based on uncontrolled vibration (i.e., Z_0).
2. **Closed-loop, off-line:** Model behavior is identified off-line. The inputs are based on measured vibration.
3. **Open-loop, adaptive:** Model behavior is identified on-line. There are two categories: (i) only the uncontrolled vibration Z_0 is identified on-line, and (ii) both Z_0 and the transfer matrix T is identified on-line. Both the categories involve feedback loops. The inputs are however still based on the identified uncontrolled vibration. Hence this is still termed open-loop.
4. **Closed-loop, adaptive:** Model behavior is identified online. The inputs are based on measured vibration.

For the off-line identification algorithms (the first two items given above) the characteristics of the multicyclic control system, Z_0 and T are assumed invariant with time. They are identified at the start and the control gains are fixed. Thus, this identification is applicable only to a global model. For the on-line identification algorithms, the characteristics of the control system are continuously updated with time; the control gains also vary with time. Thus this identification is applicable to both global and local models. In case of the local model, the T -matrix need to be identified for each and every time cycle. The meaning of open-loop control is that the inputs Θ_n depend only on the uncontrolled vibration level, Z_0 . For closed-loop control Θ_n depend on the measured vibration level of the previous time cycle, Z_{n-1} .

In this section, we assume a deterministic controller i.e., the properties of the model are known. In this case, for optimal control, the dependance, which relates the control inputs to the vibration levels, is based on the minimization of a performance function.

$$J = Z_n^T W_Z Z_n + \Theta_n^T W_\Theta \Theta_n + \Delta \Theta_n^T W_{\Delta\Theta} \Delta \Theta_n \quad (10.20)$$

where W_Z , W_Θ , and $W_{\Delta\Theta}$ are the weighting matrices for response, pitch controls, and the pitch control rates. Typically, these are diagonal matrices. The first term controls the vibration. Setting any of the diagonal entrees to zero unconstrains that component of vibration. The diagonal entrees can be selected differently to introduce different weights to different components of vibration depending on their severity. The second term controls the inputs, e.g. constrains the actuator displacement. The third term controls the control rate and reduces large transients. For optimal control inputs the performance function J is minimized, which means

$$\frac{\partial J}{\partial \Theta_n} = 0 \quad \text{for each component of } \Theta_n$$

Assume that equal weight is given to all loads, i.e. $W_Z = I$, and the control inputs are unconstrained, i.e. $W_\Theta = 0$. The optimization result can be put in one of the following two forms

$$\begin{aligned} \Theta_n &= \Theta_{n-1} + CZ_{n-1} \quad \text{used in closed loop control} \\ \Theta_n &= CZ_0 + C_{\Delta\Theta} \Theta_{n-1} \quad \text{used in open loop control} \end{aligned} \quad (10.21)$$

where

$$C = -DT^T W_Z \quad (10.22)$$

$$C_{\Delta\Theta} = DW_{\Delta\Theta} \quad (10.23)$$

$$D = (T^T W_Z T + W_{\Delta\Theta})^{-1} \quad (10.24)$$

$W_{\Delta\Theta}$ does not affect the steady-state solution but affects the convergence time due to control sluggishness. The gain matrix C depends on the transfer matrix T . For on-line identification, T is updated continuously and hence C is updated continuously. In open-loop control Θ_n depends on Z_0 and T (via C), not Z_{n-1} , hence the name open-loop. But Z_0 and T can be identified at time n using Z_{n-1} . Then the system is called open-loop adaptive system. Note that it is a feedback system but as the inputs do not depend directly on Z_{n-1} it is classified as open loop.

In the next sections methods by which the control parameters of the system can be identified are described. The following symbols will be used.

T, Z_0 : Actual helicopter characteristics

\hat{T}, \hat{Z}_0 : Estimated or identified helicopter characteristics

10.7.3 Off-line Identification

For off-line identification, a set of input-output measurements are used with a least-squared-error method. The off-line identification is useful not only for control algorithms which use this method, but also for control algorithms which use on-line identification. In the latter case, a good off-line estimate of initial rotor characteristics are important for stabilizing the system, reduce transients, and faster convergence. Consider the following dimensions

$Z : j \times 1$ for example $j = 12$

$Z_0 : j \times 1$ same dimension as Z

$\Theta : m \times 1$ for example $m = 6$

$T : j \times m$ for example 12×6

The measurement noise v introduced in the output harmonics (eqn. 10.17) is assumed to be random with a Gaussian distribution. They are identified by their mean and standard deviation. Θ is assumed to contain no noise. For off-line identification, both T and Z_0 can be estimated simultaneously. Alternatively, Z_0 can be obtained directly by setting $\Theta = 0$. Then identify only the T matrix. For a set of N control inputs, independent of each other, the T matrix is identified by the least-squared-error method as

$$T = Z\Theta^T (\Theta\Theta^T)^{-1} \quad (10.25)$$

Θ here consists of N columns of independent control inputs. Z consists of N columns of output vibration. Thus

$Z : j \times N$ for example $12 \times N$

$\Theta : m \times N$ for example $6 \times N$

The minimum number of measurements N necessary is same as the dimension of input harmonics, m . For a good estimate typically N is two or three times this value.

10.7.4 On-line Identification

For on-line identification, the model characteristics are continuously updated with time, using a Kalman filter estimation [17]. The reason for using a Kalman-filter is as follows. Let us say there are 6 control inputs, i.e. $m = 6$, and 12 vibration measurements, i.e. $j = 12$. Then the T matrix has $j \times m = 12 \times 6$ entries. At a given time n we have only 12 measurements. Thus the number of unknowns is greater than equations. Through the Kalman filter, the T matrix is divided into 12 states (instead of 12×6 entries); a prior estimation of the state is made at the time of measurement and then the estimation of the state is updated using the current measurement. This is the basic idea of a Kalman filter, the combining of the previous estimate with the current measurement based on the relative accuracy of the two quantities, to refine the estimate of unknowns which are greater in number than the number of equations.

For purposes of notation let each row of T be organized into a column vector denoted by t_j . A typical form of the j -th measurement Z_j is then

$$Z_j = \Theta^T t_j + v_j$$

$$Z_j : 1 \times 1$$

$$\Theta_T : 1 \times m$$

$$t_j : m \times 1$$

To denote that the j -th measurement is taken at time n the above can be re-written as

$$Z_{jn} = \Theta^T t_{jn} + v_{jn}$$

The actual form depends on whether Z_0 is being identified and whether the global or local model is being used. For convenience, drop j , and write the j -th measurement of Z at time n as

$$Z_n = \Theta^T t_n + v_n \quad j\text{-th measurement of } Z$$

The variation of t is assumed to follow

$$t_{n+1} = t_n + u_n$$

where u is the process noise. The process noise u is assumed to be Gaussian white noise with zero mean that has a variance or noise level defined by

$$E(u_n u_i) = Q_n \delta_{ni}$$

The elements of Q represent the variation of the actual t from the estimated one. For changing flight conditions, Q can be large. A large value of Q can cause convergence problems. Thus, while the measurement noise level r is relatively easy to assign, Q is difficult to assign. An acceptable value can be found using trial and error based on the quality of estimation that results. Assume that we have an estimate of t (i.e. t_j , the j -th row of the transfer matrix T) at the $(n-1)$ -th cycle. Now want a new estimate of t based on the current measurements made in the n -th cycle. The Kalman filter gives a minimum-error variance solution

$$\hat{t}_n = \hat{t}_{n-1} + K_n (Z_n - \Theta_n^T \hat{t}_{n-1}) \tag{10.26}$$

$$\hat{t}_n, \hat{t}_{n-1} : m \times 1$$

$$K_n : m \times 1$$

$$Z_n - \Theta_n^T \hat{t}_{n-1} : 1 \times 1$$

where

$$\begin{aligned} K_n &= \frac{P_n \Theta_n}{r_n} \\ P_n &= M_n - \frac{M_n \Theta_n \Theta_n^T M_n}{r_n + \Theta_n^T M_n \Theta_n} \\ M_n &= P_{n-1} + Q_{n-1} \end{aligned} \quad (10.27)$$

M_n is the covariance of error in the estimate of t_n before measurement. P_n is the covariance of error in the estimate of t_n after measurement. To simplify calculations, it is possible to assume Q and r do not vary with time. Also, Q , r and P_0 can be assumed to be proportional to the same function f_j , where j represents the measurement. This results in

$$P_{jn} = f_j P_n \quad \text{and} \quad M_{jn} = f_j M_n$$

where P_n is a function of time and f_j is a function of measurement. The Kalman gain matrix is same for all measurements. Assume that the ratio Q_{jn}/r_{jn} is the same for every measurement. Then the Kalman state equations put together gives

$$\hat{T}_n = \hat{T}_{n-1} + \left(Z_n - \hat{T}_{n-1} \Theta_n \right) K_n^T \quad (10.28)$$

Note that P_n and K_n are calculated only once during each time cycle. The entire matrix T_n is then identified in a single step, a big reduction in computation time.

10.7.5 Open-Loop Off-Line Control

T and Z_0 are identified off-line. The weighting function for input rates $W_{\Delta\Theta}$ must be zero. The optimal control solution is

$$\Theta = C \hat{Z}_0 \quad (10.29)$$

When implemented gradually in n cycles, $n = 1, 2, \dots, N$, it becomes

$$\Theta_n = \frac{n}{N} C \hat{Z}_0 \quad (10.30)$$

10.7.6 Closed-Loop Off-Line Control

The model characteristics are identified initially and assumed invariant. This controller is applicable only to a global model. The optimal control solution is

$$\Theta_n = \Theta_{n-1} + C Z_{n-1} \quad (10.31)$$

Substitute

$$Z_{n-1} = Z_0 + T \Theta_{n-1} + v_{n-1}$$

to obtain

$$\Theta_n = D \left[\hat{T}^T \left(\hat{T} - T \right) + W_{\Delta\Theta} \right] \Theta_{n-1} - D \hat{T}^T \left(Z_0 + v_{n-1} \right) \quad (10.32)$$

where

$$D = \left(\hat{T}^T W_Z \hat{T} + W_{\Delta\Theta} \right)^{-1} \quad (10.33)$$

The stability of the closed system is determined by the eigenvalues of

$$D \left[\hat{T}^T \left(\hat{T} - T \right) + W_{\Delta\Theta} \right]$$

10.7.7 Open-Loop On-Line Control

The model characteristics are continuously updated with time. The open-loop on-line (i.e., adaptive) controllers are classified according to the parameter being identified. There are two types: (i) Z_0 is identified on-line; T is identified off-line initially and assumed invariant, and (ii) both Z_0 and T are identified on-line. Both require an initial transfer function T .

On-Line Identification of Z_0 only

The Kalman estimate of Z_0 is

$$\hat{Z}_{0n} = \hat{Z}_{0n-1} + \left(Z_n - \hat{T}\Theta_n - \hat{Z}_{0n-1} \right) K_n \quad (10.34)$$

where K_n is determined as follows

$$M_n = P_{n-1} + Q \quad (10.35)$$

$$P_n = rM_n / (r + M_n) \quad (10.36)$$

$$K_n = M_n / (r + M_n) \quad (10.37)$$

Note that P_n and M_n are simply scalars in this case. The optimal controls are

$$\Theta_n = C\hat{Z}_{0n-1} + C_{\Delta\Theta}\Theta_{n-1} \quad (10.38)$$

where C and $C_{\Delta\Theta}$ are feedback gains fixed with time. The vibration response is

$$Z_n = Z_0 + T\Theta_n + v_n$$

where T and Z_0 are the true model characteristics. The estimation and control equations can be combined to obtain

$$\begin{bmatrix} I & 0 \\ (\hat{T} - T)K_n & I \end{bmatrix} \begin{Bmatrix} \Theta_n \\ Z_{0n} \end{Bmatrix} = \begin{bmatrix} C_{\Delta\Theta} & C \\ 0 & (I - K_n)I \end{bmatrix} \begin{Bmatrix} \Theta_{n-1} \\ Z_{0n-1} \end{Bmatrix} + \begin{Bmatrix} 0 \\ (Z_0 + v_n)K_n \end{Bmatrix} \quad (10.39)$$

The stability of the system is determined by the eigenvalues of

$$\begin{bmatrix} I & 0 \\ (\hat{T} - T)K_n & I \end{bmatrix}^{-1} \begin{bmatrix} C_{\Delta\Theta} & C \\ 0 & (I - K_n)I \end{bmatrix}$$

On-Line Identification of T and Z_0

Here both T and Z_0 are identified continuously with time-cycles using a Kalman-filer estimation. This is therefore more suitable for varying flight conditions than the first case where only Z_0 is identified. The Kalman estimation is

$$\begin{bmatrix} \hat{T}_n \\ \hat{Z}_{0n} \end{bmatrix} = \begin{bmatrix} \hat{T}_{n-1} \\ \hat{Z}_{0n-1} \end{bmatrix} + \begin{bmatrix} K_n \\ Kz_n \end{bmatrix} \left(Z_n - \hat{Z}_{0n-1} - \hat{T}_{n-1}\Theta_n \right) \quad (10.40)$$

where K_n is determined as follows

$$M_n = P_{n-1} + Q_{n-1} \quad (10.41)$$

$$P_n = M_n - \frac{M_n \begin{bmatrix} \Theta_n \\ 1 \end{bmatrix} (\Theta_n^T I) M_n}{[r_n + (\Theta_n^T I) M_n] \begin{bmatrix} \Theta_n \\ 1 \end{bmatrix}} \quad (10.42)$$

$$K_n = \frac{P_n \begin{bmatrix} \Theta_n \\ 1 \end{bmatrix}}{r_n} \quad (10.43)$$

The optimal controls are same as before

$$\Theta_n = C\hat{Z}_{0n-1} + C_{\Delta\Theta}\Theta_{n-1} \quad (10.44)$$

except that the feedback gains, C and $C_{\Delta\Theta}$, are now continuously updated with time.

10.7.8 Closed-Loop On-Line Control

The model characteristics are updated continuously with time. The controller may use both global and local models.

Global Model

The controller here is similar to the open-loop adaptive case with on-line identification of both T and Z_0 , except that here the control inputs are based on the measured response, not the estimated uncontrolled response.

$$\Theta_n = \Theta_{n-1} + CZ_{n-1} \quad (10.45)$$

Local Model

This controller is applicable even to a nonlinear model. The transfer function T is assumed linear about the current control inputs. The control inputs are based on the measured response.

$$\Delta\Theta_n = CZ_{n-1} \quad (10.46)$$

where $\Delta\Theta_n = \Theta_n - \Theta_{n-1}$. The feedback gain C gets updated with time via T . The Kalman estimation of T is given by

$$\hat{T}_n = \hat{T}_{n-1} + \left(\Delta Z_n - \hat{T}_{n-1} \Delta\Theta_n \right) K_n^T \quad (10.47)$$

where we have

$$\Delta Z_n = Z_n - Z_{n-1} \quad (10.48)$$

$$M_n = P_{n-1} + Q_{n-1} \quad (10.49)$$

$$P_n = M_n - \frac{M_n \Delta\Theta_n \Delta\Theta_n^T M_n}{r_n + \Delta\Theta_n^T M_n \Delta\Theta_n} \quad (10.50)$$

$$K_n = \frac{P_n \Delta\Theta_n}{r_n} \quad (10.51)$$

Table 10.2: Longitudinal Hub Load H Transmitted by Blades to Hub

Drag Shear at Blade Root Harmonics s_x	Radial Shear at Blade Root Harmonics s_r	Hub Load H in Fixed Frame		
		2-Bladed Rotor	3-Bladed Rotor	4-Bladed Rotor
s_{x_0}	s_{r_0}	0	0	0
$s_{x_{1c}} \cos \psi_m$	$s_{r_{1c}} \cos \psi_m$	$s_{r_{1c}} + s_{x_{1c}} \sin 2\psi + s_{r_{1c}} \cos 2\psi$	$(3/2)s_{r_{1c}}$	$2s_{r_{1c}}$
$s_{x_{1s}} \sin \psi_m$	$s_{r_{1s}} \sin \psi_m$	$s_{x_{1c}} - s_{x_{1s}} \cos 2\psi + s_{r_{1s}} \sin 2\psi$	$(3/2)s_{x_{1c}}$	$2s_{x_{1c}}$
$s_{x_{2c}} \cos 2\psi_m$	$s_{r_{2c}} \cos 2\psi_m$	0	$(3/2)s_{x_{2c}} \sin 3\psi + (3/2)s_{r_{2c}} \cos 3\psi$	0
$s_{x_{2s}} \sin 2\psi_m$	$s_{r_{2s}} \sin 2\psi_m$	0	$-(3/2)s_{x_{2s}} \cos 3\psi + (3/2)s_{r_{2s}} \sin 3\psi$	0
$s_{x_{3c}} \cos 3\psi_m$	$s_{r_{3c}} \cos 3\psi_m$	$-s_{x_{3c}} \sin 2\psi + s_{r_{3c}} \cos 2\psi + s_{x_{3c}} \sin 4\psi + s_{r_{3c}} \cos 4\psi$	0	$2s_{x_{3c}} \sin 4\psi + 2s_{r_{3c}} \cos 4\psi$
$s_{x_{3s}} \sin 3\psi_m$	$s_{r_{3s}} \sin 3\psi_m$	$s_{x_{3s}} \sin 2\psi + s_{r_{3s}} \cos 2\psi + s_{x_{3s}} \sin 4\psi + s_{r_{3s}} \cos 4\psi$	0	$-2s_{x_{3s}} \sin 4\psi + 2s_{r_{3s}} \sin 4\psi$
$s_{x_{4c}} \cos 4\psi_m$	$s_{r_{4c}} \cos 4\psi_m$	0	$-(3/2)s_{x_{4c}} \sin 3\psi + (3/2)s_{r_{4c}} \cos 3\psi$	0
$s_{x_{4s}} \sin 4\psi_m$	$s_{r_{4s}} \sin 4\psi_m$	0	$(3/2)s_{x_{4s}} \cos 3\psi + (3/2)s_{r_{4s}} \sin 3\psi$	0
$s_{x_{5c}} \cos 5\psi_m$	$s_{r_{5c}} \cos 5\psi_m$	$-s_{x_{5c}} \sin 4\psi + s_{r_{5c}} \cos 4\psi + s_{x_{5c}} \sin 6\psi + s_{r_{5c}} \cos 6\psi$	$(3/2)s_{x_{5c}} \sin 6\psi + (3/2)s_{r_{5c}} \cos 6\psi$	$-2s_{x_{5c}} \sin 4\psi + 2s_{r_{5c}} \cos 4\psi$
$s_{x_{5s}} \sin 5\psi_m$	$s_{r_{5s}} \sin 5\psi_m$	$s_{x_{5s}} \sin 4\psi + s_{r_{5s}} \cos 4\psi + s_{x_{5s}} \sin 6\psi + s_{r_{5s}} \cos 6\psi$	$-(3/2)s_{x_{5s}} \cos 6\psi + (3/2)s_{r_{5s}} \sin 6\psi$	$2s_{x_{5s}} \cos 4\psi + 2s_{r_{5s}} \sin 4\psi$
$s_{x_{6c}} \cos 6\psi_m$	$s_{r_{6c}} \cos 6\psi_m$	0	0	0
$s_{x_{6s}} \sin 6\psi_m$	$s_{r_{6s}} \sin 6\psi_m$	0	0	0

Table 10.3: Lateral Hub Load Y Transmitted by Blades to Hub

Drag Shear at Blade Root s_x Harmonics	Radial Shear at Blade Root s_r Harmonics	Hub Load Y in Fixed Frame		
		2-Bladed Rotor	3-Bladed Rotor	4-Bladed Rotor
s_{x_0}	s_{r_0}	0	0	0
$s_{x_{1c}} \cos \psi_m$	$s_{r_{1c}} \cos \psi_m$	$-s_{r_{1c}}$	$-(3/2)s_{x_{1c}}$	$-2s_{x_{1c}}$
		$s_{x_{1c}} \cos 2\psi$		
		$s_{r_{1c}} \sin 2\psi$		
$s_{x_{1s}} \sin \psi_m$	$s_{r_{1s}} \sin \psi_m$	$s_{r_{1c}} - s_{x_{1s}} \sin 2\psi$	$(3/2)s_{r_{1s}}$	$2s_{r_{1s}}$
		$s_{r_{1s}} \cos 2\psi$		
$s_{x_{2c}} \cos 2\psi_m$	$s_{r_{2c}} \cos 2\psi_m$	0	$-(3/2)s_{x_{2c}} \cos 3\psi +$	0
			$(3/2)s_{r_{2c}} \sin 3\psi$	
$s_{x_{2s}} \sin 2\psi_m$	$s_{r_{2s}} \sin 2\psi_m$	0	$-(3/2)s_{x_{2s}} \sin 3\psi -$	0
			$(3/2)s_{r_{2s}} \cos 3\psi$	
$s_{x_{3c}} \cos 3\psi_m$	$s_{r_{3c}} \cos 3\psi_m$	$-s_{x_{3c}} \cos 2\psi$	0	$-2s_{x_{3c}} \cos 4\psi$
		$s_{r_{3c}} \sin 2\psi$		$2s_{r_{3c}} \sin 4\psi$
		$s_{x_{3c}} \cos 4\psi$		
		$s_{r_{3c}} \sin 4\psi$		
$s_{x_{3s}} \sin 3\psi_m$	$s_{r_{3s}} \sin 3\psi_m$	$-s_{x_{3s}} \sin 2\psi$	0	$-2s_{x_{3s}} \sin 4\psi$
		$s_{r_{3s}} \cos 2\psi$		$2s_{r_{3s}} \cos 4\psi$
		$s_{x_{3s}} \sin 4\psi$		
		$s_{r_{3s}} \cos 4\psi$		
$s_{x_{4c}} \cos 4\psi_m$	$s_{r_{4c}} \cos 4\psi_m$	0	$-(3/2)s_{x_{4c}} \cos 3\psi -$	0
			$(3/2)s_{r_{4c}} \sin 3\psi$	
$s_{x_{4s}} \sin 4\psi_m$	$s_{r_{4s}} \sin 4\psi_m$	0	$-(3/2)s_{x_{4s}} \sin 3\psi +$	0
			$(3/2)s_{r_{4s}} \cos 3\psi$	
$s_{x_{5c}} \cos 5\psi_m$	$s_{r_{5c}} \cos 5\psi_m$	$-s_{x_{5c}} \cos 4\psi$	$-(3/2)s_{x_{5c}} \cos 6\psi +$	$-2s_{x_{5c}} \cos 4\psi$
		$s_{r_{5c}} \sin 4\psi$	$(3/2)s_{r_{5c}} \sin 6\psi$	$2s_{r_{5c}} \sin 4\psi$
		$s_{x_{5c}} \cos 6\psi$		
		$s_{r_{5c}} \sin 6\psi$		
$s_{x_{5s}} \sin 5\psi_m$	$s_{r_{5s}} \sin 5\psi_m$	$-s_{x_{5s}} \cos 4\psi$	$-(3/2)s_{x_{5s}} \sin 6\psi -$	$-2s_{x_{5s}} \sin 4\psi$
		$s_{r_{5s}} \sin 4\psi$	$(3/2)s_{r_{5s}} \cos 6\psi$	$2s_{r_{5s}} \cos 4\psi$
		$s_{x_{5s}} \cos 6\psi$		
		$s_{r_{5s}} \sin 6\psi$		
$s_{x_{6c}} \cos 6\psi_m$	$s_{r_{6c}} \cos 6\psi_m$	0	0	0
$s_{x_{6s}} \sin 6\psi_m$	$s_{r_{6s}} \sin 6\psi_m$	0	0	0

Table 10.4: Hub Roll Moment M_X

Flap Moment at Blade Root n_f Harmonics	Hub Roll Moment M_X in Fixed Frame		
	2-Bladed Rotor	3-Bladed Rotor	4-Bladed Rotor
n_{f_0}	0	0	0
$n_{f_{1c}} \cos \psi_m$	$n_{f_{1c}} \sin 2\psi$	0	0
$n_{f_{1s}} \sin \psi_m$	$n_{f_{1s}} (1 - \cos 2\psi)$	$(3/2)n_{f_{1s}}$	$2n_{f_{1s}}$
$n_{f_{2c}} \cos 2\psi_m$	0	$(3/2)n_{f_{2c}} \sin 3\psi$	0
$n_{f_{2s}} \sin 2\psi_m$	0	$-(3/2)n_{f_{2s}} \cos 3\psi$	0
$n_{f_{3c}} \cos 3\psi_m$	$-n_{f_{3c}} \sin 2\psi$ +	0	$2n_{f_{3c}} \sin 4\psi$
	$n_{f_{3c}} \sin 4\psi$		
$n_{f_{3s}} \sin 3\psi_m$	$n_{f_{3s}} \cos 2\psi$ -	0	$-2n_{f_{3s}} \cos 4\psi$
	$n_{f_{3s}} \cos 4\psi$		
$n_{f_{4c}} \cos 4\psi_m$	0	$-(3/2)n_{f_{4c}} \sin 3\psi$	0
$n_{f_{4s}} \sin 4\psi_m$	0	$(3/2)n_{f_{4s}} \cos 3\psi$	0
$n_{f_{5c}} \cos 5\psi_m$	$-n_{f_{5c}} \cos 4\psi$ +	$(3/2)n_{f_{5c}} \sin 6\psi$	$-2n_{f_{5c}} \sin 4\psi$
	$n_{f_{5c}} \cos 6\psi$		
$n_{f_{5s}} \sin 5\psi_m$	$n_{f_{5s}} \sin 4\psi - n_{f_{5s}} \sin 6\psi$	$-(3/2)n_{f_{5s}} \cos 6\psi$	$2n_{f_{5s}} \cos 4\psi$
$n_{f_{6c}} \cos 6\psi_m$	0	0	0
$n_{f_{6s}} \sin 6\psi_m$	0	0	0

Table 10.5: Hub Pitch Moment M_Y

Flap Moment at Blade Root n_f Harmonics	Hub Pitch Moment M_Y in Fixed Frame		
	2-Bladed Rotor	3-Bladed Rotor	4-Bladed Rotor
n_{f_0}	0	0	0
$n_{f_{1c}} \cos \psi_m$	$-n_{f_{1c}} (1 + \cos 2\psi)$	$-(3/2)n_{f_{1c}}$	$-2n_{f_{1c}}$
$n_{f_{1s}} \sin \psi_m$	$-n_{f_{1s}} \sin 2\psi$	0	0
$n_{f_{2c}} \cos 2\psi_m$	0	$-(3/2)n_{f_{2c}} \cos 3\psi$	0
$n_{f_{2s}} \sin 2\psi_m$	0	$-(3/2)n_{f_{2s}} \sin 3\psi$	0
$n_{f_{3c}} \cos 3\psi_m$	$-n_{f_{3c}} \cos 2\psi$ +	0	$-2n_{f_{3c}} \cos 4\psi$
	$n_{f_{3c}} \cos 4\psi$		
$n_{f_{3s}} \sin 3\psi_m$	$-n_{f_{3s}} \sin 2\psi$ -	0	$-2n_{f_{3s}} \sin 4\psi$
	$n_{f_{3s}} \sin 4\psi$		
$n_{f_{4c}} \cos 4\psi_m$	0	$-(3/2)n_{f_{4c}} \cos 3\psi$	0
$n_{f_{4s}} \sin 4\psi_m$	0	$-(3/2)n_{f_{4s}} \sin 3\psi$	0
$n_{f_{5c}} \cos 5\psi_m$	$-n_{f_{5c}} \cos 4\psi$ -	$-(3/2)n_{f_{5c}} \cos 6\psi$	$-2n_{f_{5c}} \cos 4\psi$
	$n_{f_{5c}} \cos 6\psi$		
$n_{f_{5s}} \sin 5\psi_m$	$-n_{f_{5s}} \sin 4\psi$ -	$-(3/2)n_{f_{5s}} \sin 6\psi$	$-2n_{f_{5s}} \sin 4\psi$
	$n_{f_{5s}} \sin 6\psi$		
$n_{f_{6c}} \cos 6\psi_m$	0	0	0
$n_{f_{6s}} \sin 6\psi_m$	0	0	0

Bibliography

- [1] Crews, S. T., "Rotorcraft Vibration Criteria, A New Perspective," In *Proceedings of the 43rd Annual Forum of the American Helicopter Society*, St. Louis, MO, May 1987.
- [2] Schrage, D. P., Peskar, R. E., "Helicopter Vibration Requirements," *Proceedings of the 33rd Annual Forum of the American Helicopter Society*, May 1977.
- [3] William G. Bousman, "Putting the Aero Back Into Aeroelasticity," 8th Annual ARO Workshop on Aeroelasticity of Rotorcraft Systems, University Park, PA, October, 1999.
- [4] Bousman, W. G. and Maier, T. "An Investigation of Helicopter Rotor Blade Flap Vibratory Loads," *American Helicopter Society 48th Annual Forum Proceedings*, Washington D.C., June 3–5, 1992.
- [5] Datta, A., and Chopra, I., "Validation of Structural and Aerodynamic Modeling using UH-60A Airloads Program Data," *Journal of the American Helicopter Society*, Vol. 51, (1), January 2006, pp. 43–58.
- [6] Datta, A., Sitaraman, J., Chopra., I, and Baeder, J., "CFD/CSD Prediction of Rotor Vibratory Loads in High Speed Flight," *Journal of Aircraft*, Vol. 43, (6), November–December 2006, pp. 1698–1709.
- [7] Roget, B., Chopra, I., "Individual Blade Control Methodology for a Rotor with Dissimilar Blades," *Journal of the American Helicopter Society*, July 2003.
- [8] Roget, B., Chopra, I., "Wind Tunnel Testing of an Individual Blade Controller for a Dissimilar Rotor," Presented at the American Helicopter Society 60th Annual Forum, Baltimore, MD, June 7-10, 2004.
- [9] Chopra, I., "Status of Application of Smart Structures Technology to Rotorcraft Systems," *Journal of the American Helicopter Society*, Vol. 45, No. 4, October 2000, pp 228-252.
- [10] Straub, F. K., "A Feasibility Study of Using Smart Materials for Rotor Control," *Smart Materials and Structures*, Vol. 5, (1), February 1996, pp. 1-10.
- [11] Bao, J., Nagaraj, V. T., Chopra, I., Bernhard, A. P. F., "Wind Tunnel Testing of Low Vibration Mach Scale Rotor with Composite Tailored Blades," Presented at the American Helicopter Society 58th Annual Forum, Baltimore, MD, June 7-10, 2004.
- [12] Chopra, I., "Review of State of Art of Smart Structures And Integrated Systems," *AIAA Journal*, Vol. 40, No. 11, November 2002.
- [13] Chopra, I. and McCloud, J. L., "A Numerical Simulation Study of Open-Loop, Closed-Loop and Adaptive Multicyclic Control Systems," *Journal of the American Helicopter Society*, Vol. 28, (1), January, 1983, pp. 529–541.

- [14] Johnson, W., "Self-Tuning Regulators for Multicyclic Control of Helicopter Vibration," NASA TP 1996, March 1982.
- [15] McCloud, J. L., III, "The Promise of Multicyclic Control," *Vertica*, Vol. 4, (1), 1980.
- [16] Shaw, J. and Albion, N., "Active Control of the Helicopter Rotor for Vibration Reduction," *Journal of the American Helicopter Society*, Vol. 26, (3), 1981.
- [17] Bryson, A. E., Jr. and Ho, Y. C., *Applied Optimal Control*, Blaisdell Publishing Company, Waltham, Mass., 1969.

Chapter 11

Rotor Tests in Wind Tunnel and in Flight

11.1 Wind Tunnel Models

Scaled models are built and tested in the wind tunnel to study aeromechanical stability, vibratory blade response and loads, performance and concept feasibility. The models simulate the essential characteristics of the full-scale system, depending on the phenomenon under investigation. The models generally fall under the following three categories:

1. Rigid models
2. Froude-scaled models
3. Mach-scaled models

Rigid models simulate only aerodynamic profile and are used to study the basic aerodynamic characteristics under ideal conditions. Such models are useful to validate computational fluid dynamic and other aerodynamic analyses as well as to generate basic data base. These models incorporate geometric details but are often less expensive to build than Froude and Mach scaled models. For example, catilevered blade models (nonrotating) are used to determine airfoil characteristics as well as three-dimensional characteristics at the tip. Rigid blades with offset hinges (rotating) are frequently used to study the basic performance. Simple rotor and body are used to determine rotor-body interactional aerodynamics

Froude-scaled models are used to study aeromechanical stability of rotors. These models are less complex and less expensive to build than Mach scale models. Froude-scaled models essentially simulate steady elastic deflections. Scaled structural, inertial and aerodynamic characteristics are simulated in these models. Compressibility effects are not simulated.

Mach-scaled models are used to study basic performance and vibratory loads characteristics. These models simulate compressibility effects, i.e. the same tip Mach number. If compressibility effects are important for aeromechanical stability, then it is necessary to build Mach scaled models. These models are complex and expensive to build. In practice, Froude number and Mach number of full-scale cannot be simulated at the same time unless the test media is changed (from air to freon), that too for a selected few flight conditions. Also, it is not possible to represent the Reynolds number in the scaled rotor model. It is important however, to keep the Reynolds number high enough to ensure the proper viscous flow on the model. Aeroelastic rotor models are normally tested in large size low speed wind tunnels because of testing cost, safety, simulation of more details and less tunnel interference.

11.1.1 Froude-Scaled Models

In Froude-scaled models, the blade deflection under its own weight is scaled in the same manner as the model dimensions. If the model is s -times smaller than full scale then the deflections will also be s -times smaller. Because aeromechanical stability is a nonlinear phenomena it is important to simulate its static deflections. Therefore, Froude-scaled models are used to determine aeroelastic behavior of rotor systems. The aeroelastic stability equations are governed by the following non-dimensional parameters:

1. Locke number $\gamma = \frac{\rho ac R^4}{I_b}$
2. Nondimensional mass distribution $\bar{m} = \frac{m}{m_0}$
3. Froude number $\frac{m_0 g R^3}{EI}$
4. Nondimensional stiffness $\frac{EI}{m_0 \Omega^2 R^4}$ or $\frac{GJ}{m_0 \Omega^2 R^4}$
5. Advance ratio $\mu = \frac{V \cos \alpha}{\Omega R}$
6. Structural damping ξ
7. Airfoil profile

The maximum dimension of the model is determined by the size of the wind tunnel test section. Let the model properties be denoted by the subscript m , and the full scale properties by f . If the model is s times smaller than full scale, where s is the scaling parameter, then the ratio of the model radius to the full scale radius is given by

$$\frac{R_m}{R_f} = s \quad (11.1)$$

Similarly the chord ratio is also

$$\frac{c_m}{c_f} = s \quad (11.2)$$

The ratio of air density is fixed. Assume both are at sea level. The acceleration due to gravity is same.

$$\begin{aligned} \frac{\rho_m}{\rho_f} &= 1 \\ \frac{g_m}{g_f} &= 1 \end{aligned} \quad (11.3)$$

From the equality of Lock number we have

$$\frac{m_{0m}}{R_m^2} = \frac{m_{0f}}{R_f^2}$$

Thus the equivalent mass per unit length is scaled by

$$\frac{m_{0m}}{m_{0f}} = s^2 \quad (11.4)$$

The mass distribution has to be the same

$$\frac{m_m}{m_{0m}} = \frac{m_f}{m_{0f}}$$

Hence the mass per unit length is also scaled by

$$\frac{m_m}{m_f} = s^2 \quad (11.5)$$

From the equality of Froude number we have

$$\frac{EI_m}{EI_f} = \frac{GJ_m}{GJ_f} = \frac{m_{0m}}{m_{0f}} \left(\frac{R_m}{R_f} \right)^3 = s^5 \quad (11.6)$$

Because the nondimensional stiffness must remain the same, the rotor rpm ratio can be determined

$$\frac{\Omega_m}{\Omega_f} = \frac{m_{0m}}{m_{0f}} \left(\frac{R_m}{R_f} \right)^4 \frac{EI_m}{EI_f} = s^{-\frac{1}{2}} \quad (11.7)$$

The nondimensional frequencies of the system must be kept same as the full scale (e.g. $\nu_\beta=1.04/\text{rev}$, $\nu_\zeta = 0.3/\text{rev}$, $\nu_\theta = 4.5/\text{rev}$, say, for both the model and full scale rotors), thus the dimensional frequencies also scale in the above manner

$$\frac{\omega_m}{\omega_f} = s^{-\frac{1}{2}} \quad (11.8)$$

Also note that, because the blade azimuth is given by $\psi = \Omega t$, for a given time t , the azimuthal angle traversed by the model blade is related to the angle traversed by the full scale blade by the same ratio

$$\frac{\psi_m}{\psi_f} = s^{-\frac{1}{2}} \quad \text{at same time } t \quad (11.9)$$

From the equality of advance ratio we have the required tunnel speed as a ratio of flight speed. The shaft tilt is same for both.

$$\frac{V_m}{V_f} = \frac{\omega_m R_m}{\omega_f R_f} = s^{\frac{1}{2}} \quad (11.10)$$

It is not possible to scale structural damping, but attempt is made to keep it as low as possible. The equality of nondimensional mass and stiffnesses, the scaling of rotor radius, and the equality of the Froude number, produces blade deformations that are scaled in the same manner as the dimensions

$$\frac{w_m}{w_f} = s \quad (11.11)$$

Using the azimuthal scaling, the nondimensional velocity and acceleration are scaled as

$$\begin{aligned} \frac{w_m^*}{w_f^*} &= s^{\frac{1}{2}} \\ \frac{w_m^{**}}{w_f^{**}} &= 1 \end{aligned} \quad (11.12)$$

The other structural properties are scaled as follows. The flap moment of inertia ($\text{kg}\cdot\text{m}^2$) is scaled by

$$\frac{I_{bm}}{I_{bf}} = \frac{m_m}{m_f} \left(\frac{R_m}{R_f} \right)^3 = s^5 \quad (11.13)$$

The pitch link stiffness (N/m) is scaled by

$$\frac{k_m}{k_f} = \frac{m_{0m}}{m_{0f}} \frac{\Omega_m^2 R_m}{\Omega_f^2 R_f} = s^2 \quad (11.14)$$

A torsional spring (N-m/rad) is scaled by

$$\frac{k_{\theta m}}{k_{\theta f}} = \frac{m_{0m} \Omega_m^2 R_m^4}{m_{0f} \Omega_f^2 R_f^4} = s^4 \quad (11.15)$$

An example of a Froude-scaled model is the Boeing four-bladed bearingless ITR (Integrated Technology Rotor) model tested in December 1984, by Boeing Vertol (now Boeing Helicopters) at the University of Maryland's Glenn L. Martin Wind Tunnel. The model diameter was 6 ft, and it was a 1/8-th Froude-scaled dynamic model of the full-scale rotor.

11.1.2 Mach-Scaled Models

A Mach-scaled model reproduces the exact Mach number at the blade tip. For performance and dynamic loads studies, compressibility effects are important and therefore Mach-scaled models are used. For standard wind tunnels, Froude and Mach numbers cannot be satisfied simultaneously.

The important nondimensional parameters in this case are as follows. These parameters must be same between the model and full scale rotors.

1. Locke number $\gamma = \frac{\rho a c R^4}{I_b}$
2. Tip Mach number $M = \frac{\Omega R}{a}$
3. Advance ratio $\mu = \frac{V \cos \alpha}{\Omega R}$
4. Nondimensional mass distribution $\bar{m} = \frac{m}{m_0}$
5. Nondimensional stiffness $\frac{EI}{m_0 \Omega^2 R^4}$ or $\frac{GJ}{m_0 \Omega^2 R^4}$
6. Structural damping ξ
7. Airfoil profile

The model size is determined by the wind tunnel test section. Let the model dimensions be s -times the full scale dimensions. Then the ratio of the model radius to the full scale radius is given by

$$\frac{R_m}{R_f} = s \quad (11.16)$$

Similarly the chord ratio is also

$$\frac{c_m}{c_f} = s \quad (11.17)$$

The ratio of air density is fixed. Assume both are at sea level. Assume that the speed of sound is same in the wind tunnel as in flight.

$$\begin{aligned} \frac{\rho_m}{\rho_f} &= 1 \\ \frac{a_m}{a_f} &= 1 \end{aligned} \quad (11.18)$$

From the equality of Mach number we have

$$\frac{\Omega_m}{\Omega_f} = \frac{R_m}{R_f} \frac{a_m}{a_f} = s^{-1} \quad (11.19)$$

To simulate the sectional Mach numbers in forward flight, the advance ratio must be the same between the model and the full scale rotor. From the equality of advance ratio we have

$$\frac{V_m}{V_f} = 1 \quad (11.20)$$

Thus the wind speed in the test section is the same as flight speed. From the equality of Lock numbers we have the ratio of equivalent mass per unit length

$$\frac{m_{0m}}{m_{0f}} = \left(\frac{R_m}{R_f}\right)^2 = s^2 \quad (11.21)$$

The nondimensional mass distributions must be the same. Thus the mass per unit length also scales by the same ratio

$$\frac{m_m}{m_f} = s^2 \quad (11.22)$$

From the equality of nondimensional stiffness we have

$$\frac{EI_m}{EI_f} = \frac{GJ_m}{GJ_f} = \frac{m_{0m}}{m_{0f}} \left(\frac{\Omega_m}{\Omega_f}\right)^2 \left(\frac{R_m}{R_f}\right)^4 = s^4 \quad (11.23)$$

The airfoil profile is very important and must be simulated precisely. The structural damping is impossible to scale and is kept as small as possible. From the above scaling, the static deflection of the model with respect to the full scale rotor under its own weight is given by

$$\left(\frac{w}{R}\right)_m / \left(\frac{w}{R}\right)_f = \left(\frac{m_0 g R^3}{EI}\right)_m / \left(\frac{m_0 g R^3}{EI}\right)_f = \frac{m_{0m}}{m_{0f}} \left(\frac{R_m}{R_f}\right)^3 \frac{EI_m}{EI_f} = s \quad (11.24)$$

or

$$\frac{w_m}{w_f} = s^2 \quad (11.25)$$

If the model is 1/8-th scale, then elastic deflection will be 1/64-th scale. Mach-scaled models are much more stiff than Froude-scaled models. The velocity and accelerations are scaled as

$$\begin{aligned} \frac{w_m^*}{w_f^*} &= s \\ \frac{w_m^{**}}{w_f^{**}} &= 1 \end{aligned} \quad (11.26)$$

The static strains in these models are much smaller than the full scale values.

11.1.3 Model Fabrication

Ideally, one must build a replica construction which scales all the details. In practice it is not feasible. Therefore models are built to simulate the essential characteristics approximately. Fabrication of models is an art, and success comes with practice and experience. There is no hard and defined rule in the selection of materials, type of construction and fabrication process. Simple design and adequate details are enough. The blades are typically built using a single spar made of Aluminum, Magnesium, Kevlar, or glass, ribs made of balsa, and skin made of fabric or glass sheet. A typical construction is shown in Fig. 11.1

11.1.4 Model Instrumentation

The models are instrumented with several pickups. Typically strain gages are mounted near the blade root. These gages are installed in a conventional bridge arrangement to measure blade flapping, lead-lag and torsional moments. Static and unsteady pressure pickups are used to determine pressures at different stations. Accelerometers are typically placed near the blade tip and in the

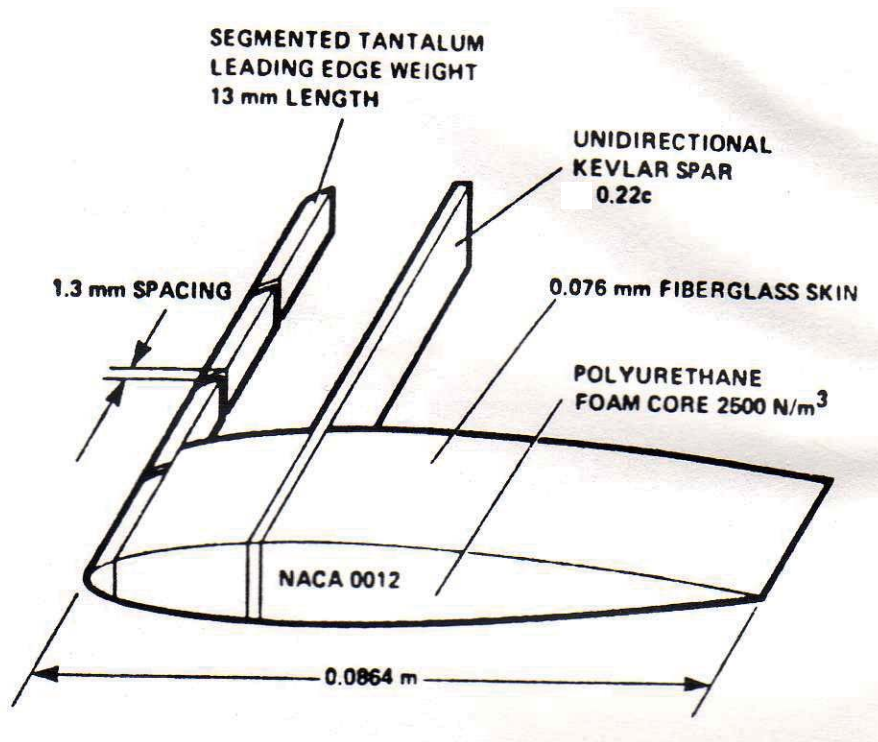


Figure 11.1: A typical experimental model blade design

airframe to obtain vibration levels (in terms of accelerations). Potentiometers and Hall-effect sensors are used at the hinges and pitch bearing to measure angular displacements. The swashplate position and hence the blade pitch input are determined by linear potentiometers mounted at each actuator. A gear tooth and photocell arrangement is used to provide 1/rev pulse. Data signals from various pickups on blades are transferred through a multi-channel slip-ring assembly to the fixed frame. Rotor loads are measured with a six component strain-gauge balance. The rotor balance is isolated from the transmission by means of a flexible diaphragm coupling. All signals are conditioned and amplified by bridge amplifiers with anti-aliasing filter, digitized using Analog to Digital (A/D) converters before being analyzed by the computer.

11.2 Model Testing

Five types of model tests are performed. They are

1. Static tests
2. Vacuum chamber tests
3. Hover tests
4. Vibration tests, and shake tests of the wind tunnel mounts
5. Wind tunnel tests

The static tests are performed on the model and the individual components of the model to check the simulation of structural stiffness and inertial characteristics. The vacuum chamber tests are performed to check the integrity of the structure to centrifugal loads. The hover tests are performed to check the integrity of the structure to both centrifugal and steady aerodynamic loads. The blade

to blade dissimilarities lead to imbalance in the rotor system. This imbalance is rectified. Usually the hover test stands are very stiff. Before, the model is tested in the wind tunnel, extensive vibration tests are performed after set up on the non-rotating model to obtain the natural frequencies and damping characteristics of all modes. Shake tests are performed on the rotating model to determine the natural frequencies and structural damping of the support structure and the rotor. These frequencies are used to check the possibility of ground resonance instability at the operating rotational speed. The rotor is then tracked in hover conditions using a strobe light at increasing speeds up to the nominal operating speed. Tracking is accomplished iteratively by making minor adjustments to the length of each pitch link. The rotor is also checked for tracking at higher collective pitch angles. With the rotor tracked correctly, it is then carefully balanced by adding small weights and short lengths of adhesive backed aluminum tape at the blade pitch housing.

In forward flight, the rotor is first brought to the operating rpm at a small collective pitch, and then the wind is turned off. The wind speed is slowly increased in a step wise manner, while adjusting the cyclic pitch inputs at each step to minimize first harmonic flapping, and thus the oscillatory bending loads at the root. This is the trim procedure. Once the desired forward speed is obtained, the collective pitch is raised to the desired level. For each test point, the rotor is re-trimmed for the particular combination of shaft angle and collective pitch setting by adjusting the longitudinal and lateral cyclic to minimize the blade cyclic flapping. This ensures that the tip path plane is perpendicular to the rotor shaft axis.

11.2.1 Testing for Isolated Rotor Stability

For blade stability measurement, the swashplate is cyclically oscillated at the regressing lag mode frequency to excite the rotor. After the rotor reaches a new steady state, the excitation is cut off and the transient response is recorded. Then, typically the Moving-Block technique is used to estimate the damping and frequency from transient signals. The testing for isolated rotor stability depends on the number of blades.

1. *One blade*: Single lead-lag and flap modes. The lead-lag mode couples with the drive system, but the drive system must have infinite impedance to represent isolated rotor. The flap mode couples with the stand.
2. *Two blades*: Two lead-lag and two flap modes. The collective lead-lag mode couples with the drive system. The differential lead-lag mode is a good approximation of isolated rotor but couples with the stand. The collective flap mode is uncoupled. The differential flap mode couples with the stand. Blade matching is not critical.
3. *Three blades*: Three lead-lag and three flap modes. Collective lead-lag mode couples with the drive system. Cyclic lead-lag modes are a good approximation of the isolated rotor but couple with stand and wake. The collective flap mode is uncoupled. The cyclic flap modes couple with stand. Blade matching is critical.

11.2.2 Spectra for Various Inputs

11.3 Major Model and Full Scale Rotor Tests

Accurate prediction of helicopter vibration and rotor vibratory loads is a complex, multi-disciplinary and difficult problem. Development of a reliable prediction capability requires careful comparison of theory and experiment. Over the last fifty years, major wind tunnel and flight tests have been conducted where detailed blade airloads and structural loads were measured. An enormous volume of data is available from the NACA/Langley 2 bladed, 15 ft dia. teetering model tested by Rabbott

and Churchill in the 1950s to the most recent U.S.Army/NASA Ames 4 bladed, 52 ft dia. articulated Black Hawk flight tests in the 1990s.

Test data, model scale and full scale, for various types of rotor systems and blade numbers are necessary for the development and validation of theoretical analysis. A theoretical analyses is successfully validated when - (i) it captures the fundamental loading patterns common to all rotor systems and (ii) captures the differences observed among different rotor configurations.

An survey of all major rotor tests, wind tunnel and full-scale, from the 1950s to the first half of the 1980s can be found in Hooper [1]. It focussed on measured airloads and identified consistent patterns that are common to all rotor systems - regardless of blade number, size and trim conditions. The work showed that the vibratory airloads are remarkably consistent in the transition regime. At high speed, they were similar but in general more variable.

Bousman [2] made a comprehensive survey of full scale rotor tests focusing on the vibratory structural response. Like in the case of vibratory airloads, consistent patterns were identified in vibratory structural response behavior, largely independent of rotor configuration. For example, the dominant vibratory flap response always occurs at 3/rev, the root chord bending moment shows a negative to positive loading at the start of the third quadrant and the pitch-link loads for articulated rotors showed large positive-negative oscillations between the first and second quadrants. On the other hand the vibratory chord bending moments differed significantly between rotor to rotor. The pitch-link load of teetering rotors like the AH-1G differed significantly from that of articulated rotors like the UH-60A.

A summary of the major rotor tests, which focussed on airloads and blade loads of main rotor systems are given in table 11.1. Tiltrotor tests have been left out of this summary. Acoustic tests have also been left out, except, the HART and ONERA tests, from which airloads measurements are often used for validation purposes.

Other rotor test programs for loads measurements are those of Lynx fitted with BERP blades [19], NASA model hover test [20], DNW tests of the Boeing 360 rotor [21] and McDonnell Douglas HARP rotor [22]. The BERP data were helpful in identifying regions of blade stall and the NASA model rotor was used to study blade-vortex interactions. UTRC and Sikorsky, under sponsorship of U.S.Army (USAAATD) have carried out extensive wind-tunnel testing (at Duits Nederlands Windtunnel, DNW, in Holland) of a 4 bladed 9.4 ft dia scale (1:5.73) model of the UH-60A Black-Hawk articulated rotor system [23]. The hover test program included blade pressures, surface flow, performance, wake geometry and flow field velocities (using a laser velocimeter). The tests were extended to forward flight in 1989 and included acoustic, dynamic, performance and airloads measurements of baseline pressure-instrumented rotors and non-instrumented rotors with modified tip geometries. An detailed discussion of the measured airloads can be found in Lorber [24].

In addition, two recent acoustic tests provide reliable airloads data. They are the HART/HART II [26] and HELISHAPE [25]. The HART test was conducted on 40% geometrically and aeroelastically scaled model of a hingeless BO-105 rotor in the DNW tunnel, in 1994. The HART II test was conducted in 2001. The HART II tests were carried out to emphasize on wake measurements. Both were collaborations between German DLR, French ONERA, NASA Langley and U.S.Army. The HELISHAPE program was an initiative between all 3 European manufacturers, Eurocopter, Augusta and Westland, and 13 other Research Institutes and Universities. Airloads measurements are available for the ONERA-Eurocopter swept-back parabolic/anhedral tip 7AD1 blade and rectangular tip 7A blades [25].

Although all the above tests were used to validate numerical models, in general, each test focussed on a specific set of phenomenon. None of them were fully comprehensive, covering steady and maneuvering flight, high thrust dynamic stall conditions, pressure data, strain gauge data, pitch link loads and fuselage vibration measurements. Wind tunnel models, even when full scale, do not include full helicopter components. For example, the model UH-60A rotor did not have a non-linear lag damper or bifilar pendulums at the hub. On the one hand, wind tunnel tests are

Table 11.1: Major Rotor Tests

Rotor Test	Configuration	Reference
NASA Langley model rotor	2 bladed teetering rotor 15 ft dia	1956 [3]
Bell UH-1 flight tests	2 bladed teetering rotor	1961 [4]
Sikorsky H-34 (CH-34) flight test, NASA Langley	4 bladed articulated	1964 [5]
H-34 (CH-34) full scale wind tunnel test, NASA Ames	4 bladed articulated	1966 [6]
Vertol CH-47A flight tests, USAAVLABS	3 bladed tandem rotor	1968 [7]
Lockheed XH-51A flight tests	4 bladed compound helicopter	1968 [8]
Sikorsky NH-3A flight tests	5 bladed, compound version of the S-61	1970 [9]
Sikorsky CH-53A flight tests, U.S.Navy	6 bladed articulated	1970 [10]
Bell AH-1G flight tests, U.S.Army	2 bladed teetering. Test conducted for aero and structural loads	1976 [11]
Bell AH-1G flight tests, NASA	2 bladed teetering. Test conducted for aero-acoustic measurements	1983 [12]
Sikorsky S-76 full scale wind tunnel tests	4 bladed articulated	1980 [13]
Bell AH-1G flight tests	2 bladed teetering	1988 [14]
Aerospatial SA-330 Research Puma flight tests	4 bladed articulated	1983, 1986.[15]
Aerospatial SA 349/2 Gazelle flight tests	3 bladed articulated	1986 [16]
Westland Lynx flight tests	4 bladed hingeless	1993 [17]
McDonnell Douglas MDART full scale wind tunnel tests	4 bladed advanced bearingless rotor, pre-production version of MD900 rotor	1993 [18]

more controlled thereby limiting uncertainties in atmospheric conditions, variations in speed due to gusts and sideslip angles, pilot error etc. On the other hand, the real objective of measuring fuselage vibration cannot be accomplished by wind tunnel models. Only a full-scale flight test program can provide fuselage vibration data, with associated rotor airloads, blade loads, control loads, performance data and vehicle trim data, which can then be used to validate all aspects of a comprehensive analysis consistently. A truly extensive flight test program would cover steady level flight, steady and unsteady maneuvers, low speed and high speed flight, low thrust and high thrust flight, each conducted multiple times to ensure repeatability and accuracy of the data. The test conditions and the blade and helicopter properties (fuselage properties, c.g. location, fuel content, armament weight and placement etc) must be accurately and carefully documented before and after each flight, minimizing uncertainties as much as possible. The U.S.Army/NASA-Ames UH-60A Black Hawk Airloads Program [27] is such a detailed flight test program. The comprehensive set of repeatable test data from the UH-60A Airloads Program have established benchmarks to validate various aspects of a comprehensive rotor analyses.

The UH-60A flight test program conducted 31 flights. They covered Steady flight (7 flights), Maneuver flight (3), Ground Acoustic Measurements (9), In-flight Acoustic Measurements (6) and

Flight dynamics (6). Pressure gauge measurements (airloads obtained by integrating) were taken at 9 stations, flap bending gauges at 9 stations, chord bending gauges at 8 stations and torsion bending gauges at 4 stations. All four pitch links were instrumented to measure control loads. This is perhaps the most extensive instrumentation suites used in a flight test, providing reliable and repeatable test data. The present work uses the UH-60A flight test data. Details of the structural, aerodynamic and trim data sets are discussed in the appropriate chapters.

Bibliography

- [1] W.E.Hooper, "The Vibratory Airloading of Helicopter Rotors," Paper No.46, 9th European Rotorcraft Forum, Stresa, Italy, September, 1983.
- [2] W.G.Bousman, "Response of Helicopter Rotors to Vibratory Airloads," *Journal of the American Helicopter Society*, Vol. 35, No. 4, Oct, 1990, pp. 53-62.
- [3] Rabbot, J. P., Churchill, G. B., "Experimental Investigation of the Aerodynamic Loading on a Helicopter Rotor Blade in Forward Flight," NACA RM L56107, Oct. 1956.
- [4] Bell Helicopter, "Measurement of Dynamic Air Loads on a Full-Scale Semi-Rigid Rotor," TCREC TR 62-42. Dec. 1962.
- [5] Scheiman, J., "A Tabulation of Helicopter Rotor-Blade Differential Pressures, Stresses, and Motions as Measured in Flight," NASA TM X-952, March 1964.
- [6] Rabbott, J. P., Lizak, A. A., Paglino, V. M., "A Presentation of Measured and Calculated Full-Scale Rotor Blade Aerodynamic and Structural Loads", USAAVLABS TR66-31, July 1966.
- [7] Pruyne, R. R., "In-Flight Measurement of Rotor Blade Airloads, Bending Moments, and Motions, Together with Rotor Shaft Loads and Fuselage Vibration, on a Tandem Rotor Helicopter," USAAVLABS TR 67-9A,B,C and D, Nov. 1967.
- [8] Bartsch, E. A., "In-Flight Measurement and Correlation with Theory of Blade Airloads and Resources in the XH-51A Compound Helicopter Rotor," USAAVLABS TR 68-22A, May 1968.
- [9] Fenaughty, R., Beno, E., "NH-3A Vibratory Airloads and Vibratory Rotor Loads," Department of the Navy SER 611493, Jan. 1970.
- [10] Beno, E., "CH-53A Main Rotor and Stabilizer Vibratory Airloads and Forces," Department of the Navy SER 65593. June 1970.
- [11] Shockey, G. A., Cox, C. Z., Williams, J. W., "AH-1G Helicopter Aerodynamic and Structural Load Survey," USAAMRDL TR-76-39.
- [12] Shockey, G. A., et al, "AH-1G Tip Aero-Acoustic Test," NASA.
- [13] Johnson, W., "Performance and Loads Data on a Full-Scale Rotor with Four Tip Planforms," NASA TM 81229, 1980.
- [14] Cross, J. L., Watts, M. E., "Tip Aerodynamics and Acoustics Test," NASA RP 1179, Dec. 1988.

- [15] Bousman, Young, C., Toulmay, F., Gilbert, N. E., Strawn, R. C., Miller, J. V., Maier, T. H., Costes, M. and Beaumier P., "A Comparison of Lifting-Line and CFD Methods with Flight Test Data from a Research Puma Helicopter," NASA TM 110421, October 1996.
- [16] Heffernan, R., Gaubert, M., "Structural and Aerodynamic Loads and Performance Measurements of an SA 349/2 Helicopter with an Advanced Geometry Rotor," NASA TM 88370, Nov. 1986.
- [17] Lau, B. H., Louie, A. W., Sotiriou, C. P., Griffiths, N., "Correlation of the Lynx-XZ170 Flight-Test Results Up To and Beyond the Stall Boundary," American Helicopter Society Forum. May 1993.
- [18] Nguyen, K., Lauzon, D., Anand V., "Computation of Loads on the McDonnell Douglas Advanced Bearingless Rotor," American Helicopter Society Forum, May 1994.
- [19] Isaacs, N. C. G., Harrison R. J., "Identification of Retreating Blade Stall Mechanisms Using Flight Test Pressure Measurements," American Helicopter Society 45th Annual Forum, Boston, MA, May 1989.
- [20] Caradonna, F. X., Tung, G., "Experimental and Analytical Studies of a Model Helicopter Rotor in Hover," NASA TM 81232, USAAVRADCOTR-81-A-23, 1980.
- [21] Dadone, L., Dawson, S., Boxwell, D., Ekquist, D., "Model 360 Rotor Test at DNW - Review of Performance and Blade Airload Data," American Helicopter Society 43rd Annual Forum, St. Louis, MO, May 1987.
- [22] Dawson, S., Jordan, D., Smith, S., Ekins, J., Silverton, L., Tuttle, B., "HARP Model Rotor Test at the DNW," American Helicopter Society 45th Annual Forum, Boston, MA, May 1989.
- [23] Yu, Y. H., Liu, S. R., Landgrebe, A. J., Lorber, P. F., Pollack, M. J., Martin, R. M., Jordan, D., "Aerodynamic and Acoustic Test of a United Technologies Model Scale Rotor at DNW," American Helicopter Society 46th Annual Forum, Washington D.C., May 1990.
- [24] Peter F. Lorber, "Aerodynamic Results of a Pressure-Instrumented Model Rotor Test at the DNW," *Journal of the American Helicopter Society*, Vol. 38, No. 3, July 1993, pp. 26-34.
- [25] Philippe, J. J., "Survey on ONERA Code Developments and Validation Studies for Multi-disciplinary Research on Rotor Aeromechanics," American Helicopter Society Aeromechanics Specialists' Conference, San Francisco, CA, January 19-21, 1994.
- [26] Yung, H. Y., et al, "The HART-II Test : Rotor Wakes and Aeroacoustics with Higher-Harmonic Pitch Control (HHC) Inputs - The Joint German/French/Dutch/US Project," American Helicopter Society 58th Annual Forum, Montreal, Canada, June 11-13, 2002.
- [27] Kufeld, R. M., Balough, D., Cross, J. L., Studebaker, K. F., Jennison, C. D., Bousman, W. G., "Flight Testing the UH-60A Airloads Aircraft," American Helicopter Society 50th Annual Forum Proceedings, Washington, D.C., May, 1994.


Alfred Gessow Rotorcraft Center
University of Maryland


Dynamic Aspects in Design of a Bearingless Rotor



Inderjit Chopra
 Director Alfred Gessow Rotorcraft Center &
 Alfred Gessow Professor of Aerospace Engineering
 Presentation At: Korea Aerospace Research Institute (KARI), Daejeon
 June 27-30, 2011

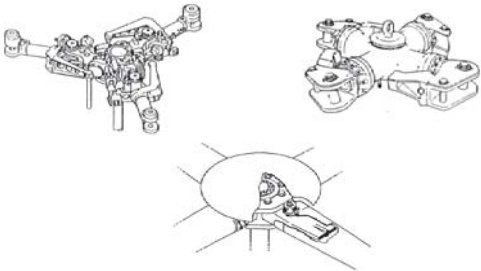

Bearingless Rotor


Bearingless Main Rotor (BMR)

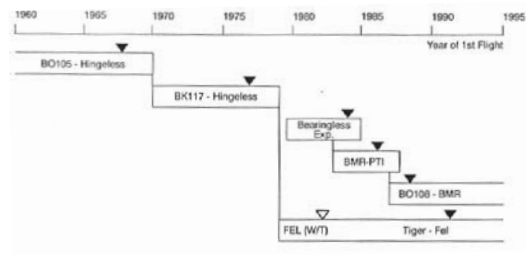
Flap and lag hinges as well as pitch bearing are eliminated:

- Reduction in parts count and maintenance cost
- Reduction in drag and weight
- **Redundancy in load paths at root**
- **Large elastic deformations**
- **Became possible because of composite materials and elastomeric dampers**

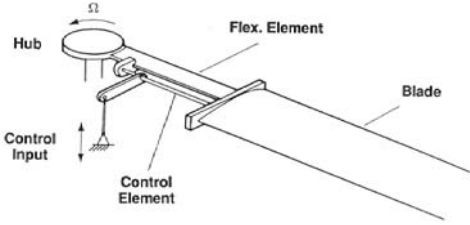

Rotor Systems Development

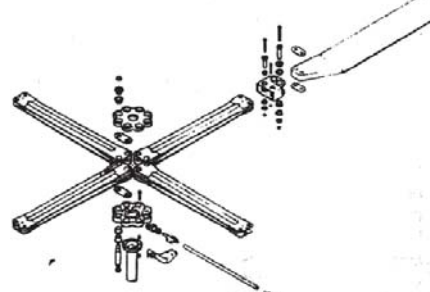

MBB's Main Rotor Technology Development


Principal Build-up of a Bearingless Rotor System


Boeing Vertol Bearingless Rotor (1978)

Matched BO 105 (hingeless) rotor characteristics (flap freq. 1.12/rev, e/R=14%, lag freq. .68/rev)
 Flexbeam: Twin C-channel cross-section; Torque Rod: mid-section; Prepitch 12.5 deg

Aerospatiale/Eurocopter France: Triflex (1972)

Matched SA 341 Gazelle characteristics; flap freq. 1.06/rev, lag freq. 0.72/rev
 Flexbeam: fiberglass-epoxy yarns embedded in elastomeric matrix, Low damping

Highes/MDHC/Boeing: HARP (1982)

4-Bladed flap hinge 8%, elastomeric damper
 Flexbeam: Single Kevlar/Graphite beam with cruciform section
 Transitioned into MD-900 Explorer 5-bladed rotor

Westland/AW

Matched Lynx rotor; 4-Bladed

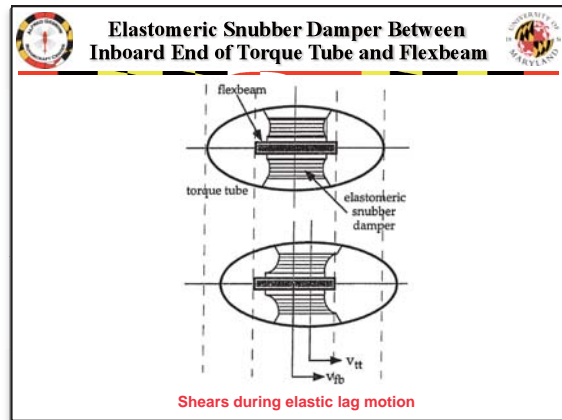
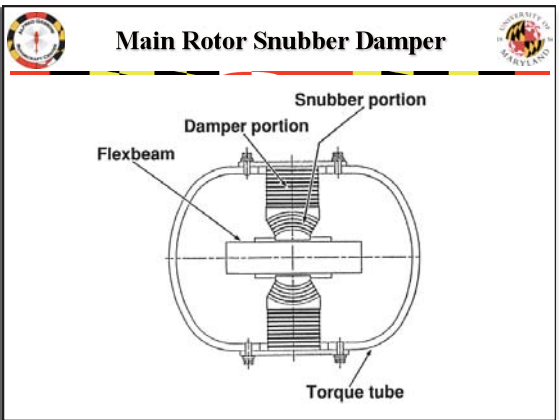
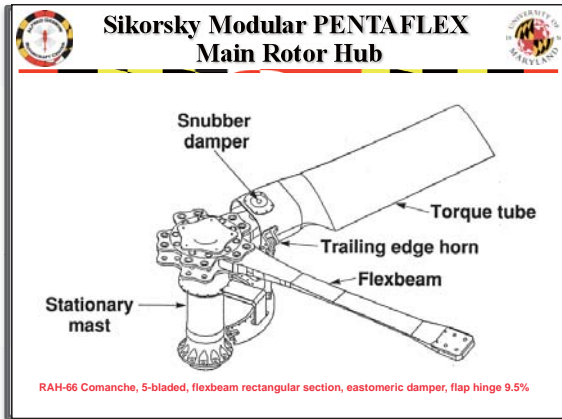
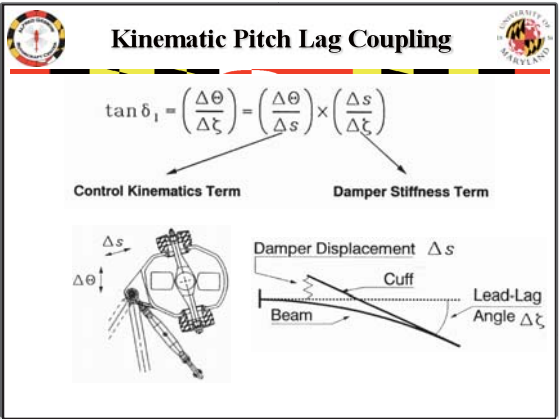
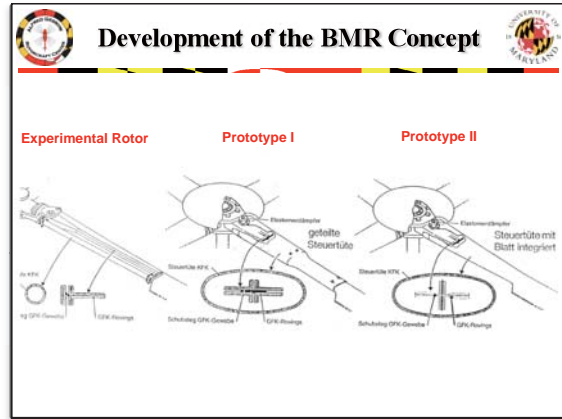
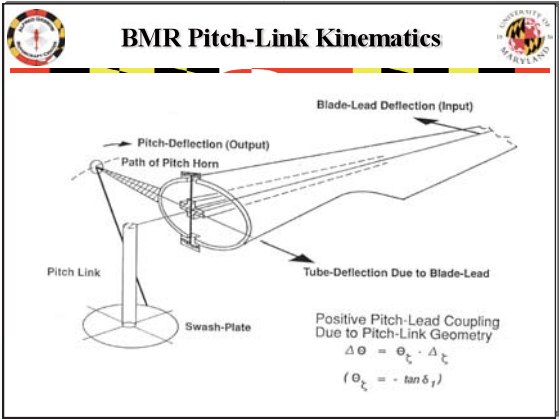
Bell Model 680 Rotor System (1982)

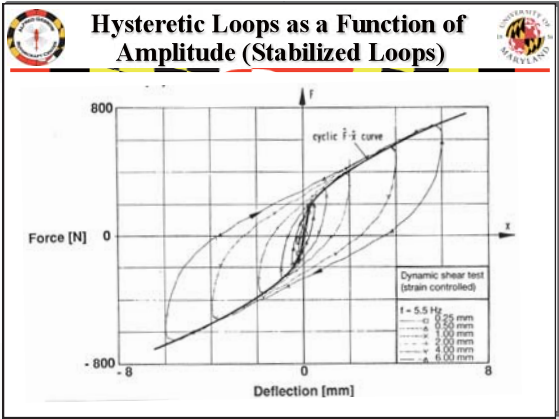
Flexbeam: One piece fiberglass, flap flexure inboard and torsionally flexible outboard; Torque Tube: torsionally stiff cuff wrapped around flexbeam; Flap hinge 2-3%

Basic Design Parameters

- Fundamental blade flap frequency or “hinge”-offset
- Fundamental blade lead-lag frequency
- Pitch-lag coupling
- Inplane damping

Evolution of Flexbeam Cross Sections





Modeling of Elastomeric Dampers and Effects on Aeromechanical Stability

- Dampers are nonlinear; Behavior dependent on the amplitude, frequency of motion, temperature, prestress
- Early efforts in elastomeric modeling were inadequate
 - Hausmann: modeled in *frequency domain*, need nonlinear hysteresis cycles, iterative solution process
 - Felker: G' , G'' independently obtained, lacks generality
- Goal is to seek a *consistent* Damper Model represented in the *time-domain* by a nonlinear differential equation
 - Predict behavior under multi-frequency/large amplitude excitations, include effects of equilibrium deformations
 - Easily integrated into a comprehensive rotor analysis

Spring-Dashpot Model

NONLINEAR

LINEAR

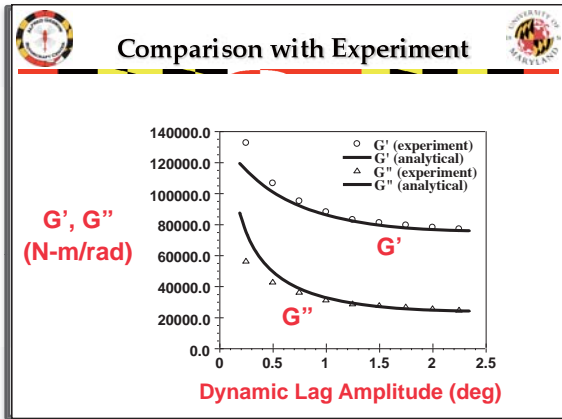
Elastomeric modeled by combination of linear and nonlinear springs and dashpots

- Derive constitutive differential equation (symbolically) For nonlinear spring + single Kelvin Chain

$$K_2 \zeta + C_2 \dot{\zeta} = K_2 f(D) + C_2 \frac{df(D)}{dD} \dot{D} + D$$

K_2, C_2 : Spring/Dashpot parameters in Kelvin chain
 $\zeta = f(D)$: nonlinear force/displacement relation of lead spring
 D : Total damper force

- Parameters determined through System Identification



Augmented Elastomeric Damper Model

OLD MODEL

AUGMENTED MODEL

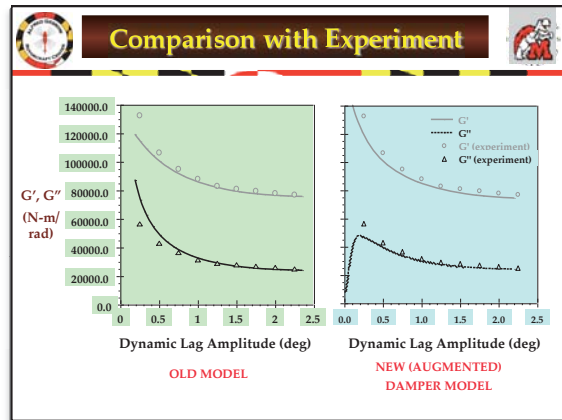
$$f(D) = (\text{sign } D) \left(c_1 |D| + c_2 |D|^2 + c_3 |D|^3 + c_4 |D|^4 \right) + (\text{sign } D) \frac{1}{c_6} \ln \left(\frac{|D|}{c_5} + 1 \right)$$

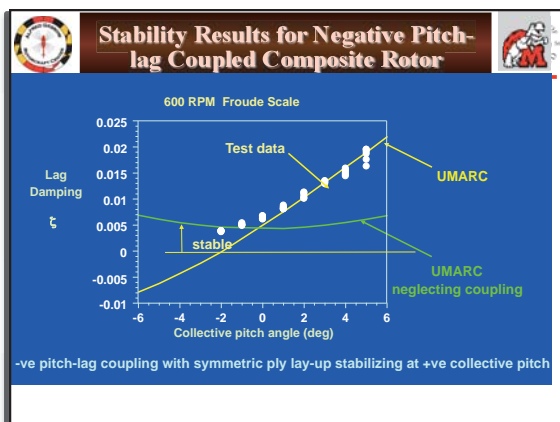
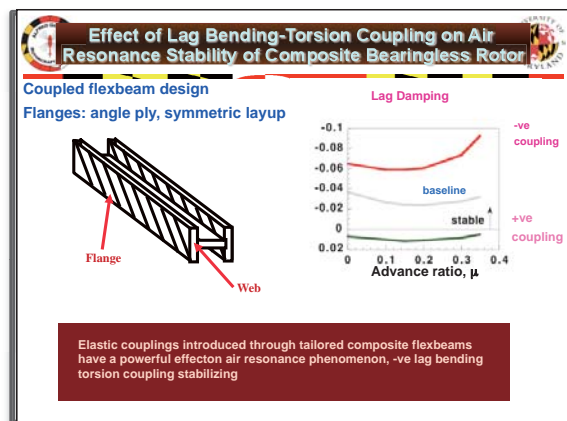
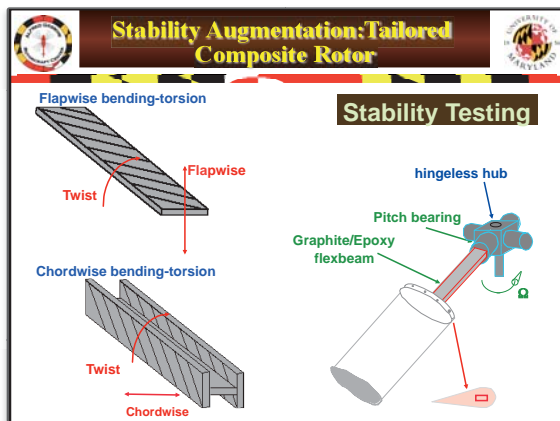
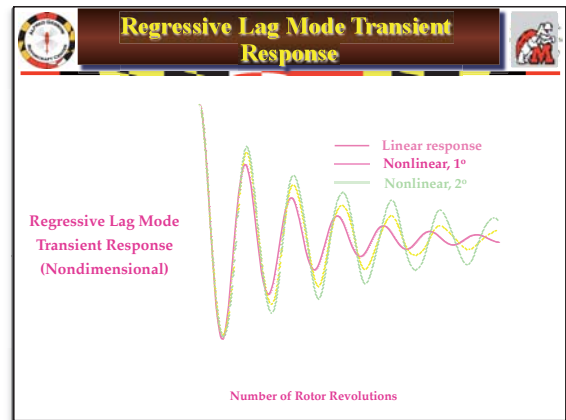
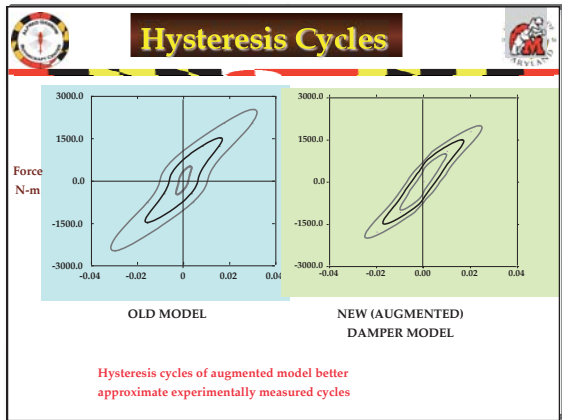
$$K_2 \zeta + C_2 \dot{\zeta} = K_2 f(D) + C_2 \frac{df}{dD} \dot{D} + D$$

$$D_{S1} = g(\zeta) = (\text{sign } \zeta) c_7 (1 - e^{-c_8 |\zeta|})$$

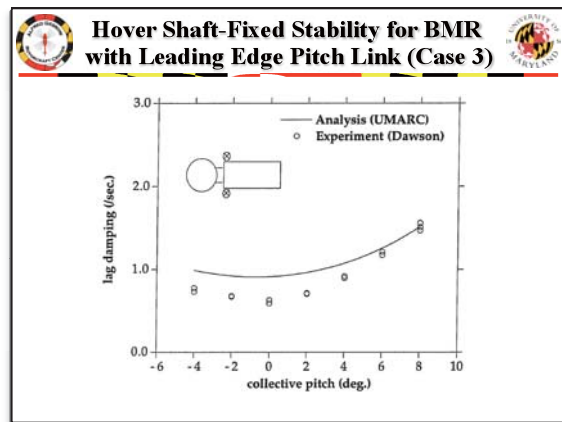
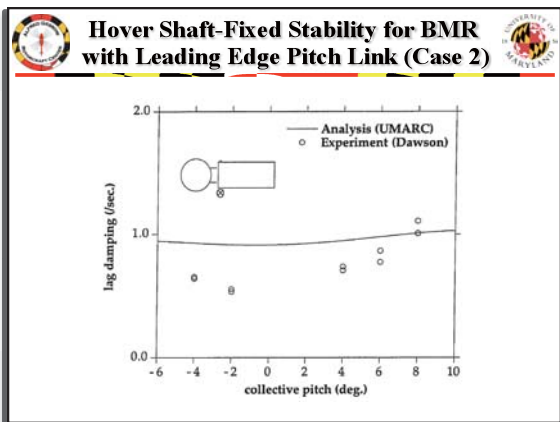
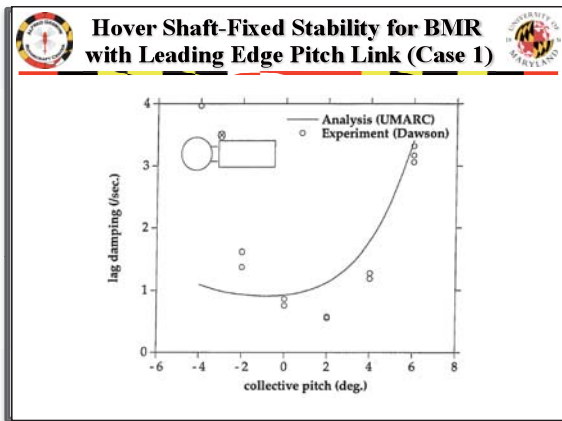
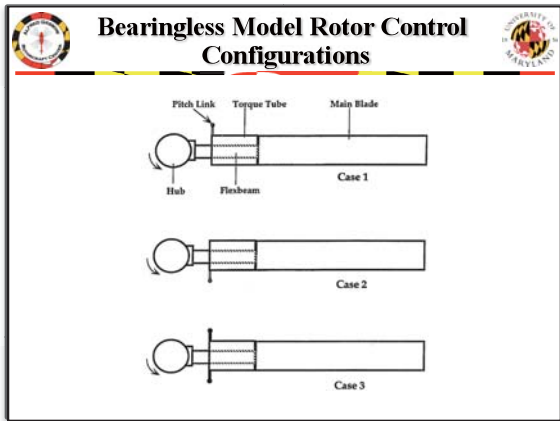
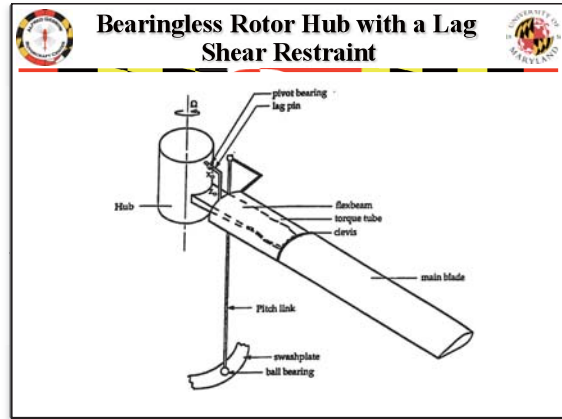
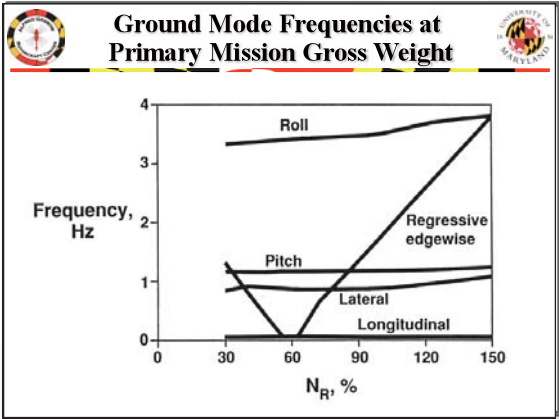
Total Damper Force = D

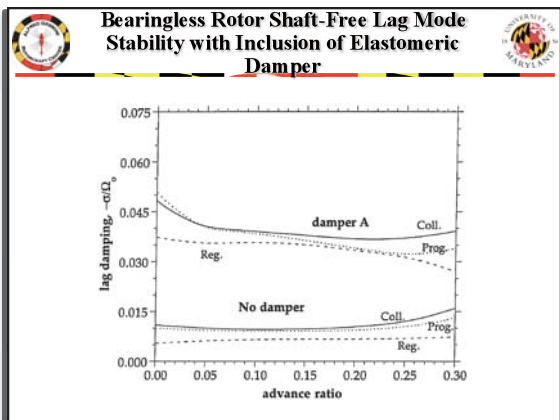
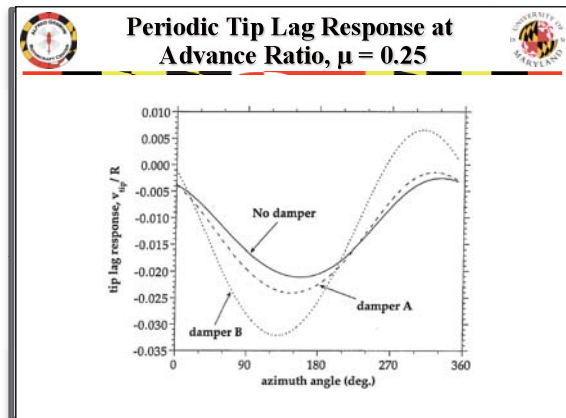
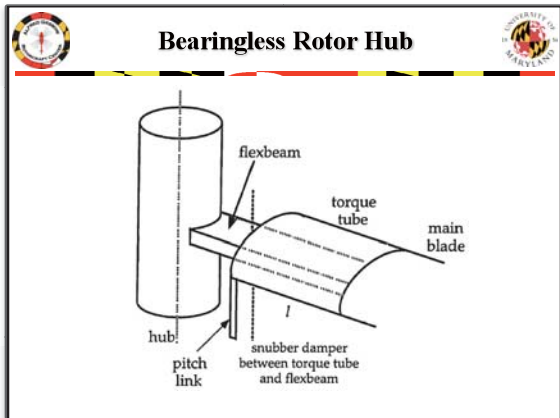
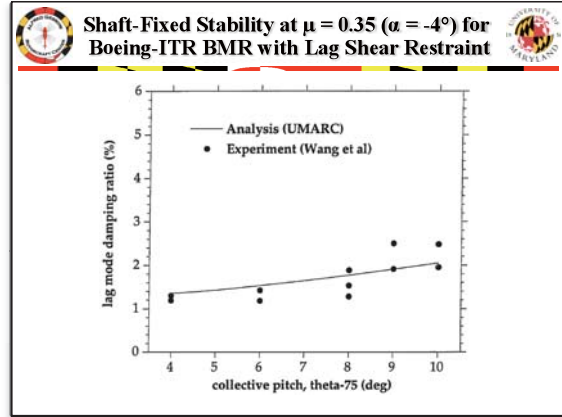
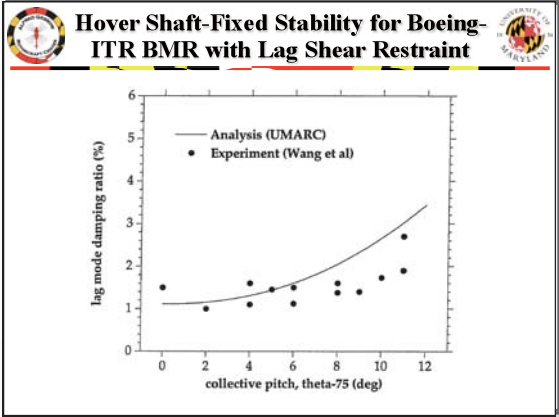
Total Damper Force = $D + D_{S1}$





- ### Snubber Design Issues
- Trade off between high loss factor and snubber life
 - Design for 1P motions superimposed on subharmonic motions
 - Stiffness and damping characteristics non-linear with amplitude
 - High stiffness at cold temperatures
 - Snubber stiffness variability affects 1P vibration
 - Stiffness variability may affect frequencies of modes contributing to 5P vibration





Analysis of Bearingless Main Rotor Aeroelasticity Using an Improved Time Domain Nonlinear Elastomeric Damper Model



Farhan Gandhi*
Rotorcraft Fellow



Inderjit Chopra
Professor and Director

Center for Rotorcraft Education and Research
Department of Aerospace Engineering
University of Maryland at College Park

An elastomeric damper model comprising a nonlinear spring and a Kelvin chain is augmented to represent experimentally observed degradation in G'' (damping) at very low dynamic amplitudes, and occurrence of limit cycle oscillations (jitter) due to applied perturbations. The damper model is described in the time domain by a nonlinear differential equation. Integration into a bearingless rotor comprehensive analysis results in the addition of damper states to the rotor/fuselage state vector, and augmentation of the baseline modal mass, damping and stiffness matrices, and load vector. The influence of the damper is examined on bearingless rotor aeroelastic behavior, including aeromechanical stability in forward flight. Damper stiffness results in a significant variation of second lag frequency with advance ratio. The nonlinear characterization of the damper results in greater stability augmentation of the lag mode at low advance ratios than at higher advance ratios.

Introduction

The main rotor is a key component on the helicopter, providing thrust, propulsive force, and most vehicle controls. It has traditionally involved complexity of hinges, bearings and dampers. Over the last two decades, strong emphasis on design simplicity has culminated in the development of the bearingless main rotor (Ref. 1). In this type of rotor, the flap and lag hinges, as well as the pitch bearing, are eliminated resulting in a substantial reduction in parts count, weight, drag, and maintenance cost, along with increased control power. The main blade of the bearingless rotor is attached to the hub by means of a torsionally soft flexure that allows most of the flap and lag bending, as well as elastic twist. Pitch control of the main blade is achieved by rotating a torsionally rigid torque tube, surrounding the flexbeam, with the pitch link. This in turn rotates the main blade, and twists the flexbeam in the process.

Since the bearingless main rotor is usually designed as a soft-inplane rotor, it is susceptible to aeromechanical instabilities (Ref. 2). To alleviate these instabilities, most bearingless rotors need to be equipped with lag dampers. In contrast to the conventional hydraulic lag dampers seen on articulated rotors, elastomeric material based lag dampers have been popular for bearingless rotors, as they provide simplicity and a reduction in moving parts, ease in maintenance, and ease in installation. Rapid advances in material science, leading to the development of specialized high loss-factor elastomers (Refs. 3, 4) has greatly contributed to the increasing popularity of elastomeric material based dampers. However, analytical modeling of the complex, nonlinear behavior of elastomeric dampers has been a challenge. This paper formulates

and implements an improved elastomeric damper model in a bearingless rotor comprehensive analysis, and examines its effects on the aeroelastic behavior of the bearingless rotor.

The aeroelastic analysis of bearingless rotors is more challenging than hingeless or articulated rotors due to the presence of redundant load paths, complex hub kinematics, and large elastic twisting of the flexbeam during the application of pitch control. The earlier analytical models for bearingless main rotors, such as FLAIR (Refs. 5, 6) and GRASP (Ref. 7), were developed for hover condition only. Sivaneri and Chopra (Ref. 8) were the first to apply the finite element method to the analysis of bearingless main rotors. Researchers at the University of Maryland (Refs. 9-13) used the finite element formulation developed in Ref. 8 to examine the aeroelastic and aeromechanical stability of several bearingless rotor configurations in hover and forward flight conditions. In the above analyses, the blade periodic response in forward flight was calculated using a temporal finite element formulation, after transforming the spatially discretized blade equations to a few normal mode equations, to reduce computation time.

Recognizing that the direct use of normal modes is fraught with difficulty on account of the large elastic deformations due to the application of pitch control (particularly the large twist in the flexbeam), the authors (Ref. 14) recently developed a refined aeroelastic analysis for bearingless rotor helicopters in forward flight. In this analysis, large elastic deformations due to pitch control application are purged from the total deformations and calculated independently, in vacuo. Since the elastic deformations due to aerodynamic and inertial loads have been separated from the large elastic deformations due to pitch control, normal mode methods can now be used for the aeroelastic analysis.

Since elastomeric dampers strongly influence the dynamic and aeroelastic characteristics of the bearingless main rotor (Ref. 1), a reliable analytical damper model that can be conveniently integrated into bearingless rotor comprehensive analyses is required. Development of such a model, that can characterize the behavior over the complete

Presented at the AHS 51st Annual Forum, Fort Worth, Texas, May 9-11, 1995. Manuscript submitted April 1995; accepted April 1996.

*Currently Assistant Professor of Aerospace Engineering, The Pennsylvania State University

range of operating conditions, has been a challenge, as the behavior of elastomeric dampers is extremely complex and nonlinearly dependent on several factors such as the amplitude and frequency of motion, the equilibrium condition, damper configuration and temperature. Current bearingless rotor analyses use very simple elastomeric damper models, or table look-up methods (Ref. 15).

Previous efforts toward the analytical modeling of these dampers by Hausmann (Refs. 16, 17), and Felker *et al* (Ref. 18), had certain limitations. For example, in the Felker time-domain model there is no provision for derivatives of damper force and displacement, and the model does not account for dependence of damper behavior on *equilibrium condition*. The Hausmann model addresses these issues, but is a frequency domain approach based on complex modulus. Such an approach is less attractive for nonlinear viscoelastic materials because of the variation of the complex moduli, G' and G'' , with *dynamic amplitude*, and the inability to use superposition for multifrequency excitations. A more detailed discussion on these models is available in (Ref. 19).

Gandhi *et al* (Ref. 20) recently developed a nonlinear elastomeric damper model that overcomes many of the limitations of the previous models. The elastomeric damper is represented by a combination of linear and nonlinear springs and dashpots, and its behavior is described in the *time-domain* by a nonlinear differential equation. The constitutive equation characterizes the nonlinear behavior of the elastomeric damper, for large amplitude vibrations, at different equilibrium conditions and under multi-frequency excitations. The authors examined the influence of this elastomeric damper model on hover aeromechanical stability (Ref. 21) and forward flight flap-lag stability (Ref. 22) of articulated and hingeless rotor helicopters represented by simple *rigid blade* approximations. It was concluded that the rotor lag mode stability characteristics are influenced by the steady lag displacement in hover, and the periodic lag response in forward flight.

More recently, additional behavioral characteristics of elastomeric dampers have been observed, such as the degradation of complex modulus component G'' at very small dynamic amplitudes (Refs. 17, 23), and the existence of limit cycle oscillations of rotor blades with these nonlinear elastomeric dampers. The analytical model developed in Ref. 20 does not account for these characteristics. Thus, the objectives of the present paper are three-fold: (i) Augment the damper model in Ref. 20 to represent the additional behavioral characteristics — reduction in G'' (damping) at very low dynamic amplitudes, and limit cycle oscillations, (ii) Systematically integrate the damper model into the bearingless rotor comprehensive analysis developed in Ref. 14, and (iii) Examine the effects of the nonlinear damper on bearingless rotor aeroelastic behavior, including aeromechanical stability, in different operating conditions.

Augmented Spring-Dashpot Model for Nonlinear Elastomeric Damper

The elastomeric damper model developed in Ref. 20 consisted of a nonlinear spring, S1, in series with a linear Kelvin chain (denoted as *original model* in Fig. 1). The spring S1 was softening in nature to represent the instantaneous force/displacement behavior of an elastomer, and was described by

$$\zeta_{S1} = f(D) = \text{sign}(D) \left(c_1|D| + c_2|D|^2 + c_3|D|^3 + c_4|D|^4 \right) \quad (1)$$

where D is the force and ζ_{S1} is the displacement in S1. The original model was able to represent the experimentally measured variation of complex moduli (G' and G'') with dynamic amplitude, as shown in Fig. 2. Recent investigations, however, have revealed that the imaginary part, G'' , of the complex modulus can be considerably degraded at very low dynamic amplitudes (Refs. 17, 23). This behavior has not

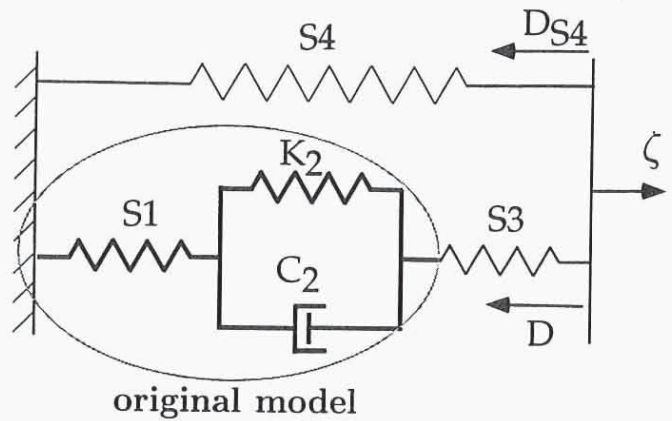


Fig. 1. Schematic spring-dashpot representation of elastomeric damper.

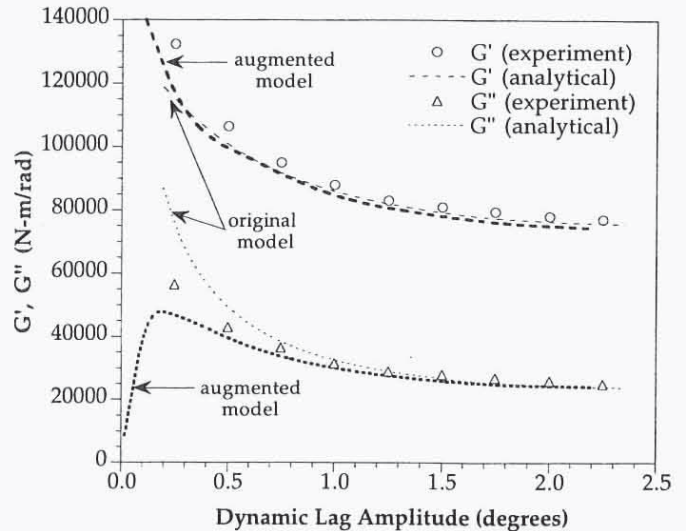


Fig. 2. Variation of complex modulus components, G' (stiffness) and G'' (damping), with dynamic amplitude.

been represented in the original model presented in Ref. 20. It has also been observed that perturbation of rotor blades with elastomeric dampers can result in a transient that settles to constant amplitude stable limit cycle oscillations (jitter phenomenon). The original elastomeric damper model is augmented with additional nonlinear springs S3 and S4 (Fig. 1) to model these behavioral characteristics.

An understanding of the nonlinear damping mechanism in the original model is a useful guide in determining the behavior of the augmenting springs S3 and S4. The high stiffness of S1 at low displacement amplitude results in considerable damping (high G'') as the majority of the damper motion occurs in the Kelvin chain (comprising of linear spring K_2 and dashpot C_2). As displacement amplitude increases, significant motion is obtained in the spring S1 due to its softening behavior, causing a decrease in G'' (damping) associated with the reduced motion in the Kelvin chain.

It is hypothesized that a reduction in G'' at small displacement amplitudes could be obtained by introducing a series spring, S3, that is very soft in the small displacement regime (so that the majority of the damper motion occurs in *this spring* rather than the dashpot in the Kelvin chain) and *rapidly hardens* thereafter, rendering it ineffective in the large displacement regime. The force/displacement behavior of

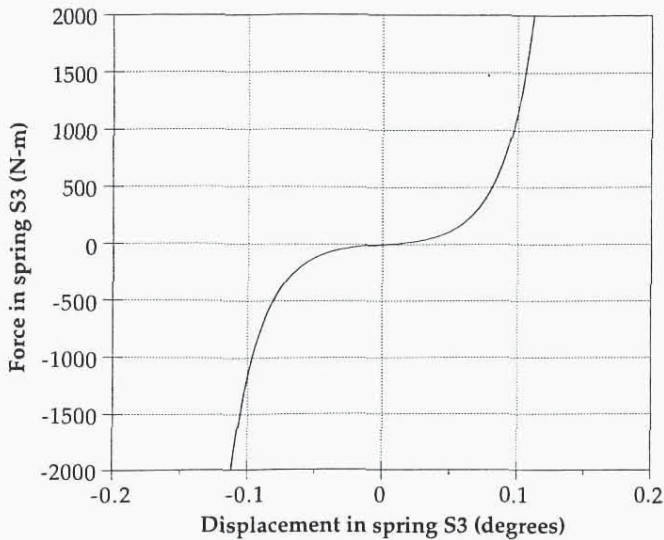


Fig. 3. Force versus displacement behavior of nonlinear spring S3 of the augmented model.

spring S3 is shown in Fig. 3 and described by

$$D = \text{sign}(\zeta_{S3}) \left[c_5(e^{c_6|\zeta_{S3}|} - 1) \right] \tag{2}$$

$$\text{or } \zeta_{S3} = \text{sign}(D) \left[\frac{1}{c_6} \ln \left(\frac{|D|}{c_5} + 1 \right) \right] \tag{3}$$

where D is the force and ζ_{S3} is the displacement in S3. While augmenting the model with such a spring alone expectedly reduces G'' at low amplitudes of excitation, it results in a decrease in G' , as well. To alleviate the reduction in G' at small amplitudes, spring S4 is introduced in parallel with the series configuration consisting of the Kelvin chain and springs S1 and S3, as shown in Fig. 1. The nonlinear behavior of spring S4 is expressed as

$$D_{S4} = g(\zeta) = \text{sign}(\zeta) \left[c_7(1 - e^{-c_8|\zeta|}) \right] \tag{4}$$

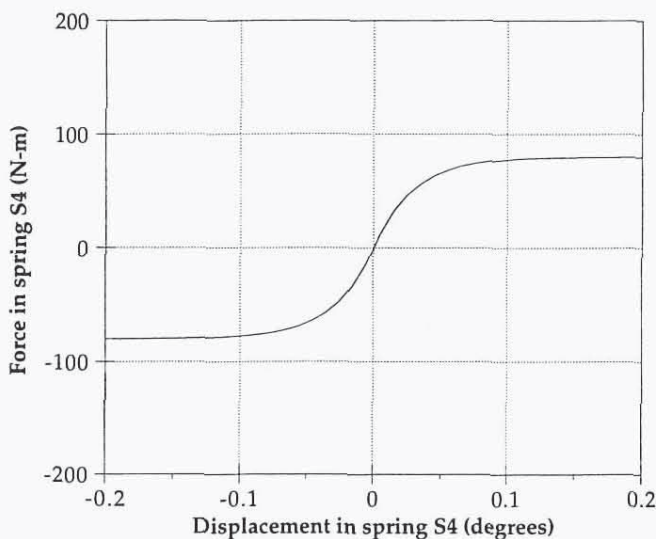


Fig. 4. Force versus displacement behavior of nonlinear spring S4 of the augmented model.

and is shown in Fig. 4. In the above equation, D_{S4} is the force in the spring S4, and ζ is the total damper displacement. The high stiffness at small displacement amplitudes prevents the decrease of G' , whereas the very low stiffness at higher amplitudes renders the branch virtually ineffective in the large displacement regime.

In Ref. 20, a rigorous mathematical procedure was presented for the evaluation of the parameters (c_1, c_2, c_3, c_4) of the nonlinear spring S1, and the linear elements (K_2, C_2) in the Kelvin chain. These parameters were determined by employing a least square fit to experimental complex modulus data, at various amplitudes of excitation. Fig. 2 shows the variation of G' and G'' with dynamic amplitude, obtained using the augmented model (with a judicious selection of parameters c_5, c_6 , and c_7, c_8 , of springs S3 and S4 respectively). From the figure it can be seen that the additional springs in the augmented model effectively decrease G'' at small amplitudes, while having no additional detrimental effect on the variation of G' or G'' with increasing dynamic amplitude.

For analysis purposes, the two nonlinear springs S1 and S3 can be treated as a single nonlinear spring. If $\zeta_{non} = \zeta_{S1} + \zeta_{S3}$ is the total displacement in the two nonlinear springs S1 and S3, and D is the force, from Eqs. (1) and (3)

$$\begin{aligned} \zeta_{non} &= \bar{f}(D) \\ &= \text{sign}(D) \left[c_1|D| + c_2|D|^2 + c_3|D|^3 \right. \\ &\quad \left. + c_4|D|^4 + \frac{1}{c_6} \ln \left(\frac{|D|}{c_5} + 1 \right) \right] \end{aligned} \tag{5}$$

The relation between D and the total damper displacement ζ can then be written as

$$K_2\zeta + C_2 \dot{\zeta}^* = K_2\bar{f}(D) + C_2 \frac{d\bar{f}(D)}{dD} \dot{D}^* + D \tag{6}$$

Note that the total elastomeric damper force is the sum of the forces D (in the branch containing the Kelvin chain), and D_{S4} (in the parallel spring S4), as shown in Fig. 1.

Hysteresis Cycles

The force/displacement hysteresis cycles of the augmented elastomeric damper model can be calculated by the application of a single frequency sinusoidal excitation $\zeta = \zeta_0 e^{i\Omega t}$ to Eqs. (4) and (6). For a linear viscoelastic material, the hysteresis cycles are ellipses, and can be described mathematically by standard equations. However, for the nonlinear elastomeric damper, the nature of the hysteresis cycles changes with both dynamic amplitude and static preload. Fig. 5 shows hysteresis cycles of different amplitudes at zero static preload for the augmented damper model developed in the previous section. These hysteresis cycles better represent the nature of experimentally measured cycles (Refs. 16, 17) than do cycles based on the original damper model in Ref. 20. Fig. 5 also shows the static force/displacement behavior of the augmented elastomeric damper model. It can be seen that the model represents the softening behavior of elastomeric materials under static loads.

Limit Cycle Oscillations

To examine whether the augmented elastomeric damper model can predict limit cycle oscillations, the damper nonlinear differential equation is solved simultaneously with the isolated blade lag equation in the rotating frame. The blade lag equation can be written as

$$\zeta^{**} + \nu\zeta^2 + \bar{D} = M\zeta \tag{7}$$

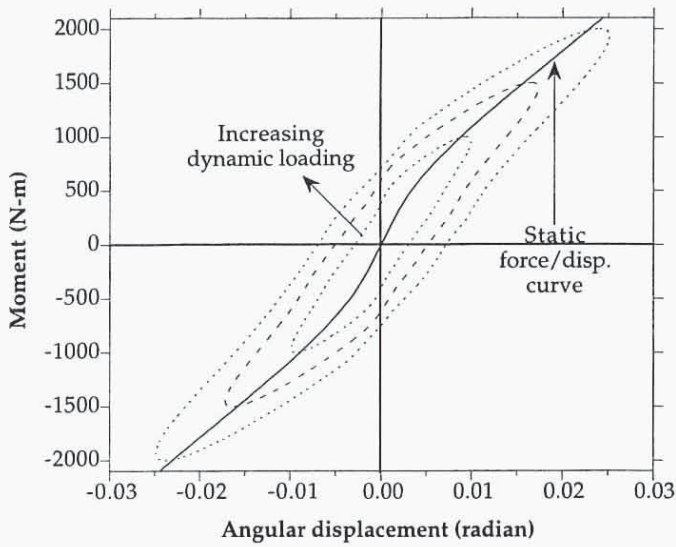


Fig. 5. Nonlinear hysteresis cycles for augmented damper model, about zero equilibrium position, and at different dynamic loads.

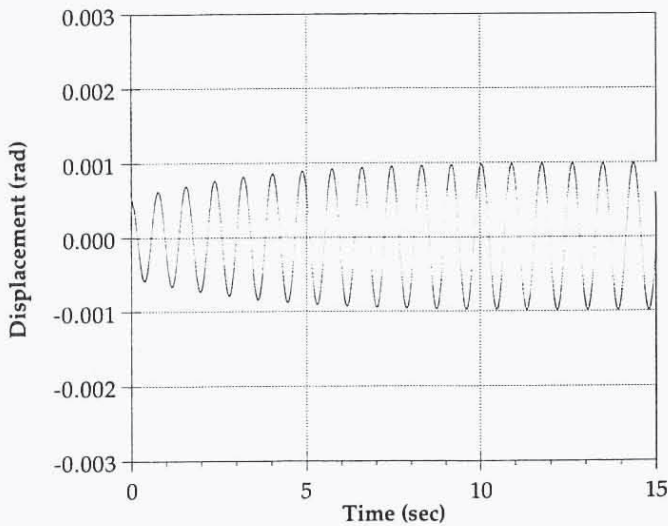


Fig. 6a. Transient lag response for a perturbation $\xi_0=0.0005$ radian.

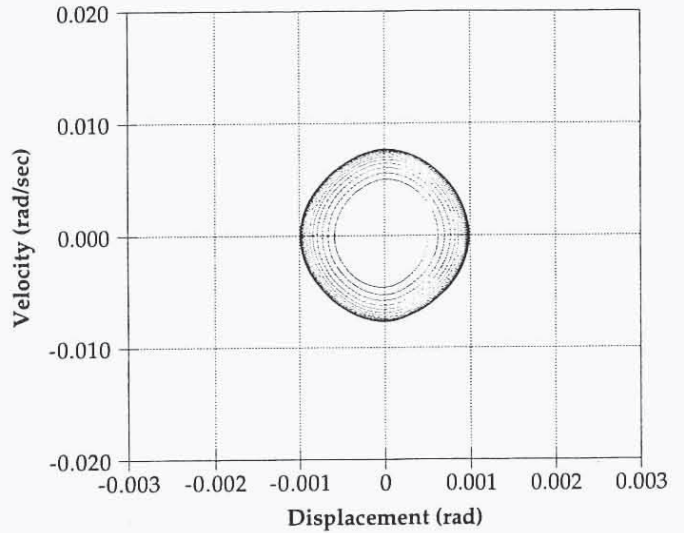


Fig. 6b. Transient lag response for a perturbation $\xi_0=0.0005$ radian.

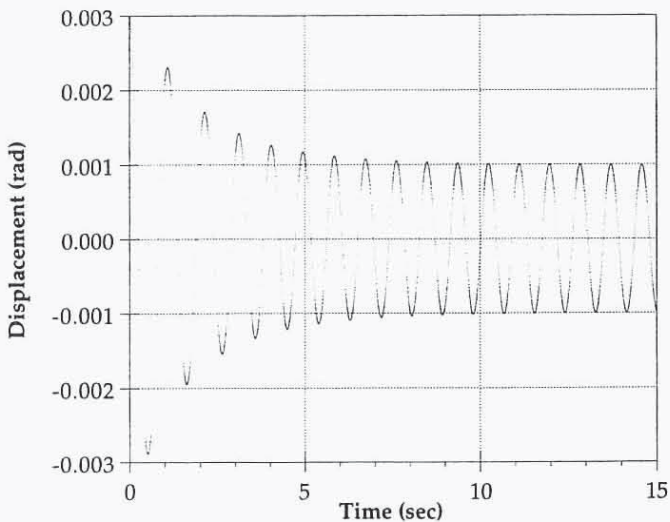


Fig. 7a. Transient lag response for a perturbation $\xi_0=0.0030$ radian.

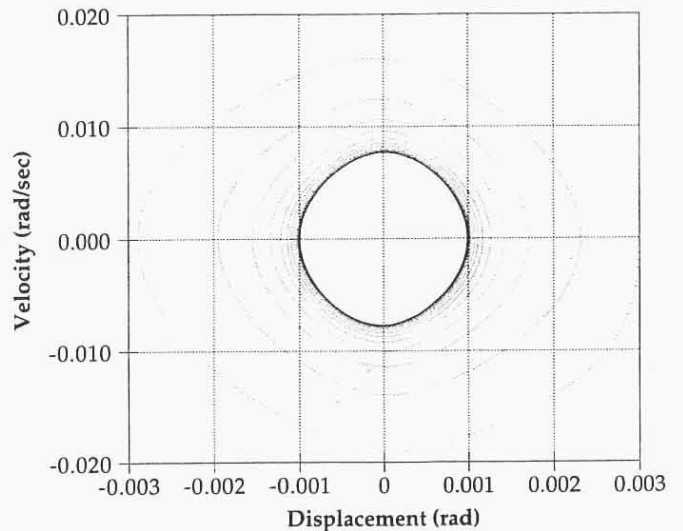


Fig. 7b. Transient lag response for a perturbation $\xi_0=0.0030$ radian.

where \bar{D} is the nondimensional elastomeric damper force, ζ is the lag displacement, ν_ζ is the rotating lag frequency, and M_ζ is the aerodynamic lag moment. Expressing the total damper force \bar{D} as the sum of D and D_{s4} , and using Eq. (4) for D_{s4} , the lag equation can be written as

$$\zeta^{**} + \nu_\zeta^2 \zeta + D + g(\zeta) = M_\zeta \quad (8)$$

Eq. (8) is solved simultaneously with the nonlinear differential equation, (6), for the force, D , in the Kelvin chain branch of the damper.

To evaluate the transient response of the system, the aerodynamic lag moment, M_ζ , is set to zero, and the system is successively given initial perturbations of $\xi_0 = 0.0005$ radian and 0.003 radian. In both cases, within a short time the transient settles to stable self-sustained limit cycle oscillations, as shown in Figs. 6a and 7a. Figs. 6b and 7b show the transient responses represented in the phase-plane (velocity/displacement plane). Limit cycles are known to be characterized by *orbits* in the phase plane, implying a periodic motion. In Figs. 6 and 7, the different initial perturbations, expectedly, yield stable limit cycle oscillations of the same amplitude, as it is known that the amplitude is dependent only on the characteristics of the nonlinear system and is independent of the initial perturbation size.

Integration of Damper Into Bearingless Rotor Analysis

To study the effects of the elastomeric lag damper on the aeroelastic behavior of a bearingless main rotor helicopter, the damper model is integrated into a bearingless rotor comprehensive analysis developed by the authors in Ref. 14. The rotor blades are modeled as elastic beams undergoing coupled flap bending, lag bending, elastic torsion, and axial deformations. The finite element method is used in the structural modeling of the rotor blades as it is extremely convenient for bearingless rotors with redundant load paths and complex hub kinematics. The refined aeroelastic analysis is carried out in two steps: (i) Calculation of elastic deformations (particularly the large flexbeam twist) experienced by the bearingless blades as a result of a prescribed washplate motion, in the absence of aerodynamic forces, and (ii) Use of *modified nonlinear equations*, obtained by the systematic inclusion of the effect of control deformations on the strain energy, to determine the behavior of the bearingless rotor under aerodynamic forces. Thus, by purging the large elastic control deformations from the total blade deformations, this approach has the advantage of permitting the use of normal modes for low computational cost, while including the *effect of the control deformations* on the nonlinear blade response under aerodynamic loads. The analysis is robust, showing good convergence behavior in the evaluation of blade periodic response even at high advance ratios.

Lag damping in the bearingless rotor is generally introduced by means of an elastomeric snubber damper, attached between the inboard end of the torque tube and the flexbeam (Figs. 8 and 9). The snubber damper, in addition to augmenting the stability of the lowly damped lag mode, alleviates pitch-flap coupling and keeps the flexbeam centered with respect to the torque tube.

Since the lag damper behavior is governed by a nonlinear *differential equation*, an expression for damping force in terms of lag displacement and velocity is not available for direct substitution into the blade lag equation. Thus, the damper differential equation is solved simultaneously with the blade and fuselage equations, with damper force or an internal damper displacement appearing as an independent state.

The coupled bending-torsion-axial equations of motion of the bearingless rotor blade are obtained by introducing expressions for the variations in strain energy, δU , kinetic energy, δT , and the virtual work δW due to external aerodynamic loads, in Hamilton's Principle:

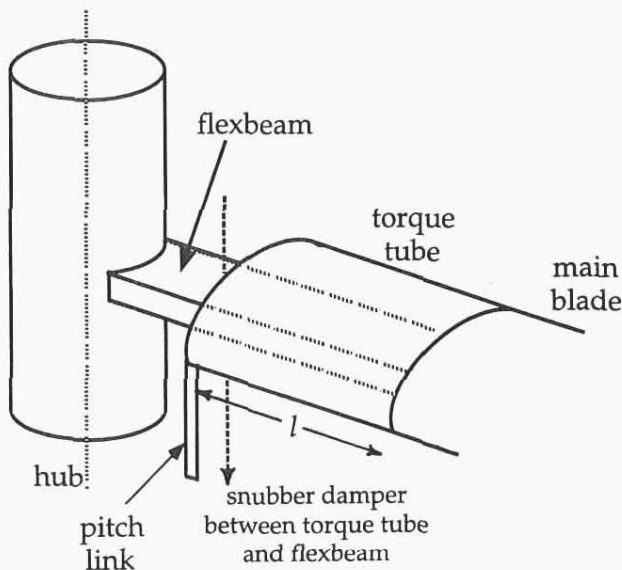


Fig. 8. Bearingless rotor hub.

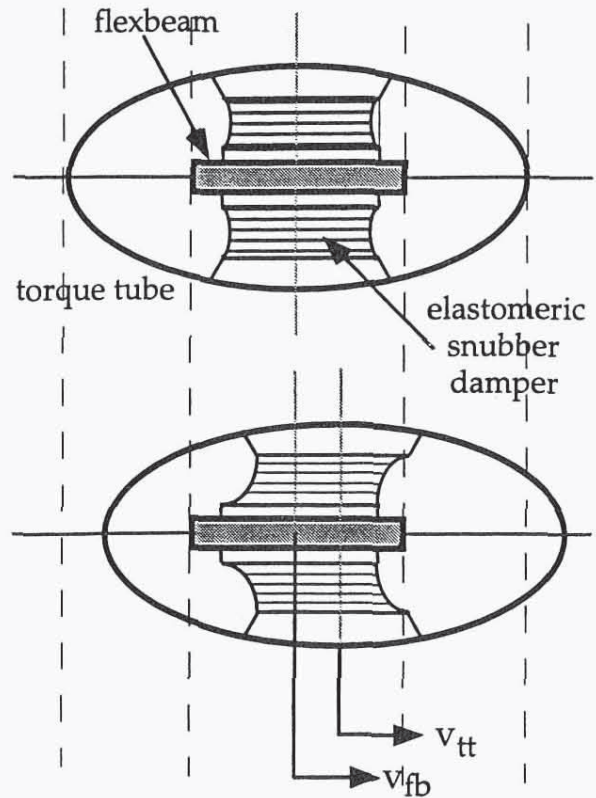


Fig. 9. Elastomeric snubber damper attached between inboard end of torque tube and flexbeam shears during relative lag motion.

$$\delta\pi = \int_{\psi_1}^{\psi_2} (\delta U - \delta T - \delta W) d\psi = 0 \tag{9}$$

Spatial discretization of Hamilton's Principle results in a set of finite element equations

$$\delta\pi = \int_{\psi_1}^{\psi_2} \delta\mathbf{q}^T \left[\mathbf{M}(\psi) \ddot{\mathbf{q}} + \mathbf{C}(\psi) \dot{\mathbf{q}} + \mathbf{K}(\psi)\mathbf{q} - \mathbf{F}(\psi, \mathbf{q}) \right] d\psi = 0 \tag{10}$$

where \mathbf{M} , \mathbf{C} , and \mathbf{K} are the assembled global mass, damping, and stiffness matrices, respectively, \mathbf{F} is the global load vector, and \mathbf{q} is the blade nodal displacement vector. The blade aerodynamic loads are obtained using quasi-steady strip theory and linear inflow assumption. The solution of Eq. (10) yields the rotor blade periodic response.

Rotor Periodic Response and Vehicle Trim

Since Eq. (10) represents a system of *nonlinear* differential equations with *periodic coefficients*, its solution is obtained iteratively, using a temporal finite element method. To reduce the computational time, Eq. (10) is first transformed into a system of normal mode equations, expressed as

$$\delta\pi = \int_0^{2\pi} \left(\delta\mathbf{p}^T \delta \dot{\mathbf{p}}^* \right) \left\{ \begin{matrix} \bar{\mathbf{F}} - \bar{\mathbf{C}} \dot{\mathbf{p}}^* - \bar{\mathbf{K}}\mathbf{p} \\ \bar{\mathbf{M}} \dot{\mathbf{p}}^* \end{matrix} \right\} d\psi = 0 \tag{11}$$

where $\bar{\mathbf{M}}$, $\bar{\mathbf{C}}$, and $\bar{\mathbf{K}}$ are the modal mass, damping, and stiffness matrices, respectively, $\bar{\mathbf{F}}$ is the modal load vector, and \mathbf{p} and $\dot{\mathbf{p}}$ are the modal displacement and velocity vectors. Typically 6 to 8 coupled rotating

modes are used to evaluate the rotor response.

Introducing the elastomeric damper nonlinear differential equation yields

$$\int_0^{2\pi} \left(\delta \mathbf{p}_a^T \delta \dot{\mathbf{p}}_a^* \right) \left\{ \begin{matrix} \bar{\mathbf{F}}_a - \bar{\mathbf{C}}_a \dot{\mathbf{p}}_a^* - \bar{\mathbf{K}}_a \mathbf{p}_a \\ \bar{\mathbf{M}}_a \dot{\mathbf{p}}_a^* \end{matrix} \right\} d\psi = 0 \quad (12)$$

where the subscript *a* denotes augmented matrices and vectors due to the additional damper state. In Eq. (12),

$$\bar{\mathbf{K}}_a = \begin{bmatrix} \bar{\mathbf{K}} & \bar{\mathbf{K}}_{bd} \\ \bar{\mathbf{K}}_{db} & \bar{\mathbf{K}}_{dd} \end{bmatrix} \quad (13)$$

$$\bar{\mathbf{C}}_a = \begin{bmatrix} \bar{\mathbf{C}} & \mathbf{0} \\ \bar{\mathbf{C}}_{db} & \mathbf{0} \end{bmatrix} \quad (14)$$

$$\bar{\mathbf{M}}_a = \begin{bmatrix} \bar{\mathbf{M}} & \mathbf{0} \\ \mathbf{0} & \mathbf{0} \end{bmatrix} \quad (15)$$

$$\bar{\mathbf{F}}_a = \begin{bmatrix} \bar{\mathbf{F}} \\ \bar{\mathbf{F}}_d \end{bmatrix} \quad (16)$$

$$\mathbf{p}_a = \begin{bmatrix} \mathbf{p} \\ D \end{bmatrix} \quad (17)$$

where $\bar{\mathbf{K}}_{bd}$ is the blade-damper coupling vector, $\bar{\mathbf{K}}_{db}$ and $\bar{\mathbf{C}}_{db}$ are the damper-blade coupling vectors, $\bar{\mathbf{K}}_{dd}$ is the damper stiffness, $\bar{\mathbf{F}}_d$ contains the damper nonlinear terms, and *D* is the damper force. Since inclusion of the damper requires only the augmentation of the original rotor matrices and vectors, it is extremely convenient and simple to implement.

To obtain expressions for $\bar{\mathbf{K}}_{bd}$, $\bar{\mathbf{K}}_{db}$ and $\bar{\mathbf{C}}_{db}$, the lag displacement ξ in the damper equation, (6), is related to the torque tube and flexbeam nodal lag displacements (v_{tt} and v_{fb}) at the damper attachment points, (Fig. 9), and expressed in terms of modal coordinates. Eq. (6) is then written as

$$\begin{aligned} & K_2 f(D) + C_2 \frac{df}{dD} \dot{D} + D \\ & - K_2 \sum \frac{\phi_{fb}^{(j)} - \phi_{tt}^{(j)}}{l} p^{(j)} \\ & - C_2 \sum \frac{\phi_{fb}^{(j)} - \phi_{tt}^{(j)}}{l} \dot{p}^{(j)} = 0 \end{aligned} \quad (18)$$

In Eq. (18) the torque tube radial length *l* is used to convert the relative translational lag displacement at the damper attachment points, v_{tt} - v_{fb} (expressed as a summation of modal contributions), into an angular lag displacement, required in the damper equation, (6). $\phi^{(j)}$ denotes the *j*th normal mode vector, and the subscripts *tt* and *fb* denote the elements of that vector corresponding to lag motion at the points of damper attachment to the torque tube and the flexbeam, respectively. The summation is over the number of modes used to estimate the response.

Using Eq. (18), the *j*th element of the damper-blade coupling vectors can be obtained as

$$\bar{\mathbf{K}}_{db}^{(j)} = \frac{K_2}{l} (\phi_{fb}^{(j)} - \phi_{tt}^{(j)}) \quad (19)$$

$$\bar{\mathbf{C}}_{db}^{(j)} = \frac{C_2}{l} (\phi_{fb}^{(j)} - \phi_{tt}^{(j)}) \quad (20)$$

Similarly, the *j*th blade-damper coupling element can be expressed as

$$\bar{\mathbf{K}}_{bd}^{(j)} = \frac{1}{l} (\phi_{fb}^{(j)} - \phi_{tt}^{(j)}) \quad (21)$$

Remaining damper related terms in Eqs. (13) and (16) are

$$\bar{\mathbf{K}}_{dd} = -1 \quad (22)$$

$$\bar{\mathbf{F}}_d = K_2 f(D) + C_2 \frac{df}{dD} \dot{D} \quad (23)$$

Eq. (12) can be symbolically expressed as

$$\int_0^{2\pi} \delta \mathbf{y}^T \mathbf{Q} d\psi = 0 \quad (24)$$

where

$$\mathbf{y} = \begin{bmatrix} \mathbf{p}_a \\ \dot{\mathbf{p}}_a^* \end{bmatrix}$$

and

$$\mathbf{Q} = \begin{bmatrix} \bar{\mathbf{F}}_a - \bar{\mathbf{C}}_a \dot{\mathbf{p}}_a^* - \bar{\mathbf{K}}_a \mathbf{p}_a \\ \bar{\mathbf{M}}_a \dot{\mathbf{p}}_a^* \end{bmatrix} \quad (25)$$

The matrices $\bar{\mathbf{K}}_a$ and $\bar{\mathbf{C}}_a$ contain periodic terms while $\bar{\mathbf{F}}_a$ is both nonlinear and periodic. To solve the nonlinear periodic system, (24), the time interval for one rotor revolution of 2π is divided into a number of temporal elements. The blade governing equations can then be expressed as the sum of the elemental equations. Further, Eq. (24) is expanded as a first order Taylor series about a steady value \mathbf{y}_o , to yield

$$\sum_{i=1}^{N_t} \int_{\psi_i}^{\psi_{i+1}} \delta \mathbf{y}_i^T [\mathbf{Q}_i(\mathbf{y}_o) + \mathbf{K}_{ti}(\mathbf{y}_o) \Delta \mathbf{y}_i] d\psi = 0 \quad (26)$$

where $\psi_1 = 0$, $\psi_{N_t+1} = 2\pi$, N_t is the number of time elements used and \mathbf{K}_{ti} is the tangential stiffness matrix of the *i*th temporal element, given by

$$\mathbf{K}_{ti} = \begin{bmatrix} \frac{\partial \bar{\mathbf{F}}_a}{\partial \mathbf{p}_a} - \bar{\mathbf{K}}_a & \frac{\partial \bar{\mathbf{F}}_a}{\partial \dot{\mathbf{p}}_a^*} - \bar{\mathbf{C}}_a \\ \mathbf{0} & \bar{\mathbf{M}}_a \end{bmatrix}_i \quad (27)$$

The blade response \mathbf{p}_a is expressed within each time element in terms of temporal shape functions, and nodal values, ξ_i . Introducing such an expression into Eq. (26) yields a system of nonlinear algebraic equations

$$\sum_{i=1}^{N_t} \int_{\psi_i}^{\psi_{i+1}} \delta \xi_i^T \mathbf{N}^T [\mathbf{Q}_i + \mathbf{K}_{ti} \mathbf{N} \Delta \xi_i] d\psi = 0 \quad (28)$$

where \mathbf{N} is the matrix of temporal shape functions and derivatives. During assembly of the global temporal finite element equations, periodicity is imposed by connecting the first and last azimuthal elements. The solution of Eq. (28) for the global response ξ is obtained using an iterative procedure based on the Newton-Raphson method.

A coupled trim procedure is adopted, whereby, convergence of the blade periodic response and vehicle equilibrium, are simultaneously accomplished. The updated blade response obtained after successive Newton-Raphson iterations is used in the calculation of the hub loads, which influence vehicle orientation and control settings. These new controls, in turn, are used in the subsequent blade response iteration. This procedure accurately determines the vehicle trim, blade periodic response and periodic damper force, which are known to have a significant influence on the stability characteristics of the system (Refs. 21, 22).

Stability of Perturbation Equations

To evaluate the stability of the rotor-fuselage-damper system, the state variables are subject to small perturbations about the trim condition. Hamilton's Principle, Eq. (9), can then be written as

$$\delta\pi = \delta\pi_o + \delta\Delta\pi = 0 \tag{29}$$

where $\delta\pi_o$ is due to the trim condition, and $\delta\Delta\pi$ is due to the perturbation motion about the trim condition. Since the trim condition is evaluated as the solution to $\delta\pi = 0$, from Eq. (29),

$$\delta\Delta\pi = \delta\Delta\pi_F + \delta\Delta\pi_R = \delta\Delta\pi_F + \sum_{i=1}^{N_b} \delta\Delta\pi_i = 0 \tag{30}$$

In Eq. (30), the subscripts *F* and *R* refer to fuselage and rotor, respectively. Further, the rotor contribution, $\delta\Delta\pi_R$ is due to the sum of the contributions of N_b individual blades. After spatial finite element discretization, and transformation to normal mode coordinates, Eq. (30) can be expressed as,

$$\begin{bmatrix} \mathbf{K}_1 & \dots & 0 & \mathbf{K}_{1F} & \mathbf{K}_{bd}^{(1)} & \dots & 0 \\ \dots & \dots & \dots & \dots & \dots & \dots & \dots \\ 0 & \dots & \mathbf{K}_{N_b} & \mathbf{K}_{N_bF} & 0 & \dots & \mathbf{K}_{bd}^{(N_b)} \\ \mathbf{K}_{F1} & \dots & \mathbf{K}_{FN_b} & \mathbf{K}_{FF} & 0 & \dots & 0 \\ \mathbf{K}_{db}^{(1)} & \dots & 0 & 0 & \mathbf{K}_{dd}^{(1)} & \dots & 0 \\ \dots & \dots & \dots & \dots & \dots & \dots & \dots \\ 0 & \dots & \mathbf{K}_{db}^{(N_b)} & 0 & \dots & \dots & \mathbf{K}_{dd}^{(N_b)} \end{bmatrix} \begin{Bmatrix} \Delta p_1 \\ \dots \\ \Delta p_{N_b} \\ \Delta x_F \\ \Delta D_1 \\ \dots \\ \Delta D_{N_b} \end{Bmatrix} + \begin{bmatrix} \mathbf{C}_1 & \dots & 0 & \mathbf{C}_{1F} & 0 & \dots & 0 \\ \dots & \dots & \dots & \dots & \dots & \dots & \dots \\ 0 & \dots & \mathbf{C}_{N_b} & \mathbf{C}_{N_bF} & 0 & \dots & 0 \\ \mathbf{C}_{F1} & \dots & \mathbf{C}_{FN_b} & \mathbf{C}_{FF} & 0 & \dots & 0 \\ \mathbf{C}_{db}^{(1)} & \dots & 0 & 0 & \mathbf{C}_{dd}^{(1)} & \dots & 0 \\ \dots & \dots & \dots & \dots & \dots & \dots & \dots \\ 0 & \dots & \mathbf{C}_{db}^{(N_b)} & 0 & \dots & \dots & \mathbf{C}_{dd}^{(N_b)} \end{bmatrix} \begin{Bmatrix} \Delta \dot{p}_1 \\ \dots \\ \Delta \dot{p}_{N_b} \\ \Delta \dot{x}_F \\ \Delta \dot{D}_1 \\ \dots \\ \Delta \dot{D}_{N_b} \end{Bmatrix} + \begin{bmatrix} \mathbf{M}_1 & \dots & 0 & \mathbf{M}_{1F} & 0 & \dots & 0 \\ \dots & \dots & \dots & \dots & \dots & \dots & \dots \\ 0 & \dots & \mathbf{M}_{N_b} & \mathbf{M}_{N_bF} & 0 & \dots & 0 \\ \mathbf{M}_{F1} & \dots & \mathbf{M}_{FN_b} & \mathbf{M}_{FF} & 0 & \dots & 0 \\ 0 & \dots & 0 & 0 & 0 & \dots & 0 \\ \dots & \dots & \dots & \dots & \dots & \dots & \dots \\ 0 & \dots & 0 & 0 & \dots & \dots & 0 \end{bmatrix} \begin{Bmatrix} \Delta \ddot{p}_1 \\ \dots \\ \Delta \ddot{p}_{N_b} \\ \Delta \ddot{x}_F \\ \Delta \ddot{D}_1 \\ \dots \\ \Delta \ddot{D}_{N_b} \end{Bmatrix} = 0 \tag{31}$$

where \mathbf{K}_i , \mathbf{C}_i , and \mathbf{M}_i are the linearized modal stiffness, damping and mass matrices of the i^{th} blade; \mathbf{K}_{iF} , \mathbf{C}_{iF} , and \mathbf{M}_{iF} are blade-fuselage coupling matrices; \mathbf{K}_{Fi} , \mathbf{C}_{Fi} , and \mathbf{M}_{Fi} are fuselage-blade coupling matrices; and x_F is the fuselage motion vector. A detailed description of these is available in Ref. 24. The damper related terms are described below.

The j^{th} element of the blade-damper coupling vector, $\mathbf{K}_{bd}^{(i)}$, in Eq. (31) is given by

$$\mathbf{K}_{bd}^{(i)} \Big|_j = \frac{1}{l} (\phi_{fb}^{(j)} - \phi_{tt}^{(j)}) \tag{32}$$

The j^{th} elements of the damper-blade coupling vectors, $\mathbf{K}_{db}^{(i)}$, and $\mathbf{C}_{db}^{(i)}$, in Eq. (31) are

$$\mathbf{K}_{db}^{(i)} \Big|_j = -\frac{K_2}{l} (\phi_{fb}^{(j)} - \phi_{tt}^{(j)}) \tag{33}$$

$$\mathbf{C}_{db}^{(i)} \Big|_j = -\frac{C_2}{l} (\phi_{fb}^{(j)} - \phi_{tt}^{(j)}) \tag{34}$$

In Eqs. (32)-(34), the superscript *i* refers to vectors pertaining to the i^{th} blade and damper. The stiffness and damping of the i^{th} damper are respectively expressed as

$$K_{dd}^{(i)} = 1 + K_2 \frac{df}{dD} \Big|_{D_T^{(i)}} + C_2 \frac{d^2f}{dD^2} \Big|_{D_T^{(i)}} \dot{D}_T^{(i)} \tag{35}$$

$$C_{dd}^{(i)} = C_2 \frac{df}{dD} \Big|_{D_T^{(i)}} \tag{36}$$

where $D_T^{(i)}$ and $\dot{D}_T^{(i)}$ denote the trim or equilibrium i^{th} damper force and its derivative. After transforming the blade-damper-fuselage equations, (31), to nonrotating coordinates using multiblade coordinate transforms, stability of the linearized periodic system can be evaluated using Floquet transition matrix theory, as described in Ref. 24.

Results and Discussion

A numerical study of elastomeric damper effects on the lag mode stability of a 3-bladed model bearingless rotor is presented in this section. The baseline rotor (without damper) was tested in hover at the Ames Research Center by the US Army Aeroflightdynamics Directorate as part of the Integrated Technology Rotor (ITR) program (Ref. 25). Recently, validation of the experimental results in Ref. 25, and a comprehensive analytical investigation of the shaft-fixed and shaft-free lag mode stability of the baseline rotor in forward flight has been carried out in Ref. 14. For the dynamic and aeroelastic analysis in the present paper, the bearingless rotor blade is discretized into eight spatial elements, three each for the main blade and the flexbeam, and two elements for the torque tube. The nondimensional stiffness and inertial properties, and geometry, for the different elements are available in Table 1. The nondimensional fundamental lag frequency for the baseline rotor is $\nu_\xi = 0.75/rev$. Blade aerodynamic loads in the evaluation of both periodic response and perturbation stability are obtained using quasi-steady strip theory and linear inflow assumption.

The elastomeric damper is attached between the inboard end of the torque tube, and the flexbeam, as indicated in Figs. 8 and 9. Since the damper analytical model was developed based on full scale damper experimental data, it is scaled down appropriately for integration into the model rotor. Two different damper sizes are considered. Damper A increases the fundamental lag frequency, ν_ξ , to 0.785/rev, while Damper B is stiffer and increases ν_ξ to 0.88/rev. Although the stiffness of the two dampers is different, both have the same nonlinear behavioral characteristics as the full scale damper. It should be pointed out that the result-

Table 1: Bearingless Rotor Blade Properties.

Element	$\frac{l_i}{R}$	$\frac{m_i}{m_o}$	$\frac{EI_y}{m_o \Omega^2 R^4}$	$\frac{EI_z}{m_o \Omega^2 R^4}$	$\frac{GJ}{m_o \Omega^2 R^4}$	$\frac{EA}{m_o \Omega^2 R^2}$	
1	0.5	0.702	0.0055	0.1488	0.0029	113.5	main blade
2	0.234	0.702	0.0055	0.1488	0.0029	113.5	main blade
3	0.0684	26.29	0.2621	0.4321	0.2904	184.5	main blade
4	0.1018	0.979	0.00157	0.00616	0.000205	365.3	flexbeam
5	0.1018	0.979	0.00157	0.00616	0.000205	365.3	flexbeam
6	0.0454	75.42	8.064	4.910	16.61	275.1	flexbeam
7	0.0509	11.25	4.473	4.495	1.664	304.7	torque tube
8	0.0509	11.25	4.473	4.495	1.664	350.0	torque tube

radius, $R=3'$, $m_o=3.0745 \times 10^{-3}$ slug/ft, $\Omega = 1100$ rpm

ing high lag frequencies would be unusual on an actual rotor due to the larger dynamic stresses they would produce. In a typical rotor design, the stiffness of the baseline rotor (without damper) would be lower (say ν_ζ of about 0.5 to 0.6/rev), with the addition of the elastomeric damper increasing the lag frequency, ν_ζ , in the range of 0.6 to 0.7/rev.

In the evaluation of the blade periodic response in forward flight, the blade modal matrices and vectors were first calculated *without considering the damper*. Inclusion of the damper nonlinear differential equation then resulted in the augmentation of the system with damper states. However, the above method can require more iterations for the convergence of the blade response, even in hover. This is because the lag modes used are not accurately representative of the physical deformations. The damper imposes a restraint resulting in modes with reduced or constrained motion between the flexbeam and torque tube. Fig. 10 shows the first lag mode deformations in the hub region with and without inclusion of the damper. Fig. 11 shows the second lag mode for the two cases. In Figs. 10 and 11, O and P' denote the radial points of attachment of the damper to the flexbeam and torque tube, respectively. Neglecting damper influence yields a mode, in which the inboard end of the torque tube, P, is less restrained, relative to the flexbeam. This effect is more pronounced for the second lag mode than the first lag mode. In order to improve blade response convergence, damper stiffness may be considered between the torque tube and the flexbeam in the *evaluation of the modes*. These modes are used in the calculation of the *baseline* bearingless rotor modal matrices, which are subsequently

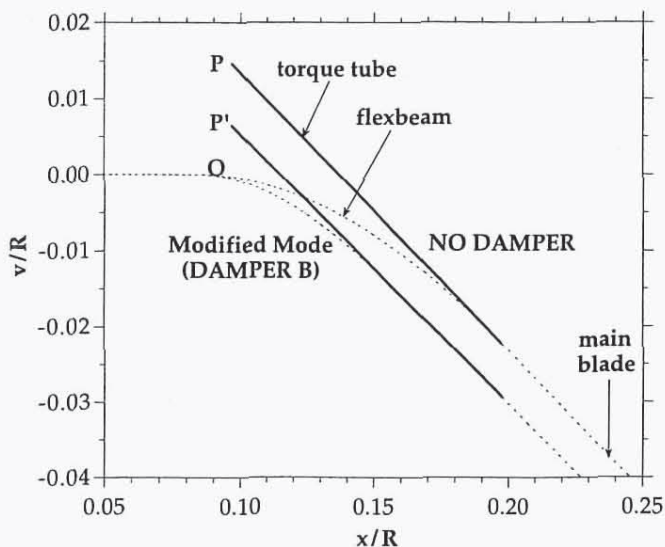


Fig. 10. Bearingless main rotor blade first lag mode shape, with and without inclusion of damper stiffness.

augmented due to the inclusion of the damper nonlinear differential equation. Thus, the stiffer damper, B, which increases ν_ζ to 0.88/rev, results in a larger lag response than damper A, which increases ν_ζ to 0.785/rev. The phase shift (damping effect) for damper B is also seen to be greater.

Figs. 13 and 14, respectively, show the variation of shaft-fixed and

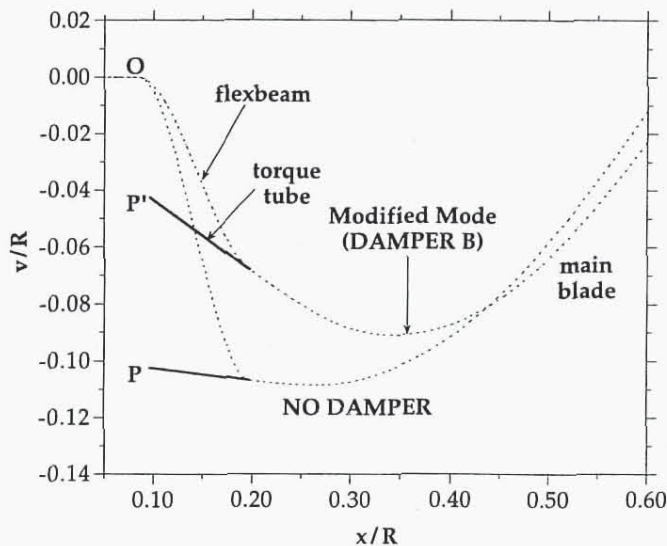


Fig. 11. Bearingless main rotor blade second lag mode shape, with and without inclusion of damper stiffness.

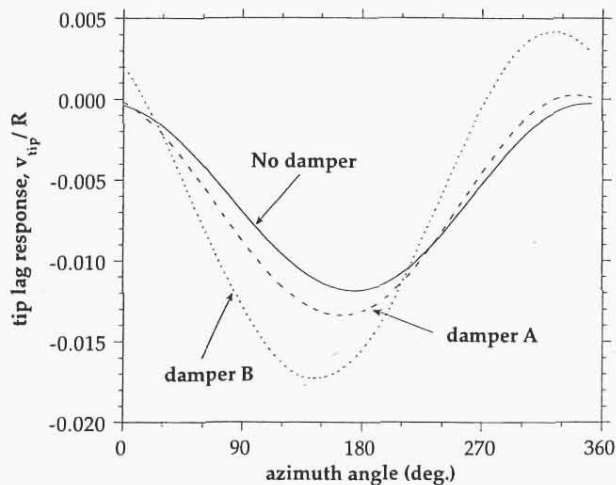


Fig. 12. Periodic tip lag response at advance ratio $\mu=0.15$.

shaft-free lag mode damping with advance ratio, for the baseline rotor (no elastomeric damper) at $C_r/\sigma = 0.07$. For the isolated rotor (Fig. 13), as expected, the damping in the collective, progressive and regressive modes is practically the same. Structural damping in the lag mode was assumed to be 1%. The increased damping at higher advance ratios is due to aerodynamic effects. When fuselage motion is included, the damping in the regressive lag mode decreases due to its interaction with body pitch/roll motion (Fig. 14).

Fig. 15 shows the shaft-fixed isolated rotor lag mode stability with the inclusion of the elastomeric damper. The stiffer damper B results in greater stability of the lag mode, over the entire range of advance ratios. The inclusion of the elastomeric damper is seen to bring about a qualitative change in the nature of lag damping variation with advance ratio. Unlike the baseline rotor, the lag damping shows a general decrease with increasing advance ratio. This can be attributed to the nonlinear behavior of the damper, specifically, the decrease in G'' (damping) at higher amplitudes of periodic lag motion (Fig. 2). Since the amplitude of the periodic lag response increases with advance ratio, it results in a

decrease in damping capabilities of the nonlinear elastomeric damper. Thus, there are two factors contributing to the lag mode damping: (i) aerodynamic effects, which result in an increase in lag damping at higher advance ratios, and (ii) nonlinear damper behavior which results in the decrease in lag damping at higher advance ratios. For the stiffer damper B, the damper nonlinear behavior predominates, and lag damping is seen to decrease with advance ratio. For the less stiff damper A, its nonlinear behavior is dominant at low advance ratios, but the increasing aerodynamic damping at high advance ratios causes a slight increase in the lag mode damping. The above hypothesis is verified by examining the lag damping calculated using a *linear* elastomeric damper. Fig. 16 shows that if a *linear* elastomeric damper is assumed, the overall lag mode stability is greater than that of the damperless rotor, but the *variation with advance ratio* is almost identical to the case of the damperless rotor. Thus it is clear that the nonlinear characterization of the damper results in the reduced lag mode stability at higher advance ratios.

Figs. 17 and 18 show the shaft-free aeromechanical stability of the bearingless rotor with the inclusion of dampers A and B, respectively.

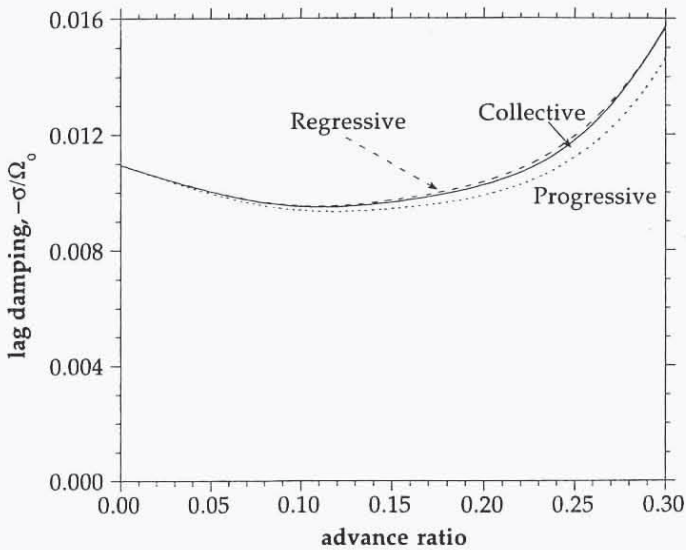


Fig. 13. Variation of shaft-fixed lag mode stability of the baseline (damperless) rotor with advance ratio.

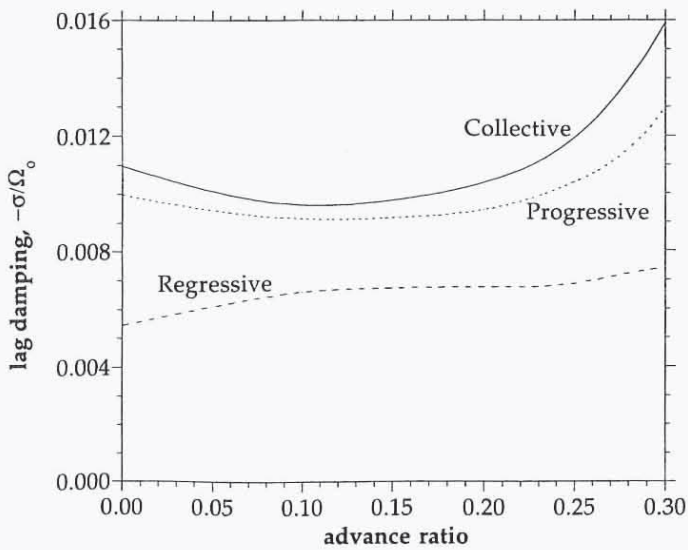


Fig. 14. Variation of shaft-free lag mode stability of the baseline (damperless) rotor with advance ratio.

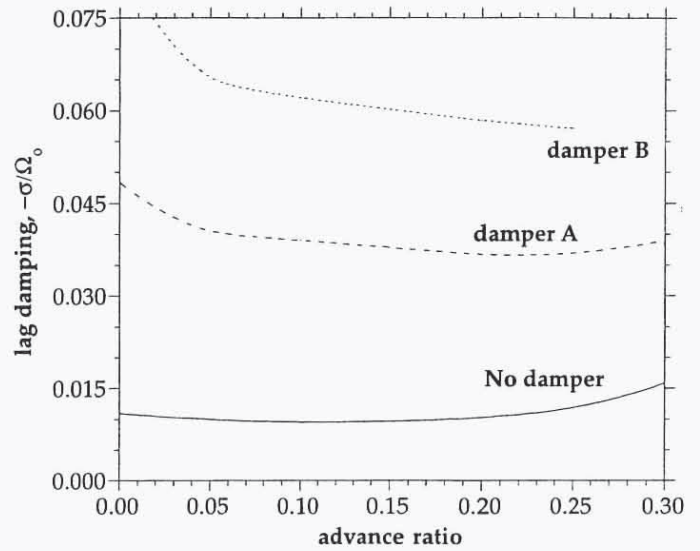


Fig. 15. Bearingless rotor shaft-fixed lag mode stability with inclusion of nonlinear elastomeric damper.

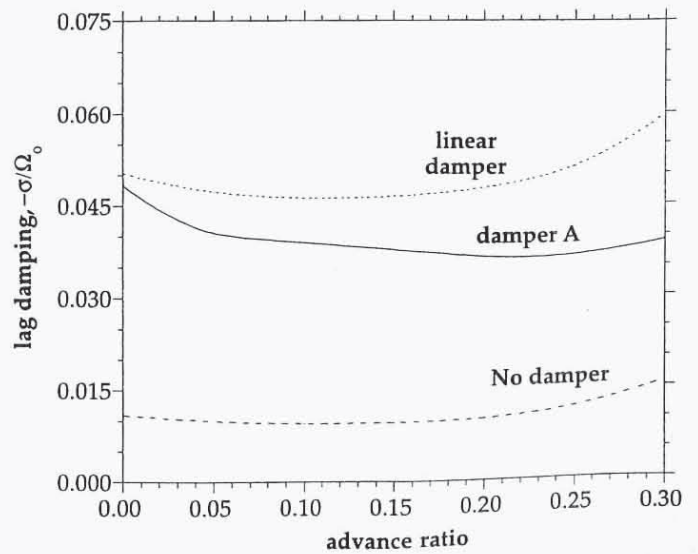


Fig. 16. Comparison of bearingless rotor shaft-fixed lag mode stability using linear and nonlinear damper.

While the elastomeric damper has a stabilizing influence on the collective, progressive as well as regressive lag modes, the damping of the regressive lag mode is considerably lower than that of the progressive and collective modes, with damper B (Fig. 18). Since this phenomenon is not observed for the shaft-fixed case, nor with the use of the weaker damper A (for both shaft-fixed and shaft-free conditions), it may be concluded that the lower regressive mode damping must be due to the influence of damper B dynamics on the coupled regressive lag/fuselage mode.

Another interesting observation is the effect of the elastomeric damper on the *second lag mode frequency*. Fig. 19 shows the variation of the second lag mode frequency with advance ratio, due to the nonlinear characterization of the damper. While the elastomeric damper also increases the first lag mode frequency, such a *variation with advance ratio* is not observed. To understand this phenomenon, it is useful to consider the damper equilibrium deformations as a sum of modal contributions. From Eq. (18), the damper deformation can be expressed

in modal coordinates as $\sum \frac{\phi_{fb}^{(j)} - \phi_{ft}^{(j)}}{l} p_j$. Although the first lag

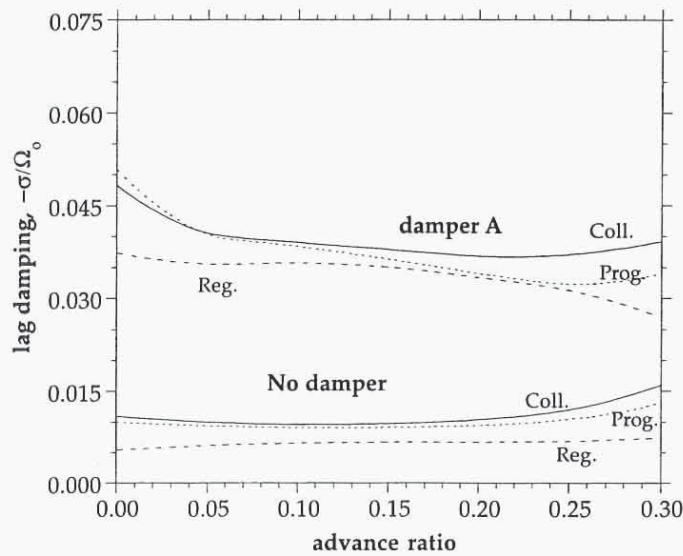


Fig. 17. Bearingless rotor shaft-free lag mode stability with inclusion of damper A.

mode coordinate, p_1 , could be larger than the second lag mode coordinate, p_2 , a comparison of Figs. 10 and 11 clearly shows that $(f_{fb}^{(j)} - f_{ft}^{(j)})$ (distance from O to P or P') for the second lag mode is substantially larger (7-8 times) than the first lag mode. Thus, if the damper periodic motion is predominantly second mode, it stands to reason that decrease in damper stiffness with increasing periodic motion (Fig. 2) obtained at higher advance ratios, will also manifest itself in the second mode. Fig. 20 shows the second lag mode frequency versus advance ratio for a *linear* damper. Expectedly, since the nonlinear characterization is not considered, a constant increase in frequency is obtained, and no variation in frequency is observed with advance ratio.

Summary and Concluding Remarks

An elastomeric damper model comprising of a nonlinear spring and a Kelvin chain is augmented with additional nonlinear springs to represent experimentally observed degradation in G'' (damping) at very low dynamic amplitudes, and occurrence of limit cycle oscillations (jitter)

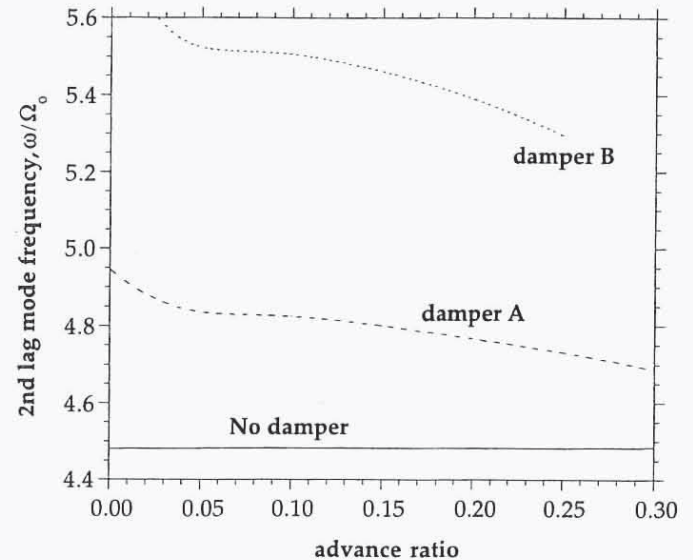


Fig. 19. Effect of elastomeric damper on second lag frequency.

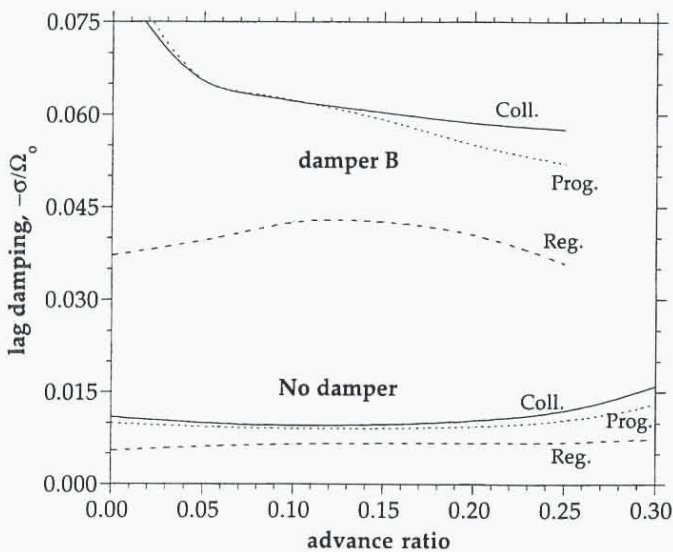


Fig. 18. Bearingless rotor shaft-free lag mode stability with inclusion of damper B.

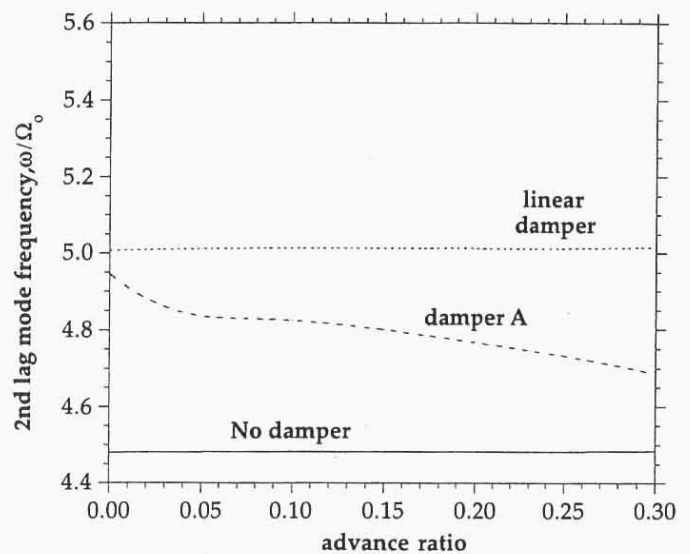


Fig. 20. Comparison of linear and nonlinear damper effects on second lag frequency.

due to applied perturbations. The hysteresis cycles calculated with the augmented model better represent the experimentally measured force/displacement behavior under cyclic loading. The damper model is described in the time domain by a nonlinear differential equation.

Integration of the damper into a bearingless rotor comprehensive analysis results in the augmentation of the rotor/fuselage state vector with additional damper states. The rotor/fuselage mass, damping and stiffness matrices, and load vector, are first evaluated without considering the damper. The damper differential equation is then introduced, resulting in augmented system matrices and vectors. This approach is easy to implement since it requires very few changes in an existing bearingless rotor comprehensive analysis.

The influence of the damper on bearingless rotor aeroelastic and aeromechanical behavior in forward flight is examined. The following observations were made:

(i) Consideration of damper stiffness between the torque tube and flexbeam in the *evaluation of modes* improves blade response convergence significantly. These modes can be used in calculation of baseline blade modal matrices and load vector, which are subsequently augmented due to inclusion of the damper nonlinear differential equation.

(ii) Since an elastomeric damper increases the fundamental lag frequency closer to the first rotor harmonic ($1/rev$), it results in an increase in amplitude of periodic lag response.

(iii) Since damper stiffness and damping capabilities are directly dependent on its periodic motion (both decreasing at higher amplitudes), its behavior varies, accordingly, with advance ratio. The lag mode damping trends with advance ratio depend on the relative contributions of the nonlinear elastomeric damper and aerodynamic effects. Additionally, influence of damper dynamics on coupled regressive lag/fuselage motion could result in a diminished damping effect, for some cases.

(iv) An estimate of modal contributions of damper motion shows that second lag mode is much more predominant than the first lag mode. Thus, the nonlinear characterization of the damper results in a variation of second lag mode frequency with increasing advance ratio (increasing periodic motion), not observed for the first lag mode frequency.

Acknowledgments

This research work is supported by the Army Research Office under the Center for Rotorcraft Education and Research, Grant No. DAAH04-93-G-0001; Technical Monitors Dr. Tom Doligalski and Dr. Robert Singleton.

References

- ¹Huber, H., "Will Rotor Hubs Lose Their Bearings? A Survey of Bearingless Main Rotor Development," Proceedings of the 18th European Rotorcraft Forum, Avignon, France, Sept 1992.
- ²Chopra, I., "Perspectives in Aeromechanical Stability of Helicopters," *Vertica*, Vol. 14, No.4, 1990, pp. 457-508.
- ³Potter, J.L., "Improving Reliability and Eliminating Maintenance with Elastomeric Dampers for Rotor Systems," Lord Library No. LL2120, 1976.
- ⁴McGuire, D.P., "The Application of Elastomeric Lead-Lag Dampers to Helicopter Rotors," Lord Library No. LL2133, 1976.
- ⁵Hodges, D.H., "A Theoretical Technique for Analyzing Aeroelastic Stability of Bearingless Rotors," *AIAA Journal*, Vol. 17, No. 4, Oct 1978, pp. 400-407.
- ⁶Hodges, D.H., "An Aeromechanical Stability Analysis for Bearingless Rotor Helicopters," *Journal of the American Helicopter Society*, Vol. 24, No. 1, Jan 1979, pp. 2-9.
- ⁷Hodges, D.H., Hopkins, A.S., Kunz, D.L., and Hinnant, H.E., "Introduction to GRASP - General Rotorcraft Aeromechanical Stability Program - A Modern Approach to Rotorcraft Modeling," Proceedings of the 42nd Annual Forum of the American Helicopter Society, Washington DC, June 1986.

⁸Sivaneri, N.T., and Chopra, I., "Finite Element Analysis for Bearingless Rotor Blade Aeroelasticity," *Journal of the American Helicopter Society*, Vol. 29, No. 2, Apr 1984, pp. 42-51.

⁹Dull, A.L., and Chopra, I., "Aeroelastic Stability of Bearingless Rotors in Forward Flight," *Journal of the American Helicopter Society*, Vol. 33, No. 4, Oct 1988, pp. 38-46.

¹⁰Jang, J., and Chopra, I., "Ground and Air Resonance of an Advanced Bearingless Rotor in Hover," *Journal of the American Helicopter Society*, Vol. 33, No. 3, July 1988, pp. 20-29.

¹¹Jang, J., and Chopra, I., "Air Resonance of an Advanced Bearingless Rotor in Forward Flight," Proceedings of the 2nd International Conference on Rotorcraft Basic Research, College Park, Maryland, Feb 1988.

¹²Hong, C.H., and Chopra, I., "Aeroelastic Stability Analysis of a Composite Bearingless Rotor Blade," *Journal of the American Helicopter Society*, Vol. 31, No. 4, Oct 1986, pp. 29-35.

¹³Tracy, A.L., and Chopra, I., "Aeroelastic Analysis of a Composite Bearingless Rotor in Forward Flight with Improved Warping Modeling," Proceedings of the American Helicopter Society Aeromechanics Specialists' Conference, San Francisco, California, Jan 1994.

¹⁴Gandhi, F., and Chopra, I., "A Refined Analysis Methodology for Bearingless main Rotor Helicopters in Forward Flight," Presented at the ASME Winter Annual Meeting (Special Symposium on Aeroelasticity and Fluid Structure Interaction), Chicago, Illinois, Nov 1994.

¹⁵Wang, J.M., Duh, J., and Fuh, J-S., "Stability of the S-76 Bearingless Main Rotor," Proceedings of the 49th Annual Forum of the American Helicopter Society, St. Louis, Missouri, May 1993.

¹⁶Hausmann, G., "Structural Analysis and Design Considerations of Elastomeric Dampers with Viscoelastic Material Behavior," Proceedings of the 12th European Rotorcraft Forum, Garmisch-Partenkirchen, Federal Republic of Germany, Sept 1986.

¹⁷Hausmann, G., and Gergley, P., "Approximate Methods for Thermoviscoelastic Characterization and Analysis of Elastomeric Lead-Lag Dampers," Proceedings of the 18th European Rotorcraft Forum, Avignon, France, Sept 1992.

¹⁸Felker, F., Lau, B., McLaughlin, S., and Johnson, W., "Nonlinear Behavior of an Elastomeric Lag Damper Undergoing Dual Frequency Motion and its Effect on Rotor Dynamics," *Journal of the American Helicopter Society*, Vol. 32, No. 4, Oct 1987, pp. 45-53.

¹⁹Gandhi, F., and Chopra, I., "Analysis of Bearingless Main Rotor Dynamics with the Inclusion of an Improved Time Domain Nonlinear Elastomeric Damper Model," Proceedings of the AHS 51st Annual Forum, Fort Worth, Texas, May 1995.

²⁰Gandhi, F., Chopra, I., and Lee, S.W., "A Nonlinear Viscoelastic Damper Model: Constitutive Equation and Solution Scheme," Proceedings of the 1994 (SPIE) North American Conference on Smart Structures and Materials, Orlando, Florida, Feb 1994.

²¹Gandhi, F., and Chopra, I., "An Analytical Model for a Nonlinear Elastomeric Lag Damper and its Effect on Aeromechanical Stability in Hover," *Journal of the American Helicopter Society*, Vol. 39, No. 4, Oct 1994, pp. 59-69.

²²Gandhi, F., and Chopra, I., "Elastomeric Lag Damper Effects on Flap-Lag Stability in Forward Flight," Proceedings of the AIAA/ASME/ASCE/AHS/ACS 35th Structures, Structural Dynamics and Materials Conference, Hilton Head, South Carolina, Apr 1994.

²³Ingle, S.J., Weber, T.L., and Miller, D.G., "Concurrent Handling Qualities and Aeroservoelastic Specification Compliance for the RAH-66 Comanche," Proceedings of the American Helicopter Society Aeromechanics Specialists' Conference, San Francisco, California, Jan 1994.

²⁴Bir, G., Chopra, I., et al., "University of Maryland Advanced Rotor Code (UMARC) Theory Manual," UM-AERO Report 92-02, Aug 1992.

²⁵Dawson, S., "An Experimental Investigation of a Bearingless Model Rotor in Hover," *Journal of the American Helicopter Society*, Vol. 28, No. 4, Oct 1983, pp. 29-34.

An Aeroelastic Analysis Methodology for Bearingless Main Rotor Helicopters



Farhan Gandhi
Assistant Professor
Rotorcraft Center of Excellence
Department of Aerospace Engineering
The Pennsylvania State University
University Park, PA 16802



Inderjit Chopra
Minta Martin Professor and Director
Alfred Gessow Rotorcraft Center
Department of Aerospace Engineering
University of Maryland
College Park, MD 20742

A methodology for the aeroelastic analysis of bearingless main rotor helicopters in forward flight is presented. The large elastic twist experienced by the flexbeam during pitch control application can influence the nonlinear aeroelastic behavior. Including its effects by eliminating the rigid pitch control rotation, θ , and using an angle, $\hat{\phi}$, to represent the spanwise distribution of cross-sectional torsional orientation would preclude the use of normal mode equations in the evaluation of blade periodic response in forward flight. In the present analysis, the elastic deformations due to pitch control are independently evaluated as the in vacuo structural response to a prescribed swashplate motion. Modified nonlinear equations of motion that include the effect of flexbeam elastic deformations due to pitch control, are used in the aeroelastic analysis. The present analysis is robust and has good convergence behavior in the evaluation of blade periodic response. Good correlation with experimental lag damping data is obtained for two different bearingless rotor configurations. Different types of pitch-flap coupling due to leading edge or trailing edge pitch links in a snubberless configuration are seen to have a strong effect on torsional response. The forward flight shaft-fixed and shaft-free stability characteristics are examined for the two pitch link configurations.

Notation

a	Bearingless rotor pitch horn chordwise offset	w_{pl}	Pitch link elastic deformation
C_T	Rotor thrust coefficient	w_{sp}	Pitch link vertical motion due to swashplate control
e_A	Chordwise offset of tensile axis ahead of elastic axis	W	Work done
EA	Axial stiffness	x, y, z	Undeformed blade coordinate system
EB_1, EB_2	Section stiffness constants	x_o	Lag pin radial offset
EC_1	Warping rigidity	z_o	Lag pin vertical offset
EC_2	Section warping constant	δT	Variation in kinetic energy
EI_y, EI_z	Flap bending stiffness, lag bending stiffness	δU	Variation in strain energy
F^{NL}	Load vector due to structural nonlinearities	δU_b	Strain energy variation for blade
GJ	Torsional stiffness	δU_{pl}	Strain energy variation for pitch link
k_A	Radius of gyration of blade cross-section	δW	Virtual work
K^G	Global structural stiffness matrix	ϵ_{xx}	Axial strain
K_{pl}	Pitch link axial stiffness	$\epsilon_{xy}, \epsilon_{xz}$	Engineering shear strain
p	Bearingless rotor pitch horn radial offset	θ_o	Rigid pitch angle due to control
q_b	Global nodal displacement vector	λ_T	Warping function
u	Blade displacement in x direction	ξ, η, ζ	Rotating deformed blade coordinate system
u_e	Displacement in x direction due to elastic stretching (Note, $u'_e = u' + \frac{v'^2}{2} + \frac{w'^2}{2}$)	σ	Rotor solidity ratio
U	Strain Energy	σ_{xx}	Axial stress
v	Blade displacement in y direction	σ_{xy}, σ_{xz}	Shear stresses
w	Blade displacement in z direction	$\hat{\phi}$	Elastic cross-sectional torsional orientation (Note, $\phi = \hat{\phi} + \int_0^x w' v''$)
		()'	$\partial(\)/\partial x$
		()''	$\partial^2(\)/\partial x^2$
		$\delta(\)$	Variation in ()
		() _c or () _f	due to control application via swashplate
		() _{tt}	denotes inboard end of the torque tube
		() _{total}	due to control application as well as aeroelastic loads

Introduction

Over the last three decades, strong emphasis on rotor design simplicity has culminated in the development of the bearingless main rotor. In this type of rotor, the flap and lag hinges, as well as the pitch bearing, are eliminated, resulting in a substantial reduction in parts count, weight, drag, and maintenance costs. The main blade of the bearingless rotor is attached to the hub by means of a torsionally soft flexure that allows flap and lag bending as well as elastic twist. The flexbeam is generally surrounded by a torsionally stiff torque tube, which is attached to the main blade/flexbeam at the outboard end, and to a pitch link at the inboard end. Pitch control of the main blade is achieved by rotating the torque tube with the pitch link. This in turn rotates the main blade, elastically twisting the flexbeam in the process. It is this pitch control mechanism that primarily distinguishes a bearingless rotor from a hingeless rotor.

Since production bearingless rotors are designed as soft-inplane rotors, their susceptibility to aeromechanical instability is a major concern. Consequently, a large number of model as well as full scale configurations have been tested by both the major helicopter manufacturers as well as NASA/Army Labs, to examine their aeroelastic and aeromechanical stability characteristics. A very detailed and comprehensive description of the various experimental as well as design and developmental efforts is available in a recent review by Huber (Ref. 1).

Simultaneously, considerable efforts have also been directed towards the analytical modeling of bearingless main rotors. This is much more involved than the analysis of hingeless or articulated rotors due to presence of multiple load paths, complex hub kinematics, and large elastic deformations in the flexbeam during pitch control application. The major rotorcraft manufacturers have individually developed and refined their own in-house methodologies and computational codes for the prediction of bearingless rotor aeroelastic behavior. These are based on a variety of methods such as the Mykelstead method, modal method, etc. However, no detailed documentation of these analyses is available in the literature. One of the earliest analytical models for bearingless main rotors reported in the literature was the FLAIR program, developed at the Army Aeroflight-dynamics Directorate (Refs. 2,3). In this analysis, the flexbeam was modeled as a Bernoulli-Euler beam undergoing elastic bending, torsion and axial deformation, while the main blade was assumed to be rigid. While this formulation was useful in calculating the aeromechanical stability characteristics of a few bearingless rotor configurations, it could not be used for evaluating blade dynamic stresses, rotor vibratory hub loads, or even flutter type instabilities involving higher modes. Soon after, the Aeroflight-dynamics Directorate developed GRASP (Ref. 4) which considered the elastic deformations in the main blade, as well. However, both the analyses were developed only for a hover condition.

The first report in the literature on the application of the finite element method to bearingless rotor analysis was by Sivaneri and Chopra (Ref. 5). This is a very suitable approach for bearingless rotor analysis as it can accurately model the complex hub kinematics and the redundant load paths of such a rotor. Using this finite element model as the basis, researchers at the University of Maryland (Refs. 6-10) conducted analytical investigations on the aeroelastic and aeromechanical stability characteristics of various bearingless rotor configurations in hover and forward flight conditions. Dull and Chopra (Ref. 6) examined the shaft-fixed aeroelastic stability of bearingless rotors with and without torque-tube shear restraints. This was followed by a study of the shaft-free aeromechanical stability characteristics of the Boeing-ITR model bearingless rotor (with torque tube shear restraint), in hover (Ref. 7) and forward flight conditions (Ref. 8), by Jang and Chopra. The dynamics of bearingless main rotors with tailored composite flexbeams was examined by Hong and Chopra (Ref. 9), in a hover condition. Tracy and Chopra (Ref. 10) used an improved structural model, including transverse shear effects and refined

cross-section warping for composite flexbeams, and examined the aeroelastic stability in forward flight. In the above analyses, the blade periodic response in forward flight was first calculated using a temporal finite element method, after transforming the spatially discretized elastic blade equations to a few normal mode equations, to reduce computation time. Stability of the perturbation equations was then calculated using Floquet theory.

Since bearingless rotor flexbeams experience large elastic twisting during pitch control application, the use of normal modes in the evaluation of blade periodic response is fraught with difficulty. In References (Refs. 6-10), the effects of the flexbeam elastic twist due to pitch control were only approximately included in the bearingless rotor analysis. However, in order to successfully design optimized or tailored flexbeams for improved stability and performance, and reduced hub loads, it is necessary to more carefully include the flexbeam deformations due to pitch control application in the analysis, as the aeroelastic behavior could depend significantly on the initially deformed configuration. In the present paper, an aeroelastic analysis for bearingless main rotors in forward flight is developed. The analysis is carried out in two steps: (i) calculation of the elastic deformations experienced by the bearingless blade as a result of pitch control application *in the absence of aerodynamics*, and (ii) use of a *modified set of equations*, which includes the influence of the previously calculated elastic deformations due to pitch control, to evaluate the aeroelastic characteristics of the bearingless rotor. Validation of the present analysis with experimental lag damping data is presented, and a systematic study of the aeroelastic and aeromechanical stability in forward flight is undertaken for bearingless rotors with leading edge and trailing edge pitch link configurations.

Analysis

Strain Energy Associated with Elastic Deformations due to Blade Pitch Control

The rotor blades are modeled as elastic beams undergoing coupled flap bending, lag bending, elastic torsion, and axial displacements. The nonlinear equations of motion, adapted from the work of Hodges and Dowell (Ref. 11), are derived using Hamilton's principle:

$$\int_{t_1}^{t_2} (\delta U - \delta T - \delta W) dt = 0 \quad (1)$$

where δU and δT are the variations in strain energy and kinetic energy, respectively, and δW is the virtual work done by external (aerodynamic) forces. In Ref. 11, δU was formulated for bending, stretching, and elastic twisting deformations about a pitch setting, θ_0 . Since θ_0 represented a rigid rotation and not an elastic deformation, it did not directly contribute to the strain energy variation, δU . While this is an appropriate modeling assumption for articulated and hingeless rotors, it is not entirely valid for bearingless rotors. This is because in the pitch control of a bearingless rotor a rigid rotation, θ_0 , of the main blade (and torque tube) is accompanied by a corresponding elastic twisting of the flexbeam. The elastic twisting can be of significant magnitude and its spanwise distribution for a nonuniform flexbeam can be quite complex. For the analysis of bearingless main rotors, it is necessary to take into consideration the elastic twist deformations in the flexbeam due to pitch control, as the aeroelastic behavior of the rotor can be affected by its initially deformed configuration.

Before elaborating on methods for including the effects of the elastic twisting of the bearingless rotor flexbeam during pitch control application, it is useful to briefly discuss the kinematics of deformation of the elastic rotor blade. The rotor blade is assumed to undergo elastic bending deformations, w and v , elastic stretching, u_c , and twisting. When moderate deflections are assumed, the final orientation angle of any cross-section is de-

noted as $\hat{\phi}$ (with respect to a pitch setting). The elastic twist rate required in the computations of the strain energy can then be expressed as

$$\phi' = \hat{\phi}' + w'v'' \quad (2)$$

In the present analysis $\hat{\phi}$ is used as the fundamental torsional variable due to convenience in calculation of aerodynamic loads.

To include the effect of flexbeam elastic twist due to pitch control, one possible method would be through the elimination of the rigid pitch rotation, θ_0 , and the use of a distributed cross-sectional orientation angle, $\hat{\phi}_{\text{total}}$, to include both pitch control effects as well as the subsequent aeroelastic deformations. Pitch control application would, of course, result in a zero twist rate over the blade and torque tube, so that the only contributions to the strain energy would come from the flexbeam. In this case, the strain-displacement relations are, in general,

$$\epsilon_{xx} = u'_e - \lambda_T \phi''_{\text{total}} + (\eta^2 + \zeta^2) \left\{ \frac{\phi'^2_{\text{total}}}{2} \right\} - v'' \{ \eta \cos(\hat{\phi}_{\text{total}}) - \zeta \sin(\hat{\phi}_{\text{total}}) \} - w'' \{ \eta \sin(\hat{\phi}_{\text{total}}) + \zeta \cos(\hat{\phi}_{\text{total}}) \} \quad (3a)$$

$$\epsilon_{x\eta} = -\xi \phi'_{\text{total}} = -\xi (\hat{\phi}'_{\text{total}} + w'v'') \quad (3b)$$

$$\epsilon_{x\zeta} = \hat{\eta} \phi'_{\text{total}} = \hat{\eta} (\hat{\phi}'_{\text{total}} + w'v'') \quad (3c)$$

The main drawback of such an approach is that the small angle assumption cannot be made on $\hat{\phi}_{\text{total}}$ since it inherently contains the pitch control angle which can assume values in excess of 20° in high speed forward flight or maneuvering flight. This would preclude the use of normal mode approximations of the blade equations of motion. The inability to transform spatially discretized blade finite element equations to a few normal mode equations would result in a significant increase in computation time for the evaluation of the blade periodic response in forward flight.

The approach taken in the present paper is to consider $\hat{\phi}_{\text{total}}$ (or ϕ_{total}) to be composed of two distinct components

$$\phi_{\text{total}} = \phi_c + \hat{\phi} \quad (4)$$

(i) ϕ_c — the elastic deformations of the bearingless blade due to the application of pitch control, calculated in the rotating condition. Unlike the rigid pitch rotation, θ_0 , in Ref. 11, ϕ_c directly contributes to the elastic strain energy of the bearingless rotor flexbeam. The term ϕ_c , evaluated as the deformation field to a given swashplate displacement, would take on a constant value over the main blade and torque tube ($\phi'_c = 0$, implying that they undergo rigid rotations), while varying over the flexbeam length ($\phi'_c \neq 0$, implying that elastic twisting occurs).

(ii) $\hat{\phi}$ — due to aeroelastic loads (as in Ref. 11) superposed over the known twist distribution, $\hat{\phi}_c$. Since large control rotations due to swashplate input are not present in $\hat{\phi}$, small angle approximations are made, and trigonometric expansions $\sin(\hat{\phi}_{\text{total}}) = \sin \hat{\phi}_c + \hat{\phi} \cos \hat{\phi}_c$ and $\cos(\hat{\phi}_{\text{total}}) = \cos \hat{\phi}_c - \hat{\phi} \sin \hat{\phi}_c$ are carried out (in Eq. 3a) to obtain algebraic expressions for $\hat{\phi}$. The spatially discretized blade equations of motion are transformed to the normal mode domain for the evaluation of periodic response in forward flight. The normal modes used for this purpose are the structural normal modes calculated in the rotating condition in the absence of aerodynamic loads, i.e., about the undeformed configuration.

Some bearingless configurations, such as a snubberless single pitch link configuration, or a configuration with a torque-tube shear restraint, result in kinematic pitch-flap or pitch-lag couplings. For such configurations, a swashplate control motion can produce flapwise or lagwise bending in addition to the elastic twisting of the flexbeam. Thus, it is assumed in general that the swashplate control motion results in an elastic twist as well as elastic flap bending, w_c , lag bending, v_c , and axial deformation,

u_{e_c} , all calculated in the rotating condition. The total deformation field is represented by Eq. 4 and

$$\begin{aligned} w_{\text{total}} &= w_c + w \\ v_{\text{total}} &= v_c + v \\ u_{e_{\text{total}}} &= u_{e_c} + u_e \end{aligned} \quad (5)$$

Figure 1 shows the undeformed cross-section, as well as the configuration achieved after undergoing the total deformation due to swashplate control [$\phi_c, w_c, v_c, u_{e_c}$] and aeroelastic influences [$\hat{\phi}, w, v, u_e$]. Strain-displacement relations based on the total deformation field [$\phi_{\text{total}}, w_{\text{total}}, v_{\text{total}}, u_{e_{\text{total}}}$], are used to obtain the strain energy variation δU , which is introduced into Hamilton's principle (Eq. 1). The strain-displacement relations are written as

$$\begin{aligned} \epsilon_{xx} &= u'_e + u'_{e_c} - \lambda_T (\phi'_c + \phi') + (\eta^2 + \zeta^2) \frac{(\phi'_c + \phi')^2}{2} \\ &\quad - (v'' + v''_c) \{ \eta \cos(\phi_c + \hat{\phi}) - \zeta \sin(\phi_c + \hat{\phi}) \} \\ &\quad - (w'' + w''_c) \{ \eta \sin(\phi_c + \hat{\phi}) + \zeta \cos(\phi_c + \hat{\phi}) \} \end{aligned} \quad (6a)$$

$$\epsilon_{x\eta} = -\xi (\phi'_c + \phi') = -\xi \{ \hat{\phi}'_c + \hat{\phi}' + (w' + w'_c)(v'' + v''_c) \} \quad (6b)$$

$$\epsilon_{x\zeta} = \hat{\eta} (\phi'_c + \phi') = \hat{\eta} \{ \hat{\phi}'_c + \hat{\phi}' + (w' + w'_c)(v'' + v''_c) \} \quad (6c)$$

The strain energy variation is

$$\delta U = \int_0^R \int_A (E \epsilon_{xx} \delta \epsilon_{xx} + G \epsilon_{x\eta} \delta \epsilon_{x\eta} + G \epsilon_{x\zeta} \delta \epsilon_{x\zeta}) d\eta d\zeta dx \quad (7)$$

On evaluating the integrals over the cross section, δU can be written in the following form

$$\begin{aligned} \delta U &= \int_0^R (U_{u_e} \delta u' + U_{v_c} \delta v'' + U_{w_c} \delta w' + U_{w''} \delta w'' \\ &\quad + U_{\hat{\phi}} \delta \hat{\phi} + U_{\hat{\phi}'} \delta \hat{\phi}' + U_{\hat{\phi}''} \delta \hat{\phi}'') dx \end{aligned} \quad (8)$$

Baseline expressions $U_{u_e}^0, U_{v_c}^0, U_{w_c}^0, U_{w''}^0, U_{\hat{\phi}}^0, U_{\hat{\phi}'}^0$ and $U_{\hat{\phi}''}^0$ (based on strain-displacement relations in Ref. 11) are available in Ref. 12. The augmented expressions due to the use of strain-displacement relations (Eqs. 6) are given below:

$$\begin{aligned} U_{u_e} &= U_{u_e}^0 + E A k_A^2 \frac{\phi_c'^2}{2} + E A k_A^2 \phi_c' w_c' v'' + E A k_A^2 \phi_c' w' v'' \\ &\quad + E A k_A^2 \phi_c' w_c' v_c'' - E A e_A w_c'' \sin \phi_c - E A e_A w_c'' \hat{\phi} \cos \phi_c \\ &\quad - E A e_A v_c'' \cos \phi_c + E A e_A v_c'' \hat{\phi} \sin \phi_c + E A u_{e_c} \\ U_{v_c} &= U_{v_c}^0 - E C_2 \phi_c'' \sin \phi_c - E C_2 \phi_c'' \hat{\phi} \cos \phi_c - E B_2 \frac{\phi_c'^2}{2} \cos \phi_c + E B_2 \frac{\phi_c'^2}{2} \hat{\phi} \sin \phi_c \\ &\quad + E B_1 w' \frac{\phi_c'^3}{2} + E B_1 w' \frac{\phi_c'^2}{2} \hat{\phi}' + w_c'' (E I_z - E I_y) \cos \phi_c \sin \phi_c \\ &\quad + w_c'' (E I_z - E I_y) \hat{\phi} \cos 2\phi_c + E A k_A^2 \phi_c' u_e' w_c' + E B_1 \phi_c'^2 w_c' \hat{\phi}' \\ &\quad + E B_1 w_c'' \frac{\phi_c'^3}{2} + E B_1 w_c'' \frac{\phi_c'^2}{2} \hat{\phi}' + v_c'' (E I_z \cos^2 \phi_c + E I_y \sin^2 \phi_c) \\ &\quad - \hat{\phi} v_c'' (E I_z - E I_y) \sin 2\phi_c - E A e_A u_{e_c}'' \cos \phi_c + E A e_A u_{e_c}'' \hat{\phi} \sin \phi_c \\ &\quad + E A k_A^2 \phi_c' u_e' w_c' + E A k_A^2 \phi_c' u_e' w' + G J w_c' \phi_c' + G J w' \phi_c' + G J w_c' \hat{\phi}' \\ U_{w_c} &= U_{w_c}^0 + E B_1 v'' \frac{\phi_c'^3}{2} + E B_1 v'' \frac{\phi_c'^2}{2} \hat{\phi}' + E B_1 v_c'' \frac{\phi_c'^3}{2} + E B_1 v_c'' \frac{\phi_c'^2}{2} \hat{\phi}' \\ &\quad + E B_1 v_c'' \phi_c'^2 \hat{\phi}' + E A k_A^2 \phi_c' v_c'' u_e' + E A k_A^2 \phi_c' v_c'' u_e' + E A k_A^2 \phi_c' v'' u_e' \\ &\quad + G J v_c'' \phi_c' + G J v'' \phi_c' + G J v_c'' \hat{\phi}' \end{aligned}$$

$$\begin{aligned}
 U_w'' &= U_w^0'' + \underline{EC_2\phi_c'' \cos \phi_c} - \underline{EC_2\phi_c'' \hat{\phi} \sin \phi_c} - \underline{EB_2\frac{\phi_c'^2}{2} \sin \phi_c} \\
 &\quad - \underline{EB_2\frac{\phi_c'^2}{2} \hat{\phi} \cos \phi_c} + \underline{w_c'' EI_z \sin^2 \phi_c} + \underline{w_c'' EI_y \cos^2 \phi_c} \\
 &\quad + \underline{v_c'' (EI_z - EI_y) \hat{\phi} \sin 2\phi_c} + \underline{v_c'' (EI_z - EI_y) \cos \phi_c \sin \phi_c} \\
 &\quad + \underline{v_c'' (EI_z - EI_y) \hat{\phi} \cos 2\phi_c} - \underline{EAe_A u_{ec}' \sin \phi_c} - \underline{EAe_A u_{ec}' \hat{\phi} \cos \phi_c} \\
 U_{\hat{\phi}} &= U_{\hat{\phi}}^0 - \underline{EC_2 w'' \phi_c'' \sin \phi_c} - \underline{EC_2 v'' \phi_c'' \cos \phi_c} - \underline{EB_2 w'' \frac{\phi_c'^2}{2} \cos \phi_c} \\
 &\quad + \underline{EB_2 v'' \frac{\phi_c'^2}{2} \sin \phi_c} + \underline{w_c''^2 (EI_z - EI_y) \cos \phi_c \sin \phi_c} - \underline{EC_2 w_c'' \phi_c'' \sin \phi_c} \\
 &\quad - \underline{EB_2 v_c'' \frac{\phi_c'^2}{2} \cos \phi_c} + \underline{2w_c'' w'' (EI_z - EI_y) \cos \phi_c \sin \phi_c} \\
 &\quad + \underline{v_c'' w_c'' (EI_z - EI_y) \cos 2\phi_c} - \underline{v_c''^2 (EI_z - EI_y) \cos \phi_c \sin \phi_c} \\
 &\quad + \underline{v_c'' w_c'' (EI_z - EI_y) \cos 2\phi_c} - \underline{EC_2 v_c'' \phi_c'' \cos \phi_c} + \underline{EB_2 v_c'' \frac{\phi_c'^2}{2} \sin \phi_c} \\
 &\quad - \underline{2v_c'' v'' (EI_z - EI_y) \cos \phi_c \sin \phi_c} + \underline{v_c'' w'' (EI_z - EI_y) \cos 2\phi_c} \\
 U_{\hat{\phi}'} &= U_{\hat{\phi}'}^0 + \underline{EB_1 \frac{\phi_c'^3}{2}} + \underline{EB_1 \frac{\phi_c'^2}{2} \hat{\phi}'} - \underline{EB_2 \phi_c' w_c'' \sin \phi_c} - \underline{EB_2 \phi_c' v_c'' \cos \phi_c} \\
 &\quad + \underline{EAk_A^2 \phi_c' u_{ec}'} + \underline{EAk_A^2 \hat{\phi}' u_{ec}'} + \underline{GJ\phi_c'} + \underline{GJw_c' v_c''} + \underline{GJw_c' v''} + \underline{GJw' v_c''} \\
 U_{\hat{\phi}''} &= U_{\hat{\phi}''}^0 + \underline{EC_1 \phi_c''} + \underline{EC_2 w_c'' \cos \phi_c} - \underline{EC_2 v_c'' \cos \phi_c} \tag{9}
 \end{aligned}$$

In Eqs. 9, two distinct types of terms are present:

- (i) Underlined terms: These depend only on the elastic deformation field as a result of pitch control application (ϕ_c, w_c, v_c and u_{ec}). They represent the strain energy stored in the system (primarily in the flexbeam) due to the work done in pitching the blade.
- (ii) Non-underlined terms: These depend on both the known elastic deformation field due to pitch control application, and the elastic deformations (ϕ, w, v , and u_e) due to aeroelastic forces. These terms represent the change in aeroelastic behavior of the blade due to its initial elastic deformation during pitch control application.

It should be noted that inclusion of the work done during pitch control application in δW would result in the cancellation of the underlined terms. Thus, the underlined terms, as well as the work done in pitching the blade, can both be dispensed with in the analysis. The non-underlined terms, however, need to be retained.

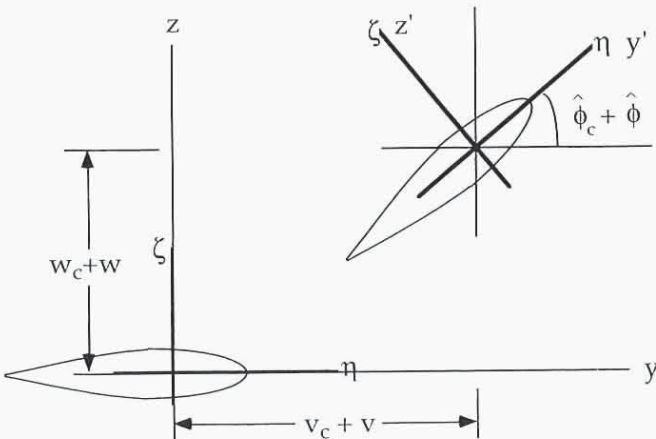


Fig. 1. Deformed configuration due to swashplate control and aerodynamic forces.

Finite Element Discretization of the Bearingless Blade

Expressions for the strain energy variation, δU , with the inclusion of elastic deformations effects due to pitch control, are used in Hamilton's principle, Eq. 1, to obtain a modified set of nonlinear equations for the bearingless rotor blade. The finite element method used to spatially discretize these equations, is well suited for application to bearingless rotor blades as it enables the accurate modeling of the redundant load paths and complex hub kinematics. The main blade, torque tube, and flexbeam are each discretized into a number of elements, with each element having two end nodes, three internal nodes, and a total of fifteen degrees of freedom (Ref. 5). Individual elements are assembled to enforce continuity of flap and lag bending displacements and slopes (w, v, w', v'), axial displacement (u_e), and torsional orientation angle ($\hat{\phi}$), between elements. Special attention is required to enforce (i) kinematic constraints at the inboard end of the torque tube, and (ii) compatibility between the main blade inboard element and torque tube and flexbeam outboard elements, at their interface.

Kinematics at the Inboard End of the Torque Tube, and Evaluation of Deformations due to Pitch Control Application

Elastic Pitch Link

Figure 2 shows the kinematics of deformation at the inboard end of the torque tube of a bearingless blade with a vertical elastic pitch link. When the swashplate is moved, the pitch link is assumed to move vertically. In practice it may deviate slightly from the vertical position but this inclination is not included in the analysis. From the figure it can then be seen that

$$w_{sp} + w_{pl} - w_{tt} = a \sin \theta_{tt} \tag{10}$$

where w_{sp} is the applied swashplate displacement, w_{pl} is the elastic deformation in the pitch link, w_{tt} and θ_{tt} denote torque tube flapwise displacement and pitch, respectively, and a is the pitch horn chordwise offset. The torque tube and pitch link deformations include contributions due to both swashplate motion and aerodynamic loads. Thus Eq. 10 can be written as

$$w_{sp} + (w_{pl}^c + w_{pl}^{aero}) - w_{tt}^c - w_{tt}^{aero} = a \sin \phi_{tt}^c + a \cos \phi_{tt}^c \phi_{tt}^{aero} \tag{11}$$

The quantities with the superscript 'c' are the contributions due to swashplate control motion, and the quantities with the superscript 'aero' are due to aeroelastic loads. For swashplate control motion, alone,

$$w_{pl}^c = w_{tt}^c + a \sin \phi_{tt}^c - w_{sp} \tag{12}$$

If the pitch link stiffness is k_{pl} , its elastic strain energy due to swashplate motion is

$$U_{pl} = \frac{1}{2} K_{pl} w_{pl}^c{}^2 \tag{13}$$

From Eqs. (12) and (13) we can obtain

$$\delta U_{pl} = (\delta w_{tt} \delta \phi_{tt}) \left(K_{pl} \left\{ \frac{w_{tt} + a \sin \phi_{tt}}{w_{tt} a \cos \phi_{tt} + \frac{a^2}{2} \sin 2\phi_{tt}} \right\} - K_{pl} w_{sp} \left\{ \frac{1}{a \cos \phi_{tt}} \right\} \right) \tag{14}$$

δU_{pl} adds to the strain energy variation, δU_b , of the blade, so that the total strain energy variation of the bearingless blade is

$$\delta U_{total} = \delta U_b + \delta U_{pl} \tag{15}$$

δU_b can be expressed as

$$\delta U_b = \delta q_b^T K^G q_b + \delta q_b^T F^{NL} \quad (16)$$

where K^G is the global structural stiffness matrix of the bearingless blade, q_b is the global nodal displacement vector, and the vector, F^{NL} , contains the nonlinear structural terms. After introducing Eqs. (14) and (16) into (15), a solution for the deformation field, q_b , of the bearingless blade can be obtained for a given swashplate control displacement, w_{sp} , in the absence of aerodynamic forces. In forward flight, w_{sp} varies along the azimuth, and q_b would have to be evaluated at several different azimuthal locations, ψ , as solutions to the input $w_{sp}(\psi)$.

However, if F^{NL} is neglected in the expression for δU_b (Eq. 16), and a small angle assumption is made on ϕ_{tt}^c in the expression for δU_{pl} so that Eq. 14 reduces to

$$\delta U_{pl} = (\delta w_{tt}^c \quad \delta \phi_{tt}^c) \left(K_{pt} \begin{bmatrix} 1 & a \\ a & a^2 \end{bmatrix} \begin{Bmatrix} w_{tt}^c \\ \phi_{tt}^c \end{Bmatrix} - K_{pl} w_{sp} \begin{Bmatrix} 1 \\ a \end{Bmatrix} \right) \quad (17)$$

only a single evaluation of the deformation field (\bar{q}_b) is required, for a unit displacement, $\bar{w}_{sp} = 1$. The deformation field at any azimuthal location could then be obtained as

$$q_b(\psi) = \bar{q}_b w_{sp}(\psi) \quad (18a)$$

$$\text{or} \quad q_b(\psi) = \bar{q}_b \frac{(\theta_o + \theta_{1c} \cos \psi + \theta_{1s} \sin \psi)}{\phi_{tt}^c} \quad (18b)$$

where θ_o is the collective pitch, θ_{1c} and θ_{1s} are cyclic pitch control components, and $\bar{\phi}_{tt}^c$ is the torque tube pitch due to $\bar{w}_{sp} = 1$. Although such an approach gives only an approximate elastic deformation field due to pitch control application, it results in considerable simplification of the solution process. The control deformations, q_b (consisting of ϕ_c , w_c , v_c , and u_c), thus obtained, are used in the modification of the bearingless blade strain energy expressions (non-underlined terms in Eq. 9).

For the evaluation of the blade steady response under aeroelastic force, Eq. 11 gives

$$w_{pl}^{aero} = w_{tt}^{aero} + a \cos \phi_{tt}^c \phi_{tt}^{aero} \quad (19)$$

Eq. 19 can be used to obtain

$$\delta U_{pl} = (\delta w_{tt} \quad \delta \phi_{tt}) K_{pt} \begin{bmatrix} 1 & a \cos \phi_{tt}^c \\ a \cos \phi_{tt}^c & a^2 \cos^2 \phi_{tt}^c \end{bmatrix} \begin{Bmatrix} w_{tt} \\ \phi_{tt} \end{Bmatrix} \quad (20)$$

Introducing Eq. 20 into Eq. 15 results in the augmentation of the bearingless blade global stiffness matrix due to the effects of pitch link stiffness.

If the pitch horn has a non-zero radial offset, p , Eq. 10 becomes

$$w_{sp} + w_{pl} - w_{tt} + p w'_{tt} = a \sin \theta_{tt} \quad (21)$$

where w'_{tt} is the flap bending slope at the inboard end of the torque tube. Again, augmentation of the bearingless blade global stiffness, and the evaluation of the deformation field due to w_{sp} , is carried out by adding the pitch link strain energy variation to δU_b .

Rigid Pitch Link

If the axial stiffness of the pitch link is very high, as is very often the case, the analyst may choose to model the pitch link as a 'rigid' member, in which case w_{pl} in Eqs. 10 and 21 is zero, yielding the kinematic constraint

$$\phi_{tt} = -\frac{1}{a} w_{tt} + \frac{p}{a} w'_{tt} + \frac{1}{a} w_{sp} \quad (22)$$

Introducing this constraint into Hamilton's principle (Eq. 1) results in the reduction in size of the inboard torque tube element matrices and vectors from 15 to 14, due to the elimination of the torsional degree of freedom.

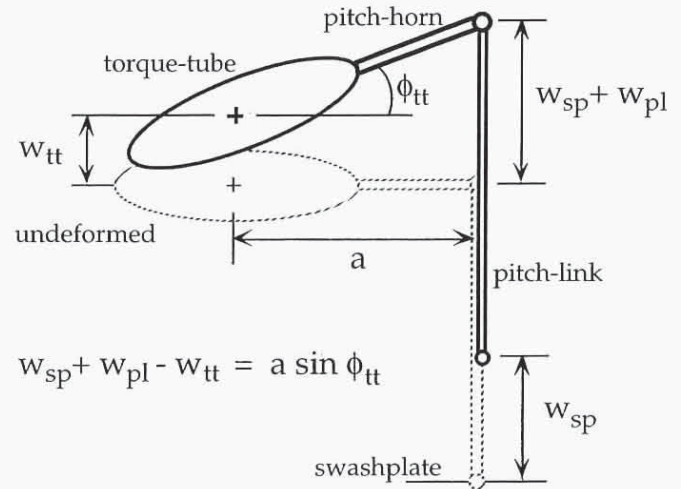


Fig. 2. Kinematics of deformation of a bearingless rotor blade with single vertical pitch link at the leading edge.

Torque tube or Lag shear restraint

Figure 3 shows a bearingless rotor blade with torque tube or lag shear restraint. The presence of a lag shear restraint imposes additional constraints at the inboard end of the torque tube. In addition to the pitch link kinematics, its presence imposes the following kinematic constraint relations.

$$-z_o \phi_{tt} + v_{tt} = v'_{tt} x_o \quad (23a)$$

$$w_{tt} = w'_{tt} x_o \quad (23b)$$

In Eqs. 23, z_o and x_o are the vertical and radial offsets of the lag pin, and v_{tt} and v'_{tt} are the torque tube lagwise bending displacement and slope. If the pitch link is rigid, the three kinematic constraints are used to eliminate three degrees of freedom, ϕ_{tt} , w_{tt} and v_{tt} , resulting in a reduction in size of the inboard torque tube element matrices and vectors from 15 to 12. Once again, the deformation field due to swashplate control motion, w_{sp} , is used to modify the blade strain energy expressions (Eq. 9).

Although the lag shear restraint concept described above was studied and tested during the bearingless rotor development phases, an elastomeric snubber is most commonly used in modern bearingless rotors to keep the flexbeam centered with respect to the torque tube. The snubber additionally provides lead-lag damping to alleviate aeromechanical instabilities. For a configuration with an elastomeric snubber damper, none of the degrees of freedom at the inboard end of the torque tube are eliminated, but the relative motions between the torque tube and the flexbeam are constrained due to the presence of the snubber.

Compatibility Conditions at the Clevis

The main blade inboard end and the flexbeam and torque tube outboard ends connect at the clevis, as shown in Fig. 3. The axial displacement, u_c , flap-bending displacement, w , and slope, w' , lag-bending displacement, v , and slope, v' , of the main blade, flexbeam and torque tube are identical at the clevis. The elastic twist at the clevis end of the flexbeam is equal to the main blade and torque tube elastic twist at the clevis ($\hat{\phi}$, due to aeroelastic loads) plus the elastic twist due to pitch control. However, by having sep-

arately accounted for the effects of elastic twist due to pitch control, only the elastic twist in the flexbeam due to aerodynamic loads ($\hat{\phi}$) needs to be considered. $\hat{\phi}$ for the flexbeam, torque tube and main blade are identical at the clevis, enabling assembly of the spatial finite elements.

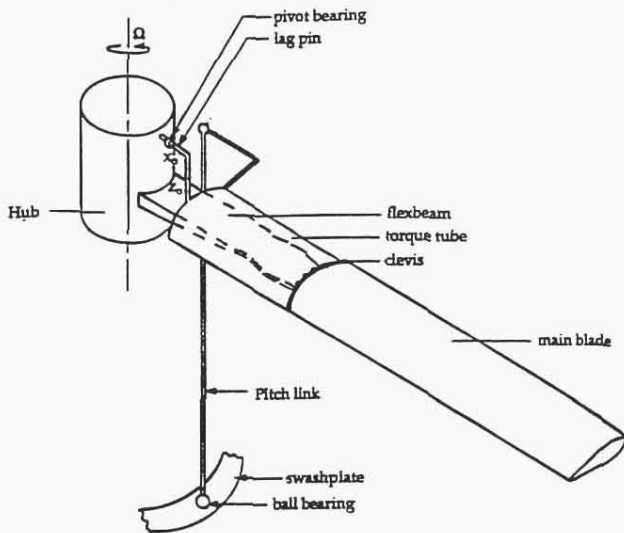


Fig. 3. Bearingless rotor hub with torque shear restraint.

Aeroelastic Analysis

The aeroelastic analysis involves the calculation of the vehicle trim, steady blade response and stability of the rotor-body perturbation motion. The steady periodic blade response is calculated using a temporal finite element method after the nonlinear equations in space are transformed into normal mode equations. In the temporal finite element method, the azimuth is discretized into a number of time elements, with a polynomial distribution for response being assumed within each element. Periodicity of response is imposed by connecting the first and last elements in one rotor revolution, during assembly of time element matrices. The nonlinear vehicle trim and blade response equations are solved iteratively as a coupled solution. The blade response in each iteration is used to calculate the hub loads, which influence the vehicle orientation and control settings. The new pitch control settings are used to calculate the blade response in the following iteration, and the procedure continues until specified convergence criteria are met. It should be noted that at this stage only the deformations due to aeroelastic forces ($\hat{\phi}$, w , v , u_c) are being evaluated. Since the largest part of the deformations, due to pitch control application, had already been evaluated and removed from the total deformations, the normal mode method could be applied, resulting in a substantial decrease in problem size. The influence of the deformations due to pitch control are accounted for in Eq. 9. For the stability analysis, the linearized normal mode perturbation equations are obtained about the steady state condition. Here, the structural normal modes used are obtained about the deformed condition, resulting from collective pitch only. The equations have periodic coefficients in forward flight and are solved using Floquet transition matrix theory. Additional details on the aeroelastic analysis procedure are available in Ref. 12.

Results and Discussion

Validation with Experiment

Two different test cases for which experimental data were available, were analyzed to validate the aeroelastic stability results pre-

dicted by the present bearingless rotor analysis. The 3-bladed model bearingless rotor consisted of a flexbeam with wrap-around torque tube, attached rigidly to the main blade at the clevis. The inboard end of the torque tube was connected to a pitch link but did not have any connection to the flexbeam whatsoever (floating cuff). This rotor was tested in hover and results of this test are available in Ref. 13. The rotor structural properties for the two cases were identical, with the only difference being the pitch link location. The pitch link was attached to the leading edge for case 1 and to the trailing edge for case 2. Case 1 was tested at 1100 RPM, while case 2 was tested at 900 RPM as it experienced flutter instability at 1100 RPM. The bearingless blade was modeled with eight elements, three elements each for the main blade and the flexbeam, and two elements for the torque tube. The nondimensionalized stiffness and inertial properties and geometric dimensions for the different elements are presented in Table 1. Note that the value of rotational speed used in nondimensionalizing the stiffness and inertial properties is $\Omega = 1100$ RPM.

Figures 4a and 4b show the variation of lag damping with collective pitch in hover, for the two cases. For the leading edge pitch link (case 1) Fig. 4a shows good correlation with experiment and generally predicts the trend with collective pitch. For the trailing edge pitch link (case 2) Fig. 4b shows even better correlation over the range of collective pitch, with the analysis accurately capturing the much gentler variation of lag damping with collective pitch.

The difference in lag damping at higher collectives between the two cases can be related to the kinematic pitch-flap couplings, which result in substantially different thrust conditions for the same collective pitch setting. For a leading edge pitch link configuration (Fig. 5a) the lift generated on the main blade due to a given collective pitch setting (position A), results in the main blade coning upward and the torque tube inboard end moving downward (to position B). Since this results in an increase in the effective blade pitch the thrust level and aerodynamic damping, increase as well. For the trailing edge pitch link configuration (Fig. 5b), the downward motion of the torque tube inboard end due to lift on the main blade results in a nose down rotation that decreases the effective angle of attack of the blade. The thrust of the blade and the aerodynamic damping, decrease accordingly. For both pitch-link configurations, the solution for the pitch orientation angles, $\hat{\phi}$, contain moderate kinematic rotations, in addition to elastic twisting. It should be noted that a bearingless rotor configuration with a shear restraint would significantly limit the kinematic pitch-flap couplings.

Blade Response, Aeroelastic and Aeromechanical Stability, in Forward Flight

The shaft-fixed aeroelastic stability characteristics and the shaft-free aeromechanical stability characteristics for the leading edge and trailing edge pitch link configurations (cases 1 and 2, respectively) are examined in forward flight. Perturbation stability was evaluated about a propulsive trim condition in cruise, at a thrust coefficient $C_T/\sigma = 0.07$.

Table 1. Bearingless rotor blade properties

Element	$\frac{I_i}{R}$	$\frac{m_i}{m_o}$	$\frac{EI_y}{m_o \Omega^2 R^4}$	$\frac{EI_x}{m_o \Omega^2 R^4}$	$\frac{GJ}{m_o \Omega^2 R^4}$	$\frac{EA}{m_o \Omega^2 R^4}$	
1	0.5	0.702	0.0055	0.1488	0.0029	113.5	main blade
2	0.234	0.702	0.0055	0.1488	0.0029	113.5	main blade
3	0.0684	26.29	0.2621	0.4321	0.2904	184.5	main blade
4	0.1018	0.979	0.00157	0.00616	0.000205	365.3	flexbeam
5	0.1018	0.979	0.00157	0.00616	0.000205	365.3	flexbeam
6	0.0454	75.42	8.064	4.910	16.61	275.1	flexbeam
7	0.0509	11.25	4.473	4.495	1.664	304.7	torque tube
8	0.0509	11.25	4.473	4.495	1.664	350.0	torque tube

radius, $R = 3'$, $m_o = 3.074 \times 10^{-3}$ slug/ft, $\Omega = 1100$ rpm

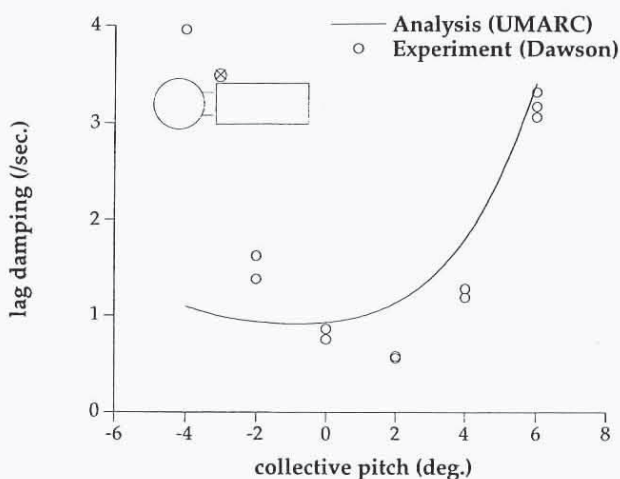


Fig. 4a. Hover shaft-fixed stability for BMR with leading edge pitch link (Case 1).

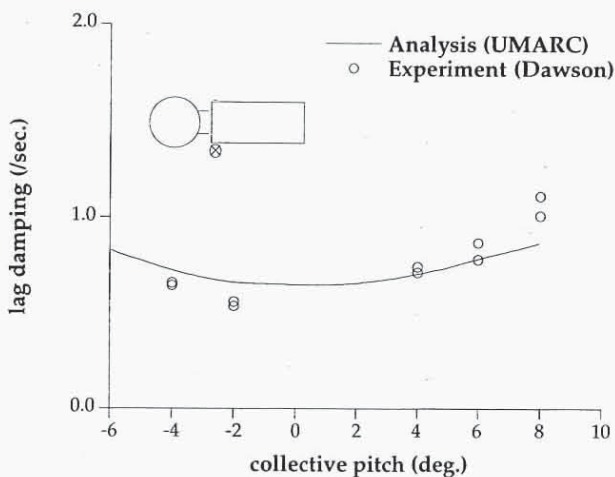


Fig. 4b. Hover shaft-fixed stability for BMR with trailing edge pitch link (Case 2).

Shaft-fixed aeroelastic stability

Figures 6a and 6b show the variation of the regressing lag mode damping with advance ratio for cases 1 and 2, respectively. Note that the stability results for both cases are calculated at 1100 RPM. For both cases, it can be seen that the lag damping increases at high advance ratios. It is assumed that this increase is associated with the higher aerodynamic damping due to large cyclic flap. Results obtained using both 'flexible' and 'rigid' pitch link analyses revealed that a 'flexible' pitch link with a nondimensional stiffness $K_{pl}/m_o\Omega^2R = 291$, behaves much like a rigid pitch link. Reduction in pitch link stiffness was generally found to have a small effect on the lag damping. This differs from the case of a bearingless rotor with torque tube shear restraint, (Ref. 6), where the influence of pitch link stiffness on lag damping was much more significant. Softening the pitch link had virtually no influence on the aeroelastic stability of the trailing edge pitch link configuration (Fig. 6b) while the leading edge configuration (Fig. 6a) showed a slight decrease in stability. A pitch mode flutter instability was observed for the trailing edge pitch link configuration (Fig. 7). From the figure the flutter instability is seen to grow weaker with increasing advance ratio, and finally the pitch mode becomes stable at advance ratios greater than $\mu = 0.3$. It should be noted that a flutter instability for this configuration was also observed experimentally by Dawson (Ref. 13) in hover condition.

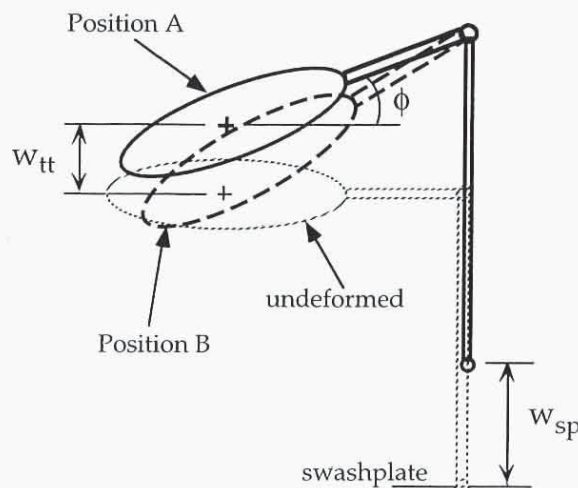


Fig. 5a. Flap up-pitch up kinematic coupling of the leading edge pitch link configuration.

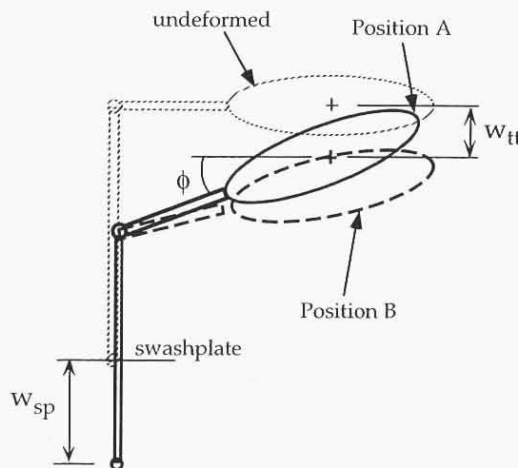


Fig. 5b. Flap up-pitch down kinematic coupling of the trailing edge pitch link configuration.

It is interesting to note that the pitch control settings required to trim the two configurations to the same thrust condition, vary significantly. For example, in hover, the pitch control angle, θ , required to trim to a thrust coefficient $C_T/\sigma = 0.07$, is 3.146° for case 1, and 8.986° for case 2. The corresponding tip torsional orientations, $\hat{\phi}$, are 2.302° and -3.583° , respectively. It can be easily seen that the effective aerodynamic angle of attack, $\theta + \hat{\phi}$, is virtually the same for the both cases (about 5.4°). Consequently, the blade tip flap displacement values were also identical ($w_{tip}/R = 0.0641$, for both cases). In Ref. 13, a third configuration with dual pitch links (at both the leading as well as trailing edge) was also examined. For this configuration, when the leading edge pitch link was moved upward, the trailing edge pitch link was moved downward by the same amount, so that the torque tube did not experience any vertical motion during pitch control application. This eliminated the pitch flap coupling. For such a configuration, it is found that a collective pitch setting of 5.748° was required to trim to a C_T/σ of 0.07, and the tip torsional deflection, $\hat{\phi}$, took on a much smaller value, -0.283° . The effective angle of attack, $\theta + \hat{\phi}$, was once again very nearly equal to 5.4° , and w_{tip}/R took a value of 0.0621. The wide variation in cross-sectional orientations, $\hat{\phi}$, between the configurations can be attributed to a nose-up rigid rotation component in case 1, a nose-down rigid rotation component in case 2, and virtually no kinematic rotations in the case of the dual pitch link configuration.

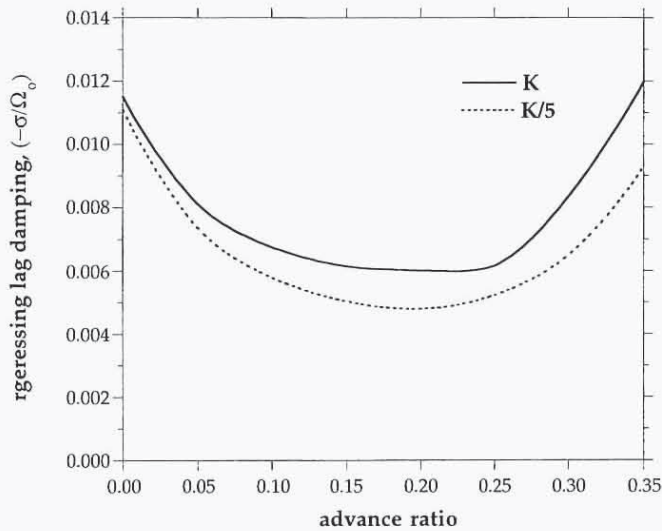


Fig. 6a. Shaft-fixed stability in forward flight (Case 1 — leading edge pitch link).

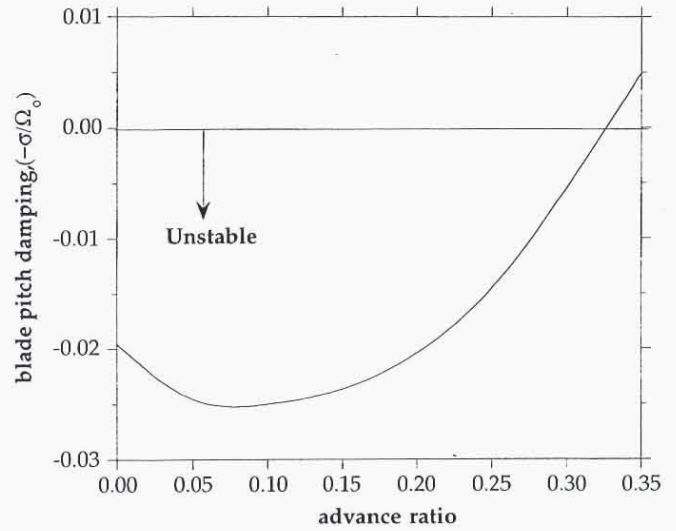


Fig. 7. Pitch-flap flutter for trailing edge pitch-link configuration at 1100 RPM.

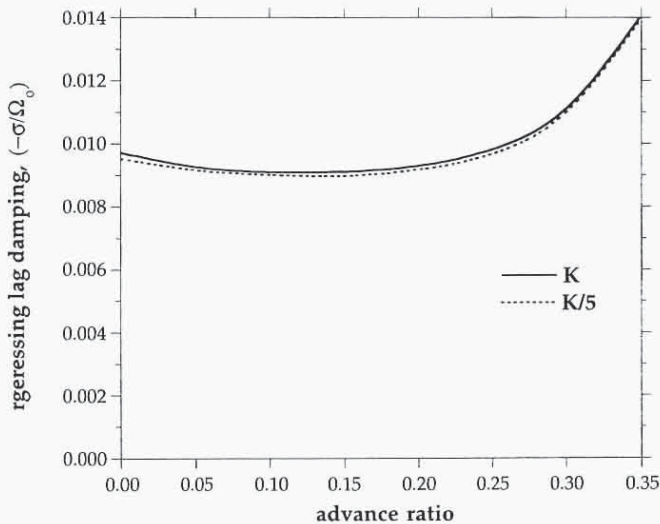


Fig. 6b. Shaft-fixed stability in forward flight (Case 2 — trailing edge pitch link).

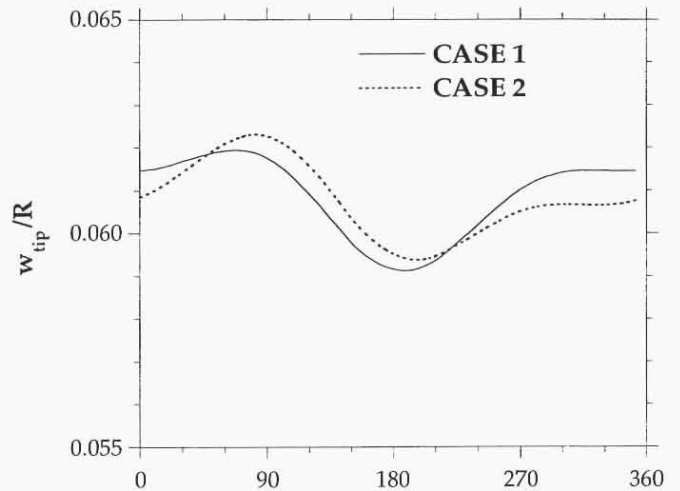


Fig. 8. Flap response at blade tip at advance ratio, $\mu = 0.1$.

This trend of virtually identical flap displacements and widely differing cross-sectional orientations between the different pitch link configurations persists in forward flight as well. From Fig. 8 it can be seen that at an advance ratio, $\mu = 0.1$, both the leading as well as trailing edge pitch link configurations have a very similar tip flap response versus azimuth. Tip cross-sectional orientation angle, $\hat{\phi}$, at various advance ratios is presented in Figs. 9a and 9b, for cases 1 and 2, respectively. The large cross-sectional orientations, $\hat{\phi}$, for cases 1 and 2 are of opposite sign and contain substantial rotations of the blade due to kinematic pitch-flap coupling, in addition to elastic twist.

From Figs. 6a and 6b it can also be observed that the leading edge pitch link configuration (case 1) shows a considerable decrease in lag damping at low to moderate advance ratios, as compared to case 2. A possible explanation to this could be due to the interaction with the flap modes. The first flap frequency for the leading edge pitch link configuration (with a flap-up, pitch-up kinematic coupling), is significantly reduced to approximately 0.36/rev as compared to a frequency of 1.05/rev for the case with almost zero pitch-flap coupling. The corresponding frequencies for the re-

gressing and progressing flap modes are 0.64/rev and 1.36/rev. As the advance ratio increases, the two low frequency flap modes are seen to converge toward and interact with each other (Fig. 10a) resulting in a pair of modes that cannot be clearly classified as 'collective' and 'regressing.' These low frequency modes have substantially different aerodynamic damping, one high and the other very low (Fig. 10b). The low damping in one flap mode may possibly be influencing the reduced lag damping observed in Fig. 6a. In contrast, for the trailing edge pitch link configuration, the first flap frequency is increased to approximately 1.44/rev. The corresponding progressing and regressing flap frequencies are 2.44/rev and 0.44/rev, and no coalescence occurs between these well separated modes as the advance ratio increases. The first lag frequency for the both configurations is approximately 0.757/rev.

Shaft-free aeromechanical stability

Figures 11a and 11b show the variation of shaft-free lag damping with advance ratio, for the leading and trailing edge pitch link configurations,

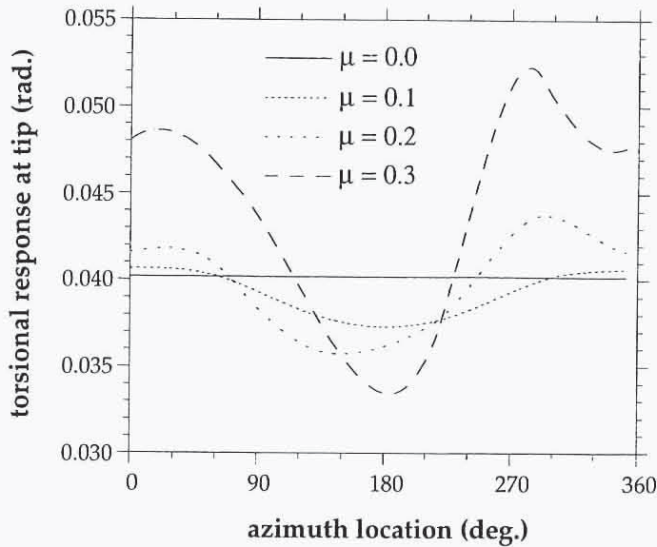


Fig. 9a. Blade tip torsional response (Case 1 — leading edge pitch link).

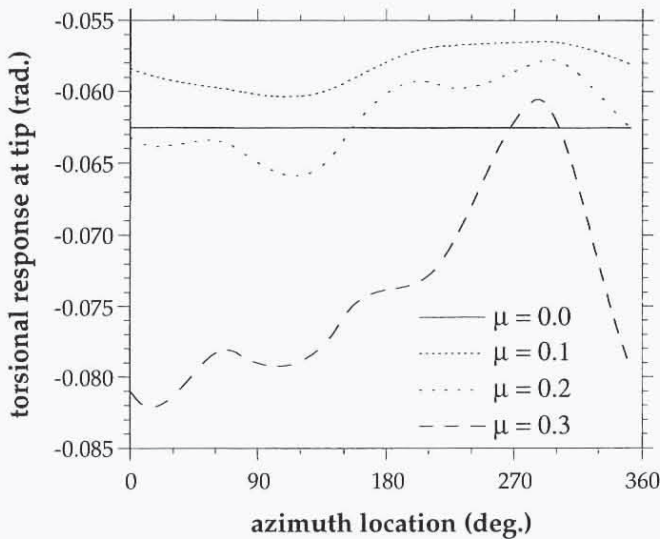


Fig. 9b. Blade tip torsional response (Case 2 — trailing edge pitch link).

respectively. Comparing these figures with the corresponding shaft-fixed lag damping variations (Figs. 6a and 6b) reveals that hub motion has a small effect on the collective and progressing lag modes, but a significant influence on the damping of the regressing lag mode. In hover, the regressing lag damping is considerably reduced for both pitch link configurations. For the leading edge pitch link configuration, the regressing lag damping rapidly increases with advance ratios (Fig. 11a). For the trailing edge pitch link configuration, a much smaller variation in regressing lag damping with advance ratio is observed (Fig. 11b).

Other than the damping in the regressing mode, inclusion of hub motion barely affected the dynamic and aeroelastic characteristics of either configuration. For the trailing edge pitch link configuration, pitch-flap flutter was again seen much as it was in the absence of hub motion.

Summary and Concluding Remarks

An aeroelastic analysis methodology for bearingless main rotor helicopters in forward flight is developed. The significant elastic twist experi-

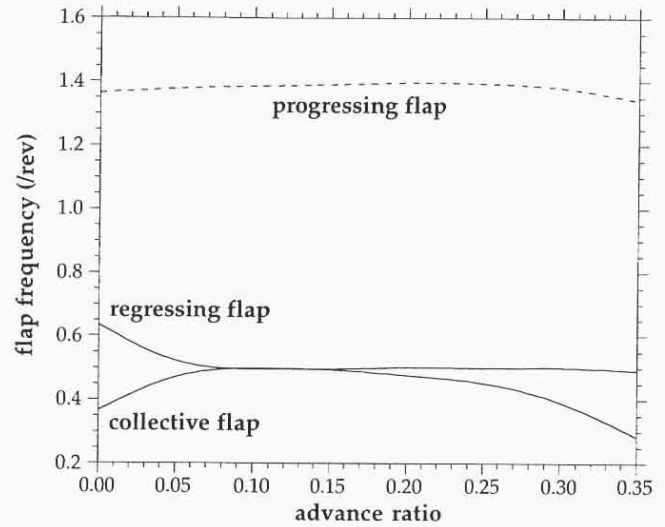


Fig. 10a. First flap modal frequencies (Case 1 — leading edge pitch link).

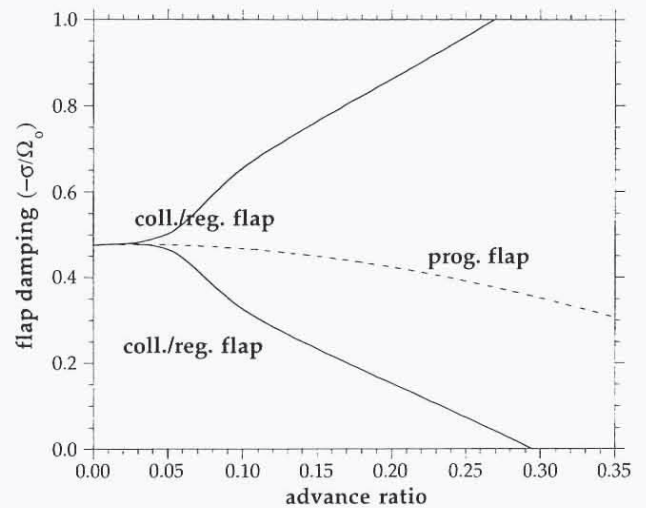


Fig. 10b. First flap modal damping (Case 1 — leading edge pitch link).

enced by the flexbeam during pitch control application can influence the nonlinear behavior of the blade under aeroelastic forces. In the present analysis, the elastic deformations due to pitch control are independently evaluated as the invacuo structural response to a prescribed swashplate motion. The aeroelastic response is obtained by the use of modified nonlinear equations of motion which account for the influence of the elastic deformations due to pitch control. The present analysis is robust and has good convergence behavior in evaluation of blade periodic response.

Good correlation with experimental lag damping data is obtained for a model bearingless rotor without shear restraint, and with pitch links located at the leading or trailing edge. Pitch link location at the leading or trailing edge (which induces different types of pitch-flap coupling) is seen to have a strong effect on torsional response and thrust of the rotor. For a given blade pitch setting, flap up-pitch up kinematic coupling of a leading edge pitch link configuration results in large positive torsional response, which increases the thrust. The flap up-pitch down kinematic coupling of a trailing edge pitch link configuration has the opposite effect. The large negative torsional response in this case, decreases the thrust. The blade tor-

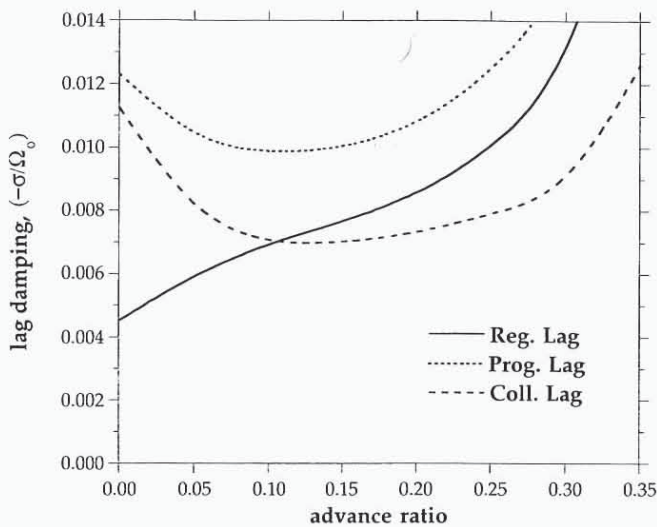


Fig. 11a. Shaft-free stability in forward flight (Case 1 — leading edge pitch link).

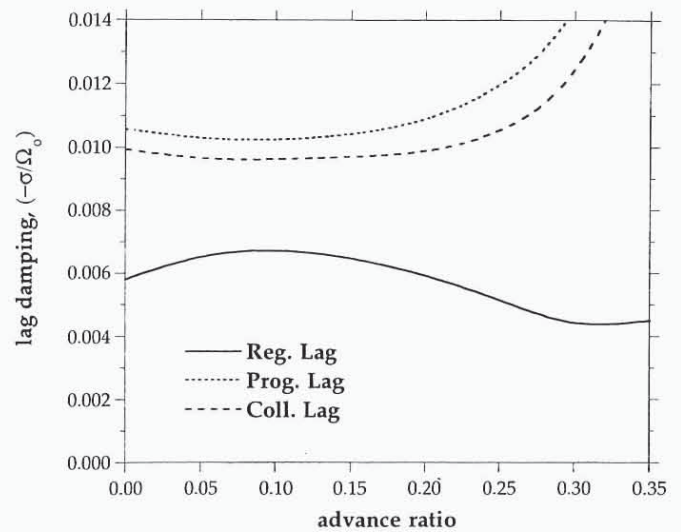


Fig. 11b. Shaft-free stability in forward flight (Case 2 — trailing edge pitch link).

sional responses for both configurations contain moderate kinematic rotations, in addition to elastic twist. Consequently, lower pitch settings would be required for the leading edge pitch link configuration to achieve the same thrust.

Shaft-fixed stability of both pitch link configurations improves at high advance ratios. It is assumed that this increase is associated with the higher aerodynamic damping due to large cyclic flap. Pitch link flexibility is seen to have a minimal influence on the shaft-fixed forward flight lag mode stability characteristics of the trailing edge configuration, and the influence is only slightly greater for a leading edge pitch link configuration. For the leading edge pitch link configuration, coalescence of the collective and regressing flap modes is seen at moderate advance ratios.

The inclusion of hub motion results in a reduction of regressing lag damping for the trailing edge pitch link configuration over the range of advance ratios. For the leading edge pitch link configuration, regressing lag damping is reduced at hover, but increases with advance ratio.

For the trailing edge pitch link configuration, occurrence of pitch-flap flutter is predicted by the analysis. The instability grows weaker with increasing advance ratio. The inclusion of hub motion does not influence the flutter instability.

Acknowledgements

This research work is supported by the Army Research Office under the University of Maryland Center for Rotorcraft Education and Research, Grant No. DAAH04-93-G-0001; Technical Monitor Dr. Tom Doligalski.

References

¹Huber, H., "Will Rotor Hubs Lose Their Bearings? A Survey of Bearingless Main Rotor Development," Presented at the Eighteenth European Rotorcraft Forum, Avignon, France, Sep 15-18, 1992.
²Hodges, D. H., "A Theoretical Technique for Analyzing Aeroelastic Stability of Bearingless Rotors," *AIAA Journal*, Vol. 17, No. 4, 1978.
³Hodges, D. H., "An Aeromechanical Stability Analysis for Bearingless Rotor Helicopters," *Journal of the American Helicopter Society*, Vol. 24, No. 1, Jan 1979, pp. 2-9.
⁴Hodges, D. H., Hopkins, A. S., Kunz, D. L., and Hinnant, H. E., "Introduction to GRASP — General Rotorcraft Aeromechanical Stability

Program — A Modern Approach to Rotorcraft Modeling," *Journal of the American Helicopter Society*, Vol. 32, No. 2, 1987, pp. 78-90.

⁵Sivaneri, N. T., and Chopra, I., "Finite Element Analysis for Bearingless Rotor Blade Aeroelasticity," *Journal of the American Helicopter Society*, Vol. 29, No. 2, Apr 1984, pp. 42-51.

⁶Dull, A. L., and Chopra, I., "Aeroelastic Stability of Bearingless Rotors in Forward Flight," *Journal of the American Helicopter Society*, Vol. 33, No. 4, Oct 1988, pp. 38-46.

⁷Jang, J., and Chopra, I., "Ground and Air Resonance of an Advanced Bearingless Rotor in Hover," *Journal of the American Helicopter Society*, Vol. 33, No. 3, Jul 1988, pp. 20-29.

⁸Jang, J., and Chopra, I., "Air Resonance of an Advanced Bearingless Rotor in Forward Flight," Proceedings of the 2nd International Conference on Rotorcraft Basic Research, College Park, MD, Feb 1988.

⁹Hong, C. H., and Chopra, I., "Aeroelastic Stability Analysis of a Composite Bearingless Rotor Blade," *Journal of the American Helicopter Society*, Vol. 31, No. 4, Oct 1986, pp. 29-35.

¹⁰Tracy, A. L., and Chopra, I., "Aeroelastic Analysis of a Composite Bearingless Rotor in Forward Flight with Improved Warping Modeling," Presented at the American Helicopter Society Aeromechanics Specialists' Conference, San Francisco, California, Jan 19-21, 1994.

¹¹Hodges, D. H., and Dowell, E. M., "Nonlinear Equations for the Elastic Bending and Torsion of Twisted Nonuniform Rotor Blades," NASA-TND-7818, Dec 1974.

¹²Bir, G., Chopra, I., et al, "University of Maryland Advanced Rotorcraft Code (UMARC) Theory Manual," UM-AERO Report 92-02, Aug 1992.

¹³Dawson, S., "An Experimental Investigation of a Bearingless Model Rotor in Hover," *Journal of the American Helicopter Society*, Vol. 28, No. 4, Oct 1983, pp. 29-34.

"WILL ROTOR HUBS LOSE THEIR BEARINGS?"

A SURVEY OF BEARINGLESS MAIN ROTOR DEVELOPEMENT

Helmut Huber
Eurocopter Deutschland GmbH
Munich, Germany

Abstract

Main rotor systems have since long been the subject of intensive research and development work in the helicopter industry. This is due to the fact that, historically, rotor heads have always been the most complex helicopter components, difficult to maintain and costly to operate. Advances in composite materials have made it feasible to develop new rotor concepts during the past 25 years, which totally eliminate the system of hinges and bearings - the bearingless-rotor design.

A review of the developments in BMR-technology is presented. The paper includes a history of the BMR concepts that have been developed and flown by the different manufacturers over the past 20 years. The critical aspects of bearingless-hub design are summarized; they include the design of the flexbeam and pitch-control structure, the possibilities of providing inplane-damping through various couplings and emphasizes design aspects of elastomeric materials damping devices. Representative results of recent designs are presented to illuminate the achievements made. Finally, an outlook into possible future trends in BMR-technology is given.

Introduction

Helicopter main rotors are commonly recognised as the more complex components which make up for the general complexity of this type of air vehicle. Indeed, the design of a main rotor is not a simple task and conceals a number of difficult problems to guarantee proper functioning.

Having that in mind, since the birth of the helicopter, the classical constructors have always been active in looking for novel ideas - both in terms of novel concepts and for detail improvement. New designs for rotor heads have been proposed fairly regularly. In the quest for design simplicity, there were mainly two developments that practically provided the necessary conditions for the design of new rotor heads in the past 20 years. These are: (1) The development of composite materials, which, besides its light weight, have "fail-safe" features inherent to their fibrous nature, and (2) the development of viscoelastic (elastomeric) materials which can be efficiently used for the design of laminated

bearings or for high hysteresis type of elastomeric elements, which provide high levels of damping.

These technological developments have made it feasible to design and develop new rotor concepts, eliminating partly or totally the system of hinges and bearings, the Bearingless Main Rotors (BMR). These rotors aim for a complete deletion of all three hinges of a conventional rotor. Figure 1 shows a schematic of a bearingless rotor build-up. Blade motions in the flapwise and chordwise directions are accomplished through elastic bending, and blade pitch-control is achieved by elastically twisting the inboard (flexbeam) portion of the spar. The moment applied to the blade from the pushrod is transmitted through a pitch-control element, which has to be rather rigid in torsion. The main goal in such design is simplicity, because of the favourable implications for rotor system weight, cost, reliability and maintainability.

The purpose of the present paper is to provide a review of the BMR-systems designed and tested, to discuss the main aspects in the design, and the achievements made so far. Finally, some prospects for future developments in BMR technology are presented.

Bearingless Main Rotor Developments

At one time or another, most of the companies of the helicopter industry have worked towards the development of bearingless rotors and have investigated in eliminating the blade retention/pitch change bearings from their main rotor systems.

Interestingly, the first successful efforts to apply bearingless rotor technology were made on tail rotors, during the design competition for the UTTAS-Helicopter in the early 1970's, in which both competitors used stiff-inplane bearingless designs for the tail rotors (References 1 and 2). These efforts have continued at Hughes with the AH-64A composite Flexbeam Tail Rotor (Reference 3), and with prototype tail rotors development at Aerospaiale (Reference 4), and MBB (Reference 5).

The design of a bearingless main rotor, quite obviously, remained a more difficult problem. When examining the variety of BMR baseline concepts, the manufacturers went different ways in their design approaches. The following is a brief history of the BMR concepts that have been developed and tested.

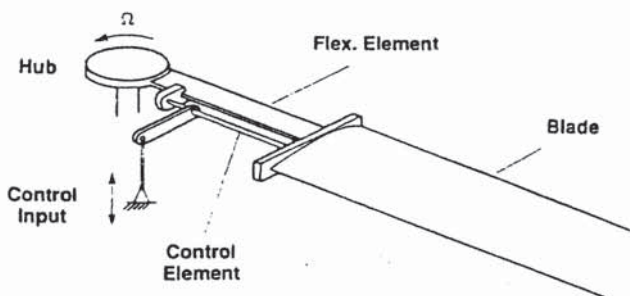


Fig. 1 Schematic of a bearingless rotor built-up

Lockheed

The first major effort to develop a bearingless main rotor was conducted by Lockheed, California, who developed a matched-stiffness rotor installed on the XH-51A helicopter in 1966. The rotor was four-bladed and used steel flexures at the root with polar symmetry for a matched stiffness configuration. Pitch control was by means of a steel torque rod forward of the flexbeam. The low inplane stiffness was mainly necessary to achieve the desired torsional flexibility. The rotor had negative pitch/flap and pitch/lag coupling, which was destabilizing.

The rotor underwent flight testing on a XH-51A helicopter (Figure 2). The testing was only partially successful, the aircraft showed marginal air resonance stability, and ground resonance stability was acceptable only on a smooth prepared surface. From the today's point of view, this development, was somewhat premature, due to the limited knowledge of aeromechanical stability and of the use of conventional materials at that date. Reference 6 described the development of the Lockheed BMR system.



Fig. 2 Matched-stiffness rotor test aircraft XH-51A

Boeing Vertol

Boeing Vertol, Philadelphia, USA began the development of a Bearingless Rotor in 1978 under a US-Army Government contract. For flying qualities, the design goal was set to depart as little as possible from the characteristics of the BO 105 Hinge-

less Rotor, i.e. to match both the basic first flap frequency dynamics (1.12/rev), corresponding to an equivalent hinge-offset around 14 percent, and the first chord frequency of 0.68/rev (soft inplane design). References 7 and 8 described the development of the BMR design.

The rotor (Figure 3) consisted of two parallel fiberglass flexures with a C-channel cross section that were rigidly attached to a rotor shaft fitting. A torque rod was placed between the two C-beams, at the center of twist. The flexbeam used 12.5 degrees prepitch to introduce structural flap/lag coupling, and 2.5 degrees negative droop to improve stability. At the outboard end of the beam, the blades were attached to individual blade-to-beam joints. The rotor had no sort of elastomeric or other type of damping device.

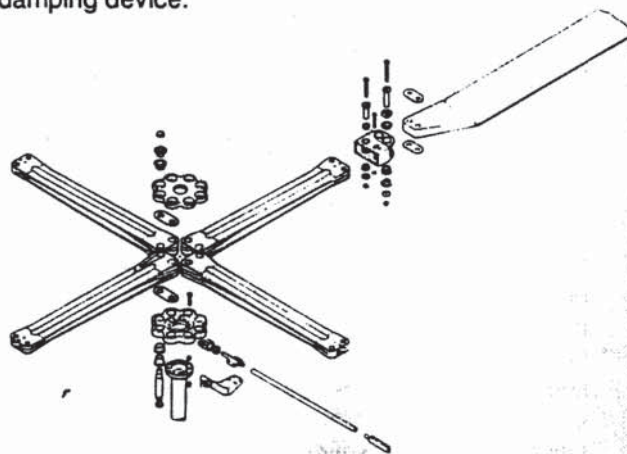


Fig. 3 Boeing Vertol bearingless rotor

The Boeing BMR first flew in 1978 on a BO 105 test vehicle (Figure 4). Initial flight tests indicated that ground resonance damping was inadequate, which was cured by stiffening the landing gear. It had similar air resonance characteristics to the Baseline BO 105 rotor, except at lower collective pitch settings. The original Boeing BMR was subsequently tested in the NASA Ames Wind tunnel, where some elastomeric damping material was bonded to the beams. The rotor was finally destroyed in the tunnel in 1982 due to an operator's error.



Fig. 4 BO105 with BMR in flight

Boeing Vertol continued its BMR efforts under the US-Army's Integrated Technology Rotor (ITR) Programme. This activity was cancelled when Boeing teamed with Sikorsky for the LHX program.

Aerospatiale/ECF

Aerospatiale, France, was always investing a large part of its research and design work to finding new solutions for simplifying the basic functions of rotorheads, as summarized in Reference 9. Among the various types of heads experimented on a SA 341 "Gazelle" helicopter was also a bearingless rotor head, called Triflex. Its development began in 1972. The three-bladed, soft-inplane rotor (Figure 5) was an attempt to eliminate not only the blade retention/pitch change bearings, but also the control rod reaction bearing as well. The rotor head consisted primarily of a set of fiberglass-epoxy yarns that were imbedded in an elastomeric matrix to form a flexible arm. The elastomeric matrix served also a second role, i.e. to introduce some structural damping for the lead-lag motion. The ends of the flexible arms were rigid fiberglass attachment blocks that connected the arms to the rotorshaft and blades. These arms had torsional flexibility, while the flapping and inplane stiffness was relatively high. The rotor had a flap frequency of 1.06/rev, a lag frequency of 0.72/rev and 2.5 degrees precone.

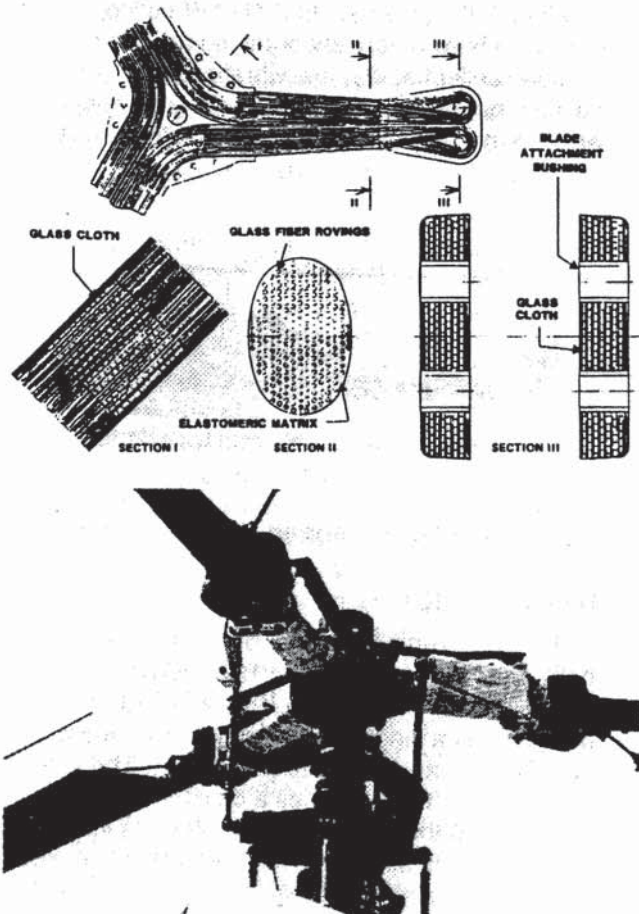


Fig. 5 Triflex hub construction



Fig. 6 SA 341 Gazelle helicopter

The flight tests of the 3-bladed Triflex rotor head were performed on a "Gazelle" (Figure 6). Apparently, most of the results were rather successful, however, the lead-lag damping was very low, resulting in a weak tendency for ground resonance instability, which was cured by installation of a hydraulic damper on the landing gear. Due to some coupling problems, also the lead-lag stresses and vibration levels were very high in certain flight conditions. The knowledge of the effect of several head and blade parameters was not yet developed at that time, and practical solutions to these problems were not found. Reference 10 reviews this development.

In further development of the Triflex rotor, Aerospatiale increased the number of blades to four, to reduce vibrations, and installed a lag damper to ensure ground resonance stability. A limited flight test was conducted. Primary development of the Triflex rotor hub configuration was completed and the conclusion was made that solutions of the various problems noted would be possible. In the following phase, Aerospatiale has shelved development of its Triflex BMR in favour of its Spheriflex elastomeric rotor (Reference 9).

Bell

Bell Helicopter Company, Texas, throughout the 1970's and 1980's has been experimenting on composite hubs (References 13). The four-bladed BMR, the Model 680 rotor (Figure 7), consists of a one-piece fiberglass structure that forms the flexbeams for all four blades. Each arm has a torsionally flexible feathering element outboard and a flapping flexure inboard. Pitch change is transmitted from the pitch links to the blade by torsionally stiff cuff assemblies that surround the arms of the flexbeams. The inboard portion of the cuffs are connected to elastomeric shear restraints and elastomeric lead-lag dampers. The flexbeams extend to 22 percent of rotor radius, where the beam, blade and cuff are bolted together. This rotor systems incorporates the Bell design philosophy of low flapping hinge offset (2-3 percent), including flexible mast and transmission suspension for some

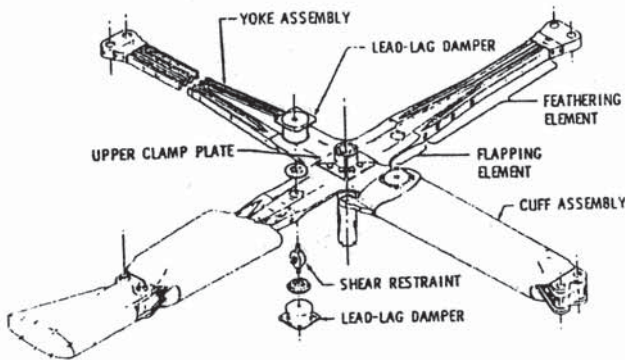


Fig. 7 Bell Model 680 rotor system

rotor flapping relief. Further design criteria were high structural lead-lag damping and uncoupled flapping, lead-lag, and pitch-change motions. Also, the flex-beam shows a highly tailored geometry for optimum stiffness and stress distributions.

The Model 680 BMR first flew in 1982 on a Model 222 helicopter (Figure 8). There were basically two problems with the Model 680 rotor: (1) The hub drag associated with the blade/cuff/flexbeam attachment was worse than expected, however, this problem could be significantly improved on the next Bell design. (2) The flapping ability of the low hinge offset flexbeam: A flapping failure mode from inter-laminar shear stresses was limiting the design to only 3 degrees flapping although the design was made for 5 degrees. With 3.5 percent rotor damping available from the lag dampers alone, ground and air resonance was no problem. The biggest advantage of the rotor was the excellent vibration level, well below 0.1 g for all flight conditions, which was achieved through a linked-focused pylon and the LIVE-isolation in the vertical axis. References 11 and 12 described the Model 680 development.



Fig. 8 Model 222 with 680-BMR

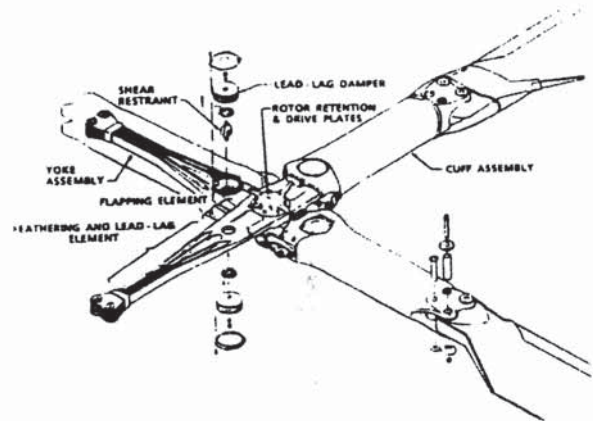


Fig. 9 4BW bearingless rotor

Having the basis of previous IR&D developments, the logical step was to apply the 680 BMR system technology to other helicopters products. Such new design is the 4-bladed Main Rotor System for the AH-1W-helicopter. The 4 BW main rotor hub (Figure 9) has now two single piece structural members, called yokes, that are bolted together at the top of the mast. Relative to the Model 680 rotor, the rotor hub drag was reduced by a cuff with elliptical cross section and fairings in the hub to blade attachment area.

Flight tests on a modified AH-1W-helicopter (Figure 10) showed very encouraging results, indicating excellent agility, low vibrations and good handling qualities. A description of the development work on this rotor system is given in Reference 14.



Fig. 10 4BW on a modified AH-1W helicopter

Hughes/MDHC

Hughes, Tempe/Arizona, began its bearingless main rotor development late 1982, within its HARP-Program. The 4-bladed HARP-Rotor is designed as a single flexbeam type, the beam made out of Kevlar and Graphite (Figure 11). The longest portion of the flexbeam has a cruciform cross section, inboard the cruciform transmissions into two flat legs, which allow for flap motion. The flapping hinge offset is approximately 8 percent and the flex-beam extends to 23 percent rotor radius. The HARP

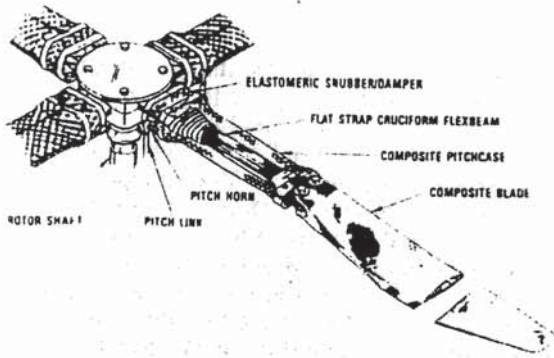


Fig. 11 HARP rotor configuration



Fig. 12 HARP rotor on MDHC Model 500E

also has pitch change cuffs, consisting of a hollow graphite box, and supported in its inboard end through an elastomeric snubber/damper unit. The manual folding arrangement has two attachment joints on each arm, which adds complexity and weight.

A comprehensive flight test program was conducted in 1985, using a 500 E helicopter (Figure 12). The flight test revealed the expected results regarding rotor stability, loads, performance and vibration characteristics. A summary of the development work and the results achieved is given in References 15 and 16.

With this basis, MDHC continued with the application of the BMR technology to its new project, the MD-900 Explorer light twin commercial helicopter. The rotor basically follows the basis worked out during the HARP-Program, but is the first five-bladed BMR ever built (Figure 13). The 33.8 ft diameter rotor has a slightly lower hinge offset and a rectangular flexbeam cross section. Five blades were chosen for the rotor to minimize noise and vibration. The characteristics of the rotor were successfully demonstrated on the whirl stand and in the 40x80 tunnel at NASA Ames up to wind speeds of 200 kts. The rotor is due to fly on the MD-900 first prototype aircraft in summer 1992.

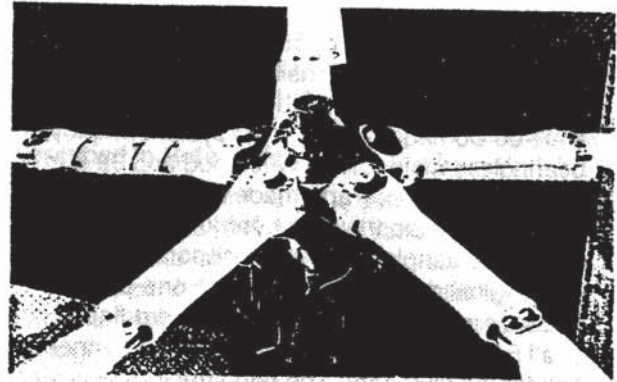


Fig. 13 MDHC five-bladed BMR for the Explorer

Sikorsky

Sikorsky Aircraft in Stratford, Connecticut, began the research and development of bearingless concepts on bearingless tail rotors, which are in production today on the Black Hawk and S-76.

The search for a low-offset main rotor bearingless concept have first lead to a unique stiff-inplane design, the Dynaflex (Figure 14). The Dynaflex rotor is a so-called "Gimballed" rotor system in which a stiff hub is attached to the driveshaft via an elastomeric constant-velocity joint to allow the hub to tilt and relieve the lead-lag stresses. The drive torque and flapping restraint are provided by a composite diaphragm, which transmits the torque from the shaft to the rotor, while at the same time retaining it by means of the carbon-fibre spring. Thus, the rotor provides an equivalent 5 percent hinge-offset, which is similar to articulated rotors. The gimbal concept allows to gain a substantially higher rotor tip path plane tilt over a conventional rotor (Reference 17).

The Dynaflex rotor, obviously, has the best drag of the BMR designs, but at the same time shows also a higher complexity. Sikorsky was performing many model tests with this hub concept, and completed a design of a full-scale rotor suitable for a high-speed Black-Hawk type helicopter, but never went into hardware.

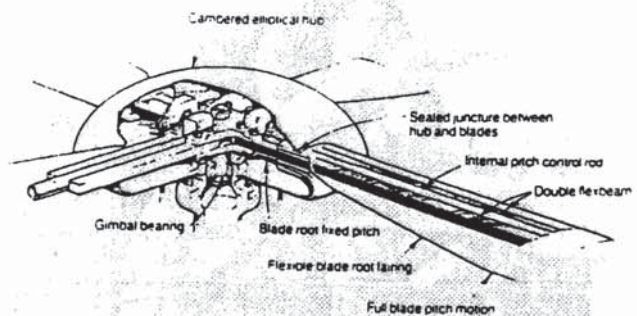


Fig. 14 Dynaflex Gimballing bearingless rotor configuration

During the LHX-Proposal phase to the US-Army, Sikorsky became responsible for the main rotor design, but did not follow the Dynaflex concept. The RAH-66 Comanche main rotor system employs a bearingless main rotor, five-bladed and 39 ft in diameter (Figure 15). Parts made using composite materials include the blade, torque tube, flexbeam, rotating swashplate, rotating scissors and quill shaft. The original design consisted of a one-piece fiberglass structure that formed the inboard flap flexures of all 5 blades and extended out to the connection bolt for the flexbeam. The hub structure was slightly changed, the PENTAFLEX rotor head being replaced by inboard blade attachments with modular fittings, that allow individual blade removal from the hub assembly for airtransportability and in case of damage. The flexbeam has rectangular cross section and inboard elastomeric damping/shear restraint elements. The equivalent flapping hinge offset lies around 9.5 percent of radius (Reference 18).

In 1991, a S-76 BMR test article, representative of the RAH-66 design concept was tested on the whirl stand (Figure 16). It is also scheduled to be tested at the NASA Ames wind tunnel facility.

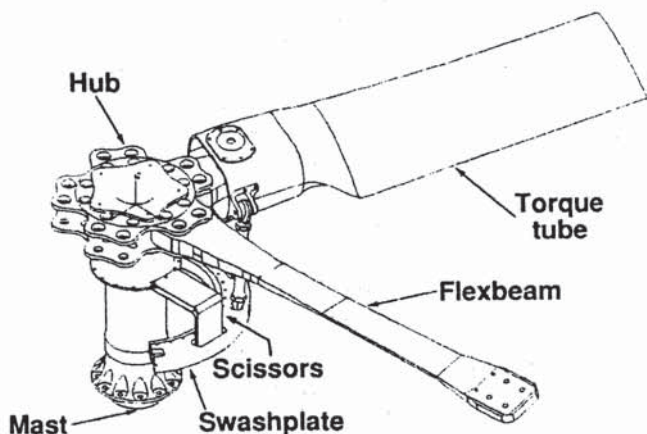


Fig. 15 RAH-66 Comanche rotor system



Fig. 16 S-76 BMR demonstrator on whirl tower

MBB/ECD

MBB (now Eurocopter Deutschland), Ottobrunn, Germany, began its fiberglass technology development in 1961, which resulted in the successful Hingeless Rotor System. Based on this tradition, MBB began experimenting with bearingless rotors in 1981. The development was conducted in three steps: In the first concept, which was a pure research configuration, a BO 105 hingeless hub was modified to carry experimental flexbeam blades, with the original pitch change bearings fixed at a 10 degrees prepitch angle (Figure 17). Similar to the Boeing approach, the design goal was to match the BO 105 rotor system dynamics as far as possible and, hence, the flapping hinge offset was outboard at 14 percent radius. The first chord frequency was at 0.69/rev. The flexbeam had a T-shaped cross-section, and a pitch control tube was placed behind it, mounted with flexible couplings to the hub and blades. In order to provide acceptable stability, elastomeric damping strips were bonded to the flexbeam, and constrained by an outer layer of graphite epoxy laminate.

The rotor was flown on a BO 105 test helicopter in 1984 (Figure 17). Although compromised, the experimental rotor yielded basically promising flight test results; however, the rotor stability was low and the hub drag was high. The development is summarized in Reference 19.

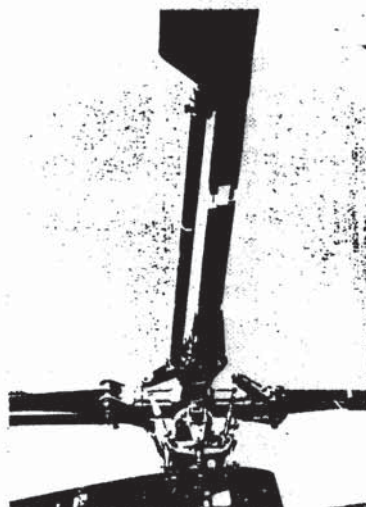


Fig. 17 MBB's FVW-Rotor experimental configuration

MBB was then developing a second prototype rotor in a more advanced design, where the stability and drag issues were particularly addressed (Figure 18). It uses a cruciform cross section flexible beam, and around this is an elliptical carbonfibre control cuff. It is made in two pieces which could be telescoped for flexbeam inspection. In this design the flapping hinge offset was reduced to about 9 percent, to provide the best compromise between agility, vibration/loads and structural integrity. The flexbeam could be shortened down by 25 percent. The rotor was tested on the whirlstand with several modifications on the hardware, to optimize the cuff

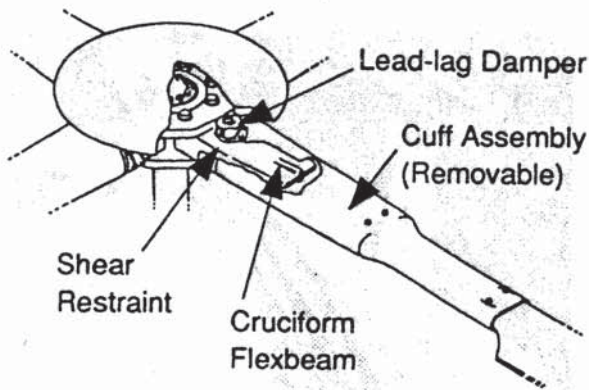


Fig. 18 BMR-P1 bearingless rotor concept



Fig. 19 Rotor installed on the BO105

design and elastomeric damper effectiveness. In 1986, the rotor was flight tested on a BO 105 with good results (Figure 19). Publications on the development of these MBB Bearingless Rotors are listed as References 20 to 22.

The results achieved during these campaigns provided a good foundation for the final BMR design for the new BO 108 helicopter. The configuration in principle follows the concept tested in the phase before, but was very much refined in the details (Figure 20). The cruciform beam shows a flatplate cross section inboard, which places the flapping hinge offset at 9 percent of radius. The carbonfibre cuff is directly bonded to the inner end of the blades' airfoil section, which results in an exceptionally smooth surface from the hub out to the aerodynamic blade part. Such a design and the inboard attachment of the beam have obvious benefits in reducing the rotor hub drag.

The total development, i.e. the flexbeam and torque tube sizing and the introduction of coupling effects was an intensive, interactive approach, which finally resulted in very satisfactory damping characteristics. Through 9 percent hinge offset, the rotor shows a proper balance of inherent dynamic stability and high maneuverability, and very low

loads and vibration levels. The rotor first flew in October 1988 on the BO 108 Prototype aircraft (Figure 21), with excellent results in aeromechanical stability, handling qualities, loads and vibration, as described in Reference 23.

Besides the BMR, ECD is developing its FEL-fibre elastomeric rotor for the Franco-German PAH-2 and the Indian ALH. This rotor follows the hingeless concept and comprises a stiff composite hub and flexible blades; pitch change is achieved through elastomeric bearings.



Fig. 20 BMR refined configuration

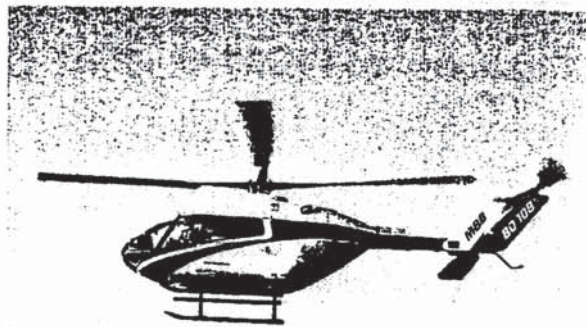


Fig. 21 BO108 with BMR during first flight

Westland Helicopters

Westland, Yeovil, England has been studying BMR's since 1980. Design feasibility studies and analytical work were performed, mainly concentrating on the assessment of ground and air resonance stability margins of such rotors in combination with existing and projected airframe configurations. To support the work, ground and air resonance tests of a four-bladed model rotor were performed. Reference 24 is a review of the analytical and experimental studies.

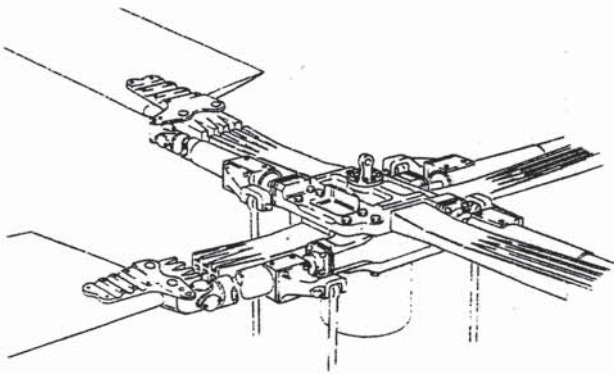


Fig. 22 Westland bearingless rotor design

In order to provide the "hard data", Westland, under a demonstrator contract of the UK-MoD, started design and manufacturing of a BMR flexure, sized for the Lynx helicopter. The rotor design, which emerged, comprised two double-ended composite glass/epoxy flexures housed in a titanium hub assembly (Figure 22). Blade pitch control is provided by a parallel torque tube, which houses an elastomeric lead-lag damper. Four full-sized flexure mouldings were produced and fatigue testing of the flexure is underway. The hardware is shown in Figure 23.

ITR/FRR - Project

In the mid-1970s, the U.S. Army Research and Technology Laboratories and NASA Ames Research Center have joined into a program to develop an Integrated Technology Rotor/Flight Research Rotor (ITR/FRR). The objective of the ITR/FRR program was to make significant advances over a broad spectrum of technologies. In the concept-definition studies a variety of hub concepts were proposed by the five US-Helicopter

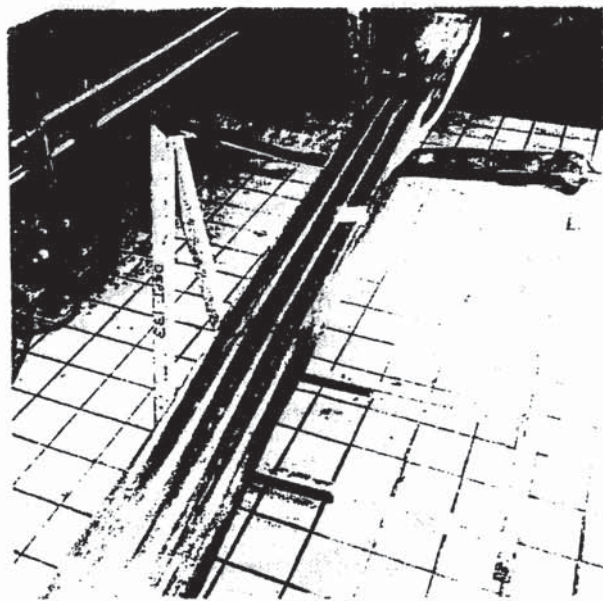


Fig. 23 Full-sized flexure hardware

manufacturers. Their description is given in References 25 to 29. Thirty-three hub-concepts were proposed, amongst them were 21 bearingless designs. Although no real design and development work was performed within this program, many of advanced design issues for new rotor hubs were examined, particularly with respect to bearingless rotor designs. The studies have also been very useful in identifying areas of weakness in the design methods. Reference 30 is a comprehensive analysis and a useful review of the concept-definition studies of the ITR/FRR-Program.

A summary and data comparison of the various bearingless hub concepts developed is given in Table 1.

Company	Type	Diameter (m)	No of Blades	Flap Hinge Offset (%)	Lag Frequency (1/rev)	Hub Precone (deg)	Control Device	Lead-Lag Damping Device	Beam Cross Section	Hub/Beam Attachment	Flown/ Tested in
Lockheed		10.70	4		0.65		Tube	No	Steel-Flex.	Bolted	1966
AS/ECF	Triflex	10.4	3	8.5	0.72	2.5	Horn	Elast/Emb	Elliptical	one Piece	1976
Bell	Model 680	12.8	4	4 (2.5)			Cuff	Elastomeric	Triple-H	one Piece	1982
	4BW	14.4	4	4 (2.5)			Cuff	Elastomeric	Triple-H	2 Pieces	1989
Boeing Vertol	BMR	9.82	4	14	0.74	0	Tube	No	Double-C	Bolted	1978
Sikorsky	Dynaflex	Model	4	5 (Gimbal)	Stiff		Tube	No	Double-C	Bolted	(Model)
	S76-Demo	13.4	5	9.5	0.7	2.5	Cuff	Elastomeric	Rectangular	Bolted	1991
MBB/ECD	FVW-Exp.	9.82	4	13.6	0.69	0	Tube	Elastomeric	T-Shape	Bolted	1984
	BMR-P1	10.0	4	9	0.75	0	Cuff	Elastomeric	Cruciform	Bolted	1986
	BMR-BO108	10.0	4	9	0.70	0	Cuff	Elastomeric	Cruciform	Bolted	1988
MDHC	HARP	8.5	4	8	0.6	2.5	Cuff	Elastomeric	Flat-X	Bolted	1985
	MD900	10.34	5				Cuff	Elastomeric	Rectangular	Bolted	1992
WHL	Exp.		4				Tube	Elastomeric	Triple-H	2 Pieces	(Model)

Table 1 Comparison of bearingless main rotor design concepts

Main Design Considerations

In order to better understand the problems related to a bearingless-hub design, it is helpful to review briefly the important design attributes and to summarize the present state of understanding.

Hub-Moment Stiffness:

A primary parameter in designing any type of rotor system is the fundamental flap stiffness, expressed also as hub-moment stiffness, or equivalent flap hinge offset. Usually, a low hub-moment stiffness is desired to improve vibratory characteristics, gust response and some aspects of flight stability. Conversely, a moderate or high hub-moment stiffness is desired to improve maneuverability, agility and fatigue life. These very basic design considerations have been addressed very systematically in the 1960's, early 1970's, when the development of the Hingeless Rotorcraft began (References 31, 32 for example). There are many literatures available; useful surveys are given in Reference 33 and 34.

When examining the variety of hub concepts and classifying them under the aspect of hub-moment stiffness (or flap hinge-offset), there were basically two categories which characterized the two ends of the full spectrum of rotor concepts, the conventional flap hinge (articulated) designs and the newer hingeless rotor designs. In terms of the flap-hinge offset, the first category, quite obviously, is limited to values below - say 5 percent. On the other side, the newer hingeless hubs show a trend towards relatively high values of flap-hinge offset, due to the fact, that the flap and lag "hinges" were no real hinges, but were realized through blade flexibilities, which lie more outboard. These concepts are characterized by flap-hinge offsets in the order of 11 to 15 percent of radius.

When looking on the current bearingless category, the design concept obviously allows for shifting the effective flap hinge more inboard, mainly due to the simple hub/flexbeam attachment, which is also desirable in order to minimize weight and hub drag. To further illustrate this trend, flap-hinge offsets are shown in Figure 24, where the values of the BMR developments during the last 15 years are plotted against a time axis (year of first flight). It does appear that there is a trend to be observed: With the exception of the pure experimental designs of BV and MBB, the more recent designs of ECD, MD and Sikorsky show hinge-offset values between 8.5 to 10 percent of radius. The Bell concepts show values in the lower range of 2.5...4 percent, which reflects its particular design philosophy of low hinge-offsets.

In-plane Stiffness:

The principal design considerations with respect to the fundamental in-plane natural frequency are very well known from many literatures (Reference

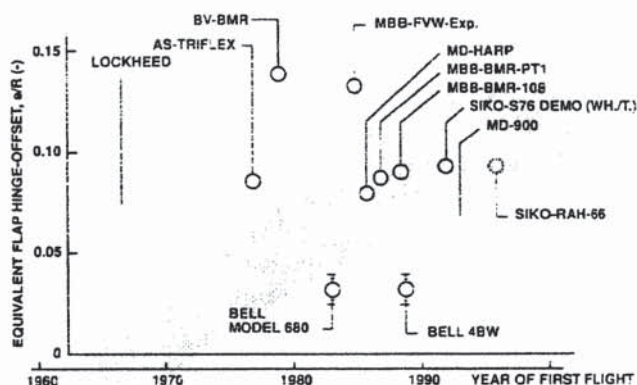


Fig. 24 Trends in BMR rotor stiffness

34). From the 10 BMR hub concepts developed and tested so far, all designs were of the soft-inplane type, with frequencies ranging from 0.6/rev to 0.75/rev (see Table 1). The soft-inplane designs give more design freedom for tailoring the flexbeam cross section, the critical chordwise loadings are low and the small dimensions of the flexbeams is a prerequisite for designing a beam with low torsional rigidity. Furthermore, the technical goals for reducing the hub weight and drag require that BMR designs be as light and compact as possible.

The critical loading conditions and the aeromechanical stability requirements for soft-inplane BMR designs were in principle known, from the substantial work that had been done on the past designs of soft-in-plane hingeless rotors (Reference 34).

Flexbeam Design

The key element of a bearingless rotor is the inboard portion of the spar, commonly called the "flexbeam". This part connects the blade to the mast and has to carry all the primary flight loads. It accommodates the elastic blade motions in flap- and chordwise directions and the elastic twist deformation for pitch control. By proper stiffness tailoring of the beam along its length, it is possible to separate the individual functions of the flexbeam. Figure 25 shows a typical flexbeam design with the different sections tailored to their specific function.

Torsional Stiffness:

The primary criterion in the flexbeam design is the torsional stiffness and strength, since the control requires to twist the beam collectively and cyclically. The shear stresses mainly depend on the achieved torsional rigidity.

In the early stages of its BMR-program, Boeing Vertol did a systematic study of several cross section shapes, like solid sections, split-tubes, I-beams and cruciforms (Reference 8). Figure 26 is a summary of the main results, and shows the tradeoff between the critical fatigue stresses under a

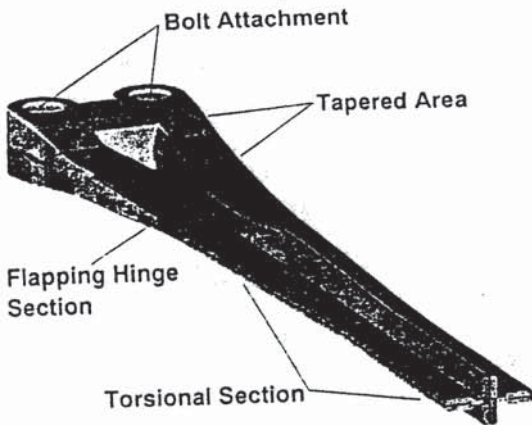


Fig. 25 Flexbeam key design areas

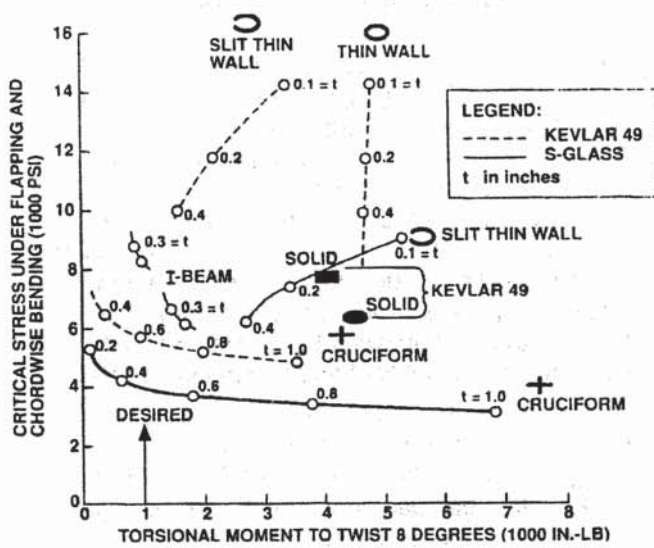


Fig. 26 Beam cross section tradeoff

given load case (alternating flap and chord moments), and the torsional moment necessary to twist the beam by a certain angle. The influence of the cross section materials is also shown.

The variety of design approaches on the present BMR designs suggests, that there is no true optimum cross section: Some of them are using highly tailored cross sections, like cruciform or Triple-H-type sections, others are using flat rectangular cross sections (Table 1). The torsional stiffness goals of all these designs can obviously be met, with careful selection of materials, tailoring of the geometry and orientation of lay-ups.

Bending Tailoring:

The need for inboard flapping flexibility leads usually to a design with a "hinge" section (Figure 25). The length of the hinge section is optimized for a minimum of mainly dynamic stresses caused by blade flapping. Current BMR designs usually apply ± 5 degrees of flapping angles without fatigue damage.

The radial variation of the cross section geometry is often highly tailored along the length of the flexbeam.

The design goal of such configurations is to achieve minimal dimensions, maximum flapping flexibility with reasonable endurance limits and low shear stresses. An example of a flexbeam with a nearly constant strain distribution can be seen in Figure 27. In the lead-lag direction, the flexbeam stiffness is governed by frequency requirements and by the need to tailor the bending mode shape in order to achieve maximum lead-lag damper efficiency.

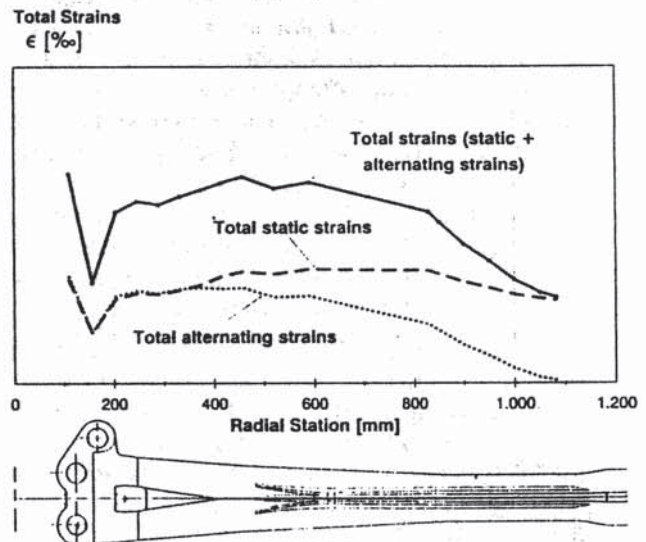


Fig. 27 Constant strain distribution

The flexbeam of the BO108 BMR uses unidirectional E-Glass/epoxy and quasi-isotropic glassfiber/epoxy fabric. Fiberglass belts are used for the attachment lugs. A flexbeam undergoing layup is shown in Figure 28.

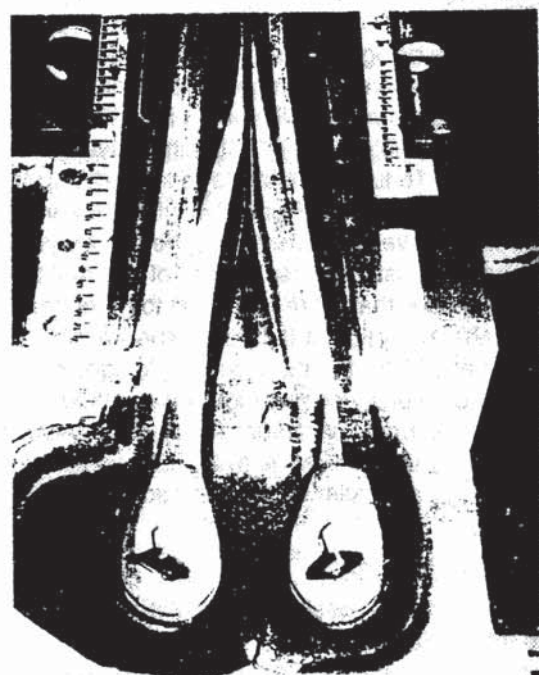


Fig. 28 Flexbeam Manufacturing

Control cuffs or pitch cases are designed to have high torsional stiffness and high chordwise stiffness to transmit the in-plane motions to the inboard damping device. Most of the current BMR designs are using primarily graphite/epoxy material in order to achieve the stiffness goals for their cuffs. Dual torsional load transfer diminishes vulnerability and increases the damage tolerance characteristics.

Design Approaches for Damping

In general, any sort of main rotor system must be carefully designed to avoid potential aeromechanical instabilities. As is well known, for soft-in-plane rotors air and ground resonance is of primary interest. Both types of resonances are dominated by the rotor blade lead-lag motion, coupled with body motion. Whenever the regressing mode chord frequency crosses a body frequency, the potential for instability exists. To suppress these potential instabilities, some source of damping has to be introduced into the blade motions for air resonance and into the blade and/or landing gear motions for ground resonance.

The amount of mechanical damping, inherent in composite structures, typically lies in the order of 0.5 to 1 percent. Aerodynamic damping through airloads is contributing some part at 1 g thrust conditions, but has only negligible effect at zero thrust. These two sources of lead-lag damping look to be insufficient for bearingless designs. Hence, blade damping must usually be augmented by mechanical damping in the rotor system or through discrete mechanical coupling of the blade motions such that aerodynamic damping is activated.

Pitch-Lag and Flap-Lag Coupling

Pitch-lag and structural flap-lag coupling, either separately or in combination, are known to have beneficial stabilizing effects for aeromechanical stability. However, these effects are not a general rule; each particular design must be carefully analyzed and the introduction and functioning of these types of couplings must be well understood.

The phenomenon of bending-torsion coupling on helicopter rotor blades can easily be realized by considering the blade bending behaviour (Figure 29). With the total dynamic and aerodynamic forces acting the elastic blade is deflected and, in case of a hingeless rotor, bends away from the line of the feathering axis. If the blade is bent in the flapping plane, the inplane forces create a pitching moment on the arm of the flapping deflection. Likewise, when the blade is bent in the lead-lag direction, a pitching moment on the lead-lag arm is created by the lift forces. References 35 and 36 examined pitch/lag and flap/lag coupling effects on soft-in-plane rotors stability.

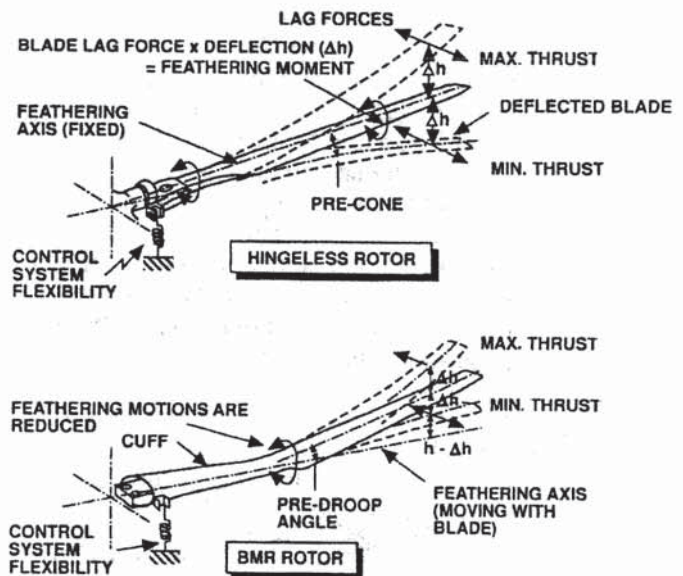


Fig. 29 Principles of lag bending-torsion coupling

When comparing a bearingless rotor with a BO 105 type hingeless concept (Figure 29) it is noticed that the inboard geometry and the sequence of the bending and feathering motions is dissimilar: The BMR does not have inboard feathering bearings and, since the effective feathering hinge for the BMR occurs outboard of the flap and lag equivalent hinges, the stabilizing coupling between the bending and feathering modes is somewhat different. Lag-torsion coupling on the BMR is reduced at low thrust due to reduction in blade-to-feathering-axis offset. Conversely, for the BO 105-rotor, minimum lag/torsion coupling occurs at around 1 g thrust collective (minimum off-axis deflection) and increases as thrust is increased or decreased.

One way of introducing beneficial pitch/lag coupling in BMR's is negative pre-droop in the portion outboard of the blade-to-beam joint. However, it must be kept in mind that blade deflections outboard of that station can partially eliminate the built-in pre-droop effect, hence, reducing the corresponding coupling. The stiffness of the control system also influences this type of mechanical coupling.

Another source of damping in bearingless rotors can be achieved through incorporation of flap-lag coupling. This coupling can principally be affected by the inclination of the principal axes of the flap and chordwise bending. This can be achieved by a pre-inclination of the flexure, as was done on the Boeing BMR. In this case, asymmetric bending of the flexure causes flap motions from chord to lag motions.

Kinematic Coupling

An additional coupling effect can result from the specific concept of the pitch-control. The most common configuration in present BMR designs involve a control cuff to twist the blade outboard of the

flexbeam. To be effective, such a cuff has to be stiff in chordwise direction and in the cuff-to-blade attachment area, such that the lag shear loads are transmitted from the blade to the shear bearing, thus activating the elastomeric damping elements. From Figure 30 it can be seen that, when the blade moves backwards, the cuff moves forward, thus deflecting the elastomeric damping elements. Depending on the geometry of the control rod, a geometric pitch-lag coupling can be introduced, which can substantially alter the damping behaviour - both positively or negatively.

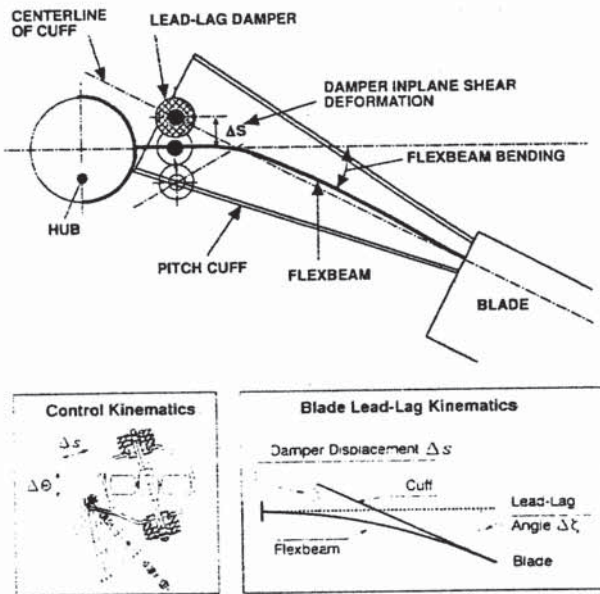


Fig. 30 Pitch/lag coupling due to blade lead-lag and control kinematics

An elementary expression of this type of pitch/lag coupling can be seen from Figure 30 (lower part), where the coupling term can be expressed by

$$\tan \delta_1 = \Delta\theta / \Delta\zeta = \Delta\theta / \Delta s \times \Delta s / \Delta\zeta$$

The first term in the equation is a control kinematics term, whereas the second one reflects the damper deflection or stiffness term.

As an example from an early MBB-concept, Figure 31 illustrates clearly, how in-plane damping could be improved by changing the damper stiffness and by introducing proper geometric pitch-lag coupling through a change in the inclination of the damper support axis. The combined effect was a doubling of damping over the whole collective pitch range. However, it should be noticed, that in case of a complete rotor-body-dynamics system like ground resonance, the influence of positive pitch-lag coupling on stability may change, and may even be negative in the resonance point. This has been demonstrated by analytical studies (Reference 37).

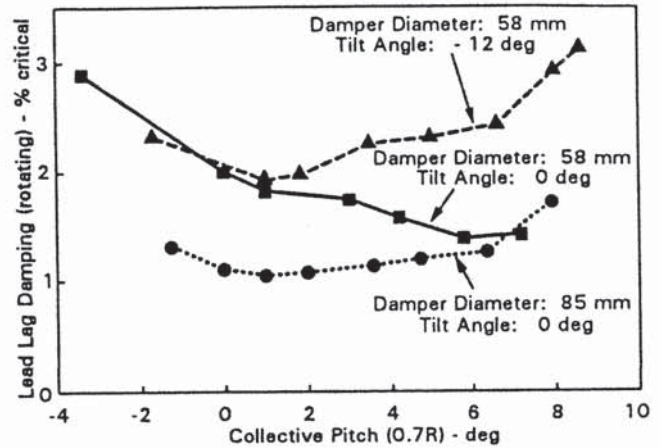


Fig. 31 Test results on coupling sensitive parameters

It is evident from these discussions, that aeroelastic coupling, on the one side, offers considerable potential for augmenting rotor damping. On the other side, stability improvements through sensitive concept parameters of this nature is a highly complex problem, which requires thorough investigation and a high level of confidence in the predictive capability of aeroelastic mathematical models.

Elastomeric Damping

The concepts described before indicate that the most common BMR configuration today involves a combined snupper/damper element at the inboard section, to control the pitch/bending coupling and to augment structural damping. A typical arrangement is shown in Figure 32. To be effective, such elements have to be strained through the inboard motion of the torque structure, thus providing an additional damping in the order of 2 to 4 percent.

The design of such elements is rather complex task. The two main characteristics which are of considerable interest are the mechanical material non-linearities and the thermoviscoelastic characteristics. Some major influences are presented below (from Reference 38).

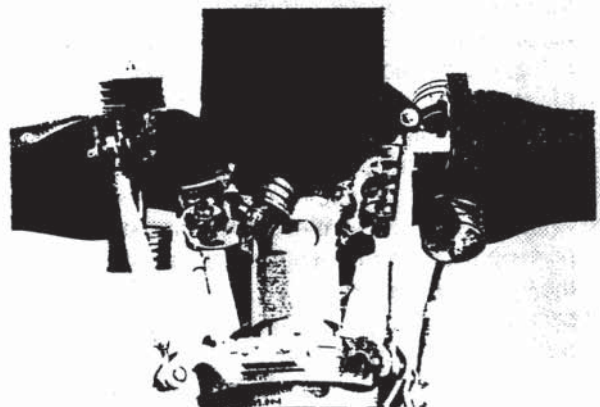


Fig. 32 Elastomeric damper elements on a BMR

Effect of Amplitude: First, the viscoelastic response of high damping elastomers shows a strong non-linear dependence on the shear loading deflections of the damping elements. Figure 33 shows the results of component tests conducted on one type of silicon damper (Reference 38). In the plotting of shear force vs. shear deflection, the strongly non-linear behaviour can clearly be seen: At small amplitudes a dynamic "hardening" of the material is observed, accompanied by a reduction in the loss factor. Conversely, with decreasing amplitudes a strain-softening is noticed.

The analysis of these results indicates that both the dynamic spring rate (curve slope) and the mechanical loss factor (hysteresis loop area) is a highly non-linear function of amplitude. A sufficiently high loss factor can only be achieved with a certain amount of damper displacement. For a concrete design it is essential to understand where this optimum working point is and how the whole system can be forced into working around this point.

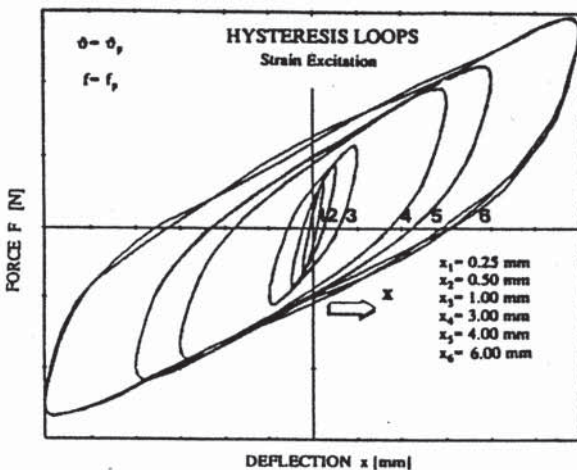
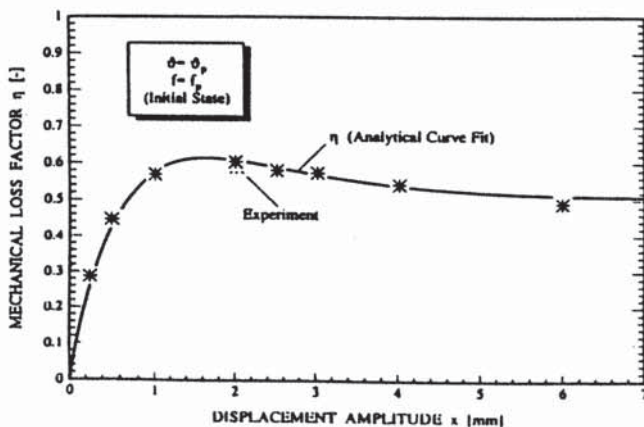


Fig. 33 Damper characteristics (complex stiffness and mechanical loss factor) as a function of displacement amplitude



Effect of Frequency: A second important effect on elastomeric damper characteristics is the influence of frequency. Component testing for a selected damper material indicate, that both the dynamic spring rate and the loss-factor (damping) increases with frequency, and it is evident again, that thorough understanding of the working conditions is required to achieve a successful design.

Effect of Temperature: Due to the particular thermomechanical behaviour of elastomeric material, the temperature is a third important parameter which has considerable influences on damper efficiency. Figure 34 shows representative effects of ambient temperature on the dynamic characteristics of a silicon type of damper. At very low temperatures a stiffening effect in the spring rate is seen, which is an important consideration in the cold start characteristics of a BMR design.

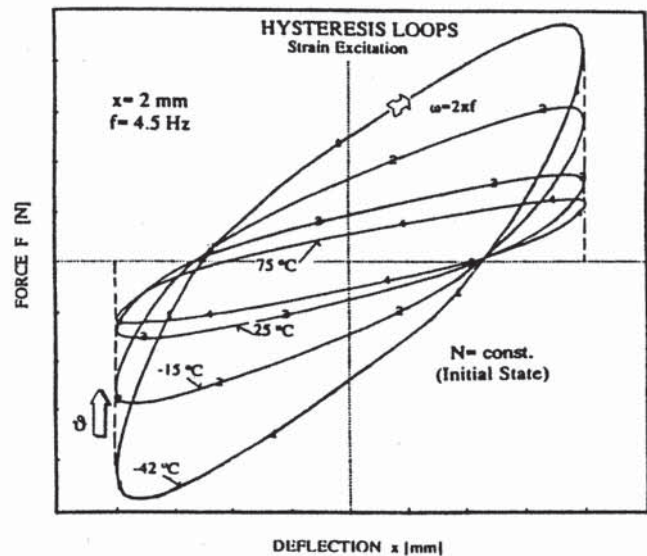


Fig. 34 Damper characteristics as a function of ambient temperature

In this context, the self-heating effect on damper characteristics during the run-up time is of importance. These effects have been thoroughly investigated through experiments during the recent years. The results show that the materials used today, even at very low temperatures show a rapid softening due to the selfheating effect, requiring only a very small number of cycles during rotor run-up.

As an example, a complete coupled thermo-viscoelastic analysis of the internal temperature field inside a damper with metal shims is presented in Figure 35. The picture shows the local temperature concentrations through internal heat buildup for a maximum amplitude case, as analyzed by FEM. The silicon rubber material can well accommodate the temperature levels shown here. The cooling effect of the two metal shims can clearly be seen. The peak temperature inside the damper would be significantly higher without the metal shims.

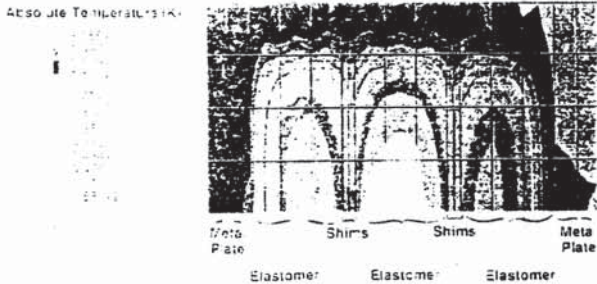


Fig. 35 Calculated temperature distribution inside an elastomeric damper (max. amplitude case)

Analytical Modelling: Due to the particular non-linear behaviour of elastomeric materials, the requirements for the analytical formulation and the procedures in the design process have changed. Pure mechanical damping can no more be treated as a simple linear term, and chordwise stiffness is no longer a constant parameter. It is important to consider that these values are depending on the operational conditions such as lead-lag amplitude, frequency and ambient temperature, for example. Hence, non-classical effects of this nature have to be incorporated into the dynamic modelling of a bearingless rotor.

Figure 36 shows a simplified steady-state model for the prediction of the modal characteristics and the aeroelastic stability behaviour, including a specific model for the elastomeric damper. The non-linear system is solved in a stepwise manner.

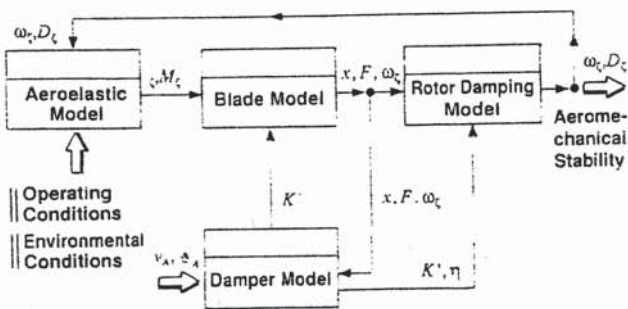


Fig. 36 Non-linear dynamics modelling

Achievements to Date and Prospects

The bearingless-rotor development efforts to date have reached a status, where a critical assessment of the achievements can be made and where future perspectives should be given.

Aeromechanical Stability Developed

Aeromechanical stability of the ground and air resonance type - a major concern in the early design - can be considered to be sufficiently developed today, as can be seen from the damping levels achieved in the various testings (References 14, 39). Inplane damping typically lies in the order of 3 to 4 percent (Figure 37). Quite obviously, the stabilizing effects of coupling parameters are understood, although other design requirements do not always allow the application of the optimum choice.

The technology of elastomeric dampers, most commonly used on the BMR-designs today, has also rapidly developed in the past decade and the understanding of the main material characteristics has strongly improved. Although, some questions have still to be finally answered to master this technology. Further work has to be done in the improvement of life-time, definition of replacement criteria, unsymmetric operations and failure analysis, for example.

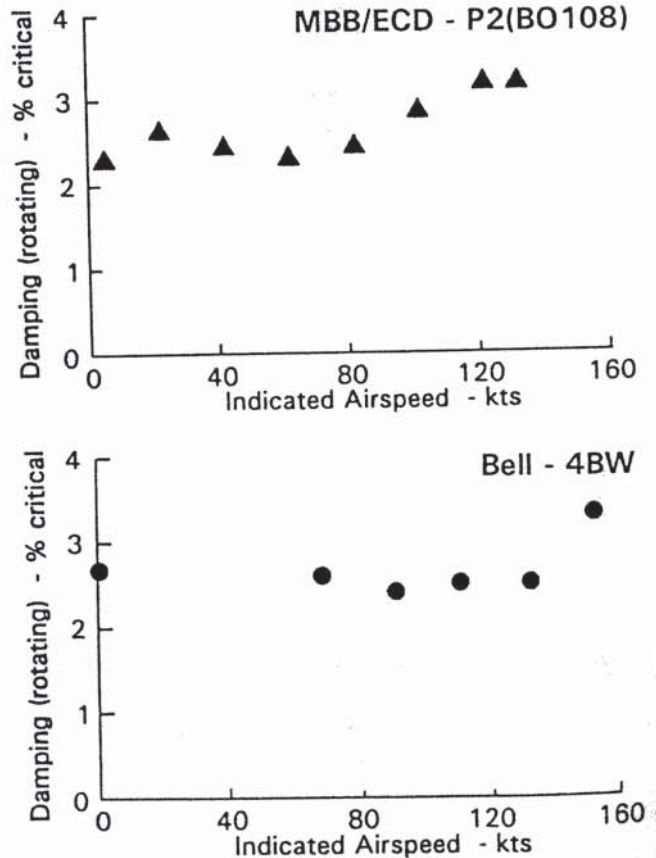


Fig. 37 Typical rotor lead-lag damping levels in flight

From the technological standpoint, the question is sometimes raised, whether such elements could even be completely dispensed in future BMR-designs. From the today's view, a complete elimination looks not likely, but any efforts should be made to minimize the damper size and the required operating amplitudes, in order to increase life-time.

Good Ride Qualities

A discussed, handling qualities and vibrations depend mainly on the hub-moment stiffness, and are not directly characteristic for the type of hub design itself. Nevertheless, the experiences gained from the handling qualities evaluations of past BMR's flight testing is in all cases very positive: The Bell 222 with a low (2,5...4 percent) hinge-offset BMR's flight testing showed significant improvements in the piloting efforts; the measured 4/rev-vibrations, particularly with the LIVE-units installed, were very low (Figure 38).

Beneficial handling qualities and vibrations were also confirmed by the BO 108 BMR prototype testing. The bearingless rotor with 9 percent hinge-offset provided the aircraft very pleasant control response, improved stability characteristics, and very good ride quality, in general. With a passive anti-resonance vibration system (ARIS) installed, the vibration levels were also highly satisfactory, with 4/rev-levels well below 0.1 g over the whole flight envelope, at all seats and in all axes (Figure 38).

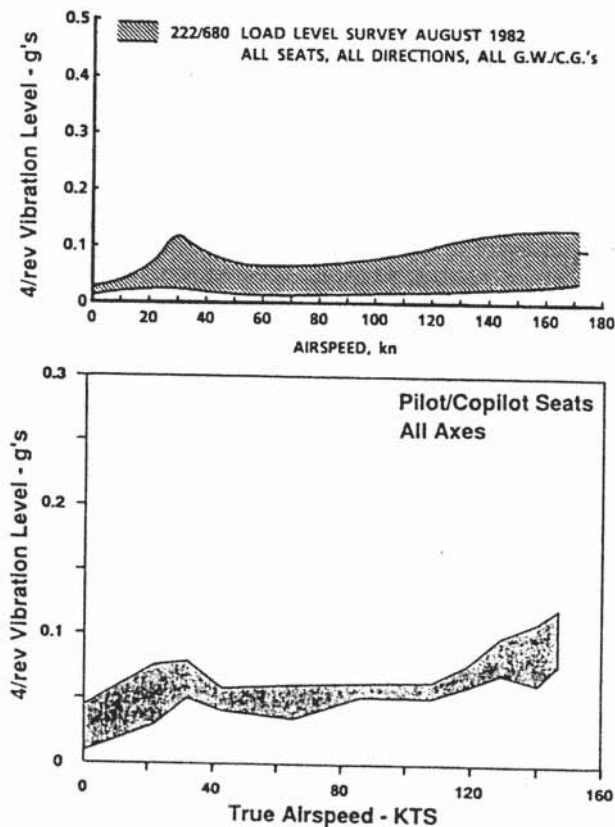


Fig. 38 Fuselage vibrations on BMR-aircraft (Top: Bell 222/680; Bottom: MBB BO108/BMR)

Low Weight

Simplicity and its favourable implications for rotor system weight is one major goal in BMR design. Although the data weight available is not enough to provide a reliable basis for such comparison, a rough assessment of the current informations should be of interest (Figure 39).

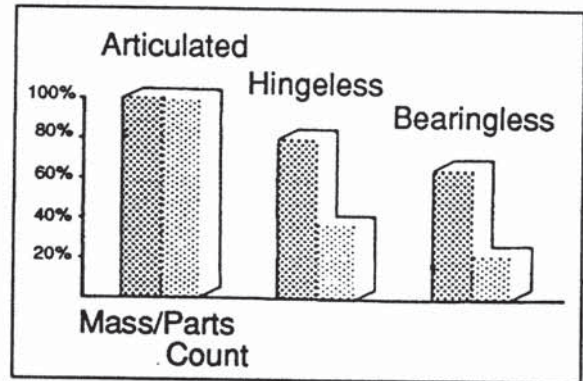


Fig. 39 Relative rotor weight and complexity

Boeing Vertol, on the basis of its experimental design, gave an early estimate for a production BMR, which would be 22 percent lighter when compared to the BO 105 hingeless rotor. Aerospatiale's Triflex hub was reported to be 48 percent lower in weight than the corresponding standard SA 341 Gazelle hub. This would compare to a weight saving of roughly 20 percent on the complete rotor. Bell, from the experience with its Model 680 rotor with 412 type of blades, shows a 9 percent lighter hub weight, which would increase to 15 to 20 percent saving with new blade designs. MBB/ECD's experience shows savings in rotor system weight of 40 kg (18 percent) on its first BMR-prototype, and of 50 kg (22 percent) in the BO-108-BMR design, when compared to the BO 105 hingeless rotor.

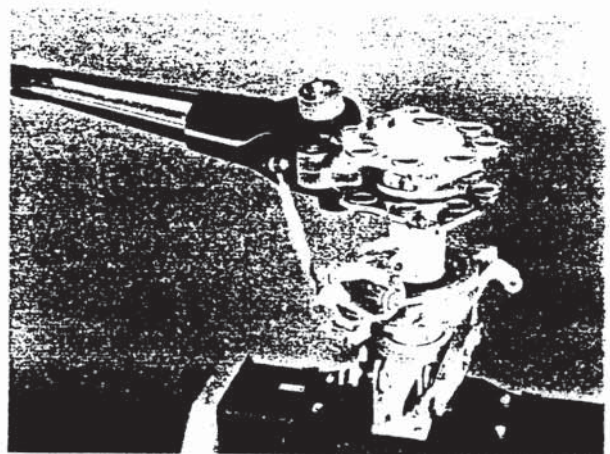


Fig. 40 Simplicity of BO108 BMR design

The reasons for the substantial weight savings are the simplification of the hub design and the intensive use of composite materials, as is evident from the BMR hardware shown in Figure 40. The composite material systems used in the design of modern bearingless rotors (hubs and blades) account for around 60 percent of the total materials used, as compared to only 12 percent for older articulated or 35 percent for hingeless rotors.

Lower Manufacturing Efforts

In examining progress in this field, parts count is a quite descriptive parameter. A high parts count is generally typical of older conventional designs, in which a system of hinges and bearings is applied on the hub. Again, based on the small data base of bearingless rotor designs, the reductions in parts count range from 50 percent (Bell) up to about 85 percent (Aerospatiale), compared to older articulated designs. In comparison to more modern designs (like hingeless rotors), the reduction is in the range of 40 percent (MBB/ECD), Figure 39.

Improved Reliability and Maintenance

The relevant drivers with respect to maintenance efforts and operating costs of conventional designs are wearing parts as bearings and joints and all life-time critical components. The progress in the new technology design stems from the fact that these parts are replaced through composites which allow for unlimited fatigue-life and show pronounced damage tolerance features inherent to their fibrous nature. Similarly, mechanical degradation in the elastomeric part shows also typical damage tolerant behaviour.

An evaluation of the fatigue characteristics indicates that, with careful design, life in excess of 10,000 hours is achievable in the composite parts. The numbers for elastomeric dampers are projected today to at least 2500 hours. These data are unquestionably a big step forward towards full on-condition replacement.

Application to New Products

It is the result of the past 10 to 15 years' research and experimental work that bearingless rotor systems are suitable for production rotors today. Recognizing the requirements for advanced components, three major new-generation civil and military projects have selected the all composite BMR system as their prime lifting device (Figure 41): The ECD BO108 (flying since 1988), the MDHC Explorer (due to fly mid 1992), and the Boeing Sikorsky Comanche (first flight scheduled for 1995). Bell did not specify to what extent its Model 680 or 4BW technology will go into production for its new products.

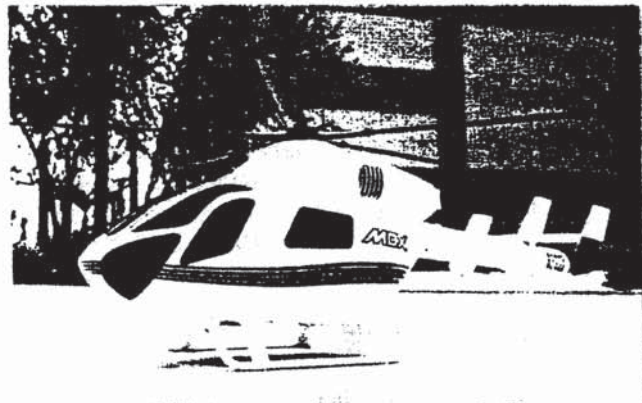


Fig. 41 ECD BO108, MDHC Explorer and Boeing Sikorsky Comanche using composite BMR systems

The expectations of the manufacturers are to take full advantage of the simplified design, the improved flight efficiency, the increased reliability and low weight, which are enabled through the introduction of the bearingless main rotor concept.

A Look to the Future

Despite all the progress made during the past decade, it can be imagined that aeromechanics and composite structural technology will not slow down in the future. Scientists and rotor design engineers will continue in thinking and creating new ideas how to make rotors better again. There are two innovative technologies coming up to date, and these are the HHC/IBC technology and, probably even more promising, the smart materials/structures technology. Currently, there are many research and experimental efforts running, to work out the fundamental technologies and to check the proof of concepts (Reference 40, 41 for example).

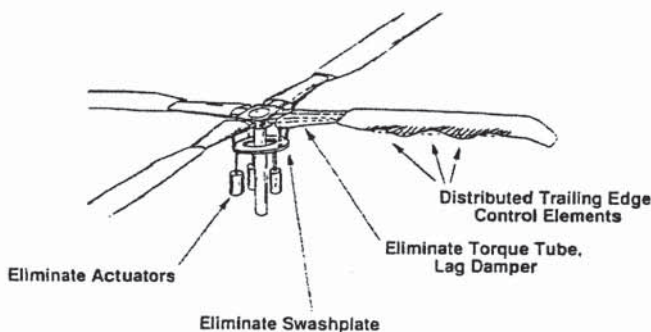


Fig. 42 "Ideal" concept possibilities

How "ideal" rotor concept possibilities could look like in the future, is shown in Figure 42, taken from Reference 42. The technology assessment indicates, that some of the required disciplines are ready today and some of them have still to be pushed forward. In this context, the aeroelastic and structural technology, worked out during the bearingless-rotor technology development, unquestionably, is an excellent basis for a full integration of smart material "actuators" within an "Intelligent Rotor".

Conclusions

There has been substantial progress in the design and development of bearingless main rotor concepts in the past decade. Nearly all of the helicopter manufacturers have worked, among other rotor systems, toward the development of bearingless-rotors, with different design approaches and with different success.

The most common bearingless-rotor configuration today involves a flexbeam with an inboard flap flexure, plus an external pitch cuff, supported by a snubber/damper at the root for the control of the pitch/bending coupling and augmentation of the structural damping. The main secrets lie in the proper design of the flexible element, and of the

damping elements. They have to accommodate the flexible blade bending and pitch-control motions, and to provide the required in-plane damping.

The successful development of such components requires an interactive approach: Material properties, load and modal analyses, kinematic/elastic coupling effects and non-linear elastomeric properties must be interactively optimized to assure proper stress distributions, adequate frequency and damping characteristics, and general structural integrity. The extensive and often non-linear finite elements analyses required within this process are available today, and most of the complex influences are understood today. Although, some questions have still to be finally answered, to fully master this technology.

A review of the recent accomplishments indicates that the aeromechanical stability of the soft-in-plane design is developed, and it is evident, that the realized concepts provide excellent flying characteristics and low vibration levels. These advantages are achieved with simplified hub designs and through a rigorous usage of composite materials, which lead to a substantial saving of weight, lower manufacturing efforts, improved reliability and reductions in maintenance.

Three new helicopter projects have selected the bearingless-rotor technology as their prime lifting device: The BO108, the Explorer and the Comanche. They are in different stages of development.

It can be imagined that aeromechanics and composite structures technology will continue to develop. New technologies are on the horizon today, which, together with the existing bearingless technology base, could lead to the "Intelligent Rotor" within the next decade.

References

1. Fenaughty, R.R., and Noehren, W.L., "Composite Bearingless Tail Rotor for UTTAS", *Journal of American Helicopter Society*, Vol. 22, No. 3, July 1977
2. Shaw, J., Jr., and Edwards, W.T., "The YUH-61A Tail Rotor: Development of a Stiff-Inplane Bearingless Flexstrap Design", *Journal of American Helicopter Society*, Vol. 23, No. 2, April 1978
3. Banerjee, D., Head, R.E., Marthe, R. and Ploudre, M., "The YAH-64A Composite Flexbeam Tail Rotor", *AHS-Specialists Meeting on Rotor Design*, Philadelphia, Oct. 1980
4. Blachere, C., and D'Ambra, F., "Tail Rotor Studies for Satisfactory Performance, Strength, and Dynamic Behaviour", *Vertica*, Vol. 6, No. 4, 1982

5. Huber, H., Klöppel, V. and Enenkl, B., "Development of Bearingless Tail Rotors", RAE's and AHS Helicopter Yaw Control Concepts Conference, London, February 1990
6. Donham, R.E., Cardinale, S.V., and Sachs, I.B., "Ground and Air Resonance Characteristics of a Soft Inplane Rigid Rotor System", Journal American Helicopter Society, Vol. 14, No. 4, Oct. 1969
7. Staley, J.A., Gabel, R., and Mac Donald, H.J., "Full Scale Ground and Air Resonance Testing of the Army-Boeing Vertol Bearingless Main Rotor", American Helicopter Society 35th Annual National Forum, Washington D.C. May 1979
8. Dixon, P.G.C. and Bishop, H.E., "The Bearingless Main Rotor", Journal American Helicopter Society, Vol. 25, No.3, 1980
9. Mouille, R., "Design Philosophy for Helicopter Rotor Heads", Second European Rotorcraft and Powered-Lift Aircraft Forum, Bückeberg, Germany, September 1976
10. Cassier, A., "Development of the Triflex Rotor Head", Fifth European Rotorcraft and Powered-Lift Aircraft Forum, Amsterdam, September 1979
11. Metzger, R., "Smooth and Simple: The Bell Model 680 Bearingless Main Rotor", Vertiflite, Vol. 29, No. 4, May-June 1983
12. Weller, W.H., "Correlation and Evaluation of Inplane Stability Characteristics for an Advanced Bearingless Main Rotor Model", NASA CR-166448, May 1983
13. Alsmiller, G., Metzger, R., and Sonneborn, W., "All-Composite Rotorcraft", American Helicopter Society, 39th Annual Forum, St. Louis, May 1983
14. Harse, J.H., "The Four-Bladed Main Rotor System for the AH-1W Helicopter", American Helicopter Society, 45th Annual National Forum, Boston, May 1989
15. Banerjee, D. and Silverthorn, L.J., "Dynamic Considerations in the Design and Flight Test of an Advanced Bearingless Rotor System", American Helicopter Society, 45th Annual National Forum, Boston, May 1989
16. Head, R.E., Alexander, J.V., and Hughes, C.W., "Design of the McDonnell Douglas Helicopter Company Advanced Composite Rotor System", American Helicopter Society, 42nd Annual National Forum, Washington D.C., 1986
17. Fradenburgh, E.A. and Dr. Carlson, R.G., "The Sikorsky Dynaflex Rotor -an Advanced Main Rotor System for the 1990's", American Helicopter Society, 40th Annual Forum, Arlington, Virginia, May 1984
18. Blackwell, R.H., "Dynamics Considerations in the Design of the Comanche Helicopter", Fourth Workshop on Dynamics and Aeroelastic Stability Modeling of Rotorcraft Systems", University of Maryland, Washington, November 1991
19. Huber, H., "Gelenk- und Lagerloser Hauptrotor in Faserverbundbauweise für dynamische Systeme zukünftiger Hubschrauber", 3. BMFT Status Seminar Luftfahrtforschung und -technologie, Hamburg, May 1983
20. Seitz, G. and Singer, G., "Structural and Dynamic Tailoring of Hingeless/Bearingless Rotors", Ninth European Rotorcraft Forum, Stresa 1983
21. Klöppel, V., Kampa, K., Isselhorst, B., "Aeromechanical Aspects in the Design of Hingeless/Bearingless Rotor Systems", American Helicopter Society, 40th Annual National Forum, Washington 1984
22. Strehow, H., Frommlet, H., "Entwicklung Neuartiger Lagerloser Rotorsystem", 4. BMFT-Statusseminar Luftfahrtforschung und Luftfahrttechnologie, München, April 1986
23. Huber, H., "BO108 Development Status and Prospects", 16th European Rotorcraft Forum, Glasgow, September 1990
24. Juggins, P.T.W., "Substantiation of the Analytical Prediction of Ground and Air Resonance Stability of a Bearingless Rotor, Using Model Scale Tests", 12th European Rotorcraft Forum, Garmisch-Partenkirchen, Sept. 1986
25. Harse, James H., "Integrated Technology Rotor/Flight Research Rotor (ITR/FRR) Concept Definition", NASA CR 166443, 1983
26. Dixon, Peter G.C., "Integrated Technology Rotor/Flight Research Rotor Hub Concept Definition", NASA CR 166447, 1983
27. Hughes, Charles W., "Integrated Technology Rotor/Flight Research Rotor (ITR/FRR) Concept Definition Study", NASA CR 16444, 1983
28. Howes, H.E. and Tomashofski, C.A., "Integrated Technology Rotor/Flight Research Rotor (ITR/FRR) Concept Definition", NASA CR 166445, 1983
29. Carlson, Raymond G., Beno, Edward A., and Ullisnik, Harold D., "Integrated Technology Rotor/Flight Research Rotor (ITR/FRR) Concept Definition Study", NASA CR 166446, 1983

30. Bousman, W.G., Ormiston, R.A., and Mirick, P.H., "Design Considerations for Bearingless Rotor Hubs", American Helicopter Society 39th Annual National Forum, St. Louis, May 1983
31. Reichert, G. and Oelker, P., "Handling Qualities with the Bölkow Rigid Rotor System", American Helicopter Society 24th Annual National Forum, Washington D.C., May 1968
32. Huber, H., "Parametric Trends & Optimization - Preliminary Selection of Configuration - Prototype Design and Manufacture", AGARD-LS-63, 1973
33. Hohenemser, K.H., "Hingeless Rotorcraft Flight Dynamics", AGARDograph No. 197, September 1974
34. Johnson, W., "Recent Developments in the Dynamics of Advanced Rotor Systems", AGARD-LS-139, 1985
35. Ormiston, R.A. and Hodges, D.H., "Linear Flap-Lag Dynamics on Hingeless Helicopter Rotor in Hover", Journal of the American Helicopter Society, Vol. 17, No. 2, 1972
36. Huber, H.B., "Effect of Torsion-Flap-Lag Coupling on Hingeless Rotor Stability", American Helicopter Society 29th Annual National Forum, Washington, May 1973
37. Jang, J. and Chopra, I., "Ground and Air Resonance of an Advanced Bearingless Rotor in Hover", Journal of the American Helicopter Society, Vol. 33, NO. 3, July 1988
38. Hausmann, G. and Gergely, P., "Approximate Methods for Thermoviscoelastic Characterization and Analysis of Elastomeric Lead-Lag Dampers", Eighteenth European Rotorcraft Forum, Avignon, 1992
39. Schimke, D., Enenkl, B. and Allramseder E., "MBB BO108 Helicopter Ground and Flight Test Evaluation", Fifteenth European Rotorcraft Forum, Amsterdam, Sept. 1989
40. Hanagud, S., Babu, G.L.N., Won, C.C. and Obal, M.B., "Smart Structures for Helicopters", Sixteenth European Rotorcraft Forum, Glasgow, September 1990
41. Chen, P.C., Samak, D.K. and Chopra, I., "Development of an Intelligent Rotor", Fourth Workshop on Dynamics and Aeroelastic Stability Modeling of Rotorcraft Systems", University of Maryland, Washington, November 1991
42. Ormiston, R.A., "Can Smart Materials Make Helicopters Better?", Fourth Workshop on Dynamics and Aeroelastic Stability Modeling of Rotorcraft Systems", University of Maryland, Washington, November 1991




Alfred Gessow Rotorcraft Center
UNIVERSITY OF MARYLAND



**Alfred Gessow Rotorcraft Center:
Past, Present and Future**

Inderjit Chopra
*Director Alfred Gessow Rotorcraft Center &
Alfred Gessow Professor of Aerospace Engineering*

Presentation At: Korea Aerospace Research Institute (KARI), Daejeon
June 27-30, 2011




Agenda

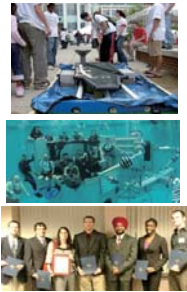
- Monday June 27**
Introduction: Alfred Gessow Rotorcraft Center
Dynamics: Introduction to Hover & Forward Flight, Flap Dynamics
- Tuesday June 28**
Dynamics: Flap-Lag-Torsion, Unsteady Aerodynamics
MAV Challenges & Opportunities
- Wednesday June 29**
Dynamics: Aeroelastic Stability in Hover, Ground/Air Resonance
CFD Applications
- Thursday June 30**
Dynamics: Bearingless Rotor, Vibration
Review Aeromechanics
- Friday July 1: Visit to SNU & Review Cyclocopter Work**

**Department of Aerospace
Engineering**
in
A. James Clark School of Engineering
University of Maryland



Undergraduate Program

- 19 Faculty members
- 337 undergraduates
- Average SAT score 1316
- 16% female
- 92 BS degrees in 2009
- **Ranked 6th by US News and World Report**



Graduate Program

- Graduate students 170
- MS Students 78
- PhD Students 92
- Female Grad students 29
- Minority Grad students 13
- Non-US Citizens 54
- 69 MS awarded in 2009
- 19 PhD awarded in 2009
- **Ranked 9th by US News and World Report**




**Department of Aerospace Engineering
Vital Statistics 2009-10**

- **8 Major Research Program (Lead)**
VLRCEO: Army/Navy/NASA (2011-16) Vertical Lift Research Center of Excellence
MURI: ONR (2006-11): Galfenol Smart Material Actuators
MURI: AFOSR (2008-13): Helicopter Brownout
CTA-MAST: ARL (2008-18): Micromechanics Center
NAVAIR: Rotorcraft & Propulsion + Education: (2009-14)
CUIP: Constellation University Institute Program; (2002-cont)
Space: Institute for Dexterous Space Robotics
Neuro-Bio Program: AFOSR (2009-14): Flying Insect Performance
- **Major Research Programs (Support Role)**
MURI: AFOSR (2007-12) Flapping MAV
MURI: ONR (2010-15) Micro Biological Systems
- **Research Grants FY09:**
Total number of grants 84
Total research expenses \$17.3M

Alfred Gessow Rotorcraft Center

Mission of Rotorcraft Center

To advance rotorcraft technology through:

- Provide an exciting and effective educational environment to train the next generation rotorcraft engineers
- Carry out inter-disciplinary, multi-disciplinary basic research in rotorcraft
 - Timely solution of technical barrier problems
 - Introduce innovative and disruptive technologies
- Speedily transfer technology to industry and government laboratories



Alfred Gessow Rotorcraft Center Vital Statistics 2010

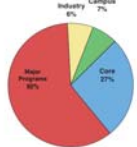
• Faculty: Rotorcraft	9	
• Faculty: Non-Rotorcraft	5	
• Research Scientists/ Visiting Prof.	4	
• Graduate Students	50	
• M.S. Degrees awarded	10	
• Ph. D. Degrees awarded	5	
• Presentations at Conferences	80	
• AHS (28), SDM (10), SPIE(12), Other (30)	16	
• 2008 AHS Forum		
• Journal Publications: Published	40	
• Accepted	49	
• 2011 Vertical Flight Scholarships	10	

Rotorcraft Tech Base

Core Rotorcraft funding from Navy, NASA, NRTC \$2M/year

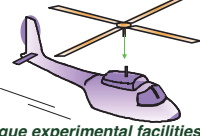
Other Major Programs:
 Army-MURI: MAV
 Army-CTA: MAST
 Airforce-MURI: Brownout \$4.5M/year
 Industry: \$0.4M/year

9 Faculty
50+ Graduate Students
40 Undergraduate Students
 (AHS Student Chapter, Elective Research projects)

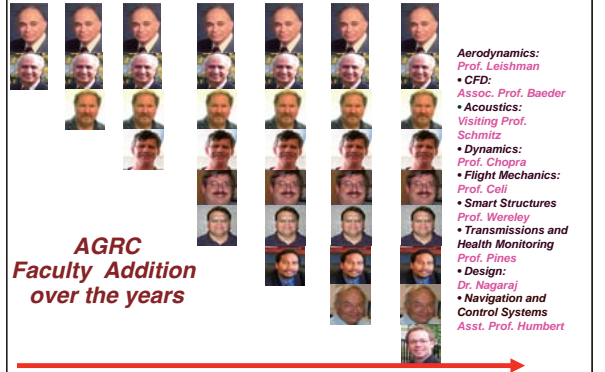


Significant Support from Campus: Fellowships, Travel budget, Fabrication, etc \$0.5M/year

Alfred Gessow Rotorcraft Center Overall Accomplishments

• M.S. Degrees awarded	200+	Established in 1982 by Army as one of three Rotorcraft Centers of Excellence; Competitive renewal every 5 years; Program ended in June 2006
• Ph.D. Degrees awarded	100+	
• Presentations at Conferences (All) AHS Forum	800+ / 200+	
• Journal Publications (All) AHS Journal	500+ / 130	
• VFF Scholarships (last 5 years)	45	
• Significant technology transfer		
• Developed specialized graduate courses & unique experimental facilities		
• Graduates employed by Army Labs, Industry, NASA, Navy, FAA, Academia and Army-Uniform		

AGRC Faculty Addition over the years



Aerodynamics: Prof. Leishman
CFD: Assoc. Prof. Baeder
Acoustics: Visiting Prof. Schmitz
Dynamics: Prof. Chopra
Flight Mechanics: Prof. Celli
Smart Structures: Prof. Woreley
Transmissions and Health Monitoring: Prof. Pines
Design: Dr. Nagaraj
Navigation and Control Systems: Asst. Prof. Humbert

1982 1985 1987 1993 1995 1999 2005 2007 2008

Rotorcraft Courses

Graduate:

- Rotorcraft Aerodynamics 1 & 2 (Leishman)
- Rotorcraft Dynamics (Chopra)
- Rotorcraft Stability and Control (Celi)
- Rotorcraft Design (Chopra, Nagaraj, Tishchenko)
- CFD 1 & 2 (Baeder)
- Composite Structures (Wereley)
- Engineering Optimization (Celi)
- Smart Structures (Chopra)
- Rotorcraft Aeroacoustics (Schmitz)
- Advanced Structural Dynamics (Pines, Hubbard)
- Multi-Body Dynamics (Celi)

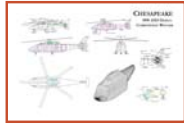
Undergraduate:

- Rotorcraft Analysis (Baeder)





UM Winning Designs (98-02)







UM Winning Designs (03-07)







UM Winning Designs (08-09)



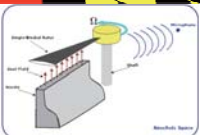

Rotorcraft Experimental Facilities








Rotorcraft Experimental Facilities



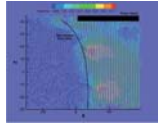





Rotorcraft Experimental Facilities



Open-Jet Wind Tunnel



PIV System for flow studies



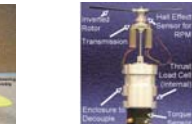
MAV System



Autonomous Lab



Insect-Motion-Based Flapping-Wing Apparatus



MAV Hover Test Rig

Alfred Gessow Rotorcraft Center Research Programs

I. Core Aeromechanics (RCOE: 1982-2006, VLRCOE 2011-16)

- Aerodynamics
- Dynamics
- Flight Dynamics and Control
- CFD
- Acoustics
- Transmission and Drive Trains
- Smart and Composite Structures
- Advanced Designs including Heavy Lift Rotorcraft

II. Army: MURI: Micro Hovering Air Vehicles (2004-10)

III. MAST CTA: Center for Microsystem Mechanics (2008-18)

IV. Airforce: MURI: Brownout of Rotorcraft (2008-13)

V. Smart Structures Programs (URI, 2 MURI, DARPA)

- Army: URI(92-97), MURI (96-01) Smart Structures Applications
- DARPA Gallenol Compact Actuator Development (2003-05)
- Navy-MURI on Gallenol actuators (06-11)

VI. ONR: Heavy Lift Rotorcraft Aeromechanics (2010-12)

VII. NASA: 5 NRAs (2007-11): Rotorcraft Aeromechanics

VIII. NAVAIR: (2008-13): Rotorcraft Aeromechanics

IX. Other Programs (NRTC, Sikorsky, Boeing, etc):

- Boeing: Active Rotor, Morphing Rotor
- NRTC: CFD Applications, High Performance actuators, Crashworthy seat
- Sikorsky/UTRC: Composite Rotor, Swashplateless rotor, etc.

10-Ft Diameter Vacuum Chamber



Notable Technical Capabilities

- State-of-Art Experimental facilities:**
Glenn L. Martin wind tunnel (6.5-ftx11-ft), 2 rotor rigs, 10-ft diameter vacuum chamber, hover tower, State-of-art PIV system, anechoic hover chamber, model fabrication facility, modern composite lab, extensive smart structures labs and growing MAV facilities
- Extensive set of specialized up-to-date rotorcraft courses
- Breadth and depth of core rotorcraft programs:
Expanded activities in MAV, brownout and CFD
- Extensive micro air vehicles research program (MAST-CTA & MURI)
- Opportunity-driven faculty and team-work
- High caliber graduate students (Largest number of Veriflite scholarships, 40% of total awards during past 10 years)
- Alfred Gessow Rotorcraft Chair & Scholarships
- Significant campus support:
 - Extensive labs
 - Co-location of grad students

Alfred Gessow Rotorcraft Center: Major Accomplishments & Technology Transfer

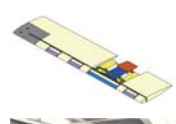
- Provided trained talented graduate students to industry and government laboratories
- Provided comprehensive aeromechanics analysis and design tools to industry and laboratories
UMARC, Free-wake and unsteady models, TURNS CFD
- Provided strategic leadership in rotorcraft technologies:
 - Bearingless rotor aeromechanics
 - Composite rotor technology
 - Advanced CFD methodology
 - Smart Structures technology
 - UAV and MAV technologies
 - Rotor wakes and unsteady aerodynamics
 - Vibration prediction & active control methodologies



Smart Structures Activities at Maryland



6-ft dia Froude scale rotor model in Glenn Martin Wind tunnel: active twist with embedded piezoelectric elements



6-ft dia Mach scale rotor model in Glenn Martin Wind tunnel: trailing edge flaps actuated with multi-layered piezobimorphs



6-ft dia Mach scale rotor model on hover tower: tip actuated with embedded piezos in conjunctions with bending-torsion composite couplings



6-ft dia Mach scale rotor model on hover tower: tip actuated with embedded piezos in conjunctions with bending-torsion composite couplings

Example: Technology Transfer

Smart Structures Technology



Smart Actuator Development:
Piezostacks with L-L Amplification



Smart Rotor Development:
Mach-Scale with Piezo Actuated Flap

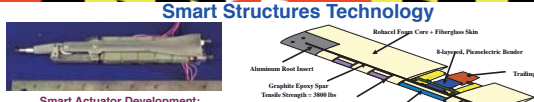


Diagram labels: Reinforced Edge Core + Fiberglass Skin, Kevlar[®] Piezoelectric Bender, Trailing-Edge Flap, Aluminum Root Insert, Graphite Epoxy Spar (Tensile Strength >300 lbs), Rib Cage, LE edge wings for non-hubbing



Boeing: Full-Scale Smart Rotor Development: MD-900 Rotor with Smart Flaps, Successfully tested in 40x80-ft wind tunnel in April 2008, Demonstrated 90% reduction in vibration and acoustic signatures



Smart Rotor Test in Glenn Martin Tunnel Mach-Scale with Smart Flaps

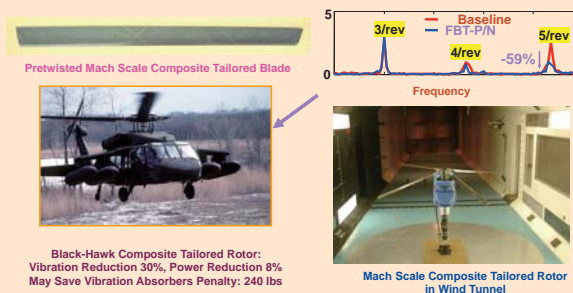
Technology Transfer

- Upgraded comprehensive rotorcraft code UMARC provided to industry, federal laboratories and academia.
- Boeing-Mesa: Helped them in their development of full-scale smart rotor system with flap actuated with piezostacks (Friedrich Straub).
- Unsteady aerodynamic analysis codes (Leishman) provided to industry and federal labs, inserted in many comprehensive codes.
- Free wake codes provided to industry, federal labs and academia, inserted in many comprehensive codes.
- Army-Ames: Assessment of active vibration control from perspective of flight mechanics (Mark Tischler)
- NREL: Helped them in identification of aerodynamic issue focused to windmills (Bir).
- Lord Corp.: Development & characterization of MR dampers (Mark Jolly).
- Sikorsky: Helped them in the assessment of composite couplings to control vibratory load and improve performance (Andy Bernhard)
- Army Science Board: Heavy Lift Cargo Rotorcraft design studies
- DARPA: Technology assessment of heavy lift systems (Don Woodbury)
- Progeny/Army: Helped them in the development of RotorChute (Murphy)

Technology Transfer

- Bell: Quadrotor performance and download studies (Bob Moullins)
- CSA: Helped them in the development of compact hybrid actuator (Eric Anderson)
- Baldwin: Helped in the design and aeromechanics issues related to mono-tiltrotor (Baldwin)
- FAA: Wire strike assessment of civil helicopters (Dy Le)
- Kaman: Helped them in the development of tab actuated flaps for primary controls (Mike Bielefeld)
- Army Picatinny Arsenal: Development of MR recoil dampers (Mike Mattice)
- Army-ARDEC: Helped them in the development of active/passive hybrid APPN smart actuator gun-fuselage vibration isolation and precision control
- Navy David Taylor Carderock: Helping them in their initiative on "Rotor Head Fault Detection" called JAHUM (David Haas).
- NASA-Ames: provided assessment for an all electric helicopter (Bill Warmbrodt)
- Army Science Board: Carried out heavy lift cargo rotorcraft design studies

Composite Rotor Technology



Pretwisted Mach Scale Composite Tailored Blade

Black-Hawk Composite Tailored Rotor:
Vibration Reduction 30%, Power Reduction 8%
May Save Vibration Absorbers Penalty: 240 lbs

Mach Scale Composite Tailored Rotor in Wind Tunnel

Black Hawk Loads Prediction: Technology Barrier Problem

Black Hawk Airloads at High Speed



Lift 92% R lbs/ft

25 deg Phase error

Flight 8534

UMARC lifting-line (dashed green line) vs UMARC/TURNS coupling (solid red line)

Comprehensive analysis + CFD

- Lift Phase error resolved
- Vibratory air loads resolved
- Transonic pitching moments captured

Unresolved Issues:

- High thrust condition (stall)
- Maneuvering flights

Vibratory Lift 92% R

Pitching Mom. 96.5% R

Accomplishments: Technology Barrier Problems (00-11)

- Rotor loads prediction: Resolving phase issue for predicted vs measured loads (Collaboration with NASA, Army & Industry)
- Composite rotor blade modeling: adequate coupled beam modeling, comprehensive aeromechanics analysis and unique vacuum chamber and wind tunnel test data
- Active vibration control (HHC & IBC) coupling with flight control stability (issue with hingeless and bearingless rotors)
- Power minimization with 2/rev active pitch input: expect nominal gain less than 5%
- Smart rotor development: smart actuator stroke limitation and innovative amplification
- Rotor wakes: resolving vortex core issue and its interaction, precise model under steady flight condition
- Rotor wakes in maneuvering flight: Time domain non-steady model and resolving off-axes response issues
- Unsteady aerodynamics of flapping rotor
- CFD couplings with comprehensive aeroelastic analyses: issue of moment coupling
- HUMS for transmissions & drive-trains: Robust ID schemes to overcome false alarms
- Comprehensive aeromechanics analyses for advanced rotor systems: bearingless (multiple load paths), tiltrotor, circulation-control, trailing-flap and smart rotor
- Flight stability and acoustics analysis in maneuvering flight

RCOE Accomplishments: Technology Barrier Problems

Damperless Rotor



Past: Hydraulic Dampers Articulated Rotors, Heavy



Present: Elastomeric Dampers Hingeless & Bearingless, Expensive



Future: ER/MR Fluid Dampers Composite Couplings and IBC Flaps active damping, Cheap and reliable

Swashplateless Rotor



Past: Swashplate with pitchlinks, Drag penalty plus maintenance cost



Present: Servo-Flap Rotor, SH-2, Mach-Scale Black-Hawk Model test in wind tunnel



Future: Smart flaps using hybrid actuators for primary controls.

Major Accomplishments over past 28 years Research

Comprehensive Analysis UMARC

Composite Rotor Analysis and Development

Bearingless Rotor Analysis

Smart Rotor Development

Free Wake Modeling

CFD/CSD Blackhawk Loads Prediction

Free Wake Models
Bagai-Leishman (Relaxation)
Bhagwat-Leishman (Time-marching)
Shreyas-Leishman (Vortex filament)

Alfred Gessow Rotorcraft Center National & International Impact

- **Publications in Archival Journals and Presentation at Helicopter Conferences: Especially AHS**
- **Graduates: Extremely successful in academia, industry and federal laboratories, For example at recent American Helicopter Society Annual Forum, every fourth paper was from or had roots in Maryland.**
- **Significant technology transfer to industry and government via publications and presentations, trained graduates and comprehensive codes and cooperative arrangements.**

Major Accomplishments over past 28 years Education

Comprehensive Graduate Curriculum

Quality of graduate students
- Placement & success
- Largest number of Vertiflite Scholars
- 7 received AHS Bagnoud Awards
- 4 became Technical Fellows of AHS
- 800+ Conference papers
- 200+ AHS Forum papers
- 500+ Journal papers
- 130 AHS Journal papers
- 19 took academic appointments
- Many now in high level positions

Balanced research: between theory and experiment

AGRC: Graduates in Rotorcraft Industry

Sikorsky

- David Matuska (MS, 83)
- John Bate (MS 86)
- Chris Van Buten (BS 86)
- Mark Scott (MS 88)
- Mike Torok (PhD 89)
- James Wang (PhD 91)
- Ashish Bagai (PhD 95)
- Vinit Suhasrabudhe (PhD 97)
- Alan Coyne (MS 97)
- Cliff Smith (PhD 99)
- Andy Bernhard (PhD 00)
- Dan Griffin (MS 01)
- Mat Tarascio (MS 01)
- Jinsong Bao (PhD 04)
- Robin Preator (MS 04)
- Ben Hein (MS 05)
- Eric Parsons (MS 05)
- Michael Brigley (MS 06)
- Jayant Sirohi (PhD 01)
- Lin Leo (PhD 03)

Boeing

- Brahamananda Panda (PhD 85)
- Hieu Ngo (MS 87)
- Alan Stemple (PhD 89)
- Antonio Llanos (MS 89)
- Dan Newman (MS 89)
- Steven Ingle (MS 90)
- Curtis Waiz (MS 94)
- M. Daghir (MS 94)
- Joseph Orso (MS 94)
- Josh Ellison (MS 04)
- Justin Kearns (MS 05)
- Dan Clingman (MS 06)
- Lynn Gravatt (MS 06)
- Patrick Downey (PhD 08)

Bell

- Brian Schweissow (MS 85)
- Bob Idol (BS 85)
- D. K. Samak (MS 87)
- David Platz (MS 94)
- Melanie Hurt (MS 96)
- J. S. Park (MS 03)
- Chehab Mustafa (MS 03)
- Taeoh Lee (PhD 99)
- Marc Gervais (PhD 04)

AGRC: Graduates in NASA/Army/Navy

Ames: NASA/Army

- Bimal Aponso (MS 83)
- Joon Lim (PhD 88)
- Hyonsoo Yeo (PhD 99)
- Theodore Colin (PhD 00)
- Mahindra Bhagwat (PhD 01)
- Preston Martin (PhD 01)
- Randy Cheng (PhD 01)
- Anubhav Datta (PhD 04)
- Mani Ramasami (PhD 05)
- Carlo Malpica (PhD 08)

Navy: David Taylor/Pax River

- David Haas (PhD 89)
- Neipei Bi (PhD 91)
- Judah Milgram (Ph 97)
- Mark Kammeyer (MS 86)
- John Vorwald (MS 86)
- Randy Barber (MS 86)
- Steve Wunder (MS 88)
- William Pogue (MS 89)
- Chris Bruner (MS 89)
- Joe Leifner (MS 89)
- Darryl Lenhardt (MS 89)
- Nancy Mueller (MS 89)
- Steve Dirlik (MS 90)
- Jody Smith (MS 92)
- Andy Baker (MS 95)
- Divyang Shukla (MS 00)
- William Facey (MS 03)
- Youngjoon Kim (MS 04)
- Daniel Everson (MS 05)
- Eric Silberg (MS 06)
- Kristi Kleinhesselink (MS 07)
- Sean Roark (MS 07)

Langley: Army

- Mark Nixon (PhD 93)
- Kevin Noonan (MS 85)
- Junwei Shen (PhD 03)
- Jayana Sitaraman (PhD 03)
- Beatrice Roget (PhD 04)
- Ugrina Sandra (PhD 06)
- Terry Ghee (MS 90)
- Eric Greenwood (MS 08)
- Rajneesh Singh (PhD 98)

UM Graduates in Academics: Faculty

- Ed Smith (PhD 92) Professor Penn State
- Farhan Gandhi (PhD 95) Professor, Penn State
- Nikhil Koratkar (PhD 00) Professor, RPI
- Chang-Ho Hong (PhD 85) Professor Choong-Nam University
- James Milke (PhD 91) Professor, University of Maryland
- Yong Hyup Kim (PhD 89) Professor, Seoul National University
- Gil Crouse (PhD 92) Associate Professor, Auburn University
- Ranjan Ganguli (PhD 94) Professor, IISc Bangalore
- Anne Spence (PhD 94) Assistant Professor, UMBC
- David Flemming (PhD 95) Professor, Florida Institute of Tech
- Yang Mao (PhD 02) Associate Professor, Northwest University, China
- Z. Xie (PhD 03) Associate Professor, Northwest University, China
- Karthik Duraisamy (PhD 05) Lecturer, Glasgow University
- Jayant Sirohi (PhD 01) Asst. Professor, University of Texas at Austin
- Beatrice Roget (PhD 03) Asst. Professor, Wyoming University
- Jaina Sitaraman (PhD 02) Asst. Professor, Wyoming University
- Atul Atulsimha (PhD 06) Asst. Professor, Virginia Commonwealth University
- Gang Wang (PhD, 02) Asst. Professor, University of Huntsville

Alfred Gessow Rotorcraft Center Important Honors & Awards

- **Chaired Professorships:** Alfred Gessow Professor (Chopra), Minta-Martin Professor (Leishman), Farvardin Professor (Pines), Techno-Sciences Professor (Wereley)
- **AHS Hon Fellow:** Gessow (81), Chopra(98); **AHS Fellows:** Schmitz(93), Chopra (96), Leishman (07)
- **AHS Alexander Nikolsky Honorary Lectureship:** Gessow (85), Schmitz (08)
- **AIAA Fellows:** Gessow (82), Chopra (91), Schmitz (04), Pines (10)
- **Royal Aero Soc Fellow:** Leishman (05); **ASME Fellow:** Chopra (03), Wereley (08), Flatau (07), Pines (09)
- **AIAA SDM Award:** Chopra(02)
- **AHS Alexander Klein Award:** Life-time Achievement Award in rotorcraft: Gessow(96), Chopra (09)
- **ASME Adaptive Structure and Material Systems Prize:** Chopra (01)
- **SPIE Life-Time Achievement Award:** Chopra (04), Flatau (10)
- **Francois Xavier Bagnoud Vertical Flight Award:** In recognition of outstanding contributions to rotorcraft by a young engineer: Smith (94), Torok (96), Gandhi (98), Bernhard (99), Koratkar (04), Sohasrabudhe (05), Datta (06)
- **Grover E. Bell Award:** Given for outstanding research contributions to AGRC: 1992, 2002
- **ARO Young Investigator Awards (Smith, Wereley, Koratkar)**
- **NSF Young Investigator Awards (Pines, Wereley, Elkins, Koratkar)**
- **Other Important Lectureships:** Pilcher Memorial Lectureship & Medal (02), von Karman Lectureship (04), Cierva Memorial Lectureship (05), AGARD Lectureship (91), Blasplinghoff-Mar-Plan (93), Paul Hamke Lectureship (04), Henry Kelley Lecture (03), Roy Aero Aus(01), AIAA SDM Lecture (03), ASME Adaptive Structures Lecture (2001)
- **Editor-in-Chief:** AHS Journal, Leishman (2004-07)
- **Editor:** Journal Intelligent Materials Systems & Structures (JIMSS): Wereley
- **Associate Editors:** JIMSS (Chopra, Pines, Flatau), Smart Mat & Struc (Chopra, Pines, Wereley), J. of Aircraft (Chopra), AHS Journal (Chopra, Vizzini, Celi, Nagaraj)
- **AHS Lichten Award:** Bernhard (96), Gervais (01)
- **AHS Student Design Competition:** Graduate Category First Place for 9 years (1999-2005, 08), 2nd Place (2006-07, 09)
- **AJ Clark School of Engineering Faculty Outstanding Research Award:** Chopra (2002)

Some RCOE Graduates in Key Positions: Industry, Government and Academia

- COL Keith Robinson, PM, Armed Scout Helicopter
- Dr. Mike Torok, Vice President & Chief Engineer CH-53K, Sikorsky
- Dr. James Wang, Vice President Research & Development, Agusta-Westland
- COL(RET) Andy Dull, Manager Lockheed Martin
- Dr. Mark Nixon, Director U.S. Army Research Laboratory Vehicle Technology Directorate
- Dr. Ed Smith, Professor, and Director Rotorcraft Center of Excellence at Penn State
- Dr. Jeanette Epps, NASA Astronaut
- Dr. & Col (Ret) Shmuel Fiedel, Senior Vice President Maintenance & Engineering, El Al Israel Airline
- Dr. Jinseok Jang, Principal Researcher & Head of Rotorcraft Program, Agency for Defense Development, Korea
- Ms Kelly McCool, Chief Engineer VH-71 (Presidential Helicopter) Program
- Col (Ret) Lazar Alon President & CEO Elbit Systems
- Mr. Chris Van Bulten, Technical Fellow & Director of Technology & Innovation, Sikorsky
- Mr. Simal Aponso, Chief NASA Aerospace Simulation Operations Branch
- Mr. Philippe Benquet, Program & Key Account Director, Thales Avionics, France
- Mr. David Matuska, Manager Engineering System Safety, Sikorsky
- Mr. Mark Scott, Chief Design Group, Sikorsky
- Dr. Andy Bernhard, Chief Engineer SAS, Sikorsky
- Ms. Megan McCluer, Program Manager Wind & Hydropower Technology, DOE
- Dr. David Haas, Head Surface Aviation Group, David Taylor, Navy
- Mr. Dan Newman, Program Manager DARPA, Formerly Head Design Office, Boeing
- Dr. Farhan Gandhi, Professor Penn State
- Dr. Bernd G. van der Wall, Head Simulation in Wind tunnel, DLR
- Mr. Carl Ockler, Head of Civil Flight Test, Eurocopter, Germany
- Mr. Mat Tarascio, Specialist Business Development/Strategic Planning, Sikorsky
- Dr. Chang-Ho Hong, Professor and Department Head Aerospace Engineering, Chooong-Nam National University
- Dr. Nikhil Koratkar, Professor Aerospace Engineering, RPI
- Dr. Srinivas Turam, Manager, Elbit, Mechanical, Business Helicopters

Notable Graduates

2007 Academy of Distinguished Alumni



2008 AHS Hon. & Technical Fellows



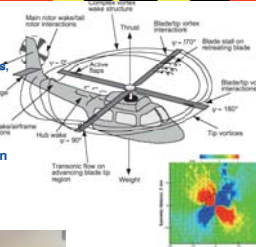
1982 1985 1987 1993 1995 1999 2005 2007

Graduate Students of Alfred Gessow Center National & International Impact

 Director of Penn State Rotorcraft Center of Excellence: Ed Smith	 Director Vehicle Technology Army/ARL Aberdeen: Mark Nixon	 Vice President Sikorsky Aircraft Co. Mike Torok
 Program Director, Thales Avionics: Philippe Benquet	 Senior VP Engineering El Al Col. Ret Fiedel Shamuel	 Head of Korea Rotorcraft Program: Jinseok Jang
 Vice President S&T James Wang	 PM Armed Scout, AMCOM Col. Keith Robinson	 NASA Astronaut Jeanette Epps

Rotorcraft Aeromechanics: Future Directions

- **Expand & nurture core multidisciplinary aeromechanics programs:**
 - Maintain balance between theory & experiment
 - Tackle barrier problems systematically such as maneuvering flight aeromechanics, variable speed rotors, robust HUMS, swashplateless rotors, etc.
- **High efficiency mission-adaptive morphing rotor**
- **Expand micro air vehicle program**
 - Revolutionary concepts in gusty environment
- **Brownout/whiteout: Understanding and mitigation**
- **Exploit advanced CFD methodology to develop next-generation rotorcraft**
- **All electric/hybrid rotorcraft: green aviation**







Alfred Gessow Rotorcraft Center
University of Maryland at College Park

Emerging CFD as a Viable Tool to Predict Vibratory Loads in a Helicopter



Inderjit Chopra
Alfred Gessow Professor and Director
chopra@umd.edu

Presentation At: Korea Aerospace Research Institute (KARI), Daejeon
June 27-30, 2011

Outline

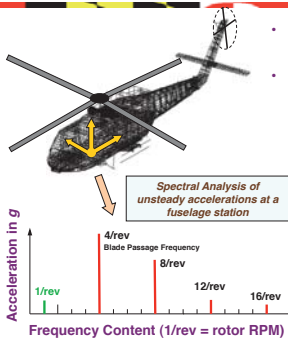
- **Introduction: Vibration**
 - Barrier Issues
- **Identification Critical Flight Conditions**
 - High speed
 - Low speed transition
 - High altitude dynamic stall
 - Severe pull-up maneuver
- **Systematic Vibration Solution using CFD**
- **Other CFD Activities and Future Work**

Swashplateless Rotor with Integrated Flaps



MR RPM : 375 rpm
Empty Weight: 1100 kg
Fuel Weight: 150 kg
Payload: 500 kg
MTOW 1750 kg

Helicopter Vibration: Definition



- Unsteady accelerations at a station in airframe
- Intrusion Index: weighted mean of 4 largest frequencies in vertical, lateral and longitudinal directions up to 60 Hz
- Source of vibration: Rotor Blades are excited at all harmonics, only harmonics consisting integer multiples of blade number, pN_b/rev are filtered through hub
- 1/rev due to rotor asymmetry

Rotor Dynamics in Forward Flight

Mach = 0.57 compressibility

produce 0, 4, 8, ... /rev

High Angle Dynamic stall

Blades respond in flap, lag, torsion, extension 0, 1, 2, 3, 4, 5, ... /rev

Sources of Vibration

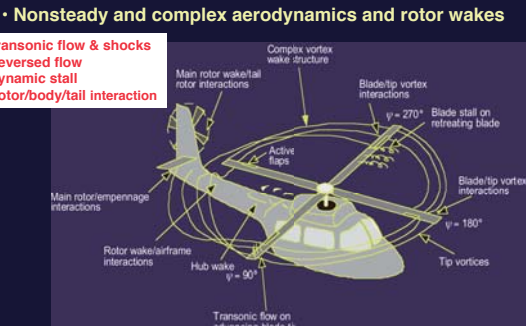
- Asymmetric flow in forward flight
- Complex wake
- Compressibility on advancing side and dynamic stall on retreating side
- Flexible rotor blades

- Blade undergoing moderately large deformations involving coupled flap, Lag, torsion and axial motion, nonlinear inertial couplings
- Airframe 3-D structure with complex joints and cutouts, Gyroscopic nonlinear couplings in vehicle dynamics

Aerodynamics: Challenges

• Nonsteady and complex aerodynamics and rotor wakes

Transonic flow & shocks
Reversed flow
Dynamic stall
Rotor/body/tail interaction



Rotor Wakes: Challenges

Main rotor wake interactions with fuselage, empennage, tail-rotor

Blade Tip Vortices: High induced velocities

Blade/Vortex Interactions: Rotor loads, Performance & Acoustics

Vortex/Vortex Interactions: Highly three-dimensional induced flow-field

Structural Layout

Structural Layout

- Nano-composite Erosion Protection Tape
- Graphite Composite Skin
- Nomex Honeycomb Core
- Steel Shim
- High Frequency De-icing Actuator
- Tungsten Nose Mass
- Uni-directional S-glass D-spar

Airframe Assembly

Airframe Assembly

- Tail Rotor Gear Box and Overhaul Actuator
- Supercritical Tail Rotor Blade
- Monocoque Composite Tail Boom
- Integration Subhood for Easy Removability
- Active Vibration Isolation Seats
- Rigid Booms
- Transmission and Engine Deck
- More: Lowered Barrel Cocks for Improved Access and Safety
- Energy Absorbing Bend Moment Composite Coupler
- Now: Shaped for the Earth Flying
- Greenability Landing Gear with Low Drag Fairing
- Lightweight, Greenability A/L Primary Subhoods

Lift Variation in Low Speed Transition Flight UH-60A

40 knots, $\mu = 0.110$;
16,500 lbs; $C_w/\sigma = 0.080$

Lift, lbs / ft

Azimuth

Radius

Helicopter Vibration vs. Forward Speed

Measured Vibration at pilot floor UH-60A 16,500 lbs

Intrusion Index

Advance Ratio Speed μ

Low-Speed 40 kts

High-Speed 155 kts

ADS-27

UTTAS / AAH

ADS-27 : Revised Aeronautical Design Standard set by the U.S. Army, 1986

UTTAS/AAH : Original design standard of 0.05g which none of the helicopters could meet

- Excessive vibration: Discomfort, reduced life (cost), degraded performance
- 90% of vibration at low speed and high speed from main rotor loads
- Non-rotor sources : transmission, tail rotor, engine, external systems

Analysis Methods : Blade Structural Model

Blade Modeled as elastic 1-D beam undergoing flap bending, lag bending, elastic twist and axial deformation

Blade Model

- Linear flap-lag-torsion dynamics for small deformations (Houbolt and Brooks 1958, Ormiston 1972)
- Nonlinear equations for moderate deformations (Hodges/Dowell 1974, Hodges/Ormiston/Peters 1980, Friedmann/Rosen 1978, Johnson 1977, Kvaternik 1976)
- Anisotropic, composite rotor with cross-sectional warping and transverse shear (Hodges 1990, Smith/Chopra 1993, Bauchau 1998)
- Advanced geometry rotors with sweep and droop (Celli/Friedmann 1992, Benquet/Chopra 1989, Ganguli/Chopra, 1992)

Spatial discretization

- Lumped parameter methods, transfer matrix, Myklestad (Murthy 1986, Sangha 1990)
- Finite element approach (Straub/Friedmann 1980, Chopra/Sivaneri 1982)
- Modal reduction vs. full finite element
- Topology independent multi-body formulations (Johnson 1998, Saberi 2004, Bauchau 1993, Ghiringhelli/Masarati 1999) large deformations

Analysis Methods : Unsteady Aerodynamic Modeling

- Classical inviscid, incompressible, thin airfoil theories (Theodorsen, Wagner)
- Semi-empirical indicial models
 - attached flow (Beddoes 1984, Leishman 1988)
 - separated flow (Beddoes 1983)
 - dynamic stall (Leishman/Beddoes 1989)
 - effect of sweep on dynamic stall (Leishman 1989)
 - Boeing dynamic stall model (Gormont 1970)
 - Johnson dynamic stall model (Johnson 1970)
 - ONERA EDLIN dynamic stall model (Petot 1990)
 - ONERA BH dynamic stall model (Truong 1998)
- Detailed CFD models (Euler, Full Potential, Navier-Stokes)

Analysis Methods: Wake Geometry Calculation

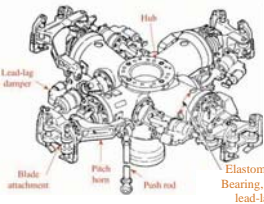
Prescribed geometry	Free Geometry	Free, time accurate
<ul style="list-style-type: none"> Prescribed wake (Piziali/DuWaldt 1962) Refined by experimental induced velocities (Landgrebe 1969) to improve hover performance Kocurek/Berkovitz 1982 Refined for forward flight, (Landgrebe/Egolf 1983, Beddoes 1985) 	<ul style="list-style-type: none"> Relaxation model (Scully 1975) General free wake method (Johnson 1995) Pseudo-implicit predictor-corrector (Bagai/Leishman 1995) Multiple trailer method (Johnson 2002) Constant vorticity contour method (Wachspress 2003) Multiple rotors, multiple trailers, dual peak, dissimilar blades (Bagai/Leishman 1996, Johnson 1988) 	<ul style="list-style-type: none"> Hover (Crimi 1965, Scully 1967) instability Clark/Leiper 1970 (enforced periodicity), forward flight (Landgrebe 1969, Sadler 1971) Vortex lattice model (Egolf 1988), Baron/Baffadossi 1993 Jain 1998, Chung 2000 studied hover instability Bhagwat/Leishman 2003 for hover, steady and maneuvering flight, explained hover instabilities



Analysis Methods: Trim, Response and Loads

- Trim models**
Free flight propulsive trim - solve for 3 rotor controls, 2 fuselage attitudes, tail rotor collective with 3 force/3 moment equations
- Rotor Response Calculation (periodic in level flight)**
 - Harmonic balance (Johnson 1980) : CAMRAD, RCAS
 - Floquet theory (Dugundji/Wendell 1983)
 - Finite element in time (Panda/Chopra 1987) : UMARC
 - Numerical integration : Lockheed REXOR, Bell C81, Sikorsky DYMORE
- Blade Loads Calculation**
 - Deflection or curvature or modal method
 - Force summation method superior in case of spatial discontinuity, rigid members, concentrated loads
 - Mixed formulation

Analysis Methods : Coupled Rotor-Fuselage Vibration

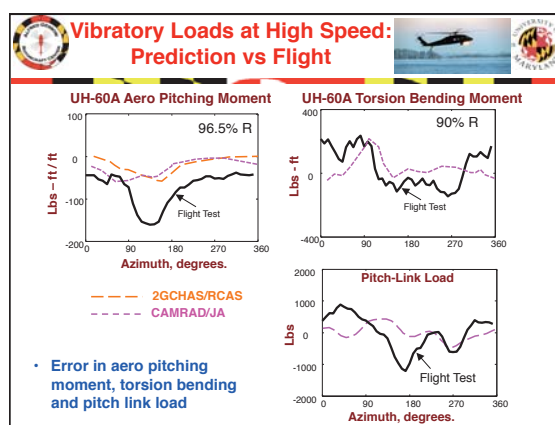
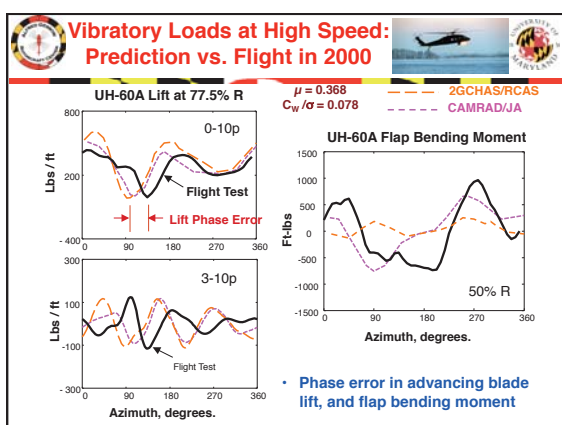
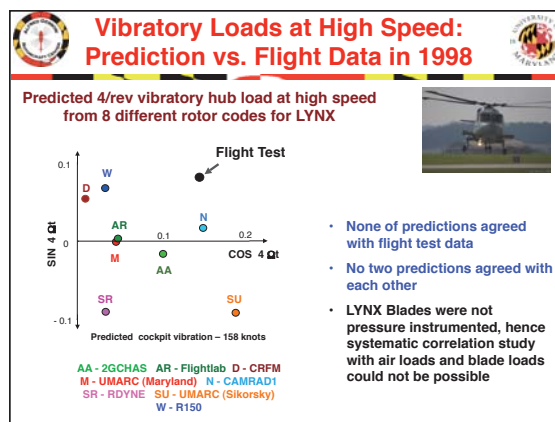
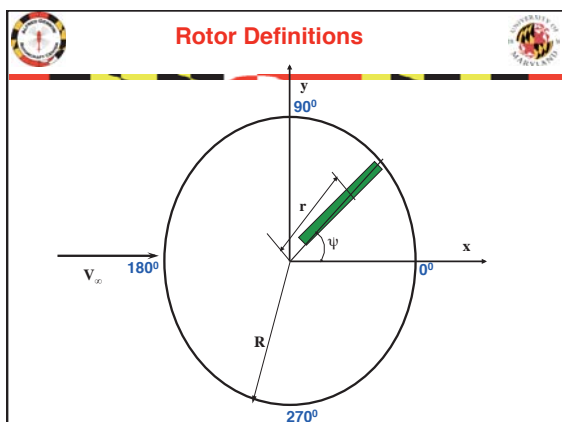



- Rotor vibratory hub harmonics (4/rev, 8/rev, etc) transmitted to elastic airframe
- Say 1P = 300 RPM or 6 Hz, 4P=24 Hz
- Airframe 20 modes less than 25 Hz, requires detailed modeling of airframe including joints, cutouts and secondary structures

Analysis Methods : Rotor Codes vs. Comprehensive Analyses

Specialized Rotor Codes	Comprehensive Codes
<ul style="list-style-type: none"> Greater details, accuracy and scope to model some physical mechanisms while simplifying most other interactions RotorCRAFT to CHARM – detailed free wake, rotor-fuselage aerodynamic interaction KTRAN-RDYNE-GENHEL – structural dynamics and flight dynamics DYMORE II – multibody rotor-fuselage dynamic model R150 and Westland/DERA C81 and COPTER R85/METAR 	<ul style="list-style-type: none"> Includes all basis components to handle multidisciplinary loads, vibration and stability, Can perform trim, transient and flutter interaction CAMRAD family UMARC family 2GCHAS to RCAS free wake model unsteady aero, stall model flexible blade dynamics free flight trim airframe dynamics advanced geometry blades composite, modern rotors 3D CFD loose coupling

Vibration Prediction: Barriers



"... we have not made any significant progress in the last 30 years in the accuracy of our prediction methods."
Bousman, 8th ARO Workshop 1999

"...we do not understand the basics : is this discrepancy from the structural or aerodynamic modeling (especially wake) or both ?"
Lim, 1st UH-60A Airloads Workshop 2001

Prediction of Vibration

Vibration Validation Study

Major undertaking in 2001: Team involving industry, academia, NASA/ Army to resolve vibration barrier issues. Loads Workshop: Meet every 6 months since 2001

Vehicle: UH-60A Black Hawk, extensive flight test data with pressure instrumented blades

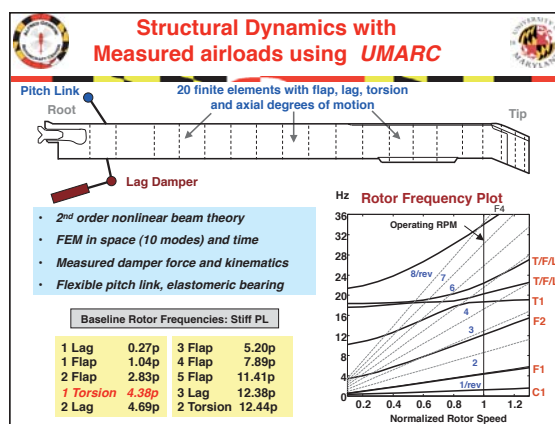
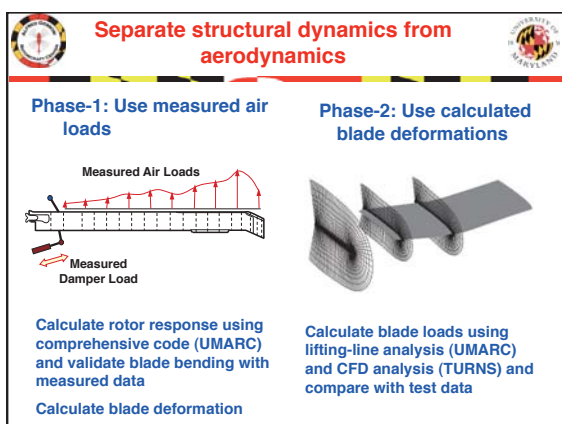
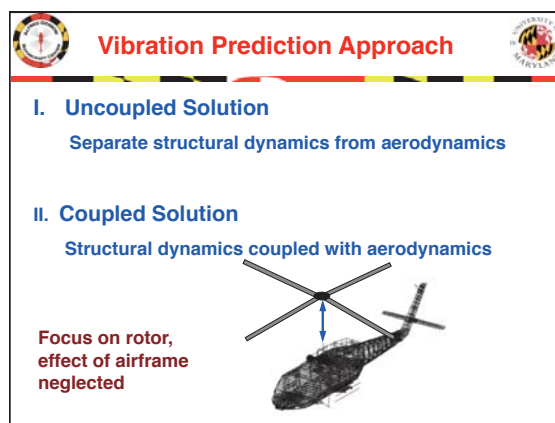
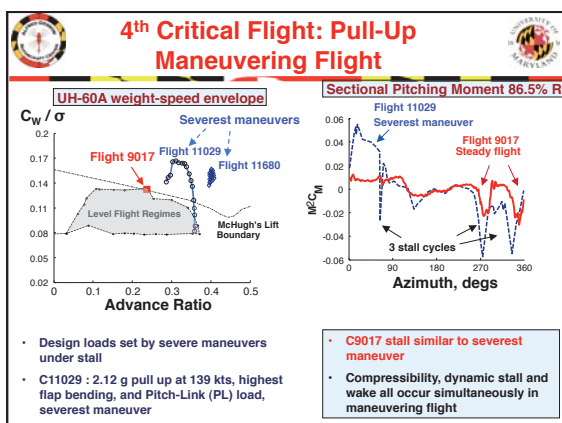
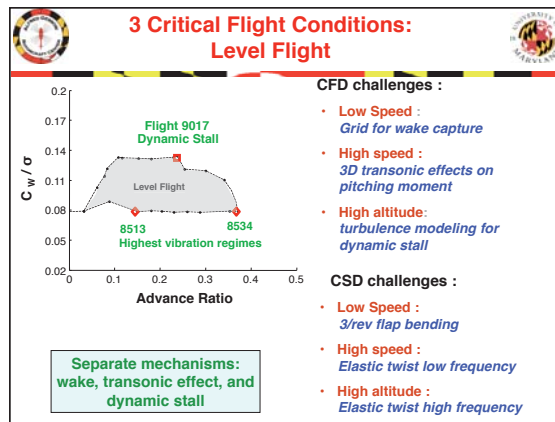
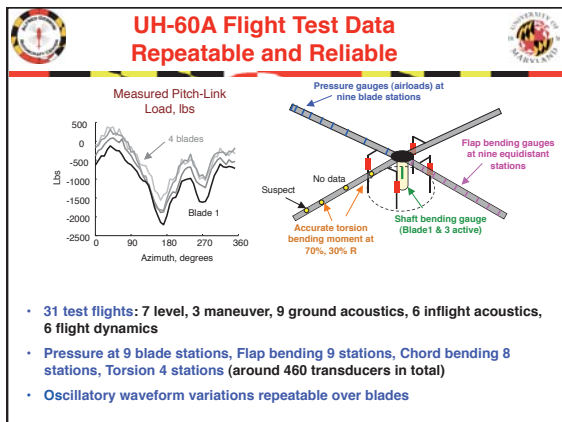
Identified 4 critical flight conditions:

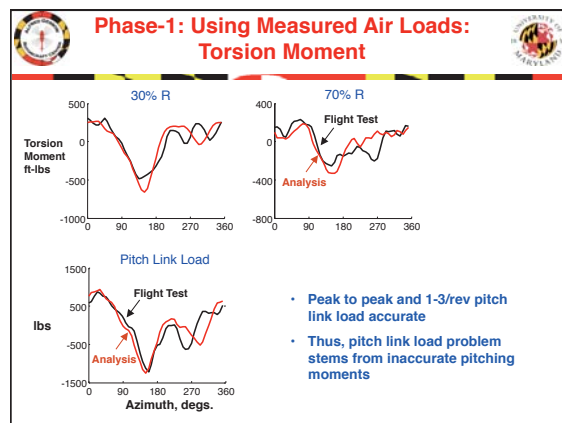
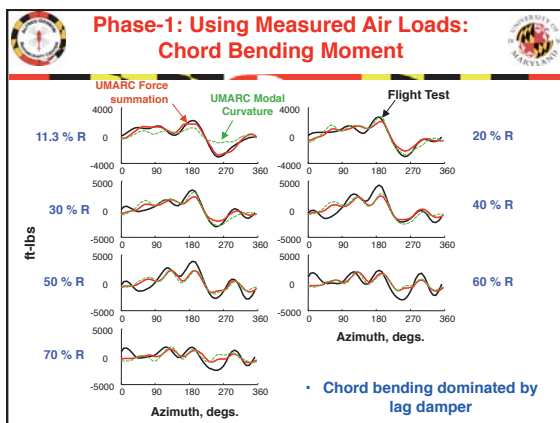
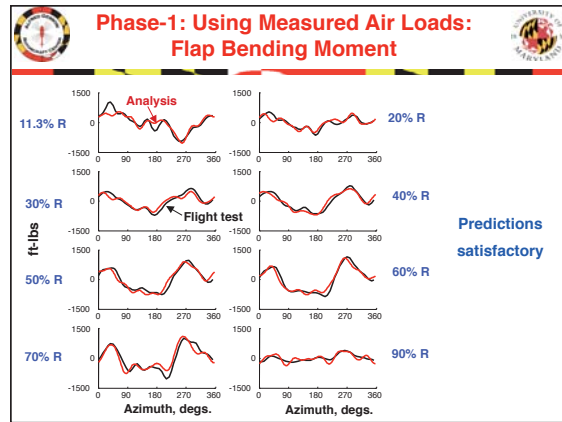
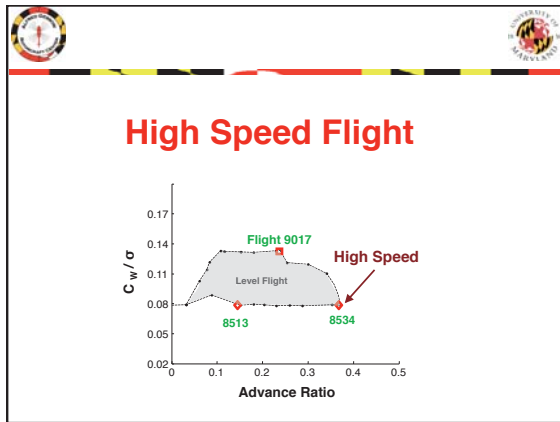
Level Flight:

1. High speed $\mu = 0.37$ UH-60A flight 8534
2. Low speed transition $\mu = 0.15$ UH-60A flight 8513
3. High altitude dynamic stall $\mu = 0.24$ UH-60A flight 9017

Maneuver:

4. Severe pull-up Maneuver $\mu = 0.341$ UH-60A flight 11029 (load factor = 2.09)



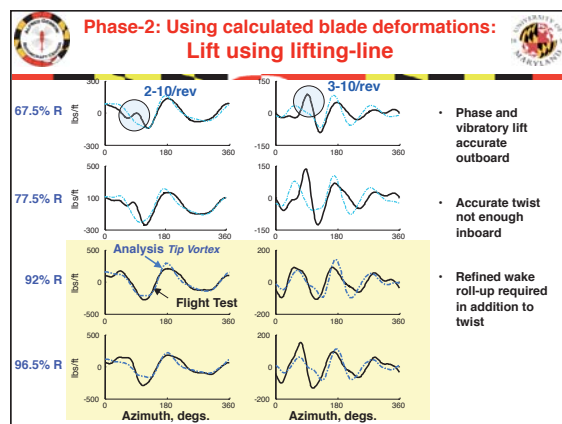


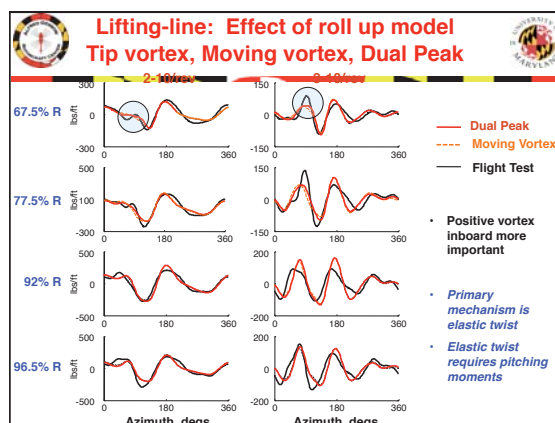
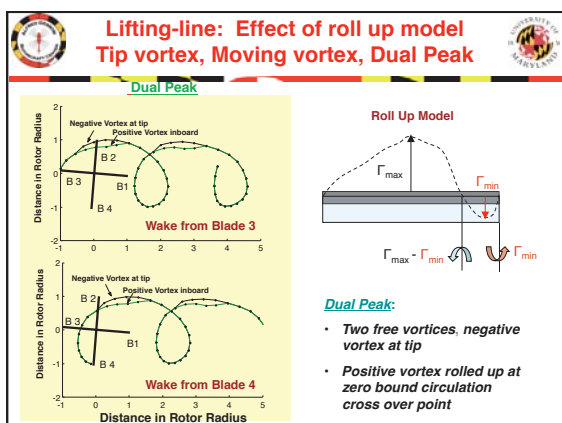
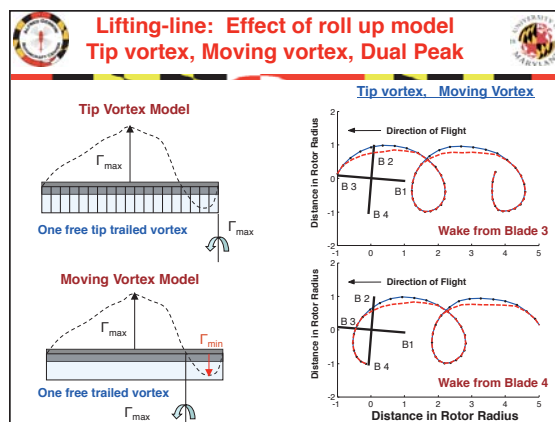
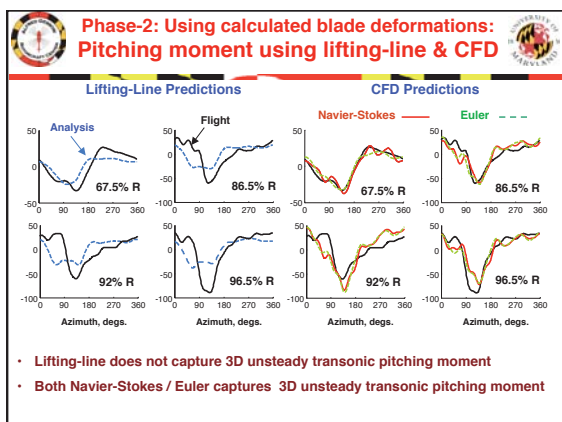
Phase-2: Using calculated deformations: Blade aero loads

UMARC (University of Maryland Advanced Rotorcraft Code)

- Lifting line model
- Bagai-Leishman free wake fully rolled up, 5 degs., 4 turns single, moving, dual, full-span, root vortex, inboard trailers, vortex lattice
- Leishman-Beddoes unsteady model attached, separated, dynamic stall extracted for SC1095, SC1095 R8
- 2D test airfoil tables
- Weissinger-L based nonlinear near wake

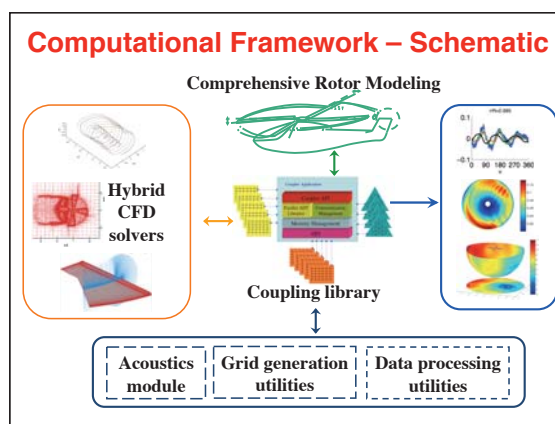
SC1095, SC1095 R8, SC1095

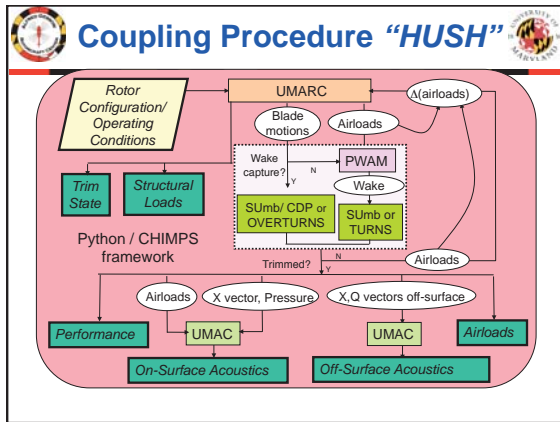




II. Coupled Solution

CFD Methodology





Wake-coupling vs. Wake-capturing

- Two strategies for predicting rotor far wake geometry and induced velocities
- Wake Coupling**
 - Stand-alone Lagrangian free-wake model (PWAM) coupled to CFD using field velocity approach
 - CFD solves only the near-body flow-field
 - Captures near wake evolution
 - Single blade sufficient for steady flight
- Wake capturing**
 - Wake calculated using CFD. Solve both near-body and off-body flow-field
 - Captures wake sheet evolution and roll-up from first principle
 - Grid resolution critical in preserving vorticity
 - Computational intensive

UMTURNS & OVERTURNS

- UMTURNS (wake coupling)**
 - Near-body solution using a C-O mesh
 - Single blade only
 - Wake effects included using field-velocity approach
 - Roe's flux differencing with MUSCL-type limiter
 - Second-order stencil for viscous terms
 - Baldwin-Lomax and Spalart-Allmaras turbulence models
- OVERTURNS (wake capture)**
 - C-O mesh used for near-body solution
 - Models all blades
 - Wake-capturing using overset meshes
 - Cylindrical background meshes
 - Essentially an overset version of UMTURN

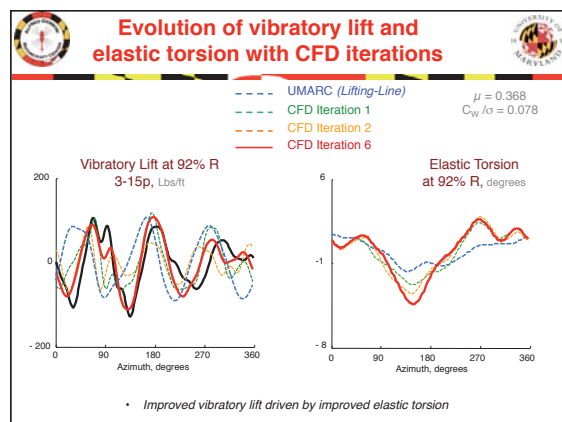
CFD-CSD Coupling

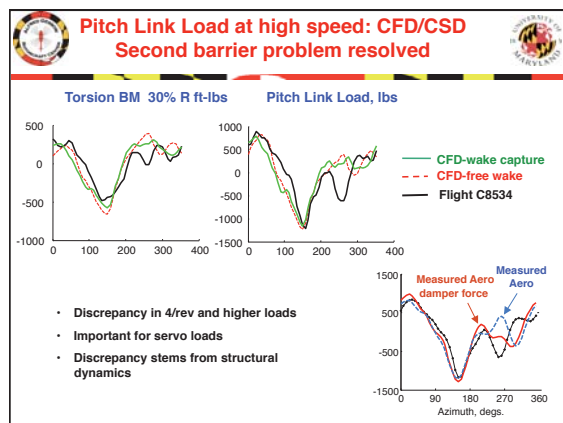
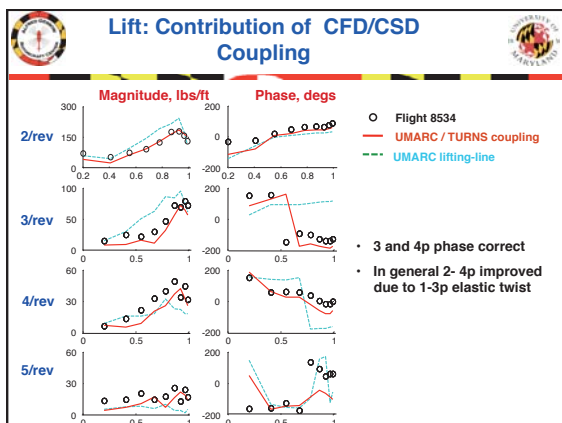
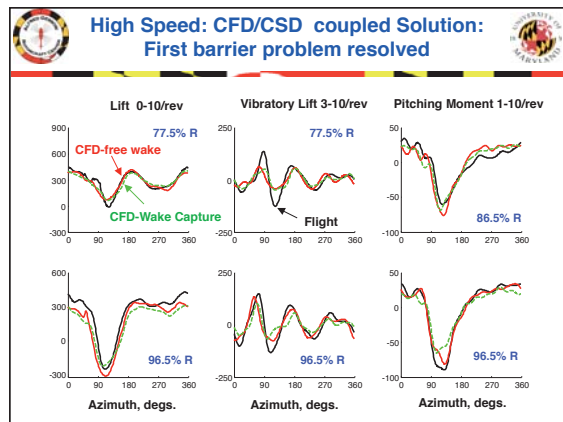
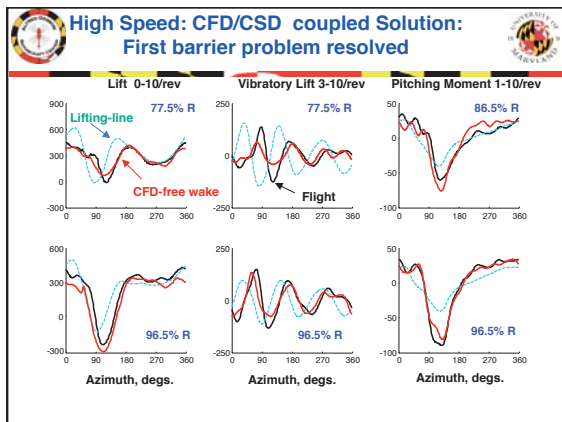
- Tight coupling**
 - Exchange data at every timestep/sub-iteration
 - Computationally intensive
- Loose coupling**
 - Exchange data every rotor revolution
 - Delta airloads methodology
 - Determine trim solution within comprehensive analysis
 - Iterate until trim convergence

Details of CFD analysis

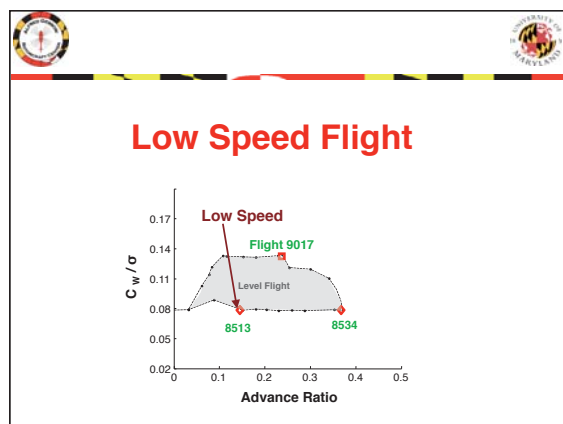
Grid spacing:

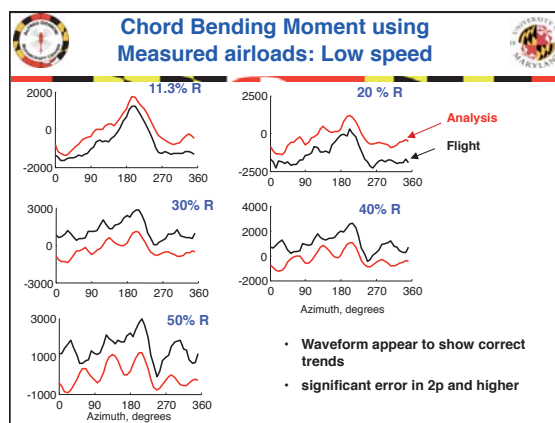
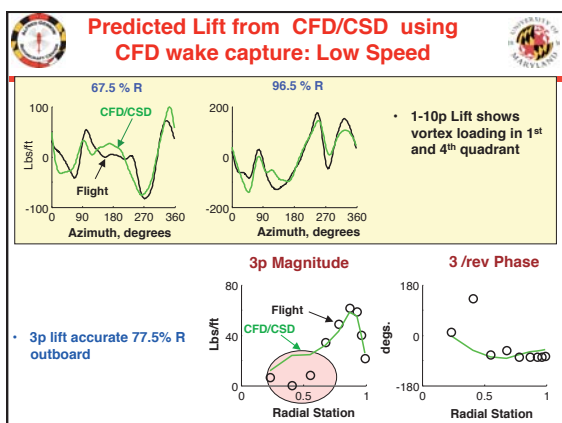
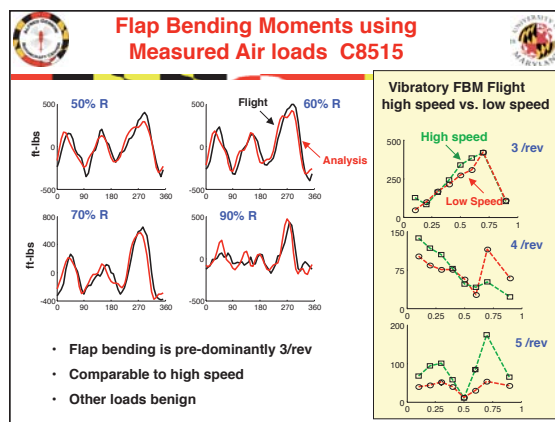
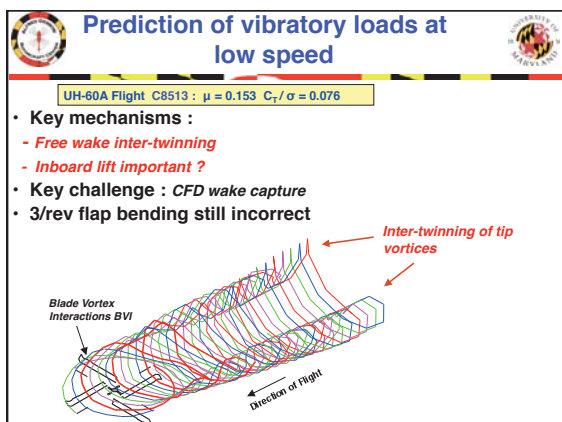
- Partial CFD: 133-43-43 (total 0.25M) coarse grid
- Full CFD: 133-125-48 (0.8 M) + background grid 2.2 M (total 3M)
- high speed airloads – grid independent
- low speed – Practically independent; refinement necessary to see grid dependency is beyond today's capability (BVI)
- Stall airloads – sensitive to grid spacing
- Power predictions – profile power (airfoil drag) sensitive to grid





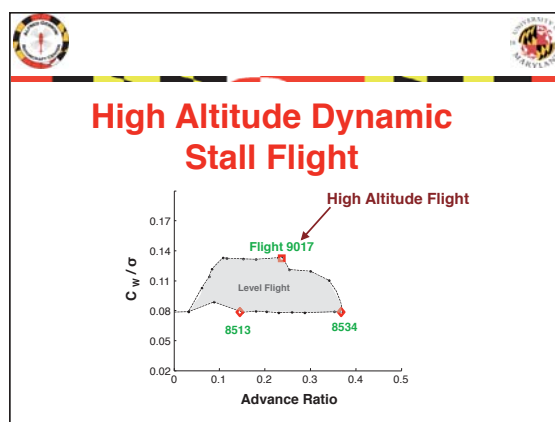
- ### Loads in High Speed Flight: Conclusions
- Key barrier problems resolved
 - Physics of vibratory lift in place: phase problem resolved
 - Peak-to-peak pitch link load captured
 - Outstanding Issues
 - 4p and higher pitch link load less satisfactory: *structure*
 - Phase error of 7-10 degree in flap bending: *aerodynamic*





Loads in Low Speed Transition : Summary

- Vibratory air-loads can be captured by CFD, but only slightly changed from lifting line results
- 0.05c background grid adequate
- artificial dissipation of tip vortices does not prevent capturing 3-5/rev air loads
- Key Technical Barrier :
 - 3/rev flap bending moment still wrong



Fundamental Understanding and Prediction of Dynamic Stall Loads

UH-60A Flight C9017 : $\mu = 0.237$ $C_T / \sigma = 0.129$

- Key barriers :
 - 2 retreating blade stall cycles
 - 3-5/rev pitch link load
- Key mechanisms : Trim stall and Twist stall
- Key challenge : CFD turbulence model

Dynamic Stall Flight 9017

High pitch link servo, and blade root loads

2 cycles in retreating side

- 3 - 5/rev torsion loads excite swashplate servo
- Peak flap bending and pitch link load important for design
- Trim, torsion response, and turbulence important for prediction

Flap Bending Moments: CFD/CSD vs. Measured airloads

CFD/CSD Prediction

Measured airloads

20% R

50% R

70% R

Coupled

Uncoupled

Torsion Moments and Pitch Link Load: CFD/CSD

Torsion Moment 1-10p

Pitch Link Load

30% R

50% R

70% R

Spallart-Allmaras

Balwin-Lomax

Flight

CFD/CSD

Lbs

Azimuth, degrees

Harmonic Number

Predicted Pitching Moment and Stall Map: CFD/CSD

Pitching Moment

86.5% R

Azimuth, degrees

180

90

0

270

Measured boundaries of Separated flow

Flight MS

Analysis MS

Flight LS

Analysis LS

Spallart-Allmaras

Balwin-Lomax

- 2nd stall cycle mostly 2D
- 1st cycle is 3D; stall vortex moving across span

Physical Mechanism of the two Stall Cycles: Trim and Twist

Angle of Attack study at 86.5% R

Contribution of elastic twist

Effect of twist harmonics

degrees

Azimuth, degrees

Net angle of attack

Rigid pitch angle

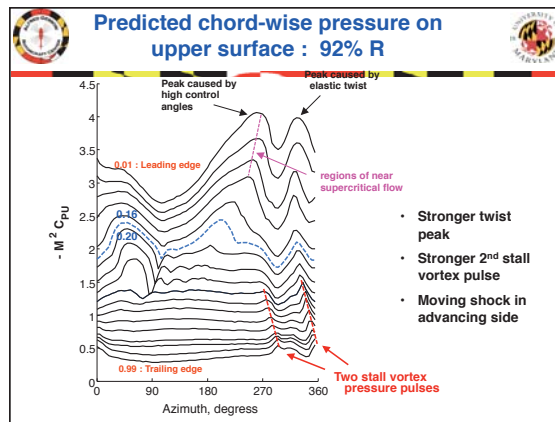
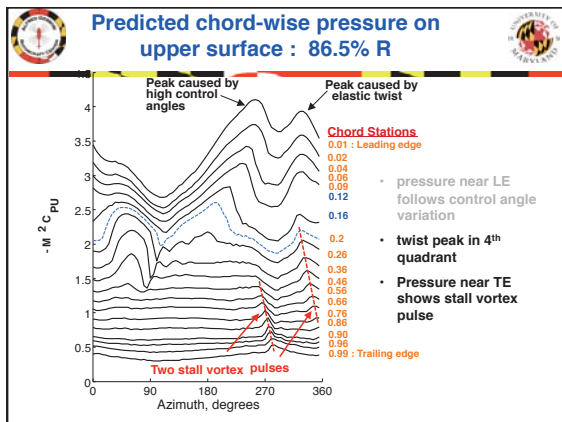
Elastic twist

total

0-3p

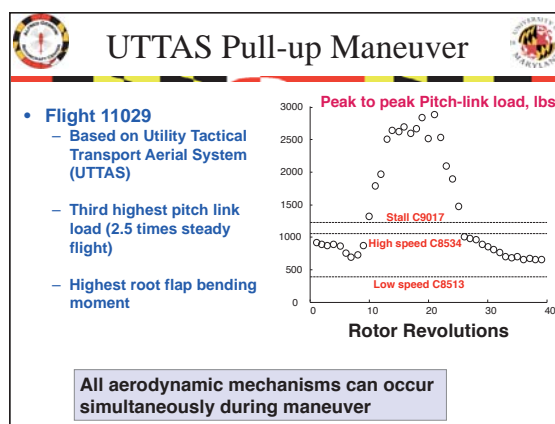
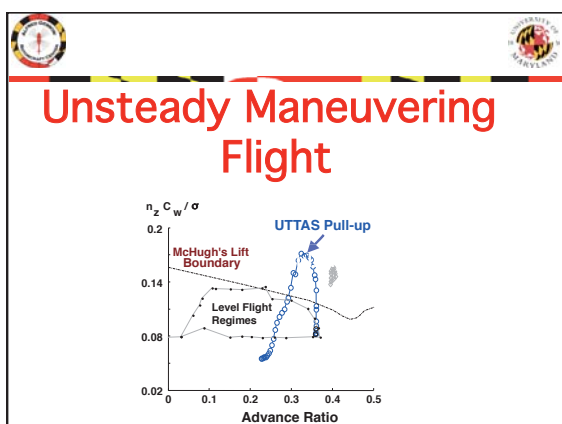
0-2p

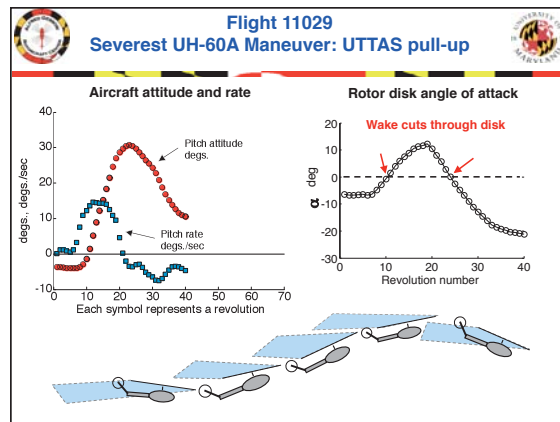
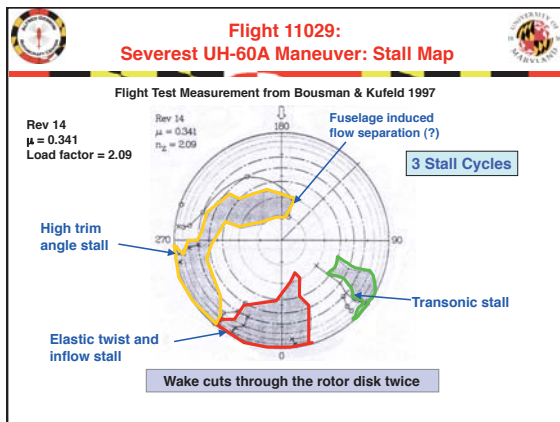
- Rise in 3rd quadrant due to high trim angles: 1st cycle is a trim stall
- 4th quadrant excitation due to 4 and 5p twist: 2nd cycle triggered by twist



- ### Loads in Dynamic Stall Flight : Summary
- Mechanism of retreating blade stall understood
 - 1st cycle due to high trim angles
 - 1st cycle excites 4 and 5p twist (torsion freq 4.38p)
 - 4 and 5p twist sets location of 2nd stall cycle
 - Inflow important
 - CFD turbulence model important
 - Stall near tip 96.5% R not captured
 - Peak to peak blade loads satisfactory
 - 4p and higher pitch link load unsatisfactory : *struct problem*
 - Important for servo loads

- ### Level Flight: Key Conclusions: CFD/CSD Coupling
- CFD provides **fundamental capability** at high speed – 3D unsteady transonic pitching moments
 - CFD provides **improved capability** at low speed and stall
 - no semi-empirical wake roll up or stall models
 - key for *calculating* loads on new rotor designs
 - Structural loads not significantly improved as air loads
 - 4p and higher torsion unsatisfactory – *struct. Problem*
 - 4p and higher chord bending unsatisfactory – *struct. Problem*





Multibody Analysis

- **Structural dynamics model**
 - Full finite element large frame (multibody) analysis capable of modeling large deformations

Pitch Link

- **Aerodynamics model: N_b bladed transient model**
 - Unsteady lifting surface including roll and pitch rates
 - Weissinger-L type lifting surface model iteratively coupled to 2D airfoil tables
 - Dynamic Stall (Leishman-Beddoes)
 - Transient Freewake (Ananthan-Leishman)

Large Deformation Analysis

Large deformations can be modeled:

Approach 1: Geometrically exact beam theory

Approach 2: Second order non-linear beam theory coupled to multibody formulation

Approach 2: (Followed)

- Additional frame attached to individual elements
- Elements undergo only moderate deformation
- Rigid body motions accommodated by finite rotation of frames

Swashplate Model

Direction of flight

$\psi = 270^\circ$

$\psi = 180^\circ$

$\psi = 90^\circ$

$\psi = 0^\circ$

Aft Lateral Forward

Pitch-link

Lateral Servo

Forward Servo

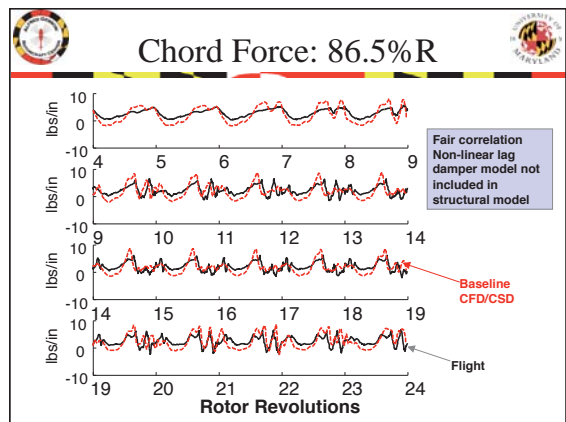
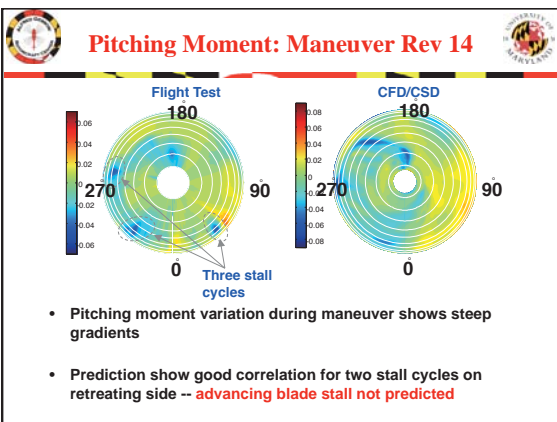
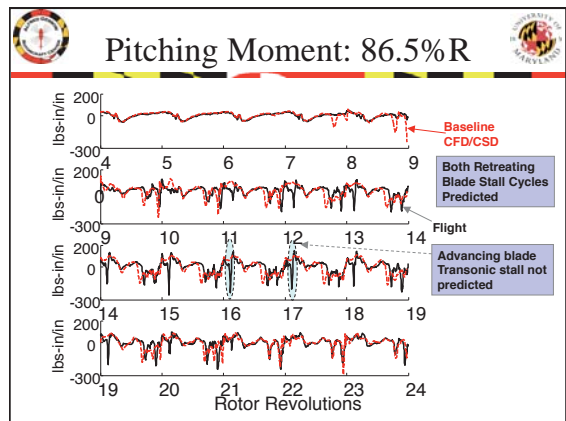
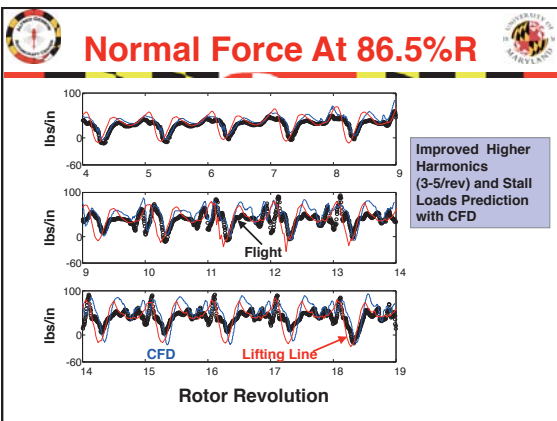
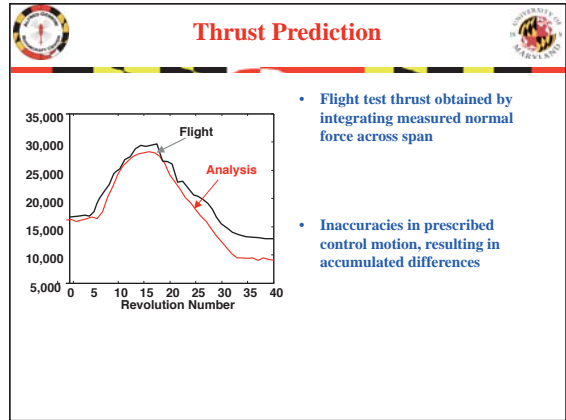
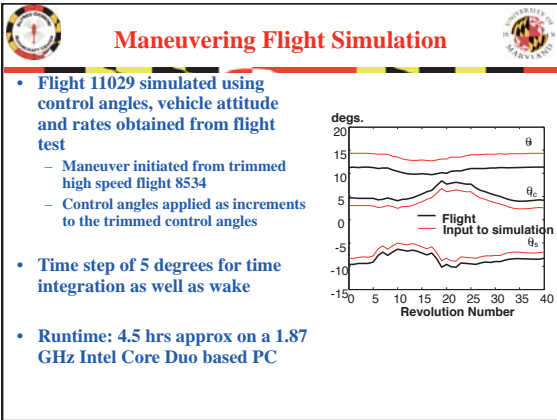
Aft Servo

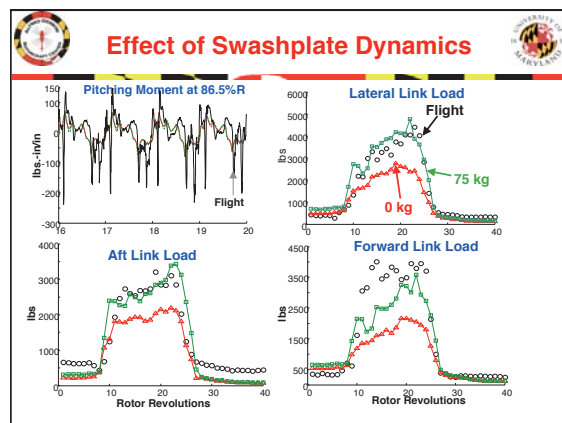
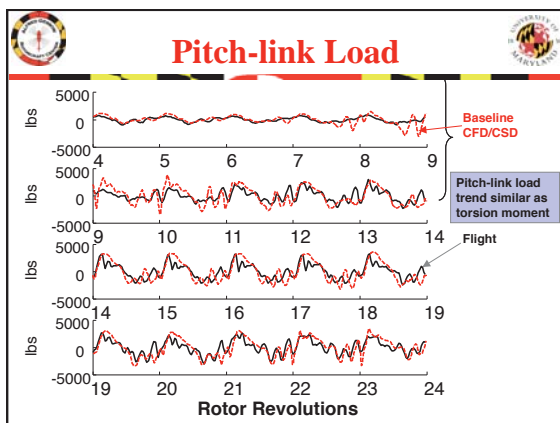
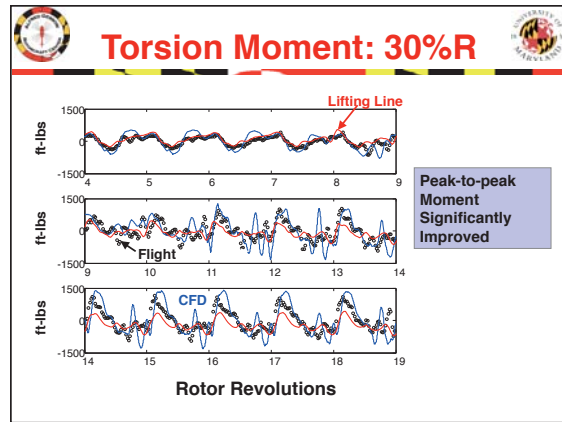
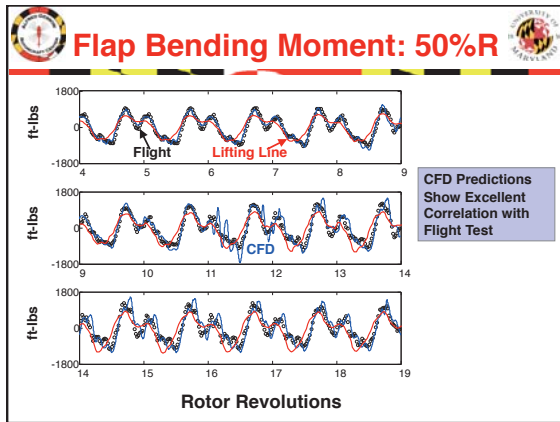
Swashplate

- 4-bladed full FEM multibody model, 20 finite elements for each blade
- Pitch link stiffness (1090 ft-lbs)
- Elastomeric bearing: flap/lag damper : 100 ft-lb/rad/s
- 3 dof Swashplate model
 - Heave (z), pitch (α), and roll (α_r)
 - Swashplate idealized as rigid disk
 - Servos modeled as linear spring-damper system

Fluid Structure Coupling

- **Inputs to aerodynamic model**
 - Blade deformations for all blades
 - Instantaneous advance ratio, shaft tilt angle, rotor pitch and roll angles, angular rates and the control angles
- **Output: instantaneous air-loads and inflow velocities**
- **Tight coupling: structure, aerodynamic, and free wake model exchange information at every time step**
 - Similar to CFD/CSD serial staggered tight coupling without sub iterations
 - Transfer of information via subroutine calls





Conclusions

- Pull-up maneuver studied is a stall dominated flight.
 - Two distinct stall cycles predicted on retreating side
- Predicted peak-to-peak torsion moment and pitch-link load show trend similar to test data.
 - Peak-to-peak magnitude under-predicted
- Servo loads predicted satisfactorily
- Average thrust prediction showed trend similar to test data.

Other CFD Applications in Rotorcraft

- Generation of 2-D airfoil data tables (c_L , c_D , c_M) for current and future airfoils
- Performance evaluation of new rotor configurations:
 - Coaxial rotors
 - Washplateless system with trailing-flaps
- Stall Alleviation with leading-edge slats
- Micro air vehicle systems (low Reynolds aerodynamics)
 - rotor based system
 - Avian-based flapping
 - Insect-based flapping
- Mission adaptive morphing rotor
- Parallelization of CFD methodology



Acknowledgements



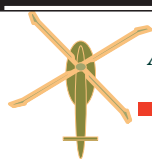
PhD Students:
Anubahv Datta (Ames)
Jaina Sitaraman (NIA)
Shreyas Ananthan (UM)
Beatrice Roget (NIA)
A.Abhishek (Grad)
Jaye Falls (Grad)
Ben Silbaug (Grad)
Brandon Bush (Grad)
L. Lakshminarayanan
(Grad)

Faculty Colleagues
Jim Baeder (Key CFD Person)
Gordon Leishman

Sponsors:
Army/NRTC
NASA/NRA
Navy/ONR
Sikorsky/UTRC

Collaborators: Stanford
Juan Alanso

Alfred Gessow Rotorcraft Center
UNIVERSITY OF MARYLAND



Hovering Micro Air Vehicles: Challenges & Opportunities

Inderjit Chopra
Alfred Gessow Professor &
Director Alfred Gessow Rotorcraft Center
(chopra@eng.umd.edu)

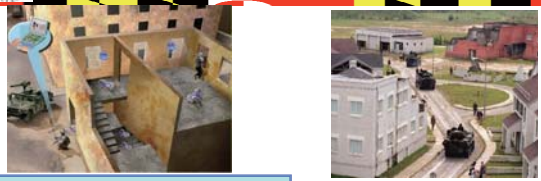
Presentation At: Korea Aerospace Research Institute (KARI), Daejeon
June 27-30, 2011

Micro Air Vehicles: Definition

- Design Requirements**
 - No dimension exceeds 15 cm (6 inch)
 - Gross takeoff weight 100 grams
 - Loiter time of 60 minutes
 - Payload capacity of at least 20 grams
- Additional considerations**
 - Fully autonomous (out of sight operations)
 - All weather operations
 - Low production cost
 - Rapid deployment
 - Low detection



Future Vision of Microsystems



Scenario 1: Small unit building search
Challenges: hover and low speed, medium endurance, quiescent airflow

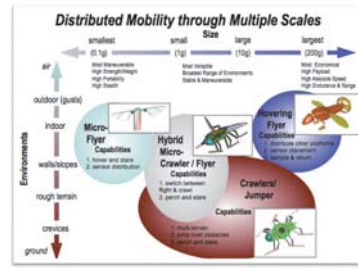
Scenario 3: Autonomous small unit perimeter defense
Challenges: High speed, range and endurance, strong wind gusts

Scenario 2: Small unit cave / demolished building search
Challenges: Hover and low speed, high endurance, mediocre gust

Microsystem Platforms

Range of platforms at:
- **Macroscale (50-100 cm)**
To verify modeling tools, performance, functionality and mobility

- Mesoscale (1-10 cm)
Final design goal
- Aerial: Rotary and flapping wings
- Hybrid: Thrust augmented entomopter, hybrid crawler/flyer

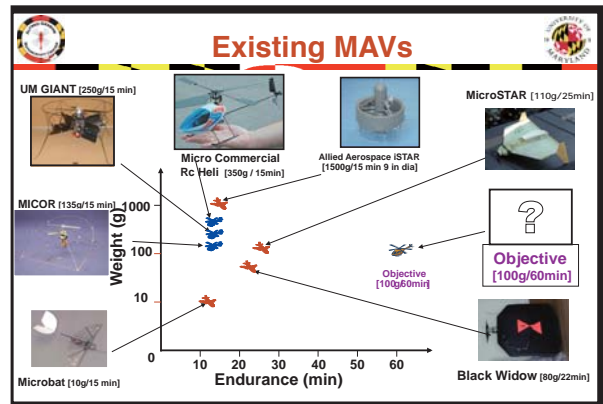
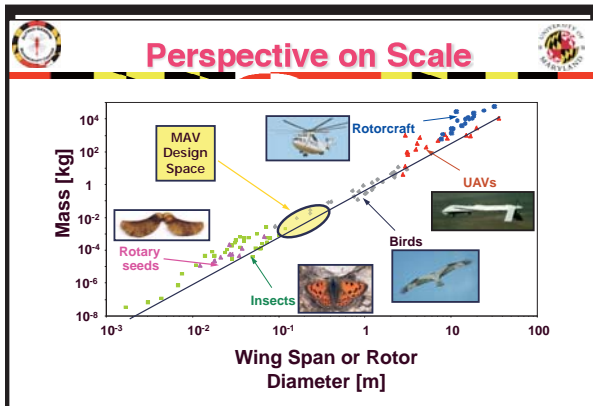


Size Scaling for MAV platforms
(Mobility)(Intelligence)(Multiplicity) = Capability

	Larger	Smaller	N*small=large
Mobility	↓	↑	↑
Gust Sensitivity	↑	↓	No change
Frequency	↓	↑	No change
CPU MIPS	↑	↓	no change
Multiplicity	↓	↑	N/A
Sensing	no change	no change*	O(N ²) ↑
Communication	↑	↓	O(N ²) ↑

Micro Air Vehicles: Key Drivers!!

- Asymmetric warfare environment: urban warfare**
- Micro-electronics: Miniaturized sensors availability**
- Micro-processing: IT and transmission power growing**
- Low cost systems: (can be organic with a soldier)**
- Increasing focus on biologically-inspired flight systems**



- ### Micro Air Vehicles: Key Challenges!!
- Lack of knowledge how scaling affects micro-vehicle performance and limitation of existing aeromechanics tools.
 - Low efficiency of existing air vehicles
 - Extreme vulnerability to gust
 - Low mobility, maneuverability and autonomy of existing vehicles
 - Requires fundamental understanding in key areas:
 - Efficient aerodynamic performance in highly unsteady vortex dominated flows at low Reynolds number
 - Bio-inspired actuation and articulation air vehicles
 - Lightweight and adaptive structures
 - Insect-like navigation and control for autonomous operations in uncertain environment (such as gusty environment)
 - Efficient bio-inspired propulsion and efficient power distribution

- ### MICRO HOVERING AIR VEHICLES
- Non-Hovering Vehicles: Fixed-wing based
 - Hovering Vehicles: Rotor Based
 - Single main rotor (with & without tail rotor)
 - Ducted fan rotor
 - Co-axial rotor
 - Tiltrotor, tiltwing, quadrotor, hybrid systems
 - Revolutionary designs
 - Hovering Vehicles: Flapping-Wing Based
 - Bird-flight based
 - Insect-flight based (Efficiency at small scale?)
 - Hovering Vehicles: Reaction Based (power intensive)

Micro Hovering Air Vehicles: Rotor-Based

Coaxial Rotor MAV

- MICOR (University of Maryland)
- 15 cm (6") dia coaxial 2-bladed rotors

Weight~100 g, Payload ~10g
 8% camber circular arc airfoils
 $Re_{75R} \sim 20,000$
 Endurance ~ 10 minutes
 Fixed pitch, variable speed rotors (feedback on lower)

Swashplate controls only lower rotor

Coaxial Rotor MAV Development at UM

Evolution of the MICOR MAV



1st Gen. 2nd Gen. 3rd Gen. 4th Gen.

1999

1st Generation

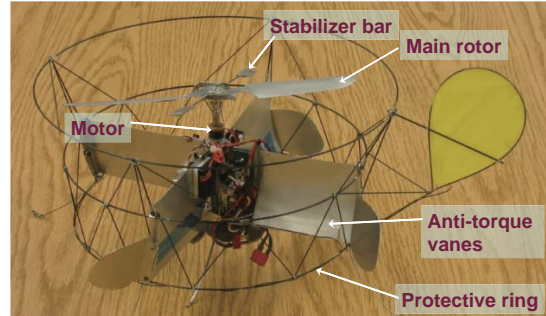
- 100 g Weight
- Maximum Single Rotor FM - 0.4
- No Payload Capacity
- No Lateral Control - Unstable
- 3 Minute Hover Endurance

2008

4th Generation

- Two bladed teetering rotors
- 135 gr. Single rotor max FM - 0.65
- Swashplate for cyclic control
- 20 minute hover endurance
- 25 g payload

MAV: Single Rotor & Anti-Torque Vanes



MAV: Single Rotor & Anti-Torque Vanes

Evolution of the Giant MAV



1st Gen. 2nd Gen. 3rd Gen. 4th Gen.

1999

1st Generation

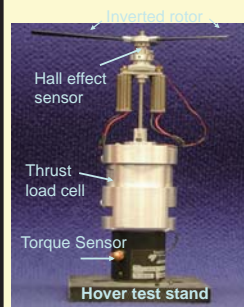
- 27 cm diameter
- 310 gm gross weight
- Aluminum construction
- Basic RC Components

2008

4th Generation

- 20 cm rotor diameter
- 200 gm gross weight
- Carbon fiber construction
- Refined spider-type swashplate
- On-board stability augmentation

Rotor Hover Test



Measurement of Hover Performance:

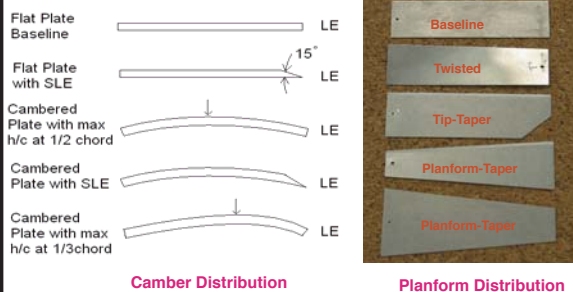
- Thrust
- Torque
- Rotational speed

FM
 C_T
 C_P

Figure of Merit

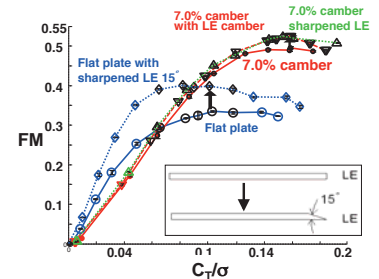
$$FM = \frac{\text{Ideal Power required to hover}}{\text{Actual Power required to hover}}$$

Blade Airfoil Variations



Sharpened Leading-Edge Airfoils

- Sharp leading-edge increases FM
- Smaller rise in FM for cambered airfoil



Sharpened LE can improve airfoil performance

Flow Visualization

7% camber, 2.75% thickness with sharpened LE
D=6" 2-bladed rotor, 3600 RPM, $Re=36.8 \cdot 10^3$

Strong tip vortices
High induced velocities in tip region
Vortical shed wake obstruction increases DL and lowers FM

Labels in image: Rotor Plane, Main Vortex, Vortex Sheet, Wake Obstruction.

Rotating-Wing MAV Performance

Profile Effects (Left Y-axis)
Induced Effects (Right Y-axis)

Curves for FM: 0.6, 0.7, 0.6, 0.55, 0.5. A 'Design goal' is marked at FM=0.6, κ=1.25. A 'Current rotating-wing MAV' is marked at FM=0.5, κ=1.75.

Better designs may come through careful aerodynamic optimization that minimizes both induced power and profile power

Shrouded Rotor System

Rotor Hover Efficiency

Figure of Merit M: Hover Efficiency is defined in terms thrust production per unit input power
For present designs: M is less than 0.6
Goal: Increase M over 0.8

Improvement of hover efficiency using duct around the rotor (plus safety protection of rotor)

Shrouded-Rotor Concept

Key Design Parameters

- Expansion ratio/Diffuser angle**
 - Want this to be as large as possible for best performance
- Inlet lip radius**
 - Incoming flow forms a suction peak on the inlet lip; cause of thrust augmentation
- Blade tip clearance**
 - Proximity of shroud wall reduces strength of blade tip vortices; reduces blade tip losses

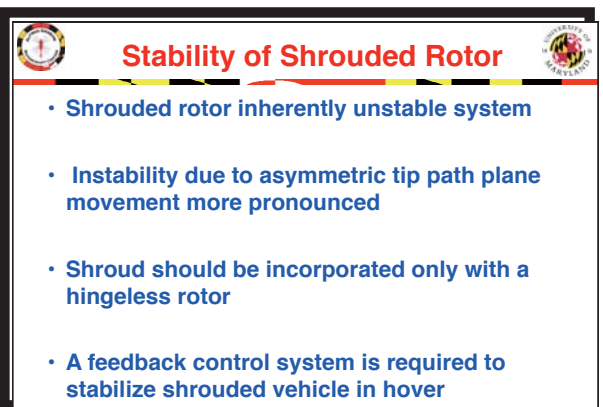
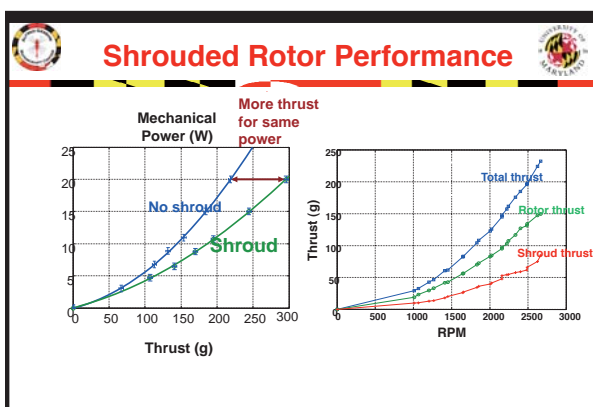
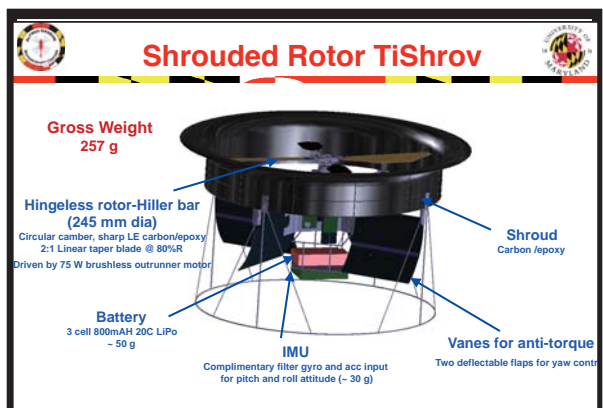
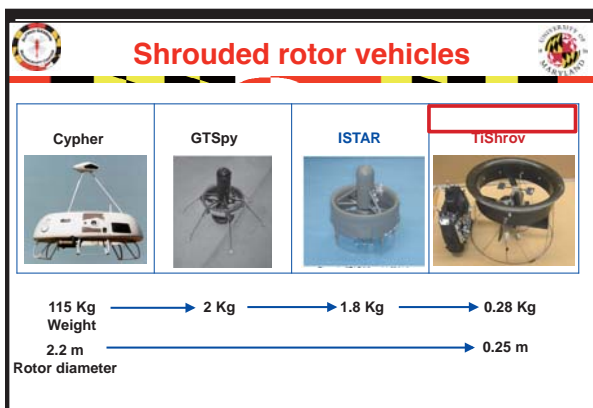
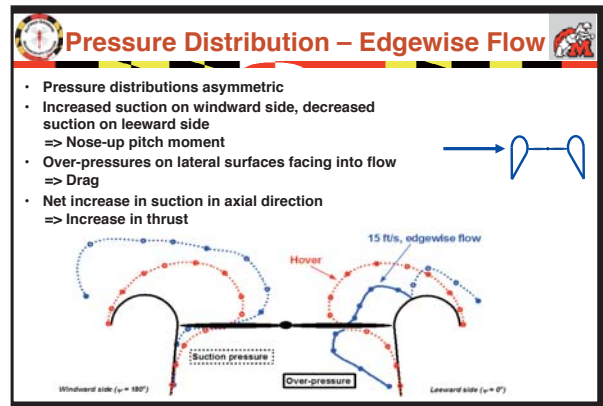
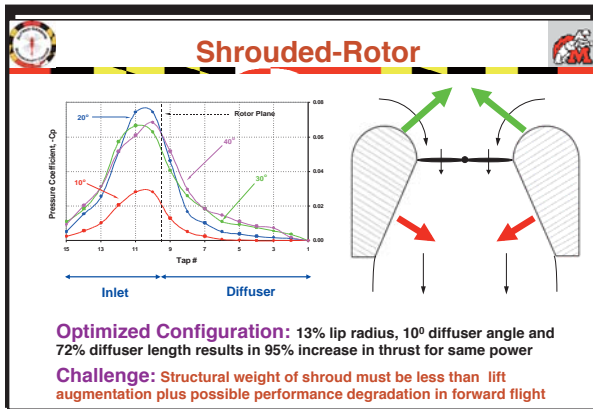
Experiment: Thrust Ratio vs. Total Power

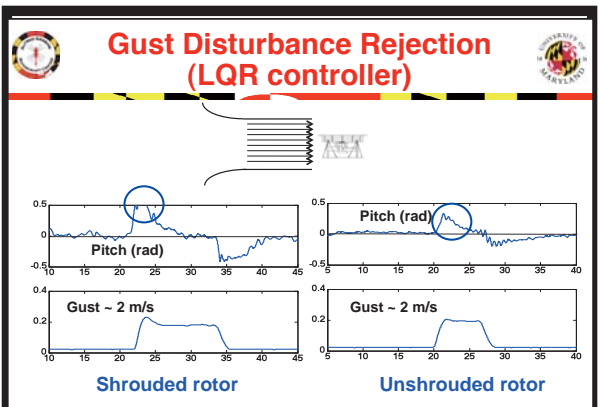
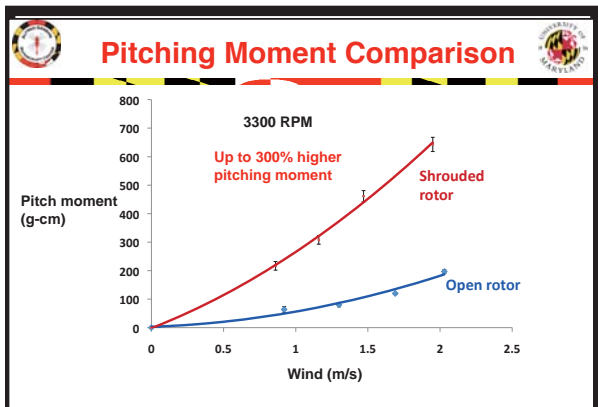
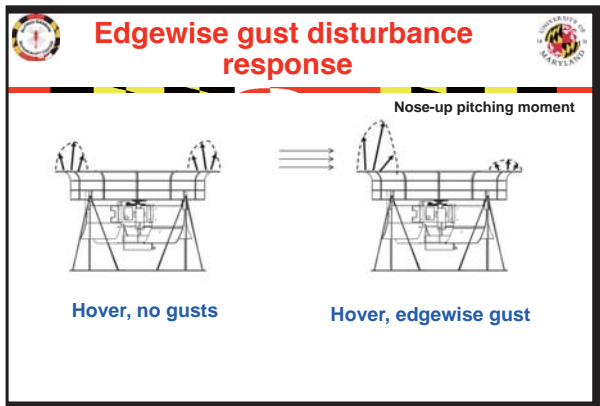
Thrust Coefficient, C_T (Left Graph)
Thrust Ratio, T_{total} / T_{free} (Right Graph)

Designs shown: LR09-D20-4, LR13-D00, LR09-D20, LR06-D10, Free Rotor.

Increase lip radius: Increase thrust
Decrease tip clearance: Increase thrust

Diffuser angle: Thrust increases with small angle $<10^\circ$





Conclusions

- MAV shroud should be designed for high hover performance and low adverse pitching moment simultaneously
- Shrouded rotor
 - 30% higher power loading
 - 80% higher control authority (hingeless rotor, washplate)
 - can accept higher cyclic pitch range (stall delay)
 - 300% higher adverse pitching moment
- Adverse pitching moment of shrouded rotor not a function of operating RPM or rotor collective

Conclusions (2)

- Control authority varies quadratically with RPM, (linearly with operating thrust)
- Improve control authority
 - Increase cyclic pitch range
 - High operating RPM, high rotor solidity and low collective
- Gust tolerance increased from 2 m/s to 3 m/s with suggested changes (increased pitch and rectangular platform)

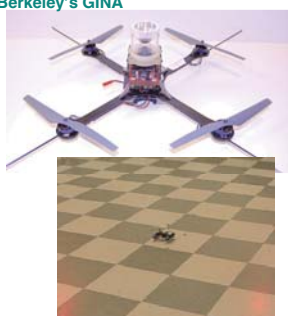
Shrouded rotor MAV viable platform for low gust environments

Micro Quad Rotor

185-g quadrotor with 10-cm rotor with off-the-shelf electronics



35-g quadrotor with 3-cm rotor with Berkeley's GINA



Quad-Rotor: 6-DOF Terrain Following + Centering Response using Optic Flow Sensor



**Rotary Wing Micro Air Vehicles:
Unconventional Configurations**

Cyclocopter

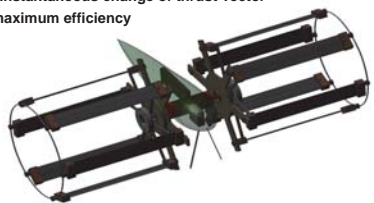
A set of blades rotate around an axis of rotation parallel to blades; pitch varies periodically once per revolution to produce thrust in desired direction

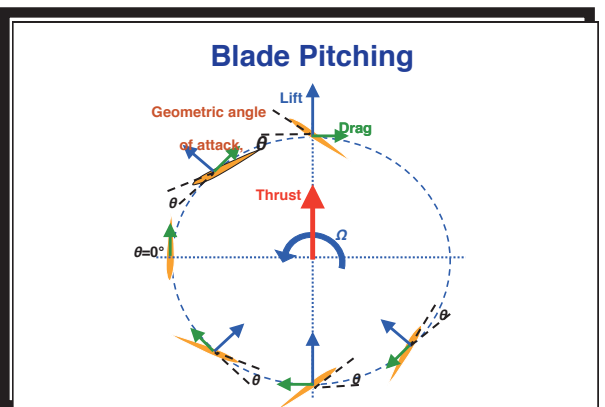
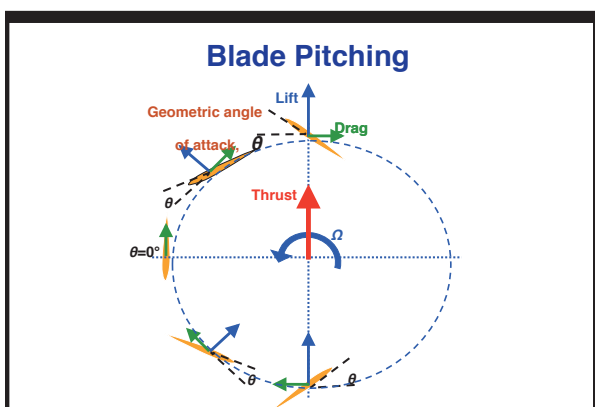
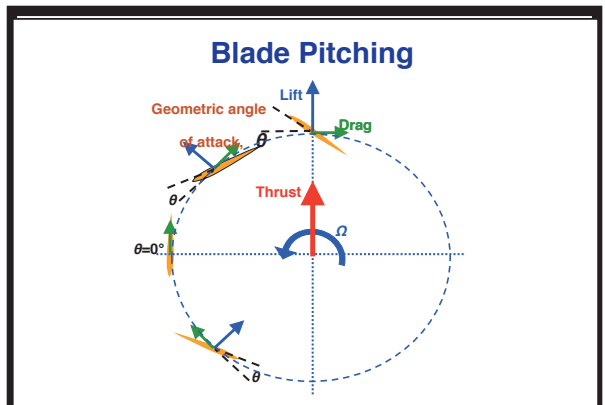
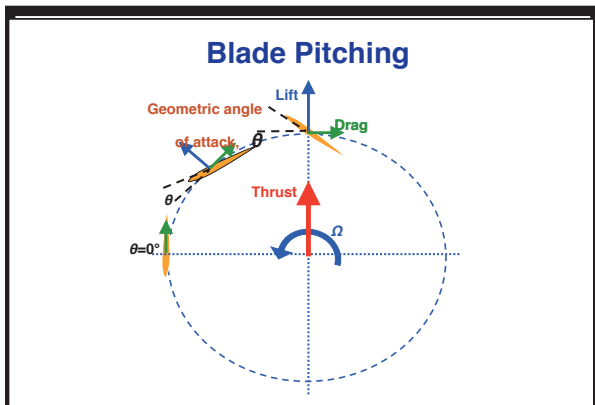
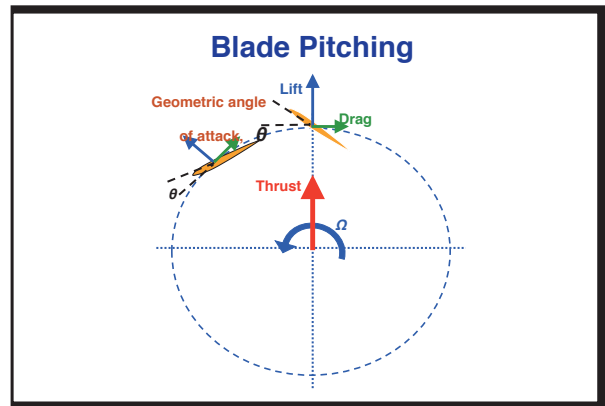
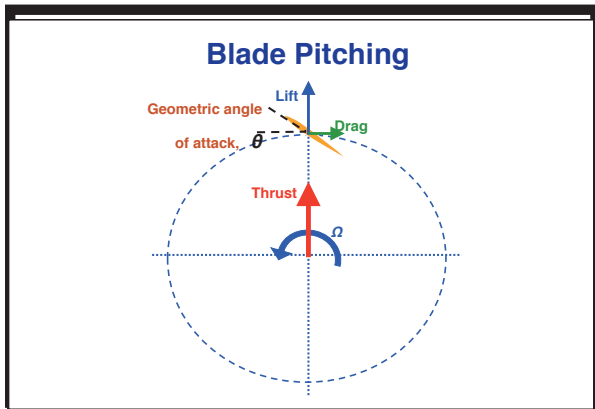
Advantages:

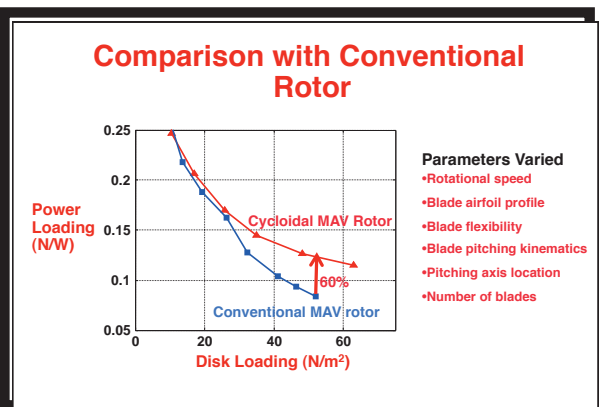
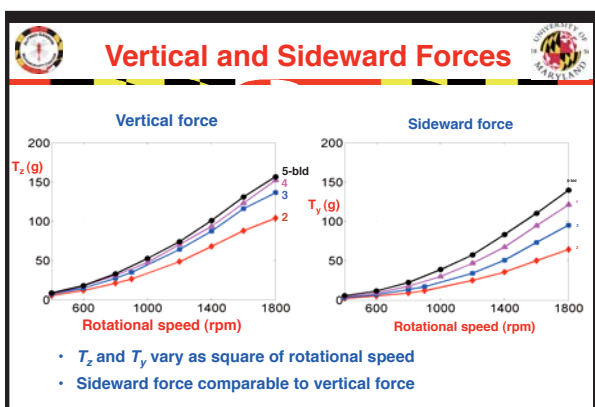
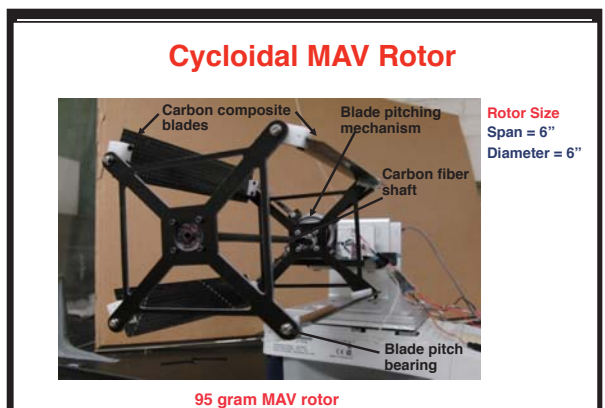
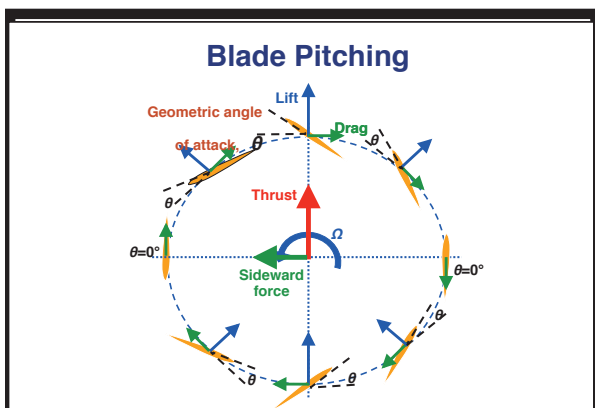
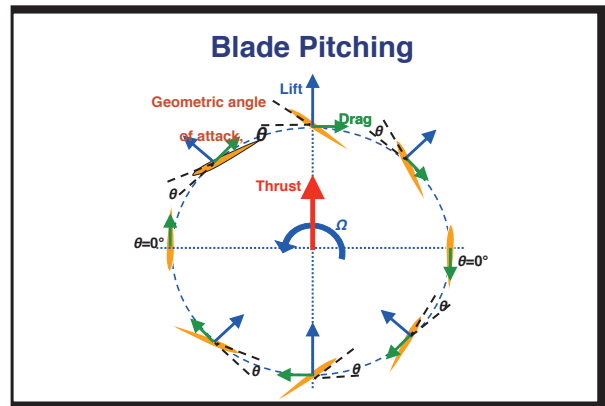
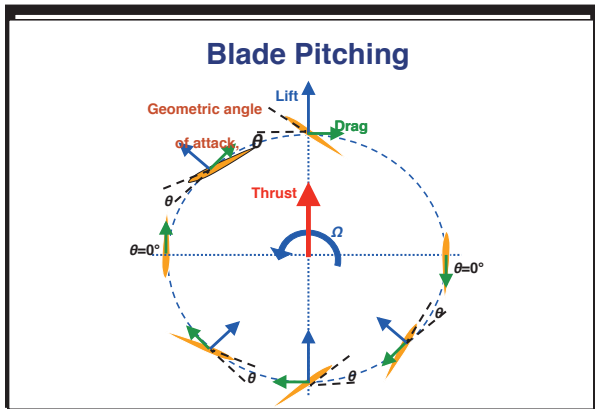
- High maneuverability: Instantaneous change of thrust vector
- All airfoils operate at maximum efficiency

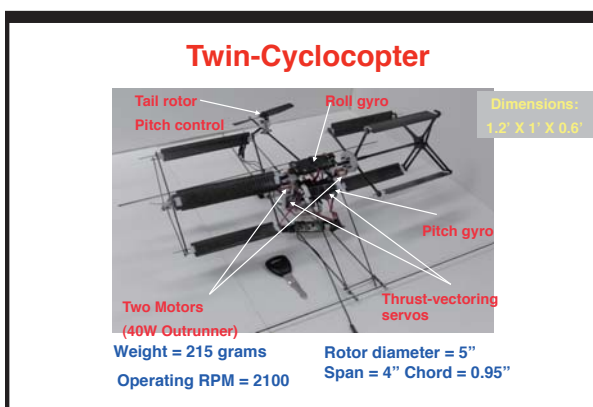
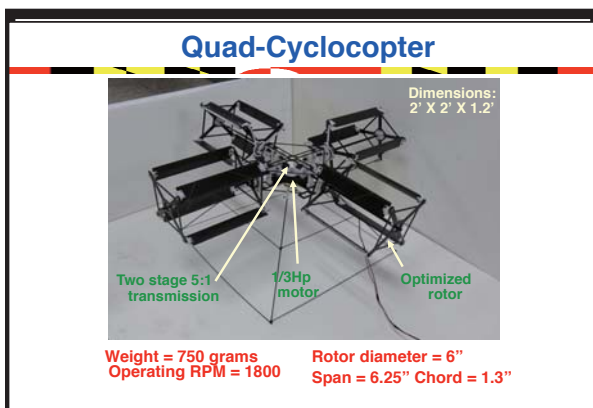
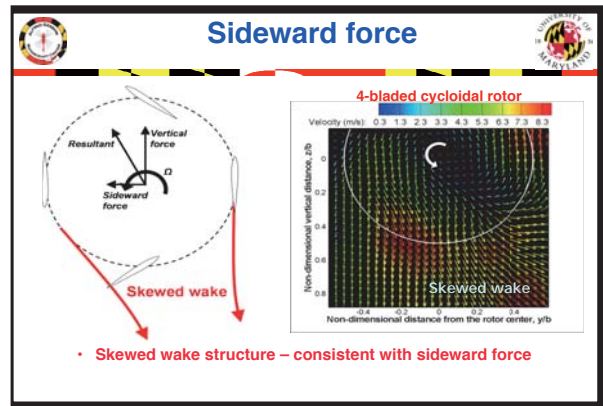
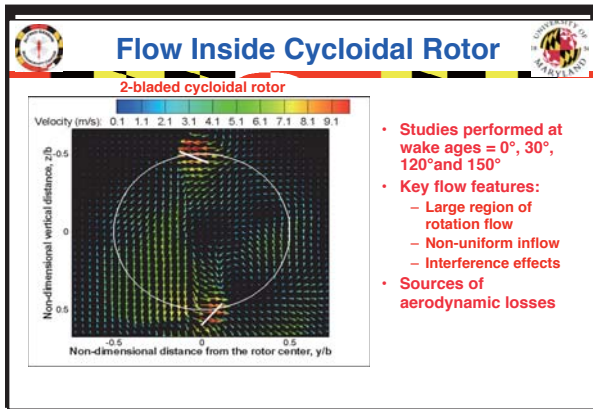
Major Concerns:

- Complex wake interaction
- Complexity of pitch change mechanism









Conclusions

- Power loading better than a conventional rotor
- Optimum cycloidal rotor based on parametric studies
 - 4-bladed, pitch amplitude = 40°, blade chord = 1.3"
- PIV measurements showed presence of a skewed wake
 - explaining side-force
- Absence of blade stall at high pitching amplitudes (45°)
 - high induced velocities in wake

Micro Hovering Air Vehicles: Flapping-Wing Based

**Mechanism of Flapping-Wing Flight
Insects vs Birds**

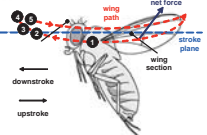



Birds vs Insects

Function	Bird	Insect
Weight	20g to 15 kg	Less than .2g
Size	0.15 to 3m	.1m and less
Aerodynamics	Quasi-steady Drag-reduction	Unsteady Lift enhancement
Morphing	Active wing morphing	Rigid wing, base motion
Wing frequency	Modest <10 Hz	High >50Hz
Hovering	Very rare	Quite common
Speed	High, wing morphing	Modest, tilting body and stroke plane
Reynolds No.	>10,000	<10,000

Insect Flight Fundamentals

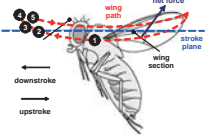
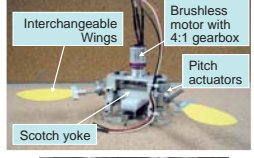
► The wing stroke of a hovering insect is divided into four kinematic stages:



1. **Upstroke** → **TRANSLATIONAL phase** – when the wings sweep through the air with a high pitch angle
2. **Downstroke** → **TRANSLATIONAL phase** – when the wings sweep through the air with a high pitch angle
3. **Pronation** → **ROTATIONAL phase** – when the wings rapidly rotate and reverse direction
4. **Supination** → **ROTATIONAL phase** – when the wings rapidly rotate and reverse direction

Flapping-Wing MAV

Background: Insect-Based MAV

► Examined insect-based flapping bio-mimetics.
 ► Hover-capable insect-based flapping causes delayed dynamic stall, rotational circulation and wake capture.
 ► A folded wake with the presence of multiple vortices on top and bottom surfaces.

► Key Parameters are: wing frequency, flap amplitude, pitch angle, aeroelastic couplings (flexibility)

Objective of Flapping-wing MAV

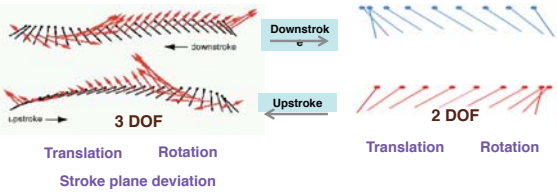
- Develop simplified flapping wing flight worthy system that can emulate insect kinematics
 - Simple and lightweight
- Exploit wing kinematics for control



CHALLENGE

- Heaviest hovering bird = 20 grams
- Flapping MAV with payload = 20 grams
- Gross Weight ~ 50 – 100 grams

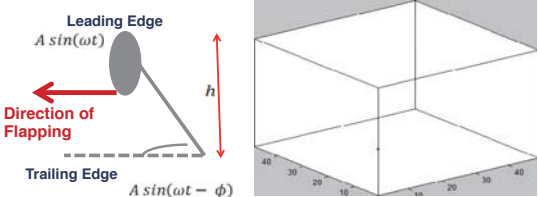
Flapping Mechanism



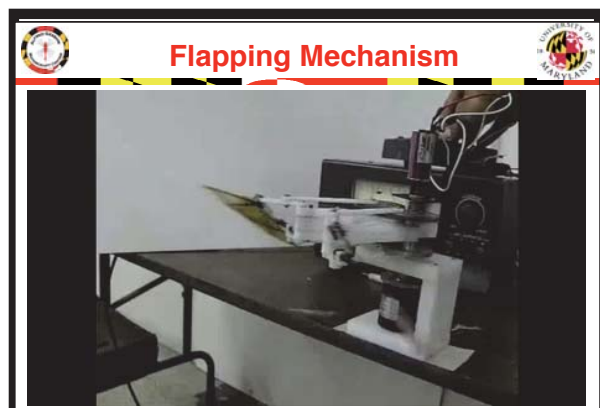
Insect Kinematics

Simplified Kinematics

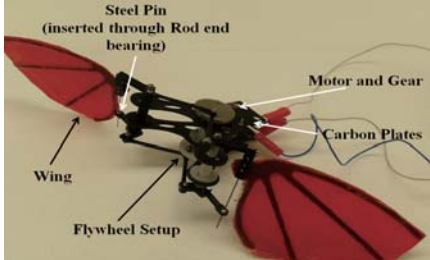
Flapping Mechanism Principle



$$\theta = \tan^{-1} \left(\frac{A \sin(\omega t) - A \sin(\omega t - \phi)}{h} \right)$$



Second Generation Flapping MAV



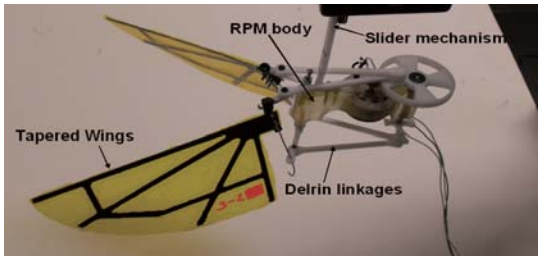
Wings hinged at different locations

Two carbon plates for increased stiffness

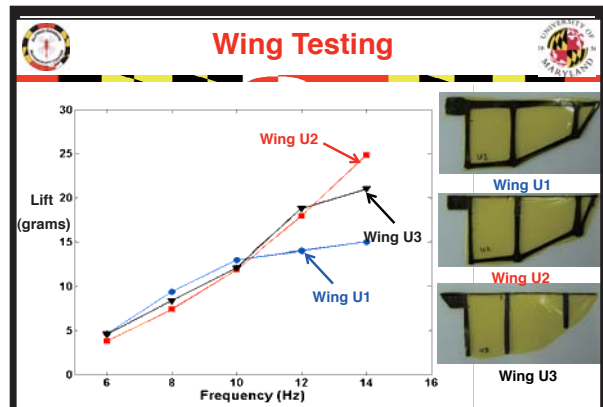
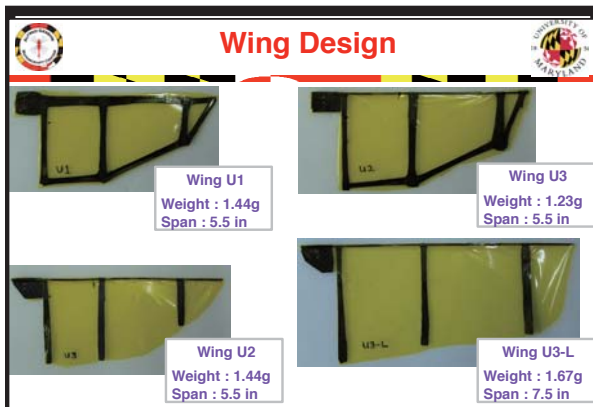
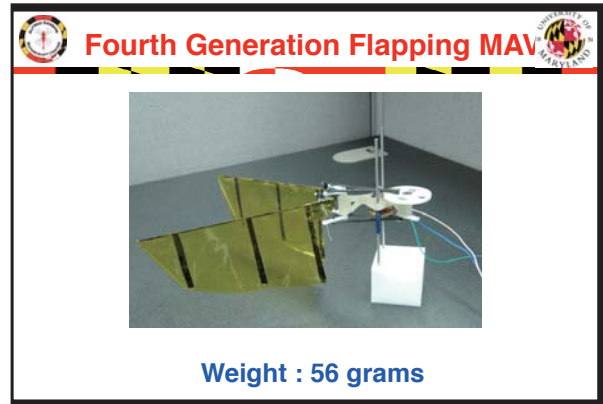
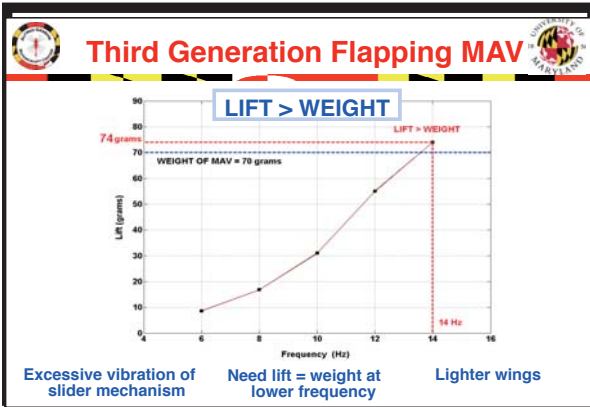
Total weight 130 grams

Motor power 140 W

Third Generation Flapping MAV



Weight : 70 grams



- ### Summary and Conclusions
- Demonstrated tethered hover capability of a 60 gram flapping MAV using insect kinematics
 - Active pitching improved MAV performance
 - Figure of merit 0.1 – 0.2
 - Wing design
 - Light – reduce power and inertial loads
 - Maintain bending stiffness and reduce torsional stiffness

Micro Flapper

Developed 10-g flapper and demonstrated yaw control in VICON and carried out detailed DPIV studies

Physics and Actuation of Flapping Flight

1) increase in stroke amplitude

2) tilt of stroke plane

Biomechanics / Control (Humbert)

0.25 1.0

Computational Fluids / Structures (Baeder / Chopra)

Particle Image Velocimetry (Leishman)

Conclusions

MAV is a multidisciplinary system and requires synthesis of:

- Aeromechanics (low Re)
- Micropropulsion
- Microelectronics
- Microprocessing
- Microfabrication

Many Challenges:

- Modeling and simulation
- Adaptive feedback controllers
- Communication and guidance
- Building and flight testing

Flight Inspired by Nature at Low Re

Propulsion and Power

- efficient batteries
- micro engines
- energy Storage/distribution

Sensing and Navigation

- miniature electronics
- Insect based guidance

Low Reynolds Number

- delayed Stall
- flow separation control
- wake capture

Biomimetic Kinematics

- actuation (thorax)
- efficiency
- frictionless

Maneuvering Capability

- distributed control surfaces
- gust prone

Lightweight Wing Structures

- active shape deformation
- wing morphing




Alfred Gessow Rotorcraft Center
 UNIVERSITY OF MARYLAND

Review of Rotorcraft Aeromechanics and Advanced Designs
Inderjit Chopra
 Director Alfred Gessow Rotorcraft Center & Alfred Gessow Professor of Aerospace Engineering

Presentation At: Korea Aerospace Research Institute (KARI), Daejeon
 June 27-30, 2011


Definition of Rotorcraft


An air vehicle whose primary means of vertical lift is a rotating airfoil

Is This Air Vehicle a Rotorcraft?

Yes **Maybe** **No**



Swashplateless Rotor with Integrated Flaps



MR RPM : 375 rpm
 Empty Weight: 1100 kg
 Fuel Weight: 150 kg
 Payload: 500 kg
 MTOW 1750 kg

Rotorcraft Aeromechanics Research


Today's Technology Drivers

- All round desire to increase performance & efficiency SFC, Figure of merit, power loading, L/D etc 
- Explosion of IT & wireless technology 
- Maturation of composite technology & upcoming smart structures technology 
- Availability of sophisticated prediction tools 
- Availability of miniaturized sensors & reliable measurement techniques 

Rotorcraft Aeromechanics Research


Today's Non-Technology Drivers

- All-round desire to reduce Cost! & Cost!! (Acquisition, maintenance and Operating: life cycle) 
- More Safety & ease of flying 
- Green legislations!!! Noise! & CO₂ level 
- More autonomy requirements 
- Runway saturation & terminal area gridlock 
- Asymmetric & urban warfare 

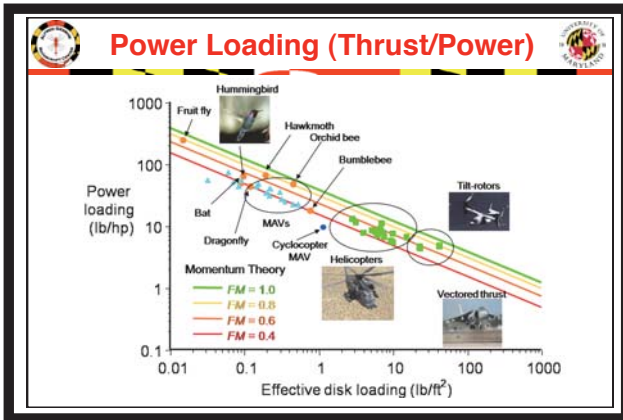

Index of Efficiency


Figure of Merit

$$FM = \frac{\text{Ideal Power required to hover}}{\text{Actual Power required to hover}}$$

Power Loading

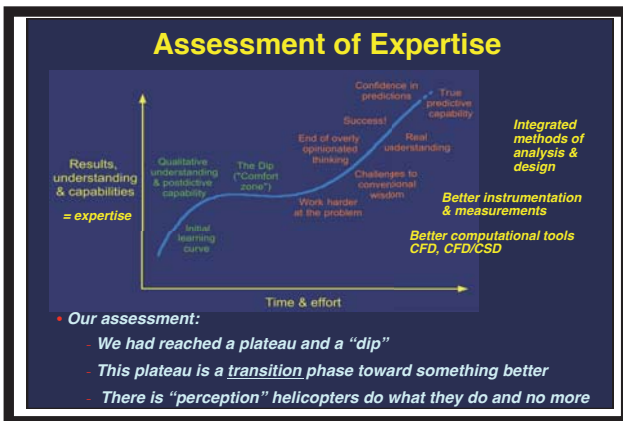
$$PL = \frac{\text{Thrust Produced}}{\text{Actual Power required}}$$



State-of-Art of Helicopter Technology

Speed	~150 Knots	Airplane of 1920's
Range	<500 nm	low
Payload	<40,000 lbs	low
Ceiling	<15,000 ft	low
Figure of merit	<0.8	Up from 0.6 in 1940
Lift-to-drag ratio	5-6	Up from 4-5 in 30 years
Productivity	Low c.f. of airplane	Small increase in 30 years
Vibration levels	High "	Uncomfortable
Noise levels	High "	Obtrusive

Despite all of the understanding of aeromechanics, why has the helicopter apparently reached a peak in its capabilities?
 By our estimate, it HASN'T!!
 But, we need to get better at implementing solutions to the problems!



- ### Postdictive Versus Predictive Capabilities
- **POSTDICTIVE modeling capability:**
 - Significant simplification of physics
 - Too many empirical "constants"
 - Usually operate on the "top" level
 - Calibrated to specific or "favorite" data sets
 - Cannot "predict" outside bounds of validation
 - **PREDICTIVE modeling capability:**
 - Requires in-depth understanding
 - Need very detailed experiments for proper validation
 - Built from upward from governing equations (first principle)
 - Appropriate predictive capability (especially for new configurations)
 - More expensive but needed for getting over the dip

- ### Why Does the "Dip" Happen?
- We reach our "comfort zone"
 - Rooted in "postdictive" capabilities
 - As methods are brought to bear on new problems, limitations realized
 - Priorities change or low (or no) funding for apparently "well-studied" problems
 - "Cultural barriers"
 - We close our wind tunnels!
 - Helicopter has "reached its peak"!
 - Expertise also slowly lost in time:
 - People move on, retire, etc.
 - We forget the fundamentals!
 - Fewer people with "sense of physics"
 - Experience not passed on effectively
 - Information hard to find (rediscovery!)
 - Work not written down in archival literature

- ### Continuation of "Dip"?
- **R&D Funds**
 - Erratic flow of funds
 - Following of milestones (creativity secondary)
 - Too much bureaucracy
 - **Future Rotorcraft**
 - Overindulgence in upgrades
 - Pursuing infeasible projects
 - Industry: too short sighted
 - **Government Laboratories (Buyers)**
 - Becoming weak in talent and facilities

Rotorcraft Aeromechanics



Coverage

Aeromechanics involves coupled, multi-, inter-disciplinary

- Dynamics (Aeroelasticity)
- Aerodynamics & Performance
- CFD
- Acoustics
- Flight Dynamics & Controls
- Composite Structures
- Transmission & Power-Trains
- Smart & Adaptive Structures

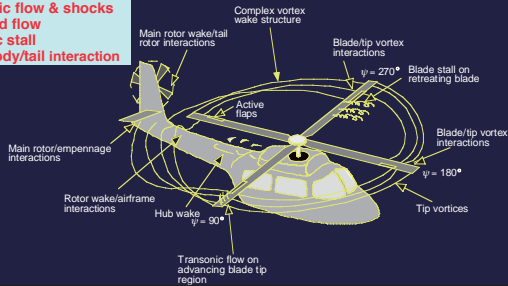


Aerodynamics

Aerodynamics: Challenges

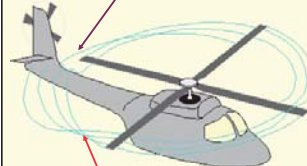
- Nonsteady and complex aerodynamics and rotor wakes

- Transonic flow & shocks
- Reversed flow
- Dynamic stall
- Rotor/body/tail interaction



Rotor Wakes

Main rotor wake interactions with fuselage, empennage, tail-rotor



Blade/Vortex Interactions: Rotor loads, Performance & Acoustics

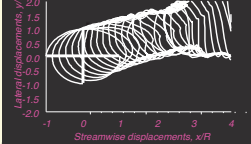
Vortex/Vortex Interactions: Highly three-dimensional induced flow-field



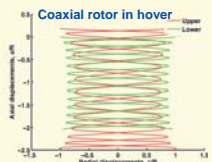
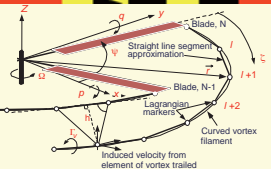
Free Vortex Wake Model

- Rotor wake modeled using vortex filaments
- Blade modeled by lifting lines (Weissinger L)
- Vortex filaments discretized into segments

Rotor in maneuvering flight



Rotor in Vortex Ring State



Rotor Wakes: Measurement



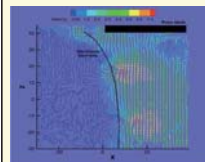
Wide-Field Shadowgraphy



Laser Doppler Velocimetry



Schlieren System



Particle Image Velocimetry

Future: DPS-DPIV (Dual-Plane Stereoscopic Digital Particle Image Velocimetry) can measure 3 velocity and 9 velocity gradients using 3 pair of lasers and 3 synchronized cameras.

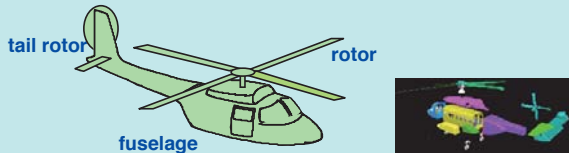
Aerodynamic Modeling: State-of-Art

	Past	Present	Future
Blade Aero	Lifting line Table-lookup Empirical stall	Indicial response functions for unsteady and dynamic stall	CFD/CSD tight coupling
Rotor Wake	Linear inflow Prescribed	Free wake Frequency & time-domain	CFD- generated wake capture
Airframe	Flat plate area	Table lookup Panel method	CFD rotor/ body coupled
CFD Modeling	Euler Uncoupled	Navier-Stokes CFD/CSD loose coupling	CFD/CSD tight coupling

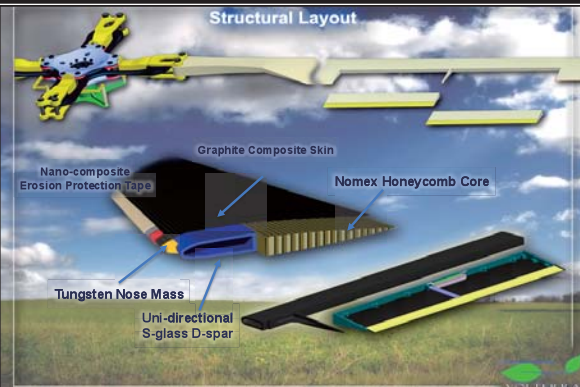
Structural Modeling

Structural Modeling: Challenges

- Coupled and nonlinear phenomena involving complex Coriolis/Gyroscopic forces
- Blade undergoing moderately large deformation involving coupled flap and lag bending, torsion and axial deformation
- Airframe 3-D structure with complex joints and nonuniformities



Structural Layout



Airframe Assembly



Composite Structures

Rotor and airframe are now increasingly being built out of composites

Key Issues:

- Modeling of composite blades and airframe (coupled, nonlinear, non-classical structural effects important)
- Structural integrity including ply delamination (flexbeam undergoing large dynamic twisting)
- Energy absorption due to landing and ballistic impact (off-axis landing, damaged blades)
- Repair of composites (field, depot and factory)

FEM vs Multibody

Classical FEM

- Typically uses single body coordinate frame
 - Deformations and loads in body coordinates
 - Topology dependent

Multibody

- Body and element coordinates
 - Deformation and loads in element coordinates
 - Increased scope of modeling

Multibody Analysis

- Increased scope of structural modeling
- Detailed modeling of control system and hub assembly
 - Exact pitch link, damper kinematics
 - Swashplate servo dynamics
- Large blade deformations
 - Moderate deformation within element frame
 - Large deformations accommodated by finite rotation of frames (important for maneuvering flight)

Structural Modeling: State-of-Art

	Past	Present	Future
Deflections	Moderate large Ordering scheme	Moderate/large	Large (no ordering)
Blade Modeling	FEM/modal	FEM/Multibody	Multibody
Airframe	Stick model	3-D FEM/modal	Multibody
Materials	Small strain Isotropic	Small strain Anisotropic	Large strain Coupled laminates

Rotorcraft Analysis

Rotorcraft Analysis: Challenges

- Governing Equations:** Coupled and nonlinear equations with periodic coefficients
- Solutions:** Trim and rotor response, aeroelastic stability, flight stability, transient response
- Steady Level Flight Analysis:** Periodic response analysis
- Non-Steady Maneuvering Analysis:** Time marching analysis

$$[A(\psi, y, \dot{y})]\{y\} = \{G(\psi, y, \dot{y})\}$$

Comprehensive rotorcraft codes: CAMRAD, RCAS, UMARC

Analyses: State-of-Art

	Past	Present	Future
Trim/Steady Response	Modal method/ Harmonic Balance	Modal/ Complete FEM time	Time integration coupled equations
CFD/CSD Coupling	Iteratively	Loose	Tight
Stability	Linear Modal/ Floquet	Linear Modal/ Full Floquet	Time marching Prony method
Maneuver Analysis	Modal/Time integration	Modal/Time integration	Fully coupled time marching

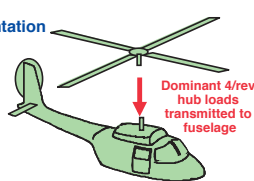
Dynamics

Dynamics

Interaction of structural, aerodynamics and inertial forces (aeroelasticity)

Issues:

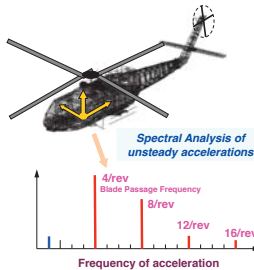
- Vibration & Loads:** prediction, measurement & suppression (level flight, maneuvering flight and gusty environment)
- Aeromechanical Stability:** augmentation (flap-lag flutter, pitch-flap flutter, ground/air resonance)



Dominant 4/rev hub loads transmitted to fuselage

Helicopter Vibration: Definition

Vibration : Accelerations in fuselage



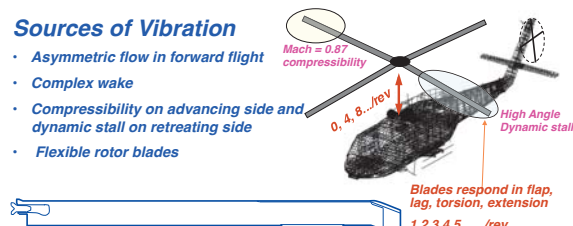
Spectral Analysis of unsteady accelerations

- Intrusion Index:** weighted mean of 4 largest frequencies in vertical, lateral and longitudinal directions up to 60 Hz
- Vibratory Forces:** Rotor blades are excited at all harmonics, only harmonics consisting integer multiples of blade number, pN_b/rev are filtered through hub
- 1/rev due to rotor asymmetry

Rotor Dynamics in Forward Flight

Sources of Vibration

- Asymmetric flow in forward flight
- Complex wake
- Compressibility on advancing side and dynamic stall on retreating side
- Flexible rotor blades



Mach = 0.87 compressibility

0, 4, 8, ... /rev

High Angle Dynamic stall

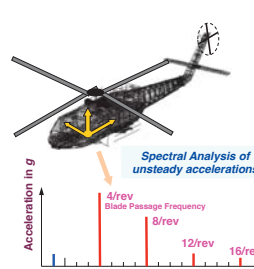
Blades respond in flap, lag, torsion, extension

1, 2, 3, 4, 5, ... /rev

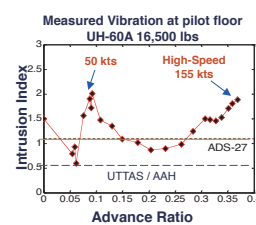
- Blades undergo moderately large deformations involving coupled flap, Lag, torsion and axial motion, nonlinear inertial couplings
- Airframe 3-D structure with complex joints and cutouts, Gyroscopic nonlinear couplings in vehicle dynamics

High Vibration: Flight Conditions

Vibration : Accelerations in fuselage



Spectral Analysis of unsteady accelerations



Measured Vibration at pilot floor UH-60A 16,500 lbs

Intrusion Index

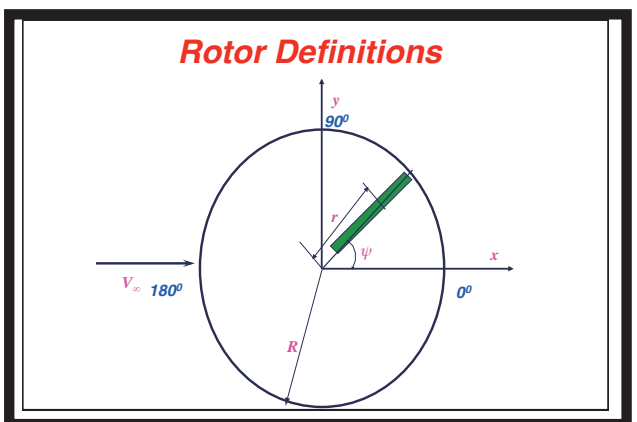
Advance Ratio

50 kts High-Speed 155 kts

ADS-27

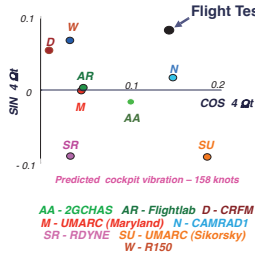
UTTAS / AAH

- 3 Critical regimes : low speed transition, high speed, and high altitude-high thrust
- Enormous vibration: High operating cost, Reduced crew / system performance



Vibratory Loads at High Speed: Prediction vs. Flight Data in 1998

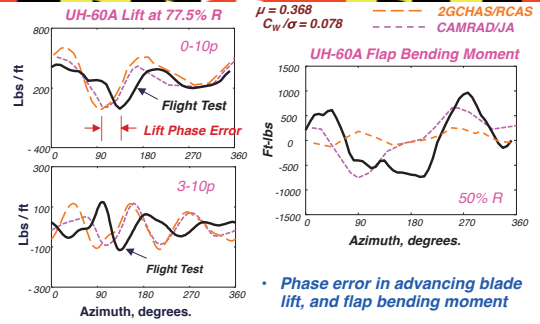
Predicted 4/rev vibratory hub load at high speed from 8 different rotor codes for LYNX



- None of predictions agreed with flight test data
- No two predictions agreed with each other
- LYNX Blades were not pressure instrumented, hence systematic correlation study with air loads and blade loads could not be possible

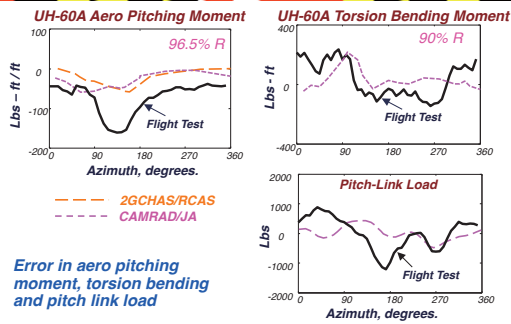


Vibratory Loads at High Speed: Prediction vs. Flight in 2000



- Phase error in advancing blade lift, and flap bending moment

Vibratory Loads at High Speed: Prediction vs Flight in 2000



- Error in aero pitching moment, torsion bending and pitch link load

Vibration Validation Study

Major undertaking in 2001: Team involving industry, academia, NASA/ Army to resolve vibration barrier issues. Loads Workshop: Meet every 6 months since 2001

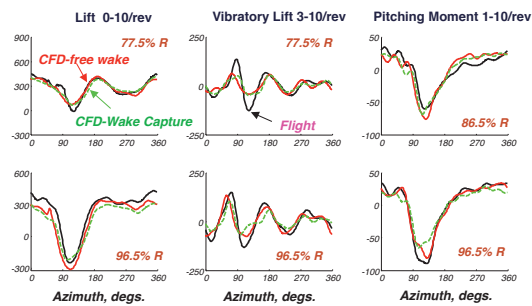
Vehicle: UH-60A Black Hawk, extensive flight test data with pressure instrumented blades

Identified 4 critical flight conditions:

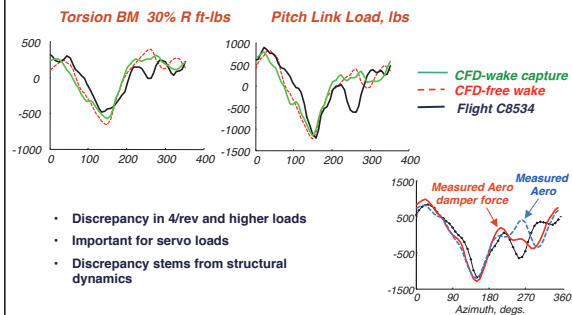
- Level Flight:**
1. High speed $\mu = 0.37$ UH-60A flight 8534
 2. Low speed transition $\mu = 0.15$ UH-60A flight 8513
 3. High altitude dynamic stall $\mu = 0.24$ UH-60A flight 9017
- Maneuver:**
4. Severe UTTAS pull-up Maneuver $\mu = 0.341$ UH-60A flight 11029 (load factor = 2.09)



High Speed: CFD/CSD coupled Solution: First barrier problem resolved

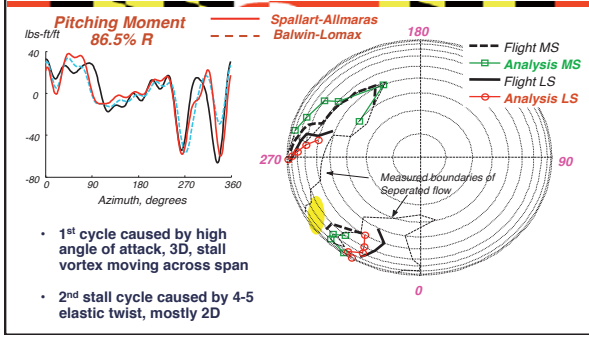


Pitch Link Load at high speed: CFD/CSD Second barrier problem resolved

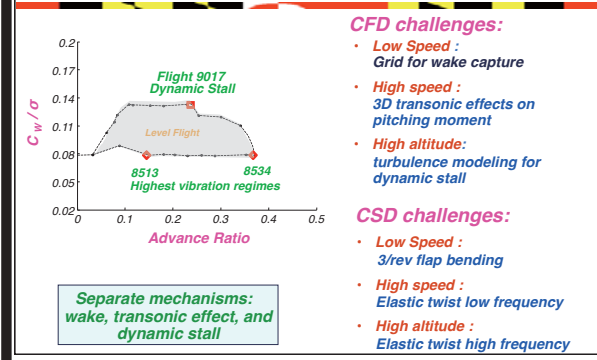


- Discrepancy in 4/rev and higher loads
- Important for servo loads
- Discrepancy stems from structural dynamics

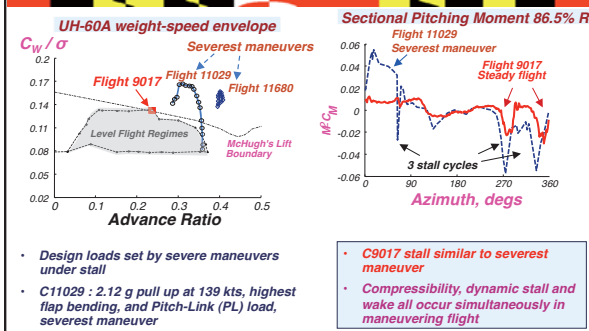
Predicted Pitching Moment and Stall Map at High Altitude & High Thrust



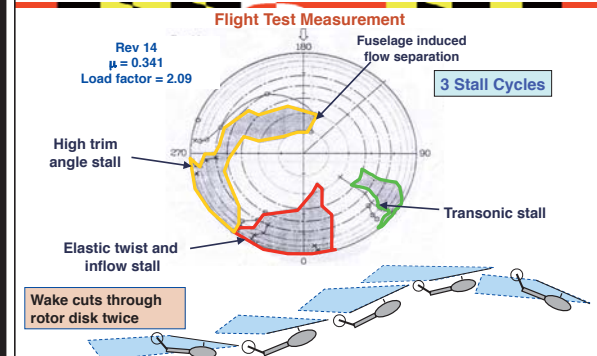
3 Critical Flight Conditions: Level Flight



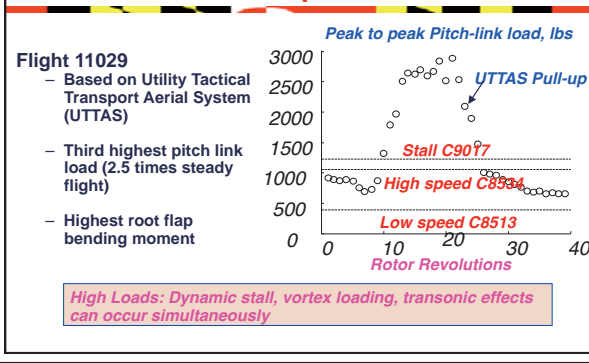
4th Critical Flight: Pull-Up Maneuvering Flight



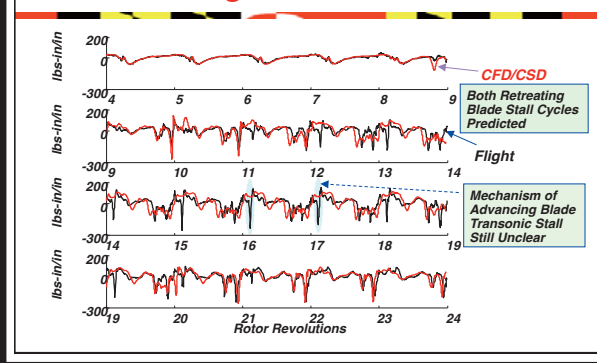
Flight 11029, Severest UH-60A Maneuver: Stall Map



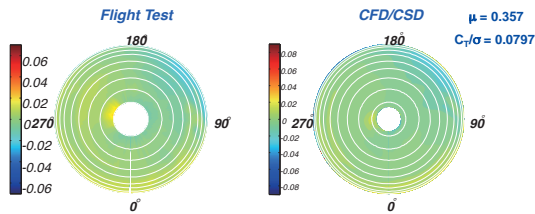
UTTAS Pull-up Maneuver



Pitching Moment: 86.5%R

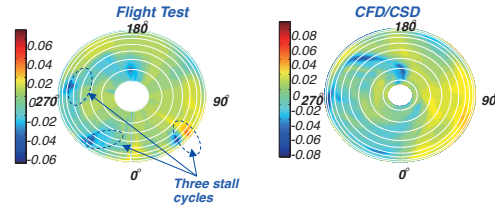


Pitching Moment: Level Flight Rev 1



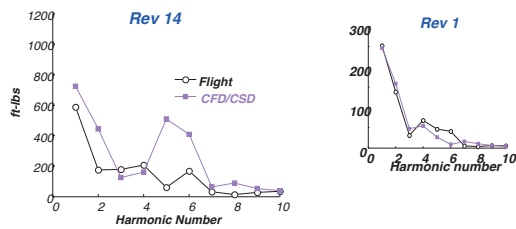
- Pitching moment variation during steady flight regime benign
 - shows no steep gradients across the rotor disk
- Prediction show good correlation with flight test

Pitching Moment: Maneuver Rev 14



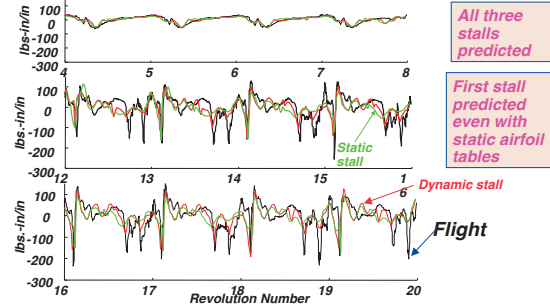
- Pitching moment variation during maneuver shows steep gradients
 - Three stall cycles
- Prediction show good correlation for two stall cycles on retreating side – **advancing blade stall not predicted**

Torsion Moment Harmonics: 30%R

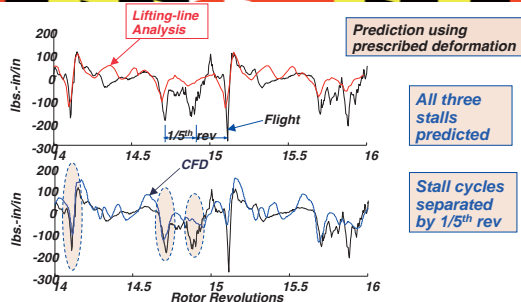


- Over-prediction of 40%–60% in the peak-to-peak magnitude
 - over-prediction of 5 and 6 rev torsional moment stemming from over-prediction of pitching moment stall peaks

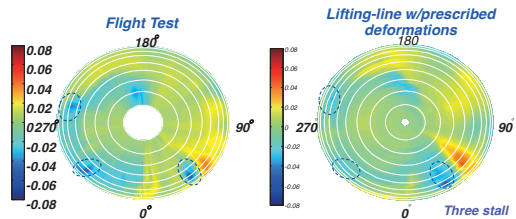
Pitching Moment Using Prescribed Deformation (From Measured Airloads): 86.5%R



Pitching Moment Using Prescribed Deformation: 86.5%R



Pitching Moment C11029: Rev 18



Advancing blade stall predicted accurately

Prediction of Vibratory Loads

Critical Flight Conditions:

- High speed forward flight: vibration
- Low speed transition flight: vibration
- High altitude dynamic stall: loads
- Severe maneuvers: pitch link loads

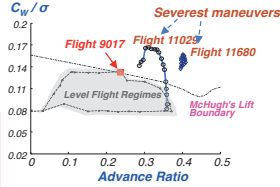
Key Conclusions:

CFD provides fundamental capability

- At high speed: 3D unsteady transonic pitching moment

At low speed: capturing of inter-twinning of wakes

- For dynamic stall flight: capturing of second cycle due to 4 and 5P twist, placement depends upon wake and turbulence model



Pull-Up Maneuver:

3 dynamic stall cycles, Advancing-side stall triggered by 5/rev twist. Two dynamic stall cycles on retreating side separated by 1/5th cycle excites 5/rev twist deformation

Vibration and Loads

Suppression

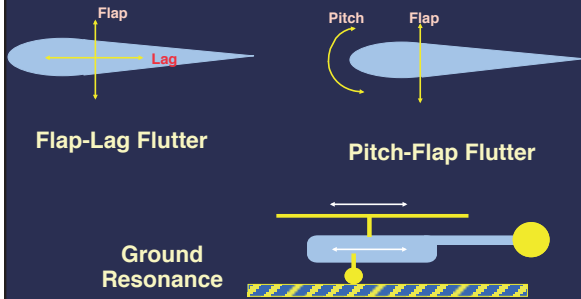
Currently: passive devices such as absorbers and isolators routinely used, also avoid rotor harmonics coupling with airframe modes

- mostly ad-hoc approaches
- extensive weight penalty (up to 3% of gross weight)

Future: towards active vibration control and structural optimization of rotor and airframe using robust prediction methodology

Goal: Reduction in vibratory loads by one-third from current values, weight penalty less than 1% of gross weight

Aeromechanical Stability



Air Resonance



- Occurs on airborne vehicle with soft-Inplane hingeless and bearingless rotors
- Caused by coupling of low frequency flap & lag modes and body airframe modes (aerodynamics very important)
- Soft Instability: To stabilize, needs mechanical damping in lag mode or negative pitch-lag coupling

Aeromechanical Stability

Prediction: For hover & forward flight with normal loading, current analyses predict satisfactorily for hingeless & bearingless rotors

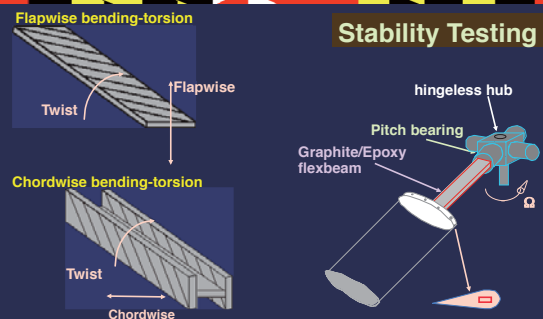
- Needs robust aerodynamic modeling (dynamic stall) for highly loaded rotors (maneuvers)
- Needs refined structural model for complex hubs (bearingless rotors)

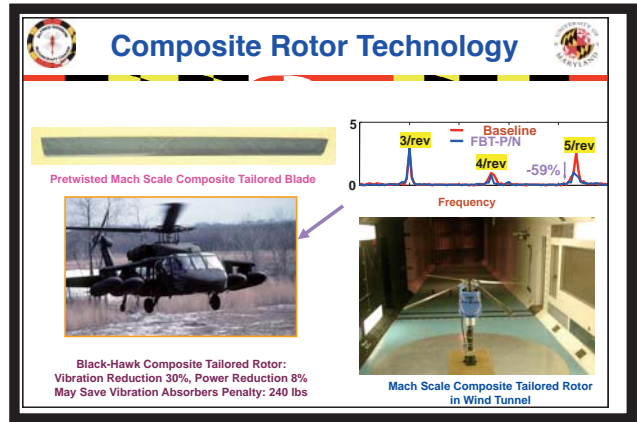
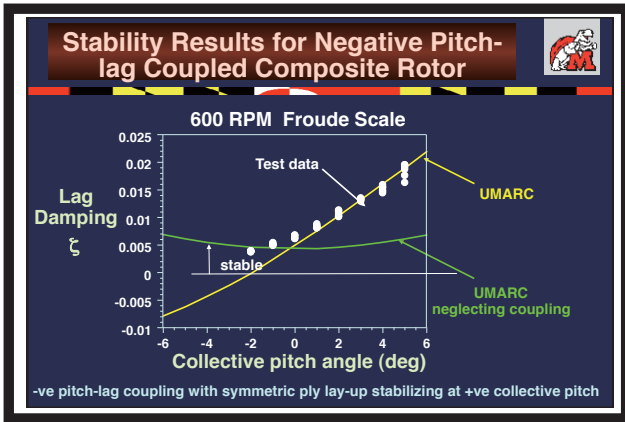
Measurement: Challenging to measure high damping modes

Stability Augmentation: Mechanical dampers routinely used
Possibility of using composite couplings to increase stability

Goal: Build a damperless rotor

Stability Augmentation: Tailored Composite Rotor





Dynamics: State-of-Art

	Past	Present	Future
Vibration Prediction (normal flight) Prediction (Maneuvering) Suppression	>50% error Not reliable Passive Penalty 3% GW	~ 20% error Inadequate tools Passive/active (few) 1-3% penalty	<10% desirable ~10% desirable Active/passive/Optimized <1% penalty
Composites Couplings	Tools development	Showed potential to improve vibration and stability, but no implementation	Composite tailoring Full-scale implementation for performance and stability
Aeromechanical Stability Prediction (Normal flight) Prediction (Maneuvering) Suppression	Adequate for conventional rotors Inadequate Hydraulic/Elastomeric	Adequate for advanced rotors Tools development Elastomeric	Exploit couplings Reliable tools needed Damperness

Acoustics

External/Internal Acoustics

Rotorcraft suffer from too much noise

External Aeroacoustics:

- Blade Vortex Interaction (BVI) low speed noise
- High speed impulsive (HSI) noise (transonic waves)
- Low frequency noise (thickness and loading)

Internal Airframe Acoustics:
Rotors, transmission and gear boxes

Rotor Aeroacoustics

Predictive capability
CFD/CSD coupled analysis to predict noise source (unsteady pressure) and apply in acoustic propagation scheme (Flowcs-Williams-Hawkin) Prediction less than satisfactory.

Noise Control

Passive Blade Design: Tip shape, aspect ratio, number of blades and tip speed using CFD tools, uneven blade spacing in fenestron (tail rotor).

Flight Path Management: Optic-based tip-path-plane tracking system to direct flight trajectory for minimum noise.

Active noise control: Using trailing-edge and leading-edge slats, actively control phasing and miss distance of vortices, and low frequency detection noise.

Goal: 5-10 db reduction of noise

Blade-Vortex Interaction Noise

When a trailing tip vortex intersects another blade, dramatic aerodynamic changes occur which generate noise

Results - Sweep Effect

Hover Tip Mach No. = 0.90; In-Plane Mach Contours

Forward Swept

Not Delocalized
Shock Bends Forward & Weakens

Rectangular

Backward Swept

- Large noise reduction for forward swept rotor
- Strong phasing effects with sweep

Results - Individual Parameter

Hover Tip Mach No. = 0.90; In-Plane Mach Contours

Forward Dogleg

Thin

Taper

- Greater noise reduction for thin and swept rotors
- Shock bends forward for swept blade

Flight Path Management for Noise Control

Technology Goal: Control External Noise by Control of Main Rotor Tip-Path-Plane (TPP) Angle using high-resolution camera. Successfully flight tested on Bell 206 & 407.

Rotorcraft Internal Acoustics

Motivation: Undesirable interior noise levels
Main/tail rotors & gas turbines (40-500 Hz), gears (500-6000Hz)

Passive means for noise reduction: Constrained layer damping and piezo shunting for high frequency suppression

Active noise control: Using piezo patches on fuselage frame and trim panels and with adaptive control strategies for low frequency suppression, active transmission mounts and constrained layer damping for high frequency noise

Goal: 20 db reduction of noise

Acoustics: State-of-Art

	Past	Present	Future
Exterior Noise Prediction	Lifting-line & Flowcs-Williams-Hawkins (FWH) Not satisfactory	CFD & FWH loose coupling Not satisfactory	CFD/CSD & FWH tight coupling Validations
Exterior Noise Suppression	Passive	Passive	Passive/Active/ Flight path management
Interior Noise Suppression	Passive	Passive	Passive/Active

Flight Mechanics and Controls



Key Issues:

- System identification for coupled rotor-fuselage system for a wide frequency band
- Flight control systems for mission tailored handling qualities
- High quality simulations, real and non-real time

Barriers:

- Free wake modeling for maneuvering flight
- Robust system ID tools
- Modeling of multidisciplinary phenomena

Advanced Rotor Systems

Swashplateless Rotor

Conventional Helicopter Primary Flight Control

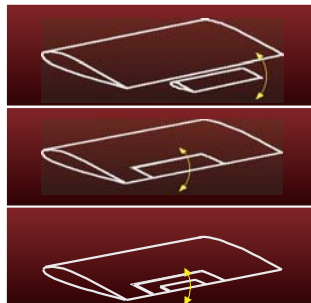
- Conventional helicopter flight control system via swashplate mechanism
 - Main rotor collective system (controls thrust)
 - Main rotor cyclic system (controls direction of thrust)
- Swashplate system involves pitch links, pushrods, and fixed frame hydraulic actuators
 - Weight & drag penalty
 - Mechanical complexity



Swashplate System

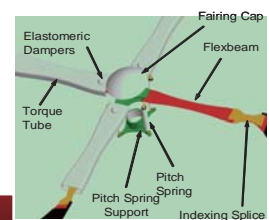
Flap Configurations

- **Servo Flap**
 - ▶ Large pitch moments
 - ▶ Exposed linkages, large drag
 - ▶ Hinge gaps reduce effectiveness
- **Integrated flap**
 - Modify lift & pitching moment
 - Internally mounted actuator and linkages (smart actuation)
- **Tab-actuated flap**
 - Tab moves flap
 - Modify lift & pitching moment
 - Least actuation power



Swashplateless Rotor System

- Swashplateless flight control via smart trailing-edge flaps
 - ▶ Flap deflections: collective and cyclic: in turn induce collective and cyclic blade pitch motion
 - ▶ Requires torsionally soft blade with blade pitch indexing
 - ▶ Potential of low drag and lightweight primary control
 - ▶ Hydraulicless system



Swashplateless System

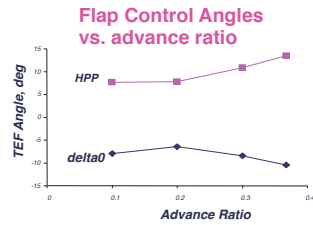


Primary Flight Control Requirements

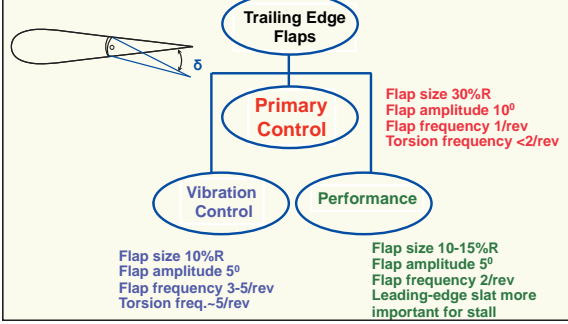


- Black Hawk
- $C_W/\sigma = 0.0783$ (16500 lb)
- $V_\theta = 2.0$ /rev
- $\theta_{dx} = 15^\circ$

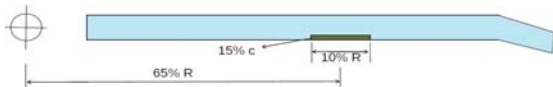
Primary control requires greater flap angles and hinge moments



Trailing Edge Flaps Rotor

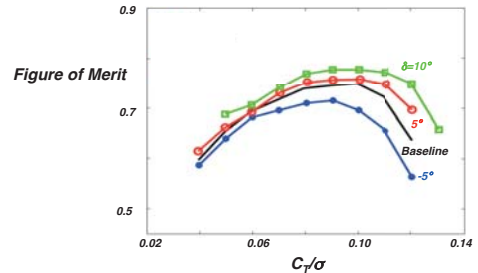


- **TEF geometry**
 - 10% span, 15% chord, midspan at 65%R
- **TEF operation**
 - Primarily moment flap
 - Alters section pitching moment and induces blade twist
 - Effect of reducing blade torsional stiffness on TE flap effectiveness



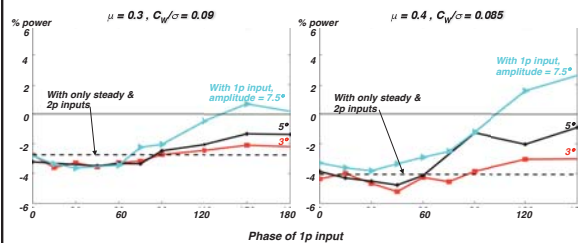
Hover Performance

Effect of steady TEF deflections



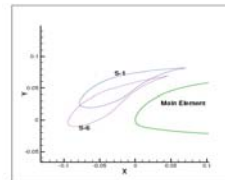
TEF geometry : 10%R, 15%c, mid-span at 65%R

Rotor Performance with Trailing-Edge Flaps



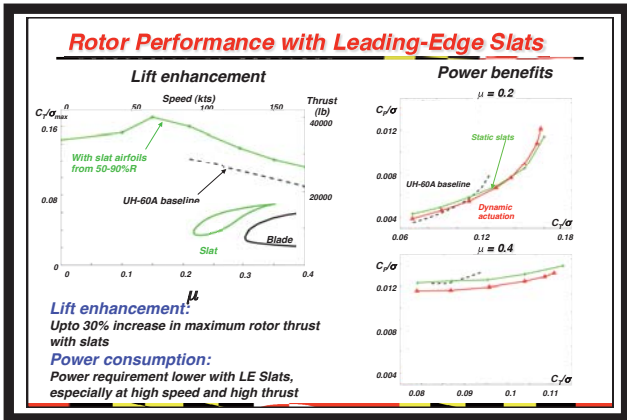
- Over 5% power reduction possible:
- Using a combination of steady, 1/rev and 2/rev flap inputs
 - Flap geometry : 10% span, 15% chord, midspan at 65% blade span

Leading Edge Slat Geometry



- S1 – Baseline position
- S6 – High Lift position
- Slat is ~15% of baseline chord





Trailing Edge Flaps Rotor

Past: Kaman SH-2 servo-flap rotor operational since 60s, servo-flaps for primary controls (collective & cyclic)

Present: Feasibility studies of integrated flaps to minimize vibration and noise using IBC (individual blade control)
Flight test: Eurocopter-Germany: BK117
Full-scale tunnel tests: Boeing-Mesa: MD900

Future: Development of full-scale integrated smart flap rotors for primary control (Eurocopter, Sikorsky, Boeing)

SH-2

Bo105

MD 900

Smart Rotor

Smart Rotor

Application of smart structures technology to actively control vibration, noise, stability and performance
Concepts: Flaps, blade twist, active tips

Present: Feasibility studies: Smart flaps
UM: successfully tested Mach-scaled models
Boeing: full-scale tests in 40x80 tunnel (April 08)
Eurocopter: successfully flight tested Sept 2006

Future: Full-scale smart rotor for primary and noise control and performance enhancement: Sikorsky, Eurocopter & Boeing

Challenges: actuators stroke, integrity

Smart Structures Activities at Maryland

6-ft dia Froude scale rotor model in Glenn Martin Wind tunnel: active twist with embedded piezoelectric elements

6-ft dia Mach scale rotor model in Glenn Martin Wind tunnel: trailing edge flaps actuated with multi-layered piezomorphs

6-ft dia Mach scale rotor model on hover tower: tip actuated with embedded piezos in conjunctions with bending-torsion composite couplings

Example: Technology Transfer

Smart Structures Technology

Smart Actuator Development: Piezostacks with L-L Amplification

Smart Rotor Development: Mach-Scale with Piezo Actuated Flap

Boeing: Full-Scale Smart Rotor Development: MD-900 Rotor with Smart Flaps, Ready for Flight Testing for Active Vibration Control (expects >80%)

Smart Structures: Enormous Potential to Minimize Vibration & Noise and improve performance

Smart Rotor Test in Glenn Martin Tunnel Mach-Scale with Smart Flaps

Eurocopter: Trailing Edge Flaps

trailing edge flaps

piezoelectric actuators

Flaps sized for vibration control
Must be scaled up for primary flight control

- BK 117 rotor blade with piezoactuated trailing edge flaps
- Successfully flight tested September 2006

Boeing: Trailing Edge Flaps

trailing edge flaps

MD900 rotor blade with piezoactuated trailing edge flaps
Successfully hover tested in May 2004
Successfully tested in 40x80 wind tunnel in April 2008

Flaps sized for vibration control
Must be scaled up for primary flight control

Tiltrotor Aircraft

Tiltrotor Dynamics Issues

- **Aeroelastic instabilities**
 - Rotor instabilities
 - Fixed-wing instabilities
 - Tiltrotor whirl flutter
- **Loads & Vibration**
 - Rotor-wing-body-tail interactional aerodynamics
 - Fountain effect
 - Gust loading
 - Tail buffeting
 - Conversion flight mode

Tiltrotor Aircraft

Past: Bell XV-15 flight tested successfully Whirl flutter stability and tail buffeting were major issues; Bell-Boeing V-22 fully operational and large descent speed a major concern (flight stability).

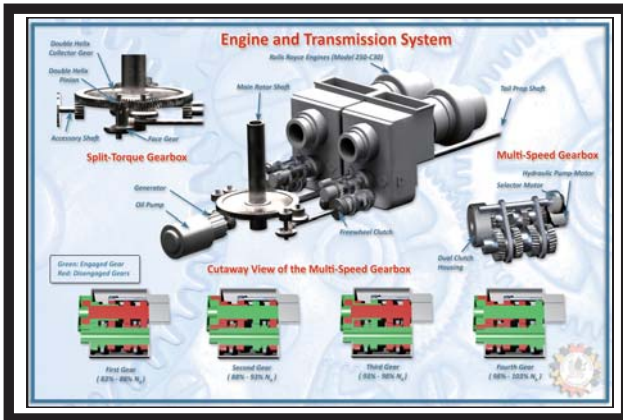
Present: Bell-Agusta 609 Civil tiltrotor under development, dynamics problems and performance.

Future: High speed heavy-lift tiltrotor with variable speed morphing rotor; and Quad-rotor

Challenges: Complexity and cost, variable speed engine, high speed dynamic instability

Challenges

- Whirl Flutter instability in high speed flight
- Interactional Aerodynamics Modeling
- Detailed Drive-shaft Dynamics
- Tail Buffeting
- Gust Response
- Detailed Hub and Gimbal Modeling
- Multi-rotor Wake Geometry



Conclusions

- ✓ 77% increase in payload delivery efficiency
- ✓ 22% increase in productivity
- ✓ Total cost of ownership over an assumed 20 year service life: \$18.6 million for *Griffin* - nearly a 5% savings over EC-145
- ✓ *Griffin's* performance meets, and in some cases exceeds, the requirements of the DARPA Mission Adaptive Rotor (MAR) Program

Aerodynamics and Dynamics of High Speed Coaxial Rotor Systems

Objective: Develop comprehensive aeromechanics analysis of coaxial rotor system.

Advantages: Compact size (lower foot print), no tail rotor, lower aerodynamic asymmetry in forward flight

Disadvantages: Aerodynamic interference between rotors, complex hub and swashplate (more drag), poor yaw control

Challenges: Limited aeromechanics analysis, aerodynamic interference, trim complexity, variable speed impact (power train, performance and rotor separation)

Future: Sikorsky has built X2 high speed coaxial rotor with proprotor to achieve 250 knots, Sikorsky is also building X2 crane as a heavy lifter. Coaxial UAVs possible.

Rotorcraft Brownout

Brownout: Loose dust, sand, snow, etc. blown up by rotor flow in ground effect (IGE) Cloud of visually restrictive material causes pilot to lose outside visual references and situational awareness. Significant number of accidents caused by brownout.

Objective: Develop comprehensive understanding and mitigation of "brownout" of rotorcraft

Challenges: Interdisciplinary phenomenon involving rotor wake near ground effect and sediment (dust) particle dynamics (particles mass, size and shape, and uplift process)

- highly unsteady 3-D "jet-like" flow
- Embedded vortices near the ground
- 2-Phase fluids with fluid particle and particle/particle collisions

Airforce-MURI: Rotorcraft Brownout: Advanced Understanding, Control, and Mitigation

Objective: Develop a design methodology that will capture physical mechanisms of potential mitigation solutions of rotorcraft brownouts

Team: UM (lead), Arizona State University, Iowa State, Dartmouth College 5 years program (2008-13)

Task-1	Fundamental of Rotor and Airframe Aerodynamics in Ground Effect Operations
Task-2	Fundamentals of Particle Suspension
Task-3	Brownout Synthesis Mitigation and Validation

Flight Dynamics and Stabilization with Suspended Loads in High-Speed Flight

Objective: Study aerodynamics, dynamics and flight stability of a suspended load in hover and forward flight, examine role of unsteady aerodynamics and nonlinearities.

Background & Challenges: In high speed, possibility of dynamic instabilities of suspended loads, but would increase radius of action and productivity index, predictions poor; unsteady aero of sling load important, aero nonlinear, stabilizing challenging, lock-in phenomenon of large amplitude motion

Technical Approach:

1. CFD based model of containers and bluff body
2. Develop transfer function type aerodynamic models
3. Develop dynamic model of rotorcraft with suspended load
4. Investigate trim, aeromechanical stability, handling qualities and dynamic loads
5. Suspended load model tests in GLM Tunnel and validations
6. Stabilization of suspended loads using static and active controls

Major Outcome: Increase speed of rotorcraft with suspended load, improve handling qualities and reduce pilot work load, increase load carrying productivity index

Rotorcraft Technology Needs

Technology Needs

- **High Performance Index**
 - Low airframe drag (exploit CFD)
 - Modular engine, high SFC
 - Variable speed transmission (exploit automotive technology)
- **Ultralight Structures**
 - Next generation composites
 - Multidisciplinary optimization
- **Mission Adaptive Rotors**
 - Active morphing for "quantum jump" in performance
 - Composite couplings for performance and loads
- **HUMS**
 - Beyond transmission & drivetrains (rotor head, servo failures, etc)

Technology Needs

- **Increased level of autonomy**
 - Collision avoidance
 - Embedded miniaturized sensors and transmitters
- **Green rotorcraft**
 - High SFC
 - Hybrid Engines
 - Re-cycling composite materials
 - All electric rotorcraft (swashplateless, hydraulicless)
- **Rapid Prototyping**
 - Numerical milling and rapid prototyping
- **Jet Smooth Rotorcraft**
 - Active controls using smart materials

Recommendations

- **For competitiveness of rotorcraft industry, seek new state-of-art production rotorcraft (not upgrades!!!).**
- **Nurture rotorcraft centers of excellence (not fragmentations!!!)**
- **Reward creativity and depth in research (let us not create a culture of milestones!!!!)**
- **Experimental facilities are key to methodology robustness, product refinements and revolutionary designs (let us not close wind tunnels!!!)**
- **Use creativity to reduce life cycle cost (real not fake!!)**
- **Discourage infeasible designs (too many paper studies!!!)**

Crossing the Dip?

- **Advances in aeromechanics appear poised for enormous potential in rotorcraft, especially towards the development of a mission adaptive rotor with a quantum leap in performance**

Wonderful World of Rotorcraft Aeromechanics



Research frontiers are expanding and moving up rapidly

- Rotor designs are tending towards low vibration and low noise rotors (jet-smooth goal)
- Performance (speed, endurance, range) improving
 - Variable rotational speed morphing rotor in future
- Increasing pay-load/gross weight fraction
- Cost: Manufacturing and maintenance costs going down
- Product reliability and survivability increasing
- Autonomy is increasing by leaps and bounds
- Future vehicles tending towards "Green"
 - Fuel efficiency, CO₂ emission and recycling material
- *How about all electric or hybrid helicopter?*

